

# **EFTF 1998**

**12th European Frequency and Time Forum**  
**12ème Forum Européen Fréquence et Temps**

10, 11, 12 March 1998  
**WARSZAWA, POLAND**

***PROCEEDINGS***

# 12th European Frequency and Time Forum

10, 11, 12 March 1998  
WARSAWA, POLAND

## *PROCEEDINGS*

Conference organizer and proceedings publisher:



Tele & Radio Research Institute  
*Piezoelectric Department*  
Ratuszowa 11  
03-450 Warszawa, Poland

For any further information about EFTF please contact the:

## Permanent EFTF Secretariat

either

### in Switzerland

#### FSRM

Swiss Foundation for Research  
in Microtechnology  
Rue Jaquet-Droz 1 / Case postale 20  
CH-2007 Neuchâtel, Switzerland

☎ +41 32 7 200 900

Fax : +41 32 7 200 990

e-mail : [eftf@fsrc.ch](mailto:eftf@fsrc.ch)

<http://www.fsrc.ch>

### in France

#### SFMC

Société Française des Microtechniques  
et de Chronométrie  
c/o LCEP/ENSMM  
26, Chemin de l'Épitaphe  
F-25030 Besançon Cedex, France

☎ +33 3 81 40 28 21

Fax : +33 3 81 88 57 14

e-mail : [isabelle.bourgon@ens2m.fr](mailto:isabelle.bourgon@ens2m.fr)

*Additional copies of these proceedings can be purchased  
from the:*

## Tele & Radio Research Institute

*Piezoelectric Department*

Ratuszowa 11

03-450 Warszawa, Poland

Tel./ Fax: + 48 22 619 64 60

E-mail: [wojcicki@itr.org.pl](mailto:wojcicki@itr.org.pl)

http: [//www.itr.org.pl/~b3](http://www.itr.org.pl/~b3)

*The organizer would like to thank the following institutions and companies for their sponsorship*

State Committee for Scientific Research

Ministry of Economy

Mayor of Warsaw



**TELEKOMUNIKACJA POLSKA S.A.**





## TABLE OF CONTENTS

Table of contents	V
◆ = abstract only	
Organization 1998 + Executive Committee	XVI
Scientific Committee	XVII

### Opening session

Radio astronomy an exciting international scientific endeavor (invited)	3
<i>A. Kus</i> , Centre for Astronomy, Nicolaus Copernicus University, Torun, Poland	
Past and present of piezoelectricity in Poland	9
<i>M. Wójcicki</i> , Tele & Radio Research Institute, Warsaw, Poland	

### Resonators I

1. Theory and design of piezoelectric resonators immune to acceleration: present state of the art (invited)	19
<i>J. A. Kosinski</i> , US Army Communications-Electronics Command, Fort Monmouth, USA	
2. Influence of the mounting structure on main performances of the BVA resonator	29
<i>J.J Boy, P. Maitre</i> , ENSMM/LCEP, Besançon, FRANCE	
<i>F. Deyzac</i> , ONERA, Chatillon, FRANCE,	
<i>R. Petit</i> , CELAR, Bruz, FRANCE	
3. The SC-cut lateral field quartz resonator working on anharmonic antisymmetric mode	34
<i>K. Weiss, W. Szulc</i> , Tele & Radio Research Institute, Warsaw, POLAND	
4. A comparative study of the idiosyncratic behaviors of 3 <sup>rd</sup> overtone and 5 <sup>th</sup> overtone precision quartz resonators ◆	39
<i>T. E. Wickard, G. L. Weaver</i> , PiezoCrystal Company, Carlisle Pa, USA	

### Optically pumped & cold atom Cs standards

1. Some properties of an optically pumped cesium beam tube depending on the microwave amplitude	43
<i>C. Audoin, F. Hamouda, L. Chassagne, R. Barillet</i> C.N.R.S. Laboratoire de l'Horloge Atomique, Orsay, FRANCE	
2. Estimation of the end to end phase shift without beam reversal in Cs beam frequency standards	49
<i>A. Makdissi, E. de Clereq</i> , BNM-LPTF, Observatoire de Paris, Paris, FRANCE	

- 3. The accuracy evaluation of the LPFT cesium fountain frequency standard at the  $10^{-15}$  level and future prospects** ♦ 54  
*S. Ghezali, Ph. Laurent, E. Simon, G. Santerelli, P. Lemonde, M. Bahoura, M. Santos, S. Bize, Y. Sortais, F. Pereira dos Santos, A. Clairon,*  
 BNM/LPTF, Observatoire de Paris, Paris, FRANCE,  
*L. Cognet,* IOTA-ESO Paris XI University, Orsay, FRANCE  
*K. Szymaniec,* University of Durham, UK

- 4. A simple configuration of clock using cold atoms** 55  
*Ch. Guillemot, P. Petit, S. Forget, C. Valentin, N. Dimarcq*  
 C.N.R.S., Laboratoire de l'Horloge Atomique, Orsay, FRANCE

## Materials

- 1. Langasite as a material for piezoelectric devices (invited)** 61  
*G. D. Mansfeld,* Russian Academy of Sciences, Moscow, RUSSIA

- 2. Defect centers in crystalline quartz by sweeping process** 66  
*M. Smaali\*\* , J.J. Boy\* , P. Zecchini\*\**  
 \*ENSMM / LCEP, BESANÇON - FRANCE  
 \*\*LCCM - UFR Sciences, BESANÇON - FRANCE

- 3. Sources of growth rate changes of quartz single crystals in the hydrothermal method** ♦ 71  
*W. Hofman,* Institute of Electronic Materials Technology, Warsaw, POLAND

- 4. Determination of high - order constants using the resonant and laser interferometry methods** 72  
*J. Nosek, L. Kretschmerova, P. Kretschmer*  
 Technical University of Liberec, Liberec, CZECH REPUBLIC

## Time transfer & comparisons I

- 1. GLONASS/GPS time transfer and the problem of the determination of receiver delays** 79  
*G. De Jong,* NMi Van Swiden Laboratorium, Delft, NETHERLANDS  
*W. Lewandowski,* Bureau International des Poids et Mesures, Sevres, FRANCE

- 2. A new approach to international time transfer: multi-channel and multi-code GPS+GLONASS common-view observations** 87  
*J. Azoubib, W. Lewandowski,* Bureau International des Poids et Mesures, Sevres, FRANCE  
*G. De Jong,* NMi Van Swiden Laboratorium, Delft, NETHERLANDS

- 3. GPS time transfer using geodetic receivers (GeTT): results of European baselines** 94  
*F. Overney, L. Prost, G. Dudle,* Federal Office of Metrology, Wabern, SWITZERLAND,  
*Th. Schildknecht, G. Beutler,* University of Bern, SWITZERLAND  
*J.A. Davis, J.M. Furlong,* National Physical Laboratory, Teddington UK,  
*P. Hetzel,* Physikalisch-Technische Bundesanstalt, Braunschweig, GERMANY

## Resonators II (Whispering Gallery Modes)

1. **New frequency-temperature compensation techniques for high-Q sapphire resonators** 103  
*M.E. Tobar, J.G. Harnett, A.G. Mann, E.N. Ivanov*, University of Western Australia, Nedlands, AUSTRALIA  
*J. Krupka*, University of Technology, Warsaw, POLAND
2. **Phase noise performances of cryogenic whispering gallery mode resonator frequency references** 108  
*O.Di Monaco, V. Giordano, J. Gros Lambert, I. Lajoie, Y. Kersalé*, LPMO/CNRS, Besançon, FRANCE
3. **Temperature compensated cryogenic whispering gallery mode resonator for microwave frequency standard applications** 112  
*L. Hao, W.J. Radcliffe, J.C. Gallop*, National Physical Laboratory, Teddington, UK  
*I.S. Ghosh, N. Klein*, Forschungszentrum Julich GmbH, Julich, GERMANY
4. **Whispering gallery mode microwave characterisation of Ba(MG<sub>1/3</sub>,Ta<sub>2/3</sub>)O<sub>3</sub> dielectric resonators** 115  
*R. Ratheesh<sup>a,b</sup>, M. T. Sebastian<sup>c</sup>, M.E. Tobar<sup>a</sup>, J. Harnett<sup>a</sup>, D.G. Blair<sup>a</sup>*  
<sup>a</sup>University of Western Australia, Nedlands, AUSTRALIA  
<sup>b</sup>Centre for Materials for Electronic Technology, Thrissur, INDIA  
<sup>c</sup>Regional Research Laboratory, Trivandrum, INDIA

## Classical Cs standards & H masers

1. **The SHM compact hydrogen maser for space applications report on the PEM physics package design verification** 121  
*A. Jornod, L.G. Bernier, H. Schweda, G. Busca*, Observatory of Neuchâtel, Neuchâtel, SWITZERLAND
2. **Influence of environmental factors on hydrogen maser frequency stability** 126  
*T. E. Parker*, National Institute of Standards and Technology, Boulder, U.S.A.
3. **Aging and environmental stability of Oscilloquartz CS-standards** 132  
*K. Kalliomäki*, University of Oulu, Oulu, FINLAND  
*T. Mansten, A. Rautiainen*, VTT Automation, VTT, FINLAND
4. **Extension of the second harmonic level monitoring in commercial cesium frequency standards** 134  
*K. Radecki*, Warsaw University of Technology, Warsaw, POLAND

## Oscillators I

1. **Nonlinear analysis of noise in quartz crystal oscillators** 141  
*R. Brendel, N. Ratier, L. Couteleau, G. Marianneau*, LPMO/CNRS, Besançon, FRANCE  
*P. Guillemot*, Centre National d'Etudes Spatiales, Toulouse, FRANCE

**2. OCXO spectrum analysis** 150  
*A. Masiukiewicz, B. Gniewinska*, Tele & Radio Research Institute, Warsaw, POLAND

**3. PSPICE simulation of a phase modulation noise measuring system of quartz crystal resonators** 155  
*F. Sthal, M. Mourey*, LCEP, Besançon, FRANCE

**4. Comparison of the output phase noise in an amplifier working in linear and nonlinear modes** 161  
*S. Galliou, R.J. Besson, M. Mourey*, ENSMM/LCEP, Besançon, FRANCE

## Time transfer & comparisons II

**1. The performance characteristics of a two-way time transfer earth station incorporating a new satre modem** 169  
*J. A. Davis, J. M. Furlong, J. D. Clarke*, National Physical Laboratory, Teddington, UK

**2. Delay stability of the TWSTFT earth station at VSL** 175  
*G. De Jong*, NMI Van Swiden Laboratorium, Delft, NETHERLANDS

**3. Tests with externally applied joint electronic and numerical control of commercial atomic clocks** 182  
*P. Eskelinen, O. Pyrhönen*, Lappeenranta University of Technology, Lappeenranta, FINLAND

## SAW I

**1. Optimization of broadband SAW transducers with polarity weighting** 189  
*E. V. Bausk*, Institute of Semiconductor Physics of RAS, Novosibirsk, RUSSIA  
*L. P. Solie*, SAWTEK Inc., Orlando, USA

**2. Comparison between theoretical and experimental properties of SAW on Z-cut of langasite** 193  
*E. Henry Briot, E. Bigler, S. Ballandras, G. Marianneau, G. Martin*, LPMO/CNRS, Besançon, FRANCE  
*M. Solal*, Thomson Microsonics, Sophia Antipolis, FRANCE

**3. Design of SAW resonators on ST cut quartz** 198  
*W. Soluch*, Institute of Electronic Materials Technology, Warsaw, POLAND

## Instrumentation & Measurement I

**1. Clock prediction uncertainty** 205  
*A. Lepek*, Newton Metrology Ltd., Jerusalem, ISRAEL

**2. Noise characterisation of irregularly spaced data** 209  
*P. Tavella*, Istituto Elettrotecnico Nazionale "G. Ferraris", Torino, ITALY  
*M. Leonardi*, Politecnico di Torino, Torino, ITALY

**3. The high gain phase comparator for reduction of close-to-carrier phase noise** 215  
*M. J. Underhill*, University of Surrey, Guildford, UK

**4. Estimation of the measurement uncertainty of drift coefficient versus the noise levels** 222  
*F. Vernotte, M. Vincent*, Observatoire de Besançon, Besançon, FRANCE

## Oscillators II

**1. Long term stability of high quality OCXOs** 231  
*J. Mannermaa*, Nokia Mobile Phones, Tampere, FINLAND  
*K. Kalliomäki*, University of Oulu, Oulu, FINLAND  
*T. Mansten*, VTT Automation, VTT, FINLAND

**2. Quartz crystal oscillator with an effective aging rate compensation** 234  
*Y. S. Shmaliy, A.Ph. Kurotchka, E.G. Sokolinskiy*, "Sichron" Center, Kharkiv, UKRAINE  
*A.V. Marienko*, St. Co. "IRVA", Kyiv, UKRAINE

**3. Oscillator selection to support CDMA holdover requirements** 240  
*W. Weidemann*, Datum Inc., Irvine CA, USA

**4. An ultra-low thermal sensitivity in the microwave synthesis for high performance frequency standards** 246  
*R Barillet*, C.N.R.S. Laboratoire de l'Horloge Atomique, Orsay, FRANCE

## Telecom & space applications

**1. Robust estimation of TDEV** 253  
*A. Dobrogowski, M. Jessa, M. Kasznia*,  
Poznan University of Technology, Poznan, POLAND

**2. Reference signal management in WDM networks** 258  
*M. Kihara, K. Hisadome*  
NTT Optical Network Systems Laboratories, Kanagawa, JAPAN

**3. Additive time synchronous system in existing SDH networks** 263  
*Y. Serizawa, K. Kitamura, M. Myoujin*, Central Research Institute of Electric Power Industry, Tokyo, JAPAN  
*T. Matsushima, O. Masui, R. Takada*, NEC Corporation, Tokyo, JAPAN

**4. Doppler wind experiment - first test results from space** 269  
*R. Kohl, K. Wagner*, Dornier Satellitensysteme GmbH, MCnchen, GERMANY  
*M. Bird, R. Dutta-Roy*, Universität Bonn, Bonn, GERMANY

## Instrumentation & measurement II

**1. Different approaches for ns-class delay lines** 275  
*J. Vainikka*, Lappeenranta University of Technology, Lappeenranta, FINLAND

- 2. Aspects of calibration of a six-port circuit for precise measurements of piezoelectric resonators parameters** **280**  
*A. Lisowiec, M. Wojcicki*, Tele & Radio Research Institute, Warsaw, POLAND
- 3. VHF and microwave interferometric PM and AM noise measurements** **286**  
*E. Rubiola*, Politecnico di Torino, Torino, ITALY,  
*V. Giordano, J. Gros Lambert*, LPMO/CNRS, Besançon, FRANCE
- 4. The Anti Jitter Circuit for low spurious DDS square waves and low cost fractional-n synthesis** **292**  
*M. J. Underhill, S. Stavrou, M. Blewett*, University of Surrey, Guildford, UK  
*N. Downie*, Maran & Co., Guildford, UK

## Laser instrumentation & optical standards

- 1. Characterization of the sub-Doppler modulation transfer spectroscopy at 612 nm** **301**  
*E. Bava, G. Galzerano*, Politecnico di Milano, Milano, ITALY  
*F. Bertinetto, M. Bisi, D. Magoga, P. Miglietta*, Istituto di Metrologia Gustavo Colonnetti, Torino, ITALY
- 2. The phase-locking scheme for the OPO frequency chain by using optical frequency comb generator** **305**  
*S. Slyusarev, T. Ikegami*,  
 National Research Laboratory of Metrology, Ibaraki-ken, JAPAN
- 3. Absolute frequency stabilization of erbium microlasers to C<sub>2</sub>H<sub>2</sub> and <sup>13</sup>C<sub>2</sub>H<sub>2</sub> in the 1530-1550 nm wavelength interval** **308**  
*C. Svelto, S. Taccheo, P. Laporta, E. Bava*, Politecnico di Milano, Milano, ITALY
- 4. A potassium vapor magnetometer optically pumped by a diode laser** **312**  
*N. Beverini<sup>a, b</sup>, E. Alzetta<sup>a</sup>, C. Carmisciano<sup>b</sup>, O. Faggioni<sup>b</sup>, F. Francesconi<sup>a</sup>, E. Maccioni<sup>a</sup>*  
<sup>a</sup>Universita di Pisa, Pisa, ITALY  
<sup>b</sup>Consorzio Universitario della Spezia, La Spezia, ITALY

## SAW II

- 1. Temperature sensitivity of Surface Transverse Wave resonators built using different combinations of grooves and strips** **319**  
*S. Ballandras, W. Daniau, E. Bigler, G. Martin, G. Marianneau*  
 LPMO/CNRS, Besançon, FRANCE
- 2. Theoretical analysis of a reciprocal BAW to SAW coupler** **326**  
*B. Dulmet, H. Watchueng*, ENSMM/LCEP, Besançon, FRANCE
- 3. GHz range STW resonators on quartz and langasite** **332**  
*A. V. Grouzdev, S. I. Kort, I. S. Mitrofanov, A. V. Perevalov*,  
 "Avangard-Elionica", St.Petersburg, RUSSIA  
*S. Gawor, A. Milewski*, Tele & Radio Research Institute, Warsaw, POLAND

## Piezoelectricity & measurement techniques (posters)

- 1. Improvements of X-ray orientation determination methods applicable in quartz oscillator industry** 339  
*H. Berger*, EFG International, Berlin, GERMANY
  
- 2. Ultra stable oscillators** 345  
*W. Candelier, J. Chauvin, C. Gelle, G. Marotel*, CEPE, Argenteuil, FRANCE,  
*M. Brunet*, CNES, Toulouse, FRANCE,  
*R. Petit*, CELAR, Bruz, FRANCE
  
- 3. Nonlinearly generated 1/f frequency noise in modelockings** 352  
*S. Dos Santos, F. Lardet-Vieudrin, M. Planat*, LPMO/CNRS, Besançon, FRANCE
  
- 4. A new 5 MHz mini-BVA OCXO** 358  
*G. Robichon*, bva INDUSTRIE S.A., Besançon. FRANCE
  
- 5. New thermal transient model of crystal resonator of thickness-shear vibrations** 362  
*Y. S. Shmaliy*, "Sichron" Center, Kharkiv, UKRAINE
  
- 6. Calculation and measurement of anharmonic vibration modes in SC-cut quartz resonators** 368  
*K. Weiss*, Tele & Radio Research Institute, Warsaw, POLAND  
*I. Mateescu, G. Pop, A. Ch. Ghita*, National Institute of Materials Physics, Bucharest-Magurele, ROMANIA
  
- 7. Simulation of pierce oscillators with digital inverters using the negative resistance model** 374  
*D. Gohring, J. Haffelder*, TELE QUARZ GROUP, Neckarbischofsheim, GERMANY
  
- 8. OCXO oscillator with direct temperature measurement of quartz vibrator** 379  
*A. Smolarski, W. Szulc, B. Gniewinska, K. Weiss, A. Masiukiewicz, B. Kalinowska*  
Tele & Radio Research Institute, Warsaw, POLAND
  
- 9. Studies of crystal oscillator with output signal controlled phase** 384  
*A. S. Vasilenko, Y. S. Shmaliy*, "Sichron" Center, Kharkiv, UKRAINE
  
- 10. Random walk and first crossing times: applications in metrology** 388  
*L. Di Piro, E. Perone*, Universita di Torino, Torino, ITALY  
*P. Tavella*, Istituto Elettronico Nazionale G. Ferraris, Torino, ITALY
  
- 11. About the radiofrequency spectrum of a phase noise modulated carrier** 392  
*A. Godone, F. Levi*, Istituto Elettrotecnico Nazionale "G. Ferraris", Torino, ITALY
  
- 12. New approach to long term frequency stability measurement data analysis** 397  
*B. Kalinowska, B. Gniewinska*, Tele & Radio Research Institute, Warsaw, POLAND

<b>13. The arithmetic of frequency mixings in an electronical loop</b>	<b>402</b>
<i>M. Planat, S. Dos Santos</i> , LPMO, Besançon, FRANCE	
<b>14. Microwave synthesizer</b>	<b>408</b>
<i>W. Wojtasiak, T. Morawski, D. Gryglewski, R. Michnowski</i> Warsaw University of Technology, Warsaw, POLAND	
<b>15. Two detection axis vibrating gyroscope structure intended for navigation</b>	<b>414</b>
<i>Y. Ansel, P. Lerch, P. Renaud</i> , Institute of Microsystem, Lausanne, SWITZERLAND	
<b>16. Two classes of transitional filter transfer functions applied in crystal filter designing</b>	<b>420</b>
<i>S. Dedic-Nesic</i> , Institute "Mihajlo Pupin", Belgrade, YUGOSLAVIA	
<b>17. Comparison of TE<sub>01n</sub> and whispering gallery modes for dielectric resonator frequency standards</b>	<b>425</b>
<i>L. Hao, J. Gallop</i> , National Physical Laboratory, Teddington, UK <i>N. Klein</i> , KFA, Julich, GERMANY	
<b>18. Quartz-crystal tuning-fork tactile sensor</b>	<b>430</b>
<i>H. Itoh, M. Nomura, M. Nakazawa</i> , Shinshu University, Wakasato, JAPAN	
<b>19. The SAW acceleration sensor</b>	<b>434</b>
<i>J. Filipiak, C. Kopycki, J. Ostrowski, L. Solarz</i> Military University of Technology, Warsaw, POLAND	
<b>20. Investigations on behaviour of coupling coefficient of monolithic structure</b>	<b>438</b>
<i>I. Mateescu, G. Pop, A. Manea, M. Lazarescu, C. Ghita</i> National Institute of Materials Physics, Bucharest-Magurele, ROMANIA	
<b>21. Experimental verification of non-linear drive level dependence of the resonant frequency in BAW quartz resonators</b>	<b>443</b>
<i>J. Nosek</i> , Technical University of Liberec, Liberec, CZECH REPUBLIC	
<b>22. Temperature dependence and compensation of GaPO<sub>4</sub> thickness resonators</b>	<b>447</b>
<i>C. Reiter</i> , AVL List GmbH + Technical University Graz, Graz, AUSTRIA <i>H. Thanner</i> , AVL List GmbH + University of Graz, Graz, AUSTRIA <i>W. Wallnöfer, P.W. Krempl</i> , AVL List GmbH, Graz, AUSTRIA	
<b>23. A new miniature quartz Y+5 temperature sensor</b>	<b>451</b>
<i>K. Weiss, W. Szulc, E. Zuchowski, M. Tupaj</i> , Tele & Radio Research Institute, Warsaw, POLAND <i>B. Dulmet</i> , ENSMM/LCEP, Besançon, FRANCE	
<b>24. One-port SAW resonator using series connected IDTs and its application</b>	<b>457</b>
<i>T. Kojima, N. Kawai</i> , Tamagawa University, Tokyo, JAPAN	
<b>25. SAW conversion in chirp pulse expanders and compressors</b>	<b>463</b>
<i>V.F. Dmitriev, I.S. Mitrofanov</i> , "Avangard-Elionica", St.Petersburg, RUSSIA	

- 26. Influence of dispersive delay lines matching networks  
on compressed signal parameters** 469  
*W. Niemyjski*, Telecommunications Research Institute, Warsaw, POLAND  
*S. Gawor*, Tele & Radio Research Institute, Warsaw, POLAND

- 27. Surface mount hybrid SAW modules for mobile transceivers** 472  
*S. A. Dobershtein, A.V. Martynov, V.A. Malyukhov*, ONIIP, Omsk, RUSSIA

- 28. Improvement of SAW filter parameters by the application  
of a single-electrode interdigital transducer** 477  
*P. Nagłowski, Dabrowska*, Institute of Electronic Materials Technology, Warsaw, POLAND

## **T/F techniques & atomic standards**

(posters)

- 1. Very low aging rate  $^{87}\text{Rb}$  frequency standard** 483  
*D. Taiqian, L. Shuqin*, Peking University, Department of Electronics, CHINA

- 2. The modification of a HP 105B frequency standard and its use  
as a portable frequency reference** 484  
*K. Kalliomaki*, University of Oulu, Oulu, FINLAND  
*T. Mansten*, VTT Automation, VTT, FINLAND

- 3. Polarization gradient cooling effect in the outer potential field** 487  
*M. Kajita, K. Fukuda, T. Morikava*, Communications Research Laboratory, Tokyo, JAPAN

- 4. RFH 100 a ruggedized time & frequency system for navy** 493  
*J.F. Schuh, B. Cailliez, H. Belivier*, MORS - Défense, Le Puy Sainte Réparate, FRANCE

- 5. Use of a dual-frequency multi-channel geodetic GPS receiver  
for the estimation of ionospheric delays applied to accurate time transfer** 499  
*K. Jaldehag*, Swedish National Testing and Research Institute, Boras, SWEDEN  
*C. Thomas, J. Azoubib*, Bureau International des Poids et Mesures, Sèvres, FRANCE

- 6. The local restitution of GPS time at Shanghai Observatory** 505  
*H. Jinlun, H. Peicheng*, Shanghai Observatory, Shanghai, CHINA

- 7. GPS multi-channel common-view time transfer using Motorola Oncore  
receiver with CCDS standards** 510  
*J. Nawrocki*, Astrogeodynamical Observatory, Borowiec, POLAND  
*W. Lewandowski, J. Azoubib*, Bureau International des Poids et Mesures, Sevres, FRANCE

- 8. Real time access to international time scale using GPS** 516  
*A. Niculescu*, National Institute of Metrology, Bucharest, ROMANIA

- 9. Low-cost time synchronisation and tagging using satellite  
TV teletext broadcasts** 519  
*J.J. Lennon, J.J. O'Riordan, C.T. O'Sullivan, P.W. Twomey, P.J. Murphy*  
University College, Cork, IRELAND

<b>10. Time and frequency standard of GUM and activities toward its improvement</b>	<b>525</b>
<i>J. Siemicki</i> , Central Office of Measures, Warsaw, POLAND	
<b>11. On line uniformity optimization of the high C-field magnet in the Politecnico cesium beam standard</b>	<b>531</b>
<i>G. A. Costanzo, M. Siccardi, A. De Marchi</i> , Politecnico di Torino, Torino, ITALY	
<i>V. Barychev</i> , VNIIFTRI, Mendeleevo, RUSSIA	
<b>12. Atomic fountain development at U.S.N.O.</b>	<b>534</b>
<i>Ch. R. Ekstrom, E. A. Burt</i>	
United States Naval Observatory, Washington, U.S.A.	
<b>13. GPS disciplined oscillators as 'internationally' traceable time and frequency reference</b>	<b>538</b>
<i>C. Green</i> , Quartzlock UK Ltd., Gothic, UK	
<b>14. HORACE: a new advance for compact clocks with cold atoms ♦</b>	<b>543</b>
<i>E. Guillot, P. Petit, C. Valentin, N. Dimarcq</i>	
C.N.R.S. Laboratoire de l'Horloge Atomique, Orsay, FRANCE	
<b>15. Progress of the PTB caesium fountain frequency standard</b>	<b>544</b>
<i>U. Hübner, S. Weyers, D. Griebisch, R. Schröder, C. Tamm, A. Bauch</i>	
Physikalisch-Technische Bundesanstalt, Braunschweig, GERMANY	
<i>J. Castellanos</i> , CENAM, Queretaro, MEXICO	
<b>16. Advances in modular time &amp; frequency system design incorporating powerful status &amp; alarm management &amp; GPS corrected caesium technology</b>	<b>548</b>
<i>D. F. Wright, N. C. Helsby, M. R. Sagin</i> , Radiocode Clocks Ltd., Helston, UK	
<i>G. H. Smith</i> , Brandywine Communications Inc., Costa Mesa, USA	
<b>17. A versatile PC controlled servo-system for high performance optically pumped cesium beam frequency standard</b>	<b>553</b>
<i>F. Hamouda, R. Barillet, P. Cerez</i> ,	
C.N.R.S. Laboratoire de l'Horloge Atomique, Orsay, FRANCE	
<b>18. Progress at CENAM toward the construction of a short cesium beam optically pumped frequency standard</b>	<b>557</b>
<i>J. M. López-Romero, F. Garcia-Nava, J.M. Figueroa-Estrada</i> , Centro Nacional de Metrologia, Querétaro, MÉXICO	
<i>D.A. Jennings</i> , National Institute of Standards and Technology, Boulder, USA	
<b>19. An experiment in frequency proficiency testing</b>	<b>560</b>
<i>H.T. Lin, C.S. Liao</i> , Chunghwa Telecom Co. Ltd., Taoyuan, TAIWAN	
<b>20. GLONASS frequency and time signals monitoring network</b>	<b>566</b>
<i>Y. Smirnov, M. Medvedev, N. Shienok</i>	
Coordination Scientific Information Center, Moscow, RUSSIA	

<b>21. GLONASS as instrument for precise UTC transfer</b>	<b>570</b>
<i>M. Lebedev</i> , Coordination Scientific Information Center, Moscow, RUSSIA	
<b>22. Work towards a cesium fountain standard at Peking University</b>	<b>574</b>
<i>Y. Wang, J. Hou, Y. Li, J. Fu, X. Wang, X. Chen, D. Yang</i> , Peking University, CHINA	
<b>Meeting report</b>	<b>576</b>
<b>List of the participants</b>	<b>578</b>
<b>List of the exhibitors</b>	<b>590</b>
<b>Index of the authors</b>	<b>591</b>

## **EFTF Local Organization**

Tele & Radio Research Institute, Warsaw, POLAND

*Marek Wójcicki* - Chairman

*Andrzej Czarnecki*

*Barbara Gniewińska*

*Antoni Masiukiewicz*

*Aleksander Lisowiec*

*Tadeusz Szustka*

*Marek Świdorski*

*Krzysztof Weiss*

## **Technical Programme Chairman**

*Waldemar Soluch*

Institute of Electronic Materials Technology, Warsaw, POLAND

## **Executive Committee**

*Claude Audoin*

Laboratoire de l'Horloge atomique, CNRS - Orsay - FRANCE

*Raymond J. Besson*

Laboratoire de Chronométrie, Electronique et Piézoélectricité de l'Ecole nationale Supérieure de Mécanique et des Microtechniques  
Besançon – FRANCE

*Marcel Ecabert*

Fondation Suisse pour la Recherche en Microtechnique, FSRM -  
Neuchâtel – SWITZERLAND

*Jean-Jacques Gagnepain*

Département Sciences pour l'ingénieur, CNRS – Paris - FRANCE

*Peter Kartaschoff*

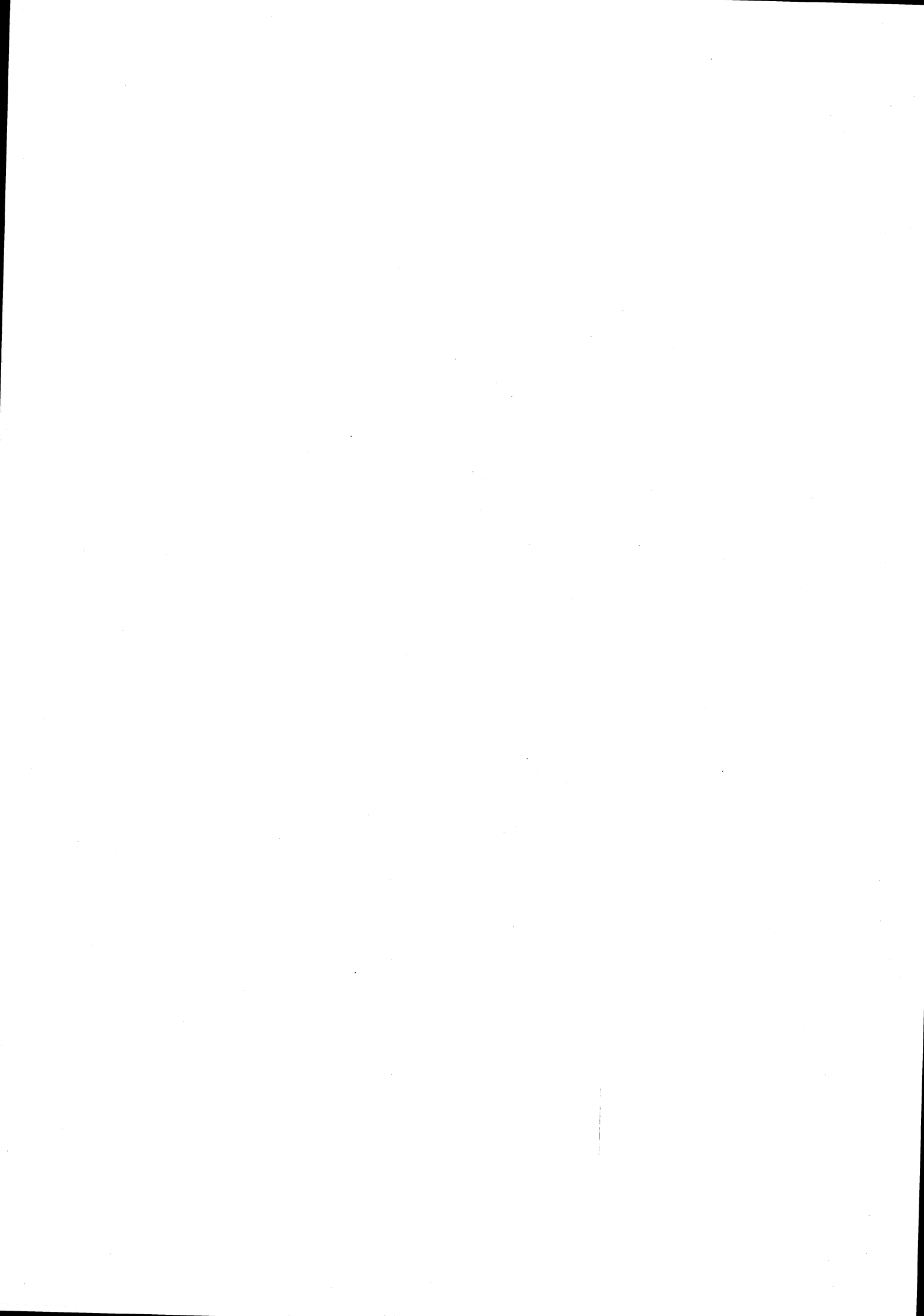
Retired from Section Recherche et Développement de la Direction  
Générale des PTT – Bern – SWITZERLAND

*Bernard Schlueter*

Rue des Mésanges 7  
25130 Villers-Le-Lac - FRANCE

SCIENTIFIC COMMITTEE

<b>Soluch</b>	<b>Waldemar</b>	<i>Institute of Electronic Materials Technology, Warsaw, Chairman 1998</i>	<b>POLAND</b>
<b>Aubry</b>	<b>Jean - Pierre</b>	Oscilloquartz SA, Neuchâtel	SWITZERLAND
<b>Audoin</b>	<b>Claude</b>	CNRS / LHA, Université Paris Sud, Orsay	FRANCE
<b>Ballato</b>	<b>Arthur</b>	US Army Research Laboratory, Fort Monmouth	USA
<b>Bauch</b>	<b>Andreas</b>	Physikalisch-Technische Bundesanstalt, Braunschweig	GERMANY
<b>Besson</b>	<b>Raymond J.</b>	L C E P / E N S M M, Besançon	FRANCE
<b>Bolox</b>	<b>Rafael</b>	Real Instituto y Observatorio de la Armada, San Fernando, Cadiz	SPAIN
<b>Brunet</b>	<b>Michel</b>	CNES, Toulouse	FRANCE
<b>Busca</b>	<b>Giovanni</b>	Observatoire Cantonal, Neuchâtel	SWITZERLAND
<b>Cutler</b>	<b>Leonard</b>	Hewlett Packard Laboratories, Palo Alto	USA
<b>De Jong</b>	<b>Gerrit</b>	NMi Van Swiden Laboratorium, Delft	THE NETHERLANDS
<b>De Marchi</b>	<b>Andrea</b>	Politecnico di Torino, Torino	ITALY
<b>Defranould</b>	<b>Philippe</b>	Thomson-Microsonics, Sophia Antipolis	FRANCE
<b>Deyzac</b>	<b>François</b>	ONERA, Châtillon sous Bagneux	FRANCE
<b>Dorenwendt</b>	<b>Klaus</b>	Physikalisch-Technische Bundesanstalt, Braunschweig	GERMANY
<b>Dowsett</b>	<b>John</b>	London	UNITED KINGDOM
<b>Duchaussoy</b>	<b>Hugues</b>	DRET, Paris Armées	FRANCE
<b>Eskelinen</b>	<b>Pekka</b>	Lappeenranta University of Technology, Lappeenranta	FINLAND
<b>Feltham</b>	<b>Steeve</b>	European Space Agency ESTEC, Noordwijk	THE NETHERLANDS
<b>Godone</b>	<b>Aldo</b>	Instituto Elettronico Nazionale "Galileo Ferraris", Torino	ITALY
<b>Graf</b>	<b>Erhard</b>	Bevaix	SWITZERLAND
<b>Granveaud</b>	<b>Michel</b>	LPTF - Observatoire de Paris, Paris	FRANCE
<b>Hartl</b>	<b>Philipp</b>	Universität Stuttgart, Stuttgart	GERMANY
<b>Hauden</b>	<b>Daniel</b>	C N R S / L P M O, Besançon	FRANCE
<b>Heighway</b>	<b>James</b>	Goulens	FRANCE
<b>Hilty</b>	<b>Kurt</b>	SWISSCOM, Bern	SWITZERLAND
<b>Hruska</b>	<b>Carl K.</b>	York University, North York	CANADA
<b>Kalliomäki</b>	<b>Kalevi</b>	University of Oulu, Oulu	FINLAND
<b>Kartaschoff</b>	<b>Peter</b>	Cormondréche	SWITZERLAND
<b>Kihara</b>	<b>Masami</b>	NTT Optical Network Systems Laboratories, Kanagawa	JAPAN
<b>Kirchner</b>	<b>Dieter</b>	Technische Universität Graz, Graz	AUSTRIA
<b>Krempf</b>	<b>Peter W.</b>	AVL List GmbH, Graz	AUSTRIA
<b>Leschiutta</b>	<b>Sigfrido</b>	Politecnico di Torino, Torino	ITALY
<b>Nakagiri</b>	<b>Koji</b>	Kinki University, Nishi-Mitani	JAPAN
<b>Nau</b>	<b>Hartmut</b>	DRL, Wessling	GERMANY
<b>Neubig</b>	<b>Bernd W.</b>	Tele Quarz GmbH, Neckarbischofsheim	GERMANY
<b>Prost</b>	<b>Léon</b>	Office Fédéral de Métrologie, Wabern	SWITZERLAND
<b>Quinn</b>	<b>T.J.</b>	Bureau International des Poids et Mesures, Sèvres	FRANCE
<b>Reid</b>	<b>Andy</b>	British Telecom, London	UNITED KINGDOM
<b>Schlüter</b>	<b>Wolfgang</b>	Institut für Angewandte Geodäsie, Kötzing	GERMANY
<b>Steele</b>	<b>James Mc A.</b>	National Physical Laboratory, Teddington	UNITED KINGDOM
<b>Thomann</b>	<b>Pierre</b>	Observatoire Cantonal, Neuchâtel	SWITZERLAND
<b>Uljanov</b>	<b>Adolph A.</b>	Kvarz Institute of Electronic Measurements, Nizhny Novgorod	RUSSIA
<b>Underhill</b>	<b>M.J.</b>	University of Surrey, Guildford	UNITED KINGDOM
<b>Unverdross</b>	<b>Rainer</b>	Unverdross Technik, Wörthsee	GERMANY
<b>Vanier</b>	<b>Jacques</b>	Ste-Foie, Quebec	CANADA
<b>Walls</b>	<b>Fred L.</b>	National Institute of Standards and Technology, Boulder	USA
<b>Winkler</b>	<b>Gernot M. R.</b>	Innovative Solutions International, Vienna	USA
<b>Yannoni</b>	<b>Nicholas</b>	Newton, MA	USA
<b>Zampetti</b>	<b>George</b>	Telecom Solutions, San Jose	USA
<b>Zingg</b>	<b>Walter</b>	Micronas, Bevaix	SWITZERLAND



*12th E F T F* - 10÷12 March 1998 - Warsaw - POLAND

**Opening session**

Chairman:

*Waldemar Soluch*



## RADIO ASTRONOMY AN EXCITING INTERNATIONAL SCIENTIFIC ENDEAVOUR

*Andrzej J. Kus*

Centre for Astronomy,  
Department of Radio Astronomy,  
Nicolaus Copernicus University,  
Gagarina 11, 87-100 Torun, Poland

### SUMMARY

From the earliest times understanding the Universe has been the greatest challenge to mankind. Our present knowledge about nature was gathered laboriously over a very long period of human activity in many areas of fundamental research. Astronomy, one of them, which by definition studies the Universe, belongs to the oldest of the sciences; still, the actual scientific activity in this field is remarkably high. New branches of astronomy emerged in this century. Radio astronomy, one of the most advanced at the present time, allows us to study the universe in the radio domain.

In this presentation the development of tools for radio astronomy over the last decades in connection with progress in fields of applied research was briefly reviewed. Modern radio telescopes and various specialised auxiliary equipment for signal processing and image reconstruction were generally described. Research in astronomy puts up the highest demands on modern technology and thus indirectly accelerates commercial applications

International activities, present and future projects of radio astronomy, among them VLBI - Very Long Baseline Interferometry, VLBI Space Observatory Programme, Square Kilometre Radio Telescope and others were given special attention. Areas of common interest for radio astronomers and electronics engineers as well as the dependence on frequency and time standards were pointed out.

The impact of recent discoveries on our understanding of mankind's place in the Universe is a particularly attractive area and is often explored in public debates. A brief review of the most recent results was given.

Finally, global relations and worries about the use of radio wave bands, demands for higher quality commercial electronics, and possible solutions on protection of the environment around world radio observatories were described. The action to preserve part of the radio spectrum for the passive use of radio astronomy is high priority and has international support under the umbrella of OECD, URSI and IAU.

### INTRODUCTION

For all of us the Universe is an open and infinite laboratory to study the extreme, the exotic and the unknown. Investigations at different wavelengths of

electromagnetic waves reveal the diverse, rich and inter-related nature of cosmic matter. Gamma-rays and X-rays show the presence of extremely energetic activities, occurring close to high density matter such as massive black holes or pulsars. Light in the visible range of wavelengths provides us with information on "normal" stars and the interstellar medium. Radio waves inform us about high energy plasma and magneto-hydrodynamic phenomena. The whole spectrum of electromagnetic waves gives us complementary information on various objects, starting from those located inside the Solar System through those in the Galaxy up to the entire Universe.

The study of the Universe brings us near the answer (or at least leads to the better formulation of) the fundamental questions:

What is the universe? How did it start, will it end? Is there any purpose in it? How did life originate? Are we alone? What is the role of intelligent life? Such unsolvable problems stimulate our imagination and have always been the source of rich inspiration for art and for science.

Astronomy has yet another dimension. The expanding nature of modern man creates new challenges, this time on much bigger scale - the colonisation of nearby planets and space. At the moment this remains a future dream but will one day emerge as reality.

### TIME

In the past times, practical considerations were the prime reasons for studying astronomy (time, calendar, astrology). The main task - time measurement - was to combine the natural periodic rhythms like a year or day/night with well defined objective and useful shorter units. Obviously our clocks have to be synchronized with the natural basic rhythms observed in nature. In fact we have too many such constraints to meet all the requirements. The rhythms can be astronomical: (year, month, week, day/night), solar rotation and solar activity; geophysical: ionosphere electromagnetic resonance frequencies and biological: heart beat, brain waves. None of these can serve as a fundamental frequency standard. Increased accuracy of time measurements has shown higher order instabilities which are due to complex nature of the Earth's rotation and orbital period.

The simplest clocks, like Sun dials, are the oldest among time keeping devices. Still being used for fun, however, they have given only quantitative measure of the flow of time. Frequency stable sources are the basic elements which run clocks. There were various approaches. The early clocks were based on a steady rate of fluid flow - water and sand clocks, latter on a mechanical oscillations - pendulum or spring driven balance and finally in modern time on the piezoelectric and atomic oscillations. Practical applications were again the driving force for the development of accurate and reliable time keeping devices.

The precision of early epoch time keeping systems was sufficient until the need for the navigation of ships put up new, higher demands. A combination of classical astronomical measurements and the precise time keeping allowed the location of a ship to within few nautical miles in XIX century. Today, GPS satellites give an accuracy very often higher than the size of the navigated object itself. This remarkable achievement is possible thanks to the use of atomic frequency standards, knowledge of earth rotation, and satellite orbit prediction.

Time keeping systems seem to be complicated as there is a need for combining the astronomical second (variable length) and the atomic second. Historical baggage left us with quite complex definitions and relations. Just to remind you I list below the basic definitions of the time systems, which were actually used: LAST - local apparent solar time, LMST - local mean solar time, GMST - Greenwich Mean Solar Time, UT - Universal Time, LST - local sidereal time, GST - Greenwich Sidereal Time, UT0 - UT as observed, UT1 - UT0 minus polar motion correction, UT2 - UT1 minus periodic earth rotation terms, ET - ephemeris time, AT, A.I, TAI - atomic time, TDT - terrestrial dynamic time, TDB - barycentric dynamical time, UTC - Coordinated Universal Time.

All the above listed systems are being used in various astronomical applications and research. Of course we would like to have the standard which could give us the "absolute" reference but we all well know that time and its measurement is relative and thus relativistic effects play significant role in high precision time measurements. The development of today's astronomy strongly depends on the quality and reliability of atomic standards. In particular, radio astronomy has a high interest in progressing the field being discussed at this conference.

## **RADIO ASTRONOMY**

Radio astronomy had its beginnings in the experiments of Karl Jansky in 1931. Since then it has been the best example of enormous progress resulting from technological development of our era. The need for high angular resolution and sensitivity, obvious in the pioneers' time, remains an open challenge. Over the last four decades entirely new observing

techniques and sophisticated data analysis methods were developed. The use of these methods provided astronomers with results which dramatically changed our understanding of the Universe. Even though radio waves are a million times longer than optical waves, the angular resolution obtained now is three orders of magnitude higher than that of the largest optical telescopes. The sensitivity of our radio telescopes enables the study of the most distant objects in the visible Universe.

Many recent discoveries made in the radio domain have received the highest international recognition. The detection of relic microwave background emission - the afterglow of the Big Bang, the discovery of pulsars, observational tests of general relativity, and the development of aperture synthesis techniques are just examples of subjects awarded the Nobel Prize.

Research in astronomy has always been limited by instrumental problems. The struggle for increased sensitivity, higher angular resolution and higher dynamic range is a continuous problem of observational radio astronomy.

Single dish limitations result from the finite physical size of the aperture. The diffraction limit defines the angular resolution. For the presently used large single telescopes it varies between few degrees to about 10 arc sec depending on the frequency used. Sensitivity is defined by the effective collecting area, the noise of receiver and the interference level.

Among others, the limited instantaneous field of view of present telescopes is a particular problem. High angular resolution results in more pixels per unit area of sky which then takes correspondingly longer to image. Multi-beam systems go some way towards reducing the problem. Paradoxically enough, we can get more detailed information from smaller and smaller areas when we enlarge the aperture to gain sensitivity. Time resolution is also an important limitation in certain applications, in particular in the study of pulsars.

Frequency resolution and the instantaneous available bandwidth, the recording and data handling methods, are all "back-end" related subjects. Sensitivity to rapid bursts of sporadic emission and ways to distinguish these from man-made interference should also become a common feature of future telescopes.

A dramatic improvement of angular resolution has been achieved by the use of radio interferometry. The technique was developed in parallel at Cambridge University and Sidney University. In the mid sixties the angular resolution of interferometers, which is defined by the distance between its elements, broke the 1 arc minute limit of the naked eye. This technique allows very accurate position measurements and thus leads to the optical identifications of many discrete radio sources of unknown nature. It has also proven to be less sensitive to local radio interference.

The major further step was made by the genius idea of aperture synthesis. This new technique was developed at the MRAO Cambridge University by Sir Martin Ryle and his co-workers. Today it remains as the most powerful method of modern radio astronomy. The major world radio telescopes operate under this principle. VLA in the USA, MERLIN in the UK, GMRT in India and VLBI (Very Long Baseline Interferometry) - the global array of radio telescopes, all are the aperture synthesis instruments. These instruments have a diffraction equivalent aperture ranging from about 30 km up to continental and global sizes. The resulting angular resolution of radio images reconstructed from the gathered data is better than 0.001 arc sec. The VLBI technique became possible in the late sixties. The radio signal received by an individual telescope of the network is converted to the video band and then independently recorded on magnetic tapes with the phase stability of atomic clocks. Thus the availability of frequency standards (Rubidium in the past, now mostly H-maser) was crucial for the technique. VLBI, or any other future array, will have to rely on high precision frequency standards; the only foreseeable change could eventually occur in the way data are transmitted to the central correlator.

High angular resolution of VLBI allows astrometric and geodetic measurements. Point-like objects are measured in the sky with milli arc sec precision. At the same time an individual antenna of the network can be located to within few millimetres on intercontinental baselines. The technique is routinely used for study of Earth rotation, tectonic plate motion and the prediction of earth quakes.

In February, 1997 the Japanese Institute of Space and Astronautical Science launched an 8 m antenna into an elliptical orbit around Earth. The project is known as VSOP - VLBI Space Orbiting Programme. Together with the ground based radio telescopes the VSOP antenna expands the capability of the existing array. The maximum baseline, which is defined by the satellite orbit, exceeds 20 000 km. The angular resolution is 3-4 times better than that achieved with the ground network. VSOP is a major step towards the synthesis of a radio telescope bigger than the Earth. Future projects such as Russia's Radioastron consider larger antennas and the maximum baseline comparable to the Earth - Moon distance. Such projects are realistic and most probably will be successfully completed within the next decade.

### Radio astronomy in Poland

Radio astronomy in Poland was initiated in the mid fifties independently at Torun's Copernicus and Cracow's Jagiellonian Universities. The dedicated hard work of Torun's team of scientists and engineers over last three decades placed us among well-developed European radio observatories. Our major

instrument, the 32m precise parabolic antenna, designed and built in Poland, is one of the best of its class. The new 32m telescope is a fully steerable classical Alt-Az mounted Cassegrain. Its main parabolic reflector is made of 336 panels, each with an accuracy better than 0.35 mm rms. They have been mounted and then adjusted to an accuracy better than 0.2 mm by a classical laser based surveying technique. The final accuracy of the surface is therefore limited by the quality of individual panels. The construction of the dish backing-structure is stiff and based on homological principle. The gravitational deviation from the parabolic shape has been designed to be 0.14 mm rms. The position of the 3.2 m subreflector is continuously adjusted to conform with the homological deformation of the dish. There are four azimuth drives each containing two AC motors and two gear boxes, and two elevation drives each with one gear box but with two AC motors. The complex scheme was chosen to ensure very smooth tracking by having opposed motors working in antbacklash mode. The telescope can point with absolute accuracy of 0.002 deg. Receivers covering the bands 1.4, 1.6, 5, 6.8 and 22 GHz are mounted simultaneously in the vertex cabin. All input amplifiers and waveguides are cooled down to 15 and 50 K respectively. The achieved system noise of all receivers is around 30K. Auxiliary equipment for the telescope consist of a Hydrogen Maser time and frequency standard (EFOS-15), a GPS timing receiver, a VLBA compatible terminal, the PSPM2 pulsar machine, a narrow band digital autocorrelating spectrometer and a weather station. The 32m high precision antenna with best available auxiliary instruments provides Polish astronomers with a unique tool to study the Cosmos. The telescope is part of the European and world-wide network of interferometers - VLBI. This system allows our antenna to be a part of the synthesis radio telescope which has an equivalent aperture size of ~10 thousand kilometres.

This new instrument and the involvement of Polish radio astronomers into international co-operation resulted in the flowering of radio research. VLBI studies of distant galaxies and quasars, the search for new planetary systems around pulsars, the study of interstellar and stellar molecules are the subjects worth mentioning here. The importance of the Torun 32m has been recognised in the astronomical community. The size of the antenna, position (important extension to the east) and a highly professional team of scientists and engineers make the addition of Torun a significant improvements to the European VLBI Network. Radio astronomy is a very challenging area of modern research for a country like Poland. The European research within EVN is seen in Poland as one of the best examples of scientific, cultural and political co-operation on our continent.

## FUTURE OF RADIO ASTRONOMY

An ideal future radio telescope should have a sensitivity of a few  $\mu\text{Jy}$ , an antenna sensitivity of much less than  $0.1 \text{ Jy/K}$  (preferably  $\sim 1 \text{ mK/Jy}$ ), and an instantaneous field of view of  $2\pi$  steradians. It should also have an available angular resolution selectable between  $\sim 1$  arc min to  $\sim 1$  milliarc second depending on the application, an available time resolution down to microseconds, and frequency resolution selectable between  $\sim 1 \text{ Hz}$  to  $\sim 10 \text{ MHz}$ . These last features are, of course, more dependent on back-end design than on antenna itself; however, the antenna and receiver's sensitivities are crucial for time and frequency resolutions and this is why they are mentioned here. Is this an unrealistic dream or can we really design and build such an instrument? I personally think that it will be possible to meet most of these requirements within 20 to 30 years, and some of them much sooner.

At the moment, the most sensible approach is to build special purpose telescopes dedicated to particular tasks; arrays to get high angular resolution and big collecting area elements to get high sensitivity.

Earth-rotation aperture synthesis is very powerful. It provides a relatively large field of view, which is defined by the properties of the individual antennae, and achieves high angular resolution. One of its weaknesses however is that it is insufficiently fast to image variable sources. But it is of course a well established and extremely successful technique.

Very large fully steerable single dishes, built the conventional way, have proved to be very expensive and there are no proposals at present for building any more. The weightless environment of space or the far side of the Moon could be better places for the building large apertures, but we know they will not be cheap. Fixed spherical dishes of the Arecibo type are being discussed and they might serve as elements of bigger arrays but it should be noticed that they are not well suited for use at high frequencies, which we may be forced to use for ground-based radio astronomy sooner than we expect. The rising tide of interference may well deny us the use of the lower frequencies.

To minimise the interference problem and to further enlarge the angular resolution, space missions with large orbiting antennas combined with ground based telescopes will synthesise a future cosmic radio telescope. The first successful attempt - VSOP - shows the direction how to use existing, as well as how to create entirely new space technologies in astronomical research.

Despite the push for higher and higher angular resolution - better and sharper images - there is a continuous need for increased sensitivity. One of the big future international projects is known as the Square Kilometre Telescope (SKT). There are several presently proposed forms of such a large telescope. All assume the effective aperture surface of about 1 square kilometre. What improvement in sensitivity would

this mean? Let me give you a science fiction example. This aperture size would allow direct reception of a typical ground TV transmitter from a distance of nearby stars. For astronomy SKT would mean entirely new quality of research. More than 100000 normal stars will become accessible instead of the few hundred available today. SKT sensitivity should allow detection of HI absorption from many more systems and the study of galaxy formation at very early stages of the evolution of the Universe. New radio sources located in the nuclei of distant galaxies will be found and studied. HI emission will allow us to build up the dynamic picture of galaxy motion around local gravitation centres - great attractors. There will also be direct cosmological implications since we could study the most distant and thus the youngest objects in the Universe in greater detail.

The proposals comprise a single aperture with large  $f/d$  or else an array of big spherical dishes or a big flat tile integrated antenna & receiver system.

I personally support the idea of a global real-time fibre-optic connected VLBI array with one global correlator centre. This would be a VLBA type array consisting of up to 1000 single elements, each 32m in diameter. Used as a phased array this would provide a collecting area comparable to  $1 \text{ km}^2$  and at the same time would give the maximum angular resolution achievable on our planet. Such an array would also allow great frequency flexibility. Individual countries could contribute effectively since such an enterprise would bring local benefits both scientific and technological. A large number of telescopes similar to Torun's new 32m could be afforded by many countries and therefore this scheme might be a very realistic way of evolving a truly world array of telescopes at a minimal and well shared cost. Questions of concern are related to the cost of the data transmission and to the cost of a mega-baseline correlator at the control centre. The first problem will be solved very soon as multimedia communication systems using fibre optics are being developed with enormous speed. The continuous upgrading of existing correlators could provide the basis for mega-baseline correlator of the future.

One additional feature of radio astronomy research, which adds to the importance of the field is the unique possibility to study complex molecules. The radio band is the only window in the electromagnetic spectrum where the rotational and vibrational transitions of molecular energy stages can occur. Since the first discovery of the OH radical, molecular radio astronomy has mushroomed and the interstellar medium has been found to be a veritable soup of diverse molecular species. Today we study more than 60 species, starting from a simple ones like OH, CO, SO,  $\text{H}_2\text{O}$  and ending with as complex as ethanol, methanol and other C,N,O,H,S complexes which I would have difficulty naming. The role of the interstellar molecular clouds in the formation of stellar

and planetary systems is being investigated. The molecules in circumstellar envelopes of evolved giant stars give information on physical conditions and inform us about envelope dynamics. Many molecules show maser amplification. Some are so bright, called mega-masers, that could have been found in distant galaxies. The study of molecules in the mm and sub-mm range is becoming a major attraction and activity field for many astronomers. A new project of a multi element mm array is being discussed between the USA, Japan and European countries. The system will be built and will become operational within next 5-7 years.

## CONCLUSIONS

Several important points concerning the future of radio astronomy research arise. First, the radio interference problem is a major concern that must be taken into account from the beginning in the planning future ground instruments. The success of the future Large Telescope, no matter how it is designed, depends very much on its location and legal protection. The increasing commercial use of the radio spectrum is pushing astronomers higher and higher in frequency, so we have to remember that our future instruments must be capable of working at mm and sub-mm wavelength. Being squeezed very exactly into our allocated bands, we cannot in the future improve sensitivity by enlarging bandwidth. Large apertures therefore seem to be the only reliable way to address the problem. Modern receivers have now brought us to practically noiseless preamplifiers (working at 15K), so the main struggle to reduce system noise must concentrate on minimising the ground contribution. Thus the screening of the area around antennas will also have to be considered an important part of future telescope design. To obtain high angular resolution and thus to measure distances, the future instruments would have to be multi-element arrays. The large ground apertures together with the space born antennas, plus radio telescopes located on the Moon and possibly Mars, will serve as our cosmic ear to listen and analyse the most beautiful natural music of the Universe.

## SPECTRUM MANAGEMENT

To protect future research in astronomy we need co-ordinated world-wide action. The first and most important issue is to protect the allocated bands. We need to make other users of electromagnetic waves understand that radio astronomy is a passive use of the band. We never transmit nor generate radio signals. To improve reception of cosmic information we can not go there and increase the transmitted power as the active users would do. The signals which we analyse

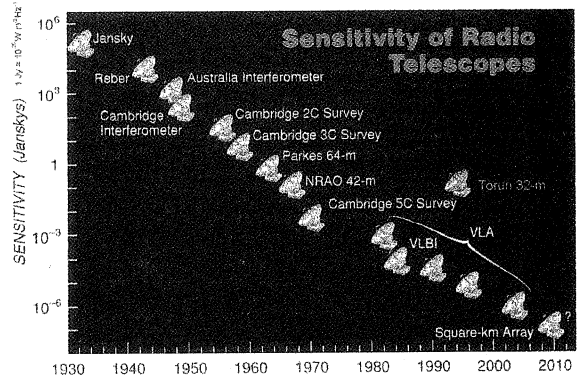
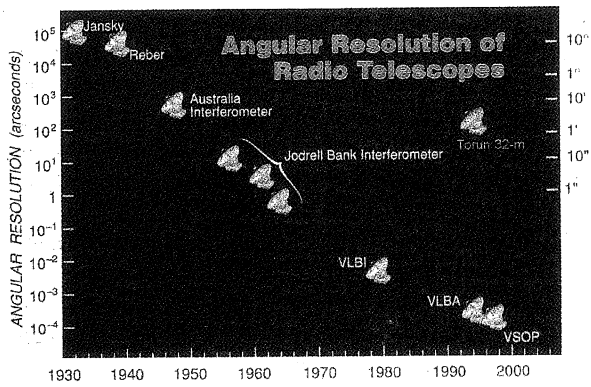
are so weak that sometimes we integrate for hours in order to get a sufficient S/N ratio. Usually it is 20-30 dB below the noise generated in the receiver and the atmosphere. Any terrestrial interference can ruin our measurements if it falls into our protected bands. Observations of distant quasars, pulsars and molecules can be compromised by commercially used devices such as microwave ovens, cellular telephones faulty TV and radio signals even garage-door openers. Recent experience shows that out of band emission and strong emission in adjacent bands causes severe problems for radio astronomers.

Conditions for coexistence are being discussed in international committees. An agreement has to be reached. Radio quiet zones around observatories, high quality electronics, linearity of power amplifiers and strict protection of radio astronomy bands are absolutely necessary.

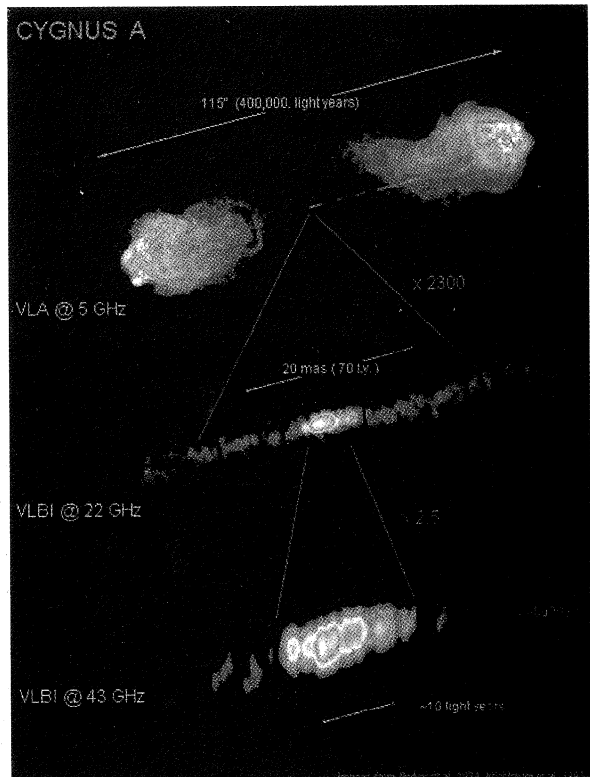
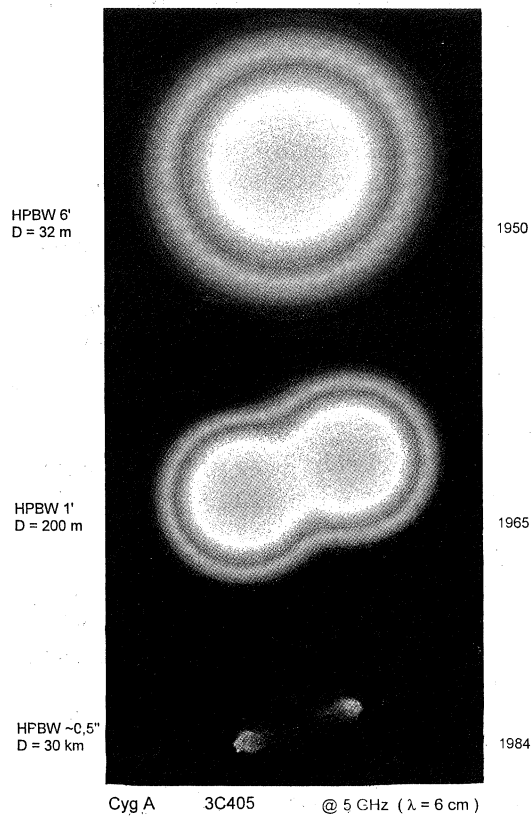
If we do not show sufficient motivation and dedication to this important activity, human kind may lose the unique chance to study the Universe in radio waves in the future.

## References:

1. Burke B.F., Graham-Smith F., 1997, An Introduction to Radio Astronomy, Cambridge University Press.
2. Kraus J.D., 1988, "Radio Astronomy", 2<sup>nd</sup> edition, Cygnus-Quasar Books.
3. Thompson A.R., Moran J.M., Swenson G.W., 1986, Interferometry and Synthesis in Radio Astronomy, John Wiley & Sons.
4. Rohlfs K., 1986, Tools of Radio Astronomy, Springer-Verlag.
5. Kellermann K.I., 1997, "Radio Astronomy in the 21<sup>st</sup> Century", *Sky & Telescope*, February, p.26-33.
6. Roth J., 1997, "Will the Sun Set on Radio Astronomy", *Sky & Telescope*, April, p.41-43.
7. "CRAF Handbook for Radio Astronomy", 1997, ESF & NFRA, 7990 Dwingeloo, The Netherlands, <http://www.nfra.nl/craf>.
8. Square Kilometre Telescope, 1998, NFRA, The Netherlands, <http://www.nfra.nl/skai>.
9. Butcher H., 1998, OECD Working Group on Radio Astronomy, NFRA, The Netherlands, [www.oecd.org/dsti/sti/s\\_t/ms/act/introra.htm](http://www.oecd.org/dsti/sti/s_t/ms/act/introra.htm)



Sensitivities and angular resolution of radio telescopes after Kellermann 1997.



Cyg A, a bright radio galaxy shown at different angular resolution. The image made with VLA comes from Perly et al., *Astrophys. J.*, **285**, L35., 1984, VLBI images are from Krichbaum, private communication, 1998.

## PAST AND PRESENT OF PIEZOELECTRICITY IN POLAND

*Marek S Wójcicki*

Tele & Radio Research Institute, Warsaw, Poland

### INTRODUCTION

Almost 70 years ago the Radio Research Institute was founded in Warsaw.

This fact can be considered as a starting point in piezoelectric research activity in Poland.

At the same time in 1929 first polish paper concerning application of quartz resonators was published [1]. It was only a few years after first world paper on this subject by Prof. Cady [2].

During the next decades up to now range of works has been extended significantly covering the following areas of interest:

- piezoelectric materials
- theory of excitation and propagation of bulk and surface acoustic waves in piezoelectric materials,
- piezoelectric devices,
- application of piezoelectric devices in electronic circuits,
- measuring methods and systems

All types of works have been developed: theoretical, experimental, designing and technological.

The most important results have been published in Polish and world technical journals.

Many of these results have been applied in practice in a form of new theories, methods, products or technologies.

Usually research works realized here were and are very close to the actual trend existing in world technique.

The most significant institutions involved in this branch are localized in Warsaw.

Three main periods of time may be distinguished in piezoelectricity development in Poland:

I - Beginnings /1929-1939/,

II - War period /1939-45/,

III - Development of research and industrial activity starting from post-war up to now /1945-98/.

Each of these periods will be characterized shortly.

### BEGINNINGS

An initiator of research works in this field was a famous Polish scientist Prof. J. Groszkowski. Prof. Groszkowski is an author of fundamental theory explaining the influence of harmonics (caused by circuit nonlinearity) on frequency of self-excited oscillators [3].

He was an animator and first director of the Radio Research Institute (IR), founded in 1929 /from 1934 reorganized in State Institute of Telecommunications (PIT)/.

Problems connected with piezoelectricity were very close to his scientific interests, from the very beginning of his career.

It can be confirmed by the titles of his papers published at that time: "Quartz crystal resonators in dynatron circuits" [1], "Quartz spectral frequency meter" [4].

A laboratory of piezoelectric stabilizers was organized in the Institute /IR/.

Various research works were carried on at the laboratory during first period. They concerned among others:

- methods of mechanical treatment of quartz and tourmaline plates and their electrical properties [5],
- effect of piezoelectric plate dimensions on its resonance frequency and temperature coefficient,
- search for cuts of zero temperature coefficient [6],
- quartz resonators properties of AT, R and X cut,
- properties of ring piezoelectric resonators,
- different vibration modes in spherical quartz resonators [7],
- optical quartz resonators, using gas ionization effect caused by high tension of electrical field accompanying maximum amplitude of mechanical vibration [8].

The optical resonator was applied in quartz frequency meter, used for frequency tuning of radio transmitters.

One of the most outstanding achievements was elaboration of quartz oscillating circuit for the transmitter of WILNO broadcast station [9].

The quartz resonator of special construction, enabling precision frequency correction, and the sophisticated oven system, minimizing ambient temperature effect, were used. High quality of the applied solution was confirmed by the official protocol from U.R.I. office in Brussels, containing results of long term stability measurements of WILNO station frequency.

According to the protocol this broadcast station was the most stable in comparison to other European broadcast stations tested at that time.

Very positive opinion about high frequency stability had also quartz clock made, during 30's, for the Polish National Bureau of Standards [10].

Piezoelectric crystals were very expensive at that time and because of that works connected with exploration of natural quartz and tourmaline sources were undertaken on the Polish territory in early 30's. Unfortunately quality of sought crystals was insufficient for piezoelectric components application.

During this period of time a first serial production of quartz resonators started in Poland. There were two enterprises involved in this activity: established in 1928 "AVA" Radio Components Company and "JAN FURSIEJ" Piezoelectric Stabilizer Company, both localised in Warsaw.

## WAR PERIOD

When war began a small group of former PIT/IR/ employees found relatively safe place of work in the above mentioned "JAN FURSIEJ" Company.

This company became at that time a part of German Company ZEISS from Jena.

Formally working for German Army the company became simultaneously a very good source of quartz resonators for the Polish Underground Army Signal Corps [11].

According to security reasons they had to change all the time frequencies of their radio transmitters and because of that their needs were very high.

Due to special order a secret magazine for quartz resonators was organized where resonators were stored and tested [12].

In spite of difficult war conditions, polish quartz specialists, still working in the domain, elaborated at that time several instruments:

- instruments for quartz optical orientation ,
- set for measurements of frequency/temperature response,
- oscillating circuit for quartz resonator testing.

Their experience was very helpful in post-war period.

## FROM POST-WAR TO PRESENT TIME

Soon after the war was finished the Institute /PIT/ was reactivated and started again its activity in piezoelectricity area.

Ten years later PIT was reorganized in, existing till now, Tele and Radio Research Institute /ITR/. During next decades the following /in majority new established/ research and industrial institutions were involved in this area too.

- Military Academy of Technology /WAT/,
- Institute of Electronic Materials Technology /ITME/,
- Warsaw University of Technology /PW/,
- Institute of Fundamental Technical Research /IPPT/,
- Radio ceramic factory CERAD,
- Radio components factory OMIG /now OMIG S.A./
- ESO Co. Ltd.

The most important facts characterizing their activity are given below.

## MATERIALS

In late 40's and early 50's ,according to actual trends, works were carried on synthetic piezoelectric crystals such as:

- EDT / ethylene diamine tartrate/
- ADP / ammonium dihydrogen phosphate/
- KDP / kalium dihydrogen phosphate/

Technology of crystallization was elaborated and crystal of regular shapes was obtained [13].

Properties of the crystal were investigated. In early 50's first works on cultured quartz started in PIT/ITR/. The hydro-thermal method was applied in

experimental autoclave. In mid 50's first small but regular crystals were obtained [14].

During next years a new experimental autoclave was constructed enabling much larger crystal growing. Large scale production of quartz monocrystals started in ITME in late 70's .

Works on technology of low dislocation and seed free 3" and 4" quartz monocrystals are being carried on now.

The following piezoelectric crystals manufactured by Czochralski method are also investigated in ITME: lithium niobate, lithium tantalite, berlinite, lithium tetraborate and bismuth silicone oxide.

At present quartz production potential is about 10 tons a year. Monocrystals of lithium niobate are produced on a small scale [15].

In the field of piezoceramic works began in late 40's in PIT and they were continued in ITR till mid 60's. At the beginning ceramic based on barium titanate was elaborated, soon after discovering its interesting properties. In mid 50's works on modified lead zirconate titanate /PZT/ ceramics were undertaken, especially on hot pressed ceramic.

Further works on various kinds of PZT ceramics were continued in CERAD factory and accompanying ceramic research center. As a result whole family of piezoceramics /PZT/ was put into large scale production in CERAD.

## QUARTZ RESONATORS

### Precision quartz resonators

In post-war period, responding to urgent needs of the Polish tele and radiocommunications as well as broadcast and measuring services, several types of XY, X+5, X+18.5, GT and AT cut resonators were manufactured in PIT.

Among others these resonators were used in first frequency standard operating at the National Bureau of Standards and for frequency stabilization of WARSAW I broadcast station transmitter.

In 60's soon after Prof. Warner papers, concerning high stability AT-cut resonators [16], there were elaborated in ITR / former PIT/ resonators of 2.5 & 5.0 MHz in glass high vacuum enclosure operating at 5<sup>th</sup> overtone. Technical parameters of these resonators were very close to that presented by the world producers, /e.g.  $Q \sim 3.6E6$ ,  $df/f/year < 1E-8$ , for 2.5MHz and  $Q \sim 2.5E6$ ,  $df/f/month < 2E-8$  for 5MHz./ [17].

5MHz resonator was put into large scale production in OMIG in early 70's.

In 70's a new type of highly stable resonator was introduced.

It was AT cut 3<sup>rd</sup> overtone 5MHz resonator enclosed in cold weld high vacuum TO-3 holder. Application of new cold weld hermetization technique made the technological process much more efficient and for that much easier serial production /OMIG/.

In early 80's, soon after first information on SC-cut resonator [18], guaranteeing much better parameters than AT-cut, works were undertaken in ITR [19].

As a result up to now a whole family of SC-cut resonators of frequencies from 4-30 MHz has been elaborated and introduced into small scale production. From several years works have been carried on new types of SC LFE resonators [20][21].

Very encouraging results have been obtained till now, especially lower aging rate and B mode elimination [22].

To perform above mentioned works a whole series of theoretical and technological problems had to be solved, such as:

- theoretical design of resonator temperature frequency characteristics [23],
- double-rotated precision crystallographic orientation[24],
- processes of chemical polishing and calibration [25],
- grinding and lapping process with current frequency control [26]

#### **Standard and medium stability quartz resonators**

First works in this field started in PIT in late 40's. Till mid 60's various low frequency resonators ( $f < 200\text{kHz}$ ) of NT, X+5, X-18.5, GT, AT cuts as well HF ( $f < 20\text{MHz}$ ) AT resonators in metal enclosures were elaborated and manufactured in PIT/ later ITR/ premises on laboratory scale [27].

In 60's construction and technology of AT-cut resonators excited at 3<sup>rd</sup> and 5<sup>th</sup> overtones up to 85 MHz were mastered.

In 80's thin plates technology was elaborated enabling manufacturing resonators at fundamental mode up to 40MHz.

At the beginning of 90's theoretical works on AT-strip resonator design started.

Analytical and numerical /finite elements method/ methods were used and experimental verification was carried on [28][29][30].

Industrial production of quartz resonators started in mid 50's in the biggest at that time electronic factory in Poland, nowadays not existing.

During 60's this activity was transferred to OMIG /enterprise established in late 50's/.

At the beginning limited types of standard AT cut resonators in metal holders in frequency range 1.5-50 MHz as well as selection of low frequency resonators from 4kHz to 300kHz were in production.

During next two decades production was extended to many types of the medium stability HF sub- and microminiature resonators operating at frequencies well over 100 MHz .

Actually OMIG is specializing in production of broad range of resonators for use in the professional tele- and radiocommunications circuits in frequency range 4 kHz - 150MHz .

In early 90's a new quartz company was established as a joint venture of Polish, German and Austrian partners.

ESO operates on local and mainly on international market. Its products are certified by several foreign customers.

The company is specializing in short series production of professional customer-designed quartz resonators within frequency range from 1 to 200 MHz also for SMT.

Actually ESO is going towards manufacturing quartz resonator operating on fundamental mode at frequencies above 40 MHz.

#### **QUARTZ OSCILLATORS**

##### **Oven controlled quartz oscillators**

At ITR this area always was and still is one of the most important field of activity.

Till early 70's several works concerning OCXO design and their application in quartz clocks have been also performed at PW.

OCXO oscillators of improved stability using 100kHz Y-cut and 200kHz DT-cut resonators and self-excited temperature control circuit were elaborated and manufactured on laboratory scale during 50's .

In 60's a new type of crystal oven was introduced [31]. Using this oven and precision 2.5 & 5MHz AT-cut resonators in glass vacuum enclosures a new family of fully transistorised oscillators was elaborated [32]. These oscillators had very good technical parameters at the expense of rather sophisticated technology [33].

Other oven constructions with dewars container and bridge tcc circuit were also applied.

Answering to growing customer demands a new generation of OCXOs of considerably improved technical parameters /reduced external dimensions, higher long term stability/ was designed during 70's.

It was possible thanks to introduction of several new technical solutions:

- new optimized oscillating circuits,
- new oven construction of low thermal capacity equipped with precision proportional tcc with thermistor bridge,
- miniaturized AT-cut 3<sup>rd</sup> overtone precision resonators encapsulated in high vacuum cold weld TO-3 metal enclosures.

At the beginning of 80's with advent of SC-cut resonators further improvements were made [ 34].

Up to now whole family of SC OCXOs from miniature low power to ultra-stable with LFE resonator has been elaborated [35][36][38].

Works on synchronized ultra-stable quartz source have been undertaken during last few years. First model of 5 MHz generating system synchronized with 1pps external signal has been elaborated and tested [37].

The ITR Piezoelectric Department started in the beginning of 90's with serial production of several types of OCXO oscillators equipped with SC-cut high stability resonators operating in frequency range 4-30 MHz.

These customer-specified OCXOs are mainly used by telecommunications industry and time and frequency measurement laboratories.

Various categories of the OCXO oscillators operating within frequency range 4-30 MHz are offered:

- highly stable -- of 24 hours frequency stability better than  $5E-11$ ,
- miniature -- of less than 25ccm volume,
- low power--of power consumption less than 0.5 W,
- quick warm-up -- of warm-up time less than 1min.

Till early 90's OCXOs large production took place also in OMIG factory. These 5MHz OCXO's were based only on AT-cut precision resonators.

### **Temperature compensated & voltage controlled quartz oscillators**

Works on temperature compensated quartz oscillators /TCXO/ were carried on in ITR during 70's [39]. Several types of TCXO's were elaborated and put into high volume production in OMIG company.

These oscillators were characterized by high technical parameters, especially very good frequency temperature stability and reduced external dimensions [27].

In 80's, voltage controlled quartz oscillators /VCXO/ with direct frequency modulation of extremely linear characteristic were elaborated[40].

In second half of 80's, some works were undertaken upon digital temperature quartz oscillators /DTCXO/ with SC-cut resonators using "B" mode as a temperature sensor [41].

At the beginning of 90's voltage controlled temperature compensated quartz oscillator /TCVCXO/ of wide tuning range / 150PPM/ was elaborated.

The number of various TCVCXO types and production volume is still increasing .

In the actual ITR production offer there are several customer designed TCVCXO's operating in frequency range 8 - 60 MHz within temperature range -30 to 80 °C of wide frequency adjustment range /150-200 PPM/ [35].

Selected types of TCXO & VCXO's oscillators for professional and military applications are in OMIG production program [42].

### **MEASUREMENT METHODS AND EQUIPMENT**

Range of original measuring methods and systems was elaborated during last few decades for investigation of quartz resonators and oscillators parameters.

These systems were designed for laboratory purpose but some of them also for industrial environment.

The following parameters have been taken into account:

*resonators* - basic parameters [43-53], inherent noise[54], unwanted response [55], nonlinearity [56][57], aging [58][59][60] and temperature characteristics [61][62][63],

*oscillators* - phase & amplitude noise, short, medium and long term instability [64-67,69], retrace

characteristic, stabilization time, static & dynamic temperature characteristic [68].

Works on above mentioned subjects were performed mainly in ITR and some of them at PW.

### **PIEZOELECTRIC FILTERS**

During last few decades works on quartz BAW filters were carried in ITR and OMIG .

First models of quartz filters for radio and telecommunications purposes were designed in ITR in late 50's. During next years a whole family of LF stopband and passband channel filters operating at various frequencies was elaborated and produced in small quantities in ITR. Radiocommunications filters 10.7MHz was also elaborated at this time [27].

In 60's filter's technology was transferred to OMIG and then serial production started.

In early 80's first monolithic 10.7 MHz filters were designed and put into serial production in OMIG.

During next years frequency range of the offered filters was extended to 45 MHz / with possibility of further extension to 150 MHz / [42].

Besides a whole range of specialized tele and radiocommunications filters consisting of discrete resonators are in OMIG production program.

### **PIEZOCERAMIC COMPONENTS**

Domain of piezoceramic devices was developed in Poland in late 40's. First ultrasonic transducer basing on barium titanate was designed and experimentally tested in PIT/ later ITR/ in early 50's [13].

During next years piezoceramic resonators and ladder filters with the use of modified lead zirconate titanate /PZT/ were designed [70].

In mid 50's the main activity in the field of piezoceramic components was transferred to newly established Radio ceramic factory CERAD and accompanying research center.

Basing on various kinds of PZT ceramics, produced at the same factory, whole range of resonators and filters, at first ladder type later monolithic, were designed and manufactured on a large scale [71].

Whole range of piezoelectric transducers for acoustic and ultrasonic applications was also designed and put into high volume production.

From early 90's research and industrial activity has been significantly limited and now is concentrated on selected types of piezoceramic resonators dedicated for oscillating circuit [72] as well as on different acoustic transducers.

It should be mentioned that many theoretical and experimental works concerning piezoelectric transducers have been performed in IPPT during last few decades.

### **SAW DEVICES**

First works on surface acoustic wave began in Poland in mid 60's at the Military Academy of Technology (WAT) in Warsaw. It was at the same time when first interdigital transducer, directly at a surface of a

piezoelectric substrate, was made in USA [73]. These works concerned an interaction of SAW and electron beam in vacuum and in piezoelectric semiconductors.

First experiments on passive SAW devices, delay lines (DL) and dispersive delay lines (DDL) on quartz were done in late 60's.

First models of these devices which could be used in practice were made in early 70's and soon after a small scale production was initiated in ITR [74].

During next years several new models, operating at 30MHz, were designed at WAT [75][76].

Later on a new family of DDL for the centre frequency 70 MHz were designed in ITR and put into production. Next SAW component, intermediate frequency bandpass TV filter (IFTV filter) was developed in ITR at the beginnings of 80's [77] and put into serial production in early 80's in co-operation with ITME [78].

Up to now 13 types of IFTV filters are in production at ITME. Also several types of professional filters for digital communication systems (operating at 70 MHz), digital radio receivers (centre frequency 118 MHz), cable TV modulators (35&36 MHz) were designed and put into serial production at ITME [79].

First one port SAW resonator was designed and experimentally verified in frequencies range 140-200MHz in ITR in early 90's.

Several models of SAW two port resonators were designed, fabricated and test at ITME. They are applied in crystal controlled oscillators in the frequency range from 200MHz to 1000MHz.

The fundamental research related to the SAW devices is performed mainly at IPPT and ITME. They concern:

- new types of waves[80] and devices [81], spectral theory of interdigital transducers and reflective couplers [82][83] (IPPT),
- properties of Bleustein-Gulyaev waves in lithium tetraborate [84], applications of a stopband coupler and synchronous coupling IDT's in SAW filters[85][86](ITME).

## CONCLUSIONS

An overview of research and production activity in piezoelectricity domain in Poland has been presented in this paper.

It can be seen that during last 70 years, in spite of very serious obstacles and barriers, this branch of Polish technique was always and is still alive and tries to be close to the actual world trends.

## ACKNOWLEDGEMENTS

I'd like to express many thanks to my colleagues, involved deeply in the subjects presented above, who helped me to collect necessary information.

Especially thanks to Prof. Wincenty Pajewski from IPPT PAN, Prof. Stefan Hahn from PW and Prof. Waldemar Soluch from ITME.

## REFERENCES

- [1] J.Groszkowski "Quartz resonator in dynatrone circuits", *Przeegl"d Radiotechniczny*, No.23-24,1929 /in Polish/
- [2] W.G.Cady "The Piezoelectric Resonator", *Proc. I.R.E.*, vol.10, 1922
- [3] J.Groszkowski "The interdependence of frequency variation an dharmonic content and the problem of constant-frequency oscillators", *Proc.I.R.E.*, vol.21, 1933
- [4] J.Groszkowski "Quartz spectral frequency meter", *Przeegl"d Radiotechniczny*, No.3-4, 1931 /in Polish/
- [5] P.Modrak "Quartz and Tourmaline", *The Wireless Engineer*, No.162-163, 1937
- [6] P.Modrak "Small Temperature Coefficient of Frequency of Quartz Plates", *The Wireless Engineer*, No.184, 1939
- [7] S.Kamienski "Spherical piezoelectric resonators", *Przeegl"d Radiotechniczny* No.9-10, 1936 /in Polish/
- [8] P.Modrak "Optical quartz resonators", *Przeegl"d Radiotechniczny*, No.9-10, 1935 /in Polish/
- [9] J.Groszkowski, Z.Jelonek "Oscillating Circuit for the Transmitter of WILNO Broadcast Station", *Przeegl"d Radiotechniczny*, No.9-10, 1939 /in Polish/
- [10] J.Groszkowski, K.Dobrski "Research Works in the State Telecommunications Institute in years 1935-36", *Przeegl"d Radiotechniczny*, No.9-10, 1937 /in Polish/
- [11] W.Pajewski, *Private Communications*, 1998
- [12] S.Hahn, *Private Communications*, 1998
- [13] W.Pajewski "Piezoelectric materials in ultrasonics", *Proc. of Ultrasonic Conference*, Warsaw, November 1953
- [14] W.Pajewski "Synthetic Quartz Crystals",
- [15] *Catalogue of the ITME Products*, 1997
- [16] A.W.Warner "Design and performance of ultraprecise 2.5MHz quartz crystal unit", *Bell System Technical Journal*, 1960
- [17] W. Pajewski "Properties of high stability quartz resonators" *Czechoslovak Journal of Physics*, vol. B16, 1966 /in Russian/
- [18] A.Ballato "Doubly rotated thickness mode plate vibrators", *Physical Acoustics*, vol.13, Academic Press, 1977
- [19] W.Szulc, M.Moniuk "High stability SC-cut quartz resonator", *Proc. of EPPC Conference*, Liberec, 1983
- [20] W.Szulc, K.Weiss, *ITR Technical Report B3-2*, 1993 /in Polish/
- [21] A.Masiukiewicz, B.Gniewinska, W.Szulc "Study of SC-cut lateral field excited resonators features", *Proc of 9<sup>th</sup> EFTF*, Besancon, 1995
- [22] K.Weiss, W.Szulc "The SC-cut lateral field quartz resonator working on anharmonic antisymmetrical mode", *Proc. of 12<sup>th</sup> EFTF*, Warsaw, 1998
- [23] E.Zuchowski, M.Lysakowska "The nonlinearity of the frequency temperature characteristics of quartz resonators with LC-cut" *Proc. of 7<sup>th</sup> Piezoelectric Conference PIEZO'90*, Serock, 1990

- [24] K.Weiss "Measurement results of the crystallographic orientation of the 6<sup>th</sup> EFTF, Noordwijk, 1992
- [25] J.Grzegorzewicz, W.Szulc "Etching of quartz crystal blanks", Prace ITR, No.83, 1980 /in Polish/
- [26] K.Weiss, ITR Technical Report Z-585, 1985 /in Polish/
- [27] C.Klimek " Research activity in piezoelectricity domain in Poland from 1945 to 1985", Prace ITR, No.101, 1985 /in Polish/
- [28] E.Zuchowski "Theoretical analysis and design of AT-cut miniature resonators, Proc. of EPPC'88, Liberec, 1988
- [29] E.Zuchowski , ITR Technical Report Z-519, 1991 /in Polish/
- [30] E.Zuchowski, M.Tupaj "Design of strip AT-cut quartz resonators with use of FEM", Proc of 8<sup>th</sup> Piezoelectric Conference PIEZO'94, Zakopane, 1994
- [31] D.Kwiatkowska "Change of state crystal oven", Prace ITR, No.2(27), 1964 /in Polish/
- [32] B.Gniewinska "Transistorised reference quartz oscillator of 2E-8/month frequency instability, Prace ITR, No.2(27), 1964 /in Polish/
- [33] A.Sowinski "Review of ITR research works on high stability quartz frequency standards", Prace ITR, No.2(35), 1966 /in Polish/
- [34] A.Masiukiewicz, B.Kalinowska " Miniature low power consumption OCXO oscillator", Proc. of 7<sup>th</sup> EFTF, Neuchatel, 1993
- [35] Catalogue of the ITR products, 1998
- [36] A.Masiukiewicz, B.Gniewinska, W.Szulc "Application of LFE-SC-cut resonators at high stability oscillators, Proc. of IEEE FCS, Boston, 1994
- [37] A.Lisowiec, A.Czarnecki "Set of GPS synchronised 5MHz frequency sources for telecommunications", Proc. of 9<sup>th</sup> Piezoelectric Conference PIEZO'96, Waplewo, 1996
- [38] A.Masiukiewicz, B.Gniewinska, W.Szulc " Precise quartz oscillators with lateral field excited resonators", Proc. of 8<sup>th</sup> Piezoelectric Conference PIEZO'94, Zakopane, 1994
- [39] M.Jeziorowski " Analysis of frequency variation of thermally compensated oscillators", Prace ITR, No.2(59), 1972 /in Polish/
- [40] B.Gniewinska, C.Norek "Computer aided design of VCXO oscillators", Prace ITR, No.113, 1991 /in Polish/
- [41] M.Olesiuk, M.Moniuk, B.Busko, A. Masiukiewicz "Analysis of possible application of SC-cut resonators in the oscillators with digital temperature compensation", Prace ITR, No. 111-112, 1991 /in Polish/
- [42] Catalogue of the OMIG S.A. products, 1998
- [43] A.Fiok "Transmission methods for measurement of multiresonance one-ports", Wyd. Politechniki Warsz. Elektronika, No.12, 1973 /in Polish/
- [44] A.Fiok, M.Wernik "FM-method for measurement of quartz resonator parameters", Proc. of EPCC'73, Liberec, 1973
- [45] A.Fiok, S.Zmudzyn, J.Cichocki, A.Słowikowski "An automated system for measuring frequency and resistance of HF quartz crystal units", Acta IMEKO, 1982
- [46] A.Smolarski, M.Wójcicki "Quartz crystal unit measurement method based on transmission line T-network", IEEE Trans. On Sonics and Ultrasonics, No5, 1978
- [47] M.Wójcicki "Method for measurement of basic parameters of HF quartz resonators", Prace ITR, No.84, 1980 /in Polish/
- [48] M.Wójcicki "A new method especially for VHF and UHF crystal unit measurement", Proc. of the Second Int. Conf. ACOUSTOELECTRONICS'85, Plovdiv, 1985
- [49] M. Wójcicki "A new single port reflection method for measurement of crystal unit equivalent parameters in very wide frequency range", Proc. of the Conference on Frequency Control and Synthesis, Surrey, 1987
- [50] M. Wójcicki, A. Lisowiec "Application of direct reflection method in quartz resonators metrology", Proc. of 8-th Piezoelectric Conference PIEZO'94, Zakopane, 1994
- [51] M. Wójcicki, A. Lisowiec "A direct reflection method and six-port measuring system for accurate determination of piezoelectric resonator basic parameters", Proc. of 8th European Frequency and Time Forum, Munich, 1994
- [52] A. Lisowiec, M. Wójcicki "Six-port technique in reference measurements of piezoelectric resonators parameters", Proc. of 9th EFTF, Besanon, March 1995
- [53] A.Lisowiec, M.Wójcicki "Aspects of calibration of a six-port circuit for precise measurements of piezoelectric resonators", Proc. of 12<sup>th</sup> EFTF, Warsaw, 1998
- [54] B. Gniewinska "Computer controlled short term frequency stability measurement system with the application of covariance method", Proc of 5th EFTF, Besanon, 1991
- [55] J.Ksiazek, A.Smolarski "Bridge circuit for measurement of parasitic resonances of quartz crystals", Prace ITR, No.4(57), 1971 /in Polish/
- [56] A.Smolarski "Free oscillation frequency method for investigation quartz resonators", Bull. Acad. Pol. Sc., No.6, 1964
- [57] A.Smolarski "An attempt at phenomenological determination of a non-linear equation for quartz resonators", Bull. Acad. Pol. Sc., No.5, 1966
- [58] J.Jamiołkowski "Measuring circuit for aging investigation of precision quartz resonators", Prace ITR, No.1(54), 1971 /in Polish/
- [59] M.Wójcicki, A.Smolarski " System for investigation of quartz resonators aging characteristics", Prace ITR, No.1(70), 1975 /in Polish/
- [60] A. Smolarski, A. Lisowiec "A high accuracy automated system for investigating the aging process of quartz resonators, Proc. of IMEKO-TC-4 Symp., Vienna, 1992

- [61] M.Wójcicki, A.Smolarski "Automation of laboratory measurement of quartz crystal unit temperature characteristic", Proc. of 3<sup>rd</sup> Conf. ACOUSTOELECTRONICS'87, Varna, 1987
- [62] A.Smolarski "Distortion of quartz crystal temperature characteristic existing during continuous and stepwise temperature changes", Proc. of URSI Symp., Warsaw, 1975
- [63] M. Wójcicki, A. Lisowiec "A new batch oriented system for quick and accurate determination of quartz resonators temperature characteristics", Proc. of IMEKO-TC-4 Symp., Vienna 1992
- [64] B.Gniewinska, ITR Technical Report Z-583, 1986 /in Polish/
- [65] B. Gniewinska: A new short term frequency stability measuring systems, Proc. of EPCC'88, Liberec, 1988
- [66] B.Kalinowska, B.Gniewinska, A.Czarnecki, G.Wojtas "Computer controlled system for measurement of phase noise and short-term frequency instability", Prace ITR, No.113, 1992 /in Polish/
- [67] B.Kalinowska, S.Gawor "Automated system for investigation of long-term instability of precision quartz oscillators", 8th Piezoelectric Conference PIEZO'94, Zakopane 1994
- [68] B.Kalinowska, ITR Technical Report B-3/S/96, 1996
- [69] B.Kalinowska, B.Gniewinska "Investigation of medium-term frequency instability of OCXO oscillators", Proc. of 10<sup>th</sup> EFTF, Brighton, 1996
- [70] W.Kaminski "Application of piezoelectric ceramics in electronics", Proc. of 1<sup>st</sup> Piezoelectric Conference, Warsaw, 1970 /in Polish/
- [71] W.Roguski "Piezoelectric ceramic components - present state and future trends", Proc. of 6<sup>th</sup> Piezoelectric Conference PIEZO'85, Jadwisin, 1985 /in Polish/
- [72] W.Roguski, B.Zmudzki "Ceramic resonators for stabilisation of a simple oscillatory circuit in the range of 6 to 10 MHz", Proc of 9<sup>th</sup> Piezoelectric Conference PIEZO'96, Waplewo, 1996
- [73] R.M.White, F.W.Voltmer "Direct piezoelectric coupling to surface elastic waves", Appl. Phys. Lett., vol.7, No.12, 1965
- [74] W.Soluch "Surface acoustic wave delay lines", Proc. 2<sup>nd</sup> Radiolocation and Microwave Conference, Pardubice, 1975 /in Russian/
- [75] E.Danicki, J.Filipiak "SAW dispersive delay line with constant period interdigital transducers", Elektronika, No.9, 1984 /in Polish/
- [76] E.Danicki, J.Filipiak, A.Kawalec "SAW dispersive delay line utilising apodised IDT with periodic electrodes", Electron. Lett., vol.19, 1986
- [77] W.Soluch "SAW television filters", Proc. of 5<sup>th</sup> Piezoelectric Conference, Warsaw, 1980 /in Polish/
- [78] W.Soluch, B.Koczynski, L.Kozłowski "SAW tv filter type FT-381", Elektronika, No.10, 1987 /in Polish/
- [79] E.Dabrowska, H.Majewska, P.Nagłowski, T.Wróbel "TV-IF filters in Poland - design, fabrication and parameters", Proc. of the 8<sup>th</sup> Piezoelectric Conference PIEZO'94, Zakopane, 1994
- [80] E.Danicki "New interfacial shear wave in piezoelectrics", Appl. Phys. Lett., vol.64, No.8, 1994
- [81] E.Danicki "New configuration of SAW resonator", Electron. Lett., vol.29, No.13, 1993
- [82] E.Danicki "Theory and application of RMSC", Proc. of IEEE Ultras.Symp., 1992
- [83] E.Danicki "Spectral theory for IDTs", Proc. of IEEE Ultras. Symp., 1994
- [84] W.Soluch "Measurements of Bleustein-Gulyayev waves in  $\text{Li}_2\text{B}_4\text{O}_7$  crystal", IEEE Trans. On UFFC, vol.42, No.5, 1995
- [85] W.Soluch Application of a stopband multistrip coupler in a SAW resonator filter", Proc. of IEEE Ultras. Symp., 1994
- [86] W.Soluch "SAW two resonator filter using synchronous coupling interdigital transducers", Proc. of 10<sup>th</sup> EFTF, Brighton, 1996



*12th E F T F* - 10÷12 March 1998 - **Warsaw - POLAND**

**Resonators I**

Chairman:

*Daniel Hauden*



## THEORY AND DESIGN OF PIEZOELECTRIC RESONATORS IMMUNE TO ACCELERATION: PRESENT STATE OF THE ART

John A. Kosinski

U.S. Army Communications-Electronics Command, ATTN: AMSEL-RD-IW-TI, Fort Monmouth, NJ 07703-5211  
USA

### INTRODUCTION

The need for low acceleration sensitivity in quartz crystal resonators for use in commercial applications is increasing rapidly due to the proliferation of mobile and satellite personal communication systems. Progress in low acceleration sensitivity design has been hampered to date by two widely held misconceptions regarding its cause:

1. The name given to the phenomenon is misleading. The phenomenon is referred to as acceleration sensitivity (or alternatively, *vibration* sensitivity or 'g'-sensitivity) based upon the practical situations in which it is observed. In reality, the resonator has a generic sensitivity to *deformation*.
2. Material nonlinearities are an important part of the phenomenon, but are not the *cause* of the phenomenon. Even a resonator made using an ideal, perfectly linear material will have an acceleration sensitivity.

Recently, significant progress has been made in understanding the cause of acceleration sensitivity (1). Practical advice on low acceleration sensitivity design has followed directly.

### DEFORMATION SENSITIVITY FUNDAMENTALS

The basic principle of operation of a generic resonator is shown in Figure 1. A traveling wave is combined with a confinement structure to produce a standing wave whose frequency is determined jointly by the velocity of the traveling wave and the dimensions of the confinement structure. In the case of crystal resonators, the traveling wave is either a bulk acoustic wave propagating through the interior of a piezoelectric crystal substrate or an acoustic surface wave propagating on the surface of a piezoelectric crystal substrate. In the case of bulk acoustic wave (BAW) resonators, the wave is confined by the substrate surfaces, while in the case of acoustic surface wave

resonators, the wave is confined by metal-strip Fabry-Perot reflectors deposited on the propagation surface.

Given that the frequency of the crystal resonator is determined jointly by the velocity of the acoustic wave and the dimensions of the confinement structure, there are only two possible effects which a mechanical bias, such as that produced by acceleration, can have on the crystal resonator:

1. The wave velocity can be perturbed.
2. The confinement dimensions can be changed.

The first effect is primarily a result of the nonlinear elastic behavior of the piezoelectric substrate, while the second effect is primarily a linear mechanical effect.

The portion of the frequency shift caused by the wave velocity change is typically substantially larger than that caused by the confinement dimension change, and hence such phenomena are often thought of in the purely nonlinear sense. However, techniques exist which can readily reduce the nonlinear part to levels such that the linear part cannot be ignored. The linear portion of the problem also causes an asymmetry in the effective material constants such that  $\hat{c}_{L\gamma M\alpha} \neq \hat{c}_{\gamma L\alpha M}$  with the important practical implication that both strains and rotations must be considered when determining the mechanical biasing state.

The driving factor behind the frequency shift induced by a mechanical bias is the deformation of the resonator. Acceleration sensitivity is simply a special case where the deformation arises from the reaction of the crystal resonator against its mounting structure. This is illustrated in Figure 2, wherein the effects of acceleration on a resonator constrained by a mounting structure are compared to the effects of acceleration on an unconstrained resonator.

The relationship of acceleration sensitivity to the force-frequency effect, planar stress compensation, etc. is clarified in Table 1. All of the listed phenomena are special cases of deformation sensitivity, each

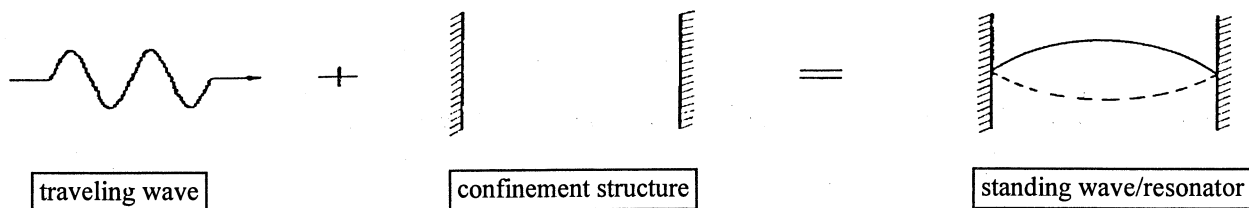


Fig. 1. Basic principle of operation of a generic resonator.

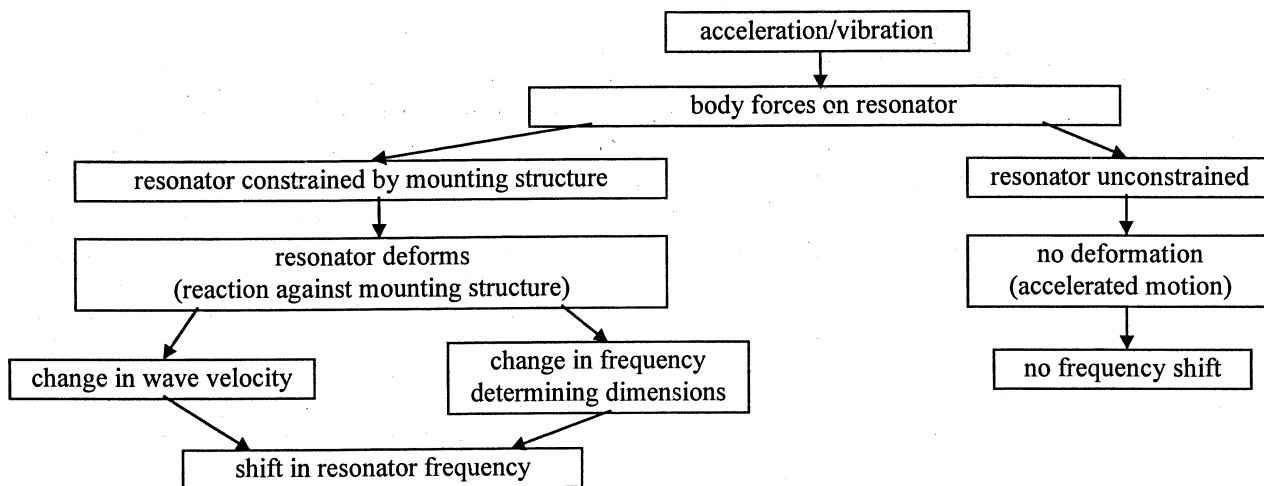


Fig. 2. Flow chart of acceleration effects for constrained and unconstrained resonators.

TABLE 1 - Deformation Sensitivities

Phenomenon	Deformation Driver
acceleration sensitivity	reaction against mounting structure in response to external acceleration
aging (stress relief)	relaxation of resonator and/or mounting structure
force-frequency effect	diametric compression
planar stress/thermal transient compensation	electrode/substrate interfacial stress

distinguished by a particular driving deformation.

#### THEORETICAL ANALYSIS

How to accurately calculate acceleration sensitivity is now well understood. One can, in theory, directly solve for the frequency under acceleration using a set of differential equations with spatially varying effective elastic constants. It has been shown to be much more

efficient to calculate the first perturbation in eigenvalue using the formalism of Tiersten (2). In this technique, one examines essentially a weighted average of the spatially varying effective elastic constants in that portion of the plate where the mode is driven. It is this effective averaging that is the basis of the various "mode-shaping" proposals recently put forth (3-8).

The basic equations employed in the perturbation approach as developed by Tiersten for the case of purely elastic nonlinearities are

$$\omega = \omega_{\mu} - \Delta_{\mu}, \quad (1)$$

$$\Delta_{\mu} = \frac{H_{\mu}}{2\omega_{\mu}}, \quad (2)$$

and

$$H_{\mu} = - \int_V g_{\alpha, M}^{\mu} \hat{c}_{L\gamma M\alpha} g_{\gamma, L}^{\mu} dV, \quad (3)$$

where

$$g_{\gamma}^{\mu} = \frac{u_{\gamma}^{\mu}}{N_{\mu}}, \quad (4)$$

and

$$N_{\mu}^2 = \int_V \rho u_{\gamma}^{\mu} u_{\gamma}^{\mu} dV. \quad (5)$$

Equation (1) shows that the frequency under acceleration,  $\omega$ , is shifted from the unperturbed frequency,  $\omega_{\mu}$ , by a small amount  $\Delta_{\mu}$  which can be calculated using equation (2) and “the perturbation integral” of equation (3). The perturbation integral given by equation (3) looks quite complicated but actually has a rather simple interpretation: it is essentially a weighted average of the acceleration induced bias throughout the volume of the quartz plate, where the weighting factor for the averaging is determined by the acoustic mode shape. Equations (4) and (5) provide the necessary normalization of the acoustic mode shape with particle displacements  $u_{\gamma}^{\mu}$  (Note: the subscript/ superscript  $\mu$  in (1) through (5) denotes the  $\mu^{\text{th}}$  eigenmode).

The acceleration-induced biasing state is most conveniently written using the material cofactor representation (9)

$$\hat{c}_{L\gamma M\alpha} = k_{L\gamma M\alpha KN} w_{N,K}, \quad (6)$$

where

$$k_{L\gamma M\alpha KN} = c_{L\gamma M\alpha KN} + c_{LMKN} \delta_{\gamma\alpha} + c_{L\gamma KM} \delta_{\alpha N} + c_{LK M\alpha} \delta_{\gamma N} \quad (7)$$

and  $\delta_{\gamma\alpha}$  represents the Kronecker delta. The  $w_{N,K}$  factor in equation (6) represents the nine acceleration-induced biasing deformation gradients (N and K take values 1,2,3), and contains all of the required information on how the shape of the crystal plate is deformed by the acceleration. Which  $\hat{c}_{L\gamma M\alpha}$  terms are required is determined by the mode of operation, and each  $\hat{c}_{L\gamma M\alpha}$  term is the sum of the deformation gradients, each multiplied by the relevant material cofactors  $k_{L\gamma M\alpha KN}$  as defined in equation (7). As applied to the calculation of the normal acceleration sensitivity, equations (1) through (3) readily yield

$$\Gamma_i = \frac{1}{8\pi^2 v^2 a_i} \int_V g_{\alpha,M}^{\mu} \hat{c}_{L\gamma M\alpha} g_{\gamma,L}^{\mu} dV, \quad (8)$$

where  $v$  denotes the resonant frequency and  $a_i$  denotes the external acceleration applied along the  $x_i$  direction.

Equation (8) may be evaluated analytically or numerically. The major advantage of the analytic approach is that it can be used to derive design equations yielding a clear understanding of the functional dependencies of the acceleration sensitivity upon real-world design and fabrication parameters (10,11). The numerical approach using finite element techniques to determine the acceleration-induced biasing state has advantages in the analysis of complicated support structures and resonator geometries.

## NORMAL SENSITIVITIES OF SIMPLE MODES

It is generally known that the acceleration sensitivity of a given resonator type depends upon the support configuration, choice of substrate material, substrate orientation, substrate dimensions, type of mode, acoustic mode profile, acoustic mode location, etc. In order to obtain a more detailed understanding of the roles these parameters play in determining the acceleration sensitivities of both bulk and surface wave resonators, it is useful to examine the instructive cases of the typically dominant, normal acceleration sensitivities of rotated Y-cut quartz resonators simply supported along rectangular edges.

The bulk acoustic wave (BAW) modes considered here are the simple thickness modes described by

$$u_2 = M_a \cdot \sin[\beta_p(x_2 - \Delta)] \quad (\text{AT-cut a-mode}), \quad (9a)$$

$$u_3 = M_b \cdot \sin[\beta_p(x_2 - \Delta)] \quad (\text{AT-cut b-mode}), \quad (9b)$$

$$u_1 = M_c \cdot \sin[\beta_p(x_2 - \Delta)] \quad (\text{AT-cut c-mode}), \quad (9c)$$

for

$$\delta - w \leq x_1 \leq \delta + w, \quad (9d)$$

$$-h \leq x_2 \leq +h, \quad (9e)$$

$$\varepsilon - l \leq x_3 \leq \varepsilon + l, \quad (9f)$$

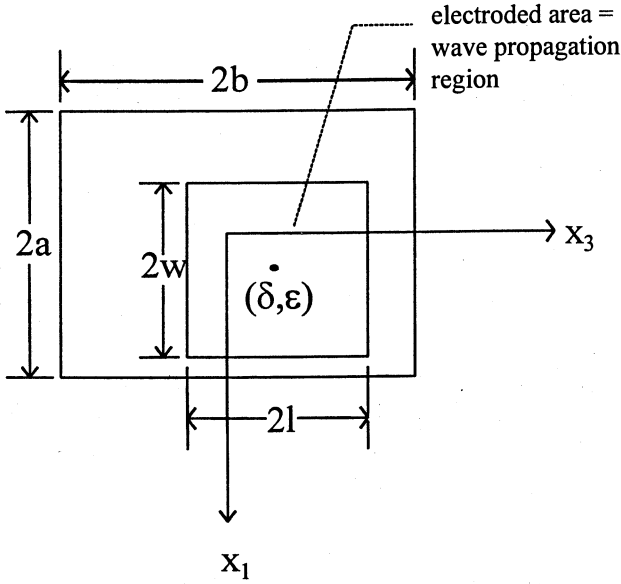


Fig. 3a. BAW device plan view.

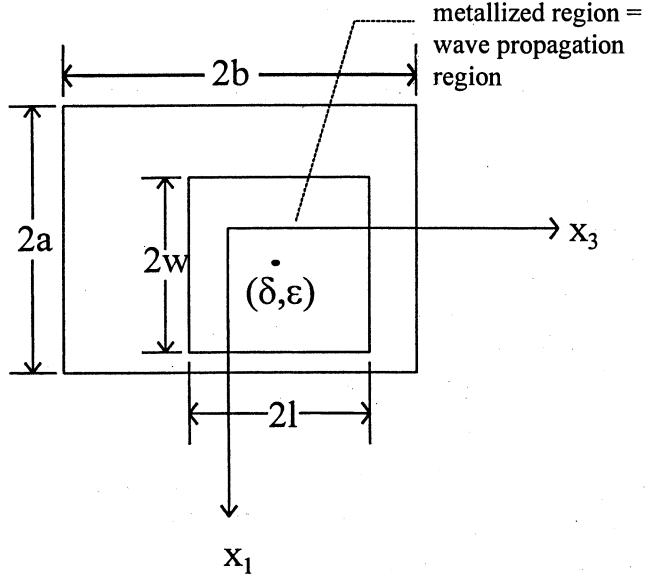


Fig. 4a. STW device plan view.

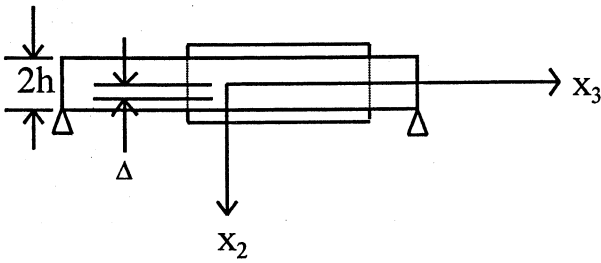


Fig. 3b. BAW device cross-section.

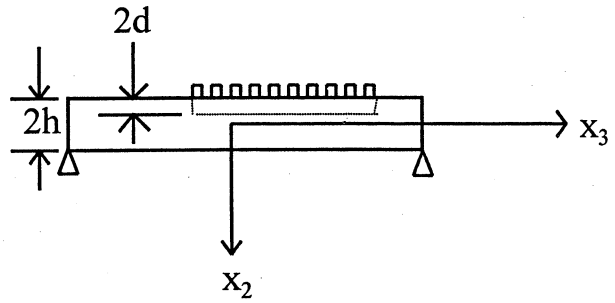


Fig. 4b. STW device cross-section.

and the simple surface transverse wave (STW) mode described by

$$u_1 = M \cdot \cos[\beta(x_3 - \epsilon)], \quad (10a)$$

for

$$\delta - w \leq x_1 \leq \delta + w, \quad (10b)$$

$$-h \leq x_2 \leq -h + 2d, \quad (10c)$$

$$\epsilon - l \leq x_3 \leq \epsilon + l. \quad (10b)$$

In equations (9) and (10),  $M$  represents the modal amplitude, and  $\beta \equiv 2\pi/\lambda$  represents the relevant propagation constant. For the BAW modes, we consider  $2h = p\lambda/2$  with  $p=1,3,5,\dots$  denoting the

harmonic number. For the STW mode, we take the length  $l$  of the active area to be a large, integer number of wavelengths and consider  $h \gg d$ .

The modes are considered to be propagating in flat, rotated Y-cut quartz plates simply supported along rectangular edges as illustrated in Figures 3 and 4. For the BAW case, we allow the mode location to be displaced from the central plane of the substrate by a distance  $\Delta$  along the thickness direction. For both BAW and STW modes, we consider the in-plane mode location to be displaced by  $(\delta, \epsilon)$  along the rotated X- and Z-axes respectively. The calculated normal acceleration sensitivities are listed in Table 2.

The various terms in the simplified solutions clarify the basic properties of the normal acceleration sensitivities:

TABLE 2 - Normal Acceleration Sensitivities of Simple Bulk and Surface Modes for Rotated Y-Cut Quartz Flat Plate Resonators Simply Supported Along Rectangular Edges

Mode	Normal Acceleration Sensitivity
BAW a-mode	$\sum_m^{\text{odd}} \sum_n^{\text{odd}} -\frac{1}{p} \frac{1}{v_a^2} \frac{96}{\pi^5} \frac{a^2 b^2 \left[ \left(\frac{m}{n}\right) E_{2222} b^2 + \left(\frac{n}{m}\right) F_{2222} a^2 \right]}{\gamma_{11} m^4 b^4 + \gamma_{33} n^4 a^4 + (2\gamma_{13} + 4\gamma_{55}) m^2 n^2 a^2 b^2} \cos(\alpha_m \delta) \sin(2\beta_p \Delta) \cos(\kappa_n \epsilon) \frac{\sin(\alpha_m w)}{\alpha_m w} \frac{1}{h} \frac{\sin(\kappa_n l)}{\kappa_n l}$
BAW b-mode	$\sum_m^{\text{odd}} \sum_n^{\text{odd}} -\frac{1}{p} \frac{1}{v_b^2} \frac{96}{\pi^5} \frac{a^2 b^2 \left[ \left(\frac{m}{n}\right) E_{2323} b^2 + \left(\frac{n}{m}\right) F_{2323} a^2 \right]}{\gamma_{11} m^4 b^4 + \gamma_{33} n^4 a^4 + (2\gamma_{13} + 4\gamma_{55}) m^2 n^2 a^2 b^2} \cos(\alpha_m \delta) \sin(2\beta_p \Delta) \cos(\kappa_n \epsilon) \frac{\sin(\alpha_m w)}{\alpha_m w} \frac{1}{h} \frac{\sin(\kappa_n l)}{\kappa_n l}$
BAW c-mode	$\sum_m^{\text{odd}} \sum_n^{\text{odd}} -\frac{1}{p} \frac{1}{v_c^2} \frac{96}{\pi^5} \frac{a^2 b^2 \left[ \left(\frac{m}{n}\right) E_{2121} b^2 + \left(\frac{n}{m}\right) F_{2121} a^2 \right]}{\gamma_{11} m^4 b^4 + \gamma_{33} n^4 a^4 + (2\gamma_{13} + 4\gamma_{55}) m^2 n^2 a^2 b^2} \cos(\alpha_m \delta) \sin(2\beta_p \Delta) \cos(\kappa_n \epsilon) \frac{\sin(\alpha_m w)}{\alpha_m w} \frac{1}{h} \frac{\sin(\kappa_n l)}{\kappa_n l}$
STW	$\sum_m^{\text{odd}} \sum_n^{\text{odd}} \frac{1}{v_{\text{STW}}^2} \frac{96}{\pi^4} \frac{a^2 b^2 \left[ \left(\frac{m}{n}\right) E_{3131} b^2 + \left(\frac{n}{m}\right) F_{3131} a^2 \right]}{\gamma_{11} m^4 b^4 + \gamma_{33} n^4 a^4 + (2\gamma_{13} + 4\gamma_{55}) m^2 n^2 a^2 b^2} \cos(\alpha_m \delta) \cos(\kappa_n \epsilon) \frac{\sin(\alpha_m w)}{\alpha_m w} \frac{1}{h} \frac{\sin(\kappa_n l)}{\kappa_n l}$

NOTE:  $\alpha_m \equiv \frac{m\pi}{2a}$ ;  $\kappa_n \equiv \frac{n\pi}{2b}$ ;  $E_{L\gamma M\alpha}$  and  $F_{L\gamma M\alpha}$  as defined in (10,11);  $\beta_p \equiv \frac{2\pi}{\lambda} = \frac{p\pi}{2h}$

- $\sum_m^{\text{odd}} \sum_n^{\text{odd}}$  - the summations reflect the fact that the flexural deformation is described by a Fourier series expansion
- +/- - reflects that the sign of the frequency shift can be correctly determined
- $\frac{1}{p}$  - proportional to inverse of the harmonic number for BAW modes
- $\frac{1}{v_{\text{mode}}^2}$  - proportional to inverse square of the modal velocity
- $\frac{96}{\pi^4}$  or  $\frac{96}{\pi^5}$  - proportionality constant depends on whether the device is a bulk or surface wave resonator
- quotient - directly proportional to complicated sum of linear and nonlinear stiffnesses via  $E_{L\gamma M\alpha}$  and  $F_{L\gamma M\alpha}$
- inversely proportional to linear stiffnesses controlling flexural rigidity via Voigt's anisotropic plate stiffnesses  $\gamma_{11}$ ,  $\gamma_{33}$ ,  $\gamma_{13}$ , and  $\gamma_{55}$
- net proportionality to the square of the lateral dimensions, i.e., proportional to area of the major surface
- $\left[ \left(\frac{m}{n}\right) E_{L\gamma M\alpha} b^2 + \left(\frac{n}{m}\right) F_{L\gamma M\alpha} a^2 \right]$  enables aspect-ratio compensation when  $E_{L\gamma M\alpha}$  and  $F_{L\gamma M\alpha}$  are of opposite sign
- $\cos(\alpha_m \delta)$  - proportionality to an  $x_1$ -direction mode center offset
- $\sin(2\beta_p \Delta)$  - proportionality to an  $x_2$ -direction mode center offset for BAW modes
- $\cos(\kappa_n \epsilon)$  - proportionality to an  $x_3$ -direction mode center offset

- $\frac{\sin(\alpha_m w)}{\alpha_m w}$  - proportionality to the  $x_1$ -direction mode profile
- $\frac{1}{h}$  - inversely proportional to plate thickness, with no proportionality to the  $x_2$ -direction mode profile
- $\frac{\sin(\kappa_n \epsilon)}{\kappa_n \epsilon}$  - proportionality to the  $x_3$ -direction mode profile

#### PROPERTIES OF THE SIMPLE MODE SOLUTIONS

The properties of the BAW and STW solutions are essentially identical with regard to most design parameters, particularly with respect to in-plane variations such as mode center offset. The differences in sign and the additional  $1/\pi$  factor in the BAW case are not significant with regard to the nature and properties of the solutions.

There are two factors which appear only in the BAW solution. First, the consideration of harmonic operation in the BAW case leads to a factor of  $1/p$  not found in the STW case, where only fundamental mode operation is considered. Second, the BAW case includes a term  $\sin(2\beta\Delta)$  causing the BAW acceleration sensitivity to be proportional to the thickness direction mode center offset, whereas the STW acceleration sensitivity has no dependence upon the thickness direction properties of the acoustic mode shape.

The BAW and STW acceleration sensitivities both depend upon the plate thickness. In the BAW case,

TABLE 3 - Comparison of Simple and Trapped Energy STW Mode Normal Acceleration Sensitivities

Mode Type	Normal Acceleration Sensitivity
Simple	$\sum_m^{\text{odd}} \sum_n^{\text{odd}} \frac{1}{v_{\text{STW}}^2} \frac{96}{\pi^4} \frac{a^2 b^2 \left[ \left( \frac{m}{n} \right) E_{3131} b^2 + \left( \frac{n}{m} \right) F_{3131} a^2 \right]}{\gamma_{11} m^4 b^4 + \gamma_{33} n^4 a^4 + (2\gamma_{13} + 4\gamma_{55}) m^2 n^2 a^2 b^2} \cos(\alpha_m \delta) \cos(\kappa_n \epsilon) \frac{\sin(\alpha_m w)}{\alpha_m w} \frac{1}{h} \frac{\sin(\kappa_n l)}{\kappa_n l}$
Trapped Energy	$\sum_m^{\text{odd}} \sum_n^{\text{odd}} -\frac{1}{v^2} \frac{24}{\pi^2} \left[ \frac{a^2 b^2 \left[ \left( \frac{m}{n} \right) E_{3131} b^2 + \left( \frac{n}{m} \right) F_{3131} a^2 \right]}{\gamma_{11} m^4 b^4 + \gamma_{33} n^4 a^4 + (2\gamma_{13} + 4\gamma_{55}) m^2 n^2 a^2 b^2} \right] \cos(\alpha_m \delta) \cos(\kappa_n \epsilon)$ $* \left[ \frac{2 \sin(\alpha_m w)}{\alpha_m w} + \frac{\sin(\{2\chi + \alpha_m\} w)}{(2\chi + \alpha_m) w} + \frac{\sin(\{2\chi - \alpha_m\} w)}{(2\chi - \alpha_m) w} \right] \left[ \left( \frac{1}{h} \right) \cdot \left( \frac{1 - 2\xi h \cdot \coth(2\xi h)}{2\xi h} \right) \right]$ $* \left\{ \left[ \frac{2 \sin(\kappa_n s)}{\kappa_n s} + \frac{\sin(\{2\beta + \kappa_n\} s)}{(2\beta + \kappa_n) s} + \frac{\sin(\{2\beta - \kappa_n\} s)}{(2\beta - \kappa_n) s} \right] + \left[ \frac{2\{2\zeta \cos(\kappa_n s) - \kappa_n \sin(\kappa_n s)\}}{[4\zeta^2 + \kappa_n^2] s} \right. \right.$ $\left. \left. - \frac{2\zeta \cos[(2\beta + \kappa_n) s] - (2\beta + \kappa_n) \sin[(2\beta + \kappa_n) s]}{[4\zeta^2 + (2\beta + \kappa_n)^2] s} - \frac{2\zeta \cos[(2\beta - \kappa_n) s] - (2\beta - \kappa_n) \sin[(2\beta - \kappa_n) s]}{[4\zeta^2 + (2\beta - \kappa_n)^2] s} \right] \right\}$ $* \left[ 1 + \frac{1}{2\zeta s} + \left( \frac{\beta \zeta}{\beta^2 + \zeta^2} \right) \frac{\cos(2\beta s)}{2\beta s} + \left( \frac{\zeta^2}{\beta^2 + \zeta^2} \right) \frac{\sin(2\beta s)}{2\beta s} \right]^{-1}$ <p>+ 12 other smaller terms</p>

the thickness is also the frequency determining dimension. As a result, there is a net 1/f frequency dependence of the BAW acceleration sensitivity for scaled designs (i.e., similar diameter- and electrode-to-thickness ratios) provided that fabrication tolerances are properly controlled. Hence a  $10^{-10}/g$  design at 10 MHz could yield  $10^{-12}/g$  when implemented as a 1 GHz microresonator.

The BAW acceleration sensitivity depends upon the harmonic number in two ways. First, there is a direct 1/p dependence upon harmonic number p. Second, the propagation constant  $\beta_p = 2\pi/\lambda = p\pi/2h$  appears in the  $\sin(2\beta_p \Delta)$  term, which may be rewritten as  $\sin(p \times 2\beta_1 \Delta)$ . The direct 1/p dependence tends to decrease the acceleration sensitivity with increasing harmonic. If the thickness direction mode center offset  $\Delta$  is taken to be the same for the various harmonics, then the  $\sin(2\beta_p \Delta)$  term increases with increasing harmonic, tending to increase the acceleration sensitivity with increasing harmonic. Published experimental results on the harmonic dependence of acceleration sensitivity

indicate an initial decrease in acceleration sensitivity with increasing harmonic number, after which the acceleration sensitivity is essentially constant or slightly increased (12).

The qualitative effects of energy trapping on the acceleration sensitivity can be understood readily from the solutions presented here by taking the case of a more tightly trapped mode to correspond to an increased modal amplitude  $M_a$ ,  $M_b$ , or  $M_c$  in conjunction with a decrease in the active area given by  $2l \times 2w$ .

The various terms in the solutions listed in Table 2 arise from specific aspects of the phenomenon. For example, the Fourier series expansion, direct proportionality to substrate area, inverse proportionality to substrate thickness, and inverse proportionality to the stiffnesses governing flexure are all reflections of the flexural biasing deformation. By considering the similarities and differences between the cases of normal and in-plane accelerations, the results given for the normal

acceleration sensitivities readily can be extended to the understanding of the in-plane acceleration sensitivities.

#### NORMAL SENSITIVITIES OF TRAPPED ENERGY MODES

The simple mode solutions as listed in Table 2, while instructive, are exact only for the considered cases of uniform amplitude, pure-mode propagation (only  $u_1$  or  $u_2$  or  $u_3$  present). In reality, the modes driven in practical resonators have spatially varying amplitudes and components of the particle displacement along all three axes ( $u_1$ ,  $u_2$ , and  $u_3$  all present). Such modes lead to solutions with slightly more complicated functional behaviors, and to solutions that are the sum of multiple terms. This is illustrated in Table 3 wherein the simple mode STW solution is compared to the trapped energy STW solution from (10). Additional complications are introduced in the Rayleigh wave case where the surface acoustic wave (SAW) mode is composed of the sum of four partial waves.

It is important to note that the simple mode solutions correspond to the dominant terms in the trapped energy solutions. Hence, where aspect-ratio compensation is not used (as, for example, in 4-point mounted BAW resonators), the simple mode solutions provide useful guidance for the design of  $10^{-10}/g$  performance devices.

The dominant term in the trapped energy solutions can be minimized readily through the use of aspect-ratio compensation, in which case the properties of the smaller terms must be considered. The most significant difference in the properties of the smaller terms as compared to the dominant term is in their proportionalities to in-plane mode center offsets. Whereas the dominant term is proportional to the cosines of the mode center offsets, the various smaller terms have combinations and permutations of sine and cosine proportionalities.

Techniques for minimizing the acceleration sensitivity through control of the acoustic mode shape have been proposed by Ballato (3), EerNisse, et al. (4-7), and Smythe and Horton (8). The solutions presented in Table 2 clarify the distinctly different roles of mode shape, i.e. "profile", and mode location. Note that the theoretical zero acceleration sensitivity of the ideal (symmetric), rotated Y-cut simple BAW resonator considered here arises solely from the thickness direction symmetry. While the trapped energy resonator will, in fact, require a full three-dimensional symmetry to obtain zero acceleration sensitivity, the dominant and hence most important symmetry in

practice in the AT-cut is not the in-plane symmetry but, rather the thickness-direction symmetry (see, for example, (13)).

#### REDUCTION TO PRACTICE

The essential form of all of the design equations presented in Tables 2 and 3 is

$$\Gamma = \sum (\text{multiple terms}) \quad (11)$$

where each term is of the form

$$(\text{proportionality constant} \times \text{dimensional tolerances}) \quad (12)$$

The form of equation (12) is particularly instructive, as it establishes two basic approaches to minimizing the acceleration sensitivity:

1. Develop improved designs which minimize the proportionality constant. This can be done by applying basic structural engineering principles to the resonator/mounting system and/or aspect-ratio compensation.
2. Fabricate to tighter dimensional tolerances. Note that this reduces the acceleration sensitivity both directly as shown in equation (12), but also indirectly through the proportionality constant when aspect-ratio compensation is employed. A detailed analysis of the dimensional tolerance terms leads to the conclusion that the thickness direction asymmetry is on the order of 100x more significant than the in-plane asymmetries for common BAW device designs.

These approaches are valid for all types of piezoelectric resonators including BAW, SAW, STW, TFR, etc.

#### WHAT WORKS AND WHY

A number of low acceleration sensitivity resonator types have been discussed in the literature. Of particular note are the successes of BVA, viscoelastic mount, aspect-ratio compensated SAW, and miniature STW technologies (14-17). These technologies have in common one very important aspect - *they work!* Each of these technologies has at its heart one or both of two fundamental techniques, namely the reduction of the resonator deformation or the application of compensation techniques.

## Deformation Reduction

The resonator is sensitive to deformation. Therefore, improved device and mounting structure designs which minimize the resonator deformation directly reduce the observed acceleration sensitivity.

The BVA embodies this principle in two ways (14). First, the resonator mounting structure is symmetric with respect to the top and bottom of the plate, thus eliminating the shear deformations which would be generated by in-plane accelerations using conventional mounting techniques. Second, the "condensers" which carry the electrodes serve to stiffen the structure with respect to the flexural deformations generated by normal accelerations.

The viscoelastic mount embodies this principle by providing vibration isolation between a set of rigid support posts and the resonator blank (15).

SAW technology embodies this principle in the use of ceramic stiffeners attached to the oscillator package (16).

The miniature STW also embodies this principle through the use of rigid ceramic packages and ceramic hybrid circuits. In addition, the miniature STW reduces the flexural deformation by minimizing the plate area and maximizing the plate thickness (17).

Note that reducing the deformation of the resonator improves the acceleration sensitivity regardless of the fabrication tolerances involved. Note also that the design of improved resonator/mounting structures which minimize the deformation is a structural engineering problem and does not per se require any expertise in piezoelectricity.

## Compensation Techniques

Two distinctly different but equally useful compensation techniques are available for low acceleration sensitivity design, namely aspect-ratio compensation and mode shape symmetry compensation.

Aspect-ratio compensation refers to the minimization of acceleration sensitivity through the use of rectangular crystal blanks with carefully controlled length-to-width or aspect-ratios. This works because the deformation sensitivities are of different signs and different magnitudes along different directions. As a result, a positive sensitivity along one direction can be compensated for by a negative sensitivity along another direction, with the lengths of the sides adjusted to

equalize the net magnitudes of the two sensitivities. This principle has been embodied in state-of-the-art SAW devices.

The use of mode shape symmetry to achieve low acceleration sensitivity has been demonstrated for both BAW and STW devices (18,19). What has not been appreciated to date is that mode shape symmetry is a compensation technique. That is, mode shape symmetry compensation relies upon having positive and negative sensitivities being exactly equal and opposite in all three-dimensions. The importance of this point cannot be understated, as there is a significant difference between the understanding communicated by the statement that "the theoretical acceleration sensitivity of an ideal BAW resonator is zero" as opposed to "the ideal BAW device is intrinsically compensated."

Both aspect-ratio and mode shape symmetry compensations are by nature dependent upon the dimensional tolerances achievable in production. For aspect-ratio compensation, each additional order of magnitude in acceleration sensitivity compensation requires a corresponding order of magnitude improvement in dimensional tolerances.

Mode shape symmetry compensation also requires the use of a resonator/mounting structure which is fully symmetric in three dimensions. This then requires the use of plano-plano or biconvex resonator geometries jointly with exceptional control of electrode thicknesses or the use of BVA technology.

## CANDIDATE RESONATOR DESIGNS

Understanding what works and why leads directly to a variety of candidate low acceleration sensitivity resonator designs. The designs which follow are not presented as optimum designs, but rather are intended to stimulate the creative process.

### Damped Package

One way to minimize the deformation is through the incorporation of vibration isolation into the mounting structure. The vibration isolator acts as a mechanical low pass filter, and isolates the resonator from vibrations at frequencies higher than the mechanical resonance frequency of the mounting structure. The primary difficulty in implementing such a system is the need to limit the Q of the mechanical resonance. For resonators such as STW, this may be

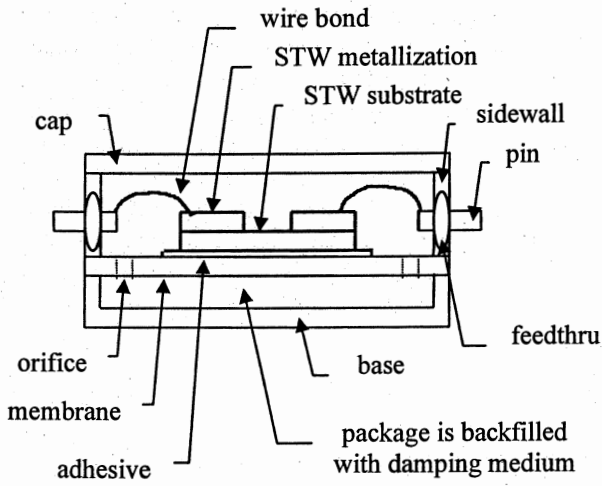


Fig. 5. Cross-sectional view of damped package.

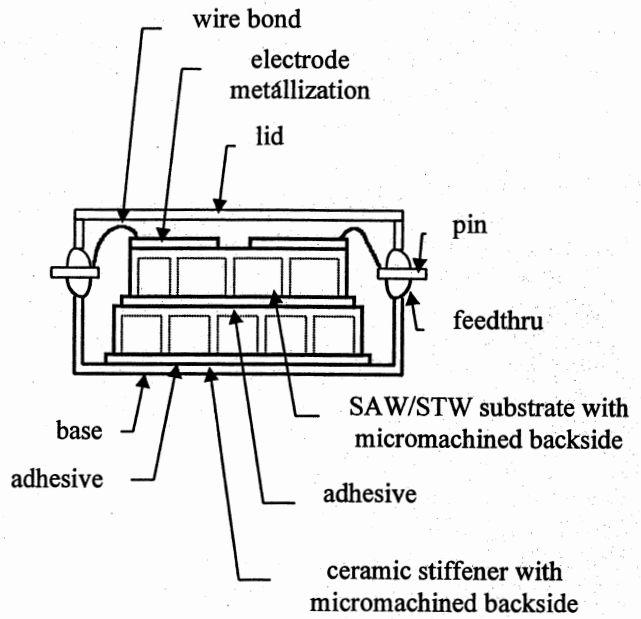


Fig. 6. Cross-sectional view of "waffle" mount.

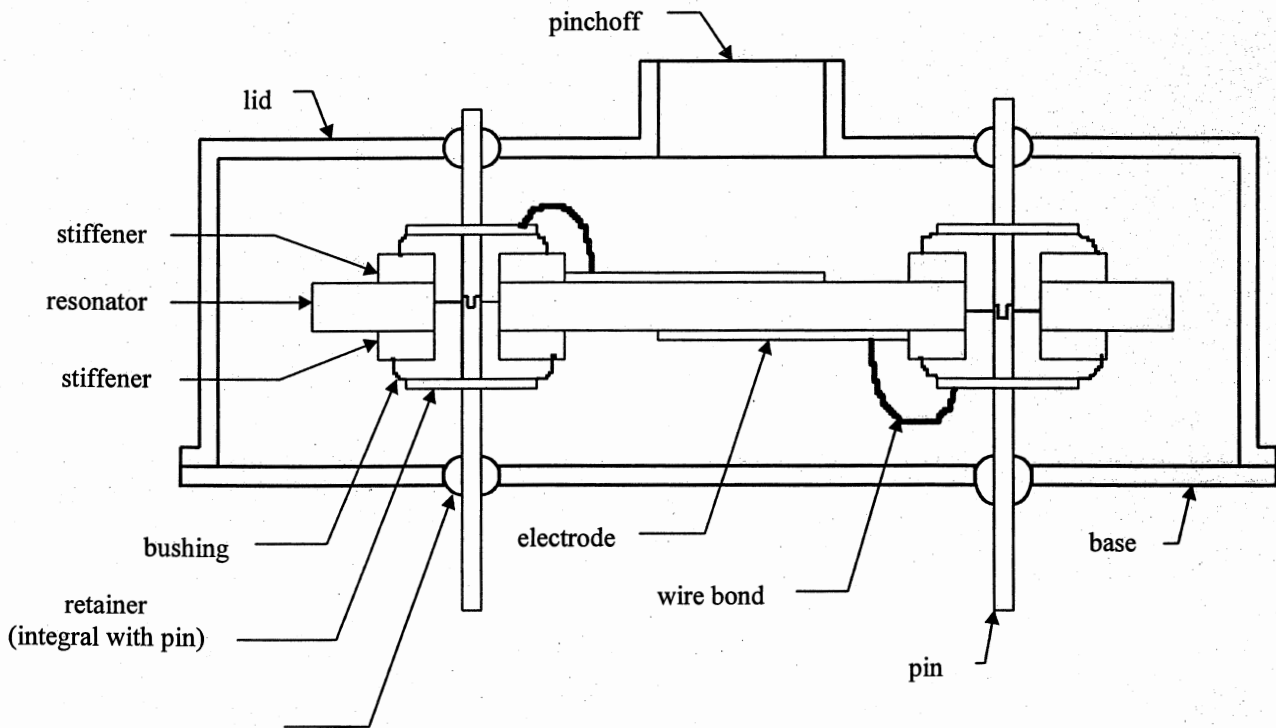


Fig. 7. Cross-sectional view of improved four-point mount.

accomplished by filling the resonator package with a damping medium. Hence, a damped package could be built as shown in Figure 5.

#### “Waffle” Mount

Another way to minimize the deformation is through the incorporation of micromachined stiffening members into the resonator and/or mounting structure. This technique is particularly appropriate for SAW and STW resonators where the structural members can be formed as an integral part of the resonator substrate by a simple backside etch. A device fabricated using a “waffle” shaped etch pattern is illustrated in Figure 6.

#### Improved Four-Point Mount

The deformation of conventional four-point mounted BAW resonators can be reduced in several ways. As noted above, the mounting structure may be designed to incorporate vibration isolation. In addition, the deformation may be reduced by the addition of suitable stiffeners and/or a cantilever construction.

The four-point mounted BAW device may also implement both aspect-ratio and mode shape symmetry compensations. Aspect-ratio compensation is readily applied through the use of a rectangular blank whose lateral dimensions can be controlled with great precision using currently available fabrication technologies. Mode shape symmetry is somewhat more difficult to apply, owing to the difficulty of achieving in practice a full three-dimensional symmetry of both the mounting structure and the acoustic mode shape. This is particularly true when the electrodes are deposited upon the quartz substrate.

A proposal for an improved four-point mount which applies both deformation reduction and compensation techniques is shown in Figure 7.

#### CONCLUSIONS

The cause of acceleration sensitivity is now well understood. The driving factor behind the acceleration-induced frequency shift is the deformation of the resonator.

Design equations for BAW, SAW, and STW resonators have been derived using the perturbation theory of Tiersten. The design equations clarify the functional dependencies of the acceleration sensitivities on the full

range of crystal resonator design and fabrication parameters.

Low acceleration sensitivity can be achieved by minimizing the resonator deformation and/or by using compensation techniques. Minimization of the resonator deformation is a basic structural engineering problem. This approach has the advantage of achieving low acceleration sensitivity without regard to fabrication tolerances. The application of compensation techniques is conceptually simpler, but requires extreme attention to fabrication tolerances in order to achieve substantially low acceleration sensitivity.

#### REFERENCES

1. Kosinski J, 1996, Proc 1996 IEEE Int'l Freq Cont Symp, 439-448
2. Tiersten H, 1978, J Acoust Soc Am, 64, 832-837
3. Ballato A, 1989, U.S. Patent 4,836,882
4. EerNisse E and Ward R, 1989, U.S. Patent 4,837,475
5. EerNisse E et al., 1990, U. S. Patent 4,935,658
6. EerNisse E et al., 1991, U.S. Patent 5,022,130
7. EerNisse E et al., 1992, U.S. Patent 5,168,191
8. Smythe R and Horton W, 1990, Proc 44th Ann Freq Cont Symp, 437-443
9. Kosinski J and Ballato A, 1993, IEEE Trans UFFC, 40, 532-537
10. Kosinski J et al., 1995, Proc 1995 IEEE Int'l Freq Cont Symp, 486-493
11. Kosinski J, 1995, 1995 IEEE Int'l Ultrason Symp Proc, 187-196
12. Filler R et al., 1983, Proc 37th Ann Freq Cont Symp, 265-271
13. Filler R et al., 1982, Proc 36th Ann Freq Cont Symp, 215-219
14. Besson R et al., 1996, Proc 1996 IEEE Int'l Freq Cont Symp, 457-463
15. Weglein R, 1989, Proc 43rd Ann Freq Cont Symp, 433-438
16. Andres D et al., 1995, 1995 IEEE Int'l Ultrason Symp Proc, 177-182
17. Cavin M and Almar R, 1995, Proc 1995 IEEE Int'l Freq Cont Symp, 476-485
18. EerNisse E et al., 1990, IEEE Trans UFFC, 37, 566-570
19. Huynh D et al., 1995, Proc 1995 IEEE Int'l Freq Cont Symp, 494-498

## INFLUENCE OF THE MOUNTING STRUCTURE ON MAIN PERFORMANCES OF THE BVA RESONATOR

J.J. Boy\*, F. Deyzac\*\*, R. Petit\*\*\*, P. Maitre\*

\* LCEP / ENSMM - Route de Gray - La Bouloie - 25030 Besançon Cedex - FRANCE

\*\* Office National d'Etudes et de Recherches Aéronautiques - BP 72 - 93322 Châtillon Cedex - FRANCE

\*\*\* CELAR, BP 7419 - 35174 BRUZ Cedex - FRANCE

### ABSTRACT

In previous paper, we have shown that G-sensitivity of a BVA quartz resonator, attributed for the main part to the design, is very low (largely lower than  $10^{-10}/G$ ) and can reach zero when its structure presents a perfect symmetry around the three axes. By finite elements analysis, we had quantified the influence of some symmetry defects due to manufacturing process (as orientation of the mounting, shift between the vibration area center and the blank center, ...) and summarized comparisons with experimental measurements.

In this paper, we present new theoretical points of view and experimental measurements of the influence of the resonator suspension on other parameters as resonant-frequency. We have calculated the frequency shift due to the clamping of the four rigid clips which hold the three quartz pieces of the resonator (the 2 « condensers » electrode-holders and the vibrating part). We note also that a difference in the tightening of one or two clips can produce larger frequency shift and consequently larger accelerometric sensitivity. Furthermore, we have observed that the long term drift can be affected by this kind of manufacturing defect.

At least, we show that the BVA SC-cut 10 MHz 3<sup>rd</sup> Over. produced by LCEP does not exhibit frequency jumps during a complete survey of its long term drift when some cares in the manufacturing process are taken.

**Keywords :** Quartz crystal, BVA resonators, accelerometric sensitivity.

### 1. INTRODUCTION

Last years we have implemented some improvements in the industrialization process of "tactical" mini-BVA (SC-cut 10 MHz third Overtone) to tentatively reduce the accelerometric sensitivity. That is why some keypoints had been systematically discussed and tested, particularly in [1, 2], in order to define how the performances can be reproduced according to different specifications.

As indicated in [3] and [4], the principal keypoints of the design work towards perfecting the symmetries around  $\Psi$ -axis and the median plane. For that, the resonator is composed of two "condensers" electrode-holders on both sides of the active part, these three quartz pieces being holdered by four rigid clips associated to a symmetrical suspension consisting in 4 pairs of springs.

Furthermore, the vibrating part of the resonator is linked to its external support by four rigid and short quartz bridges, oriented along the projection of the crystallographic axes.

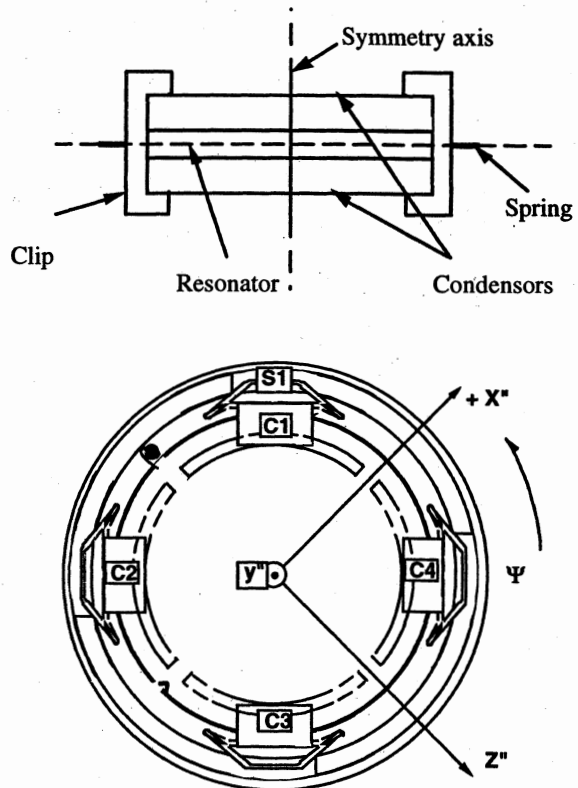


Fig. 1 : Diagram and top view of the mini-BVA (called BVA<sub>2</sub>)

So, after having pointed out selected geometrical defects of the vibrating part of the resonator, we are interested here by the influence of the mounting structure (so called « suspension ») on the resonant frequency in the intention of taking into account the unavoidable defects of manufacturing and improving its.

### 2. BRIEF REVIEW ON FINITE ELEMENTS METHOD MODELLING

With the support of DRET, ONERA, engaged in studies dedicated to reduce sensitivities of quartz

resonators, has developed an appropriate simulation tool to better understand the sensitivity mechanisms of resonators and to evaluate the influence of manufacturing defects. This tool involves a finite elements method for modelling the resonator and the mounting structure. At least, we use a theoretical stress/frequency model [5].

We recall just here that the model takes into account the crystallographic cut ( $\phi$ ,  $\theta$ ), the crystal orientation ( $\psi$ ) in the section plate (which is defined by the direction of the 2 bridges along Z'' ideally positioned at  $\psi = 0^\circ$ ) and calculates the wave polarization directions and the rotated coefficients of elasticity.

At least, we note that the main hypothesis for calculation is that the frequency shift depends only on stress variations in the central zone of the vibrating area (i.e. center of plate without defect) because the resonator is designed to confine energy at its center (with, for example, the realisation of a convexity in one face of the plate).

### 3. INFLUENCE OF MECHANICAL DEFECTS ON THE RESONANT FREQUENCY

#### 3.1. Estimation of the nominal stresses induced by the mounting structure :

The first simulation was performed on a model presenting a perfect symmetry around the three axes. It included the mounting structure (i.e. clips and springs) which was perfectly fit into the median plane and embedded in the ring. We have verified that this BVA structure can be ideally "super-symmetric" and, consequently, non sensitive to the acceleration. By introducing the radius curvature and some mechanical defects of the vibrating part, we have shown that the accelerometric sensitivity increases up a few parts of  $10^{-11}/g$  [1]. However, we have established that the measured accelerometric sensitivity stays slightly higher than the calculated one. It is why we want to complete our study by introducing mechanical defects of the suspension.

We have pointed out two kinds of influences : first in the positioning of each clip around the three quartz pieces, and second in the stresses induced by the clip and/or the spring.

Each clip holders the three quartz pieces along the vertical axis (i.e. Y''-axis) with a nominal clamping estimated at 2.8 N (Fig. 2a). This value depends on the material used, the difference between the thickness of the « sandwich » and the gap between the 2 lips of the clip and, of course, on the temperature. So, the stress induces by one clip on the quartz crystal can be very different from one clip to other one. This stress is called « axial force » :  $F_a$ . Finally, the total stress induces axially on the edge of the vibrating part of the resonator is nominally equal to 11.2 N, distributed in 4 small areas.

As the radial force  $F_r$  induced by each pair of springs, it has been evaluated as indicated in Fig. 2b. For a differential of about 20  $\mu m$  between the diameter defined by the ends of springs and the internal diameter of the ring supporting its, the radial force is equal to about 1 N.

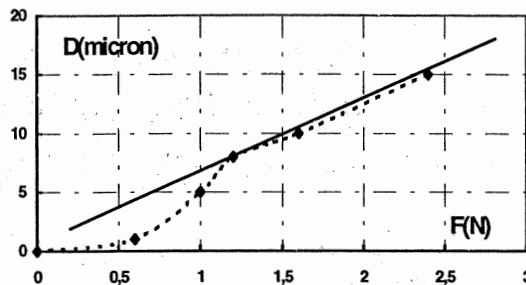


Fig. 2a : Measurements of the stiffness of one clip

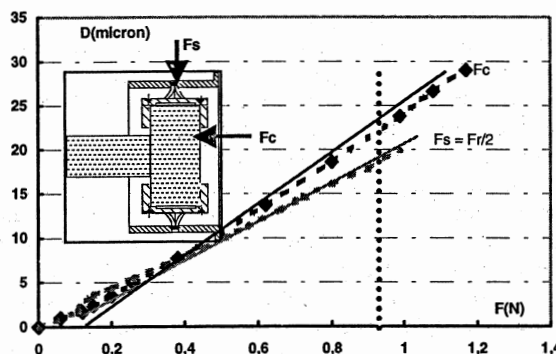


Fig. 2b : Measurements of the mounting structure stiffness

First of all, we have calculated these two effects of clamping by finite elements modelling to compare experimental way and theoretical point of view. So, for  $F_s = 1$  N, we calculate a 20.4  $\mu m$  displacement in the direction of the applied force which has to be compared to the 20  $\mu m$  measured. As for the axial displacement due to  $F_c$ , the agreement is not so good, but the associated frequency-shift is in accordance to the measured one (see item 3.4). In conclusion, to calculate the force-frequency effect, we have used the following values as nominal stresses induced by the mounting structure :

$$F_a = 2.8 \text{ N for each clip}$$

$$F_r = 1 \text{ N for each pair of springs}$$

#### 3.2. Force-frequency effect :

The following table indicates the frequency shifts induced by a nominal clamping and the contribution of, in one hand, each clip and in other one, a pair of opposite springs. We note that the influence of these stresses on the resonant frequency is translated by the bridges in the vibrating part of the resonator. The four bridges are, in the nominal position, directed along the projection of the crystallographic axes and, so, defined by  $\psi = 0^\circ$ . The clips are numbered as indicated in the Fig. 1.

**Table 1** : Mounting structure effect on the resonant freq.

Axial forces (clips)	$\Delta f/f$ (in $10^{-9}$ )	Radial Forces (Springs)	$\Delta f/f$ (in $10^{-9}$ )
Clip #1	-2.95		
Clip #3	+7.30		
		Pairs #1-3	-14.5
Clip #2	-3.49		
Clip #4	+7.20		
		Pairs #2-4	+16.2
<b>TOTAL</b>	<b>+8.06</b>		<b>+1.7</b>

We see that the total frequency shift induced by the entire mounting structure is close to  $+1 \cdot 10^{-8}$ , i.e. 0.1 Hz for a 10 MHz  $3^{rd}$  Overtone.

We remark, in this table, that the force-frequency effects due to each clip or each pair of springs are very different. And the model being linear up to the anelastic behavior of the material used for clips and springs, a clamping two times higher than the nominal one induces a double frequency-shift. For example, if one spring is not well positioned in the ring (eventually due to the hyperstaticity of the structure), the radial force can increase and reach 5 to 10 times the nominal stress. Consequently, the frequency could shift of 1 to 2 Hz. So, if we do not take care on the manufacturing process, the mounting structure can slip during test under high random or sinusoidal vibrations without risk of damage because the resonator is still working but on a slightly different frequency...

As term of comparison, we give here the frequency-shift induces by the mounting structure of a « classical » resonator. For it, the stresses existing in the vibrating part of the resonator are generally trapped around the sealing due to the used technique. Indeed, the implementation of the sealing is realized at high temperature (i.e. higher than the working temperature) and so creates stresses when it is cooled down to the ambient. Furthermore, the differential dilatation of the base and the piece of quartz can induce more stresses in the plane of the resonator. Finally, the whole contribution of stresses induces a frequency-shift of a few  $10^{-7}$ , i.e. 10 to 50 times higher than for the BVA resonator.

We have calculated now the relative shift of the resonant frequency due to a slight variation of each clip around its nominal position (at  $45^\circ$  in respect to bridge direction). The associated frequency shifts are illustrated in the following figure. Fig. 3a is just for the clips (numbered #1 to #4) and Fig. 3b concerns only the effects of springs. We remark that the total frequency shift does not change if the entire structure rotates around the axis of symmetry. In contrary, the frequency-shift can become relatively important when just one clip is not positioned at its nominal place.

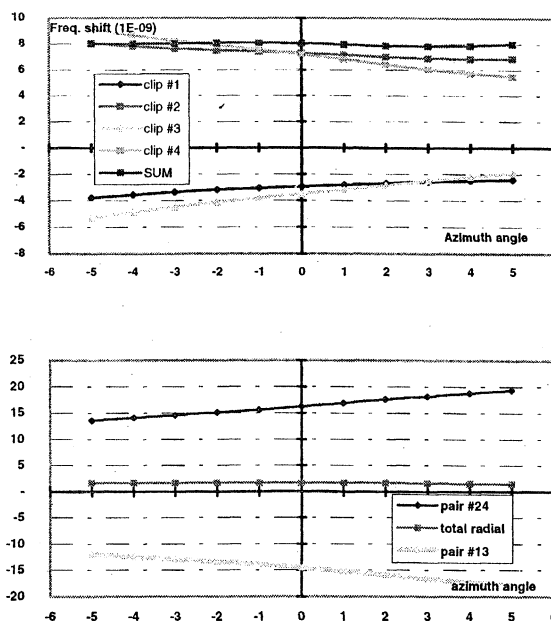


**Fig. 3** : Positioning default of clips and pair of springs (with nominal clamping)

### 3.3. Frequency-shift due to angle variations :

The frequency-shift due to variations of the cutting angles is illustrated by the following figure (Fig. 4). If for the nominal cut angles ( $\varphi_0, \theta_0$ ) the variation of the frequency is close to  $1 \cdot 10^{-8}$ , it is possible to find a couple of angles ( $\varphi, \theta$ ) for which the effect of the mounting structure reaches zero, without forgetting that the directions of bridges are defined by  $\psi = 0^\circ$ . But, we have to keep in mind the specification concerning the inversion point of the frequency-temperature curve (which is, for a time base, its operating temperature).

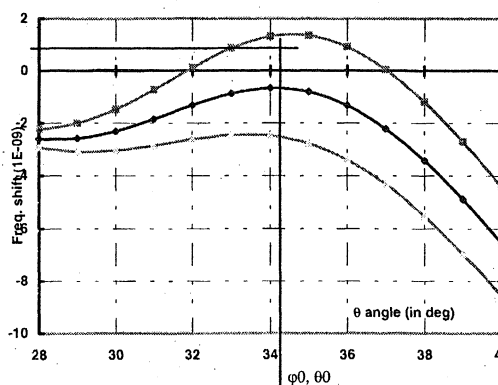


**Fig. 4** : Frequency-shift versus  $\theta$ -angle

Since the effect of the mounting structure is more or less important on the nominal frequency and not always well defined, it appears more interesting to search the direction of the bridges in which the clamping effect is negligible. In other words, we have to calculate the influence of a nominal clamping when  $\psi$ -angle is rotated.

Fig. 5 illustrates the frequency-shift due to a 90° rotation of the 4 bridges around the axial axis, Y''. It is evident that the springs follow the clips, being welded together, but the knowledge of each contribution is necessary when the stresses induce by springs or clips are different of the nominal ones. We note two directions of insensitivity to radial and axial stresses which are close to 0 and 45°. The two zero crossings are quasi similar for  $\psi = 43^\circ$ . So, this direction seems more interesting than the previous one.

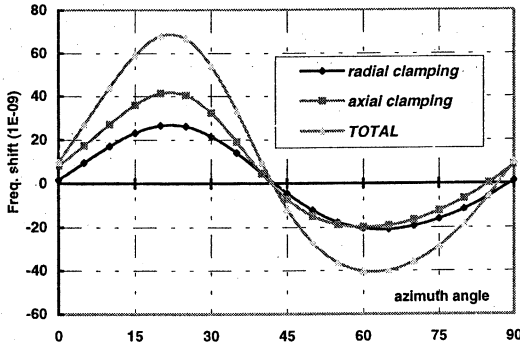


Fig. 5 : Frequency-shift versus bridges orientation

Unfortunately, it is not possible to perform this calculation at other temperatures than 25 °C due to the unknowledge of the temperature variation of the third order elastic coefficients, used for this kind of calculation. So, complementary experiments are needed.

### 3.4. Experimental measurements :

Our first experiment has been realized at ambient temperature. We have applied an axial force « Fc » on the top condenser of a working resonator (at 10 MHz, 3<sup>rd</sup> Ov.). Though temperature was not controlled, it has been possible (as indicated in Fig. 6) to follow the output frequency of the oscillator when force is applied. This figure shows first a good repeatability when force is stabilized and second a linear behavior up to 2 N. This experiment exhibits a frequency variation of about  $1.3 \cdot 10^{-7}$  for 1 N, when the calculated value is  $1.03 \cdot 10^{-7}$ , taking into account the contribution of the gap which is decreased under pressure. This contribution is of  $2 \cdot 10^{-8}$ .

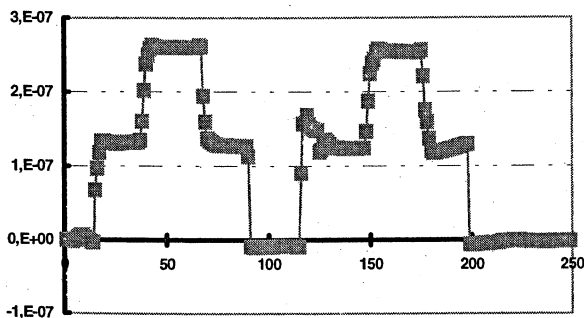


Fig. 6 : Frequency-shift versus axial force Fc (steps at 1 and 2N)

But, we have also observed that the mounting structure can be move and leave its positioning in the ring. In that case, the radial stress will be very different and will induce an important and permanent frequency jump. This disadvantage can appear under high level of vibrations and it is not always measurable, particularly, when the resonant frequency is controlled in a « PI » bridge (for which the precision is around a few parts of  $10^5$ ).

The second experiment has been realized on three different resonators for which the bridges of the vibrating part have been rotated around Y'' and are defined by  $\psi = -10$  for the first one, 0 for the second and  $+10^\circ$  for the third. After stabilization at the inversion temperature, we have checked the resonance frequency when the « sandwich » is holdered by one or two pairs of clips. At each step, the frequency is compared to this obtained without stress. So, the following table shows that the zero-sensivity of the mounting structure is located between  $\psi = 0$  and  $\psi = -10^\circ$ .

Similar results could be deduced from [6].

Table 2 : Frequency-shift versus bridges orientation (nominal position :  $\psi = 0^\circ$ ) @ TinV

$\Delta F/F$ (in $10^{-8}$ )	$\psi = -10^\circ$	$\psi = 0$	$\psi = +10^\circ$
with C1/C3	-0,6	1,0	0,8
with C2/C4	-2,3	-2,9	-4,7
with 4 clips	-0,5	0,6	-6,5

### 3.5. Influence of the mounting structure on the accelerometric sensitivity :

As we have calculated, last years, the influence on the accelerometric sensitivity of some geometrical defects of the vibrating part, we continue here in introducing the new selected defects concerning the mounting structure. The following Table indicates the ratio between the nominal frequency-shift for 1 G and this induced by a slight misorientation.

Table 3 : Accelerometric sensitivity versus position of clips (1 if  $\psi = 0^\circ$ ) – worst axis

$\Delta F/F \times 10^{-11}/g$	$-5^\circ$	$+5^\circ$
Clip #1	1.04	1.24
Clip #2	1.45	0.59
Clip #3	1.15	1.02
Clip #4	0.67	1.42
<b>TOTAL</b>	<b>1.07</b>	<b>1.065</b>

We show that the clips have not, here too, the same influence on the accelerometric sensitivity. Indeed, the clip #2 is the more influential on it and the frequency-shift increases of 45 % when it is positioned at  $-5^\circ$  of its nominal position. But globally, if the entire structure rotates around the Y''-axis, the frequency does not change really under acceleration.

In fact, we have seen that the sensitivity to an acceleration of the BVA depends strongly on the kinds of links existing between the springs and the ring which supports it. Indeed, the springs are not really embedded in the ring and so they can move under acceleration or vibrations. For example, when the acceleration is applied along X'-axis, the springs S1 and S4 are stressed against the ring when S2 and S3 become less stretched. In this case, the theoretical result of the accelerometric sensitivity is 10 times higher than in the case for which the four pairs of springs are embedded.

This observation prevails on us to define more precisely the conditions of embedding in our simulation tool in one hand and to improve part of the mounting structure, in other hand.

### CONCLUSION

If we have achieved last years some improvements in the realisation of the mini-BVA concerning particularly the vibrating area, our efforts concern today the reliability of its mounting structure. The research of a very low accelerometric sensitivity (on its worst axis) and a very good hardness under vibrations or shocks has obliged us to focus on the assembling of the suspension.

The systematic measurements of the clappings of the clips and the stresses induced by the springs have shown that the research of the « perfect » symmetry is not always very easy to obtain, particularly when it induces hyperstatic structure.

Our measurements have also shown that the elasticity of the mounting structure cannot create jumps during a complete survey of the resonant frequency (performed in CELAR) except, of course, if the ends of springs slip in the ring under high level of vibrations.

At least, due to the relative high influence of the stress induced by the suspension, we assume that the wear of the metal used for clip and spring can slightly affect the long term drift. But, a particular treatment can anneal the stresses trapped during manufacturing.

For all these reasons, it appears more interesting to check the direction of bridges for which the resonant frequency (at the operating temperature) is insensitive to the stresses induced axially or radially by the suspension.

### REFERENCES

1. J.J. BOY, F. DEYZAC, A. BERTHAUT : « Accelerometric and magnetic sensitivities of BVA resonators » - 9<sup>th</sup> Europ. Freq. and Time Forum (1995), pp. 9, 15
2. R.J. BESSON, J.J. BOY, F. DEYZAC : « Acceleration sensitivity of BVA resonators » - 50<sup>th</sup> Annual Freq. Control Sympo. (1996), pp. 457, 463
3. R.J. BESSON : « A new electrodeless resonator design » - 31st Annual Freq. Control Symp. (1977), pp. 147, 152
4. J.J. BOY, A. BERTHAUT, G. RENARD, R. ROY, D. THIEBAUD, G. ROBICHON, C. LONGET : "Characterisation of BVA in industrialisation process" - 7th Europ. Freq. and Time Forum (1993), pp. 57, 62.
5. F. DEYZAC : « Finite elements method modelling of accelerometric and barometric sensitivity of quartz resonators » - 7th Europ. Freq. and Time Forum (1993), pp. 291, 295.
6. E.P. EERNISSE : « Temperature dependance of the force frequency effect for the AT-, FC-, SC- and Rotated X-cuts » - 34th Annual Freq. Control Symp. (1980), pp. 426, 430

## The SC-cut lateral field quartz resonator working on anharmonic antisymmetric mode

Krzysztof Weiss, Wiesław Szulc

Tele & Radio Research Institute, Warsaw, POLAND

### 1. Introduction

Anharmonic modes are accompanying to first modes of fundamental or overtone vibrations of thickness shear resonators. For AT resonators they are known from many years, and there were many trails to explain theoretically this feature of resonators, and to calculate these spurious modes frequency [1] [2] [3]. But for SC - cut resonators all these theories were not adequate. In 1985 Tiersten and Stevens [4] published theory of anharmonic modes vibration in plano-convex SC cut resonators. This theory was completed in the next year by Stevens and Tiersten [5], and checked in practice, resulting good agreement of calculated and measured frequencies.

### 2. Anharmonic modes vibrations

For AT cut these vibrations were investigated by X-ray topography and were presented in many publications [6]. Theoretically perpendicular electric field excites only symmetric modes of vibrations. The antisymmetric modes will appear with very low intensity as result of error in electrodes positioning and electric field asymmetry caused by electrodes connectors. Generally we can say that anharmonic modes vibrations that are thickness shear vibrations of different regions of quartz plate in opposite directions with the same frequency. For example symmetric mode  $n 2 0$  exhibits three vibration regions presented in fig. 1.

In  $n 0 2$  mode displacements are the same but in different direction. This kind of vibrations is called symmetrical because displacements are symmetrical to plane crossing plate center. The antisymmetric mode  $n 1 0$  exhibits two vibrating regions with displacements presented in fig. 2.

In vibrating plate can exist higher order anharmonic modes of vibration :

antisymmetric :  $n 0 3, n 0 5 \dots$  and  $n 3 0, n 5 0 \dots$

symmetric :  $n 0 4, n 0 6 \dots$  and  $n 4 0, n 6 0 \dots$

and their combinations as  $n 1 1, n 2 2, n 1 2, n 1 3 \dots$

Symmetric modes can be excited with significant intensity by perpendicular and lateral field in classic resonators. Antisymmetric modes are more difficult for excitation. Bourquin at all [7], [8] presented electrodes configuration for  $n 0 1$  or  $n 1 0$  modes excitation consisting of four semicircle electrodes connected alternately to electric connectors (fig. 3).

Fig. 1. The anharmonic symmetric  $n 2 0$  mode vibrations displacements

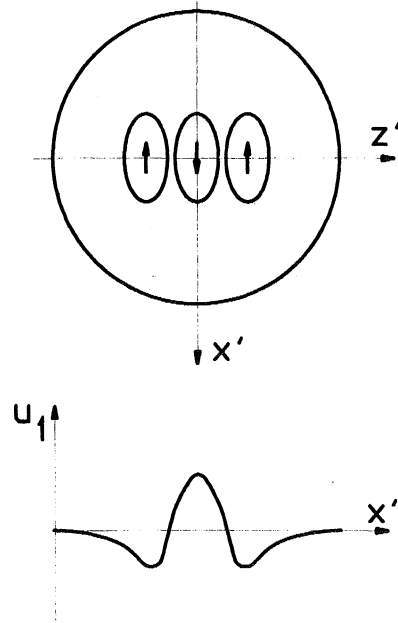


Fig. 2 The anharmonic antisymmetric  $n 1 0$  mode vibration displacements

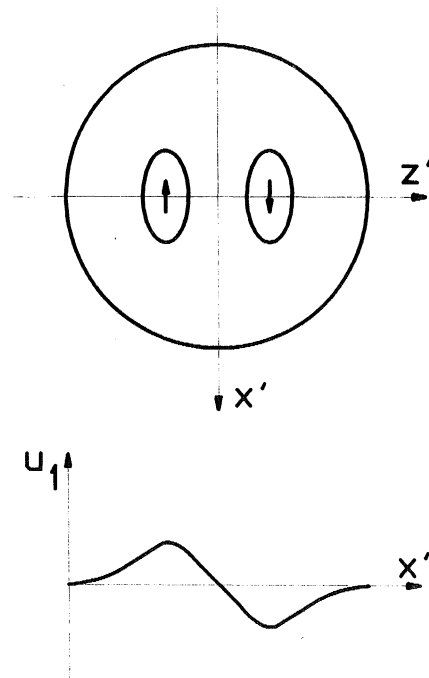
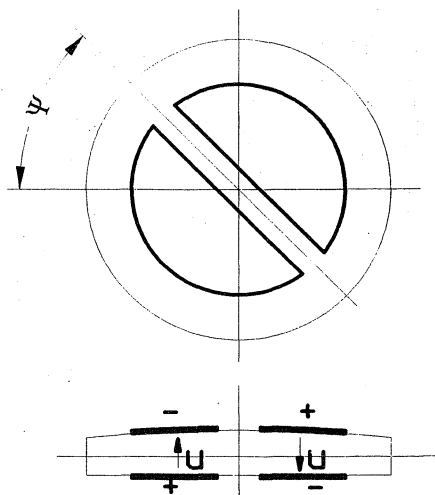
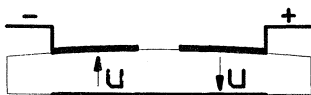


Fig. 3 The  $n 0 1$  mode perpendicular field resonator electrodes configuration



This electrodes configuration is exciting two plate regions for vibrations in opposite directions. These vibrations are coupling by plate material giving in effect anharmonic mode vibrations. The same effect can be reached by three electrodes configuration presented in fig. 4.

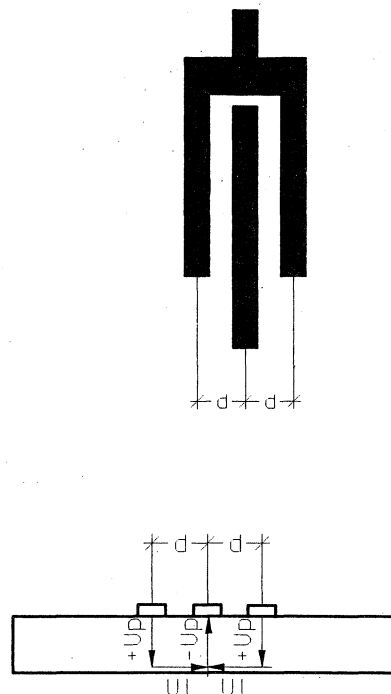
Fig. 4. The  $n 0 1$  mode resonator series electrodes configuration



### 3. Lateral field excited antisymmetric anharmonic mode resonator design

Our proposition was to excite this vibration mode by lateral field excitation. It is necessary to create on plate surface two regions with opposite direction of electric field. This conditions are realized by three finger parallel electrodes with external electrodes shorted. This electrodes configuration and electric field distribution is presented in fig. 5.

Fig 5. Electrodes configuration and electric field distribution



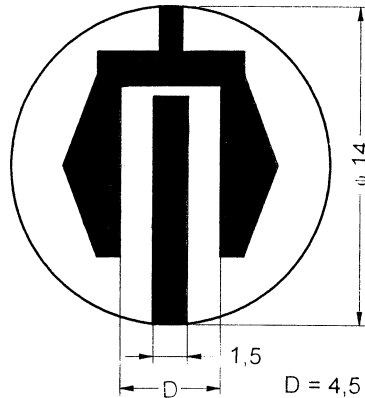
Both components of electric field  $U_l$  and  $U_p$  are generating displacements of quartz plate.  $U_p$  can excite symmetric anharmonic vibration modes.  $U_l$  gives possibility of antisymmetric modes exciting. By optimizing distance between electrodes we can modify intensity of desired mode excitation, but generally the antisymmetric mode excitation is stronger. This electrodes configuration can excite not only the first antisymmetric mode but also next modes as  $n 0 3$  or  $n 0 5$ . Intensity of these modes excitation depends on distance between electrodes. The chosen mode excitation depends also of direction of lateral field. Direction of excitation corresponds to anharmonic modes regions positions. These positions were calculated by Bourquin at all.[7], [8]

### 4. Experimental results

Anharmonic modes excitation by lateral field was started by measurement of resonant frequency of different SC- cut quartz plates without electrodes, positioned on outer electrodes configuration presented in fig. 5 with electrodes width and distance between electrodes 1mm. By quartz plate rotation we did find positions of highest intensity of different vibration modes. We did find that we can excite the main third mode of vibration with very low intensity ( over  $2000\Omega$  in  $\pi$ - network ) and anharmonic modes  $3 0 1$  and  $3 1 0$  with significant higher intensity ( about  $500 \Omega$  ). The  $3 1 1$ ,  $3 3 0$ ,  $3 0 3$ ,  $3 1 3$  and  $3 3 1$  modes were so distinguish but with significant lower intensity. The B- mode

intensity in position of highest intensity of 3 0 1 mode was very low ( about 5000  $\Omega$ ). Next we designed electrodes configuration presented in fig. 6, and we made resonators with this configuration of electrodes deposited on quartz plate surface The first resonators were made of standard SC - cut resonator 8,192 MHz 3<sup>rd</sup> overtone plates with diameter 14 mm and curvature radius 500 mm. These resonators parameters compared with classic lateral field resonator are presented in tab. 1.

Fig 6. Practical electrodes configuration.



Tab. 1 resonators parameters comparison

parameter	lateral field 3 0 1	classic resonator	classic lateral field[9]	Bourquin at all resonator[8]
frequency [MHz]	8,248	8,192	4,999	9,998
motional resistance [ $\Omega$ ]	371	54	570	85 - 100
motional capacitance [fF]	0,047	0,3	0,0252	
Q factor [E6]	1,11	1,2	2,2	1,2
B mode resistance [ $\Omega$ ]	8200	40	14000	90 - 152
fa - fr [Hz]	382	494	35	

The new lateral field resonator exhibit in comparing with classic lateral field resonator significant lower resistance, higher capacitance and very high value of difference between series and parallel resonance frequency. It is very important because in lateral field resonators the main technological problem was very precise quartz plate frequency adjustment necessary. This precision depends on electrical frequency adjustment in oscillator possibility, which can be realized in range between series and parallel resonance frequencies. In comparing with perpendicular field anharmonic mode resonator, our resonator parameters are worse except the B-mode

reduction. But this resonator construction is very simple.

In the second step many different quartz plates anharmonic 3 0 1 mode frequencies and attenuation in  $\pi$ - network values were measured. The measurements were carried out on external electrodes with different values of gap between electrodes. The internal electrode width was 0,5 mm. The distance between external electrodes was 3; 4; 4,5; 5; and 6 mm The results of measurements are presented in tab. 2.

Tab. 2. Height of resonance peak of quartz plates without electrodes

No	F [MHz] 301mode	R [mm]	Height of 3 0 1 resonance peak [dB]				
			distance	between	external	electrode	D [mm]
			3,0	4,0	4,5	5,0	6,0
1	10,055	1000	20,0	25,3	23,9	23,4	22,8
2	8,260	500	24,4	25,8	27,1	27,4	28,2
3	8,193	500	25,9	27,7	26,1	27,9	28,1
4	8,273	300	25,3	25,8	28,2	26,3	24,2
5	8,193	200	24,6	27,8	27,5	27,1	24,9
6	6,810	300	24,7	25,7	26,6	26,4	26,1
7	5,058	200	24,1	23,6	23,7	27,0	29,8
8	5,061	150	20,3	26,2	27,6	29,5	25,5
9	4,850	300	16,1	24,2	25,9	26,0	23,7
10	4,166	100	20,3	20,7	22,8	23,5	28,6

In the tab 2. The highest values of resonant amplitudes are in frames. We can see that for different radius of curvature and for different plate thickness we can observe different optimal value of distance between electrodes. It depends on vibrating region topology. This dependence is very strong. For 8,2 MHz resonators with R= 500 mm the optimal distance between electrodes (De) is between 5 and 6 mm. For R= 200 mm the optimal distance is between 4.0 and 4,5 mm. On these measurements basis the experimental resonators were designed and performed. Parameters of these

resonators are presented in tab. 3. These results show in comparing with results presented in tab. 1 that electrodes configuration is not optimal. In the first construction width of inner electrode was 1,5 mm and distance between external electrodes was 4,5 mm. In the next construction it was changed on 0,5 mm and 4 or 5 mm. This new construction did appear worse. From presented construction versions sample no 4 did appear the best. In the next experiments it is necessary to check inner electrode width optimize. The B mode suppression is in all cases to strong that in oscillator it will not excite.

Tab. 3 The lateral field excited 3 0 1 mode resonators parameters

Parameter	Resonator no.			
	1	2	3	4
F 3 0 1 mode [MHz]	8,192	8,193	8,193	8,193
R [mm]	500	500	200	200
De [mm]	5	4	5	4
Co [pF]	0,295	0,327	0,280	0,326
Cm [fF]	0,038	0,033	0,028	0,038
Rm [ $\Omega$ ]	458	522	602	390
Q [E6]	1,1	1,1	1,29	1,30
Fa -Fs [Hz]	530	417	411	482
Another modes resistance [ $\Omega$ ]				
3 0 0	21000	12500	8350	11100
3 1 0	4300	14000	1900	3800
3 1 1	9300	3100	6100	6100
3 0 3	2250	3100		
3 3 3	8900	4100		
B mode 3 0 0	13200	15300	14000	16600
3 0 1	14000	10500	9900	8800

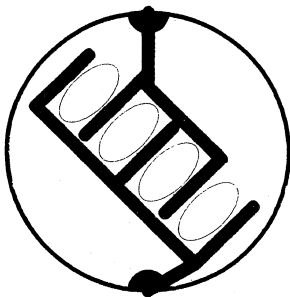
## 5. Conclusions

Presented resonators exhibit interesting parameters. In comparing with classic lateral field excited resonator they have lower resistance and the same Q-factor. The resonator construction optimizing may give better parameters but probably not to good as for classic resonators. The most important advantage of this resonator is wide range of frequency adjustment in oscillator in practice the same as for classic perpendicular field resonator. That are only initial experiments results. We did not measure long term and short term stability of these resonators, but we can expect higher frequency stability because of double resonator working on one quartz plate. In electrical circuit it can be treated as two parallel connected resonators working on the same frequency. The electrodes positioned between active regions will exhibit very low influence on resonator aging. Very simple construction and technology can decide that these resonators will be in price similar to classic resonators.

## 6. The future experiments

In presented investigations we did design only resonators working on the first anharmonic mode but presented method of anharmonic modes excitation by lateral field electrodes configuration can be utilized for another anharmonic modes excitation, for example  $n 0 3$  or  $n 3 0$  with electrodes configuration presented in fig. 7. But for this resonator design it is necessary to know with high precision this mode distribution and to find proper distances between electrodes. It is probably possible to design electrodes configuration for more complicated modes working resonator. If we will divide external electrodes we can use lateral field excited resonator as very narrow band filter similar to classic monolithic filter. All these ideas need many calculations and experiments.

Fig. 7. Electrodes configuration for  $n 0 3$  mode excitation



## 7. References

1. C.J.Wilson, Vibration modes of AT - cut convex quartz resonators, J.Phys. D: Appl. Phys. Vol. 7. 1974
2. H.F. Tiersten, R.C. Smythe, An analysis of contoured crystal resonators operating in overtones of coupled thickness shear and thickness twist, J Accoust. Soc. Am. 65(6) June 1979.
3. V.E. Bottom, Introduction to quartz crystal units design, Van Nostrand Reinhold Company 1982 p.72-80
4. H.F.Tiersten, D.S.Stevens, The evaluation of the coefficient of nonlinear resonance for SC-cut quartz resonators, Proc. 39<sup>th</sup> AFCS - 1985
5. D.S. Stevens, H.F. Tiersten, An analysis of doubly rotated quartz resonators utilizing essentially thickness modes with transverse variation. J. Accoust. Soc. Am. 79(6). June 1986.
6. B.W.Neubig, Measurement of spurious resonances of crystal units using network analysers with error correction, Proc. 8<sup>th</sup> EFTF 1994.
7. R Bourquin. B.Dulmet. J.J.Boy, SC - cut resonator operating in anharmonic modes with B mode reduction. Proc 10<sup>th</sup> EFTF 1996
8. R Bourquin. B.Dulmet. J.J.Boy, Characterization of SC cut resonators operating in anharmonic mode. Proc 11<sup>th</sup> EFTF 1997.
9. A. Masiukiewicz, B.Gniewinska, W. Szulc. K. Weiss, Study of SC cut lateral field excited resonators features. Proc. 39<sup>th</sup> AFCS 1985

## A Comparative Study of the Idiosyncratic Behaviors of 3<sup>rd</sup> Overtone and 5<sup>th</sup> Overtone Precision Quartz Resonators

Timothy E. Wickard and Gregory L. Weaver  
Piezo Crystal Company, Carlisle Pa. USA

Increased interest in the application of quartz resonators for hyperstable performance as a substitute for rubidium based frequency sources has raised several emergent issues. Specifically, the question whether to base quartz frequency sources on either 5 MHz 3<sup>rd</sup> overtone designs or 10 MHz 5<sup>th</sup> overtone designs is compelling to the extent that both resonator styles represent similar quartz masses, mounting and enclosure structures. Oscillator designers are, therefore, attracted toward 10 and 15 MHz, 5<sup>th</sup> overtone designs which would remove the complications and degradation associated with frequency multiplication.

This paper will present the results of a detailed investigation into the comparative performance between 5<sup>th</sup> and 3<sup>rd</sup> overtone SC-cut quartz resonators. Careful controls will be applied on the design and manufacture of resonators in this study so that idiosyncratic behaviors may be observed and analyzed. A particular feature of the investigation procedures will be the use of the phase separation technique which allows the direct discrimination of frequency drift contribution associated with the quartz resonators from the oscillator circuitry.<sup>1</sup> The experiments of the investigation will focus on anomalous frequency behaviors such as the recurrence of initial aging, retrace, frequency jumps and fractional frequency jitter.

---

<sup>1</sup> A presented at the 10<sup>th</sup> Annual EFTF in Brighton, United Kingdom



**12th EFTF - 10-12 March 1998 - Warsaw - POLAND**

**Optically pumped & cold atom Cs standards**

Chairman: ***Pierre Thomann***



## SOME PROPERTIES OF AN OPTICALLY PUMPED CESIUM BEAM TUBE DEPENDING ON THE MICROWAVE AMPLITUDE

Claude Audoin, Frédéric Hamouda, Luc Chassagne and Roland Barillet

Laboratoire de l'Horloge Atomique, Unité Propre de Recherche CNRS associée à l'Université Paris-Sud  
Bâtiment 221 - Université Paris-Sud, 91405 Orsay Cedex, France

### ABSTRACT

Assuming square wave frequency modulation, the response, versus the amplitude of the microwave field, of an optically pumped cesium beam tube is analyzed. The effect of the neighboring lines is considered and a model of the profile of the microwave field in each interaction region is validated.

A symmetry property of the response considered is pointed out. It enables us to implement a feedback control of the microwave amplitude with a large depth of the amplitude modulation. However, the microwave amplitude achieved is not exactly that for which the cavity pulling effect is cancelled. It is shown that with a cavity designed with  $\phi = \pi$  between the two oscillatory fields, an appropriate correction can be derived and applied to the servoed value of the microwave amplitude. Consequently, the fractional cavity pulling frequency offset can be made smaller than  $1 \times 10^{-14}$  for any cavity mistuning.

*Keywords : Atomic clocks, Optical pumping, amplitude modulation, microwave resonator, power transmission control.*

### 1. INTRODUCTION

Nowadays, it is current practice to apply a square-wave frequency modulation to cesium beam tubes. The primary purpose is to derive an error signal that can lock the frequency of a quartz crystal oscillator to the atomic resonance. This waveform is well suited to a numerical signal processing of the beam tube response. In addition, it provides the great advantage of giving an easy means to settle the microwave amplitude to a constant value [1]. This is accomplished by looking at the properties of the beam tube response at the (angular) frequency  $\omega_0 \pm \omega_m$ , where  $\omega_0$  is the atomic resonance frequency and  $\omega_m$  is the frequency modulation depth. The microwave amplitude for which this response shows an extremum has an useful feature. It is close to a value such that the frequency shift due to a cavity mistuning is eliminated [1, 2], as well as any frequency shift related to a modulation of the microwave amplitude that would be correlated to the frequency modulation [3]. Furthermore, it depends scarcely on environmental conditions and it provides a means to stabilize the other microwave dependent frequency shifts. However, as we will show, the experimentally obtained value of the microwave amplitude is not exactly the desired one since it is offset by the neighboring lines of the cesium microwave spectrum.

In this work, we will describe some properties of the cesium beam tube response at the frequency  $\omega_0 \pm \omega_m$ . We will consider more particularly the case where the preparation and the detection of the atomic states are accomplished by optical pumping. Then, the velocity distribution function of the atoms detected is well defined and it can be assumed a modified maxwellian distribution. We will take into account the effect of the

two ( $F=4, m_F=-1$ )  $\leftrightarrow$  ( $F=3, m_F=-1$ ) and ( $F=4, m_F=+1$ )  $\leftrightarrow$  ( $F=3, m_F=+1$ ) neighboring lines. We will show that their contribution to the experimentally recorded variation of the beam tube response, versus the microwave amplitude, provides a means to model the profile of the microwave amplitude variation along the beam path, in the two interaction regions. We will point out that the beam tube response at  $\omega_0 \pm \omega_m$  shows symmetry properties when plotted versus the logarithm of the microwave level. It is thus possible to find, by appropriate means, the maximum of this response by applying a square-wave modulation to this amplitude whose depth does not need to be very small. However, this maximum occurs at a value of the microwave amplitude that is shifted by the presence of the neighboring lines. We will show how it is possible, when the Ramsey pattern is observed inverted, to compensate for this error and to obtain an excellent approximation of the amplitude for which the cavity pulling effect disappears. Finally, we will specify the cavity pulling frequency offset associated with any residual bias of the value of the microwave amplitude, achieved.

In this work, we will refer to the properties of the optically pumped cesium beam tube Cs IV developed and studied in the laboratory [4]. We will also give some indications valid for other beam tube designs.

### 2. CONTRIBUTION OF THE REFERENCE LINE TO THE BEAM TUBE RESPONSE AT $\omega_0 \pm \omega_m$

In general, we will use the notations of [3] and [5 ch.5]. Let us consider the ( $F=4, m_F=0$ )  $\leftrightarrow$  ( $F=3, m_F=0$ ) reference transition of cesium atoms in the ground state in two successive oscillatory microwave fields having the same amplitude and the same frequency  $\omega$  [6 ch.5]. We assume at first that the amplitude of each of these fields is a constant along the length  $\ell$  of each atom-microwave interaction region and that it is equal to zero elsewhere. This amplitude will be represented by  $b$ . The separation between the fields is  $L$ .

The probability that a transition occurred, averaged over all the atom velocities is given by [5, 6] :

$$P_r = \int_0^\infty f(\tau) \left\{ \frac{2b}{\Omega} \sin \frac{\Omega\tau}{2} \left[ \cos \frac{\Omega\tau}{2} \cos \frac{\Omega_0 T + \phi}{2} - \frac{\Omega_0}{\Omega} \sin \frac{\Omega\tau}{2} \sin \frac{\Omega_0 T + \phi}{2} \right] \right\}^2 d\tau. \quad (1)$$

In this equation,  $\tau$  is the time of flight, in each oscillatory field, of atoms having a given velocity and  $T = \tau L / \ell$  is their transit time between the two microwave excitation regions. We have defined  $\Omega_0 = \omega - \omega_0$ , and  $\Omega^2 = b^2 + \Omega_0^2$ . The phase difference between the two fields is  $\phi$ . It can take the value 0 or  $\pi$  according to the beam tube design [3]. We neglect here the small phase shift due to imperfections in the microwave cavity. The function  $f(\tau)$  is the

normalized distribution function of the interaction time  $\tau$ . In optically pumped cesium beam tubes, the velocity distribution function is very close to a modified maxwellian distribution. This leads to [5 p.650] :

$$f(\tau) = \frac{C_n}{\tau_0} \left( \frac{\tau_0}{\tau} \right)^{n+2} \exp(-\tau_0^2 / \tau^2). \quad (2)$$

We have  $\tau_0 = \ell/\alpha$ , where  $\alpha$  is the most probable velocity in the cesium oven. In the simplest case where a single laser line is used for the atomic state preparation and the detection of the transition by optical pumping, we have  $n = 3$  and  $C_3 = 2$ . If more than one laser line is available, one may have  $n = 1$  or  $2$  with  $C_1 = 2$  and  $C_2 = 4/\sqrt{\pi}$ .

The quantities without dimension  $b\tau_0$  and  $\omega_m T_0$ , with  $T_0 = L/\alpha$ , are convenient ones to characterize the microwave amplitude and the frequency offset of the oscillatory fields, respectively. Figure 1 shows the variation of  $P_r(b\tau_0, \omega_m T_0)$ , computed for  $\omega = \omega_0 \pm \omega_m$ , versus  $b\tau_0$  for several values of  $\omega_m T_0$ . We have assumed  $n = 3$ ,  $\phi = \pi$  and  $L/\ell = 16.2$ . These values apply to the optically pumped cesium beam tube Cs IV operated in the laboratory [4]. The first maximum of  $P_r$  occurs for  $b\tau_0$  close to 1.5. Besides, it has been shown [3] that the best overall cesium beam tube performance is obtained for  $b\tau_0 \sim 1.5$  and  $\omega_m T_0 \sim 1.5$ . Then, the value of  $\omega_m$  is nearly equal to the half-width at half-maximum of the atomic resonance line. In the case where  $\phi$  would be equal to zero, we would obtain a graph similar to that of figure 1, but with  $P_r(b\tau_0, \omega_m T_0)$  a decreasing function of  $\omega_m T_0$ , for given  $b\tau_0$ . The corresponding optimum values of  $b\tau_0$  and  $\omega_m T_0$  would be approximately equal to 2 and 1.5, respectively. It should be noted that the results given do not depend greatly on the ratio  $L/\ell$ , i.e. on the cesium beam tube length, provided that we have  $L/\ell \geq 15$ .

Probability that a transition occurred:  $P_r(b\tau_0, \omega_m T_0)$

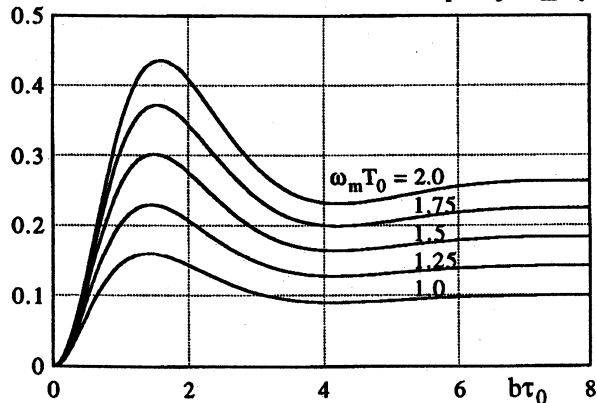


Fig-1. Variation of the probability that a transition occurred,  $P_r(b\tau_0, \omega_m T_0)$  versus  $b\tau_0$  for several values of  $\omega_m T_0$ . Only the reference line is considered. It is assumed :  $n = 3$ ,  $\phi = \pi$  and  $L/\ell = 16.2$ .

### 3. TOTAL BEAM TUBE RESPONSE AT $\omega_0 \pm \omega_m$ AND PROFILE OF THE MICROWAVE FIELD AMPLITUDE

The microwave spectrum of the cesium atom in the ground state shows seven lines. Among them, the  $(F=4, m_F=-1) \leftrightarrow (F=3, m_F=-1)$  and  $(F=4, m_F=+1) \leftrightarrow (F=3, m_F=+1)$  lines are the closest to the  $(F=4, m_F=0) \leftrightarrow$

$(F=3, m_F=0)$  reference line. For the usual value of the static magnetic field, around  $6 \mu\text{T}$ , the aisles of the Rabi pedestal of these two lines bring a noticeable contribution to the beam tube response at frequencies close to  $\omega_0$  and it must be added to that of the central line. Consequently, the curves shown in figure 1 must be corrected to represent the properties of the actual beam tube response.

Since the neighboring lines are off resonance, their amplitude is proportional to the microwave power and thus to  $(b\tau_0)^2$ . Furthermore, it is also known that the aisles of the Rabi pedestal of all the resonance lines depend greatly on the profile of the variation of the amplitude of the oscillatory field in each of the two identical interaction regions [7]. In order to obtain the corrective term to be added to  $P_r(b\tau_0, \omega_m T_0)$ , we have assumed a simple model of the field amplitude distribution. It has been suggested by the results of a computation, by means of a finite element method, of the microwave amplitude in an interaction region of a customary design [8]. We set :

$$b'(\chi) = b \left[ 1 - \frac{1}{2} \exp\left(\frac{2|\chi|-1}{2\chi_d}\right) \right] \text{ for } -\frac{1}{2} \leq \chi \leq \frac{1}{2}, \quad (3)$$

$$b'(\chi) = \frac{b}{2} \exp\left(\frac{1-2|\chi|}{2\chi_d}\right) \text{ for } -\frac{1}{2} > \chi > \frac{1}{2}. \quad (4)$$

In these equations, the normalized abscissa  $\chi$  is equal to  $x/\ell$  where  $x$  denotes the position along the beam axis. Its origin is taken at the center of an interaction region. Here, the parameter  $\ell$  must be understood as the separation between the two large faces of the X-band waveguide. We have  $\ell = 1 \text{ cm}$  as usual. The field amplitude variation is entirely determined by the damping factor  $\chi_d$ . The subsequent figure 3 shows an example of such a profile. For the value of  $\chi_d$  encountered, the mean value of the microwave amplitude, averaged over an interaction region, is very closely equal to  $b$ .

The two neighboring lines are symmetrically disposed around the central one. Let us consider the  $(F=4, m_F=+1) \leftrightarrow (F=3, m_F=+1)$  line, for instance. Its resonance frequency is  $\omega_1$  and it is excited at frequency  $\omega_0 \pm \omega_m$ . We thus have  $\Omega_0 = \omega_1 - (\omega_0 \pm \omega_m)$ . It is easy to verify that  $\omega_m$  can be neglected compared to the Zeeman separation  $\Omega_z = \omega_1 - \omega_0$  between the two lines. Furthermore, we typically have  $\Omega_z = 2.65 \times 10^5 \text{ rad/s}$  and  $b = 3.25 \times 10^4 \text{ rad/s}$ . Then, the condition  $\Omega_z \gg b$  is sufficiently well verified and the contribution of one line to the probability that a transition occurred — and thus to the beam tube response — is given by [5 p.640, 7] :

$$P' = \frac{1}{2} \int_0^\infty f(\tau) (Kb\tau)^2 |F(\Omega_z \tau)|^2 d\tau, \quad (5)$$

where  $F(\Omega_z \tau)$  denotes the Fourier transform of the profile function  $b'(\chi)/b$ . The constant  $K$  is equal to  $15^{1/2}/4$  for the lines considered [5 p.56]. The additive contribution  $P_n$  of the two closest neighboring lines is obtained from Eqs. (3-5). We have :

$$P_n(b\tau_0, \Omega_z \tau_0) =$$

$$\frac{15}{4} \left( \frac{b\tau_0}{\Omega_z \tau_0} \right)^2 \int_0^\infty f(\tau) \left[ \frac{\sin(\Omega_z \tau / 2)}{1 + (\Omega_z \tau \chi_d)^2} \right]^2 d\tau, \quad (6)$$

where a term proportional to  $\exp(-1/2\chi_d)$ , which can be neglected for the plausible values of  $\chi_d$ , has been deleted.

In well designed optically pumped cesium beam tubes, the level populations are the same for opposite values of  $m_F$ . Consequently, the Rabi and the Ramsey pullings [9, 10] do not occur, which practically means that the presence of the neighboring lines leads to a background depending on the level of the microwave field, but not on its frequency. We assume that any other background component does not depend on the microwave frequency. One may observe that the respective contributions to the beam tube response of the reference and of the neighboring lines have been calculated with different profiles of the microwave field amplitude. It has been assumed a sharp one for the central line and a smooth one for the lateral lines. In fact, it is known that, for  $L/\ell$  large enough, a simplified expression of the probability that a transition occurred can be considered and it does not depend on the microwave profile [5 p.634 and p.646]. This statement has been verified, for  $L/\ell = 16.2$ . Firstly the probability that a transition occurred has been obtained from Eq. (1). Secondly, this probability has been computed by following the change of the atom quantum state all along the atom path, assuming an amplitude profile given by Eqs. (3-4). For  $n = 3$ ,  $\omega_m T_0 = 1.5$ ,  $b\tau_0 < 4$  and the value of  $\chi_d$  experimentally obtained (see next Section), the relative difference between the two results is at most equal to  $2 \times 10^{-3}$  for  $\phi = 0$  and to  $4 \times 10^{-3}$  for  $\phi = \pi$ . It follows that the relatively simple Eq. (1) can be used for practical purposes and that the total beam tube response at  $\omega_0 \pm \omega_m$  is proportional to  $P_t$  given by :

$$P_t = P_r(b\tau_0, \omega_m T_0) + P_n(b\tau_0, \Omega_z \tau_0). \quad (7)$$

#### 4. EXPERIMENTAL VALIDATION OF THE MODEL OF THE MICROWAVE FIELD AMPLITUDE PROFILE

The variation of the beam tube response at  $\omega_0 \pm \omega_m$  versus the amplitude of the microwave field at the input of the cavity has been experimentally recorded. The amplitude of the externally applied field is proportional to  $b$  and it can be written  $Cb\tau_0$ , where  $C$  is a constant.

A set of curves representing the variation of  $P_t$  versus  $b\tau_0$  has been computed for several values of the damping factor  $\chi_d$ . It has been set  $n = 3$ ,  $\phi = \pi$ ,  $L/\ell = 16.2$ ,  $\omega_m T_0 = 1.5$  and  $\Omega_z \tau_0 = 12.3$ , which are the current values of these parameters. We denote  $P_t^{\max}/P_t^{\min}$  the first maximum and the first minimum of  $P_t$ , respectively.

The value of  $\chi_d$  that has been retained is that giving the same value of  $P_t^{\max}/P_t^{\min}$  as the experimental record. In our cesium beam tube, this leads to :  $\chi_d = 0.095 \pm 0.005$ . For this value of the damping factor, the abscissa of the maximum of  $P_t$  is equal to  $b\tau_0 = 1.523_{-0.004}^{+0.003}$ .

The value of the constant  $C$  introduced above can be obtained by comparing the values of  $b\tau_0$  and  $Cb\tau_0$  for the first maximum. This practically means that the amplitude of the microwave field fed to the cavity is calibrated in terms of the quantity  $b\tau_0$ .

Finally the ordinates of the experimental points are multiplied by an appropriate factor such that the experimental and the theoretical data coincide at their first maximum. Figure 2 shows the result of the fit. One can see that it is quite satisfactory.

Thus, the model considered provides an excellent estimate of the variation of the microwave amplitude in each interaction region, averaged over the atomic trajectories. Figure 3 shows the profile of this variation.

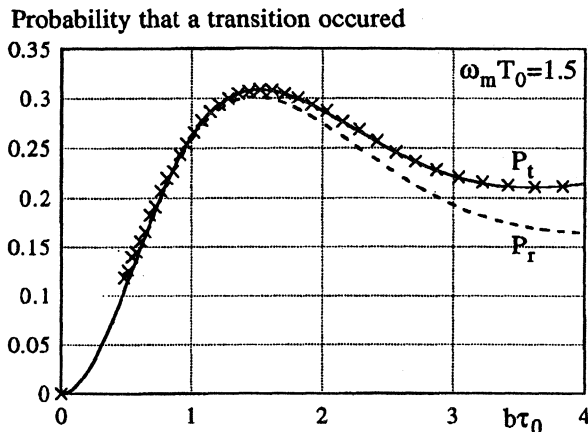


Fig-2. Result of the fit between the theoretical variation of the total probability  $P_t$  that a transition occurred (solid line) and the experimental points (crosses). We have  $n = 3$ ,  $\phi = \pi$ ,  $L/\ell = 16.2$ ,  $\omega_m T_0 = 1.5$ ,  $\Omega_z \tau_0 = 12.3$  and  $\chi_d = 0.095$ . The dashed line represents the contribution of the reference transition alone.

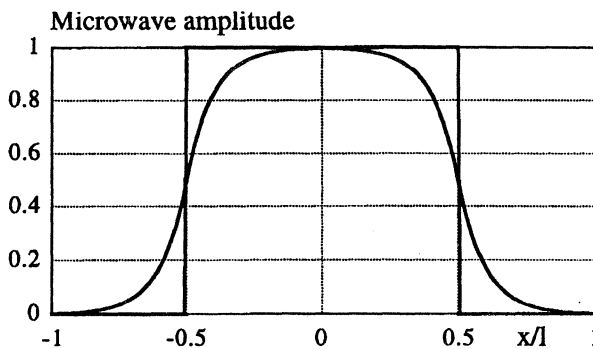


Fig-3. Variation of the amplitude of the microwave field along the atom path in an interaction region. We have  $\chi_d = 0.095$ .

#### 5. SYMMETRY PROPERTY OF THE BEAM TUBE RESPONSE AT $\omega_0 \pm \omega_m$

Let us consider the shape of the atomic resonator response at  $\omega_0 \pm \omega_m$  versus the variable  $b\tau_0$ , shown in figures 1 and 2. It presents a positive skewness in the vicinity of the maximum. This occurs i) for all the velocity distribution functions recalled in Section 2 and ii) for  $\phi = 0$  as well as for  $\phi = \pi$ . This distortion is a consequence of the large velocity distribution occurring in optically pumped cesium beam frequency standards. It is negligible in the case of sufficiently narrow velocity distribution.

Fortunately, the skewness shown in figures 1 and 2 disappears almost entirely for another choice of the abscissa.

It exists voltage variable attenuators — those using PIN diodes for instance — which, for a given input power, give an output power  $P_o$  such that  $\log(P_o)$  is a linear function of the applied voltage. The practical consequence of interest to us is that we have access to

the quantity  $\log(b\tau_0)$  as a linear function of the voltage. Figures 4a and 4b show, for the purpose of comparison, the variation of the probability that a transition occurred at  $\omega_0 \pm \omega_m$  versus  $b\tau_0$  and  $\log(b\tau_0)$ , respectively. Also represented is the locus of points at an equal horizontal distance from the two main branches of the response function. We note that in figure 4b, the locus is very close to a vertical straight line on a large part of its height. Consequently, the beam tube response can be approximated by an even function of the quantity  $\log(b\tau_0/b_\mu\tau_0)$  in the vicinity of its maximum, where  $b_\mu\tau_0$  denotes the value of  $b\tau_0$  at the first maximum. Similar results have been obtained for  $\phi = 0$  in the case  $n = 3$ , and for  $n = 1$  and 2.

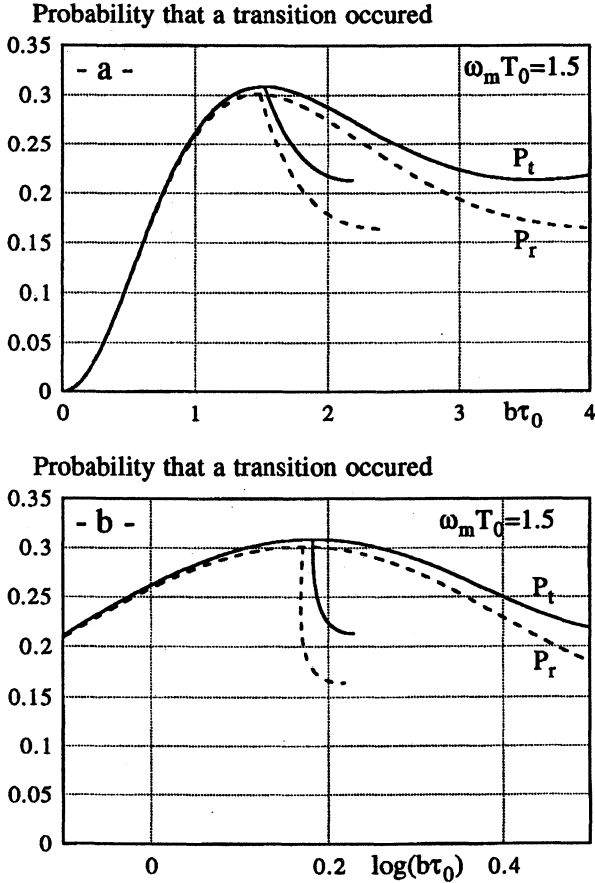


Fig-4. Variation of the probability that a transition occurred and locus of points at an equal horizontal distance from the two branches of the probability function : a) versus  $b\tau_0$ , b) versus  $\log(b\tau_0)$ . Solid line : total probability  $P_t$ . Dashed line : contribution of the reference transition only. We have :  $n = 3$ ,  $\phi = \pi$ ,  $L/l = 16.2$ ,  $\omega_m T_0 = 1.5$ ,  $\Omega_z \tau_0 = 12.3$  and  $\chi_d = 0.095$ .

## 6. CONTROL OF THE MICROWAVE AMPLITUDE

In modern manufactured cesium beam frequency standards, with magnetic state selection, the microwave amplitude is locked at the value that provides the first maximum of the total beam tube response at  $\omega_0 \pm \omega_m$

[1]. This is accomplished by producing a permanent but tiny modulation of the microwave amplitude.

In our design [11], the modulation is not a permanent one, but we take advantage of the symmetry property mentioned in the preceding Section to change significantly the microwave amplitude. The modulation is applied for a fraction of a second. Then, the microwave amplitude is hold for some length of time during which its variation under the effect of any environmental perturbation can be neglected. During the active control period of time, the microwave amplitude is square-wave modulated by applying alternately the voltages  $(V_t + \Delta V)$  and  $(V_t - \Delta V)$  to the attenuator. A feedback loop adjusts the value of  $V_t$  such that the beam tube response is the same at the two voltages. Thanks to the symmetry property pointed out in Section 5, the value of  $b\tau_0$  associated with  $V_t$ , that we denote  $b_t\tau_0$ , differs but very slightly from the theoretical value of the abscissa of the first maximum of  $P_t$ ,  $b_\mu^{(t)}$ , when the voltage modulation changes the microwave amplitude up to  $\pm 3$  dB around  $b_t$ . For  $n = 3$ ,  $L/l = 16.2$ ,  $\omega_m T_0 = 1.5$ ,  $\Omega_z \tau_0 = 12.3$ , and  $\chi_d = 0.095$ , the relative error is equal to  $2.4 \times 10^{-3}$  for  $\phi = \pi$  and to  $-8 \times 10^{-3}$  for  $\phi = 0$ . Of course, the relative error is even smaller for a smaller modulation depth. Similar results have been obtained for  $n = 1$  and 2.

## 7. CORRECTION TO THE SERVOED MICROWAVE AMPLITUDE

It has been shown that the cavity pulling effect disappears when the microwave amplitude takes the value  $b_\mu^{(r)}$  corresponding to an extremum of the contribution  $P_r$  to the reference ( $F=4, m_F=0$ )  $\leftrightarrow$  ( $F=3, m_F=0$ ) line, the first maximum for instance [2,3]. However, the measurable quantity is  $P_t$ , the sum of the contributions of the central and the lateral lines. Therefore, although the feedback loop provides an excellent estimate of  $b_\mu^{(t)}$ , this is not the desired value anyway. With the numerical values considered here, we have  $b_\mu^{(r)}\tau_0 = 1.486$  and  $b_\mu^{(t)}\tau_0 = 1.523$  for  $\phi = \pi$ . The corresponding values for  $\phi = 0$  are 2.088 and 2.131, respectively. With  $n = 1$  and 2, the relative offset is also of about  $(1 \text{ to } 3) \times 10^{-2}$ . It follows that with the value  $b_\mu^{(t)}$  of the microwave amplitude, a residual frequency offset of the cesium beam standard occurs when the cavity resonance frequency  $\omega_c$  is not tuned at the atomic resonance frequency  $\omega_0$ . This cavity pulling frequency offset can be evaluated from results given in the next Section.

However, a microwave cavity designed such that  $\phi = \pi$  offers the possibility to correct  $b_t$ , the estimate of  $b_\mu^{(t)}$  to approach more closely the desired value  $b_\mu^{(r)}$ . This opportunity is related to the fact that the atomic resonance is inverted [3] at  $\omega = \omega_0$ , with  $P_r(b\tau_0, \omega_m T_0 = 0) = 0$ . The spurious term  $P_n$  of Eq. (7) is thus measurable by setting the microwave frequency at  $\omega = \omega_0$ .

Figure 5 shows schematically the variation of the separate probabilities  $P_t$ ,  $P_r$  and  $P_n$  that a transition occurred versus the voltage applied to the attenuator, the latter being a linear function of  $\log(b\tau_0)$ . Since  $P_n$  is proportional to  $(b\tau_0)^2$ , it is represented by a straight line in this graph.

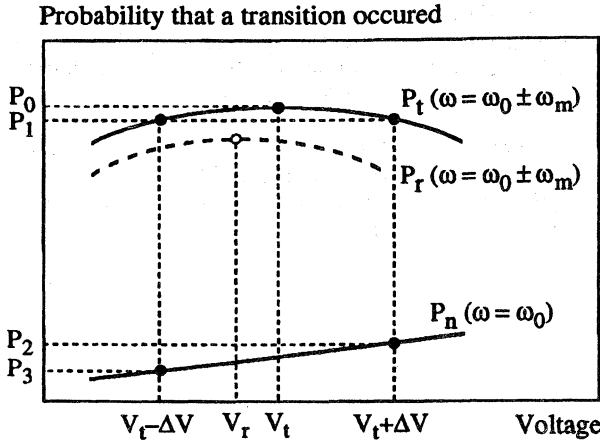


Fig-5. Schematic variation of the probabilities  $P_t$  and  $P_n$  that a transition occurred versus the voltage  $V$ . The black dots show values to be measured.

Close to its maximum,  $P_t$  can be represented by the following parabolic approximation :

$$P_t = C - A(V - V_t)^2, \quad (8)$$

where  $A$  and  $C$  are constants. The voltage  $V_t$  is that given by the microwave amplitude feedback loop. We have, from Eq. (7) :

$$P_r = C - A(V - V_t)^2 - P_n. \quad (9)$$

The maximum of  $P_r$  is obtained for the value  $V_r$  of the voltage such that :

$$V_r - V_t = -\frac{1}{2A} \frac{\partial P_n}{\partial V}. \quad (10)$$

Therefore, by adding the corrective term  $V_r - V_t$  to the servoed value  $V_t$  of the voltage, one obtains a microwave amplitude approaching more closely the desired value  $b_{\mu}^{(r)}$ .

The practical strategy to implement is the following,  $\Delta V$  being the voltage modulation depth (see fig. 5) : i) set the microwave frequency at  $\omega = \omega_0 \pm \omega_m$  and measure  $\omega_0$  when the voltage is  $V_t$  as given by the amplitude feedback loop and  $P_1$  when the voltage is  $V_t \pm \Delta V$  and ii) set the microwave frequency at  $\omega = \omega_0$  and measure  $P_2$  and  $P_3$  for  $V = V_t \pm \Delta V$ . It is easy to see that we have :

$$V_r - V_t = -\frac{\Delta V}{4} \frac{P_2 - P_3}{P_0 - P_1}. \quad (11)$$

For  $n = 3$  and the numerical values considered here, a computer simulation shows that the relative difference between the corrected value of  $b$  and the target value,  $b_{\mu}^{(r)}$ , is equal to  $-1.7 \times 10^{-3}$ ,  $-3.0 \times 10^{-3}$  and  $-4.3 \times 10^{-3}$  for a modulation depth of the microwave amplitude respectively equal to 1, 2 and 3 dB of the value  $b_t$  given by the amplitude feedback loop. The method is also well suited to approach very closely the desired value of the microwave amplitude in the cases  $n = 1$  and 2.

## 8. RESIDUAL CAVITY PULLING EFFECT

For the purpose of locking a quartz crystal oscillator to the atomic resonance, the frequency of the microwave field is switched between the two values  $\omega_i - \omega_m$  and

$\omega_i + \omega_m$ . If the cavity resonant frequency  $\omega_c$  is not equal to  $\omega_i$ , then the amplitude of the field inside the interaction regions is not the same at the two frequencies. Assuming that this amplitude is  $b^+$  at the frequency  $\omega_i + \omega_m$ , it is equal to  $b^-$  at  $\omega_i - \omega_m$ , given by :

$$b^- = b^+ \frac{[1 + T_c^2 (\omega_i - \omega_c + \omega_m)^2]^{1/2}}{[1 + T_c^2 (\omega_i - \omega_c - \omega_m)^2]^{1/2}}, \quad (12)$$

where  $T_c$  is the cavity time constant. We have  $T_c = 2Q_c/\omega_c$ ,  $Q_c$  being the cavity quality factor. The frequency feedback loop adjusts  $\omega_i$  such that the beam tube response is the same at  $\omega_i + \omega_m$  and  $\omega_i - \omega_m$ . Since the magnitude and the width of the atomic resonance depend on  $b$ , as can be seen from Eq. (1), this occurs for a value of  $\omega_i$  that is offset with respect to the atomic resonance frequency  $\omega_0$ , except if the condition  $b^+ = b_{\mu}^{(r)}$  is fulfilled. (The role of  $b^+$  and  $b^-$  can be inverted since we generally have  $\omega_m \ll |\omega_c - \omega_i|$ ).

We have computed the cavity pulling frequency offset  $(\omega_i - \omega_0)/2\pi$  versus the cavity mistuning  $(\omega_c - \omega_0)/2\pi$  by searching for the value of  $(\omega_i - \omega_0)$  that provides the same probability that a transition occurred at  $\omega_i \pm \omega_m$ . The computation does not assume that the frequency offset of the cavity is small compared to its linewidth. Figure 6 gives the cavity pulling frequency offset for several values of  $db = b^+ - b_{\mu}^{(r)}$ , with  $db/b$  varying from  $-3 \times 10^{-2}$  to  $+3 \times 10^{-2}$ . It is assumed  $n = 3$ ,  $\phi = \pi$ ,  $L/\ell = 16.2$ ,  $\omega_m T_o = 1.5$ ,  $T_o = 0.75$  ms and  $Q_c = 1000$ . The variation of  $\omega_i - \omega_0$  versus  $\omega_c - \omega_0$  has the general shape of a dispersion curve, with extrema at  $\pm \omega_c/2Q_c$ . This is to be related to the fact that the difference  $b^+ - b^-$  is closely proportional to the derivative of the cavity resonance pattern.

Since it is possible to obtain  $|db/b| < 5 \times 10^{-3}$  in the case  $\phi = \pi$ , it follows that the fractional cavity pulling frequency offset can be made smaller than  $1 \times 10^{-14}$  for any cavity mistuning.

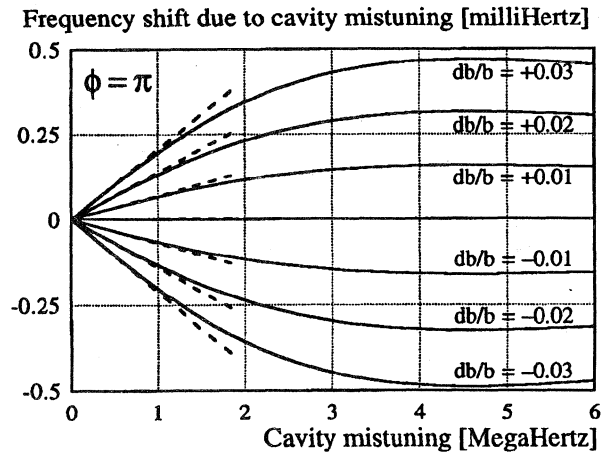


Fig-6. Frequency offset due to the cavity pulling effect versus the cavity mistuning for several values of the relative deviation of the microwave amplitude from the desired value  $b_{\mu}^{(r)}$ . We have :  $n = 3$ ,  $\phi = \pi$ ,  $L/\ell = 16.2$ ,  $\omega_m T_o = 1.5$ ,  $T_o = 0.75$  ms and  $Q_c = 1000$ . The dashed lines represent the frequency offset calculated under the approximation of a small cavity mistuning [3].

## CONCLUSION

We have described a method aimed at controlling accurately the microwave amplitude in optically pumped cesium beam frequency standards. We have shown that despite the presence of neighboring lines, it is possible to obtain a value of this amplitude such that the fractional cavity pulling frequency offset is smaller than  $1 \times 10^{-14}$  for any cavity mistuning. This result assumes that the cavity is designed so that the phase difference between the two oscillatory fields is equal to  $\pi$ , confirming the interest of such a design. A profile of the distribution of the amplitude of the microwave field in each interaction region is obtained as a by-product of the analysis supporting the results described.

## ACKNOWLEDGEMENT

We gratefully acknowledge the support of DSP (Direction des Systèmes de Force et de la Prospective).

## REFERENCES

1. L.S. Cutler and R.P. Giffard, 1992, "Architecture and Algorithms for new cesium beam frequency standard electronics", in : Proc. 1992 IEEE Frequency Control Symposium, Hershey, USA, pp. 127-133.
2. C. Audoin, P. Lesage and A.G. Mungall, 1974, "Second order Doppler and cavity phase dependent frequency shifts in atomic beam frequency standard", IEEE Trans. Instrum. Meas., vol 23, n°4, pp. 501-508.
3. C. Audoin, V. Giordano, N. Dimarcq, P. Cérez, P. Petit and G. Théobald, 1994, "Properties of an optically pumped cesium-beam frequency standard with  $\phi = \pi$  between the two oscillatory fields", IEEE Trans. Instrum. Meas., vol 43, n°4, pp. 515-520.
4. B. Boussert, P. Cérez, L. Chassagne and G. Théobald, 1997, "Frequency evaluation of a miniature optically pumped cesium beam clock", in : Proc. 11th European Frequency and Time Forum, Neuchâtel, Switzerland, pp. 58-62.
5. J. Vanier and C. Audoin, 1989, in Quantum Physics of Atomic Frequency Standards, Philadelphia : IOP Publishing.
6. N.F. Ramsey, 1956, in Molecular Beams, Oxford : Clarendon Press.
7. A. de Marchi, G.D. Rovera and A. Premoli, 1984, "Pulling by neighboring transitions and its effects on the performance of caesium beam frequency standards", Metrologia, vol 20, n°1, pp. 37-47.
8. L. Pichon and A. Razeq, Juillet 1997, "Apport de la modélisation électromagnétique à la caractérisation des horloges atomiques", Bulletin du Bureau National de Métrologie, Paris, n° 109, pp. 17-23.
9. A. de Marchi, 1987, "Rabi pulling and long-term stability in cesium beam frequency standards", IEEE Trans. Ultrason. Ferroelec. Freq. Contr., vol 34, n°6, pp. 598-601.
10. L.S. Cutler, C.A. Flory, R.P. Giffard and A. de Marchi, 1991, "Frequency pulling by hyperfine s transitions in cesium beam atomic frequency standards", J. Appl. Phys., vol 69, n°5, pp. 2780-2782.
11. F. Hamouda, R. Barillet and P. Cérez, "A versatile PC controlled servo-system for high performance optically pumped cesium beam frequency standard". Presented at this conference.

## ESTIMATION OF THE END TO END PHASE SHIFT WITHOUT BEAM REVERSAL IN Cs BEAM FREQUENCY STANDARDS

Ala'a Makdissi and Emeric de Clercq

BNM-Laboratoire Primaire du Temps et des Fréquences  
Observatoire de Paris, 61 Av. de l'Observatoire, 75014 Paris, France.  
E-mail: Alaa.Makdissi@obspm.fr

### ABSTRACT

In this paper, a new method is presented to directly determine the averaged phase difference  $\phi$  between the fields interacting with the atoms in the two regions of a Ramsey cavity. This method allows to determine  $\phi$  in commercial clocks which has been believed not to be measurable until now. We show too that it is possible to cancel the phase shift whatever the value of  $\phi$ . Experimental results in our standard are given. They are compared with those obtained by the beam reversal method which validate the new method. We show that the beam reversal method could lead to erroneous evaluation in our case. When combined with a beam reversal operation, this method allows too to make correction of the distributed phase shift which could be very harmful if not considered.

### I - INTRODUCTION

Many factors contribute to the error budget of Cs atomic beam frequency standards. At present time, the frequency shift (named the cavity phase shift or the end to end phase shift) due to the phase difference between the two interacting fields of the microwave cavity is known to have one of the biggest contribution to the error budget of both commercial and laboratory clocks. In case of laboratory clocks, a beam reversal experiment is used in order to measure this shift. Spatial phase variations due to losses in the cavity walls complicate the efforts to precisely estimate this effect by imposing stringent specifications on the retrace of the beam (see De Marchi et al (1)).

When the atomic time of flight distribution is broad or asymmetric as in optically pumped laboratory standards or in commercial clocks, the cavity phase shift is sensitive to some operational parameters like the microwave power level and the modulation depth. Here we show that it is possible to estimate the phase shift, and even to cancel it, using the dependency of this shift on the above parameters. It is then a phase shift measurement without beam reversal. The proposed method could allow to know the phase shift in a commercial clock. In a

laboratory clock this method could allow to detect the effect of the spatial phase variation and to confirm the results of beam reversal. The accuracy of proposed methods depends on the stability of the standards and on the degree to which the other shifts are known.

This paper is organized as follows. In Section II, the basic formulae are given. The problem of determination of the phase difference  $\phi$  is introduced. In Section III, we show the principle of the well known beam reversal method and discuss its accuracy and its limitations. We propose a new method that allow to estimate  $\phi$  without beam reversal in Section IV. Section V is devoted to experimental results. Conclusions are presented in Section VI.

### II - FREQUENCY SHIFTS

In cesium beam frequency standards the frequency of the local oscillator is locked to the center of the atomic resonance. For this purpose the resonator frequency is modulated. Here we consider only the square wave frequency modulation case with a modulation depth  $f_m$ . As the atomic resonance is distorted by some effects, the average frequency of the local oscillator depends on the frequency modulation depth. During the locking operation, the measurable quantity is the mean frequency difference between the locked local oscillator frequency and a reference frequency, it can be written as :

$$f = f_{LLO} - f_R = f_0 + f_{of} + \sum_i f_i - f_R \quad (1)$$

Where  $f_{LLO}$  is the frequency of the locked oscillator,  $f_R$  is the reference frequency, given by an H maser in our case.  $f_0$  is the center of the unperturbed resonance, corresponding to the value of the definition of the second.  $f_{of}$  is the offset of the resonance center, due to effects which translate the resonance without distortion, like the quadratic Zeeman effect, the black body shift, etc. The  $f_i$  terms are shifts due to effects which distort the resonance curve. They are mainly equal to:

$$\sum_i f_i = C(f_m, b) + D(f_m, b) + \phi F(f_m, b) \quad (2)$$

where  $C$  is the cavity pulling shift,  $D$  is the second order Doppler shift, and  $\phi F$  is the phase shift.  $b$  is the Rabi frequency, proportional to the square root of the microwave power and  $\phi$  is the phase difference between the two fields in the arms of the Ramsey cavity.

$f_{of}$ ,  $C$ , and  $D$ , can be measured or computed by well known methods, see for example Vanier and Audoin (2).  $F$  is computed from  $f_m$ ,  $b$ , and the Time Of Flight (TOF) distribution  $\rho(\tau)$  by:

$$F(f_m, b) = \frac{\ell \int \sin\left(2\pi \frac{L}{\ell} f_m \tau\right) \sin^2(b\tau) \rho(\tau) d\tau}{L \int \tau \sin\left(2\pi \frac{L}{\ell} f_m \tau\right) \sin^2(b\tau) \rho(\tau) d\tau} \quad (3)$$

where  $\ell$  is the width of one arm of the Ramsey cavity (1cm in our standard),  $L$  is the length of free flight between the two arms of the cavity (1m in our standard), and  $\tau$  is the time of flight across  $\ell$ .

In order to evaluate the standard and to estimate  $f_0 - f_R$ , all the shifts must be computed and considered in the correction of the measured frequency. Here we suppose that the unknowns in equation (1) are  $f_0 - f_R$  and  $\phi$ . Therefore, knowing  $\phi$  in equation (1) leads to achieve the evaluation of the standard. In the followings, the problem of estimating  $\phi$  is addressed.

### III - BEAM REVERSAL METHOD

Until now the only method used to measure the phase shift is the beam reversal technique: two atomic beams with opposite directions are successively used. The measured frequency in the first direction  $f_1$  is given by :

$$f_1 = (f_0 - f_R) + f_{of} + C + D + \phi F \quad (4)$$

In the opposite direction,  $\phi$  change its sign and the measured frequency is:

$$f_2 = (f_0 - f_R) + f_{of} + C + D - \phi F \quad (5)$$

$\phi$  can be computed from equations (4) and (5):

$$\phi = \frac{f_1 - f_2}{2F} \quad (6)$$

The uncertainty on  $\phi$  with this method is equal to:

$$\sigma_\phi = \frac{\sigma_f}{F} + \frac{\phi \sigma_F}{F} \quad (7)$$

In our standard with operational parameters,  $F \cong -35$ ,  $\sigma_F \cong 0.1$ ,  $\sigma_f \cong 6.10^{-5}$  Hz, we get  $\sigma_\phi = 2 \mu\text{rad}$  for  $\phi = 180 \mu\text{rad}$ .

The beam reversal technique has several limits. Commercially available tubes are sealed and therefore do not allow reversal measurement. In a laboratory standard it requires a perfect symmetry of the atomic trajectories with the beam reversal. Otherwise the spatial phase variation in each arm of the cavity yields to a phase difference different for each beam direction, and then to a different shift. This is the distributed phase shift. The TOF distribution must be the same for the two beam directions, if not the terms  $C$ ,  $D$  and  $F$  are different for each beam direction.

### IV - METHOD WITHOUT BEAM REVERSAL

The method of estimating the phase difference  $\phi$  with a single beam uses the asymmetry or the broadness of the TOF distribution in commercial standards and in optically pumped standards. With such a distribution the  $F(f_m, b)$  term is sensitive to the modulation depth  $f_m$  and to the Rabi frequency  $b$ , i.e. the microwave power. Figure 1 shows the computed  $F$  function versus the modulation depth  $f_m$  for two values of  $b$ ,  $b_{opt}$  is the  $b$  value which maximizes the clock signal at resonance.

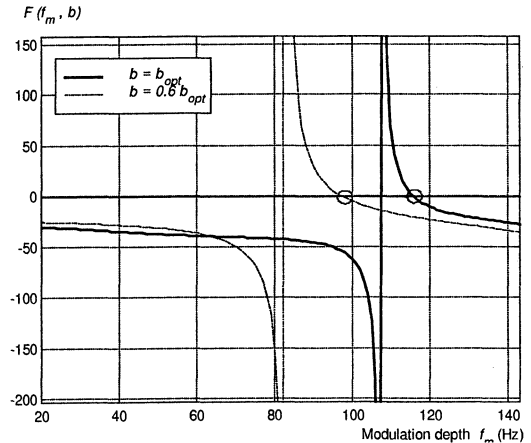


**Figure 1:** The  $F$  function versus the modulation depth  $f_m$  for two  $b$  values. The circles show the points where the phase shift is canceled

It can be noticed that the phase shift is canceled for some values of  $(f_m, b)$ . The circles in Fig. 1 show the points where the  $F$  function is null and then the

phase shift for any value of the phase difference. For these points the slope of the Ramsey fringe is small and the short term stability is reduced. However, there are a couple  $(f_m, b)$  where the stability is degraded by only a factor four.

In the following we will use the corrected frequency from all the effects except the phase shift:

$$f_x = f - f_{of} - C(f_m b) - D(f_m b) = f_0 - f_R + \phi F(f_m b) \quad (8)$$

With

$$a = f_0 - f_R \quad (9)$$

$f_x$  becomes:

$$f_x = a + \phi F \quad (10)$$

We notice the linear relation between  $f_x$  and  $F$ . In order to calculate  $a$  and  $\phi$  from equation (10) we let vary  $F$  by varying  $f_m$  and  $b$ . Using  $N$  different values for  $(f_m, b)$  we get  $N$  linear equations, that we can write in a matricial form:

$$\begin{pmatrix} f_{x1} \\ f_{x2} \\ \vdots \\ f_{xN} \end{pmatrix} = \begin{pmatrix} 1 & F_1 \\ 1 & F_2 \\ \vdots & \vdots \\ 1 & F_N \end{pmatrix} \begin{pmatrix} a \\ \phi \end{pmatrix} \quad (11)$$

or as:

$$\mathbf{f}_x = \mathbf{A}\Theta \quad (12)$$

The uncertainty  $\sigma_{f_{xi}}$  on each corrected frequency  $f_{xi}$  is maximized by:

$$\sigma_{f_{xi}} = \sigma_{f_i} + \sigma_{of} + \sigma_{C_i} + \sigma_{D_i} \quad (13)$$

$\sigma_{f_i}$  depends on the stability of the clock and the measurement time.  $\sigma_{C_i}$  and  $\sigma_{D_i}$  could be estimated by using different methods to compute  $C$  and  $D$ .  $\sigma_{of}$  is small in most standards and does not depend on  $(f_m, b)$ .

The covariance matrix  $\mathbf{R}_f$  of the vector  $\mathbf{f}_x$  express the uncertainty on this vector and under the assumption that the different  $N$  measured frequencies are uncorrelated it is given by:

$$\mathbf{R}_f = \text{diag}(\sigma_{f_{x1}}^2, \sigma_{f_{x2}}^2, \dots, \sigma_{f_{xN}}^2) \quad (14)$$

Where  $\text{diag}$  means a diagonal matrix.

In order to solve equation (12) and to estimate  $a$  and  $\phi$ , we look for a not biased solution  $\hat{\Theta}$  that has a minimum variance  $\mathbf{R}_\Theta$ . This can be seen as a minimization problem (of  $\mathbf{R}_\Theta$ ) subject to a

constraint (not biased solution). The formal solution of this problem is given by:

$$\hat{\Theta} = (\mathbf{A}^t \cdot \mathbf{R}_f^{-1} \cdot \mathbf{A})^{-1} \cdot \mathbf{A}^t \cdot \mathbf{R}_f^{-1} \cdot \mathbf{f}_x \quad (15)$$

and the covariance matrix of this solution is:

$$\mathbf{R}_\Theta = (\mathbf{A}^t \cdot \mathbf{R}_f^{-1} \cdot \mathbf{A})^{-1} \quad (16)$$

$\mathbf{R}_\Theta$  is a  $(2 \times 2)$  matrix. It express the uncertainty on the found solution. Its diagonal terms express the uncertainties on  $\phi$  and  $a$ :

$$\sigma_\phi = \sqrt{\mathbf{R}_\Theta(2,2)}, \quad \sigma_a = \sqrt{\mathbf{R}_\Theta(1,1)} \quad (17)$$

its non diagonal terms express the correlation between  $\phi$  and  $a$ .

We notice that the solution (15) is a special case of the weighted least squares solution when the weighting matrix is equal to the inverse of the covariance matrix  $\mathbf{R}_f$  of the observation  $\mathbf{f}_x$ . If the covariance matrix  $\mathbf{R}_f$  is unknown, it could be replaced by the identity matrix. Then the classical least square solution is obtained.

When the TOF distribution is narrow, changing  $f_m$  and  $b$  leads to close values of  $F_i$  and therefore the rows of the matrix  $\mathbf{A}$  in (12) are linearly dependent and  $\mathbf{A}$  is said to be ill-conditioned. Then in the presence of noisy measurement  $\mathbf{f}_x$  the solution  $\hat{\Theta}$  is not meaningful and a regularization approach (see Makdissi et de Clercq (3)) that smoothes the solution could not be applied because the elements of  $\hat{\Theta}$  have different physical meaning.

## V - EXPERIMENTAL RESULTS

In order to compare results obtained by the proposed method with results of beam reversal, we have performed the same measurements on each beam direction. We have measured three data sets for each direction. The first data set is with  $f_m = 45$  Hz,  $b$  takes seven values,  $b \in \{ 15000, 21330, 26150, 30135, 33664, 36945, 39962 \}$  rad/s.  $b$  is fixed in the second set to  $b_{opt}$ , the value of  $b$  which maximizes the clock signal at resonance,  $f_m$  takes the values : 30, 35, 40, 45, 50, 55, 60, 70 Hz. In the third data set  $b = 0.6 b_{opt}$ ,  $f_m = 25$  to 60 Hz step 5. We have then 23 distinct measurements for each beam direction. The total measurement time is a little more than 4 days for one beam direction. The relative drift of the maser frequency during this time is less than  $1 \cdot 10^{-15}$ . In our standard one beam direction is the East-West direction and the opposite direction is West-East. The cavity pulling  $C$ , the second order Doppler

effect  $D$  and the  $F$  function are computed for each value of  $(f_m, b)$  using the TOF distribution previously determined by different methods and directly from a measured Ramsey pattern for each  $b$  value (see Makdissi and de Clercq (4)). The uncertainties on  $C$  and  $D$  are taken as the standard deviation of the different values obtained by the different methods. In the three data sets  $\sigma_{f_x}$  was between  $4 \times 10^{-5}$  and  $8 \times 10^{-5}$  Hz using equation (13). The frequency is also corrected of the quadratic Zeeman effect. Fig. 2 shows the corrected frequency  $f_x$  versus the values of the function  $F$ . As expected the dependency of  $f_x$  on  $F$  is linear.

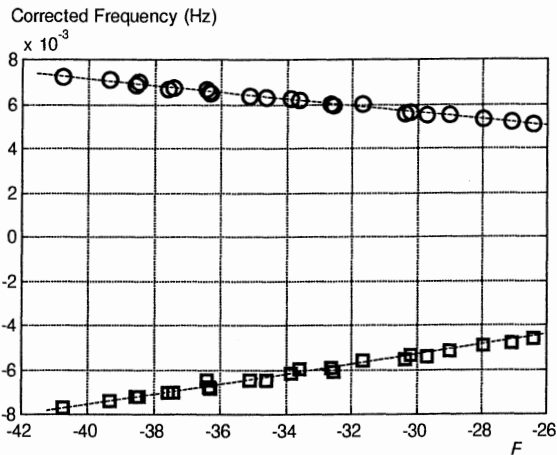


**Figure 2:** Corrected frequency versus  $F$ . Squares:  $E-W$  direction, Circles:  $W-E$  direction.

In order to compare these two straight lines, the corrected frequency  $f_x$  for the EW direction is plotted versus  $F$  in Fig. 3, with  $-f_x$  for the WE direction. The two slopes are clearly different and then the two phases differences are also different.

The proposed weighted least squares method applied to these points gives:

EW direction:

$$\phi_{EW} = 212.54 \mu\text{rad}, a = 9.89 \times 10^{-4} \text{Hz} \quad (18)$$

WE direction:

$$\phi_{WE} = 152.96 \mu\text{rad}, a = 9.86 \times 10^{-4} \text{Hz} \quad (19)$$

Equations (17) led to uncertainties  $\sigma_a = 8.3 \times 10^{-5}$  and  $\sigma_\phi = 2.5 \mu\text{rad}$  which yield a relative frequency uncertainty equal to:  $8.2 \times 10^{-15}$  in operational conditions.

With the same least squares method applied to the same points but considered as  $N$  beam reversal measurements, see Fig.4, we get:

$$\phi_{BR} = 182.68 \mu\text{rad}, \sigma_\phi = 0.4 \mu\text{rad} \quad (20)$$

Using this value of  $\phi$  for computing  $a$  from equation (10) gives:  $a = -8.6 \times 10^{-6}$  Hz.

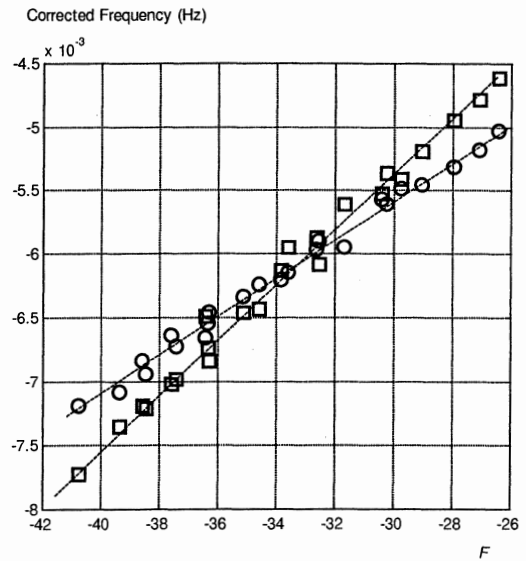


**Figure 3:** Corrected frequency versus  $F$ . Squares:  $+f_x$  is reported for the  $E-W$  direction, Circles:  $-f_x$  for the  $W-E$  direction.

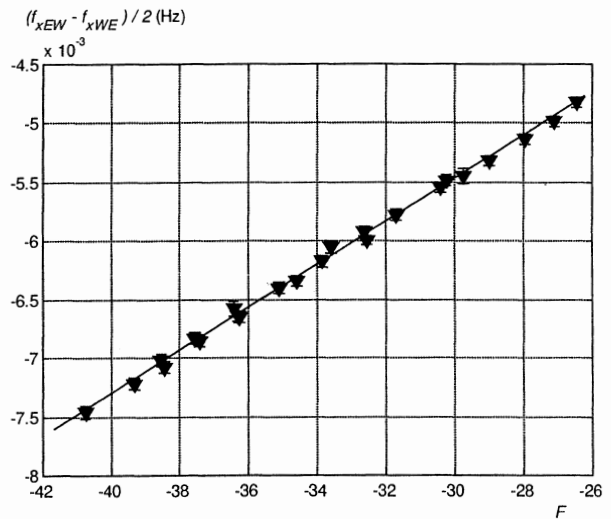


**Figure 4:** Beam reversal method,  $(f_{xEW} - f_{xWE}) / 2$  versus  $F$ .  $\phi_{BR}$  is the slope of the curve.

The values of the phase differences are different for each beam direction,  $\phi_{EW} \neq \phi_{WE}$ , and are different of the phase difference computed from beam reversal  $\phi_{BR}$ . However we can notice that  $\phi_{BR}$  is just equal to the average of the phase difference for each beam direction, taking into account the uncertainties :

$$\phi_{BR} = \frac{\phi_{EW} + \phi_{WE}}{2} = 182.75 \mu\text{rad}. \quad (21)$$

This can be easily explained. If we suppose that the two phases are different, equation (10) becomes:

$$f_{xEW} = a + \phi_{EW} F \quad (22)$$

$$f_{xWE} = a - \phi_{WE} F \quad (23)$$

The phase difference calculated by beam reversal is then:

$$\phi_{BR} = \frac{f_{xEW} - f_{xWE}}{2F} = \frac{\phi_{EW} + \phi_{WE}}{2} \quad (24)$$

The different result for each beam direction is therefore consistent with the phase difference obtained by beam reversal.

We can check if the two phase are really different by noticing that:

$$\text{If } \phi_{EW} = \phi_{WE} \text{ then: } \bar{f} = \frac{f_{xEW} + f_{xWE}}{2} = a \quad (25)$$

$$\text{If } \phi_{EW} \neq \phi_{WE} \text{ then: } \bar{f} = a + \frac{\phi_{EW} - \phi_{WE}}{2} F \quad (26)$$

The averaged corrected frequency  $\bar{f}$  versus  $F$  is shown on Fig.5.

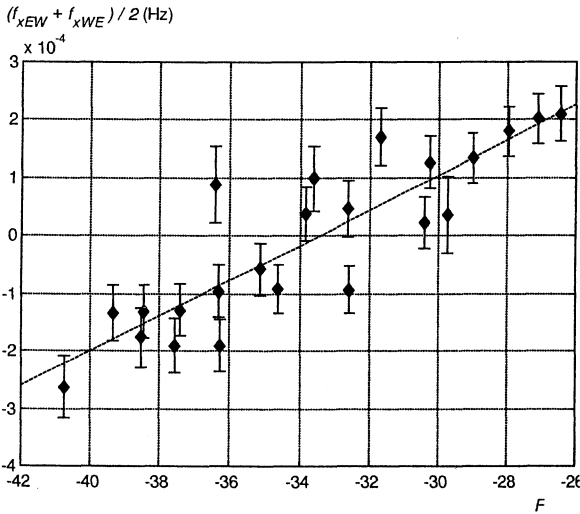


Figure 5:  $(f_{xEW} + f_{xWE})/2$  versus  $F$ . We notice a residual phase difference of  $30 \mu\text{rad}$ .

Clearly,  $\bar{f}$  is not a constant but increases linearly with  $F$ . The slope is equal to  $30 \mu\text{rad}$ , the half difference of phase differences. Consequently the phase differences are not equal, and the new method is validated and is consistent with beam reversal method. The difference of phase differences could be explained by a distributed phase shift, as this effect does not change of sign with the beam direction, or by another shift with the same behavior with  $f_m$  and  $b$  as a phase shift. This needs further investigations.

## VI - CONCLUSION.

We have proposed a new method in order to measure the phase difference for one beam direction without beam reversal. The method is based upon the sensitivity of the phase shift with the modulation depth and the Rabi frequency when the TOF distribution is asymmetric or broad. A weighted least squares method is used for extracting the numerical value of the phase difference from experimental data. The method has been checked on our optically pumped frequency standard and compared to the beam reversal method. The two methods are in agreement but the new method gives more information, it gives the phase difference for each beam direction and not the average. In our experiment the uncertainty on the measured phase difference is  $\sigma_\phi = 2.5 \mu\text{rad}$ . It can still be decreased by using a larger number of measurements or by more accurate frequency measurements (i.e. longer integration times). The new method is valid for commercial Cs clocks as well as for optically pumped clocks. We believe that when applied to commercial clocks, the proposed method could reduce their accuracy to a few times  $10^{-14}$ .

We have also shown that the phase shift can be canceled in some cases.

## ACKNOWLEDGEMENTS

We wish to thank P. Aynié, J. P. Berthet and N. Dichard for their helpful technical assistance.

## REFERENCES

1. A. De Marchi et al, 1991, "Feasibility of End to End Phase Shift Correction from the Outside of Sealed Cesium Beam Tubes", *IEEE Trans. Instr. Meas.*, vol 40, n°2, pp.165-169.
2. J. Vanier and C. Audoin, 1989, "The Quantum Physics of Atomic Frequency Standard", Adam Hilger, Bristol and Philadelphia.
3. A. Makdissi and de Clercq, 1997, "A Regularization Approach for the Determination of the TOF Distribution in the Cesium Beam Standard", *IEEE Trans. Ultra. Ferro. Freq. Contr.*, vol 44, n°3, pp 637-642.
4. A. Makdissi and E. de Clercq, 1997, "A Signal Approach Analysis of the Ramsey Pattern in Cesium Beam Frequency Standards", *IEEE Trans. Instr. Meas.*, vol 46, n°2, pp 112-116.

**The ACCURACY EVALUATION of the LPTF CESIUM FOUNTAIN FREQUENCY  
STANDARD at the  $10^{-15}$  LEVEL and FUTURE PROSPECTS.**

S.Ghezali, Ph.Laurent, E.Simon, G.Santarelli, P. Lemonde, K. Szymaniec \*,  
L. Cagnet \*\*, M. Bahoura, M. Santos, S. Bize, Y. Sortais, F. Pereira dos Santos  
and A.Clairon.

BNM /LPTF, Observatoire de Paris, 61 Avenue de l'Observatoire, 75014 Paris, France.

e-mail: Selma.Ghezali@obspm.fr

**Abstract**

Most of the frequency shifts which limit the accuracy of cesium atomic frequency standards are considerably reduced when using ultra-cold atoms and long interrogation times in a Ramsey geometry. These shifts are also more easily evaluated than in traditional cesium beam standards. Most of these shifts reduced to  $10^{-16}$  or less and can be calculated accurately such as relativistic shifts, cavity pulling, Rabi pulling... Other effects have to be directly measured. With our actual experimental set up, we have measured frequency shifts due to cold collisions, quadratic Stark effect, black body radiation, quadratic Zeeman effect, residual first order Doppler effect....

At present, the accuracy of the fountain is estimated at  $2 \cdot 10^{-15}$ . A biatomic cesium-rubidium fountain, is being built leading to a potential improvement of a factor 10 of the actual fountain's accuracy evaluation.

\*: University of Durham, Department of Physics, England.

\*\* : IOTA, ESO, Paris XI University, Orsay. France.

A SIMPLE CONFIGURATION OF CLOCK USING COLD ATOMS

Ch. Guillemot, P. Petit, S. Forget, C. Valentin, N. Dimarcq

Laboratoire de l'Horloge Atomique, Unité Propre de Recherche du CNRS associée à l'Université Paris-Sud  
Bâtiment 220, Université Paris-Sud - F-91405 Orsay Cedex - France

1. ABSTRACT

We present a new experiment named « CHARLI » (in French Configuration d'Horloge à Atomes Refroidis en Lumière Isotrope), which is an atomic clock using a source of Cesium atoms cooled in isotropic light. We describe CHARLI and expose our first experimental results.

Keywords : Cold Cesium clocks, miniature clocks

Last year [2], we proposed a new cooling configuration with isotropic light which has been demonstrated to be efficient and easy to operate.

CHARLI takes advantage of this cooling technique. Thus, CHARLI's configuration is very simple (Figure 1). The clock has a sequential operation. In a first step, atoms are cooled in a cell with isotropic light. The laser beams are then switched off and the atoms fall down, due to the gravity force. The microwave interrogation occurs under the cell in a cylindrical cavity. The clock signal is optically detected below with resonant light. This signal is expected to have a linewidth about 30 Hz.

3. COOLING OF ATOMS

The cooling experimental set-up is based on the cooling configuration we used last year [2].

The Cesium atoms are contained in a cell (diameter = 2 inches). The isotropic light is created in an integrating sphere made with SPECTRALON (produced by Labsphere). The laser light is injected inside the sphere with multimode fibers. We changed the following points. Firstly, the Cesium source is no longer located at the bottom of the experimental device. Indeed, the presence of hot Cesium atoms in the area of TOF was a source of ratio signal to noise degradation. Now, the source is located at the top of the device (see Figure 1).

Secondly, we use a quartz cell which has the same size (2 inches) as the integrating sphere : 2D computed simulations showed us that the light distribution in the cell was about the same than when the integrating sphere was bigger. That's what we can see in the figure 2.

The first graph represents light distribution (in arbitrary units) along a radius when the cell and the integrating sphere are the same size ; the second one is the light distribution when the integrating sphere is bigger (47 mm diameter for the integrating sphere and 35 mm diameter for the cell).

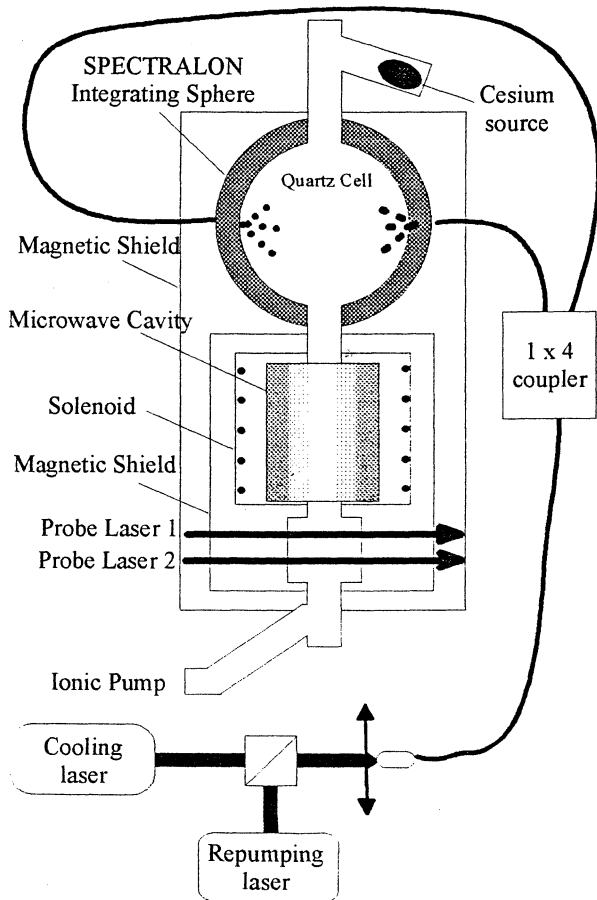
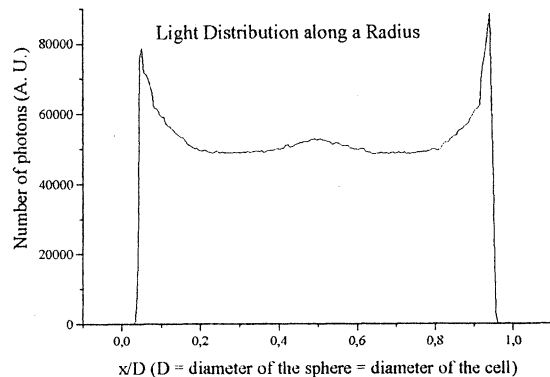


Fig-1. Experimental Set-up.

2. GENERAL POINTS

The advantages of isotropic light have been already demonstrated [1].

At the present time, the users of atomic clocks are generally satisfied by the frequency performances of the existing clocks. They now wish their size to be reduced with the same performances. The use of cold atoms is an answer to that wish.



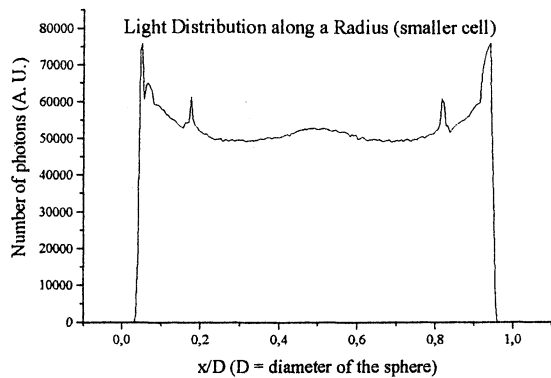


Fig-2. 2D Computed Simulations of the light distribution in the integrating sphere.

Thirdly, light is injected with 4 multimode (50/125  $\mu\text{m}$ ) fibers connected to a  $1 \times 4$  multimode coupler : previous cooling experiments have demonstrated that the cooling with only one or two optical fibers was still efficient [2]. The fibers are placed every  $90^\circ$  in the horizontal plane passing by the center of the cell.

Another important change is in the choice of the cooling light. We use no more SC extended cavity laser. The cooling light comes from a DBR laser diode which delivers about 150 mW and whose linewidth is about 5 MHz. These frequency performances are not so good as those of an extended cavity laser (linewidth in the range of 100 kHz).

The cooling laser frequency  $f_L$  is tuned below the resonance frequency of the  $4 \rightarrow 5$  transition of the cesium  $D_2$  line. For this purpose, it is locked on the frequency of the saturated absorption signal for the  $4 \rightarrow 5$  transition which we shift by Zeeman effect. The pumping laser is tuned to the  $3 \rightarrow 4$  transition of the Cesium  $D_2$  line. About 50 mW cooling light and 6 mW pumping light are injected in the integrated sphere.

#### 4. MICRO-WAVE INTERROGATION

When the atoms are cold, we switch off the laser light and the atoms fall down.

In fact, we don't cut the two laser beams at the same time. We firstly switch off the cooling laser. Thus the atoms interact with only the repumping laser during a few milliseconds. This interaction phase aims at preparing them in the  $F=4$  state.

Then they cross the microwave cavity.

This one is surrounded by a solenoid that provides a weak (several mG) but uniform magnetic field in the cavity. Firstly, this magnetic field's orientation is parallel to the longitudinal microwave magnetic field : thus, only the  $\Delta m=0$  transitions are allowed ; secondly its value is important enough to separate the transition  $m=0 \rightarrow m=0$  from the others.

This is a cylindrical copper cavity and the atoms cross it once. We chose a Rabi scheme : atoms see a single  $\Pi$  pulse during the whole crossing. The reason why we didn't choose the temporal Ramsey scheme (two short  $\Pi/2$  pulses separated by a dead time  $T$ ) is that we don't know exactly the actual size of the cold atoms clouds : if we deal with big clouds (that's what we guess), the Ramsey method is not suitable.

This cavity operates in the  $TE_{011}$  mode. Therefore, atoms do not see a constant microwave magnetic field when they cross it : this one varies in a sinusoidal way. This is why the maximum contrast for the Rabi signal is not obtained from [3] :

$$b\tau = \pi + 2k\pi$$

but from the following equation [3]:

$$b\tau = \frac{1}{2}\pi^2 + 2k\pi$$

where  $b$  is the Rabi pulsation and  $\tau$  the time spent by the atoms in the cavity. The smaller  $k$ , the narrower the Rabi signal. For  $k=0$ , the full width at half maximum is given by [3] :

$$W = \frac{6.85}{\tau}$$

The cavity is 5 cm long and is located 10 cm below the center of the cell. If we consider an atom at rest at the center of the cell, this will remain roughly 33 ms in the cavity. In such conditions, for  $k=0$ , the clock signal is expected to have a linewidth as narrow as 33 Hz, which should lead to frequency performances in the  $10^{-15}$  range. Experimentally, we injected roughly 0,1 nW microwave in the cavity.

#### 5. TIMES OF FLIGHT (TOF)

In order to know the temperature of the cooled atoms, we use the technique of time of flight

After interacting with the microwave, the atoms go on falling. They emit fluorescence when they cross a resonant probe laser. TOF have several utilities : the first one is to measure the cold atoms temperature, the second one is to deduce clock signals : to that purpose, we observe the variation of the TOF integration when the microwave frequency is swept.

In order to increase the signal to noise ratio of the clock signal, we realize a double detection.

The first one (see Figure 1) enables us to detect the atoms that did not make the microwave transition  $F=4, m=0 \rightarrow F=3, m=0$  in the cavity. These atoms are excited by the probe laser 1, whose frequency is locked on the transition  $F=4 \rightarrow F'=5$  of the  $D_2$  line and emit fluorescence. The laser light is firstly a standing wave then a progressive one that will push these atoms. The result will be that only the atoms in the  $F=3$  level will go on falling and contribute to the second detection.

The probe laser 2 consists in two waves. The first one is a progressive wave whose frequency is locked on the transition  $F=3 \rightarrow F'=4$ . It aims at repumping in the  $F=4$  state the atoms which had made the microwave transition. These atoms are then detected in a standing laser wave whose frequency is locked on the transition  $F=4 \rightarrow F'=5$ .

This double detection presents a great advantage : the number of cold atoms is not exactly controlled and can be different at each flight. If we can detect all the atoms (those who interacted with the microwave and those who didn't), we can normalize our results by the total number of atoms.

## 6. EXPERIMENTAL RESULTS

The initial number of cold atoms is a few  $10^9$ .

### 6.1. Temperature measurement

Our TOF were obtained 24 cm below the center of the cell. We cut the repumping laser beam 10 ms after the cooling laser beam. A typical TOF signal is depicted in the following figure.

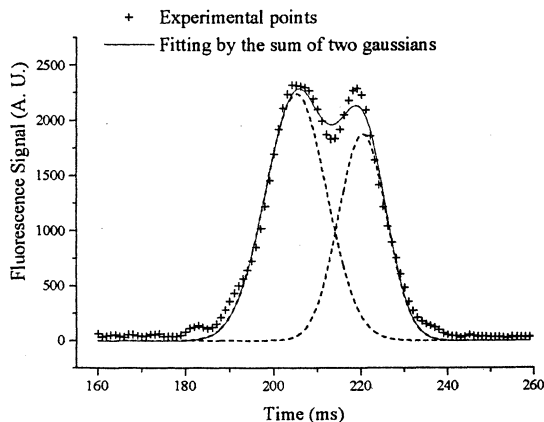


Fig- 3. Typical Time of Flight Signal

The origin of the times is the moment when the cooling light is switch off : it's the moment when the atoms begin to fall.

The dispersion of a TOF signal results both from the dispersion of the initial atomic velocities and from the initial size of the cold atoms cloud. Here, we can see that this TOF can be fitted by the sum of two gaussian lines. This could mean that there are two clouds of cold atoms in the experiment. Simple calculations make us think that the second peak, centered at 220 ms corresponds to the cold atoms at the center of the cell. The first one, centered at 205 ms could then correspond to cold atoms located in the tube below the cell but surrounded by the integrating sphere. If we only consider the second peak, this one has a full width at  $1/e$  maximum roughly equal to 11 ms. This corresponds to a temperature of about  $40 \mu\text{K}$ . Such an obtained Sub-Doppler temperature demonstrates the presence of intensity or polarization gradients in the isotropic light.

### 6.2. Clock signal

**6.2.1 Experimental conditions.** Our clock signals were obtained with the integration of only one TOF : we detected the atoms that didn't make the microwave transition. Time preparation is 10 ms.

The constant magnetic field provided by the solenoid around the cavity is 8 mG.

A typical clock signal we obtained is depicted in the following figure (Figure 4).

For each microwave frequency, the integration value reported on the graph is the average of 10 integration values.

We fit the curve by a squared cardinal sine.

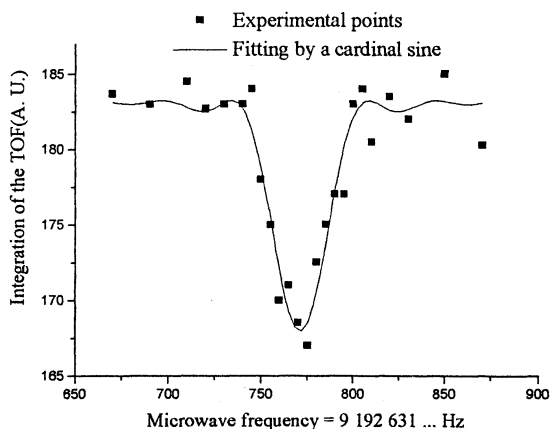


Fig.-4. Clock Signal

**6.2.2 Results and discussion.** The width of the fitted signal is about 35 Hz, which is in agreement with theory (see section 4) that predicts 33 Hz by considering an atom with constant velocity. Now, we have to study the effects of the accelerated motion of the atoms in the microwave cavity and of the atomic velocity distribution. The obtained contrast is about 9 percent : if we consider that, in the better case, all the atoms in the  $F=4, m=0$  state make the microwave transition, this leads to a  $1/9$  contrast, that is to say 11 percent.

For the time being, our signal to noise ratio is in the range several tens and can easily be enhanced. Firstly, we can better control the number of cold atoms by adding a Sisyphus cooling phase before the atomic preparation : thus, atoms will be colder (a few  $\mu\text{K}$ ) and their number will less vary from one TOF to another.

Secondly, the adding of the second probe laser will enable us to normalize our results by the total number of atoms. These two points will be our next days' work.

## 7. CONCLUSION

The cooling configuration appears to be efficient, easy to operate and well suited to a compact clock with high frequency performances.

We obtained cold atoms at temperatures colder than  $100 \mu\text{K}$  and clock signals with widths in the rang of 35 Hz. Of course, an important work remains in order to improve our results, in particular to enhance our signal to noise ratio.

## RÉFÉRENCES

- (1) W. Ketterle, A. Martin, M. A. Joffe and D. E. Pritchard, 1992, « Slowing and Cooling Atoms in Isotropic Light », *Phys. Rev. Lett.*, vol. 69, p. 2483.
- (2) C. Guillemot, Gh Varelle, C. Valentin and N. Dimarcq, 1997, « 3D Cooling of Cesium Atoms with Isotropic Light », *Proc. of 11<sup>th</sup> European Frequency and Time Forum*, Neuchâtel, Switzerland.
- (3) J. Vanier and C. Audoin, 1989, « The Quantum Physics of Atomic Frequency Standards », Vol. 2, Ed. Adam Hilger. (UK).



*12th E F T F* - 10-12 March 1998 - **Warsaw - POLAND**

**Materials**

Chairman:

*John Kosinski*



## LANGASITE AS A MATERIAL FOR PIEZOELECTRIC DEVICES

G.D.Mansfeld,

Institute of Radioengineering and Electronics,  
Russian Academy of Sciences, 11 Mokhovaya st., 103907 Moscow, Russia

### ABSTRACT

A review of the results of numerous works and publications devoted to growing up langasite crystals, experiments on material constants and their temperature dependences measurements, and applications of the material for working out acoustoelectron BAW and SAW devices and sensors is presented.

### LANGASITE AND ITS PROPERTIES

Lanthanum Gallium Silicate ( $\text{La}_5\text{Ga}_5\text{SiO}_{14}$ -Langasite-LGS) is one of the perspective crystalline materials for various applications in acoustoelectron and piezodielectric devices. It belongs to 32 point group, P321 spatial group (lattice parameters:  $a = 8.1662 \text{ \AA}$ ,  $c = 5.074 \text{ \AA}$ , mass density =  $5.751 \text{ g/cm}^3$ ).

The first published mentions of LGS date to 1982-1983 [1-3]. Further investigations and growing up were made in the Institute of Crystallography, «Giredmet» (Podolsk, Moscow region), the Institute of Monocrystals (Kharkov), the Institute «Phonon» (Moscow), IRE RAS (Moscow), and «Fomos» Company (Moscow). Now LGS is also grown up in France, USA, Japan.

Promising advantages of this material in comparison with a widely used quartz and other 32 materials are the follows: absence of phase transitions up to the melting point ( $1470^\circ \text{C}$ ), low acoustic wave propagation losses, a high value of electromechanical coupling constants, and absence of twins.

#### *Growing up LGS Crystals.*

The two methods are used for LGS growing up: Czochralski's method and selfdistributing synthesis [4-8,12]. An important part of the preparation procedure is the preparation of a mixture of high purity oxides  $\text{La}_2\text{O}_3$ ,  $\text{Ga}_2\text{O}_3$ , and  $\text{SiO}_2$  and heating these components mixture during 4 - 5 hours at  $1150 - 1200^\circ \text{C}$  to obtain a multiphase mixture which consists of  $\text{La}_5\text{Ga}_5\text{SiO}_{14} + \text{LaGaO}_3 + \text{Ga}_2\text{O}_3 + \text{SiO}_2$ . For the growth process platinum or iridium crucible is used. Traditionally growth is initiated by using seeds oriented along Z axis. But it is also possible to grow up crystals in Y direction.

Growing procedure takes time from a few hours up to a few days. The grown up crystals have a hexagonal cross-section, a diameter more than 85 mm, and weight more than 4 kg.

#### *Elastic, dielectric and piezoelectric properties of LGS.*

For calculation and prediction of acoustic properties of the media it is necessary to know a full set of elastic modulus, dielectric constants, and expansion coefficients as a function of temperature. Such information is given in [3,6-8]. The latest corrected data and additional data on temperature dependences on piezoelectric constants are published in [9]. They are listed in Table 1.

#### *Acoustic losses in LGS*

Acoustic losses were measured in a wide frequency band for all principal directions of propagation of acoustic waves and crystalline cuts using a Bulk Acoustic Wave Composite Resonator method [10]. The method is based on measurements of total losses in composite resonators consisting of rather thick, properly oriented LGS flat-parallel plates with thin piezoelectric transducer made of ZnO. The resonator is multifrequency one - its resonances (spaced by main resonant frequency of the structure) are seen in a wide frequency band (from hundreds to thousands MHz). For obtaining the attenuation data, losses in ZnO layer and additional losses due to surface roughness, were subtracted from total losses. Frequency dependences of losses revealed square dependence on frequency. Some attenuation data are shown in Table 2. These data agree with the results obtained by the echo-pulse method [11]. A high limit value of Qf product for the thermostable cut ( $Y+1.5^\circ$ ) for slow shear waves is estimated as  $2.5 \cdot 10^{13}$ .

All these data are sufficient for prediction and calculation of the parameters of BAW devices.

#### *BAW devices - monolithic filters*

First prototypes of BAW devices based on LGS were monolithic filters [8,13,14]. The progress in their development was the improvement of their characteristics and increase of frequencies. For modern LGS monolithic filters developed for communication systems reached

parameters are (at room temperature): insertion losses - 1.7 dB, central frequency - 71 MHz, bandwidth - 165 kHz, impedance - 50 Ohm.

#### *BAW devices - resonators*

Many authors [9,12,16-18] made a detailed analysis of coupling and temperature-frequency coefficients as a function of crystalline cuts and wave direction and polarization. In particular zero TCF (Euler angles) was found at  $\varphi = 1.5^\circ$ ,  $\Theta = 0$  for piezoelectric slow shear mode.

It is interesting to compare the data of the investigation of different prototypes of BAW resonators worked out by different investigators. One of BAW resonators (S.A.Sakharov, 1996) worked at a fundamental mode at  $f = 186$  MHz and had rather small Q-factor. It could be explained in part by relatively high losses due to surface and electrode roughness. Much better Q-factor (corresponding to  $Qf = 5.75 \cdot 10^{11}$ ) was achieved in 5 MHz third overtone plano-convex resonator [12].

With the increase of the number of overtone Q-factor and Qf product increase. For the same oscillation mode the value  $Q_a = 3.34 \cdot 10^6$  ( $Qf = 1.65 \cdot 10^{13}$ ) for 7-th overtone was achieved [16]. At microwaves when Y-cut LGS plate was used as vibration element of BAW composite resonator Q was 13700 ( $Qf = 1.89 \cdot 10^{13}$ ) on 1380 MHz [19]. In our experiments with LGS composite resonator designed for frequency synthesizer the value of Q =  $5.1 \cdot 10^3$  ( $Qf = 2.1 \cdot 10^{13}$ ) on the frequency 4.1 GHz was achieved.

Available experience and knowledge on material constants and principles of operation of BAW resonator are sufficient for prediction and calculation of almost all characteristics of LGS BAW resonators. Among the effects for which an adequate explanation was not found is a big difference between Q-factors at resonance and anti-resonance. Similar resonator behavior is often observed in resonators based on materials with strong piezoelectric coupling.

#### *Surface acoustic waves*

Wave velocities, TCF, electromechanical coupling constants, and beam steering angles were calculated and experimentally verified using known material constants [20-23,33].

In [20] more than 150 SAW resonators of different cuts and propagation directions and about 60 various cuts have been prepared and investigated in frequency range 400 - 700 MHz. Their frequency responses were measured at - 40... + 80° C temperature range. Some promising cuts and propagation directions with zero frequency coefficients of resonant frequency were found. For most cases a good agreement between experiments and calculations was found. Such peculiarities as a large difference in a stop-band width and

multimode operation in a narrow stop-bands were discovered. These effects require additional physical investigations.

A complete numerical analysis for arbitrary propagation directions of SAW and for a set of cuts have been made in [21]. In this work some extreme characteristics of SAW were found and the peculiarities of Gulyaev-Bleustein waves in LGS were discussed.

An agreement between calculated and measured SAW propagation data was also demonstrated in [33].

Analyzing angle dependences of SAW velocity, power flow angle, electromechanical coupling coefficient, and temperature coefficients N.F.Naumenko and V.S.Orlov [23] discovered a very promising cut ( $\Theta$  is near  $145^\circ$  and  $\psi$  is near  $20^\circ$ ). This cut is characterized by zero TCF, zero power flow angle, and rather high K (0.42%). Other types of the waves that can be useful are also studied [32].

#### *LGS as a material for sensors*

To use resonator elements made of LGS as sensors it is necessary to know nonlinear constants describing their behavior under pressure or electric fields. A complete set of third-order elastic constants, nonlinear piezoeffect constants, electrostriction constants, nonlinear dielectric permeability was measured [24] (Table 3). Some data on nonlinear third-order elastic constants were confirmed by G.D.Mansfeld and J-J.Boy in 1997.

The change in sound velocity in the material under pressure or when an electric field is applied to the crystal is described by controlling coefficients, which are expressed as a function of nonlinear constants. For example for pressure:

$$\alpha_{v_i(P)} = \frac{1}{V_i(0)} \left( \frac{\Delta V_i}{\Delta P} \right)_{\Delta P \rightarrow 0}$$

All estimated values of responses are of the same order of magnitude as that in quartz, but LGS is preferable due to the absence of phase transitions in a wide temperature region.

Usually twins in LGS do not manifest themselves. But like to quartz at a very high uniaxial pressure the effect of lattice ferrobielastic switching of LGS in a twin state is possible. This effect was observed in [25]. It was detected as a jump in a curve of a relative change in the frequency of a composite BAW resonator versus supplied pressure. The sign of a frequency jump at the threshold pressure when the switching occurs is opposite to that of quartz [26]. This is explained by different signs of elastic stiffness constants in LGS and quartz.

Important results are obtained in [27]. These results characterize LGS as a material appropriate for high temperature applications. It was experimentally confirmed that the LGS filter chips with electrodes made of Pt withstand high temperatures up to 1000°C. Frequency decrease at high temperatures was registered and explained.

Above 30 compounds with the structure similar to LGS have been synthesized by now [11,28-30]. One of them is langanite ( $\text{La}_3\text{Ga}_5\text{Nb}_{0.5}\text{O}_{14}$  - LGN) [28,29]. All the main characteristics of this material have been investigated. Temperature dependences of elastic constants, piezoelectric constants, velocities of acoustic waves, dielectric permeability, and thermal expansion coefficients of this material were found. LGN was found to be slightly favorable because of higher piezoelectric constants and less thermal expansion coefficients.

In spite of the fact that there are no publications on mass commercial production of BAW and SAW devices and sensors based on LGS our analysis indicates that this material is perspective for acoustoelectron and piezoelectric applications.

### CONCLUSIONS

1. The technology of growing up a very high quality langasite crystals has been developed. At present the price of a perfect material is still a few times higher than that of quartz but some parameters of langasite essentially excel that of quartz, namely: absence of phase transitions in a wide temperature range, higher electromechanical coupling constants, less attenuation coefficients. It opens a real possibility for a wide use of acoustic components made of langasite in resonators, filters, delay lines, and sensors.

2. All main material characteristics have already been investigated, material parameters which are necessary for development of piezoelectric components have been known.

3. Principal possibilities of using langasite in acousto- and piezoelectronics for the creation of BAW and SAW devices have been demonstrated.

### ACKNOWLEDGEMENTS

The author of the review is grateful to the Organizing Committee of 12-th EFTF for its kind invitation. The author is grateful to Dr.S.A. Sakharov, Dr.N.F.Naumenko, Dr.Yu.V. Pisarevsky, and Dr.V.I.Fedoretz for useful discussion on the report material and presentation of their original results. The author is grateful to Academician Yu.V.Gulyaev (IRE RAS) and Prof. R.J.Besson (LCEP, ENSNN) for their support in obtaining some original results presented. Some

original results presented were obtained in the works supported by RFBR (grant N 96-02-17480).

### REFERENCES

1. Kaminskii, S.E.Sarkisov, et.al. Generation of Stimulated Nd-ion Radiation in Trigonal Acentric  $\text{La}_3\text{Ga}_5\text{SiO}_{14}$ - crystal. Reports of the USSR Academy of Sciences, 1982, v.264, N1, pp.93-35
2. A.A.Kaminskii, B.V.Mill, Yu.V.Pisarevsky, I.M.Silvestrova,  $\text{La}_3\text{Ga}_5\text{SiO}_{14}$  - New Piezoelectric Material, Proc. 10 All-union Acoustic Conference, Moscow, 1983, p.20.
3. A.A.Kaminskii, I.M.Silvestrova, S.E.Sarkisov, G.A.Denisenko, Investigation of Trigonal  $(\text{La}_{1-x}\text{Nd}_x)_3\text{Ga}_5\text{SiO}_{14}$  Crystals, Phys.Stat.Sol., v.80, pp.607-620, 1983.
4. I.A.Andreev, M.F.Dubovik, Pisma v JTF, Langasite ( $\text{La}_3\text{Ga}_5\text{SiO}_{14}$ ), a Material with Zero Temperature Coefficient of Elastic Vibration Frequency, Pis'ma v ZhTF 1984, v.10, N8, pp.487-491.
5. A.N.Gotalskaya, D.I.Drezin, V.V.Bezdelkin, V.N.Stasceovich, Peculiarities of Technology, Physical Properties and Applications of a New Piezoelectric Material: Langasite ( $\text{La}_3\text{Ga}_5\text{SiO}_{14}$ ), Proc. 1993 IEEE Int.Freq.Contr.Symp., p..339-346 (1993).
6. I.M.Silvestrova, V.V.Bezdelkin, P.A.Senyushenkov, Y.V.Pisarevsky, New Piezoelectric Material: Langasite ( $\text{La}_3\text{Ga}_5\text{SiO}_{14}$ ) Proc. 1993 IEEE Int.Freq.Contr.Symp., pp.351-352.
7. A.B.Ilyaev, B.S.Umarov, L.A.Shabanova, M.F.Dubovik, Temperature Dependence of Electromechanical Properties of LGS Crystals, Phys.Stat.Sol., A, v.98, N2, pp. K109-K114, 1986.
8. S.A.Sakharov, I.M.Larionov, A.V.Medvedev, Application of Langasite Crystals in Monolithic Filters Operating in Shear Modes, Proc. 1992, IEEE Freq.Control Symp., pp.713-723.
9. S.A.Sakharov., P.A.Senushcenkov, A.V.Medvedev, Yu..V.Pisarevsky, New Data on Temperature Stability and Acoustical Losses of Langasite Crystals, 1995 IEEE Frequency Control, Symp., pp.647-652.

10. G.D.Mansfeld, Measurements of Acoustic Wave Attenuation in  $\text{La}_3\text{Ga}_5\text{SiO}_{14}$  Using HBAR Technology, 1994 IEEE International Frequency Control Symposium, Boston, USA, pp.35-39
11. A.A.Kaminskii et.al., Pure and  $\text{Nd}^+$ -Doped  $\text{Ca}_3\text{Ga}_2\text{Ge}_4\text{O}_{14}$  and  $\text{Sr}_3\text{Ga}_2\text{Ge}_4\text{O}_{14}$  Single Crystals, Their Structure, Optical, Spectral Luminescence, Electromechanical Properties, and Stimulated Emission, Phys.Stat.Sol.(a), 86, 345 (1984), pp.345-362.
12. A.N.Gotalskaja, et.al., Langasite Crystal Quality Improvement Aimed at High-Q Resonators Fabrication, 1995 IEEE International Frequency Control Symposium, pp.657-666.
13. S.A.Sakharov, A.V.Medvedev, I.M.Larionov, Y.A.Samsonov, Extension of Monolithic Filter Application Field and Their Miniaturization, 7-th European Freq. and Time Forum, Neuchatel, 16-18 March, 1993, pp.555-560.
14. S.A.Sakharov, I.M.Larionov, V.A.Isaev, Monolithic Filters Using Strong Piezoelectric, 45 Annual Symp. on Freq.Contr., pp.181-183.
15. V.V.Bezdelkin, E.E.Antonova, Fundamental Characteristics of Thickness Vibration of Langasite Plates for BAW Resonators J. de Physique, IV, vol.4, n.2-139, 156.
16. J.Detaint, J.Schwartzel, A.Zarka, B.Capelle, D.Cochet-Muchy, E.Philippot, Properties of the Plane and Plano-Covexe Resonators Using Berlinite, Gallium Phosphate and Langasite, 1994 Ultrasonics Symp., pp.1051-1056.
17. J.Detaint, A.Zarka, B.Capelle, D.Palmier, E.Philippot, Optimization of the Design of the Resonators Using the New Materials: Applications to Gallium Phosphate and Langasite, 1997 International Frequency Control Symposium, pp.566-578.
18. A.Ballato, J.G.Gualtieri, J.Kosinski, 1pPA5. High Q Piezoelectric Resonators, ASA 100th Meeting M.I.T. 1994.
19. V.V.Bezdelkin, A.S.Karasev, B.A.Martynov, Kh.B.Chan, Generator with BAW Resonator, Radiotechn. i Electron., v.42, N4, 1997, pp.500-505.
20. V.N.Fedoretz, Yu.P.Kondratyev, B.V.Mill, V.A.Pankov, Yu.V.Pisarevsky, V.V.Timashev, Surface Acoustic Wave Characteristics on  $\text{La}_3\text{Ga}_5\text{SiO}_{14}$  Crystals, 1997 IEEE International Frequency Control Symposium, pp. 816-820.
21. I.B.Yakovkin, R.M.Taziev, A.S.Kozlov, Numerical and Experimental Investigation SAW in Langasite, 1995 IEEE Ultrasonics Symposium, pp.389-392.
22. J.G.Gualtieri, J.A.Kosinski, A.Ballato, Piezoelectric Material Constants for Surface Wave Research, 7-th European Frequency and Time Forum, Neuchatel, 1993, pp.231-234.
23. N.F.Naumenko, V.S.Orlov, High Frequency SAW Devices, Patent H03H 9/17, 9/02, PCT US 96/17906.S.A.Sakharov,
24. K.S.Aleksandrov, B.P.Sorokin, P.P.Turchin, S.I.Burkov, D.A.Glishkov, A.A.Karpovich, Effects of Static Electric Field and of Mechanical Pressure on Surface Acoustic Waves Propagation in  $\text{La}_3\text{Ga}_5\text{SiO}_{14}$  Piezoelectric Single Crystals, 1995 IEEE Ultrasonic Symposium, pp.409-412.
25. G.D.Mansfeld, J.J.Boy, Observation of Ferrobielastic Switching in Langasite Crystals under a Uniaxial Static Pressure, JETP Lett., V.66, N 5, 1997, pp.362-364.
26. G.D.Mansfeld, R.J.Besson, P.Guzzo, HBAR Study of Ferrobielastic Twinning in Quartz Subjected to a Uniaxial Pressure, Fiz.Tv.Tela, 1997, v.39, N2, pp.290-294.
27. J.Hornsteiner, E.Born, E.Riha, Langasite for High Temperature Surface Acoustic Wave Applications, Phys.St.Sol., Rapis Research Notes, 97-035. Yu.V.Pisarevsky,
28. P.A.Senjushenkov, T.V.Hristoforova, B.V.Mill, V.N.Hristoforov, Tu.V.Pisarevsky, Temperature Characteristics of Langanite Bulk Wave Vibrations, 1996 IEEE International Frequency Control Symposium, pp.137-140.
29. Yu.V.Pisarevsky, P.A.Senjushenkov, P.A.Popov, B.V.Mill, New Strong Piezoelectric  $\text{La}_3\text{Ga}_{5.5}\text{Nb}_{0.5}\text{O}_{14}$  with Temperature Compensation Cuts, 1995 International Frequency Control Symposium, pp.653-656.

30. A.A.Kaminskii, I.M.Silvestrova et al. Investigation of Trigonal  $(La_{1-x}Nb_x)Ga_5SiO_{14}$ -crystals, Phys.Stat.Sol., (a), 80, 607 (1983).
31. S.A.Sakharov, A.V.Medvedev, P.A.Senushcenkov, V.Lider, Surface and Volume Defects in Langasite Crystals, 1995 IEEE Frequency Control Symp., p..642-646.
32. E.Danicki, W.Laprus, Piezoelectric Interfacial Waves in Langasite and Dilithium Tetraborate, 1995 IEEE Ultrasonics Symposium, pp.1011-1014.
33. H.Saton, A.Mori, Surface Acoustic Wave Propagation Characteristics on a Langasite Crystal Plate, Jap.J.Appl.Phys., vol.36 (1997), pp.3071-3073.

Table 2. Attenuation of BAW in principal crystalline directions on 1 GHz.

Wave direction and polarization	Velocity Km/S	Attenuation dB/( $\mu$ S GHz <sup>2</sup> )
X-longitud	5.78±0.01	0.52±0.04
Z-longitud	6.75±0.01	1.30±0.04
Y-quasilongitud	5.79±0.01	0.75±0.05
Y-slow shear	2.77±0.01	1.05±0.05

Table 1. Elastic modulus of LGS.

Absolute quantities		Temperature coefficients	
Elastic stiffness ( $10^{10} N/m^2$ )		First order ( $10^{-6} K^{-1}$ )	Second order ( $10^{-9} K^{-2}$ )
$C_{11}^E$	18.93	-53	-4.2
$C_{12}^E$	10.50	-92	+25
$C_{13}^E$	9.528	-88	-131
$C_{14}^E$	1.493	-205	+870
$C_{33}^E$	26.24	-104	-109
$C_{44}^E$	5.384	-62	-111
$C_{66}^E$	4.216	-4.7	-40.7

Table 3. Third-order elastic constants  $c_{ijk}$  ( $10^{10} N/m^2$ ), nonlinear piezoeffect constants  $e_{ijk}$  (Coul/m<sup>2</sup>), electrostriction constants  $H_{ij}$  ( $10^{-11} F/m$ ), nonlinear dielectric permeability  $\epsilon_{111}$  ( $10^{-20} F/V$ ). All data are given in the table (for 20° C).

$c_{111}$	-97.2±0.5	$c_{134}$	-4.1±0.1
$c_{112}$	0.7±0.1	$c_{144}$	-4±0.2
$c_{113}$	-11.6±0.3	$c_{155}$	-19.8±0.4
$c_{114}$	-2.2±0.1	$c_{222}$	-96.5±0.3
$c_{123}$	0.9±0.2	$c_{333}$	-83.4±0.7
$c_{124}$	-2.8±0.1	$c_{344}$	-38.9±0.3
$c_{133}$	-72.1±0.5	$c_{444}$	20.2±0.7
$\epsilon_{111}$	-0.5±0.1	$H_{11}$	-26±10
$e_{111}$	9.3±0.7	$H_{12}$	65±7
$e_{113}$	-3.5±0.5	$H_{13}$	20±8
$e_{114}$	1.0±0.3	$H_{14}$	-43±9
$e_{122}$	0.7±0.3	$H_{31}$	24±15
$e_{124}$	-4.8±0.6	$H_{33}$	40±30
$e_{134}$	6.9±0.6	$H_{41}$	170±13
$e_{144}$	-1.7±0.3	$H_{44}$	-44±10
$e_{315}$	-4±1.2		

Piezoelectric stress constants (C/m<sup>2</sup>)

$e_{11}$	-0.431	456	1032
$e_{14}$	+0.108	-628	1480

Dielectric permeability constants

	18.97	137	82
$\frac{\epsilon_{11}^T}{\epsilon_0}$	52.00	-795	1076

Thermal expansion coefficients ( $10^{-6} K^{-1}$ )

$\alpha_{11}$	5.07
$\alpha_{33}$	3.60

## DEFECT CENTERS IN CRYSTALLINE QUARTZ BY SWEEPING PROCESS

M. SMAALI\*\*, J.J. BOY\*, P. ZECCHINI\*\*

\*ENSM / LCEP – 26, chemin de l'Épitaphe - 25030 BESANÇON Cedex - FRANCE

\*\*LCCM - UFR Sciences – Route de Gray - 25030 BESANÇON Cedex - FRANCE

### ABSTRACT

Trivalent aluminum ions are the principal substitutional impurities within quartz crystals, by replacing tetravalent silicon ions during the growth of natural or synthetic crystals. To have the total electrical neutrality, the difference of valence is compensated by alkali ions ( $\text{Na}^+$ ,  $\text{Li}^+$ ) or protons. These defect centers (Al-M and Al-OH) induce typical absorption bands which can be correlated to each ion by IR measurements. In order to clearly correlate the absorption bands and the treatment effects, on one hand, many synthetic samples have been swept and, on the other hand, they have been doped with alkali ions.

Variations of some characteristics measured or calculated parameters in the middle infrared range, such as the  $\alpha_{3500}$  coefficient and the  $s_2$  and  $e_2$  absorption bands are studied on vacuum swept synthetic quartz.

The modifications induced by electrolytic exchange experiments, in natural or cultured crystals, lead to correlate absorption bands and created defects. In case of cultured quartz, lithium doping process increases "e" bands, when no effect has observed by sodium doped quartz. As for natural quartz, very important modifications have observed. Then the  $3473 \text{ cm}^{-1}$  band is responsible of  $[\text{AlO}_4/\text{Li}]^0$  vibration, and the  $3448 \text{ cm}^{-1}$  is due to  $[\text{AlO}_4/\text{Na}]^0$  vibration centers.

### 1. INTRODUCTION

Alpha quartz is the material currently used for Ultra-Stable Oscillators, for which the purest quality is needed. Many studies [1-4, 7] have shown the presence of some defects that can alter the material properties after it has been submitted to various treatments and more particularly,  $\gamma$ -radiations. These defects are substitutional aluminum, incorporated as  $\text{Al}^{3+}$  by replacing silicon ions. In order to get the electrical neutrality within the quartz lattice, compensating monovalent charges, such as the alkali ions and protons, are also trapped during the crystal growth of natural or

synthetic quartz. Alkali ions lead to the Al-M centers (M is  $\text{Li}^+$  or  $\text{Na}^+$ ), protons leading to the Al-OH centers. Aluminum-hole centers (Al-h) can also be formed under special experimental conditions, as irradiation or sweeping [3, 4, 6]. The structure of those defects can be modified by treatments such as sweeping or ionizing radiations. Sweeping out a quartz crystal leads to eliminate impurities out of the crystal. It can be performed in vacuum when to swept out all impurities is aimed. In that case, Al-h center defects can be created. If the sweeping out process is performed in air, Al-OH centers are created by replacing alkali ions by protons. The sweeping process can be done in the opposite way ; then it is called sweeping into. The way leads to introduce at once only one kind of interstitial impurity within the crystal. To see what kind of sweeping induces new defect configurations, IR spectra are recorded in each case.

In this paper, the effect of various sweeping processes on natural and cultured quartz crystals are reported in order to correlate defects and IR absorptions.

### 2. EXPERIMENTAL PROCEDURES

The samples used for this study are rectangular in shape with parallel and polished faces. The origin of the crystals is natural and synthetic. As indicated in table I, synthetic samples have been vacuum swept at first. In the second step both naturel and synthetic samples have been swept into by hydrogen atoms using air atmosphere or alkali ions. For many details about equipment and sweeping technique procedure see [5, 8]. With these treatments new infrared measurements lead to know the evolution and the modification of the absorption bands at each step of the treatments. To verify sweeping treatments, chemical analyses have been done with ICP instrument ( all results are given in table IV ).

**TABLE 1 - Origin of materials and treatments the samples have been submitted to.**

quartz sample	origin	1 <sup>st</sup> treatment	2 <sup>nd</sup> treatment
A1	synthetic	vacuum swept	-
A2	synthetic	vacuum swept	H swept
A3	synthetic	vacuum swept	Li swept
A4	synthetic	vacuum swept	Na swept
NS1	natural	air swept	Li swept
NS2	natural	air swept	Na swept

### 3. RESULTS AND DISCUSSIONS

Table 2 summaries the sweeping results, by giving the values of absorption coefficients corresponding to the appeared bands. Figure 1 shows the spectra obtained with cultured quartz. The infrared spectrum of the untreated sample exhibits all "s" bands except "s<sub>1</sub>". In the case of H-swept quartz, the "s" bands intensities decrease strongly. The appearance of "e<sub>2</sub>" band is the modification that air sweeping process has induced. The same result is obtained when quartz is swept under vacuum.

The infrared spectrum of lithium doped sample gives a low "e<sub>2</sub>" band intensity in comparison with swept samples. Because "e" bands are responsible of the

vibrations of [AlO<sub>4</sub>/H]<sup>0</sup> centers, lithium ions by replacing a part of hydrogen atoms involves the obtained result. Thus lithium ions, when introduced in quartz lattice, stand close to [AlO<sub>4</sub>]<sup>-</sup> centers. This suggestion is confirmed by Howarth et al [9]. Monitoring <sup>17</sup>O enriched quartz crystals by EPR technique, these authors found that lithium cation is very nearly to one of the four oxygen atoms surrounding aluminum atom in the case of [AlO<sub>4</sub>/Li]<sup>0</sup>.

As for sodium doped sample, no modification has been observed between swept quartz and sodium doped one, even though a chemical analysis reveals a high content of Sodium. This confirms that Sodium cations do not take a particular position in lattice.

**TABLE 2 - Absorption coefficient of synthetic samples after electrolytic exchange experiments.**

wavenumbers (cm <sup>-1</sup> )	A1	A2	A3	A4
3366	0.794	0.786	0.650	0.796
3396	-	-	-	-
3438	-	-	-	-
3580	0.098	0.102	0.105	0.102
$\alpha_{3500}$	0.018	0.0175	0.019	0.018

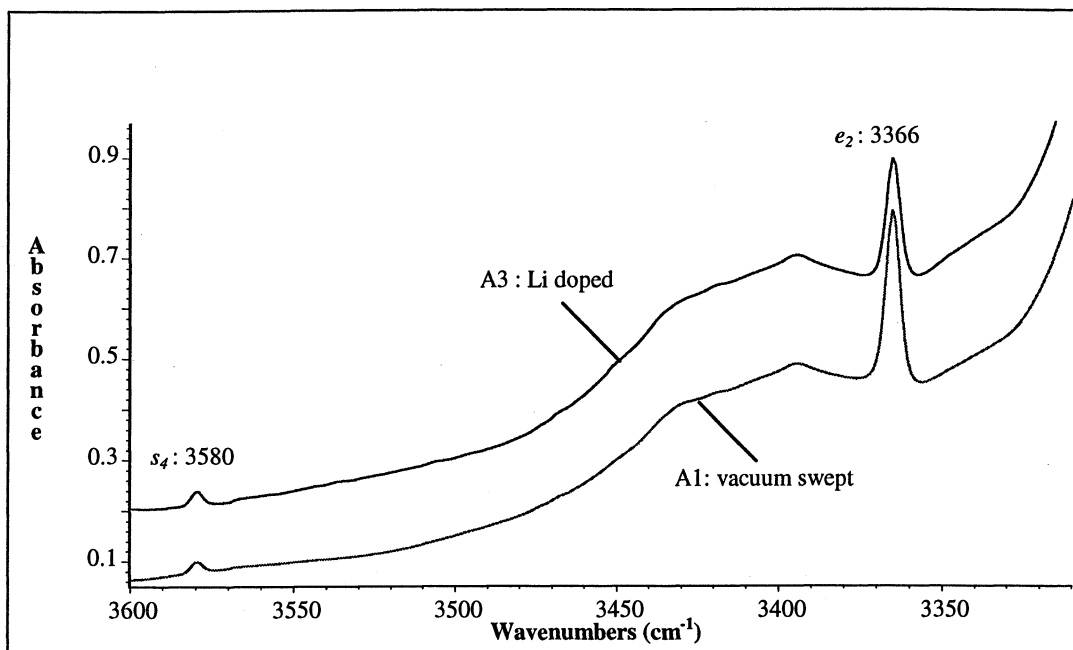


**Figure 1 : Infrared spectra of cultured quartz crystals.**  
Spectra of samples A2 and A4 are similar to this of A1.

Natural quartz is also used to distinguish the effect of electrodiffusion on it. Figure 2 gives IR spectra in each case. Each spectrum exhibits an absorption band at  $3593\text{ cm}^{-1}$ , whose the origin is not very known. Furthermore, we note that it is not affected by the sweeping treatment. An other narrow band located at  $3580\text{ cm}^{-1}$  observed in a few untreated natural quartz, vanishes after sweeping and reappears after doping treatment.

Many authors have attributed the  $3473\text{ cm}^{-1}$  band to Lithium defects [5, 7, 10]. To verify it, we have doped many air swept natural quartz with Lithium. The results, presented in figure 2, show that the  $3473\text{ cm}^{-1}$  band decreases until a total vanishing, after air swept process. And after doping with Lithium cations, this band reappears.

Using Sodium salts to do electrolytic exchange on air swept natural quartz, the band due to  $[\text{AlO}_4/\text{Li}]^0$  vibration is not observed. According to the previous result, it is evident that the band does not appear in IR spectrum. And the band which may be attributed to  $[\text{AlO}_4/\text{Na}]^0$ , as shown in figure 2, is the  $3448\text{ cm}^{-1}$ . Note that in case of natural quartz the "e" bands have not

been affected by any electrolytic exchange experiment. We can compare our results with a work of H. Bahadur [5] who has used sweeping process to sweep alkali cations under vacuum. He has observed that the lithium swept material gives an identical spectrum as unswept quartz using Brazilian natural quartz. With Arkansas natural quartz, he has found the Li-OH center at  $3476\text{ cm}^{-1}$  and Na-OH center at  $3451\text{ cm}^{-1}$ . At least, in case of synthetic quartz, hydrogen sweeping adds typical bands as  $e_1$  and  $e_2$ , but any band has affected by Lithium or sodium sweepings.

Finally these experiments have permitted to us to distinguish between untreated natural quartz, swept materials and alkali doped ones. The  $3473\text{ cm}^{-1}$  band in untreated natural quartz is more intensive or in the same range as the  $3430\text{ cm}^{-1}$  band. Swept material is easily recognized because of the absence of the  $3473\text{ cm}^{-1}$ . For Lithium doped quartz, in contrast with the untreated, the intensity of  $3473\text{ cm}^{-1}$  band is lower than this of  $3430\text{ cm}^{-1}$  band. And as for the sodium doped quartz, the  $3448\text{ cm}^{-1}$  band is infrared characteristic.

**Table 3 - Absorption coefficient of characteristic bands in treated natural quartz.**

Wavenumbers ( $\text{cm}^{-1}$ )	NS1 swept	NS1 Li doped	NS2 swept	NS2: Na doped
3448	-	-	-	0.156
3473	-	0.096	-	-
3580	-	0.04	-	0.056
$\alpha_{3500}$	0.039	0.04	0.025	0.026

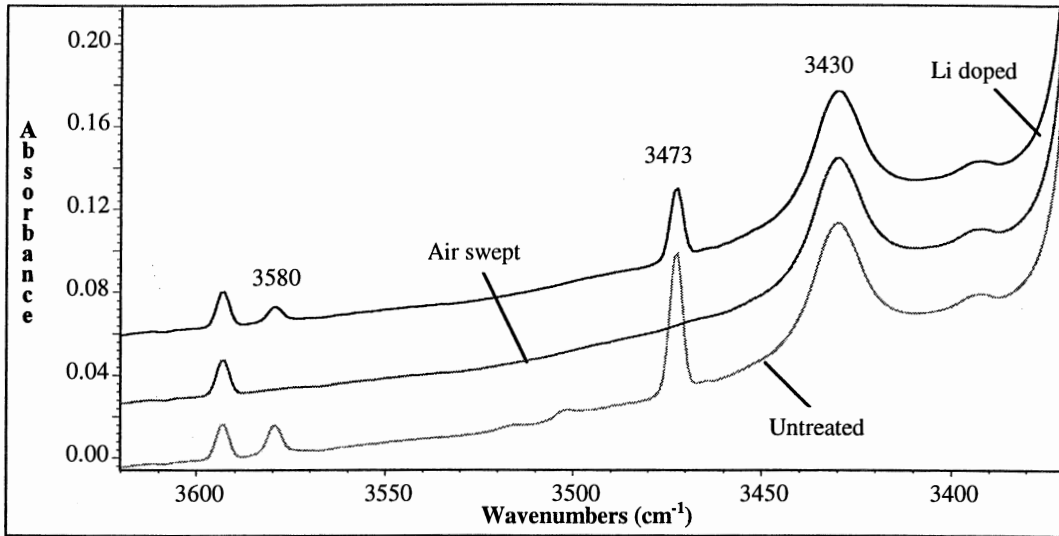


Figure 2 : Infrared spectra of natural quartz (untreated, air swept and Li doped quartz).

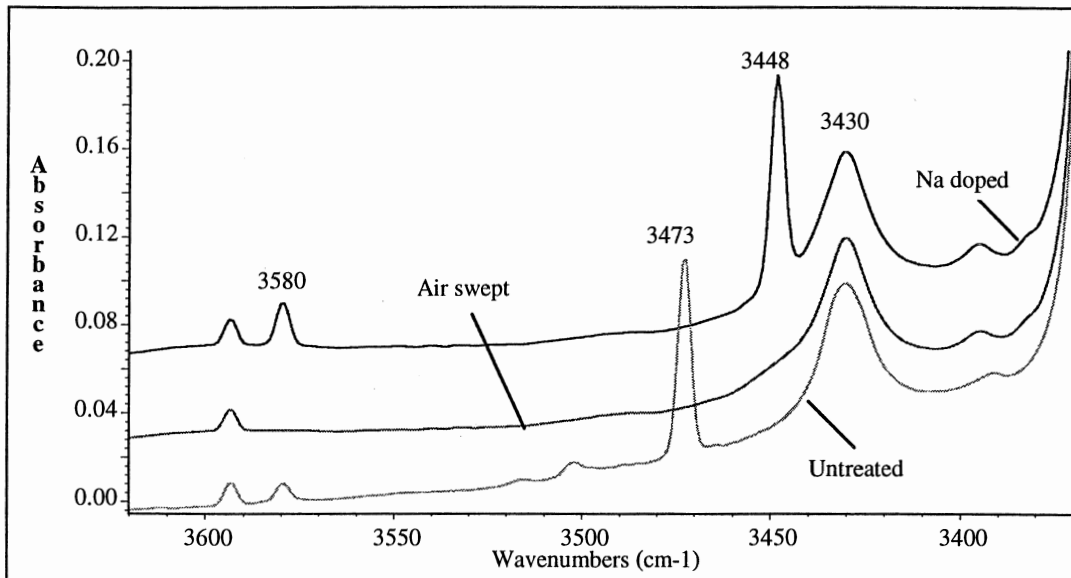


Figure 3 : IR spectra of natural quartz (air swept and Na doped quartz).

Table 4 - Chemical analyses results in atomic ppm.

Element	Na	Li	K	Al
A1: untreated	1.11	0.25	< 0.05	3.2 – 3.6
A1: swept	0.1 - 0.2	< 0.05	-	3.2 – 3.6
A3: Li doped	0.18	1.48	-	3.2 – 3.6
A4: Na doped	1.73	0.20	-	3.2 – 3.6
NS1: untreated	0.55	6.23	-	7.1 – 7.5
NS1: swept	< 0.05	< 0.05	-	7.1 – 7.5
NS1: Li doped	< 0.05	7.65	-	7.1 – 7.5
NS2: untreated	0.70	3.78	-	4.2 – 4.5
NS2: swept	<0.05	< 0.05	-	4.2 – 4.5
NS2: Na doped	2.10	< 0.05	-	4.2 – 4.5

#### 4. CONCLUSION

We have swept alkali cations into the lattice of vacuum swept synthetic and air swept natural quartz, to know how kinds of modifications we read in infrared spectra. In summary, sweeping results are origin of quartz depending. Furthermore, it is important to note that different kinds of sweepings, as for synthetic or natural quartz crystals, do not modify the obtained results. So, we can summarize our results as described below :

- For synthetic quartz : Each treatment affects first  $e_2$  absorption band intensity. No modifications on IR spectrum have been observed when Sodium ions are used to sweep it into the crystal. In case of Lithium doped quartz, a part of protons in  $[AlO_4/H]^0$  centers is replaced by Lithium as  $[AlO_4/Li]^0$ .
- For natural quartz : If we perform an air swept treatment, the  $3473\text{ cm}^{-1}$  band vanished and by using Lithium cations to do electrolytic exchange, it reappears. With Sodium ions one band is easily distinguishable at  $3448\text{ cm}^{-1}$ , though it was not observed before.

#### REFERENCES

1. KING J.C., and KOEHLER D.R., 1985, Radiation Effects on Resonators, Precision Frequency Control, **1**, 147-159
2. MARTIN J.J., 1989, Radiation Induced Frequency Offsets and Acoustic Loss In AT-Cut Quartz Crystals, 43rd Annual Symposium On Frequency Control, 526-535
3. WEIL J.A., 1975, The Aluminum Centers in Alpha Quartz; Radiation Effects, **26** (4), 261-265
4. WEIL J.A., 1984, A Review of Electron Spin Spectroscopy and Its Application to the Study of Paramagnetic Defects in Crystalline Quartz, Physics and Chemistry of Minerals, **10**, p 149-165
5. BAHADUR H., 1991, Electrodiffusion (Sweeping) and Irradiation Effects in Crystalline Quartz, 5th European Frequency and Time Forum, 148-156
6. GUALTIERI J.G., and VIG R., 1984, Sweeping and Irradiation Studies in Quartz, 38th Annual Frequency Control Symposium, 42-49
7. KATS A., 1962, Hydrogen in alpha quartz, Philips Research Reports, **17**, 133-195
8. PANKRATH R., and FLÖRKE O.W., 1994, European Journal of Mineralogy, **6** (4), 435-457
9. HOWARTH D.F., MOMBOURQUETTE M.J., and WEIL J.A., 1997, Canadian Journal of Physiques, **75**, 99-115
10. BOY J.J., PASQUALI M.A., VIARD B., YAMNI K., 1995, 9th European Frequency and Time Forum, 255-260.

## SOURCES OF GROWTH RATE CHANGES OF QUARTZ SINGLE CRYSTALS IN THE HYDROTHERMAL METHOD

*Władysław Hofman*

Institute of Electronic Materials Technology  
Wólczyńska 133, 01-919 Warsaw, Poland

When marking of current crystallization front is applied to hydrothermal processes, the time dependent function of quartz crystal extension can be determined what in turn makes possible to find a current growth rate variation of crystal faces. This method was used for crystals grown in a common temperature - pressure conditions with a good repeatability of initial hydroxide concentration, pressure and constant control temperatures of solution in the subsequent hydrothermal processes. However, these runs were different with respect to cooling conditions applied to the baffle and autoclave head. **This work describes how growth rate changes, detected for these processes, can be explained.**

The greatest changes was observed for the current crystal growth rate which decreases from 1.6 to 2.4 time in every process between the beginning and the termination of run.

This fall can be caused by three different mechanisms:

- a. a gradual decrease of solution supersaturation in consequence of fill factors changes of crystallization and dissolution chamber,
- b. an increase of diffusion layer around crystals due to convection velocity decrease which is modified by fall of radial temperature gradients in the growth chamber during hydrothermal process,
- c. changes of volumetric properties of crystals which modify local concentration gradients of fluid in diffusion layer along crystal faces.

A distinct smaller growth rate variations (1.1 time) were related to bars taken from different tiers of crystal rack for given process. A character of these changes was correlated to,

- d. local fluid supercoolings modified by axial temperature profiles along autoclave walls.

Comparable to those last variations were growth rate changes between crystals coming from the same tier of rack but from different cooling processes as mentioned above. In these case all causes were important but probable that related to supercooling play the main role.

## DETERMINATION OF HIGH - ORDER CONSTANTS USING THE RESONANT, AND LASER INTERFEROMETRY METHODS

Jaroslav Nosek, Lenka Kretschmerová, Petr Kretschmer  
Technical University of Liberec, Hálkova 6, CZ-461 17 LIBEREC, Czech Republic  
E-mail: jaroslav.nosek@vslib.cz

### ABSTRACT:

The paper deals with the short description of the non-linear effects in the quartz resonator and with the determination of the 4<sup>th</sup> order elastic constants of the quartz. The verification of some elastic constants is provided using resonant methods. A laser interferometry method can be used for the determination of the piezoelectric or pyroelectric coefficients and modules.

### 1. INTRODUCTION

It is well known that the linear theory of piezoelectricity is used for describing the acoustic waves propagation in solid piezoelectric materials and for solving motional equations, provided that the amplitudes of vibrations are small. Also, the vibrating solids must not be subjected to any elastic pre-stressing or strong electric field. If these requirements are not fulfilled, the results of calculation have to be modified by various correction factors, or the calculations must include some non-linear relations desired from the particular initial conditions - Ref. (1). The properties of the acoustic waves of the resonator or of other piezoelectric selective devices are usually influenced by internal or external parameters on account of the non-linear properties of the crystal. These nonlinearities are at the origin of many non-linear effects, as frequency-amplitude effects, intermodulation, and the sensitising to various physical quantities, like electric field, temperature, mechanical forces, acceleration or pressure as it was shown by Gagnepain (2) and Nosek (3). It is obvious that a part of this non-linear effects is non desired, and, at the opposite, nonlinearities can be used for sensing functions - Ref. (4), making the selective BAW or SAW resonators.

The description of the non-linear behaviour of the resonator requires the knowledge of not only the regular second order fundamental material constants, but also of the higher order constants of the third, and in some cases of the fourth order. The paper will be related with the phenomena resulting mainly in elastic nonlinearities of the quartz, used for the AT- and BT-cuts resonators vibrating in a thickness-shear mode.

### 2. NON-LINEAR FUNDAMENTAL EQUATIONS

The non-linear theory takes into consideration the final deformation  $\eta_{ij}$ . Elastic stiffnesses of higher order can be derived from the internal energy  $U$ . As shown in Ref.

(1), the elastic coefficients of  $n$ -order, as well as higher order coefficients characterising the dielectric, piezoelectric and pyroelectric properties of crystals, can be derived from various thermodynamic potentials. The electro-optical, electrostriction and other coefficients can be specified by the same method. The thermodynamic stress  $t_{LM}$ , the thermodynamic electric displacement  $D_N$  and the thermodynamic intensity of electric field  $E_N$  can be taken as the basis for the study of non-linear electro-elastic properties of piezoelectric substances. For an adiabatic process, the components  $t_{LM}^{e,\sigma}$  of a thermodynamic stress tensor and the components of electric displacement  $D_N$  can be expressed as it was shown by Zelenka (1).

The stress equations of motion and charge equation of electro-elasticity for an electro-elastic solid with small piezoelectric coupling may be written in the form

$$\hat{K}_{LM,L} = \rho^0 \ddot{u}_M \quad (1)$$

$$D_{L,L} = 0, \quad (2)$$

where the symbols  $\rho^0$ ,  $\hat{u}_M$ ,  $\hat{K}_{LM}$  and  $D_L$ , denote the reference mass density, the mechanical displacement, the Piola-Kirchhoff stress tensor, and the electric displacement vector, respectively.

In the view of small piezoelectric coupling in the quartz, we have included non-linear elastic terms only and kept the electric and electro-elastic terms linear.

The second family of non-linear problems corresponds to the propagation of a small amplitude wave in a pre-strained medium. The theoretical analysis is simplified by considering that the wave has no influence on the static deformation. Only the modifications of the wave characteristic by the pre-strain are usually considered.

### 3. NON-LINEAR ELASTIC CONSTANTS

We would like to determine some elastic coefficients using the mathematical description and experimental verification of two non-linear effects in the quartz.

#### 3.1 AMPLITUDE-FREQUENCY EFFECT

The steady-state solutions to the non-linear forced vibration problems are obtained by Tiersten (7). The analysis was employed in the determination of the frequency change caused by driving voltage, showing the influence of quality factor, load resistance and

harmonic overtone, for the AT-cut quartz resonator. Nosek (5) gives the results of simplified mathematical analysis of the non-linear amplitude-frequency effect and some experimental results. A value of the elastic stiffness  $\tilde{c}_{4666}^E = 7.8 * 10^{12} \text{ Nm}^{-2}$  was experimentally obtained.

### 3.2 INTERMODULATION OF PIEZOELECTRIC RESONATOR

If two (or more) harmonic signal levels  $V_1$  and  $V_2$  with frequencies  $\omega_1$  and  $\omega_2$  positioned uniformly with respect to resonant frequency act simultaneously in electronic circuit, the intermodulation signal of the voltage  $\hat{V}_\Omega$  and angular  $\Omega = 2\omega_1 - \omega_2$  is created due to the cubic non-linearities. This frequency  $\Omega$  will be located also within the bandwidth, and therefore, will not be filtered.

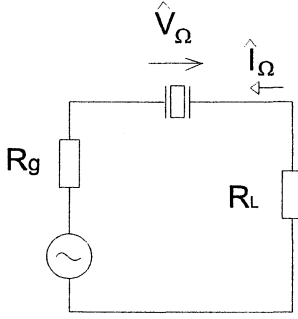


Figure1: Circuit with intermodulation current

The complex value of the intermodulation voltage for the circuit in Fig. 1 can be derived from Ref. (6). Now, if we calculate the current  $\hat{I}_\Omega$ , after simple arrangement we get to an interesting relation for :

$$\hat{I}_\Omega = -(\hat{Y}_\Omega \cdot \hat{V}_\Omega + jA_{1\Omega} \cdot A_4 \frac{V_1^2 V_2}{\Delta\Omega}), \quad (3)$$

where  $\hat{Y}_\Omega$  is the resonator admittance at angular frequency  $\Omega$ . Significance of symbols for admittance  $Y$ ,  $A_{1\Omega}$ ,  $A_4$  and  $\Delta\Omega$  is shown in Ref. (12).

It follows from Eqn. (3), that the intermodulation current consists of a component dependent on the admittance  $\hat{Y}_\Omega$  and a component affected by control signals of levels  $V_1$ ,  $V_2$ , and effective elastic stiffness  $\gamma$ , which include the linear and non-linear elastic stiffness of the 2nd, 3rd and 4th order.

For the AT-cut quartz resonator of 10 MHz, the measured values are:

$$\tilde{c}_{4666}^E = 7.6 * 10^{12} \text{ Nm}^{-2} \quad (V_\Omega = -98 \text{ dB} \quad \text{and} \\ V_{1,2} = 4.5 \text{ dB}, \quad \Delta f = \pm 1 \text{ kHz}, \quad f_N = 9 \ 995.35 \text{ kHz}, \\ R_L = 135 \ \Omega).$$

### 4. DETERMINATION OF OTHER NON-LINEAR CONSTANTS

Tiersten (6) derived the relation, from which it is possible to determine the nonlinear elastic stiffness  $\tilde{c}_{6666}^E$  of AT-cut quartz resonator. Based on the same principle, we are trying to specify an effective elastic stiffness  $\tilde{c}_{6666}^E$  of the 4<sup>th</sup> order for the BT-cut quartz resonators or some other cuts of quartz resonators. Read the relation for a nonlinear stiffness

$$\gamma = \frac{1}{2} \tilde{c}_{22}^E + \tilde{c}_{4266}^E + \frac{1}{6} \tilde{c}_{4666}^E, \quad (4)$$

where the symbols  $\tilde{c}_{22}^E$ ,  $\tilde{c}_{266}^E$ ,  $\tilde{c}_{6666}^E$  denote the effective elastic stiffnesses of the 2<sup>nd</sup>, 3<sup>rd</sup>, or 4<sup>th</sup> order. We express

$$\tilde{c}_{4666}^E = 6\gamma - 3\tilde{c}_{22}^E - 6\tilde{c}_{266}^E, \quad (5)$$

from Ref. (4).

The basic elastic stiffnesses are found out from tabular values of basic elastic stiffnesses of the 2<sup>nd</sup> and the 3<sup>rd</sup> orders for different cuts. Now, a computer program to carry on the computations of effective elastic stiffnesses was made. It calculates effective elastic stiffness of the 2<sup>nd</sup> and the 3<sup>rd</sup> order for any cutting angle.

We found out that the stiffness  $\tilde{c}_{6666}^E$  consists of five basic stiffnesses by the application of this program on the elastic stiffness of the 4<sup>th</sup> order:

$$\tilde{c}_{4666}^E = A_1 c_{4555}^E + A_2 c_{4556}^E + A_3 c_{4566}^E + A_4 c_{4566}^E + A_5 c_{4666}^E \quad (6)$$

The coefficients  $A_1$ ,  $A_2$ ,  $A_3$ ,  $A_4$  and  $A_5$  in the relation (6) depend on the rotation angle of the resonator. We measure  $\tilde{c}_{6666}^E$  for five different cuts of piezoelectric resonators and specify the constants  $A_1$ ,  $A_2$ ,  $A_3$ ,  $A_4$ ,  $A_5$  for each of these cuts. We get a set of five equations. By the solution of this equations set, we obtain the values of basic elastic stiffnesses of the 4<sup>th</sup> order  $c_{5555}^E$ ,  $c_{5556}^E$ ,  $c_{5666}^E$ , and  $c_{6666}^E$ .

Nevertheless, it is obvious that the values being obtained in this way neither allow to set the linkage with other elastic stiffnesses of the 4<sup>th</sup> order or the symmetry of this matrix. But, the elastic module  $\tilde{c}_{6666}^E$  for any angle of rotated cuts of a quartz resonator can be determined by substitution in the relation (6).

The following processing was provided by the program for computing the coefficients  $A_1 - A_5$  in the equation (6), or in (7) generally:

$$\tilde{c}_{ijklmnop} = \sum_{abcdefgh} c_{abcdefgh} \alpha_{ia} \alpha_{jb} \alpha_{kc} \alpha_{ld} \alpha_{me} \alpha_{nf} \alpha_{og} \alpha_{ph} \quad (7)$$

In the Eqn. (7),  $\alpha_{ia} - \alpha_{ph}$  there are direction cosines of rotation angles, which means that this is the equation for uncompounded components of elastic stiffnesses tensor of the 8<sup>th</sup> order. As seen in Fig.2, when indexes  $i, j, k, l, m, n, o, p$  and rotation angle  $\alpha$  are entered, the program in the right window will write out the influence of the elastic stiffnesses  $c_{abcdefgh}$  of basic matrix of elastic stiffnesses tensor of the 8<sup>th</sup> order. In this description, the symbol  $\alpha$  denote the angle of the rotation around X-axis. If the right side of the Eqn. (7) is converted back to compounded indexes with assuming symmetry, we get to Eqn. (6) in our case. The calculation of components of elastic stiffnesses tensor of the 8<sup>th</sup> order is shown in Fig. 2.

## 5. LASER INTERFEROMETRY POSSIBILITIES

Our laboratory with a double beam laser interferometer has been built since spring 1997. Its construction is based on a grant support of Ministry of Education of the Czech Republic. The goal of this activity is accurate measurement of strained specimens made from piezoelectric materials in the temperature range 10 K - 330 K, if an optical He cryostat is used. The accuracy of displacement measurement in the order of 10 - 100 pm is expected. We suppose that the precise strain measurement makes possible a more accurate determination of piezoelectric, dielectric and temperature parameters of piezoelectric materials or composite structures based on the definition of the piezoelectric strain constant

$$d_{i\lambda} = \frac{\partial S_{\lambda}}{\partial E_i} \quad (8)$$

(or piezoelectric stress constant  $h_{i\lambda}, e_{i\lambda}$ ) for the adiabatic and isothermic processes,

pyroelectric module

$$\rho_i = - \frac{\partial \theta}{\theta \partial E_i} \quad (9)$$

or heath extension coefficient

$$\alpha_{\mu} = \frac{\partial S_{\mu}}{\partial \theta} \quad (10)$$

for the adiabatic processes.

Interferometer type selection was made on the bases of the following requirements:

- Elimination of sample strain due to its own vibrations or optical path change due to the substrate motion.
- Achievement of maximum modulation of interferometric pattern.

The first condition limits strongly the use of Michelson interferometer and leads to the construction of double beam Mach-Zender interferometer. The ray of one branch of interferometer meets the front and back specimen surface successively, it ensures that the substrate or specimen displacement is added once and subtracted next.

The second condition leads to the use of a single mode stabilised 1 mW laser of long length of coherency, half-wave plate, diaphragm in front of the laser and anti-reflective layers on the elements of an optical path.

The stabilised single mode He-Ne laser with the wavelength of 632 nm, type *Coherent* was selected. The laser exhibits the linear polarisation ratio of 1:1000, the ray diameter of 0.5 mm and the ray divergency of 1.6 mrad. It is necessary to use 3 polarised ray dividers and other components in order to construct the double ray interferometer. Mechanical components of the optical path, for example specimen holders, have micro-positioning of accuracy of 0.01 mm.

Interferometer electronic equipment should ensure

- a) Positioning of reference mirror into its initial position
- b) Periodical movement of reference mirror in order to calibrate the photodiode
- c) Suppression of incidental movement of reference mirror
- d) Measurement of light intensity entering the photodiode
- e) Excitation of vibrations in the sample
- f) Instantaneous display of results
- g) Measured data saving and processing.

The set up of initial reference mirror position is performed by an actuator driven from the high voltage amplifier. The mirror displacement of 7500 nm is produced by actuator voltage of 1500 V.

Harmonic mirror movement is ensured by control harmonic voltage at the high voltage amplifier input. Photodiode calibration is performed by HP generator at frequency of 30 Hz. Suppression of incidental mirror movement is made by a feedback. The intensity of light entering the photodiode is measured by a lock in amplifier (phase sensitive detector).

The sample vibration requires power source and knowledge of sample parameters, for example its static capacity. HP oscilloscope with mathematical module

for FFT is used for instantaneous display of results. The interferometer is on the granite optical desk.

In final stage of the interferometer construction, we will develop the measured data storage and processing by the use of control computer and GPIB bus.

A wide temperature range for measured specimens can be achieved with the aid of optical cryostat from Oxford Instruments at defined suppression of cooling system vibrations.

## 6. CONCLUSION

This review shows that the amplitude frequency effect and intermodulation products depend not only on the 2nd and 3rd order fundamental elastic constants, but also on the 4th order ones. This is a serious difficulty for evaluating this effects, from such models, because the values of the 4th order fundamental elastic stiffness are almost completely unknown, and even those of quartz crystal.

The measurement performed on quartz AT-cuts resonators gives an access to obtain the effective non-linear constants. A computer determination of the basic non-linear constants of higher order is possible.

A laser interferometry gives the possibility to obtain the piezoelectric and pyroelectric constants from the measurement of the displacements of the order 10 - 100 pm.

## ACKNOWLEDGEMENT

This work was supported in part by the Grant of Ministry of Education of the Czech Republic under Contract No. VS 96006 and No. G388.

The authors wish to thank J. Zelenka from Technical University of Liberec for valuable recommendations.

## REFERENCES:

1. Zelenka J., 1986, Piezoelectric Resonators and their Applications. Prague: Academia, Amsterdam: Elsevier Science Publishers.
2. Gagnepain, J.J., 1987, Non-linear constants and their significance. Proc. 41st Annual Frequency Control Symposium, 266-276.
3. Nosek J., 1997, Some Second-order Effects in the Electromechanical Systems with Bulk- and Surface Acoustic Waves. Proc. 11<sup>th</sup> European Frequency and Time Forum, Neuchatel, Switzerland, 243-248.
4. Nosek J., Zelenka, J., 1996, Quartz Strip Resonator as a Temperature Sensor for Mechatronics. Proc. of the 3rd International Conference Mechatronics 96 and M2VIP96, Guimaraes, Portugal, 233-237
5. Nosek J., 1997, Drive Level Dependence of the Resonant Frequency in BAW Quartz Resonators and his

Modeling. Proc. 1997 IEEE Int. Frequency Control Symposium, Orlando, Florida, USA, 687 - 695.  
IEEE Transactions on Ultrasonics, Ferroelectric, and Frequency Control (to be published).

6. Tiersten, H.F., 1975, An analysis of intermodulation in rotated Y-cut quartz thickness shear resonators. J. Acoust. Soc. Am., Vol. **57**, 667- 681.
7. Tiersten H.F., Stevens D.S, 1986, An analysis of nonlinear resonance in contoured-quartz crystal resonators. J. Acoust. Soc. Am., Vol. **80**, 4, 1122-1132.
8. Hruska K., 1981, IEEE Trans. Son. Ultrason. SU-28 108.
9. Nosek J., 1995, Highly precise and stable sensors with surface acoustic wave. Proc. 15th Int. Congress on Acoustics ICA 95, Trondheim, Norway, Vol. I, 397-400.
10. Nosek, J., Zelenka, J. 1997, Recent Activities of Crystal Properties at the Technical University of Liberec. Annales de Chimie. Science des Matériaux. Masson Paris, Milan, Barcelone, Vol. **22**, 8, 661-668.
11. Nosek, J., 1997, New Experimental Possibilities of Investigation of Basic Properties of Crystals and Smart Materials. Annales de Chimie. Science des Matériaux. Masson Paris, Milan, Barcelone, Vol. **22**, 8, 691- 693.
12. Nosek J., 1995, Intermodulation products of quartz resonators and their measurement. Proc. 9th European Frequency and Time Forum EFTF 95, Besancon, France, 447-449.

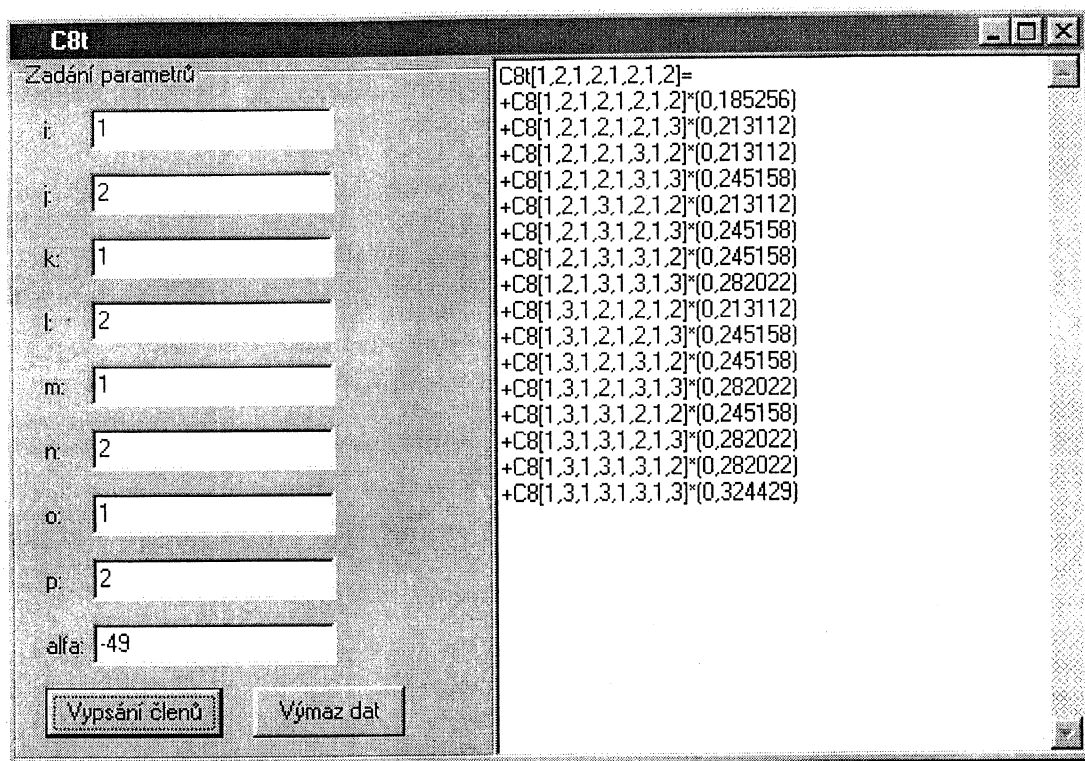


Figure 2: Calculation of components of the elastic stiffnesses tensor of the 8<sup>th</sup> order with the rotation around the axis X.

(Ad Nosek, Kretschmerová, Kretschmer: Determination of the high- order constants.....)

*12th E F T F* - 10÷12 March 1998 - Warsaw - POLAND

**Time transfer & comparisons I**

Chairman:

*Giovanni Busca*



## GLONASS/GPS TIME TRANSFER AND THE PROBLEM OF THE DETERMINATION OF RECEIVER DELAYS

Gerrit de Jong  
NMI van Swinden Laboratorium, P.O.Box 654, 2600 AR, Delft  
Netherlands

Włodzimierz Lewandowski  
BIPM, Pavillon de Breteuil, F-92312 Sevres Cedex  
France

### ABSTRACT

GPS and recently also Glonass receivers are widely used for navigation. When these receivers are used for time and frequency transfer, then all the internal delays and their associated stability become very important. For accurate navigation they are in 'common mode' and only need to be constant during an integration period of less than about one minute. This nanosecond level problem is sometimes not understood by manufacturers and users of those GPS and Glonass timing receivers that were converted from navigation receivers. In the paper this problem is addressed and also the specific Glonass problem caused by the Frequency Division Multiplexing (FDM) used in stead of Code Division Multiplexing (CDM) used in GPS. Some delay measurement results are presented. The calibration and characterization of these delays is important for the international atomic time scale.

### INTRODUCTION

Since the introduction of the Global Positioning System (GPS), many manufacturers have developed and produced receivers for navigation or geodetic positioning. Those receivers consist of an antenna unit, a receiver with a correlator to lock to the coded bi-phase modulated satellite signals, a time reference (usually an internal quartz or rubidium clock), and a time interval counter (TIC) to measure the arrival time of the received signal from each satellite  $s$  with respect to the time reference (fig. 1).

For each satellite  $s$ , the TIC reading  $TI(s)$  is:

- the time offset of the satellite clock (1),
- + the propagation time (2) from satellite  $s$  to the antenna (including ionosphere delay, Sagnac effect and troposphere excess delays),
- + the signal delay in the antenna unit (3) (including delays in its filters and amplifiers),
- + the signal delay in the cable (4) from antenna unit to the receiver input,

- + the signal delay in the receiver (5) (filters, amplifiers, down converters),
- the time offset (6) of the reference clock (including the reference cable delay in case of the use of an external reference clock)

For each satellite the above delays 3, 4, 5 and 6 are equal, but delays 1 and 2 are different. The clock offset of each satellite clock is transmitted, so can be accounted for.

**Navigation and positioning** use the **propagation delay differences (2)** for their calculations, so the delays 3, 4, 5, 6 in Antenna, Cable, Receiver, Reference and Clock offset are **common** and should only not change within the (short) sequence time to measure 4 or more satellites. The propagation delays (2) are transformed into distances using the speed-of-light constant, these distances are the pseudo ranges. From pseudo ranges to 4 different satellites the position of the antenna is calculated.

**Time Transfer** uses known fixed antenna coordinates and calculates the local or internal **reference clock offset** from the  $TI(s)$ . Then the delays in Antenna(3), Cable (4), Receiver (5), reference cable (6) have to be known in an absolute value: they should have been measured and thus been **calibrated**. Unknown changes due to changes in temperature etc. in any of these delays become attributed to the calculated reference clock offset and are limiting the accuracy and precision of the time and frequency transfer.

The **necessity of knowing continuously** the values of hardware delays 3, 4, and 5 as well as the cable delay from delay 6 is often neglected when GPS and Glonass receivers developed firstly for positioning, are being transformed into timing receivers by changing only its software! This extra necessity is also the reason why geodesists have a problem to understand that, while they obtain centimetre position accuracy (equivalent to 30 ps time uncertainty), timing experts obtain for long-term (half day or longer) only about 3 ns time accuracy which translates into metre position accuracy! This paper will further point to some sources of the

(slow changing) delays (3), (4) and (5).

## SOURCES OF SIGNAL OR GROUP DELAYS

The listing below shows a number of sources of signal delays.

- ▶ Coaxial cables: typical 5 ns per metre for  $Z = 50$  Ohm (with solid polyethylene insulator)
- ▶ Amplifiers with transistors, resistors and (parasitic) capacitances, depending on bandwidth and frequency: wider bandwidth results in lower delay
- ▶ HF tuned L-C circuits, high, low and band pass filters, depending on bandwidth and frequency: wider bandwidth and higher frequency gives lower delay
- ▶ Surface Acoustic Wave (SAW) filters using ceramic or glass resonators: depending on excitation mode, propagation velocity in the material, bandwidth.
- ▶ Optical fibre cables: see SAW filters

## FACTORS OF SIGNAL DELAY CHANGES

When these delays are known once, they may change due to sensitivity to some factors as given in the list below:

- ▶ Temperature
- ▶ Humidity
- ▶ Air Pressure
- ▶ Mechanical strain
- ▶ Aging
- ▶ Reflections in cables/fibres due to mismatch
- ▶ Supply Voltage
- ▶ Signal Power level in amplifiers, specially near the compression point

So all such factors should be examined to determine if they may result in significant changes of the delays for GPS, Glonass and Two-Way Satellite Time and Frequency Transfer [11, 12] equipment.

## DELAYS IN GPS TIME TRANSFER RECEIVERS

In fig. 2 and 3 the signal delay calibration curves of two different pre-correlation filters are shown for the GPS L1 frequency (1575.42 MHz). It is clearly seen that wide band filters exhibit less delay than narrow band filters. Also when both filters would have the same percentage of temperature dependency, the wide filter is more stable with temperature. Of course, the overall temperature

coefficient depends on the temperature sensitivity of the used components [1, 3, 6, 7, 8, 9, 10, 11, 12]. For the P-code a ten times wider bandfilter is required compared to the C/A code. That is one reason why (geodetic) P-code receivers (mostly also dual-frequency) receivers generally could have smaller temperature sensitivities compared to C/A (mostly single-frequency) receivers.

Fig. 4 shows an example of a good characterization of a commercial filter, a linear group delay factor is given, as well as a parabolic and a ripple value.

## DIFFERENTIAL DELAY IN DUAL FREQUENCY L1 & L2 RECEIVERS

The excess delay due to the ionosphere cannot simply be determined. In receivers for the GPS L1 frequency (1575.42 MHz) using the C/A code, a model for the ionosphere and a parameter from the navigation message is used to calculate it. Fortunately, the ionosphere delay is frequency dependant. So from pseudo range measurements using the same signal from the same satellite (fig. 5) but at a different frequency, the momentary ionosphere delay can be determined more accurately. The second frequency, L2, is 1227.6 MHz, and the delay in the receiver for this signal may differ from the L1 delay (see fig. 9); this differential delay has to be calibrated in advance and should be subtracted from the measured L1-L2 pseudo-range difference to obtain the true ionosphere delay difference. Then the absolute ionospheric delay correction at L1 is calculated and used in the positioning and time transfer calculations.

## SIGNAL DELAYS IN GLONASS (=MULTI-FREQUENCY) RECEIVERS

In the GPS all satellites transmit at the same nominal frequency for L1 and L2. The satellite signals are distinguishable because of the difference in their unique codes used for the bi-phase modulation. In the Glonass, the codes on all satellites are equal, but the transmit carrier frequencies are different for each satellite; at L1:  $(1602 + k \cdot 0.5625)$  MHz and at L2:  $(1246 + k \cdot 0.4375)$  MHz, (where  $k=0$  to 24), a difference of about 0.5 MHz between satellites. The L1 frequency range spans 13.5 MHz and L2 needs 10.5 MHz for the 24 satellites. The delay in antenna unit and receiver over these bands should be identical or its frequency dependency should be calibrated and corrected for (see an example in fig. 9). This is necessary both for positioning and for time transfer, but is not easy to do at the 1 ns level or better.

A L1 & L2 Glonass receiver thus needs 24 L1 and 24 L2 differential calibration values, apart from one L1-L2 differential delay calibration for accurate positioning and for time transfer at least one additional absolute calibration is needed. Due to the planned re-use of Glonass frequencies, now not all 24 calibrations are needed, in the future 12 will be enough. For Glonass receivers delay stability with temperature is also a great necessity [2,3,4,5].

### **SIGNAL DELAYS MULTI-CHANNEL GPS AND GLONASS RECEIVERS**

In single channel receivers all measurements are using the same receiver channel. In multi-channel receivers (fig. 7) there is a chance of differential delays between channels. These delays should be calibrated and corrected for in the software; or at least these differences should be smaller than a specified level such as 1 ns.

### **SIGNAL DELAYS IN DIGITAL SIGNAL PROCESSORS (DSP'S)**

Presently new GPS and Glonass receivers are using digital signal processors for the digitization, correlation, time interval and code generation functions. The pseudo-ranges are determined using these very fast processors with the appropriate software. The processing in these DSP's take some time, which leads to an apparent receiver delay time, which is equivalent to the delay in filters and in digital circuitry. This delay will normally be identical for all tracked satellites and so will not normally be a problem with positioning applications, but are a big problem for time transfer. This delay has been reported to amount up to 2000 ns! This delay should be calibrated for time transfer applications. A better solution would be to minimize this DSP delay or even avoid it by optimizing the design of the hard and software of the DSP for time transfer.

### **CARRIER PHASE AND RECEIVER DELAYS**

The use of carrier phase smoothed data for time transfer improves the short term stability due to averaging more cycles in the same averaging time and less multipath, but the timing of the code sequence is still needed for initially identifying a carrier cycle. For the long term (a half day or

longer), the phase of the carrier is also affected by the same filter and cable delay changes due to temperature, humidity, etc. as the coded bi-phase modulated carriers and these receivers need the same precautions to improve its long-term delay stability necessary for time transfer [8,9].

### **SIGNAL DELAYS IN DUAL SYSTEM (GPS+GLONASS) DUAL FREQUENCY MULTICHANNEL RECEIVERS**

See fig. 8. It is obvious that in a complicated system as mentioned above all the appropriate calibrations are needed to obtain accurate time transfer results.

### **DELAY DIFFERENCES BETWEEN TWO RECEIVERS**

For time transfer two receivers can be calibrated by bringing the one receiver to the other receiver site, putting the antennas close together, connect them to the same reference clock and do a set of observations during several days. So the differential delays are found. After installing the first receiver at the remote site time transfer can be done between the two sites and use the earlier determined differential delay (for example see fig. 10) as a correction. But temperature, humidity, etc. may differ at both sites and limit the obtained accuracy. So still the long-term stability is limited by the sensitivity of each receiver to temperature, etc. However, when the delays are specified by the manufacturer, then clocks at any site can be compared to any other site within the specified uncertainty. Only periodically checks by a visiting receiver are needed for verification.

### **CONCLUSIONS**

The adaptation of navigation or positioning receivers for accurate time transfer is possible, but need besides relative calibrations a few additional absolute calibrations (see table 1 below), as well as a much improved longer term delay stability (temperature, humidity, etc.) for the signal delays in antenna unit, the cable connection between antenna and receiver, the internal receiver delays and reference clock cable.

Table 1. Required Delay Calibrations

Receiver configuration	No. of bands	No. of frequencies per band	Total no. of frequencies	Navigation: no. of Calibrations	Time Transfer: no. of Calibrations
GPS C/A, single freq.	1	1	1	0	1 Absolute
GPS dual freq., P-code	2	1	2	1 Relative	2 Absolute = 1 Abs. + 1 Rel.
Glonass C/A, single band	1	24	24	24 Relative	24 Absolute = 1 Abs. + 23 Rel.
Glonass dual band, P-code	2	24	48	49 Relative	49 Absolute = 1 Abs. + 48 Rel.
Dual system GPS C/A & GLO C/A, Glonass dual band, P-code	3	1/24/24	49	50 Relative	50 Absolute = 1 Abs. + 49 Relative

**RECOMMENDATION**

It is recommended that manufacturers of GPS and/ or Glonass receivers for time transfer provide the values of the relative and absolute delays in each antenna and receiver unit on a calibration report or in a calibration data file; also that the receiver is prepared to use such a calibration file to correct the calculated time transfer data output.

Further research should be done to improve the long term stability (specially temperature sensitivity) of GPS and Glonass receiver circuitry.

**REFERENCES**

[1] G. de Jong 1985, " Measuring the propagation time of coaxial cables used with GPS receivers", Proceedings 17<sup>th</sup> Precise Time and Time Interval (PTTI) Applications and Planning Meeting, 3 - 5 December, Washington, DC, USA, pp.223 - 232.

[2] W. Lewandowski, P. Moussay, J. Danaher, R. Gerlach, E. Vasseur, 1997, "Temperature-protected antennas for Satellite Time Transfer Receivers", Proceedings 11<sup>th</sup> European Frequency and Time Forum (EFTF), 4 - 7 March 1997, Neuchatel, Switzerland, pp. 498-503.

[3] W. Lewandowski, J. Azoubib, M. Weiss, V. Zhang, V. Hanns, A.G. Gevorkyan, P.P. Bogdanov, N. Tutolmin, J. Danaher, G. de Jong, J. Hahn. M. Miranian 1997, "Glonass Time transfer and its comparison with GPS", Proceedings 11<sup>th</sup> European Frequency and Time Forum (EFTF), 4 - 7 March 1997, Neuchatel, Switzerland, pp. 187-193.

[4] W. Lewandowski, J. Azoubib, A.G. Gevorkyan, P.P. Bogdanov, J. Danaher, G. de Jong, J. Hahn, 1996, "First results from Glonass common-view time comparisons realized according to the BIPM international schedule", Proceedings 28<sup>th</sup> Precise Time and Time Interval (PTTI) Applications and Planning Meeting, 3 - 5 December, Reston, Virginia, USA, pp. 357 - 365.

[5] W. Lewandowski, J. Azoubib, M. Weiss, A.G. Gevorkyan, P.P. Bogdanov, W.J. Klepczynski, M. Miranian, J. Danaher, N.B. Koshelyaevsky, D.W. Allan 1996, "A contribution to the standardization of GPS and Glonass time transfers", Proceedings 28<sup>th</sup> Precise Time and Time Interval (PTTI) Applications and Planning Meeting, 3 - 5 December, Reston, Virginia, USA, pp. 367 - 386.

[6] W. Lewandowski, P. Moussay, P. Guerin, F. Meyer, M. Vincent 1997, "Testing Motorola On-core GPS receiver and temperature-stabilized antennas for time metrology", Proceedings 28<sup>th</sup> Precise Time and Time Interval (PTTI) Applications

and Planning Meeting, 3 - 5 December, Reston, Virginia, USA, pp. 387 - 396.

[7] W. Lewandowski, P. Tourde 1990, "Sensitivity to the external temperature of some GPS time receivers", Proceedings 22<sup>th</sup> Precise Time and Time Interval (PTTI) Applications and Planning Meeting, 4 - 6 December, Vienna, Virginia, USA, pp. 307 - 316.

[8] P. Baeriswyl, T. Schildknecht, J. Utzinger, G. Beutler 1995, "Frequency and time transfer with geodetic GPS receivers: first results", Proceedings 9<sup>th</sup> European Frequency and Time Forum (EFTF), - March 1995, pp. 46-51.

[9] F. Overney, L. Prost, U. Feller, T. Schildknecht, G. Beutler 1997, "GPS time transfer using geodesic receivers: middle-term stability and temperature dependency of the signal delay", Proceedings 11<sup>th</sup> European Frequency and Time Forum

(EFTF), 4 - 7 March 1997, Neuchatel, Switzerland, pp. 504-508.

[10] R.J. Douglas, J. Popular 1994, "PTTI applications at the limits of GPS", Proceedings 26<sup>th</sup> Precise Time and Time Interval (PTTI) Applications and Planning Meeting, 6 - 8 December, Reston, Virginia, USA, pp. 141 - 151.

[11] J.A. Davis, P.R. Pearce 1993, "Characterization of the signal delays in a ground station designed for Two-Way Time Transfer", Proceedings 7<sup>th</sup> European Frequency and Time Forum (EFTF), 16 - 18 March 1993, pp. 113-118.

[12] G. de Jong 1997, "Delay stability of the TWSTFT earth station at VSL", Proceedings 29<sup>th</sup> Precise Time and Time Interval (PTTI) Applications and Planning Meeting, 2 - 4 December, Long Beach, California, USA,.

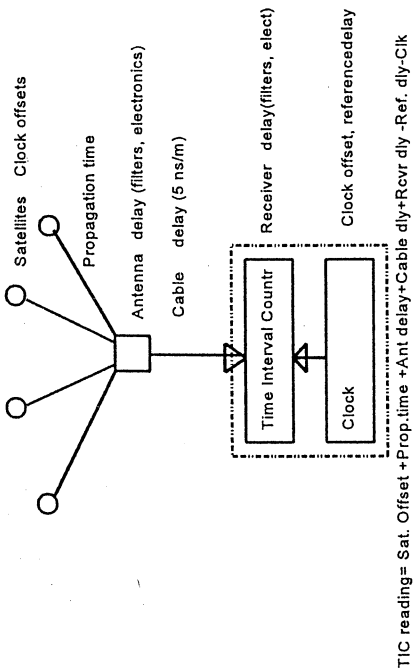


Figure 1. GPS receiver principle with delays

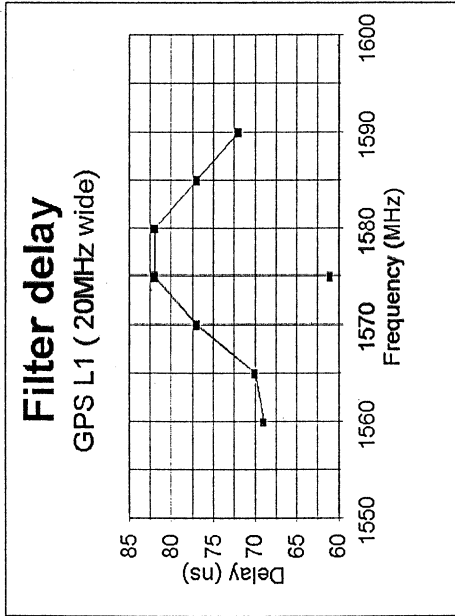


Figure 2. Delay versus frequency

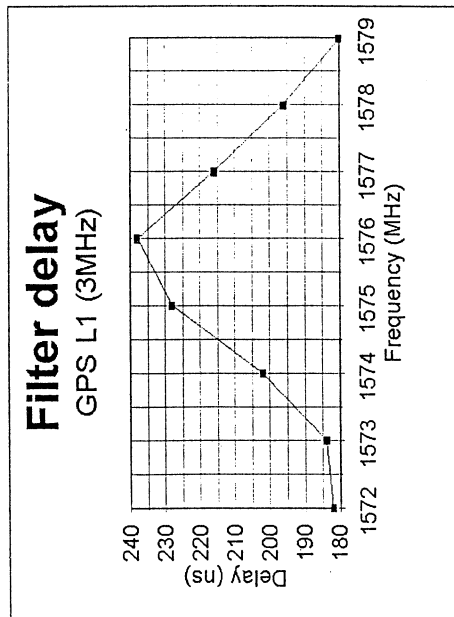


Figure 3. Delay versus frequency

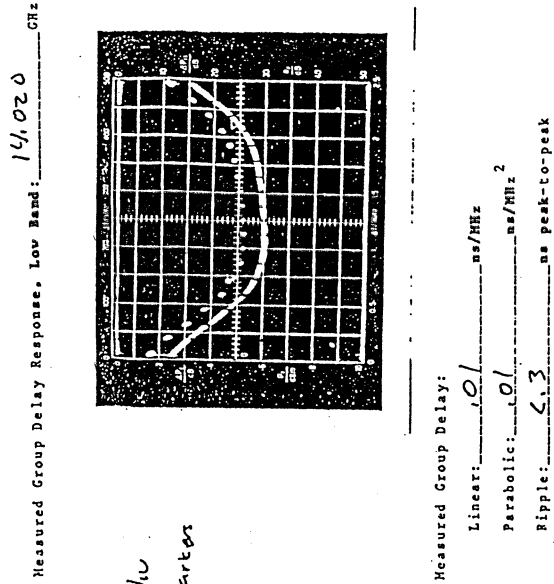


Figure 4. Filter delay versus frequency (Y-axis top-down)

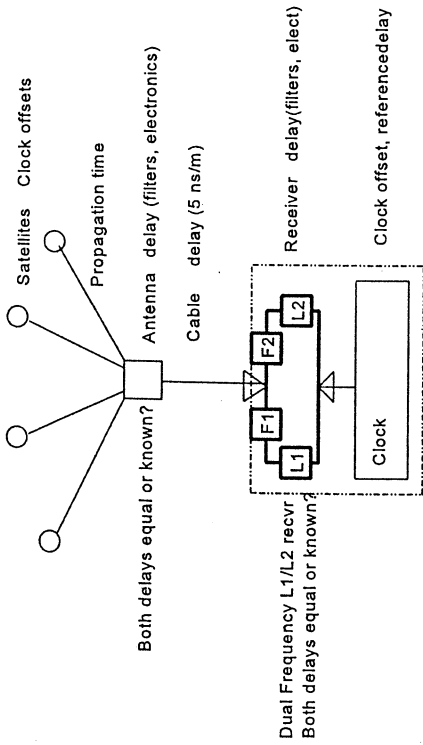


Figure 5, Dual frequency Receiver

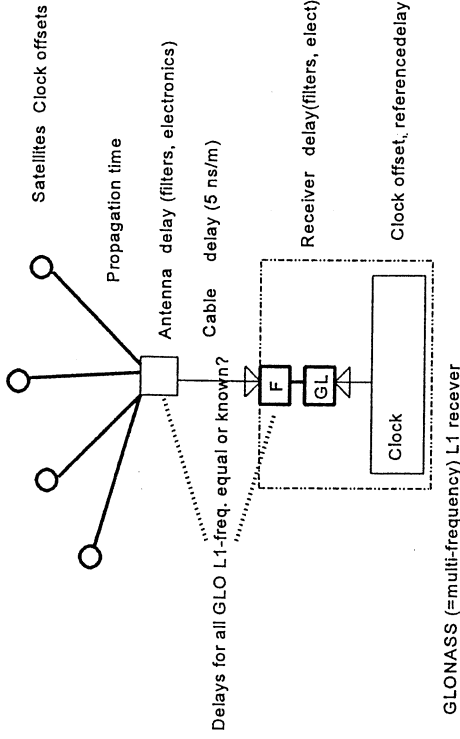


Figure 6. Glonass Receiver

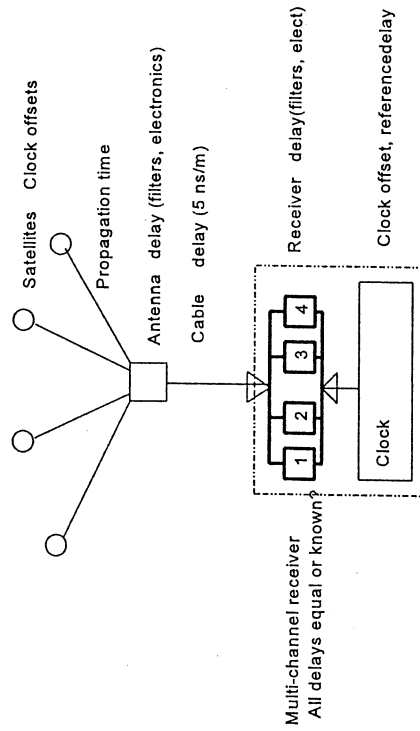


Figure 7. Multi-channel Receiver

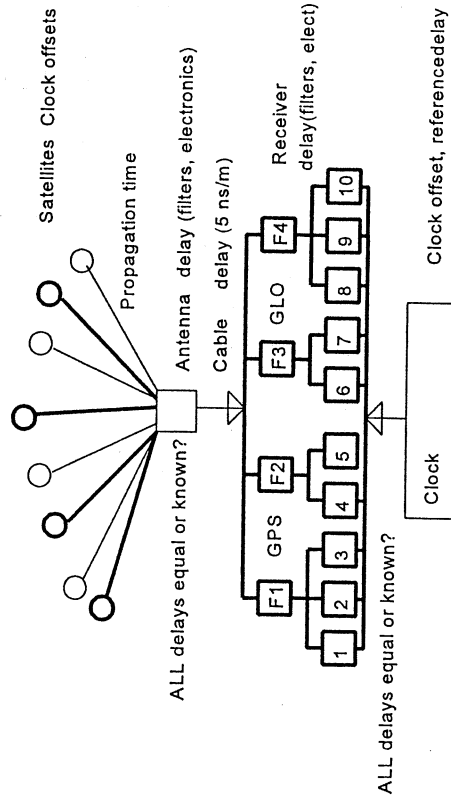


Figure 8. Combined Glonass / GPS Receivers

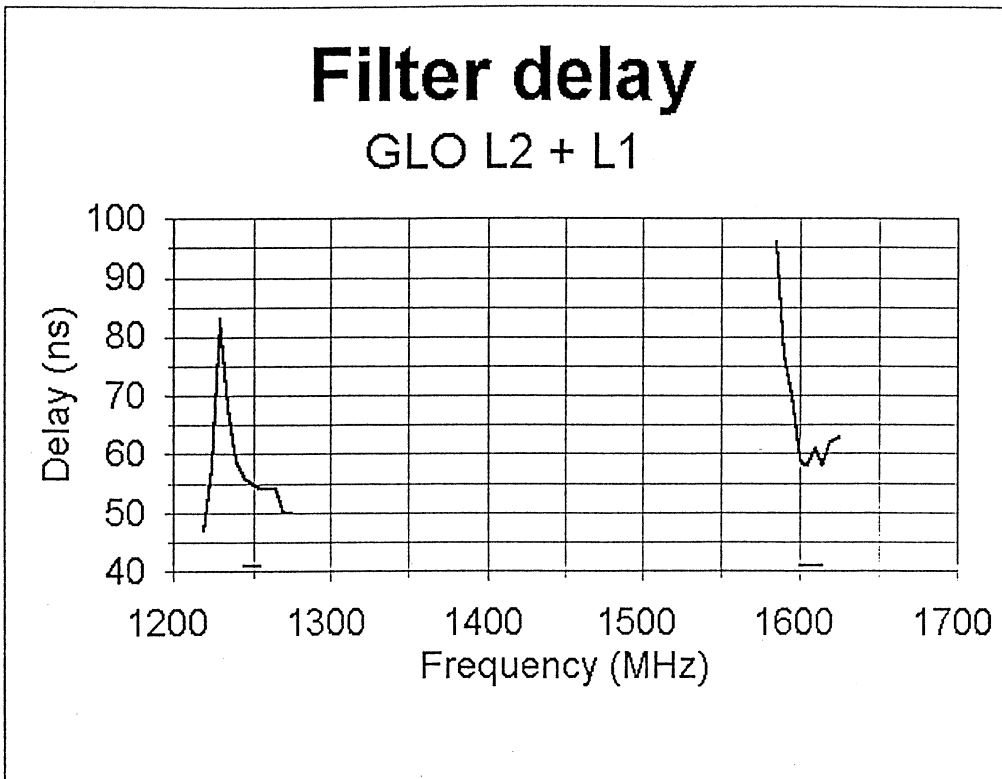


Figure 9. L2 & L1 Filter delays

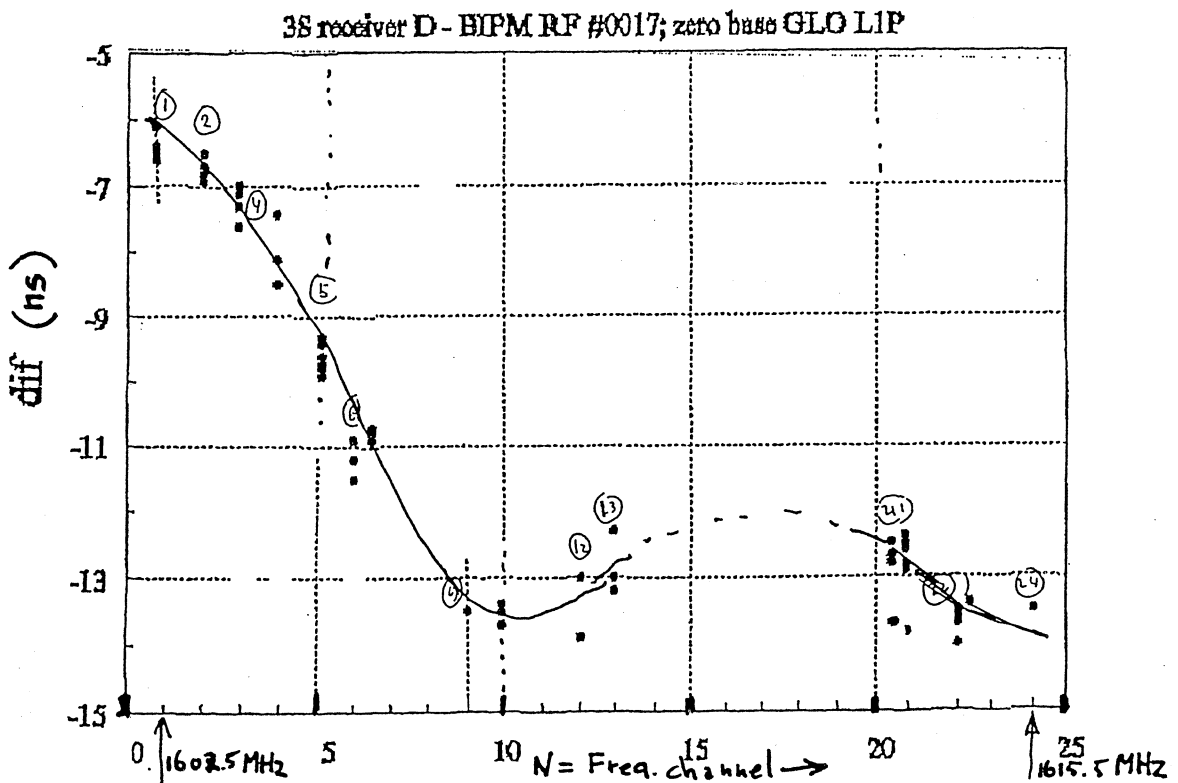


Figure 10. Delay difference of two Glonass Receivers versus freq. channels

**A NEW APPROACH TO INTERNATIONAL TIME TRANSFER:  
MULTI-CHANNEL AND MULTI-CODE GPS + GLONASS COMMON-VIEW OBSERVATIONS**

J. Azoubib and W. Lewandowski  
Bureau International des Poids et Mesures, Sevres, France

G. de Jong  
NMi Van Swinden Laboratorium, Delft, the Netherlands

**Abstract**

*The combined use of GPS and GLONASS for international time and frequency transfer is feasible despite differences between the two systems. The use of two systems in multi-channel mode increases the number of observations by a factor of 20 in comparison to a single-channel one-system mode. This results in an improvement in time and frequency comparisons. In addition GLONASS P-code is accessible to civil users and it shows an outstanding performance in time transfer. Specially designed receivers for GPS + GLONASS multi-channel and multi-code time and frequency comparisons are described and some initial results are provided. The use of temperature-stabilized antennas brings further improvement and is described briefly.*

**1. INTRODUCTION**

For the past fifteen years international time transfer, as used for the computation of TAI, has been carried out using single-channel C/A-code GPS receivers and an international common-view schedule of standard 13 minute tracks [1]. For regional time comparisons, within 1000 km, about 40 tracks are usually available, and for intercontinental distances about 10. At present, the estimated uncertainty for operational GPS atomic clock comparisons is 5 -10 nanoseconds for a single common-view observation and a 2 - 3 nanoseconds for a daily average, which corresponds to a few parts in  $10^{14}$ . This performance is barely sufficient for the comparison of current atomic clocks, and needs to be improved rapidly to meet the challenge of clocks now being designed.

For this reason the timing community is engaged in the development of new approaches to remote clock comparison. Among them is approach based on multi-channel two-system C/A-code GPS and GLONASS receivers, and multi-channel P-code GLONASS receivers.

The multi-channel receivers considered here use C/A-code to observe all GPS and GLONASS satellites in view and use standard 13 minute tracks at the standard hours. In addition, they observe GLONASS satellites with P-code on one or two channels. The standard hours are defined at 16 minute intervals beginning at 00 h 02 min UTC on reference date 1st October 1997 (MJD = 50722) [2] and are decremented by 4 minutes each next day to take account of the sidereal periods of the satellite orbits.

The use of two systems in 'all-in-view' multi-channel mode increases the number of observations by a factor of 20 relative to the single-channel one-system mode. A consequent improvement in the quality of time and frequency transfer is to be expected. Of course these observations are subject to systematic variations, mainly caused by environmental effects on the receivers but, if temperature-stabilized antennas (TSA) are used, these effects are greatly reduced.

This paper provides an analysis of the first results for multi-channel double-system GPS + GLONASS time transfer between two sites distant by about 400 km and for a one-site comparison. It also applies the results of the first differential calibration of remote GPS + GLONASS time equipment. The advantages of the use of GLONASS P-code are discussed, including a solution for the delay biases caused by the use of different GLONASS frequencies.

**2. WHY GLONASS?**

The Russian Global Navigation Satellite System (GLONASS) was inaugurated in 1982 and is still under development. Because the GLONASS signal is free of Selective Availability (SA) and is available world-wide, it offers the international time metrology community a useful additional tool for high-accuracy time transfer. However, the use of GLONASS signals, which have characteristics similar to those of GPS, was restricted for a long time because no commercial time receivers were available. This has changed recently: new GLONASS time receivers are now readily available [3].

The GLONASS constellation not only offers an additional 24 satellites and a C/A-code signal free of SA, but it is also broadcast using unencrypted P-code signal, unlike the GPS P-code which is subject to Anti-Spoofing (AS) encryption. GLONASS P-code has two main advantages for precision time synchronization. First, GLONASS P-code has a wavelength that is 1/10th that of GLONASS C/A-code and about 1/5th that of GPS C/A-code. This has the effect that GLONASS P-code pseudo-range measurements are considerably more precise than comparable GPS or GLONASS C/A-code measurements. Second, GLONASS P-code is transmitted on both L1 and L2 frequencies, so it allows high-precision ionospheric delay measurements. Until now GLONASS P-code time receivers have only processed data for L1 frequencies. After a minor change in the software, already accepted by the manufacturer, P-code data on L2 frequencies will also be treated to produce 13 minute tracks. This will double the number of P-code observations, which adds an additional value to the process we describe below.

GLONASS signals are broadcast on 48 frequencies (in the future 24 frequencies) in contrast to GPS, which is broadcast on 2. This causes some difficulties with the delay biases, which vary with frequency. These, however, can be resolved, so the GLONASS system provides the net advantage that it is less vulnerable to intentional or unintentional jamming.

At present no post-processed GLONASS precise ephemerides are available. This will soon change as the Scientific Assembly of the International Association of Geodesy decided, on 3-9 September 1997 in Rio de Janeiro, to organize an International GLONASS Experiment (IGEX) in 1998. Participation by many geodetic and timing institutions is expected and the first GLONASS precise ephemerides expressed in the ITRF could become available to civil users at the end of 1998. This will make it possible to use GLONASS more efficiently for intercontinental time links. Other improvements will follow, among them rigorous transformation parameters between the WGS 84 reference frame used by GPS and the PZ-90 reference frame used by GLONASS.

### 3. NEW TYPE OF TIME RECEIVERS

A few years ago the first commercial GLONASS two-channel time receivers became available. More recently new GPS + GLONASS multi-channel and multi-code time receivers have been developed. Already a number of major timing centres around

the globe observe GPS and GLONASS in multi-channel and multi-code mode. Their receivers are all of type R-100/30, manufactured by 3S Navigation. These take the form of a 12-channel GPS + GLONASS C/A-code card, and two or more cards with GLONASS P-code channels. The number of GLONASS P-code cards can be increased. Four to six satellites of each system can usually be observed simultaneously on the 12-channel C/A-code component of the receiver. Each receiver uses a single antenna. The receivers are controlled by a PC and use a standard format, developed for the GPS single-channel common-view technique by the CGGTTS [4], which has been adapted to suit two-system two-code multi-channel observations [2, 5]. These receivers have operated correctly over long periods of time and no bugs have been identified in the software. Their metrological quality has been confirmed by comparison with other GPS time receivers [6]. 3S Navigation has recently introduced a new GPS + GLONASS time receiver, an 18-channel C/A-code GNSS-300T.

An important feature of all these receivers is that they provide carrier phase measurements for GPS and GLONASS under a standard Receiver Independent Exchange Format (RINEX) [7]. Carrier phase data is already used by these receivers to smooth GLONASS P-code measurements of the ionosphere. Data recorded in RINEX format will be shortly used in the IGEX campaign and possibly for carrier phase based techniques of frequency transfer now under development (the IGS/BIPM Pilot Project to Study Accurate Time and Frequency Comparisons Using GPS and Phase Measurements).

### 4. SINGLE-CHANNEL VERSUS 'ALL-IN-VIEW' MULTI-CHANNEL COMMON-VIEW OBSERVATIONS

The BIPM issues GPS and GLONASS single-channel international common-view schedules for international time and frequency comparisons twice a year. These indicate to receivers which satellites to observe at which time. Until recently, the times of observation were redefined for each new schedule so that a first 13 minute track begun at 00 h 02 UTC on the first day of implementation of a new schedule and continued at 16 minute intervals until the end of the day. These times were decremented by 4 minutes each next day, to take account of sidereal orbits of the satellites.

This convention of reference dates has changed recently: the CCTF Sub-group on GPS and GLONASS Time Transfer Standards (CGGTTS), at its meeting in Long Beach on 1st December 1997, set

1st October 1997 (MJD = 50722) as the definitive date of reference for all future GPS and GLONASS schedules, whatever their implementation dates [2].

The multi-channel GPS + GLONASS time receivers considered here observe all the GPS and GLONASS satellites in view, in standard 13 minute tracks every 16 minutes at scheduled standard times. For these receivers, there is obviously no need to specify which satellites to observe, as is done for single-channel receivers, because such an ensemble of 'all-in-view' tracks necessarily includes the international single-channel schedules. This greatly simplifies the parallel introduction of GPS + GLONASS multi-channel time receivers into the present system of scheduled GPS and GLONASS single-channel receivers. The adoption by the CGGTTS of a permanent reference day for standard times is a further simplification, as multi-channel receivers will not have to be updated when international schedules are changed for single-channel receivers. In the future, when all single-channel receivers have been withdrawn from operation, the use of a fixed reference date will make it possible to cease publication of the common-view schedules.

Although, in theory, up to 12 GPS or GLONASS satellites can be observed simultaneously, only about 5 satellites from each system may be observed above  $15^\circ$  (and thus be of interest for time transfer) from an average urban site. As there are 89 useful 16 minute periods in a day, this is the number of tracks, which may be observed in each channel. Using all five channels, we may therefore observe 445 tracks per day for each system, and 890 for the combined system. All of these tracks can be used for regional common-view links. For very large baselines, between continents, 160 to 200 common-view tracks may be available for the combined system using a multi-channel approach. In most cases single-channel receivers are limited by their software to 48 tracks per day. In practice, single-channel receivers provide about 45 tracks per day for regional links and about 10 for intercontinental links. The increase by a factor of twenty in the number of common views made available in the combined system multi-channel approach, makes it reasonable to expect an improvement in the quality of time transfer. Of course, all observations are subject to systematic variations, mainly related to the effects of environmental change on the receivers. When using temperature-stabilized antennas, however, these effects are greatly reduced.

## 5. TEMPERATURE-STABILIZED ANTENNAS

It is now well documented, and generally admitted, that most of GPS time equipment is sensitive to external temperature [8]. The variation is typically about  $0.2 \text{ ns}/^\circ\text{C}$ , but can approach  $2 \text{ ns}/^\circ\text{C}$  for some types of receiver. Even for the lower value, the consequent change in signal delay can be the dominant noise contribution in measurements involving time transfer by GPS common-view for periods of several days over baselines of several hundred kilometres.

This sensitivity to external temperature suggests an effect linked to those parts of the time equipment located in the open-air, that is to the antenna and its cable. The receiver itself is usually located in an air-conditioned room. For several years different hypotheses were considered to explain the temperature dependence of timing equipment. All linked the problem to the electronics of the antenna, but none were verified. The length and material of the cables are important and must be also considered.

As no practical way was found to resolve the problem electronically, another approach was suggested [8]: an oven with a stabilized temperature should protect the antenna. The primary objective of the antenna temperature stabilization process is to maintain the critical components at some constant temperature. The exact temperature is not critical.

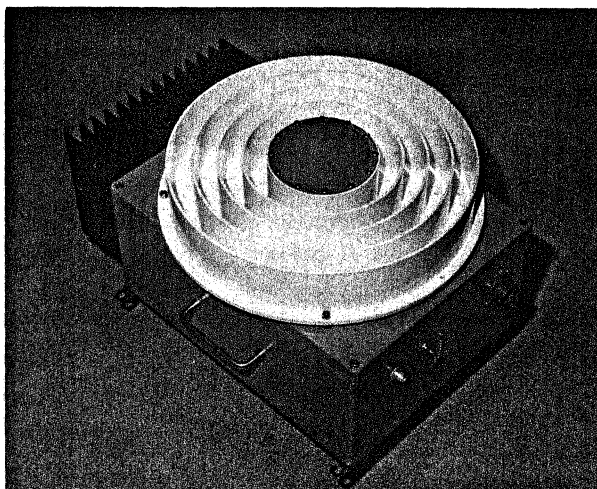


**Figure 1.** Industrial temperature-stabilized GPS + GLONASS TSA-100 antenna. Integrated chock-ring multipath protection can also be seen.

First prototypes of the ovens for receiver time antennas were built at the BIPM, quickly followed by a commercial version, referred to as a Temperature

Stabilized Antennas (TSA) (Figure 1). A preliminary one-site comparison of two GPS multi-channel receivers equipped with TSA antennas at the BIPM is reported below.

## 6. TIME TRANSFER OVER 400 km

The time link between the BIPM and the VSL considered in the trial comparison described here has a baseline of about 400 km. Both laboratories are equipped with R-100/30 receivers and their ground-antenna coordinates are expressed in the ITRF with an uncertainty of 0.3 m. At the time of our trial comparison the neither receiver was not equipped with a TSA antenna. At both laboratories, receivers were connected to HP5071A clocks. For this study we used data covering roughly 10 days. Both receivers were calibrated using a portable R-100/30 receiver [6]. We observed a constant bias of 6 ns between the GPS and GLONASS links. After application of this correction, the GPS and GLONASS data could be mixed and we computed  $[BIPM\ clock - VSL\ clock]$  using GPS + GLONASS. Table 1 shows the number of common views available for the different kind of time link. Figures 2 and 3 show the time differences between the clocks, using the same receivers over a common period of time, for a single-channel GPS link and for multi-channel GPS + GLONASS links.

**Table 1.** Number of common views per day by different methods for  $[BIPM\ clock - VSL\ clock]$  comparison.

Method	Average number of common views per day	Average number of simultaneous common views
GPS single-channel	38	1
GLONASS single-channel	25	1
GPS multi-channel	350	4.5
GLONASS multi-channel	255	3.3
GPS+GLONASS Multi-channel	605	7.8

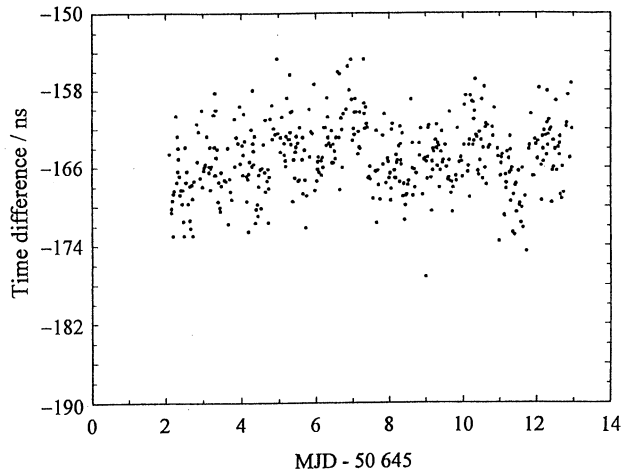


**Figure 2.**  $[BIPM\ clock - VSL\ clock]$  by single-channel GPS common views.

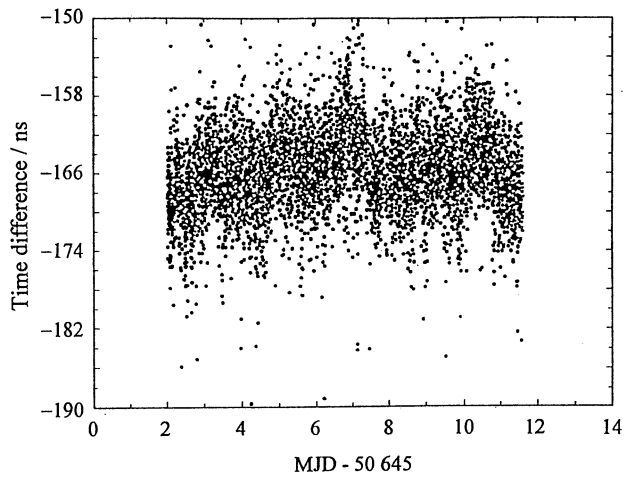


**Figure 3.**  $[BIPM\ clock - VSL\ clock]$  by GPS + GLONASS multi-channel common views.

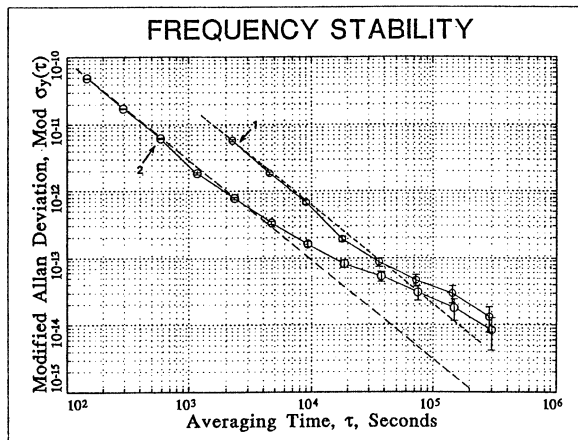


**Figure 4.** Modified Allan Standard Deviation of  $[BIPM\ clock - VSL\ clock]$  as given by single-channel GPS (1) and by multi-channel GPS+GLONASS (2) observations.

The level of noise for all these links is about 3 ns. However, we observe an important advantage obtained by increasing the number of daily common views from 38, for the single-channel GPS link, to the 605, for the multi-channel GPS + GLONASS link. A theoretical gain in stability of  $(605/38)^{1/2} = 4$  is expected in the regions where white phase noise is preponderant. This can be seen on the stability curves of Figure 4 for averaging times of less than  $10^4$  seconds. Additional systematic effects are observed for averaging times above  $10^4$  seconds. These are probably linked to the environmental sensitivity of the antennas which were not temperature-stabilized. We address this problem below in a one-site comparison.

## 7. ONE-SITE COMPARISON

A one-site comparison calls for the computation of common views for two independent time receivers located at the same site, connected to the same clock, and with antennas distant by no more than several metres. Comparisons at short distances allow the cancellation of common clock errors and certain other systematic errors. If the software used by the receivers is identical, no error should arise from satellite broadcast ephemerides, antenna coordinates or imperfect modelling of the ionosphere and troposphere. Any constant bias measured is caused by delay differences of the two time-receiving systems, including the receiver itself, the antenna and the cables, and any observed noise arises in the hardware and in multipath effects. In fact, the noise ascribed to space factors for the comparison over several hundred kilometres is almost as well cancelled as that for the one-site comparisons. The particularity of a one-site comparison, however, is the elimination of the clock, so that only the noise of the receiving equipment is observed. This can serve to characterize the receiving equipment. We used a one-site test specifically to analyse the noise of our time receiving equipment 1) when used with GPS and GLONASS C/A-code in single-channel and multi-channel modes, both with and without a TSA antenna, and 2) when used with GLONASS P-code in single-channel mode, both with and without a TSA antenna.

Figure 5 shows some examples of one-site comparisons over a period of about two weeks using the same pair of receivers throughout. We observe that C/A code comparisons are affected by some systematic changes. GLONASS C/A-code data is slightly noisier than GPS C/A-code data as the delays are affected by different GLONASS

frequencies. After removing the bias specific to each GLONASS frequency and activating the TSA antennas the GLONASS P-code comparison shows outstanding performance.

Time deviations of one-site comparisons were computed for four cases (Figure 6):

- GPS C/A-code single-channel with non-protected antennas,
- GPS C/A-code multi-channel with non-protected antennas,
- GPS C/A-code multi-channel with TSA antennas,
- GLONASS P-code single-channel with TSA antennas and biases for different GLONASS frequencies removed.

Except for GLONASS P-code the level of noise for the all above comparisons is about 3 ns. The gain in stability between GPS C/A-code single-channel and a multi-channel comparison is in line with our expectations, according to considerations reported above. The multi-channel comparison is affected by a systematic effect which becomes evident at about  $3 \times 10^4$  second. This effect is removed when the TSA antennas are activated. However, a smaller systematic effect with a period of several hours persists: this may have its origin in the antenna cables. Recent data from another pair of receivers of the same type equipped with TSA antennas exhibits no systematic effect.

The level of noise for the GLONASS P-code comparison using TSA antennas and after removing the bias specific to each frequency, is about 600 picoseconds. The gain in level noise between GPS C/A-code single-channel and GLONASS P-code single-channel comparison is about 5. The use of GLONASS P-code in multi-channel mode should provide an improvement in stability similar to that found for C/A-code. Consequently, the expected time stability with an averaging time of one day should be several tens of picoseconds: this corresponds to a frequency stability of several parts in  $10^{16}$ . Multi-channel GLONASS P-code time transfer will be object of our next study as suitable receivers are now available.

## 8. CONCLUSIONS

- This study confirms the feasibility of GPS + GLONASS multi-channel time transfer. The dual-system multi-channel and multi-code receivers operate smoothly and no bugs have been found in the software. They use standard software and standard format. Comparison with other GPS time receivers provides a test of their metrological quality.

### ONE-SITE COMPARISON

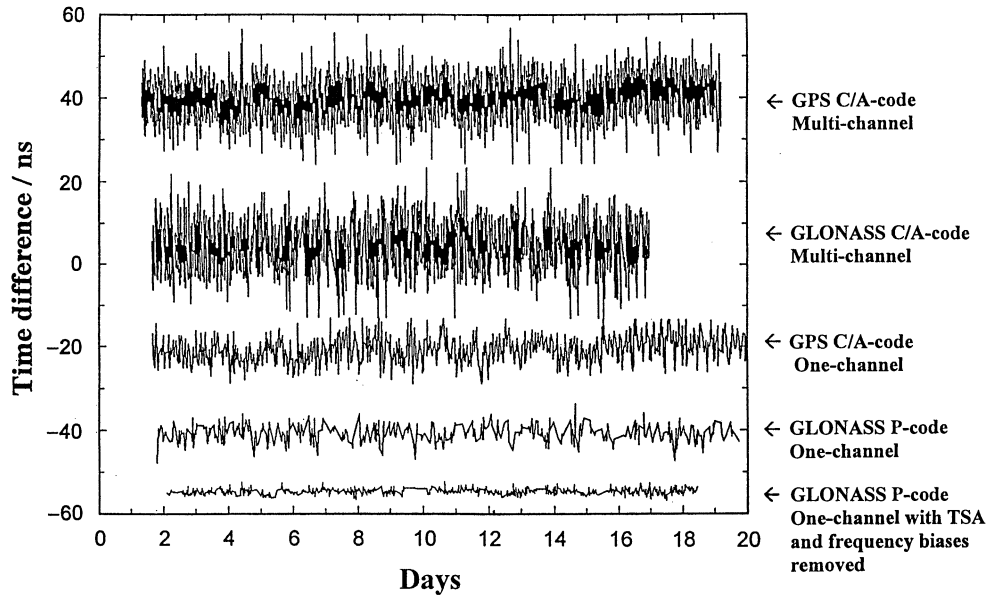


**Figure 5.** One-site comparisons (two separate antennas on a single site). For the top four traces the X-axis shows the days from MJD 50661; for the bottom trace 0 corresponds to MJD 50765.

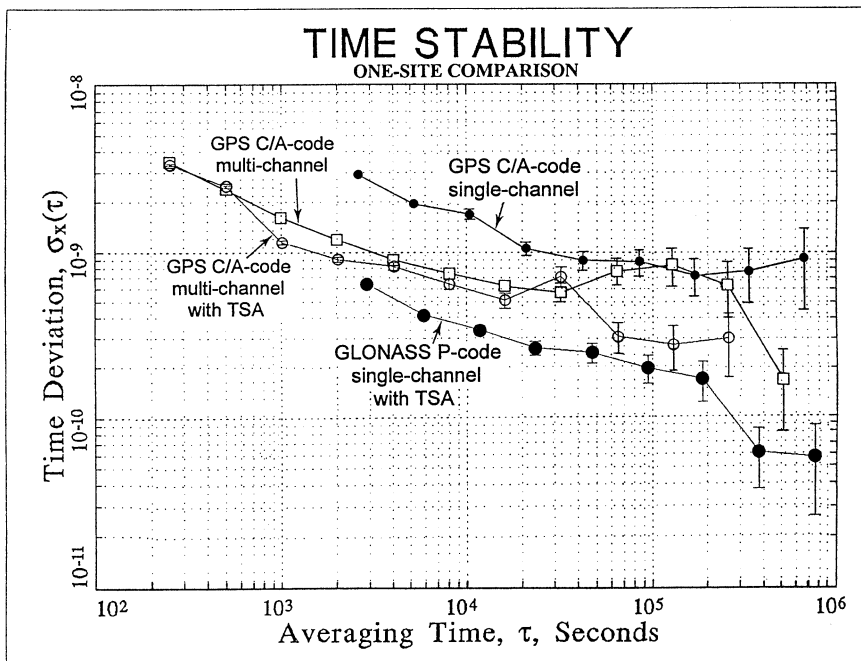


**Figure 6.** Time Deviation for one-site comparisons (two separate antennas on a single site).

- Increasing the number of daily common views by a factor of about 20 between a single-channel GPS link and multi-channel GPS + GLONASS link greatly improves the reliability of time transfer.

- A stability gain of 4 was observed between a single-channel GPS and a GPS + GLONASS multi-channel links for averaging times less than  $10^4$  seconds.

- Additional systematic effects were observed for averaging times above  $10^4$  seconds for 400 km and one-site comparisons. These are linked to the environmental sensitivity of the antennas. These systematic effects can be removed by using temperature-stabilized antennas.

- Multi-channel GPS and GLONASS C/A-code measurements with TSA antennas can provide, for integration times of one day, estimates of the frequency difference between remote atomic clocks with an uncertainty of a few parts in  $10^{15}$ .

- A test of TSA antennas on one site (two separate antennas) demonstrates the removal of systematic effect with a period of several-days during multi-channel GPS C/A-code comparison. A smaller systematic effect of several hours persists, but this may be ascribed to the antenna cables or to the receivers themselves. Recent data from another pair of the same type of receivers equipped with TSA antennas exhibits no systematic effect.

- GLONASS P-code single-channel data obtained in the course of a one-site comparison shows the noise gain of 5 relative to GPS C/A-code single-channel data performance. The use of GLONASS P-code in multi-channel mode promises a gain in stability by a factor of at least 3. Consequently, the expected time stability for an averaging time of one day should be of several tens of picoseconds, which corresponds to a frequency stability of several parts in  $10^{16}$ . This performance corresponds to the theoretical potentiality of carrier phase measurements and Two-Way Satellite Time Transfer.

- The receivers considered in this paper have the important feature that they record carrier phase measurements for GPS and GLONASS under standard RINEX format at the same time as they record standard 13 minute code measurements. The carrier phase data is already used to smooth GLONASS P-code measurements of the ionosphere and will be used for the determination of GLONASS precise ephemerides during the IGEX campaign. It may also be used in carrier-phase based techniques for frequency transfer now under development. This underlines universal character

of these new type of receivers for the purposes of time metrology.

#### Acknowledgements

The authors wish to express their gratitude to 3S Navigation for providing equipment essential for this work.

#### REFERENCES

[1] Allan D., Weiss M., 1980, Accurate Time and Frequency Transfer During Common-view of a GPS Satellite”, Proc. 1980 Frequency Control Symposium, pp. 334-346.

[2] “Report of the Open Forum on GPS and GLONASS Standardization”, 1998, 6th CGGTS Meeting on 1 December 1997 in Long Beach, California.

[3] Lewandowski W., Azoubib J., de Jong G., Nawrocki J., Danaher J., 1997, “A New Approach to International Satellite Time and Frequency Comparisons: ‘All-in-View’ Multi-channel GPS+GLONASS Observations”, Proc. ION GPS-97, pp. 1085-1091.

[4] Allan D.W. and Thomas C., 1994, “Technical Directives for Standardization of GPS Time Receiver Software”, Metrologia, 31, pp. 67-79. .

[5] Lewandowski W., Azoubib J., Gevorkyan, A.G., Bogdanov P.P., Klepczynski W.J., Miranian M., Danaher J., 1996, “A Contribution To the Standardization of GPS and GLONASS Time Transfers”, Proc. 27th PTTI Meeting, pp. 367-383.

[6] Azoubib J., de Jong G., Lewandowski W., 1997, “Determination of differential time corrections for multi-channel GPS and GLONASS time equipment located at 3S Navigation, BIPM and VSL”, Rapport BIPM-97/6, Part 1of 2.

[7] Gurtner W., 1994, “RINEX: The Receiver Independent Exchange Format Version 2”, Astronomical Institute, University of Berne.

[8] Lewandowski W., Moussay P., Danaher J., Gerlach R., LeVasseur E., 1997 “Temperature-Protected Antennas for Satellite Time Transfer Receivers”, Proc. 11th EFTF, pp. 498-503.

## GPS TIME TRANSFER USING GEODETIC RECEIVERS (GeTT): RESULTS ON EUROPEAN BASELINES

E. Overney, L. Prost, G. Dudle, Th. Schildknecht<sup>†</sup>, G. Beutler<sup>†</sup>, J. A. Davis<sup>††</sup>, J. M. Furlong<sup>††</sup>, P. Hetzel<sup>‡</sup>

Swiss Federal Office of Metrology, Switzerland

<sup>†</sup> Astronomical Institute of the University of Berne, Switzerland

<sup>††</sup> National Physical Laboratory, United Kingdom

<sup>‡</sup> Physikalisch-Technische Bundesanstalt, Germany

### ABSTRACT

Two time and frequency comparison campaigns were carried out between three European laboratories with the purpose to demonstrate the reliability, precision and accuracy of the GeTT method. The GeTT method has been compared to the GPS Common-View (CV) over two baselines: firstly between the Swiss Federal Office of Metrology (OFMET) and the National Physical Laboratory (NPL) and secondly between the Physikalisch-Technische Bundesanstalt (PTB) and the NPL. The difference of the time comparison obtained using CV and GeTT is analysed for both baselines. Some preliminary measurements by Two-Way Satellite Time and Frequency Transfer (TWSTFT) between PTB-NPL were realised using a new SATRE modem. The Allan variance of the comparisons of a Cs clock against a H-maser and between two masers is also analysed.

### INTRODUCTION

Accuracy in time metrology not only depends on the performances of the atomic clocks but also on the time and frequency comparison capabilities.

Up to now, the two most used methods in the time transfer domain are the so-called GPS Common-View (CV) [1] and the Two-Way Satellite Time and Frequency Transfer (TWSTFT) [2]. The first one is rather simple to use but limited to a precision of few nanoseconds for an observation time of 1 day and does not permit to compare the clocks at their best performance. The second is more precise (typically 50 ps at  $\tau=300$  s) but relatively complicated and expensive to use. Furthermore the cost of the satellite time often makes continuous TWSTFT comparisons between clocks prohibitively expensive.

Like the CV method, the Geodetic Time Transfer method (GeTT) [3] uses the satellites of the Global Position System (GPS) and hence is also relatively simple and cheap to use. In contrast to the CV, the GeTT takes full advantage of the potential of the GPS signals: all five observables are taken into account, all satellites in view are tracked and the data are processed in an interferometric mode. Adapted from geodetic techniques, this method permits a theoretical precision of some 10 ps (at  $\tau=30$  s) and the accuracy should reach the subnanosecond level.

In order to investigate the performance of this new technique two GeTT terminal prototypes have been built, characterised and calibrated over a zero-baseline [4].

In this communication first results over a non-zero baseline are presented and compared to the well established tools in the time and frequency community (CV and TWSTFT). In next sections we present a short description of the GeTT terminal and of the principle of the technique. Then first results of the campaigns between the Swiss Federal Office of Metrology (OFMET) and the National Physical Laboratory (NPL) and between the Physikalisch-Technische Bundesanstalt (PTB) and the NPL are presented. In either case time and frequency comparisons have been carried out.

### DESCRIPTION OF THE GeTT TERMINAL

As shown in the Figure 1, the GeTT terminal built and characterised at OFMET can be divided into four components: the receiver Box (RBox), the PC, the Time Interval Counter (TIC) and the Uninterrupted Power Supply (UPS). The RBox is the main component of the terminal, since it contains the GPS receiver. The geodetic GPS receiver (Ashtech Z-XII) was modified by the manufacturer to lock the internal receiver clock used to tag the GPS observation to an external clock (local clock). These modifications are mainly:

- the internal receiver reference frequency is derived from an external 20 MHz signal which is obtained by multiplying the 5 MHz output of the local clock.
- the receiver internal 1 PPS is synchronised with the external 1 PPS coming from the local clock through the 1 PPS fan out.

As shown in a previous study [4], the variation of the delay through the electronic boards and the GPS receiver can be greater than 200 ps/°C for the code observation. Furthermore, both GPS receivers have not the same temperature dependence. To reduce this effect, the temperature of the RBox is stabilised. The RBox is supplied with 24 VDC from the UPS that ensures a continuous GPS data acquisition even during short power failures. Other components like the PC and the TIC are directly supplied from the power line (230 VAC/50 Hz) and thus not protected against power failure.

The purpose of the PC is to download the GPS-observation file once a day from the receiver memory to its hard disk and to send the file to the processing centre. The PC is also used to acquire the temperature data from the antenna, the local environment and the RBox.

The TIC measures the delay between the 1 PPS input and 1 PPS output of the GPS receiver (see the right hand side of Figure 1). The stability of this delay indicates that the GPS receiver is working correctly.

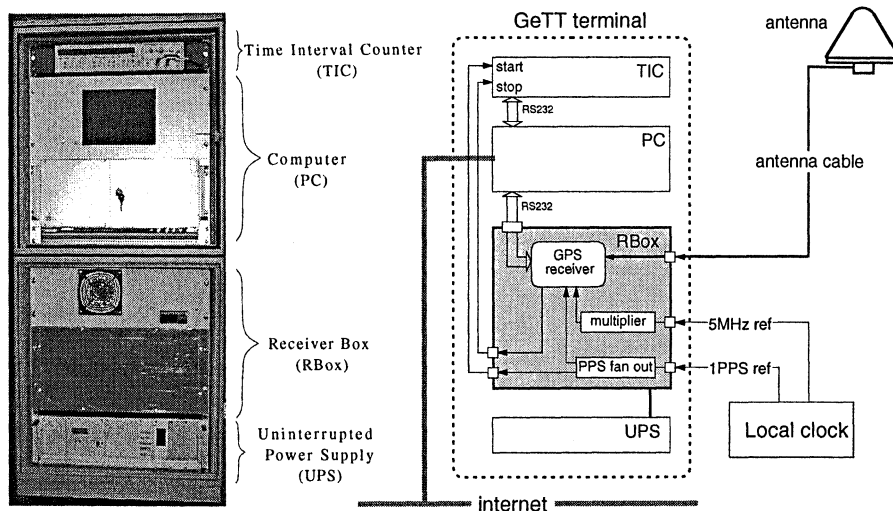


Figure 1: Picture and schematic representation of the GeTT terminal

## DESCRIPTION OF GeTT TECHNIQUE

Figure 2 shows the basic set-up of the GeTT measurements. One GeTT terminal is placed on site A and controlled by the local clock A. The second GeTT terminal is placed on site B and controlled by the local clock B. Each terminal acquires the GPS signals from all satellites in view and stores the phase and the code observations every 30 seconds. Every 24 hours, the observation files of the previous day are automatically sent (by FTP) from both terminals to the processing centre at the Astronomical Institute of the University of Berne. There, a first estimate of the comparison of both local clocks is available 12 hours after the last observation. Final results are obtained five days later.

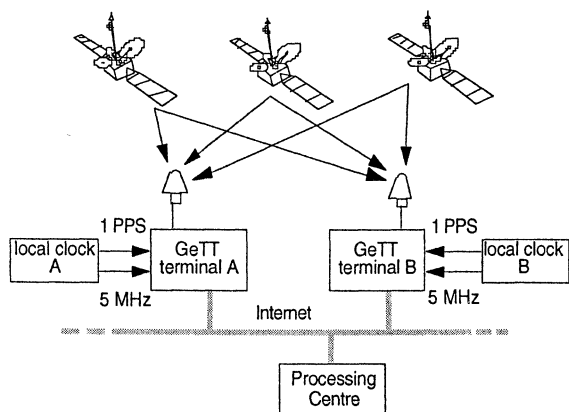


Figure 2: Schematics of the basic set-up of a GeTT campaign between two laboratories A and B

The data processing yields two types of comparisons: the first, called P3, is computed from the code observations of the GPS signals. The second, called L3, is computed from the phase observations of the GPS signals. Both are the results of the ionosphere free linear combination of the two frequencies of the GPS signals. The tropospheric delays are also estimated during the

data processing and both Sagnac effect and other relativistic effects are allowed for. Earth rotation parameters and precise orbits are obtained from the International GPS Service for Geodynamics (IGS).

While the code observations give directly an absolute time comparison between the two terminals, an unknown bias due to the phase ambiguity exists for the phase observations. This bias remains constant as long as the GPS observations are not interrupted. Therefore, it is possible to use many code measurements to determine this constant with a high precision (typically 50 ps for 1 day observation) and to correct the phase observations accordingly. With this technique, the high precision of the phase observation can also be used for the time comparison.

The results  $\Delta t$  given by the processing is not actually the comparison of the local clocks but rather the comparison of the internal signals of both GPS receivers. To obtain the comparison of both local clocks the difference of the local delays have to be taken into account.

$$[A - B] = \Delta t - \left\{ \left( D_A^a - D_B^a \right) + \left( D_A^c - D_B^c \right) + \left( D_A^{RBox} - D_B^{RBox} \right) \right\} \quad (1)$$

$$= \Delta t - D_{A,B}$$

where  $[A - B]$  is the time difference between the signals of the local clock A and B at the input of the terminals,  $D_{A,B}$  is the difference between local delays through the antenna ( $D_k^a$ ), the antenna cable ( $D_k^c$ ) and the RBox ( $D_k^{RBox}$ ) of both terminals ( $k=A,B$ ). The total delay can be divided into a constant term  $D_{A,B}^0$  and a correction term  $\Delta D_{A,B}^T$  depending on the temperature :

$$D_{A,B} = D_{A,B}^0(T = 20^\circ C) + \Delta D_{A,B}(T) \quad (2)$$

The constant term is the calibration value measured between both terminals placed next to each other and steered by the same clock. The correction term has to be calculated using the temperatures measured at both sites and a calibrated model of the thermal coefficients of the

delay through the antenna, the antenna cable and the RBox. The correction term was not taken into account for the time and frequency comparisons shown in this study.

### CAMPAIGN'S SETTING

Three European laboratories were involved in two comparison campaigns: the first measured time and frequency differences between clocks located at the OFMET and NPL. For the second, the comparison took place between PTB and NPL. The length of the baseline is about 750 km in both cases. The first campaign was carried out during 47 days (MJD 50686-50733) and the second during more than 120 days (MJD 50751-50873).

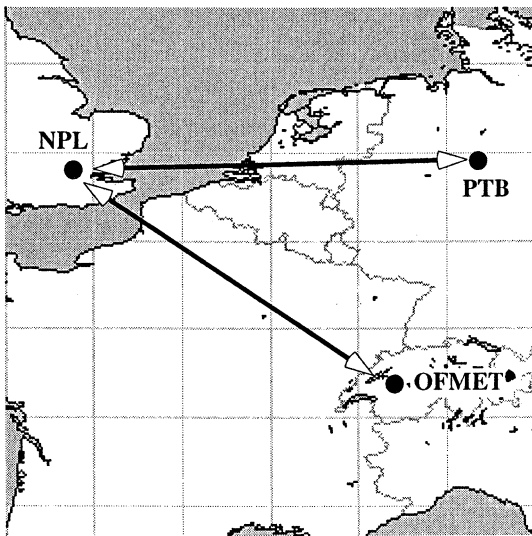


Figure 3: Localisation of European laboratories involved in both campaigns

At OFMET there are a set of 7 commercial cesium clocks. The GeTT terminal and the CV GPS receiver (AOA TTR5A) were steered by the same HP 5071A clock named ACs#1 in this study.

At NPL there are two active H masers (SIGMA TAU) named BH1 and BH2 in this study. The CV GPS receiver (AOA TTR5A), the TWSTFT earth station and the GeTT terminal were in general steered by the same maser used to produce UTC(NPL). On MJD 50759 the clock used at NPL was swapped from maser BH1 to maser BH2. On MJD 50865 the maser steering the GeTT terminal was swapped back to BH1. NPL has also purchased a geodetic Ashtech Z-XII GPS receiver. This receiver, steered by the same clock that controls the GeTT terminal offers an additional possibility of comparison. On the TWSTFT side, a new SATRE modem was in use for which no experience has been acquired before this study. The TWSTFT earth station at NPL has not been optimised.

At PTB there are two active H masers (SIGMA TAU) but the UTC(PTB) is derived from their primary cesium clock #2 (named ACs in this study). The CV GPS receiver (Rockwell Collins) and the TWSTFT earth

station are steered by the primary cesium clock while the GeTT terminal was connected to the maser named AH1 in this study. To be able to compare results obtained by GeTT to CV or TWSTFT results, a local comparison of AH1 against the primary cesium ACs was done once an hour. The TWSTFT earth station at PTB is equipped with a MITREX modem.

The TWSTFT equipment at PTB and NPL is described in more details in [5].

All CV GPS measurements were made according to the BIPM schedule.

### OFMET-NPL COMPARISON

Figure 4 shows the residuals ( $\Delta t$  minus a linear drift of 17 ns/day) of the GeTT comparisons between OFMET-NPL as derived from the P3 and L3 observations. The whole period of the campaign is represented in the top Figure while the bottom one is a detailed plot over one day. One notes the small noise of the phase observations (solid line). The much noisier code observations (open circles) were only used to determine the initial phase ambiguity.

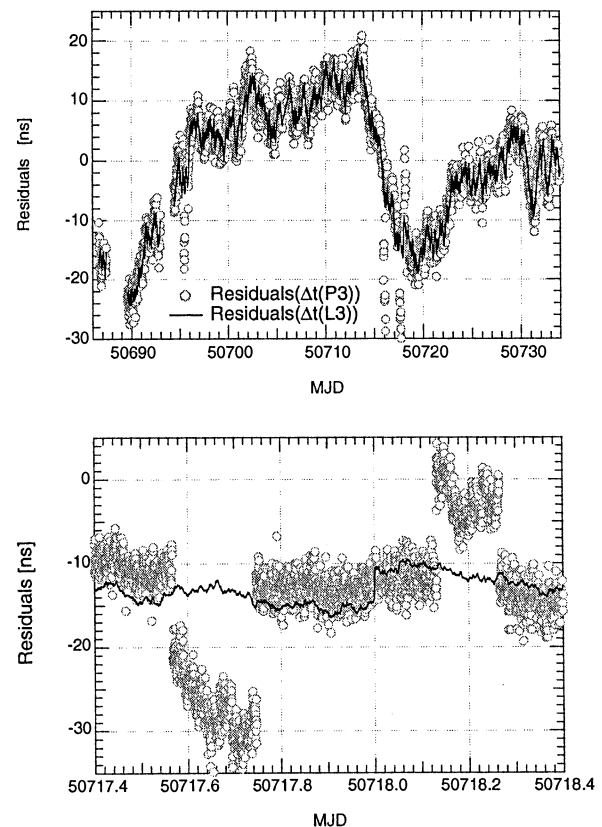


Figure 4: Residuals ( $\Delta t$  minus linear drift of 17 ns/day) of the GeTT measurements between a cesium clock (OFMET) and a H-maser (NPL). Open circles denote P3 residuals, L3 residuals are shown by solid lines.

A step of a few nanoseconds appears clearly for P3 results and disappears abruptly after a few hours. The origin of such steps which occurred only 4 times during

the campaign is not fully understood yet. Even if the phase L3 measurements do not show such steps, the time comparison obtained from L3 is also distorted by the misbehaviour of P3. One can indeed observe a small step in L3 results at the day's transition. As we previously explained, the shift between phase and code results was computed and removed. A new value of the shift is generally computed each day. As a consequence of the steps in the P3 results, the value of the shift is overestimated on MJD 50717 while it is underestimated on MJD 50718. The day's transition step visible on the L3 results shown on Figure 4 is thus resulting from the steps in the P3 results. A better estimate of the shifts and consequently an improved continuity of the L3 results at day boundaries can easily be achieved by screening the P3 data for this kind of "outliers".

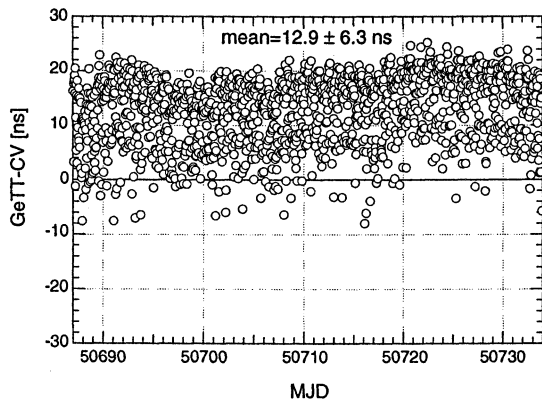


Figure 5: Comparison of the GeTT method to the CV method between the OFMET and the NPL.

The CV comparison of the ACs#1 at OFMET and BH1 at NPL was also carried out during the campaign. Figure 5 shows the difference between the results obtained by GeTT and by CV. Even if the scattering of the data is larger than one can expect from the CV, it is entirely due to this method. The problem was that the coordinates of the antenna of the CV receiver at NPL were not optimised. The difference seems to be relatively stable within the CV precision during all the campaign with a mean value of about 13 ns. This offset can be attributed to two reasons at least: firstly, the CV link between OFMET and NPL has not been calibrated yet. Secondly, an error in the antenna position of the CV receiver at NPL could also induce an offset in the CV measurement.

Figure 6 shows the square root of the Allan variance ( $\sigma_y$ ) of the measurements. An estimate of the Allan variance of the ACs#1 alone has been computed using a linear combination of the comparison of the ACs#1 against a set of six cesium clocks collocated at OFMET. For the GeTT measurement, the Allan variance was directly computed from the L3 residuals over a period of 19 days (MJD: 50696-50715).

$\sigma_y[\text{ACs\#1-BH1}]$  computed from the GeTT(L3) measurements is in excellent agreement (for  $\tau < 2-3$  days) with the estimate for ACs#1 alone. Firstly, this means that the noise of the comparison is entirely dominated by the noise of the ACs#1 as expected for a short integration time. Secondly, these results show that, over

a baseline of 750 km, the GeTT method has a lower instrumental noise than commercial, high-performance cesium clocks. This implies that GeTT is well suited for comparisons of these kind of clocks.

For  $\tau > 3$  days, one observes an apparent discrepancy between the two Allan variances shown in Figure 6: the comparison appears to be better than the performance of ACs#1 alone ! Three reasons might explain this difference:

- The data used in the calculation were not taken over the same period for both curves. Therefore, a change in the behaviour of the clock can not be excluded.
- The method used to estimate  $\sigma_y[\text{ACs\#1}]$  (linear combination of different clock comparisons) could introduce some error.
- Another unknown parameter is the long-term noise of the phase comparator used in the local comparison of cesium clocks at OFMET. For example the effect of the variation of the room temperature.

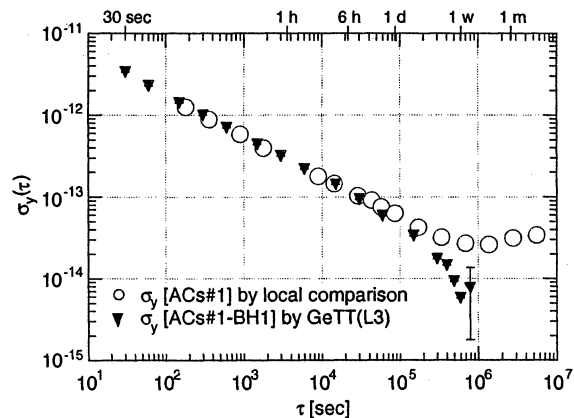


Figure 6: Square root of the Allan variance computed for the ACs#1-BH1 comparison (filled triangles) and for ACs#1 alone (open circles).

## PTB-NPL COMPARISON

The campaign between NPL and PTB can be divided into three periods: For a first set of data the GeTT terminal located at NPL was steered by the maser BH1 (MJD 50751 to MJD 50759), for a second set BH2 was used (MJD 50759 to MJD 50865) and finally, BH1 was again connected to the terminal (after MJD 50865). Figure 7 shows typical results obtained with the carrier phase for each of these periods. For clarity a linear drift has been removed from the comparison NPL-PTB. Whereas the comparison PTB - BH1 at the beginning and the end of the campaign behaves as expected, a modulation is clearly visible over the period when maser BH2 was steering the GeTT terminal. This modulation has a amplitude of 50 ps and a period of 724 s. Different tests have shown that a misbehaviour of the GeTT terminals and the PTB maser can be ruled out and the oscillation must originate from the maser BH2 steering the GeTT terminal at NPL.

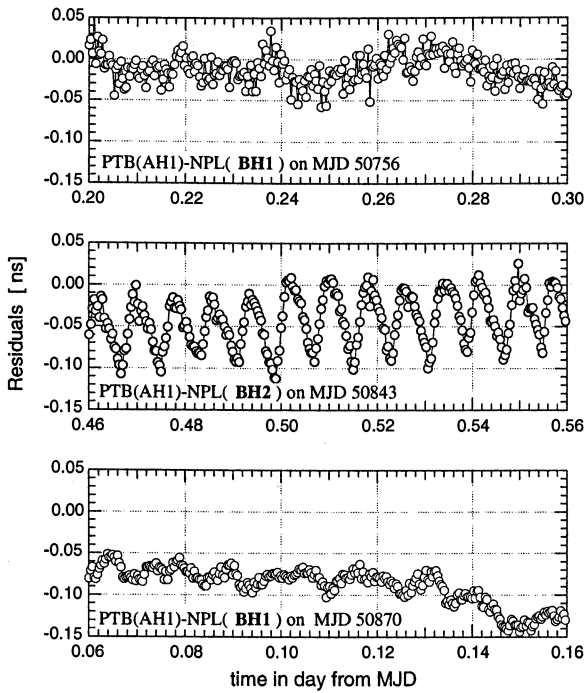


Figure 7: GeTT(L3) comparison of the PTB maser (AH1) to the NPL masers BH1 (on the top and bottom) and BH2 (in the middle).

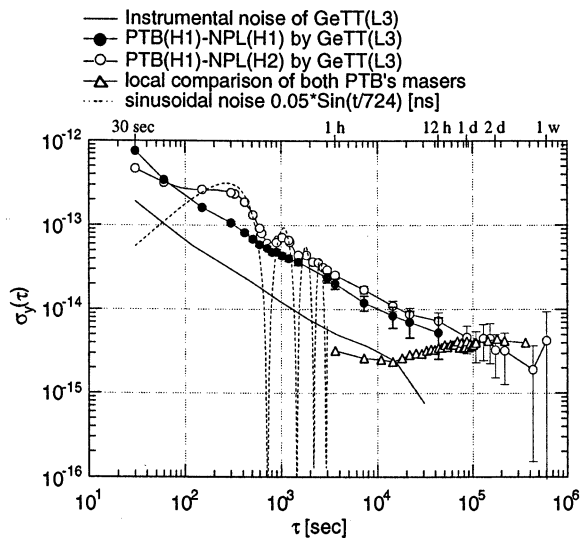


Figure 8: Square root of the Allan variance computed for the GeTT(L3) comparison PTB(AH1)-NPL(BH2) (open circles) and PTB(AH1)-NPL(BH1) (plain circles). Triangles are associated to local comparison of the two masers located at the PTB.

The influence of such a modulation on the Allan variance can be seen in Figure 7. The open circles indicate  $\sigma_y(\tau)$  of the comparison PTB(AH1)-NPL(BH2) while the plain circles are associated to the PTB(AH1)-NPL(BH1) comparison. The dashed line shows the Allan variance of a sine wave with an amplitude of 50 ps and a period of 724 s (i.e. corresponding to the detected

noise). The solid line indicates the level of instrumental noise of the GeTT method. This curve has been obtained by steering two GeTT terminals with the same local clock. The triangles, finally, show the Allan variance of the local comparison of the masers in use at PTB. From this Figure, it is clearly visible that the GeTT method is not used at its full potential but is limited by the modulation of one of the steering clocks. The instrumental noise, estimated over a zero-baseline (5 meters), is almost a factor of ten lower than the figures computed from the comparison between NPL(BH2) and PTB(AH1).

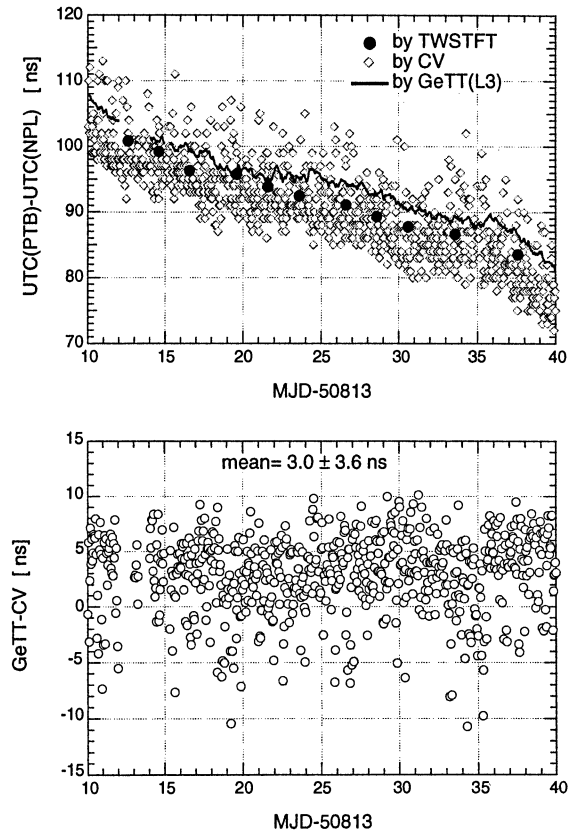


Figure 8: Top: comparison of time scale between PTB and NPL by means of CV (diamonds), TWSTFT (circles) and GeTT(L3) (plain line). Bottom: difference between the GeTT method and the CV method.

A comparison of the time scales by means of CV (diamonds), TWSTFT (circles) and GeTT(L3) (solid line) is shown in Figure 8 (top). As explained above, the GeTT terminal at PTB and UTC(PTB) were not controlled by the same clock. An hourly local comparison allows nevertheless to compare UTC(PTB) by means of GeTT to another time scale at this repetition rate. A direct comparison of CV and GeTT(L3) is presented over the same period (bottom). Although an unknown offset has to be adjusted daily (due to the phase ambiguity), the difference between the two methods remains stable over the 30 days shown on this graph. As for Figure 5 the scattering of the difference can be attributed to the noise of the CV measurement. As the coordinates of the antenna of the CV receiver at NPL have been optimised between the

two campaigns, the scatter was reduced from 6.3 ns (Figure 5) to 3.6 ns. As the CV link between PTB-NPL has recently been calibrated, the difference between both methods should be close to zero. The mean value of 3.0 ns is slightly larger than expected for a period of 30 days. However, one has to keep in mind that the CV receiver and the GeTT terminal were not steered by the same clock at the PTB. The intermediate comparison between ACs and AH1 could also introduce some systematic offset into the GeTT-CV difference.

## CONCLUSIONS

One can draw two types of conclusions: the first concerning the time comparison and the second regarding the frequency comparison.

- 1) In terms of precision the GeTT method outperforms the classical CV by at least one order of magnitude. For both campaigns the difference between these two methods (GeTT-CV) is stable, within the noise of the CV, over more than 30 days. GeTT-CV is relatively close to 0 (3.1 ns) when a calibrated CV comparison is used. Thus, the calibration constant  $D_{A,B}^0$  measured over a zero-baseline remains stable when the setting is changed and the length of the baseline increased. A more detailed analysis of the TWSTFT results obtained during the PTB-NPL campaign will give us more information about the performance of the GeTT method.
- 2) The experiment has shown that the instrumental noise of the GeTT technique over a 750 km baseline and time intervals of 10 days is lower than the noise of commercial, high performance cesium clocks. The GeTT method is well suited to detect a misbehaviour of a H-maser because a small variation of few 10 ps over few 100 sec can easily be detected. When two good masers are connected to the GeTT terminals we could expect the instrumental noise of the GeTT method to become smaller than the clock noise for  $\tau > 6$  hours. GeTT is a most promising method to compare the new generation of atomic frequency standards over long baselines

The next steps evaluating the GeTT method will be to investigate the longer time stability (1 year and more), and to try a transatlantic GeTT comparison.

## REFERENCES

- [1] N. Ashby, M. Weiss, "Accurate time transfer during common-view of a GPS satellite", Proc. 34th Ann. Symp. on Frequency Control, pp. 334-346, 1980.
- [2] D. Kirchner, "Two-Way Time Transfer Via Communication Satellites", in Proc. IEEE, Vol. 79, No 7, pp. 983-989, 1991
- [3] Th. Schildknecht, G. Beutler, W. Gurtner, M. Rothacher, "Towards sub-nanosecond GPS Time Transfer using Geodetic Processing Technique", Proc. 4th EFTE, pp. 335-346, 1990.

- [4] F. Overney, Th. Schildknecht, G. Beutler, L. Prost, U. Feller, "GPS Time Transfer Using Geodetic Receivers: Middle-Term Stability and Temperature Dependence of the Signal Delays", Proc. 11th EFTE, pp. 504-508, 1997.
- [5] J. A. Davis et al, "Two-Way Satellite Time Transfer Experiments Between Six European Laboratories Using The INTELSAT (VA-F13) Satellite", Proc. 9th EFTE, pp. 296-314, 1994.



*12th E F T F* - 10-12 March 1998 - **Warsaw - POLAND**

**Resonators II (Whispering Gallery Modes)**

Chairman: *Raymond J. Besson*



## NEW FREQUENCY-TEMPERATURE COMPENSATION TECHNIQUES FOR HIGH-Q SAPPHIRE RESONATORS

\* M.E. Tobar, \* J.G. Hartnett, \* A.G. Mann, † J. Krupka and \* E.N. Ivanov.

\* The University of Western Australia, Nedlands 6907, WA Australia

† Institute of Microelectronics and Optoelectronics, Department of Electronics, Warsaw University of Technology, Koszykowa 75, 00-662 Warsaw Poland.

**Abstract** - New electromagnetic techniques to compensate the frequency-temperature dependence of high-Q sapphire resonators above liquid helium temperature have been investigated. These techniques have involved various applications of the titanium atom. The doping of  $Ti^{3+}$  and  $Ti^{4+}$  ions into the sapphire lattice was investigated. In the  $Ti^{3+}$  doped sample compensation points were measured to be in the range 27-77 K with Q values of order a million. The  $Ti^{4+}$  doped sample compensation points were measured below 40 K with Q values of order ten million. The mechanism behind the compensation is likely due to paramagnetic effects from the  $Ti^{3+}$  ions. Another technique investigated was dielectric compensation, achieved by constructing a composite resonator from monocrystalline sapphire and rutile ( $TiO_2$ ). Compensation was achieved in different modes from 50 to 150 K, with Q-values varying from 5 million to 0.3 million respectively.

These methods give the possibility of building frequency stable fly-wheel oscillators with a frequency instability of  $10^{-14}$  without the necessity of cooling to liquid helium temperatures.

## INTRODUCTION

Various methods to compensate the frequency-temperature dependence of a high-Q sapphire resonator near 77 K have been described previously. A mechanical compensation technique by Santiago et. al. [1], at 87 K, was developed. They constructed a resonator using two closely spaced identical cylindrical sapphire disks. The thermal expansion of the copper post causes a widening of the gap between the disks which modulates the mode frequency with opposite temperature dependence to the permittivity. However vibration sensitivity in this design can be problematic.

Recently, dielectric techniques have also been investigated. This technique has been investigated by Klein et. al. [2], Gallop et. al [3] and Tobar et al. [4-7]. The technique uses a low-loss dielectric material of opposite frequency-temperature dependence to sapphire to create a turning point in the frequency-temperature characteristic of the composite resonator. This technique also requires separate pieces to be held together rigidly and problems can occur because of mechanical stability and thermal impedance between the separate structures. The modes with highest Q-values have come from resonators designed to operate on

whispering gallery modes [6, 7] rather than low-order modes in HTS enclosures [2, 3, 8].

At liquid helium (He) temperature the residual paramagnetic impurities in commercially produced sapphire (~ few ppm concentration) have provided temperature compensation of the mode frequencies in the range 5 to 13K. Mann et al. [9] have used  $Cr^{3+}$  impurities, while Luiten et. al. [10] have used  $Mo^{3+}$  and  $Ti^{3+}$  impurities. It has been determined that the Van Vleck paramagnetic susceptibilities explain the mode frequency-temperature dependence.

In the work presented in this paper we focus on techniques to frequency-temperature compensate resonators near 77 K using the titanium atom. We investigated three possible methods; 1. paramagnetic susceptibility effects of excess  $Ti^{3+}$  ions doped into the sapphire lattice [11]; 2. dielectric effects of  $TiO_2/Al_2O_3$  composite structures, and; 3. the doping of  $Ti^{4+}$  into the sapphire monocrystal to form  $TiO_2$  dielectric pockets within the sapphire lattice.

## $Ti^{3+}$ DOPED SAPPHIRE

Two bulk-doped laser-quality  $Ti^{3+}$  HEMEX sapphire samples of 25 mm diameter and 20 mm height were manufactured by Crystal Systems with 0.03-0.1% doping by weight. One sample was kept as made, while the other went through a conversion process to transform the majority of the  $Ti^{3+}$  ions to  $Ti^{4+}$ . The colouring of the 3+ sample was bright pink, while the 4+ sample appeared transparent with a slight pinkish tinge due to a slight fraction of unconverted 3+ ions. In this section we report on results obtained from the 3+ doped sample, the 4+ sample is described in detail later.

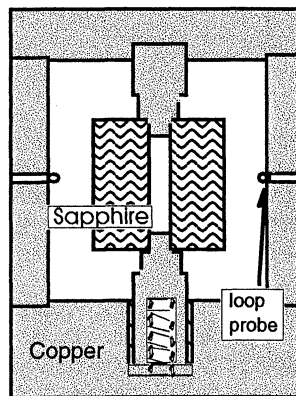


Figure 1: Schematic of the  $Ti^{3+}$  doped sapphire loaded copper cavity.

The fixture was mounted in a vacuum can inside a cryogenic dewar. Platinum and carbon glass thermometers were used to read out the temperature depending on the temperature range. Measurements down to 50 K were done in a liquid nitrogen environment, temperatures below 77 K were obtained by pumping on the cryogenic fluid. To make measurements down to 4 K liquid helium was used.

Mode frequencies of the resonator were measured between 8 to 20 GHz. They were excited by loop probes as shown in figure 1. The resonator was analysed in transmission with small values of coupling of less than 0.01 on both ports. A stable swept frequency was created by mixing a 8673H HP synthesiser with a 8662A HP synthesiser as shown in figure 2. This technique was appropriate when measuring from 8 to 13 GHz, to measure higher frequencies we made use of a microwave active doubler in the circuit. When measuring a resonance either the upper or the lower side band was transmitted while the other was filtered by a YIG filter. To determine which sideband was measured a microwave frequency counter was used to read out the frequency. The resonant frequencies were determined by the maximum frequency of transmission, and the loaded Q-factor was determined by measuring the half power bandwidth. Because of the low cavity coupling we assumed the loaded Q-factor was equal to the unloaded Q-factor. An automated measurement system was used that read directly the resonance curve from the detector. A curve fit to the resonance was implemented to calculate the frequency and Q-factor. Details of this technique can be found in Luiten et. al. [12].

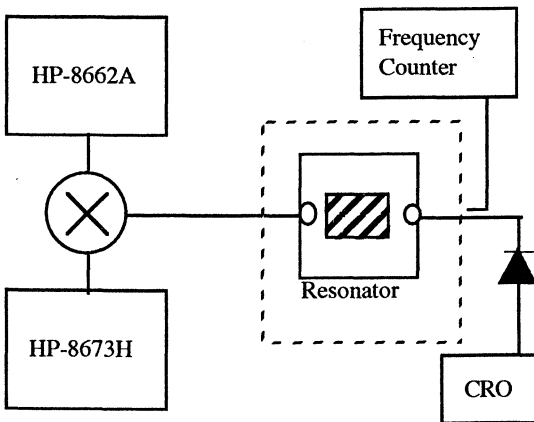


Figure 2: A stable swept frequency source from 2-13 GHz was created by mixing the 8662A synthesiser with a 8673H synthesiser. To obtain swept frequencies between 13 and 20 GHz an active frequency doubler was implemented. The resonators were measured in transmission with low coupling on the input ports.

In general all the measured modes were hybrid modes and had both an axial electric field dependence and an axial magnetic field dependence. It is common to denote a mode with a dominant axial electric field dependence as an E-mode (quasi TM) and a dominant magnetic field dependence as a H-mode (quasi TE). Because all modes are hybrid,

we adopt the N-S notation where N refers to an antisymmetric magnetic field (symmetric electric field) along the z axis of the resonator, and S refers to a symmetric magnetic field (antisymmetric electric field) [13].

We observed temperature compensation (turning points) in all modes. Figure 3 illustrates the observed frequency-temperature dependencies. The maximum turning point of 74-76 K was found in quasi-TE modes, while the minimum of 28 K was found in quasi-TM modes. Hybrid modes that exhibit both TE and TM components fall in between.

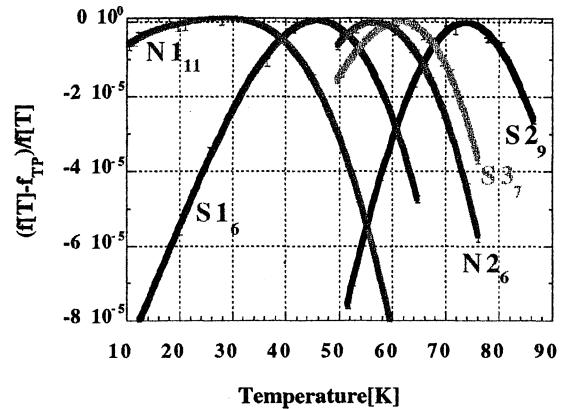


Figure 3: Frequency-temperature dependence of various modes in the  $Ti^{3+}$  doped sapphire resonator. Here,  $f(T)$  is the absolute frequency shift and  $f_{TP}$  is the turning point frequency.  $N1_{11}$ : Quasi-TM at 16.49 GHz with turning point at 29 K.  $S1_6$ : Quasi-TM at 10.99 GHz with turning point at 43 K.  $N2_6$ : Hybrid at 12.24 GHz with turning point at 53 K.  $S3_7$ : Hybrid at 14.78 GHz with turning point at 61 K.  $S2_9$ : Quasi-TE at 16.63 GHz with turning point at 76 K.

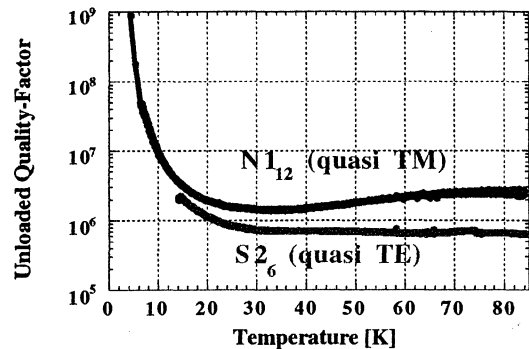


Figure 4: Unloaded quality-factor versus temperature.  $N1_{12}$ : Quasi TM mode.  $S2_6$ : Quasi TE mode.

Q-factors in the  $Ti^{3+}$  doped sapphire are generally around a million, an order of magnitude less than pure sapphire at 77 K. On cooling below 10 K the Q factor increases rapidly, reaching  $2 \times 10^9$  at 4.2 K in a quasi TM mode, but only  $4 \times 10^7$  in a quasi TE mode. Further investigation is warranted to understand the physics of these observations.

## TiO<sub>2</sub>-SAPPHIRE COMPOSITE RESONATORS

Two 2 cm thick rutile slices were polished down to 0.21 mm thickness. A cavity holding these slices to the ends of a 24.9 mm diameter sapphire crystal, was constructed as shown in figure 5.

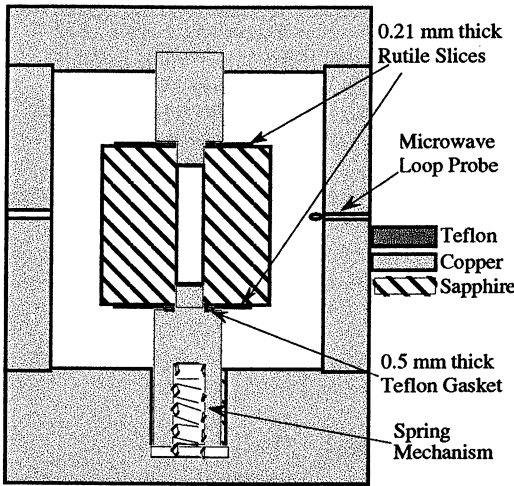


Figure 5: Sapphire-rutile composite resonator. The sapphire crystal is 23.6 mm high by 24.9 mm wide with two 0.2 mm thick by 20 mm wide rutile crystals held tightly to the top and bottom of the sapphire crystal with a spring mechanism

To measure the properties of the composite resonator in figure 5, the same configuration as shown in figure 2 was set up. The frequency and Q-factor as a function of temperature was measured for a variety of modes from 300 K to 50 K. Rutile has an opposite temperature coefficient of permittivity to sapphire, so the annulment in frequency comes from the two effects becoming opposite and equal. Details of how this is achieved have been published recently[5, 7].

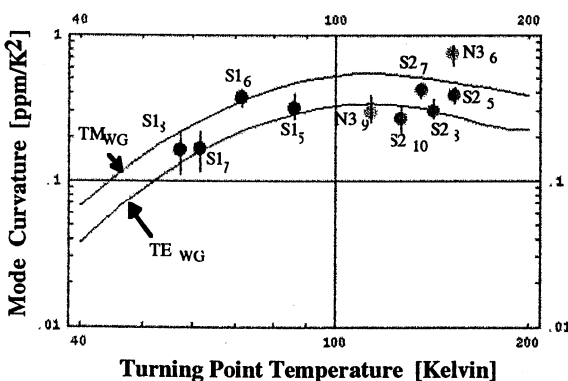


Figure 6: Curvature of the frequency-temperature turning point of the sapphire/rutile resonator at the turning point temperature. The upper curve is the predicted curvature for E-modes that depend on the permittivity parallel to the c-axis, and the lower curve is the predicted curvature for H-modes that depend on the permittivity perpendicular to the c-axis. The points are the experimentally measured mode curvature at the turning point temperature for a variety of WG modes.

The frequency-temperature characteristics of the resonator modes agree very well with what was

expected. This is evident from figure 6. However, the Q-values are smaller than what can potentially be achieved in such a resonator. The S1 ( $E_{m 1 1+\delta}$ ) is significantly less than the potential Q-value given by the  $Q_{TM}$  curve of figure 7. The N3<sub>6</sub> ( $H_{6 1 1+\delta}$ ) mode is also below the  $Q_{TE}$  curve but not as significantly as the E-modes.

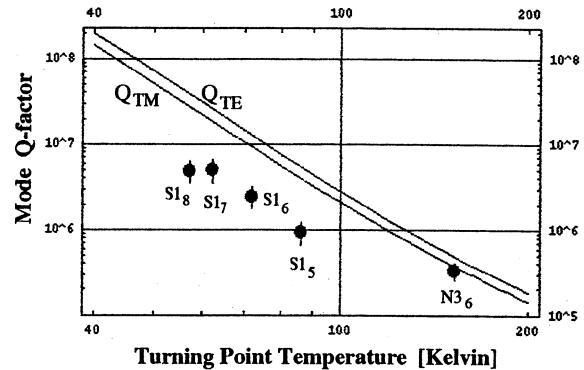


Figure 7: Effective Q-factor given for a compensated sapphire/rutile resonator operating at a specific temperature[7]. The upper curve considers the perpendicular components of the loss tangent while the lower curve considers the parallel components. The points show experimentally determined Q-values at the turning point temperatures for some of the WG modes.

An estimation of the quality factor due to the limit imposed by the dielectric loss tangents ( $\tan\delta$ ) can be determined by[5, 7];

$$Q^{-1} = p_{e \text{ rutile}} \tan \delta_{\text{rutile}} + p_{e \text{ sapphire}} \tan \delta_{\text{sapphire}} \quad (1)$$

$$\approx \frac{p_{e \text{ r/l/s}} \tan \delta_{\text{rutile}}}{1 + p_{e \text{ r/l/s}}} + \frac{\tan \delta_{\text{sapphire}}}{1 + p_{e \text{ r/l/s}}}$$

where,

$$p_{e \text{ r/l/s}} = \frac{p_{e \text{ rutile}}}{p_{e \text{ sapphire}}} = - \frac{\alpha_{\epsilon \text{ sapphire}}^{TP}}{\alpha_{\epsilon \text{ rutile}}^{TP}} \quad (2)$$

Here  $\alpha_{\epsilon \text{ sapphire}}^{TP}$  is the effective temperature coefficient of permittivity (TCP) for sapphire at the turning point temperature and  $\alpha_{\epsilon \text{ rutile}}^{TP}$  is the effective TCP for rutile at the turning point temperature, and  $p_e$  is the electrical energy filling factor. The approximation given by (1) is true assuming the sum of the filling factors in the two dielectric materials is equal to one. This is a very good approximation for a WG mode.

Based on individual results measured for both rutile and sapphire the potential Q-values of a composite sapphire-rutile resonator are plotted in figure 7. To understand the nature of the Q degradation the resonator of figure 5 was measured without the rutile slices. It was found that there were now excess losses other than dielectric added by the rutile slices and the source of the Q degradation was internal to the sapphire cavity itself.

Mode	Temperature [K]	Q (composite resonator)	Q (sapphire only)	Q (pure TM sapphire)	Q (calculated)
S1 <sub>8</sub>	52	5.2×10 <sup>6</sup>	6.8×10 <sup>6</sup>	2.7×10 <sup>8</sup>	5.8×10 <sup>6</sup>
	77	3.8×10 <sup>6</sup>	6.6×10 <sup>6</sup>	5.2×10 <sup>7</sup>	4.8×10 <sup>6</sup>
S1 <sub>6</sub>	52	3.3×10 <sup>6</sup>	4×10 <sup>6</sup>	2.7×10 <sup>8</sup>	3.4×10 <sup>6</sup>
	77	2.3×10 <sup>6</sup>	3.3×10 <sup>6</sup>	5.2×10 <sup>7</sup>	2.4×10 <sup>6</sup>
S1 <sub>5</sub>	77	1.2×10 <sup>6</sup>	2.0×10 <sup>6</sup>	5.2×10 <sup>7</sup>	1.5×10 <sup>6</sup>

Table 1. Analysis of the Q degradation in the sapphire-rutile composite resonator for some selected quasi TM modes at 52 and 77 K. The resonator Q-values with and without the rutile slices are given in columns 3 and 4 respectively. The Q-values are significantly degraded to that of pure sapphire[7, 14, 15]. From data in column 3 combined with the measured properties of rutile[16], the expected Q based on equation (1) is calculated in the final column. These values are consistent to within the measurement uncertainties of the measured values in column 3.

The sources of Q degradation are probably due to:

1. The copper support is quite thick and can contribute conductor losses especially to lower azimuthal m values. This would explain the Q value increase with azimuthal mode number.

2. We have shown that some residual Ti<sup>3+</sup> paramagnetic impurities exist as the H-modes exhibit turning points around 25 K. This leads to a loss plateau in the range of 90-20 K, which could explain some of the Q-degradation.

This technique has the potential to obtain very high Q-values if larger and purer samples are implemented to eliminate conductor and paramagnetic losses.

#### Ti<sup>4+</sup> DOPED SAPPHIRE

The same fixture and measurement technique that was used for the 3+ doped sample (figure 1-2) was also used for the 4+ doped sample. Temperature compensation was observed in all modes. The maximum turning point of 33 K was found in quasi TE modes, while a minimum of 10 K was found in quasi TM modes.

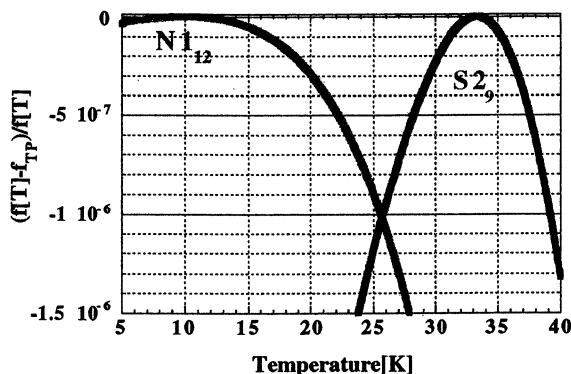


Figure 8. Frequency-temperature dependence of a quasi TM mode (N1<sub>12</sub>) and a quasi TE mode (S2<sub>9</sub>), in the Ti<sup>4+</sup> doped sapphire resonator.

Q-factors of the Ti<sup>4+</sup> doped sapphire are generally around 10 million. It is evident that the losses are still worse than in pure sapphire but are much less than in the Ti<sup>3+</sup> doped sample. However, the structures of the Q-factor curves shown in figure 9 are similar to the Ti<sup>3+</sup> sample, ie. they have a plateau like structure from 20-70 K and the Q starts to increase exponentially above 20 K. Thus, we believe

the mechanism for compensation in both resonators is the same.

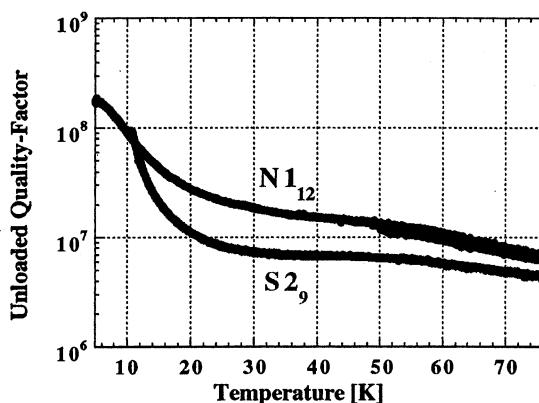


Figure 9. Unloaded quality-factor versus temperature. N1<sub>12</sub>: Quasi TM mode. S2<sub>9</sub>: Quasi TE mode.

It was thought that a dielectric effect may be measured in a Ti<sup>4+</sup> doped sample. This is because the ion will sit in the sapphire lattice like TiO<sub>2</sub>. However, the conversion process leaves a residual of Ti<sup>3+</sup> ions, and from our results presented in figure 8 and 9 it is evident that we are looking at a lesser effect due to the smaller concentration of Ti<sup>3+</sup> ions with the Ti<sup>4+</sup> ions remaining neutral. The mechanism is paramagnetic, the details are too long to describe in this paper and will be published elsewhere.

#### DISCUSSION

In general in all the techniques investigated, the lower the temperature of a mode compensation (turning point), the more shallow the mode curvature. Figure 10 shows a comparison in mode curvature as a function of the turning point (compensation) temperature. This fact is also true for the composite resonator (see figure 6). Above 40 K all techniques exhibit curvatures from 0.1 ppm/K<sup>2</sup> to a few by 0.1 ppm/K<sup>2</sup>. Below 40 K the curvatures reduce dramatically, as shown in figure 10.

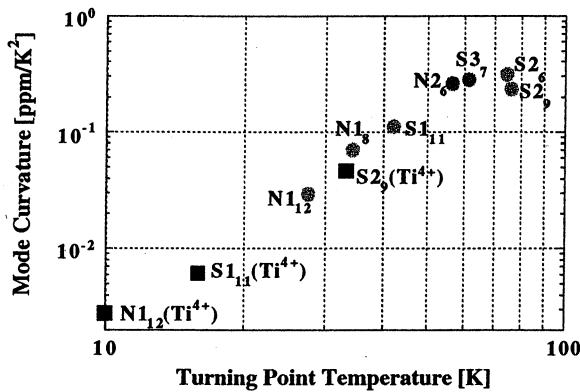


Figure 10. Measured mode curvatures of some frequency-temperature turning points of the  $Ti^{3+}$  and  $Ti^{4+}$  doped sapphire resonators.

Also, in general the lower the temperature the higher the Q-factor. The exception is in the  $Ti^{3+}$  doped sample where a slight increase in loss due to paramagnetic effects can exist around 70-40 K. Thus, if the resonator is temperature controlled to operate on a compensation point, one can expect better performance the lower the temperature. To free oneself from the burden of liquid helium a closed cycle or liquid nitrogen system can be considered.

The advantage of the  $Ti^{3+}$  method is that compensation may be achieved in one monolithic sapphire structure. This adds simplicity to the resonator design and eliminates time constants and vibration problems between a design made of more than one structure. We have shown that at temperatures as high as 77 K the technique still works. The disadvantage is an order of magnitude reduction in Q-factor due to the losses introduced by the paramagnetic ions. Reducing the concentration of the ions reduces this effect but also reduces the temperature of the compensation points.

The advantage of the composite rutile-sapphire resonator is that very high Q-factors close to the intrinsic performance of sapphire can be achieved. Results presented in this paper showed degraded Q-factors of order of a few million between 80-50 K. We showed that this could be eliminated by using a larger sample of pure sapphire to eliminate residual paramagnetic and conductor losses.

## REFERENCES

1. Santiago D, Dick G, and Wang R, 1996, "Frequency stability of  $10^{-13}$  in a compensated sapphire oscillator operating above 77 K", *Proc. IEEE Int. Freq. Cont. Symp.*, 772-775
2. Klein N, Scholen A, Tellmann N, Zuccaro C, and Urban K, 1996, "Properties and applications of HTS-shielded dielectric resonators: a state-of-the-art-report", *IEEE Trans. on MTT*, 44, 1369-73
3. Gallop J, Hao L, Abbas F, and Langham C, 1997, "Frequency stability of dielectric loaded HTS microwave resonators", *IEE Appl. Supercon.*, 7, 122-125

4. Tobar M, Krupka J, Woode R, Ivanov E, 1996, "Dielectric frequency-temperature compensation of high quality sapphire dielectric resonators", *Proc. IEEE Int. Freq. Cont. Symp.*, 799-806
5. Tobar M, Krupka J, Ivanov E, and Woode R, 1997, "Dielectric frequency-temperature-compensated microwave whispering-gallery-mode resonators", *J. Phys. D: Appl. Phys.*, 30, 2770-2775
6. Tobar M, Krupka J, Hartnett J, Ivanov E and Woode R, 1997, "Sapphire-rutile frequency-temperature compensated whispering gallery microwave resonators," *Proc. IEEE Int. Freq. Cont. Symp.*, 1000-8
7. Tobar M, Krupka J, Hartnett J, Ivanov E, and Woode R, 1998, High-Q sapphire-rutile frequency-temperature compensated microwave dielectric resonators, *IEEE Trans. UFFC*, 45
8. Ghosh I, Schemion D, and Klein N, 1997, "Temperature compensated high-Q dielectric resonators for long term stable low phase noise oscillators", *IEEE Int. Freq. Contr. Symp.*, 1024-9
9. Mann A, Giles A, Blair D, and Buckingham M, 1992, "Ultra-stable cryogenic sapphire dielectric microwave resonators: mode frequency-temperature compensation by residual paramagnetic impurities", *J. Phys. D: Appl. Phys.*, 25, 1105-1109
10. Luiten A, Mann A, and Blair D, 1996, "Paramagnetic susceptibility and permittivity measurements at microwave frequencies in cryogenic sapphire resonators", *J. Phys. D: Appl. Phys.*, 29, 2082-2090
11. Hartnett J, Tobar M, Mann A, Krupka J, and Ivanov E, 1998, "Temperature dependence of  $Ti^{3+}$  doped sapphire whispering gallery mode resonator", *Electron. Lett.*, 34, 195-196
12. Luiten A, Mann A, and Blair D, 1996, "High resolution measurement of the temperature-dependence of the Q, coupling and resonant frequency of a microwave resonator", *Meas. Sci. and Technol.*, 7, 949-953
13. Krupka J, Cros D, Luiten A, and Tobar M, 1996, "Design of very high-Q sapphire resonators", *IEE Electron. Lett.*, 32, 670-671
14. Krupka J, Derzakowski K, Abramowicz A, Tobar M, and Geyer R, 1997, "Complex permittivity measurements of extremely low loss dielectric materials using whispering gallery modes", *IEEE MTT Int. Micr. Sym. Digest*
15. Woode R, Tobar M, Ivanov E, and Blair D, 1996, "An ultra-low noise microwave oscillator based on a high-Q liquid nitrogen cooled sapphire resonator", *IEEE Trans. UFFC*, 43, 936-41
16. Tobar M, Krupka J, Ivanov E, and Woode R, 1998, "Anisotropic Complex Permittivity Measurements of Mono-Crystalline Rutile Between 10-300 Kelvin", *J. Appl. Phys.*, 83, 1604-9.

PHASE NOISE PERFORMANCES OF CRYOGENIC WHISPERING GALLERY MODE RESONATOR FREQUENCY REFERENCES.

O. Di Monaco, V. Giordano, J. Gros Lambert, I. Lajoie, Y. Kersalé

Laboratoire de Physique et Métrologie des Oscillateurs  
L.P.M.O- C.N.R.S.

Associé à l'Université de Franche-Comté - Besançon

32 Avenue de l'Observatoire  
-25044 Besançon Cedex - France

INTRODUCTION.

The ultra low dielectric losses of the sapphire monocrystal make it an ideal material for the realisation of high-Q microwave resonators. Nevertheless, the permittivity of the sapphire ( $\sim 9$ ) does not allow to confine efficiently the electromagnetic energy in the sapphire monocrystal if a low order resonance mode, as the  $TE_{018}$ , is used. High order hybrid resonance modes, i.e. Whispering Gallery Modes (WGM) have to be excited in order to obtain unloaded Q-factor values only limited by the intrinsic losses of the sapphire monocrystal. With such resonant modes, Q-factors of  $2 \cdot 10^5$  at room temperature and as high as  $3 \cdot 10^7$  at 77K have already been obtained [1;2;3].

In our laboratory, we develop cryogenic sapphire Whispering Gallery Mode frequency references for phase noise measurement purposes. For this applications, high Q-factor resonators could be used in a passive configuration (Frequency discriminator) or as a reference oscillator.

In this paper we present preliminary experiments demonstrating the potentialities of the two configurations.

Special design of the resonant cavity has been implemented in order to reject the spurious modes around the main resonance.

1) DESIGN OF THE CRYOGENIC SAPPHIRE RESONATOR.

Figure 1 shows the WGM sapphire resonator geometry. A sapphire disk (50 mm diameter and 20 mm thick) is centred in a cylindrical copper cavity whose dimensions are about twice the resonator's one. For this sapphire cavity, several high-Q resonance modes, corresponding to  $WG_{m,0,0}$  with  $4 < m < 12$ , can be used as a frequency reference in the band 4-10 GHz. This frequency range is sufficient today for most of our applications. The high quality sapphire disk used in this experiment is produced with the HEMEX technique by Crystal Systems company. This method provides high purity and quasi perfectly orientated monocrystals.

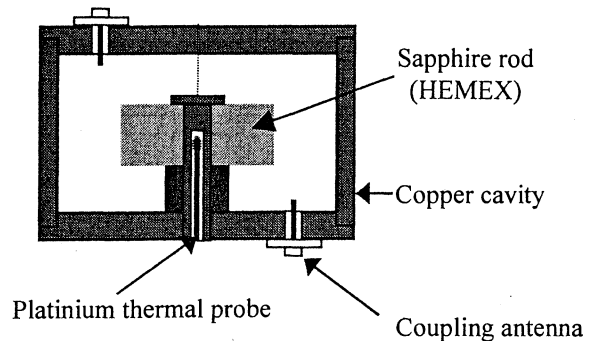


Figure 1 : Design of the Sapphire cavity.

Two electrical probes parallel to the axis of the structure allows to excite the quasi-TM modes. We have chosen to operate on quasi-TM modes (WGH) because preliminary experiments have shown that these modes are more easily excited than the quasi-TE Whispering Gallery modes (WGE).

MODE SELECTION.

We choose the  $WGH_{9,0,0}$  mode as the operational resonance. Its resonance frequency is 7.34 GHz. This mode presents a Q-factor equal to 250000 at 300K and  $30 \cdot 10^6$  at cryogenic temperature. Figure 2 shows the amplitude of the transmission coefficient of our resonator around the  $WGH_{9,0,0}$  resonance at 77K.

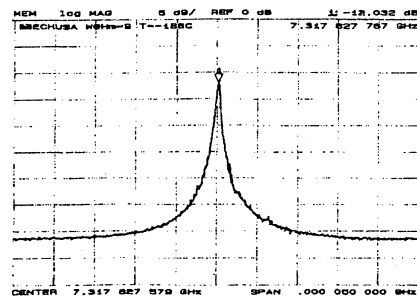


Figure 2 : Amplitude of the transmission coefficient around the  $WGH_{9,0,0}$  resonance.

However, the configuration shown in figure 1 is not suitable for an oscillator assembly. In fact, a

number of highly coupled spurious resonance exists around the operational mode. An oscillator tends naturally to lock itself on the more intense resonant mode of the resonator. So, the spurious modes have to be rejected or at least attenuated. Consequently, we have modified the resonator upper-plate, as shown in figure 3.

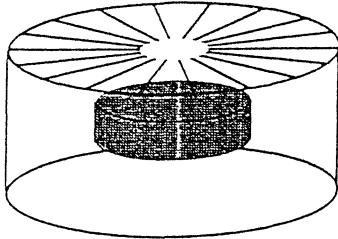


Figure 3 : Design of the modal selector for the WGH<sub>9,0,0</sub> mode.

Thin slots (0.05 mm thick) have been manufactured along the 2x9 radial directions. Their angular positions correspond to the location of the eighteen E-field minima of the WGH<sub>9,0,0</sub> mode, which is then not perturbed.

On an other hand, the spurious resonance presenting different azimuthal electromagnetic configurations are strongly affected. We observe an increase from 2 to 10 dB of the insertion losses (see table I and figure 4) for the nearest perturbing resonance, whereas the WGH<sub>9,0,0</sub> performances remain unchanged.

	Without selector			With selector		
	f0 (GHz)	I.L. (dB)	Q	I.L. (dB)	Q	Attenuation (dB)
MK1	7,08	-12,4	2230	-15,2	1500	2,8
MK2	7,18	-30,4	38000	-33,3	21000	2,9
MK3	7,29	-28	8000	-30	6100	2
MK4	7,38	-14,8	17000	-24,4	11000	9,6
MK5	7,43	-14,8		-21		6,2

Table I : Insertion losses of spurious modes with and without modal selector.

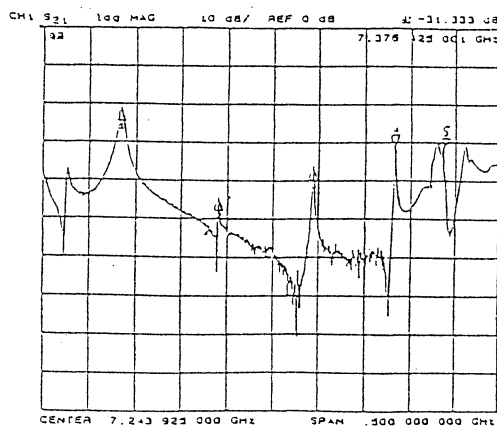


Figure 4 : Spurious resonance modes around 7.35 GHz.

This new cavity configuration associated with a 200 MHz bandwidth filter, allows to obtain a very stable oscillation on the WGH<sub>9,0,0</sub> resonance mode.  
II) PHASE NOISE MEASUREMENTS :

Sapphire WGM resonators present a large sensitivity to temperature fluctuations. This sensitivity is of an order of -10 ppm/K at cryogenic temperature. In such conditions, near carrier frequency fluctuations measurement, i. e. down to 1 kHz Fourier frequency, requires sophisticated temperature control. In order to avoid such technical difficulty, we implemented two identical cavities in the same thermal environment. The experimental set-up is described in figure 5. Two identical sapphire cavities are centred in the liquid nitrogen trap. This assembly is placed in a vacuum enclosure where a pressure lower than 10<sup>-14</sup> Torr is maintained. Moreover, to assure a good thermal link between the two cavities, they have been connected to each other by a high thermal conductor copper post. Each sapphire cavity is coupled by two HF connectors to the external circuit kept at room temperature.

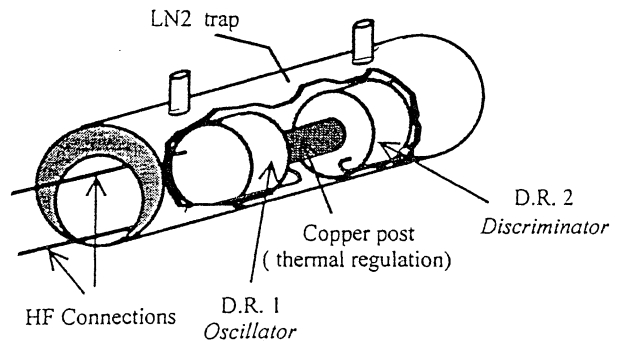


Figure 5 : Experimental apparatus for the cryogenic characterisation of the sapphire cavities.

The thermal enclosure we used is an old ammoniac maser tube available at the laboratory. The thermal contact between the liquid nitrogen bath and the sapphire cavities has not optimised.

Thus, the lowest temperature presently available is 133K. At this temperature, and for each resonator, the WGH<sub>9,0,0</sub> mode presents a loaded Q-factor of 2.6 10<sup>6</sup>.

### 1) DISCRIMINATOR PERFORMANCES

In the scheme of the figure 5, one of the cavities (R1) is mounted in a conventional transmission oscillator configuration and the second cavity (R2) is used as a FM-PM converter, to characterise the R1-oscillator.

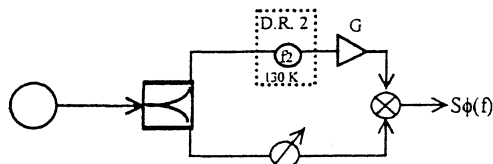
#### Sensitivity of the discriminator :

The measurement set-up is depicted in figure 6. The RF oscillator output signal is divided into two equal parts by a power splitter. In the first arm, the sapphire cavity discriminator converts the

frequency fluctuations  $\Delta\omega$  of the oscillator into phase fluctuations with a converting factory proportional to the loaded Q-factor of the cavity (figure 7):

$$\Delta\Phi = -\frac{2Q_1}{\omega_2} \Delta\omega$$

An amplifier G has been added to compensate the insertion losses of the cavity.



Oscillator under test  
(Wiltron 68 B)

Figure 6: Discriminator sensitivity measurement set-up.

In the second arm, an adjustable phase shifter allows to obtain a phase of  $\pi/2$  between the two signals at the mixer input.

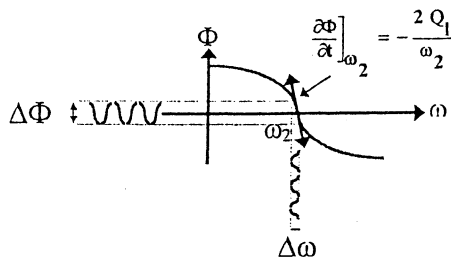


Figure 7: FM-PM sapphire cavity converter.

The mixer output can be written :

$$V_s(t) = \alpha \frac{V_0^2}{2} |S_{21}(\omega_2)| \sqrt{G} \sin\left(\frac{2Q_1}{\omega_2} \Delta f\right)$$

with:  $\alpha$  : mixer sensitivity  
 $V_0$  : oscillator output amplitude  
 $|S_{21}(\omega_2)|$  : Modulus of the transmission coefficient of the cavity at the resonance

Assuming the frequency fluctuations of the oscillator under test are low enough, the output signal is linearly dependant with the frequency variations of oscillator :

$$V_s(t) \approx K_d \Delta f$$

The sensitivity  $K_d = \alpha \frac{V_0^2}{2} |S_{21}(\omega_2)| \sqrt{G}$  can be determined experimentally by changing by  $\Delta f$  the frequency of the driver oscillator. A sensitivity value of  $2.3 \cdot 10^{-5} \text{ V Hz}^{-1}$  has been obtained.

#### Phase noise floor measurement:

To determine the discriminator phase noise floor, we replaced the R2 sapphire resonator with an

attenuator corresponding to sapphire cavity insertion losses.

The frequency fluctuations of the source are not converted into phase fluctuations and are the same in the two arms of the device. Then, they are rejected at the mixer output. The signal  $V_s$  reflects only the intrinsic phase noise of the active components, i. e. the mixer and the amplifier. The Power spectral density (PSD) of the discriminator phase noise floor can be deduced from the PSD of the output tension fluctuations by the relationship :

$$S_{\Phi}^{\text{floor}}(f) = \frac{S_{V_s}(f)}{K_d^2 f^2} = \frac{f_2}{2Q_1} \frac{1}{f^2} \left[ S_{\Phi}^{\text{ampli}}(f) + S_{\Phi}^{\text{mixer}}(f) \right]$$

Figure 8 shows the results obtained with our sapphire discriminator compared with other classical discriminators: delay line of 3 m length, multiplied SAW and RF synthesiser (see table 2). The phase noise floor improvement obtained with our device at 133K is already very clear. At 1 kHz offset, the phase noise floor is reduced to  $-135 \text{ dB rad}^2/\text{Hz}$ , that corresponds to a gain of at least 15  $\text{dB rad}^2/\text{Hz}$  compared with other classical discriminators.

Delay line	$-65 \text{ dB rad}^2/\text{Hz}$
RF Synthesiser	$-20 \text{ dB rad}^2/\text{Hz}$
SAW 50 MHz	$-15 \text{ dB rad}^2/\text{Hz}$

Table 2: Comparison of the phase noise floor of the sapphire cavity with classical discriminators.

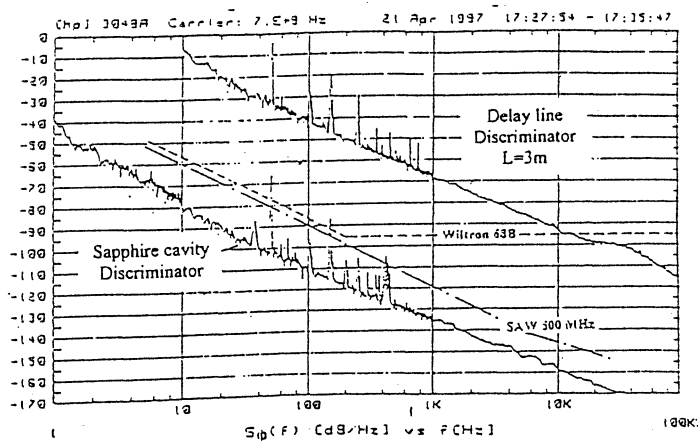


Figure 8 : Comparison of the phase noise floor of different discriminators.

#### OSCILLATOR PERFORMANCES :

The sapphire discriminator has been used to determine experimentally the phase noise performances of the cryogenic sapphire oscillator

R1. The scheme of the experimental set-up is shown in the figure 9.

The resonance frequencies of two cavities differ from 1 MHz. An external low-noise synthesiser is needed to compensate this frequency difference. At the mixer RF output, two side bands  $f_1-f_2$  and  $f_1+f_2$  are generated. By changing the IF signal frequency, it is possible to let  $f_1-f_2$  equate with  $f_2$ , frequency of the sapphire discriminator.

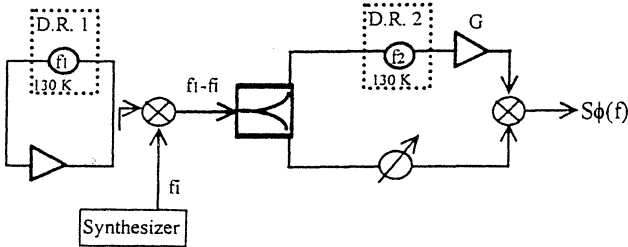


Figure 9: Experimental set-up to characterise the R1 oscillator phase noise.

The frequency fluctuations of the R1 oscillator signal are then converted in phase modulation throughout the R2 cavity. The output tension  $V_s$  expresses the frequency fluctuations of our oscillator, so that its PSD of phase noise can be deduced by :

$$S_{\phi}(f) = \frac{1}{K_d^2 f^2} S_{V_s}(f).$$

The results of the R1 oscillator PM noise measurement are shown in figure 10.

This result (-117 dB/Hz at 1 kHz offset), obtained at 133K, is already satisfactory and demonstrates the sapphire resonator potentialities.

At 77K, with a Q-factor ten times higher than the present one, an excellent phase noise should be

obtained. An value of  $S_{\phi}(f) = -137 \text{ dB rad}^2/\text{Hz}$  at 1 kHz offset is expected. This will correspond to an improvement of  $20 \text{ dB rad}^2/\text{Hz}$  compared with the presently available performances.

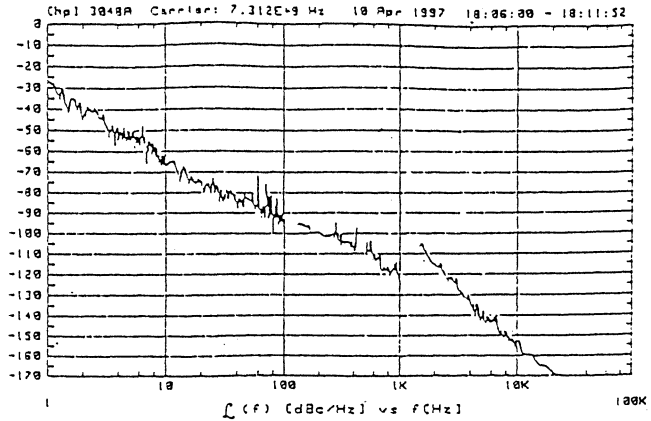


Figure 10 : Single Side Band phase noise of the sapphire oscillator versus frequency offset.

## CONCLUSION.

In this work, we have conceived two WGM sapphire resonators presenting loaded Q-factors better than  $2 \cdot 10^6$  at 7.3 GHz and at 133K. A special cavity design allowed to reject the spurious modes around the main resonance. These cavities, mounted in the same thermal environment, are used to measure the PM noise of the frequency discriminator and of the oscillator configuration simultaneously. Noise floor of  $-135 \text{ dB rad}^2/\text{Hz}$  and  $-117 \text{ dB rad}^2/\text{Hz}$  at 1 kHz offset were obtained respectively.

These results demonstrate the potential of the WGM sapphire resonators for providing ultra-low noise floor.

## Acknowledgement :

We thank the B.N.M. (Bureau National de Métrologie) for its interest and financial support.

## References:

- [1]:M.E. Tobar, A.J. Giles, S. Edwards and J.H. Searls. "High-Q thermoelectric Stabilised Sapphire Microwave Resonators for Low-Noise Applications" IEEE Transactions on Ultrasonics, Ferroelectrics and Frequency Control; Vol. 41, n°3, May 1994, pp. 391-396.
- [2]:D.G. Santiago, D.J. Dick. " Microwave frequency discriminator with a cooled sapphire resonator for ultra-low phase noise." Proceedings of the 1992 IEEE International Frequency Control Symposium, 27-29 May 1992, Hershey Penn. (US), pp. 176-182.
- [3]:O. Di Monaco, W. Daniau, I. Lajoie, Y. Gruson, M. Chaubet, V. Giordano. "Mode Selection for a Whispering Gallery Mode Resonator". Electronics Letters, 28 March 1996, Vol. 32, n° 7, pp. 669-670.

## TEMPERATURE COMPENSATED CRYOGENIC WHISPERING GALLERY MODE RESONATOR FOR MICROWAVE FREQUENCY STANDARD APPLICATIONS

L Hao<sup>+</sup>, N Klein<sup>\*</sup>, W J Radcliffe<sup>+</sup>, J C Gallop<sup>+</sup> & I S Ghosh<sup>\*</sup>

NPL<sup>+</sup>, Teddington, UK & FZ<sup>\*</sup>, Jülich, Germany

### ABSTRACT

We have investigated a miniature composite dielectric resonator employing a sapphire puck and a single crystalline platelet of rutile, excited in a whispering gallery mode. At the time of writing we have achieved values of the Allan variance as low as  $4 \times 10^{-12}$  for an integration time of 1000 seconds with the first prototype system.

### INTRODUCTION

There is a rapidly increasing demand for improved compact stable frequency standards, driven by the needs of the telecommunications industry, global navigation (GPS, GLONASS and their successors), military requirements and basic science. The Cs atomic clock and the H maser, first developed 40 years ago, remain the best clocks available but these are no longer confined to standards laboratories and are increasingly found in broadcast stations, digital telephone exchanges, satellites for navigation and power distribution networks. As a result of this widespread increase in use of state-of-the-art frequency standards it is clear that simpler and better clocks and frequency standards are now required.

Atomic clocks have relatively poor short term signal to noise because inter-atomic interactions perturb the transition frequency and require that the atom density be kept very low. However, unlike atoms, photons do not interact with one another so that a cavity resonator can contain a very high density of photons without any degradation of stability and with a resulting large improvement in signal to noise. The high Q and excellent short-term stability achievable with cryogenic resonators complements the good, intrinsic atomic stability of Cs clocks or H masers.

### HIGH Q RESONATORS AS FREQUENCY STANDARDS

The frequency discrimination function of a resonator depends on its Quality Factor (Q value). It is possible

in practice to divide the resonance linewidth with an accuracy of  $\sim 1$  in  $10^6$ . Thus the frequency resolution  $\delta f$  is limited to:

$$\delta f / f \sim 10^{-6} / Q$$

With superconducting cavity resonators Q values as high as  $10^{11}$  have been achieved using the conventional low temperature superconductor niobium ( $T_c \sim 9.2$  K) so that  $\delta f/f$  levels as low as  $1$  in  $10^{17}$  are possible in principle. But resonator *stability* is currently a bigger challenge than achieving the highest Q. The main contributions to frequency instability arise from thermal expansion due to temperature changes, variation of conductor skin depth with temperature and mechanical instability from shocks or changing thermal gradients. At 4.2 K the thermal expansion coefficient of niobium is  $10^{-8}/K$  so that an unachievable temperature stability of  $1 \mu K$  is required for the relatively modest  $\delta f/f \sim 10^{-14}$ . At 4.2 K small tilts by  $\sim$  seconds of arc cause the resonator to distort under its own weight to give fractional frequency shifts  $\delta f/f \sim 10^{-14}$ . Single crystal dielectric materials such as sapphire ( $Al_2O_3$ ) are much stronger than niobium at cryogenic temperatures and also exhibit remarkably low microwave losses so that although the Q values attained with dielectric resonators are not yet as high as those for superconducting cavity resonators they exhibit the potential for much improved long term stability.

### IMPLEMENTATION OF COMPOSITE PUCK OSCILLATOR

Excellent performance of superconducting shielded dielectric resonators cooled with liquid helium has already been reported by a number of groups (see for example [1]). However the use of liquid helium is expensive, time consuming and adds complexity to the operation. There has been much development recently of closed cycle coolers operating in the range 40 K to 100 K where the loss tangent is already below  $10^{-6}$  [2]. The major problem for sapphire resonators in this temperature range arises from its relatively large temperature coefficient of permittivity. Below we describe progress made in compensating this unwanted temperature coefficient by the use of composite dielectric pucks consisting

of two different dielectric components, both having low loss.

Whispering gallery modes in general provide strong confinement of the electromagnetic field and therefore the resonator unloaded quality factor  $Q_0$  is nearly unaffected by ohmic losses due to the normal metal shielding cavity in use. For sapphire at  $T < 70\text{K}$  the dielectric losses at microwave frequencies are fairly low, corresponding to values of the loss tangent  $\tan\delta$  below  $10^{-7}$ . Single crystal rutile ( $\text{TiO}_2$ ) provides low losses as well, but in contrast to sapphire has a negative temperature coefficient of the permittivity  $\epsilon_r(T)$  ( $\partial\epsilon_r(T)/\partial T < 0$ ) [3], resulting in a potential frequency versus temperature compensation point for a composite dielectric resonator made from an appropriate combination of these two materials [4]. Fig 1. shows the calculated  $f(T)$  of a sapphire - rutile composite resonator using fits to literature data of  $\epsilon_r(T)$ . The quantity  $\kappa$  is the fraction of electromagnetic field energy stored in rutile. Fig. 1 shows that a small amount of a few parts in  $10^{-3}$  results in a turning point ( $1/f \partial f / \partial T = 0$ ) at temperatures attainable with single-stage low-power cryocoolers. For such a small volume fraction of rutile  $Q_0$ s in excess of  $10^7$  are still possible, since the losses in high-quality rutile single crystals are very small [5].

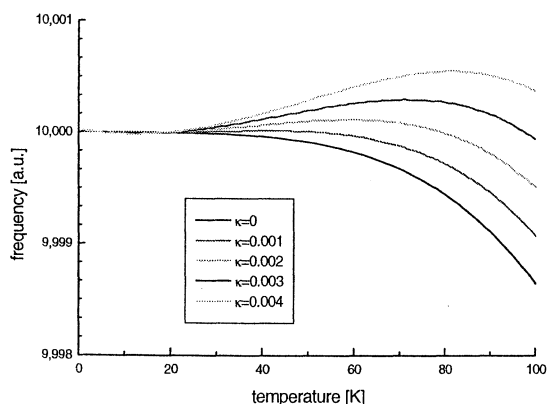


Fig. 1 Calculated resonance frequency vs temperature for a composite rutile - sapphire resonator for different values of the fraction of field energy in rutile  $\kappa$

Specifically, for  $\kappa=0.001$  (0.002) the turning point is at 41K (59K), the relative frequency change for a temperature deviation of 1mK is about  $10^{-14}$ , and the maximum  $Q_0$  is above  $10^7$  at 10 GHz. Our present configuration consists of a 100  $\mu\text{m}$  thin platelet of rutile, glued to a sapphire puck, providing a resonant frequency of 17.1 GHz for a whispering gallery mode of azimuthal order  $n=7$ , a turning point at 40.8

K (in good agreement with calculation), and an unloaded quality factor of  $3 \times 10^6$ .

## CONSTRUCTION OF COMPOSITE RESONATOR

In the prototype system a HEMEX single crystal sapphire puck (17 mm in diameter) is glued with a very thin layer of adhesive to a 100  $\mu\text{m}$  thick single crystal rutile disc of the same diameter. The composite puck is mounted in an OFHC copper housing, spaced from the walls by single crystal quartz tubes (see fig. 2), the whole structure being held rigidly in place by springs. The copper housing has a heater wound on it and two Si diode temperature sensors, mounted top and bottom. This is suspended inside a vacuum jacket from low thermal conductivity support tubes and the jacket is immersed in a bath of liquid He at 4.2 K. Electrical power applied to the heater is controlled by a pc to stabilise the resonator housing at the (previously measured) frequency versus temperature turning point for this mode ( $\sim 40.8$  K).

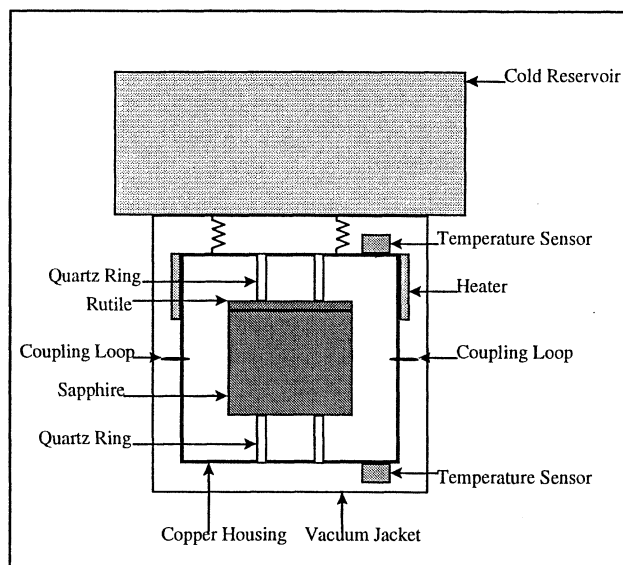


Fig. 2 Schematic of the composite puck and its cryogenic environment.

## REALISATION OF STABLE OSCILLATOR

At present, frequency locking techniques are being optimised to utilise the performance of the high  $Q$  whispering gallery mode for setting up an ultrastable

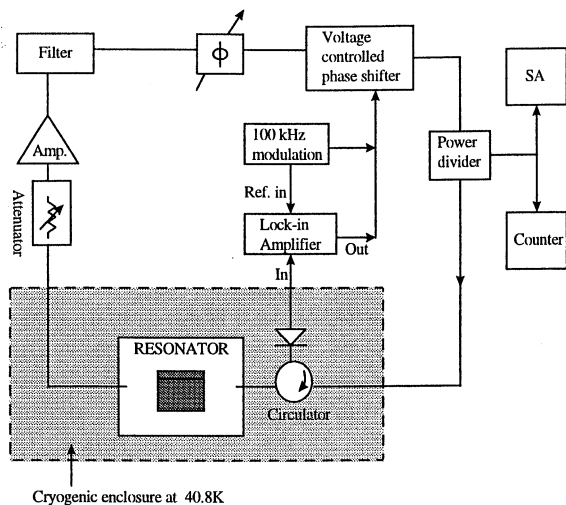


Fig. 3 Loop oscillator schematic, including Pound stabilisation circuit.

microwave oscillator (see fig. 3). A loop oscillator configuration is being used for which the thermal noise within the resonator whispering gallery mode bandwidth is amplified by a room temperature GaAs low noise amplifier and fed back to the input via manual and electronic phase shifters and a 1% bandwidth filter in series so that the loop oscillator condition, that the total phase change around the loop, is  $2n\pi$  ( $n$  an integer) is satisfied. The output from a splitter is taken to a frequency counter (gated by a signal derived from a H maser clock) and a spectrum analyser.

A Pound stabilisation technique is being used to reduce the effects of drifts in room temperature circuit components. Sidebands at  $\pm 100$  kHz are imposed on the carrier using an electronic phase shifter. The reflected signal from the resonator input has a component at 100 kHz if the oscillator is not tuned exactly to the resonator centre frequency. This error signal is detected by a lock-in amplifier and the correction signal is applied to the phase shifter to maintain the oscillator output frequency equal to the resonator centre frequency.

Fig. 4 shows the Allan variance calculated from the measured frequency counts of a counter (gated with reference to a H maser) as a function of gate time  $\tau$ . It is clear that, as the gate time increases the Allan variance  $\sigma^2(\tau)$  continues to fall, indicating that approximately white noise is still limiting performance at the longest averaging times. We plan to investigate this source of noise (which may represent counter gate jitter or interference on the 50 m long line which connects to the H maser) to further improve performance.

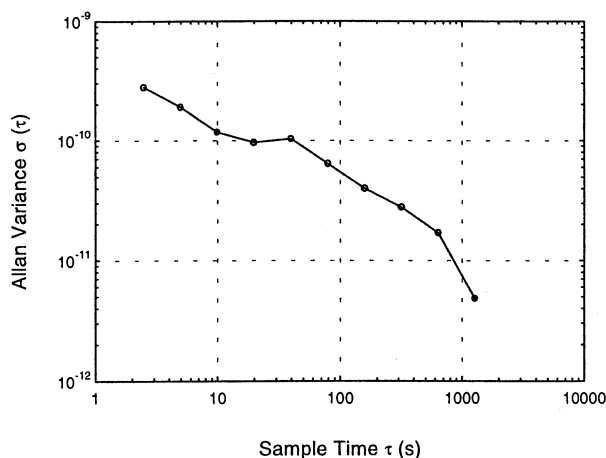


Fig. 4. Results of Allan variance for prototype composite puck resonator operated at 41K, for gate times up to  $10^3$  s.

## CONCLUSIONS AND FUTURE WORK

At present the measurements have been performed in a liquid helium cryostat to produce a rather vibration free environment for operating the oscillator. We plan shortly to install the resonator in a closed cycle Giffard-McMahon cooler to provide long term stable operation with minimal attention. This will involve careful attention to vibration isolation but successful achievement of this will also allow the oscillator to provide state-of-the-art low phase noise performance.

By suitable choice of mode and volume ratio of sapphire to rutile the turning point may be shifted anywhere in the range between  $\sim 30$  K and 90 K. We plan to redesign the resonator to raise this to  $\sim 60$  K, accessible to single stage Stirling coolers. A further two orders of magnitude improvement in performance should be possible, provided that sufficient levels of mechanical vibration isolation can be achieved.

## REFERENCES

1. A N Luiten, A G Mann & D G Blair, IEEE 47th Intl. Freq. Control Symp. pp757-62 (1993)
2. V B Braginsky, V S Ilchenko & K S Bagdassarov, Phys. Lett. A 120 pp300-5 (1987)
3. N Klein, N Tellmann, C Zuccaro, P Swiatek & H Schulz, Applied Superconductivity (IOPP Special Publication 148) pp743-8 (1995)
4. J C Gallop, C D Langham, L Hao & F Abbas, IEEE Trans. Instrum. Meas. 46 pp122-5 (1997)
5. N.Klein et al., J.Appl. Phys. 78, 6683 (1995)

## WHISPERING GALLERY MODE MICRO-WAVE CHARACTERISATION OF $Ba(Mg_{1/3}, Ta_{2/3})O_3$ DIELECTRIC RESONATORS

R Ratheesh<sup>ab</sup>, M T Sebastian<sup>c</sup>, M E Tobar<sup>a</sup>, J Harnett<sup>a</sup> and D G Blair<sup>a</sup>

<sup>a</sup>Department of Physics, University of Western Australia, Nedlands 6907 Australia

<sup>b</sup>Centre for Materials for Electronics Technology, M.G.Kavu, Athani, Thrissur 680771 India

<sup>c</sup>Regional Research Laboratory, CSIR, Trivandrum 695 019, India

*Abstract: Microwave dielectric ceramic resonators based on  $Ba(Mg_{1/3}, Ta_{2/3})O_3$  have been prepared by conventional solid state ceramic route. The DRs have a dielectric constant of 24 at 6.8GHz. The Whispering Gallery Mode technique was employed for the determination of the dielectric properties in the microwave frequency range. The  $Ba(Mg_{1/3}, Ta_{2/3})O_3$  have a quality factor of 22500 at 13.024 GHz. The temperature coefficient of resonant frequency ( $\tau_f$ ) has been measured accurately using different resonant modes.*

### INTRODUCTION

With recent advance in microwave telecommunications and satellite broadcasting, a variety of microwave devices such as band pass filters, band stop filters etc. have been developed using dielectric resonators as the frequency determining components. Dielectric resonators provide significant advantages in terms of compactness, light weight, temperature stability, and relatively low cost in the production of high frequency devices. Three parameters, dielectric constant ( $\epsilon_r$ ), Quality factor (Q<sub>u</sub>), and temperature coefficient of resonant frequency ( $\tau_f$ ) must be carefully controlled for such applications. In view of this, a number of dielectric ceramic materials such as  $(Zr, Sn)TiO_4$ ,  $Ba_2Ti_9O_{20}$ ,  $Ba_5Nb_4O_{15}$ ,  $Ba(Ln_{1/2}, Nb_{1/2})O_3$ ,  $Ba(Mg_{1/3}, Ta_{2/3})O_3$ ,  $Ba-Ln_2O_3-TiO_2$  etc. [1-7] have been investigated for microwave applications. Out of these  $Ba(Mg_{1/3}, Ta_{2/3})O_3$  (BMT) is expected as a very promising material for a dielectric resonator operating at the microwave frequency region because of its ultra low dielectric loss property.

Dielectric Resonators are normally operated using  $TE_{016}$ ,  $TM_{016}$ , or  $HE_{116}$  modes [8-10]. But the measured quality factor of these modes can be significantly low due to the conducting plates, radiation losses etc. However, recently it has been established that

Whispering Gallery Modes are necessary to obtain the high level of dielectric field confinement which in turn gives rise to low loss tangents for dielectric resonators at microwave frequencies. The quality factor of WG-mode DRs is limited only by intrinsic losses in the dielectric material and cannot exceed  $1/\tan\delta$ . They also offer good suppression of spurious modes that leak out the resonator and can be absorbed without perturbing the desired ones [11-14]. In the present paper we discuss the microwave dielectric properties of  $Ba(Mg_{1/3}, Ta_{2/3})O_3$  dielectric resonators. Both whispering Gallery Mode and microstripline methods are employed to accurately determine the loss tangent of these ceramic and results are presented.

### EXPERIMENTAL

The  $Ba(Mg_{1/3}, Ta_{2/3})O_3$  (BMT) samples were prepared by conventional solid state ceramic route. The dielectric constant ( $\epsilon_r$ ) of these ceramics were measured by the Hakki & Coleman [15] method and the quality factor by the stripline method of Khanna & Garault [16]. To determine the loss tangent in the Whispering Gallery mode ceramic, cylindrical pucks of 10mm in diameter and 5 to 7mm in height were used. The Cu post used for holding the ceramic puck (See Fig.1) was designed to minimize the losses. The loss tangents were measured in the 8 to 18 GHz region using the reflection configuration. Loop probes were used to excite

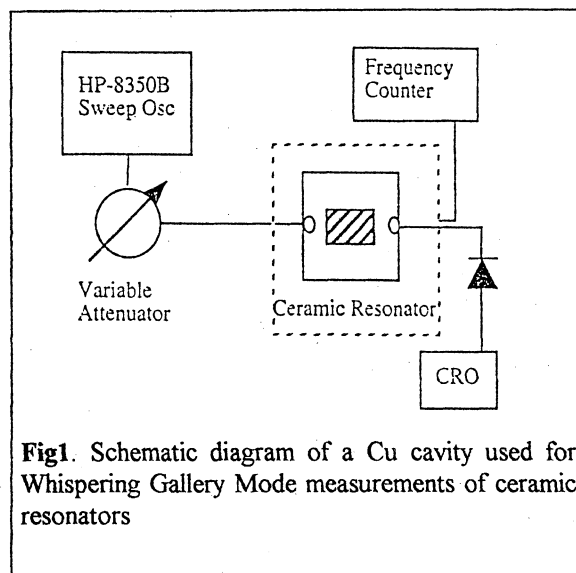


**Fig1.** Schematic diagram of a Cu cavity used for Whispering Gallery Mode measurements of ceramic resonators

the resonator. A Hp 86260 A and HP 86250 D sweep oscillator were used for the measurements. A microwave frequency counter was used to read out the frequency. The resonant frequencies determined by the frequency of minimum reflection, and the loaded Q-factor (QL) was determined by measuring the half power bandwidth. The coupling was measured using an Hp X 382A variable attenuator. The unloaded quality factor was calculated from the coupling factor  $\beta$ , using the equation  $Q_0 = QL(1 + \beta)$ . The schematic diagram of the experimental set-up used for the WGM measurement is shown in Figure 2.

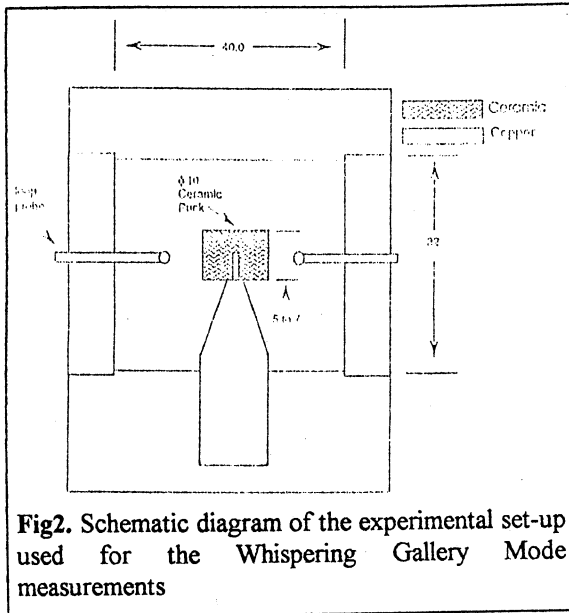


**Fig2.** Schematic diagram of the experimental set-up used for the Whispering Gallery Mode measurements

For the temperature coefficient of resonant frequency ( $\tau_r$ ), the sample was mounted inside a vacuum can and a peltier circuit was used for varying the temperature. Platinum and Germanium thermocouples were used to read out and control the temperature inside the can from -14 to 47 °C.

**RESULTS AND DISCUSSION**

The BMT green compacts were sintered into dense ceramics with cream homogeneous appearance. The dielectric constant of the sample with 94% density is 24 at 6.8 GHz (TE<sub>011</sub> mode). The Qu measured by the stripline method is 21,400 at 7.2 GHz.

The Whispering Gallery Mode microwave measurement of these ceramic samples were performed for the accurate determination of the intrinsic quality factor of the BMT samples. The measurements were made in the

reflection configuration. X-band quasi-TM<sub>mnp</sub> resonant mode families with azimuthal mode numbers, m, from 2 to 6 were identified for BMT ceramics. The mode families were identified by the excitation and observation of the H-field, using two magnetic loop probes in a radial plane. The measurements were made in transmission with one probe stationary as the other was moved relative to the ring. For each mode the unloaded quality factor (Qu) was accurately determined from a measurement of loaded Q and the corresponding coupling.

In general all the measured modes were hybrid in nature and had both axial electric field dependence and axial magnetic field dependence. It is common to denote a mode with a dominant axial electric field dependence as an E mode (quasi TM) and a dominant magnetic field dependence as a H-mode (quasi TE). Even though the material is isotropic we implemented anisotropic software [8] to determine the hybrid nature of the modes under investigation. The resonant frequencies were calculated from the value determined using the 'post resonator' method, assuming  $\epsilon_{||} = \epsilon_{\perp}$ , where  $\epsilon_{||}$  is the permittivity parallel to the anisotropic axis, and  $\epsilon_{\perp}$  is the permittivity perpendicular to the anisotropic axis. The electric energy filling factors for both E and H modes parallel,  $P_{e||}$  and perpendicular,  $P_{e\perp}$  from equation (2)

$$P_{e\perp} = 2 \frac{\partial f}{\partial \epsilon_{\perp}} \frac{\epsilon_{\perp}}{f}$$

$$P_{e||} = 2 \frac{\partial f}{\partial \epsilon_{||}} \frac{\epsilon_{||}}{f}$$

For quasi TE mode, the energy will be mainly stored in the perpendicular direction and  $P_{e\perp} > P_{e||}$  while for

**TABLE 1- Measured and predicted frequencies and corresponding filling factors of quasi TM modes of Ba(Mg<sub>1/3</sub>Ta<sub>2/3</sub>)O<sub>3</sub>**

m	Quasi TM modes	Freq. Meas. (GHz)	Freq. Pred. (GHz)	Electrical energy filling factor	Electric energy filling factor	Electric energy filling factor (Tot.)
2	TM <sub>2,1,0</sub>	8.597	8.535	0.4142	0.5761	0.9903
3	TM <sub>3,1,0</sub>	10.8151	10.762	0.2888	0.7064	0.9951
4	TM <sub>4,1,0</sub>	13.024	12.983	0.2106	0.7865	0.9971
5	TM <sub>5,1,0</sub>	15.2179	15.166	0.1597	0.8383	0.998
6	TM <sub>6,1,0</sub>	17.396	17.371	0.1251	0.8738	0.999

a quasi TM mode the energy will be mainly stored in the parallel direction and  $P_{e||} > P_{e\perp}$ .

The dielectric loss tangent for the isotropic dielectric

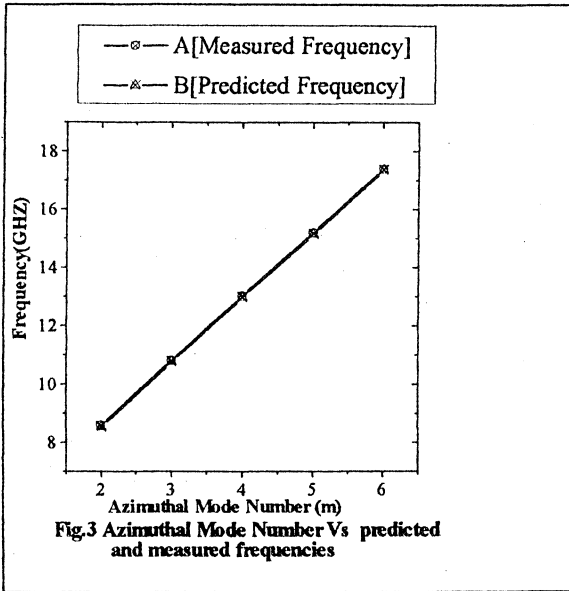


Fig.3 Azimuthal Mode Number Vs predicted and measured frequencies

can be solved using the following equation

$$Q_{(E)}^{-1} = \tan \delta (P_{e\perp} + P_{e||}) + Rs/G^{(E)}$$

$$Q_{(E)}^{-1} = \tan \delta (P_{e\perp} + P_{e||}) + Rs/G^{(H)}$$

where Rs is the surface resistance of the cavity enclos-

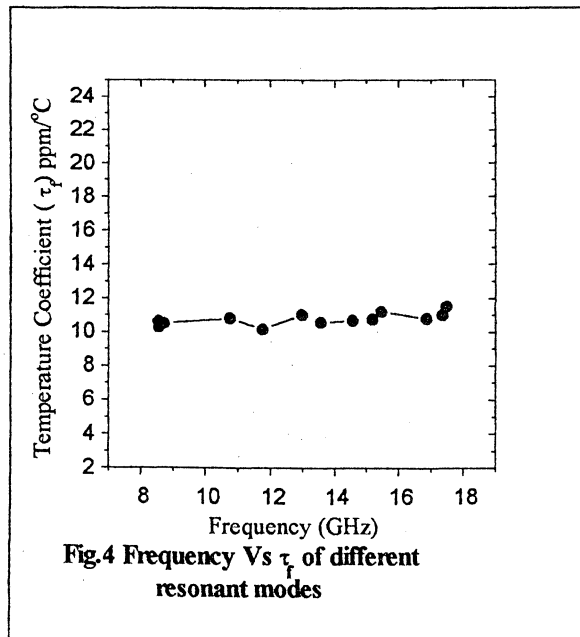


Fig.4 Frequency Vs  $\tau_f$  of different resonant modes

ing the dielectric resonators. For whispering gallery modes the geometric factor G is significantly large that the effect of the cavity can be ignored when compared to the loss tangent. The electric energy filling factors of DR for all these modes are close to unity (Table 1). It can be seen from Figure 3 that the predicted and measured quasi-TM modes are in good agreement. We

obtained a maximum quality factor of 22,500 at 13.024 GHz for BMT ceramics.

The temperature variation of resonant frequency of these ceramics were measured from -14 to 47 °C. We obtained a  $\tau_f$  of nearly 10ppm/°C for BMT ceramics in the 8-18 GHz region for thirteen different resonant frequencies (Fig.4)

## CONCLUSION

The Whispering Gallery Mode method has been employed to measure the dielectric properties of  $Ba(Mg_{1/3}, Ta_{2/3})O_3$  ceramic dielectric resonators. A better understanding of the behaviour of frequency on quality factor has been established. Highest quality factor of 22,500 is obtained for this dielectric resonator at 13.02 GHz. Predicted and measured frequencies show excellent agreement with each other. We obtained a temperature coefficient of 10ppm/°C for BMT ceramics using peltier circuit.

## REFERENCES

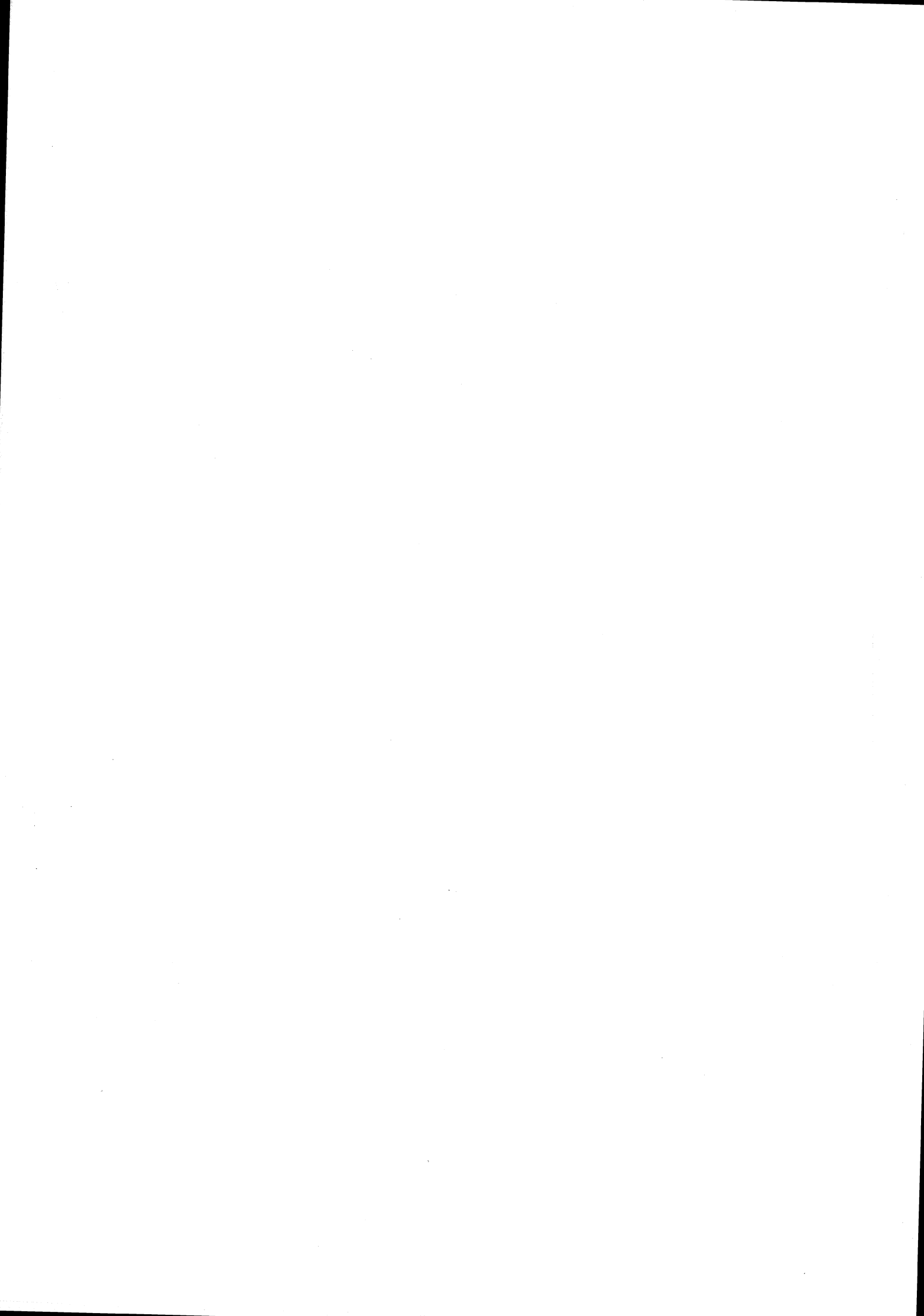
- 1 G.Wolfram and H.E.Gobel, 1981, *Mater. Res. Bull.* **16**, 1455
- 2 S.Nomura, K.Toyama and K.Kaneta, 1982, *Jap. J. Appl. Phys.* **21** L624.
3. D.Kolar, S.Gaberscek, Z. Stadler and D. Sovora, 1980 *Ferroelectrics* **27**, 269
4. J.M. Dyrand and J.P.Boilot, 1987, *J. Mater.Sci. Lett.* **6**, 134
5. H.Sreemoolanadhan, M.T.Sebastian and P.Mohanan, 1996, *Ferroelectrics* **27**, 43.
6. M.Taketa and K.Kageyama, 1989, *J. Amer. Cer. Soc.* **72**, 1955
7. Sam Soloman, H.Sreemoolanadhan, M.T.Sebastian and P.Mohanan, 1996, *Mater. Lett.* **28**, 107.
8. M.E.Tobar and A.G. Mann, 1993, *IEEE Trans. MTT* **41**, 632.
9. J.R.Wait, 1967, *Radio Sci.*, **Vol.2**, 1005
10. J.Krupka, D.Cros, M.Aubourg, and P. Guillon, 1994, *IEEE Trans. MTT* **42**, 56
11. R.A.Wood, E.N.Ivanov, M.E.Tobar and D.G.Blair, 1994, *Elect. Lett.*, **30 (25)**, 2129.
12. E.N.Evanov, D.G.Blair and V.I. Kalinichev, 1993, *IEEE Trans MTT-41*, 632.
13. M.E.Tobar and A.G.Mann, 1991, *IEEE Trans. MTT-39(12)*, 2077.
14. J.Krupka, K.Derzakowski, A.Abramowicz, M.E.Tobar and R.G. Geyer, 1997, *IEEE MTT, IMS, Dec.*
15. B.W.Hakki and P.D. Coleman, 1960, *IRE Trans MTT* **8(7)**, 402.
16. A.P.S. Khanna and Y. Garault, 1983, *IEEE Trans. MTT* **31(3)**, 261.



*12th EFTF* - 10÷12 March 1998 - Warsaw - POLAND

**Classical Cs standards & H masers**

Chairman: *Claude Audoin*



THE SHM COMPACT HYDROGEN MASER FOR SPACE APPLICATIONS  
REPORT ON THE PEM PHYSICS PACKAGE DESIGN VERIFICATION

*Alain Jornod, Laurent-Guy Bernier, Hartmut Schweda, Giovanni Busca,*  
Observatoire Cantonal de Neuchâtel, Switzerland

1. ABSTRACT

The SHM-RA instrument is a compact (50 kg, 70 W) atomic hydrogen maser clock for space applications being developed by the Observatory of Neuchâtel in view of the Radioastron orbital VLBI mission.

The miniaturised Physics Package is based on a sapphire loaded microwave cavity concept that, in conjunction with a novel automatic cavity tuning system, yields frequency stability performances  $\sigma_y(10^5\text{s}) < 1.5 \times 10^{-15}$  comparable with that obtained from a conventional full size maser physics design.

The PEM Physics Package is now being evaluated in conjunction with a breadboard Electronics Package for the purpose of design verification. A detailed structural analysis was performed in 1997 based on a Finite Element Model. The microwave cavity and magnetic shields assembly, the heart of the Physics Package, was also successfully tested in random vibration at Radioastron qualification levels. The formal Preliminary Design Review of the PEM Physics Package was started at the end of October 1997 under the supervision of ESA. The breadboard electronics package is also under evaluation and has given good results.

Keywords: hydrogen maser, frequency standards, atomic clocks, space applications, sapphire loaded microwave cavity.

2. THE SHM INSTRUMENT

2.1 INTRODUCTION

The Observatory of Neuchâtel (ON) is developing a compact hydrogen maser for space applications, based on a miniature sapphire loaded microwave cavity. The hydrogen maser is a high performance frequency standard capable of a frequency stability of about  $1 \times 10^{-15}$  over averaging intervals from 1'000s to 10'000 s. If used as a clock, this is equivalent to a time stability of 0.7 ps over a 1000 s time interval or 7 ps over a 10'000 s time interval. The SHM instrument was developed for the international Radioastron (RA) orbital VLBI mission to be used as the alternate master clock. The SHM instrument was also designed to be used for an accurate measurement of the red-shift effect, i.e. the time dilatation due to the gravitational field. This is the purpose of the CRONOS experiment proposed by ON and sponsored by the Swiss PRODEX

program of ESA. The RA mission and the CRONOS experiment were reported previously in references [Valtaoja (1), Andreyanov (2), Bernier et al. (6)].

2.2 DEVELOPMENT STEPS

The SHM compact hydrogen maser frequency standard is based on a Miniature sapphire loaded Microwave Cavity (MMC) designed by ON in 1993 under a first ESTEC contract for the development of the SHM instrument [Bernier (3), Bernier et al. (6)]. The development was continued up to now through several design and breadboarding steps that are reported in references [Bernier (3) to Bernier et al. (7)]. The design of the SHM Physics Package (PP) makes use of several sophisticated technologies and many problems had to be overcome in the course of development. Technologies and development activities worth to be mentioned are : optimisation of the atomic storage volume in the sapphire loaded microwave cavity, manufacturing of a very large sapphire cylinder, vacuum-tight diffusion bonding of sapphire to titanium, vapour deposition plating of the internal surface of a titanium cylinder, machining by electro-erosion of the main titanium structural part, teflon coating of the composite titanium-sapphire atomic storage bulb, development of a special process of the magnetic shields that optimises the permeability in zero field, evaluation of the pumping speed, capacity and brittleness of the hydrogen getters.

2.3 DESIGN VERIFICATION PROGRAMME

The last major step of development was the manufacturing and the first integration of the Prototype Engineering Model Physics Package (PEM-PP). The PEM-PP was manufactured during the first half of 1996 and first integrated in October and November 1996. The first atomic signal from the fully integrated PEM-PP was obtained in December 1996.

A first evaluation of the PEM-PP was performed in January and February 1997. The atomic quality factor, the atomic signal power and the short-term frequency stability characteristics of the PEM-PP were verified experimentally. The PEM-PP was then disassembled and several design modifications were implemented during the first half of 1997. These modifications were known to be necessary but had been postponed in order to allow for a quick first integration and evaluation.

A detailed structural analysis of the PEM design was performed in 1997 by CSEM, a Swiss engineering company. For the purpose of analysis CSEM has developed a finite elements structural model of the SHM instrument with more than 7'000 nodes. The detailed structural analysis included : static loading, random vibration analysis, shock analysis, load safety margins, buckling analysis, thermal stress analysis and fracture control analysis. The main conclusion of CSEM's engineering analysis is that the PEM design is compliant with the Radioastron requirements without modifications. Several design improvements to the mechanical design were also suggested by CSEM.

The Reduced Microwave Cavity & magnetic Shields Assembly (RMCSA), the heart of the Physics Package which contains the atomic hydrogen storage bulb, is also the most complex part of the Physics Package from the structural point of view. A spare RMCSA unit, identical to the one used in the PEM-PP, was tested successfully for shocks (40 g shock response spectrum) and for random vibration (7.5 g rms) to the Radioastron qualification levels on May 14-15 1997. The same unit was also successfully tested for random vibration to the GPS clocks qualification levels (14 g rms) on September 25 1997 in preparation to future applications of the SHM design for Global Navigation Satellite System (GNSS) applications.

The Preliminary Design Review (PDR) of the PEM SHM instrument was opened on October 29 1997 under the technical supervision of ESA. The reviewed material includes the design definition documents, the design verification by inspection and analysis, and the design verification by test on the PEM-PP.

## 2.4 RECENT DEVELOPMENT AND TEST ACTIVITIES

The PEM-PP design verification activities obviously involve a lot of fine tuning and debugging work since the PEM-PP is the first prototype of a completely new hydrogen maser physics package design.

The use of titanium for the microwave cavity implies relatively high thermal gradients because titanium has a very low thermal conductivity as compared to other metals. We have observed that the combination of bi-metallic junctions and thermal gradients is sufficient, in certain cases, to generate local thermo-electrical current loops that produce magnetic inhomogeneities large enough to impair the stimulated emission of the stored hydrogen atoms.

A large part of the recent activities have therefore concentrated on the improvement of the control of the thermal gradients and of the thermo-electrical current loops in the sapphire loaded microwave

cavity. After a number of investigations we are now in a position to achieve the required level of control but minor modifications to the microwave cavity assembly are necessary.

Another area of recent development activities is the reduction of the hydrogen consumption. Hydrogen consumption with the original design of the dissociator collimator is about 3 litres/year (volume of molecular hydrogen at normal temperature and pressure). This yields an autonomy of 3 years with the 10 litres supply of molecular hydrogen. We are now working on an improved design of the dissociator collimator that will yield a hydrogen consumption of 1 litre/year or less in order to make possible an autonomy of at least 10 years with the existing supply of hydrogen.

The activation of the bulk getters situated inside the thermal and the hydrogen vacuum enclosures generates a lot of heat and a lot of outgassing. Both the heat dissipation and the outgassing pressure must be kept under strict control during activation in order to achieve the specified pumping speed and pumping capacity. Part of the recent development activities was dedicated to the improvement of the getter activation procedures.

Several modifications of the PEM-PP are still necessary before the final configuration is achieved. Therefore one more integration is necessary before the final tests can be conducted to close the PDR.

The results of the design verification tests already performed on the PEM-PP are reported below.

On the other hand, the breadboard electronics developed to enable testing the PEM-PP is also under evaluation. A first demonstration of the performance of the breadboard ACT (Automatic Cavity Tuning system) is reported below.

## 2.5 PERSPECTIVES FOR FUTURE DEVELOPMENT

In parallel with the closure of the PEM-PP PDR, the next step will be to kick-off a contract for the development of a PEM SHM space compatible Electronics Package (EP).

On the basis of the existing breadboard electronics, the development of the space compatible PEM-EP is expected to take one year. The fully integrated and tested PEM SHM instrument will then be delivered to Astro Space Centre in Moscow for the purpose of ground testing the Radioastron payload. In particular it is planned to perform a VLBI session on ground using the full EM (Engineering Model) Radioastron payload.

Another flight opportunity for the SHM instrument is the ACES atomic clocks experiment proposed by a team of French scientists for the early utilisation of the International Space Station. The ACES experiment has already been officially endorsed by ESA and involves the demonstration in space of a cold atoms caesium fountain and other atomic clocks [Lemondé (7) et al. Feustel-Büechl et al. (8)]. The present phase of the ACES experiment activities is concerned with the funding of the required instruments by the participating European countries. The ACES SHM design will be very close to the Radioastron design. The extra effort of development will concern mainly the adaptation of the instrument interfaces. A system study of the ACES concept has already been performed by CNES for the Space Station Applications and Promotion Office of ESA [CNES (10), MATRA (11)].

Besides, ESA plans to include the SHM hydrogen maser as part of the payload for an experimental technology demonstration flight (part of GNSS-2 activities) in preparation to the future GNSS European Global Navigation Satellite System.

### 3. SHM INSTRUMENT DESIGN

#### 3.1 CONDENSED SPECIFICATIONS

- long-term drift :  $< 3 \times 10^{-12} \text{ year}^{-1}$
- output levels : 0.4 Vrms in 50  $\Omega$
- frequency stability

$\tau$ [s]	Allan deviation
1	$< 1.5 \times 10^{-13}$
10	$< 2.1 \times 10^{-14}$
100	$< 5.1 \times 10^{-15}$
1'000	$< 2.1 \times 10^{-15}$
10'000	$< 1.5 \times 10^{-15}$

Table 1  
Short-Term Stability

- phase noise

	14.71 MHz output	5 MHz output
f [Hz]	L (f) [dBc]	L (f) [dBc]
1	$< -100$	$< -110$
10	$< -122$	$< -132$
100	$< -132$	$< -143$
1'000	$< -141$	$< -151$
10'000	$< -145$	$< -155$

Table 2  
Phase Noise

- temperature range: 10°C to 35°C
- thermal sensitivity:  $\leq 3 \times 10^{-15} \text{ K}^{-1}$
- magnetic field range:  $\pm 1 \text{ Gauss}$
- magnetic sensitivity:  $\leq 2 \times 10^{-14} \text{ Gauss}^{-1}$
- DC input voltage: 22 to 50 V
- power consumption:  $< 70 \text{ W}$
- largest diameter : 460 mm
- full height (vertical) 600 mm
- mass 50 kg
- operational lifetime  $> 3 \text{ years}$

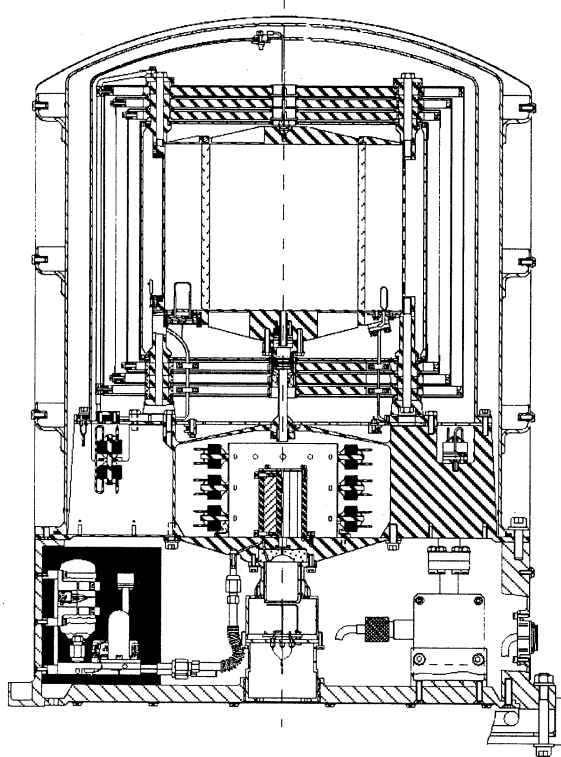


Figure 1  
Top Assembly Drawing of SHM Physics Package

#### 3.2 MASER PHYSICS DESIGN

The heart of the PP design concept is the sapphire loaded MMC. The internal volume of the MMC is 4.4 litre. This is to be compared with the 20 litre of a conventional unloaded microwave cavity tuned to the hydrogen hyperfine frequency. The storage volume for hydrogen is 1.7 litre which is comparable to a conventional design based on a full size cavity. It is basically the size reduction of the microwave cavity that has made possible the realisation of a 50 kg SHM instrument. The sapphire cylinder of the MMC has both a microwave function, the dielectric loading of the cavity, and a maser physics function

since, together with the bonded titanium covers, it also constitutes the hydrogen storage bulb.

State selection is performed by a conventional quadrupole magnetic state selector. The dissociator is a small fused quartz bulb. The hydrogen supply is stored in the form of a solid-state hydride material. Magnetic shielding is performed by a set of four 0.5 mm magnetic shields around the MMC and by a fifth 0.5 mm magnetic shield that surrounds the whole instrument.

There are two vacuum systems: the hydrogen vacuum enclosure and the thermal vacuum enclosure. Each enclosure is pumped by a set of getters and by a set of two 2 l/s ion pumps. For each enclosure, one ion pumps would be sufficient. The second pump is there for redundancy. The sealed part of the PP is closed by an aluminium bell jar that closes the thermal vacuum enclosure.

### 3.3 MECHANICAL DESIGN

The Top Assembly Drawing of the SHM Physics package is shown on figure 2. The SHM instrument is designed to pass the Radioastron qualification vibration levels i.e. 40 g shocks and 7.5 g rms random vibration.

### 3.4 THERMAL DESIGN

In orbit the instrument is covered by a MLI thermal insulation blanket. All thermal exchanges are performed by conduction to a dedicated thermally controlled base plate which is part of the spacecraft. The temperature of the MMC is controlled with a design goal thermal stability of  $\sigma_T(10'000s) \leq 7mK$ . This is achieved by three concentric layers of active thermal control around the MMC.

The thermal coefficient of the MMC  $TE_{011}$  resonant frequency is 65 kHz/°C. With such a thermal coefficient it is not possible to achieve the specified thermal coefficient of the instrument with thermal control of the MMC resonant frequency only. An Automatic Cavity Tuning (ACT) system is necessary in order to reduce the cavity pulling effect by an additional electronic frequency control of the MMC.

### 3.5 ELECTRONICS DESIGN

The ACT system is the most important performance critical element of the electronics. Its purpose is to stabilise the resonant frequency of the microwave cavity in order to minimise the cavity pulling effect on the atomic signal frequency.

The specified maximum thermal coefficient of the PP is  $6 \times 10^{-12} K^{-1}$  with only thermal control of the MMC resonant frequency and  $3 \times 10^{-15} K^{-1}$  with the

ACT system in operation, i.e. with electronic frequency control of the MMC.

## 4. EVALUATION OF PEM PHYSICS PACKAGE

### 4.1 MICROWAVE CAVITY

The measured loaded quality factor of the MMC is 34'000. The thermal coefficient of the  $TE_{011}$  mode is -65 kHz/K.

### 4.2 ATOMIC QUALITY FACTOR

The operating atomic quality factor at -104 dBm is  $1.5 \times 10^9$ .

### 4.3 THERMAL CONTROL

The measured thermal stability of the MMC is  $\sigma_T(10'000s) \leq 0.2mK$ , i.e. 35 times better than the design goal.

### 4.4 AUTOMATIC CAVITY TUNING (ACT)

With only a thermal control of the MMC the measured thermal coefficient is  $5 \times 10^{-12} K^{-1}$  which is compliant with the specification. On the other hand, the thermal coefficient becomes  $3 \times 10^{-14} K^{-1}$  with the breadboard ACT in operation. This is still one order of magnitude far from the specification and further improvement of the breadboard ACT is necessary.

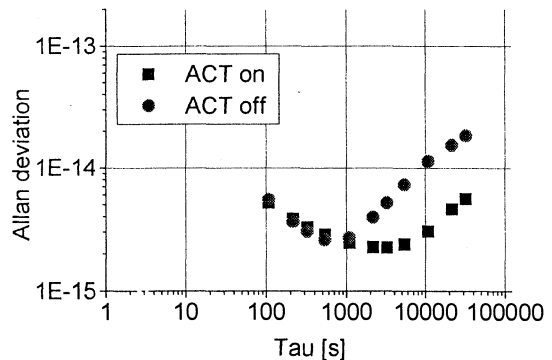


Figure 2  
Allan deviation with and without breadboard ACT as measured on an EFOS-C ground maser

The measured frequency stability with the breadboard ACT in operation is  $\sigma_T(1'000s) \leq 3 \times 10^{-15}$ . This is already very close to the specification.

Figure 2 shows the improvement of Allan deviation achieved by the breadboard ACT in a recent test performed on an EFOS-C ground hydrogen maser.

Similar results are expected to be obtained soon on the PEM PP.

#### 4.5 MAGNETIC SHIELDING

The measured shielding factor with only the four cavity shields is 20'000. A global shielding factor of 200'000 is expected with 5 shields.

#### 4.6 GETTERS & ION PUMPS

It was verified that the vacuum system has an autonomy of at least 10 days without electrical power to the ion pumps (getters only). This requirement is specific to the Radioastron I mission.

### 5. CONCLUSION

The evaluation of the PEM SHM-PP reported in this paper is still in progress but most of the important conclusions have been drawn already.

Most of the design parameters have been measured and analysed and have been shown to be compliant with the specifications. In particular the maser physics parameters, i.e. atomic quality factor and short-term stability, have been verified and the detailed structural analysis performed by CSEM has shown that the design is compliant with the random vibration and shock requirements of Radioastron. The shock and random vibration tests of the spare RMCSA assembly have validated the finite elements model of CSEM and confirmed the conclusions of the structural analysis.

On the other hand, the breadboard electronics package is still in development and does not reach yet all the performance goals set by the instrument specifications.

One more integration cycle of the PEM PP has to be performed before the final configuration is achieved and before the final design verification tests can be performed.

### 6. REFERENCES

1. Valtaoja E., « *The Radioastron Space VLBI Project* », Proc. 4th EFTF, Neuchâtel, March 13-15, 1990, pp. 707-710.
2. Andreyanov V.V., « *Time-Frequency Synchronization in Radioastron OVLBI Project* », Proc. 7th EFTF, Neuchâtel, March 16-18, 1993, pp. 33-38.
3. Bernier L.G., « *Preliminary Design and Breadboarding of a Compact Space Qualified Hydrogen Maser Based on a Sapphire Loaded Microwave Cavity* », Proc. 8th EFTF, Munich, March 9-11, 1994, pp. 965-980.
4. Couplet C., Bernier L.G., « *Proton Irradiation Test of the Teflon Wall Coating in the Atomic Hydrogen Maser in Preparation to Space Applications* », Proc. 8th EFTF, Munich, March 9-11, 1994, pp. 952-958.
5. Bernier L.G., « *Preliminary Design and Breadboarding of a Compact Space Qualified Hydrogen Maser Based on a Sapphire Loaded Microwave Cavity* », Proc. 5th Time & Space Metrology Symposium, Mendeleevo, Russia, October 11-13, 1994, pp. 412-417.
6. Bernier L.G., Busca G., Jornod A., Schweda H., « *The SHM Space Borne Hydrogen Maser : First Evaluation of the PEM Physics Package* », Proc. 11<sup>th</sup> EFTF, Neuchâtel, March 4-7, 1997, pp. 664-667.
7. Bernier L.G., Jornod A., Schweda H., Gentsch R., Busca G., « *The SHM Atomic Clock for Space Applications - Development and Test of the PEM Physics Package* », to be published in Proc. 29<sup>th</sup> PTTI, Long Beach, California, December 2-4 1997.
8. Lemonde P., Salomon C., Laurent P., Simon E., Santarelli G., Clairon A., Dimarcq N., Petit P., Audoin C., Jamin-Changeart F., Gonzales F., « *PHARAO : A compact Clock Using Laser Cooled Cesium Atoms* », Proc. 11<sup>th</sup> EFTF, Neuchâtel, March 4-7, 1997, pp. 646-650.
9. Feustel-Büechl J., Isakeit D., « *The International Space Station - A Challenge for Global Cooperation* », Proc. 11<sup>th</sup> EFTF, Neuchâtel, March 4-7, 1997, pp. 3-11.
10. « *ACES Concept - Programme, Organisation and Development Plan* », CNES report document ACES-MS-0-1-CNS, issue 1, revision 0 of June 10, 1997.
11. « *ACES Concept - Accommodation on the Express Pallet Adapter & Related Interface Constraints* », MATRA MARCONI SPACE report, document EXT/PP/NT/062.97 issue 1, revision 0 of May 29, 1997.

## INFLUENCE OF ENVIRONMENTAL FACTORS ON HYDROGEN MASER FREQUENCY STABILITY

T. E. Parker

National Institute of Standards and Technology  
Time and Frequency Division, 847.5  
325 Broadway, Boulder, CO 80303 USA

### ABSTRACT

It is necessary to have a complete understanding of the environmental sensitivities of hydrogen masers in order to obtain optimum frequency stability, and to avoid common-mode frequency fluctuations. Measurements of environmental sensitivities (temperature, relative humidity, atmospheric pressure, line voltage and magnetic field) made at the National Institute of Standards and Technology (NIST) have demonstrated that the frequency stability of cavity-tuned hydrogen masers is not significantly degraded if the masers are contained in a controlled environment. Under these conditions common-mode frequency fluctuations are not a problem.

### INTRODUCTION

The number of hydrogen masers being used in time scales around the world has increased significantly over the last ten years [1-3]. The Bureau International des Poids et Mesures (BIPM) now uses data from 38 masers in the generation of International Atomic Time (TAI). Masers are also now commonly used as reference oscillators for primary frequency standards since they offer fractional frequency stabilities below  $1 \times 10^{-15}$  at time intervals on the order of hours to days. With cavity tuning this stability can be extended to tens of days. The National Institute of Standards and Technology (NIST) has five cavity-tuned masers [4] at its site in Boulder, Colorado, USA, four of which are currently used in the NIST AT1 time scale [1]. The remaining maser will very likely be included in the scale by the end of 1998. One of the masers is also routinely used as the reference oscillator for the primary frequency standard NIST-7 [5], and for research on new technologies for primary frequency standards. Each maser at NIST is contained in its own environmental chamber to control temperature ( $\sim \pm 0.1$  °C peak to peak) and relative humidity ( $\sim \pm 2$  % peak to peak).

With the increased role of masers in time scales and as references for primary frequency standards it is important to have accurate knowledge concerning the environmental sensitivities of the masers for time

intervals up to at least several days. In most laboratories the only frequency source with short-term frequency stability comparable to that of a maser is another maser. Therefore, it is necessary to know if there are any common-mode frequency fluctuations which would not be visible in a comparison between masers. Since common-mode fluctuations generally come from environmental sensitivities, these sensitivities must be known. Consequently, NIST has conducted a series of measurements to determine these sensitivities. The results of these measurements are reported here.

Pressure sensitivity is of particular concern since controlling pressure is very expensive and, if not controlled, all of the masers at a given site will respond to the same fluctuations in atmospheric pressure. Furthermore, the lowest pressure sensitivity currently guaranteed by the manufacturer [4] could result in fractional frequency fluctuations larger than  $1 \times 10^{-14}$  occurring simultaneously in all of the masers just due to barometric pressure fluctuations. These fluctuations may not be observable in comparisons among masers at the same site. Previous measurements of the pressure sensitivity of hydrogen masers without cavity tuning have shown evidence of fractional frequency fluctuations as large as  $1 \times 10^{-13}$  [6]. Fortunately, we have found that the pressure sensitivity in the cavity-tuned masers is more than 10 times smaller than the manufacturer's specification.

In a more general sense, it is also desirable to know to what extent environmental fluctuations degrade the maser stability even if the frequency fluctuations are not common-mode. To accomplish these goals a program has been carried out at NIST to measure the environmental sensitivities of the masers, as well as to monitor the stabilities of the environmental parameters during normal operation. The sensitivities of the maser frequencies to (a) temperature, (b) relative humidity, (c) barometric pressure, (d) line voltage, and (e) vertical magnetic field (the most sensitive axis) have been measured on several units. Previous measurements of environmental sensitivities of cavity-tuned hydrogen masers have been made [7], but not over the appropriate time interval or at the accuracy required for use in time scales or as references for primary frequency standards.

Contribution of the U.S. Government not subject to copyright.

## ENVIRONMENTAL SENSITIVITIES

Frequency sensitivities to temperature, relative humidity, line voltage, and magnetic field were all measured in the same type of chamber in which the masers normally operate. This was done to ensure that gradients in temperature and humidity present in the chambers used for normal operation are also present during the measurements of the sensitivities. However, pressure sensitivity had to be measured in a specially constructed chamber that has approximately the same internal dimensions as the other chambers. This chamber is capable of pressure changes up to  $\pm 15\%$  about the ambient barometric pressure. Preliminary results were presented at the 1997 IEEE International Frequency Control Symposium, and details of the techniques used to measure the environmental sensitivities can be found in [8]. No attempt was made to investigate the physical cause of any particular environmental sensitivity, but simply to characterize its value. Apparent sensitivities to pressure, humidity, and line voltage may in fact be caused partially or entirely by changes in temperature or temperature gradients inside the maser. Knowing these details is important to reducing the environmental sensitivities of the masers, but this information is not needed to quantify the sensitivities.

## SUMMARY OF RESULTS

Table 1 summarizes the results of all of the

environmental tests. Table blocks with no values indicate that those parameters have not been measured. This table is more complete than that given in [8]. The five masers at NIST were purchased between 1990 and 1996 and are numbered in the order in which they were obtained. The most recently purchased masers have been more thoroughly characterized since the environmental testing could be done before the masers were put to use in the NIST time scale. Older masers can be tested only when they are taken out of the time scale for various reasons. Masers 3 and 5 have been completely characterized, while masers 1 and 4 have been partially characterized. No data are available for maser 2 since it has been in the NIST time scale continuously since 1994. The first column of the table lists the coefficients for temperature, relative humidity, pressure, line voltage, and magnetic field (at  $10 \mu\text{T}$  and  $100 \mu\text{T}$ ). The next four columns list the values of the measured sensitivities for each maser expressed as fractional frequency changes ( $10^{-15}$ ) per unit change of the environmental parameter. The last column gives the duration for which the environmental parameter was changed from its nominal value in order to determine the environmental sensitivity.

**Temperature** -  $S_T$  is the static temperature coefficient and corresponds to the fractional frequency shift per degree Celsius after all of the transient frequency shifts have disappeared. All of the values of  $S_T$  are within the manufacturer's specifications, though there is a large variation from maser to maser. The manufacturer has

TABLE 1 - Summary of environmental sensitivities

Sensitivity	Maser 1	Maser 3	Maser 4	Maser 5	Step Interval (days)
$S_T(10^{-15}/^\circ\text{C})$	$+1.3 \pm 0.2^*$	$-9 \pm 1$	$-8 \pm 1$	$-3.4 \pm 0.2^{**}$	3 - 7
$S_{RH}(10^{-15}/\%)$	-	$+0.4 \pm 0.2$	$-0.2 \pm 0.2$	$-0.04 \pm 0.2$	14 - 21
$S_P(10^{-15}/\text{kPa})$	-	$+0.08 \pm 0.4$	$+0.16 \pm 0.04$	$+0.004 \pm 0.04$	3
$S_V(10^{-15}/\text{V})$	-	$-0.09 \pm 0.2$	-	$-0.08 \pm 0.1$	3
$S_H(10^{-15}/10 \mu\text{T})$	-	$-13 \pm 2$	-	$+4.7 \pm 1.4$	3
$S_H(10^{-15}/100 \mu\text{T})^\dagger$	4	17	6	5	0.02

\* Dynamic temperature response of  $\sim -/+4 \times 10^{-14}$  for a  $\pm 2^\circ\text{C}$  temperature step is not included

\*\* Dynamic temperature response of  $\sim -/+2 \times 10^{-14}$  for a  $\pm 2^\circ\text{C}$  temperature step is not included

† As measured by manufacturer at  $\pm 100 \mu\text{T}$  ( $\pm 1$  gauss)

made a number of changes to the masers over the years so it is difficult to identify the exact cause for the variations. All of the masers exhibited transient frequency shifts when the temperature steps were first applied and this indicates the presence of a dynamic temperature response (see ref. 8). Because of small static coefficients, the dynamic responses on masers 1 and 5 could be quantified and are  $-4 \times 10^{-14}$  and  $-2 \times 10^{-14}$  respectively for a  $+2$  °C step. It is difficult to quantify the dynamic responses on masers 3 and 4 because of the larger static temperature effects, but they appear to be about the same as that of maser 5.

**Relative humidity** - Sensitivities to relative humidity ( $S_{RH}$ ) are small, and large steps ( $\pm 9\%$ ) in relative humidity had to be used to measure them. Small changes in temperature sometimes coincided with the humidity steps, but correcting for these steps has no significant impact on the values of  $S_{RH}$  in Table 1. A humidity step of 14 to 21 days in length was used to ensure that processes with long time constants would be observed. Test cycles much longer than this are of limited value since frequency drift or aging in masers is usually large enough to make environmental parameters irrelevant in the long-term.

**Pressure** - The manufacturer guarantees a pressure sensitivity ( $S_p$ ) less than  $3 \times 10^{-15}/\text{kPa}$  and the observed values are smaller than this by more than a factor of 10. (1 kPa is on the order of the average day to day barometric pressure variations.) This effectively eliminates one potential cause of common-mode frequency fluctuations. The large uncertainty for the pressure sensitivity of maser 3 in Table 1 stems from the fact that this maser exhibited occasional erratic frequency transients during the measurements. These transients were not reproducible like the dynamic temperature effects and did not always occur simultaneously with the pressure steps. Sometimes they would occur many hours after the pressure change, or not at all. Also, the signs of the frequency transients were not consistent with the signs of the pressure steps. It is clear, however, that the transients are related to large, relatively sudden pressure excursions, since they do not occur at all during extended periods when the pressure changes only gradually due to normal barometric pressure variations. No significant coherent temperature changes were observed during the pressure tests, but small changes ( $\sim 1\%$ ) in the relative humidity did coincide with the pressure changes. Making corrections for coherent variations in temperature and/or relative humidity has little impact on the observed pressure sensitivities.

**Line voltage** - Frequency sensitivity to line voltage ( $S_V$ ) is very small and is not cause for concern as a source of common-mode frequency fluctuations. None of the other environmental parameters showed any coherent variations with the line-voltage variations.

**Magnetic field** - Sensitivity to magnetic field ( $S_H$ ) was measured by placing a set of Helmholtz coils around one of the environmental chambers. The coils were oriented to create a vertical magnetic field since this is the most sensitive axis of the masers. Calibration was accomplished by measuring the field strength and uniformity inside the chamber as a function of electrical current but without a maser present. During testing with the maser in the chamber the vertical field strength is monitored on the top surface of the maser. The field on the maser in the test chamber is typically around  $-73$   $\mu\text{T}$  ( $100$   $\mu\text{T} = 1$  gauss) just due to the Earth's magnetic field. Changes about this value caused by current in the Helmholtz coils were approximately twice the magnitude of those observed in the empty coils due to flux concentration by the maser. For the purposes of calculating the magnetic field sensitivity, however, the field values for the empty coils were used.

Tests were performed for field changes of  $\pm 10$   $\mu\text{T}$  and  $\pm 5$   $\mu\text{T}$ .  $S_H$  appears to be nonlinear since the magnitude of the observed frequency change is about 50% larger when the total field strength is increased as opposed to when the field is decreased by the same amount. The values listed in Table 1 are the average of the responses for the two directions.

Sensitivity to vertical magnetic field is of particular interest since the frequency shifts of masers 3 and 5 measured in our laboratory for 10  $\mu\text{T}$  changes in magnetic field are almost as large as those measured by the manufacturer on the same masers for 100  $\mu\text{T}$  field changes. See Table 1. No sign information was available for the manufacturer's measurements. The effectiveness of passive magnetic shielding is highly nonlinear, and this may explain the differing results. Also, the manufacturer's tests were conducted for a much shorter time interval. Another possible reason for the discrepancy is that the magnetic shielding may have degraded during transportation of the masers from the manufacturing site to our facility. Unfortunately we cannot duplicate the manufacturer's test conditions in our laboratory because of the proximity of the magnetic-field test chamber to other masers used in the NIST time scale. Therefore, the discrepancy between our measurements and the manufacturer's observations remains unexplained. However, the lower field variations of our tests are more meaningful for our situation since the normal field fluctuations in our laboratory are on the order of  $\pm 1$   $\mu\text{T}$  or less. Except for magnetic field sensitivity, no significant nonlinearity was observed in any of the other environmental sensitivities, even though a range of values in the steps was used.

TABLE 2 - Stability characteristics of NIST environmental chambers

Environmental Parameter	Maser 3 MJD's 50755-50850		Maser 5 MJD's 50710-70805	
	TOTAL Allan Dev. ( $\tau=1$ day)	Std. Dev.	TOTAL Allan Dev. ( $\tau=1$ day)	Std. Dev.
Temperature ( $^{\circ}\text{C}$ )	$16 \times 10^{-3}$	$35 \times 10^{-3}$	$8 \times 10^{-3}$	$25 \times 10^{-3}$
RH (%)	0.14	0.50	0.16	2.29
Pressure (kPa)	0.32	0.53	0.33	0.59
Power-line (V)	0.44	1.01	0.55	1.23
Magnetic field ( $\mu\text{T}$ )	0.05	0.30	0.03	0.15

**IMPACT OF ENVIRONMENTAL FACTORS ON MASER FREQUENCY STABILITY**

In addition to the determination of the maser environmental sensitivities, the stabilities of the environmental parameters in the maser chambers and maser room are also being monitored. Temperature, relative humidity, and vertical magnetic field (the most sensitive axis of the masers) are all monitored in the chambers in which the masers normally operate, while barometric pressure and power-line voltage are monitored in the maser room. The measurements are made every 2 hours. Detailed examples of the characteristics of the various environmental parameters are given in [8]. A two-sample (Allan) variance analysis of the observed environmental parameter fluctuations, along with the measured sensitivities, allows one to estimate the influence of the environment on the observed FM noise of the masers.

Table 2 summarizes the stability characteristics of the five environmental parameters for masers 3 and 5 over two different 95 day periods. The table gives values for

the Allan deviation at  $\tau = 1$  day along with the standard deviation for the entire 95 day period. The same sensors used in the environmental sensitivity tests were used to monitor the environment in the chambers. Since, as discussed earlier, the magnetic field sensors on the masers measure about twice the actual external field changes, the magnetic field values in Table 2 are half the measured variations. The chamber in which maser 5 is housed has no humidity control at this time, which explains the large standard deviation for relative humidity in Table 2. Air flow through this chamber is very slow so the short-term fluctuations in humidity are small, but over the long-term the changes can be large.

Figure 1 shows the TOTAL Allan deviation,  $\sigma_{y,TOTAL}(\tau)$ , of the maser 3 frequency (drift removed) as determined from a 3 corner hat measurement (solid circles). (For details on the TOTAL Allan deviation see [9].) Figure 1 also shows the estimated frequency instabilities caused by the five environmental parameters being monitored (static temperature - hollow squares, humidity - crosses, magnetic field - solid squares, line voltage - solid triangles, and barometric pressure - hollow diamonds) as well as that estimated for the dynamic temperature effect (hollow triangles). These instabilities were determined by calculating the TOTAL Allan deviation of the measured environmental data and then multiplying this by the maser 3 sensitivities in Table 1. For example, the estimated TOTAL Allan deviation at 1 day due to the static temperature effect is obtained by multiplying 0.016 from Table 2 by  $9 \times 10^{-15}$  from Table 1.

In a dynamic temperature effect the frequency change is proportional to the time rate of change of temperature. The estimated Allan deviation due to this effect is obtained by first performing a first difference on the temperature data to obtain a new time series representing temperature changes per unit time. The Allan deviation is then calculated from this new time series and multiplied by the dynamic response observed on the masers. For maser 3 a dynamic response of

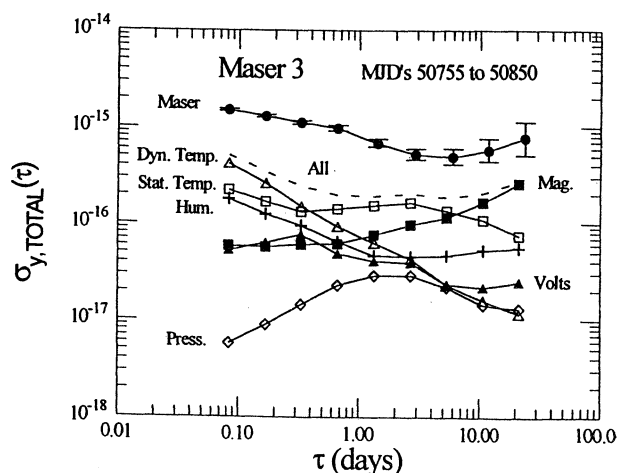


Figure 1 Allan deviation of maser 3, along with environmental contributions.

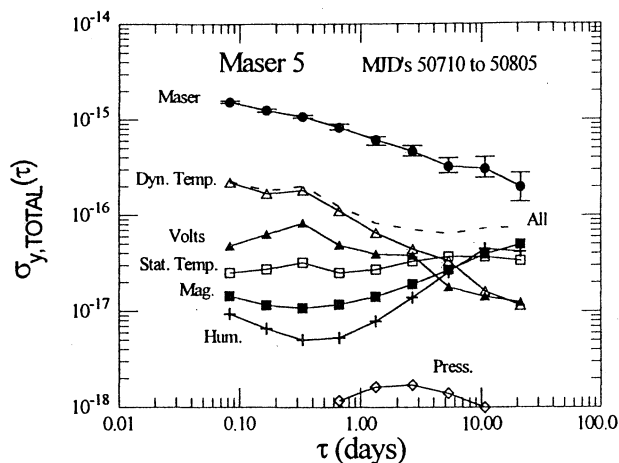


Figure 2 Allan deviation of maser 5, along with environmental contributions.

$1 \times 10^{-14}$  for a  $1^\circ\text{C}$  step was used to calculate the data in Fig. 1. The response time of the maser frequency to a temperature step is on the order of 4 to 6 hours [8]. This obviously has an influence on the two-sample deviation data at intervals less than the response time. However, no attempt was made to correct for this since it is a complicated process and would only result in making a small effect even smaller.

The dashed line in Fig. 1 with no symbols is calculated from the square root of the sum of the squares for all of the environmental parameters and represents the estimated total contribution from environmental factors.

Figure 2 shows the same type of plots for maser 5, one of our most stable masers. The decreasing value of  $\sigma_y(\tau)$  at  $\tau = 20$  days is very likely not real, but caused by drift removal.

Figures 1 and 2 are similar to Figs. 8 and 9 in [8], but these new results are for two different, fully characterized masers, and no estimates of environmental sensitivities had to be made. Though the maser noise levels are as low as  $3$  to  $4 \times 10^{-16}$ , Figs. 1 and 2 show that fluctuations in environmental parameters do not play a significant role in determining the frequency stability of the masers in our laboratory. This is particularly true for maser 5, which generally has very low environmental sensitivities. Temperature and magnetic field fluctuations are the largest contributors, but the resulting frequency fluctuations are more than a factor of 2 below the maser noise. The other environmentally induced fractional frequency fluctuations are generally below  $1 \times 10^{-16}$ . Combining all of the environmental contributions in a root-sum-square process does not change the conclusion. Eliminating the observed environmentally induced frequency fluctuations entirely would produce at most a

10% improvement in maser frequency stability at some values of  $\tau$ .

In Figs. 1 and 2 the general shapes of the curves representing all of the environmental contributions (dashed lines) are similar to that of the maser noise characteristics. Could this be an indication that there is an error in estimating the magnitudes of the environmental effects? This is not likely for several reasons. First of all, the environmental effects have been carefully measured. Second, there is some structure in each of the maser frequency and combined environmental curves that is not consistent. Third, no statistically significant correlations were observed between the environmental parameters and the maser frequencies. However, the similarities in shape may not be totally coincidental. The manufacturer believes that the maser stability beyond about 1000 s (excluding long-term drift due to wall shift) is dominated by cavity pulling and the cavity servo [10]. It is very possible that temperature fluctuations *internal* to the maser caused by convection, conduction, and instabilities in the thermal control circuitry, play a role in determining the maser frequency stability. In this case the static and dynamic temperature effects would be present, and similarly shaped curves would be generated. However, they would be more closely related to the internal environment of the maser than to the external environment. This possibility is consistent with the observation that maser 5, which has the lowest noise levels at 10 days, also has an extra layer of thermal control on the cavity [11].

## CONCLUSIONS

The flicker floors of the best masers in our laboratory are about  $\sigma_y(\tau) = 3$  to  $4 \times 10^{-16}$  at  $\tau$  of a few days, and our analysis indicates that none of the external environmental fluctuations are large enough to be a significant contributor to such frequency fluctuations. This also means that none of the observed environmental parameters can be a significant source of common-mode frequency fluctuations. However, some of the environmental sensitivities are large enough that care must be exercised to ensure that they are not a problem. Generally, temperature and magnetic field sensitivities require the most attention.

## ACKNOWLEDGMENTS

The author acknowledges the valuable assistance of Jim Gray, Trudi Pepler, Laurent Gaudron, and Valentin Hanns, and very useful discussions with Bryan Owings.

## REFERENCES

- [1] T.E. Parker and J. Levine, "Recent Improvements in the Performance of the NIST AT1 Time Scale," in *Proc. 1996 IEEE International Frequency Control Symposium*, pp. 1131-1136, 1996.
- [2] L. A. Breakiron, "Timescale Algorithms Combining Cesium Clocks and Hydrogen Masers," in *Proc. 23rd Annual Precise Time and Time Interval (PTTI) Applications and Planning Meeting*, pp. 297-305, 1991.
- [3] C. Thomas, "Impact of New Clock Technologies on the Stability and Accuracy of the International Atomic Time TAI," *IEEE Trans. Ultrason., Ferroelect., Freq. Contr.*, vol. 44, no. 3, pp. 693-700, 1997.
- [4] Sigma Tau Standards series 2000 cavity-tuned hydrogen masers. Commercial equipment has been identified since it would be impossible to duplicate the results without this information. Such identification does not imply recommendation or endorsement by the National Institute of Standards and Technology.
- [5] W.D. Lee, J.H. Shirley, J.P. Lowe and R.E. Drullinger, "The Accuracy Evaluation of NIST-7," *IEEE Trans. Instrum. Meas.*, vol. IM-44, no. 2, pp. 120-123, 1995.
- [6] R.A. Dragonette and J.J. Suter, "Barometric Pressure Induced Frequency Offsets in Hydrogen Masers," in *Proc. 45th Annual Symposium on Frequency Control*, pp. 586-590, 1991
- [7] T.K. Tucker, "Operating and Environmental Characteristics of Sigma Tau Hydrogen Masers used in the Very Long Baseline Array (VLBA)," in *Proc. 20th Annual Precise Time and Time Interval (PTTI) Applications and Planning Meeting*, pp. 325-336, 1988.
- [8] T.E. Parker, J.E. Gray and T.K. Pepler "Environmental Sensitivities of Cavity-Tuned Hydrogen Masers," in *Proc. 1997 IEEE International Frequency Control Symposium*, pp. 273-279, 1997.
- [9] D.A. Howe, "An Extension of the Allan Variance with Increased Confidence at Long Term," in *Proc. 1995 IEEE International Frequency Control Symposium*, pp. 321-329, 1995.
- [10] H.E. Peters and H.B. Owings "Hydrogen Maser Improvements and Future Applications," in *Proc. 1997 IEEE International Frequency Control Symposium*, pp. 280-285, 1997.
- [11] H.B. Owings, Sigma Tau Standards Corp., 1711 Holt Road, Tuscaloosa, AL 35403, USA, private communication.

## AGING AND ENVIRONMENTAL STABILITY OF OSCILLOQUARZ CS-STANDARDS

K.Kalliomäki<sup>(1)</sup>, T. Mansten<sup>(2)</sup>, A.Rautiainen<sup>(2)</sup>

1) University of Oulu, Department of Electrical Engineering, FIN-90570 Oulu, Finland

2) VTT AUTOMATION, Measurement Technology, P.O. Box 1304, FIN-2044 VTT, Finland

## ABSTRACT

The time scale of Finland is derived from four Cs-clocks: three Oscilloquarz 3210 and a HP 5071A. Oscilloquarz clocks are situated in a special access controlled subterranean facility. Clock phases are compared to GPS-time using different remote measurement techniques. Thus possible annual delay variations of remote measurement systems can be checked. The frequencies of all clocks are drifting into the same direction, even the magnitude ( $-0.04 \dots -0.1 \cdot 10^{-12}$ /year) is quite the same. Environmental factors affect the frequency. In laboratory conditions variation of relative humidity is the most important thing causing nearly 500 ns<sub>pp</sub> annual phase variation.

## INTRODUCTION

The time scale of Finland is derived from four Cs-clocks: three Oscilloquarz 3210 and a HP 5071A. The one year old HP clock belongs to National Standards Lab of Time and Frequency (VTT/AUT).

Oscilloquarz clocks belong to Telecom Finland and their purpose is to provide the main synchronisation source to digital telecommunication networks. Oscilloquarz clocks are situated in a special access controlled subterranean facility about ten kilometres from VTT/AUT. Clocks are situated into the same rack, one on the other.

It is well known that environmental factors affect clock performance. Clocks kept in the same place tend even to behave similarly due to common surroundings, i.e. clocks do not provide independent time or frequency information. Temperature stabilisation is relatively easy but protection against humidity and especially pressure variations is difficult. Those changing environmental factors cause diurnal and annual phase variations. Because most of laboratories use HP Cs-clocks or at least the tube itself is from the same manufacturer, the annual variation may be similar and could be difficult to extract from the data.

However, one can evaluate the effect of those factors to clock performance from observations as-

suming that enough data is available. Minimum data is one year long.

## MEASUREMENT SYSTEM

Local clock monitoring system at Telecom compares the phases of the three Cs-clocks to the TV-frame sync. pulse and to the GPS (Navstar XR5) pps-pulse every ten minutes and transfers time differences via modem connection to VTT/AUT. In addition, 2048 kHz main synchronisation signal derived from those clocks is extracted from optical fibre at VTT telephone exchange and monitored directly at VTT/AUT. Thus there exists three independent ways to monitor those clocks allowing to gather information simultaneously from the diurnal stability of those time links.

In addition to clock phases, temperature, pressure and humidity is monitored.

## RESULTS AND DISCUSSION

Phase difference UT(GPS)-UT(Cs1) during the last four years using optical connection is shown in Fig 1. This curve resembles parabola, indicating frequency drift. The corresponding frequency deviation (10 day average) is shown in Fig 2. From this curve systematic frequency drift and annual frequency variation is clearly visible. Aging seem to be  $-0.1 \cdot 10^{-12}$  per year and annual relative frequency variation  $0.09 \cdot 10^{-12}$  (pp).

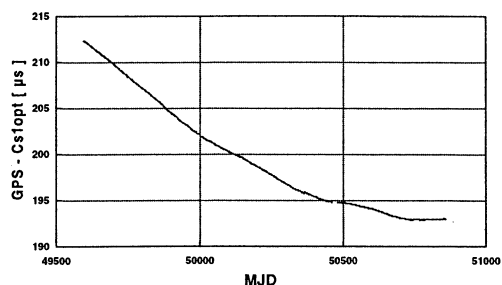


Fig. 1: Telecom Finland, Cs1 phase versus GPS via optical link

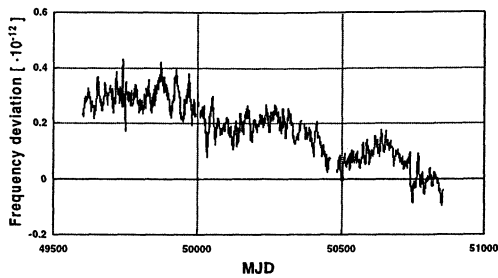


Fig. 2: Telecom Finland, Cs1 frequency via optical link

After applying parabolic regression, the 2<sup>nd</sup> order residuals are plotted into Fig 3. Annual phase variation of 500 ns<sub>pp</sub> is clearly visible.

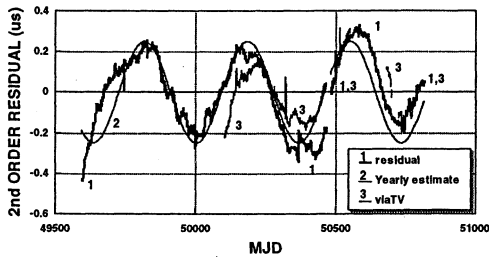


Fig. 3: Telecom Finland, Cs1 phase versus GPS via optical link, 2nd order residual

Cs1 is the main reference, Cs2 and Cs3 work as a reserve. To reduce measurement noise, Cs2 and Cs3 are compared locally to Cs1. As mentioned above, clocks are situated in the same rack, one on the other.

Therefore it is not a surprise that the annual phase fluctuations are similar. Fig 4 shows the differential frequency variations of Cs2 and Cs3, GPS as reference. The relative frequencies of Cs1 and Cs3 are quite the same but frequency of Cs2 is quite far, its sign is even in opposite direction. Cs-clocks are not locked to each other; this fact can be realised from the frequency plot.

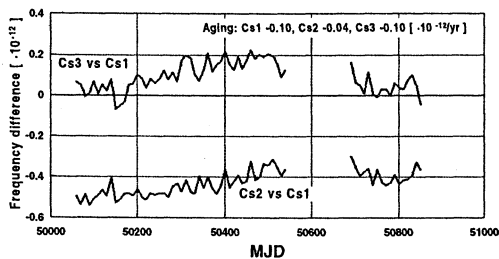


Fig. 4: Telecom Finland, frequency of Cs clocks 1996-1998

As can be seen from the picture, differential variations are negligible as compared to absolute variation. Therefore we have not calculated individual environmental coefficients for all the clocks.

The frequency of Cs1 is drifting;  $-0.1 \cdot 10^{-12}$  per year. This is little bit more than that of our new HP 5071A ( $-0.08 \cdot 10^{-12}$  per year).

Humidity coefficient is quite easy to calculate because humidity variation is slow (annual) allowing long integration time. Relative humidity seem to vary between 20 % (winter) and 60 % (summer) near Oscilloquartz clocks. Humidity is not stable at our National Laboratory too, because air conditioning system is ineffective during hot and wet weather and relative humidity may increase from nominal 40 % to 55 %. The observed humidity coefficient is  $2 \cdot 10^{-15} / \% \text{ RH}$  which seems to be quite the same to our HP 5071A ( $1.5 \cdot 10^{-15} / \% \text{ RH}$ ).

Temperature and pressure coefficients are difficult to calculate reliably. Temperature is quite well stabilised ( $\pm 1 \text{ }^\circ\text{C}$  during two year follow up) and natural pressure variations are too fast compared to measurement resolution of frequency. Our first estimate is  $8 \cdot 10^{-15} / ^\circ\text{C}$  which is surprisingly lower than that of HP 5071A. Pressure coefficients are very vague but the first estimate is  $-0.4 \cdot 10^{-15} / \text{mb}$ . In practise aging and humidity explain practically all phase variations in laboratory conditions.

## REFERENCES

1. Kalliomäki K, Mansten T, 1992, "Control of Environmental and Clock Parameters in Time and Frequency Standards Laboratory", Proc. 6th EFTE, 191-193
2. Kalliomäki K, Mansten T, 1995, "Stability of a Cs-Clock based 2048 kHz Optical ISDN Synchronization Signal", Proc. 9th EFTE, 498-501

**EXTENSION OF THE SECOND HARMONIC LEVEL MONITORING  
IN COMMERCIAL CAESIUM FREQUENCY STANDARDS**

*K. W. Radecki*

Warsaw University of Technology, Institute of Radioelectronics  
Nowowiejska 15/19, 00-665 Warsaw, Poland

**ABSTRACT**

In commercial caesium frequency standards the second harmonic of the caesium tube response is used as a standard health and status indicator [1]. In this paper the extension of the second harmonic amplitude (SHA) monitoring is proposed. It is shown that the SHA variations versus frequency deviation correspond to inverted caesium resonance line. The SHA variations versus frequency deviation were measured in Oscilloquartz caesium beam frequency standard with sine wave modulated microwave interrogation signal, for a set of microwave power levels. In practice it is a good approximation of the shape of highly symmetrical line. Second harmonic level monitoring has high sensitivity to microwave power variations. Extension of measurements for a large number microwave deviations offers additional advantage of line shape monitoring in normal mode of operation (feedback loop is locked) of frequency standard.

In a digital caesium standard it is easy to implement the function „microwave deviation sweep” and the SHA data processing.

**THEORETICAL BACKGROUND**

We consider a conventional thermal caesium beam tube with two identical microwave excitation regions and drift region between them [2]. The signal at the tube output is determined by the Ramsey probability averaged over atomic time of flight distribution across these regions. The central fringe of the Ramsey pattern is given by:

$$U(\lambda) = \int_0^{\infty} \rho(T) \sin^2(b\tau) \cos^2\left(\frac{1}{2}\lambda T\right) dT \quad (1)$$

where  $\rho(T)$  is an atomic time of flight distribution,  $\tau$  and  $T$  are the transit times for an atom across the excitation and drift regions respectively;  $\tau = LT/l$ ,  $L$  is the drift region length,  $l$  is the excitation region length,  $b$  is the Rabi frequency and  $\lambda = \Omega - \Omega_0$  is detuning from the atomic resonance frequency ( $\Omega = 2\pi f$  - microwave angular frequency).

The resonance pattern (1) may be represented by an algebraic polynomial

$$x = 1 + A_2 y^2 + A_4 y^4 + A_6 y^6 + \dots \quad (2)$$

where  $x = U/U_r$  is a normalised output voltage ( $U_r$  is the resonance output voltage),

$y = (f_r - f)/W$  is the normalised frequency detuning from the is the resonant frequency  $f_r$  ( $W$  is the representative line width) and the coefficients  $A_n$  are:

$$A_n = (-1)^{n/2} (2\pi W y)^n \frac{\int_0^{\infty} \rho(T) \sin^2(2b\tau) T^n dT}{2n! \int_0^{\infty} \rho(T) \sin^2(2b\tau) dT}$$

for  $n = 2, 4, \dots$

Further, we assume that the normalised frequency of modulated microwave signal is of the form:

$$y = y_0 + \bar{y}[\sin \omega t + m_2 \sin(2\omega t + \varphi_2) + m_3 \sin(\sin 3\omega t + \varphi_3)] \quad (4)$$

where  $y_0 = (f_r - f_0)/W$  is the normalised offset of the interrogation frequency,  $\bar{y} = \Delta f/W$  is the normalised frequency deviation,  $\omega$  is the modulating angular frequency and  $m_2, m_3$  are the harmonic contents ( $m_2 \ll 1$  and  $m_3 \ll 1$ ).

The spectral components of the output signal of the atomic beam detector may be derived by substituting (4) into (2). The expression (5) given below is correct if intermodulation products with coefficients equal  $m_2 \cdot m_3$  and higher orders may be neglected.

In the case of synchronous detection and six order approximating polynomial the second harmonic amplitude  $\bar{x}_2$  versus microwave deviation  $\bar{y}$  takes form:

$$\begin{aligned} \bar{x}_2 = & \bar{y} \Delta A_1 - \frac{1}{2} \bar{y}^2 (A_2 + \Delta A_2) + \bar{y}^3 \Delta A_3 + \\ & - \frac{1}{2} \bar{y}^4 (A_4 + \Delta A_4) + \bar{y}^5 \Delta A_5 \\ & - \frac{15}{32} \bar{y}^6 (A_6 + \Delta A_6) \end{aligned} \quad (5)$$

where:

$$\begin{aligned} \Delta A_1 = & m_2 \sin \varphi_2 (2A_2 y_0 + 4A_4 y_0^3 + 6A_6 y_0^5) \\ \Delta A_2 = & -2m_3 \cos \varphi_3 (A_2 + 6A_4 y_0^2 + 15A_6 y_0^4) + \\ & + 6A_4 y_0^2 + 15A_6 y_0^4 \end{aligned}$$

$$\begin{aligned}\Delta A_3 &= \frac{3}{2} m_2 \sin \varphi_2 (A_4 y_0 + 20 A_6 y_0^3) \\ \Delta A_4 &= -3 m_3 \cos \varphi_3 (A_4 + A_6 y_0^2) + 15 A_6 y_0^2 \\ \Delta A_5 &= \frac{105}{8} m_2 A_6 y_0 \sin \varphi_2 \\ \Delta A_6 &= -\frac{22}{5} m_3 A_6 \cos \varphi_3\end{aligned}$$

In practice the resonance line may have a small asymmetry and the following terms must be added:

$$\begin{aligned}\Delta A_1' &= m_2 \sin \varphi_2 A_1 + 3 A_3 y_0^2 \\ \Delta A_2' &= -2 m_3 \cos \varphi_3 3 A_3 y_0 + 3 A_3 y_0 \\ \Delta A_3' &= \frac{3}{2} m_2 A_3 \sin \varphi_2\end{aligned}$$

where  $A_1$  and  $A_3$  describes line asymmetry. In the normal mode of operation of frequency standard under lock on condition  $y_0 = y_{0r}$ . The value of  $y_{0r}$  is very small and depends on line asymmetry and the effect of imperfections in the modulation and demodulation processes. In this case the  $y_{0r}$  is sensitive to microwave power level [2] and frequency deviation also [4, 3]. With a properly constructed phase modulator ( $m_2 \ll 1, m_3 \ll 1$ ), small line asymmetry ( $A_1 \ll 1, A_3 \ll 1$ ) the terms  $\Delta A$  in equation (5) may be neglected. For example for  $m_2 = m_3 \leq 10^{-4}$ , line factor  $Q = 2.5 \cdot 10^7$  and  $\bar{y} < 1$ , the level of neglected terms  $\Delta A_{2n}$  is 70 dB below the value of the coefficients  $A_{2n}$ . Therefore equation (5) takes the form:

$$\bar{x}_2 = -\frac{1}{2} \bar{y}^2 A_2 - \frac{1}{2} A_4 \bar{y}^4 - \frac{15}{32} A_6 \bar{y}^6 \quad (6)$$

From equations (6) and (2) we see that the SHA variations versus microwave deviation correspond to inverted caesium resonant line. Comparing these equations we can notice that for a linear phase modulator and  $y = \bar{y}$ ,

$$x \approx x' = 1 - 2\bar{x}_2 \quad (7)$$

The difference is  $x - x' = 6.25 \cdot \bar{y}^6 A_6 \%$  (better conformance may be achieved with higher order approximation of the resonance line shape)

## EXPERIMENTAL RESULTS

The second harmonic amplitude versus amplitude of modulating signal were measured in Oscilloquartz caesium beam frequency standard (model 3200 with FTS caesium beam tube) for a set of microwave power. It was verified that the characteristic of phase modulator is linear up to frequency deviation 380 Hz.

Examples of these measurements, made by means of lock-in nanovoltmeter, are shown in Fig.1. Each curve corresponds to the resonance line shown in Fig.2.  $\Delta P = 0$  dB corresponds to the largest possible value of Ramsey peak response. The level of microwave power in manufactured caesium tube is standardised to about 2 dB less than for maximum beam tube signal.

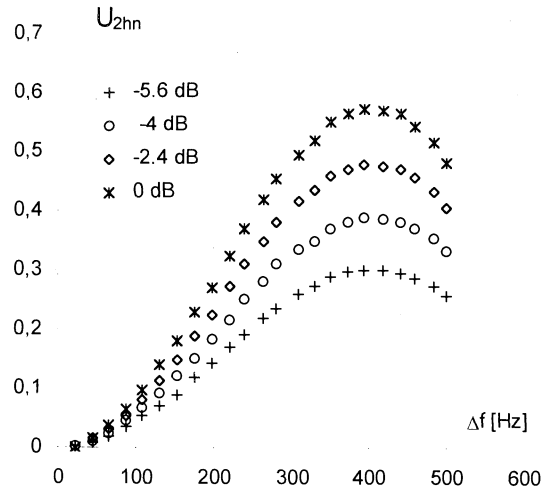


Fig.1. Second harmonic amplitude versus frequency deviation for various microwave power levels  $\Delta P$

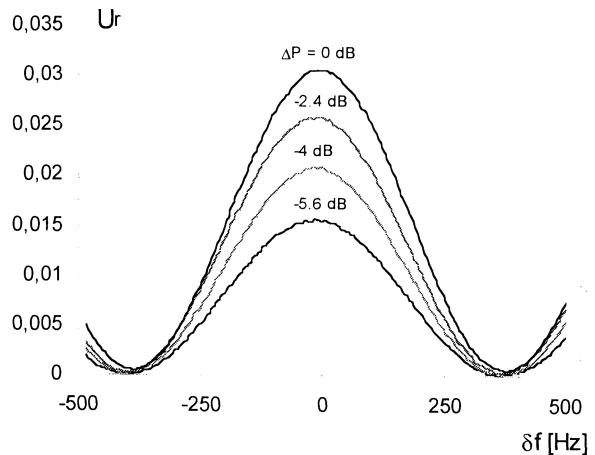


Fig.2. Variation of beam tube response for various microwave power levels  $\Delta P$

The SHA variations versus microwave deviation were compared with appropriate inverted resonance line shape. In Fig.3 is shown the comparison of normalised the SHA and the resonance line for

$\Delta P = -2.4$  dB. The normalisation to unity was done for both curves and  $\delta f = \Delta f = 280$  Hz. The SHA fairly good approximates measured line up to 400 Hz (linear characteristic of modulator)

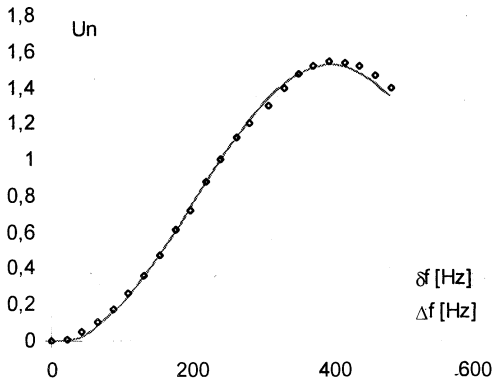


Fig.3. Comparison the SHA versus frequency deviation  $\Delta f$  (continuous line) and inverted Ramsey response (points) for  $\Delta P = -2.4$  dB.

Fig.4 shows the dependency of SHA on microwave power level measured for various frequency deviations. Each of curve reaches the maximum for the power  $\Delta P = 0$  as described above (Fig.1). The peak of SHA is somewhat narrower and more symmetrical (not shown here) than the beam current peak (DC level).

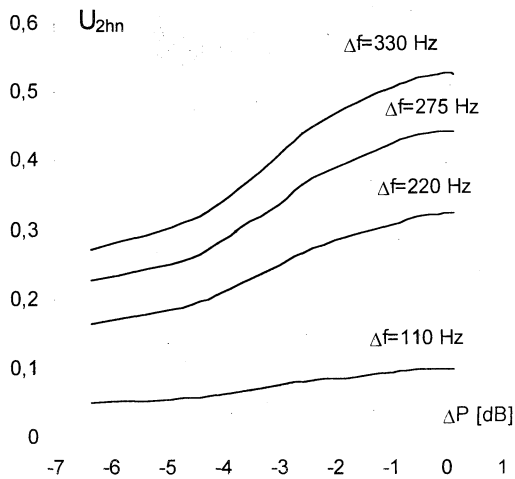


Fig4. Variation of the SHA versus microwave power level  $\Delta P$  for various frequency deviations  $\Delta f$

## CONCLUSIONS

We have shown that the extension of measurements of the second harmonic amplitude for a large number microwave deviations offers an additional advantage of the Ramsey response monitoring in normal mode of operation of frequency standard. The SHA curve versus frequency deviation approximates highly

symmetrical beam tube response for sine-wave frequency modulation well. In the case of square wave frequency modulation the SHA dependency also approximates the Ramsey response but in narrower range of frequency deviation (Appendix).

Monitoring of the SHA at the output of a caesium beam tube versus frequency deviation allow to distinguish influence of power level changes from other situations (like ionizer temperature and preamplifier gain changes) because the slope of the SHA can be analysed.

It seems that the digital servos can stabilise the interrogation power level by analysing the slope of the SHA or maximising the SHA versus power response of the tube. Implementation of the function „microwave deviation sweep” and SHA data processing could be easy in commercial digital caesium standard.

## APPENDIX

Square wave frequency modulation is best achieved by switching the interrogation frequency between two values obtained in frequency synthesiser.

The normalised frequency of square wave modulated interrogation signal is given by:

$$y = y_0 + \bar{y}g(t) \quad (8)$$

where  $g(t)$  is the modulation function defined as

$$g(t) = \begin{cases} +1, & \text{for } 0 < t < \frac{T}{2} \\ -1, & \text{for } \frac{T}{2} < t < T \end{cases}$$

$T$  is the modulation period,  $y_0$  is the normalised offset of the interrogation frequency and  $\bar{y}$  is the normalised frequency deviation.

The SHA may be derived by inserting the value of frequency  $y$  (8) into equation (2). When the line asymmetry is small ( $A_1 \ll 1$ ,  $A_3 \ll 1$ ), offset  $y_0 = 0$ , the resonance pattern is represented by an algebraic polynomial (2) and modulation function is approximated by a sum of odd harmonics (up to eleven harmonic of the modulation frequency), the amplitude  $\bar{x}_2$  takes form:

$$\bar{x}_2 = (-7.4\bar{y}^2 A_2 - 3.3\bar{y}^4 A_4 + 4.9\bar{y}^6 A_6) \cdot 10^{-2} \quad (9)$$

Then we can choose the following approximation of the resonance pattern:

$$x' = 1 - 13.5\bar{x}_2 = 1 + A_2\bar{y}^2 + 0.45\bar{y}^4 A_4 - 0.66\bar{y}^6 A_6 \quad (10)$$

Comparing the expressions (10) with (2) we see that the SHA curve versus frequency deviation can approximate well the inverted resonance line near the resonant frequency only (for frequency deviations smaller than the half line width).

#### REFERENCES

1. Jaduszwiler B and Hurrell J.P, 1994,"Second Harmonic Level Monitors in Cesium Atomic Frequency Standards", IEEE Int. Freq. Symp. Control, 769-775
2. Vanier J and Audoin C, 1989, The Quantum Physics of Atomic Frequency Standards, A.Hilger, Bristol
3. Hahn, S.L, 1970,"Analysis of Modulation Method for Measuring Atomic Resonant Frequency", IEEE Trans. Instrum. Meas., IM-19, 209-215
4. Radecki K.W, 1993,"A method of the resonant line analysis in a cesium beam frequency standard under operation conditions", VII Polish National Symp. Radio Science URSI, Gdansk, 17-20.



*12th E F T F* - 10-12 March 1998 - **Warsaw - POLAND**

**Oscillators I**

Chairman:

*Michael J. Underhill*



## NONLINEAR ANALYSIS OF NOISE IN QUARTZ CRYSTAL OSCILLATORS

R. Brendel, N. Ratier, L. Couteleau, G. Marianneau, P. Guillemot\*

Laboratoire de Physique et Métrologie des Oscillateurs du CNRS

associé à l'Université de Franche-Comté-Besançon - 32, avenue de l'Observatoire - 25044 Besançon Cedex - France

\*Centre National d'Etudes Spatiales - 18, avenue Edouard Belin - 31055 Toulouse Cedex - France

### ABSTRACT

By using formal manipulation capability of commercially available symbolic calculation code, it is possible to automatically derive the characteristic polynomial describing the oscillation condition of a circuit. The analytical expression of the characteristic polynomial is obtained through a successive encapsulation process starting from the SPICE netlist description of the circuit. In this method, the nonlinear component is described by its large signal admittance parameters obtained from a set of SPICE transient simulations of larger and larger amplitude.

The encapsulation process involving linear and nonlinear components as well as noise sources leads to a perturbed characteristic polynomial.

In the time domain, the perturbed characteristic polynomial becomes a nonlinear non autonomous differential equation. By using an extension of the slowly varying function method, this differential equation is transformed into a nonlinear differential system with perturbation terms as the right hand side.

Eventually, solving this system with classical algorithms allows to obtain both amplitude and phase noise spectra of the oscillator.

### INTRODUCTION

Steady state and transient behaviour of quartz crystal oscillators can be obtained by using the nonlinear characteristic polynomial method stemmed from a generalization of the popular Barkhausen criterion method [1, 3]. The oscillation condition of a circuit is described by a polynomial in the Laplace's variable whose coefficients are expressed in terms of the circuit components some of them depending on the signal amplitude. Solving this nonlinear polynomial in the frequency domain leads to the steady state oscillation amplitude and frequency. In the time domain, the characteristic polynomial expresses the nonlinear differential equation the solution of which gives the signal transient [4, 5].

Because of the large number of oscillator circuit components, this method cannot be managed by hand. Thus, a dedicated program calling for a symbolic calculation software has been developed so as to automatically generate the characteristic polynomial directly from a SPICE description netlist [6].

Solving the nonlinear differential equation in the time domain may lead to unacceptable computer time because of the high quality factor involved in the quartz oscillator circuits. Asymptotic method, like the slowly varying function method, can be used to overcome this difficulty: the initial nonlinear differential equation is transformed into a first order nonlinear differential system in the amplitude and phase variables. Because this associated system involves much slower functions than the initial differential equation, it can be solved much faster by using classical numerical algorithms.

This method has been demonstrated to accurately predict the oscillator transient behaviour. These accurate method and model have been extended to the study of noise mechanism in the oscillating loop. By using an automatic symbolic reduction method similar to the one used to derive the characteristic polynomial, the circuit, and the different noise sources located inside, are progressively transformed in a reduced circuit. At each step of the transformation process, new components and their associated noise source are encapsulated into an equivalent circuit. The parameters of this new circuit are expressed in terms of the new component introduced and the previous step parameters. At each step, these symbolic functions and their transformation equations are coded and stored so that, at the end of the reduction process one obtains the perturbed characteristic polynomial, the perturbation terms coming from the various noise sources spread out in the circuit.

### NOISE SOURCES IN OSCILLATORS

Perturbation sources in electronic circuits may be divided into two categories:

- Macroscopic noise coming from environmental perturbations like temperature fluctuation, vibration, electromagnetic influence, etc.
- Microscopic noise originating in the random motion of carriers in the components, in this category fall the thermal noise in resistive components and the shot noise in semi conductor junctions.

From the designer point of view, the noise sources may act on the oscillator frequency through two main mechanisms:

- Additive noise, in this case the perturbation source can be modeled by voltage or current generators associated with some circuit components. In the particular case of quartz crystal oscillator, the high quality factor of the resonator makes the circuit strongly selective so that only noise Fourier components near the oscillation frequency have to be considered.
- Parametric noise, so called because it affects the value of the component itself and therefore the frequency of the oscillator which depends on all circuit parameters. Parametric noise mainly comes from macroscopic effect like temperature fluctuation, ionizing effect, etc. Its effect results in an oscillation frequency modulation so that only very low noise Fourier components whose modulation lines are located near the carrier have a significant contribution.

### NOISE SOURCE MODELING

Noise sources are modeled according to their nature. For additive noise, they appear under the form of a current generator in parallel with resistive components (Fig. 1) or at the input and output ports of the active device (Fig. 2).

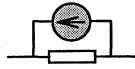


Fig. 1.

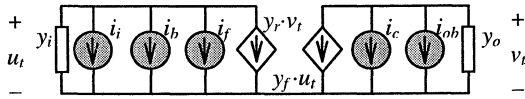


Fig. 2.

The thermal noise source mean square current is given by:

$$\overline{i_n^2} = 4kTG \cdot \Delta f \quad (1)$$

Where  $k$  is Boltzmann's constant,  $T$  the absolute temperature,  $G$  the conductance of the component and  $\Delta f$  the effective band pass.

The shot noise source mean square current is given by:

$$\overline{i_s^2} = 2qI \cdot \Delta f \quad (2)$$

Where  $q$  is the electron charge,  $I$  the bias current of the junction and  $\Delta f$  the effective bandpass.

In the case of parametric noise, the value of the component is modulated by some internal or external mechanism so that it can be represented by a

polynomial expression. For example, under temperature fluctuation, a resistor should exhibit parametric noise given by :

$$R = R_0 (1 + \alpha_R \cdot \Delta T(t)) \quad (3)$$

Where  $R_0$  is the nominal resistor value,  $\alpha_R$  the linear temperature coefficient and  $\Delta T(t)$  the temperature vs. time function.

### REDUCTION PRINCIPLE

When all perturbation sources have been identified and modeled, the oscillator circuit looks like Fig. 3 where parametric noise is represented by an arrow through a components.

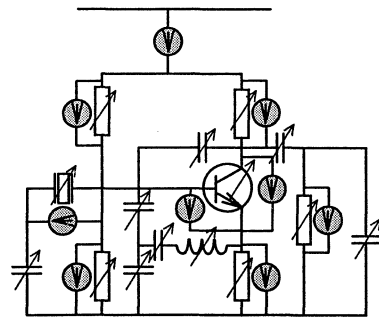


Fig. 3.

Automatic formal equation derivation needs systematic reduction process analogous to the one used for the unperturbed oscillator [7]. In this method, because of its particular role in the oscillator behavior, the resonator is left out of the reduction process, and by successive encapsulations, the remaining amplifier circuit is reduced to the form shown in Fig. 4

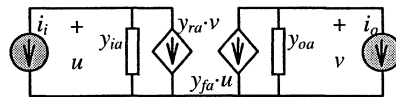


Fig. 4.

The four parameters  $y_{ia}$ ,  $y_{fa}$ ,  $y_{ra}$  and  $y_{oa}$  represent the unperturbed amplifier y-parameters while  $i_i$  and  $i_o$  represent the equivalent reduced noise sources. All parameters in Fig. 4 are in fact symbolic rational functions in the Laplace's variable  $s$  expressed in terms of the initial circuit components and noise sources. The reduction process starts with the identification of elementary transforms like series or parallel associations or star-to-triangle transforms. When all elementary transforms have been performed, the circuit is reduced to the form shown in Fig. 4, by using a limited number of simple transformations represented in Fig. 5.

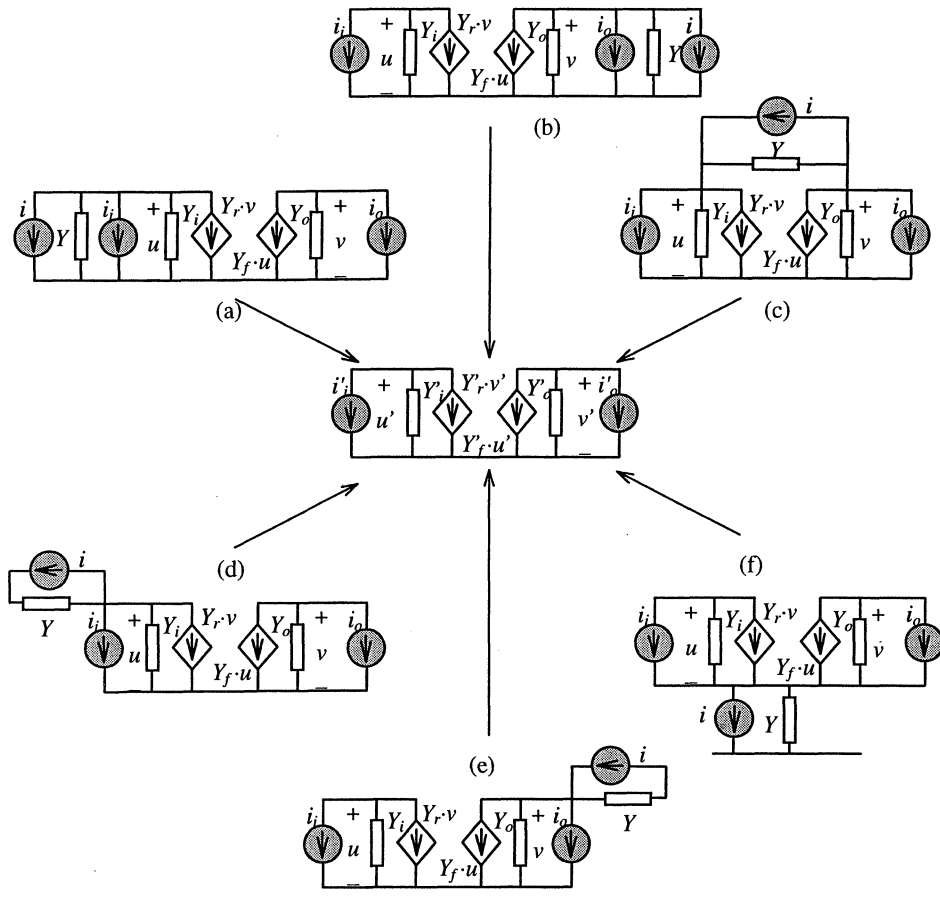


Fig. 5.

At each step of the reduction process, a new circuit component is introduced in the equivalent circuit and the parameters of the new equivalent circuit are expressed in terms of the former ones and the new component. Meantime, the input and output voltage and the input and output noise source current of the new circuit are expressed in terms of the former ones.

**OSCILLATION CONDITION**

When all transformation steps are completed, the resonator is put back in the circuit where it may occupy one of the three basic positions shown in Fig. 6.

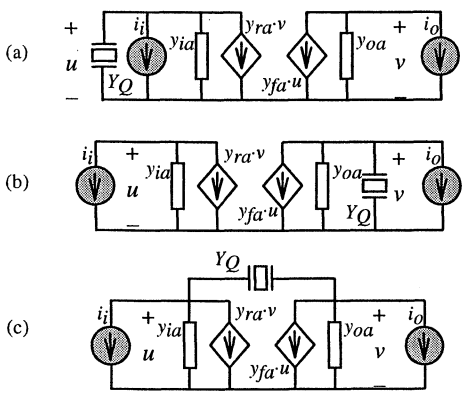


Fig. 6.

By an ultimate transform summarized in Table I, the oscillator circuit is reduced to the form shown in Fig. 7.

Table I.

	$Y_i$	$Y_r$	$Y_f$	$Y_o$	$V_Q$
(a)	$y_{ia} + Y_Q$	$y_{ra}$	$y_{fa}$	$y_{oa}$	$u$
(b)	$y_{ia}$	$y_{ra}$	$y_{fa}$	$y_{oa} + Y_Q$	$v$
(c)	$y_{ia} + Y_Q$	$y_{ra} - Y_Q$	$y_{fa} - Y_Q$	$y_{oa} + Y_Q$	$u - v$

	Amplifier gain	Oscillation condition
(a)	$\frac{y_{fa} \cdot i_i - (y_{ia} + Y_Q)i_o}{y_{ra} \cdot i_o - y_{oa} \cdot i_i}$	$(\Delta y_a + y_{oa} \cdot Y_Q)u = y_{ra} \cdot i_o - y_{oa} \cdot i_i$ $(\Delta y_a + y_{oa} \cdot Y_Q)v = y_{fa} \cdot i_i - (y_{ia} + Y_Q)i_o$
(b)	$\frac{y_{fa} \cdot i_i - y_{ia} \cdot i_o}{y_{ra} \cdot i_o - (y_{oa} + Y_Q)i_i}$	$(\Delta y_a + y_{ia} \cdot Y_Q)u = y_{ra} \cdot i_o - (y_{oa} + Y_Q)i_i$ $(\Delta y_a + y_{ia} \cdot Y_Q)v = y_{fa} \cdot i_i - y_{ia} \cdot i_o$
(c)	$\frac{(y_{fa} - Y_Q)i_i - (y_{ia} + Y_Q)i_o}{(y_{ra} - Y_Q)i_o - (y_{oa} + Y_Q)i_i}$	$(\Delta y_a + y_{sa} \cdot Y_Q)u = (y_{ra} - Y_Q)i_o - (y_{oa} + Y_Q)i_i$ $(\Delta y_a + y_{sa} \cdot Y_Q)v = (y_{fa} - Y_Q)i_i - (y_{ia} + Y_Q)i_o$
	$y_{sa} = y_{ia} + y_{ra} + y_{fa} + y_{oa}$	$\Delta y_a = y_{ia} \cdot y_{oa} - y_{ra} \cdot y_{fa}$

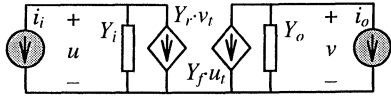


Fig. 7.

Under this form, the oscillation condition can be obtained by writing down the equilibrium condition of the circuit:

$$\begin{cases} Y_i \cdot u + Y_r \cdot v = -i_i \\ Y_f \cdot u + Y_o \cdot v = -i_o \end{cases} \quad (4)$$

Solving this system with respect input and output voltages  $u$  and  $v$  leads to the oscillation condition equations:

$$\begin{cases} \Delta Y \cdot u = Y_r \cdot i_o - Y_o \cdot i_i \\ \Delta Y \cdot v = Y_f \cdot i_i - Y_i \cdot i_o \end{cases} \quad \Delta Y = Y_i Y_o - Y_r Y_f \quad (5)$$

As previously mentioned, all parameters and current sources in the reduced circuit of Fig. 7. are in fact rational functions of the initial circuit components in the Laplace's variable  $s$  so that in the time domain the oscillation condition represents in fact a nonlinear differential system.

Note that under this form it is possible to take into account the resonator isochronism defect given by [8]:

$$f_q = f_{q0}(1 + \alpha \cdot Pa) \quad (6)$$

Where  $f_q$  is the actual resonant frequency,  $f_{q0}$  is the natural low power resonant frequency and  $\alpha$  the isochronism defect parameter. The active power in the crystal is obtained by:

$$P_a = \frac{1}{2} \Re e(Y_Q) \cdot |V_Q|^2 \quad (7)$$

Where  $Y_Q$  is the series branch admittance of the resonator and  $V_Q$  the voltage across the resonator (see Table I).

## SLOWLY VARYING FUNCTION METHOD FOR PERTURBED OSCILLATORS

As for the unperturbed oscillator transient analysis [4], because of the high quality factor involved in the oscillator circuit, the oscillation condition can be put under the form of a quasi harmonic integro-differential equation of the form:

$$\ddot{x} + \omega_0^2 x = \lambda h(x, \dot{x}, \ddot{x}, x, \dots, t) \quad (8)$$

where  $x$  is the chosen variable (e.g. transistor input voltage),  $\dot{x}$ ,  $\ddot{x}$  are derivatives with respect to time  $\dot{x} = s \cdot x = dx/dt$ ,

$\underline{x}$ ,  $\underline{\underline{x}}$  are primitives with respect to time  $\underline{x} = \frac{x}{s} = \int x \cdot dt$

$\lambda$  is so-called *small parameter* which determines the closeness of the system to a linear conservative system.

Resolution of this kind of equation can be performed by using asymptotic method like the slowly varying function method [9, 10]. In the present case, the right hand side of the equation exhibits non autonomous terms coming from the noise sources. These terms, which depend explicitly on time, need to be specified. Because they represent noise source effects, their amplitude is assumed to be small enough so that perturbation method can be used. Furthermore, any time signal being expandable in Fourier series, it is possible to restore the overall output spectrum from the envelope of the system response to the individual Fourier components of the excitation signal. Thus the non autonomous terms in the oscillation equation can be separated from the autonomous part and the equation takes the form:

$$\ddot{x} + \omega_0^2 x = \lambda f(x, \dot{x}, \ddot{x}, x, \dots) + \alpha \omega_0^2 \sin \omega t + \beta \omega_0^2 \cos \omega t \quad (9)$$

In this equation,  $\omega$  represents the actual Fourier frequency of the perturbation source (which is different from the natural oscillation frequency  $\omega_0$ ),  $\alpha \omega_0^2$  and  $\beta \omega_0^2$  are the small amplitude of the Fourier component which, in the general case, depend on the Fourier frequency  $\omega$

As in the case of unperturbed equation, the initial oscillation second order equation is transformed into a first order equation system by using the variable change:

$$x = y \cos \psi \quad \text{where} \quad \psi = \omega_0 t + \varphi \quad (10)$$

$y(t)$  and  $\varphi(t)$  are respectively the amplitude and phase of the quasi sinusoidal solution  $x(t)$  of the initial system and are slowly varying time functions. Under this form, the instantaneous oscillation frequency is the derivative with respect to time of the total phase  $\varphi(t)$ .

It can be shown that the variable change leads to the following system:

$$\begin{cases} \dot{y} = \frac{-\lambda}{\omega_0} f(y, \psi) \sin \psi - g_y(t) \\ y \dot{\varphi} = \frac{-\lambda}{\omega_0} f(y, \psi) \cos \psi - g_\varphi(t) \end{cases} \quad (11)$$

$$\begin{cases} g_y(t) = \alpha \omega_0 \sin \omega t \sin \psi + \beta \omega_0 \cos \omega t \sin \psi \\ g_\varphi(t) = \alpha \omega_0 \sin \omega t \cos \psi + \beta \omega_0 \cos \omega t \cos \psi \end{cases}$$

Because  $y$  and  $\varphi$  are slowly varying functions, in the first order approximation in  $\lambda$ , these quantities keep the same value for one period of the signal so that it is possible to get a simplified form of the initial system

by averaging all terms over one period of the signal e.g.:

$$\dot{y} = \bar{\dot{y}} = \frac{1}{T_0} \int_0^{T_0} \dot{y}(t) dt + O(\lambda^2) \quad (12)$$

In the case of additive noise, as previously stated, only noise Fourier components close from the oscillation frequency have a significant contribution. Thus, the excitation frequency can be taken under the form:

$$\omega = \omega_0 + \Omega \quad \text{with} \quad \Omega \ll \omega_0$$

Averaging the system over one period of the signal and keeping only first order terms, leads to the so called associated system:

$$\begin{cases} \dot{y} = \frac{-\lambda}{\omega_0} F_y(y, \psi) - G_y(t) \\ y\dot{\psi} = \frac{-\lambda}{\omega_0} F_\psi(y, \psi) - G_\psi(t) \end{cases} \quad (13)$$

where:

$$\begin{cases} G_y(t) = \frac{\alpha\omega_0}{2} \cos(\Omega t - \varphi) - \frac{\beta\omega_0}{2} \sin(\Omega t - \varphi) \\ G_\psi(t) = \frac{\alpha\omega_0}{2} \sin(\Omega t - \varphi) + \frac{\beta\omega_0}{2} \cos(\Omega t - \varphi) \\ F_y(y, \psi) = \frac{1}{2\pi} \int_0^{2\pi} f(y, \psi) \sin \psi d\psi \\ F_\psi(y, \psi) = \frac{1}{2\pi} \int_0^{2\pi} f(y, \psi) \cos \psi d\psi \end{cases} \quad (14)$$

Note that when the perturbation terms do not exist ( $\alpha = \beta = 0$ ) the associated system becomes identical to the unperturbed associated system [4].

### SIMPLE COLPITTS OSCILLATOR

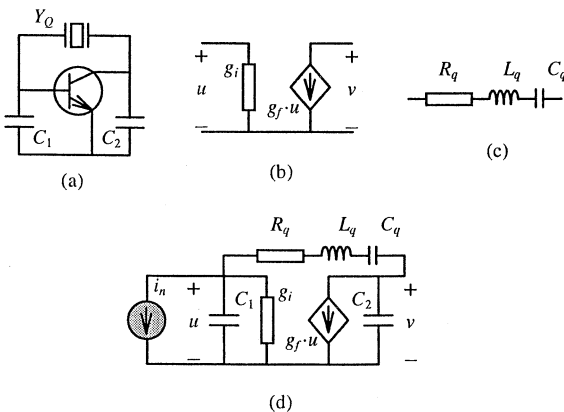


Fig. 8.

So as to demonstrate how the slowly varying amplitude and phase method can be used to obtain the oscillation transient and the noise spectrum of a circuit, let us consider the circuit shown in Fig. 8a in which components are reduced to their simplest equivalent

form (Fig. 8b and 8c). The dynamical equivalent circuit is represented in Fig. 8d.

So as not to obscure the purpose with unnecessary complicated expressions, the noise source is assumed to be an independent current source  $i_n$  located at the amplifier input port. Remember that the large signal transistor parameter  $g_i$  and  $g_f$  depend on the transistor input voltage amplitude  $y$  (Fig. 9).

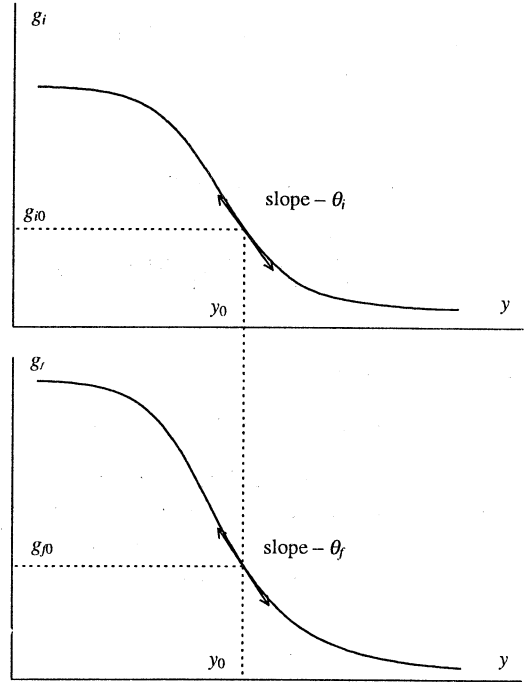


Fig. 9.

Referring to Table I, the transistor input voltage  $u$  obeys the oscillation condition:

$$(\Delta y_a + y_{sa} \cdot Y_Q) \cdot u = -(y_{oa} + Y_Q) \bar{i}_n \quad (15)$$

Where  $\bar{i}_n$  is the root mean square amplitude of the noise source current.

Developing and ordering all terms of this equation so as to put the smallest of them at the right hand side leads to the initial differential equation.

$$\begin{aligned} \ddot{u} + \omega_0^2 u = & - \left[ \frac{\omega_q}{Q_q} + \frac{g_i}{C_1} \right] \dot{u} - \frac{g_i \omega_q}{Q_q C_1} u - \left[ \frac{\omega_q^2 g_i}{C_1} + \frac{g_i + g_f}{L_q C_1 C_2} \right] u \\ & - \frac{1}{C_1} \dot{\bar{i}}_n - \frac{\omega_q}{Q_q C_1} \bar{i}_n - \omega_q^2 \left( 1 + \frac{C_q}{C_2} \right) \bar{i}_n \end{aligned} \quad (16)$$

In this equation  $\omega_q$  and  $Q_q$  are respectively the series branch resonant frequency and the unloaded  $Q$  of the resonator.

The natural frequency  $\omega_0$  is given by:

$$\omega_0^2 = \omega_q^2 + \frac{C_1 + C_2}{L_q C_1 C_2} \quad (17)$$

Eq. (16) then looks like the general form (8):

$$\ddot{u} + \omega_0^2 u = \lambda f(u, \dot{u}, u) + g(t) \quad (18)$$

Where  $g(t)$  is the perturbation term.

Assuming that the noise source  $\bar{i}_n$  is an harmonic current generator of the form:

$$\bar{i}_n = i_0 \cos \omega t$$

The perturbation term takes the form:

$$g(t) = \frac{i_0}{C_1 \omega} \left[ 1 - \frac{i_0 \omega_q^2}{\omega^2} \left( 1 + \frac{C_q}{C_2} \right) \right] \sin \omega t - \frac{\omega_q i_0}{Q_q C_1} \cos \omega t \quad (19)$$

which is of the form:

$$g(t) = \alpha \omega_0^2 \sin \omega t + \beta \omega_0^2 \cos \omega t \quad (20)$$

By using the slowly varying function method described in the previous section and considering only the Fourier components close to the oscillation frequency, the associated system can be expressed as:

$$\begin{cases} \dot{y} = \frac{y}{2} \left[ \frac{1}{\omega_0^2 L_q C_1} \left( \frac{g_f}{C_2} - \frac{g_i}{C_1} \right) - \frac{\omega_q}{Q_q} \right] - G_y(t) \\ y \dot{\phi} = \frac{g_i \omega_q y}{2 \omega_0 Q_q C_1} - G_\phi(t) \\ G_y(t) = \frac{\alpha \omega_0}{2} \cos(\Omega t - \varphi) - \frac{\beta \omega_0}{2} \sin(\Omega t - \varphi) \\ G_\phi(t) = \frac{\alpha \omega_0}{2} \sin(\Omega t - \varphi) + \frac{\beta \omega_0}{2} \cos(\Omega t - \varphi) \end{cases} \quad (21)$$

with

$$\begin{aligned} \alpha \omega_0 &= \frac{i_0 \omega}{C_1 \omega_0} \left[ 1 - \frac{\omega_q^2}{\omega^2} \left( 1 + \frac{C_q}{C_2} \right) \right] \\ \beta \omega_0 &= - \frac{i_0 \omega_q}{C_1 \omega_0 Q_q} \\ \omega &= \omega_0 + \Omega \end{aligned} \quad (22)$$

## PERTURBATION METHOD

The steady state is obtained by solving the unperturbed system given by:

$$\begin{cases} \dot{y} = \frac{y}{2} \left[ \frac{1}{\omega_0^2 L_q C_1} \left( \frac{g_f}{C_2} - \frac{g_i}{C_1} \right) - \frac{\omega_q}{Q_q} \right] \\ \dot{\phi} = \frac{g_i \omega_q}{2 \omega_0 Q_q C_1} \end{cases} \quad (23)$$

When the steady state is reached, the amplitude  $y$  becomes constant so that  $\dot{y} = 0$ , Eq. (23) shows that this happens for the amplitude  $y_0$  such that:

$$\frac{g_{fo}}{C_2} - \frac{g_{io}}{C_1} = \omega_0^2 R_q C_1 \quad (24)$$

Where  $g_{fo} = g_f(y_0)$  and  $g_{io} = g_i(y_0)$  (see Fig. 9). In this case, the oscillator exhibits a frequency offset given by the second equation (23):

$$v_0 = \dot{\phi}(y_0) = \frac{g_{io} \omega_q}{2 \omega_0 Q_q C_1} \quad (25)$$

Thus, the unperturbed steady state oscillation frequency is given by:

$$\omega_s = \omega_0 + v_0 \quad (26)$$

Because noise usually deals with very small amplitude excitation terms its effect on the oscillation signal can be expected to be obtained by using perturbation method in the vicinity of the steady state. Thus, the amplitude  $y$  in Eq. (21) will take the form:

$$y = y_0 + z(t) \quad (27)$$

The amplitude  $\bar{z}$  of the perturbation  $z(t)$  being much smaller than the unperturbed steady state amplitude ( $\bar{z} \ll y_0$ ).

Furthermore, the second equation (21) gives the frequency perturbation which take the form:

$$\dot{\phi} = v_0 + v(t) \quad (28)$$

As for the signal amplitude, the frequency perturbation amplitude  $\bar{v}$  of  $v(t)$  is much smaller than the unperturbed steady state oscillation frequency  $\omega$  ( $\bar{v} \ll \omega_s$ ).

By looking at Fig. 9 we can see that for small amplitude perturbations, the nonlinear transistor parameters  $g_i$  and  $g_f$  can be expanded in Taylor's series around the unperturbed steady state amplitude:

$$\begin{cases} g_i = g_{io} - \theta_i \cdot z \\ g_f = g_{fo} - \theta_f \cdot z \end{cases} \quad (29)$$

where  $-\theta_i$  and  $-\theta_f$  are the slopes of  $g_i(y)$  and  $g_f(y)$  at  $y = y_0$ .

Putting expressions (27), (28) and (29) into (21) taking into account steady state conditions (24) and (25) and keeping only first order terms leads to the perturbation system :

$$\begin{cases} \dot{z} + \lambda\omega_0 z = -\frac{\alpha\omega_0}{2} \cos(\Omega t - \varphi) + \frac{\beta\omega_0}{2} \sin(\Omega t - \varphi) \\ v = -\varepsilon\omega_0 z - \frac{\alpha\omega_0}{2y_0} \sin(\Omega t - \varphi) - \frac{\beta\omega_0}{2y_0} \cos(\Omega t - \varphi) \end{cases} \quad (30)$$

where:

$$\begin{aligned} \lambda\omega_0 &= \frac{y_0}{2\omega_0^2 L_q C_1} \left( \frac{\theta_f}{C_2} - \frac{\theta_i}{C_1} \right) \\ \varepsilon\omega_0 &= \frac{\theta_i \omega_q}{2\omega_0 Q_q C_1} \end{aligned} \quad (31)$$

## FREQUENCY AND AMPLITUDE PERTURBATION

It can be shown that the solution of the perturbation system (30) can be expressed under the form of a signal modulated both in frequency and amplitude. The modulation frequency  $\Omega_m$  is equal to the difference between the excitation frequency  $\Omega$  and the frequency offset  $\nu_0$ :

$$\Omega_m = \Omega - \nu_0 \quad (32)$$

So that the frequency perturbation can be taken as:

$$v = \bar{v} \cos \Omega_m t \quad (33)$$

while the amplitude perturbation is expressed as:

$$z = \bar{z} (\cos \Omega_m t - \varphi_a) \quad (34)$$

Where  $\varphi_a$  represents the phase shift between frequency and amplitude modulations. Assuming small modulation factor and index it is possible to obtain the expression of the amplitude and frequency modulation amplitudes:

$$\bar{z}^2 = \frac{1}{4} \frac{(\alpha\omega_0)^2 + (\beta\omega_0)^2}{(\lambda\omega_0)^2 + \Omega_m^2} \quad (35)$$

$$\bar{v}^2 = \frac{\bar{z}^2}{y_0^2} \left[ (\lambda\omega_0)^2 + (\Omega_m - y_0 \varepsilon \omega_0)^2 \right] \quad (36)$$

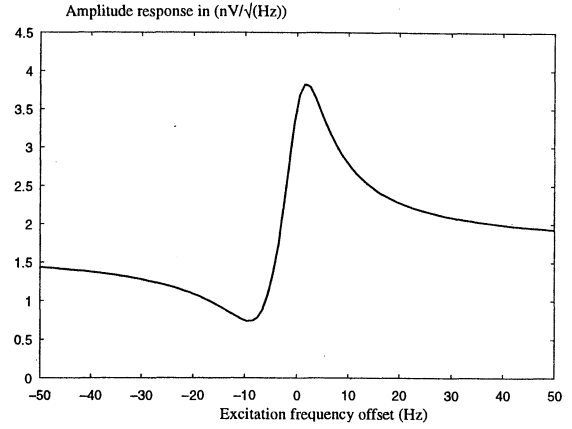


Fig. 10.

Figures 10 and 11 represent respectively the amplitude of the amplitude modulation and the amplitude of the frequency modulation as a function of the difference between the unperturbed steady state oscillation frequency and the excitation frequency. Curves have been obtained assuming that the noise source current  $i_0$  is induced by a  $50 \Omega$  resistor value.

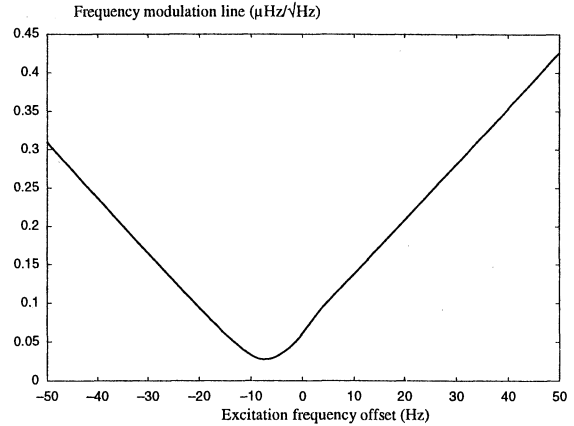


Fig. 11.

## AMPLITUDE NOISE AND PHASE NOISE SPECTRA

The previous analysis showed that the noise source induces a frequency and an amplitude modulation of the oscillation signal which can thus be expressed as:

$$u = (y_0 + \bar{z} \cos \Omega_m t) \cos(\omega_s t + \bar{v} \cos \Omega_m t) \quad (37)$$

The amplitude spectrum can be obtained from the envelope of the amplitude modulation line as a function of the modulation frequency:

$$S_z(\Omega_m) = \frac{\bar{z}^2}{2} = \frac{1}{8} \frac{(\alpha\omega_0)^2 + (\beta\omega_0)^2}{(\lambda\omega_0)^2 + \Omega_m^2} \quad (38)$$

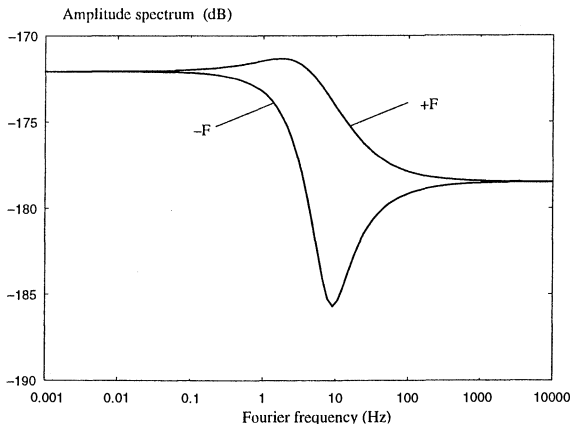


Fig.12.

Furthermore, the phase spectrum is given by the envelope of the phase modulation line:

$$S_{\varphi}(\Omega_m) = \frac{\bar{v}^2}{2\Omega_m^2} = \frac{\bar{z}^2}{2\Omega_m^2} \left[ (\lambda\omega_0)^2 + (\Omega_m - \gamma_0 \epsilon \omega_0)^2 \right] \quad (39)$$

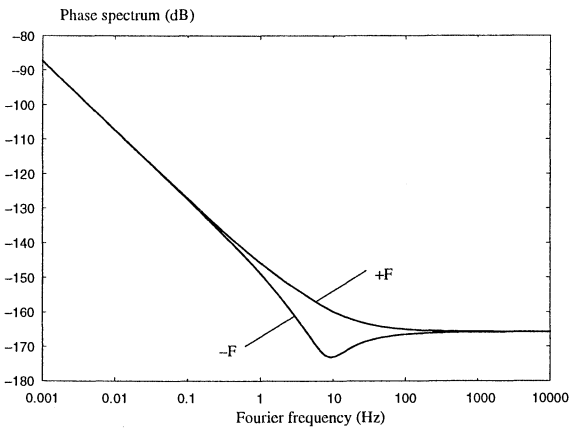


Fig. 13.

Figures 12 and 13 show the amplitude and phase noise spectra induced by the 50  $\Omega$  resistor value previously mentioned.

The spectra shown in Figs. 12 and 13 have been obtained by varying the modulation frequency on both sides of the carrier. It is obvious here that the shape of the spectrum is different depending on whether the modulation frequency is lower or higher than the carrier. In fact, when dealing with noise, all modulation frequencies are simultaneously present in the noise source so that a spectrum analyzer cannot discriminate between lower or higher modulation frequencies. Nevertheless, the overall noise spectra can be obtained by assuming that both upper and lower parts have an equal contribution.

The effective noise spectra are then obtained by:

$$\begin{cases} S_z(\Omega_m) = \frac{1}{2} [S_z(\Omega_m < 0) + S_z(\Omega_m > 0)] \\ S_{\varphi}(\Omega_m) = \frac{1}{2} [S_{\varphi}(\Omega_m < 0) + S_{\varphi}(\Omega_m > 0)] \end{cases} \quad (40)$$

These spectra are represented in Figs. 14 and 15.

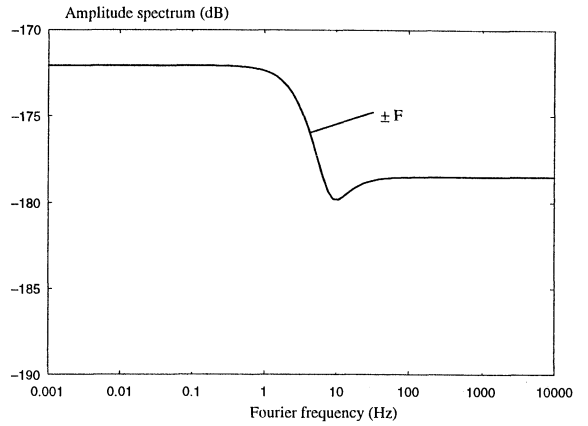


Fig. 14.

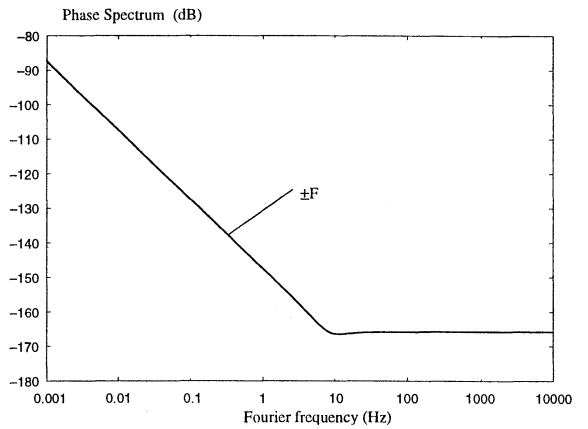


Fig 15.

## CONCLUSION

By using a methodical symbolic reduction process it is possible to automatically derive the oscillation condition of a circuit. This condition takes the form of a characteristic polynomial whose coefficients are expressed in terms of the circuit components and the active device large signal  $\gamma$ -parameters. Reduction process also involves noise sources spread out in the circuit which appear as perturbation terms in the characteristic polynomial.

In the time domain, characteristic polynomial becomes a nonlinear second order differential equation with time dependent excitation terms. By calling on asymptotic method, this equation is transformed into a first order differential system in the amplitude and phase variables which can be solved by classical numerical algorithms

to obtain steady state oscillation amplitude and frequency.

By using a perturbation method around the steady state, it is possible to show that noise sources induce both frequency and amplitude modulations.

The amplitude and phase noise spectra are then obtained from the envelope of the amplitude and phase response to an harmonic noise source of variable frequency in the vicinity of the oscillation frequency.

The results obtained show that the phase spectrum agrees very well with the classical Leeson's model [11] but, unlike the Leeson's model which globally assess the effect of all noise sources in the oscillating loop, the present approach enables us to calculate individual contribution of each noisy component in the circuit on both the amplitude and the phase spectra.

It should be emphasized that symbolic circuit reduction model generation, steady state and transient solution as well as perturbation analysis and spectrum calculation can be fully automated so as to give the user an efficient and powerful analysis tool for quartz crystal oscillator design.

#### ACKNOWLEDGMENTS

This work has been supported by CNES and DGA under contracts :

#832/CNES/88/5374/00, #962/CNES/91/1476/00,  
#962/CNES/94/1230/00.

#### REFERENCES

- [1] R. Brendel, G. Marianneau, E. Robert, March 1991, "Nonlinear modeling techniques for quartz crystal oscillators", Proc. of the 5<sup>th</sup> European Frequency and Time Forum.
- [2] R. Brendel, F. Djian, E. Robert, May 1991, "High precision nonlinear computer modeling technique for quartz crystal oscillators", Proc. of the 45<sup>th</sup> Annual Symposium on Frequency control.
- [3] R. Brendel, G. Marianneau, T. Blin, M. Brunet, July 1995, "Computer aided design of quartz crystal oscillators", IEEE Trans. On Ultrasonics, Ferroelectrics and Frequency control, vol. 42, n°4.
- [4] R. Brendel, N. Ratier, L. Couteleau, G. Marianneau, P. Guillemot, March 1997, "Transient simulation in quartz crystal oscillators", Proc. of the 11<sup>th</sup> European Frequency and Time Forum.
- [5] R. Brendel, N. Ratier, L. Couteleau, G. Marianneau, P. Guillemot, March 1998, "Slowly varying function method applied to quartz crystal oscillator transient calculation", IEEE Trans. on Ultrasonics, Ferroelectrics and Frequency Control, vol. 45, n°2.
- [6] N. Ratier, R. Brendel, P. Guillemot, March 1996, "Quartz oscillators : deriving oscillation condition by symbolic calculus", Proc. of the 10<sup>th</sup> European Frequency and Time Forum.
- [7] N. Ratier, L. Couteleau, R. Brendel, P. Guillemot, May 1997, "Automatic formal derivation of the oscillation condition", Proc. of the 51<sup>st</sup> International Symposium on frequency Control.
- [8] J.J. Gagnepain, R. Besson, 1975, "Nonlinear effects in piezoelectric quartz crystal", Physical Acoustics, vol. XI, Academic Press.
- [9] N.N. Bogoliuboff, 1943, "Introduction to nonlinear mechanics", Princeton.
- [10] J. Haag, "Les mouvements vibratoires", PUF, vol. 1 (1951), vol. 2 (1955).
- [11] Leeson, 1966, "Simple model of feedback oscillator noise spectrum", Proceedings Letters.

## OCXO SPECTRUM ANALYSIS

A.Masiukiewicz, B.Gniewinska

Tele & Radio Research Institute, Ratuszowa 11, 03-450 Warsaw, Poland

### ABSTRACT

Complex phase noise model of the OCXO oscillator was proposed, basing on typical OCXO block diagram.

This model was verified during analysis of the OCXO 2001 type oscillator employing LFE (lateral field excited) SC cut resonator.

Quite good compatibility between theoretical considerations and direct phase noise measurement was obtained.

### 1. INTRODUCTION

Analysis of the output signal spectrum of the high stability oscillator requires consideration of several possible noise sources which are neglected in the oscillators of lower frequency stability. Leeson's feedback oscillator model [1] with resonator flicker [2,3,4,5] and output buffer [6] noise included doesn't discuss many random processes of fluctuations which caused instantaneous frequency fluctuations.

Complex phase noise model of the OCXO oscillator was proposed basing on typical OCXO block diagram. This model was used for analysis of the oscillator type OCXO-2001 with LFE type SC cut resonator.

Quite good compatibility between theoretical considerations and direct phase noise measurements was obtained.

Short term frequency stability better than  $1E-12$  for 1 to 10 sec averaging time of the OCXO-2001 oscillator was achieved.

### 2. PHASE NOISE MODEL OF OCXO OSCILLATOR

Phase noise models of the quartz oscillators based at present on Leeson's formula of the feedback oscillator. Typical model consists of the active element (amplifier), the selective element (resonator) and output buffer. The lack of several random fluctuations processes limits the validity of theoretical analysis.

The complex model basing on typical block diagram of the OCXO (fig.1) oscillator was proposed. The model idea was presented in fig.2.

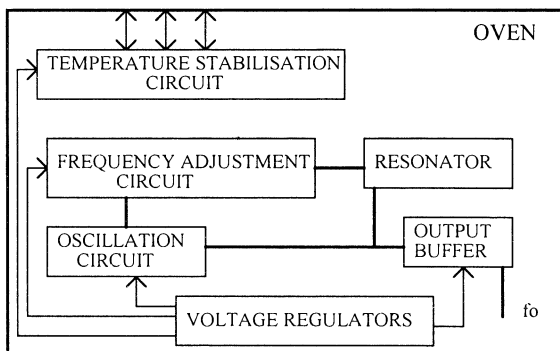


Fig.1 Block diagram of the OCXO's

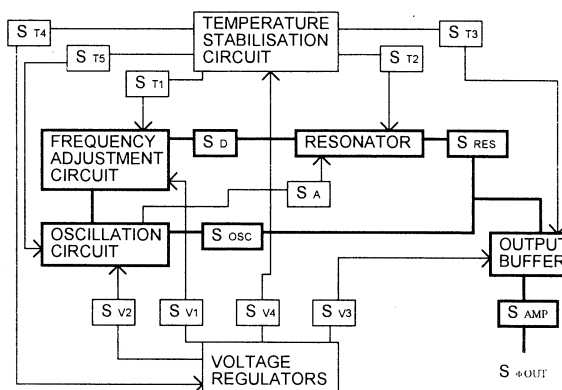


Fig.2 Phase noise model of the OCXO's

Comparing with Leeson's model this one includes such circuits as frequency tuning circuit, thermostabilisation circuit and voltage regulators. Both the thermostabilisation circuit and voltage regulators produce fluctuations processes which can modify the phase noise characteristics of the hf elements and circuits. These processes can cause also the parametric type noise connected with circuits parameters which decided of phase and frequency of the output signal. The output signal phase noise was determined basing on mechanisms presented in references and author's experience. As it is shown in fig.2 the hf elements and circuits have its own phase noise characteristics which can be defined according to references [1, 2, 6, 7]. All formulas are included in table 1.

The model includes also three types of fluctuations processes:

a/ temperature fluctuations  $S_{T1...5}(F)$ ,

b/ dc voltage fluctuations  $S_{V1...4}(F)$ ,

c/ ac voltage fluctuations  $S_{A(F)}$ .

The final number of fluctuations processes in different oscillators depends on details of construction and electronic circuits configuration. The way of acting of different factors on the power density of phase noise fluctuations of the output signal are shown in fig.3

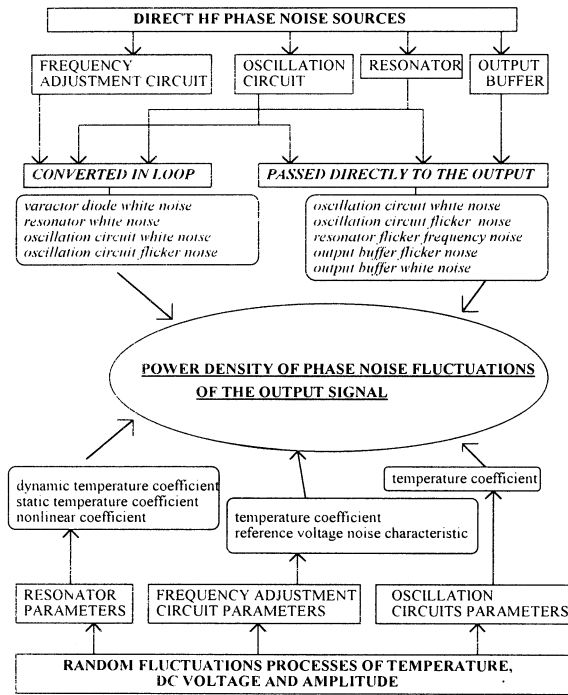


Fig.3 The mechanisms of of the output signal phase noise characteristic erection

Taking into account all mentioned above noise sources and noise transformation mechanisms the elements of oscillator output spectrum in frequency domain are listed in Table 1.

Modulation and parametric type noise processes are characterized by coefficients which connect fluctuations with the parameter of the resonator or other element, responsible for the frequency change. Coefficients included in Table 1 can be described as:

*a/ resonator parameters*

- $\alpha_R$  resonator flicker noise coefficient
- $f_0$  nominal frequency
- $Q_l$  load resonator Q factor
- $P_R$  resonator excitation power
- $a$  dynamic resonator temperature coefficient
- $b$  static temperature coefficient
- $K_1$  resonator nonlinear coefficient
- $K_2$  selfheating resonator coefficient

*b/ oscillation circuit parameters*

- $A$  oscillation circuit flicker noise coefficient
- $B$  oscillation circuit white noise coefficient
- $K_3$  oscillation circuit temperature coefficient

*c/ output buffer parameters*

- $\alpha$  output buffer flicker noise coefficient
- $\beta$  output buffer white noise coefficient

*d/ frequency adjustment circuits parameters*

- $r_s$  tuning diode series resistance
- $K_{21}$  resonator sensitivity to series reactance
- $K_2$  temperature coefficient of series reactance
- $K_5$  tuning slope

*e/ fluctuation processes characteristics versus Fourier frequency*

- $S_{T1}$  temperature fluctuations in the resonator chamber
- $S_{T2}$  temperature fluctuations in the oscillation circuit chamber
- $S_{T5}$  temperature fluctuations in the adjustment circuit chamber
- $S_{V1}$  reference voltage noise
- $S_A$  amplitude fluctuations

The output spectral power density of phase noise fluctuations can be described, with the assumption that all noises are uncorrelated as the sum of all noises presented in Table 1:

$$S_{\phi OUT}(F) = \sum S_{\phi k}(F)$$

### 3. THE ANALYSIS OF THE OCXO-2001 OSCILLATOR SPECTRUM

The oven controlled oscillator type OCXO-2001 includes three chamber oven where all electronic circuits are placed [8]. The hf circuit and temperature control circuit have separate dc voltage regulators. The phase noise model of this oscillator is presented in fig.4.

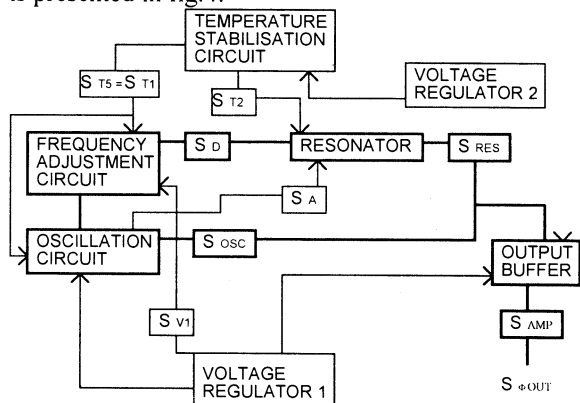


Fig.4 The OCXO2001 phase noise model

Fluctuations processes are taken into account by means of two methods. Some of them were measured while the influence of others is included in measurement results of noise characteristics of hf elements and circuits.

The temperature fluctuations  $S_{T2}(F)$  in the resonator chamber was measured by means of B mode of the SC cut resonator. This mode represents

the frequency versus temperature slope of -25ppm/K. Results of measurements are presented in Table 2.

Table 2 Temperature fluctuations in the resonator chamber

$\tau$ [sec]	0.1	1	10
$\sigma_{T_2}(\tau)$ [K]	6E-7	2.6E-7	4.8E-7

The temperature fluctuations in the second chamber ( where the oscillation and tuning circuits are placed) was measured by means of Y+5 temperature sensor of F-T slope 100ppm/K, sustaining in Colpitts circuit. Results are presented in Table 3.

Table 3 Temperature fluctuations in the second chamber

$\tau$ [sec]	0.1	0.2	0.5	1	10
$\sigma_{T_1}(\tau)$ [K]	8E-6	4E-6	2E-6	2E-6	4E-6

The dc reference voltage ( for tuning circuit) fluctuations were measured directly by low frequency HP spectrum analyzer. Results are presented in Table 4.

Table 4  $S_{V_2}(F)$  voltage regulator

	$S_{V_2}(F)$ [dB/Hz]/ $F$ [Hz]					
Regulator type	5	10	30	100	1k	10k
LT1021	-135	-136	-137	-138	-139	-150

The amplitude fluctuations in the oscillation circuit were determined according to the method proposed in reference [9]. These fluctuations represents the worst case. The results are presented in Table 5.

Table 5 Amplitude fluctuations

$F$ [Hz]	0.1	1	3	10
$S_A(F)$ [dB/Hz]	-80	-110	-122	-129

Information concerning several coefficients and operating conditions of the resonator and oscillation circuit are necessary for calculation of the output spectrum. These coefficients are determined basing on measurements and other methods and results are presented in Table 6.

Table 6

Data for analysis	Value	Methods of determination
$\alpha_R$	5E-12	measurement
$f_o$ [Hz]	5E6	
$Q_i$	1E6	calculations
$K_1$ [Hz/W]	5000	measurement
$P_R$ [W]	2E-6	simulation
$\dot{\alpha}$	2E-7	measurement
$A$	2E-13	measurement
$B$	5E-15	measurement

$K_3$ [rad/K]	3.5E-3	measurement
$r_s$ [ $\Omega$ ]	1.2	catalogue data
$K_4$ [Hz/K]	2E-3	measurement
$K_5$ [Hz/V]	0.35	measurement
$\alpha$	4E-13	measurement
$\beta$	5E-15	measurement
$K_2 K_{21}$ [1/K]	2E-3	calculations
$a_a$ [1/K]	1E-8	calculations
$K_3$ [Hz/K]	7E-5	measurement

The characteristics of separate noise sources and the final theoretical characteristic of the oscillator output spectrum are presented in fig.5.

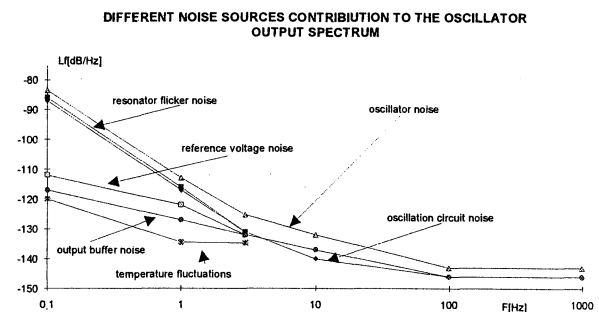


Fig.5 Phase noise structure of the OCXO2001 oscillator

To check the sensitivity of the spectrum to temperature influence some calculations were made when the SC-cut resonator was replaced by at-cut (of much more worse dynamic temperature coefficient ) and while the temperature fluctuations in the resonator chamber were of one order higher. The results are shown in fig.6.

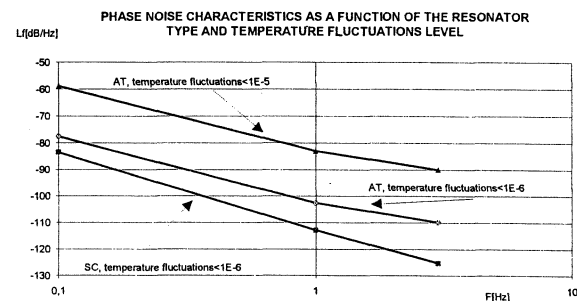


Fig.6 Phase noise characteristic as a function of the resonator type and temperature fluctuations level.

In the worse case (AT-cut resonator, temperature fluctuations  $\approx 1E-5$ ) the phase noise degradation of 20dB was observed.

Good compatibility between theoretical approach and measurement results was obtained. The calculations were made for data included in table 6. The difference between characteristics is below 3dB (fig.7), however it is necessary to remember that so called theoretical approach based in many cases on very precise measurement.

The power spectral density of phase fluctuations level which was achieved corresponds to short term frequency stability of  $8E-13/1\text{sec}$  and  $7.5E-13/10\text{sec}$ .

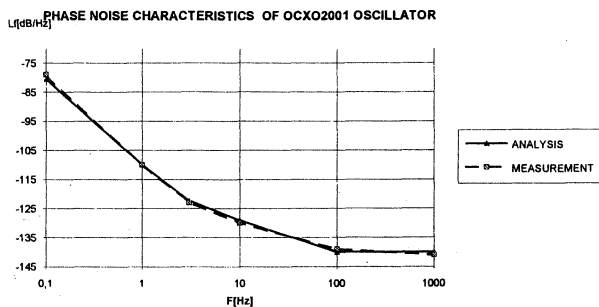


Fig.7 Comparison of calculations and measurement results  
Tests with higher excitation level as well as with resonators of different Q factor were carried out and the results are presented in fig.8

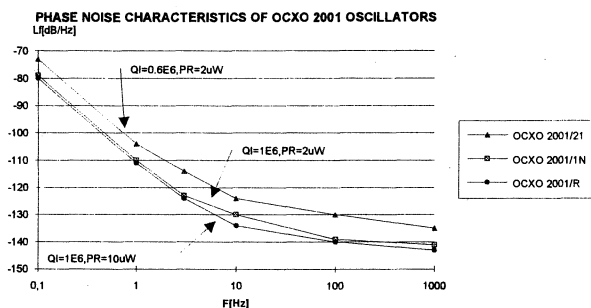


Fig.8 Phase noise as a function of the excitation level  
The most significant noise sources are presented in table 7.

Table 7

F[Hz]	DOMINANT PHASE NOISE SOURCES
0.1	-resonator frequency flicker noise -oscillation circuit flicker phase noise converted in loop
1	-resonator frequency flicker noise -oscillation circuit flicker phase noise converted in loop -parametric noise in adjustment circuit caused by reference voltage noise
3	-resonator frequency flicker noise -oscillation circuit flicker phase noise -resonator parametric noise caused by temperature fluctuations -output buffer flicker phase noise
10	-oscillation circuit flicker phase noise -resonator parametric noise caused by temperature fluctuations -output buffer flicker phase noise
100	-output buffer white noise -oscillation circuit white noise

#### 4. CONCLUSIONS

There could be several applications of proposed phase noise model of OCXO such as :

- analysis of the oscillator to find dominant noise sources,
- establishing the requirements for the oscillator elements and circuits,
- evaluating of the new design oscillator phase noise characteristic.

For power density of phase noise fluctuations close to  $-110\text{dB/Hz}$  for  $F=1\text{Hz}$  difference between analysis and direct phase noise measurement below 3dB was achieved.

There are several factors which limits the accuracy of the model:

- some resonator, circuits parameters and fluctuations processes were measured only for examples (dynamic temperature coefficient, resonator phase noise, temperature fluctuations),
- correlations between different phase noise sources were neglected,
- some factors were not included in analysis (the problem of harmonic distortion contribution),
- measurements accuracy,
- influence of environmental fluctuations processes.

#### 5. REFERENCES

1. D.B.Leeson, A simple model of feedback oscillators noise spectrum. Proceedings of IEEE 1966
2. T.E.Parker, Characteristics and sources of phase noise in stable oscillators. 41st ASFC, 1987
3. G.S.Curtis, The relationship between resonator and oscillator noise and resonator noise measurement techniques. 41st ASFC, 1987
4. V.F.Kroupa, The state of art of flicker frequency noise in BAW and SAW quartz resonator. IEEE Transactions On Ultrasonics, Ferroelectrics And Frequency Control. Vol.35, No 3, 1988
5. F.L.Walls, R.H.Handel, R.Besson, J.J.Gagnepain, A new model of 1/F noise in BAW quartz resonators. 46th ASFC, 1992
6. J.J.Gagnepain, Fluctuations and noises in quartz oscillators and resonators, Prace ITR no 99/100, 1985
7. J.K.A.Everard, Low noise oscillators, theory and design. 10th EFTF, Brighton, 1996
8. A.Masiukiewicz, B.Gniewinska, W.Szulc, Application of LFE SC cut resonators at high stability oscillators. IEEE Frequency Control Symposium, Boston, 1994
9. L.M.Nelson, C.W.Nelson, F.L.Walls, Relationship of AM to PM noise in selected RF oscillators, IEEE Transactions On Ultrasonics, Ferroelectrics And Frequency Control. Vol. 41, No 5, 1994
10. F.L.Walls, "The quest to understand and reduce 1/f noise in amplifiers and BAW quartz oscillators", Proc. of 9th EFTF, 1995
11. A.Masiukiewicz, "Analysis of operating conditions of the oscillator with piezoelectric frequency stabilisation and their optimisation for the maximal spectral purity" (in Polish) , Ph.D. Thesis, Technological University of Warsaw, Faculty of Electronics and Informatics, 1997

Table 1 Elements of output spectrum

Source of phase noise	$S_{\phi_k}(F)$ Formula
resonator frequency flicker noise	$\frac{\alpha_R}{F^3}$
resonator white noise	$\frac{1}{F^2} \beta_R \left(\frac{f_o}{2Q_l}\right)^2 = \frac{1}{F^2} \frac{2kT}{P_R} \left(\frac{f_o}{2Q_l}\right)^2$
resonator parametric noise caused by ac voltage fluctuations	$\frac{1}{F^2} S_A(F)^2 K_1^2 P_R^2$
resonator parametric noise caused by temperature fluctuations and connected with resonator dynamic temperature coefficient	$\frac{1}{F^2} S_{T2}(F) d^2 F^2 f_o^2$
resonator parametric noise caused by temperature fluctuations and connected with resonator static temperature characteristic	$\frac{4f_o^2}{F^2} S_{T2}(F) b^2$
resonator parametric noise caused by temperature fluctuations connected with resonator power fluctuations and related to dynamic and static behaviour	$\frac{4b^2}{F^2} S_A(F)^2 K_4^2 P_R^2 f_o^2 + f_o^2 d^2 K_4^2 P_R^2 S_A(F)^2$
oscillation circuit noise	$\frac{1}{F^2} \left(\frac{f_o}{2Q_l}\right)^2 \left(\frac{A}{F} + B\right) + \frac{A}{F} + B$
oscillation circuit parametric noise caused by temperature fluctuations	$\frac{1}{F^2} [S_{T5}(F) K_3^2 \left(\frac{f_o}{2Q_l}\right)^2 + S_{T5}(F) K_3^2]$
varactor diode white noise	$\frac{1}{F^2} 4kTr_s \left(\frac{f_o}{2Q_l}\right)^2$
frequency tuning circuit modulation noise caused by temperature fluctuations	$\frac{1}{F^2} S_{T1}(F) K_{21}^2 K_2^2$
frequency tuning circuit modulation noise caused by reference voltage noise	$\frac{1}{F^2} S_{V1}(F) K_5^2$
output buffer noise	$\frac{\alpha}{F} + \beta$

## PSPICE SIMULATION OF A PHASE MODULATION NOISE MEASURING SYSTEM OF QUARTZ CRYSTAL RESONATORS

F. STHAL, M. MOUREY

Laboratoire de Chronométrie, Electronique et Piézoélectricité,  
Ecole Nationale Supérieure de Mécanique et des Microtechniques  
26, Chemin de l'Épitaphe - 25030 BESANÇON CEDEX - France

**Abstract:** A PSPICE simulation of a new phase modulation noise measuring system of high stability quartz crystal resonators is presented. The measuring system has been split in several parts for the simulation. The low-noise source is studied as a frequency modulated source. The power splitter is simulated with a passive circuit. We used a classical equivalent circuit for the quartz crystal resonator around its resonant frequency. Both quartz are followed by a low-noise amplifier. The double balanced mixer which makes the phase difference between each path is represented by its passive equivalent circuit. The system output is constituted by an amplifier, which allows the connection with a spectrum analyzer. This simulation is applied to 10 MHz BVA resonator and the system is optimized for this kind of resonators.

### 1. INTRODUCTION

The phase noise of quartz crystal resonators is an important parameter in the frequency stability of quartz crystal-controlled oscillators. In the phase noise measurements of quartz crystal oscillators, it is difficult to distinguish the respective contributions of the electronic amplifier and of the quartz crystal resonator to the phase fluctuations in the output signal.

New techniques have been developed to measure the inherent phase noise of quartz resonators.

The quartz crystal phase noise is measured in a passive measuring system. Two crystals chosen to be as identical as possible are driven through a  $\pi$  transmission network by a unique low-noise source. This technique is suited to measurements at room temperature (1)-(8) and at very low temperature (9).

These techniques were used for studying a great number of AT and BT cut resonators. These studies have shown that, according to the short-term stability, the  $1/f$  frequency noise is preponderant in quartz crystal resonators. Thereafter, it was shown that the noise was proportional to  $Q^{-4}$ , where  $Q$  is the unloaded inherent quality factor of the quartz crystal (9)-(14).

In practice, identical resonators which are very difficult to obtain are necessary for the smooth running of the measuring benches. The rejection of the source noise is indeed very dependent on the differences between both resonators. In order to extend the study to the third overtone, SC-cut, 10 MHz BVA resonators developed in our laboratory, a PSPICE simulation of a measuring system similar to the F. L. Walls device (2) has been developed. This simulation is closer to the real

measuring system than a numerical simulation (15)-(16). More electronic problems are taken into account and the amplitude noise rejection can be evaluated in comparison with the phase noise.

In this paper, the measuring system and its PSPICE simulation are presented. The measuring system has been split in several parts for the simulation. The low-noise source is studied as a frequency modulated source. The power splitter is simulated with a passive circuit. We used a classical equivalent circuit for the quartz crystal resonator around its resonant frequency. Both quartz are followed by a low-noise amplifier. The double balanced mixer which makes the phase difference between each path is represented by its passive equivalent circuit. The system output is constituted by an amplifier which allows the connection with a spectrum analyzer. This simulation is applied to third overtone, SC-cut, 10 MHz BVA resonator and the system is optimized for this kind of resonators.

### 2. MEASURING SYSTEM

The simulated measuring device is presented in figure 1.

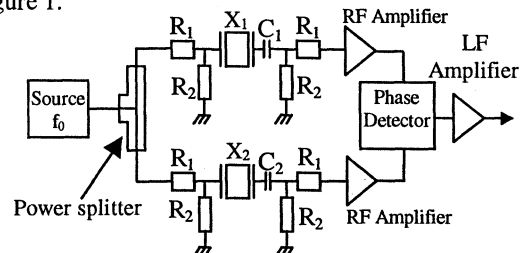


Fig. 1: Passive phase noise measuring system of quartz crystal resonators.

A low-noise source of frequency  $f_0$  drives two quartz crystals  $X_i$  ( $i = 1, 2$ ). To preserve its resonance quality, each quartz crystal resonator is placed in an impedance adaptation network which is composed of resistors  $R_1$  and  $R_2$ . Resistors are settled according to the impedance of the quartz crystal and of the source. The inherent quality factors of the resonators are  $Q_i$ , the resonant frequency  $f_{qi}$ . Tuning capacitors  $C_i$  ( $i = 1, 2$ ) are associated in series to the quartz crystals, thus allowing the resonant frequency of each path of the bridge to be adjusted. These adjustments are necessary in order that each path of the bridge resonate at the frequency of the source. The RF amplifiers allow to adjust the output signal amplitude of the quartz resonator. These signals must have a sufficient amplitude to drive the phase detector. The output signal

of the phase detector is filtered by the LF amplifier which allows the spectrum analyzer to be connected with an impedance matched to 50 Ω. A spectrum analyzer, connected at the output of the LF amplifier, allows the power spectral density of the phase fluctuations  $S_{\phi}(f)$  to be obtained as a function of the square difference of each path phase.

### 3. PSPICE SIMULATION

#### 3.1. Source simulation

Generally, the signal of the source can be represented by the following expression:

$$v(t) = (V_0 + \varepsilon(t)) \sin[2\pi f_0 t + \phi(t)] \quad (1)$$

where  $V_0$  is the amplitude of the signal,  $f_0$  the source frequency. The amplitude fluctuations  $\varepsilon(t)$  and the phase fluctuations  $\phi(t)$  of the source are considered as random ergodic and stationary processes. With PSPICE we can suppose that the phase modulation is a sinusoidal modulation at the frequency  $f_m$  (17). Random phase noise is replaced with sinusoidal modulation for a 1 Hz bandwidth.

$$v(t) = V_0 \sin[2\pi f_0 t + \Delta\phi \sin(2\pi f_m t)] \quad (2)$$

Equation (2) can be also written as:

$$v(t) = V_0 \sum_{n=-\infty}^{+\infty} J_n(\Delta\phi) \cdot \sin 2\pi(f_0 + n f_m)t \quad (3)$$

where  $J_n$  is the Bessel function of first kind and  $n$  order. This modulated source is simulated by a Value-Controlled Voltage Source (fig 2).

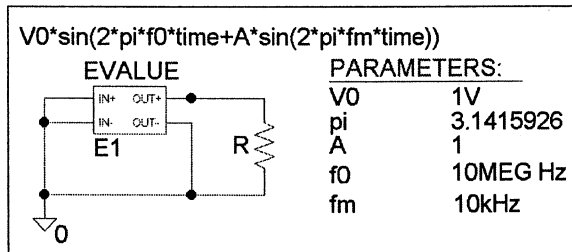


Fig. 2: PSPICE model of the source.

The value of the value-controlled voltage source can be a sinusoidal time function with a modulation frequency  $f_m$  or several modulation functions at different frequencies. A constant phase shift as  $\pi/2$  can be used. We can also create an amplitude modulation if  $V_0$  is a time function (this case is not represented here). Figure 3 gives the amplitude of the source in the frequency domain for  $f_0 = 10$  MHz and the modulation coefficient  $A = \Delta\phi$  equal to 1.

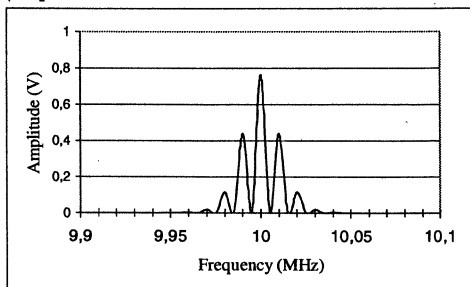


Fig. 3: Source spectrum,  $f_0 = 10$  MHz,  $f_m = 10$  kHz.

The source frequency is equal to 10 MHz. We can observe the amplitudes of the peaks which are given by the Bessel functions. Errors are less than 1 % for  $J_0$  and  $J_1$ , and less than 5 % for  $J_2$  and  $J_3$ .

Analysis of the source must be computed in the time domain, thus, to obtain a good separation of the different frequencies is very difficult. For example, one hour of computation is necessary to obtain the two frequencies 10 MHz and 1 kHz.

When  $\Delta\phi \ll 1$ ,  $v(t)$  can be written as:

$$v(t) \approx V_0 \sin 2\pi f_0 t + \frac{1}{2} V_0 \Delta\phi \sin 2\pi(f_0 + f_m)t - \frac{1}{2} V_0 \Delta\phi \sin 2\pi(f_0 - f_m)t \quad (4)$$

In frequency domain, the single-sideband-to-carrier power ratio allows to evaluate  $\Delta\phi$ . The power spectral density of the phase fluctuations is given by the following expression in dBc/Hz (17).

$$S_{\phi}(f_m) = 20 \cdot \text{Log} \left( \frac{\Delta\phi}{\sqrt{2}} \right) \quad (5)$$

The simulator allows to distinguish a single-sideband amplitude when  $\Delta\phi$  is equal to  $10^{-8}$  thus the resolution of the simulator is equal to  $-163$  dBc/Hz.

#### 3.2. Power Splitter simulation

Figure 4 shows the passive equivalent circuit of the power splitter.

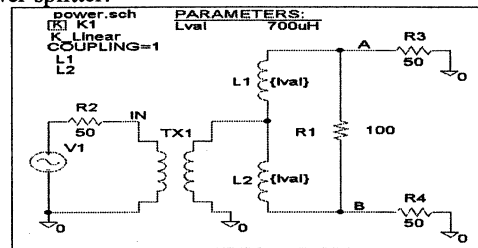


Fig. 4: Equivalent circuit of the power splitter.

The magnetic coupling between the inductors is ideal and linear. The source  $V_1$  gives a sinusoidal excitation at 10 MHz. It is associated in series with a resistor of 50 Ω, thus it simulates a 50 Ω adapted source at the point IN. The input of the power splitter is adapted at 50 Ω by the 2-to-1 transformer. We can verify that the power is well shared in both paths with an equal value (figure 5).

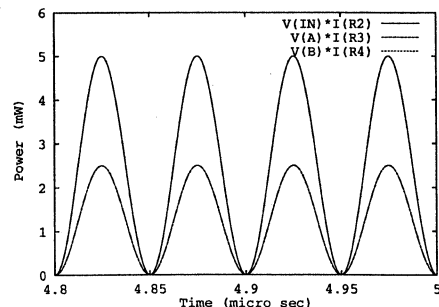


Fig. 5: Input and output powers of the power splitter.

Considering the ratio of the inductors, the output voltage of each path is equal to the input voltage divided by the square root of 2 (figure 6).

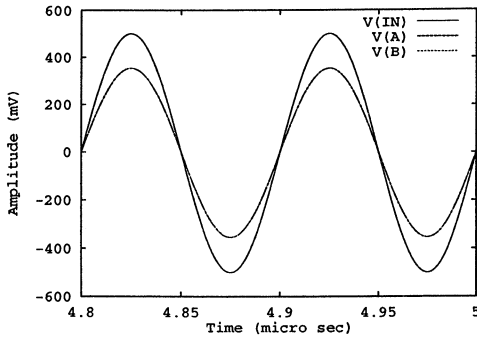


Fig. 6 : Input voltage (IN) and output voltage (A, B).

The signals are perfectly in phase but this power splitter doesn't allow to introduce a  $\pi/2$  phase shift.

### 3.3. Quartz crystal resonators

Third overtone, SC-cut, 10 MHz BVA resonators are used (18).  $R_q$ ,  $L_q$ , and  $C_q$  are the motional parameters which give the resonant frequency  $f_q$  of the quartz crystal. For both resonators, the motional resistor  $R_q$  is set at  $100 \Omega$ . The static capacitor  $C_0$  is 2.4 pF. The Q-factor is  $1.36 \cdot 10^6$ . The motional inductor is approximated using the following equation:

$$L_q = \frac{Q \cdot R_q}{2 \cdot \pi \cdot f_q} \quad (6)$$

The motional capacitor  $C_q$  is computed from a dichotomy method with a  $10^{-15}$  accuracy to obtain the quartz crystal resonant frequency equal to  $f_q$ .

The 10 MHz BVA resonators, used in time base, are designed so that their serial resonant frequency is equal to  $9\,999\,983 \text{ Hz} \pm 10 \text{ Hz}$ . The range of the tuning capacitor is determined by the extreme frequency values. The tuning capacitor  $C_i$  is also computed to obtain the resonant frequency  $f_i$  with the same precision as  $C_q$ . The source frequency  $f_0$  and the resonant frequency  $f_i$  of each path of the bridge are set at 10 MHz. Figure 7 gives an example of a quartz crystal resonator which has a frequency  $f_q = 9\,999\,993 \text{ Hz}$ . The resonator is associated to its tuning capacitor  $C_1 = 81 \text{ pF}$  and placed in an impedance adaptation network.

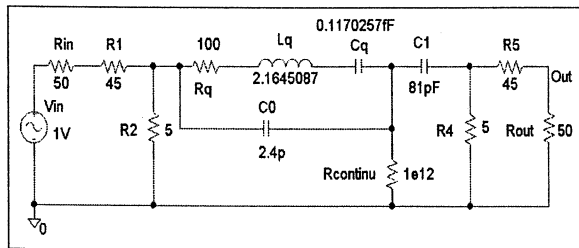


Fig. 7: BVA resonator associated to its tuning capacitor and impedance adaptation network.

Figure 8 and 9 show the frequency adjustment which is represented by the amplitude and the phase of the transfer function of the quartz crystal.

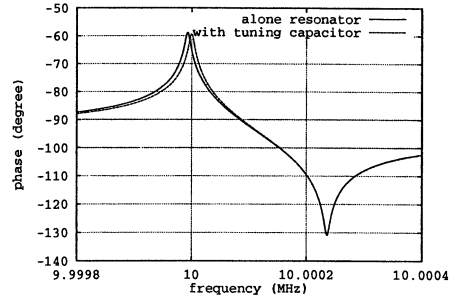


Fig. 8: Transfer function amplitude of the BVA setup.

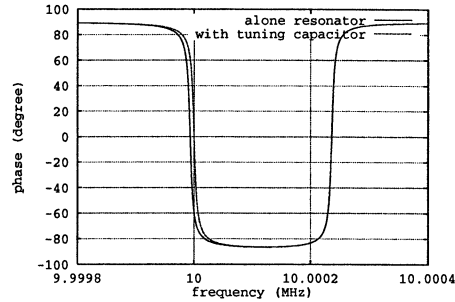


Fig. 9: Phase of the transfer function of the BVA setup.

The simulator precision is limited to eight significant digits. The frequencies are obtained with a precision equal to  $10^{-1}$  Hertz. This kind of simulation is less accurate than a numerical simulation (15). A software like MAPLE V allows to have more than thirty significant digits.

### 3.4. RF amplifier

Figure 10 presents the RF amplifier.

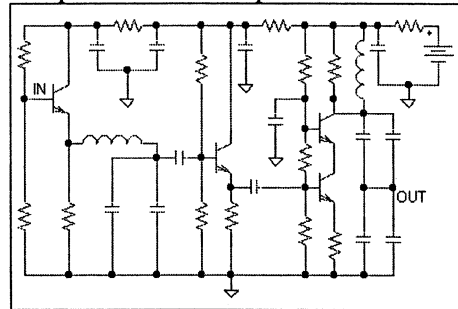


Fig. 10: RF amplifier following the resonator circuit.

It is designed with three low-noise amplifying stages. The circuit is tuned at 10 MHz. The gain and the cut-off frequency are given in figure 11. The gain is close to 20 dB at 10 MHz and the cut-off frequency bandwidth is around 800 kHz.

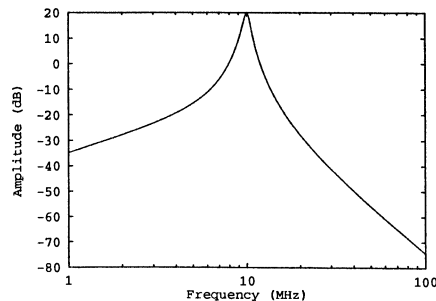


Fig. 11: Gain of the RF amplifier.

Figure 12 shows the phase of the RF amplifier.

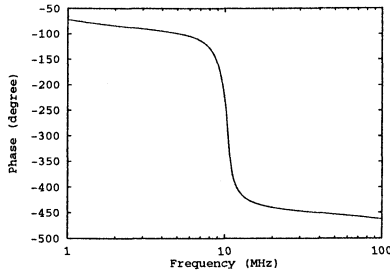


Fig. 12: Phase of the RF amplifier.

### 3.5. Phase detector

The phase detector is simulated by its passive equivalent circuit (figure 13).

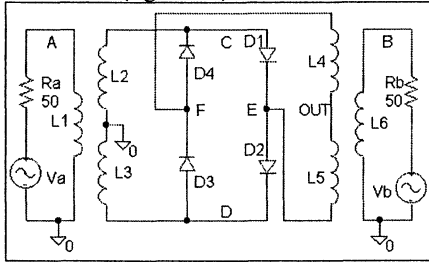


Fig. 13: Equivalent circuit of the phase detector.

It is designed with a double balanced mixer (DBM) which is composed of a four diode ring.

Two sinusoidal sources at 10 MHz drive the input transformers of the phase detector. Their phases can be adjusted. The transformers are ideal (inductors are coupled with a coupling coefficient  $K$  equal to 1). Ring mixer operation can be described in simple terms by treating the diodes as switches which are turned on and off by the A signal. The A signal is applied to the primary of one transformer and the B signal is applied to the primary of the other. The center tap of the A transformer secondary is grounded, and the center tap of the B secondary constitutes the output. Since the load represented by each diode is identical, points E-F are virtual ground for the A and points C-D are virtual ground for the B.

When the A power is applied, an AC-voltage is applied to points C and D. This voltage alternately turns on and off diode pairs D1/D2 and D3/D4. This switching on and off of the diode pairs alternately connects points E and F between virtual ground and high impedance. The result is that the polarity of the B signal, applied to the OUT, is reversed at the A frequency. This phase reversal of the B signal is illustrated in figure 14.

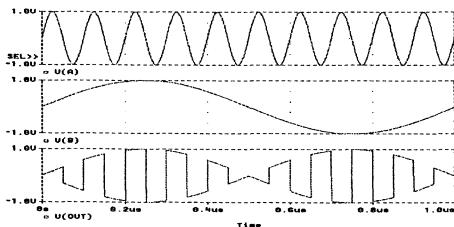


Fig. 14: Input signals A and B and output signal OUT of the phase detector,  $f_A = 10$  MHz and  $f_B = 1$  MHz.

This is equivalent to multiplying the B signal by a square wave which has an amplitude of  $\pm 1$  at the A frequency. The output is the product of the B signal and the fundamental component of the A square wave. The output signal can be written as the following equation:

$$\text{OUT}(t) = B(t) \cdot \frac{4}{\pi} [\sin(2\pi f_A t) + \frac{1}{3} \sin(3 \cdot 2\pi f_A t) + \frac{1}{5} \sin(5 \cdot 2\pi f_A t) + \dots] \quad (7)$$

As  $B(t) = B \cdot \sin(2\pi f_B t + \phi)$ , equation (7) becomes

$$\text{OUT}(t) = \frac{2B}{\pi} [\cos(2\pi(f_A - f_B)t - \phi) - \cos(2\pi(f_A + f_B)t + \phi) \dots] \quad (8)$$

if we consider the first harmonic.

When the A and B frequencies are equal, the OUT signal is composed of a DC-voltage which is proportional to the cosine of the phase difference of the A and B signals.

$$\text{OUT}(t) = \frac{2B}{\pi} [\cos \phi - \cos(2\pi \cdot 2f \cdot t + \phi) \dots] \quad (9)$$

In fact, the A amplitude has an effect on the output voltage because A is a sinusoidal signal and the diode are not perfect switches. The non-linear conductance of the diodes produces intermodulation and distortion. The DBM must be operated in a saturated mode (as a limiter) and thus the OUT becomes independent of the input signal level variations.

The OUT and the A spectra are given in figure 15. A and B are in phase and their amplitude are equal to 715 mV. We can observe the DC-voltage and the 2f component of the output signal. The A and B signals are limited by the diode threshold voltage and have a 3f and 5f components.

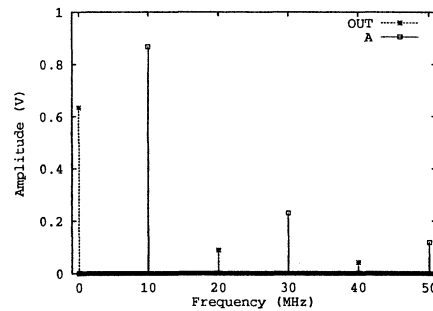


Fig. 15: OUT and A spectra for  $f_A = f_B = 10$  MHz.

In the simulation, all diodes are identical. The diode model is modified to have an output voltage amplitude around 600 mV. Figure 16 shows the phase detector response versus the phase difference of the A and the B.

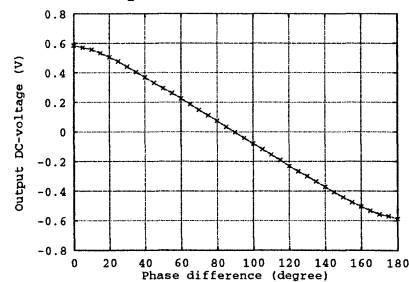


Fig. 16: Output amplitude of the phase detector versus the phase difference of A and B.

Around a phase shift of  $90^\circ$  between A and B, we can consider that the output DC-voltage is directly proportional to the phase difference of the two input signals. The sensitivity for an input equal to 5 mW is around  $8 \text{ mV}^\circ$  (or  $460 \text{ mV}\cdot\text{rad}^{-1}$ ) and corresponds to our real phase detector which is used in the measuring system.

The sensitivity of the phase detector to the input power is given by the curve in figure 17.

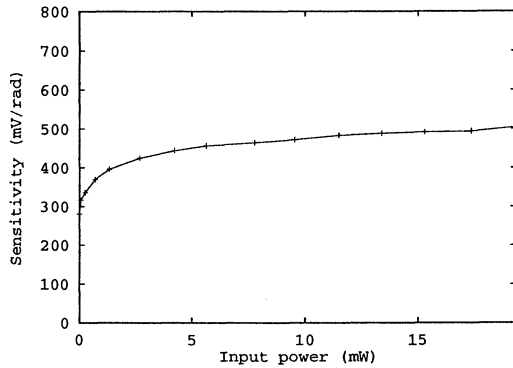


Fig.17: Phase detector sensitivity versus input power.

For an input power less than 1 mW, the sensitivity is equal to  $77 \text{ mV}\cdot\text{rad}^{-1}/\text{mW}$ . After 5 mW, the sensitivity to the input power is  $3.3 \text{ mV}\cdot\text{rad}^{-1}/\text{mW}$ , thus, we have a great interest to work at a power above 5 mW to saturate the DBM and have a minimum dependence of the amplitude variations of the input signal.

### 3.6. Output LF amplifier

This amplifier allows an adjustment of the signal amplitude which drives the spectrum analyzer. The offset voltage can be adjusted to have 0 V for a phase shift equal to  $90^\circ$ . It is associated to a low-pass filter that eliminates the 20 MHz frequency signal which is obtained at the output phase detector after the signal multiplication. The amplifier is presented in figure 18.

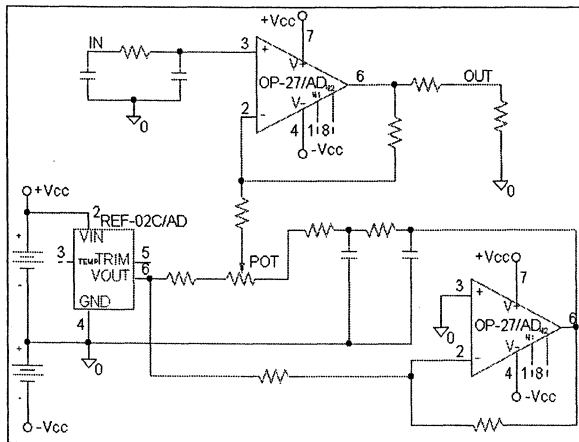


Fig. 18: Output LF amplifier.

Figure 19 and 20 give the amplifier characteristics. The cut-off frequency is around 160 Hz. In this figure, the gain is equal to 1 and can be adjusted in accordance with the spectrum analyzer.

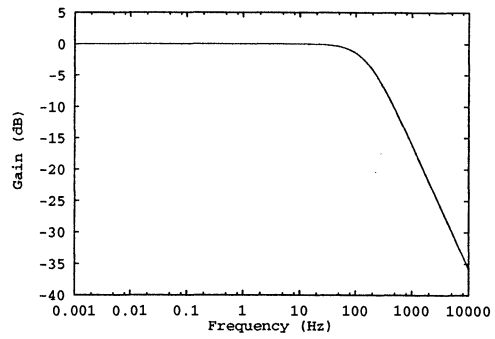


Fig. 19: Amplifier gain in dB.

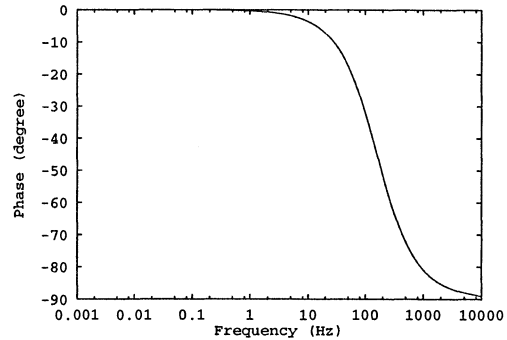


Fig. 20: Amplifier phase.

### 3.7. Complete simulation

The complete simulation is obtained when we put together all previous parts except the LF amplifier and the power splitter. Four cases have been performed. In all cases, the phase detector is saturated with input voltages equal to 800 mV.

In the first case, the simulation is computed without any modulation. The quartz resonators have been tuned at the source frequency  $f_0 = 10 \text{ MHz}$ . In this case, the output voltage floor is given in the frequency domain using the FFT. The output amplitude is equal to  $0.2 \mu\text{V}$  and allows to define the system limit. The corresponding power spectral density of the phase fluctuations  $S_\phi(f)$  is equal to  $-130 \text{ dBc/Hz}$ .

In the second case, the simulation is computed with a quartz crystal modulation. A signal which is modulated at 1 MHz is applied in one of the path of the measuring system. The quartz resonators remain adjusted to the source frequency. This configuration allows to simulate a resonator noise. The minimum of the modulation amplitude  $A = \Delta\phi$  that the system can distinguish above the voltage floor is  $10^{-6}$ . The corresponding power spectral density of the phase fluctuations  $S_\phi(f)$  is equal to  $-123 \text{ dBc/Hz}$ .

In the third case, the simulation is computed with a source modulation at 1 MHz. The quartz resonators remain adjusted to the source frequency. The rejection of the source modulation is given by this configuration. The output level is above the first case and equal to  $0.4 \mu\text{V}$  ( $S_\phi(f) = -124 \text{ dBc/Hz}$ ). Therefore the source modulation is rejected because of the measuring system symmetry.

The last case is the same as the third case but the quartz resonator frequencies are not adjusted. The resonators are chosen with a frequency equal to 9 999 993 Hz and 9 999 973 Hz, respectively. In this case, the source modulation gives a peak at 1 MHz which has an amplitude equal to 7  $\mu$ V instead of 0.2  $\mu$ V. The corresponding power spectral density of the phase fluctuations  $S_{\phi}(f)$  is equal to -99 dBc/Hz. This case shows that the frequency tuning of the quartz crystal resonators is an important parameter to reject the source modulation.

#### 4. CONCLUSION

In this paper, we have presented a PSPICE simulation of a phase noise measuring system of quartz crystal resonators. We have proposed a modulated source model. The simulator allows to tune the quartz crystal resonator frequencies to the source frequency.

The phase detector can be modified. The diode model allows to adjust the output voltage amplitude and the phase sensitivity. For most phase detector, manufacturers prefer an output level around 300 mV and a sensitivity around 300 mV·rad<sup>-1</sup>. Generally, they use schottkey diodes. Thus, the saturation of the diodes is obtained for a weaker input signal and a weaker input power level.

The complete simulation shows us the detection limit of the system. The frequency adjustment of the quartz crystal frequencies is an important parameter to have a good rejection of the source noise. It agrees with the previous numerical simulation (15)-(16).

The drawback of this kind of simulation is the computation time which is very long if we want a good resolution near the frequency carrier.

#### 5. REFERENCES

- (1) A.E. WAINWRIGHT, F.L. WALLS, W.D. McCAA, 1974, "Direct measurement of the inherent frequency stability of quartz crystal resonators", Proc. 28th Ann. Freq. Cont. Symp., pp. 177-180.
- (2) F.L. WALLS and A.E. WAINWRIGHT, 1975, "Measurement of the short-term stability of quartz crystal resonators and the implications for crystal oscillator design and applications", IEEE Trans. Instrum. Meas., Vol. IM-24, N° 1, pp. 15-20.
- (3) J.J. GAGNEPAIN, 1976, "Fundamental noise studies of quartz crystal resonators", Proc. 30th Ann. Freq. Cont. Symp., pp. 84-91.
- (4) J.J. GAGNEPAIN, M. OLIVIER, F.L. WALLS, 1983, "Excess noise in quartz crystal resonators", Proc. 37th Ann. Freq. Cont. Symp., pp. 218-225.
- (5) J.J. GAGNEPAIN, 1985, "A comparison of frequency noise of quartz resonators", Proc. 39th Ann. Freq. Cont. Symp., pp. 135-137.
- (6) S.S. ELLIOTT, R.C. BRAY, 1984, "Direct phase noise measurements of SAW resonators", Proc. 38th Ann. Freq. Cont. Symp., pp. 180-185.
- (7) T.E. PARKER, 1985, "1/f frequency fluctuations in acoustic and other stable oscillators", Proc. 39th Ann. Freq. Cont. Symp., pp. 97-106.
- (8) T.E. PARKER, 1985, "1/f frequency fluctuations in quartz acoustic resonators", Appl. Phys. Lett., 46, (3), pp. 246-248.
- (9) J.J. GAGNEPAIN, J. UEBERSFELD, G. GOUJON, P. HANDEL, 1981, "Relation between 1/f noise and Q-factor in quartz resonators at room and low temperatures, first theoretical interpretation", Proc. 35th Ann. Freq. Cont. Symp., pp. 476-483.
- (10) F.L. WALLS, P. H. HANDEL, R. BESSON and J.-J. GAGNEPAIN, 1992, "A new model of 1/f noise in BAW quartz resonators", Proc. 46th Ann. Freq. Cont. Symp., pp. 327-333.
- (11) T.E. PARKER, D. ANDRES, 1993, "Dependence of SAW resonator 1/f noise on device size", Proc. 47th Ann. Freq. Cont. Symp., pp. 178-185.
- (12) P. H. HANDEL, F.L. WALLS, 1994, "Analysis of quantum 1/f effects in frequency standards", Proc. 48th Ann. Freq. Cont. Symp., pp. 539-540.
- (13) T.E. PARKER, D. ANDRES, 1994, "1/f noise in surface acoustic wave (SAW) resonators", Proc. 48th Ann. Freq. Cont. Symp., pp. 530-538.
- (14) F.L. WALLS, 1995, "The quest to understand and reduce 1/f noise in amplifiers and BAW quartz oscillators", Proc. 9th EFTE, pp. 227-243.
- (15) F.STHAL, M. MOUREY, 1997, "Numerical simulation of a phase modulation noise measurement system of quartz crystal resonators", Proc. 11th EFTE, pp. 359-363.
- (16) F.STHAL, M. MOUREY, 1997, "Numerical model of phase bridge method used for measuring the phase modulation noise in quartz crystal resonator pair", Proc 51st Ann. Freq. Cont. Symp., pp. 456-463.
- (17) M. MOUREY, S. GALLIOU, R.J. BESSON, 1997, "A Phase Noise Model to Improve the Frequency Stability of Ultra Stable Oscillators", Proc 51st Ann. Freq. Cont. Symp., pp. 502-508.
- (18) R.J. BESSON, J.J. BOY, M. MOUREY, 1995, "BVA resonators and oscillators : a review. Relation with space requirements and quartz material characterization", Proc. 49th Ann. Freq. Cont. Symp., pp. 590-599.

# COMPARISON OF THE OUTPUT PHASE NOISE IN AN AMPLIFIER WORKING IN LINEAR AND NONLINEAR MODES

S. GALLIOU, R.J. BESSON, M. MOUREY

Laboratoire de Chronométrie, Electronique et Piézoélectricité  
 Ecole Nationale Supérieure de Mécanique et des Microtechniques  
 26 Chemin de l'Épitaphe - 25030 BESANÇON CEDEX - FRANCE  
 Fax : 33 3 81 88 57 14

## ABSTRACT

This paper is based on simulation results provided by the MicroSim PSpice CAD software. The performed analysis leads to power spectral density of phase fluctuations at the output of a transistor amplifier. This is done, first, when the amplifier signal is small, and second, when the output RF signal is high and distorted. The resulting comparison gives information about the influence of nonlinearities without any link to the amplifier inner noise. These nonlinearities are responsible of the LF noise spectrum translation around the carrier frequency.

This preliminary work is easily applied to an oscillator configuration where nonlinearities basically exist whatever the amplifier bandwidth is. Indeed, one can understand that the largest the transistor bandwidth is the lower the phase fluctuation level. But results will also improve by use of a transistor stage working at an optimized operating point where nonlinearity effects are very low.

As a conclusion, some practical applications are driven in the case of low noise 10MHz oscillators.

## INTRODUCTION

Designing transistor amplifiers which minimize phase noise is a very important investigation [1] [2]. Indeed, oscillator phase noise reduction is first the result of phase noise reduction in the loop amplifier and second phase noise reduction in the output amplifier stages.

The Power Spectral Density (PSD) of phase fluctuations in the oscillator loop (i.e., loop amplifier + quartz crystal resonator in the closed-loop) can be expressed from the PSD of phase fluctuations of the opened loop using models which are obviously limited [3] [4] [5]. These models are only available in a linear working mode. They use a general expression of the PSD of phase fluctuations  $S_{\phi}(f)$  including each of the transfer functions in the loop.

Works on phase noise (and amplitude noise) in transistor stages have been published recently [6] [7] [8]. Amplifier stages working in a linear way are described and analyzed in details. These models perfectly apply for the external output amplifier. However in the case of the oscillating closed loop the problem is very different because the signal amplitude in the oscillating loop is determined by non linearities and the linear assumption is no more valid.

This paper follows the same approach by the use of simulations instead of analytical developments and intends to introduce non linearities.

## THE ANALYSED AMPLIFIER STAGE

The amplifier studied here is, as an example, a bipolar junction transistor amplifier which can be the active part of an oscillator similar to the Clapp type. Its input is at the transistor base and two outputs must be considered:

- The first one is at the transistor collector. It is the output towards the amplifiers providing the main output signal of the system. Seen from the transistor collector, its load impedance is very large and can be ignored.
- The second one is at the transistor emitter. It feeds the tank circuit as shown in figure 1, where the quartz resonator model is the usual set {CO, LQ, CQ, RQ}. This tank circuit has its own load impedance which will be here the input impedance of this loaded transistor stage when the loop is closed !

In other words the load at the transistor emitter has to be considered. The simplest way to take into account the fact that the system will be closed is to copy the studied stage at its input and at its output (one time is a minimum) as illustrated in figure 1.

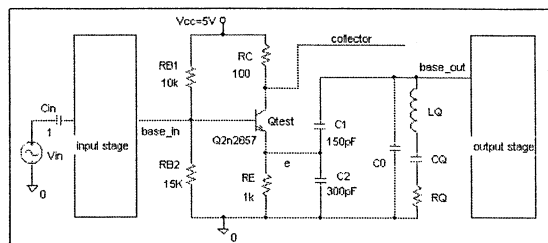


Figure 1 : The studied stage is sandwiched between two identical stages in order to simulate equivalent loads of the closed loop.

Main features of the 2N2857 are :  $f_T=1.6\text{GHz}$ ,  $C_{be}=0.9\text{pF}$ ,  $C_{bc}(\text{at } V_{cb}=10\text{V})=0.9\text{pF}$ ,  $r_b=10\Omega$ ,  $r_c=4\Omega$ ,  $\beta=280$ ,  $NF=3\text{dB}$ . The biasing point is here  $I_c=2\text{mA}$ ,  $V_{cb}=2\text{V}$ .

The quartz resonator has an unloaded quality factor equal to  $Q = 1.3 \cdot 10^6$ .

Looking at the required accuracy it is important to pay attention to the option set up before simulation.

## LINEAR ANALYSIS

In references [6] [7] [8] the calculation principle of the PSD of phase fluctuations consists of expressing the analytical form of the transfer function  $G(v)$  of the studied stage as a function of passive elements surrounding the transistor and inner elements of the transistor small signal model. All of these elements are denoted  $x_i$  in the following expressions.

Assuming an ideal input signal  $v_{in}(t) = V_{in} \sin(2\pi f_0 t)$  where  $f_0$  denotes the "carrier" frequency (in our case  $f_0 = 10$  MHz) then the output signal is given by :

$$v_{out}(t) = V_{out}(f_0, x_i) \cdot \sin(2\pi f_0 t + \Phi(f_0, x_i)) \quad (1)$$

parameters  $x_i$  being affected by noise, with :

$$V_{out}(f_0, x_i) = V_{in} \times |G(f_0, x_i)| \quad \text{and} \quad \Phi(f_0, x_i) = \text{Arg} G(f_0, x_i) \quad (2)$$

for small changes  $dx_i$  of  $x_i$  around  $x_{i0}$  at frequencies  $f \ll f_0$  ( $f$  being the frequency of a noise component) the phase of  $v_{out}(t)$  yields :

$$\begin{aligned} \Phi(f_0, x_{i0} + dx_i) &= \text{Arg} G(f_0, x_{i0} + dx_i) \\ &= \text{Arg} G(f_0, x_{i0}) + \left. \frac{\partial}{\partial x_i} \text{Arg} G(f_0, x_i) \right|_{x_i=x_{i0}} \times dx_i \\ &= \Phi_0 + \Delta\Phi \end{aligned} \quad (3)$$

where  $\left. \frac{\partial}{\partial x_i} \text{Arg} G(f_0, x_i) \right|_{x_i=x_{i0}} \times dx_i$  may be a sum of terms depending on the number of  $x_i$  affected by noise.

Considering the noise component at frequency  $f$  such that  $dx_i = \Delta x_i \sin 2\pi f t$  where  $\Delta x_i$  is sufficiently small so that terms of second order can be neglected in the series development of (1),  $v_{out}(t)$  can be expressed in components at frequencies  $f_0$ ,  $f_0 \pm f$ ,  $f_0 + f$  whose amplitudes are :

$$\begin{aligned} &- V_{in} G_0 \quad \text{for the component at } f_0, \\ &- V_{in} G_0 \frac{1}{2} \frac{\Delta G_i}{G_0} \quad \text{and} \quad V_{in} G_0 \frac{1}{2} \Delta\Phi_i \quad (\text{not at the same} \end{aligned}$$

phase) at  $f_0 + f$  and  $f_0 - f$ .  
where

$$\begin{aligned} G_0 &= |G(f_0, x_{i0})|, \\ \Delta G_i &= \left. \frac{\partial}{\partial x_i} |G(f_0, x_i)| \right|_{x_i=x_{i0}} \times \Delta x_i \quad \text{and} \\ \Delta\Phi_i &= \left. \frac{\partial}{\partial x_i} \text{Arg} G(f_0, x_i) \right|_{x_i=x_{i0}} \times \Delta x_i \end{aligned} \quad (4)$$

Then, the PSD of phase fluctuations becomes :

$$\begin{aligned} S_\Phi(f) &= \Delta\Phi^2(f) \text{ rd}^2/\text{Hz} = \\ &\left[ \left. \frac{\partial}{\partial x_i} \text{Arg} G(f_0, x_i) \right|_{x_i=x_{i0}} \right]^2 \times S_{x_i}(f) \end{aligned} \quad (5)$$

and the PSD of amplitude fluctuations is :

$$\begin{aligned} S_A(f) &= \left( \frac{\Delta G(f)}{G_0} \right)^2 \text{ V}^2/\text{Hz} = \\ &\left[ \left. \frac{\partial}{\partial x_i} |G(f_0, x_i)| \right|_{x_i=x_{i0}} / G_0 \right]^2 \times S_{x_i}(f) \end{aligned} \quad (6)$$

This working frequency  $f_0$  of the amplifier is here the frequency of oscillation of the closed loop system, that is to say the frequency which satisfies the phase conditions  $V_p(\text{base\_out}) - V_p(\text{base\_in}) = 0$  ( $V_p(x)$  means phase of  $V(x)$ ) and also the amplitude condition  $V(\text{base\_out}) \geq V(\text{base\_in})$ , where "base\_in" and "base\_out" denote both ends that must be joined in the closed-loop (see fig. 2 and fig. 1)

We note that for a series resonance frequency of the crystal at 10 000 000.0 Hz, the frequency of oscillation in fig. 2 is 10 000 010.9 Hz that is a frequency shift of 10.9 Hz with the values of C1 and C2 of fig. 1, for instance. This shift is also predictable using a calculation based on a basic circuit model of the oscillator giving :  $\frac{\Delta f_0}{f_0} = \sqrt{C_Q \left( \frac{1}{C_1'} + \frac{1}{C_2'} \right)} - 1$  with  $C_1' = \alpha C_1$  and  $C_2' \approx C_2$  where  $\alpha$ , is a function of  $R_E$  (here  $\alpha \approx 0.8$ ).

Fig. 2 shows the behavior of the three interesting nodes referred to the input "base\_in" versus frequency. This is the result of the Spice "AC analysis" performing a frequency sweep of the input generator  $V_{in}$  (see fig. 1) on a small signal model of the circuit at its operating point. So, this is the numerical form of what is analytically done in references [6] and [7]. The AC analysis just needs a few seconds on a PC.

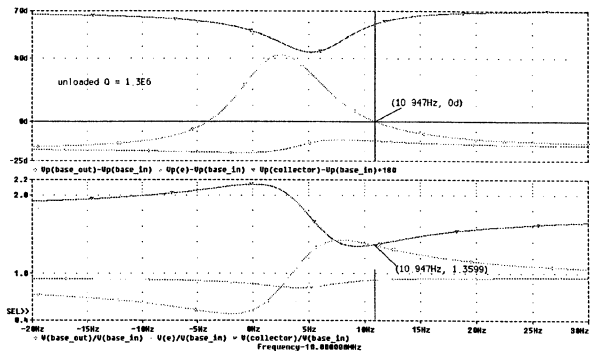


**Figure 2 :** Gain and phase of the three interesting transfer function of fig. 1 versus frequency around  $f_0 = 10$  MHz.

Fig. 3 shows the influence of change of the resonator quality factor on input-output phase of the open-loop amplifier (this is equivalent to a change of the amplifier load). These phase changes imply changes of the frequency of oscillation of the closed-loop amplifier. Here, a relative change  $\Delta Q/Q = \pm 30\%$  of the unloaded quality factor gives a frequency change of  $\frac{\Delta f_0}{f_0} \approx \pm 5 \cdot 10^{-7}$ .

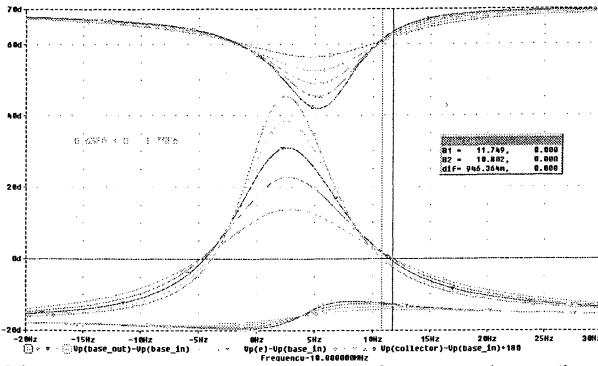


Figure 3 : Influence of the quality factor on phases (in degrees) and on the frequency of oscillation (when phase is 0).

Those previous remarks were necessary before examining consequences of the transistor internal noise on the phase noise of this amplifier stage.

We assume that the main origin of  $1/f$  noise is the charge carrier recombination rate fluctuation. This can be simulated by saturation current fluctuations in the transistor base-emitter junction expressed as  $I_s = I_{s0}(1 + \text{gamIs})$  where  $\text{gamIs}$  denotes the relative fluctuation of current  $I_s$  (i.e.  $\gamma$  as in [6]). The typical values of  $I_{s0}$  for the 2N2857 is  $69.28 \cdot 10^{-18}$  at  $27^\circ \text{C}$ .  $\text{gamIs}$  is just defined as a parameter for simulations which consist in as many AC analysis as parameter values. Fig. 4 shows results on phase versus frequency around the zero phase of the open-loop when  $I_s$  changes from  $-6 \cdot 10^{-5}$  to  $+6 \cdot 10^{-5}$  for a resonator unloaded quality factor  $Q = 1.3 \cdot 10^6$ .

The phase change of  $V_p(\text{base\_out}) - V_p(\text{base\_in})$  versus  $\text{gamIs}$  can be looked like a frequency noise considering that a phase shift of the amplifier would be compensated by an opposite phase shift of the tank circuit, once the loop is closed. Here the frequency shift is  $\Delta f_0 = 9 \mu\text{Hz}$  for  $\Delta \text{gamIs} = 5 \cdot 10^{-5}$  the phase change can also be seen as a consequence of frequency noise inside the loop. The corresponding phase change is then calculated from the slope around the frequency of oscillation  $f_0$  (strongly dependent of the loaded resonator quality factor). With a slope of  $0.05 \text{ rd/Hz}$ , the PSD of phase fluctuations becomes  $S_\Phi(f) = \Delta\Phi^2(f) \cdot \text{rd}^2/\text{Hz} = (0.05 \cdot 9 \cdot 10^{-6})^2 \text{ rd}^2/\text{Hz} = 2 \cdot 10^{-13} \text{ rd}^2/\text{Hz}$  that is  $-127 \text{ dBc/Hz}$  for a basic white noise such that  $\Delta \text{gamIs} = 5 \cdot 10^{-5}$ . Generalizing to some noise affecting  $\text{gamIs}$  with PSD  $S_\gamma(f)$ , the PSD of phase fluctuations into the loop at the transistor base, would be  $S_\Phi(f) = \Delta\Phi^2(f) \cdot S_\gamma(f) = 8 \cdot 10^{-5} S_\gamma(f)$ .

The phase change on  $V_p(\text{collector}) - V_p(\text{base\_in})$  shows that a frequency noise into the loop induces a phase noise at the collector output. A specific phase value  $\Phi = V_p(\text{collector}) - V_p(\text{base\_in})$  is associated to each value of the frequency of oscillation  $f_0$  (at  $V_p(\text{base\_out}) - V_p(\text{base\_in}) = 0$ ).

As shown in fig. 4, the set of these points can be approximated by a straight line whose slope  $\Delta\Phi / \Delta f_0 = 139 \mu\text{degree}/22.6 \mu\text{Hz} = 0.1 \text{ rd/Hz}$ . Nevertheless, it is impossible to go ahead in the calculation of the induced frequency change without any time relationship (the instantaneous frequency being defined by  $2\pi f(t) = \frac{d}{dt} \Phi(t)$ ).

In the case of an open-loop amplifier, the collector phase change measurement is more simple : it is the  $V_p(\text{collector}) - V_p(\text{base\_in})$  change at a constant frequency  $f_0$  (where  $f_0$  is the input signal frequency). This leads to a collector phase change 0.8 times less than previously, that is:  $S_\Phi(f) = 4 \cdot 10^{-13} \text{ rd}^2/\text{Hz}$  for  $\Delta \text{gamIs} = 5 \cdot 10^{-5}$  or  $S_\Phi(f) = 1.5 \cdot 10^{-4} S_\gamma$ .

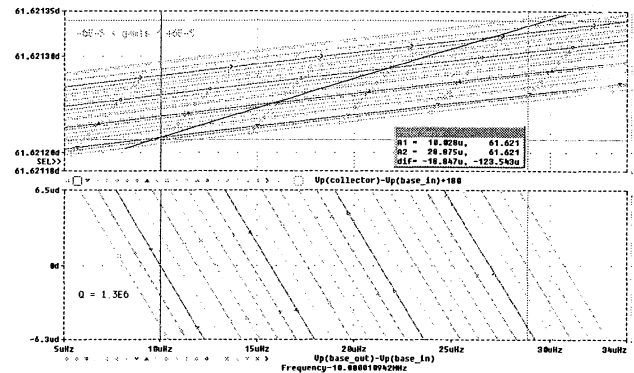


Figure 4 : Phases in degrees resulting from AC analysis when  $\text{gamIs}$  changes from  $-6 \cdot 10^{-5}$  to  $+6 \cdot 10^{-5}$  by step of  $0.5 \cdot 10^{-5}$ .

## INFLUENCE OF THE OPERATING POINT

Biasing of the transistor base as performed in fig. 1 with the set  $\{V_{cc}=5\text{V}, R_{B1}=10\text{k}\Omega, R_{B2}=15\text{k}\Omega\}$  can also be done with the equivalent set  $\{V_{BB}=3\text{V}, R_{BB}=6\text{k}\Omega\}$ . Thus, transistor biasing can easily be modified without changing the input impedance of the amplifier.

Fig. 5 shows such a simulation result when  $V_{BB}$  increases from  $1.3 \text{ V}$  to  $4.9 \text{ V}$  by step of  $0.2 \text{ V}$  (in fact, oscillation conditions are not verified for  $1.3 \text{ V}$ ) which also leads the emitter current to increase by step of about  $0.2 \text{ mA}$ . It is obvious that the frequency of oscillation  $f_0$  at  $V_p(\text{base\_out}) - V_p(\text{base\_in}) = 0$  is less sensitive to  $V_{BB}$  changes for high values of  $V_{BB}$ , and thus for high values of  $I_E$ . The frequency change  $\Delta f_0$  is roughly proportional to  $\Delta V_{BB}/V_{BB}$  and then to  $\Delta I_E/I_E$ . This is in accordance with the following relationship calculated from a simplified small signal model :

$$\Delta f_0 \approx \frac{\epsilon R_E g_m}{8\pi^2 L_Q C_1 f_0} \frac{\Delta I_E}{I_E} \text{ where } \epsilon \approx 3 \cdot 10^{-3}, g_m \text{ being the transistor transconductance.}$$

On the other hand, one can see that the quality factor decreases when  $I_E$  increases (like  $V_{BB}$ ) : the slope

$\Delta\Phi/\Delta f_0$  is about  $97.10^{-3}$  rd/Hz at  $I_E = 0.92$  mA ( $V_{BE} = 1.7$  V) whereas it decreases down to  $34.10^{-3}$  rd/Hz at  $I_E = 2.93$  mA ( $V_{BE} = 3.9$  V). Such a decrease in the quality factor is due to a decrease in the resonator load depending on the input transistor resistor  $r_{BE} \approx \beta V_T/I_E$ .

**As a first conclusion, from the point of view of the phase noise into the loop, it is better to work with low currents  $I_E$  !**

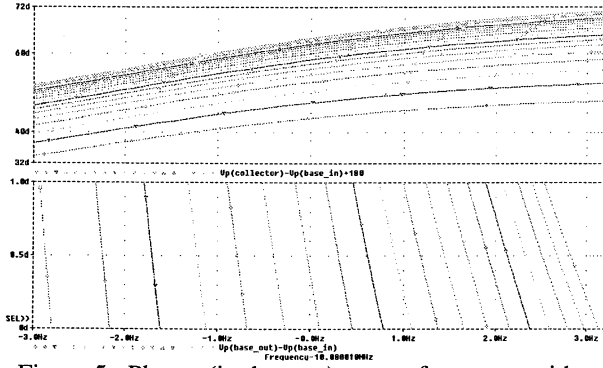


**Figure 5 :** Phases (in degrees) versus frequency with unloaded  $Q = 1.3 \cdot 10^{-6}$ . The equivalent bias voltage  $V_{BE}$  comes from 1.3 V to 4.9 V by step of 0.2 V.

Moreover, the  $V_p(\text{collector})-V_p(\text{base\_in})$  characteristics in fig. 5 indicate that the curve of this phase versus frequencies of oscillation  $f_o$  is non linear and its slope decreases as  $I_E$  increases (like  $V_{BE}$ ).

Then, this is the second conclusion : **it is better to have a high value of  $I_E$  in order to reduce phase noise at the collector output !**

Both conclusions indicate opposite directions. Finally, the solution is a compromise and this is largely confirmed by experiments, pointing out differences between oscillator and amplifier design.

## NON LINEAR ANALYSIS

In the above linear analysis there is a direct noise modulation of the signal and, as a consequence, the low frequency noise spectrum automatically comes around the carrier frequency. A second mechanism of this up-conversion is the modulation through a non linearity like the base-emitter junction characteristic. The relationship between the collector current  $I_c$  and the base-emitter voltage  $V_{BE}$ , when developed at the second order, is a good description of the signal to noise modulation :

$$\begin{aligned}
 I_c &\approx \beta I_s \exp \frac{V_{BE}}{U_T} = \beta I_s \exp \frac{V_{BE0}}{U_T} \cdot \exp \frac{v_{BE}(t)}{U_T} \\
 &\approx I_{c0} \cdot \left[ 1 + \frac{v_{BE}(t)}{U_T} + \frac{1}{2} \left( \frac{v_{BE}(t)}{U_T} \right)^2 \right] \\
 &= I_{c0} + \frac{I_{c0}}{U_T} v_{BE}(t) + \frac{1}{2} \frac{I_{c0}}{U_T} \frac{v_{BE}^2(t)}{U_T} \\
 &\approx I_{c0} + g_m v_{BE}(t) + \frac{1}{2} g_m \frac{v_{BE}^2(t)}{U_T}
 \end{aligned} \tag{7}$$

where subscripts 0 denotes bias components,  $v_{BE}(t)$  being the time-varying component of  $V_{BE}$  including noise as well as the signal. Direct modulation due to the inner transistor noise affects the transconductance  $g_m$  (in phase and amplitude modulation). Signal and noise intermodulation into the loop appears from the second order term. Noise into the loop may have an outer origin or be the amplifier caused noise or resonator caused noise.

In order to take into account non linearities it is necessary to perform a transient analysis. This type of analysis is very realistic but needs large calculation times and important memory space, especially in our case where high resolution is needed with a large  $Q$  factor, that is to say a long transient time before steady state.

In the following simulations the quality factor is set at  $Q = 1000$  and thus noise effects are emphasized.  $Q$  could be increased up to 500 000 without too much complexity.

Unfortunately, dynamic change of an inner transistor parameter is impossible. Like in AC analysis, only static change are authorized. Nevertheless, an outer dynamic disturbance can be superimposed (see (7)) in order to generate intermodulation.

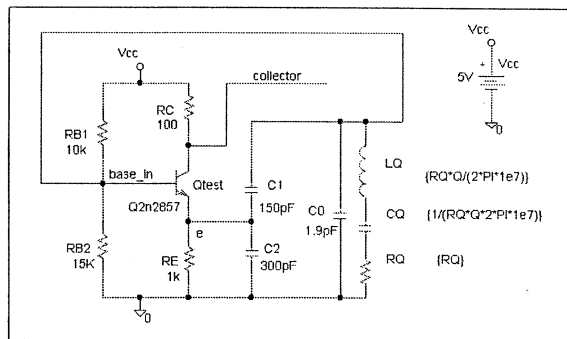


**Figure 6 :** The closed loop system.

Fig. 6 shows the analyzed oscillator in transient analysis whose results in fig. 7 shows very well the effects of non linearities. The Fast Fourier Transform (FFT) performed on these signals provides the respective amplitude of each component.

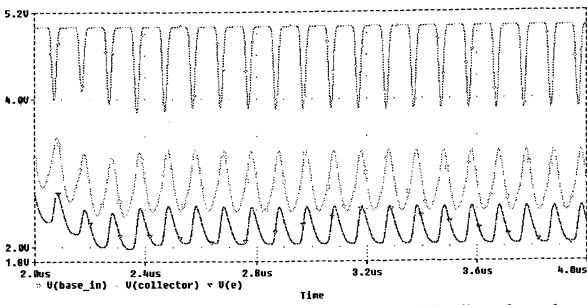


**Figure 7-a :** Shapes of voltages marked in fig. 6 at the end of the transient period.  
Simulation conditions :  $Q = 1000$  and  $CQ$  initially charged at 100 V.

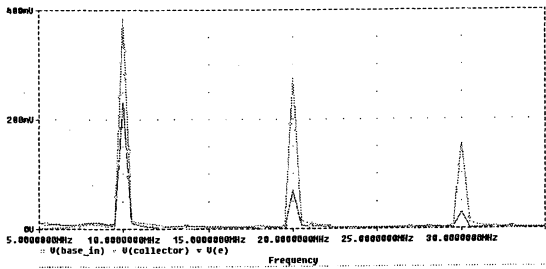


**Figure 7-b :** FFT result (amplitude spectrum) of voltages in fig. 6, without their DC components.

Superimposing a disturbance can be performed like in fig. 8 for instance, where a current sine wave "Imodul" is added at one node. The disturbance effect measurement needs comparison of the noisy signal to a reference one. This explains the second oscillator in fig. 8 which is identical to the Device Under Test (DUT) but without any disturbance. The ability to built such a reference is a great advantage of simulation compared with experiments.

Each voltage of the DUT compared with its corresponding reference voltage is shown in fig. 9-a. In this example the added noise frequency is at  $f = 1$  MHz (frequency of the "Imodul" wave). The up-conversion of this noise around the carrier at  $f_0 = 10$  MHz is well illustrated by the amplitude spectrum in fig. 9-b : two components rise on both sides (at 10 MHz-1 MHz and 10 MHz+1MHz) close to the carrier here suppressed by the comparison. But still remains to separate phase noise from amplitude noise in this result. This will be the next step of our work.

Nevertheless, by use of results indicated here it has been possible to design 10 MHz Ultra Stable Oscillator (USO) with short term stabilities  $\sigma_y(\tau)$  in the order of  $7.10^{-14}$  ( $1 \text{ s} < \tau < 100 \text{ s}$ ).

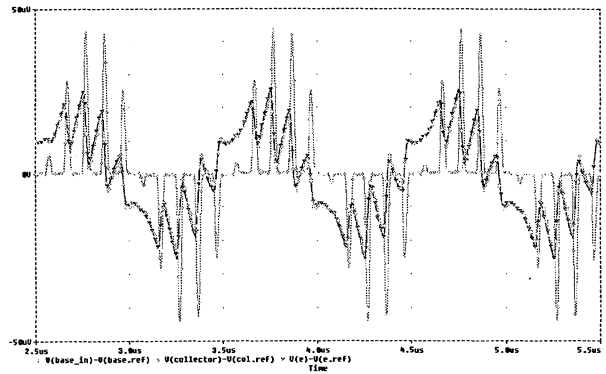


**Figure 9a :** Perturbation effect of the emitter current with a relative change of  $5.10^{-5}$  at 1 MHz. Here is the comparison result.

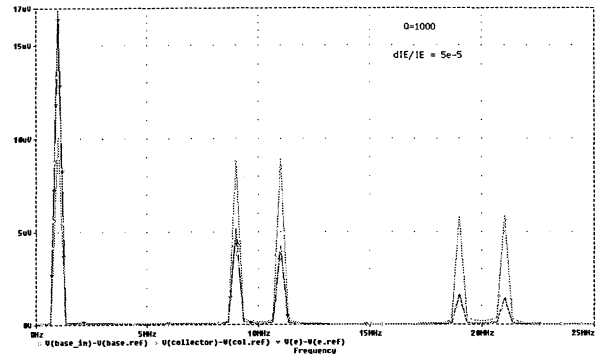


**Figure 9-b :** The FFT operation on voltages of fig. 9-a limited at 25 MHz.

## CONCLUSION

Though the work is still going on it is possible to derive provisional conclusions :

- \* Simulations can be extremely useful in quest of low phase noise oscillators because :
  - analytical calculation is almost impossible to solve the non linear problem ;
  - devices without noise are possible in simulation for instance in view of differential measurements.
- \* It is now clear that the choice of the current  $I_E$  is a compromise because :
  - Low  $I_E$  favors low phase noise in the loop ;
  - High  $I_E$  favors low phase noise at the collector output of the amplifier.
- \* The above analysis method allows to reach the noise in a non linear closed-loop amplifier.
- Still remains to separate phase noise from amplitude noise in result of non linear analysis.

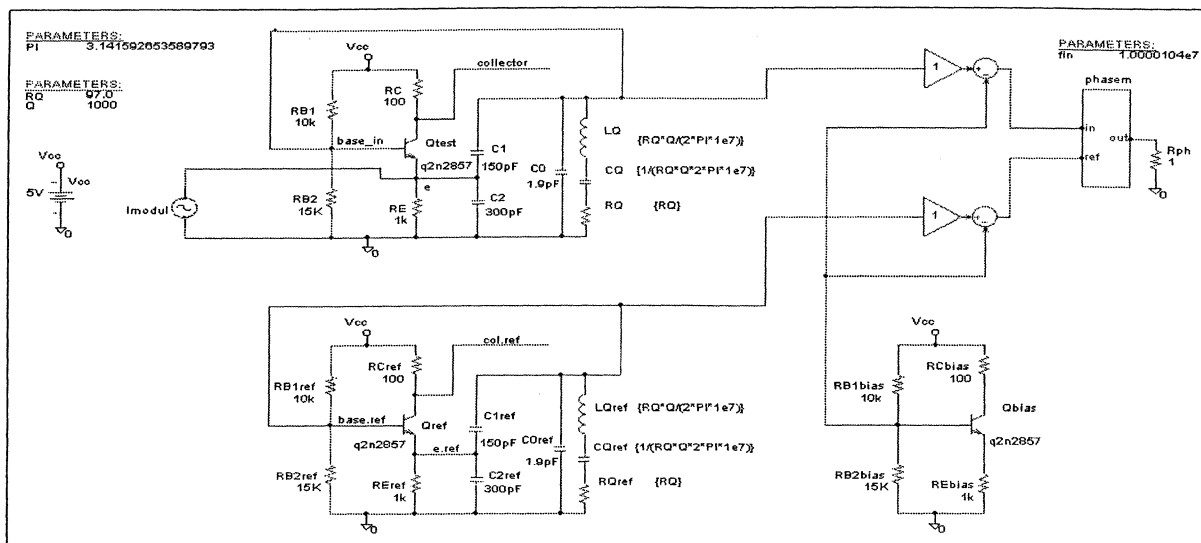


Figure 8 : The disturbed oscillator and the reference oscillator working in same conditions.

## REFERENCES

- [1] T.E. PARKER, 1985, "1/f Frequency Fluctuations in acoustic and Other Stable Oscillators", Proceedings 39th Annual Frequency Control Symposium, pp 97-106.
- [2] F.L. WALLS, 1995, "The quest to understand and reduce 1/f noise in amplifiers and baw quartz oscillators", Proceedings 9th EFTF, pp 227-243..
- [3] D.B. LEESON, 1966, "A simple model of feedback oscillator noise spectrum", Proc. of the IEEE, Vol. 54, N° 2, pp 329-330.
- [4] G. SAUVAGE, 1977, "Phase noise in oscillators : a mathematical analysis of Leeson's model", IEEE Transactions on Instrumentation and Measurement, Vol. IM26, N° 4..
- [5] M. MOUREY, S. GALLIOU and R.J. BESSON, 1997, "A phase noise model to improve the frequency stability of ultra stable oscillator", Proc. of the IEEE International Frequency Control Symposium, , pp 502-508
- [6] F.L. WALLS, E.S. FERRE-PIKAL and S.R. JEFFERTS, 1995, "The origin of 1/f noise in bipolar junction transistor amplifiers", Proc. of the IEEE International Frequency Control Symposium, San Francisco, pp 294-304.
- [7] V.N. KULESHOV and T.I. BOLDYREVA, 1997, "1/f AM and PM noise in bipolar transistor amplifiers : sources, ways of influence. Techniques of reduction", Proc. of the IEEE International Frequency Control Symposium, Orlando, pp 446-455
- [8] R. BESSON, M. MOUREY, S. GALLIOU, Ph. GUILLEMOT, 1996, "Phase noise figures comparison in transistor amplifiers of different types", Proceedings 10th EFTF. Brighton, pp 447-451
- [9] MicroSim corporation 20 Fairbanks, Irvine, California 92718 USA  
<http://www.MicroSim.com>

**Time transfer & comparisons II**

Chairman:

*Kurt Hilty*



## THE PERFORMANCE CHARACTERISTICS OF A TWO-WAY TIME TRANSFER EARTH STATION INCORPORATING A NEW SATRE MODEM

John A Davis, Joan M Furlong and Jon D Clarke

Centre for Time Metrology, National Physical Laboratory, Queens Road, Teddington, Middlesex, TW11 OLW.

### ABSTRACT

The Two Way Satellite Time and Frequency (TWSTFT) earth station at the NPL has been re-engineered, both to fully automate its operation, and to improve its performance. A description is given of the new TWSTFT earth station configuration. The performance of a new SATRE TWSTFT modem is compared with that of the existing MITREX modem. Measurements have been made to determine the delay stability of the TWSTFT station. Results are presented that may provide an insight into the errors arising from correcting TWSTFT instrumentation delay changes using a near field satellite simulator.

### 1) INTRODUCTION

Two Way Satellite Time and Frequency Transfer (TWSTFT) is one of the most precise methods of time and frequency transfer available (Kirchner (1)). Because of the symmetry of the TWSTFT method, many sources of error that occur in receive only time transfer methods, for example due to earth station or satellite positioning errors, ionospheric and tropospheric delays are either eliminated or very substantially reduced. The ultimate time and frequency transfer accuracy of the TWSTFT system is limited by instabilities in the earth station instrumentation delays. The use of TWSTFT near field satellite simulators to measure the delay stability of TWSTFT instrumentation, has been reported by several authors, (de Jong (2)), (Ressler et al (3)) including previous measurements made at NPL (Davis and Pearce(4)).

The NPL has been performing regular TWSTFT measurements since 1993. An initial evaluation of the stability of the NPL's TWSTFT earth station was reported in 1992 (4). The requirement to upgrade and automate the earth station has provided an opportunity to incorporate automated earth station delay measurements as part of the station's routine operation. This has been accomplished through the construction of two near field TWSTFT satellite simulators that operate in parallel. This configuration has enabled the study of the systematic errors present when using near field TWSTFT satellite simulators. A second series of loop delay measurements were also made using a microwave mixer located indoors in a temperature controlled room. The incorporation of a new SATRE TWSTFT modem into the earth station offers the

possibility of significantly improving the performance of the TWSTFT earth station.

### 2) TWSTFT EARTH STATION CONFIGURATION USED FOR AUTOMATIC OPERATION.

Significant hardware changes have been made to support the automation of NPL's TWSTFT earth station. Besides a new SATRE modem, a new up-converter (Miteq model U-9456-1K), counter timer (Stanford Instruments SR620), connecting cables (Rhopphase Type 1771), High Powered Amplifier (HPA) (PASCAL model PA-14145-2), PC and switch boxes (Hewlett Packard model 59307A) and directional couplers (MA-COM model TU-508) have all been incorporated into the station up-grade. A diagram of the TWSTFT earth station configuration is shown in Figure 1.

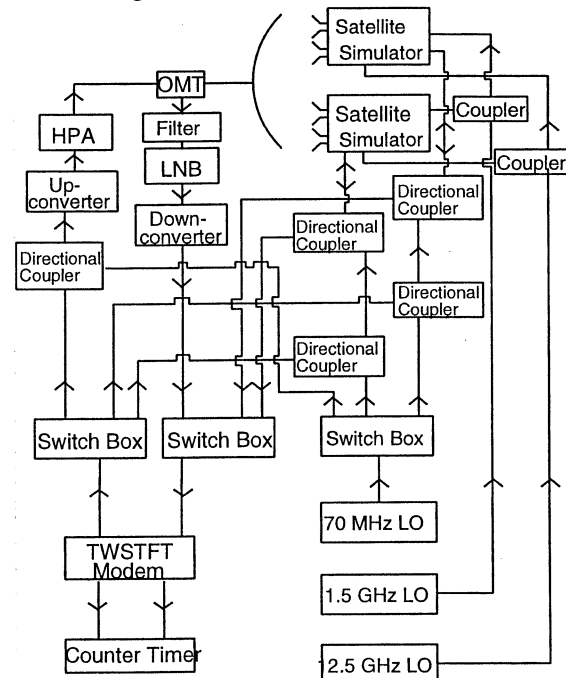


Figure 1: Configuration of the NPL earth station.

During loop test measurements the internal counter timer of the SATRE modem was used to measure the loop delay. The SR620 pico-second resolution counter timer was used with the existing MITREX modem. The high frequency switch boxes were used to switch the 70 MHz modem transmit and receive signals between a variety of TWSTFT calibration loops. The loop configurations were switched every minute, with

the last 30s of collected data being analysed. Because the TWSTFT earth station is located some distance from UTC(NPL), a standard frequency 5 MHz signal is transmitted along a cable between UTC(NPL) and the TWSTFT earth station and the 1 PPS signal supplied to the modem is generated locally. Delays in the cables between the buildings were monitored using a phase comparator (Timetech model 16-001/96). The near field TWSTFT satellite simulators are a modification of the de Jong design (Figure 2).

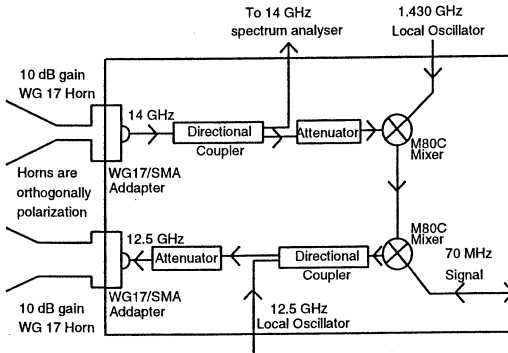


Figure 2: Near field simulator configuration.

Near field TWSTFT satellite simulators are used to make two separate measurements. The total loop delay (combined uplink and downlink delay) and the downlink delays are measured separately. These measurements enable the determination of the earth station delay asymmetry (half difference of the uplink and downlink delay). The NPL satellite simulator has been designed to independently measure the uplink delay using a 12.6 GHz local oscillator. The two satellite simulators are supplied with the same local oscillator signals and experience similar temperature and humidity changes, however in other respects they are independent.

### 3) NON-LINEAR ADDITION OF PROPAGATION DELAYS

The non-linear addition of propagation delays in TWSTFT instrumentation was first detected through the observation of closing errors in European TWSTFT time transfers (Davis et al (5)). The propagation delay through an element of a TWSTFT earth station is dependent on the characteristics of its input signal (Davis et al (6) and Davis (7)). The use of both the SATRE and MITREX modems provided NPL with two TWSTFT signal sources that have slightly different characteristics, for example in their spectral profile. This enabled studies of the non-linear propagation delay addition within the TWSTFT earth station. Non-linear delay addition is a serious problem when using a TWSTFT satellite simulator to calibrate earth station delay asymmetries. This is because the downlink calibration loop signal will have a different origin to a normal TWSTFT signal, and hence characteristics. This results in a slightly different

downlink delay and hence a calibration error. The non-linear component of the instrumentation delay is defined here as the component of the delay that is dependent on the characteristics of the input signal. The variation of the non-linear components of the instrumentation delay will also limit the accuracy with which earth station delay changes may be corrected using a near field simulator. The stability of this non-linear component may be estimated by measuring the stability of the TWSTFT closures.

### 4) COMPARISON OF THE SATRE AND MITREX MODEMS

The SATRE and MITREX modems were directly compared by measuring their loop delay. The possible modem loop configurations are shown in Figure 3.

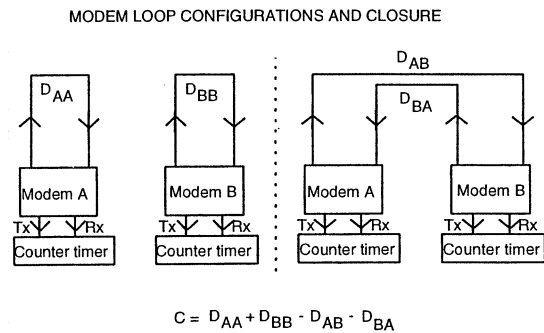


Figure 3: Modem configurations used in this work

The high frequency switch boxes, and directional couplers were used to measure in turn the delay stabilities of the modem loops. The switching arrangements are shown in Figure 4.

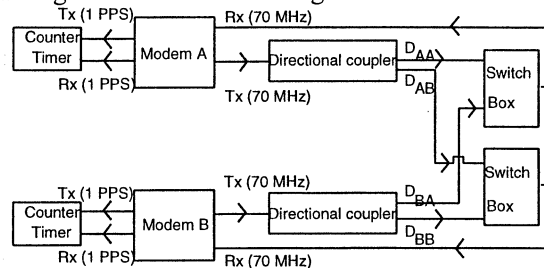


Figure 4: Modem switching configuration

The SATRE to SATRE loop delay was found to be the most stable (Figure 5). This provides a limitation to the ultimate performance of the TWSTFT earth station and demonstrated that the SATRE modem is an improvement on the existing MITREX modem. The SATRE to MITREX and MITREX to SATRE loop delays were found to be stable, indicating that the MITREX and SATRE modems are compatible.

A modem closure (C) may be obtained from combining the four delays shown in Figure 3 where:

$$C = D_{AA} + D_{BB} - D_{AB} - D_{BA} \quad (1)$$

The same cables were used in the two loop arrangements. A closure of  $(2.5 \pm 0.1)$  ns was observed. This demonstrated that when comparing SATRE and MITREX modems it is not possible to simply add the components of the propagation delays within the modems and connecting cables.

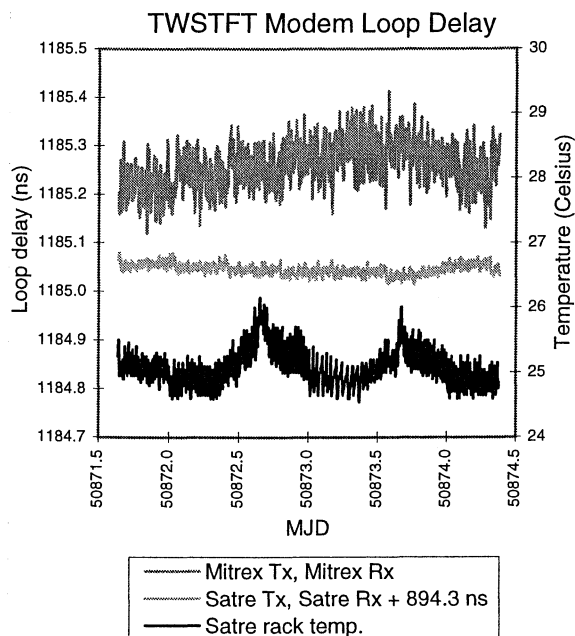


Figure 5: Modem loop delays

The closure appeared to be relatively insensitive to temperature changes. The closure was however stable suggesting that delay closures may be effectively calibrated.

### 5) MEASUREMENTS MADE USING NPL'S TWSTFT NEAR FIELD SIMULATORS.

The TWSTFT earth station configuration using the near field simulator is shown in Figure 1. Four loop configurations were measured, the total loop delays and downlink delays using both simulators. Changes in the total loop delays did correlate reasonably well between the two simulators (Figure 6), however delay instabilities may occur in the elements of the satellite simulator. The downlink loop delay changes as measured by the two simulators did not correlate well. Further work is required in developing this loop configuration.

### 6) EARTH STATION MEASUREMENTS MADE USING SIMULTANEOUS MODEM TRANSMISSIONS

The earth station configuration used in these loop measurements is shown in Figure 7. Two directional couplers were used to combine and split the two modem signals, which are transmitted through the

same earth station elements. The power levels of the two signals were equalised; different modem codes were used to identify and separate the signals. The SATRE and MITREX loop delays differed only in the modem used. There was clear correlation between the SATRE and MITREX loop delays using the same satellite simulator (Figure 8). The short term noise in the SATRE modem signal is significantly lower.

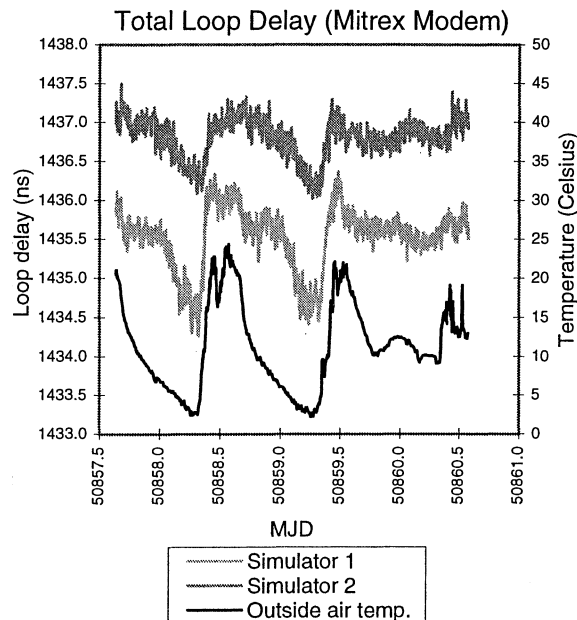


Figure 6: Total loop delay

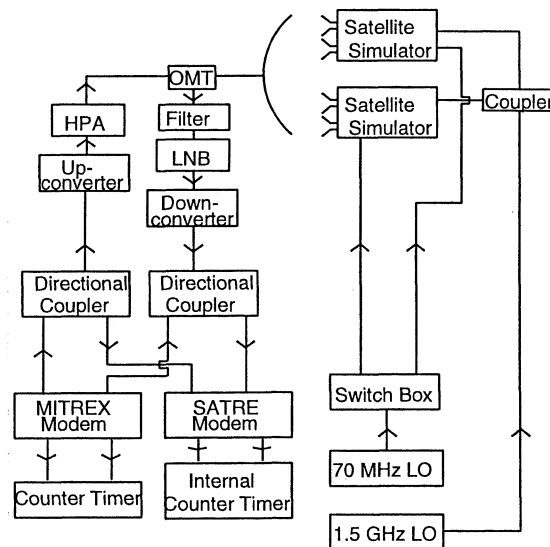


Figure 7: Configuration of simultaneous modem transmission loop.

### 7) DOWNCONVERTER AND INDOOR LOOP DELAY MEASUREMENTS

A downconverter loop delay configuration is shown in Figure 9. All of the components of the loop were located in a temperature controlled room. Plots of both MITREX and SATRE delay loops, and local temperature are shown in Figure 10.

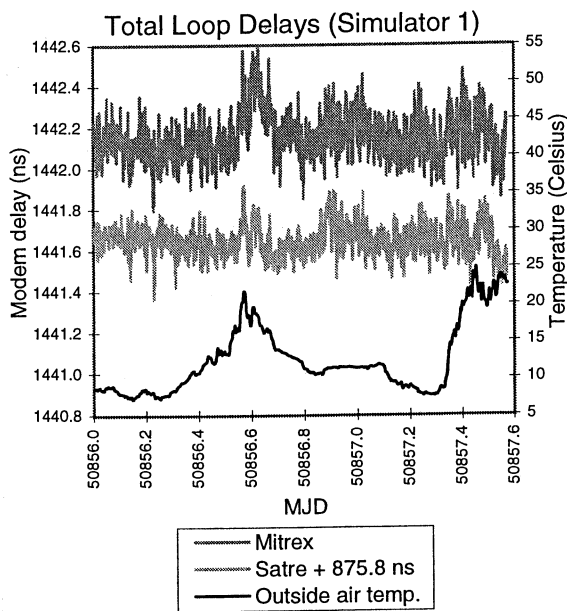


Figure 8: Satellite simulator total loop delay

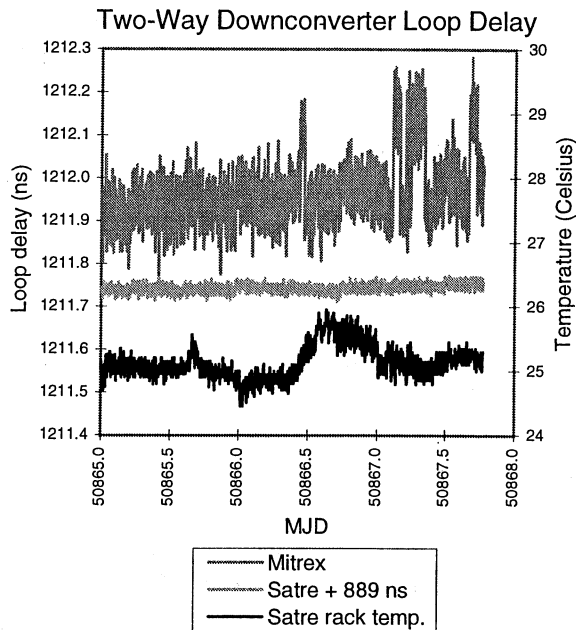


Figure 10: Downconverter delay

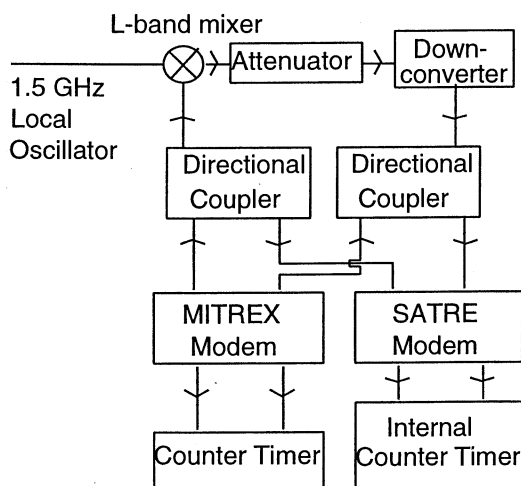


Figure 9: Downconverter loop delay configuration.

All of the loop delays were encouragingly stable. The MITREX loop delay did however show small discrete delay steps. The stability of the SATRE loop delay was significantly better. Similar loop configurations were measured that included all of the indoor components of the TWSTFT earth station.

For all of the indoor loops under examination the measured values of  $\sigma_x$  ( $\tau = 1$  day) was less than 100 ps. There was some correlation between the indoor temperature fluctuations and the loop delay changes. This was probably due to the temperature sensitivity of the mixer used in the calibrating loop. The results were encouraging, demonstrating that all of the indoor components of the TWSTFT earth station were sufficiently stable to permit time transfers with a transfer  $\sigma_x$  of 100 ps or lower for averaging times of 1 day.

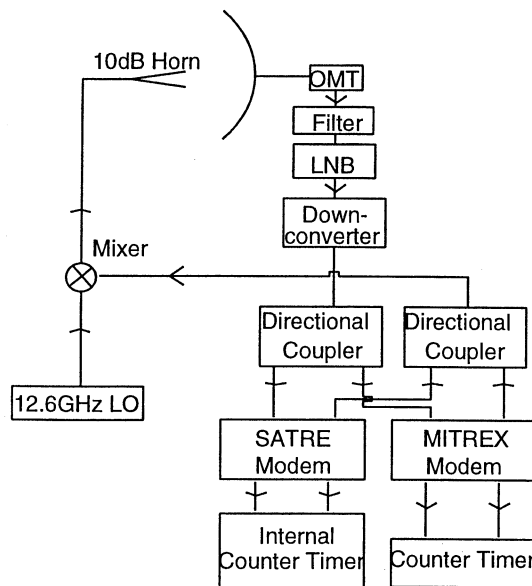


Figure 11: Downlink delay configuration

## 8) OUTDOOR LOOP DELAY MEASUREMENTS

The configuration used to measure the downlink delay, and delay stability is shown in Figures 11 and 12 respectively. The results using the SATRE and MITREX modems correlated well. The lowest short term delay instabilities were shown by the SATRE modem. Delay changes of several ns occurred. These changes did not correlate with temperature. Similar results were obtained in the 1992 NPL study (4). The MITREX-SATRE differences were also found to show significant variations of around 300 ps in the underlying delay value. This was discouraging as these non-linear components of the delay changes cannot be calibrated using a satellite simulator or

calibrating loop.

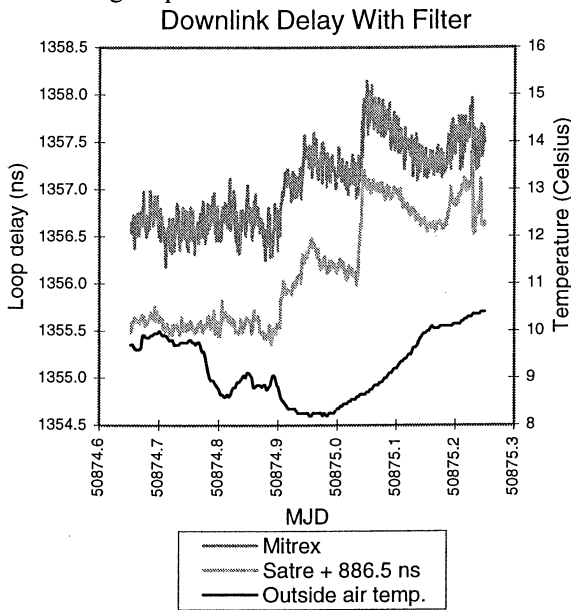


Figure 12: Downlink delay

The TWSTFT downlink contains an isolation filter that prevents the uplink transmit signal from interfering with the downlink LNB amplifier. After removing this filter it is still possible to operate the TWSTFT downlink in its test loop configuration. The results obtained are interesting and encouraging (Figure 13).

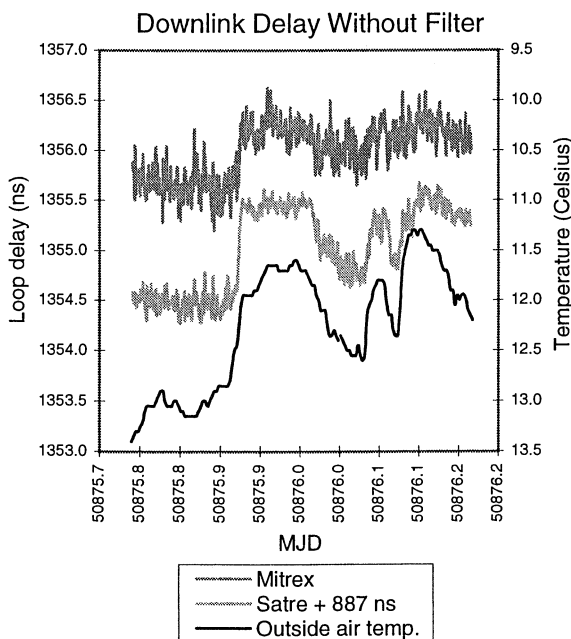


Figure 13: Downlink delay without filter

The total loop delay change is smaller and there is a strong correlation with outdoor temperature. These delay changes may be reduced by temperature control of the outdoor elements of the TWSTFT earth station.

The SATRE - MITREX delay differences also show strong correlation with temperature (Figure 14). The last result is particularly encouraging and puzzling as

in calculating the difference between measurements made with the two modems, one would expect the delay changes due to the common (outdoor) elements to cancel. This is clearly not the case. This non linear component of the delay instability cannot be corrected using either a loop measurement or a satellite simulator. However the temperature dependence suggests that temperature control of the outside elements will reduce these instabilities. Unfortunately it was impractical to operate the TWSTFT earth station for an extended period without a downlink filter.

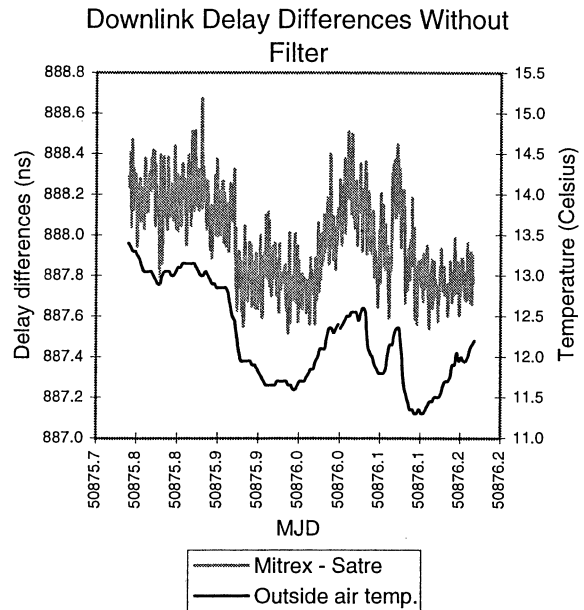


Figure 14: Downlink MITREX - SATRE delay differences without filter

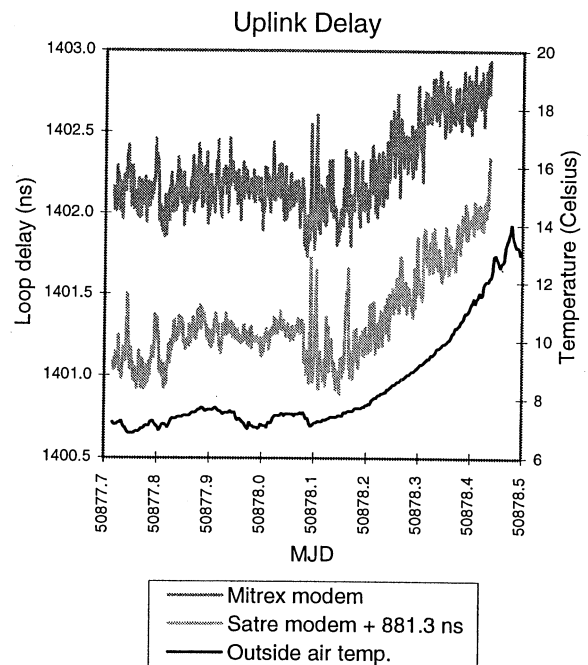


Figure 15: Uplink delay

A similar measurement configuration is used to measure the uplink delay stability. There is a strong correlation with outdoor temperature (Figure 15). The

SATRE-MITREX delay differences also show correlations with outdoor temperature. This is in contrast to the 1992 result and probably due to the change of model of up-link HPA.

## 9) CONCLUSIONS

Several conclusions may be drawn from this work:

- The SATRE modem instrumentation delay is substantially more stable than the corresponding delay of the MITREX modem
- The advantages gained through the use of the SATRE modem are being lost due to the delay instabilities present in the remainder of the TWSTFT earth station.
- There was only a partial correlation between the total loop delay changes measured using two co-located satellite simulators. Further work is required to eliminate delay changes within the simulator elements when using this configuration.
- The delay stability of all of the indoor elements of the TWSTFT was sufficient to permit time transfers with a  $\sigma_x = 100$  ps at  $\tau = 1$  day averaging time. Future efforts need to be concentrated on improving the delay stability of the outdoor elements of the TWSTFT earth station
- Delay changes in many of the outdoor elements of the TWSTFT earth station (with the exception of the downlink filter) correlated strongly with temperature. The delay stability of these elements of the TWSTFT earth station would benefit from temperature control .
- Changes in the SATRE-MITREX loop delay differences containing outdoor elements correlated strongly with outdoor temperature. This puzzling result indicated that the non-linear components of the instrumentation delay that cannot be corrected through the use of satellite simulators or calibration loops may be improved by temperature control.

## 10) FUTURE WORK

Substantial work still needs to be performed to improve the instrumentation delay stability of NPL's TWSTFT earth station. The temperature control of the active outdoor elements is being considered. Temperature control is preferred to temperature

modelling as there are some significant instrumentation delay changes that do not correlate linearly with temperature.

The use of isolators and attenuators to prevent and reduce signal reflections both within the satellite simulator and between the elements of the TWSTFT earth station will be carefully studied.

A second TWSTFT earth station is being commissioned at NPL. This will be used for zero baseline common clock experiments between the two TWSTFT earth stations. This should enable the effectiveness of the near field satellite simulator and calibration loops to be evaluated.

Studies are also underway on the effects of breaking and reforming the modem PN code lock, and any resulting delay changes. It is proposed to undertake experiments using both loop measurements and actual satellite transmissions.

## REFERENCES

1. Kirchner D, 1991 "Two-Way Time Transfer Via Communication Satellites," in Proc. IEEE, Special Issue on Time and Frequency, 79, 7, 983-990.
2. de Jong, G 1989, "Accurate delay calibration of satellite ground stations for Two-Way Time Transfer", Proc. 3rd EFTF, pp. 198-203.
3. Ressler H, Kirchner D and Robnik R, 1997, "Satellite earth stations for Two-Way Time Transfer at the Technical University Graz", Proc. 11th EFTF, 509-513.
4. Davis J A, and Pearce P R, 'Characterization of the signal delays in a ground station designed for satellite two way time transfer'. Proc. 7th EFTF, 1993.
5. Davis J A, Pearce P R, Kirchner D, Ressler H, Hetzel P, Söring A, de Jong G, Grudler P, Baumont F, Veenstra L, 1995, 'European two-way satellite time transfer experiments using the Intelsat (VA-F13) satellite at 307°E', IEEE J. Trans. Inst. and Meas. 44, 2,
6. Davis J A, Pearce P R, Bartle K A, Hetzel P, Kirchner D, Ressler H, Powell W, McKinley A, De Young J A, Klepczynski W, de Jong G, Soering A, Baumont F, Claudon P, Grudler P, Hackman C, Veenstra L, 1995, 'Closing errors observed during two-way time transfer experiments'. Proc. 9th EFTF,
7. Davis J A, 1995, 'Theoretical treatment of closing errors occurring in two-way satellite time transfers', Proc. 9th EFTF, 537-540.

DELAY STABILITY OF THE TWSTFT EARTH STATION AT VSL

Gerrit de Jong

NMi Van Swinden Laboratorium, P.O. Box 654, 2600 AR, Delft  
Netherlands

ABSTRACT

Frequency and time transfer methods rely on the stability of the propagation time of the signals through the systems involved. For TWSTFT the stability of the delays encountered in the earth station by the transmission of the local 1 PPS signal as well as that of the received remote 1 PPS signal determine the uncertainty at sub-nanosecond level for such transfers. The characteristics of the TWSTFT earth station at NMi Van Swinden Laboratorium (VSL) based on data accumulated with its automated delay measurement system during about one year are presented and discussed in more detail. Delay stabilities TDEV of 100 ps for  $\tau = 1$  h to 50 d are obtained, and frequency stabilities ADEV of  $2.2 \cdot 10^{-15}$  for  $\tau = 1$  d.

INTRODUCTION

For the measurement of the difference of the delay in the transmit part (TX) and the delay in the receive part (RX) of the TWSTFT earth station at VSL, an automatic calibration system [3] has been developed, based on the use of a specially at VSL developed satellite simulator SATSIM method [1,2]. The knowledge of this TX - RX delay is necessary if clocks at two remote sites are to be compared using the TWSTFT method; if both stations are equipped with such a system no additional visits [4] of other calibration equipment is necessary for absolute time comparisons. This paper shows what long-term performance can be expected from this TX-RX calibration. This method uses a calibrated reference cable, and this essential cable is also calibrated automatically in the automatic system. The main parts of the system used for the calibration are part of the TWSTFT equipment, only coaxial transfer switches are added, 70 MHz and 1425 MHz sine wave sources and the SATSIM, as shown in fig. 1a.

The cables and their delays are defined as follows (Fig. 1a+b):

A is the cable from the Mitrex modem 70 MHz TX output to the up-converter Fup;

B is the cable from the down-converter Fdn to the 70 MHz RX input of the Mitrex modem;

C is the cable from the 70 MHz CW generator to the output of the amplifier;

HL is the cable from amplifier output to the Sat. Simulator input;

HL' is a cable equal to cable HL, and runs from the

difference frequency generator DF to the other input of the Sat. Simulator; cable L is the sum of HL and HL';

CL is the Reference cable being calibrated each time, it is the sum of C and HL;

RX is the Receive delay: the sum of the delay from the Sat. Simulator to the Feed, the delay from Feed to the output of the down-converter Fdn and cable B;

TX is the Transmit delay: the sum of the delay of cable A, from the input of the up-converter Fup to the Feed, from the Feed to the Sat. Simulator;

TX-RX is the value of interest for TWSTFT.

STABILITY OF THE REFERENCE CABLE  
DELAY CALIBRATION

Firstly the delay of the reference cable CL is determined. Using a three corner hat method, the delay of C is determined from half of the sums of the delays of cables C+B and C+A minus the sum of cables A and B.

The stabilities of these three sums do not differ much, the structure of the variations (fig. 2a and Fig. 3a) that can be seen, are originating in the MITREX modem itself, not in the cables. Also a small slope during the year can be seen. Fig. 2a and 2b show the stability of A+B and 3a and 3b that of cable C+B. TDEV varies from 24 ps for  $\tau = 1$  h to maximum 150 ps for  $\tau = 1$  week. At MJD 50612 the original cable C has been replaced by a new cable with 70 ns less delay. The data taken after the replacement which included the delay of cable C, have been corrected for this.

The delay of HL is determined by measuring C+B+L (fig. 4a + b) and subtracting C+B and dividing the result by two. HL alone is determined with a very good long-term stability as shown in fig 5a and 5b, a TDEV of 10 ps at  $\tau = 1$  h to 23 ps for  $\tau = 50$  days! At MJD 50612 a residual step of 100 ps due to the replacement for cable C is visible and causes the rise of TDEV at  $\tau$  of 20 d and 50 d.

Now the wanted delay of the reference cable CL is the sum of C and HL and its stability is shown to be 20 ps at  $\tau = 1$  h to a maximum of 72 ps at  $\tau = 1$  week in fig. 6a and 6b.

STABILITY OF THE TOTAL TRANSMIT AND  
RECEIVE DELAY INCLUDING UP- AND  
DOWN CONVERTERS, HPA AND LNA

The next measurement is the sum of cables CL + RX

which include the RF path from SATSIM to the receiver antenna and the down-converter and cable B. The total RX delay is calculated from CL+RX and subtraction of CL. Stability is shown in figs. 7a+b, 8a+b, TDEV is constantly about 100 ps.

Then the sum of TX+RX is measured and the delay of TX (including the up-converter and RF path to the SATSIM) is calculated by subtraction of the RX delay determined before. Stability is shown in figs. 9a+b, 10a+b, again a TDEV of about 100 ps for  $\tau = 1$  h to 50 d.

### STABILITY OF THE TRANSMIT - RECEIVE DELAY DIFFERENCE

Finally the TX-RX delay is calculated by subtraction of the RX delay from the TX delay, see fig. 11a and 11b for the stability. Now TDEV varies from 250 ps at  $\tau = 1$  hr to 110 ps for  $\tau = 50$  d. The associated frequency stability is showing mainly flicker phase noise and a modified Allan deviation of  $2.2 \times 10^{-15}$  is obtained at  $\tau = 1$  day,  $2.5 \times 10^{-16}$  at 10 d and  $4.5 \times 10^{-17}$  at 50 d.

Fig 12a+b show the outside temperature and its stability. These figures help to see if correlations of delay stability with temperature exists. The 'TEMPDEV' shows a rise after 2 h and reaches a maximum as expected at a diurnal  $\tau = 12$  h of 2.2 degrees C and drops to 1.2 at  $\tau = 18$  h and 24 h. For TX-RX we also find a drop of TDEV from 150 ps at  $\tau = 12$  h to 120 ps at  $\tau = 18$  h and 110 ps at  $\tau = 24$  h.

### CONCLUSION

The TX-RX delay at the VSL earth station is **stable to a TDEV of about 100 ps for  $\tau$  of up to at least 50 days** and the system is **stable in frequency to  $2 \times 10^{-15}$  for  $\tau = 1$  day**. But while these delay changes are measured in near real time, they can be subtracted from actual Two-Way data, and enable the clock comparisons to **an even much better level than the stability reported here**. This could be demonstrated when two good H-Masers were compared using TWSTFT stations equipped with such an automated delay measuring system and the TWSTFT data be corrected for the measured delay changes. So far, a best TDEV of 0.22 ns for  $\tau = 1$  h to 0.18 ns for  $\tau = 1$  d from hourly sessions of 300 s during 32 days using an "Atlantis" modem on a baseline of 2400 km has been reported [10].

The VSL full TX-RX stability results are up to two times better than the results reported by the Technical University Graz (TUG) [5, 7, 11, 12] when taking into account that the half TX-RX delay stability was reported, maybe this difference is because at VSL the up- and down-converter are mounted inside the building, just under the roof, while at TUG they are

outside at the antenna.

### RECOMMENDATIONS

Unfortunately the improvement of the performance of TWSTFT using delay measurements cannot be demonstrated further with good clocks now: the two laboratories equipped now with automated delay measuring systems (TUG and VSL) have no H-masers available and the labs that do have H-masers do not (yet) have an automated delay measuring system. This dilemma should be solved in the near future!

Another finding is that the used MITREX modem is sensitive to environmental factors for  $\tau$  of 3 h to 10 d even when it was kept in a room at a temperature of 23 degrees Centigrade controlled to about 0.3 degrees C and a relative humidity of 45% controlled to about 5 % RH. Also it was noticed that the non-linearity of delays measured by the MITREX modem when changing the length of the cable in known increments under circumstances is 100 ps or more. Some mismatch and / or cross-talk in the modem might be the cause of this. So modems still should be improved.

### REFERENCES

- [1] G. de Jong 1989, "Accurate delay calibration of satellite ground stations for Two-Way Time Transfer", Proceedings of the 3rd European Frequency and Time Forum (EFTF), March 21-23, 1989, Besançon, France, pp. 198-203.
- [2] G. de Jong 1989, "Accurate delay calibration for Two-Way Time Transfer earth stations", Proceedings 21st Annual Precise Time and Time Interval (PTTI) Applications and Planning Meeting, November 28-30, 1989, Redondo Beach CA., USA, pp. 107-116.
- [3] G. de Jong and M.C. Polderman 1994, "Automated delay measurement system for an earth station for Two-Way Satellite Time and Frequency Transfer", Proceedings 26th Annual Precise Time and Time Interval (PTTI) Applications and Planning Meeting, December 7-9, 1994, Reston, Virginia, USA, pp. 305-318.
- [4] G. de Jong, D. Kirchner, H. Ressler, P. Hetzel, J.A. Davis, P.R. Pearce, W. Powell, A. Davis McKinley, W. Klepczynski, J.A. DeYoung, C. Hackman, S.R. Jefferts, T.E. Parker 1995, "Results of the calibration of the delays of earth stations for TWSTFT using the VSL Satellite Simulator method", Proceedings 27th Annual Precise Time and Time Interval (PTTI) Applications and Planning Meeting, November 29 - December 1, 1995, San Diego CA., USA, pp. 359 - 372.
- [5] D. Kirchner, H. Ressler, and R. Robnik 1995, "An automated signal delay monitoring system for a Two-

Way Satellite Time Transfer terminal”, Proceedings of the 9th European Frequency and Time Forum (EFTF), March 1995, Besancon (F), pp 75-79.

[6] C. Hackman, S.R. Jefferts, and T.E. Parker 1995, “Common-clock Two-Way Satellite Time Transfer experiments”, Proceedings of the 1995 IEEE International Frequency Control Symposium, 31 May - 2 June 1995, San Francisco, California, USA, pp. 1169 - 1172.

[7] D. Kirchner, H. Ressler, and R. Robnik 1995, “Signal stability of a Ku-band Two-Way Satellite Time Transfer terminal”, Proceedings 27th Annual Precise Time and Time Interval (PTTI) Applications and Planning Meeting, November 29 - December 1, 1995, San Diego CA., USA, pp. 303 - 311.

[8] J.A. Davis 1996, “Delay stability measurements made within a Two-Way Time Transfer system using satellite ranging from several locations”, Proceedings of the 10th European Frequency and Time Forum (EFTF), 5 - 7 March 1996, Brighton, UK, pp. 206-211.

[9] F.G. Ascarrunz, S.R. Jefferts, and T.E. Parker 1996, “Earth station errors in Two-Way Time

transfer”, Proceedings of the 1996 IEEE International Frequency Control Symposium, 5-7 June 1996, Honolulu, Hawaii, USA, IEEE Catalog No. 96CH35935, pp. 1169 - 1172.

[10] J.A. DeYoung, F. Vannicola, and A. Davies McKinley 1996, “A comparison of the highest precision commonly available Time Transfer methods: TWSTT and GPS CV”, Proceedings 28th Annual Precise Time and Time Interval (PTTI) Applications and Planning Meeting, 3 - 5 December, 1996, Reston, Virginia, USA, pp. 349-355.

[11] D. Kirchner, H. Ressler, and R. Robnik 1997, “Recent work in the field of Two-Way Satellite Time Transfer carried out at the TUG”, Proceedings of the 11th European Frequency and Time Forum (EFTF), 4 - 7 March 1997, Neuchatel, Switzerland, pp. 205-208.

[12] H. Ressler, D. Kirchner and R. Robnik 1997, “Satellite earth stations for Two-Way Time Transfer at the Technical University Graz”, Proceedings of the 11th European Frequency and Time Forum (EFTF), 4 - 7 March 1997, Neuchatel, Switzerland, pp. 509-513.

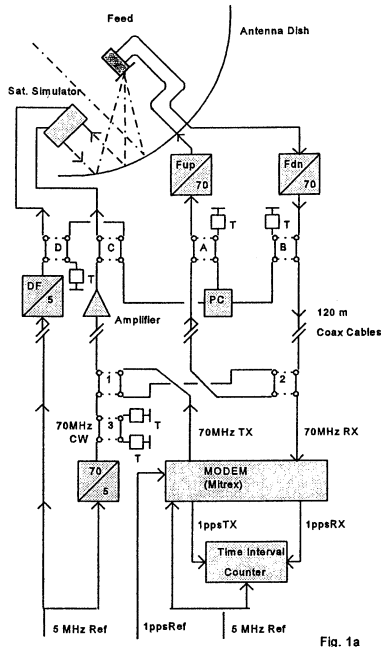


Fig. 1a

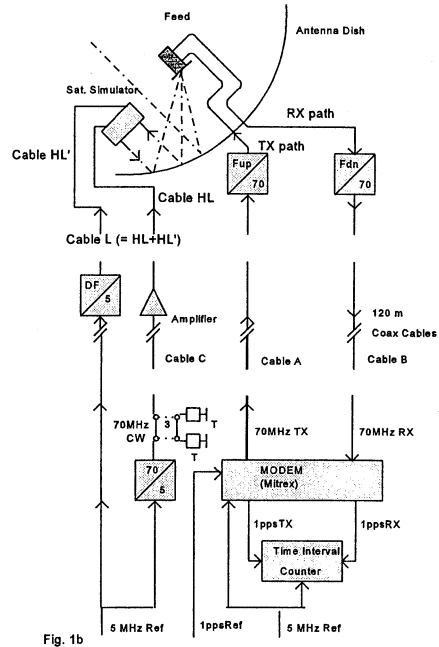


Fig. 1b

Delay TWSTFT earth station  
A&B -2347ns

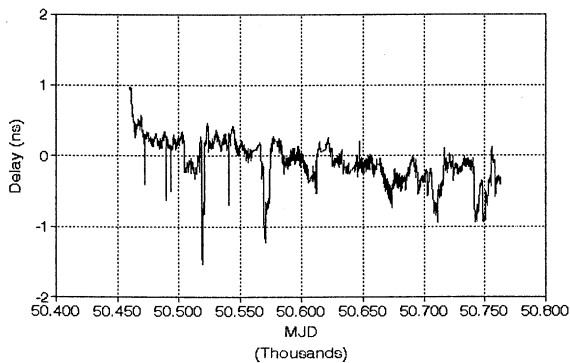


Fig. 2a

Stability of TW Earth Station Delay  
A&B

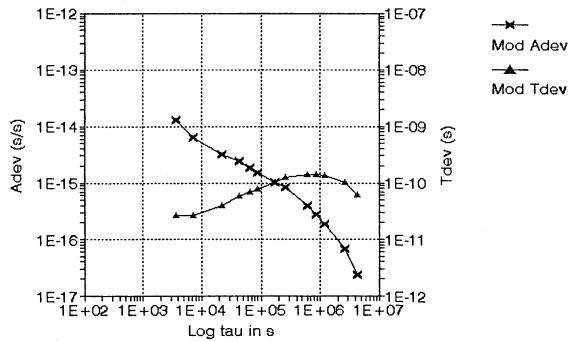


Fig. 2b

Delay TWSTFT earth station  
C&B -2438 ns

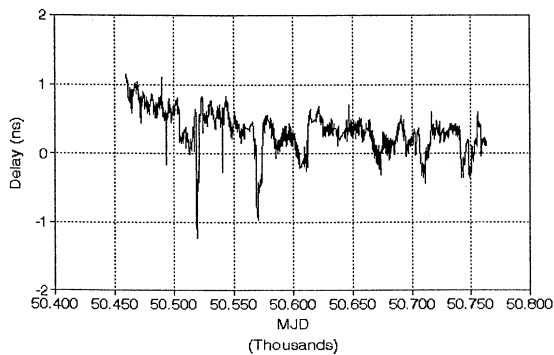


Fig. 3a

Stability of TW Earth Station Delay  
C&B

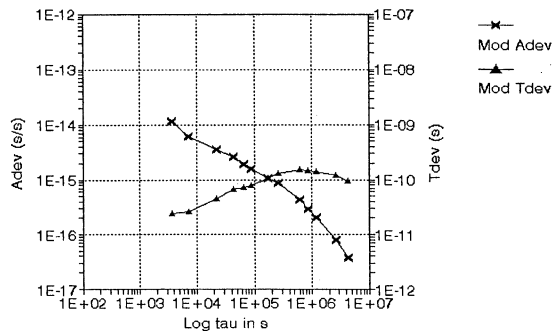


Fig. 3b

Delay TWSTFT earth station  
C&B&L -2509 ns

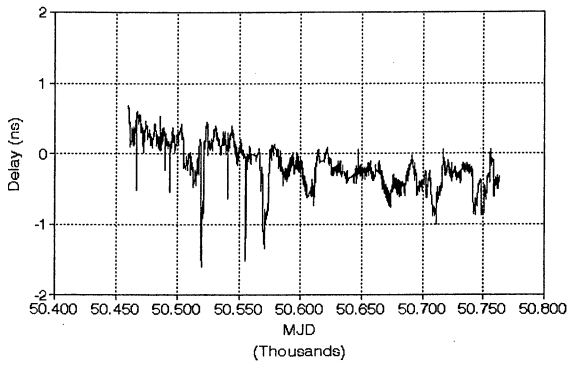


Fig. 4a

Stability of TW Earth Station Delay  
C&B&L

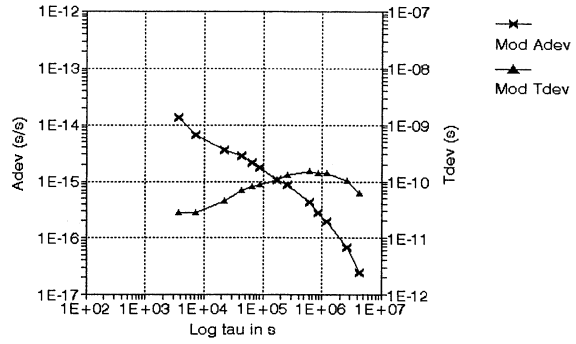


Fig. 4b

Delay TWSTFT earth station  
HL -35 ns X 10

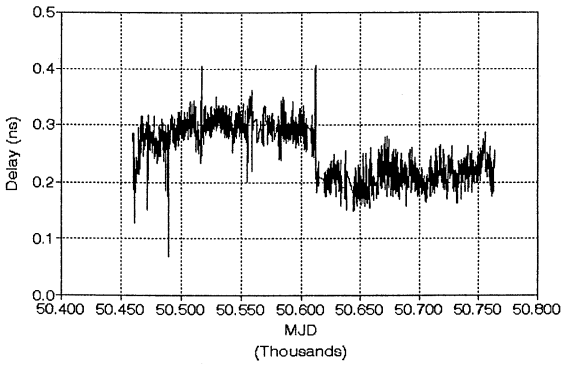


Fig. 5a

Stability of TW Earth Station Delay  
HL 10-18

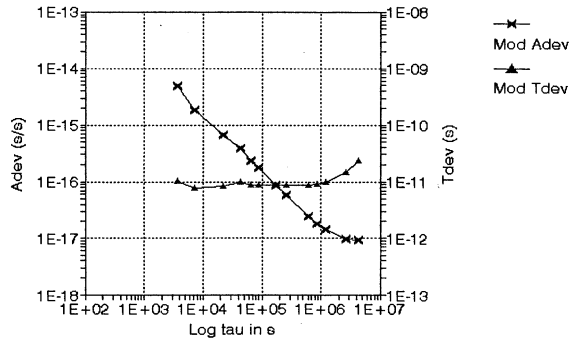


Fig. 5b

Delay TWSTFT earth station  
CL -1310 ns

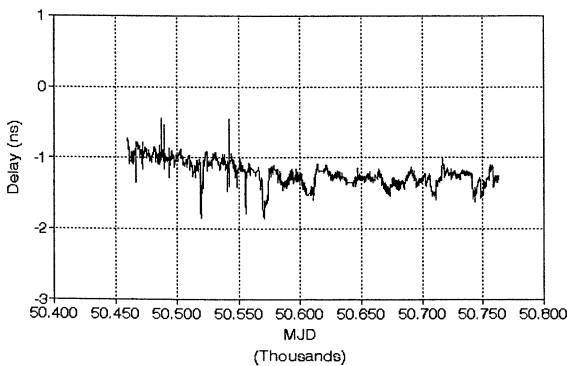


Fig. 6a

Stability of TW Earth Station Delay  
CL

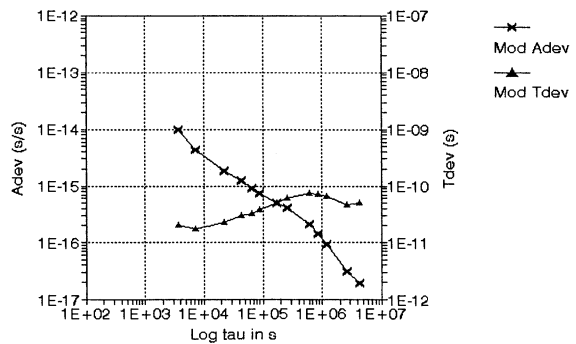


Fig. 6b

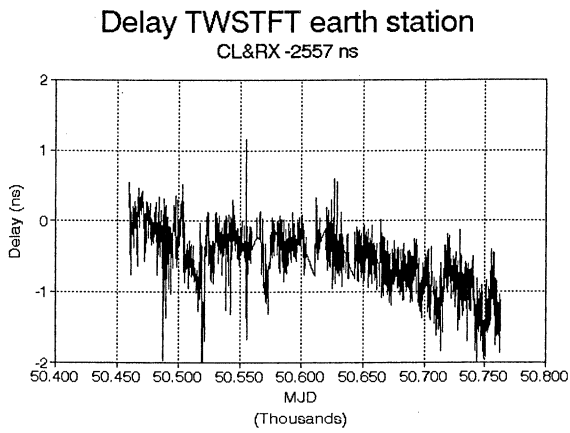


Fig. 7a

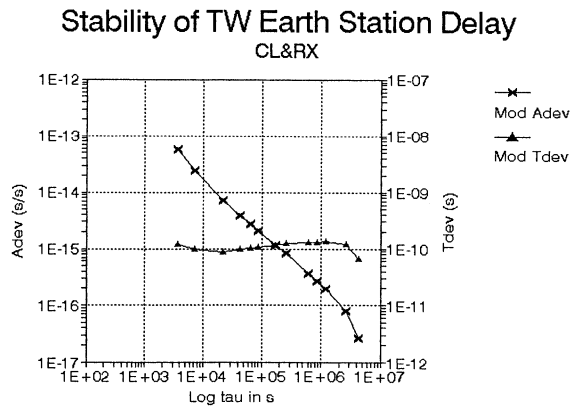


Fig. 7b

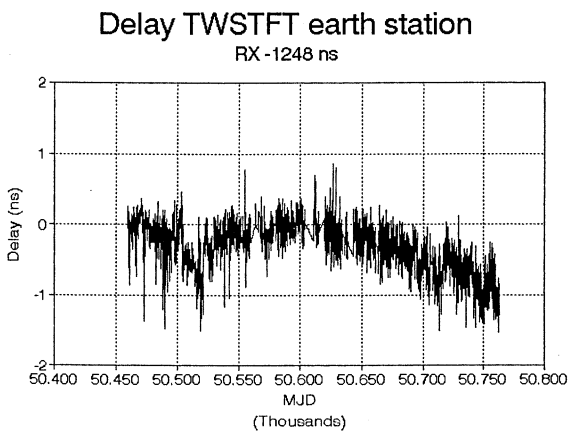


Fig. 8a

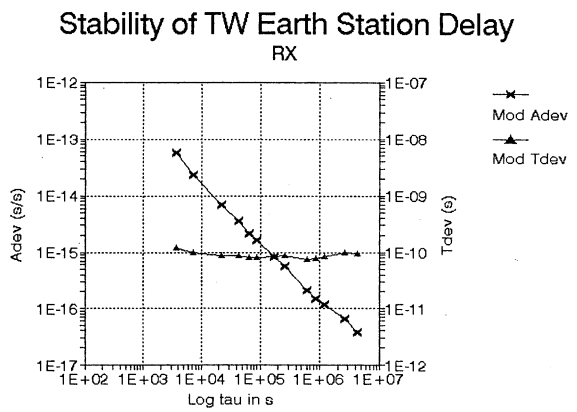


Fig 8b

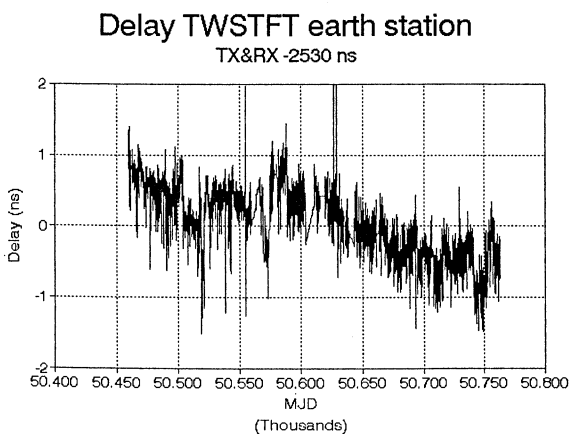


Fig. 9a

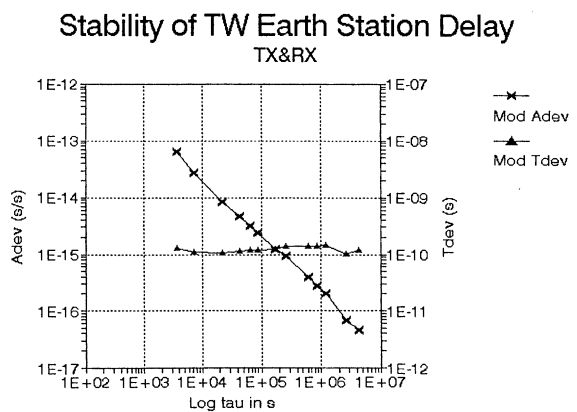


Fig. 9b

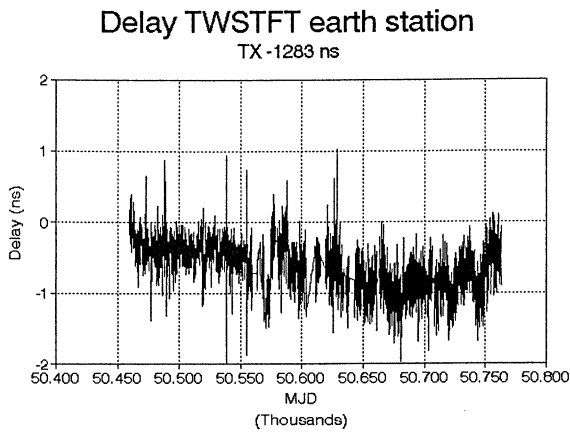


Fig. 10a

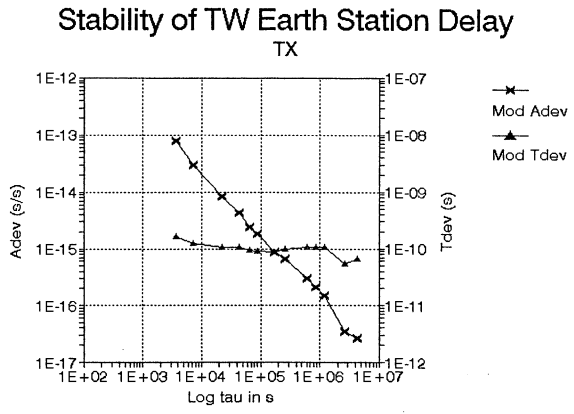


Fig. 10b

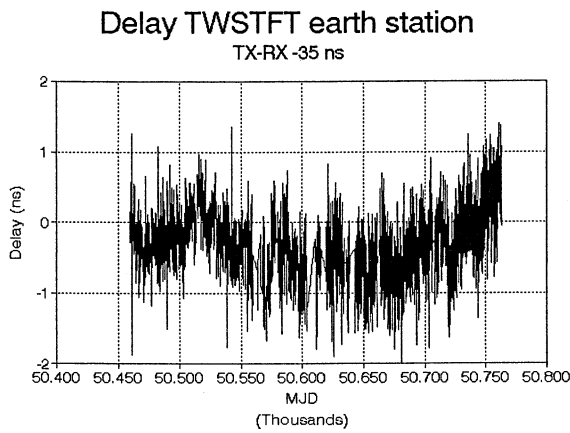


Fig. 11a

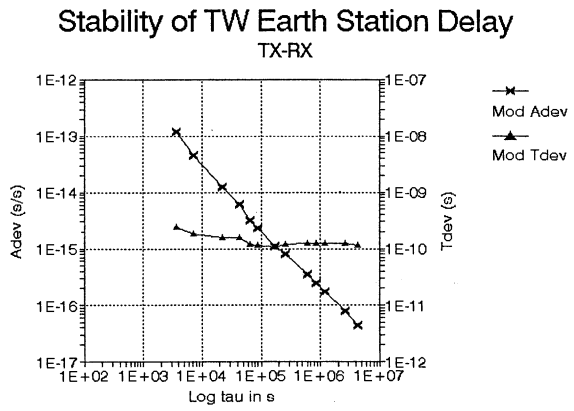


Fig. 11b

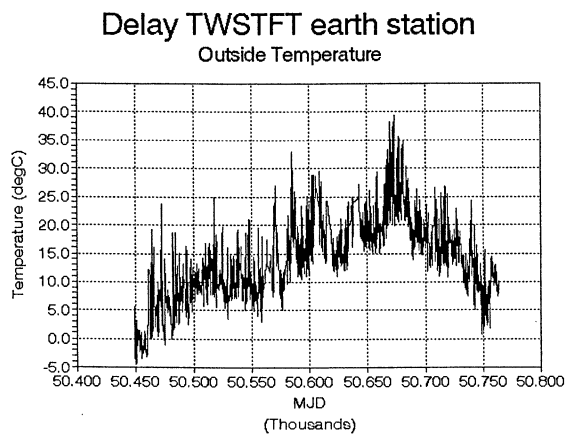


Fig. 12a

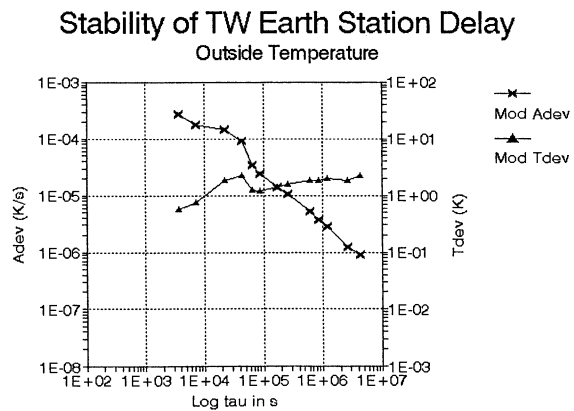


Fig. 12b

## TESTS WITH EXTERNALLY APPLIED JOINT ELECTRONIC AND NUMERICAL CONTROL OF COMMERCIAL ATOMIC CLOCKS

Eskelinen P. and Pyrhönen O.

Lappeenranta University of Technology, PL 20, 53851 Lappeenranta, Finland

### ABSTRACT

Long term timing stability of present commercial atomic clocks can be considerably improved by simple numerical algorithms and associated intelligent electronics which correct together both the inherent frequency bias and the effects of supply voltage variations and outside temperature. Often a linear subtraction of frequency offset which can be realized by a microprocessor controlled digital delay line, is sufficient. A conventional cesium clock could run at  $10^{-15}$  level, but reliable and reasonable real-time comparison or measurement techniques do not exist yet. A digital delay line, connected to the local Cs1 output has been able to reduce the timing drift and fluctuations of this unit to and below  $2.7 \cdot 10^{-14}$  level while using the previously tested 5 hour integration constant. The delay is constructed from a 100 MHz divider chain, logic gates of 3 ns steps and finally with RF transmission lines below the 1 ns increments. Better than  $2.0 \cdot 10^{-15}$  frequency reproducibility is achieved. The test sessions starting from 5/97 show periodic variations of about 100 ns, with a 546 hour cycle in the 1pps output of the CS 1.

### INTRODUCTION

The Lappeenranta University of Technology (LUT) has continued efforts to find out suitable algorithms and prototype circuit designs with which the medium and long term uncertainty of different existing commercial atomic frequency standards could be reduced. Initial results of a comparison between cesium, H-maser and GPS clocks [1. Eskelinen P. et al, 1997] showed that the medium-term stability of a suitably controlled stand-alone cesium could exceed by a factor of 5-10 that of currently available GPS designs. For these tests the laboratory has further updated its clock system by adding a third GPS-receiver (Efratom GmbH model FC), a time interval analyzer (HP) and by two computer controlled digital delay lines with associated software. A new HP5071A cesium unit with the high stability option 001 installed has been purchased for autonomous comparisons. No physical transportation like [2. Davis J. and Steele J., 1996] has been possible but an exchange of GPS data has been continued with Swisscom.

Many modern atomic oscillators which form the basis of high quality clocks lack the possibility of accurate frequency tuning, with the luxurious exception of e.g. the HP5071 cesium [3. HP Product Note]. Typical rubidium tuning resolution is around  $5E-11$  and that of older cesiums  $2E-13$ . Besides, particularly rubidium oscillators are known to be sensitive to temperature and supply voltage variations and even to load pulling which all drastically hamper sensible adjustments. A computer based analog correction of rubidium output frequency is hardly possible with an uncertainty better than  $2E-11$  as demonstrated in [4. Eskelinen P. et al, 1996]. On the other hand, any tuning intervention inside a cesium oscillator is considered among us metrology people hazardous regarding the unit's uncertainty.

A practical need for a stable flywheel clock came apparent when measurements of GPS-disciplined clocks were carried out. In an attempt to repeat the measurements described in [5. Kusters J., 1996] with a combination of a remote H-maser and a local proven cesium clock, unpredictable fluctuations of the GPS-chain exceeding 150 ns within a couple of days were demonstrated in [6. Eskelinen P. et al, 1997] but this required heavy post-processing of the remote clock data. If at least two autonomous high stability clocks were available locally such tests could be performed in almost real time. Being unable to acquire several additional new cesiums or H-masers we started to consider the possibility to improve the long term characteristics of present local clocks. Some relief for the short-term specifications of ground-based oscillators was to be expected due to the heavy averaging required anyhow in the final test system for the removal of GPS S/A and A/S effects [7. Kayton and Fried, 1997].

### TEST SETUP

The procedure applied is really straightforward and has been utilized for other purposes elsewhere, see e.g. [8. HP Application Note 200-3]. The atomic standard 5 or 10 MHz output signal is directed to two parallel paths, to one decade counter chain dividing by  $10^7$  to form a 1 pps signal and to a phase locked loop producing a suitable VHF frequency, which in this example was chosen to be

100 MHz. The VCO (MiniCircuits type POS-400) output is connected to a programmable divider, where a delay in steps of one clock cycle (10 ns) is counted. Smaller delay steps are added with a logic gate assembly or a transmission line matrix. Finally, this delay and the former 1 pps signal are combined to provide a steerable 1 Hz output.

A functional block diagram is shown in Fig.1 and a prototype circuit board in Fig. 2. The board routing of signal paths is critical because we are dealing with transitions which approach the ultimate limit of F-TTL capabilities. In Fig. 3 a possible real-life (and finally working) arrangement is demonstrated with nearly optimized interconnection distances between successive counter stages. Note that the dimensioning of the board must follow RF impedance matching rules in order to avoid multiple reflections of the logic signals. Thus e.g. the line width between two successive F-TTL components should be chosen such as to create a characteristic Z of about 50 - 75 ohms.

A test version of the coaxial transmission line system is shown in Fig. 4 where the focus has been on keeping the paths in equal temperature and well isolated from external sources of electromagnetic interference. The high quality cable performance is not of primary concern but a well-defined connection between logic IC pins and the cable is essential. Also, in the 1 ns region, differences in gate propagation delays must be measured and a balanced combination selected. The impairment of rising edge characteristics can be compensated by a line driving logic gate.

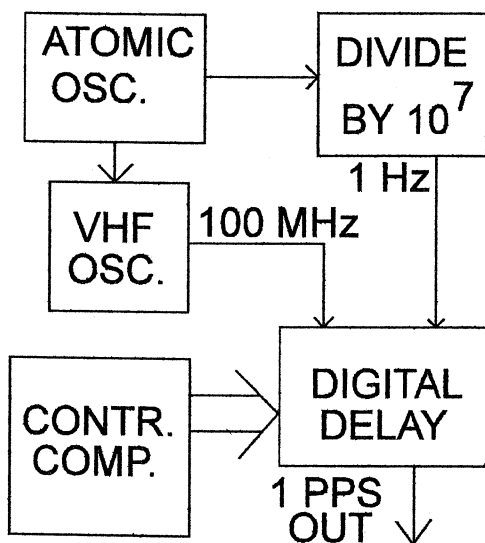


Fig.1. The 10 MHz output from an atomic oscillator is used to steer a VHF phase lock circuit and a decade counter. A digital delay line fine adjusts the position of the outgoing 1 pps signal.

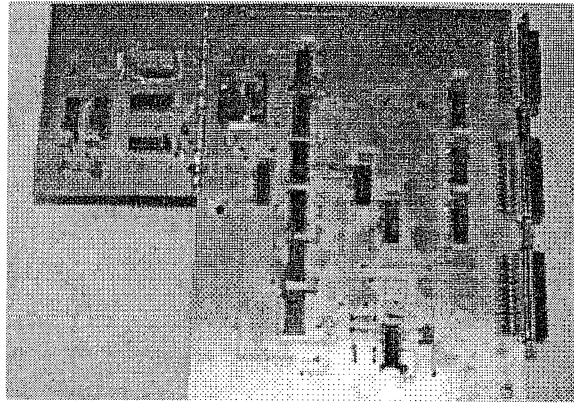


Fig. 2. The prototype of the delay electronics unit utilizes FAST TTL- programmable counters.

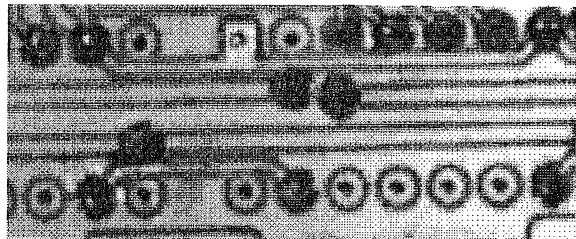


Fig. 3. An optimized path lay-out is essential in order to avoid excessive propagation delays in the counter cascade.

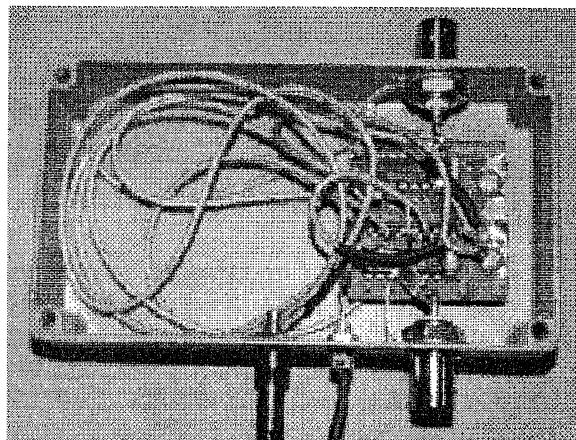


Fig. 4. The coaxial transmission-line matrix is assembled separately thus minimizing disturbances in the sub- ns world.

The software used to control the programmable dividers is very simple and has been coded in Basic. A task-oriented flow chart is shown in Fig. 5. The software looks for three most important parameters: the elapsed raw time (obviously for aging and frequency shift), supply voltage of the primary oscillator and external room temperature. Based on these figures the processor calculates the necessary wait after which the binary word at the divider parallel load inputs is incremented or decremented by one. Of course, a priori knowledge of the initial frequency offset is necessary but can be obtained in

the case of atomic oscillators with very high repeatability, usually at least better than  $1 \text{ E-}14$ .

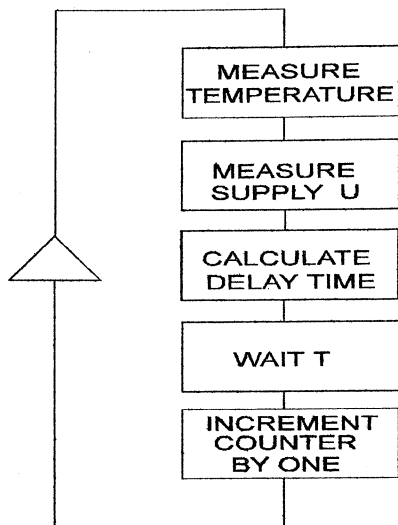


Fig.5. The software adjusts its own wait time according to supply voltage and temperature. The initial cycle period of the software is determined by preliminary measurements of oscillator aging.

Making the system as low-cost as possible, an old HP 85B desk-top computer modified for 24 V battery power was chosen as the system controller. Temperature is sensed with a commercial Fluke transducer providing a 1 mV/degree output and a 6 digit DVM is used for voltage. An air-conditioning system has not been installed in the clock room, because the thermal mass of the underground part of the building was consider large enough, see e.g. [9. Kalliomäki K. et al, 1993].

To demonstrate the system principle we can as an example assume that the frequency bias of the oscillator is  $+5\text{E-}11$  at 10 MHz. Initially this means that the raw clock output goes too fast and 10 ns must be subtracted every 200 seconds. However, if the processor measures a supply voltage increase of 0.1 V (known to produce an additional frequency bias of  $+1\text{E-}11$ ), it compensates this by adjusting the wait time to 167 s. It is essential that the loading of the binary data to the divider chain and possible adjustment of the coaxial transmission line matrix can be made "on the fly", otherwise unpredictable timing jumps will occur. However, this is not a problem as the system "knows" internally when the next 1 pps pulse will go out.

Application of the proposed algorithm to e.g. past generation cesium units does not necessarily require clock frequencies far above 100 MHz, as random fluctuations of the commercial primary oscillator generally exceed 10 ns over any relevant integration time, say e.g. 10 hours, see Fig. 6, and thus most phase jumps induced by the correction will be

masked by noise. In the case of this particular OSA cesium oscillator with a demonstrated frequency offset of  $2.7\text{E-}13$ , adjustments by 10 ns would be needed about twice per day.

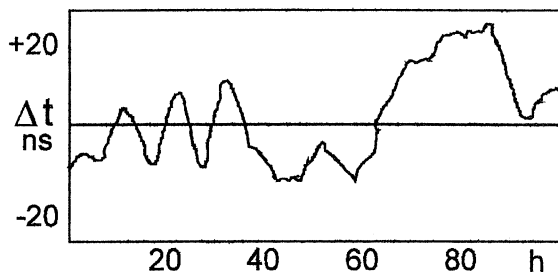


Fig.6. Typical older generation cesium units seem to have an inherent timing jitter exceeding 10 ns for integration times of 1- 20 hours. This plot is of an Oscilloquartz cesium against Swiss PTT master clock.

### NOTES ON DRIFT CORRECTION

The present test program has included an initial medium to long term stability analysis, a total intentional cesium shutdown, demonstration and complete recording of following warm-up behaviour which shows e.g. a required stabilization period of two months, see Fig. 7, and after that continuous monitoring of steady state performance. The plot quite clearly demonstrates a fast timing drift up to 800 hours from the cold start (at 0 hours on the x-axis), after that an (internal) attempt to stabilize, but again a rather rapid drift until 1500 hours where from the uncorrected output did achieve its normal ageing rate. The current total continuous measuring time exceeds 6000 hours. As a by-product, information on sample commercial clock designs has been gathered.

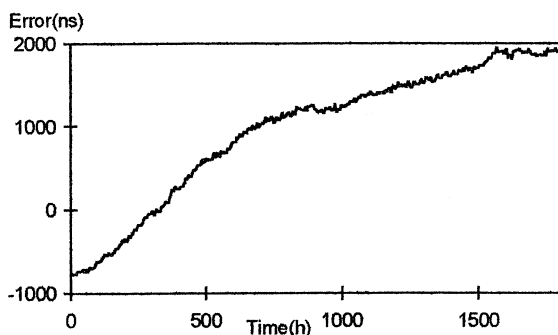


Fig. 7 Warm up characteristics of the OSA cesium (without external control) show that actually two months (1500 h) are required for stabilization.

At the time of writing this the measurements have been going on for seven months. One of the first results with an electronically corrected Oscilloquartz cesium unit is shown in Fig. 8. The VCO frequency

was intentionally divided by two to yield 50 MHz because noise, measured actually with a phase comparator, would anyhow exceed this and occasional but unavoidable phase jumps caused by the divider stepping occur at half the update speed. An overall relative timing uncertainty of  $2.4 \times 10^{-14}$  has been achieved here with an averaging over 100 seconds for each individual sample plotted.

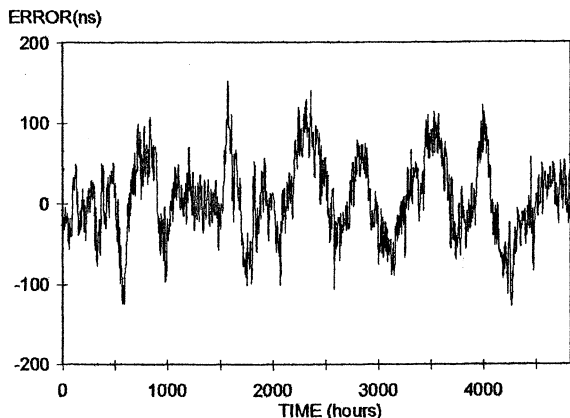


Fig.8 Numeric control with a digital delay line quite completely removes any frequency offset from the timing and we easily see cesium fluctuations

### OSCILLATIONS IN THE CLOCK OUTPUT

As could be seen already from the plot of Fig.8, there seems to be a nice sine wave of 100 ns peak amplitude and about 500 h cycle time. The following discussion is based on observations of the detailed schematic diagrams of the clock and application of general control system theory.

The primary output of the cesium standard is a 5 MHz signal supplied by a servo-controlled quartz-crystal oscillator. The signal for the cesium beam excitation is synthesized from the same oscillator output as well. A feedback is provided by the cesium beam tube for the oscillator, and the corrective control actions are done according to it. Extensive Fourier analysis of the measured (Fig.8) data shows three low frequency components listed into Table 1. The whole spectrum is plotted in Fig. 9 as obtained from a Matlab simulation.

Table 1. Unwanted oscillation components of clock output data, period and relative amplitude

$T_1 = 1275 \text{ h}$	$T_2 = 546 \text{ h}$	$T_3 = 425 \text{ h}$
$A_1 = 28.13 \text{ ns}$	$A_2 = 25.8 \text{ ns}$	$A_3 = 17.7 \text{ ns}$

If a general feedback system is asymptotically stable, and the input signal is zero, the system should go to an equilibrium point, where all the derivatives of the state variables are zero [10. Franklin & al, 1986].

One explanation for the oscillations here could be that the cesium standard feedback control does not completely fulfill this feature, but there are a small oscillations in the equilibrium point due to apparent unidealities in the control electronics, e.g. the FET detector amplifier. Large time constants could be explained for example by thermal effects of the system, particularly in the tube heating oven, together with the thermal power loss of the unit. Furthermore it is interesting to notice, that there are three different non-harmonic frequencies present.

Another source for the oscillations might be some external phenomena. In that case the error should however be more like white noise without any specific extremely low characteristic frequencies. We remind the reader however that the standard fulfills perfectly the respective specification given by the manufacturer.

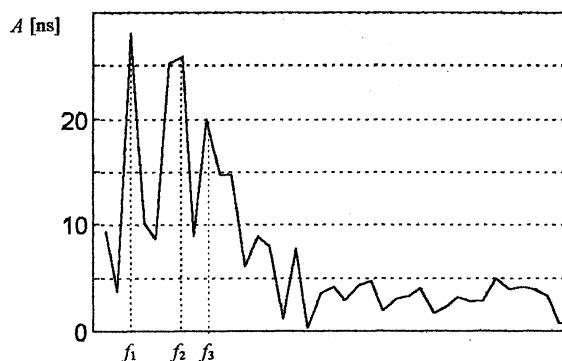


Figure 9. Fourier analysis of the measured clock output data. The error signal has three low frequency components  $f_1=1/1275 \text{ h}^{-1}$ ,  $f_2=1/546 \text{ h}^{-1}$ ,  $f_3=1/425 \text{ h}^{-1}$ .

It is obvious from the suggested operational principle that the short term behaviour is somewhat impaired by the arrangement, partly due to the electronics, mainly the VCO instabilities and partly by the apparent, roughly 1 ns jitter which is introduced by the delay chain stepping. With a steady programming input, however, a jitter of less than 300 ps has been measured.

The electronically controlled OSA (Cs1) and the HP 5071A opt.001 (Cs2) have been used in parallel in order to measure the local GPS timing uncertainty. Also the warm-up recording of Cs2 has been possible. It seems that the internal controlling algorithm of this specific HP unit is well matched to the user environment but that the home-made external electronic control could also here introduce a stability improvement. The comparison is documented in Fig. 10 where the Cs2 curve has a negative gradient reflecting a frequency bias of  $-8.7 \times 10^{-14}$  and the Cs1 a positive one of  $6.9 \times 10^{-14}$ .

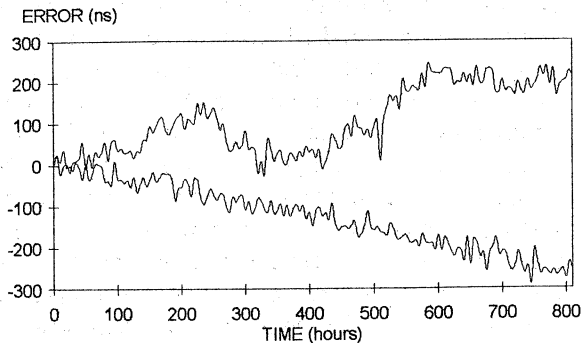


Fig. 10 The HP 5071 opt.001 (Cs2, lower) warm-up recording is seemingly stable, but the electronically controlled OSA (upper) does also very well.

In order to be able to judge the actual timing stability we decided to further subtract the obvious frequency bias from both Cs plots and then averaged the Cs1 signal results over 25 hours to reduce the noise content. An interesting view is shown in Fig. 11 where the final confirmed result of the long hunt for possibly GPS-based, user observable clock fluctuations can be seen as a modulation envelope of the Cs2 output having a good timing match with the Cs1 excursions, although the latter are of much higher amplitude.

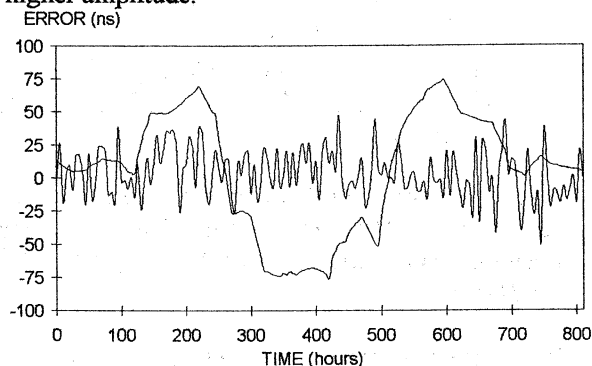


Fig. 11 Here we have a closer look at the two cesium outputs. There seems to be a correlation between Cs2 envelope pattern and Cs1 excursions.

### GPS RECEIVER OBSERVATIONS

During the local clock system update some comparisons of GPS disciplined oscillators, something like [11. Davis J. et al, 1997], was performed. An interesting result is shown in Fig. 12 where, for reasons of confidence, we have measured the electronically corrected Cs1 output against two different GPS units, the HP and the Efratom FC. A good overall agreement is visible, also the expectable reduction of noise in the HP GPS output but the long term drifting, very well indeed within specifications, between the two GPS units seems problematic.

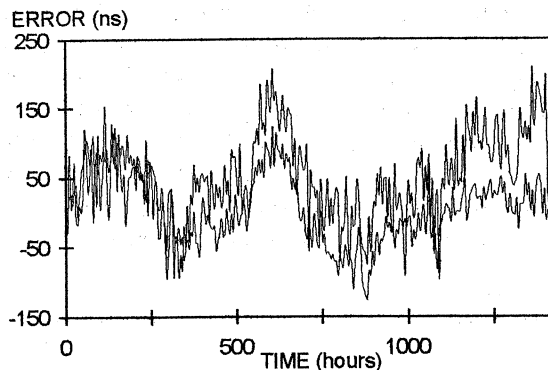


Fig. 12. A parallel measurement of corrected cesium with two different GPS disciplined oscillators.

### REFERENCES

1. Eskelinen P. et al, 1997, "Comparison of Cesium, H-maser and GPS-based Timescales", Proc. 11th EFTF'97, 477-480
2. Davis J. and Steele J., 1996, "A cesium flying clock experiment between NPL and USNO", Proc. 11th EFTF'97, 306-310
3. "HP 5071A Primary Frequency Standard", HP Product Note, Hewlett Packard
4. Eskelinen P. et al, 1996, "A Computer Controlled Clock System", Proc. 10th EFTF'96, 92-95
5. Kusters J., 1996, "The Global Positioning System and HP SmartClock", Hewlett Packard Journal 1996,
6. Eskelinen P. et al, 1997, "Experiments with controlled atomic clocks", IEEE AES Magazine vol 11, 8-10
7. Kayton M. and Fried W., 1997 "Avionics Navigation Systems", John Wiley and Sons, New York
8. "Fundamentals of Time Interval Measurements", HP Application Note 200-3, Hewlett Packard 1975
9. Kalliomäki K. et al, 1993, "Temporal and spatial temperature variations in surroundings of a clock", Proc. 7th EFTF'93
10. Franklin Gene F., Powell J. David, Emami-Naeini Abbas, 1986, "Feedback control of dynamic systems", Addison-Wesley Company
11. Davis J. et al, 1997, "A study examining the possibility of obtaining traceability to UK national standards using GPS disciplined oscillators", Proc. 11th EFTF'97, 515-519

SAW I

Chairman:

*Remi Brendel*



## OPTIMIZATION OF BROADBAND SAW TRANSDUCERS WITH POLARITY WEIGHTING

Evgeniy V. Bausk\* and Leland P. Solie\*\*

\*Institute of Semiconductor Physics of Russian Academy of Sciences, 630090 Novosibirsk, Russia

\*\*SAWTEK Inc., P.O. Box 609501, Orlando, Florida

### ABSTRACT

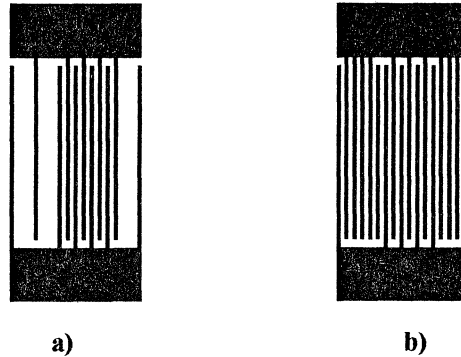
An optimization algorithm for broadband polarity weighted (PW) interdigital transducers is under consideration. Unlike the familiar methods, this algorithm compares the modelled transducer designs on the basis of how well they meet the specifications, not in the time domain, but in the frequency domain directly. For PW transducers having not more than 50-60 electrodes the algorithm gives the optimal decision because all rational combinations of electrode polarities are analyzed. As for longer transducers, a modification of the algorithm gives a suboptimal decision. When phase linearity is not needed, the algorithm can synthesize asymmetrical PW IDTs. As a rule, they have better selectivity than symmetrical structures.

A set of PW IDTs for SAW filters with bandwidths of 1-14% has been designed using this algorithm.

### 1. INTRODUCTION

The periodic, constant overlap interdigital transducer (IDT) is one of the most commonly used structures in surface acoustic wave (SAW) devices. It can be used together with an overlap weighted (apodized) transducer or with a similar uniform-beam-profile IDT to reduce an aperture without increasing the effects of diffraction.

In spite of the restrictions on its structure: constant values of period and electrode length, such IDTs are often required to provide a high level of frequency selectivity. Withdrawal weighting and weighting by assignment of polarities of individual electrodes (polarity weighting) (Fig.1) can be used effectively for this purpose. Each of them has relative advantages and disadvantages with respect to each other: withdrawal weighted (WW) IDTs are more flexible in the realization of broadband frequency responses while polarity weighted (PW) transducers are less sensitive to second-order effects and can be designed with using more simple model.



a) b)  
Fig.1. Withdrawal weighted (a) and polarity weighted (b) SAW transducers

The optimization algorithm presented here is based on the methods developed before for optimization of broadband WW transducers [1-3], however it has some distinctions.

This technique is intended for the design of SAW filters with bandwidth of about 1-15%. The key feature, which distinguishes our algorithm from optimization methods approximating a specified time response, is that the choice of the best IDT structure is based upon how well it meets the specifications, not in the time domain, but in the frequency domain directly. Specifications can assign, for example, either a uniform level of frequency response (FR) sidelobes in broad frequency regions or the maximum rejection in the most important narrow frequency regions or the minimum FR transition bands (i.e., the best FR shape factor). These specifications can be applied not only to a single transducer but also to a total filter frequency response, that is, selectivity of an input transducer can be taken into account.

### 2. OPTIMIZATION ALGORITHMS

Within the scope of the delta-function model, frequency response of both withdrawal weighted and polarity weighted transducers can be written as:

$$H_{out}(f) = \sum_{n=1}^N A_n \exp(in\pi f/f_0 + \varphi_n), \quad (1)$$

where  $f_0$  is the passband center frequency,  $A_n$  is the  $n$ -th SAW source amplitude,  $\varphi_n$  is the shift of a source position from periodicity. We suppose that in

withdrawal weighted transducers SAW sources are placed in the centers of the electrodes. If the  $n$ -th electrode is absent,  $A_n$  is equal to 0, otherwise the values of  $A_n$  and  $\varphi_n$  depend upon the presence or absence of neighboring electrodes. The magnitudes of  $A_n$  can range between about 0.2 and 1.1 (in the regular structure  $A_n$  equals 1.0), providing additional flexibility in forming a desired IDT response compared with polarity weighted IDTs. In polarity weighted transducers  $A_n = (P_n - P_{n-1})/2$ , where  $P_n = \pm 1$  is the polarity of the  $n$ -th electrode. Deleting electrodes is not considered here. Hence,  $A_n$  can only have values of 1, 0, -1, and the shifts in  $\varphi_n$  equal 0. That is why PW transducers are less flexible in forming broadband frequency responses than WW IDTs. An important advantage of such PW transducers is the uniformity of the electrode structure. Due to a constant SAW velocity in different parts of the transducer, the distortion of the frequency response is smaller than in WW IDTs.

For symmetric PW transducers the number of variables  $A_n$  can be halved by modifying the expression (1) as follows:

$$H_{out}(f) = \sum_{n=1}^{N/2} (P_n - P_{n-1}) \sin((n+0.5)\pi f/f_0), \quad (2)$$

Our method chooses the best electrode structure on the basis of how well the frequency response meets the specified characteristics. To obtain the optimal combination of electrode polarities, one must consider  $2^N$  different structures for an asymmetric structure or  $2^{N/2}$  for symmetric one, where  $N$  is the number of electrodes in the IDT. In the synthesis algorithm developed for WW transducers [1-3], the polarity of electrodes must alternate within each lobe of time response. For PW transducers there is no concept of lobes in the time domain: each electrode can have any polarity but all electrodes must be present.

One of the most important tasks in developing the optimization procedure was to increase in the speed of the transducer structure analysis. On the basis of our experience, we have developed software that can estimate 100-5000 structures per second on a personal computer. The speed depends on the frequency response specifications. In addition, we usually suppose that in some central region of a PW IDT its structure is unweighted. That is why we don't consider changing the electrode polarity there. As a result, we can design optimal structures for symmetrical PW IDTs having up to 50-60 electrodes with bandwidths in the range of 5-15%.

One can show that the computational time for the optimal solution doubles with each additional pair of electrodes in a transducer with a symmetrical structure or with each additional electrode in an asymmetrical IDT. That is why the optimization of PW transducers, which have bandwidths less than 5% (10% in case of asymmetrical IDTs) or time

responses with sidelobes, needs too much time. For such IDTs the algorithm gives suboptimal solutions. It is very important that the suboptimal solution is a close approximation to the optimal one. The search process for the suboptimal solution is complex and consists of two main stages.

The first stage forms an initial structure for the second one. For WW IDTs, this stage was a choice of the best combination of groups of 2-6 electrodes withdrawn from an unapodized transducer of a specified length [3]. However, for PW IDTs a similar method of building the transducer structure by blocks (electrode groups) has appeared ineffective. We use here a smooth time response  $A(t)$  instead of the initial electrode structure. The time response can be synthesized by any known optimization procedure [4,5]. In our software we use for this purpose the cosine-squared-on-a-pedestal time function [5]:

$$A(t) = k + (1-k) \cos^2(\pi t/2\tau) \quad (t \geq \tau, t \leq \tau)$$

with  $k=0.5$ . This value of  $k$  gives a better shape factor of the frequency response than the Hamming function, where  $k=0.08$ . Moreover, the software can use any external time response or electrode structure as the initial one for the second stage of the algorithm.

The second stage includes several steps. On each step the algorithm analyzes all possible combinations of electrode polarities in some limited region of the IDT (8-16 electrode positions, as a rule). This region scans step-by-step through the IDT. The process continues until an improvement in the FR takes place. If during a full pass through the region of the transducer there are no improvements, the process of optimization is finished.

There are two serious problems in a practical realization of the described algorithm. The first one is how to prevent selecting a local optimum in the FR which is far from the global optimum. To avoid this possibility we use consistently four varieties of the scanning region. The region consists of one or two "windows" that move towards one another from opposite edges of the IDT or in a parallel way. The second problem is related to the process of transforming the ideal time response  $A(t)$  to a real electrode structure. Often in the beginning of the second stage of the algorithm, when a group of taps within a window of the ideal time response is replaced with real electrodes, no combination of electrode polarities inside the "window" will meet the frequency response specifications. However, the algorithm should, in any case, select one combination to allow the "window" to move further through the IDT. In this case we use a temporary relaxation of the specifications. In following iterations specifications will be gradually restored.

The main disadvantage of PW transducers is caused by the fact that SAW source amplitudes can have only values of 1, 0, or -1. As a consequence, there are difficulties in realizing frequency responses with good rejection over a broad stopband

by PW transducers (see Fig.2,3). Asymmetrical PW transducers offer more flexibility in the design of broadband frequency responses than symmetrical IDTs because they give, in principle, more possibilities for achieving better selectivity due to twice the number of variables or electrodes polarities, (compare expressions (1) and (2)). That is why we often use asymmetrical structures when phase linearity is not required. However, it takes much more time than the optimization of symmetric structure of the same length.

### 3. RESULTS

For an illustration of the capabilities of the described algorithms, several different polarity weighted transducers and SAW filters have been synthesized.

Fig.2 and 3 presents frequency responses of single symmetric polarity weighted IDTs.

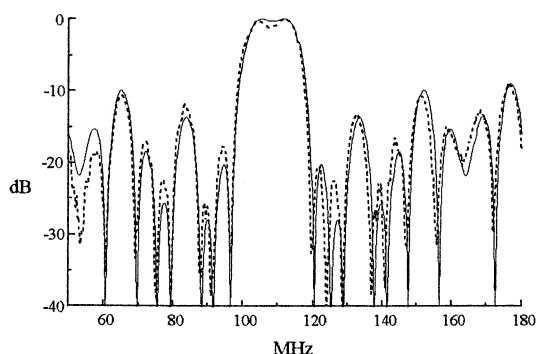


Fig.2. Calculated (solid line) and measured(broken) frequency responses of a symmetric PW IDT 37 lectrodes long; the bandwidth is 14%

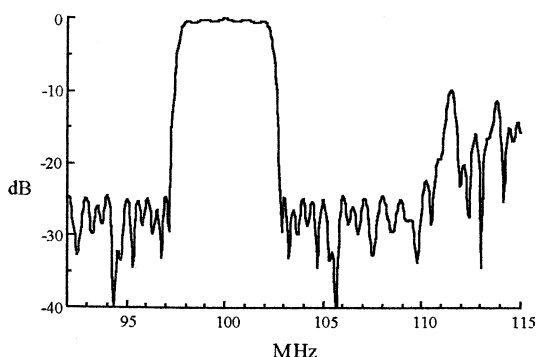


Fig.3. Calculated suboptimal frequency response of a PW IDT having 401 electrodes; the bandwidth is 4.7%.

Fig.2 shows the frequency response of the optimal PW structure, 37 electrodes long. The broken line is the measured response of this

transducer performed on YZ lithium niobate. Suboptimal structure synthesized for a transducer 401 electrodes long is shown in Fig.3. Figures 2 and 3 illustrates good possibilities of PW structures in forming frequency responses with good shape factor and close-in rejection. However, a high level of far-out sidelobes is the main disadvantage of polarity weighted IDTs.

The next three figures present frequency responses of SAW filters including one or two polarity weighted IDTs. All suboptimal PW structures have been synthesized with accounting of frequency responses of output transducers.

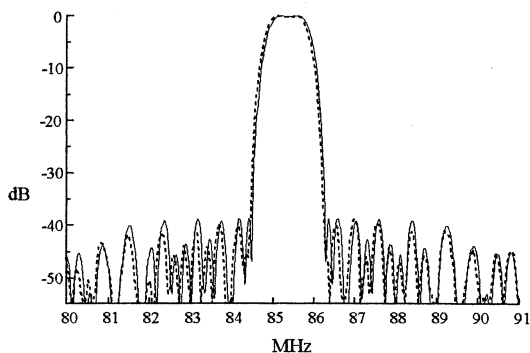


Fig.4. Calculated (solid line) and measured(broken) frequency responses of the filter including PW IDT 179 electrodes long (3rd harmonic) and unweighted IDT 122 electrodes (1st harmonic); the bandwidth is 1.2%.

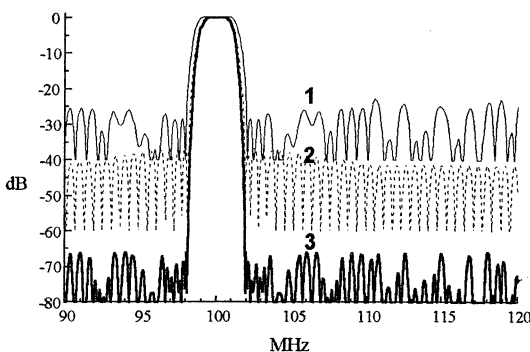
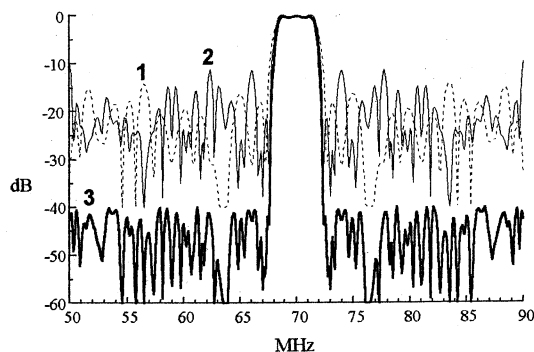


Fig.5. Calculated frequency responses: 1- of a symmetric PW IDT, 2- of an apodized IDT, 3- of the filter including both transducers, each 335 electrodes long; the bandwidth is 2.7%.



*Fig. 6. Calculated frequency responses:  
1,2- of input and output asymmetrical PW IDTs,  
3- of the filter including these transducers:  
bandwidth of 5%.*

In the filter shown in Fig.6, asymmetrical structures of PW IDTs give about 4dB improvement in the stopband rejection compared with their symmetrical analogs.

#### 4. CONCLUSION

Algorithms have been developed to synthesize both symmetric and asymmetric SAW transducers which are weighted by assigning polarities to the individual electrodes (polarity weighted). For IDTs up to 50-60 electrodes in length the software provides optimal structures. For longer transducers it gives suboptimal results.

A number of SAW devices with bandwidths of 1-14% have been designed using this algorithm.

#### REFERENCES

- [1] E.V.Bausk, “A synthesis algorithm for the design of withdrawal weighted SAW transducers with the passband width of 0.5-20%”, in Proc. of International Symp. on Surface Waves in Solid and Layered Structures, Russia, Moscow-St.Peterburg, 1994, pp.148-152.
- [2] E.V.Bausk, I.B.Yakovkin, “Design of low-shape-factor SAW filters having a single acoustic track”, in Proc. IEEE Frequency Control Symp., 1996, pp.291-295.
- [3] E.V.Bausk, I.B.Yakovkin, “Synthesis algorithm of broadband withdrawal weighted SAW transducers with specified amplitude and phase responses”, in Proc. IEEE Frequency Control Symp., 1997, pp.163-167.
- [4] A.J.Slobodnik, T.L.Szabo and K.R.Laker, “Miniature surface-acoustic-wave filters”, Proc. IEEE, 1979, v.67, pp.129-146.
- [5] C.C.W.Ruppel, A.A.Sachs, and F.J.Seifert, “A review of optimization algorithms for the design

## COMPARISON BETWEEN THEORETICAL AND EXPERIMENTAL PROPERTIES OF SAW ON Z-CUT OF LANGASITE

E. HENRY BRIOT\*, E. BIGLER\*, M. SOLAL\*\*, S. BALLANDRAS\*, G. MARIANNEAU\* and G. MARTIN\*

\* *Laboratoire de Physique et Métrologie des Oscillateurs du CNRS associé à l'Université de Franche Comté*  
32, Av. de l'Observatoire, 25044 BESANÇON CEDEX, FRANCE

\*\* *Thomson Microsonics, 399 route des Crêtes, BP 232, 06904 SOPHIA ANTIPOLIS CEDEX, FRANCE*

Langasite (LGS,  $\text{La}_3\text{Ga}_5\text{SiO}_{14}$ ) has been characterized by many research groups for Bulk Acoustic Wave (BAW) applications. However, different sets of fundamental elastic, piezoelectric and dielectric constants have been published corresponding to different manufacturing processes of LGS. Because of its interesting properties (high piezoelectric coupling, existence of temperature-compensated crystal orientations), LGS also appears as a very promising material for SAW applications. However, for high precision design, a faithful characterization of the SAW properties is required. It is then necessary to measure the principal SAW characteristics on LGS (velocity, electro-mechanical coupling coefficient, frequency-temperature curve) in order to define the best set of constants for SAW applications, or even to recalculate some constants.

The paper will focus on new measurements of velocities and temperature sensitivities of SAWs on Z-cut plates of LGS. A comparison of the experimental temperature coefficients of frequency (1-st order TCF) with already published data will be made and conclusions on the best values for the CTFs of SAWs will be proposed.

### I. INTRODUCTION

Originally developed for optical applications, Langasite ( $\text{La}_3\text{Ga}_5\text{SiO}_{14}$ , LGS) has been known to be a piezoelectric crystal with the 32 point group since the 80's [1]. Then it has been studied for Bulk Acoustic Wave (BAW) resonators and filters [2-5] exhibiting a good combination of temperature of bulk acoustic modes stability and a higher piezoelectric coupling than Quartz [6,7].

Recently, LGS single crystal has attracted much attention as a suitable Surface Acoustic Wave (SAW) substrate for SAW applications requiring good temperature stability and high coupling factor [8]. Nu-

merous investigations have been reported on LGS growth [9-13] and measurements of bulk modes and material constants [14-19].

However, to the best of our knowledge, very few papers exist on experimental measurements of SAW properties of LGS. A first general theoretical investigation of SAW application has been presented by Naumenko [8] and Yakovkin [20]. Experimental results of SAW propagation on X-cut plates have been reported by Satoh and Mori [21]. A comprehensive experimental survey of SAW properties has been presented by Fedorets and *al.* [22], however in the printed version of the 1997 IFCS proceedings it is not possible to know the proper cut angles of interesting SAW orientations (Table 4 is missing).

We present here the first experimental results of SAW propagation on Z-cut plates of Langasite. Velocities and first order temperature coefficients of frequency (1<sup>st</sup>-TCF) have been measured for Rayleigh waves. In addition, the properties of a higher velocity mode have been measured and compared to theoretical predictions based on an effective permittivity approach [23].

### II. EXPERIMENTAL PROTOCOL

The experimental devices are delay lines (shown in fig. 1) built on the surface of the LGS plate. An 1900 Å thickness Aluminum film is first deposited on the surface by E-beam evaporation. Then the delay lines are fabricated using a classical U.V. photolithography process and wet chemical etching of Aluminum.

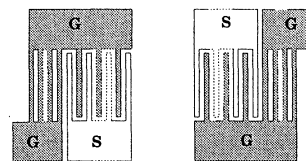


FIG. 1. Principle of the delay lines patterned on the surface of the wafer (G: ground, S:signal)

This work is supported by CNRS (France), Région de Franche-Comté (France) and Thomson Microsonics Company (Sophia Antipolis, France)

All the devices have been built with different propagation directions. This propagation direction is defined using an angle  $\psi$  between the flat and the wave's propagation direction. As shown in figure 2, many SAW devices can be built on the same wafer with identical technological parameters (Aluminum thickness, strip width, metallization ratio) allowing to measure Rayleigh wave characteristics for six different propagation directions.

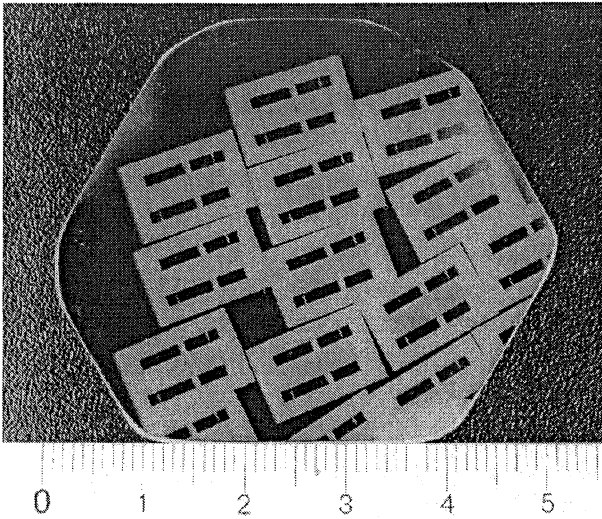


FIG. 2. Aluminum delay lines on a Z-cut plate of LGS

The synchronous frequency of propagating modes is measured using a network analyser and the velocity  $V$  can be derived from both synchronous frequency  $F$  and acoustic periodicity  $\lambda_{ac}$  imposed by the IDT period, according to  $V = F \times \lambda_{ac}$ .

The frequency temperature measurements are performed inserting delay lines in an oscillation loop operating at  $F$  and submitting them to a quasi-static temperature cycle from 20°C to 120°C and back to 20°C. The frequency and the corresponding temperature measurements are automatically controlled and recorded by a computer. The temperature is measured using a platinum resistor probe directly glued on the substrate.

### III. EXPERIMENTAL RESULTS

Figure 3 points out the existence of two modes propagating on the plate, the first one at 104.22 MHz being identified as the Rayleigh mode.

Figure 4 presents the corresponding thermal behaviour of the delay line.

It should be noted that no thermal compensation were observed for the six measured propagation angles.

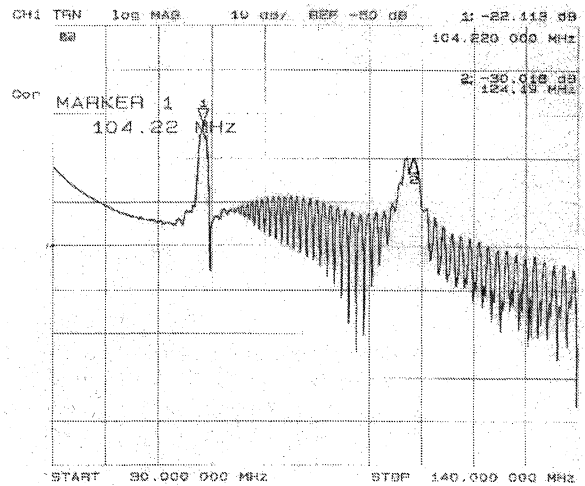


FIG. 3. Log. Magnitude of transmission response of a delay line on Z-cut of LGS ( $\psi=18$ deg.)

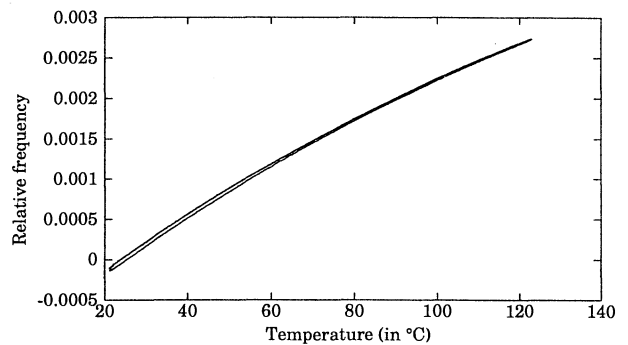


FIG. 4. Thermal dependance of the synchronous frequency of a delay line on Z-cut of LGS ( $\psi=18$ deg.)

### IV. COMPARISON WITH THEORETICAL MODELS

As mentioned in introduction, an effective permittivity approach [23] has been used to compare theoretical velocity of piezoelectrically coupled modes and experimental measurements.

Figure 5 summarises a comparison between measured velocities and theoretical predictions based on different sets of elastic constants (LGS1 [15], LGS2 [14], LGS3 [18]). The agreement between theory and experiment is fairly good as far as velocities are concerned, the agreement is better than 3% within the whole set of experimental data. The last set of constants published by Sakharov [18] seems to be the best one in the prediction of velocities of propagating modes on this Languisite samples.

A simulation has been performed, using the LGS3 [18] set of constants, to explain the presence of a second response peak in the experimental curves (*cf* figure 3). Using the effective permittivity approach, it is possible to predict the existence of the second mode with a very good agreement between predicted and measured velocities (*cf* figure 6).

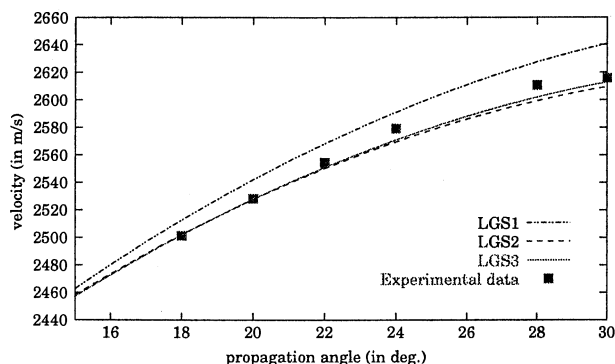


FIG. 5. Comparison between theoretical and experimental velocities of the Rayleigh mode on Z-cut of LGS for different sets of constants

There is an interesting similarity between the angular dependance of the phase velocity for the high velocity mode experimentally measured, and the quasi-transverse vertical shear bulk mode that would propagate in the corresponding crystallographic orientation ( $\phi_{bulk} = \psi_{SAW} - 90$  and  $\theta_{bulk} = \theta_{SAW} - 90$ ). Further investigations are required to check whether this mode is a pseudo surface mode (PSAW) or a surface-generated bulk mode bouncing at the bottom of the plate.

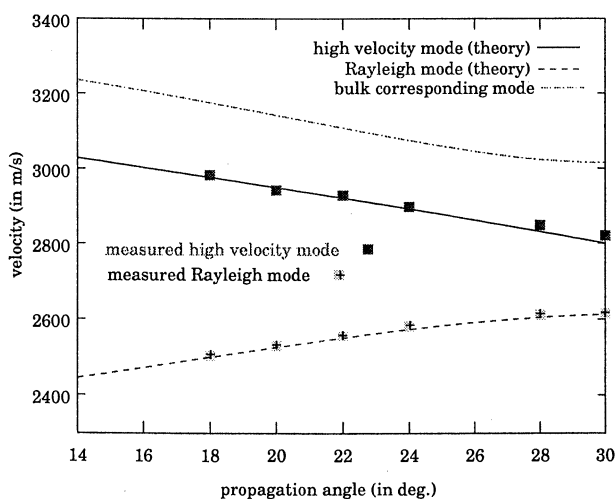


FIG. 6. Comparison between theoretical and experimental velocities on Z-cut of LGS

Figure 7 summarises a comparison between measured first order temperature coefficient of frequency

of the Rayleigh mode and theoretical predictions based on different sets of elastic constants and their temperature derivatives. The theoretical results are obtained by a classical method of variation of the elastic constants [24]. The measurements seems to be more similar to the LGS 1 & 3 sets of constants than to LGS2, except the 10 ppm/ $^{\circ}$ K difference of value. But, on the other hand, very different sets of temperature coefficients of elastic constants have been published that provide very different theoretical results. Then no conclusion could be proposed before further experiments on other cristallographic orientations. It can be noted that the 2<sup>nd</sup> order TCF were measured (*cf* fig. 4) between -60 and -70 ppb/ $^{\circ}$ K<sup>2</sup>.

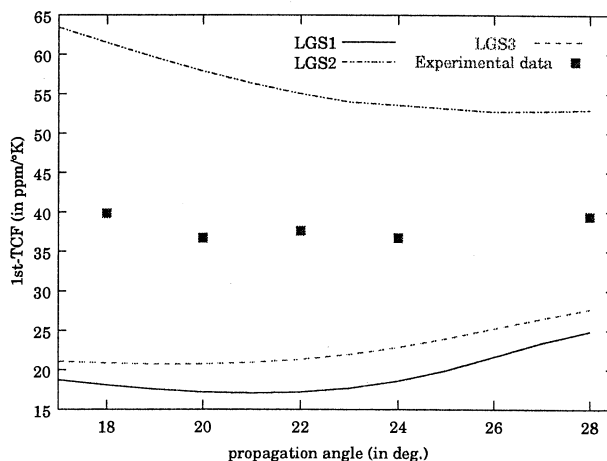


FIG. 7. Comparison between theoretical and experimental 1st-TCF on Z-cut of LGS, for different sets of constants

## V. CONCLUSION

First experimental measurement of SAW velocities and 1<sup>st</sup> order temperature coefficient of frequency have been obtained on Z-cut of Languisite. A very good agreement is found for velocities between experimental data and predicted values derived from already published material constants for LGS. Major discrepancies still exist between theory and experiment for a correct prediction of the first order TCF. It is assumed that the impurity contents of the crystal has a strong influence on the TCF, that may explain the above discrepancies since our samples may be very different from samples originally used for building the material constants data set.

A high velocity mode has been observed and it's phase velocity is correctly predicted by an effec-

tive permittivity approach. Further investigations on other crystallographic orientations are required to check the consistency of experimental values of TCF with available material constants.

#### ACKNOWLEDGEMENTS

We are indebted to M. J.-L. Van Klaveren (Escete B.V., Enschede, the Netherlands) for providing the Z-cut LGS plates used in this work.

- 
- [1] A.A. Kaminskii, I.M. Silvestrova, S.E. Sarkisov, and G.A. Denisenko. Investigation of trigonal  $(La_{1-x}Nd_x)Ga_5SiO_{14}$  crystals. *Phys. Stat. Sol. (a)*, 80:607–620, 1983.
- [2] E.G. Bronnikova, I.M. Larionov, V.A. Isaev, I.M. Silvestrova, and Yu.V. Pisarevsky. Monolithic filters and resonators based on new piezoelectric lanthane gallosilicate. *Souv. Journ. Electronnay technica*, 2(63):83–85, 1986.
- [3] V.B. Grouzinenko and V.V. Bezdelkin. Piezoelectric resonators from  $La_3Ga_5SiO_{14}$  (langasite) - single crystals. In *Proc. IEEE International Frequency Control Symposium*, pages 707–712, 1992.
- [4] I.M. Silvestrova, V.V. Bezdelkin, P.A. Senyushenkov, and Yu.V. Pisarevsky. Present stage of  $La_3Ga_5SiO_{14}$  - Research. In *Proc. IEEE International Frequency Control Symposium*, pages 348–350, 1993.
- [5] J. Detaint, J. Schwartzel, A. Zarka, B. Capelle, D. Cochet-Muchy, and E. Philipot. Properties of the plane and plano-convexe resonators using berillite, gallium orthophosphate and langasite. In *Proc. IEEE International Ultrasonics Symposium*, Cannes, France, Nov. 1994.
- [6] J. Detaint, J. Schwartzel, A. Zarka, B. Capelle, J.P. Denis, and E. Philipot. Bulk wave propagation and energy trapping in the new thermally compensated materials with trigonal symmetry. In *Proc. IEEE International Frequency Control Symposium*, pages 58–71, 1994.
- [7] J. Detaint, B. Capelle, A. Zarka, and D. Cochet-Muchy. Langasite plano-convexe resonators using lateral or perpendicular field excitation. In *Proc. European Frequency and Time Forum*, Besançon, France, Mars 1995.
- [8] N.F. Naumenko. SAW and leaky waves in a new piezoelectric crystal of langasite. *ISSWAS*, pages 245–251, 1994.
- [9] S.A. Sakharov, I.M. Larionov, and A.V. Medvedev. Application of langasite crystals in monolithic filters operating in shear modes. In *Proc. IEEE International Frequency Control Symposium*, pages 713–723, 1992.
- [10] A.N. Gotalskaya, D.I. Drezin, V.V. Bezdelkin, and V.N. Stassevich. Peculiarities of technology, physical properties and applications of new piezoelectric material langasite ( $La_3Ga_5SiO_{14}$ ). In *Proc. IEEE International Frequency Control Symposium*, pages 339–347, 1993.
- [11] B. Capelle, A. Zarka, J. Schwartzel, J. Detaint, E. Philipot, and J.P. Denis. Characterization of piezoelectric materials: old and new crystals. *Journal de Physique IV, Colloque C2, supplément au Journal de Physique III*, 4:123–134, février 1994.
- [12] A.N. Gotalskaya, D.I. Drezin, G.N. Cherpoukhina, V.V. Bezdelkin, and S.N. Shegolkova. Aspects of growing langasite crystals and their properties. *Journal de Physique IV, Colloque C2, supplément au Journal de Physique III*, 4:201–207, février 1994.
- [13] Kiyoshi Shimamura, Hiroaki Takeda, Takuya Kohno, and Tsuguo Fukuda. Growth and characterization of lanthanum gallium silicate  $La_3Ga_5SiO_{14}$  single crystal for piezoelectric applications. *Journal of Crystal Growth*, (163):388–392, 1996.
- [14] I.M. Silvestrova, Yu.V. Pisarevski, P.A. Senushenkov, and A.I. Kruppnyi. Temperature dependences of the elastic properties of  $La_3Ga_5SiO_{14}$  single crystals. *Sov. Phys. Solid State*, 28(9):1613–1614, Sept. 1986.
- [15] I.M. Silvestrova, Yu.V. Pisarevsky, V.V. Bezdelkin, and P.A. Senushenkov. New piezoelectric materials. In *Proc. IEEE International Frequency Control Symposium*, pages 351–352, 1993.
- [16] V.V. Bezdelkin and E.E. Antonova. Fundamental characteristics of thickness vibrations of langasite plates for baw resonators. *Journal de Physique IV, Colloque C2, supplément au Journal de Physique III*, 4:139–156, février 1994.
- [17] K.S. Aleksandrov, B.P. Sorokin, P.P. Turchin, S.I. Burkov, D.A. Glushkov, and A.A. Karpovich. Effects of static electric field and of mechanical pressure on surface acoustic waves propagation in  $La_3Ga_5SiO_{14}$  piezoelectric single crystals. In *Proc. IEEE International Ultrasonics Symposium*, pages 409–412, 1995.
- [18] S. Sakharov, P. Senushencov, A. Medvedev, and Yu. Pisarevsky. New data on temperature stability and acoustical losses of langasite. In *Proc. IEEE International Frequency Control Symposium*, pages 647–651, 1995.
- [19] J.A. Kosinski. New acoustoelectronic materials. In L. Spassov, A. Manov, I. Avramov, and Z. Georgiev, editors, *Proceedings of the 6<sup>th</sup> Conference Acoustoelectronics '93*, Varna, Bulgaria, Sept. 1993. Institute of Solid State Physics of the Bulgarian Academy of Sciences.
- [20] I.B. Yakovkin, R.M. Taziev, and A.S. Kozlov. Numerical and experimental investigation saw in langasite. In *Proc. IEEE International Ultrasonics Symposium*, pages 389–392, 1995.
- [21] Hiroaki Satoh and Atsushi Mori. Surface acoustic wave propagation characteristics on a langasite crystal plate. *Japanese Journal of Applied Physics*, 36 (Ultrasonic Electronics)(Part 1, 5B):3071–3073, may 1997.
- [22] V.N. Fedorets, Yu. P. Kondratyev, B.V. Mill, V.A. Pankov, Yu. V. Pisarevsky, and V.V. Timashev. Surface acoustic wave characteristics on

$\text{La}_3\text{Ga}_5\text{SiO}_{14}$  crystals. In *Proc. IEEE International Frequency Control Symposium*, pages 816–820, Orlando, Florida, May 1997.

- [23] D.P. Morgan. *Surface-wave devices for signal processing*, volume 19 of *Studies in electrical and electronic engineering*. Elsevier Ed., 1985.
- [24] J.J. Campbell and W.R. Jones. A method for estimating optimal crystal cuts and propagation direction for excitation of piezoelectric surface waves. *IEEE Trans. Sonics Ultrason.*, SU-15:209–217, 1968.

DESIGN OF SAW RESONATORS ON ST CUT QUARTZ

Waldemar Soluch

Institute of Electronic Materials Technology  
Wolczynska 133, 01-919 Warsaw, Poland

ABSTRACT

Surface acoustic wave (SAW) resonators on ST cut quartz, with synchronous placement of the interdigital transducers (IDTs), were designed, fabricated and measured. The basic structure of the resonators was a two port one. The one port resonators were obtained by parallel connection of the two IDTs or by short circuiting one of them. The IDTs were apodised to eliminate coupling to spurious modes. The transfer function of the two port resonators was calculated by using the scattering matrix method. Several models of these resonators were investigated in the frequency range from about 300 MHz to 715 MHz. The responses of the resonators were free of any spurious modes.

INTRODUCTION

Surface acoustic wave (SAW) resonators are high Q components used for frequency control in oscillators. They are generally applied as VHF/UHF local and voltage controlled crystal oscillators and low power transmitters in the frequency range from 100 MHz to 1.5 GHz. If the frequency is to be multiplied to a microwave range, the multiplication coefficient is much smaller compared to the case when bulk acoustic wave resonators (at much lower frequency) are used, and lower noise level is obtained.

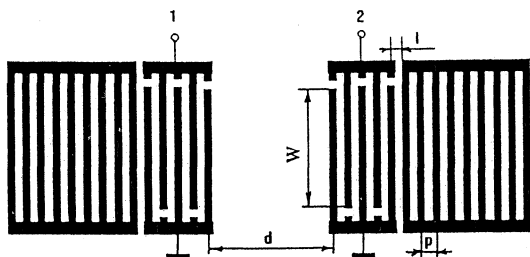


Fig.1. SAW synchronous two port resonator.

Usually the synchronous type resonators are used in practical applications [1]. The resonator (Fig.1) consists of two reflectors and two interdigital transducers (IDTs). It is assumed, that both the IDTs and the reflectors are identical, and that the IDTs are symmetrical. The electrodes of the reflectors are

short circuited. The IDTs can be apodised to eliminate coupling to spurious transverse modes.

TRANSFER FUNCTION

Transfer function  $T_{12}$  of the two port synchronous SAW resonator can be written as [2,3]:

$$T_{12} = \frac{t S_{13}^2 W_1^2}{W_2^2 - t^2 W_3^2} \quad (1)$$

where:

$$\begin{aligned} W_1 &= 1 + r(S_{12} - S_{11}), \\ W_2 &= 1 - r S_{11}, \\ W_3 &= S_{11} + r(S_{12}^2 - S_{11}^2), \\ t &= \exp(-j(\beta_f d - \pi)), \\ r &= \Gamma T_i \exp(-j2\beta_r l), \\ \beta_f &= 2\pi f/v_f, \\ \beta_r &= 2\pi f/v_r. \end{aligned}$$

Here  $S_{ij}$  are the IDTs scattering coefficients,  $\Gamma$  is the reflection coefficient of the reflectors,  $T_i$  is the loss coefficient,  $f$  is the frequency, and  $v_f$  and  $v_r$  are the SAW velocities in the areas between the reflectors and inside them, respectively. For the synchronous resonator, the IDTs are inside the reflectors, therefore  $d$  (instead of a distance between their centers), and  $l = p - p/4$  (Fig1.), are used in the expressions for  $t$  and  $r$ , respectively. The transfer function can be written as

$$T_{12} = |T_{12}| \exp(j\Phi) \quad (2a)$$

and the insertion loss IL is calculated from the expression

$$IL = 20 \log |T_{12}| \quad (2b)$$

The input admittance of the apodised IDT can be calculated by the method presented in [4]. The scattering coefficients of the IDT and the reflection coefficient of the reflector may be calculated from the expressions given in [2]. It should be remembered,

that in the case of two apodised IDTs, calculations of the transfer function are correct only near the center frequency of the resonator.

### TWO PORT RESONATORS

Using the above analytical expressions, a computer program was written to calculate the transfer function of the resonator as a function of frequency. For the ST cut quartz, the following input data were used in the program [5 -7]:  $v_f = 3158$  m/s,  $K^2 = 0.0016$ ,  $\epsilon_r = 4.5$ ,  $\gamma = -0.5 h/\lambda_f$ , where  $\lambda_f = 2p$ ,  $v_f$  is the free surface SAW velocity,  $K$  is the electromechanical coupling coefficient,  $\epsilon_r$  is the relative dielectric constant,  $\gamma$  is the reflection coefficient of one strip of the reflector,  $h$  is the aluminium layer thickness,  $\lambda_f$  is the SAW wavelength in the area of the reflectors, and  $p$  is the period of the reflectors, respectively. The center frequency of the resonator is equal to the center frequency of the reflectors (maximum reflection coefficient) if

$$d = n \lambda_f / 2 + p/2 \quad (3)$$

where  $d$  is the distance between the reflectors,  $\lambda_f$  is a SAW wavelength for the free surface (between the reflectors), and  $n$  is an integer (Fig.1). If  $n$  is odd, then the phase shift  $\Phi(f_0)$  is approximately equal to  $\pi$ , while for  $n$  even it is close to 0.

The following data were used for the resonator at a frequency near 300 MHz (Fig.1):  $W = 1$  mm,  $p = 5.2$   $\mu$ m,  $n = 21$ ,  $N_t = 91$  and  $N_r = 625$ , where  $N_t$  is the number of the IDT electrodes, and  $N_r$  is the total number of the reflector electrodes (the IDT is a part of the reflector). Cosine function was used for the IDT apodisation (Fig.2).

A negative photomask was made with electron beam photolithography and the aluminium electrodes were deposited on the ST cut substrate by the lift-off method.

The resonator chips were mounted in metal packages (TO-8), hermetically sealed by cold welding in the vacuum and measured in a 50  $\Omega$  system (HP 8752A Network Analyzer).

Several thicknesses  $h$  of the aluminium layer were used to determine the variation of the SAW velocity  $v_f$  in the area of the reflectors. In the case of equal width of the gaps and electrodes, the following expression was obtained from the measured resonance frequencies and from the known period  $p$  of the resonator:

$$v_f = v_r [1 - 2.9 \cdot 10^{-4} - 0.155 (h/\lambda_f) - 5.73 (h/\lambda_f)^2] \quad (4)$$

Fig.3. shows the measured and calculated insertion loss IL of the resonator for the aluminium layer

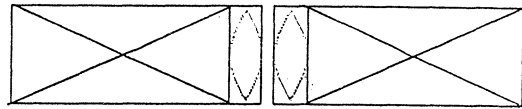


Fig.2. Structure of the resonator with apodised IDTs.

thickness  $h \approx 90$  nm. To obtain an agreement between the calculated and measured insertion loss

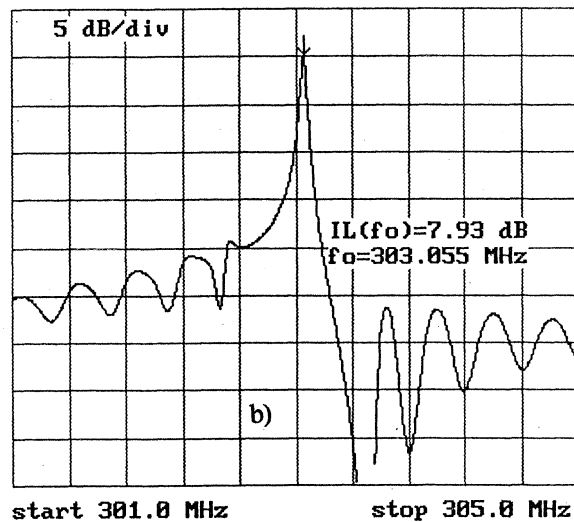
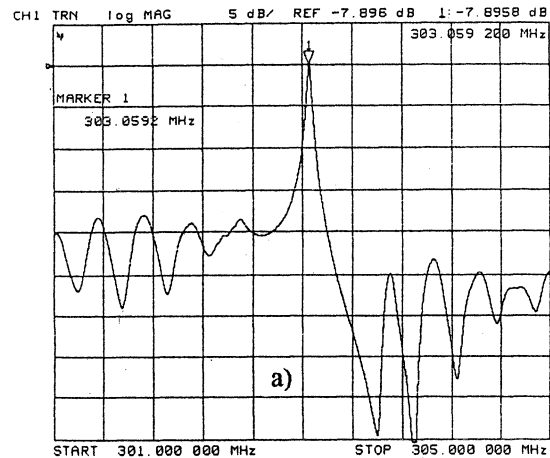


Fig.3. Measured (a) and calculated (b) insertion loss IL of the resonator.

$IL(f_0)$  at the resonance frequency  $f_0$ , the loss coefficient  $T_i = 0.98$  was used for the calculations and an additional capacitance of the resonator package (about 1 pF) was also added to the static capacitance of the IDT. The measured phase shift  $\Phi(f_0)$  was approximately equal to  $\pi$ , as expected. The loaded quality factor  $Q_L$  can be determined as  $Q_L = f_0 / \Delta f_{3dB}$ , where  $\Delta f_{3dB}$  is the 3dB bandwidth of the transfer function. For the above resonator  $Q_L \approx 9000$  was obtained. Then, from the above measured data, the equivalent circuit parameters of the two port resonator (Fig.4) can be easily calculated [8].

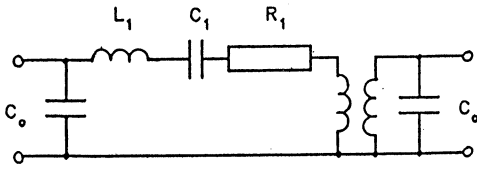


Fig.4. Equivalent circuit of a two port SAW resonator.

Several models of the two port resonators were next designed for higher frequencies up to 715 MHz. By comparing the measured and calculated parameters of the resonators, it was found, that the loss coefficient  $T_i$  may be approximately determined from the expression

$$T_i \approx 1/(1+72.3 \cdot 10^{-6} f_0) \quad (5)$$

where  $f_0$  is in MHz.

#### ONE PORT RESONATORS

If the phase shift  $\Phi(f_0)$  is close to  $\pi$ , then the one port resonator can be obtained by parallel connection of the IDTs. If this condition is not satisfied or if we need higher resistance, then only one of the IDTs may be used (the other one should be short circuited). The 303 MHz resonator was measured in both configurations by using the HP Network Analyzer in the reflection mode. Fig.5 presents the admittance circle for the IDTs parallelly connected.

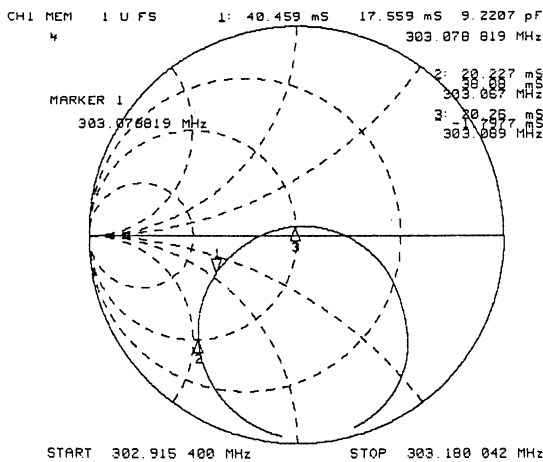


Fig.5. Admittance circle of the one port resonator for parallelly connected IDTs.

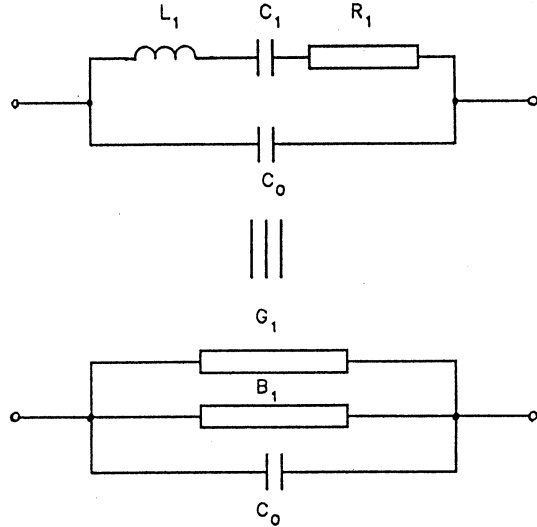


Fig.6. Equivalent circuit of a one port SAW resonator.

The equivalent circuit parameters (Fig.6) can be easily deduced from the circle. Namely

$$R_1 = 1/G_{1M} \quad (6)$$

where  $G_{1M}$  is the maximum value of conductance  $G_1$  (marker 1 at frequency  $f_0$ ),

$$Q_U = f_0/\Delta f_{3dB} \quad (7)$$

where  $\Delta f_{3dB}$  is the difference between the frequencies at which the conductance is equal to  $G_{1M}/2$  (markers 2 and 3), and

$$L_1 = Q_U R_1/\omega_0 \quad (8)$$

$$C_1 = 1/(\omega_0^2 L_1) \quad (9)$$

#### SUMMARY AND DISCUSSION

The 303 MHz SAW resonators parameters are summarized in Table.1. It can be shown, that if the phase shift of the two port resonator  $\Phi(f_0)$  would be exactly equal to  $180^\circ$ , then for the IDTs parallelly connected

$$Z_{1p} = Z_{2p}/4 \quad (10)$$

where  $Z_{1p}$  and  $Z_{2p}$  are the impedances of the series

Table 1. Parameters of the 303 MHz resonators

Configuration	Parameter						
	$C_0$ [pF]	$L_1$ [mH]	$C_1$ [fF]	$R_1$ [ $\Omega$ ]	$Q_L$ -	$Q_U$ -	$\Phi(f_0)$ [ $^\circ$ ]
Two port	2.3	1.18	0.23	150	9000	15000	190
One port, two IDTs	4.6	0.18	1.51	25	-	14000	-
One port, one IDT	2.3	1.08	0.25	142	-	14500	-

arm of the one and the two port resonator, respectively (Fig.4 and 6). It means, for example, that the resistance  $R_1$  of the one port should be 1/4 of that one in the two port resonator. In our case it is 1/6, since the phase condition is not exactly satisfied and it is some influence of the parasitic elements. If one of the IDTs is short circuited, then the above impedances should be equal, and it is approximately confirmed by the results presented in Table 1. To obtain lower resistance  $R_1$ , the number of the ITD electrodes should be larger.

### CONCLUSION

The scattering matrix approach can be used for design of the two port and one port synchronous SAW resonators. It was confirmed by the theoretical and experimental results obtained for the ST cut quartz. This approach can be also used for other piezoelectric substrates.

### REFERENCES

- [1] P.S.Cross, W.R.Shreve and T.S.Tan, "Synchronous IDT SAW resonators with Q above 10,000", 1979 IEEE Ultrason. Symp. Proc., p.824.
- [2] L.A.Coldren and R.L.Rosenberg, "Scattering matrix approach to SAW resonators", 1976 IEEE Ultrason. Symp. Proc., p.266.
- [3] W.Soluch, "Application of synchronous two port resonators for measurements of SAW parameters

in piezoelectric crystals", 1997 IEEE International Freq. Contr. Symp. Proc., p.827.

[4] W.Soluch, "Admittance matrix of a surface acoustic wave interdigital transducer", IEEE Trans. on UFFC, vol. 40, No. 6, 1993, p.828.

[5] A.J.Slobodnik, "Surface acoustic waves and SAW materials", Proc. IEEE, vol.64, No. 5, 1976, p.581.

[6] C.Dundrowicz, "Reflection of surface waves from periodic discontinuities", 1976 IEEE Ultrason. Symp. Proc., p. 386.

[7] W.J.Tanski, H. van de Vart, "The design of SAW resonators with emphasis on two ports", 1976 IEEE Ultrason. Symp. Proc., p. 260.

[8] Surface acoustic wave resonators (SAW).Part 1. General information, standard values and test conditions, IEC 1019-1-2, 1993.

### ACKNOWLEDGEMENTS

I would like to thank W.Hofman for quartz substrates fabrication, to A.Kowalik for masks fabrication, to M.Teodorczyk for the resonators chips fabrication and to T.Wrobel for measurements.

This work was supported by the State Committee for Scientific Research under Grant No. 8 S501 051 04.



*12th E F T F* - 10÷12 March 1998 - Warsaw - POLAND

**Instrumentation & Measurement I**

Chairman: *Roger Bourquin*



## CLOCK PREDICTION UNCERTAINTY

A. Lepek

Newton Metrology Ltd., PO Box 9769, Jerusalem 91091, Israel. E-mail 100264.565@compuserve.com

## ABSTRACT

It is recognized that the classical variance does not adequately describe type 'A' (statistical) measurement uncertainty of unstable measurands such as clocks and oscillators [1]. We argue that the equivalent of the classical uncertainty in measuring time (or phase) is the uncertainty in time prediction. The usefulness of a clock is in its predictability, that is, its prediction error obtained with an optimum predictor. It was shown [2, 3] that for each type of clock instability, a specific linear predictor provides optimum or close to optimum prediction. Given a series of time measurements, the deviations from optimum predictions are of white noise and therefore we can use the classical methods [4] to estimate the uncertainty in such prediction. The classical uncertainty is a special case of the prediction uncertainty when the measurand is stable. The predictability of a clock can be used to characterize and compare clocks of different instabilities. In this paper we present the various linear predictors, estimate the associated prediction uncertainties and show how to characterize clocks. We note the difference between predictability and stability (which is defined as the Allan deviation in the IEEE standard [5]).

## INTRODUCTION

Suppose we have a time series of measured values of time difference between two clocks or between a clock and a reference time scale made at time intervals  $T$ . We try to predict the next measurement before it is made. If this prediction has a small uncertainty we have a predictable clock. Consider the series of time differences  $x_m$ , chosen at the time intervals  $\tau = n \cdot T$ , where  $m$  is the time index. Using linear prediction, the predicted value of  $x_m$ ,  $p_m$  is

$$p_m = \sum_{i=0}^{N-1} a_i x_{m-N+i} \quad (1)$$

that is, a linear combination of the measured values obtained at the past  $N$  points.

We define the linear predictor  $P$  by its coefficients,

$$P = [a_0, \dots, a_{N-1}] \quad (2)$$

After measuring  $x_m$ , the deviation from the prediction  $p_m$ ,  $d_m$ , is given by

$$d_m = x_m - p_m = \sum_{i=0}^N -a_i x_{m-N+i}, \quad a_N = -1 \quad (3)$$

As in (2) we can define a deviation function,  $D$ , by its coefficients as

$$D = [-a_0, \dots, -a_{N-1}, 1] \quad (4)$$

The prediction error,  $E$ , can be estimated by

$$E = \sqrt{\frac{\sum_{m=N}^r d_m^2}{(n-1)}}, \quad (5)$$

where  $n$  is the number of predictions and  $r$  is the number of points in the  $x_m$  series. The value of  $E$  may depend on  $\tau$ .

If  $P$  is an optimum predictor on a very long time series,  $x_m$ , the average  $d_m$  is zero, the value of  $E$  is a minimum (compared to prediction errors of any other predictor acting on the same time series) and is equal to the standard deviation of  $d_m$ ,  $\sigma$ . In this case, the  $P_m$  values define the best regression curve predicting the next measurement and the time series  $d_m$  is in the form of white noise. With practical predictors which have a small number of coefficients it is not always possible to find an optimum predictor. As will become clear later, such close to optimum predictor are still useful in the estimation of the prediction uncertainty and in finding clock predictability.

## PREDICTOR COEFFICIENTS

It is possible to find optimum or close to optimum linear predictors for some instability models.

A clock time series  $x_m$  can be modeled by a slowly varying curve on which different types of noise are superimposed. The various noise types are described in terms of what is called an oscillator model [6, 7]. In the following, linear drifts and low order accelerations are modeled by a low order polynomial. The present approach does not treat periodical variations which may be removed by choosing prediction intervals equal to the period.

For example, by choosing prediction intervals of 24 hours much of the clocks' diurnal variations are eliminated [8].

The techniques used to compute the predictor coefficients for the present instability model are described in [2, 3]. Table 1 shows some deviation functions, D (limited to 8 past points for practical reasons). The instabilities are superimposed on some polynomials. The table lists the normalized prediction errors,  $E_o$ , (normalized with respect to

the prediction error of white noise obtained with the deviation function  $D=[1]$ , the optimum is 1.00).

Some of the deviation functions of table 1 are well known. The deviation function in line 1 of the table,  $D1=[1]$ , is the classical standard deviation of a random variable whose average is 0;  $D3$  (line 3) is a deviation function based on the average of  $N$  past points;  $D5$  is the first difference;  $D7$  is the linear regression;  $D11$  is the second difference which is proportional to the Allan deviation.

TABLE 1 - Normalized prediction errors,  $E_o$ , for oscillator instabilities superimposed on several polynomials. The  $E_o$  values in bold type are minima for the noise type for each polynomial. Optima are in italic.

	highest polynomial	Deviation function D	White PM	Flicker PM	White FM	Flicker FM	Random walk FM
1	horizontal line on abscissa	[1]	<b>1.00</b>	1.16	>10		
2		[-1,2]/2	1.12	<b>1.00</b>	>10		
3	horizontal line	[-1,-1,-1,-1,-1,-1,-1,-1,8]/8	<b>1.06</b>	1.19	1.80	3.19	>10
4		[-1,-1,-1,-1,-1,-1,-1,-9,16]/16	1.16	<b>1.05</b>	1.25	1.86	>10
5		[-1,1]	1.41	1.15	<b>1.00</b>	1.16	>10
6		[1,-3,2]/2	1.87	1.41	1.12	<b>1.00</b>	>10
7	straight line	[7,4,1,-2,-5,-8,-11,-14,28]/28	<b>1.26</b>	1.33	1.35	1.93	3.11
8		[3,0,0,-1,-1,-2,-13,14]/14	1.39	<b>1.21</b>	1.10	1.38	2.15
9		[1,0,0,0,0,0,-8,7]/7	1.52	1.25	<b>1.07</b>	1.19	1.70
10		[1,0,0,0,0,7,-22,14]/14	1.93	1.46	1.16	<b>1.06</b>	1.22
11		[1,-2,1]	2.45	1.87	1.41	1.15	<b>1.00</b>
12	parabola	[-8,3,5,7,5,-2,-8,-20,18]/18	<b>1.72</b>	1.67	2.3	5.62	>10
13		[-4,2,2,2,3,1,-1,-17,12]/12	1.81	<b>1.57</b>	1.33	1.45	1.44
14		[-2,1,1,1,1,1,-11,7]/7	1.92	1.59	<b>1.31</b>	1.35	1.31
15		[-3,3,0,1,0,0,11,-24,12]/12	2.44	1.83	1.44	<b>1.24</b>	1.11
16		[-1,1,0,0,0,7,-13,6]/6	2.67	1.99	1.55	1.27	<b>1.08</b>

### TYPE "A" NEXT MEASUREMENT UNCERTAINTY

When measuring a time varying measurand, the order of the measurements is significant and thus we must refer to the "next measurement uncertainty" rather than to the "measurement uncertainty". The "next measurement uncertainty" should reflect our gain in confidence about the next measurement when using a predictor. The two kinds of uncertainty, the "next measurement uncertainty" and the "measurement uncertainty" are of course identical when the measurand does not vary in time and the "measurement uncertainty" is thus a special case of the "next measurement uncertainty".

Given a clock time series, the next measurement uncertainty depends on the instability type, on the predictor and on the prediction interval. We consider two practical approaches for assessment of the next measurement uncertainty.

We note that with an optimum predictor (see  $D1$ ,  $D2$ ,  $D5$ ,  $D6$  and  $D11$  in Table 1), the prediction deviations series,  $d_m$  form white noise and the elements of the series are therefore uncorrelated. Also,  $\langle d_m \rangle = 0$ . This means that  $E = \sigma(d_m)$  and  $E$  may be used to estimate the next measurement uncertainty. With  $n$  predicted points, the "next measurement expanded uncertainty",  $U_N$ , is defined similarly to the "expanded uncertainty",  $U$ , [4],

$$U_N = t \cdot E / \sqrt{n}, \quad (6)$$

where  $n$  is the number of predictions,  $t$  is the student distribution 95% percentile for  $n-1$  degrees of freedom,  $df$ ,

$$df = n - r - N \quad (7)$$

where  $r$  is the  $x_m$  data length.

For example, with the 2nd difference predictor  $P=[-1,2]$ ,  $n$  equals the number of the points in the time series minus 2. This predictor is optimum for

random walk FM. It should have the same number of degrees of freedom as the overlapping Allan deviation for this instability. This indeed is the case [9].

In general, to be able to use an optimum predictor in the presence of a trend polynomial, the polynomial must be first removed. For example, if the instability is white FM about a straight line then in order to use  $D5=[-1,1]$  as the deviation function of the optimum predictor  $P=[1]$ , a linear regression must first be removed. This is because  $D5$  can be used only with a horizontal line as a trend polynomial.

Given a time series, the removal of a fitted polynomial will leave a time series with  $\langle x_m - X_m \rangle = 0$ , where  $X_m$  is the fitting polynomial series. Now, from table 1 it is clear that one of the deviation functions,  $D1$ ,  $D2$ ,  $D5$ ,  $D6$ , or  $D11$  or their combination will be optimum for the  $x_m - X_m$  series. If the exact instability type is unknown then the prediction error for each of these deviation functions is computed and the minimum prediction error is the sought one. The best predictor is thus {a fitted polynomial predictor} + {an optimum predictor from table 1}. The standard components of the prediction uncertainty in this case are the {prediction uncertainty of the fitting polynomial} and {the prediction uncertainty of an optimum predictor from table 1}. The number of degrees of freedom is the data length minus the degree of the regression polynomial minus  $N$ , the number of past points used by the optimum predictor. The prediction uncertainties of simple polynomials in the presence of white noise are well established (e.g. linear regression prediction).

An alternative to the removal of a fitted polynomial before the use of optimum predictors, is to use the deviation functions of table 1 (if the number of past points is 8) or other appropriate deviation function which could be prepared for the actual number of past points. Because of the way these predictors were prepared, their action includes implicitly the removal of a trend line,  $P_m$ , and thus the two approaches are equivalent.

Two minor corrections must be made to this statement. The deviation series,  $d_m$ , obtained with the best close to optimum predictors are somewhat correlated and thus do not constitute white noise, however they show white noise slope when analyzed in a  $\log[\sigma_y(\tau)]$  vs  $\log[\tau]$  plot. Also, these  $d_m$  series has the lower prediction error when tested with  $D=[1]$ . The second correction is that  $D12$ - $D13$  are simplified approximations to the fitting of a parabola but the differences are within 1%.

In the Following we illustrate the equivalence of the two approaches. WE compare the uncertainties obtained with linear regression of white noise obtained in the two ways. The prediction expanded uncertainty obtained with linear regression is well established [10]. For equally spaced  $N$  points and predicting the  $N+1$  point, the predicted expanded uncertainty becomes

$$Un = t \cdot \sigma \cdot \sqrt{(1 + 1/N + 3(N+1)/(N(N-1)))} = t \cdot \sigma \cdot B \quad (8)$$

where  $t$  is the student percentile,  $\sigma$  is the standard deviation of the white noise and  $B$  just abbreviates the rest of the formula. Substituting  $N=8$  we obtain  $B=1.26$  which is the same as the value of  $E0$  of  $D7$  obtained from the root mean square of its coefficients.

If the type of the instability is unknown, then all of the prediction errors of  $D12$  to  $D16$  should be evaluated and the minimum error is the one to be used. The two methods are equivalent.

In some cases it is possible to overcome the problem of computing the prediction errors of all the relevant predictors (when the instability type is not known) to chose an appropriate one. In the following we discuss this matter.

## CLOCK PREDICTABILITY

We define the predictability of a clock at a particular prediction interval,  $\tau$ , as the value of  $E(\tau)$  for an optimum predictor. This minimum value for  $E(\tau)$  is unique and may be used to characterize clock performance. In practice, one optimum predictor cannot be devised for all instability types. If a predictor could have the same prediction error for all instability types, knowing how much the prediction error is higher than the optimum prediction error, the predictability could be evaluated. Fortunately, it was found that there are predictors for which the values of  $E$  are uniform over a range of instabilities (that is, for adjacent columns in Table 1). The largest uniform ranges we have found are for three adjacent instabilities. Table 2 shows some predictors of this kind and some predictors whose prediction errors deviate by a small fraction over a range of instabilities. The values in the table are the normalized values,  $E_0$ , the normalization made in the same way as in Table 1.

As an example, if a nonuniformity of 15% (maximum to minimum) in the prediction error over the entire range of instabilities can be tolerated and it is known that the time series shows a frequency drift then the deviation function  $D20$  (table 2) can be used to estimate  $Z(\tau)$ ,

$$Z(\tau) = E_{20} \sqrt{(81/262)} \quad (9)$$

If only 7% non uniformity can be tolerated with the same time series then the predictability can be estimated by

$$Z(\tau) = \text{minimum}\{E_{21} \sqrt{0.3}, E_{22} \sqrt{2}\} \quad (10)$$

Note that D21 and D22 use the same number of past point.

Of interest is the simple deviation function D19=[1,-1,-1,1] (P=[-1,1,1]) whose prediction error is uniform over the range of white FM to random walk FM about a straight line. This is most important range for caesium clocks and can be used

to characterize them. The predictability in this case can be estimated from

$$Z(\tau) = E_{19} / \sqrt{2} \quad (11)$$

The advantage of estimating the predictability,  $Z(\tau)$ , using predictors which have a constant value of prediction error over a range of instabilities is that it enables to compare clocks of different instabilities without first checking the type of instability for each prediction interval,  $\tau$ . The common method of using the Allan deviation to compare clocks of different types of instabilities is inferior because of its nonuniformity (up to 245% over the range of instabilities).

TABLE 2 - Predictors which have small nonuniformities in  $E_{\theta}$  over ranges of instabilities. The bold type indicates the uniform ranges. To obtain the predictability multiply the prediction error by the correction factor. The line numbers are continued from table 1.

	highest polynomial	correction factor	Deviation functions D	White PM	Flicker PM	White FM	Flicker FM	Random walk FM
17	straight line	$\sqrt{(49/118)}$	[6,-2,-2,-2,-2,-1,-4,7]/7	<b>1.55</b>	<b>1.55</b>	<b>1.55</b>	2.19	3.45
18		$1/\sqrt{2}$	[1,0,0,-1,0,0,-1,-1,2]/2	<b>1.41</b>	<b>1.41</b>	<b>1.41</b>	2.01	3.39
19		$1/\sqrt{2}$	[1,-1,-1,1]	2.00	1.73	<b>1.41</b>	<b>1.41</b>	<b>1.41</b>
20	parabola	$\sqrt{(81/262)}$	[-5,2,4,7,1,-10,-8,9]/9	<b>2.05</b>	<b>2.08</b>	<b>1.8</b>	<b>2.08</b>	<b>2.0</b>
21		$\sqrt{0.3}$	[-2,1,1,1,1,1,-2,-2,-2,3]/3	<b>1.83</b>	<b>1.95</b>	<b>1.83</b>	2.38	2.59
22		$1/\sqrt{2}$	[-1,1,0,1,-1,0,1,0,-3,2]/2	2.12	1.73	<b>1.41</b>	<b>1.41</b>	<b>1.41</b>

## REFERENCES

- Allan D W, 1987, "Should the Classical Variance Be Used As a Basic Measure in Standard Metrology?", IEEE Transactions on Instrumentation and Measurement, IM-36, 646-654
- Lepek A, 1997, "A Time Scale Based on Optimum Linear Prediction", Frequency Control Symposium, 1997 IEEE International Frequency Control Symposium, 382-387
- Lepek A, 1998, "Clock Prediction and Characterization", Metrologia, 34, 379-386
- BIPM, IEC, IFCC, ISO, IUPAC, IUPAP, OIML, 1993, "Guide To The Expression Of Uncertainty", ISO 1993, 1st edition, pp101
- Ferre-Pikal E S, Vig J R, Camparo J C, Cutler L S, Maleki L, Riley W J, Stein S R, Thomas C, Walls F L and White J D, 1997, "Draft Revision of IEEE STD 1139-1988 Standard Definition of Physical Quantities for Fundamental Frequency and Time Metrology - Random Instabilities", 1997 IEEE International Frequency Control Symposium, 338-357
- Rutman J and Walls F L, 1991, "Characterization of Frequency Stability In Precision Frequency Sources", Proceedings of the IEEE, 79, 952-960
- Allan D W, Weiss M A and Jespersen J L, A Frequency-Domain View of Time Domain Characterization of Clocks and Frequency Distribution Systems, 45th Annual Symposium on Frequency Control, 1991, 667-678
- Lepek A, Shenhar A and Allan D W, 1996, "UTC(INPL) - a virtual time scale", Metrologia, 32, 245-252
- Howe D W, Allan D W and Barnes J A, Properties of Signal Sources and Measurement Methods, Proceedings of the 35th Annual Symposium on Frequency Control, 1981, 1-47
- Walpole R E and Myers R H, Probability and statistics for Engineers and Scientists, 1993, 5th edition, Macmillan Publication Company, NY, pp766, Page 381.

## NOISE CHARACTERISATION OF IRREGULARLY SPACED DATA

P. Tavella\* and M. Leonardi<sup>o</sup>

\*Istituto Elettrotecnico Nazionale "G. Ferraris" *Strada delle Cacce 91*, 10135 Torino, Italy; [tavella@tf.ien.it](mailto:tavella@tf.ien.it)

<sup>o</sup>Politecnico di Torino, Dip. Elettronica *C.so Duca degli Abruzzi 24*, 10129 Torino, Italy; [leonardi@tf.ien.it](mailto:leonardi@tf.ien.it)

### ABSTRACT

The new generation of frequency standards as well as two-way satellite time transfer techniques, either in microwave or optical domain, operate discontinuously in time. As a consequence, time and frequency comparisons are often an unevenly spaced data series. The noise analysis performed on irregularly spaced data by means of the Allan or related variances requires some care, because the results may be biased.

The paper deals with noise characterisation with particular attention to the current periodicity chosen for the TWSTFT technique.

The effect of the reconstruction procedure used to fill in missing data is examined by an analytical development where the transformation laws of covariance matrices are introduced. The cases of white phase, white frequency and random walk frequency noises are examined.

### 1. INTRODUCTION

Unevenly spaced data series are more and more frequent in the modern time and frequency metrology. For example, the TWSTFT (Two-Way Satellite Time and Frequency Transfer) technique operates discontinuously in time.

Currently, microwave TWSTFT comparisons are executed only on Mondays, Wednesdays and Fridays. In this case, missing data are not caused by a theoretical limitation of the measurement method. These comparisons are, in fact, intentionally worked out in a desultory way, because the satellite channels are not always available, but the periodicity of comparisons could be modified.

In case of two-way comparisons in the optical domain, where links are established with laser carriers, missing data are no more due to human decisions, but they are an intrinsic limitation of this particular measurement technique. Light connections, utilising an orbiting satellite, depend on the weather conditions, therefore sometimes measurements can not be done at all.

Other examples are the intersatellite ranging and synchronisation or in space probe navigation. In the former situation, the satellites orbiting the Earth move relatively to each other, some go out of view

and new ones come into view, thus the comparison of clocks on board is possible only intermittently in time. In the latter case, the probes might not have a straight field of view towards the Earth stations owing to possible occultations.

Even if comparisons ran continuously in time, new generation of frequency standards do not work continuously. In the analysis of the repeatability, the problem of irregularly spaced data could then arise. Unevenly spaced and missing data series, indeed, ask for particular attention in the subsequent elaboration. In particular, in T&F metrology, two points seem to be addressed.

Firstly, noise analysis is often performed by using regularly spaced data by means of the Allan or related variances. Such processings are useful to indicate the amount and the type of the noises that affect the data series. When data are not evenly spaced, missing values are usually filled in by means of some interpolation techniques and then the resultant uniformly spaced data are analysed by standard methods. The resulting noise is thus the combination of the actual noise and of the effect of data manipulations.

Secondly, a clock comparison is often requested on a particular date, for example in the computation of a time scale or in dating an event. The irregular sequence has thus to be interpolated when data are missing. In this case, the optimal interpolation technique should be sought by a suitable combination of the smoothing of the noise added by the comparison technique and a correct determination of the clock behaviour. Data reconstruction technique optimal to this aim seems to be different from the optimal in noise analysis.

The paper deals with the former of the described issue, i.e. noise characterisation, with particular attention to the current periodicity of clock comparison by TWSTFT, where data are available on Mondays, Wednesdays, and Fridays and missing values are usually reconstructed by linear interpolation between adjacent data.

This topic was covered by Hackman and Parker in [1] by the aid of simulation techniques, leading to the results that the commonly used straight-line interpolation gives biased TDEV particularly for small integration time  $\tau$ . A simulation study was also reported in [2] for pulsar data analysis.

In this paper, conversely, the effect on noise identification of the reconstruction procedure is

analytically examined by introducing the covariance matrices and their transformation laws. The cases of white phase, white frequency and frequency random walk noises are examined; the results are in perfect agreement with those obtained by simulation in [1]. Moreover the effect of a 5<sup>th</sup> order polynomial reconstruction technique is also examined.

The presented analysis helps in discriminating the effects of data reconstruction from the genuine characteristics of data and can be easily extended to other examples of missing data series or to different reconstruction technique, by the use of the same analytical development. The mathematical details are reported in the Appendix.

## 2. MATHEMATICAL TOOLS

When dealing with time comparison data, the mathematical tools commonly used to characterise the noise are the Allan variance or the associated TVAR. These tools must be applied on equispaced series. In case of unevenly data series, first of all it is thus necessary to reconstruct an evenly spaced sequence.

With the aim of developing a general treatment, an analytical formulation was preferred in the noise analysis here reported. This gives the advantages of allowing an insight on which are the parameters most affecting the results, of examining with a minimal effort another measurement periodicity or another noise case or a different reconstruction technique. The analytical processing of random variables requires the introduction of their covariance matrices. A complete noise characterisation, in fact, needs information not only on the variances of any variables but also on the possible covariance with any other variable.

To maintain conformity with the common interpretation of clock noises in terms of TVAR, the following estimations will be performed by introducing the TVAR covariance matrices in analogy to what is commonly done with "classical" covariance matrices. The TVAR matrix is a particular covariance matrix obtained by a suitable filtering on data as indicated in the Appendix A2.

A covariance matrix contains, on the main diagonal, the variance of each single variable of the series and, on the off-diagonal element, the covariance terms describing the correlation between couple of variables. For any value of the integration time  $\tau$ , there corresponds a TVAR( $\tau$ ) matrix.

For representing a series of independent variables describing a white noise, for example, it is sufficient to state that each variable has a certain variance, while the covariance terms are all equal to zero. This corresponds to a covariance matrix with equal terms on the main diagonal (the variances) and null off-diagonal terms, i.e. to a diagonal matrix.

The advantage of the use of covariance matrices stands in the fact that to any transformation of the variables, there corresponds a particular transformation of the covariance matrix and such transformation law is known and easy to be evaluated (see Appendix).

The analysis will be performed in terms of the TVAR( $\tau$ ) covariance matrix, but in the following we will speak of a general covariance matrix  $\Sigma$ , being the treatment of general validity.

In the described approach, it is not necessary to simulate any sequence of data affected by a specific noise. The noise properties are examined only by the variance/covariance transformations.

## 3. THE "RECONSTRUCTION" OF MISSING DATA: STRAIGHT LINE AND A 5<sup>TH</sup> ORDER POLYNOMIAL

Although the particular case of clock comparisons by the current TWSTFT periodicity is here examined, the presented rules have a general validity.

In the analysis of TWSTFT the missing data are commonly reconstructed by a linear interpolation between the adjacent values. The measured data, denoted by  $x_i$ , are combined by the rules illustrated in Table 1 and an equispaced series labelled as  $X_i$  is obtained.

Table 1. Linear reconstruction law.

Day of the week	Unevenly spaced measure	Reconstruction rule	Evenly spaced reconstructed series
Monday	$x_{Mon,1}$	$x_{Mon,1}$	$X_1$
Tuesday	-	$(x_{Mon,1} + x_{Wed,1})/2$	$X_2$
Wednesday	$x_{Wed,1}$	$x_{Wed,1}$	$X_3$
Thursday	-	$(x_{Wed,1} + x_{Fri,1})/2$	$X_4$
Friday	$x_{Fri,1}$	$x_{Fri,1}$	$X_5$
Saturday	-	$(2x_{Fri,1} + x_{Mon,2})/3$	$X_6$
Sunday	-	$(x_{Fri,1} + 2x_{Mon,2})/3$	$X_7$
Monday	$x_{Mon,2}$	$x_{Mon,2}$	$X_8$
...	...	...	...

The transformation that permits the passage from the  $x_i$  series  $\{x_{Mon,1}, x_{Wed,1}, x_{Fri,1}, x_{Mon,2}, \dots\}$ , to the  $X$  sequence  $\{X_1, X_2, X_3, X_4, X_5, X_6, X_7, X_8, \dots\}$  may be written in term of a suitable reconstruction matrix  $R$  as

$$X = Rx$$

as reported in App. A.

As the statistical properties of the  $x_i$  sequence are embedded in their covariance matrix  $\Sigma_x$ , the same is for the  $X_i$  sequence. Thus, the covariance matrix  $\Sigma_X$  of the  $X_i$  has to be inferred. This is done from the knowledge of the covariance matrix  $\Sigma_x$  of the

original data series and of the reconstruction matrix  $R$  as shown in the Appendix A.1.

Likewise, if we use a different reconstruction rule, the corresponding reconstruction matrix  $R^*$ , has to be determined. The case of a 5<sup>th</sup> order polynomial interpolation was also considered by the use of the Lagrange interpolation formula [3]. Whatever matrix  $R$  is used and therefore whatever reconstruction law is used, it appears that the new rebuilt data  $X_i$  do not have the same statistical properties of the original  $x_i$  series. Thus the covariance matrices  $\Sigma_X$  and  $\Sigma_x$  are different. This is because the reconstructed data are strongly intercorrelated; as an example, looking at Table 1, it is evident that the rebuilt datum  $X_2$  is completely correlated to the measured data  $X_1$  and  $X_3$ .

#### 4. RESULTS OF THE NOISE ANALYSIS

To test the proposed method, we supposed to have data  $x_i$  affected by a known noise as white PM (WPM), white FM (WFM) or random walk FM (RWFm) described by the appropriate covariance matrix  $\Sigma_x$ , whose explicit form is discussed in App. A3. The noise resulting on the reconstructed data  $X_i$  is examined by the estimation of the covariance matrix  $\Sigma_X$  through  $\Sigma_x$  and  $R$  as described in the Appendix. From a comparison of  $\Sigma_x$  and  $\Sigma_X$ , we can see the effect of the reconstruction on the noise.

Actually, for any value of  $\tau$ , we have at disposal an entire covariance matrix containing information on the variances and covariances of any day of the week, but for an easier interpretation it is better to trace the most familiar plot of  $\text{TVAR}(\tau)$ . Moreover, in the practice, there is no distinction among the TVAR of Monday or Tuesday measures because all the measured values are processed together as sample of a unique random variable. Therefore, from the  $\text{TVAR}(\tau)$  matrix, only the variances on the main diagonal are considered, averaged, and reported on the plot versus the integration time  $\tau$ . Such situation is analogous to what would appear from the statistical analysis of real data.

Results are reported in the following figures. To understand how the interpolation technique modifies the noise of the original data series, also the variances of the genuine series  $x_i$  are reported.

As a general remark, since in the case of TWSTFT data are taken with a sampling period  $\tau_0$  of about 2.5 days, the estimation of the noise for  $\tau < \tau_0$  might be strongly incorrect. For example, data affected by white PM are by definition uncorrelated. As a consequence, it is impossible to predict a white

missing value either using antecedent or subsequent data. Our aim is to understand at which value of  $\tau \geq \tau_0$  the genuine noise can be identified and, if it is possible, extrapolated to smaller values of  $\tau$ . Such threshold value of  $\tau$  depends on the noise and on the interpolation technique. Intuitively, if the noise is composed by low frequency fluctuations, then the interpolated data are close to the genuine values and the correct noise is easily identified. On the other hand, if the underlying noise is due to high frequency components (as white PM), then the filtering action of the reconstruction technique may strongly limit the possibility of identifying the correct noise.

This is evident when comparing the theoretical behavior of a daily sampled **white PM**, with the reconstructed process where missing data are reconstructed by a straight line as illustrated in Table 1 (Fig. 1).

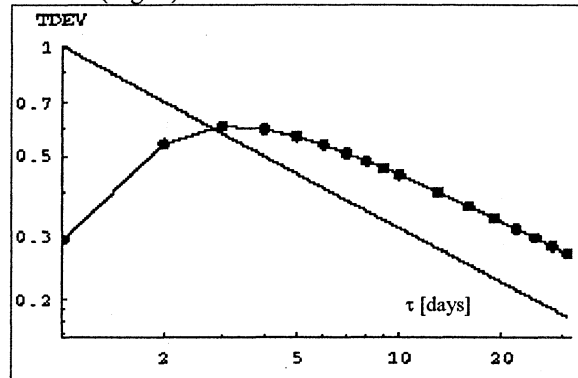


Figure 1. White Phase Noise  
True noise (solid line), reconstructed noise (line with dots)

It appears that, for  $\tau < \tau_0$ , the reconstruction completely modifies the noise behaviour and acts as a filter. For  $\tau > 7$  days, the correct slope of the white PM is identified, but at a higher level. Such higher level is probably due to the fact that, in case of white PM, the TDEV values depends on the sampling period often referred as the “software bandwidth”. Even if the reconstructed series has daily values, the true sampling period is  $\tau_0 \approx 2.5$  days in this case. Since  $\text{TDEV}(\tau) \propto \sqrt{\tau_0}$ , it is expected that the different level of TDEV should be higher of a factor  $\sqrt{2.5} \approx 1.5$ , which is in good agreement with the evaluation reported in Fig.1. Thus the true white PM noise, for the true sampling period  $\tau_0$ , is identified after the integration time  $\tau$  of about seven days. The values analytically obtained are in perfect agreement with those obtained in [1] by the aid of simulation.

It appears that in this case the straight-line interpolation is probably the worst (although the simplest) reconstruction because it drastically filters the noise, limiting the possibility of following the real behaviour of the sequence. With an higher

order polynomial interpolation the filtering effect should be less dramatic.

A 5<sup>th</sup> order polynomial reconstruction by mean of the Lagrangian polynomials [3] was estimated and the obtained stability curve is reported in Fig. 2. It can be noted that for  $\tau < \tau_0$  the reconstructed values are still unreliable, but the TDEV curve reaches faster the true value. After the integration time  $\tau \geq 4$  days, the correct slope of the white PM is identified. This could be an advantage, for example, when different noises are superimposed and the white PM appear only in a limited region of small  $\tau$  values. With the polynomial interpolation the white PM identification is possible after integration time  $\tau \geq 4$  days, conversely, the straight line interpolation needed at least an integration time of 7 days, to identify the correct noise.

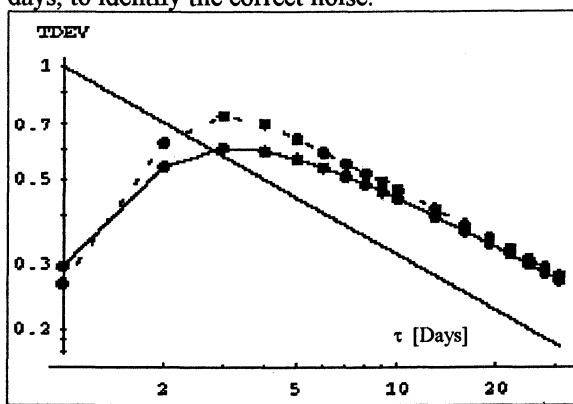


Figure 2. White phase noise. True noise (solid line); Straight line interp. (line with dots); Polynomial interp. (dashed line with dots)

In Fig. 3 and Fig. 4, the cases of white FM and random walk FM are reported. In both cases, the filtering action is less evident than in the case of white phase noise, because white and random walk FM contain a minor contribution of high frequency components. This is why the calculated curves are very closed to the theoretical curve even for small values of  $\tau$ . Also in this case, the estimated TDEV values of the reconstructed data are identical to those obtained by simulation in [1].

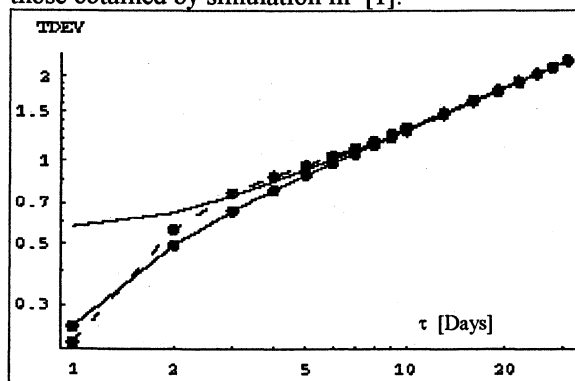


Figure 3. White Frequency Noise True noise (solid line); Straight line interp. (line with dots); Polynomial interp. (dashed line with dots)

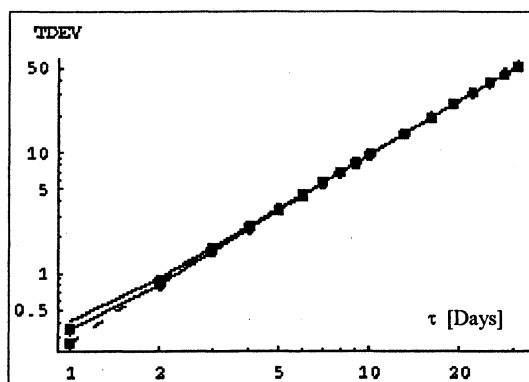


Figure 4. Random Walk Frequency Noise. True noise (solid line); Straight line interp. (line with dots); Polynomial interp. (dashed line with dots)

## 5. CONCLUSIONS

When a noise analysis is performed on unevenly spaced measure series, it is necessary to reconstruct missing data to obtain a uniformly sampled series. The reconstruction technique should not alter the genuine data noise. Of course some modification always occurs when data are manipulated, but the effect of the interpolation technique should leave the possibility to identify the real noise that affects the data, at least, in some spectral bandwidth.

By an analytical development, based on the transformation of covariance matrices, the effects of a straight line and of a 5<sup>th</sup> order polynomial interpolations were inferred. Each interpolation technique acts as a filter but with a different cut-off. In particular the straight line seems not to be optimal when a white PM noise has to be recognised. In such case, an higher order polynomial works better. On the other hand, slower noises such as white FM and random walk FM are not too much degraded by the linear interpolation. It is important to point out that the *best* reconstruction in order to characterise the noise is not the *best* solution for estimating the clock behaviour at a specific date. In the former case, we are interested in estimating the actual value we could obtain in a real measurement. In the latter case it is more important to estimate the behaviour of the clocks by reducing the noise due to the measurement technique.

The example treated in this paper regards the current two-way comparison technique, but the analysis of noise of unevenly data is to be faced, for instance, also when utilising optical synchronisation techniques or intersatellite comparisons. In these different cases, the analytical development presented here remains valid. It is only necessary to introduce the correct reconstruction matrix  $R$  that depends on the measurement periodicity, on the reconstruction technique, etc.

Moreover, the effect of the reconstruction technique was here examined only on three particular types of noises, with the aim of developing a method. The

application to other combination of noises could follow.

## 6. REFERENCES

- [1] Hackman C. and Parker T. E., *Noise analysis of unevenly spaced time series data*, Metrologia, 1996, 33, 457-466.
- [2] Vernotte F., et al., *Spectral analysis of irregularly spaced timing data: comparisons of several methods* in Proc. 10<sup>th</sup> European Frequency Time Forum, Brighton, UK, 1996, pp. 344-349.
- [3] Tretter S. A., "Introduction to discrete-time signal processing", J. Wiley, New York, 1976

## APPENDIX

### A. (Generality)

When dealing with  $n$  random variables  $x_i$  it is convenient to arrange them in a column vector denoted  $x$ . The covariance matrix  $\Sigma_x$  of the variables  $x_i$  describes the statistical characteristic of the sequence and it is defined as:

$$\Sigma_x = \left\langle \left( x - \bar{x} \right) \left( x - \bar{x} \right)^T \right\rangle$$

where  $\bar{x}$  is the column vector containing the average value of each random variable  $x_i$ , the brackets  $\langle \rangle$  denote the average value and superscript  $T$  stands for transposition.

Each element of  $\Sigma_x$  is given by:

$$\Sigma_{x_{ij}} = \sigma_{ij} = \left\langle \left( x_i - \bar{x}_i \right) \left( x_j - \bar{x}_j \right) \right\rangle$$

and denotes the covariance between  $x_i$  and  $x_j$ . When  $i=j$ ,  $\sigma_{ii} = \sigma_i^2$  is the variance of  $x_i$ .

If the variables  $x_i$  are linearly combined, a new random variable sequence  $X_i$  is obtained. The new  $m$  variables  $X_i$  are represented by the vector  $X$ . The transformation, from the vector  $x$  to the vector  $X$ , can be mathematically described with the help of a matrix  $L$  of dimension  $m \times n$  as:

$$X = Lx$$

The matrix  $L$  is useful not only to build the new sequence, but it also permits to determine the covariance matrix of the  $X$ , denoted as  $\Sigma_X$ .

The new sequence  $X_i$  is still described by a covariance matrix  $\Sigma_X$  given by:

$$\Sigma_X = L \Sigma_x L^T \quad (A1)$$

An appropriate matrix  $L$ , linearly combining the  $x_i$ , is directly useful for representing the reconstruction of missing data (section A.1), and also for representing the phase second differences and averages necessary for determining the TVAR covariance matrix (section A.2) and finally, for the expression of a known noise through the TVAR matrix (section A.3).

### A1. (Reconstructing missing data)

Each kind of data manipulation has the consequence of giving a certain degree of correlation among the reconstructed data. Let's interpret the random variables  $x_i$  as the original sequence of unevenly sampled data in case of TWSTFT clock comparison. Each datum, representing the time difference on a particular day according to Table 1, is a single random variable. The statistical properties of the  $\{x_i\}$  and thus the noise affecting the sequence are described by the covariance matrix  $\Sigma_x$ .

An evenly spaced data series  $\{X_i\}$  is generated by a linear combination of the  $\{x_i\}$ . Such reconstruction is described by a matrix  $R$ . The covariance matrix  $\Sigma_X$  of the reconstructed data series is obtained from the covariance matrix  $\Sigma_x$  of the original sequence as:

$$\Sigma_X = R \Sigma_x R^T$$

For the particular case of clock comparisons with the current TWSTFT technique, the reconstruction by linear interpolation of adjacent data, utilising the rules showed in Table 1, leads to the following matrix:

$$R = \begin{pmatrix} 1 & 0 & 0 & 0 & 0 & 0 & 0 & 0 \\ 1/2 & 0 & 1/2 & 0 & 0 & 0 & 0 & 0 \\ 0 & 0 & 1 & 0 & 0 & 0 & 0 & 0 \\ 0 & 0 & 1/2 & 0 & 1/2 & 0 & 0 & 0 \\ 0 & 0 & 0 & 0 & 1 & 0 & 0 & 0 \\ 0 & 0 & 0 & 0 & 2/3 & 0 & 0 & 1/3 \\ 0 & 0 & 0 & 0 & 1/3 & 0 & 0 & 2/3 \\ 0 & 0 & 0 & 0 & 0 & 0 & 0 & 1 \end{pmatrix}$$

Changing the type of interpolation and utilising, for example, a 5<sup>th</sup> order polynomial reconstruction, another reconstruction matrix  $R^*$  is necessary. In such case, the new covariance matrix  $\Sigma_X$  related to the new interpolation law becomes

$$\Sigma_X = R^* \Sigma_x R^{*T}$$

### A2. (AVAR and TVAR covariance matrices)

Allan variances and covariances of the variables  $X_i$  (for a fixed value of  $\tau$ ) can be obtained by interpreting the Allan variances as the classical variance of the data second differences  $\Delta_2 X$ . Thus the variables  $X_i$  are manipulated by an Allan matrix  $A$  that constructs a new vector containing the second differences

$$\Delta_2 X_i = X_i(t+2\tau) - 2X_i(t+\tau) + X_i(t) \text{ as}$$

$$\Delta_2 X = AX$$

According to the rule (A1), the Allan covariance matrix  $\Sigma_{AVAR}$  of the second differences is easily obtained:

$$\Sigma_{AVAR} = \frac{1}{2\tau^2} [A \Sigma_X A^T]$$

where  $\Sigma_X$  is the covariance matrix of the  $X_i$  variables. The matrix  $A$  is composed by the values (1, -2, 1) placed in different positions according to the integration time  $\tau$ .

In case the use of the TVAR is preferred, another transformation, through the Modified Allan variance, is necessary. To obtain the modified MVAR, an average over  $N$  consecutive second differences is necessary, where  $N = \tau / \tau_0$ . Then, it is sufficient to multiply the MVAR by the factor  $\tau^2/3$  to obtain the TVAR covariance matrix  $\Sigma_{TVAR}$ . Denoting with  $T$  the matrix which permits the passage from the Allan covariance matrix to the MAVAR covariance matrix we have:

$$\Sigma_{TVAR} = \frac{\tau^2}{3} T \frac{1}{2\tau^2} (A \Sigma_X A^T) T^T$$

Also in this case, matrix  $T$  has different expression and dimension depending on the chosen  $\tau$  value. This final matricial expression gives the complete TVAR estimation for each random variable  $X_i$ . The use of covariance matrices permits to deal with variances and covariances in a compact form. The same could be done by the algebraic summation of the correct variance and covariance terms; the fact is that, by applying such procedure, often the covariance terms are forgotten and thus the final variance estimation is not correct. For this reason a matricial formulation was preferred. Nevertheless, we may be not interested in a particular TVAR value related to a specific day of a particular week, like  $\text{TVAR}_{\text{Mon}}$ , or  $\text{TVAR}_{\text{Tue}}$ . Moreover, when experimental data are processed, the measures of different days are treated together as different samples of a unique random variable. To have a correspondence with this analytical treatment and the common processing practice, it is sufficient to calculate an average TVAR value. In particular, due the weekly periodicity of the current TWSTFT, it is sufficient to average over one week data. Therefore,

the TVAR values reported in the plots are determined by the following expression:

$$\overline{\text{TVAR}}_{\text{Week}} = \sum_{i=1}^7 \left[ \frac{\tau^2}{3} T \left( \frac{1}{\tau^2} A \Sigma_X A^T \right) T^T \right]_{i,i}$$

considering only the first seven diagonal elements of the matrix  $\Sigma_{TVAR}$ .

The  $\overline{\text{TVAR}}_{\text{Week}}$  value is obtained for any specific value of  $\tau$ . This means that if we want to generate a plot of the value of TVAR for different  $\tau$ , it is necessary to calculate the new form of the matrices  $A$  and  $T$  selecting the appropriate variables  $X_i$  for each value of  $\tau$ . The computational effort is therefore conspicuous. For example for a plot of TVAR over ten points it is necessary to determine ten  $A$  matrices of different dimension and ten  $T$  matrices. Then, it is necessary to calculate the matrix transpositions and products. Nevertheless, the computation time on a common PC is acceptable.

### A3. (WPM, WFM and RWFM covariance matrices)

The analytical method described in the text, investigates the effect of the reconstruction technique on the noise of the original sequence  $\{x_i\}$ . The noise of the  $\{x_i\}$  is expressed by  $\Sigma_x$ . Here we estimate the form of  $\Sigma_x$  in case of white phase, white frequency and random walk frequency noises. Let's suppose that the original random variables  $x_i$  are affected by WPM and that they have all the same variance  $\sigma^2$ . The covariance matrix  $\Sigma_x$  associated to these data, has all the covariance terms equal to zero, while the diagonal terms represents the variance  $\sigma^2$  of any single datum  $x_i$ . The covariance matrix  $\Sigma_{x,WPM}$  of a white phase noise sequence is:

$$\Sigma_{x,WPM} = \sigma^2 I$$

The matrix  $I$  is the identity matrix, while, in this case,  $\sigma^2$  represents the classical variance of the phase values.

The covariance matrix of any other noise with power spectral density of the type  $|\omega|^{-\alpha}$  (with even  $\alpha$ ) can be constructed by means of (A1) by expressing the noise as a linear transformation of white noise. In particular the white frequency noise can be interpreted as a random walk of phase. Thus  $\Sigma_{x,WFM}$  is constructed by a transformation matrix  $W$  that sums up white increments and defines a random walk. The covariance matrix becomes

$$\Sigma_{x,WFM} = W \sigma^2 I \cdot W^T$$

where, in this case,  $\sigma^2$  is the classical variance of the white frequency values. In a similar way, the covariance matrix of the RWFM is obtained.

## “THE HIGH GAIN PHASE COMPARATOR FOR REDUCTION OF CLOSE-TO-CARRIER PHASE NOISE”

M J UNDERHILL

School of Electronic Engineering, Information Technology and Mathematics  
University of Surrey, Guildford, Surrey, GU2 5XH - UK

### ABSTRACT

The principle of the high gain phase comparator was outlined some years ago (1, 2) and it has been used to good effect in commercial PLL (Phase Lock Loop) synthesiser chips.

In applications where the comparison frequency is low, the high gain phase comparator gives a superior close-to-carrier phase noise performance, with improvements up to 40dB or more being typically feasible. Because this phase comparator operates on the sample hold principle it gives good suppression of comparison frequency spurious sidebands.

The purpose of this paper is to reexamine the fundamental limitations of the high gain technique when applied to the higher phase comparison reference frequencies now being used in present day synthesiser designs. The conclusion is that the technique remains the best choice in many PLL applications.

**Keywords:** Phase noise, time jitter, phase comparators, phase lock loops, frequency synthesis.

### 1. INTRODUCTION

For a Phase Lock Loop (PLL) type of frequency synthesiser with small frequency steps, a low close to carrier phase noise can be difficult to achieve. The problem arises because circuit noise can never be entirely removed. In any PLL synthesiser, circuit noise modulates the Voltage Controlled Oscillator (VCO) output with a frequency spectrum depending on the loop cut off frequency and number of loop poles, see Fig. 1. The magnitude of such noise is always found to be proportional to the division ratio of the programmable divider which sets the output frequency, and inversely proportional to the phase comparator gain. The division ratio is set by the requirements for output frequency and step size. The step size always imposes an upper limit on the loop cut-off frequency  $f_c$  and limits the speed of frequency setting.

From this it can be seen that for best phase noise the programmable divider division ratio should always be as small as possible. If a multiple loop frequency synthesiser arrangement is used, faster switching speed can be achieved, because small division ratios can be used in each loop, but at greater expense in circuit complexity and power consumption.

However an alternative approach which can give much improved close to carrier phase noise (below loop cut-off sideband frequencies) is to use a high gain phase comparator (1, 2). Such a device can provide very large reductions in phase noise, but it can also allow the loop bandwidth to approach more closely to the comparison frequency  $f_r$ . As close as  $f_r/6$  can be achieved with careful design. As a consequence an improvement in switching speed of five to ten times can typically be achieved.

The high gain phase comparator reduces noise components by the attenuation which has to be inserted in the loop to compensate for the increased gain of the phase comparator (See Fig. 2). Some of the additional gain can be used to widen the loop bandwidth. The rest can provide a large attenuation of both spurious and broadband phase noise components. Spurious components at the comparison frequency and harmonics of this are also notched out by the sample hold action which is an intrinsic part of the high gain phase comparator.

The high gain phase comparator was originally announced in 1978 as the “high performance phase comparator” (3) and first incorporated in the Philips HEF4750 Reference Comparator Combination. At that time it was not disclosed that the high performance derived from the high gain principle. This chip together with the HEF4751 Universal Divider provided the first professional quality PLL frequency synthesiser in integrated circuit form (4). Subsequent Philips chips incorporated the high gain phase comparator principle, examples being the SAA1057 and its successors. It should be noted that the original patents are believed no longer to be in force.

The purpose of this paper is to show that the high gain phase comparator technique can give a PLL frequency synthesiser with higher performance and

lower cost than other methods such as the sample hold comparator technique which otherwise gives the best performance. However where it is possible to use a high comparison or reference frequency in the required synthesiser design, the high gain advantage is considerably reduced.

## 2. PRINCIPLE OF THE HIGH GAIN PHASE COMPARATOR

Fig. 3 shows the block diagram of the high gain phase comparator technique (2). The V(VCO) signal active or leading edge initiates a fast rising ramp by switching on a current source which charges the ramp capacitor. The R (reference) signal switches off the current source and so the ramp terminates with the capacitor holding a voltage proportional to the time difference and hence to the phase difference between the two signals.

A second hold circuit samples the steady ramp capacitor voltage, and this sample is provided as the phase comparator output signal. Because the sampled voltage is constant, no unnecessary glitch or pulse at the reference/comparison frequency is caused and almost perfect filtering of reference frequency components occurs.

The ramp slope determines the gain of the phase comparator. A very high comparator gain can be achieved in this way. An increase of in excess of a thousand times is possible particularly for lower comparison frequencies.

A conventional phase comparator will have an operating phase range of typically  $\pi$ ,  $2\pi$  or  $4\pi$  radians. The  $4\pi$  range phase comparator almost universally used in frequency synthesiser PLLs has the added advantage of being frequency sensitive (See Fig. 4). If a type two loop filter arrangement is used the frequency sensitive phase comparator will always ensure that phase lock is achieved whatever the initial frequency error.

The high gain phase comparator inevitably has a very small operating phase range and it is not intrinsically frequency sensitive. A gain increase of 1000 times means the phase range becomes 1000 times less, i.e. well less than one degree. Thus the high gain phase comparator has to be combined with the frequency sensitive phase comparator so that the advantages of both may be achieved as shown in Fig. 5.

When the phase error becomes sufficiently small the "coarse" frequency sensitive phase comparator output PC2 is switched off so that it then is not a source of circuit noise causing phase noise.

The high attenuation is placed between the output of the "fine" high gain phase comparator PC1 and the loop filter.

## 3. NOISE ANALYSIS

Fig. 6 shows two forms of loop filter commonly used in PLL synthesisers. The current source or charge pump type gives the "integral" action required for a type 2 loop by charging the main filter capacitor. The op amp in the other filter provides the integral action through the feedback capacitor. It is important to note that the high gain provided by the integrator is not the same as the high gain provided by the high gain phase comparator. The integral gain is always positioned in the wrong place with respect to the noise sources in the circuit and cannot provide any reduction in the noise from these sources.

It is the resistor  $R_p$  in both filters that provides the proportional part of the loop gain. It is also the dominant source of phase noise which remains after all other noise sources have been minimised. It is convenient and possible for all of the phase comparator noise also be referred to this resistor ( $R_p$ ). Then it is as if the resistor had a noise factor F which allows for these other sources of noise to be included as if they had originated from this single resistor.

The noise from the resistor  $R_p$  or any white noise appearing at the phase comparator output creates a synthesiser phase noise output spectrum which is flat at sideband frequencies below the loop cut-off frequency. Above the loop cut-off frequency the spectrum falls at 6dB per octave for every pole in the loop filter. In a low noise application it is usual to have a total of three poles in the filter; one from the integrator, one from the VCO (when treated as voltage to rate of change of phase converter) and the third one from the low pass filter usually employed on the input to the VCO. In this case the attenuation above the loop cut-off is 18dB per octave. The resultant phase noise superimposed on the VCO is shown in Fig. 7.

The level of the output noise below cut off is easily calculated because then the loop gain is greater than unity and the forward closed loop gain becomes equal to the inverse of the feedback gain.

When applied to the PLL synthesiser for a source of (RMS) noise per Hz of  $V_n$ , and division ratio  $n$  and phase comparator gain  $k_c$ , we have at the VCO output

$$S_{\phi}(f) = \frac{1}{4} L(f) = \frac{V_n^2}{4} \left( \frac{n}{k_c} \right)^2 \quad (1)$$

The equivalent or actual (if noise factor  $F = 1$ ) thermal noise  $V_n$  from the resistor  $R_p$  is in the 1Hz bandwidth

$$V_n^2 = 4kTR_p = 16 \times 10^{-21} \times R_p \quad (2)$$

where  $k$  is Boltzmann's constant and  $T$  is an ambient temperature of 293K.

#### 4. LIMIT OF HIGH GAIN NOISE PERFORMANCE

The practical limit of high gain noise performance is reached as the comparison frequency is raised. At higher comparison frequencies the gain of the high gain phase comparator becomes limited by the ramp maximum slope that can be achieved.

For example a typical full ramp length of  $1\mu\text{s}$  would mean that high gain could only be achieved up to a 1MHz comparison frequency or a bit less. This limit on the maximum ramp slope is therefore taken to define the maximum comparison frequency for which the high gain technique remains advantageous and useful.

At lower comparison frequencies the high gain technique shows an increasing advantage. For example with a  $1\mu\text{s}$  ramp limit, at 100kHz a 20dB noise improvement is achieved, at 10kHz there is a 40dB advantage, and at 1kHz a 60dB advantage is possible.

An alternative way of assessing the merits of the high gain phase comparator is to estimate the irreducible noise in a practical system and see how much extra comparator gain is needed to reduce this to an acceptable level.

A just acceptable close-in noise level at 1kHz is typically -65dBC/Hz. In a 3kHz modulation band the demodulated signal to noise ratio would then be a little better than 30dB. A better target level for close to carrier noise at 1kHz from carrier is -90dBC/Hz which gives a demodulated signal to noise ratio of better than 55dB.

We can now calculate then comparator gain  $k_c$  required if these two specification levels are applied to a 1GHz output frequency PLL synthesiser with various choices of comparison frequency.

Table 1 shows the results of applying equations 1 and 2 to the 1GHz synthesiser with the noise assumed to originate entirely as thermal noise from the resistor  $R_p$  with  $R_p = 10\text{k}$ . It can be seen that the high gain phase comparator performance is lost in this case for comparison frequencies above 2MHz. Below this frequency the high gain advantage is very substantial. The high gain

advantage is shown in Fig. 8 both for close-in phase noise and also for suppression of reference frequency sidebands. These measurements were obtained in 1976 and resulted in the high gain technique being incorporated in the Philips synthesiser chips.

#### 5. CONCLUSIONS

The high gain type of phase comparator remains the best choice for low close in phase noise frequency synthesisers for most applications. The advantage can be a phase noise reduction of as much as 40 to 60dB for comparison frequencies between 10kHz and 1kHz. At higher comparison/reference frequencies  $f_r$ , the advantage is not so great. Typically for  $f_r$  above 1 to 2MHz high gain is more difficult to achieve and the advantage over more conventional phase comparators becomes marginal. However, implementation of the high gain technique using a faster, higher frequency IC technology could potentially increase this limit.

A further advantage of the high gain technique is that for a give comparison/reference frequency a higher loop cut-off frequency and faster settling time can be achieved. Typically a 5 to 10 times improvement can be achieved.

In conclusion the high gain phase comparator technique continues to show considerable advantage in most phase lock loop applications.

#### REFERENCES

- (1) **M J Underhill & M A G Clark**, British Patents 1477584 (1975) and 15219944 (1977).
- (2) **W Gosling** (Editor) "*Radio Receivers*" Peter Peregrinus 1986. ISBN 0-86341-056-1 (Chapter on Frequency Synthesis by M J Underhill).
- (3) **M J Underhill, P A Jordan, M A G Clark & R I H Scott**, "*A general purpose LSI frequency synthesiser system*", Proc. 32nd Annual Frequency Control Symposium, 1978, pp.365-372.
- (4) **U L Rohde**, "*Digital PLL Frequency Synthesisers*", Prentice Hall Inc, N.J.1983 ISBN: 0-13-214239-2.

Comparison/Reference frequency  $f_r$  and division ratio N

	$f_r = 1\text{MHz}$ N=10 <sup>3</sup>	$f_r = 100\text{kHz}$ N=10 <sup>4</sup>	$f_r = 10\text{kHz}$ N=10 <sup>5</sup>	$f_r = 1\text{kHz}$ N=10 <sup>6</sup>
(a) <u>Digital PC</u> with $k_c = 5/4\pi$ V/rad	S $\phi(f) =$ -90	-70	-50	-30
<u>High Gain PC</u> slope=5Vin1 $\mu$ s $k_c = \frac{5 \times 10^6}{2\pi f_r}$ V/rad	-96	-96	-96	-96

**Table 1**

Close-in noise on VCO output from S $\phi(f_{PC})$  in dBC for 1GHz synthesiser with comparison frequency  $f_r$  division ratio N and two types of phase comparator for  $R_p = 10k$

Low specification target is -65dBC  
High specification target is -90dBC

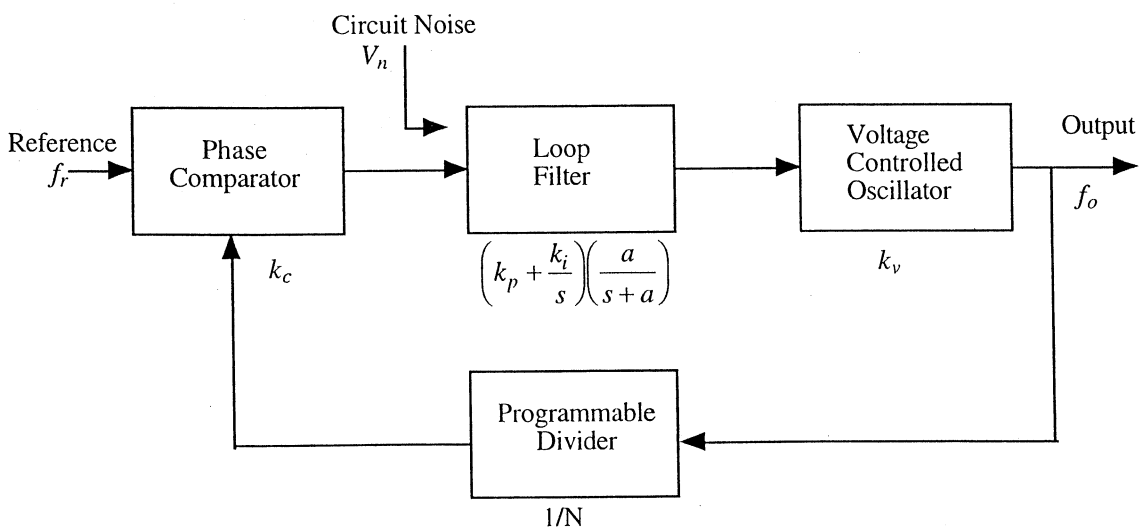


**Fig. 1: Basic Type 2 PLL Frequency Synthesiser**

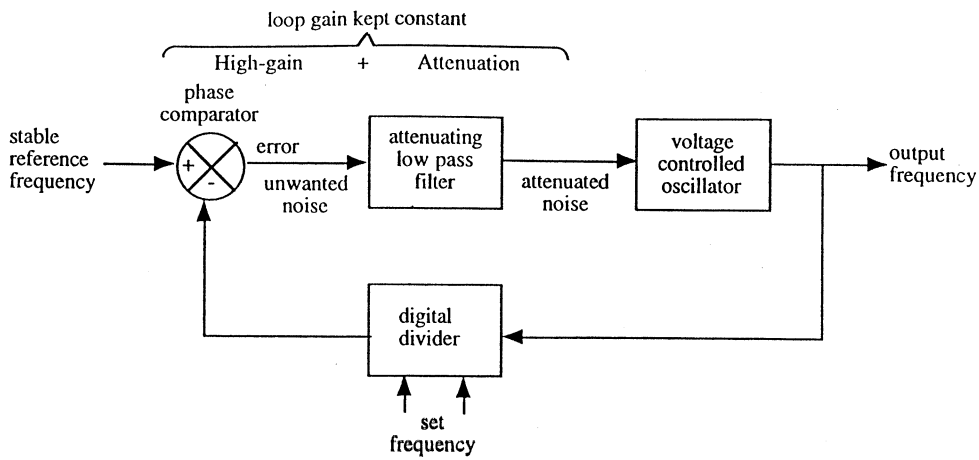


**Fig. 2: The principle of the high gain phase comparator.**  
The compensating attenuation also attenuates the sources of noise.

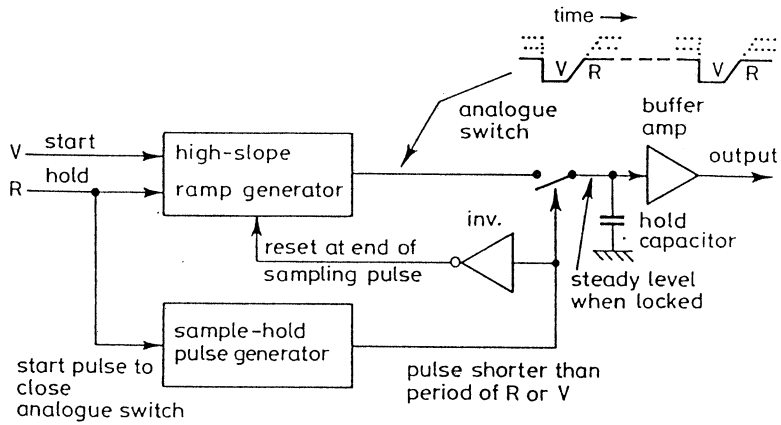


**Fig. 3: The high gain phase comparator.**

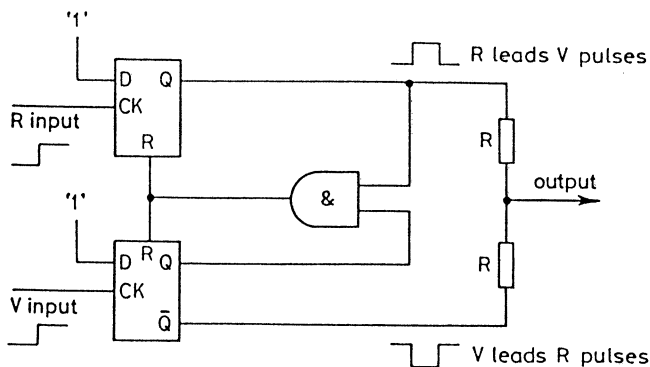


**Fig. 4: Frequency sensitive digital phase comparator.**

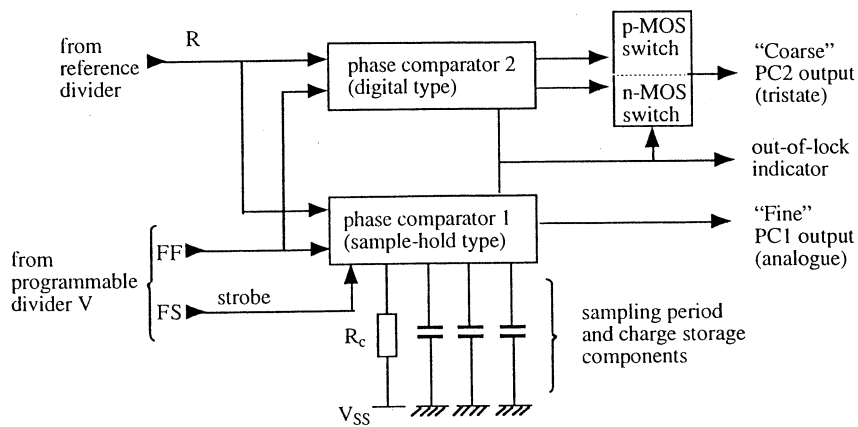


Fig. 5: Phase comparator combination (HEF 4750)

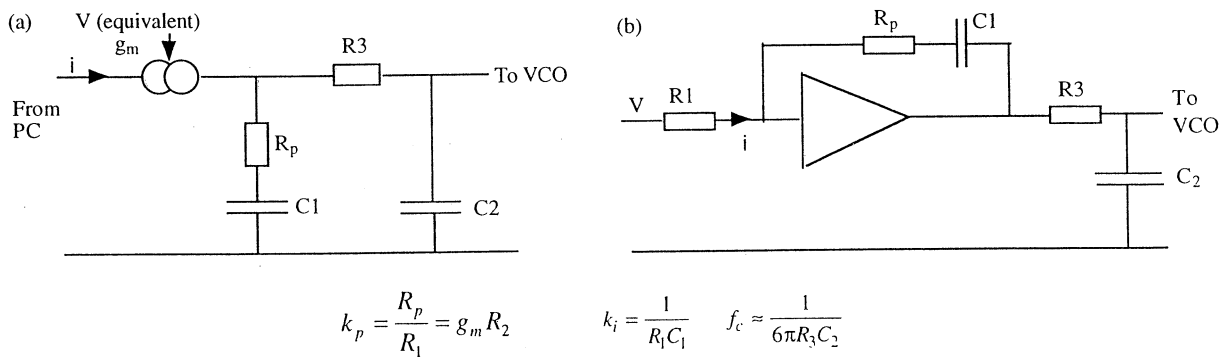


Fig. 6: Two equivalent loop filters (a) Current fed (b) Voltage fed

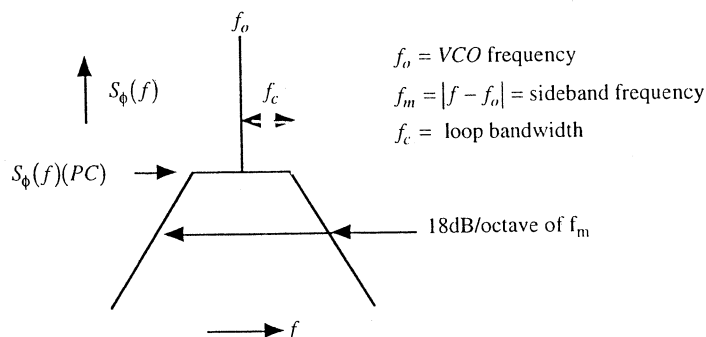


Fig. 7: VCO phase noise spectrum for phase comparator noise equivalent  $S_\phi(f)(PC)$  (in schematic form).

(a) "Digital" type PC

(b) High gain PC

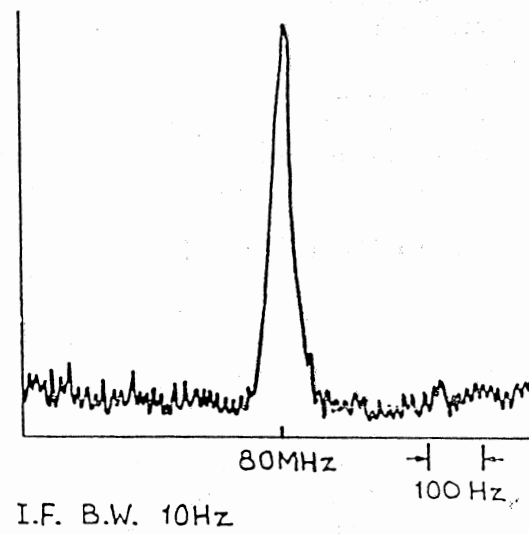
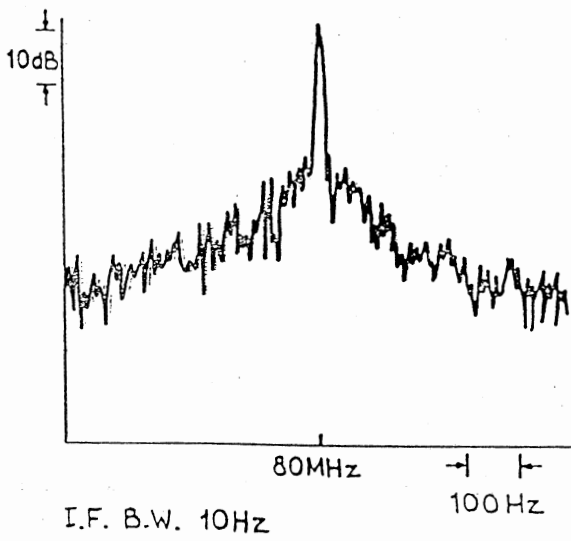
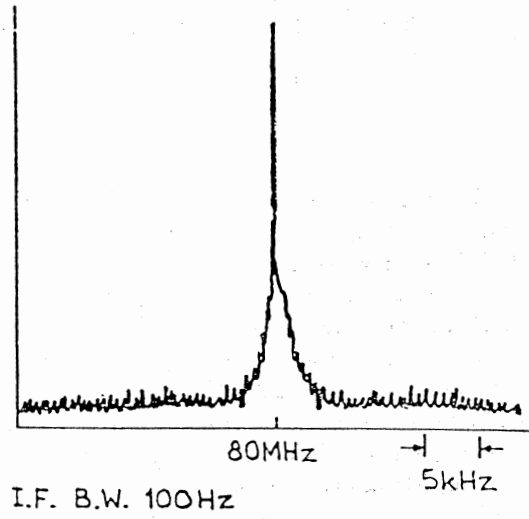
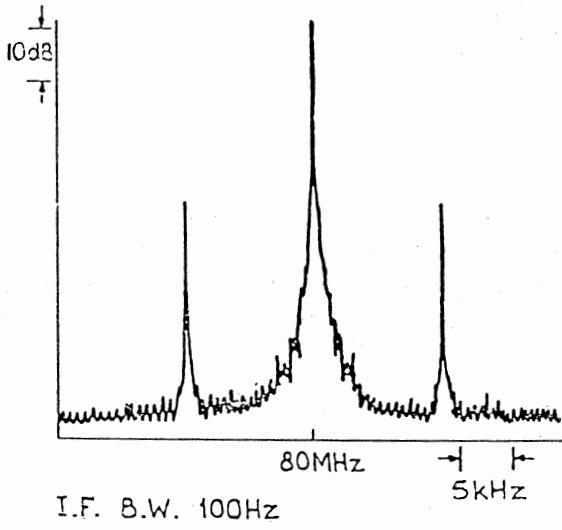


Fig. 8: Phase Noise Spectra of (a) digital PC and (b) high gain PC.

# ESTIMATION OF THE MEASUREMENT UNCERTAINTY OF DRIFT COEFFICIENTS VERSUS THE NOISE LEVELS

F. Vernotte, M. Vincent  
Observatoire de Besançon

41 bis avenue de l'Observatoire - BP 1615 - 25010 BESANCON Cedex - FRANCE  
Phone : +333.81.66.69.22 - Fax : +333.81.66.69.44 - E-mail : francois@obs-besancon.fr

## Abstract

Oscillators are affected by drifts (linear phase drift, linear frequency drift, i.e. quadratic phase drift) and different types of noise according to the power law model of power spectral density (from  $f^{-2}$  to  $f^{+2}$  frequency noise, i.e.  $f^{-4}$  to  $f^0$  phase noise). Generally, for long term instability characterization (duration greater than one hour), drift coefficients are estimated by using least squares whereas noise levels are obtained from the residuals by using variances (AVAR, MVAR, TVAR, ...).

However, the low frequency noises, such as random walk FM, induce very long term fluctuations which may be confused with deterministic drifts. This effect, due to the non-stationarity of these noises, depends on the low cut-off frequency which must be introduced in order to ensure power convergence for low frequencies. But, the real physical meaning of such a cut-off frequency is mysterious. In this paper, we propose another approach for the characterization of low frequency noises, considering a random walk FM as the integration of a white process since the switch-on of the oscillator. We also calculate the standard deviation of "artificial" drifts due to long term random fluctuations, versus the noise levels.

The first interest of these results concerns the estimation of the measurement uncertainty of drift coefficients : knowing the noise levels of an oscillator we calculate the standard deviation of the artificial drift coefficient due to these noises; thus, if a "real" deterministic drift is identified in the signal, its coefficients are determined plus or minus the artificial drift coefficients. The standard deviation of the artificial drift coefficients may be considered as the measurement uncertainty of the deterministic drift coefficient.

The second interest concerns the predictability of an oscillator affected by a deterministic drift. The reliability of a prediction depends on two factors : the relevancy of the model and the accuracy of the parameter determination. Thus, the knowledge of the drift coefficient uncertainties yields a criterion for quantifying the reliability of a time error prediction.

## 1 INTRODUCTION

We consider a sequence of frequency deviation samples composed of a deterministic part, i.e. a linear frequency drift, and a random part:

$$y(t_k) = C_1 t_k + C_0 + \epsilon_k. \quad (1)$$

An estimation by least squares yields estimates  $\hat{C}_0$  and  $\hat{C}_1$  of the real coefficients  $C_0$  and  $C_1$ . Denoting the interpolated samples by  $\hat{y}(t)$ , we obtain:

$$\hat{y}(t_k) = \hat{C}_1 t_k + \hat{C}_0. \quad (2)$$

The residuals are defined as:

$$e_k = y(t_k) - \hat{y}(t_k) \quad (3)$$

### 1.1 Random Fluctuations and Deterministic Drifts

The instantaneous frequency is defined from the nominal frequency and the frequency deviation

samples by:

$$\nu_k = \nu_0 (1 + y_k) \quad (4)$$

If the sequence  $y_k$  is not centered, there are two possibilities:

- the real nominal frequency is different from the assumed nominal frequency: this is a problem of inaccuracy of the oscillator;
- there are long term random fluctuations (with period much longer than the duration of the sequence) which are seen as constant over the sequence[1].

The same problem may occur with linear frequency drift.

It is impossible to distinguish a "true" deterministic drift from a "false" random drift.

TABLE 1 - Correlations of the  $y_k$  samples versus the noise levels  $h_\alpha$ .  $C$  is the Euler constant:  $C \approx 0,5772$ . Assuming a sampling satisfying the Shannon rule, the high cut-off frequency is  $f_h = \frac{1}{2\tau_0}$ .  $f_l$  is the low cut-off frequency.

$S_y(f)$	$R_{ij}$ (with $i \neq j$ )	$R_{ii}$
$h_{-2}.f^{-2}$	$h_{-2} \left[ \frac{1}{f_l} + \pi^2  t_j - t_i  \right]$	$\frac{h_{-2}}{f_l}$
$h_{-1}.f^{-1}$	$-h_{-1} [C + \ln(2\pi f_l) + \ln t_j - t_i ]$	$-h_{-1} \ln(2\tau_0 f_l)$
$h_0.f^0$	0	$h_0 f_h$
$h_{+1}.f^{+1}$	$h_{+1} \frac{(-1)^{(j-i)} - 1}{4\pi^2 (t_j - t_i)^2}$	$h_{+1} \frac{f_h^2}{2}$
$h_{+2}.f^{+2}$	$h_{+2} \frac{f_h \cos [2\pi f_h (t_j - t_i)]}{2\pi^2 (t_j - t_i)^2}$	$h_{+2} \frac{f_h^3}{3}$

## 1.2 Statement of the Problem

The Power Spectral Density (PSD) may be modelled as:

$$S_y(f) = \sum_{\alpha=-2}^{+2} h_\alpha . f^\alpha \quad (5)$$

- If no deterministic drift exists, what are the relationships between the noise levels  $h_\alpha$  and the estimated drift coefficients  $\hat{C}_0$  and  $\hat{C}_1$ ?
- If a deterministic drift exists, what are the uncertainties of the estimated drift coefficients  $\hat{C}_0$  and  $\hat{C}_1$ ?
- In both cases, what is the Time Interval Error (TIE) due to an extrapolation of the linear frequency drift?

## 2 LINEAR REGRESSION

### 2.1 Coefficient Calculation

We consider  $N$  measurements  $(t_i, y_i)$ :  $\{(t_0, y_0), \dots, (t_{N-1}, y_{N-1})\}$ , regularly spaced with a sampling period  $\tau_0$ :

$$t_k = t_0 + k.\tau_0 \quad (6)$$

We need to know the coefficient of the linear model:

$$y_k = \hat{C}_1 t_k + \hat{C}_0 + e_k \quad (7)$$

The most probable coefficient values, in the sense of the least squares, are given by:

$$\hat{C}_0 = \frac{2(2N-1)}{N(N+1)} \sum_{i=0}^{N-1} y_i + \frac{-6}{N(N+1)\tau_0} \sum_i t_i . y_i \quad (8)$$

$$\hat{C}_1 = \frac{-6}{N(N+1)\tau_0} \sum_i y_i + \frac{12}{N(N-1)(N+1)\tau_0^2} \sum_i t_i . y_i \quad (9)$$

### 2.2 Estimation of the Uncertainties

From (8) and (9), it is possible to calculate  $\sigma^2(C_0)$  and  $\sigma^2(C_1)$ :

$$\sigma^2(C_0) = \frac{4(2N-1)^2}{N^2(N+1)^2} \sigma^2 \left( \sum y_i \right) + \frac{36}{N^2(N+1)^2 \tau_0^2} \sigma^2 \left( \sum t_i . y_i \right) - \frac{24(2N-1)}{N^2(N+1)^2 \tau_0} Cov \left( \sum y_i, \sum t_i . y_i \right) \quad (10)$$

$$\sigma^2(C_1) = \frac{36}{N^2(N+1)^2 \tau_0^2} \sigma^2 \left( \sum y_i \right) + \frac{144}{N^2(N-1)^2(N+1)^2 \tau_0^4} \sigma^2 \left( \sum t_i . y_i \right) - \frac{144}{(N-1)N^2(N+1)^2 \tau_0^3} Cov \left( \sum y_i, \sum t_i . y_i \right) \quad (11)$$

with

$$\sigma^2 \left( \sum y_i \right) = \sum_i \sum_j \langle y_i . y_j \rangle \quad (12)$$

$$\sigma^2 \left( \sum t_i . y_i \right) = \tau_0^2 \sum_i \sum_j i . j . \langle y_i . y_j \rangle \quad (13)$$

$$Cov \left( \sum y_i, \sum t_j . y_j \right) = \tau_0 \sum_i \sum_j i . \langle y_i . y_j \rangle \quad (14)$$

where  $\langle \rangle$  denotes an average over an infinite number of identical processes (ensemble average).

### 2.3 Correlation of the Samples

The PSD  $S_y(f)$  is the Fourier Transform of the autocorrelation function. Thus, if no real drift exists in the sequence, we have:

$$\langle y_i . y_j \rangle = \int_{-\infty}^{+\infty} S_y^2(f) e^{+j2\pi f(t_j - t_i)} df = \int_0^{+\infty} S_y(f) \cos [2\pi f(t_j - t_i)] df = R_{ij} \quad (15)$$

which leads to the results given in Table 1.

## 2.4 Mean Value Subtraction

Table 1 shows that, for low frequency noises ( $f^{-2}$  and  $f^{-1}$  FM), the correlations of the samples depend on the low cut-off frequency  $f_l$ . This cut-off frequency must be introduced in order to ensure the power convergence.

If the inverse of the low cut-off frequency is much larger than the duration of the sequence  $[t_0, t_N]$ , the very long term fluctuations (period  $\approx \frac{1}{f_l}$ ) are seen as a constant[1] (see Figure 1).

As an example, let us consider a random walk frequency noise ( $f^{-2}$  FM). The ageing of the oscillator,  $z(t)$ , which is the derivative of the instantaneous frequency deviation  $y(t)$ , is then a white noise process and may be modelled as :

$$y(t) = y(t_0) + \int_{t_0}^t z(\theta) d\theta \quad (16)$$

This relationship is composed of two terms :

- $y(t_0)$  is a **constant** due to the "history" of the oscillator. It depends on the low cut-off frequency  $f_l$  ;
- $\int_{t_0}^t z(\theta) d\theta$  is a centered random variable. Its standard deviation only depends on  $T = t - t_0$ .

Therefore, the subtraction of the mean value of the sequence removes the term  $y(t_0)$  and cancels the dependence on  $f_l$ .

Denoting the mean value of the sequence by  $\bar{y}$  and the centered sequence samples by  $y'_k$  :

$$\bar{y} = \frac{1}{N} \sum_{j=0}^{N-1} y_j \quad (17)$$

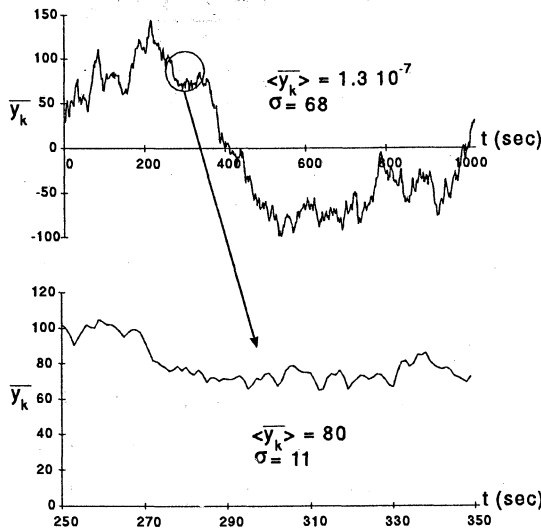


Figure 1: Sequence of frequency deviation samples for an  $f^{-2}$  FM noise. Above, the duration of the sequence is about the inverse of the low cut-off frequency. Below is an enlargement of a part of this graph: the inverse of the low cut-off frequency is far larger than the duration of the sequence, and the samples are no longer centered.

$$y'_k = y_k - \bar{y} \quad (18)$$

The subtraction of the mean value is equivalent to a correction of the nominal frequency by a factor  $(1 + \bar{y})$ :

$$\nu_k \approx \nu_0(1 + \bar{y})(1 + y'_k) \quad (19)$$

After subtraction of the mean value, it follows that:

$$\sum_{i=0}^{N-1} y'_i = 0 \quad (20)$$

$$\sum_{i=0}^{N-1} t_i \cdot y'_i = \tau_0 \left[ \sum_i i \cdot y_i - \frac{N+1}{2} \sum_j y_j \right] \quad (21)$$

Thus:

$$\begin{aligned} \sigma^2 \left( \sum t_i \cdot y'_i \right) &= \tau_0^2 \left[ \sum_i \sum_j i \cdot j \cdot R_{ij} \right. \\ &\quad \left. - (N+1) \sum_i \sum_j i \cdot R_{ij} \right. \\ &\quad \left. + \frac{N(N+1)}{4} \sum_i \sum_j R_{ij} \right] \end{aligned} \quad (22)$$

Considering the new linear frequency drift model:

$$y'_k = \hat{C}'_1 t_k + \hat{C}'_0 + e'_k \quad (23)$$

we have:

$$\sigma^2(C'_0) = \frac{36}{N^2(N+1)^2\tau_0^2} \sigma^2 \left( \sum t_i \cdot y'_i \right) \quad (24)$$

$$\sigma^2(C'_1) = \frac{144}{N^2(N-1)^2(N+1)^2\tau_0^4} \sigma^2 \left( \sum t_i \cdot y'_i \right) \quad (25)$$

It may be demonstrated that  $\hat{C}'_1 = \hat{C}_1$  and then  $\sigma^2(C'_1) = \sigma^2(C_1)$ .

## 2.5 Estimation of the Residuals

The differences between the estimated drift and the  $y_k$  samples are:

$$e_k = y_k - \hat{C}_1 t_k - \hat{C}_0 \quad (26)$$

The variance of the residuals is given by:

$$\begin{aligned} \sigma^2(e) &= \sigma^2(y) + \frac{(N-1)(2N-1)\tau_0^2}{6} \sigma^2(C_1) \\ &\quad + \sigma^2(C_0) - \frac{2}{N} Cov \left( \sum y_k, C_0 \right) \\ &\quad - \frac{2}{N} Cov \left( \sum t_k \cdot y_k, C_1 \right) \\ &\quad + (N-1)\tau_0 Cov(C_0, C_1) \end{aligned} \quad (27)$$

The residuals don't depend on the subtraction of the mean value:

$$e_k = y_k - \hat{C}_1 t_k - \hat{C}_0 = y'_k - \hat{C}'_1 t_k - \hat{C}'_0 \quad (28)$$

TABLE 2 - Standard deviation of the drift coefficients and of the residuals versus the noise level  $h_\alpha$  and the duration of the sequence  $\tau$ . The high cut-off frequency is  $f_h = \frac{1}{2\tau_0}$  and the low cut-off frequency is  $f_l$ .

$S_y(f)$	$\sigma(C_0)$	$\sigma(C'_0)$	$\sigma(C_1)$	$\sigma(e)$
$h_{-2} \cdot f^{-2}$	$\sqrt{\frac{h_{-2}}{f_l}}$	$\sqrt{\frac{3\pi^2 \tau h_{-2}}{5}}$	$\sqrt{\frac{12\pi^2 h_{-2}}{5\tau}}$	$\sqrt{\frac{2\pi^2 \tau}{15} h_{-2}}$
$h_{-1} \cdot f^{-1}$	$\sqrt{\left[\frac{3}{2} - \frac{1}{4} \ln(2f_l \tau)\right] h_{-1}}$	$\frac{3\sqrt{h_{-1}}}{2}$	$\frac{3\sqrt{h_{-1}}}{\tau}$	$\sqrt{[C + \ln(\pi\tau)] h_{-1}}$
$h_0 \cdot f^0$	$\sqrt{\frac{2h_0}{\tau}}$	$\sqrt{\frac{3h_0}{2\tau}}$	$\sqrt{\frac{6h_0}{\tau^3}}$	$\sqrt{\frac{h_0}{2\tau_0}} = \sqrt{f_h h_0}$
$h_{+1} \cdot f^{+1}$	$\sqrt{\frac{5[1.37 + \ln(2f_h \tau)] h_{+1}}{\pi^2 \tau^2}}$	$\sqrt{\frac{9[1.27 + \ln(2f_h \tau)] h_{+1}}{2\pi^2 \tau^2}}$	$\sqrt{\frac{18[1.27 + \ln(2f_h \tau)] h_{+1}}{\pi^2 \tau^4}}$	$\sqrt{\frac{f_h^2}{2} h_{+1}}$
$h_{+2} \cdot f^{+2}$	$\sqrt{\frac{10f_h \ln(2) h_{+2}}{\pi^2 \tau^2}}$	$\sqrt{\frac{9f_h \ln(2) h_{+2}}{\pi^2 \tau^2}}$	$\sqrt{\frac{36f_h \ln(2) h_{+2}}{\pi^2 \tau^4}}$	$\sqrt{\frac{f_h^3}{3} h_{+2}}$

### 3 RESULTS

Thus, after measuring the  $h_\alpha$  noise levels, we may estimate the uncertainties  $\sigma(C_0)$  and  $\sigma(C_1)$  by using Table 2.

This table shows that the subtraction of the mean value cancels the dependence of  $C_0$  on  $f_h$ . For high frequency noises,  $\sigma(C_0)$  remains very close to  $\sigma(C'_0)$ . Moreover, neither  $\sigma(C_1)$  nor  $\sigma(e)$  are modified by this subtraction.

#### 3.1 Measurement Uncertainties of Drift Coefficients

If no real deterministic drift exists, the determination of the drift coefficients yields:

$$\begin{aligned} -2\sigma(C_0) < \hat{C}_0 < 2\sigma(C_0) & \quad \text{with 95.5\% confidence} \\ -2\sigma(C_1) < \hat{C}_1 < 2\sigma(C_1) & \quad \text{with 95.5\% confidence} \end{aligned}$$

Thus, measuring a drift coefficient  $C$  within the interval  $[-2\sigma(C), +2\sigma(C)]$  is compatible with a null drift hypothesis (with a risk of the second kind of 4.5%).

On the other hand, if a real deterministic drift exists, the estimates  $\hat{C}_0$  and  $\hat{C}_1$  converge toward the real coefficients  $C_0$  and  $C_1$ :

$$\langle \hat{C}_0 \rangle = C_0 \quad \text{and} \quad \langle \hat{C}_1 \rangle = C_1.$$

The uncertainty domains of the coefficients  $C_0$  and  $C_1$  are:

$$\begin{aligned} C_0 = \hat{C}_0 \pm 2\sigma(C_0) & \quad \text{with 95.5\% confidence} \\ C_1 = \hat{C}_1 \pm 2\sigma(C_1) & \quad \text{with 95.5\% confidence} \end{aligned}$$

#### 3.2 Frequency and Time Error Prediction

##### 3.2.1 Frequency error prediction

If  $\hat{C}_0$  and  $\hat{C}_1$  are estimated over a sequence of  $N$  samples (duration  $\tau = N\tau_0$ ), what error results from an extrapolation of the linear model to  $t_N + T$ ?

$$\hat{y}(t_N + T) = \hat{C}_1 \cdot (t_N + T) + \hat{C}_0 \quad (29)$$

The Total Frequency Error (TFE) may be defined as:

$$TFE(T) = y(t_N + T) - \hat{y}(t_N + T) \quad (30)$$

The TFE is composed of a Deterministic Frequency Error (DFE):

$$DFE(T) = (C_1 - \hat{C}_1)(t_N + T) - (C_0 - \hat{C}_0) \quad (31)$$

plus a random error (see Figure 2):

$$TFE(T) = DFE(T) + y_r(t_N + T) \quad (32)$$

$y_r(t_i)$  is a centered random variable without drift, with a variance  $\sigma^2(y_r) = R_{ii}$ .

Thus, denoting  $t' = t_N + T$ , we obtain:

$$\begin{aligned} \langle TFE^2(T) \rangle = & \sigma^2(C_0) + \sigma^2(C_1) \cdot t'^2 + \sigma^2(y_r) \\ & - 2Cov(C_0, y_r(t')) - 2Cov(C_1, y_r(t')) \cdot t' \\ & + 2Cov(C_0, C_1) \cdot t' \end{aligned} \quad (33)$$

$Cov(C_0, y_r(t'))$  is the covariance between the parameter  $C_0$  estimated over the sequence  $[t_0, t_N]$  and the random sample  $y_r$  at the date  $t' = t_N + T$ .

##### 3.2.2 Time error prediction

If a sequence of  $x(t_k)$  is known over a duration  $\tau$  (from  $t_0$  to  $t_N = t_0 + \tau$ ), the Time Interval Error (TIE) at  $t_N + T$  may be defined as [2, 3]:

$$TIE(T) = x(t_N + T) - x(t_N) - T\bar{\hat{y}}_{t_N, T} \quad (34)$$

with

$$\begin{aligned} \bar{\hat{y}}_{t_N, T} &= \frac{1}{T} \int_{t_N}^{t_N+T} \hat{y}(t) dt \\ &\approx \frac{1}{M} \sum_{i=N}^{N+M-1} \hat{y}_i \end{aligned} \quad (35)$$

where  $\hat{y}_i$  is the extrapolated frequency deviation at  $t_i$  and  $M$  is defined as  $T = M\tau_0$ .

$$TIE(T) = \tau_0 \sum_{i=N}^{N+M-1} (y_i - \hat{y}_i) \quad (36)$$

Thus, denoting  $M' = N + M - 1$ , we obtain:

$$\begin{aligned} \langle TIE^2(T) \rangle &= \tau_0^2 \sum_{i=N}^{M'} \sum_{j=N}^{M'} R_{ij} + t_M^2 \sigma^2(C_0) \\ &\quad + t_M^2 \left( t_N + \frac{T}{2} \right)^2 \sigma^2(C_1) \\ &\quad + 2t_M^2 \left( t_N + \frac{T}{2} \right) Cov(C_0, C_1) \\ &\quad - 2\tau_0^2 \sum_{i=N}^{M'} \sum_{j=N}^{M'} Cov(y_i, C_0) \\ &\quad - 2\tau_0^2 \sum_{i=N}^{M'} \sum_{j=N}^{M'} t_j Cov(y_i, C_1) \end{aligned} \quad (37)$$

### 3.2.3 Example of $f^{-2}$ frequency noise

In order to use (33) the covariances  $Cov(C_0, y_r(t'))$  and  $Cov(C_1, y_r(t'))$  must be calculated:

$$\begin{aligned} \langle C_0, y_{rM'} \rangle &= \frac{2(2N-1)}{N(N+1)} \sum_{i=0}^{N-1} \langle y_i, y_{rM'} \rangle \\ &\quad - \frac{6}{N(N+1)} \sum_{i=0}^{N-1} i \langle y_i, y_{rM'} \rangle \\ &= \frac{2(2N-1)}{N(N+1)} \sum_{i=0}^{N-1} R_{iM'} \end{aligned}$$

$$\begin{aligned} &= -\frac{6}{N(N+1)} \sum_{i=0}^{N-1} i \cdot R_{iM'} \\ &= h_{-2} \left[ \frac{1}{f_i} - \pi^2(t_N + T) \right] \end{aligned} \quad (38)$$

For  $Cov(C_1, y_r(t'))$ , we obtain:

$$Cov(C_1, y_r(t')) = \frac{h_{-2}\pi^2}{\tau_0} \quad (39)$$

Therefore, for an  $f^{-2}$  frequency noise, the standard deviation of the TFE is:

$$\sqrt{\langle TFE^2(T) \rangle} = \sqrt{h_{-2} \left[ \frac{4\pi^2 t_N}{15} + \frac{12\pi^2 T}{5t_N} (t_N + T) \right]} \quad (40)$$

It is interesting to notice that the DFE and the Random Frequency Error are fully separated:

$$\sqrt{\langle TFE^2(T) \rangle} = \sqrt{2\sigma^2(e) + \sigma^2(C_1)(t_N + T)} \quad (41)$$

Thus, if  $T = 0$  (interpolation), the standard deviation of the TFE is  $\sqrt{2}$  times the standard deviation of the residuals, i.e. it is the standard deviation between two residuals.

Concerning the TIE, from (37), (38) and (39), we obtain:

$$\sqrt{\langle TIE^2(T) \rangle} = \sqrt{\frac{\pi^2 h_{-2} T^2}{15 t_N} (9t_N^2 + 13t_N T + 4T^2)} \quad (42)$$

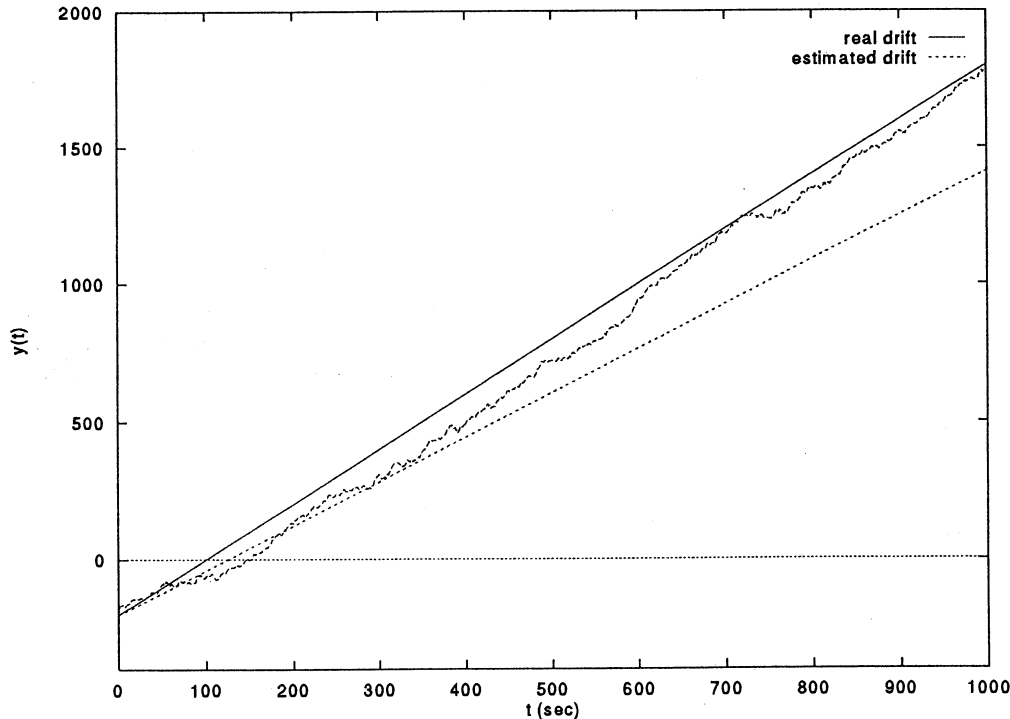


Figure 2.a: Estimation of the drift over a sequence of frequency deviation altered by  $f^{-2}$  FM noise (above). The drift was estimated over the first 256 samples (256 sec). After this time, the sequence moves away from the estimated drift.

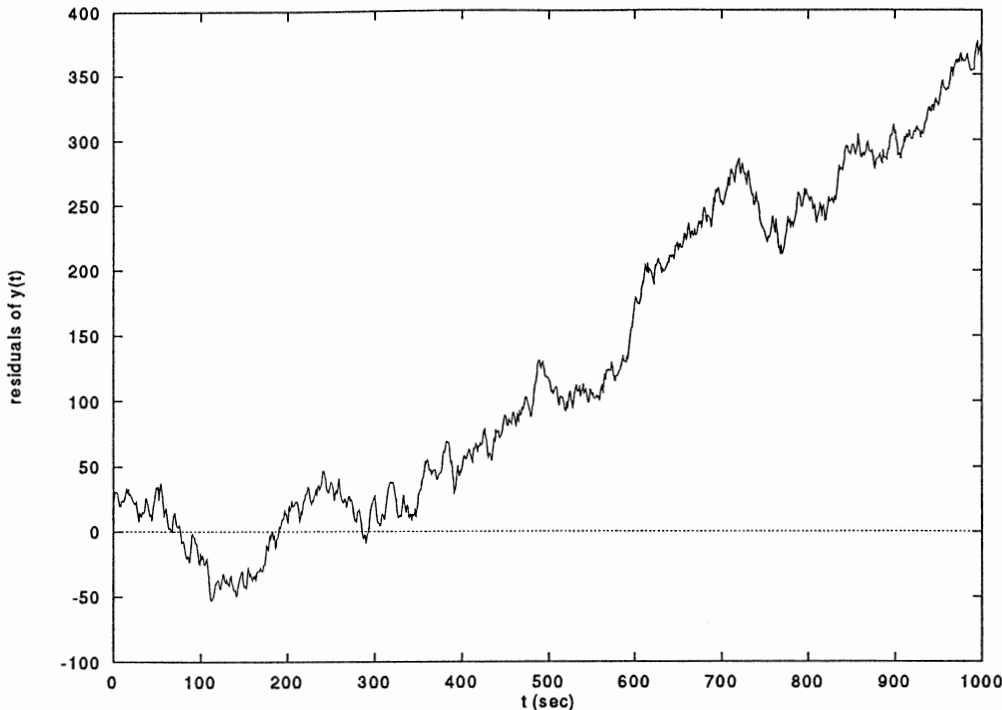


Figure 2.b: Residuals of the sequence shown in figure 2.a. The effect described in figure 2.a is more obvious here.

## 4 CONCLUSION: CHOICE OF THE FREQUENCY MODEL

What is the physical meaning of the low cut-off frequency of an oscillator? Is it a real feature of low frequency noises or a mathematical trick? In practice, it is possible to avoid its use.

For an  $f^{-2}$  frequency noise, the derivative of the frequency deviation, the ageing  $z(t)$ , is a white noise:

$$y(t) = \int_{t_0}^t z(\theta) d\theta \quad (43)$$

where  $t_0$  is the switch-on date of the oscillator. In this case, we have assumed that the oscillator was syntonized and synchronized at  $t_0$ .  $f_l$  is no longer necessary,  $y(t)$  is a centered random variable whose standard deviation increases with  $\Theta$ :

$$f_l \equiv \frac{1}{\Theta} \quad (44)$$

What is the "real" frequency of the oscillator over  $T \ll \Theta$ : its nominal frequency or its mean frequency over  $T$ ?

The answer depends on the frequency model:

- the use of the power law PSD model implies that the nominal frequency and the  $h_\alpha$  noise levels are time independent: they are the constants of this model. This model

is suitable for free running oscillators, e.g. frequency standards involved in the TAI computation;

- the determination of the nominal frequency as the mean frequency over a sequence of finite duration implies that the nominal frequency is time dependent: this nominal frequency is only valid over this whole sequence but neither over a part of this sequence nor over another sequence. This model is suitable for oscillators used for an experiment of well-defined duration.

## References

- [1] F. Vernotte and M. Vincent. Estimation of the uncertainty of a mean frequency measurement. In 11th European Frequency and Time Forum, pages 553–556, Neuchatel, Switzerland, March 1997.
- [2] C. A. Greenhall. Initializing a flicker noise generator. IEEE Trans. on Instrum. and Meas., IM-35(2):222–224, June 1986.
- [3] L. G. Bernier. Linear prediction of the non-stationarity clock error function. In European Frequency and Time Forum 1988, pages 125–137, Neuchatel, Switzerland, March 1988.



*12th E F T F* - 10÷12 March 1998 - Warsaw - POLAND

**Oscillators II**

Chairman:

*Bernd W. Neubig*



## LONG TERM STABILITY OF HIGH QUALITY OCXOs

Jari Mannermaa <sup>(1)</sup>, Kalevi Kalliomäki <sup>(2)</sup>, Tapio Mansten <sup>(3)</sup>

1) Nokia Mobile Phones, Tampere, Finland

2) University of Oulu, Department of Electrical Engineering, FIN-90570 Oulu, Finland

3) VTT AUTOMATION, Measurement Technology, P.O. Box 1304, FIN-2044 VTT, Finland

## ABSTRACT

Twenty years old OCXO:s of Hewlett Packard HP105A and HP105B, Oscilloquartz BVA8601 and Rohde Schwarz XSF (later R&S XSF) were studied. Their frequency and phase were monitored, Loran-C in the beginning and GPS later as a reference. However, long term stability of all studied oscillators are better than  $10^{-11}$ /day. Stabilities of OCXO:s were observed to be quite similar. BVA oscillator was better than others. Ambient conditions affect the performance. The OCXO:s can be stated to be much better than specified by manufacturers.

## INTRODUCTION

High quality crystal oscillators are relatively cheap compared to atomic standards like rubidium one. Their lifetime is practically infinite and short term stability is excellent. Hewlett Packard and Oscilloquartz are well-known manufacturers of frequency standards and their oscillators were used commonly in calibration laboratories like in VTT (Technical Research Center of Finland) / Automation and OY (University of Oulu) / Time Lab. The studied oscillators (HP105A, HP105B, BVA8601 and R&S XSF) have operated as a flywheel in Loran-C clocks and as a transportable frequency standard. In above mentioned calibration labs those oscillators have been replaced by atomic ones but most of accredited laboratories cannot afford them. Therefore the overall behaviour of

high quality crystal oscillators is still interesting. The long term stability of above mentioned oscillators seem to be two decades better than specified (HP105  $5 \cdot 10^{-10}$ /day and BVA8601  $2 \cdot 10^{-11}$ /day) but ambient factors like temperature, humidity and air pressure have significant influence on them. If somebody wants to achieve the best possible performance, at least, ambient temperature must be stabilized.

## DATA AND METHODS

The clocks mentioned before were provided during years 1972..1977. Their frequencies were monitored "manually" in the beginning i.e. there did not exist any continuous data of them. It was until 1986 when the first continuously operative surveillance system was developed at University of Oulu Time Lab. The advanced one was taken in use 1988 except at University of Oulu, also at Finnish National Calibration Laboratory of time and frequency. Loran -C navigation system was firstly used as a reference of time and frequency and the stability of  $10^{-11}$  per 24 hours was achieved. The reference was changed on 1989 and the new one was the GPS (Kinematics with a rubidium option) by which the inaccuracy of  $10^{-12}$  per day was achieved. After this it was possible to study the short term stability of crystal oscillators.

Table 1. The numerical values of the slopes of aging, temperature, humidity and air pressure of the studied OCXO:s with the respective standard deviations.

OCXO	Time coefficient		Temperature coefficient		Humidity coefficient		Pressure coefficient	
	AVG	SD	AVG	SD	AVG	SD	AVG	SD
Type								
HP105A	0.04	0.000	-2.7	0.15	-0.6	0.007	0.003	0.002
HP105B	-0.01	0.000	-0.3	0.10	-0.1	0.012	-0.03	0.004
BVA8601	-0.02	0.000	-0.2	0.19	0.1	0.016	0.011	0.002
R&S XSF	0.02	0.001	0.9	0.06	-----	-----	-0.002	0.008

The surveillance system also measures automatically important environmental quantities and the phase deviations of different clocks and frequency standards every ten minute. This means that even 8 years' continuously recorded data of the above mentioned crystals are in use. The recorded values were handled by Lotus Spreadsheet Program and its multivariate regression analysis was applied to find out the influence of different factors. Moreover, the Allan variances of the short term data were calculated.

## RESULTS AND DISCUSSION

Frequency drifts of studied oscillators are shown in Fig. 1 which point out that the sign of the original

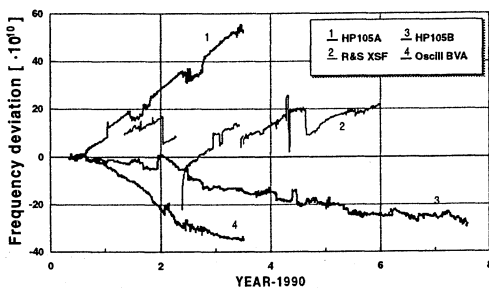


Fig. 1. Drifts of studied oscillators. The abrupt changes are due to adjustments.

direction of aging seem to be random. E.g. the HP 105A and 105 B of the same manufacturer drift into different directions. Earlier it was thought that the frequency will increase as a rule when an OCXO is becoming older. Interesting is that the absolute numerical values of the slopes are quite near each other, the order being the same.

The HP105A drifts linearly though at summer times there exists conformed deviations from the linear behavior. The HP105B also ages relative smoothly and even any essential annual exchanges can not be observed. The drift of the BVA8601 is exceptional because it seems to be parabolic or the aging changes its direction and any seasonal effects are not seen. Seasonal affect of HP 105A is due to its relative high sensitivity to humidity. The lack of an annual effect in the case of the HP 105B and BVA8601 oscillators can be explained with small sensitivity to humidity and air pressure. In addition the temperature changes in the laboratory has been unremarkable.

A multivariate regression was applied to the long term data. In the case of the HPs and BVA8601 oscillators time, temperature, humidity and pressure were used. Due to the lack of data of humidity

transducer only three factors were used in the case of the R&S XSF. The estimates were computed by means of the above mentioned variables. In general, a good compatibility of measured and computed estimate curves can be observed. Long term agings of the studied oscillators are shown in Figs. 2a-2d.

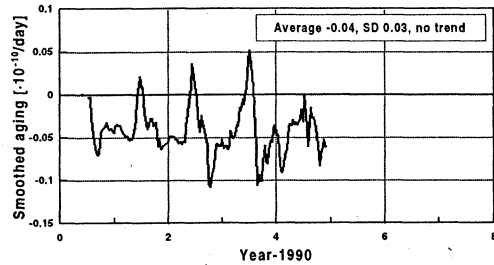


Fig. 2 a). A long term aging of HP 105A.

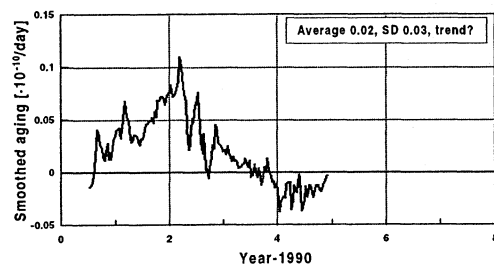


Fig. 2 b). A long term aging of Oscilloquarz BVA8601.

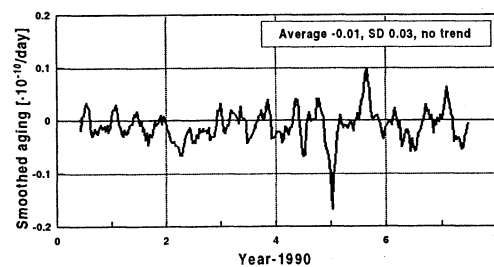


Fig. 2 c). A long term aging of HP 105B.

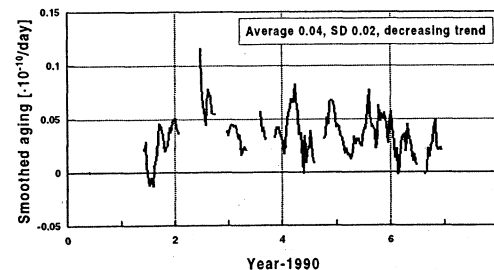


Fig. 2 d). A long term aging of R&S XSF.

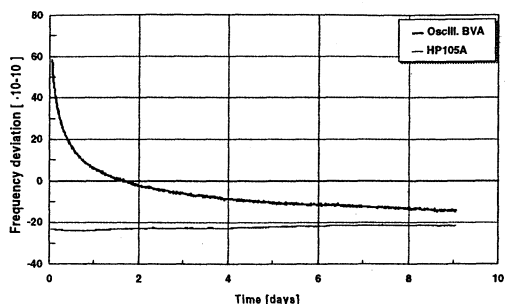


Fig. 3. Start-up of two OCXOs after one hour warm-up

In the next table is represented the numerical results of the factors of aging, humidity, temperature and pressure during years 1990..1996.

When aging is used as a criterion the HP 105B crystal is the best the BVA8601 and R&S XSF ones being the next and the HP 105A one is clearly poorest. If temperature coefficients are observed the BVA8601 is the best one though the HP 105B one is a good one and the HP 105A again is the poorest one. The situation is repeated in the case of humidity. The relative ratios in temperature and humidity coefficients are remarkably higher than in time as numerically presented about 14, 8 and 5, respectively. In statistic point of view only the pressure coefficients of the HP 105B and BVA8601 oscillators are significant (t values being about 7 and 5 ) whereas the others seem to be insensitive to air pressure.

There has been different opinions of the behaviour of an OCXO:s just after it has started to run. As a mathematical model of this start mode behaviour is among the others proposed to be a LOG(t) (logarithm) or SQRT(t) (square root) one. In Fig. 2 9s described measured behaviours of the HP 105A

and BVA8601 oscillators. As seen the curves are totally different. HP 105A achieves a smooth state after a few hours but the BVA8601 is unstable over a week. A log(t) model matches quite near in the case of BVA8601.

One way to estimate the frequency behaviour of an OCXO is to use the Allan variance. There is in Fig. 4. shown a typical example of Allan variance of an QCX oscillator.

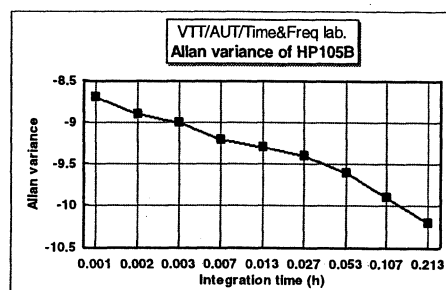


Fig. 4. The Allan variance of the HP105B.

## REFERENCES

Kalliomäki, Kalevi, Mansten, Tapio, "Control of Environmental and Clock Parameters in Time and Frequency Standards Laboratory", Proc. of the 6th EFTF, 1992, Noordwijk, the Netherlands.

Kalliomäki, Kalevi, Mansten, Tapio, Mannermaa, Jari, "A Computerised Time and Frequency Standards Monitoring System", Proc. of the 4th EFTF, 1990, Neuchatel, Switzerland.

## QUARTZ CRYSTAL OSCILLATOR WITH AN EFFECTIVE AGING RATE COMPENSATION

Yuriy S Shmaliy, Alexander Ph Kurotchka, Evgeniy G Sokolinskiy \*, Anatoliy V Marienko\*\*

\* "Sichron" Center, 4 Skripnika Str., Kharkiv, 310057, Ukraine, tel/fax: 380 572 45 09 55;  
yush@sichr.kharkov.ua

\*\* St.Co "IRVA", 12/14 Radisheva Str., Kyiv, Ukraine

## ABSTRACT

This paper discusses an application of the modulational method of quartz crystal frequency stabilization to diminution of aging rate in an OCXO within a crystal standard. Description of this last one is given, in which compensation of long-term frequency instabilities is realized with the use of the method based on use of the anharmonic properties of quartz crystal unit. General standard long-term performances obtained with and without aging compensation, and investigation results of the quartz frequency standards of Ч1-88 type are taken. It is shown that for both regimes there are aging rates per month correspondingly of  $-(6..20) \cdot 10^{-10}$  and  $(3..24) \cdot 10^{-12}$ . With this the short-term Allan variance is  $(1..3) \cdot 10^{-12} / \text{sec}$ .

## INTRODUCTION

An oven controlled quartz crystal oscillator (OCXO) have gotten at present a very small Allan variance of  $(2..10) \cdot 10^{-14} / \text{sec}$  for BVA crystal resonator [1] and of  $(1..10) \cdot 10^{-13} / \text{sec}$  for precision BAW one of SC-cut. With this its operating instabilities (long-term and temperature) are at an essential disadvantage in relation to quantum rubidium standard of frequency (Fig.1). For this reason at the last time there are investigations in direction of the ways search of self-contained (without use of quantum discriminators) decrease of an OCXO long-term aging.

There are two principal approaches in direction of this problem decision:

1. prediction of the frequency behavior during the operating time which based upon past measurements taken at arbitrary intervals;
2. measurement of frequency drifts in time that requires utilization of aging sensors within an OCXO.

A first approach had been studied, for instance, by Filler *et al* [2] with use of Kalman filtering theory and was realized by Kusters *et al* [3] within an aging prediction algorithm for HP-10811D/E oscillator, SC-cut. As may see from [4], its effectiveness is significantly limited by random nature of frequency changes, jumps of frequency, and a temperature influence. The investigations [2-4] had shown that prediction gives good results for 1-3 intervals of past measurements. With this, there are no excluded cases, when the character of frequency off-

set is changed significantly at once after the past measurement had stopped.

The second one had been realized by Shmaliy [5] in the modulational method of quartz crystal frequency stabilization [6]. Here, thanks to high aging cross-correlation of main  $f_0$  and anharmonic  $f_{npq}$  frequencies ( $k_k=0.83... 0.97$  [7]), it is carried out a continuous self-contained measuring of a long-term aging of the frequency  $f_0$  during the  $\tau_m$  time interval, which is formed by  $f_{npq}$  frequency. The measurements had shown [8] that effectiveness of the method is more than 10 and in one of the quartz crystal standard was a success in getting the aging rate of  $9 \cdot 10^{-11} / \text{year}$  [5]. Here the general limitation is the valuation errors of regression coefficients between  $f_0$  and  $f_{npq}$  frequencies in time as well as the temperature hysteresis. An analysis shows that with a use of the method there is a real possibility of an OCXO and quartz crystal standards creation with the aging rate of  $(5..10) \cdot 10^{-12} / \text{month}$  for SC-cut resonators and of  $(5..50) \cdot 10^{-13} / \text{month}$  for BVA ones (Fig.1).

## THE ESSENCE OF THE MODULATIONAL METHOD

Now we will consider a crystal resonator that is characterized, for example, by three modes  $h_{n11}$ ,  $h_{n13}$ , and  $h_{n31}$  in the operation frequency range, where  $11,13,31 \in \{pq\}$ ,  $n$  is a number of mechanical harmonic,  $pq \in \infty, \infty$  is a vibration index. An amplitude vs. frequency characteristic  $K_{QR}(f)$  of resonator has splashes in this range at the frequencies  $f_{n11}$ ,  $f_{n13}$ , and  $f_{n31}$ . During an excitation of resonator in oscillator circuit due to greater activity of the  $h_{n11}$  mode the oscillations with the frequency  $f_0 \cong f_{n11}$  within an inter-resonance gap is set with the spectral density  $S_\varphi(f)$  of phase fluctuations power, which has variations in the vicinity of  $h_{n13}$  and  $h_{n31}$  modes. There is shown in [9] that an energy distribution in variation zones is a subject to the Rayleigh-Rice law. Under FM-AM of an oscillator signal with the rather small index of FM  $\varepsilon_{FM} \ll 1$  and depth of AM  $\varepsilon_{AM} \ll 1$  two lateral components appear in the oscillations spectrum  $S_{FM-AM}$ , amplitudes of which vary with variation of modulation frequency in

the vicinity of modes  $h_{n13}$  and  $h_{n31}$  according to the law [10,11].

Under influence of the  $\theta$  component of the destabilizing factors vector  $\vec{\theta}$  (temperature, aging, pressure, etc.) the frequencies  $f_{npq}$  of single and double rotated cuts of thickness-shear vibrations of resonator change according to Tiersten's law [12].

$$f_{npq}^2(\vec{\theta}) = \frac{n\delta_1^2(\vec{\theta})}{4\pi h(\vec{\theta})\rho(\vec{\theta})} \left\{ 1 + \frac{h^{0.5}}{\pi n R} [\delta_2(\vec{\theta})(2p-1) + \delta_3(\vec{\theta})(2q-1)] \right\} \quad (1)$$

where  $h(\vec{\theta})$  and  $\rho(\vec{\theta})$  are a thickness of disc piezo crystal plate and quartz density,  $\delta_1(\vec{\theta})$ ,  $\delta_2(\vec{\theta})$ , and  $\delta_3(\vec{\theta})$  are constants, dependent on the orientation angles, geometry and physical properties of the piezo plate and electrodes. With this, the parameters of dynamic modulation characteristic change according to [13] as

$$m_\omega(j\Omega\vec{\theta}) = \frac{\Delta f(j\Omega\vec{\theta})}{f_0} = \varepsilon_\omega K_\omega(\Omega, \vec{\theta}) \exp[j\varphi_\omega(\Omega, \vec{\theta})] \quad ; \quad (2)$$

$$m_A(j\Omega\vec{\theta}) = \frac{\Delta U(j\Omega\vec{\theta})}{U_0} = \varepsilon_A K_A(\Omega, \vec{\theta}) \exp[j\varphi_A(\Omega, \vec{\theta})] \quad , \quad (3)$$

where  $\Omega = 2\pi F$ ,  $F$  is a modulation frequency,  $K_{A,\omega}(\Omega, \vec{\theta})$  and  $\varphi_{A,\omega}(\Omega, \vec{\theta})$  are amplitude vs. frequency and phase vs. frequency dynamic characteristics of AM and FM,  $\varepsilon_\omega$  and  $\varepsilon_A$  are the coefficients of static FM and AM,  $\Delta f$  and  $\Delta U$  are a frequency  $f$  deviation and amplitude  $U$  variation of an OCXO in the FM-AM process. If we use this property deriving from an OCXO output signal the information on frequencies  $F_{npq}(\theta) = f_{npq}(\theta) - f_0(\theta)$  behavior contained in parameters of dynamic modulation characteristics, and convert it into the controlling signal effecting discipline of the output frequency, we can construct frequency stabilization systems on this basis. Justification of the modulation method and general signals are given in [5].

## AN AGING OF ANHARMONIC FREQUENCIES OF AT-CUT CRYSTAL RESONATOR

Aging degradation processes in quartz crystal resonators are caused by three groups of physical processes:

1. surface processes - basically by overgrowing of microcracks, relieving stresses, oxidizing electrodes and mass transfer;
2. structural processes - basically by relaxation effects, diffusion and impurities exit, dislocations movement;
3. contact processes - changes in the places of contact of the quartz crystal piezoelectric plate with the quartz holder.

All the three groups of processes cause micro changes of physical properties and geometrical dimensions of quartz crystal resonator. Hence, these ones cause strongly correlated aging functions of resonator natural vibrations. Experimentally with the help of measuring equipment during some years with a set of AT-cut quartz units of thickness shear vibrations of PK-187 (Phonon) type under the fixed environment temperature the drifts of frequencies  $f_{511}$ ,  $f_{513}$ , and  $f_{531}$  of series resonances of the main mode  $h_{511}$  and the nearest  $h_{513}$  and  $h_{531}$  anharmonic modes from initial values of  $f_{511}^0 \cong 5 \text{ MHz}$ ,  $f_{513}^0 \cong 5.16 \text{ MHz}$ , and  $f_{531}^0 \cong 5.18 \text{ MHz}$  have been observed. Fundamental  $f_0$  frequency drifts of the same quartz crystal units also have been controlled under their excitation in the OCXO circuit.

Averaged by 10 quartz crystal units, the variation functions are received of frequencies  $\delta f_0 = (f_0 - f_0^0) / f_0^0$  and  $\overline{\delta f}_{npq} = (\bar{f}_{npq} - \bar{f}_{npq}^0) / \bar{f}_{npq}^0$ . The corresponding matrixes of correlation  $r_{ij}$  and regression  $k_{ij}$  coefficients have the forms of

$$R_{ij} = \begin{bmatrix} 1 & 0.830 & 0.937 & 0.948 \\ 0.830 & 1 & 0.885 & 0.849 \\ 0.937 & 0.885 & 1 & 0.972 \\ 0.948 & 0.849 & 0.972 & 1 \end{bmatrix} \text{ and } K_{ij} = \begin{bmatrix} 1 & 0.910 & 1.830 & 1.868 \\ 0.757 & 1 & 1.578 & 1.525 \\ 0.479 & 0.497 & 1 & 0.980 \\ 0.481 & 0.472 & 0.964 & 1 \end{bmatrix},$$

where the frequencies in lines and columns are arranged in the  $\bar{f}_{511}$ ,  $\bar{f}_0$ ,  $\bar{f}_{513}$ , and  $\bar{f}_{531}$  sequence.

The strong correlation between aging functions indicates the generality of the sources of their variations. However, the differences in the regression coefficients assuming the values of 1...15 in the set of quartz crystal units, indicates the different manifestation of the fundamental and anharmonic resonances of resonator. To approximate the  $\delta f_{npq}(t)$  aging functions the model has been taken  $\delta f_{npq}^a(t) = A_{npq}(1 - e^{-\alpha_1 t}) + B_{npq}(1 - e^{-\alpha_2 t})$ , where:  $A_{511} = 3.9 \cdot 10^{-8}$ ,  $A_{513} = 7.14 \cdot 10^{-8}$ ,  $A_{531} = 6.57 \cdot 10^{-8}$ ,  $B_{511} = 2.9 \cdot 10^{-7}$ ,  $B_{513} = 2.9 \cdot 10^{-7}$ ,  $B_{531} = 4.89 \cdot 10^{-7}$ ,  $\alpha_1 = 0.2$ ,  $\alpha_2 = 4.2 \cdot 10^{-4}$ . With this the root-mean-square errors of the experimental curves from the approximating ones are  $\sigma_{511} = 4.12 \cdot 10^{-9}$  and  $\sigma_{513} = 3.31 \cdot 10^{-9}$ ,  $\sigma_{531} = 4.05 \cdot 10^{-9}$  respectively. The functions  $\delta f_{511}(t) / \Delta t$  at the initial stage and at the end of the testing period assumed, correspondingly, the values of  $(9...20) \cdot 10^{-9} / \text{day}$  and  $(2...5) \cdot 10^{-11} / \text{hour}$  for series resonances of quartz crystal units. Behavior of the functions is in agreement with the beginning stage of the aging law [13] and, as time goes on, all frequencies show tendency to decrease with  $-(1...5) \cdot 10^{-9}$  per month average aging rate of the main frequency. Here, it is necessary to say that knowledge of the aging law of an OCXO main frequency is not obligatory to compensation system realization according to the method [5].

Creation of the system is based upon the knowledge of the regression coefficient  $k_{ij}$  of the general and anharmonic frequencies.

## THE QUARTZ CRYSTAL FREQUENCY STANDARD STRUCTURE

The structure of the quartz crystal frequency standard is shown in Fig.2. The base part of the standard consists of an OCXO with quartz crystal oscillator realized with Colpitts circuit and an AT-cut resonator of the PK-187 or PK-327 (Phonon) type. The OCXO has a single-ring proportional oven controlled system. To continuous self-contained measurement of a long-term instability of the fundamental frequency 5MHz according to above mentioned method, the modulation, and computing circuits are introduced into the structure. Under the regime of self-contained long-term aging compensation, the controlling signal  $E_{cont}$  comes from the digital-to-analog converter (D/A) to the OCXO through the switcher. Under the regime of external one, the D/A converter output is disconnected from the OCXO and the reference signal  $E_{ref}$  comes to the standard input.

Upon the stage of a standard calibration the aging functions of the main frequency of 5MHz and the additional anharmonic mode  $h_{513}$  one, which is on approximately  $1.6 \cdot 10^5$  Hz higher than the main one, are determined. After the calibration stage has completed, the necessary constants are put down into the computer memory for calculation of the compensation signal codes and the OCXO frequency steering through the D/A converter. All operations on this stage are carried out with the help of the basic special software SICHRON LELCAL for the OCXO and quartz crystal standard calibration. During the standard operation process there is possibility of self-contained (without use of reference signals, GPS, for instance) aging compensation both in the manual (by means of the aging indicator and the calculated table) and in the independent automatic regimes.

Now we will consider that

$$\delta_f(t) = \bar{\delta}_f(t) + \tilde{\delta}_f(t) , \quad (4)$$

$$\delta_F(t) = \bar{\delta}_F(t) + \tilde{\delta}_F(t) , \quad (5)$$

where  $\bar{\delta}_f$  and  $\bar{\delta}_F$  are the own deterministic, and  $\tilde{\delta}_f$  and  $\tilde{\delta}_F$  are the own random parts of relative instabilities of  $f_0$  and  $F_{npq}$  frequencies. We will find the instability of the output frequency  $f_0$  under the compensation regime as

$$\delta(t) = \delta_f(t) - \frac{1}{k_r} \delta_F(t) + \delta_A , \quad (6)$$

where  $k_r \in \{k_{ij}\}$  is a linear regression coefficient of  $f_0$  and  $F_{npq}$  frequencies,  $\delta_A$  is an error of the compensation system.

Let us evaluate the effectiveness of the aging rate compensation with account of (4-6) as

$$\text{Eff}_R(t) = \frac{|\delta_f(t)|}{|\delta(t)|} = \frac{|\delta_f(t)|}{|\delta_f(t)| \frac{\Delta k_r}{k_r} + \delta_A} \cong \frac{k_r}{\Delta k_r} , \quad (10)$$

where  $\Delta k_r$  is error of  $k_r$  valuation. If  $\delta_A \rightarrow 0$  and  $\Delta k_r \rightarrow 0$  then  $\text{Eff}_R(t) \rightarrow \infty$ . Under the real conditions there is no hard to obtain the  $\delta_A \ll \delta_f(t) \Delta k_r / k_r$ , hence, the main limitation of  $\text{Eff}_R(t)$  increase is connected with the error of  $k_r$  measurement.

Let us also define the effectiveness of  $f_0$  frequency accuracy increase as

$$\text{Eff}_A(t) = \frac{|\bar{\delta}_f(t)| + \sigma_f}{\delta_A + \sqrt{\sigma_f^2 + \sigma_F^2 k_r^{-2}}} , \quad (11)$$

where  $\sigma_f$  and  $\sigma_F$  are root-mean-square deviations of low-correlated  $\tilde{\delta}_f(t)$  and  $\tilde{\delta}_F(t)$  random functions. One may see from (11) that  $\text{Eff}_A(t)$  substantially depends on  $\bar{\delta}_f(t)$  aging rate and system effectiveness may be less than 1.0 if  $\bar{\delta}_f(t) < \sigma_f$ , that is not acceptable. Hence, main limitations to high values of  $\text{Eff}_A(t)$  advance are caused by real magnitudes of dispersions of  $\tilde{\delta}_f(t)$  and  $\tilde{\delta}_F(t)$  functions. In the limiting case ( $\sigma_f \rightarrow 0, \sigma_F \rightarrow 0$ ) the effectiveness is found as  $\text{Eff}_A(t) \rightarrow \bar{\delta}_f(t) / \delta_A$  and may reach of tens and hundreds. Let us mark that there is influence of the resonator temperature hysteresis and thermal dynamic processes within an OCXO to  $\delta_f$  and  $\delta_F$ .

## EXPERIMENTAL RESULTS

Results of the experimental studies of the standards long-term aging with and without its rate compensation are given in this chapter.

### Correlation and regression coefficients

As mentioned above stability in time of regression coefficient is a main factor that has a great influence into an effectiveness of the crystal standard aging compensation, if the modulational method is used. Accounting this, we have been watching for the frequencies  $f_0$  and  $F_{513} = f_{513} - f_0$  aging functions for a long time. The experimental plots of correlation  $k_c \in r_{ij}$  and regression  $k_r \in k_{ij}$  coefficients behavior in time for #02 standard are shown in Figures 3 and 4.

The studies have been carried out with the normal environment room temperature of  $(25 \pm 6)^\circ\text{C}$  after 30 days of continuous operation. One may see from Fig.3 that there is vary strong cross-correlation between aging functions of  $f_0$  and  $F_{513}$  frequencies. With this the coefficient  $k_c$  for all standards had a value of 0.85...0.95 after 10...30 days of studies and for the #02 had reached the value of 0.98 after 90 days (Fig.3).

Studies of the coefficient  $k_r$  were carried out with the measuring data had been obtained during 1...190 days (Fig.4). Upon the early stage of measurements, there are too small discrete points for the coefficient objective valuation. It may be seen from Fig.4 that the average value of  $k_r$  has disparity with similar valuations for resonators. The last finding is explained by an influence of the oven controlling and modulation circuits. Processes of turn-off/on and cyclical changes of a temperature, which had been took place during 14 days, also have influence to  $k_r$  valuations. Nevertheless, in whole we may speak about relatively constant and, to all appearances, fundamental nature of the regression coefficient between  $f_0$  and  $F_{npq}$  aging functions.

#### Long-term instabilities compensation

Figures 5 and 6 illustrate the results of aging measurements of frequencies  $f_0$  and  $F_{513}$  that had been obtained for a long time. Also, there is contained the prediction of the  $f_0$  frequency long-term behavior with a use of the aging compensation regime for the #02 and #03 standards.

General evaluations of these processes are given in Table 1 with the experimental values  $k_p = 15.8$  and  $k_c = 0.96$  for the #02, and  $k_p = 9.07$  and  $k_c = 0.996$  for the #03 standards.

TABLE 1 – Long-term performances of the standards

Aging rate per month	#02	#03
base	$-2.5 \cdot 10^{-9}$	$-6.3 \cdot 10^{-10}$
with compensation	$-6.2 \cdot 10^{-11}$	$-3.4 \cdot 10^{-12}$

If to take that the error of  $k_p$  valuation is (10...1)%, then one may find from (7) that prediction effectiveness has the levels  $\text{Eff}_R(\#02) = 7,1..19,9$  and  $\text{Eff}_R(\#03) = 3,86..8,84$  per month,  $\text{Eff}_R(\#02) = 9,7..75,1$  and  $\text{Eff}_R(\#03) = 5,91..43,3$  per year. The standard #03 after the first 52 operating days had shown the  $k_p = 7.4$  and, after a long time of storage and studies in a turn on/off regime, this one had shown the parameters  $k_p = 5.73$  and  $k_c = 0.996$ .

Figures 7 and 8 show the standard #02 aging functions, which had been obtained during half year (from 13 March 1995) with and without the steering. In the first

case (fig.7), the aging control had been done within the normal temperature field of  $(25 \pm 6)^\circ\text{C}$ . In the second one (fig.8) a temperature had been had the  $(26 \pm 0.5)^\circ\text{C}$  constant value. As may see from fig.7, the influence of temperature appreciably set a limit on the effectiveness of this regime and, therefore, the more efficient oven systems as well as controlling circuits are preferable.

Let us evaluate the real effectiveness of the compensation system of the #02 standard (Table 2) according to (7) and (8).

TABLE 2 – Aging and effectiveness of the standards

Performances	$(26 \pm 0.5)^\circ\text{C}$
aging rate per month / year	$-2.4 \cdot 10^{-11} / -2.9 \cdot 10^{-10}$
$\text{Eff}_R$	25,7...103,4
$\text{Eff}_A$ per month / year	3,9...7,8 / 37,5...67,5

As follows from Tables 1 and 2 comparison, the experimental valuations are in a good agreement with prediction ones.

Figures 9 and 10 show the analogous results received from 12 Nov 1996. On the beginning stage (near 80 days), there had been a calibration of an OCXO. From 100<sup>th</sup> day it had been carried out the aging compensation under condition of turn off/on with the surrounding temperature of 18...32°C. As may see, in whole we have not received good results here. However, there was quite good aging rate diminution within the all time ranges with unaffected operation conditions.

Bringing all the frequency jumps into zero level at the beginning stages of each partial process we gone to the figure 10. In this prediction case, we also had received the result that is similar to the case (figure 7) without turn off/on. Here, as may see, we obtained lesser long-term noise of frequency as a standard system had been improved (we used a new temperature compensation algorithm). Comparing results obtained by figures 7-10, we gone to the conclusion that the main limitations of aging reduce in an OCXO are errors of an instrumental compensation system and thermal hysteresis as well. Now we found out the effective ways of a system error diminution by the modulation method. With this, the thermal hysteresis will be able to limit the resulting accuracy of frequency in an OCXO by the level of  $(1..5) \times 10^{-10}$  for a long time. We suppose, it is the boundary value of accuracy in time for an OCXO with AT-cut resonator of PK-187 type within a wide temperature range.

#### CONCLUSION

The results of experimental studies of the modulational method effectiveness in quartz crystal standards with AT-cut resonators show that there is a real possibility to

obtain the values  $\text{Eff}_R(t) = 10 \dots 100$  and  $\text{Eff}_A(t) = 5 \dots 50$ . Although we have analyzed only the data for these standards, we conclude that the ended results may be more pronounced for an OCXO with SC-cut and BVA units. In the last case, by our prediction, a tendency to diminution the frequency instabilities is as shown in Fig.1.

## ACKNOWLEDGMENT

This work was supported by Ukrainian Ministry of Science and Technology under the Program 06.08.276-92, and by Ukrainian State Standard under the Program "Metrology 2.4".

## REFERENCES

1. Douglas R, Boulanger J, 1992, "Local Oscillator Requirements for Timekeeping in the  $10^{-14} \tau^{-1/2}$  Era", in Proc.of 46th IEEE IFCS, 6-26.
2. Filler R, Stien S, 1988, "Kalman Filter Analysis for Real Time Applications of Clocks and Oscillators", in Proc. of 42th IEEE AFCS, 447-452.
3. Kusters J, Ho K, Giffard R, Cutler L, Allan D, 1994, "A No-drift and less than  $1 \cdot 10^{-13}$  Long-term Stability Quartz Oscillator Using a GPS SA Filter ", in Proc.of 48th IEEE IFCS, 572-577.
4. Su W, Filler R, 1992, "Application of Kalman Filtering Techniques to the Precision Clock with Non-Constant Aging", in Proc.of 46th IEEE IFCS, 231-237.
5. Shmaliy Yu, 1995, "The Modulational Method of the Precision Quartz Crystal Oscillators and Standards Frequency Stabilization", in Proc.of 49th IEEE IFCS, 579-589.
6. Shmaliy Yu, Romanko V, Marienko A, 1995, "The Long-Term Frequency Instability Compensation in Quartz Frequency Standards", in Proc. of 7th Int. Congress-METROLOGIE-95, 279-283.
7. Shmaliy Yu, 1995, "An aging special features of natural vibrations spectrum of vacuum crystal resonator of AT-cut", Journal of Techn. Physic, 65, 81-86. (in Russian).
8. Shmaliy Yu, Kurotchka A, Marienko A, 1996, "Quartz Frequency Standard Ч1-88 with a Long-Term Frequency Instabilities Compensation", in Proc.of Int.Symp. Acoustoel., Freq. Control & Signal Generation, (Moscow), 225-229.
9. Romanko V, Shmaliy Yu, 1992, "Probability properties of dynamic modulation characteristics of crystal oscillator," Izv. VUZov, Radioelectronika, 37, 11, 37-44 (in Russian).
10. Shmaliy Yu, 1991, "Splashes of dynamic modulation characteristics in precision quartz crystal oscillator with FM," Radiotechnika, 46, 7, 36-39.
11. Shmaliy Yu, 1986, "Dynamic distortions in frequency modulating self oscillatory system," Izv. VUZov, Radioelectronika, 29, 12, 40-44 (in Russian).

12. Stevens D, Tiersten H, 1985, "An Analysis of Doubly-Rotated Contoured Quartz Crystal Resonators", in Proc.of 39th AFCS, 436-447.
13. Vig J, Meeket T, 1991, "The Aging of Bulk Acoustic Wave Resonators, Filters and Oscillators", in Proc. of 45th IEEE IFCS, 77-101.

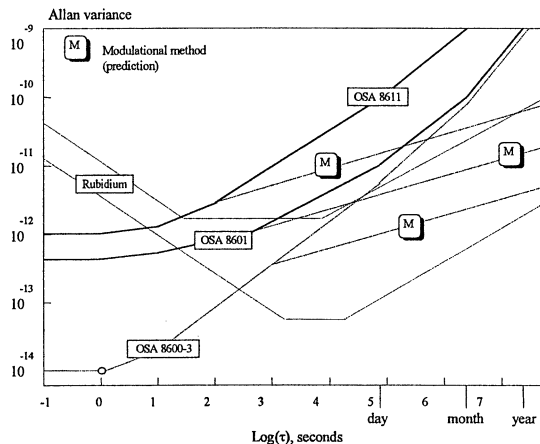


Figure 1. Allan variance of rubidium oscillators and OCXOs of OSA 8611, 8601, 8600-3 types: real curves and anticipated ones with the use of the modulational method

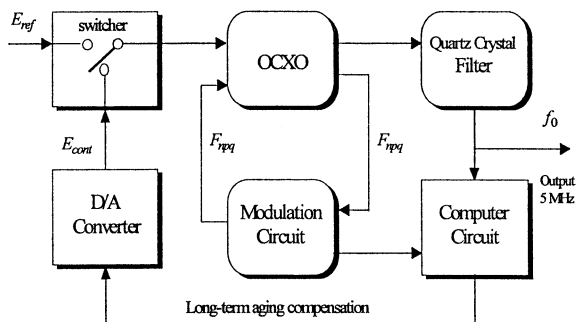


Figure 2. Block diagram of the quartz crystal frequency standard

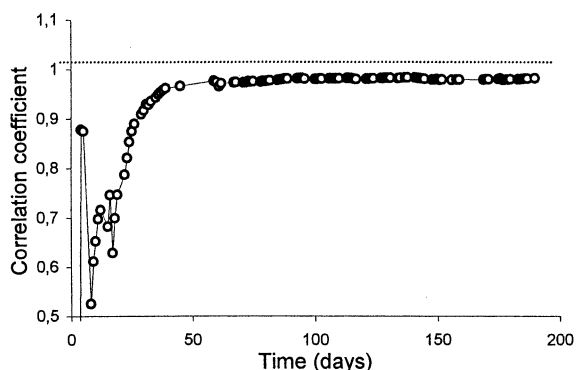


Figure 3. Dependence in time of the coefficient  $k_c$  between frequencies  $f_0$  and  $F_{513}$  of the #02 standard

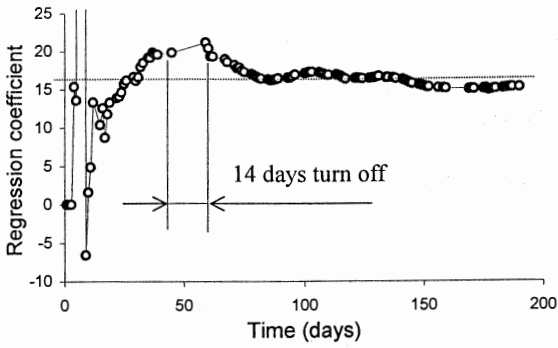


Figure 4. Dependence in time of coefficient  $k_r$  between frequencies  $f_0$  and  $F_{513}$  of the #02 Standard

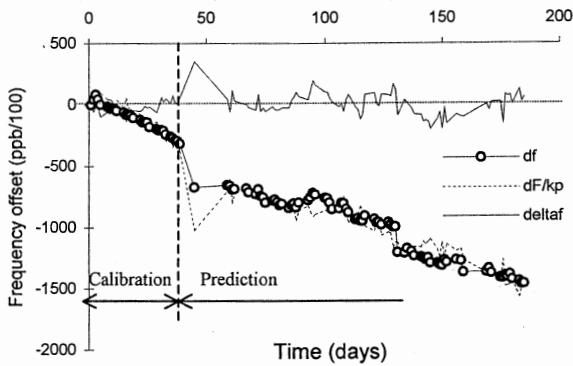


Figure 5. Aging of main (df) and anharmonic ( $dF/k_p$ ) frequencies, and prediction one ( $\text{delta}f = df - dF/k_p$ ) for the #02 standard

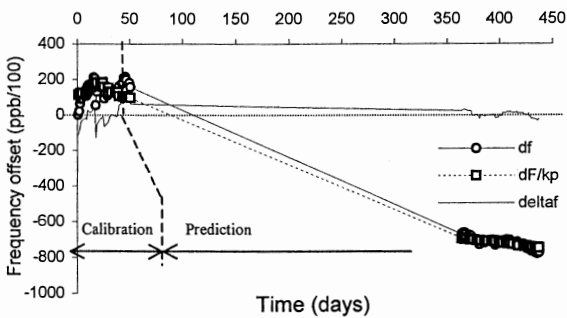


Figure 6. Aging of main (df) and anharmonic ( $dF/k_p$ ) frequencies, and prediction one ( $\text{delta}f = df - dF/k_p$ ) for the #03 standard

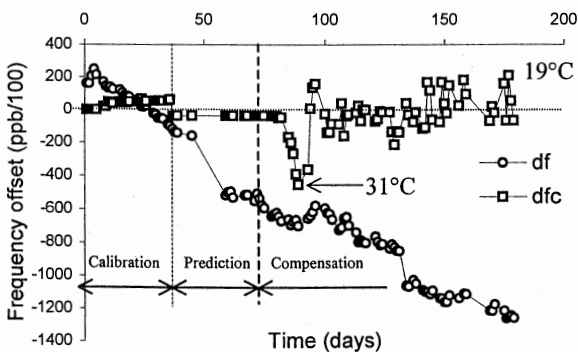


Figure 7. Aging of the frequency  $f_0$  with (dfc) and without (df) instability compensation within the temperature range of  $(25 \pm 6)^\circ\text{C}$  for the #02 standard

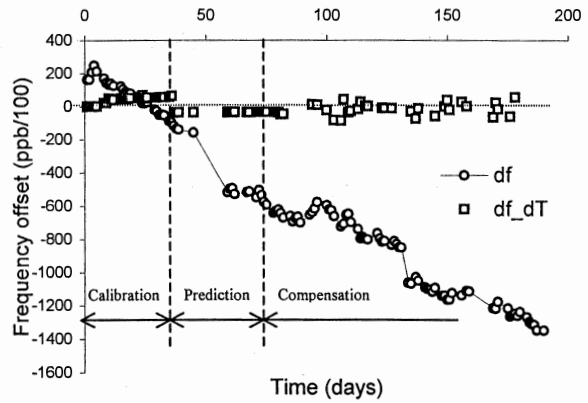


Figure 8. Aging of  $f_0$  with ( $df_{dT}$ ) and without (df) compensation within the temperature range of  $(26 \pm 0.5)^\circ\text{C}$  for the #02 standard

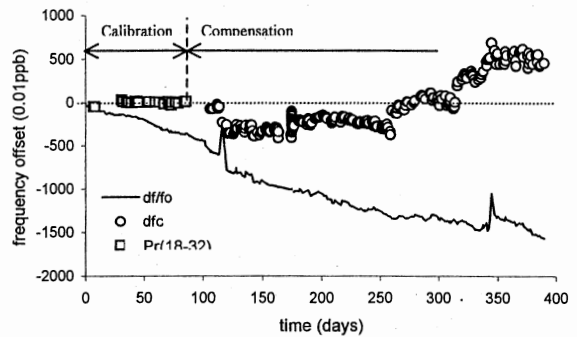


Figure 9. Aging of  $f_0$  under conditions of turn off/on and temperature influence with (dfc) and without (df/fo) compensation. Pr(18-32) is prediction curve with the temperature of 18...32°C for the #02 standard

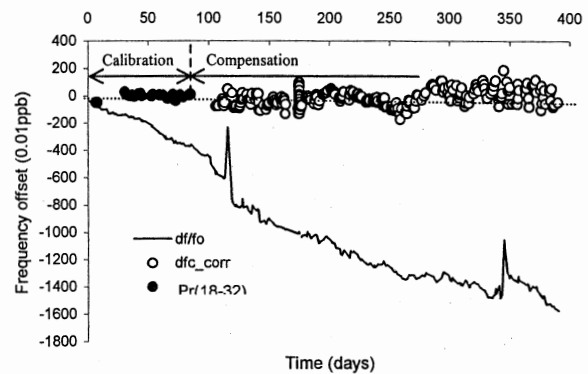


Figure 10. Aging of  $f_0$  with ( $dfc_{corr}$ ) and without (df/fo) compensation. Pr(18-32) is prediction curve with the temperature of 18...32°C for the #02 standard.

## OSCILLATOR SELECTION TO SUPPORT CDMA HOLDOVER REQUIREMENTS

Werner Weidemann,

Datum Inc., Efratom Time and Frequency Products, 3 Parker, Irvine, CA 92618

### Abstract

This paper discusses Oscillator Selection to meet the Time and Frequency Accuracy and Stability requirements for CDMA (Code Division Multiple Access) Base Stations. GPS (Global Positioning Satellite System) provides the system reference with a comfortable margin. However, GPS may not be available 100% of the time, and the local reference in each base station needs to maintain the required accuracy until GPS coverage is regained. The interval between GPS coverage is called holdover time. This paper discusses the special situations, which could arise before and during holdover. It discusses concerns relating to the local oscillator as well as benefits and limitations of "smart" compensation algorithms. Aging, environmental sensitivities, warm-up specifications, and unpredictable events (such as frequency steps) are discussed as they pertain to different oscillator technologies. Calculated and measured holdover performances are also described.

While the paper focuses on the needs of CDMA, it is basically applicable to all disciplined oscillator solutions.

### CDMA BASICS

CDMA utilizes Spread Spectrum Technology to allow multiple users to communicate via a network of base stations through a single shared wireless channel. The system requirements are outlined in the TIA/EIA Interim Standard 95, called "Mobile Station-Base Station Compatibility Standard". CDMA optimizes frequency utilization and attempts to increase capacities compared to AMPS (Advanced Mobile Phone Service) and TDMA (Time Division Multiple Access). It assigns a code to all speech bits, transmits the encoded speech and reassembles the speech in its original form at the receiver. All calls are simultaneously spread over the entire frequency band of 1.25 MHz.

The subscribers' handset must decode the pseudo random code of the transmission to reassemble a voice or data channel. Synchronization of the handset, a requirement to decode the pseudo random code, is started by the pilot channel and completed by the synchronization channel. Usually, the handset will receive multiple base stations. The pilot channels of different base stations are identical, but separated by  $n \times 52 \mu\text{s}$ .

The relative timing of the pilot channels received by the handset is dependent on: the timing accuracy of the individual base stations, the transmission delay caused by the distance between the handset and the base stations, as well as multipath conditions and other delays. The handset calculates the timing of other base stations based on the received pilot of its primary base station.

If the separation of timing signals from different base stations is not maintained at the location of the handset, it is unable to simultaneously communicate with two base stations. The simultaneous communication with two base stations is called a soft hand-off, a very important feature of CDMA. It reduces the likelihood that a call will be dropped due to the dynamics of signal fluctuations. The goal is to keep each base station within 1 to 3  $\mu\text{s}$  absolute accuracy. If a base station drifts outside its 10  $\mu\text{s}$  window, calls may not be transferred to another base station and an island cell is created.

This paper's concern is the ability to keep the transmitter timing within the TIA/EIA IS95 requirements and the importance and impact of the selection of the local oscillators.

### Base Station Requirements per TIA/EIA IS95

- Frequency Accuracy  $\pm 5\text{E-}8$
- Time Accuracy
  - Nominal  $\pm 3 \mu\text{s}$  of CDMA System Time
  - Worst Case  $\pm 10 \mu\text{s}$  of CDMA System Time
- Time Correction Rate  $\leq 101.725 \text{ ns} / 200 \text{ ms}$

### GPS AS PRIMARY SYSTEM TIMING REFERENCE

With at least four satellites visible, the GPS provides position and time. Most GPS receivers are designed to provide optimum position coordinates and velocity vectors. When the GPS user is stationary and knows his position, he can receive GPS time as long as at least one satellite is visible. GPS receivers optimized to provide accurate timing while minimizing demands on the user, include features such as:

- Automatic Site Survey
- Position Averaging
- Simultaneous Reception of eight or more channels

- Timing Mode
- T-RAIM (Time Receiver Autonomous Integrity Monitoring)
- rf Jamming Immunity
- Stable, Phase Adjustable 1 PPS output
- Diagnostic Support e.g.:
  - Satellite Tracking schedule/visibility
  - Satellite Signal Strength
  - Antenna Current Monitoring
- Fast Acquisition/Re-Acquisition Time
- Selection of satellites to minimize ionospheric delay.

The GPS system is purposely degraded through SA (Selective Availability). A stationary user can minimize the effects of SA by averaging the signals for several hours. The T-RAIM function allows the user to set a window (e.g. 1  $\mu$ s). Only data inside the window are considered valid and are included in the averaging process. This effectively removes bad satellite data as long as at least 3 satellites are visible.

How accurate is the timing information? A typical board level timing receiver produced in significant quantities provides the following performance:

130 ns (1 sigma) with SA on; 50 ns (1 sigma) with SA on, position hold mode

This is based on 8 satellites. The accuracy changes with the inverse of  $\sqrt{n}$ , when  $n$  is the number of satellites tracked. Assuming a gaussian distribution means that even in the more accurate position hold mode, 5% of all measurements are outside of a 100 ns window, when eight healthy satellites are visible. About 37% of all measurements are outside that 100 ns window, if only two satellites are visible. In order to keep base station timing changes to < 101 ns between successive timing pulses, a flywheel needs to be incorporated in the receiver.

**GPS alone does not meet all CDMA requirements; its long term accuracy is unmatched, but its short term stability needs to be improved even when the system performs within its specification and multiple satellites are visible.**

### AVERAGING OF THE GPS TIMING SIGNAL

Averaging of the GPS timing signal reduces the noise of the GPS signal including the pseudo random noise induced by SA. This can be done by creating a local time scale, derived from a local oscillator, which will be compared to and steered to the GPS timing signal (Figure 1). To reduce jitter, the noise of the local oscillator over the integration time must be lower than that of the GPS signal (Figure 2). Over relatively short periods, up to several minutes, this condition is rela-

tively simple to satisfy, especially if the requirements ( $\pm 1 \mu$ s GPS time and  $\pm 100$  ns/s change) are well within the system's capability.

An analogy is to compare the local oscillator to a flywheel which is loosely coupled to the impulse of a GPS reference. Since the flywheel provides the timing to the user, it can also cover interruptions in GPS reception.

The timing of the CDMA base station and the integrity of the telephone system must be maintained through this flywheel even if the GPS signal is not available.

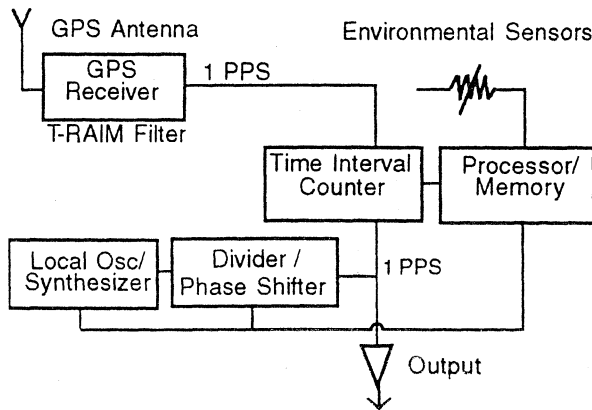


Figure 1 - Steered Time & Frequency (T/F) Source

The above diagram shows a basic block diagram of a steered T/F source, where the GPS time output is compared with a local clock. The time differences are measured and processed to steer the local oscillator. The block diagram shows a (temperature) sensor providing an additional input to the processor. It is possible to learn the performance of the local oscillator when the unit is disciplined by GPS. If the algorithms can separate the independent contributors to frequency and phase offsets, we consider the algorithm as a "smart" algorithm, and the T/F source a "Smart Solution".

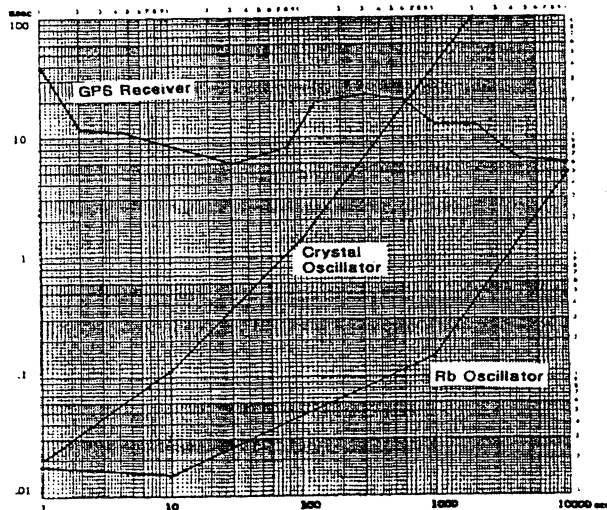


Figure 2. Time Domain Stability of GPS Reference & Local Oscillator

In order to provide robust and fault tolerant solutions, the designer must consider the normal noise processes and anomalies of the GPS reference and the local oscillator during the design. Most GPS anomalies can be effectively removed by the T-RAIM function in the receiver, when at least three satellites are in view. With only one or two satellites in view, the algorithm needs to estimate the likelihood of GPS anomalies or oscillator anomalies. In such a situation it is important to know the "health" of the local oscillator. With a crystal oscillator, the oven current can be monitored to provide some assurance that no major changes have occurred in its heater circuits, but the health of the oscillator circuitry can only be estimated based on its performance history. With a rubidium standard, a "lock monitor signal" is provided that assures that the internal crystal is locked to the rubidium hyperfine transition. This assures that the output frequency is within a few E-8 as long as the lock flag is valid. Proper use of status information and the oscillators' history allows the built-in processor to steer the local oscillator to meet the users' requirements with the greatest probability.

### Intermittent Coverage of GPS.

Potential reasons for intermittent GPS coverage:

Antenna and cable problems

Receiver failures

Intentional/unintentional unavailability of GPS

Intentional and unintentional RF jamming of the receiver

- Because the GPS antenna is often installed near high power transmitter antennas, unintentional jamming warrants special consideration during installation and may be an operational concern.
- Limited visibility of the sky is a problem in urban locations, particularly if the view of the southern sky is blocked. Trade-offs involve site selection, reducing antenna cable length, and enhancing the ability to operate through periodic GPS outages.
- Solar flares produce electro magnetic disturbances in the ionosphere and affect propagation of radio signals. The next sunspot cycle peaks around the year 2000 or 2001. The GPS system of satellites was in its infancy when the last peak occurred, so it is uncertain what the effects will be on GPS during the upcoming peak periods. To be on the safe side, the CDMA network should be capable of withstanding GPS outage for more than 24 hours.

Antenna, cable and receiver failures require a maintenance action, the other causes may correct themselves after some time. Problems related to limited sky visibility are periodic and repeat approximately every 12 hours due to the orbits of the satellites.

### Holdover Concerns.

The local oscillator must smooth the received GPS signals and provide accurate timing when the GPS signals are not available. The accumulated time error  $\Delta t$ , of an oscillator-based clock is equal to the integral of the fractional frequency offset due to all causes over the observation time  $t$ :

$$\Delta t = \int_0^t df/f(t) dt$$

The fractional frequency change  $df/f$  integrated over time  $t$  can be approximated by finite increments  $\Delta f_1/f$ , integrated over time  $t_1$  through  $\Delta f_n/f$  integrated over time  $t_n$ . These fractional frequency changes  $\Delta f/f$  can be attributed to several mechanisms and causes. Offsets can be caused by temperature changes and other environmental changes as well as changes internal to the oscillator, but also by the disciplining algorithms. A linear change in frequency  $D$  may be a reasonable approximation of the aging of the oscillator over a relatively short time. It can also be caused by a slowly and monotonically changing ambient temperature. To accommodate random frequency fluctuations we add  $\epsilon$ , representing the time error due to stochastic noise processes in the oscillator. Using the linear approximation we can write:

$$\Delta t = t_0 + \frac{\Delta f_1}{f} * t_1 + \frac{\Delta f_2}{f} * t_2 + \dots + \frac{\Delta f_i}{f} * t_i + \dots + \frac{\Delta f_n}{f} * t_n + \frac{D}{2} * t^2 + \epsilon(t)$$

### **Oscillator Parameters To Be Considered :**

**Initial Frequency Offset** - Depends on the update algorithm of T/F standard, resolution of tuning steps, noise and integration time of GPS signal. Normally the accuracy of the update increases with longer integration (averaging) times. However, this may not be the case if significant temperature changes occurred over the integration interval. Also, the unit may show appreciable aging over the integration interval resulting in an initial offset different from the calculated offsets. Note that aging and temperature compensating algorithms will minimize the temperature and aging induced errors.

**Frequency Steps** - They occur in any type of oscillators and are not predictable. They are seen most often hours to days after turn-on of the oscillator. Unlike temperature and aging induced offsets, the results of frequency steps cannot be reduced by modeling due to their unpredictability. Frequency steps in rubidium oscillators are almost always smaller than a few E-12. Quartz oscillators may show steps of  $\geq$  E-10 (Figure 3). Frequency steps are not included in the sample calculation but it must be recognized that a single step of 5E-11 accumulates 4.3  $\mu$ s over 24 hours!

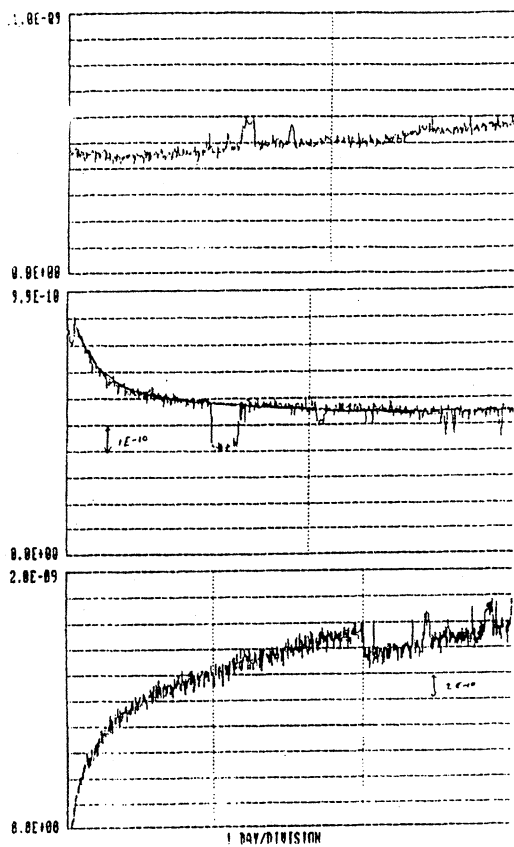


Figure 3

**Aging** – For high performance oscillators, aging improves significantly over time and can be predicted with a relatively small residual error for 24 hours if the oscillator has been operating for many days or weeks. It is very difficult to do this with confidence if the oscillator has been operating for only a few hours to a day. The aging estimate needs to be continuously updated; every turn-on is different from the previous turn-on. Rubidium oscillators age  $< 2E-11$ /day within a day of turn-on. Crystal oscillators may age  $\geq 1E-10$ /day even after several days of operation, especially if we consider oscillators which cost less than a low cost rubidium (Rb) oscillator.

**Warm-up** – Warm-up is a combination of initial aging and the subsiding of thermal gradients in the oscillator. These processes have different time constants, often have different signs and are difficult to separate. Special concern arises when the frequency needs to be predicted during the first 24 hours of operation.

**Stochastic Time Error** – The stochastic RMS time error of an oscillator driven clock is caused by the same noise processes that determine Allan Variance, the short term stability of the clock. The time error:

$$\epsilon(t) \sim t \times \delta y(t)$$

For long periods, typically  $> 3$  hours for rubidium clocks and 1 hour for crystal clocks, this error is dominated by random walk FM. In this case,  $\delta y(t) = k \times t^{1/2}$  and therefore:

$$\epsilon(t) = k \times t^{3/2}$$

## Environmentally Induced Frequency Changes To Be Considered:

**Temperature Coefficient** - Temperature has a very significant impact on an oscillators' stability. Not only is the magnitude of the change important, but also the rate and the direction. Typically, an external temperature change affects not only the internal temperature and temperature gradients of the resonator and physics package, but also its operating parameters. The latter can be a result of drive level changes, power changes or in the case of crystal oscillators, load changes. Atomic standards are additionally susceptible to RF level and servo gain changes. A concern is the possibility that the temperature sensitivity of the output frequency changes with time. This is especially true if the changes are caused by changes in the electronics and/or if the temperature sensitivity is highly compensated by other means. If the frequency of the oscillator is tuned directly, the temperature coefficient may change with the tuning voltage. This limits improvements by external compensation.

**Humidity, Barometric Pressure Changes, Magnetic Field Changes** - Typically are less significant than temperature changes. Humidity has no discernible effect on either rubidium oscillators or hermetically sealed crystal oscillators. Barometric pressure changes and magnetic field changes are well understood in rubidium oscillators, however, their effects may be hidden in crystal oscillators by temperature and humidity changes, or aging, and limit the predictability of the oscillator.

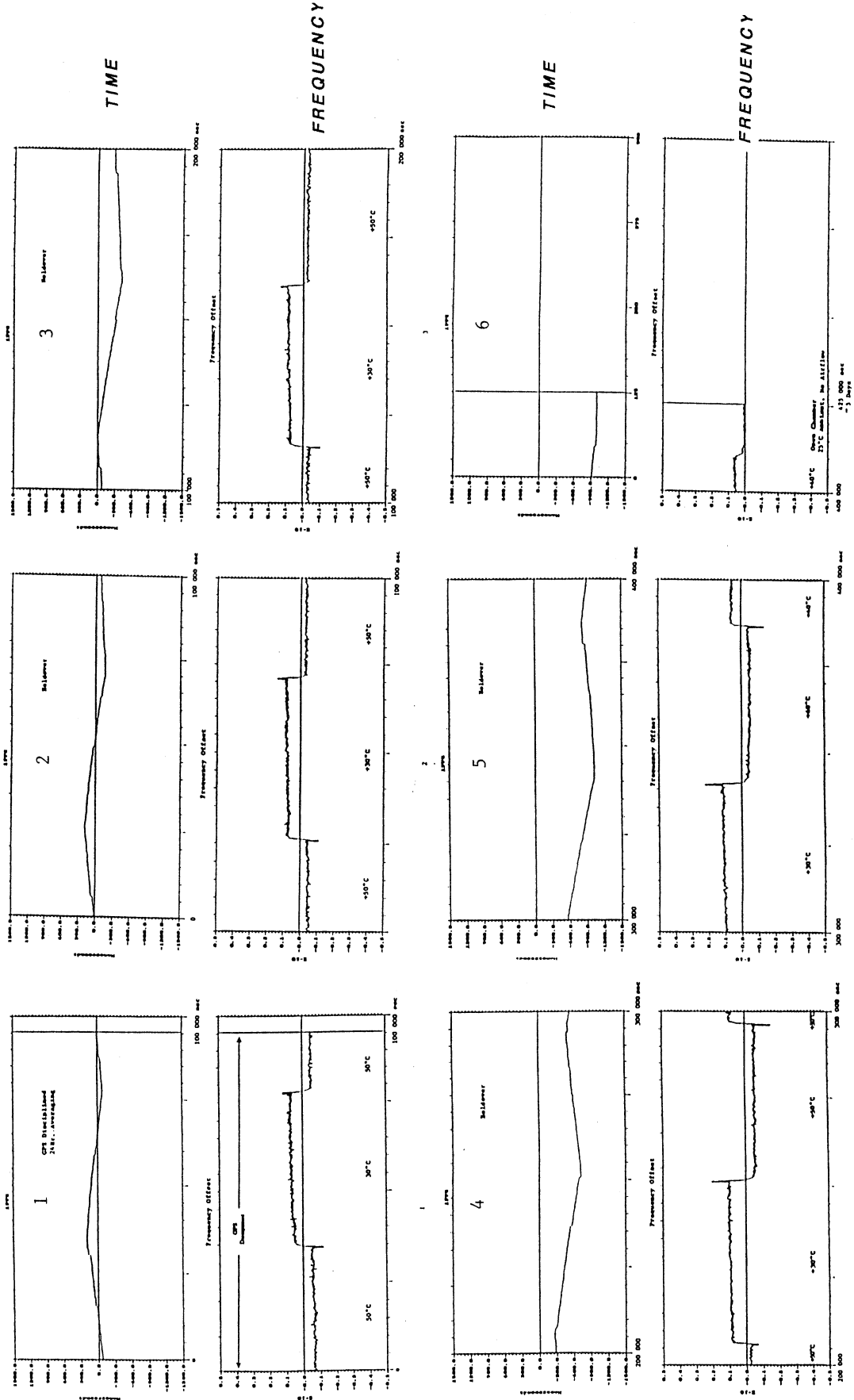
## Performance Data.

**Predicted Performance** - Table 1 predicts the holdover performance of CDMA Time/Frequency References based on rubidium and crystal oscillators under different conditions. This table gives worst case and RSS results. Table 2 predicts the performance of a Smart Solution.

**Measured Performance** - Holdover data were collected from a rubidium based T/F source in an environmental chamber. The temperature of the chamber was cycled in diurnal pattern between 30° and 60°C. The unit was powered for about 5 days before start of the tests (Figure 4).

The test should be compared to Table 2, a smart Rb based solution, exposed to  $\pm 10^\circ\text{C}$  diurnal temperature changes. The rubidium oscillator in the tested T/F source performed much better than the assumed specifications. We have seen similar performances of other T/F sources of this particular design utilizing the same type of rubidium oscillators. A major customer of ours performed two qualification tests in '96 resulting in less than 1  $\mu\text{s}$  time error over a 24 hour period. This gives credence to our expectation that we can meet the antici-

TEST RESULTS: RB BASED T/F STANDARD



±1.5 μs full scale  
±5E-11 full scale

FIGURE 4

pated performance in a large scale production environment. At this time we do not have sufficient data on quartz oscillators to make the same statement with confidence.

**HOLDOVER PERFORMANCE (μs)**

Local Oscillator	Operating Time before holdover	HOLDOVER TIME			
		24 Hrs		72 Hrs	
Rubidium Standard	> 1 day	Const. Temp.*	20°C Step	Const. Temp.*	20°C Step
				3.3 / 2.2	8.5 / 5.6
Rubidium Standard	> 3 days	1.5 / .9	6.7 / 5.3	7.1 / 4.7	22.6 / 16.2
		Crystal Oscillator	> 1 day	48.6 / 43.5	65.9 / 46.8
Crystal Oscillator	> 3 days			11.0 / 8.8	28.3 / 19.4

\* Constant Temperature or ideal diurnal temperature cycle.

**Table 1**

ASSUMPTIONS				
20°C Temperature step at beginning of holdover				Worst Case / FSS
Initial time error 100 nsec				
Operating Time Before Holdover	Rubidium		Crystal	
	Standard	"Smart"	Standard	Smart
Aging ≥ 1 day	3E-11/d	1E-11/d	10E-10/d	2E-10/d
≥ 3 days	1E-11/d	2E-12/d	2E-10/d	4E-11/d
Initial offset				
≥ 1 day	2E-11	6E-12	5E-11	2E-11
≥ 3 days	1E-11	2E-12	2E-11	4E-12
Temp. Coefficient	3E-12/°C	6E-13/°C	1E-11/°C	2E-12/°C
Stochastic Time Error : (k) > 1 day	8E-15		4E-14	
> 3 days	4E-15		2E-14	

**HOLDOVER PERFORMANCE (μs)**

Local Oscillator	Operating Time before holdover	HOLDOVER TIME, Smart Solution			
		24 Hrs		72 Hrs	
Rubidium Standard	> 1 day	Const. Temp.*	20°C Step	Const. Temp.*	20°C Step
				1.2 / .7	2.3 / 1.3
Rubidium Standard	> 3 days	.5 / .2	1.5 / 1.1	1.9 / 1.1	5.0 / 3.3
		Crystal Oscillator	> 1 day	11.5 / 8.9	14.9 / 9.5
Crystal Oscillator	> 3 days			2.7 / 1.8	6.1 / 3.9

\* Constant Temperature or ideal diurnal temperature cycle

**Table 2**

**Summary / Conclusion.**

The paper identifies the many parameters which significantly determine the performance of a T/F source in its holdover mode. Some of these parameters are inherent in the design and greatly influenced by the oscillator technology selected.

The holdover performance is mostly determined by the operating time before entering holdover, by the environmentally induced frequency changes during holdover and by the unpredictable frequency changes the oscillator may show when not disciplined by GPS. The system operator must weigh these factors as they influence the system availability. A system solution based on multiple oscillator choices seems preferable. Longer holdover time can lessen maintenance and ease the mind of the operator at a very modest cost differential. It should be noted that either technology can provide highly reliable solutions with service intervals in excess of 10 years.

Often critical oscillator parameters are not readily available to the system designer (e.g. offset and aging after power interruptions and hysteresis in temperature coefficient) and need to be discussed with the help of the manufacturer. Sometimes the manufacturer specifies performance parameters without disclosing all test conditions, leading to significant performance short-falls in the application.

**References:**

- [1] Michael King, David Busch, Mihran Miranian, **Test Results and Analysis of a Low Cost Core GPS Receiver for Time Transfer Applications**, Motorola Inc. (PNSB), 1994 National Technical Meeting, Jan 24-26, 1994
- [2] Various Data sheets from GPS Receiver Manufacturers, Rb oscillator manufacturers, and High Performance Crystal Oscillator Manufacturers
- [3] TIA / EIA IS95
- [4] Various discussions with Crystal Oscillator manufacturers.
- [5] Environmental Sensitivity of Quartz Crystal Oscillators by Fred Walls, 22nd PTTI Meeting

## AN ULTRA-LOW THERMAL SENSITIVITY IN THE MICROWAVE SYNTHESIS FOR HIGH PERFORMANCE FREQUENCY STANDARDS

Roland Barillet

Laboratoire de l'Horloge Atomique, Unité Propre de Recherche du CNRS associée à l'Université Paris-Sud,  
Bâtiment 221, UPS, 91405 - Orsay Cedex - France

Fax (33) 1 69 15 41 10 - EMail: Roland.Barillet@ief.u-psud.fr

### ABSTRACT

The frequency stability of high performance frequency standards using cold atoms should reach approximately  $10^{-16}$  for sampling times larger than 1 day. This level of performance implies very low systematic spurious effects, such as those related to the thermal sensitivity. The transfer of the frequency stability from the atomic resonator or oscillator to the output signals -usually 5MHz and/or 10MHz- requires an excellent phase coherence between the microwave local oscillator and the available output signals, which can be obtained by means of a proper PLL.

We have experimentally determined the operating conditions in which high performance or even low price mixers can provide an ultra low thermal sensitivity. The corresponding realization provides an excellent phase coherence in a multiplication or division chain : for a sinewave 5MHz to 1440MHz link, the sensitivity is about 1ps/K in a temperature range of 3 to 4 K near the usual ambient temperature, and a few ps/K in a range of 10K. The comparison with a previous generation of frequency multipliers shows a reduction of the thermal sensitivity by a factor 400.

### 1. INTRODUCTION

The theoretical estimation of the ultimate performance expected from frequency standards is classically based on "signal to noise" considerations. On that basis, the frequency stability of the cesium fountains or of the PHARAO experiment should be about  $10^{-16}$  for sampling times larger than 1 day. The practical consequence of this expectation is that systematic effects related to ageing, ambient fluctuations... must remain reasonably lower than  $10^{-16}$  in the operating conditions. In particular, the transfer of the frequency stability from the atomic resonator or oscillator to the output signals -usually 5MHz and/or 10MHz- requires an excellent phase coherence between the microwave local oscillator and the available output signals, of the order of 1ps/K versus temperature.

Wideband amplifiers and presently available low noise frequency dividers are able to provide a very low thermal sensitivity [1]: consequently, a carefully designed PLL should be able to maintain an excellent phase coherence between a 5 or 10MHz sinewave signal and a microwave LO signal if frequency mixers also show a low thermal sensitivity. An investigation of this kind of requirements was made [2] and it shows that the use of

mixers at 5 or 10MHz does not seem able to fulfill the previous requirement. However, thermal drifts about 10 or 20 ps/K at 5MHz over a wide range of temperature are not compatible at all with the usual offset specifications of the mixers : consequently, it is probable that these thermal sensitivities are not constant in the whole temperature range and that they may show optima. Or else there are other additional effects that are to be investigated.

We have decided to check the behavior of various mixers versus temperature for different operating conditions. This led us to observe that, with high performance mixers as well as with low price mixers, it is possible to find operating conditions that provide an ultra low thermal dependence in a moderate temperature range (5 to 10K) in the vicinity of the ambient temperature. The implementation of the corresponding rules in a 1440MHz- 5MHz (sine) link confirms the efficiency of this approach.

### 2. OPTIMUM CONDITIONS FOR MIXERS OPERATED AT 10MHz

On the one hand, a previous paper already mentioned [2] indicates a fundamental means that makes it possible to reduce the thermal sensitivity of mixers : a satisfactory impedance matching. We have widely used this guideline. On the other hand, we have investigated the detailed evolution of the apparent phase shift (LO-RF) versus temperature for various loads of the IF output of the mixer.

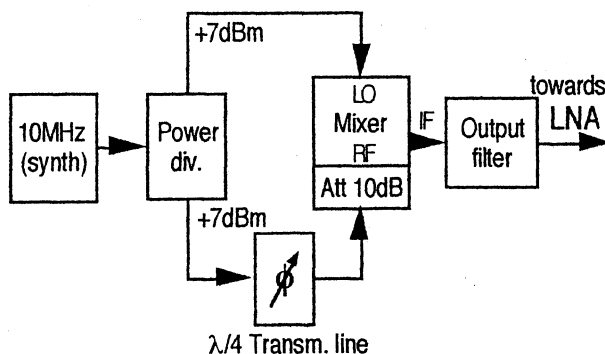


Fig.1 : 10MHz measurement system

We had observed [1] that the LO input is better matched when attacked via a 15Ω serial resistor placed just near the LO input : most of our measurements were made with this serial resistor (not mentioned in the figures). The measurement bench is shown in fig.1. It is quite classical, and a precise adjustment of the quadrature is possible in order to find the phase shift (slightly different from the apparent quadrature) that suppresses the effect of amplitude fluctuations. This operating condition is not completely necessary, but it helps a lot for the measurements.

The low noise DC amplifier (LNA) that follows the output filter is a LT1028 operational amplifier. We have measured its temperature sensitivity (0,02ps/K), which does not contribute significantly to our following measurements.

Two types of double balanced mixers have been checked at 10MHz : a high performance mixer (Hewlett Packard 10514B) which is no longer commercially available, and a low price mixer (Mini Circuits Labs. SRA1). Various loads of the IF output have been tried, either capacitive loads in order to obtain a high slope of the phase detection, or matched loads (only for the high frequency components, not at DC) in order to fulfill the usual operating conditions.

### 2.1. OPTIMUM CONDITIONS FOR A HIGH PERFORMANCE DOUBLE BALANCED MIXER

Three different IF loads were tried :

- the first one was a capacitive load (22nF) followed by a low-pass filter (50Ω, 22nF) in order to suppress the residual high frequency components. The corresponding thermal behavior of the output signal - hence of the apparent phase shift between LO and RF signal - is shown in fig2. One observes an optimum in the vicinity of 28°C and a 4K temperature range where the peak to peak phase fluctuation is ≈1ps, which is quite satisfactory. In fig.2, crosses are experimental results and the continuous line is the third order polynomial fit, also used in the next figures. Vertical unit is ps (10<sup>-12</sup>s)

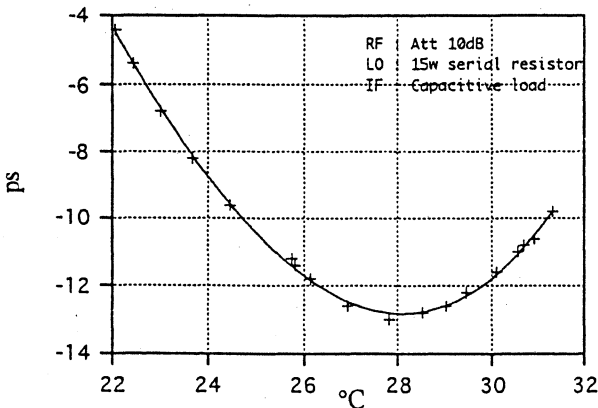


Fig 2 : Thermal sensitivity of a high performance double balanced mixer

- the second IF load was a HF matched load (50Ω at high frequency, but high impedance at DC). The

corresponding results, represented in fig.3, are similar to those of fig.2, but the optimum temperature range is at a lower temperature. This shows that for this kind of mixers, a change in the IF load can slightly change the optimum operating conditions. This effect can be related to the temperature coefficient of the load capacitor used in the previous configuration, or to a change in the behavior of the mixer itself.

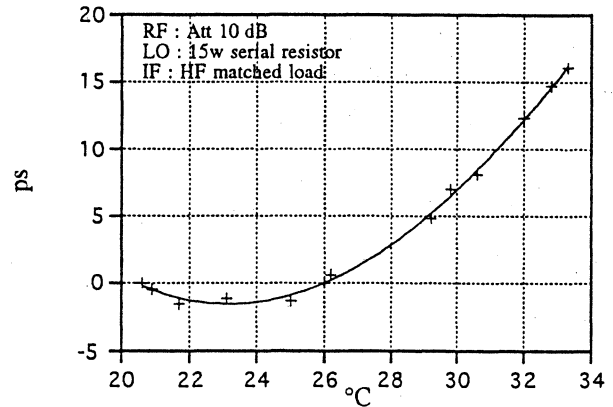


Fig 3 : Thermal sensitivity of a high performance double balanced mixer

- the third IF load was identical to the previous one (HF matched load), but the attenuation at the RF input was 16dB instead of 10dB previously : an optimum seems to be located at lower temperature, and the general behavior is similar.

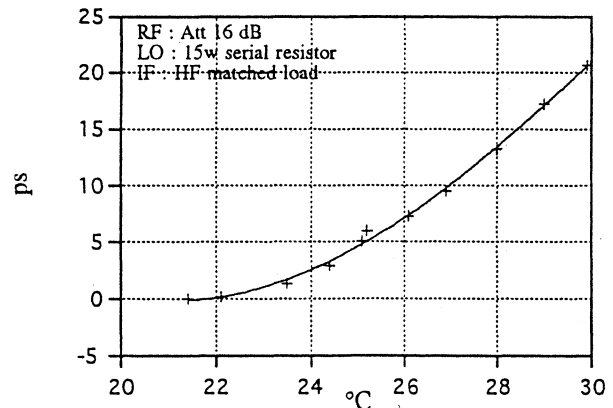


Fig 4 : Thermal sensitivity of a high performance double balanced mixer

In any case, it is possible to find a temperature range where the thermal sensitivity fulfill the 1ps/K requirement.

We think that this effect was not observed previously [2] because the temperature range was different (29 to 39°C approximately), the attenuation at the RF input was only 6dB and there was no serial resistor before the LO input.

## 2.2. OPTIMUM CONDITIONS FOR A LOW PRICE DOUBLE BALANCED MIXER

We frequently use these mixers (MCL SRA1) and it seemed interesting to determine their ultimate possibilities about thermal sensitivity. We used the same measurement bench as in fig.1 with a  $\lambda/4$  transmission line phase shifter.

- first configuration : attenuator 10 dB at the RF input, no serial resistor at the LO input and high frequency matched load at the IF output. The thermal sensitivity is shown in fig.5. Obviously, the effect is much stronger than previously, and the mean slope is approximately 7ps/K, which is not satisfactory.

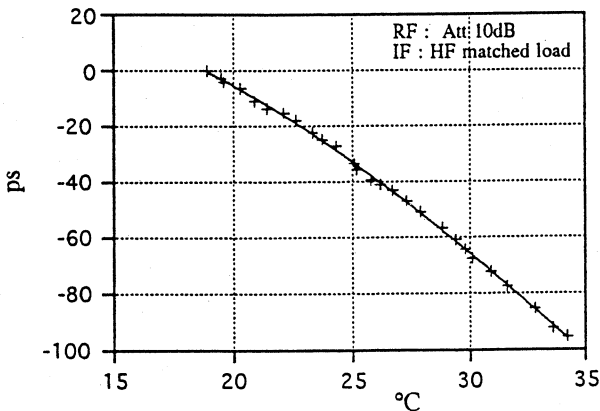


Fig 5 : Thermal sensitivity of a low price double balanced mixer

- second configuration : attenuator 10 dB at the RF input, 15 $\Omega$  serial resistor at the LO input and high frequency matched load at the IF output. One observes (fig.6) a reduced slope, slightly lower than 5ps/K. This value is not yet satisfactory compared to our requirement.

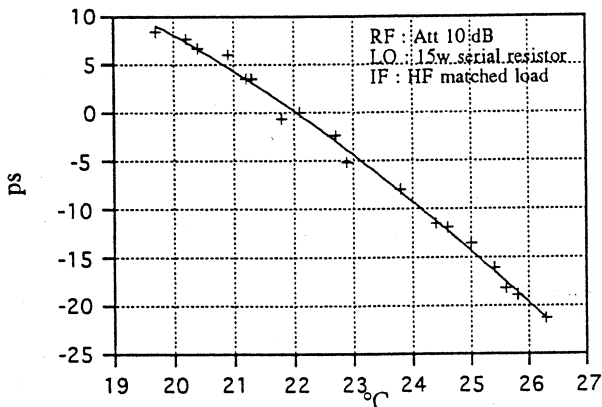


Fig 6 : Thermal sensitivity of a low price double balanced mixer

- third configuration : attenuator 10 dB at the RF input, 15 $\Omega$  serial resistor at the LO input and capacitive load (22nF) at the IF output. One observes (fig.7) a moderate slope (2ps/K), which is better around 22°C (1.4ps/K), but there is no optimum temperature. In this configuration where the gain of the mixer is the highest of the three configurations, we obtain a result which is almost satisfactory.

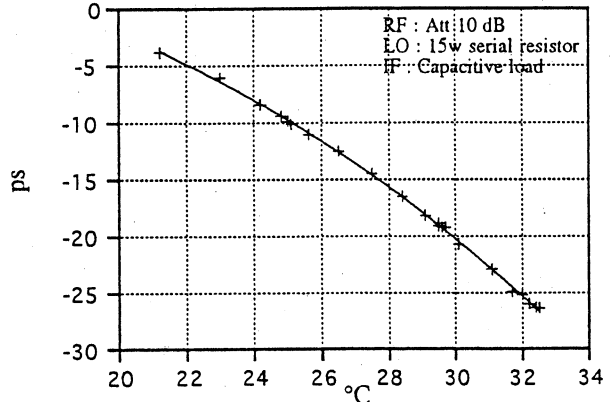


Fig 7 : Thermal sensitivity of a low price double balanced mixer

As a preliminary conclusion, we can say that low price mixers operated around 20°C show a low thermal sensitivity, that can be almost as good as that of high performance mixers.

## 3. OPTIMAL CONDITIONS FOR DIVIDERS AND MIXERS OPERATED AT 5MHz

Our plan was to use a low noise programmable divider (GEC-Plessey SP8400) in order to phaselock a 5MHz USO on a microwave signal (1440MHz). Preliminary tests were made with the apparatus presented in Fig.8. The mixer was a low price Surface Mounted Device (MCL - RMS1), loaded by 44nF. A wideband amplifier - not mentioned in fig8 - is located at the output of each divider, to attack the mixer.

One of the dividers was in a box B1, the second divider, the mixer and the low noise amplifier (LNA) in a second box B2. B1 and B2 could be cooled or heated separately by a Peltier element. We measured the phase noise of the SP8400 frequency divider : in our operating conditions - IN=1440MHz, OUT = 5MHz - the spectral density  $S_{\phi}(f)$  of the phase fluctuations shows the two usual components : a flicker phase noise (-140dBc/Hz @ 10Hz) and a white phase noise (-152dBc/Hz), measured at 5MHz. These values are consistent with those indicated in the data sheet.

The thermal sensitivity of the SP8400 divider is presented in fig.9. Its slope is almost constant  $\approx$  1ps/K.

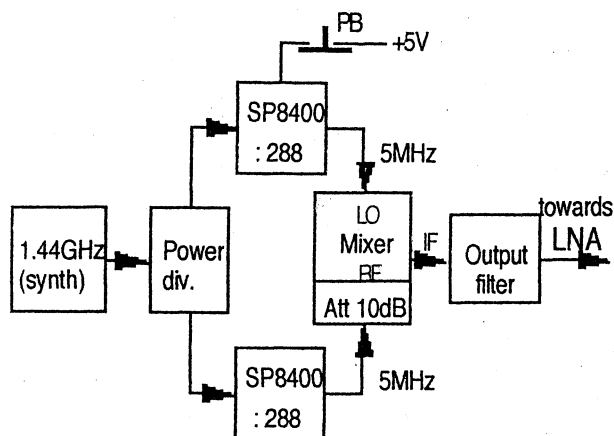


Fig.8 : measurement system with 1.44GHz input signal, frequency divider (: 288) and mixer

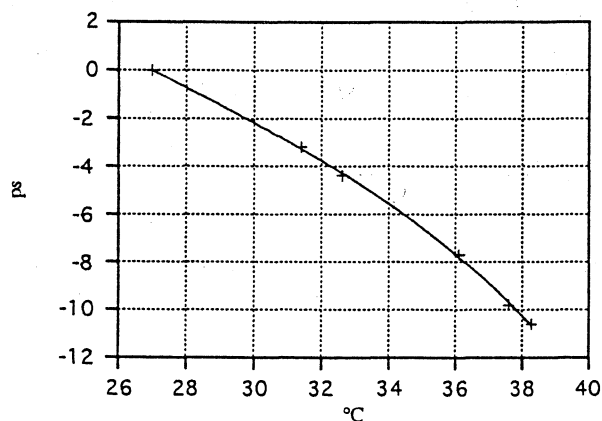


Fig 9 : Thermal sensitivity Divider SP8400

For these measurements, we had changed our experimental procedure concerning the phase adjustments. Indeed, the output level of the dividers is very stable and consequently the adjustment of the phase is less critical than in the first measurements, where we used a frequency synthesizer. Furthermore, frequent actions on SMA connectors quickly degrade their quality, so we preferred to roughly adjust the phase without any action on the connectors. It was made by means of a push-button - PB, in the upper part of fig.8- that enabled us to switch off and on the +5V supply of the divider. Statistically, we were in the vicinity of the quadrature much more quickly than with a length adjustment, and without consequence for the connectors. However, this new experimental procedure induced an unexpected problem : the first experimental results concerning B2 (divider+mixer) were not consistent ! We measured a thermal sensitivity that was either low or rather high! In fact we understood that the measurements were splitted into two groups, related to the output slope of the mixer, which was randomly positive or negative. An easy test using a 2.2pF capacitor enabled us to group the results concerning the two possible slopes.

The corresponding results are shown in fig.10 : the "bad" slope A of the mixer provides a quasi linear thermal sensitivity  $\approx 25\text{ps/K}$ , whilst the "proper" slope B shows a very low thermal sensitivity, with an optimum which provides a 3K temperature range with 1ps (p-p), not very obvious on the figure.

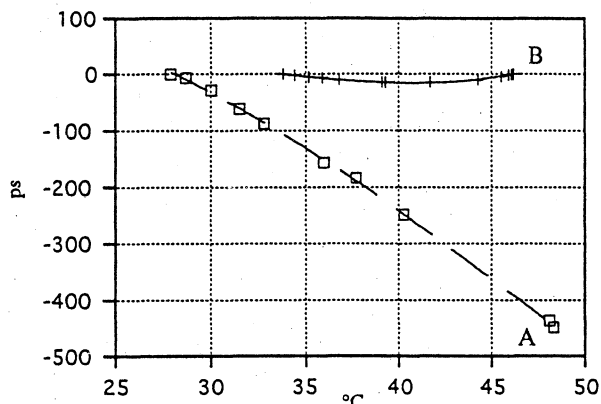


Fig 10 : Thermal sensitivity (Divider SP8400 + Mixer RMS1)

A possible explanation of the previous observation is that two phenomena are concerned : the first is related to the change of the dynamic resistance of the diodes with temperature in presence of an unbalance, the second is due to probable thermoelectric effects in the IF output of the mixer : depending on the slope of the IF signal, these effects are added or subtracted.

It must be noticed that this result is obtained with square wave signals at RF and LO inputs. For a different configuration where one or two sinewave signals are used, the result may be different : we have observed that the effect always exists, but the difference A to B is less violent than with square signals.

#### 4. OPTIMIZED PHASELOCKED LOOPS AND EXPERIMENTAL RESULTS

The previous experiments indicate useful guidelines to reduce the thermal differential sensitivity of the phase (RF-LO) in the mixer, but they do not check the possible common mode phase shift that may exist in the mixer operation. To check it, we have realized two identical PLLs : the block diagram is presented in fig11. The mixer (RMS1 by MCL) operating conditions fulfill the following conditions : 10Ω serial resistor just at the LO input, 10dB attenuator just at the RF input, capacitive load at the IF output, and choice of the proper slope by the proper sign in the feedback. Usually, with a double balanced mixer, the PLL locks by itself because it finds the proper slope. But here we must choose the slope that provides the minimum thermal effect. This adjustment is made separately for each PLL. After that, the system is approximately in optimum operating conditions. The performance of PLL B2 was checked, and is shown in fig.12.

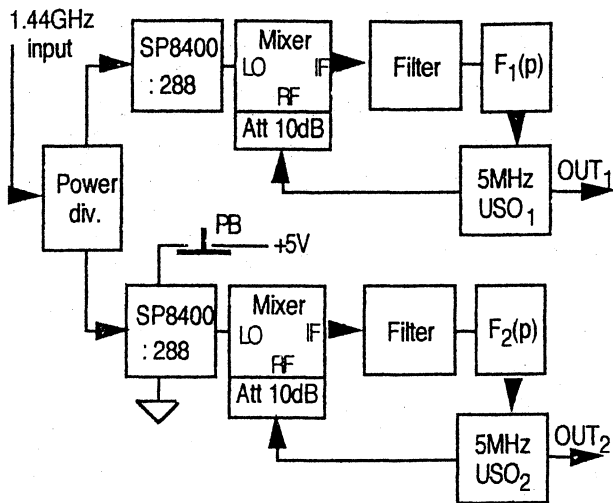


Fig.11 : measurement of the thermal sensitivity of the 1.44GHz - 5MHz PLLs

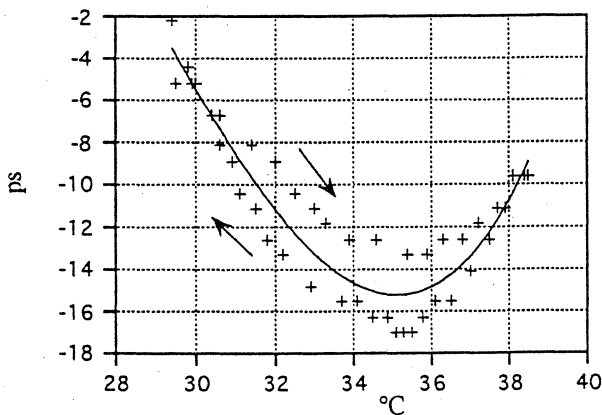


Fig 12 : Thermal sensitivity of the PLL (5-1440MHz)

The hysteresis-like behavior is in fact related to the "speed" of the temperature changes : it is twice larger when the experiment is made more quickly, which shows that it is not induced by a linear drift of the phase.

We must precise that, at such low levels of phase fluctuations ( $\approx$  a few  $10^{-5}$  rad), other tiny effects may be observed, such as the sensitivity of cables, boxes, substrates to various disturbances, for example stresses or proximity effects. We have tried to sweep very slowly the temperature of the D.U.T, but small effects probably related to ambient disturbances or to temperature fluctuations of the second PLL - the reference - have slightly disturbed our result : the "up" and "down" curves were not superimposed better than in fig12. A more complete test bench using additional thermal regulations and an improved EMC configuration are necessary in order to precisely measure the thermal response of these 5MHz-1440MHz links. Presently, we can say that the PLL B2 is able to maintain a phase coherence of a few ps between the 5MHz and 1440MHz

signals for an operating (inner) temperature of  $35^{\circ}\text{C} \pm 2^{\circ}\text{C}$ .

Finally, we have used this PLL (B2) to measure the thermal sensitivity of the phase in a frequency multiplier  $5 \rightarrow 1440\text{MHz}$  of an old generation, similar to that used in our M3 H-maser. After a 2 days acquisition, the result was about  $400\text{ps/K}$  ! Consequently, the PLL B2 will be used to provide the 5MHz output signal of M3 : this additional element should almost completely suppress the thermal sensitivity of M3 electronics.

## CONCLUSION

The optimum operating conditions of various balanced mixers make it possible to maintain the phase coherence, between a 5 or 10MHz sinewave signal and a microwave local oscillator, at the level of a few picoseconds in a temperature range of several K. With a moderate thermal regulation, a sub-picosecond phase coherence should be possible, thus allowing an easy observation of the performances expected from the future super-clocks and its link to other existing frequency standards.

## ACKNOWLEDGEMENTS

We gratefully acknowledge F. Hamouda for his help during this work, and F. Walls for our many fruitful discussions about these topics.

## REFERENCES

- [1] R. Barillet - "Thermal effects in high performance frequency synthesizers"- Proc. of the 1997 IEEE Freq. Contr. Symp., Orlando (USA), 28-30 may 1997, pp980-984
- [2] F.Walls et al, "Designing for frequency and time metrology at the  $10^{-18}$  level" - Proc. of the 1992 EFTF, ESTEC, Noordwijk, NL, 17-19 march 1992, pp477-481
- [3] R. Brendel et al, "Phase and Amplitude Modulation effects in a phase detector using an incorrectly balanced mixer", IEEE Tr. on Instr. and Meas. Vol IM26, N°2, june1977, p 98-102

*12th E F T F* - 10÷12 March 1998 - Warsaw - POLAND

**Telecom & space applications**

Chairman:

*Pekka Eskelinen*



## ROBUST ESTIMATION OF TDEV

Andrzej Dobrogowski, Mieczysław Jessa, Michał Kasznia

Institute of Electronics and Telecommunications  
Poznan University of Technology  
Piotrowo 3A, 60-965 Poznan, Poland

### ABSTRACT

In the paper the problem of time deviation calculation in the presence of impulse noise is presented. In the first section authors introduce the problem. The essence of robust preprocessing in TDEV calculation is emphasized. In the next parts some method of robust TDEV estimation is described. Then the results of TDEV computations with and without robust preprocessing are presented.

*Keywords: time error (TE), time deviation (TDEV), impulse noise, robust preprocessing*

### 1. INTRODUCTION

Measurements of the parameters of synchronization (timing) signal are very important in the exploitation of digital telecommunication network. Timing signal has a global consequence for the network. This signal provides digital processes running in the network with time scale. Proper work of all devices in the network and correct transmission of data depend on the quality of timing signal. Thus the servicemen must know the parameters of timing signal at some interfaces of telecommunication network. The parameters, measured and/or calculated at the interface should be compared with standards defined by international standardization bodies.

Unfortunately, there is possibility to get the measured timing signal contaminated. The contamination has an influence on the result of calculation of the parameters and can change the opinion about the quality of timing signal. The result of calculation differs from real value of the parameter, because the reason of contamination is outside of timing or reference signal generation mechanism. In such a case repeating the parameters' measurements and calculations is the must. In the work time deviation (TDEV) is the analyzed parameter. In order to calculate time deviation, the time error measurement must be done. The standards require the time error measurement interval for TDEV calculation to be at least twelve times bigger than the observation interval  $\tau$ . For observation interval  $\tau=100000$  s the measurement of time error have to be done during two weeks. Any contamination, which appears in timing or time error signals during this period and changes the result of TDEV calculation, ought to disqualify measured sequence. Necessity of repeating the two

weeks measurement may be inconvenient or impossible. Also, it is not certain, that the repeated measurement process will be free of contamination. Thus, for elimination of this contamination (impulse noise), the robust preprocessing of the time error sequence is proposed. The preprocessing is provided before the TDEV computation and may be realized in real time, during the measurement process.

In the paper the methods of TDEV calculation are described. The simplified algorithm of TDEV calculation is presented. Results of several computations based on contamination free and contaminated data are included and commented. The robust preprocessing algorithm for time error signal cleaning is proposed. Also the results of TDEV calculations with preprocessing are presented.

### 2. TDEV CALCULATION METHODS

The basic characteristic of timing (synchronization) signal is time error function (TE). Time error of timing signal under consideration with respect to a frequency standard, is the difference  $x(t)$  between the time of that signal and a frequency standard one. Using time error values other parameters characterizing timing signal are calculated. In the telecommunication standards some conditions for the measurement of time error are specified. Time error should be measured using an anti-aliasing filter with the cut-off frequency  $f_0$ . The minimum observation interval  $\tau_{\min}$  must be three times greater than maximum sampling interval  $\tau_0$  and the anti-aliasing filter cut-off frequency  $f_0$  must be equal  $f_0=1/\tau_{\min}$ . The minimum value of measurement period  $T$  for time deviation calculation should be twelve times longer than the observation interval  $\tau$ . For the parameters calculations the time error samples should be stored in the memory of measuring system.

In the telecommunication standards the formulas for the parameters are defined. Time deviation can be estimated from

$$\hat{TDEV}(\tau) = \sqrt{\frac{1}{6n^2(N-3n+1)} \sum_{j=1}^{N-3n+1} \left[ \sum_{i=j}^{j+n-1} (x_{i+2n} - 2x_{i+n} + x_i) \right]^2} \quad (1)$$

where

$\{x_i\}$  - sequence of  $N$  samples of time error function  $x(t)$  taken with interval  $\tau_0$ ;

$\tau=n\tau_0$  - observation interval.

The time spend for the TDEV estimate calculation can be reduced if we notice that the estimator can be presented in the form

$$T\hat{DEV}(n\tau_0) = \sqrt{c(n) \sum_{j=1}^{N-3n+1} S_j^2} \quad (2)$$

where

$$c(n) = \frac{1}{6n^2(N-3n+1)}$$

$$S_j = S_{j-1} - x_{j-1} + 3x_{j+n-1} - 3x_{j+2n-1} + x_{j+3n-1}$$

$$S_1 = \sum_{i=1}^n (x_{i+2n} - 2x_{i+n} + x_i)$$

Both formulas (1) and (2) are identical.

Time deviation converges for all major noise types affecting current timing signals. Any frequency offset of a timing signal, relative to the reference signal, has no influence on TDEV (Ref. 3).

In order to speed-up the computation of TDEV the modification of procedure given by (2) was proposed (Ref. 2). The calculations of TDEV are divided into the segments. For the sampling interval  $\tau_0=1/30$  s and the maximum observation interval  $\tau=100000$  s, the segments are as follows: 0.1 s-1 s, 1 s-10 s, 10 s-100 s, 100 s-1000 s, 1000 s-10000 s, 10000 s-100000 s. For each calculation segment the set of time error samples used for computation and the interval between samples are modified. In the first two segments the raw data are used for calculation without any change. The data interval  $\tau'_0$  used for computation equals to the sampling interval  $\tau_0$ . In the next segments the data interval  $\tau'_0$  is magnified ten times. In the third segment (10-100) we have  $\tau'_0=10\tau_0$ . The samples of time error are grouped into the subsets of ten items and the average value for each group is calculated. This average is an item in the new data set. The modifications are made for each segment. In general, for all values of  $\tau_0$ , the first segment is  $(3\tau_0-30\tau_0)$  and the modification starts for observation interval  $\tau=300\tau_0$ . As the result of the data modification we get shorter data sequence and smaller computation time. The results of TDEV computations with and without modifications were presented and compared in (Ref. 2). The relative error between the results was less than 1%.

### 3. ROBUST PREPROCESSING

The contamination, defined also as impulse noise, outliers or gross errors, are the wrong values of measurement. In the case of timing signal the most serious cause resulting in outliers are sudden or very fast changes of phase with considerable magnitude. There are many reasons of very fast phase changes. Among them are (Ref. 1):

- fading of synchronization signal;
- temporary out-of-synchronism condition of different pieces of equipment of synchronization chain along which the timing signal is transmitted;
- switching events affecting synchronization chain;

- environmental sensitivity of the measuring equipment. Very often outliers can be interpreted as an impulse noise. Because the impulse noise can change the result of TDEV calculation, the noise should be suppressed first. For that goal a preprocessing algorithm was proposed (Ref. 1). The preprocessor, based on DPCM modulator is shown in Fig. 1. In *predict-and-compare loop* the input signal (time error)  $x_i$  is compared with the predicted signal  $\hat{x}_i$ . The error  $e_i$  is cleaned in signal cleaning block. Then the cleaned value of error  $\tilde{e}_i$  corrects the predicted signal  $\hat{x}_i$  and the result  $\tilde{x}_i$  goes out of the preprocessor. For the preprocessor implemented we assumed the predicted value as an average of  $m$  last output values  $\tilde{x}_i$ . The predictor tracks the trend in time error signal  $x(t)$ . The signal cleaning block removes all the changes exceeding some threshold value. In the block two cleaning functions are used. First, the Huber's function  $\psi(\cdot)$  given as

$$\psi(u) = \min(g, \max(u, -g)) \quad (3)$$

where  $g$  is the threshold. Second cleaning function adopted  $\psi_2(\cdot)$  is given by

$$\psi_2(u) = \begin{cases} 2g & u > 3g \\ 0.5(u+g) & 3g \geq u > g \\ u & g \geq u \geq -g \\ 0.5(u-g) & -g > u \geq -3g \\ -2g & u < -3g \end{cases} \quad (4)$$

Both functions are presented in Fig. 2.

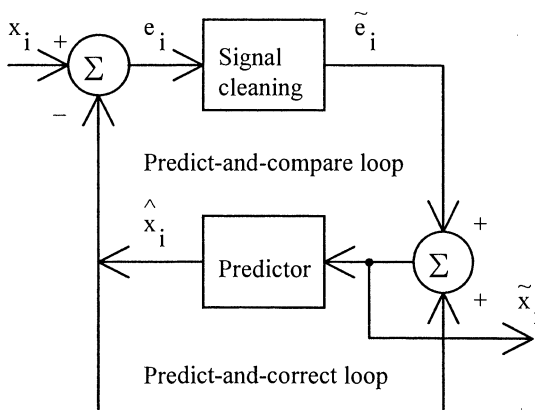


Fig. 1. Impulse noise removing preprocessor

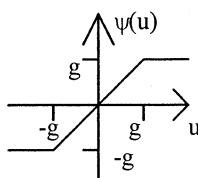


Fig. 2a. Huber's function

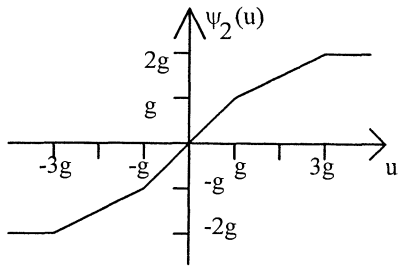


Fig. 2b.  $\psi_2(\cdot)$  cleaning function

Fig. 2. Cleaning functions

#### 4. TDEV CALCULATIONS

##### 4.1. Time error data

We get time error data from measurement lasting 4 hours. The sampling interval was  $\tau_0=1/30$  s. None impulse noise was assumed. The results of measurement are presented in Fig. 3. The corresponding results of TDEV calculations for observation intervals changing from 0.1 s to 1000 s are presented in Fig. 4. The calculations were performed without modifications described in section 2.

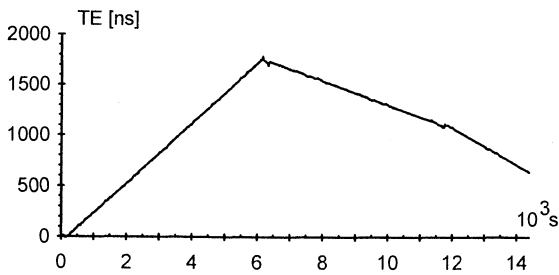


Fig. 3. Time error used for TDEV computations

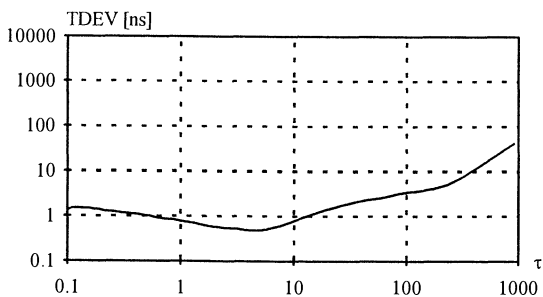


Fig. 4. Results of TDEV calculations for noncontaminated data

##### 4.2. Time error sequence contaminated by impulse noise

The time error sequence contaminated by impulse noise was considered next. For each time error sample contaminating impulse appeared with probability  $p$ . The impulse took the value from the intervals  $(-15; -5)$  and  $(5; 15)$  with uniform probability density. The impulses were generated in the burst mode. The rule for burst

generation was as follows. When the impulse appeared, the probability of impulse within the next  $k$  time error samples was increased to the value of  $p_1$ . In the work the impulse noise was generated with probabilities  $p=0.01$ ,  $p_1=0.25$  and with burst length  $k=10$ .

The preprocessor described in section 3 is used for removing the impulse noise from the time error sequence. The threshold in signal cleaning block is  $g=5$  and the number of preceded samples in the predictor block is  $m=5$ . In Fig. 5 - 7 1000 first samples used in TDEV computations are presented. We can see, that the preprocessor having Huber's clearing function clears the data. For comparison, in Fig. 8 the output of predictor is presented.

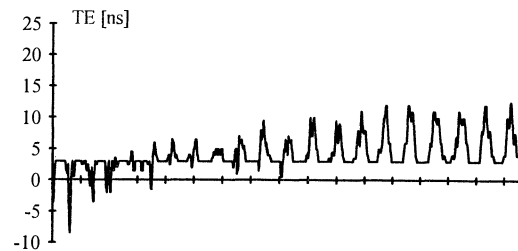


Fig. 5. First 1000 samples of time error

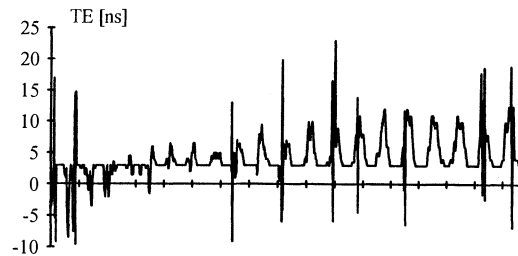


Fig. 6. Contaminated time error sequence



Fig. 7. The output of robust preprocessor

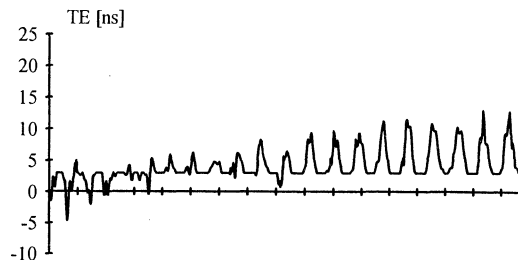


Fig. 8. The output of predictor in robust preprocessor

### 4.3. Results of TDEV calculations for contaminated data

In Fig. 4 time deviation for noncontaminated time error sequence is presented. For contaminated data the calculations of TDEV were made for three types of time error sequence:

- time error sequence with contamination without preprocessing;
- contaminated time error sequence after robust preprocessing with Huber's cleaning function;
- contaminated time error sequence after robust preprocessing with  $\psi_2(\cdot)$  cleaning function.

For each sequence the calculations were made without and with modification procedure described in section 2. The relative errors between the obtained results and the value of TDEV given in Fig. 4 were computed. The relative errors for calculations without modification are presented in Fig. 9 - 11.

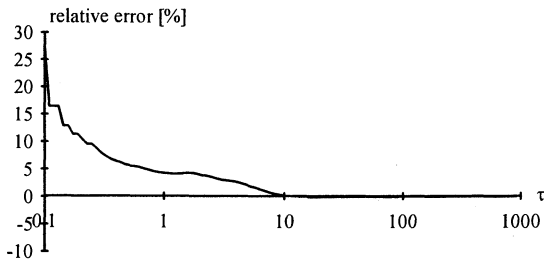


Fig. 9. Relative error for TDEV calculation without preprocessing

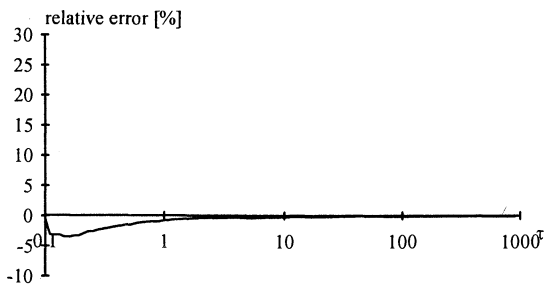


Fig. 10. Relative error for TDEV calculation with preprocessing with Huber's cleaning function

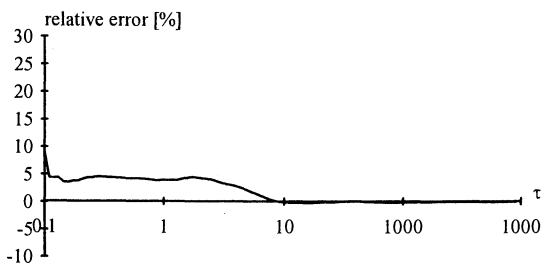


Fig. 11. Relative error for TDEV calculation with preprocessing with  $\psi_2(\cdot)$  cleaning function

The relative errors for calculation with modification procedure described in section 2 are presented in Fig. 12 - 14.

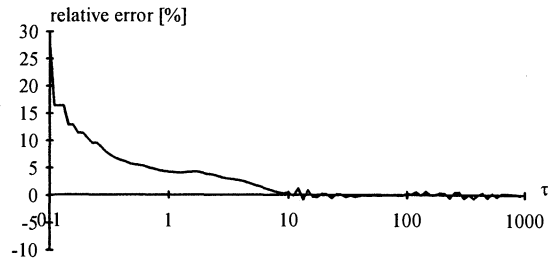


Fig. 12. Relative error for TDEV calculation without preprocessing

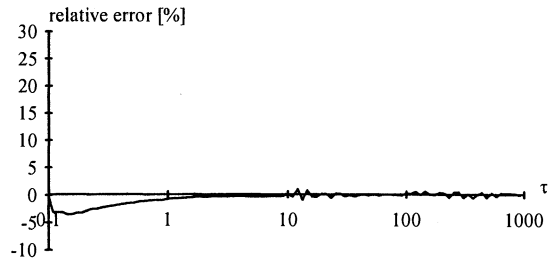


Fig. 13. Relative error for TDEV calculation with preprocessing with Huber's cleaning function

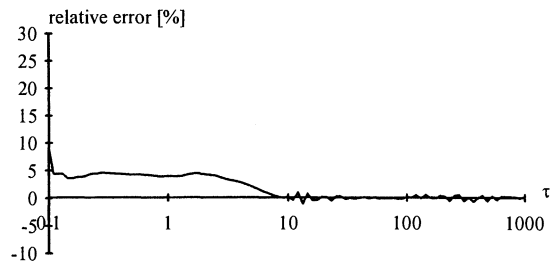


Fig. 14. Relative error for TDEV calculation with preprocessing with  $\psi_2(\cdot)$  cleaning function

In both cases (without and with modification procedure) the greatest value of the relative error for contaminated sequence is about of 25% and appears for small observation intervals. The relative error falls down with the length of observation interval. For observation intervals larger than  $\tau=10$  s the influence of contamination is very small. Relative error is falling down after using robust preprocessing. For the cleaning function (3) the relative error does not exceed 5%. For the cleaning function (4) the relative error is about 8% for the smallest observation intervals and about 5% for the intervals not greater than 10 s. For both cleaning functions the relative error is negligible for the observation intervals greater than 10 s.

## 5. CONCLUSIONS

In the paper the method of robust preprocessing in TDEV estimation is proposed. The impulse noise contaminating the results of measurement can seriously change the value of calculated parameters of timing signal. The influence of impulse noise is quite considerable for rather short observation intervals and almost completely vanishes for longer ones (for  $\tau$  greater than 10 s in our simulation experiment). The results of TDEV calculation for contaminated data sequence with and without preprocessing are presented. Presented robust preprocessing algorithm effectively limited the adverse influence of impulse noise. Time error sequence used in calculations was obtained using SP-2000 measuring system. The system was designed in Institute of Electronics and Telecommunications Poznan University of Technology. The algorithms presented in the work were applied in the software of the SP-2000 system.

This work was performed in the frame of the project TB-44-536/98/DS.

## REFERENCES

1. Dobrogowski A., 1997, Robust Statistics and Diagnostics of Timing Signal, Proc. of 11th European Frequency and Time Forum, Neuchatel 4-6 March, pp 86-90.
2. Kasznia M., 1997, Some Approach to Computation of ADEV, TDEV and MTIE, Proc. of 11th European Frequency and Time Forum, Neuchatel 4-6 March, pp 544-548.
3. European Telecommunication Standard. Transmission and Multiplexing; Generic requirements for synchronization networks. ETSI 1995.

## REFERENCE SIGNAL MANAGEMENT IN WDM NETWORKS

Masami Kihara and Kenji Hisadome

NTT Optical Network Systems Laboratories  
1-1 Hikari-no-oka, Yokosuka-shi, Kanagawa, 239 Japan  
Tel:+81-468-59-3164 Fax:+81-468-55-1282  
e-mail:kihara@exa.onlab.ntt.co.jp

### Abstract

WDM (Wavelength Division Multiplex) systems are indispensable if future transmission systems are to cope with the growth in bandwidth demand for multimedia services such as Internet applications. WDM technologies can achieve both simple multiplexing and efficient routing in optical layers with the minimum of electrical processing and conversion between optical and electrical signals. They are very effective in terms of performance such as jitter, wander, error, and reliability. Especially regarding reference signals such as timing clocks, and time and synchronization information, only WDM network can revolutionize the management of reference signals in broadband networks following the introduction of SDH systems.

This paper describes the effectiveness of WDM networks for reference signal performance, new management schemes for reference signals and reference signal distribution systems.

### 1. Introduction

While networks have evolved such as the move to Synchronous Digital Hierarchy (SDH) and Asynchronous Transfer Mode (ATM), the basic reference signal transfer network has not changed since the introduction of digital synchronous systems. The reference timing clock is transferred one way from a higher node to a lower slave node. The lower node trusts the transferred electrical reference timing clock and hastens to synchronize to it. The problem of this mechanism is that no node except the master node knows for sure what the best reference signal is and how accurate the re-

generated reference signal is.

Two methods are used in SDH-based networks to transfer reference signals: section transfer through cascaded slave clocks and additionally through SDH equipment clocks (SEC), and path transfer using paths built up by SDH virtual containers. The disadvantage in both methods in terms of reference performance is the degradation due to multi-linking and pointer processing, respectively.

The optical path concept in Wavelength Division Multiplex (WDM) networks[1] can advance reference signal management including the transfer mechanism and configuration. It can achieve both single linking in the path transfer and high performance close to the original reference.

This paper describes reference signal management based on the optical path concept, with a brief look at a unique reference signal in WDM networks, optical frequency.

### 2. Optical path in WDM networks[1]

WDM technologies can bring us to the world of broadband networks in which network nodes handle data streams wider than several hundreds of Gb/s. Figure 1 shows the future transmission network. SDH networks are partitioned and connected to each other via the WDM network. The WDM network however ought not to be regarded as the network that just connects several SDH networks in a transmission media layer. The WDM network provides SDH virtual container

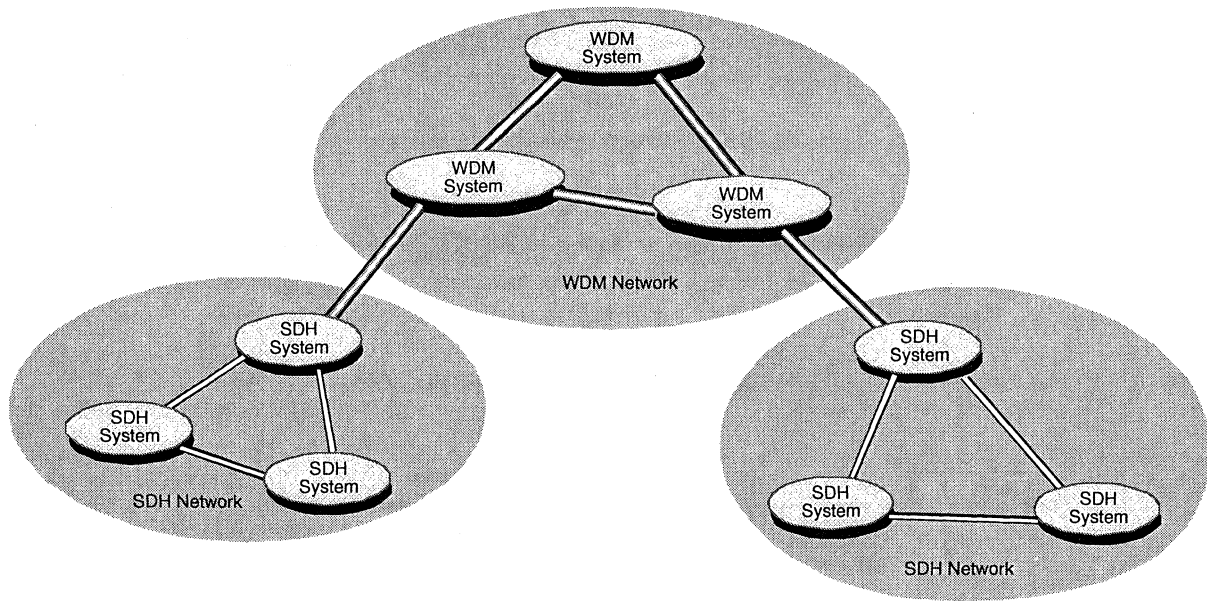


Fig. 1 - WDM network and partitioned SDH networks

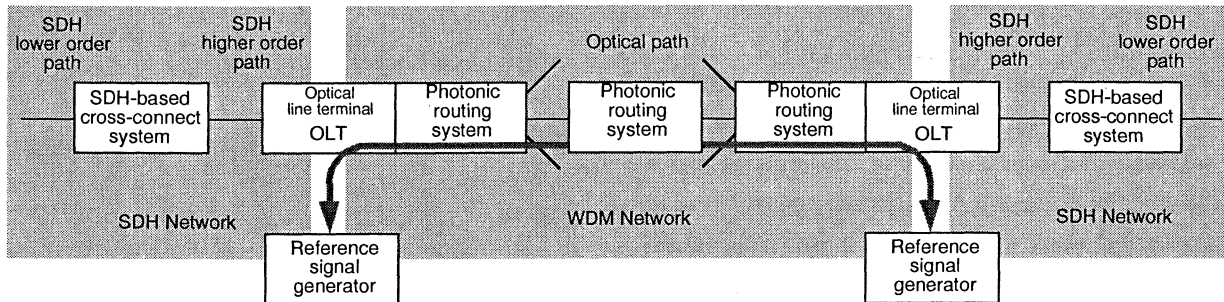


Fig. 2 - Optical Line Terminal (OLT) in the WDM network

trails throughout the network in the most reliable way and with the best quality through its routing function or the cross-connection of optical paths. Network partitioning is a most important technique in large networks, since it enables each network to perform restoration, Quality of service (QoS) management, and connection management independently.

The other important technique in the WDM network is path management based on the optical path concept. Lower order SDH paths and ATM virtual paths are bundled into higher order SDH virtual containers such as VC-4, and are managed as a single optical path. Reduce managed object number is very effective in enhancing operation system performance. Reference signal management shows the same effect as general path management.

Remapping from the SDH virtual container to the op-

tical container, and vice versa is executed in an Optical Line Terminal (OLT: Fig. 2). Multiplex and regenerator sections in the SDH network, and the optical path in the WDM network are terminated in the OLT. Since the OLT is a gate of the node, it must terminate the reference signals as well. This implies that the optical path equals a reference signal path. The reference signal path can take advantage of the optical path.

### 3. Clock distribution network based on optical paths

There are two clock distribution systems for SDH networks. One utilizes a SDH lower order path layer as shown in Fig. 3 (a). The reference timing clock, that is reference frequency, is transferred as a clock component of the path layer. This system is the same as the timing clock distribution system in PDH networks; however, we have to consider a new factor degrading reference performance, that is the jitter, wander and

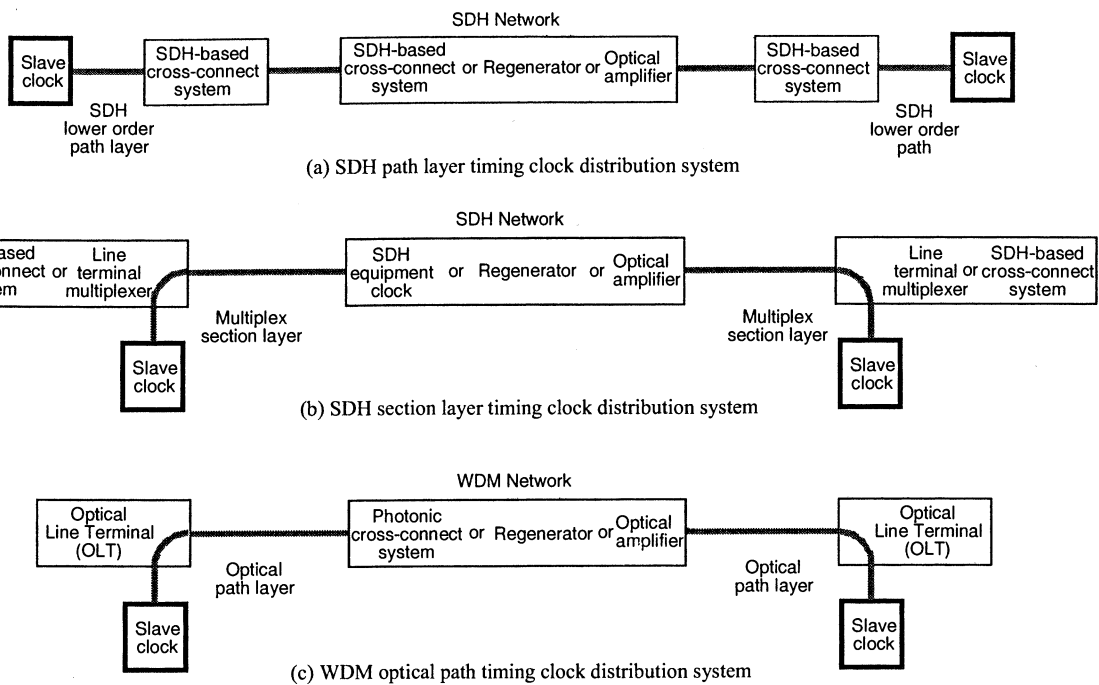


Fig. 3 - Timing distribution systems

phase jumps caused by pointer processing in SDH systems. The other system utilizes a SDH multiplex section layer as shown in Fig. 3 (b). The reference clock itself determines the transmission speed between nodes. The receiver node extracts the reference timing clock from the transmitted information without frequency control. Slave clocks are, however, cascade connected section by section, since SDH multiplex section is terminated at the entrance of SDH line terminal multiplexers or SDH-based cross-connect systems. This also degrades reference performance.

Reference signal management using the optical path system is one of the most promising concepts to improve reference performance. No frequency control process is needed in the optical paths such as pointer processing, slave clocks and SECs in intermediate nodes (Fig. 3 (c)). Regenerators are the only degradation factor, if they are introduced in WDM networks to transmit information over a long distance. The other merit is that the optical path system can be restored if failure occurs. Optical path restoration consequently reestablished the clock distribution network as well. Reference timing clock distribution networks do not need to maintain distribution paths by themselves.

#### 4. Reference frequency and time

It is very important for reference signal distribution systems to be able to setup their own data link[2]. The reference data link enables reference signal management to transfer reference information between higher and lower nodes: lower slave nodes can know the route of the reference signal distribution and which master node is generating the reference signal; higher slave nodes can determine which lower nodes are using them, and can know how accurate the lower nodes are. These functions are essential for advanced reference signal management.

The optical container used in the optical path provides a payload and AU pointer area that can transport virtual containers such as VC-4, and an optical overhead area including optical multiplex section and optical repeater section information. Reference data links can be reserved by using the optical overhead in WDM networks; this is very difficult in existing SDH networks due to additional cost and modification problems.

The OLT should offer the reference data link, and be connected with a reference signal generator as shown in Fig. 4. The OLT also receives reference frequency and time generated in the reference signal generator. The reference timing clock is generated from the ref-

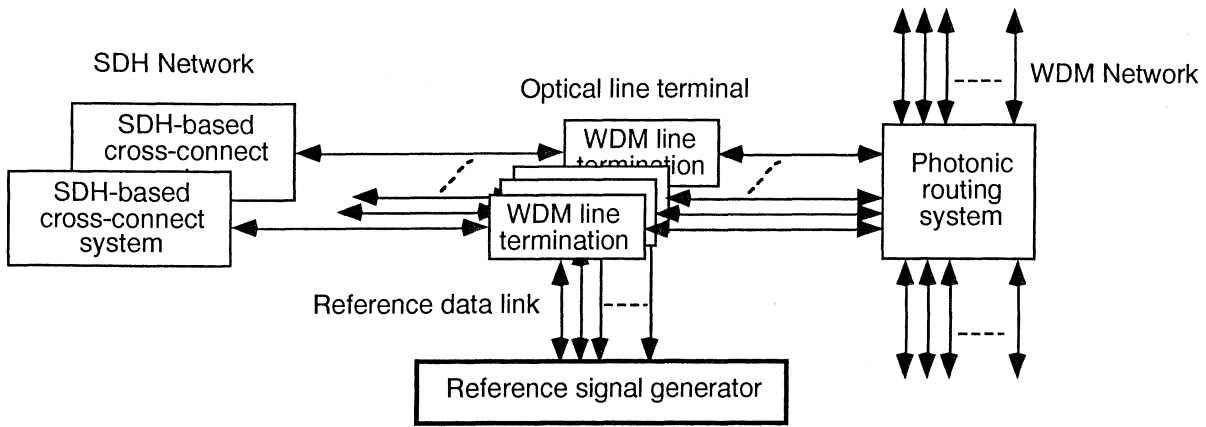


Fig. 4 - Reference data links in the optical line terminal

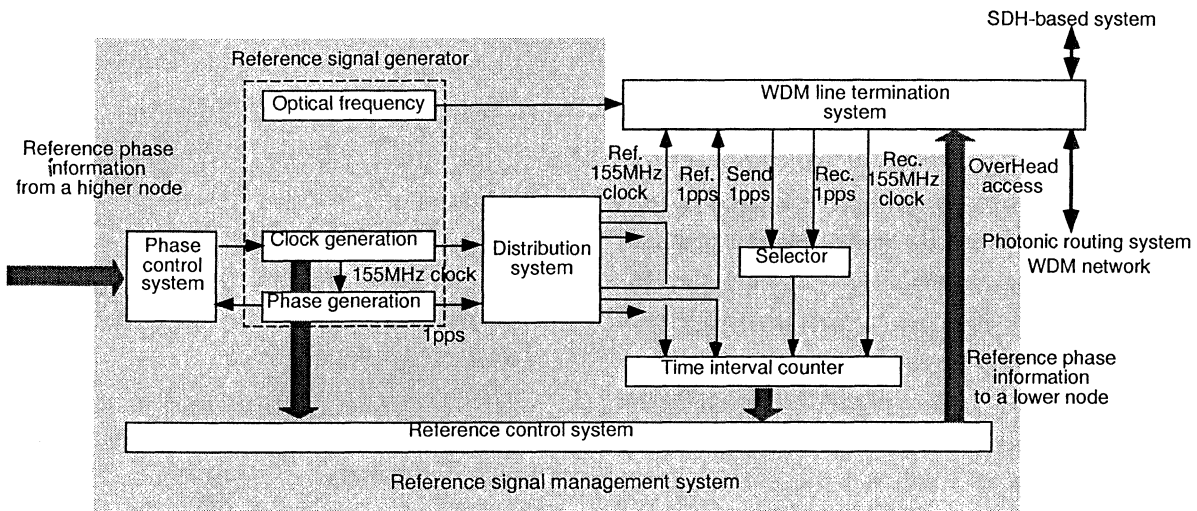


Fig. 5 - Reference signal management system

reference frequency. Reference time consists of a 1 pps signal and time information, and is transferred via the reference data link. Figure 5 shows the complete reference signal management system. Reference frequency of 155 MHz clock and reference time of 1pps are supplied to the WDM line termination system in the OLT.

WDM networks will handle transmission signals faster than 2.5Gb/s as a client for single optical frequency. Time variation in the reference management system is approximately 100ps in the temperature range of 10 to 50°C in a 2.5Gb/s transmission system. If the reference management system uses time compensation with two way time transfer, frequency transfer stability of  $10^{-14}$ - $10^{-15}$  and time transfer stability of 0.1ns over 1 day averaging could be achieved in WDM networks[3][4].

### 5. Optical reference frequency

The reference signal generator supplies reference optical frequency to the OLT (Figs. 4 and 5). WDM networks require limited accuracy for reference optical frequency to avoid interference between optical signals with different frequencies in the same optical fiber. Some papers describe optical frequency requirements [5][6]. Our initial target of optical frequency accuracy is around  $10^{-7}$  considering WDM system configuration and maintenance and measurement margins. We can now utilize two molecular absorptions of acetylene[6] and hydrogen cyanide[7] and one atomic absorption of rubidium[8]. It is possible to integrate a laser stabilizing system using these absorptions as well as other digital circuits into single package as shown in Fig. 6.

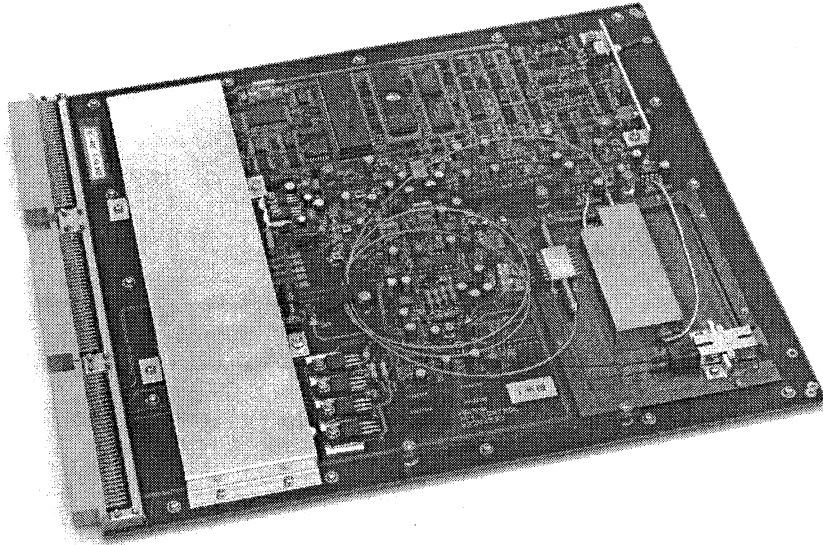


Fig. 6 - Reference optical frequency generator package using acetylene absorption line

We do not have a plan to synchronize optical frequency between nodes since these optical reference frequency packages can independently achieve the desired frequency accuracy and stability. Each node has the reference optical frequency generator as shown in Fig. 6, and its reference signals are supplied to WDM line termination systems and WDM cross-connect systems as shown in Fig. 5.

## 6. Conclusion

WDM networks are very important for reference signal management. They can support more advanced reference signal distribution mechanisms, operation systems for reference signals and improved reference performance. If international and domestic networks are connected with WDM systems and an international optical path is setup, global frequency and time transfer would be possible over WDM networks.

## Acknowledgment

The authors wish to thank Satoru Okamoto of NTT Photonic Network Laboratory for his helpful discussion and comments and Haruhiko Ichino and Kenji Kawai of NTT Photonic Network Laboratory for their helpful suggestions.

## References

- [1]S. Okamoto and K. Sato;"Iner-network interface for photonic transport networks and SDH transport networks", GLOBECOM, 1997
- [2]M. Kihara and A. Imoka;"accurate network synchronization for telecommunications networks using paired paths", EFTF, 1993
- [3]M. Kihara and A. Imaoka;"Two-way time transfer through 2.4 Gbit/s optical SDH system", PTII, 1997
- [4]T. Celano, S.R.Stein and Al.Gifford, et. al.;"Results from proof-of-concept time based communications testing", PTII, 1997
- [5]Y. Hamazumi, M. Koga and K. Sato;"Beat induced crosstalk reduction against wavelength difference between signal and for-wave mixing lights in unequal channel spacing WDM transmission", IEEE Photo. Tech. L., vol.5, no.5, pp.718-720, 1996
- [6]A. Imaoka and M. Teshima;"Optical frequency reference in optical path networks based on WDM technique",IEICE Technical report, OCS96-65, 1996
- [7]J. Ishikawa and H. Watanabe; IEEE Trans. IM, vol.42, no.2, pp.423-425, 1993
- [8]To be published in IEEE Photo. L.

## ADDITIVE TIME SYNCHRONOUS SYSTEM IN EXISTING SDH NETWORKS

Yoshizumi Serizawa, Kazunori Kitamura, Masanori Myoujin Tohru Matsushima, Osamu Masui, Riki Takada

Central Research Institute of Electric Power Industry  
Komae-shi, Tokyo 201-8511 Japan

NEC Corporation  
Minato-ku, Tokyo 108-8425 Japan

### ABSTRACT

A simplified SDH (Synchronous Digital Hierarchy)-based time synchronous system that does not need modification of existing SDH transmission equipment (STE) and clock supply equipment (CSE) is proposed. The system has auxiliary time synchronizing equipment attached to existing STE and CSE, where frequency and time are separately synchronized, and which enables us to partially time-synchronize an SDH network or to introduce a time synchronous system locally. Experimental time synchronizing devices using a data communication channel (DCC) in the section overhead (SOH) showed potentially satisfactory performance; synchronization errors of a 4-link system are of the order of sub-microseconds.

### 1. INTRODUCTION

Precise time information or timing signal is indispensable for electric power system operations, Wilson (1), such as fault location and clearance in power transmission lines where current waveforms are measured at remote stations simultaneously at an accuracy of a few microseconds or sub-microseconds. Timing synchronism has been achieved on a terminal-to-terminal basis using two-way or round-trip pulse transmissions in conventional private PDH (Plesiochronous Digital Hierarchy) networks so far. Multipoint or system-wide timing synchronization is becoming more important for such future sophisticated applications as wide-area power system protection, Serizawa et al. (2). Although GPS would be the most practical way to construct a time transfer system, it is not appropriate for whole applications to depend on a single time transfer system since reliability is a major concern for power system applications. Therefore, redundant or backup operation, or complementary use of time transfer systems composed of the satellite-based GPS and a terrestrial time synchronous digital network should be taken into account for wide-area use. Since electric power utilities are constructing private SDH (Synchronous Digital Hierarchy) networks for their broadband communications, an SDH-based time synchronous system would be promising for system reliability and operability.

Some SDH-based time synchronous systems with a synchronizing function built into SDH transmission equipment (STE) and clock supply equipment (CSE) were proposed by Jefferts et al. (3) and Kihara and Imaoka (4). Serizawa et al. (5) also made a fundamental examination of constructing a

simplified time synchronous system that does not need modification of existing STE and CSE, and conducted preliminary experiments using a pair of master-slave devices without STE. This paper first describes a multi-link configuration of the simplified additive time synchronous system in existing SDH networks, and then the performance of experimental devices using a SDH transmission circuit simulator is presented. Delay variation characteristics of overhead fiber-optic cable links that would be used for an actual system are also described.

### 2. PROPOSED SYSTEM

#### 2.1 System configuration

In terrestrial digital networks a master-slave time transfer system shown in Fig. 1 is preferable for its simplicity of operation and can be established by modifying the present digital networks which are operated based on the master-slave frequency transfer technique. A multi-stratum system can be configured by a cascaded system of slave nodes; a slave node at stratum  $n$  becomes a master node for a slave node at stratum  $n+1$ . Fig. 2 shows a basic configuration of the proposed time synchronous system. The system has auxiliary time synchronizing equipment (TSE) attached to existing STE and CSE, where frequency synchronization is conducted by CSE which usually has a digital processing phase locked loop, and phase or time synchronization is carried out by the TSE. This configuration enables us to partially time-synchronize an SDH network or to introduce a time synchronous system locally, since electric power utilities may not need wholly time synchronized networks, but only use the system for certain local applications.

To transmit a time signal, especially a reference timing pulse, in SDH networks it is preferable to use undefined bytes in the section overhead (SOH) to avoid delay variation due to an elastic store memory in a receiver module. Two SOH bytes not defined for any purpose were proposed for time synchronization by Kihara and Imaoka (3). More practically for private SDH networks, we could utilize Data Communication Channel (DCC), D1 to D12; a 192-kbps channel using D1 - D3 as a Regeneration Section DCC, or a 576-kbps channel using D4 to D12 as a Multiplex Section DCC, ITU-T (6). However, special care is needed because some currently and commercially available SDH transmission equipment actually have elastic store memories in DCC which cause large synchronization errors.

## 2.2 Synchronization scheme

Considering the following three functions that should be implemented for the time synchronization scheme between two remote stations; transmission of a time signal including a reference timing pulse, transmission delay data, and time information, transmission delay measurement, and delay compensation and phase synchronizing control, the proposed system employs a mutual or two-way pulse transmission and delay measurement method shown in Fig. 3 that is less vulnerable to delay variations. This configuration seems preferable in that it cancels the delay variation that occurs similarly on both the outgoing and incoming transmission paths. On the contrary, a round-trip pulse transmission and delay measurement method is affected by this kind of delay variation. The system can form both multi-link and branch configurations.

Each reference pulse generated by the reference timing generator (RTG) both at the master and slave nodes is mutually transmitted to the other node. Each received pulse is delayed by one-way

transmission through the outgoing or incoming transmission lines ( $\delta_1$  or  $\delta_2$ ). By using the time interval counter (TIC), each node measures the time difference between the transmission of its own pulse and the reception of the opposite node's pulse;  $T_M$  at the master node and  $T_S$  at the slave node.  $T_M$  is transmitted to the slave node which executes delay compensation corresponding to a half of the difference between the two delays,  $(T_M - T_S)/2$ , as well as frequency synchronization in its RTG composed of a phase locked oscillator (PLO) and an automatic phase control (APC). If different types of STE made by different manufacturers are used in a master-slave paired configuration, the internal delays of transmitter and receiver modules must be compensated because outgoing and incoming delays may not be reciprocal.

There are three stages of time synchronization; delay measurement, delay data transmission, and delay compensation. Fig. 4 shows the temporal sequence of time synchronization. A sequence of time synchronization is completed within two periods of pulse transmission,  $2T$ . In the mutual or two-way

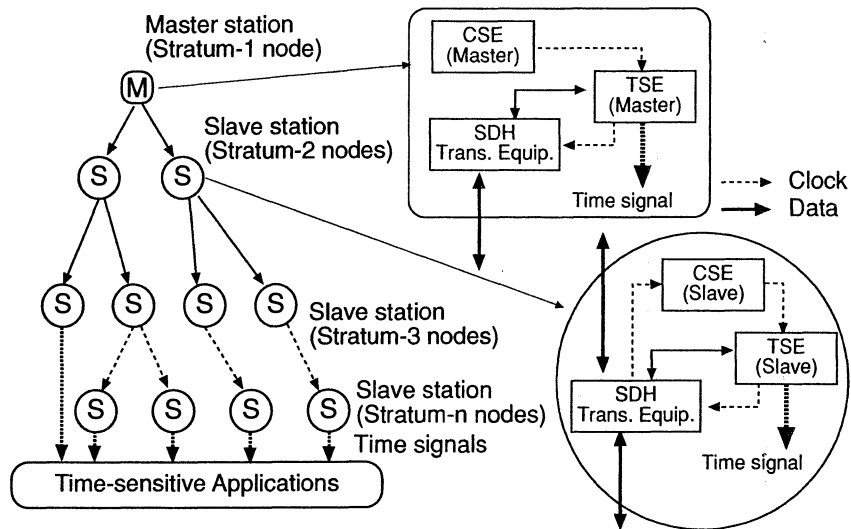


Fig. 1 Multi-stratum time synchronous network. CSE and TSE denote existing Clock Supply Equipment and external Time Synchronizing Equipment, respectively.

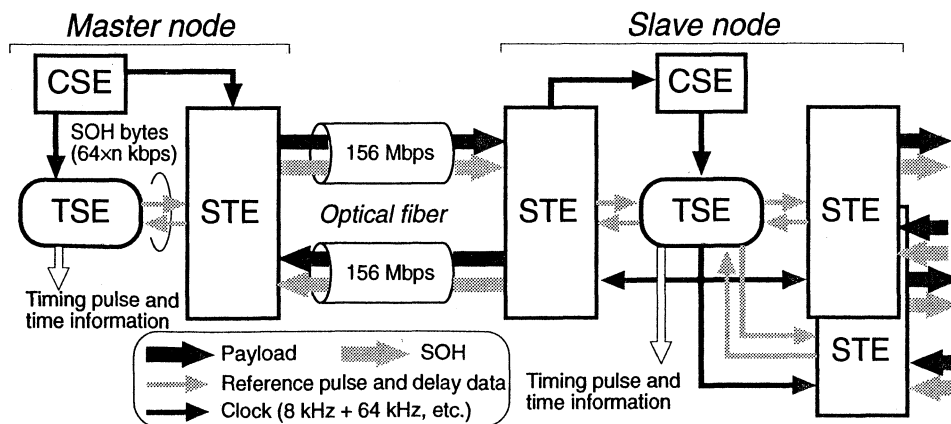


Fig. 2 Externally additive time synchronous system in a master-slave configuration. STE denotes SDH transmission equipment.



time synchronizing device. Taking into account the currently available SOH interfaces and the use in private networks, the 576-kbps DCC, D4 to D12, and a 50-Hz multi-frame format were provisionally employed instead of undefined SOH bytes and a 1-Hz multi-frame suitable for general applications, respectively. A 64-kbps channel in an undefined SOH byte can be technically used for 1-Hz signal transmissions. The frequency of the TSE internal oscillator, which is synchronized to CSE and is used for the operations of TIC and APC, is selected at 17.28 MHz, or 30 times as high as the bit rate. The higher the internal clock frequency is, the more accurate the synchronization becomes, while the slower the pull-in speed becomes. The delay measurement by a TIC is conducted every 20 milliseconds (ms), or at 50 Hz, and therefore 50-Hz reference timing pulses and time information is output for power system applications. A transmission frame of 72 bits within a period of 125  $\mu$ s includes frame synchronization bits, time information, delay data, a frame sequence number in a multiframe of a period of 20 ms consisting of 160 frames, CRC, etc. The APC operation is conducted by inserting or removing pulses to adjust the output pulse stream timing in a frequency divider circuit. The interval of APC operation or delay compensation can be set to 2.5, 5, 10, 20, 40, 80, 160 or 320 ms, or to a control frequency of 400, 200, 100, 50, 25, 12.5, 6.25 or 3.125 Hz. Delay compensation is carried out by 57 ns, say, every 10 ms (twice a multiframe), 20 ms (once a multiframe), 40 ms (once two multiframe), or 160 ms (once 8 multiframe) according to the calculation of delay difference  $T_M - T_S$ . The system continuously performs APC or delay compensation operations even when no synchronization error is detected. A

constant transmission delay can be compensated manually if different types of SDH transmission equipment are used in a master-slave paired configuration and outgoing and incoming delays may not be reciprocal. Due to the difficulty of procuring actual SDH equipment, two types of DCC simulators which consist of digital PLLs and manually adjustable constant delay circuits shown in Fig. 6 were applied. There are two types of PLLs applied; one is the same type as used for actual SDH equipment with a faster response time for a frequency change or a cutoff frequency (Type-A), and the other with a slower response time (Type-B).

Five time synchronizing devices were connected via DCC simulators forming a four-link system.

### 3.2 Results

Synchronization errors for the multi-link master-slave system are defined as the timing difference between two 50-Hz output pulses of the devices. Figs. 7 and 8 show temporal variations of synchronization errors in the ordinary state and the summary of synchronization errors with respect to the number of links, respectively. The result illustrates that the lowest synchronization error or accuracy was obtained as 0.2  $\mu$ s<sub>p-p</sub> for a one-link configuration and 0.4  $\mu$ s<sub>p-p</sub> for a four-link one with 6.25-Hz APC operations, which seems optimal for the experimental devices. The errors are mainly dependent on the time constants of PLO and APC and oscillator performance, although actual repetitive APC operations are carried out within an accuracy of a few times the 57-ns resolution, that is, the order of 0.1  $\mu$ s<sub>p-p</sub>. Fig. 9 shows the calculated time variance of the ordinary synchronization errors indicating the

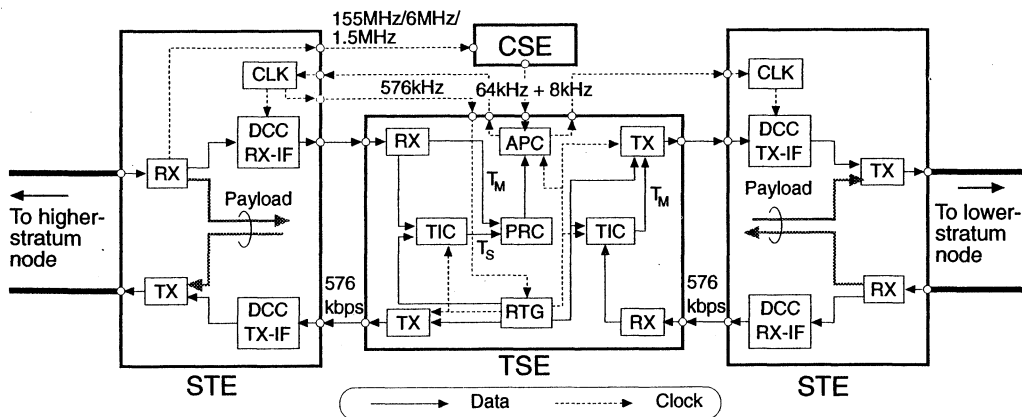


Fig. 5 Experimental slave device. DCC IF, TX (RX), and CLK denote data communication channel interface, transmitter (receiver) module, and internal clock supply module, respectively.

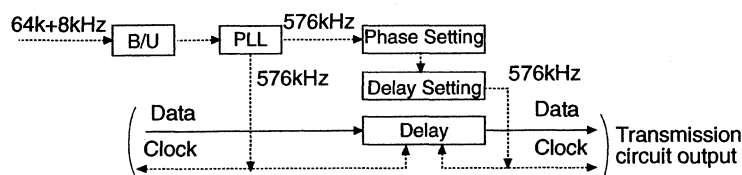
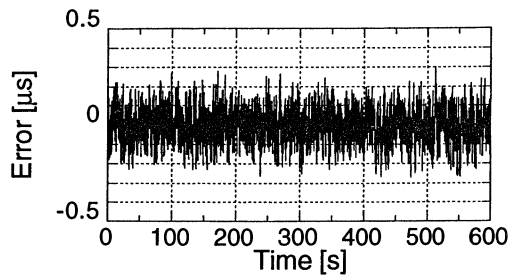
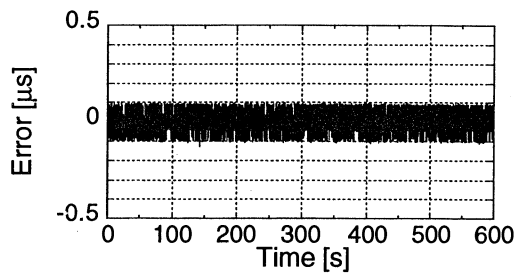


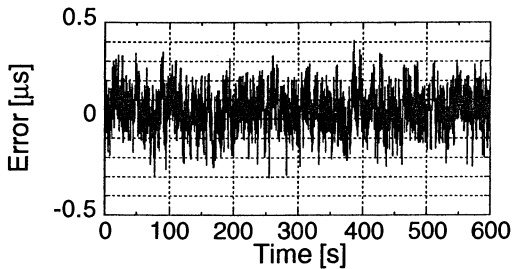
Fig. 6 DCC simulator. B/U denotes a bipolar to unipolar signal converter.



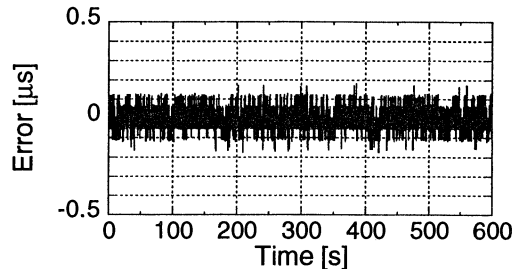
(a) DCC Type-A, 1 link.



(b) DCC Type-B, 1 link.



(c) DCC Type-A, 4 links.



(d) DCC Type-B, 4 links.

Fig. 7 Variations of synchronization errors with time for experimental devices with an APC interval of 160 ms.

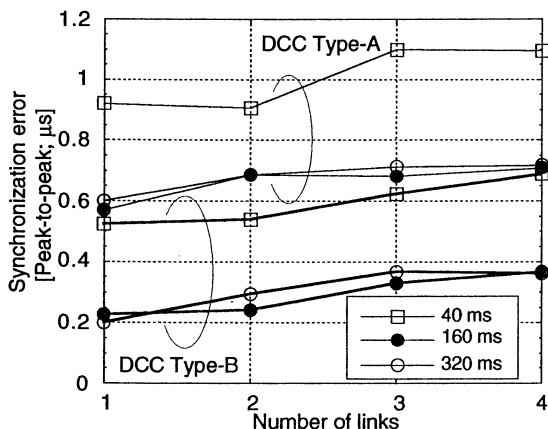


Fig. 8 Synchronization errors with respect to the number of links and APC intervals.

stability of the devices, respectively. Due to their repetitive APC operations in the ordinal state, there is a hump around averaging time  $\tau$  of 0.1 to 1 second, and white PM noise characteristics with a slope of  $\tau^{-1/2}$  are exhibited at  $\tau > 1$  s. By using two sets of actual STE and two sets of the experimental devices, a 1.544-Mbps signal was successfully transmitted in a SDH payload channel during repetitive APC operations by the devices in the ordinary state. Another configuration of asynchronous transmission, where a device that modulates the time signal from TSE using a sampling or digital-to-digital (D/D) conversion method is installed between the TSE and STE, and the time signal is thus transmitted in the 576-kbps DCC at a lower rate, say, 64 kbps, in an

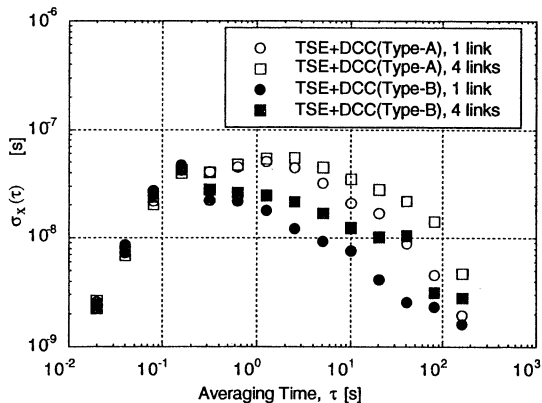
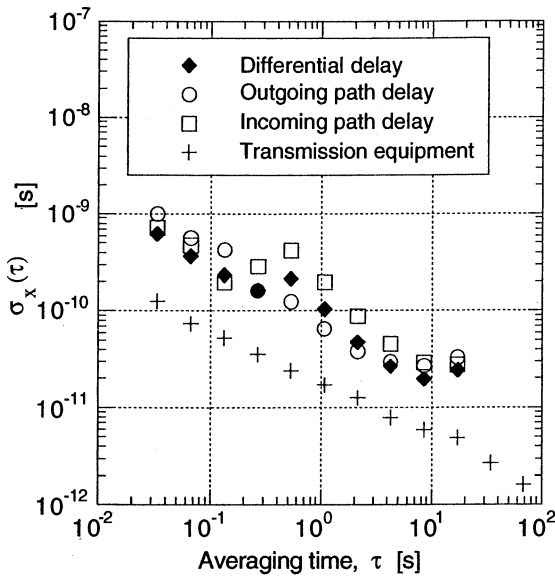


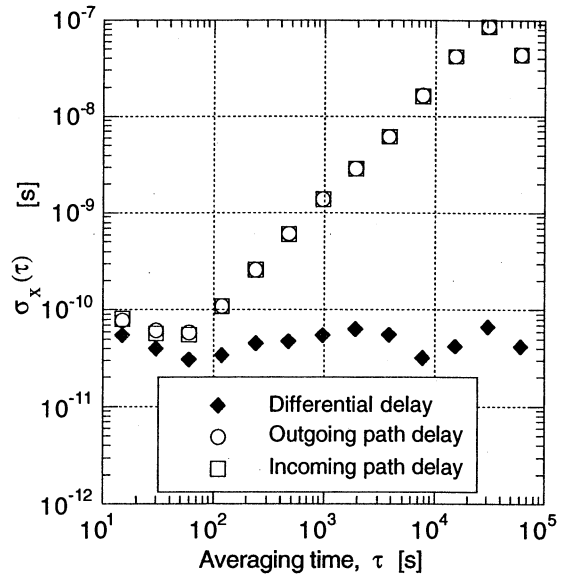
Fig. 9 Noise deviation,  $\sigma_x(\tau)$ , of synchronization errors for experimental devices with an APC interval of 160 ms.

asynchronous manner, also showed sub-microsecond synchronization errors.

These results suggest potentially satisfactory performance for electric power system applications with respect to a multi-link time transfer system consisting only of STE and TSE, taking no account of transmission media. The delay variation characteristics of transmission media, however, are crucial for these types of time transfer systems while we can neglect jitters of transmission equipment owing to jitter suppression by the phase-locked loop. The trunk fiber-optic telecommunication circuits of electric power utilities are mainly overhead cable links where optical fibers are embedded in ground wires installed along power



(a) Short-term characteristics.  
(30-Hz measurement)



(b) Long-term characteristics.  
(15-second interval measurement)

Fig.10 Noise deviation,  $\sigma_x(\tau)$ , of delay variations in an overhead fiber-optic cable link.

transmission lines, called OPGW (Optical Ground Wire). Those overhead links exhibit large diurnal and seasonal delay variations compared with underground cables, which are attributed to temperature changes, Serizawa et al. (7). If we assume that the maximum length of the fiber-optic time transfer path is 300 km, yearly temperature variation is 40°C, and the delay variation coefficient of such links is 62 ps/km/°C, then the maximum delay variation would be 744 ns. But these kinds of delay variations can be also compensated. However, two-way differential delay and variations are of concern. Fig. 10 shows delay variations measured in a 277-km 32-Mbps OPGW link. For the region with an averaging time  $\tau > 10^2$  s, delay variations both in the outgoing and incoming paths are canceled by the two-way method, leaving residual two-way differential delays. For the noises with shorter averaging time regions  $\tau < 10^2$  s, filters with a time constant of tens of seconds should be employed to suppress them.

#### 4. CONCLUSIONS

A simplified SDH-based multi-link time synchronous system was proposed. In the system, auxiliary time synchronizing equipment is attached to existing SDH networks composed of SDH transmission equipment and digital clock supply equipment, and not only frequency but also frame phase or time is synchronized. The experimental time synchronizing devices accompanied with SDH DCC simulators showed potentially satisfactory performance for the power system applications; synchronization errors of a 4-link system are of the order of sub-microseconds.

#### REFERENCES

- [1] Wilson, R. E., 1991, "Use of Precise Time and Frequency in Power Systems", *Proc. IEEE*, **79**, 1009-1018.
- [2] Serizawa, Y., Myoujin, M., Kitamura, K., Sugaya, N., Hori, M., Takeuchi, A., Shuto, I. and Inukai, M., 1998, "Wide-Area Current Differential Backup Protection Employing Broadband Communications and Time Transfer Systems", *IEEE PES 1998 Winter Meeting*, PE-203-PWRD-0-11-1997.
- [3] Jefferts, S. R., Weiss, M. A., Levine, J., Dilla, S. and T. E. Parker, 1996, "Two-way time transfer through SDH and SONET systems", *10th EFTE*, 461-464.
- [4] M. Kihara and A. Imaoka, 1996, "System configuration for standardizing SDH-based time and frequency transfer", *10th EFTE*, 465-470.
- [5] Serizawa, Y., Kitamura, K., Myoujin, M., Shimizu, K., Matsushima, T. and Morimitsu, M. 1998, "SDH-Based Time Synchronous System for Power System Communications", *IEEE Trans. Power Delivery*, **13**, 59-65.
- [6] ITU-T, 1996, "Recommendation G.707: Network node interface for the synchronous digital hierarchy (SDH)".
- [7] Serizawa, Y., Myoujin, M., Miyazaki, S. and Kitamura, K., 1997, "Transmission Delay Variations in OPGW and Overhead Fiber-Optic Cable Links", *IEEE Trans. Power Delivery*, **12**, 1415-1421.

## DOPPLER WIND EXPERIMENT - FIRST RESULTS FROM SPACE

Rudolf Kohl \*, Klaus Wagner \*, Michael Bird \*\*, Robindro Dutta-Roy \*\*

\* Dornier Satellitensysteme GmbH, POB 801169, D-81663 München, Germany

\*\* Radioastronomisches Institut der Universität Bonn, Auf dem Hügel 71, D-53121 Bonn, Germany

### 1. ABSTRACT

A Doppler Wind Experiment (DWE) will be performed during the Titan atmospheric descent of the Huygens Probe. The Probe's wind-induced motion will be derived from the residual Doppler shift of its S-Band radio link to the Cassini Orbiter. The experiment relies on Rubidium (Rb) Ultra-Stable-Oscillators (USO) to generate the transmitted signal from the Probe and to extract the frequency of the received signal on the Orbiter. Initial results from the first in-flight checkout, successfully performed 8 days after Cassini/Huygens launch, are described.

### 2. INTRODUCTION

On 15<sup>th</sup> October 1997, the American Orbiter Cassini with the attached European Probe Huygens successfully commenced its journey into deep space by a Titan launcher from Cape Canaveral in Florida. In seven years, the Huygens probe will be released from the orbiter and will travel on a ballistic trajectory to Titan. After entering the Titan atmosphere, the probe will glide down to the surface on its parachute. Six scientific instruments will gather data on the composition and dynamics of Titan's atmosphere.

One of these experiments is the Doppler Wind Experiment (DWE) [1]. DWE is performed by an international science working team led by the principal investigator M. Bird from the University in Bonn, Germany. The primary scientific goal of DWE is to determine the direction and strength of the zonal winds in the Titan atmosphere. A height profile of wind velocity will be derived from the Doppler shift of the radio link signal from the Huygens probe to the Saturn orbiter with an accuracy at the  $\pm 1$  m/s level. Further scientific objectives of the experiment are to monitor the probe descent dynamics like spin and parachute swing, to establish position and orientation of the Huygens probe at and after impact on Titan and to determine strength and spatial scales of turbulences in the Titan atmosphere by

measurement of Doppler modulation, Doppler variations and fluctuations.

A Rubidium Ultra-Stable-Oscillator (USO) accommodated on Huygens and an identical unit on Cassini make these measurements possible. The Rubidium frequency standards have expressly been developed by Dornier for DWE. The capabilities of the space USOs and the results from ground- and pre-launch testing have been described in [1] and [2].

This paper will present the first in-orbit check-out results.

### 3. DWE INSTRUMENTATION

The DWE experimental configuration is shown in Figure 1. The Transmitter Ultra-Stable-Oscillators (TUSO) drives the signal generated by the Transmitter A, one of the two redundant radio links. An internal TCXO serves as back-up in case of TUSO failure during cruise to Saturn and Titan. The TUSO output signal is multiplied by 204 to S-Band and transmitted to the dedicated Probe Support Avionics (PSA) Receiver A on the Cassini Orbiter. Cruise checkouts, which are conducted every six months, enable continuous monitoring of the DWE components and radio subsystem. At Titan the signal is amplified for free-space transmission. Timing and signal generation in the PSA are controlled by the RUSO. Like in the probe, switching to a back-up TCXO is possible. Phase-lock loop control in the receiver is governed by a numerically controlled oscillator (NCO), the output of which provides the DWE frequency measurement at 8 samples per second. The TUSO will be powered 30 minutes before initial signal transmission from the Probe, in order to warm-up and achieve the required frequency stability. The RUSO will be switched on at an even earlier time. The required fast warm-up time and insensitivity to the mechanical loads expected during the Huygens entry phase were the major drivers in the selection of Rb USOs.

The DWE instrumentation specification imposed a

requirement for a frequency drift stability  $dfo/fo \leq 2 \cdot 10^{-10}$  within a 30-minute warm-up time. This could not be guaranteed with quartz oscillators. A detailed description of the Rb USOs (see Figure 2) and their performance characteristics is given in [2].

#### 4. RESULTS OF 1<sup>st</sup> IN-FLIGHT TESTS

The first in-flight checkout of the Huygens probe payload occurred as planned on 23 October 1997, 8 days after the launch of the Cassini spacecraft. An overview of the DWE data recorded during the checkout is shown in Figure 3. The top two panels of Fig. 3 show the received frequency  $f_R$  in the two redundant radio chains at the same scale, starting 40 minutes after the start of the checkout. The received signal level (AGC = automatic gain control) is shown for chains A and B in the bottom two panels. Both  $f_R$  and AGC are recorded at a sample time of 125 ms. The initial 20 minutes are used for warming up the receivers and other probe Support Equipment, including the DWE-RUSO. Measurements of frequency relevant to the nominal mission at Titan are possible only after an additional 20 minutes, which are allocated to the same warm-up process for the DWE-TUSO. This sequential switch-on procedure is only necessary for the cruise checkouts. The sequence of events during the actual mission at Titan are such that both USOs will be warmed up and stable at the moment the Huygens signal is acquired.

Whereas the recorded frequency in chain A is governed by the TUSO/RUSO combination, the measurements in chain B are highly irregular. The jumps in frequency, which arise from a thermal feedback loop driving a TCXO, are apparently random. Upon closer inspection of the intervals between jumps, it is found that the frequency exhibits an unpredictable drift. The frequency trace in chain A remains at its nominal value near 0 Hz during the entire checkout (Huygens is obviously not moving with respect to the receivers on the Orbiter). The large deviation from zero velocity in chain B is due to the imprecise output frequencies of the TCXOs, which are constrained only to one part in  $10^6$ . The cause of the unusual time profiles seen in the signal level recordings (AGC), whereby both chains display the same irregular decrease by about 1 dB over the duration of the test, is unknown. The parallel behavior in the two independent chains implies the presence of an external source disturbing the aggregate Huygens radio subsystem.

It was determined rather late in the probe pre-launch test program that a small, but annoying, spurious oscillation was present in the chain A

frequency data. The oscillation was enhanced significantly after the Probe was mated to the Orbiter for launch configuration and was also seen to increase over the duration of the pre-launch checkout tests. A high-resolution plot of the recorded frequency in radio chain A over a one-minute interval, shown in the upper panel of Figure 4, reveals this spurious oscillation (frequency modulation) at a time when it had almost reached its maximum frequency deviation of 23 Hz peak-to-peak (p-p). The frequency of this spurious modulation, as marked by the dominant peak in the power spectrum (Fig. 4, second panel) is very constant at  $f_s = 0.366$  Hz. This spectrum is the Fourier transform of the frequency time series in the test elapsed time interval from 50 - 200 minutes (Fig. 3, upper panel). Harmonics of this frequency are also evident in the spectrum, albeit with considerably less power.

It was recognized soon after the discovery of the spurious oscillation that the unwanted modulation in the data could be eliminated by a Fourier filtering technique. The filtering procedure consists of reassigning all spectral amplitudes above a given threshold to values at the noise level, selected randomly from the spectrum baseline. The third panel of Figure 4 shows such a filtered spectrum. Although the two spectra look quite different, only 191 points of the original spectrum (from a total of 72000) with amplitudes above the (arbitrary) cutoff at  $10 \text{ Hz}^2/\text{Hz}$  were reduced to noise levels by this process. The spectral power amplitudes at frequencies below 1 mHz, which are basically responsible for long-term drifting, were left unfiltered. Finally, applying an inverse transform to the filtered spectrum, one obtains the filtered frequency trace in the time domain shown in the bottom panel of Fig.4. The spurious frequency modulation has virtually vanished. The filtered frequency measurements are centered at an frequency-offset of  $\approx 3$  Hz and the standard deviation is  $\approx 1.5$  Hz for a data sampling rate of 125 ms.

After considerable study, it has become known that the probable cause of the spurious modulation is an internal USO signal used to detect the resonance of the Rb atoms. A microwave signal of  $\approx 6.834$  GHz is applied to the Rb atoms to cause the atomic resonance. In order to detect the resonance, the microwave signal is phase modulated with an audio frequency signal of about 135.63 Hz [3]. The modulation signal (10 MHz/73730) is derived from the 10 MHz USO output signal and can be found as a spurious phase/frequency modulation on the 10 MHz operational output of the USO. The level of the spurious signal is very low on unit level (typically  $< -80$  dBc). However due to the frequency multiplication by the factor 204 in the Huygens

transmitter (see Fig.1), the modulation index, and thus the spectral power of the spurious signal is enlarged by 46 dB according to equation 1)

$$1) S_{\text{Sys}} = S_{\text{USO}} + 20\log(204) \approx -34 \text{ dBc}$$

with  
 $S_{\text{Sys}}$ : Spurious Power at System level (S-Band)  
 $S_{\text{USO}}$ : Spurious Power at USO output (10MHz)

and the spurious level at S-Band is rather high (typically -34 dBc). When this signal is sampled by the digital receiver on Cassini at the sampling rate of 125 msec, an apparent spurious oscillation appears at the frequency

$$2) f_s = n / T_{\text{sample}} - f_{\text{audio}} = 0.3663194 \text{ Hz}$$

with  
 $f_s$ : apparent spurious  
 $n$ : 17  
 $T_{\text{sample}}$ : sampling rate (125 msec)  
 $f_{\text{audio}}$ : Spurious audio modulation (135.63... Hz)

Although the internal USO signal has the correct frequency to produce the spurious oscillation, it is quite unclear why the frequency deviation (modulation index) grows from 8 to 25 Hz p-p over the duration of the checkout. An explanation might be found in the level (amplitude) stability of the phase modulation at USO level versus time. The USO electronics are warmed-up, and the modulation index might change by several dBs without any impact on the USO frequency stability. However, the index of the spurious modulation on the USO output signal may vary also by some dBs, resulting in an increase of the frequency deviation from 8 to 25 Hz p-p over the entire duration of the checkout.

### 5. CONCLUSIONS

The Huygens Doppler Wind Experiment is designed to determine the direction and strength of Titan's zonal winds from the residual Doppler Shift of the S-Band radio link to the Cassini Orbiter. The necessary frequency stability of the Probe carrier signal and its measurement on the Orbiter is realized by using Rubidium Ultra-Stable-Oscillators. In spite of a slight imperfection due to a multiplied spurious modulation on the transmit signal, the DWE instrumentation is fully functional and capable of meeting the originally defined scientific goals.

To our knowledge, it is the first time that a European Rubidium USO has been operated in space. Certainly, the DWE USOs are the first Rubidium oscillators in a deep space mission.

### REFERENCES

Ref.1: Bird, M.K. et al.,  
 The Huygens Doppler Wind Experiment - Titan Winds Derived from Probe Radio Frequency Measurements,  
 Space Science Reviews 1998

Ref.2: Kohl, R., Bird, M.K.,  
 Rubidium Frequency Standard Goes To Deep Space,  
 EFTF 1997

Ref.3: Huygens DWE Ultra-Stable-Oscillator Experiment User Manual  
 DWE Project Internal Paper

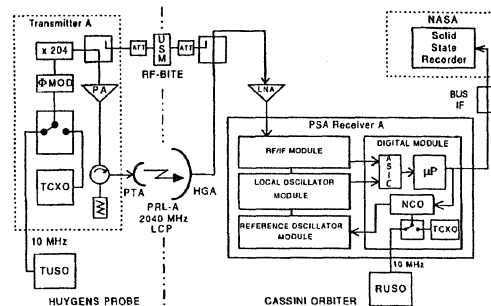


Figure 1: DWE experimental configuration

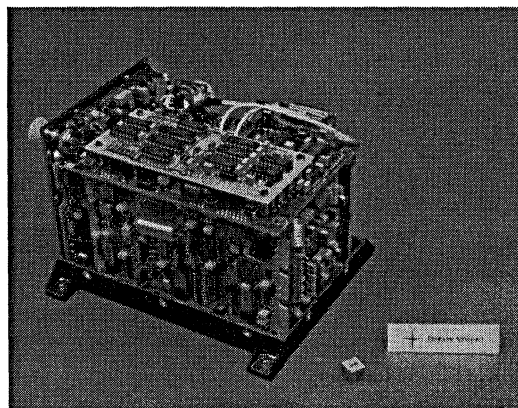


Figure 2: DWE USO cover and side walls off

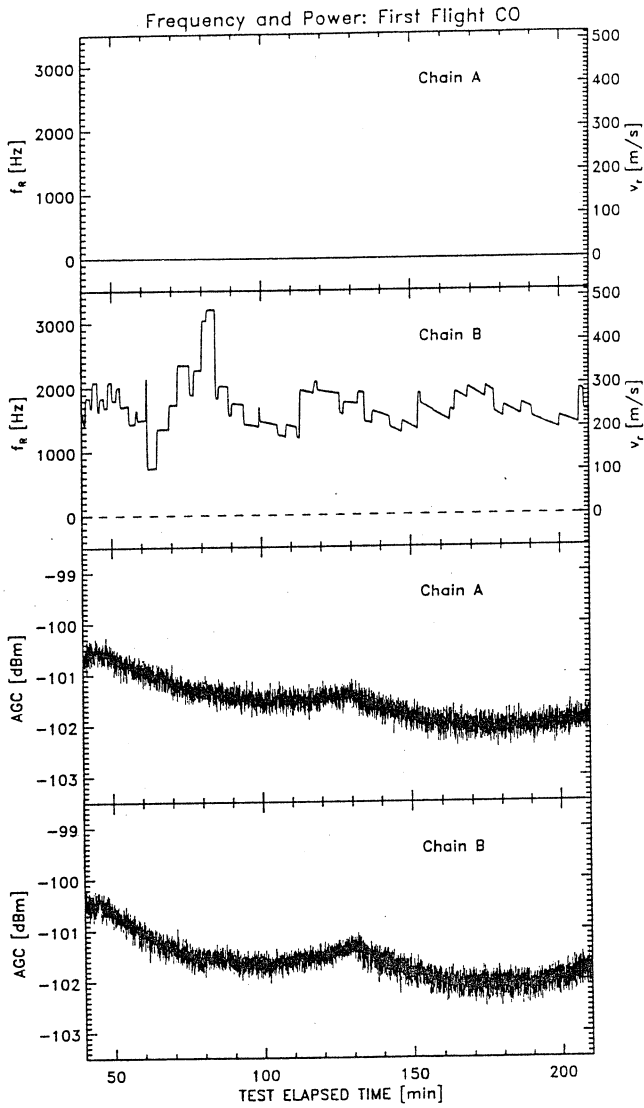


Figure 3: Huygens radio frequency signal during 1<sup>st</sup> in-flight checkout.

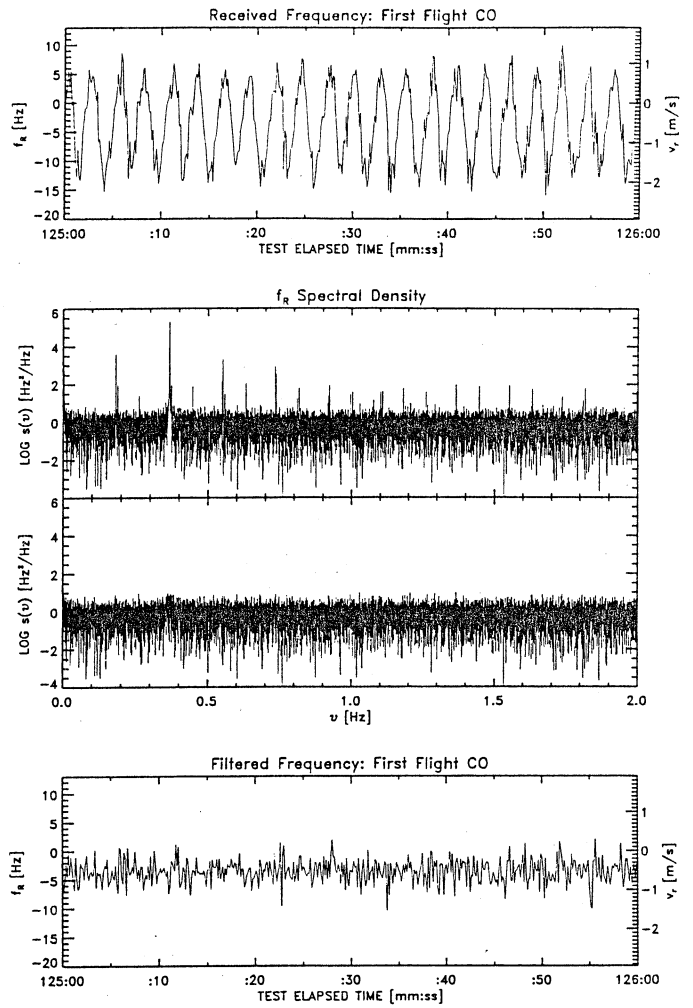


Figure 4: High-resolution frequency data during a one-minute interval

*12th E F T F* - 10÷12 March 1998 - Warsaw - POLAND

**Instrumentation & measurement II**

Chairman: *Antoni Masiukiewicz*



DIFFERENT APPROACHES FOR NS-CLASS DELAY LINES

Juha Vainikka  
 Lappeenranta University of Technology  
 PO BOX 20, 53851, Finland  
 Juha.Vainikka@lut.fi

ABSTRACT

The output frequency of any oscillator changes continuously with time. With crystal oscillators the physical properties of the quartz crystal cause a gradual change with time, mostly due to the ageing of the resonator material, resulting in cumulative frequency drift. This drift can be compensated using adjustable capacitors, which improves the long-term stability of crystal oscillators. The same type of systematic variation can be observed also in atomic frequency standards. In latter the compensation is much harder, and in the case of caesium, which is the primary standard, not always possible. However, the effects of ageing in atomic oscillators are known, and the change in frequency can be anticipated. When the error in the time base is calculated for each moment an arriving time pulse can be shifted to correct its location temporally. This shifting can be made using delay lines. In this paper different methods are presented for shifting pulses by means of accurate ns-class delay lines. These delay lines consist of either Fast TTL- or ECL-family logic gates or transmission lines with exact propagation delays and necessary control circuitry.

1. SYSTEM-LEVEL DESCRIPTION

Block diagram for error-correcting hardware is presented in figure 1. The main blocks in the picture are Primary Clock Source (PCS), Adjustable Delay Line (ADL) and Control Unit (CU).

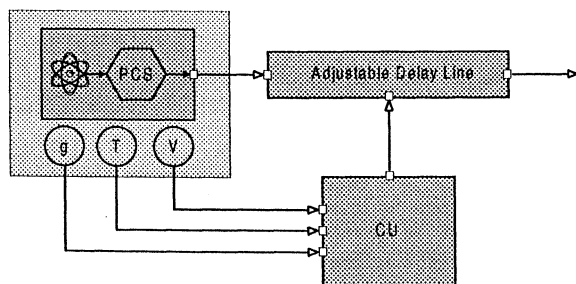


Figure 1: System level block diagram

Parameters for Control Units calibration function depend of the type of Primary Clock Source. Typical environmental factors that contribute for long-term stability of precision oscillators include temperature, supply voltage, and vibration. Anticipating the effect of these factors together with PCS ageing forms the input of calibration function in system's CU. This

function uses the model of the behaviour of the PCS for real-time simulation.

2. ADJUSTABLE DELAY LINE PROPERTIES

2.1 Length of Delay Line

The results from the simulation of PCS are used for correcting the error in time base by constantly changing the place of arriving time pulse in respect to the previous pulse. Since the pulse may have to be moved in either forward or backward in time to compensate cumulative errors, the Adjustable Delay Line must have length of  $2T_{clk}$  where  $T_{clk}$  is the cycle length of PCS output.

2.1 Resolution of Delay line

Changes in oscillator frequency can be categorised [1] into systematic variations, deterministic periodic variations, or random fluctuations. The first one is usually connected to long-term instability or ageing, whilst the latter two are the typical reasons for short-term instability of a frequency source.

Accumulated time error for oscillator with known ageing rate can be calculated with [2]

$$\Delta T = T_0 + \left( \frac{f_0}{f_r} - 1 \right) T + \frac{1}{2} DT^2 \quad (1)$$

where  $T_0$  = Initial Time Error,  
 $(f_0/f_r - 1)$  = Relative Frequency Offset,  
 $D$  = Ageing rate, and  
 $T$  = Elapsed Time

It can easily be seen that atomic frequency standards with ageing rate of none to less than  $10^{-13}$  in day, stability  $<10^{-12}$  at day, and temperature coefficient  $<10^{-10}$  over operating temperature range are mostly affected by environmental effects. Provided these effects cause deterministic errors in range  $10^{-10} - 10^{-11}$ , they produce accumulated time error in the magnitude of one to few tens nanoseconds per minute.

The length of the delay step and calibration cycle should be chosen according to time error accumulating rate and maximum acceptable time drift in the system.

### 3 DIFFERENT DELAY LINES DESIGNS

Commercial applications for delay lines are built by means of RC-networks with known  $\tau_{RC}$ , or in case of longer delays, with switched capacitor chains. Neither of these are capable for transporting a timing pulse accurately and without corrupting it. In this chapter designs are presented that consists of transmission lines with exact propagation delay. These delay lines are made of either cascade logic gates, several coaxial cables of different length or reflection stub made of single coaxial cable.

#### 3.1 Switched delay lines

Two different type of switches were tested: TTL-multiplexer and CMOS-switch, or transmission gates. The latter of these is presented in figure 2. TTL-multiplexer differs from CMOS-version only in that the switching unit is matching TTL-component.

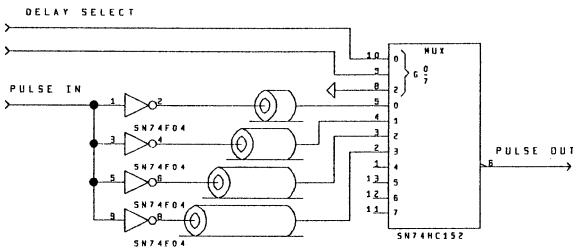


Figure 2: CMOS-switched Delay line.

In this design delay is formed with paths with different lengths. Selecting appropriate path using the multiplexer then produces the desired delay. Paths are formed of coaxial cable. If characteristic impedance of cable is

$$Z_0 \equiv \sqrt{\frac{L}{C}}, \quad (2)$$

$L$  and  $C$  being the inductance and capacitance of unit length of the cable, the length of delay paths may be calculated as [3]

$$\ell \equiv \frac{\tau}{\sqrt{LC}} \quad (3)$$

where  $\tau$  is the desired delay.

The TTL-multiplexer had relatively low impedance internal couplings between its inputs inherent to its structure which made it very difficult to adjust the length of the delay paths. This design was soon rejected as useless.

The design with CMOS transmission gates missed those unwanted features of TTL-multiplexer, and since the internal delays between output and different inputs of HC-device were quite small (less than 1ns) it proved to be easy to calibrate.

#### 3.2 Cascade ECL gates with RC-phase shift network

Second approach uses ECL gates to form basic delay and RC-network between gates to calibrate the delay of each of the states. Test circuitry is presented in figure 3.

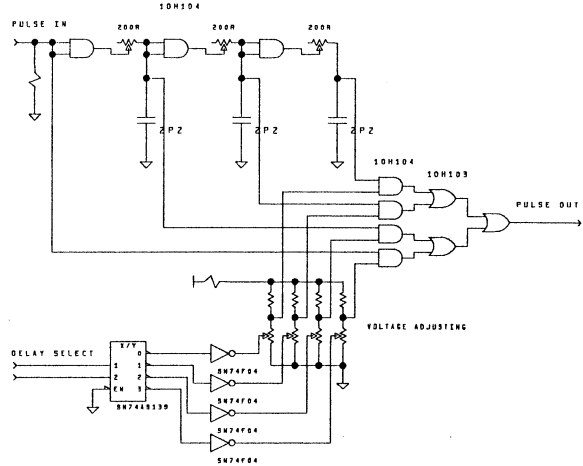


Figure 3: ECL gates with calibrating RC-network.

ECL technology has well known advantages and disadvantages, that apply also in their use in delay lines. Low power-supply noise generation and crosstalk eliminated due to internally slowed edge rates ensure robust implementations with minimal increase of timing instability caused by noisy signals.

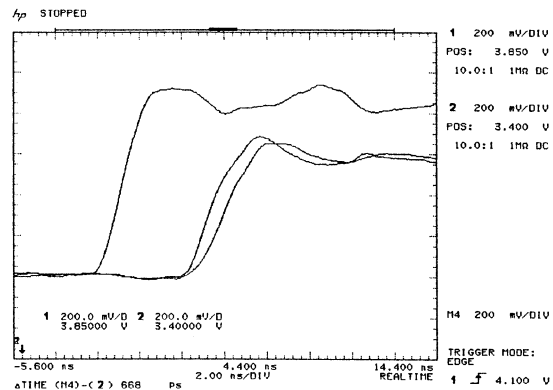


Figure 4: Delay adjusting with RC-network

This circuitry is quite easy to calibrate, and relative differences in propagation delays between individual gates are small. Performance of this circuitry could still be increased by using varactor diodes for tuning the  $\tau_{RC}$ , thus eliminating bulky adjustable resistors [3]. Adjusting with voltage-controlled varactors could also help compensate the temperature coefficient of the circuit. Figure 4 shows an oscilloscope display of delayed signal in circuitry from figure 3. Signals from left to right are input signal and delayed signal twice with adjusting at minimum and maximum values.

### 3.3 Reflection stub as a delay line

Third approach for generating deterministic delays exploits the well-known phenomena of signal reflections in a poorly terminated transmission line.

When terminating impedance  $Z$  at the end of the transmission line does not equal to transmission line characteristic impedance  $Z_0$ , a reflection develops when the signal reaches the termination. If the incident signal has amplitude of  $V$ , then the reflected signal will have amplitude of  $\Gamma V$ , where the reflection coefficient  $\Gamma$  can be calculated from

$$\Gamma = \frac{Z - Z_0}{Z + Z_0} \quad (4)$$

When reflected signal arrives back at the source, the reflection coefficient at the source determines whether there will be another reflection. If neither ends of transmission line matches  $Z_0$ , multiple reflections occur.

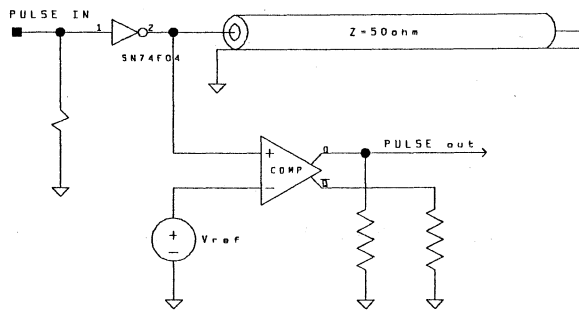


Figure 5: Delay circuitry using reflection stub

In figure 5 is a simplified schematics of a design used to test reflection stub. A 74F04 TTL inverter is driving a coaxial cable with  $Z_0 = 50\Omega$ . Since 74F-family has source resistance of  $R_S \approx 25\Omega$ , and transmission line is shorted, reflection coefficients at both ends are non-zero:

$$\text{Source end: } \Gamma_s = \frac{25\Omega - 50\Omega}{25\Omega + 50\Omega} = -0.3$$

$$\text{Load end: } \Gamma_l = \frac{0 - 50\Omega}{0 + 50\Omega} = -1$$

This produces multiple reflections which reduce the pulse voltage after each round trip of signal. Voltage from source end of transmission line is fed to a fast comparator with adjustable reference voltage at the other input. Value of reference voltage determines which round trip makes the comparator change its output. Figure 6 shows an oscilloscope display of signal with multiple reflections and outputs of three comparators with different reference voltages. The initial voltage is negative because the leading edge is negative after the inverter. The positive pulse that follows is caused by trailing edge of input pulse.

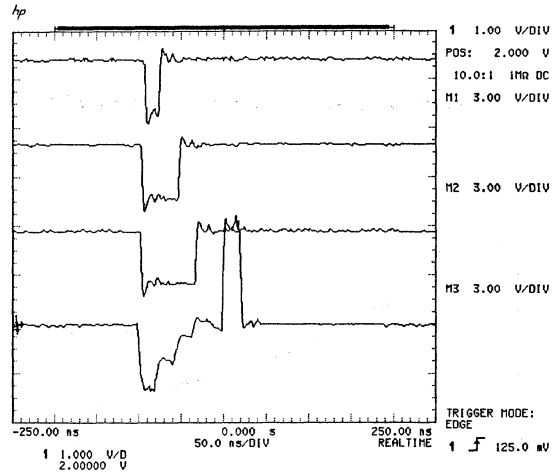


Figure 6: Reflection stub and comparator outputs

### 4 PERFORMANCE EVALUATIONS

All the measurements were made using Hewlett-Packard's HP8130A Pulse Generator, HP53310A Modulation Domain Analyser and 3631A Power Supply.

As stated in section 2.1 the main contributors for instability in high-performance oscillators are environmental factors like temperature and supply voltage variations. It is clear, that when trying to compensate the effect of such factors it is essential to know their effects of to correcting circuitry. All the plots presented in this paper are estimates of mean and standard deviation of the delay of the circuitry. Since measurement data contains also delay and distortion from signal source and cabling these must be eliminated before evaluating the results.

We know that if each  $X_i$  is a independent random variable with mean  $\mu_i$  and variance  $\sigma_i^2$ , then  $\sum X_i$  has mean  $\sum \mu_i$  and variance  $\sum \sigma_i^2$  [5].

If we have two independent variables

$$X_1 \sim N(\mu_1, \sigma_1), \text{ and}$$

$$X_2 \sim N(\mu_2, \sigma_2)$$

Then  $Y = X_1 - X_2$  is distributed as  $N(\mu_y, \sigma_y)$ , or

$$Y \sim N(\mu_1 - \mu_2, \sqrt{\sigma_1^2 + \sigma_2^2}) \quad (5)$$

The subtrahend distribution is the normal distribution of measurement system alone:

$$X_2 \sim (22.25 \text{ ns}, 96.71 \text{ ps})$$

Regression analysis is made in data and trend line is added to all the plots. All the measurements are made either from delay circuitry input to circuitry output or from circuitry input to output of one delay stage. This means, that every measurement includes delay of one 74F04 TTL-inverter, and ECL implementations plot includes also temperature coefficient of RC-network.

#### 4.1 HCMOS Transmission gate implementation

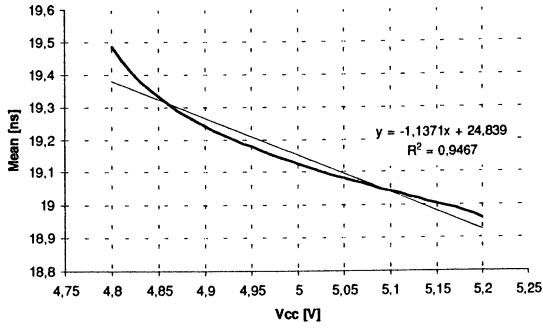


Figure 7: Delay vs. Vcc for HCMOS, mean.

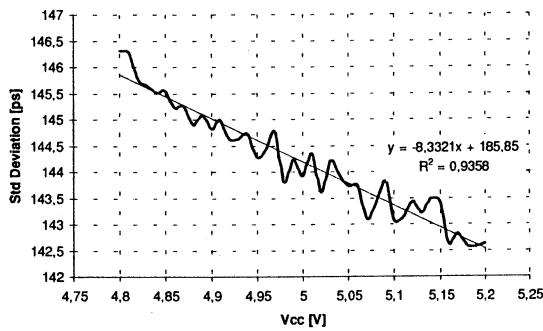


Figure 8: Delay vs. Vcc for HCMOS, standard deviation.

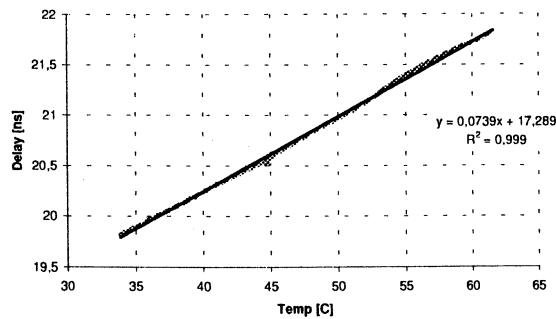


Figure 9: Delay vs. Temperature for HCMOS, mean

#### 4.2 ECL gate implementation

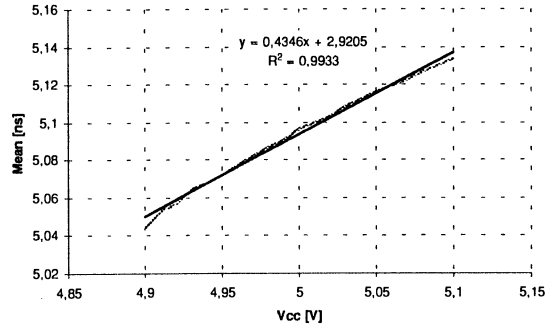


Figure 10: Delay vs. Vcc for ECL, mean.

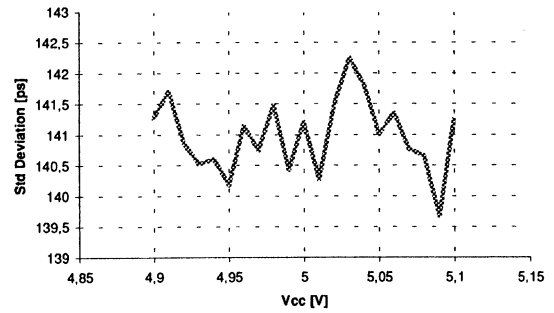


Figure 11: Delay vs. Vcc for ECL, standard deviation.

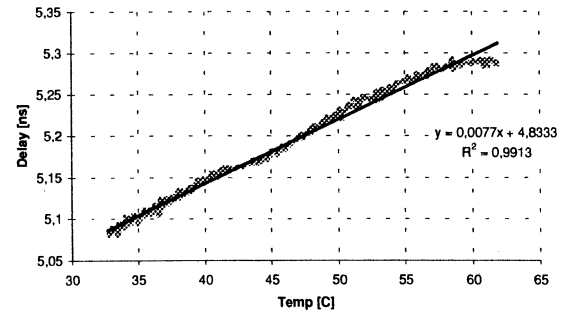


Figure 12: Delay vs. Temperature for ECL, mean.

Temperature did not have any measurable effect on standard deviation over testing range on either technology.

## 5 CONCLUSION

Three different designs for delay generation were tested and evaluated. All these designs were displaying predictable and quite linear response to environmental factors. They also displayed deviation well below desired calibration step.

Transmission gate design is capable of implementing delays down to one nanosecond, but is relatively slow to calibrate and can't be adjusted. Cascade ECL gates with RC-network is fast to calibrate and can be made adjustable to compensate its own temperature coefficient and to perform tight PCS calibration. Reflection stub is space effective when long delay steps are needed, since it can use several round trips to form several long delays with only one cable. On the other hand the comparator circuit is quite sensitive to variations in ambient temperatures so designs that are used in such environments must have temperature compensation.

## REFERENCES

- [1] Rutman, J. 1978. Characterization of Phase And Frequency Instabilities in Precision Frequency Sources: Fifteen Years of Progress. Proceedings of the IEEE, vol. 66, N #9, pp. 1048-1075.
- [2] Efratom Time & Frequency Products 1993 "Precision Time and Frequency Handbook" Ball Corporation.
- [3] Johnson, H. 1993. High Speed Digital Design, New Jersey, Prentice Hall.
- [4] Haznedar H. 1991. Digital Microelectronics, California, The Benjamin/Cummings Pub.
- [5] Barnes, J.W 1994. Statistical analysis for engineers and scientists, McGraw-Hill.

ASPECTS OF CALIBRATION OF A SIX-PORT CIRCUIT FOR PRECISE MEASUREMENTS OF PIEZOELECTRIC RESONATOR PARAMETERS

Aleksander Lisowiec, Marek Wójcicki  
Tele & Radio Research Institute, Warsaw, Poland

ABSTRACT.

An application of six-port technique in reference measurements of quartz resonator parameters has been presented. The main difficulty in such six-port technique application lies in obtaining bandwidth of over two decades with the lower end at 1 MHz. Aspects of calibrating the six-port reflectometer in the frequency range 1-500 MHz have been described. At this frequency range the six-port circuit as well as the subset of calibration items must be made in lumped elements circuit technique. The accuracy of reflection coefficient measurement in practical six-port reflectometer has been presented and basing on this the accuracy of quartz resonator parameters measurement by direct reflection method has been given.

REFERENCE METHODS OF QUARTZ RESONATOR PARAMETERS MEASUREMENT

The recommended methods for measurement of quartz resonator parameters are methods using network analyzer and automatic error correction [1].

In transmission method the resonator is connected as a two port in a measurement setup shown in figure 1. The full scattering matrix of the two-port is measured over some frequency range around resonance and the admittance of the resonator is calculated by a well known formula (1). The measured points are then fitted by a circle from which all relevant parameters of the resonator are determined.

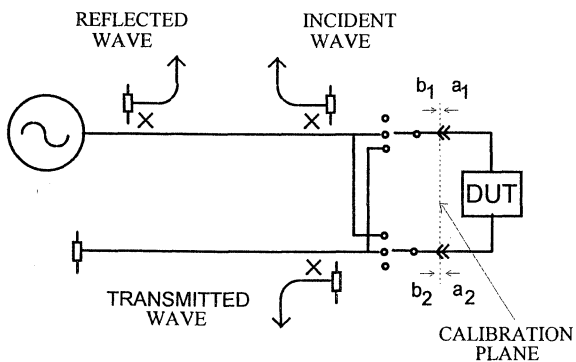


Figure 1: Quartz resonator measurement by transmission method.

$$Y = \frac{1}{Z_0} \frac{2S_{12}}{(1+S_{11})(1+S_{22}) - S_{21}S_{12}} \quad (1)$$

In reflection method the resonator is treated as one-port. Again the admittance values are

calculated from the measured reflection coefficient values, they are then fitted by a circle and resonator parameters are calculated.

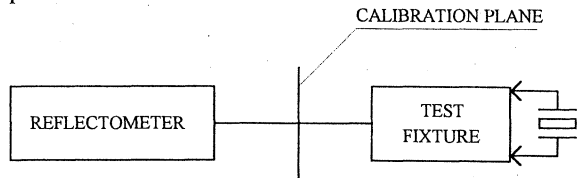


Figure 2: Quartz resonator measurement by reflection method.

$$Y = \frac{1}{Z_0} \frac{1 - S_{11}}{1 + S_{11}} \quad (2)$$

The method that offers potentially very high accuracy is direct reflection method. In this method the reflection coefficient in a transmission line terminated with quartz resonator is measured. But instead of transforming measured reflection coefficient values into admittance and approximating them by a circle, all relevant resonator parameters are calculated by simple analytic formulas from the knowledge of characteristic points of frequency characteristics of modulus and phase of reflection coefficient.

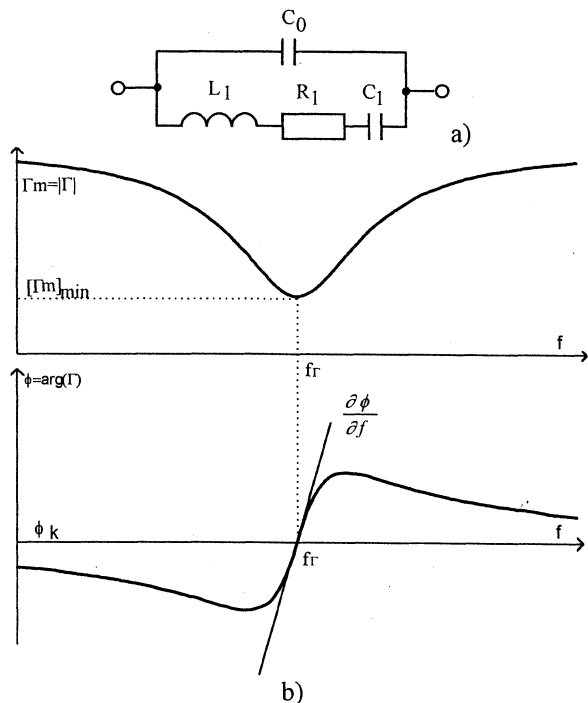


Figure 3: Modulus and phase frequency characteristics of reflection coefficient in a transmission line terminated with quartz resonator.

The necessary equations are presented below for four element equivalent electrical circuit (fig.3 a).

$$\frac{f_{\Gamma} - f_s}{f_s} = \frac{\frac{C_1}{C_0}}{2 \left[ 1 + \frac{1}{(Z_0 2\pi f_s C_0)^2} \right]} \quad (3)$$

$$R_1 = Z_0 \cdot \frac{1 + A \cdot [\Gamma_m]_{\min}}{(1 - A \cdot [\Gamma_m]_{\min}) \left( 1 + tg^2 \left( \frac{\phi_k}{2} \right) \right)} \quad (4)$$

$$Q = \frac{\partial \phi}{\partial f} \cdot f_s \cdot \frac{[\Gamma_m]_{\min}}{1 - [\Gamma_m]_{\min}^2} \quad (5)$$

$$C_0 = \frac{tg \left( \frac{\phi_k}{2} \right)}{2 \cdot \pi \cdot f_s \cdot Z_0} \quad (6)$$

$$C_1 = \frac{1}{Q \cdot 2 \cdot \pi \cdot f_{\Gamma} \cdot R_1} \quad (7)$$

In all of the before mentioned methods the proper measurement is preceded by calibration. Assuming linearity, almost all imperfections of the measurement system looking back from the calibration plane into the network analyzer can be removed.

As the resonator is basically a symmetrical device a test fixture is needed to connect it to the coaxial input of the measurement system at the calibration plane. Because the test fixture is not included into calibration path, the influence of the parameters of the test fixture on the accuracy of quartz resonator parameters measurement should be modeled mathematically.

Thus the accuracy of quartz resonator parameters measurement depends on the accuracy of scattering matrix or reflection coefficient measurement and on the accuracy of test fixture model.

## SIX-PORT PRINCIPLES

In microwave domain two methods of automatic impedance measurement have been developed. The heterodyne method introduced by Packard in mid fifties is exemplified in its modern form by an automatic network analyzer. Automatic network analyzers offer good accuracy and are extremely versatile.

The alternate method of impedance measurement is six-port technique [3]. In this technique one does not try to separate the incident and reflected waves from the measured object. Instead superpositions of these waves are arranged and then the powers of these superpositions are measured.

Simplified block diagram of the six-port reflectometer is presented in figure 2. One port is connected to the signal source, the second port is measurement port for connecting measured reflectance and the other four ports are connected to power meters.

$$\Gamma = \frac{a_2}{b_2} = \frac{k_1 \cdot \frac{P_3}{P_4} + k_2 \cdot \frac{P_5}{P_4} + k_3 \cdot \frac{P_6}{P_4} + k_4}{m_1 \cdot \frac{P_3}{P_4} + m_2 \cdot \frac{P_5}{P_4} + m_3 \cdot \frac{P_6}{P_4} + 1} \quad (8)$$

The value of the measured reflectance is calculated from the formula (8) where the complex  $k_1, \dots, k_4$  and real  $m_1, \dots, m_3$  are frequency dependent calibration constants that must be found in a special calibration procedure.

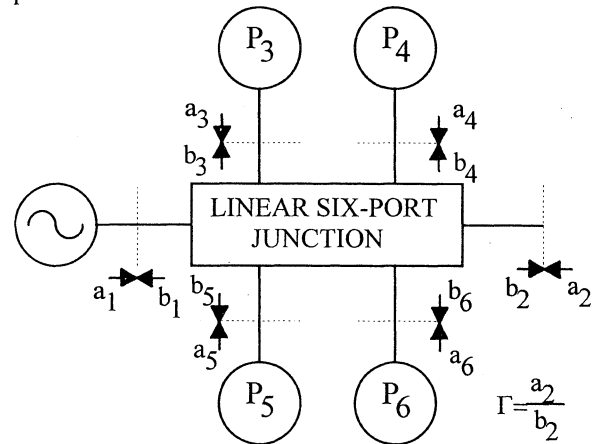


Figure 4: Block diagram of a six-port reflectometer.

There are many methods of six-port calibration. They consist generally of connecting certain number of impedance standards, taking power readings and calculating calibration constants. The mathematics of calibration routines usually demands that impedance standards are distributed on a unit circle in the reflection coefficient plane. Such standards, excluding open and short are narrow band, so to fully calibrate the six-port over two or three decade bandwidth a lot of calibration items would be needed making the calibration process very tedious.

## ASPECTS OF BROAD-BAND CALIBRATION

At present there is only one known broadband calibration method that in the sense that the same calibration items can be used in whole frequency range. It was originally developed by Engen [4] who also originated the six-port concept in

the early seventies and is known as a calibration method by reduction of six-port to four port.

In the first step of this calibration routine five calibration constants, the so called reduction coefficients are determined. As can be shown [4], the measured power ratios of a six-port reflectometer fulfill the formula (9) where  $x, y, z$  denote power ratios and  $p, q, r, a, b$  are real constants called reduction coefficients. This formula (known also in the literature as the Engen formula) describes in a space of power ratios a surface called elliptic paraboloid (fig. 5).

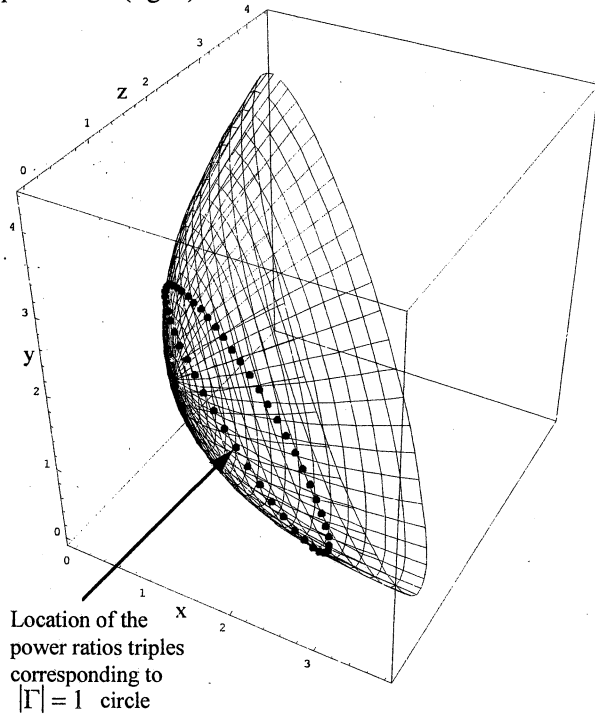


Figure 5: Location of the power ratios of the six-port junction with reduction coefficients  $p=4, q=5, r=5, a=2, b=2$ .

If we make substitutions (10) in (9), new equation (11) describing the paraboloid is obtained, which is linear in  $X_1, \dots, X_9$ .

$$px^2 + qa^2y^2 + rb^2z^2 + (r-p-q)axy + (q-p-r)bxz + (p-q-r)abyz + p(p-q-r)x + q(q-p-r)ay + r(r-p-q)bz + pqr = 0 \quad (9)$$

$$\begin{aligned} X_1 &= 1/(qr), X_2 = a^2/(pr), X_3 = b^2/(pq), \\ X_4 &= a(r-p-q)/(pqr), X_5 = b(q-p-r)/(pqr), \\ X_6 &= ab(p-q-r)/(pqr), X_7 = (p-q-r)/(qr), \\ X_8 &= a(q-p-r)/(pr), X_9 = b(r-p-q)/(pq) \end{aligned} \quad (10)$$

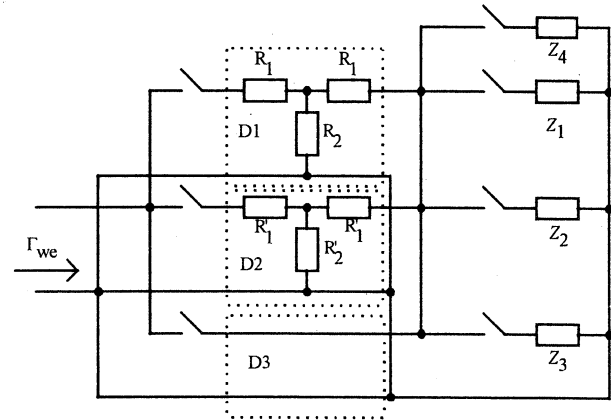
$$X_1x^2 + X_2y^2 + X_3z^2 + X_4xy + X_5xz + X_6yz + X_7x + X_8y + X_9z = -1 \quad (11)$$

Connecting at least 9 different but not necessarily precisely known reflectances, a set of equations can be obtained from which  $X_1, \dots, X_9$ , and by inverting (10), initial estimates of reduction coefficients can be calculated. As power ratio readings contain errors due to noise, limited resolution, etc., the values of reduction coefficients calculated from (10) are not precise. They must be optimized, usually by minimizing quantity

$$\sum_i \frac{(px_i^2 + qa^2y_i^2 + rb^2z_i^2 + (r-p-q)ax_iy_i + (q-p-r)bx_i z_i + (p-q-r)aby_i z_i + p(p-q-r)x_i + q(q-p-r)ay_i + r(r-p-q)bz_i + pqr)^2}{p(p-q-r)x_i + q(q-p-r)ay_i + r(r-p-q)bz_i + pqr} \quad (12)$$

where the summation is done over all power ratio readings.

In the frequency range of interest in quartz resonator measurements, which spans three decades with the lower limit at 1 MHz, the set of 9 sufficiently well separated in amplitude and phase reflectances in reflection coefficient plane can be realized only by a lumped elements circuit. An example of such circuit is shown in figure 3. If such 9-state reflection circuit is optimized so that over the whole frequency range of interest, the nine reflectances are sufficiently far separated in the reflection coefficient plane, reduction coefficients can be determined without doing any manual connections.



$$Z_1 = \frac{1}{j\omega C_1} \quad C_1 = 10 \text{ pF}$$

$$Z_2 = \frac{1}{j\omega C_2} \quad C_2 = 680 \text{ pF}$$

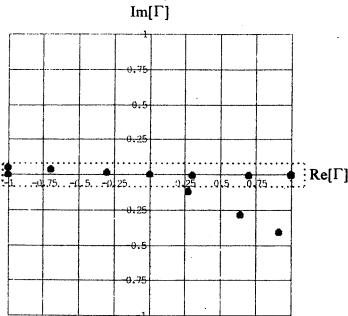
$$Z_3 = j\omega L_1 \quad L_1 = 0.2 \text{ } \mu\text{H}$$

$$Z_4 = j\omega L_2 \quad L_2 = 6.8 \text{ } \mu\text{H}$$

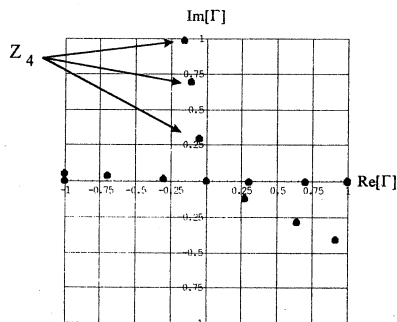
Figure 6: Augmented 9-state reflection circuit.

The condition cited in the literature that is imposed on the 9 reflectances used in the reduction process is that at least 3 out of them have different amplitudes and at least 3 have different phases [5]. This condition is not sufficient. Namely it can be

shown that if five or more of the 9 reflectances lie on the same line or on the same circle in a reflection coefficient plane, the power ratios obtained during their measurement lie on the same surface defined by a linear equation  $Ax + By + Cz + D = 0$ . Linear dependence of  $x$ ,  $y$ ,  $z$  and Engen formula (8) let obtain only four independent equations of the form (11) while at least nine are needed.



Values of the reflection coefficients of 9-state reflection circuit together with open, short and matched load at 1 MHz



Values of the reflection coefficients of the modified 9-state reflection circuit together with open, short and matched load at 1 MHz

Figure 7: Reflectances obtained by the augmented 9-state reflection circuit.

9-state reflection circuit optimized for maximal phase differences in the band 1-500 MHz (calculated values of  $C_1$ ,  $C_2$ ,  $L_1$  are given in fig.6), exhibits around 1 MHz the property that the reflectances of  $C_1$  branch lie almost on the same line as reflectances of  $L_1$  branch. This causes the set of equations of the form (11) to be badly conditioned. The remedy to this is to augment the 9-state reflection circuit by an additional reflectance (in this case a SMD inductance 6.8  $\mu\text{H}$  -  $Z_4$ ) that is switched in the range 1-5 MHz.

After the set of reduction coefficients for each frequency of interest has been determined, the second stage of six-port calibration is similar to calibrating traditional network analyzer. Three complex constants  $d=dr+jdi$ ,  $e=cr+jci$ ,  $e=er+jei$  (again each frequency dependent) must be found that relate measured reflection coefficient  $\Gamma$  to the complex quantity  $w$  by the formula

$$w = \frac{d\Gamma + e}{c\Gamma + 1} \quad (13)$$

where  $w$  is found from power ratios and reduction coefficients by the formula

$$w = \frac{x - ay + r}{2\sqrt{r}} + j \cdot \frac{r(p+q-r) + (p-q+r)x - (p-q-r)ay - 2rbz}{\pm 2\sqrt{r(2pq + 2qr + 2rp - p^2 - q^2 - r^2)}} \quad (14)$$

Conveniently open, short and matched load broadband reflection standards can be used in this stage of the calibration process.

Formula relating measured reflection coefficient to the observed power ratios and eleven constants:  $p$ ,  $q$ ,  $r$ ,  $a$ ,  $b$ ,  $dr$ ,  $di$ ,  $cr$ ,  $ci$ ,  $er$ ,  $ei$ , characterizing the six-port at each frequency is a rational function of the first order in  $x$ ,  $y$  and  $z$ .

### PRACTICAL CIRCUIT

The practical six-port circuit is presented in figure 8 together with equations describing it and a block diagram of the measurement system is presented in figure 9. In fact the six-port has been realized as a switched four-port where different superpositions of the waves incident and reflected from the measured object have been realized by changing the internal structure of the four-port by means of switched internal reflectors. This has the advantage that only two power detectors can be used in place of four (one of them is the reference detector). This switched four-port is a modified version of a circuit originally developed at Slovak Technical University, Bratislava.

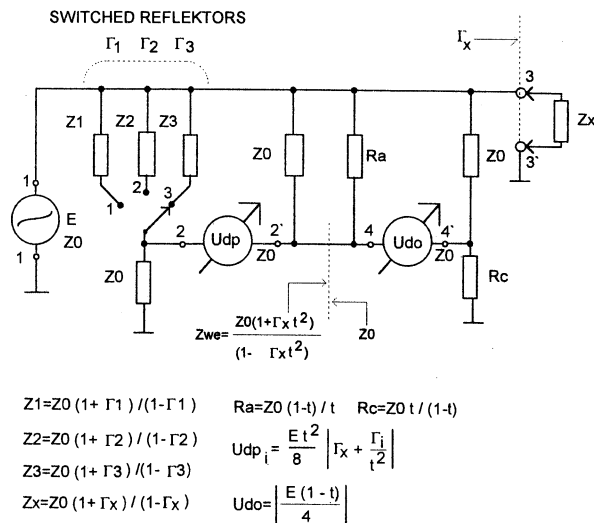


Figure 8: Simplified block diagram of the six-port junction.

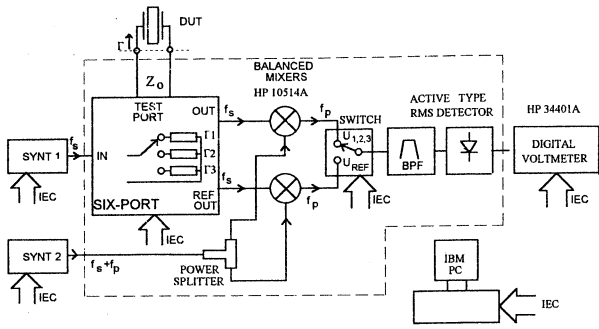


Figure 9: Block diagram of the measurement system.

### REFLECTION COEFFICIENT MEASUREMENT ACCURACY

The six-port reflectometer has been calibrated by the method just described and figure (10) shows the accuracy that has been achieved. The accuracy of the reflection coefficient measurement is comparable to the accuracy of HP automatic network analyzers.

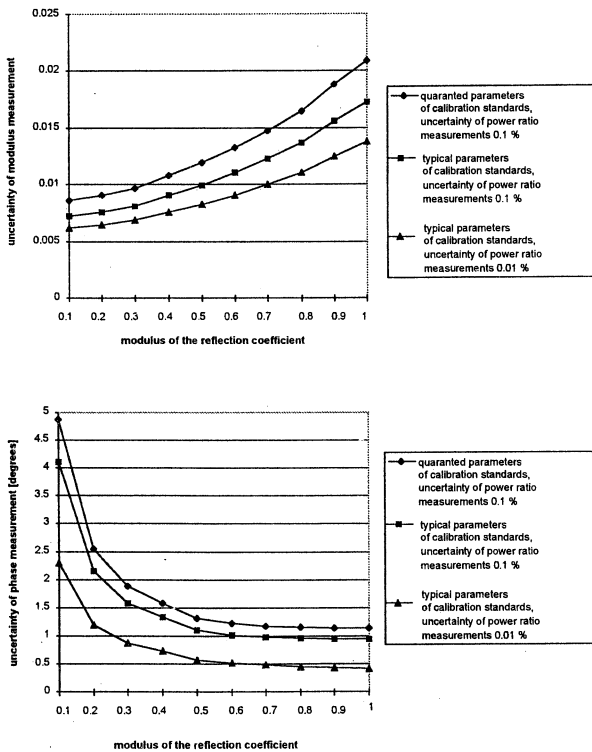


Figure 10: Accuracy of reflection coefficient measurement obtained with the practical six-port reflectometer.

### RESONATOR PARAMETERS MEASUREMENT ACCURACY

Having determined the accuracy of reflection coefficient measurement, the accuracy of quartz resonator parameters measurement by direct reflection method can be evaluated basing on the

equations (3)-(7) Figures (11) to (15) show the accuracy of resonator parameters measurement.

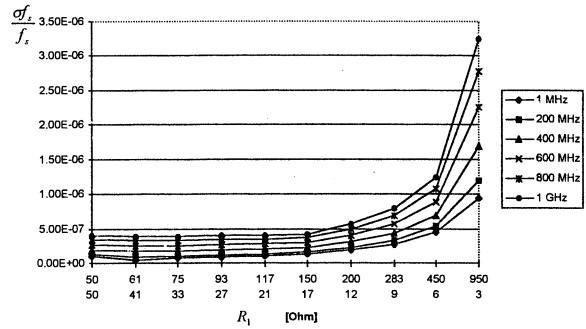


Figure 11: Relative accuracy of series resonance frequency measurement.

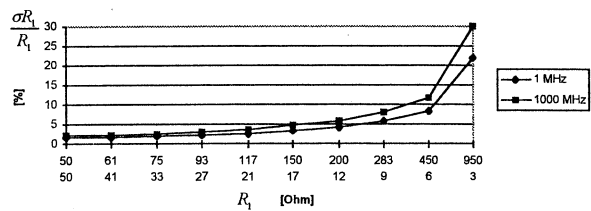


Figure 12: Relative accuracy of series resistance measurement.

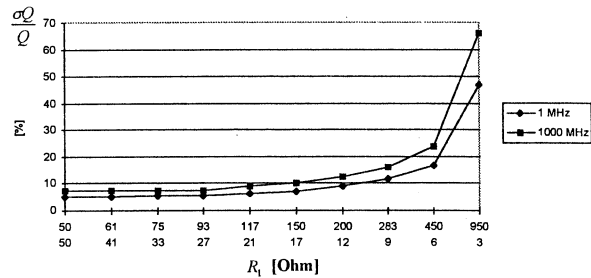


Figure 13: Relative accuracy of Q-factor measurement.

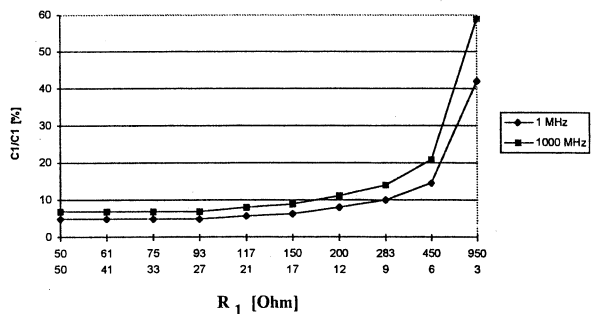


Figure 14: Relative accuracy of dynamic capacitance  $C_1$  measurement.

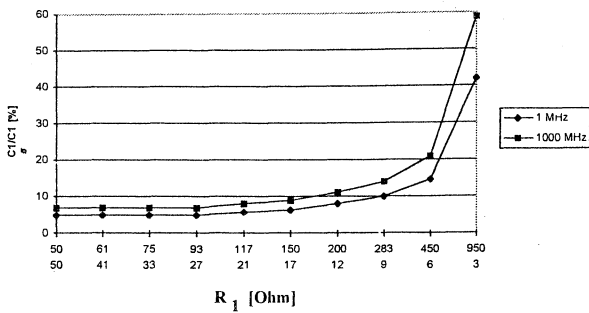


Figure 15: Relative accuracy of static capacitance  $C_0$  measurement.

## CONCLUSION

Six-port technique can be successfully applied in quartz resonator parameters measurement. Due to its technical simplicity and comparable accuracy it is an attractive alternative to heterodyne network analyzer. The main difficulty lies in obtaining over two decades bandwidth with lower limit at 1 MHz. At this frequency range the six-port junction has to be realized in lumped elements circuit technique. Six-port calibration by reduction of six-port to four port also demands the use of reflectances realized in lumped elements circuit technique as a subset of calibration standards.

Quartz resonator parameters measurement by direct reflection method enables easy accuracy assessment due to simple analytic formulas relating resonator parameter values to characteristic points of reflection coefficient modulus and phase frequency characteristics. The relative accuracy that has been achieved in a practical circuit with six-port circuit as reflection coefficient meter is better than 1 ppm for series resonant frequency, 2% for series resistance and around 5% for the rest of resonator parameters in a four element electrical equivalent circuit.

## REFERENCES.

1. IEC Norm 444-5 Part 5: Methods for measurement of quartz crystal devices for the determination of equivalent electrical parameters using automatic network analyzer and error correction.
2. Bilik V. et al., Lumped Wideband Six-Port Structures, Research report F426, Fac. of Elec. Eng., Slovak Tech. Univ., Bratislava, 1988
3. Engen G. F., The six-port reflectometer: An alternative network analyzer, IEEE Trans. Microwave Theory and Tech., 1977
4. Engen G. F., Calibrating the six-port reflectometer by means of sliding terminations, IEEE Trans. Microwave Theory and Tech. MTT-26, 1978
5. Hjiipieris G., Potter G. M., Ultra-broadband vector reflectometer using the six-port technique, MIOP 93, 7<sup>th</sup> Exhibition and Conference for Ultra High Frequency Technology, Sindelfingen, 1993
6. Lisowiec A., Wójcicki M., Six-Port Measuring System for Accurate Determination of Piezoelectric Resonators Parameters, Proc. of 8<sup>th</sup> Piezoelectric Conference PIEZO'94, Zakopane 1994
7. Lisowiec A., Wójcicki M., Six-port technique in reference measurements of piezoelectric resonator parameters, Proc. of 9<sup>th</sup> EFTF, Besancon, 1995

## VHF and Microwave Interferometric PM and AM Noise Measurements

E. Rubiola <sup>†</sup>, V. Giordano <sup>‡</sup>, J. Gros Lambert <sup>‡</sup>

<sup>†</sup> Politecnico di Torino, Dipartimento di Elettronica  
c. Duca degli Abruzzi no. 24 I-10129 Torino - ITALY

<sup>‡</sup> Laboratoire de Physique et de Métrologie des Oscillateurs  
Unité Propre de Recherche du CNRS n°1303 associé à l'Université de Franche-Comté  
32, A. de l'Observatoire 25044 Besançon Cedex - FRANCE

### Abstract

The interferometric technique allows close to the carrier measurements of both phase and amplitude noise, improving the instrument noise floor by 10–25 dB as compared to the traditional method based on a saturated mixer. In this paper we present the experiments done at the LPMO, in co-operation with the Politecnico di Torino, both in the microwave (7–9 GHz) and in the VHF (100 MHz) bands. Moreover, we propose a new scheme which combines the advantages of the cross-correlation and interferometric methods.

### I. Introduction

The interferometric method for measuring PM and AM noise close to the carrier was proposed by Sann about 30 years ago [1]. A quite similar technique was also proposed by Horn to extend the dynamic range of spectrum analysers [2]. But it was only recently that the interferometric technique revived the attention of the time and frequency metrology community, after some impressive results published by the University of Western Australia (UWA). In fact, it has been demonstrated that this method allows the improvement of the noise floor of PM and AM noise measurement set-up by 10 to 25 dB in X-band [3]. The noise of some devices, such as phase shifters and isolators, can be measured only with that method. As the interferometric scheme makes the instant value of noise available in real time, dynamic correction of amplifier and oscillator noise is also possible [4].

Studying the interferometric method at the LPMO, in co-operation with the Politecnico di Torino, we first built an interferometer operating in the 9 GHz band, obtaining results close to those reported by the UWA. Then we successfully tested the same technique in the VHF band, at 100 MHz. Finally, we experimented the well-known cross-correlation technique on two equal interferometers that measure the same DUT (Device Under Test).

In the first part of this paper, conventional phase noise measurement set-up, based on a saturated mixer, is compared with the interferometric scheme giving particular attention to the instrument noise floor. Then

microwave and VHF implementations are described in detail, giving their performances in terms of white and flicker noise. Finally the double interferometer technique is presented and discussed.

### II. Review of Noise Measurements Principles

Measurement of noise close to the carrier is something comparable to distinguishing a glow-worm beside a bright halogen lamp. The only means to avoid being dazzled is to darken the light. When measuring noise close to a carrier signal, we come up against the same kind of difficulty. Let's consider a simplified model (Fig. 1), where a pure sinusoid of power  $C$  passes through a DUT, being modulated by the internally generated phase noise of the latter. In this condition, the DUT causes phase noise sidebands of power spectral density  $N_\phi$  around the carrier.

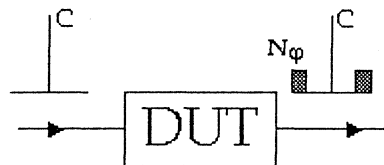


Fig 1. Challenge to measure PM noise. Phase noise only is considered here.

Close to the carrier frequency, the noise density referred to the carrier power, i.e.  $N_\phi/C$ , can be of the order of  $10^{-16}$  or less. No instrument has exhibited a dynamic range sufficient to measure such a low noise power without being blinded by the carrier. Consequently the carrier must be suppressed.

Traditionally, carrier suppression is accomplished through a multiplication which takes place inside a Double Balanced Mixer (DBM), as shown in Fig. 2. Provided that the two mixer inputs are in quadrature ( $\gamma=90^\circ$ ), a voltage  $v(t)$  proportional to the instant phase fluctuation  $\phi(t)$  induced by the DUT is present at the mixer IF output. Defining  $S_\phi(f) = 2N_\phi/C$  as the power spectrum density (PSD) of the PM noise  $\phi(t)$ , the IF voltage PSD turns out to be

$$S_v(f) = K_d S_\phi(f) \quad (1)$$

where  $K_d = \mu^2$ , and  $\mu$  is the gain of the DBM when used as phase detector. In most practical cases,  $\mu$  spans in the 0.1 to 0.3 V/rad range, depending on the mixer input power.

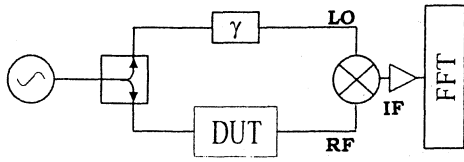


Fig 2. Conventional PM noise measurement.

White noise floor (for  $f_m > 1$  kHz) limitation for this technique is due to the equivalent input noise voltage of the low-frequency amplifier inserted at the mixer output. For reference, a typical noise floor of the order of  $-170$  dB $\text{rad}^2/\text{Hz}$  can be achieved driving the mixer with 15 dBm signals; in addition, flicker noise of  $-140$  dB $\text{rad}^2/\text{Hz}$  @ 1Hz is present, due to the mixer. Decreasing the driving level, the mixer gain decreases, and the instrument suddenly becomes unusable.

In the interferometric method (Fig. 3), carrier suppression is achieved by vector addition of an equal signal opposite in phase.

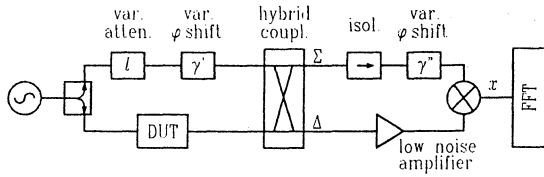


Fig 3. PM and AM noise interferometric measurement.

Setting  $l$  and  $\gamma'$  equal to the DUT attenuation and phase shift respectively, interference takes place in the hybrid coupler. In this condition, all the carrier power goes to the  $\Sigma$  output. The carrier is suppressed at the  $\Delta$  output, where only the DUT noise sidebands are present. The latter are amplified and down converted to baseband by a DBM. As no carrier power is present at the  $\Delta$  output, the amplifier operates in its fully linear regime, thus preventing the amplifier to generate flicker noise by up converting near-dc flicker. Setting the detection phase  $\gamma''$  to  $90^\circ$  or  $0^\circ$ , the mixer down converts PM or AM noise respectively.

With reference to the scheme of Fig. 2, the mixer IF output PSD is given by

$$S_{\text{IF}}(f) = \frac{g_a}{\ell_h \ell_m} N_\varphi(f) \quad (\text{W/Hz}) \quad (2)$$

where  $\ell_h$  and  $\ell_m$ , respectively, are the hybrid coupler and mixer *additional losses* (in both cases the factor 1/2 due to power splitting is not included in the definition of  $\ell_h$  and  $\ell_m$ ) and  $g_a$  is the amplifier gain. Then, the voltage noise PSD at the FFT input is

$$S_V(f) = \frac{R_0 g_a}{\ell_h \ell_m} N_\varphi(f) \quad \text{V}^2/\text{H}(z) \quad (3)$$

where  $R_0 = 50 \Omega$  is the resistive termination value. Finally, the system gain is

$$K_d = \frac{R_0 g_a C}{2 \ell_h \ell_m} \quad \text{V}^2/\text{rad}^2 \quad (4)$$

If the additional losses are  $\ell_h = 0.5$  dB and  $\ell_m = 3$  dB (typical values for real world hybrids and mixers), a  $g_a = 37$  dB amplifier is chosen and the driving power is set so that  $C = 15$  dBm,  $K_d$  turns out to be 32 dB $\text{V}^2/\text{rad}^2$ , which is equivalent to a phase-to voltage gain of 40 V/rad. The latter is 100 times higher than the gain of traditional measurement systems.

White noise floor can be derived from the equivalent noise at the RF amplifier input. Letting  $F$  be the amplifier noise figure,  $k = 1.38 \times 10^{-23}$  W/Hz, and  $T_0$  the absolute ambient temperature, which is also the temperature of the interferometer, the amplifier equivalent input noise is  $FkT_0$ . Taking into account the down conversion mechanism, the voltage noise floor is given by

$$S_V^{\text{floor}}(f) = \frac{R_0 g_a}{\ell_m} FkT_0 \quad (5)$$

Consequently, the PM noise floor of the instrument is

$$S_\varphi^{\text{floor}}(f) = \frac{S_V^{\text{floor}}(f)}{K_d} = 2 \ell_h \frac{FkT_0}{C} \quad (6)$$

All the above formulae still hold for the AM noise, provided that  $\varphi$  is replaced with  $\varepsilon$  ( $\varepsilon$  stands for the relative amplitude noise) and  $\gamma''$  is set to  $0^\circ$ .

The white noise floor decreases as the carrier power  $C$  increases. For example, with  $F=2$  dB,  $T_0 = 300$  K and  $C=10$  dBm, one obtains an  $S_\varphi^{\text{floor}}$  value of the order of  $-180$  dB  $\text{rad}^2/\text{Hz}$ . Flicker noise is also present and it could come from the intrinsic noise of the variable attenuator and phase shifter. Moreover, high carrier suppression is required to maintain the RF amplifier in its linear regime in order to avoid the conversion of dc bias noise to close to the carrier noise. Suppression values of 60 to 80 dB can be necessary, depending on the carrier power and the amplifier dynamic range. It should be noted that a carrier suppression of 80 dB implies that phase and attenuation of the interferometer ( $\gamma'$  and  $l$ ) are to be set within 100  $\mu\text{rad}$  and  $9 \times 10^{-4}$  dB, respectively, to their nominal values. Consequently, a stable mechanical arrangement must be ensured in order to keep the carrier suppression at the desired level for the duration of the experiment. According to our experience, SMA type connectors and semirigid cables are necessary even for the 100 MHz experiments, and the interferometer is to be placed on an optical table. In these conditions, we are able to

maintain a carrier suppression of 70–90 dB for about half an hour.

### III. Measurements at 9 GHz

The 9 GHz interferometer prototype is shown in Fig. 4.

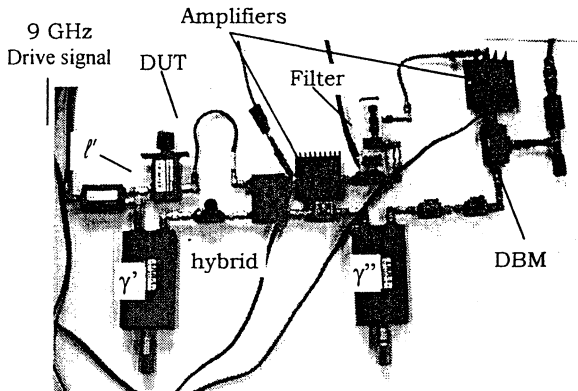


Fig. 4. X band interferometer operating at 9 GHz.

The main difficulties arising from X-band are:

*i - Wavelength.* Because at 9 GHz wavelength is about 25 mm inside coaxial cables, phase accuracy and stability equivalent to a cable length of 0.4  $\mu\text{m}$  are to be ensured if a carrier suppression of 80 dB is needed. The desired stability can be achieved only using an antivibrating table.

*ii - Amplifiers bandwidth.* As the bandwidth of our microwave amplifiers is of the order of 10 GHz, the total thermal noise could push the amplifiers out of linearity. For this reason, we inserted a dielectric filter with a bandwidth of 100 MHz in the amplifier chain.

*iii - Hybrid and mixer isolation.* Microwave devices, as hybrids and mixers, show poor isolation, typically of the order of 20 dB. Consequently, a fraction of the amplifier output signal, passing through the mixer and the hybrid, goes back to the amplifier input. In order to prevent oscillation or measurement alteration, a proper isolation must be ensured. The best configuration of the isolators must be determined with some attempts, taking into account that the isolators in this case can produce small but unpredictable phase alterations due to their interaction with reflected waves.

In order to measure the instrument noise floor we replaced the DUT with a short cable. The amplifier, which consists of two cascaded modules, shows a gain  $g_a = 41.5$  dB. A directional coupler, inserted between the two stages, allows the monitoring of the residual carrier. Our DBM shows an additional loss  $l_m = 5.5$  dB. When operating with a carrier power  $C = 14$  dBm, we expect a gain  $K_d = 33.9$  dB from the equation (4),

which is in close agreement to the measured value  $K_d = 34.3$  dB. The latter was obtained by injecting a suitable modulation in the DUT path and measuring the corresponding voltage PSD at the mixer output.

The PM noise floor of our prototype is shown in Fig. 5. The observed white noise floor is in agreement with the predicted one, given by the equation (6). Table 1 summarises the performances of our 9 GHz prototype.

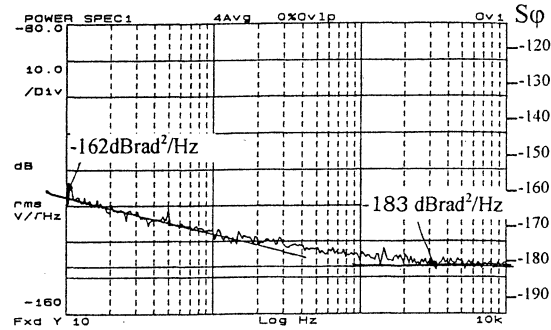


Figure 5. Phase noise floor of the 9 GHz interferometer operating with a DUT power of 14 dBm. Fourier frequency spans from 10 Hz to 10 kHz.

Frequency	: 9 GHz
Power (DUT output)	: 14 dBm
Equivalent gain	: 52 V/rad 34.3 dB
$S_{\phi}^{\text{floor}}(f_m) = -183 \text{ dBrad}^2/\text{Hz} (f_m > 1\text{kHz})$	
$S_{\phi}^{\text{floor}}(1\text{Hz}) = -152 \text{ dBrad}^2/\text{Hz}$	

Table 1. Performances of the 9 GHz Interferometer.

### IV. Measurements at 100 MHz

Fig. 6 shows the experimental set-up operating at 100 MHz.

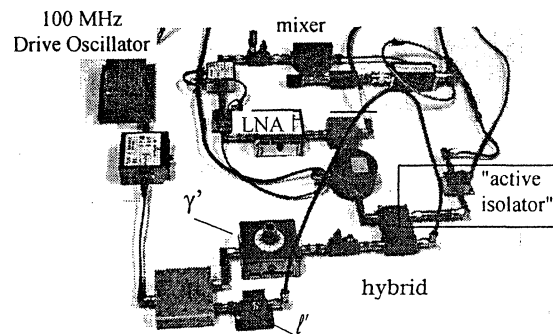


Fig. 6. 100 MHz Interferometer.

In the realisation of a VHF prototype, problems and solutions are different to those encountered in the microwave region.

*i - Ferrite isolators are not available.* Active isolators must be used, based on attenuator-amplifier pairs. Although noise is not a critical point in this part of the circuit, it is really important to drive the amplifier and the mixer with appropriate power level.

ii - Low noise phase shifters are not available. Surprisingly, all the available phase shifter — even those successfully used in the microwave experiments — could not be used in the VHF band because of their internally generated noise. This could be explained in terms of parasitic capacitance in parallel to non-perfect electrical contacts, which behave as short circuits at 9 GHz and as microphones at 100 MHz. Anyway, instead of investigating that problem we designed a specific phase shifter for this application.

iii - Almost all commercially available components have a bandwidth of 2–3 decades. Harmonic distortion is responsible for the presence of unwanted signals at frequencies multiple of the carrier frequency. Obviously, the carrier suppression mechanism has no effect on these unwanted signals. The only known solution consists of inserting low Q bandpass filters in certain key points of the circuit.

The above proposed solutions can also be used at lower frequencies, such as 5–10 MHz. Figure 7 and table 2 summarise performances of our 100 MHz interferometer.

Frequency	: 100 MHz
Power (DUT output)	: 9 dBm
Equivalent gain	: 41 V/rad
	32.3 dB
$S_{\phi}^{\text{floor}}(f_m) = -178 \text{ dBrad}^2/\text{Hz} \text{ (} f_m > 1\text{kHz)}$	
$S_{\phi}^{\text{floor}}(1\text{Hz}) = -150 \text{ dBrad}^2/\text{Hz}$	

Table 2. Performances of the 100 MHz Interferometer.

Although our interest is focused on the instrument itself, we measured some components for demonstrative purposes only. Figure 8 shows the phase noise of a commercial amplifier (UTO 512) working at an output power of 0 dBm. In this condition, the instrument gain is  $K_d = 24 \text{ dBV}^2/\text{rad}^2$  and the instrument noise floor is

$-165 \text{ dBrad}^2/\text{Hz}$ . It should be noted that this measurement would have been impossible with the traditional scheme of Fig. 2.

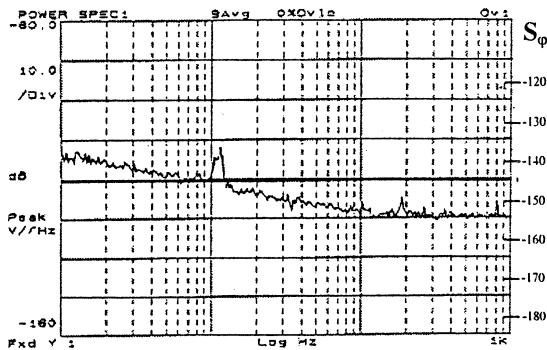


Fig. 8. PM noise of a UTO 512 amplifier driven by a low power signal. Output level is 0 dBm (Frequency span 1Hz-1kHz)

After observing that microwave phase shifters are more noisy in the VHF band than in the microwave one, we systematically measured some of them. Results are shown in Fig. 9.

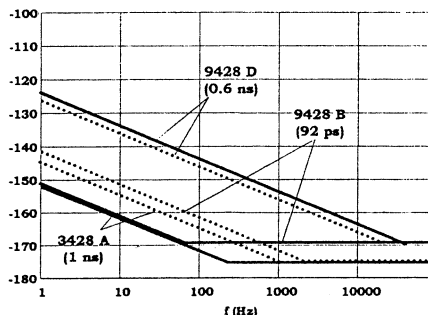


Fig. 9. PM (—) and AM (...) noise of ARRA mechanical phase shifters measured at 100 MHz.

Flicker PM noise of the 9428 B and 3428 A are close to the instrument noise floor. The available 9428D is an old component and its internal contacts could have been stressed. Finally, it should be pointed out that these phase shifters are not designed to operate in the VHF band.

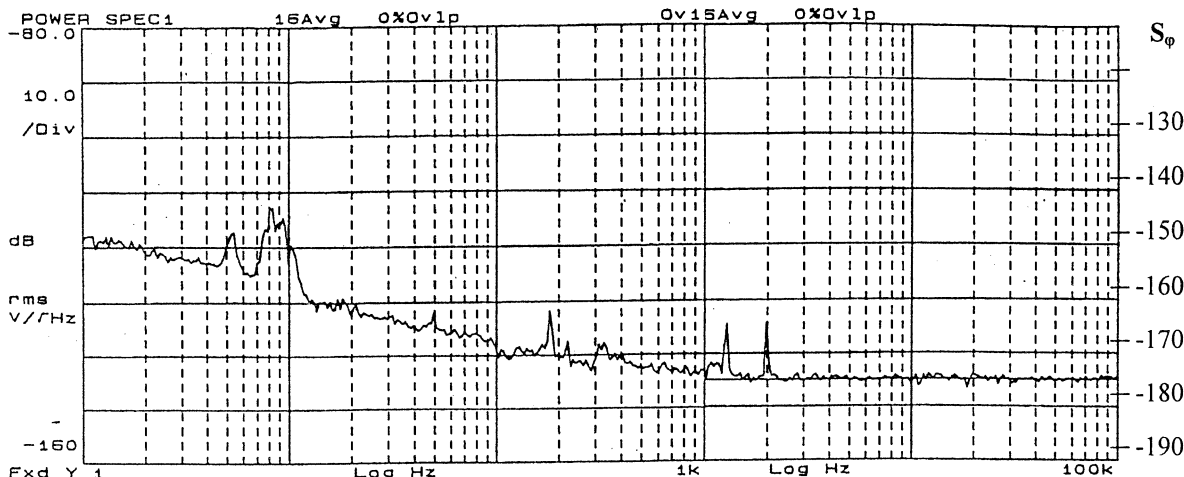


Fig. 7. 100 MHz interferometer noise floor. (Frequency span 1Hz-100kHz)

## V. Double Interferometer

We improved the interferometer idea by cross-correlating the outputs of two equal interferometers, as shown in Fig. 10; two configurations are proposed, with a single DUT or two equal ones.

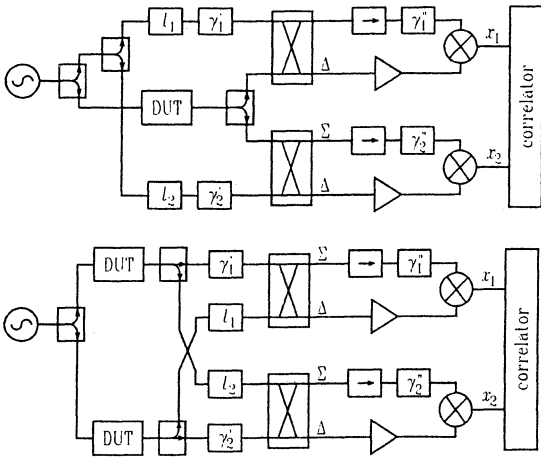


Fig. 10. Double interferometer schemes. Top: single DUT configuration. Bottom: twin DUTs variant.

We built two prototypes of the double interferometer, working at 7.3 GHz and 100 MHz; this latter is shown in Fig. 11.

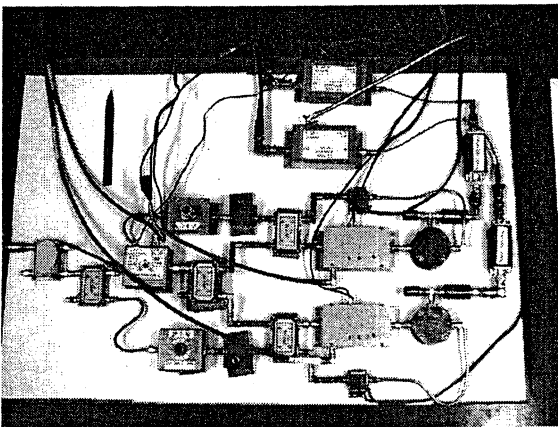


Fig. 11. 100MHz Double interferometer prototype.

The gains of amplifiers, the bandwidths of filters, the carrier suppression and all the other parameters are close to those of the above described 9 GHz and 100 MHz interferometers, respectively. Preliminary results of the microwave version are available in [5], while the VHF one is still unpublished.

If each interferometer is regarded as a sort of low noise mixer, our scheme is similar to the dual mixer cross-correlation system, known since the early 80s [6]. As the noise floor for this configuration is still not clearly understood, we are only able to give a brief statement of our knowledge.

Basically, the cross-correlation mechanism can not eliminate noise that it is present at both mixer outputs, coming from the same source. Accordingly, insufficient isolation between the two arms, made worse by signal reflections in non-perfectly matched junctions, takes in correlated noise; similarly, resistive loss at the input of the power splitters, which must be of the reactive type, causes correlated noise. In addition, there is a more relevant limitation, inherent to the power splitters. These devices are actually 4-port hybrids internally terminated (Fig. 12), otherwise they could not be impedance matched.

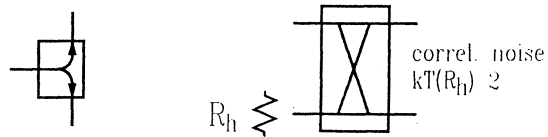


Fig. 12. A reactive power splitter is an hybrid internally terminated by a resistor  $R_n$ . Thermal noise of this latter is divided into the two outputs.

Therefore, noise power originated by that internal resistor is divided into the two outputs and it gives fully correlated noise contributions. Because of these resistors, all the three power splitters of Fig. 10 are responsible for correlated noise at the two amplifier inputs. This makes one think that the cross-correlation mechanism would not be able to overcome the thermal noise limitation.

Nevertheless, experimental results are in contrast with the above conclusion. In fact, we obtained an instrumental noise  $S_p^{\text{floor}} = -192$  dBrad<sup>2</sup>/Hz with  $C=15$  dBm for the microwave prototype and  $S_p^{\text{floor}} = -194$  dBrad<sup>2</sup>/Hz with  $C=8$  dBm for the VHF one. The instrumental noise of the latter is shown in Fig. 13.

This suggests a noise carrier - noise floor product  $CS_p^{\text{floor}}(f)$  of the order of  $-180$  dBrad<sup>2</sup>/Hz, which is well below the thermal noise. Although we have no explanation for this unexpected low noise and we are aware that the reported data are hard to believe, we wish to stress that these results are *reproducible*. In fact, the two prototypes are made with quite different components and technologies, and the instruments that make them work are different.

Although the white noise limit of the double interferometer is still under discussion, it is clear that this configuration allows the rejection of the flicker noise of attenuators and phase shifters. This feature makes an automatically tuned version of our scheme feasible, bypassing the limitation due to the higher noise of the voltage controlled attenuators and shifters as compared to the manually adjustable ones.

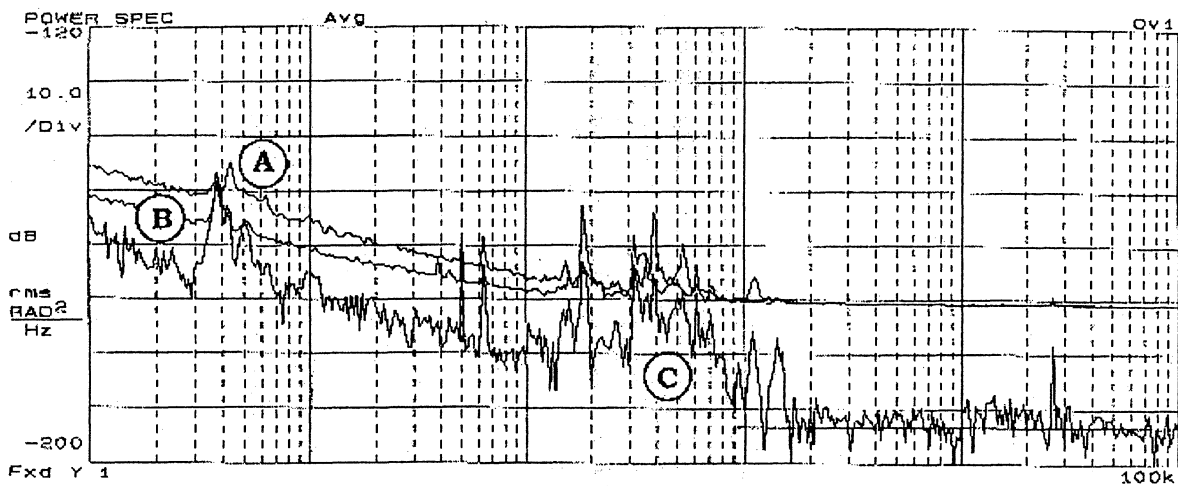


Fig. 13. Instrumental noise of the 100 MHz double interferometer prototype. The two upper plots represent the noise PSD measured at the two arm outputs, while the lower plot is the cross correlation, i.e. the instrument noise. DUT power is  $C = 8$  dBm.

## VI. Conclusion

We demonstrate the possibility to achieve low PM and AM noise floors with the interferometric method in a wide frequency range. Two prototypes have been built in the X-band (9 GHz) and in the VHF band (100 MHz). Gain values of about 40V/rad and noise floor values around  $-180$  dBrad<sup>2</sup>/Hz (white) and  $-150$  dBrad<sup>2</sup>/Hz @ 1 Hz (flicker) have been obtained, with power level from 9 to 15 dBm. Furthermore, we improved the interferometer by cross-correlating the outputs of two identical ones. Two double interferometer prototypes have been built and tested, working at 7.3 GHz and 100 MHz. Both these instruments show noise floor of the order of  $-190$  dBrad<sup>2</sup>/Hz. As the theory of the double interferometer configuration is still not clearly understood, further work is in progress,

## Acknowledgements

We wish to acknowledge our colleagues, M. Olivier of the LPMO, S. Leschiutta, A. Ferrero, M. Siccardi, F. Maddaleno and G.P. Bava of the Politecnico di Torino for contributing to this work with fruitful discussions.

## References

- [1] K.H. Sahn, "The measurement of near-carrier noise in microwave amplifiers", *IEEE Trans. Microw. Theory Tech.*, vol. MTT-16 no. 9 pp. 761-766, 1968.
- [2] C.H. Horn, "A carrier suppression technique for measuring S/N and carrier sideband ratios greater than 120 dB", *Proc. of the 23<sup>rd</sup> Annual Frequency Control Symposium* pp. 223-235, Atlantic City, NJ (USA), 6-8 May 1969.
- [3] E.N. Ivanov, M.E. Tobar, R.A. Woode, "A study of noise phenomena in microwave components using an advanced noise measurement system", *IEEE Trans. Ultrason. Ferroelectr. Freq. Control*, vol. 44 no. 1 pp. 161-163, 1997.
- [4] E.N. Ivanov, M.E. Tobar, R.A. Woode, "Ultra-low noise microwave oscillator with advanced phase noise suppression system", *IEEE Trans. on Microwave and Guided Wave Letters*, vol. 6, no 9 pp. 312-315, 1996.
- [5] E. Rubiola, V. Giordano, J. Gros Lambert, "Double correlating interferometer scheme for measuring PM and AM noise", *Electronics Letters* vol. 34 no. 1 pp. 93-94, 8<sup>th</sup> Jan. 1998.
- [6] D. Fest, J. Gros Lambert, J. J. Gagnepain, "Individual characterisation of an oscillator by means of cross-correlation or cross covariance method", *IEEE Trans. on Instr. & Meas.* vol. 32 no. 3 pp. 447-450, Sept. 1983.

## “THE ANTI JITTER CIRCUIT FOR LOW SPURIOUS DDS SQUARE WAVES AND LOW COST FRACTIONAL N SYNTHESIS”

M J UNDERHILL, S STAVROU & M BLEWETT

School of Electronic Engineering, Information Technology and Mathematics  
University of Surrey, Guildford, Surrey, GU2 5XH - UK

N. DOWNIE

Maran & Co, 1 Eustace Road, Guildford, GU4 7EB - UK

### ABSTRACT

The Anti Jitter Circuit (AJC) was first announced at the EFTF Conferences in 1996 and 1997 (1, 2). The purpose of this paper is to show application of the circuit to two important types of frequency synthesiser.

A conventional Direct Digital Synthesiser (DDS) cannot produce low spurious square waves directly. A squarer placed directly on the DDS output reduces the effective precision of the output DAC of any precision to one bit. For an output of about one third of the DDS clock frequency the spurious sidebands can be as little as -10dBC. Results obtained so far show that improvements to -65dBC can be obtained by two AJC arrangements in cascade, each giving about 28dB spurious suppression.

A second proposed application of the AJC is for a fractional-n PLL (Phase Lock Loop) frequency synthesiser. In this case the AJC technique can in principle totally replace any noise spreading or noise cancellation circuitry. The result is a much simpler synthesiser circuit taking less power and giving better performance.

These two applications indicate that the Anti Jitter Circuit could well prove to be the most significant circuit development since the Phase Lock Loop.

**Keywords:** Phase noise, time jitter, direct digital synthesis, fractional-n synthesis.

### 1. INTRODUCTION

The “Anti-Jitter Circuit” (or AJC) is the name now adopted for the “Self Adjusting Delay Compensator” as originally announced at the 1996 and 19897 EFTF Conferences (1, 2).

In its discrete component form a single AJC has now been shown to be capable of giving in excess of 20 to 25dB cancellation of time jitter and phase noise at frequencies up to 20 MHz. Further cancellation can easily be achieved by cascading a number of AJCs. Plans are in hand to implement the AJC in an integrated circuit. For this implementation a performance of 10-20dB minimum cancellation per stage at in excess of 50MHz is expected. In an integrated circuit it is

easier to achieve a much shorter time for the jitter reduction action to be restored after a large frequency step. Frequency switching nonetheless remains instantaneous.

The purpose of this paper is to disclose some recent results on the performance of the AJC in discrete component form, and to reveal two potentially important applications of the circuit to frequency synthesis. These are Direct Digital Synthesis (DDS) of square waves and low cost fractional-n PLL synthesis. Before describing these applications the basic AJC technique is now described.

### 2. THE BASIC ANTI JITTER CIRCUIT TECHNIQUE

The anti-jitter circuit (1, 2) operates as shown in Fig. 1. It detects and cancels time jitter of either the up transitions or the down transitions of the input waveform. The mean level of the waveform at the output of the first short pulse monostable is proportional to input frequency. The (feedback) DC removal circuit leaves all phase noise and time jitter components unchanged apart from removing the DC and very low frequency components up to the DC removal circuit bandwidth. The higher frequency time jitter (phase noise) components can be seen to be removed at the time points  $t_5$  when the integrator waveform crosses the switching level of the comparator.

The output monostable is triggered from the comparator output transition which has (theoretically) no time jitter, and its pulse length is chosen to typically provide a square wave output with approximately a one to one mark-space ratio.

The AJC has a number of variants. For example it is easy to arrange that the first short pulse monostable is triggered from both edges of the input waveform. A divide by two circuit on the comparator output will then restore the output frequency to be equal to the input frequency and give an extra 6dB noise suppression. In this case the output mark space ratio is essentially the same as the input mark space ratio over, theoretically at least, all input frequencies. This arrangement also provides a double frequency output if desired from the second monostable. The disadvantage is that

the maximum frequency that can be handled is halved. There are a number different integrator circuits which can be used in the AJC. Also DC removal can be removed either by an input capacitor or by feedback from various points in the circuit.

### 3. SQUARE WAVES FROM A DDS

The Direct Digital Synthesiser (DDS) cannot give a low spurious square wave output directly. The problem is that a squarer placed on the DDS output effectively removes the ability of the DDS output DAC (Digital to Analog Converter) to reduce the spurious noise components. A low pass filter followed by the squarer can be used but then for a wide frequency range of operation the cut off frequency of the low pass filter has to be switched. The solution to this problem is to use one or up to three AJCs to replace the DDS DAC. Considerable saving, in current consumption and a possible increase in speed of DDS operation can potentially be achieved in this way.

Fig. 2 shows how the AJC can be placed directly on the output of a DDS in order to produce square waves with reduced level of "spurs" (spurious signals). The AJC does not operate correctly if the phase jitter is greater than  $2\pi$  radians. This occurs if more than one consecutive pulses are missing. In this case the DDS pulse source has to be divided by a ratio and the AJC followed by a frequency multiplier to restore the original input frequency.

For the results shown in Fig. 3 an Analog Devices AD9830EB DDS was used but with an LT1016 comparator operating on the DAC output. Ideally the AJC should have been connected directly to the MSB (Most Significant Bit) input of the DAC, but access to this point in the DDS system was not available. By switching at the same level on the DDS DAC output waveform the comparator output has the same time jitter and phase noise spurs as if the DAC had not been present. The results shown were obtained in this way.

Fig. 3 (a) shows the output spectrum of the comparator on the DDS output. The unbalanced first spurious sidebands are believed to be as a result of AM to PM conversion occurring as a result of the actual comparator switching levels on the DDS DAC output waveform. Figs. 3(b) and 3(c) show the result of respectively one AJC and two cascade AJC units applied to the comparator output. It can be seen that a total improvement of about 54dB in spur suppression is achieved with the two units.

### 4. SIMPLE FRACTIONAL-N SYNTHESIS

The second AJC application is for fractional-n frequency synthesis. There are two main methods currently used for ensuring low spurious

frequency components from the fractional-n process. The first uses analogue cancellation of the digitally predicted phase errors; such phase errors cannot be avoided in the fractional-n synthesis process. The main problem is that it is difficult to achieve or maintain good cancellation over a wide frequency range or if temperature variations have to be taken into account.

The second method is what is called "noise spreading". The unavoidable phase jitter energy has its spectrum altered so that individual components become more noise like and the energy is concentrated away from the low sideband frequencies at the expense of higher noise at the higher sideband frequencies around the comparator reference frequency. The overall noise power is increased four or nine times but the high frequency components can easily be filtered out by using a narrow enough loop bandwidth.

If the AJC method is used a much simpler fractional-n synthesis scheme is the result. A considerable reduction in circuitry ensues, with consequent reductions in power consumption. Furthermore provided at least a sample hold if not a high gain phase comparator (3) is used a higher loop bandwidth becomes possible and the resulting synthesiser can switch faster (for the same reference frequency).

Fig. 4 shows the use of the AJC in a fractional-n PLL synthesiser. The AJC cancels the time jitter originating from the rate multiplier and pulse subtraction process. Rate multipliers give time jitter because the output pulses can only appear synchronised to the clock and are not therefore evenly spaced. If the time jitter is removed from the divider chain, the phase comparator sees a jitter free signal. Thus no phase noise spurs appear on the VCO output.

The rate multiplier provides output pulses at a selectable rate which is always lower than the output frequency of the programmable divider. It can be of the "successive addition" type where a number is added successively in an accumulator until an overflow occurs. The overflow is the output and the rate of overflow is proportional to the number selected for successive addition.

Alternatively a binary rate multiplier or decimal rate multiplier may be used. In these devices, rate select switches select the 0 to 1 transitions from binary or decimal counter stages. Since the transitions from the various stages interlace and never occur simultaneously, the pulse trains from each stage can be combined in binarily weighted form to give any pulse rate up to (but not including) the rate multiplier input clock frequency. The pulse subtracter is a divide by 1 or 2 variable modulus prescaler. Each time it is commanded to divide by 2, one pulse is subtracted at the input of the programmable divider.

The AJC circuit, which can also be a cascade of several individual AJC circuits, is shown placed between the pulse subtracter and programmable divider. If it is necessary to operate the AJC at a lower frequency it is possible to move it to a point between two stages inside the programmable divider. In this case it is best to implement the programmable divider using the multiple feedback technique which has been used in the Philips HEF4751, SAA1057 and other Philips frequency synthesiser chips (3, 4).

The loop filter design in this fractional-n arrangement can be the same as if the fractional-n part were not present. However, it is possible to raise the comparison frequency in a fractional-n synthesiser by increasing the number of stages in the fractional-n part and correspondingly decreasing the number of stages in the programmable divider. A high comparison frequency can give much improved PLL switching speed and a much lower close-in phase noise.

To prove the principle of the simple fractional-n method a PLL synthesiser was constructed using a MC12022A 64/65 prescaler in place of the 1/2 prescaler shown in Fig. 4. This prescaler provides a pulse subtract function, but since the multiple feedback divider arrangement was not used, there were large gaps in the frequency coverage. For the purpose of assessing the method the gaps in coverage did not matter since it was the fractional-n performance that was being assessed. Two BCD rate multipliers type CD4522B were used in cascade to provide steps of 1/100th of the 6.991kHz comparison/reference frequency.

The programmable divider was MC14060B and the phase comparator was an MC14046B. A loop filter was designed according to the information in the data sheet, but the size of the integrator capacitor was increased keeping the proportional loop gain the same. As a result the loop filter behaves as if it was a type 1 system loop filter after initial phase lock has been achieved. The VCO used was the Motorola MC1648 with an output frequency of about 115MHz.

Figs. 5 and 6 show the fractional-n synthesisers performance with and without the AJC in place.

Figs. 5(a) and 5(b) show the surprising result that the reference and its harmonic spurious signals are significantly suppressed by the AJC in the divider chain. This meant that significant wide-band phase noise spur improvement could be achieved with the loop filter bandwidth being made otherwise much too high. An unexpected 19dB reduction of 6.991kHz spaced components was the improvement obtained.

Figs. 6(a) and 6(b) show about 10dB suppression of the 139.82Hz spaced components. Had a

sample hold or high gain phase comparator been used rather than then "digital" or pulse width type the overall level of close-in phase noise would have been much reduced (5). The poor phase comparator performance is in fact masking the suppression actually being achieved by the AJC.

## 5. CONCLUSIONS

Two important applications of the Anti-Jitter Circuit (AJC) have been investigated in this paper.

The AJC provides a simple method of producing low spurious square waves from a DDS (Direct Digital Synthesiser). Results indicate that one to three cascaded AJCs can improve the DDS spurs to better than the -60dBC level typically achieved with a sinewave output DDS.

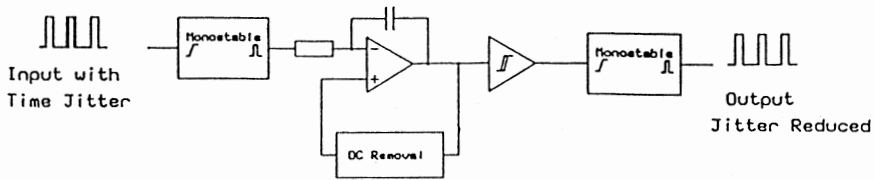
A much simplified fraction-n PLL frequency synthesiser can be made using the AJC technique. Results so far achieved indicate that this technique can significantly improve on the typical spur levels of -60dBC achieved by more complicated fractional-n arrangements.

These applications are just two of the many possible applications envisaged for the AJC. If implemented in integrated circuit form the AJC could well prove to be the most significant circuit development since the ubiquitous Phase Lock Loop.

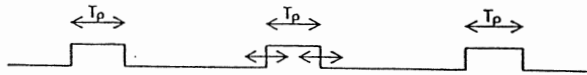
## REFERENCES

- (1) **M J Underhill & M J Blewett**, "Spectral Improvement of direct digital frequency synthesisers and other frequency sources". Proc. 10th EFTF, Brighton, March 1995, pp. 452-460 (IEE Conf. Pub. 418).
- (2) **M J Underhill & M Blewett** "Performance of a delay compensation phase noise and time jitter reduction method". Proc. 11th EFTF, Neuchatel, March 1997, pp.364-368.
- (3) **W Gosling (Ed)**, "Radio Receivers", Peter Peregrinus Ltd, 1996. ISBN: 0-86341 056-1
- (4) **M J Underhill, P A Jordan**, "A General Purpose LSI Frequency System", Proc. 32nd Annual Frequency Control Symposium 1978, pp.365-372.
- (5) **M J Underhill**, "The high gain phase comparator for reduction of close to carrier phase noise", EFTF Conference, Warsaw, 10-12 March 1998.

(a) Block diagram



(b) Input waveform



(c) Integrator output waveform

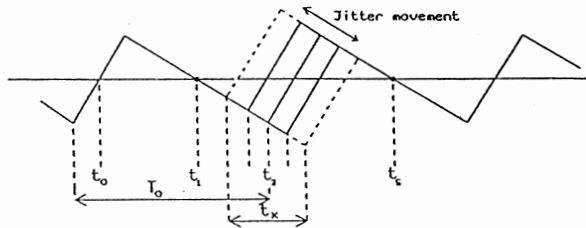
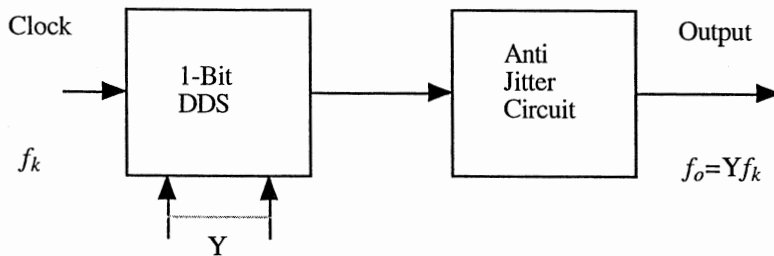


Fig. 1 The Anti Jitter Circuit



1 bit DDS can also be:

- (a) Successive Addition Rate Multiplier
- (b) Binary or BDC Rate Multiplier
- (c) Any digital pulse train with not more than one consecutive missing pulses

Fig. 2 Low spurious DDS using the AJC

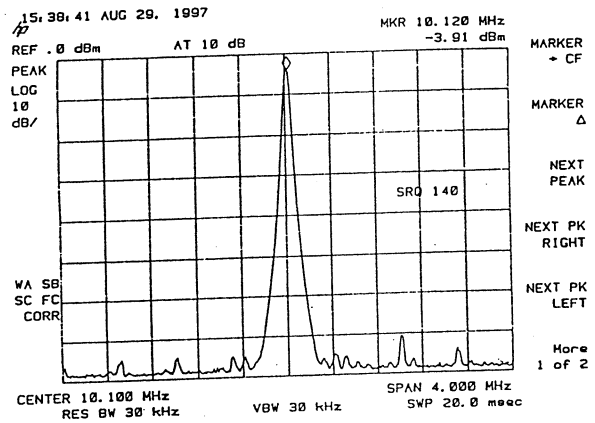
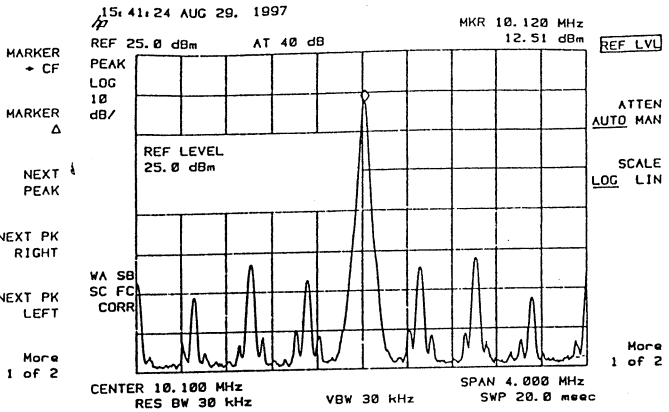
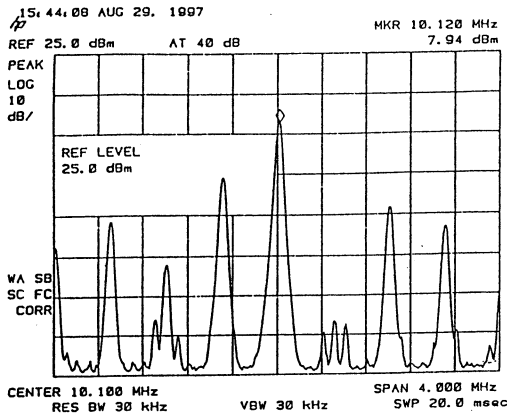


Fig. 3: Output spectrum of DDS  
 (a) without AJC  
 (b) with single AJC  
 (c) with 2 AJC units in cascade.

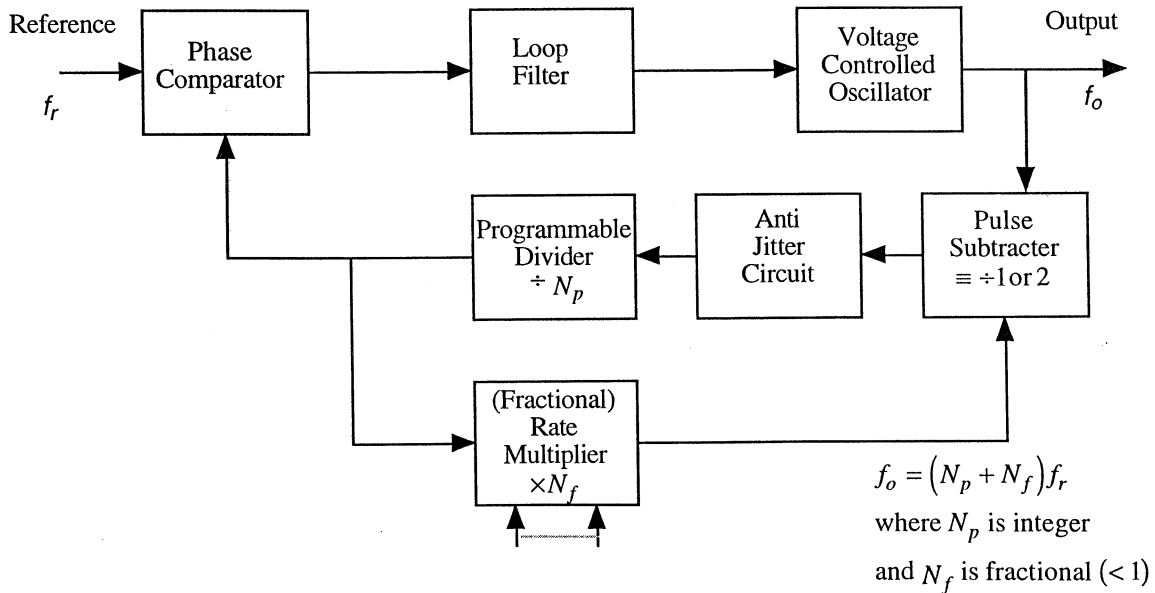
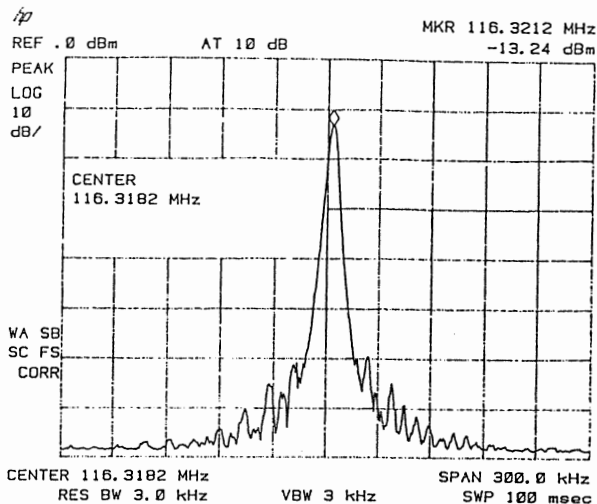
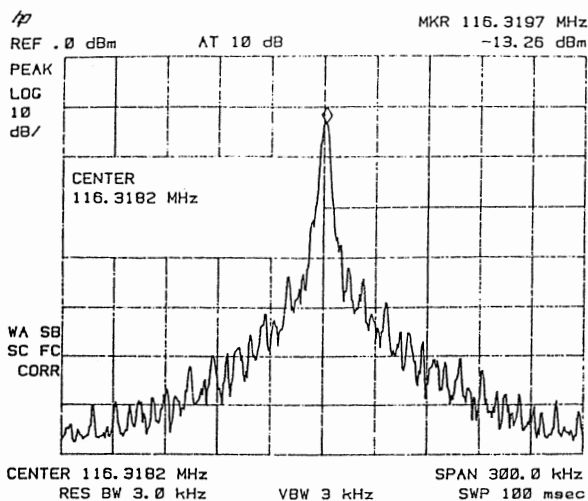
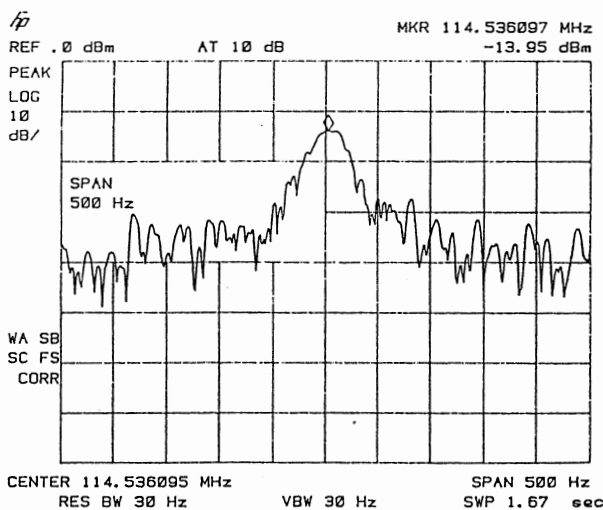
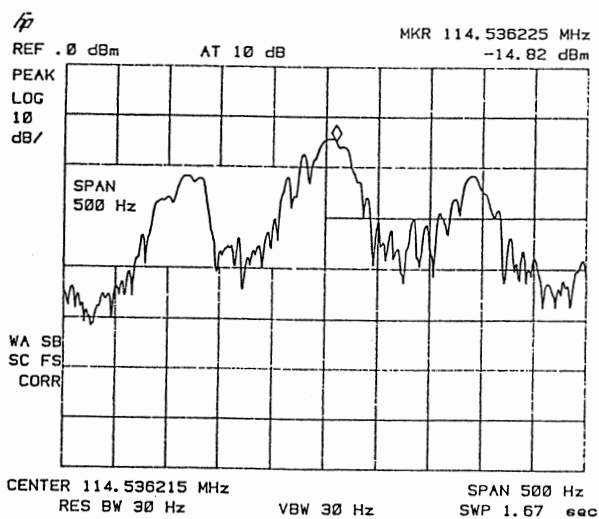


Fig. 4 Fractional-N synthesiser using AJC for spurious component suppression



**Fig. 5: Wideband spectrum of fractional-n frequency synthesiser (a) without AJC, (b) with AJC. Shows suppression of 6.9991kHz components.**



**Fig. 6: Close in phase noise of fractional-n frequency synthesiser (a) without AJC (b) with AJC. Shows suppression of 139.82Hz components.**



*12th E F T F* - 10÷12 March 1998 - **Warsaw - POLAND**

**Laser instrumentation & optical standards**

Chairman: *André Clairon*



## CHARACTERIZATION OF THE SUB-DOPPLER MODULATION TRANSFER SPECTROSCOPY AT 612 nm

E. Bava, G. Galzerano, F. Bertinetto\*, M. Bisi\*, D. Magoga\*, P. Miglietta\*

Dipartimento di Elettronica e Informazione-Politecnico di Milano, Milano-ITALY

\*Istituto di Metrologia Gustavo Colonnetti, CNR Torino-ITALY

### ABSTRACT

We report on the experimental characterization of the non-linear Modulation Transfer spectroscopy method by means of He-Ne lasers at 612 nm. The obtained frequency stability of He-Ne lasers locked against a hyperfine structure component of iodine, a spectroscopy of the iodine transition R(47)9-2 and the comparison with the results obtained in a previous work on the frequency modulation spectroscopy have been reported.

### INTRODUCTION

Sub-Doppler optical frequency modulation (FM) spectroscopy (1, 2) is a very sensitive technique to realize practical optical frequency standards. By this method however the background coming either from the linear absorption or from the spurious interferometric fringes, induced by imperfect optical isolation, can not

be canceled completely limiting the standard accuracy. Several four-wave mixing processes can transfer modulation from a modulated beam to an originally unmodulated probe beam (3, 4, 5). This effect takes place in an optical layout where there is no direct path to feed the modulation sidebands into the detector. Only the sub-Doppler resonances achieve this result, thus the baseline stability is largely improved (6, 7).

In this work the characterization of the sub-Doppler modulation transfer method (TM) using two He-Ne lasers at 612 nm locked to a rovibronic transition of  $^{127}\text{I}_2$  is reported.

### EXPERIMENTAL SET-UP

The experimental arrangement for the modulation transfer characterization is shown in figure 1. A 1 m long He-Ne laser operating at 612 nm is forced to oscillate on a single axial mode by an internal iodine cell. In this way, a relatively large tunability is achieved

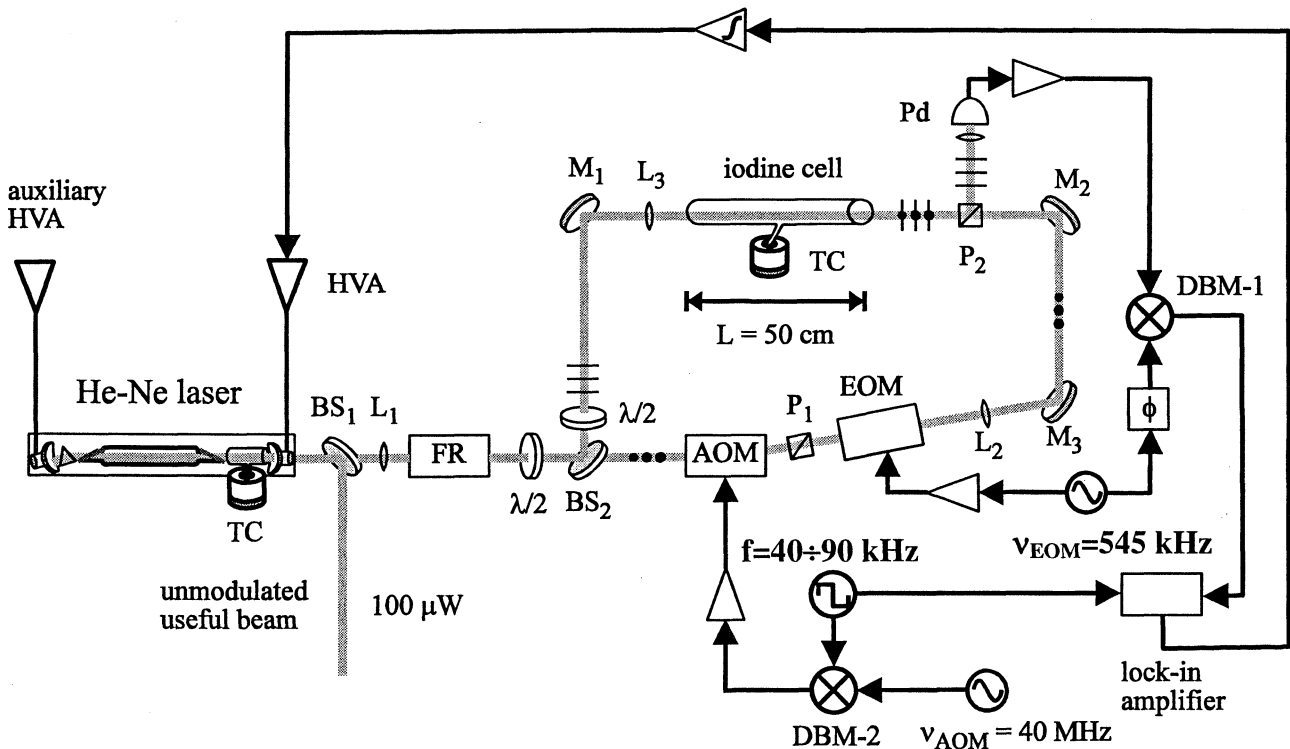


Figure 1. Experimental set-up for Modulation Transfer spectroscopy. AOM acousto-optic modulator, EOM electro-optic modulator, FR Faraday rotator, Pd photodetector, DBM's doubled balanced mixers, HVA high voltage amplifier, TC thermoelectric cooler,  $\Phi$  phase shifter, M mirror, L lens, BS beam splitter,  $\lambda/2$  half-wave plate, P polarizer.

from component  $b_{11}$  of transition P(48)11-3 to component  $a_{14}$  of transition R(47)9-2. A second laser, similar to the one described above, but stabilized to iodine using the FM spectroscopy technique, is used as a reference. In both systems the modulated and unmodulated beams were counter-propagating with orthogonal polarizations through the external  $^{127}\text{I}_2$  cells. Both saturating and probe beams have a power of approximately  $500 \mu\text{W}$  when coupled to the iodine cell, so that the collimated beams inside the cell have to be maintained with a relatively small diameter, i.e. 1.5 mm. The pump beams have been frequency shifted (40 MHz) and intensity chopped (40÷90 kHz) by means of acousto-optic modulators (AOM's). The acousto-optic modulators are useful for coherent detection of the signal from DBM-1 and provide further optical isolation. Unlike the FM configuration, in the TM system the modulated beam was the pump beam. Frequency modulation is imposed using an electro-optic modulator driven at 545 kHz; this frequency has been chosen because the hyperfine structure (hfs) components of the two main iodine transitions coincident with the emission of He-Ne lasers at 612 nm, i.e. P(48)11-3 and R(47)9-2, present a linewidth of approximately 1.2 MHz, at a pressure of 3 Pa (cold finger temperature of  $-5 \text{ }^\circ\text{C}$ ). New sidebands on the probe beam were generated by four-wave mixing processes associated with the non-linear effect of the third order susceptibility,  $\chi^{(3)}$ , of  $^{127}\text{I}_2$  resonance. These sidebands together with the remaining unmodulated probe (carrier) generate a photocurrent at the detector output whose lineshape should be free of DC offset due to background slope (4, 5). This signal, therefore, can be efficiently used to stabilize the laser frequency against the iodine resonances.

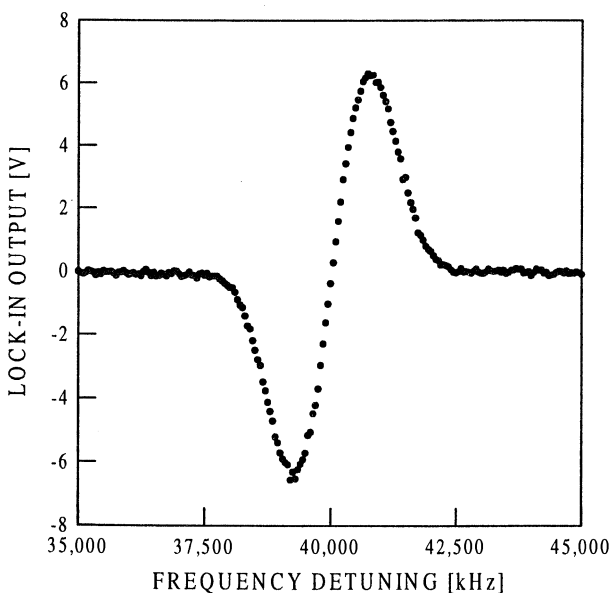


Figure 2. Lineshape of the hfs  $b_{15}$  component at the lock-in output. Modulation frequency is 545 kHz and phase modulation index is 2.5.

## EXPERIMENTAL RESULTS

Modulation transfer lineshapes have been accurately recorded using RF offset phase-locking techniques. A typical lineshape record of the  $b_{15}$  hfs component of P(48)11-3 at lock-in output with a modulation frequency of 545 kHz and a phase modulation index of 2.5 is shown in figure 2.

This signal presents an S-shaped discriminant curve with a very steep zero crossing and can be used as an error signal to lock the laser frequency to the iodine transition. The obtained frequency stability has been evaluated through the Allan variance of the beat frequency between reference and measurement lasers both stabilized against component  $b_{15}$ . With the above modulation parameters for an integration time longer than 1000 s, a fractional frequency instability  $\sigma_y = 4.3 \cdot 10^{-13}$  has been obtained whereas, when both lasers were frequency stabilized by means of FM spectroscopy (better signal to noise ratio),  $\sigma_y$  was  $8 \cdot 10^{-14}$  (8). Both diagrams reported to the optical frequency are shown in figure 3. Since the signal to noise ratio (SNR) obtained with the TM technique is worse than the one obtained with the FM method, the sensitivity of TM technique seems to be slightly lower.

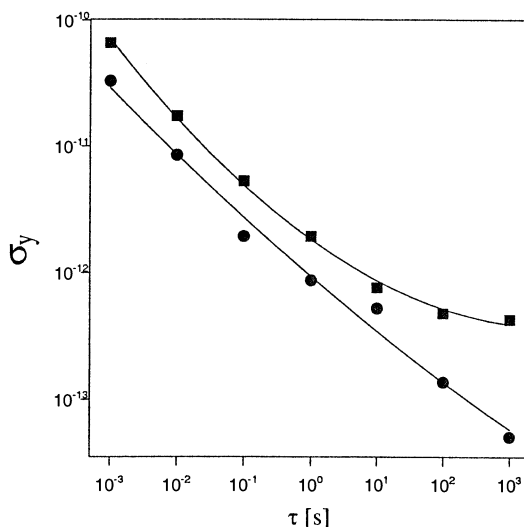


Figure 3. Allan standard deviation for the two lasers stabilized to the component  $b_{15}$  using the FM technique (●) and one laser stabilized with the MT (■).

In the laser tuning frequency range several hfs components of different iodine transitions have been observed. Figure 4 is a record of these lines, obtained with the measurement laser locked with a frequency-offset to the reference one. From this figure it can be seen that using an external iodine cell the hfs  $b_{15}$  component of P(46)11-3 is stronger than the hfs  $a_7$  component of R(47)9-2 recommended by CIPM. By means of an analysis of the beat frequency values at

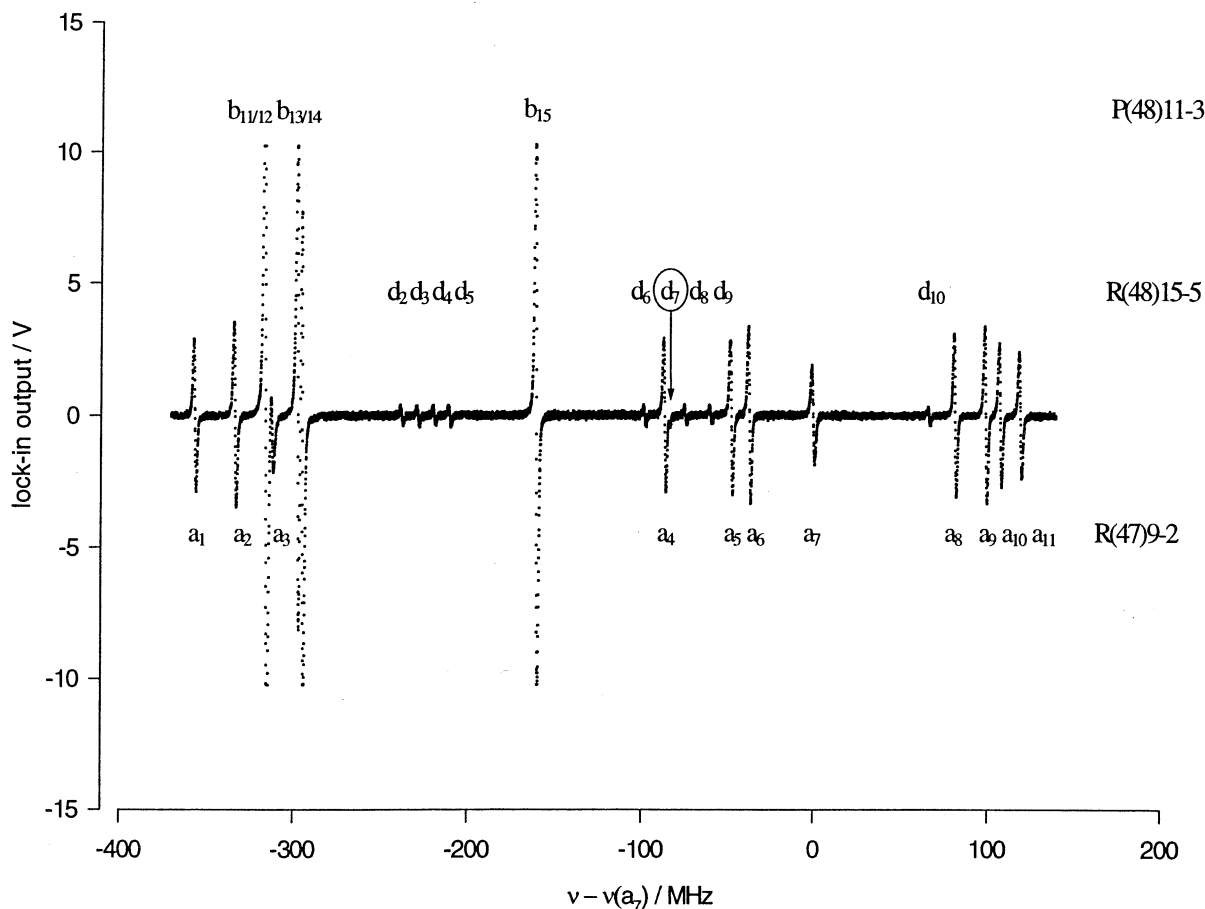


Figure 4. Digital record (output signal from the lock-in amplifier) of the hfs components of iodine transitions at 612 nm inside the laser tuning range. As a consequence of the relatively low modulation frequency adopted, the doublet  $b_{13}$ - $b_{14}$  is resolved and component  $a_3$  is apart from  $b_{11/12}$ .

different iodine vapour pressures, pressure shifts of  $(-10.7 \pm 0.8)$  kHz/Pa and  $(-9.1 \pm 0.5)$  kHz/Pa for the hfs components  $a_7$  and  $b_{15}$ , respectively, have been measured.

Component	Observed [MT] (kHz)	Observed [FM] (kHz)	Recommended by CCDM (kHz)
$a_1$	$-357173 \pm 5$	$-357156 \pm 2$	$-357160 \pm 20$
$a_2$	$-333987 \pm 5$	$-333967 \pm 2$	$-333970 \pm 10$
$a_3$	-	-	$-312460 \pm 20$
$a_4$	$-86171 \pm 5$	$-86162 \pm 2$	$-86168 \pm 7$
$a_5$	$-47282 \pm 5$	$-47279 \pm 2$	$-47274 \pm 4$
$a_6$	$-36783 \pm 5$	$-36776 \pm 2$	$-36773 \pm 3$
$a_7$	-	-	-
$a_8$	$81447 \pm 5$	$81448 \pm 2$	$81452 \pm 3$
$a_9$	$99098 \pm 5$	$99108 \pm 2$	$99103 \pm 3$
$a_{10}$	$107462 \pm 5$	$107464 \pm 2$	$107463 \pm 5$
$a_{11}$	$119048 \pm 5$	$119048 \pm 2$	$119045 \pm 6$
$\Delta_{eq}Q/MHz$	1948.1	1948.0	
$\Delta C/kHz$	25.175	25.160	

Table 1. Frequency interval measurements between a few components of transition R(47)9-2 at 612 nm and the obtained change in hyperfine coupling constants.

The hyperfine splittings for the R(47)9-2 transition have been obtained with the two (FM and TM) methods.

The measured frequency intervals are fit to a 4-term hyperfine Hamiltonian which includes electric-quadrupole, spin-rotation, tensor spin-spin and scalar spin-spin interactions (9). The results are given in table 1. The obtained values are in quite good agreement with the recommendation of CCDM but in the case of TM technique an uncertainty higher than FM (better signal to noise ratio) has been calculated. The sensitivity of the TM method, for various modulation frequencies and indexes, was then characterized by means of lineshape recordings. The measurement of the phase modulation indexes has been performed using a confocal resonator, with a 500 kHz linewidth, placed behind the EOM. Figure 5 shows the signal slope variations as a function of the modulation frequency scaled by the resonance width and figure 6 shows the signal slope as a function of modulation index. The data show a maximum of sensitivity for modulation frequencies near the half width of the transition, and, at the fixed modulation frequency of 545 kHz (EOM is made resonant at this value), for a phase modulation index higher than 2. These behaviors are in good agreement with theory (3, 4, 6).

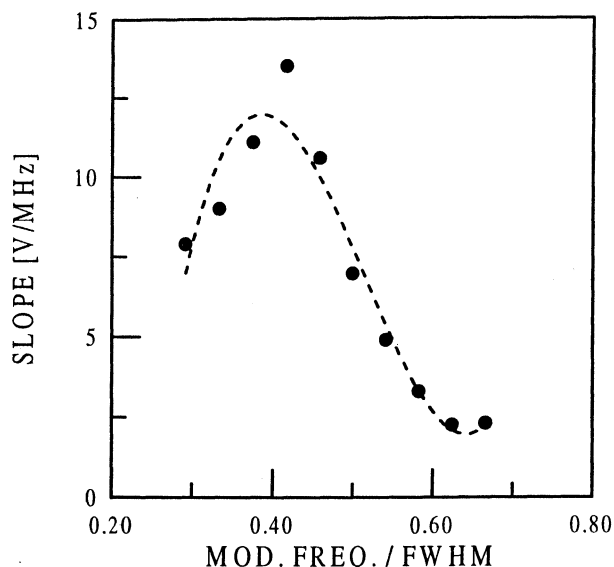


Figure 5. Sensitivity of the TM signal at different modulation frequencies divided by the resonance width (FWHM $\approx$ 1.2 MHz).

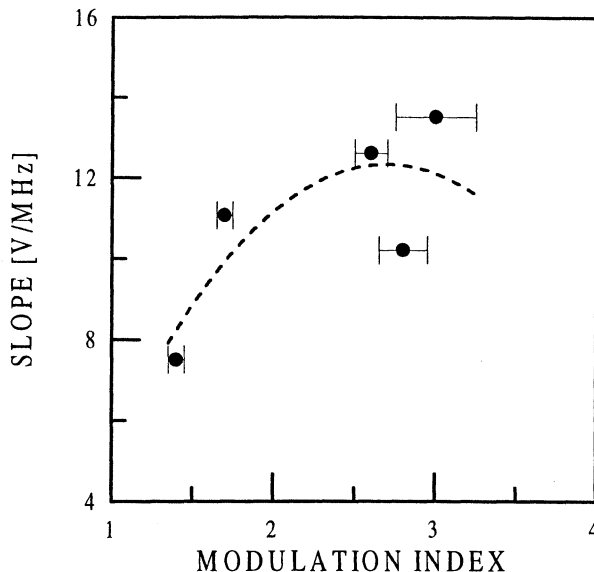


Figure 6. Sensitivity of the TM signal as a function of the phase modulation index values at a fixed modulation frequency of 545 kHz. The uncertainty in the modulation index was due to the measurement resonator linewidth.

## CONCLUSIONS

Sub-Doppler modulation transfer spectroscopy represents a very sensitive and nearly systematic-free baseline technique and, for these reasons, it is quite suitable for the realization of practical optical frequency standards. However, in the case of He-Ne lasers at 612 nm, the signal to noise ratio is worse than that obtained with a standard FM spectroscopy method as it was found comparing the stability level obtained with the two methods. This should be due to the lower sensitivity of the TM method with respect to the FM one. We would apply the TM technique to Nd:YAG frequency doubled lasers in order to compare the stability and accuracy of the TM and FM standards in the 532 nm optical range (7, 10). This is a program within the cooperation between the Politecnico di Milano and the Istituto di Metrologia G. Colonnetti in Torino.

## REFERENCES

1. G. C. Bjorklund, M. D. Levenson, W. Lenth and C. Ortiz, 1983, "Frequency modulation (FM) spectroscopy-theory of lineshapes and signal to noise analysis", *Appl. Phys. B*, **32**, 145
2. J. L. Hall, L. Hollberg, T. Baer and H. G. Robinson, 1981, "Optical heterodyne saturation spectroscopy", *Appl. Phys. Lett.*, **39**, n. 9, 680-682
3. M. Ducloy and D. Bloch, 1984, "Polarization properties of phase-conjugate mirrors: angular

dependence and disorienting collision effects in resonant backward four-wave mixing for Doppler-broadened degenerate transitions", *Phys. Rev. A*, **30**, n. 6, 3107-3122

4. J. H. Shirley, 1982, "Modulation transfer processes in optical heterodyne saturation spectroscopy", *Optics Letters*, vol. **7**, n. **11**, 537-539
5. G. Camy, Ch. J. Bordé and M. Ducloy, 1982, "Heterodyne saturation spectroscopy through frequency modulation of the saturating beam", *Optics Comm.*, **41**, n. **5**, 325-330
6. M. Long-Sheng and J. L. Hall, 1990, "Optical heterodyne spectroscopy enhanced by an external optical cavity: toward improved working standard", *IEEE J. of Q.E.*, **26**, n. **11**, 2006-2012
7. M. L. Eickhoff and J. L. Hall, 1995, "Optical Frequency Standard at 532 nm", *IEEE Trans. On Instr. And Meas.*, vol. **44**, n. **2**, 155-158
8. M. Bisi and F. Bertinetto, 1996, "Frequency reproducibility of He-Ne lasers at 612 nm using frequency modulation spectroscopy technique", to be published on *Metrologia*, vol. **34**, n. **6**
9. S. Picard-Fredin and A. Razet, 1991, "On the hyperfine structure of iodine:2. To calculate hyperfine constants on the basis of experimental data", *Rapport BIPM-91/2*, Bureau Int. Des Poids Et Mesures.
10. G. Galzerano, E. Bava, M. Bisi, F. Bertinetto and C. Svelto, 1998, "Frequency stabilization of frequency doubled Nd:YAG laser", submitted at *CPEM 98*, July 6-9, Washington (USA)



0.7% for 1064nm light. A PZT was attached to the output mirror for cavity tuning. The typical distance between the mirrors was 49mm. The crystal was rotated around the z-axis. Thus, the output wavelength could be tuned by about 5THz (19nm) around 1064nm because of the change in the phase-matching condition (Fig.3a). The phase-locking apparatus was described elsewhere (5). Next we used KTPs with the cutting angles of  $(90^{\circ}, 30^{\circ})$  and  $(90^{\circ}, 40^{\circ})$ . The oscillation wavelength was 1050nm-1178nm ( $\nu_{\text{sig}} - \nu_{\text{idler}} = 7.5\text{THz}$ ) and 1001nm-1135nm ( $\nu_{\text{sig}} - \nu_{\text{idler}} = 35.4\text{THz}$ ).

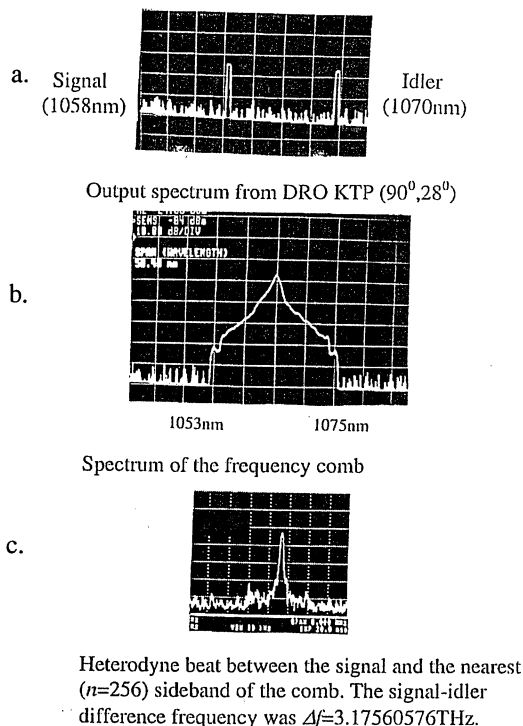


Fig.3.

### 3. OPTICAL FREQUENCY COMB GENERATOR

For the comb generator, a monolithic OFCG (6) was used. It consists of an EO crystal ( $\text{LiNbO}_3$ ,  $1.25 \times 1 \times 21\text{mm}$ ) with high reflection coatings (99.5% at the wavelength of 1064nm) on the both ends, i.e., the EO crystal becomes a monolithic optical FP cavity so that the OFCG can be made to have lower optical round-trip loss. The top and bottom sides was gold plated for E-field control of the cavity length. The EO crystal is installed in the microwave waveguide resonator which was made of brass to increase the microwave electric field intensity in to the EO crystal for highly efficient EO modulation. The FSR and the modulation frequency were 3.1GHz and 6.1527GHz ( $=2\text{FSR}$ ),

respectively. Apart of the output from the OFCG was split off and detected to high-speed photodiode. The output from the photodiode was then demodulated at the modulation frequency to provide an error signal for locking the OFCG cavity to the IR YAG laser by E-field control. Fig.3.b. shows the examples of observed OFCG spectrum for the particular case of modulation index equal  $0.35\pi$  rad. Since the resolution (0.2nm) was larger modulation frequency, the envelope of the OFCG was observed.

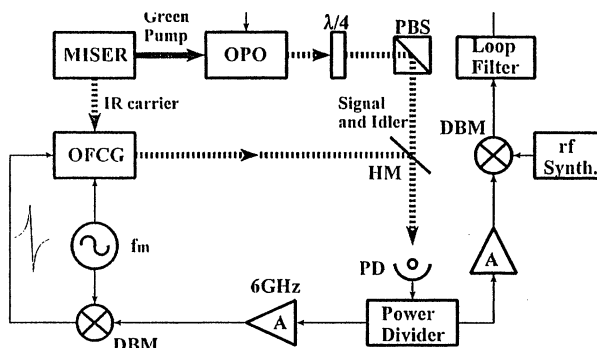


Fig.4. Setup of the OPO-OFCG phase-locking scheme

### 4. THE PHASE-LOCKING SCHEME FOR THE OPO FREQUENCY CHAIN

The OFCG can be used for measuring terahertz frequency differences between two optical frequencies (7). We have applied it to phase lock the signal (idler) outputs of DRO as shown in Fig.4. The DRO was tuned so that the heterodyne beat between the signal (idler) and the nearest sideband of the comb was less than 1GHz (Fig.3c). The heterodyne beat was amplified and then downconverted to  $\sim 120\text{MHz}$ . The resultant beat was amplified, bandpass filtered, and phase locked to a rf signal by means of the electro-optic effect of the DRO.

The DRO was tuned so that the signal was near the 256th sideband of the modulated IR YAG laser radiation. We determined the sideband order  $n$  by dithering  $f_m$  by 1MHz and measuring the change in the beat frequency on  $n$  MHz. In the phase-locking experiment, the modulation frequency was 6.15427GHz. Therefore the exact signal-idler difference frequency of the phase-locked DRO was 3.17560576THz.

### 5. SUMMARY

We have adjusted a set of DROs with outputs center at frequency of IR YAG laser to cover a range of 20THz and to facilitate the difference-frequency measurement in the optical frequency chain. We have phase locked a DRO to a microwave synthesized source at a signal-idler difference frequency of 3.1756THz. To our knowledge, this frequency difference was larger than ever before in 1 $\mu$ m optical range. For the construction of our frequency chain, following things are remained to be done:

Demonstration of 3:1 divider (532nm pumped 798nm signal and 1596nm idler DRO). This is considered to be possible with the (90<sup>0</sup>,50<sup>0</sup>) CTA crystal, 5% MgO:LiNbO<sub>3</sub> type 1 (90<sup>0</sup>,0<sup>0</sup>,200<sup>0</sup>C) crystal or the PPLN crystal.

Demonstration of the parallel connection of DROs using the OFCGs.

Construction of the system using SUM&SHG dividers with KN crystals.

## REFERENCES

1. N.C.Wong, 1992, Opt.Lett. **17**,1156.
2. N.C.Wong,1995, Appl.Phys. B **61**,143.
3. H.R.Telle *et al*,1990, Opt. Lett. **15**,532.
4. T.Ikegami *et al*, 1996, Proc.5<sup>th</sup> Symposium on Frequency Standards and Metrology, ed.J.C.Berquist, World Scientific, 333.
5. D.Lee and N.C.Wong, 1993, J.Opt.Soc.Am. B **10**, 1659.
6. M.Kouroggi, 1994, IEEE Photon. Technol.Lett.,214.
7. L.R. Brothers *et al*, 1994, Opt.Lett. **15**,245.

# ABSOLUTE FREQUENCY STABILIZATION OF ERBIUM MICROLASERS TO $C_2H_2$ AND $^{13}C_2H_2$ IN THE 1530-1550 nm WAVELENGTH INTERVAL

C. Svelto<sup>o</sup>, S. Taccheo<sup>\*</sup>, P. Laporta<sup>\*</sup>, and E. Bava<sup>o</sup>

POLITECNICO DI MILANO - P.zza Leonardo da Vinci 32, 20133 Milano, Italy  
E-mail: cesare.svelto@polimi.it Phone: +39(2)2399.3610 Fax: +39(2)2399.3413

<sup>o</sup>Dipartimento di Elettronica e Informazione and CSTS-CNR

<sup>\*</sup>INFN-Dipartimento di Fisica and CEQSE-CNR

## ABSTRACT

Diode-pumped Er-Yb:glass microlasers operating at 1.5  $\mu\text{m}$  have been frequency stabilized against  $C_2H_2$  and  $^{13}C_2H_2$  absorption lines with two different locking techniques. Frequency stabilities below 200 kHz over one hour period were obtained with a Pound-Drever locking on  $C_2H_2$ . Using the  $^{13}C_2H_2$  molecule, absolute frequency stabilization over the 1540-1550 nm wavelength interval was demonstrated. In all cases, the short term (1-ms) laser linewidth is narrower than 50 kHz.

## INTRODUCTION

Laser frequency stabilization in the 1.5- $\mu\text{m}$  region is of great interest for many of the proposed optical communication applications involving wavelength-division multiplexing such as in multiwavelength transport networks and passive optical networks. In addition, frequency reference lines in this region are important for metrological applications and high-resolution spectroscopy. To date, several studies have been devoted to the absolute frequency stabilization of 1.5  $\mu\text{m}$  semiconductor lasers using various atomic (1,2) or molecular lines (3-5). Diode lasers, however, generally exhibit a quite large oscillation linewidth, typically ranging from a few megahertz to a few tens of megahertz. On the other hand, due to their high-quality spatial and spectral characteristics of the output beam, diode-pumped Er-Yb:glass microlasers at 1.5  $\mu\text{m}$  (6) appear to be a very interesting source for both optical communications and metrology. In fact, these solid-state laser sources operate in single transverse and longitudinal mode, exhibiting very narrow linewidths and an extremely wide wavelength tunability (continuous tunability interval from 1530 nm to 1565 nm) compared, e.g., to single-frequency laser diodes. For both dense wavelength division multiplexing (7) and frequency metrology, the absolute stabilization of the emitted wavelength(s) is of great interest. In this work recent results obtained in frequency stabilization with respect to  $C_2H_2$  and  $^{13}C_2H_2$  rovibrational lines in the 1530-1550-nm wavelength interval will be reported. The attained frequency

stability has been directly evaluated by beat note experiments (beat frequency temporal and spectral analysis as well as beat note Allan's variance) between pairs of identical and independently stabilized erbium microlasers.

## SPECTROSCOPIC MEASUREMENTS WITH THE Er-Yb LASER

Before moving into stabilization of the Er-Yb:glass lasers against  $C_2H_2$  lines, some detailed spectroscopic measurements of transition P(15) at 1534.099 nm were performed. To this purpose the Er-Yb microlaser was first wavelength tuned at  $\sim 1534$  nm, by means of an intracavity etalon, and then frequency scanned feeding a linear ramp voltage signal to the piezoelectric (PZT) transducer (Pickelmann, mod. HPSt 500/10-5/15) controlling the cavity length. Using the experimental set-up depicted in Fig. 1, the transmission profiles of three  $C_2H_2$  sealed gas cells at different pressures have been recorded. Quartz cells, with 100-mm optical length (Hellma, mod. QS-225), filled at 1 kPa, 2 kPa and 5 kPa gas pressures were used in the

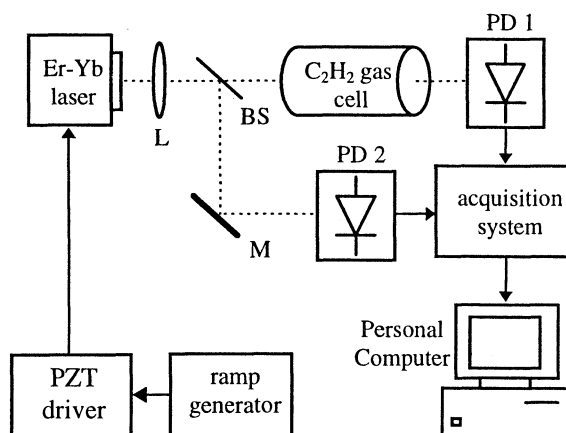


Figure 1. Spectroscopic measurements set-up.

experiments. The laser output beam is divided into a first beam sensing the cell absorption and impinging on the transmitted power recording detector and a second beam used as power reference. The recorded voltage signal of the first detector was divided by the power reference signal. In this way, amplitude

fluctuations occurring while frequency scanning the Er-Yb laser and amplitude noise of the laser source were canceled out allowing the acquisition of clean and well resolved transmission spectra, as shown in Fig. 2 (transmitted power has been normalized to unity when outside the transition). To calibrate the

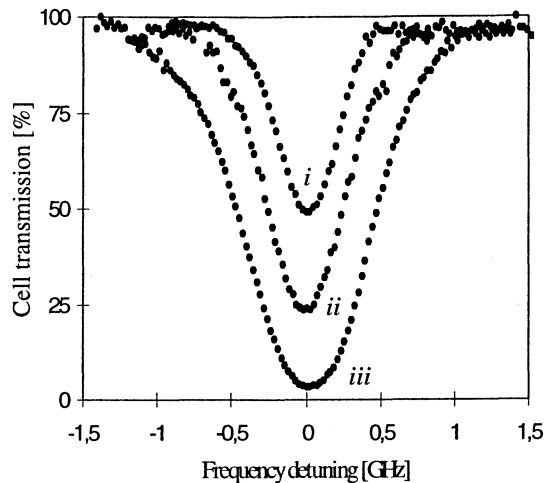


Figure 2. Recorded transmission spectra for the P(15)  $C_2H_2$  line at different gas pressures  $p$ . (i)  $p=1$  kPa, (ii)  $p=2$  kPa and (iii)  $p=5$  kPa.

frequency axis of the curves depicted in Fig. 2, the PZT frequency actuating factor was measured by applying a 1-V signal to the actuator and observing the consequent frequency shift on a scanning Fabry-Perot interferometer (Burleigh, mod. RC-110-IR) set to a 1-GHz free spectral range. The measured actuating factor corresponds to  $\sim 210$  MHz/V and remains approximately constant while changing the PZT bias voltage.

### POUND-DREVER EXPERIMENTS ON $C_2H_2$

The experimental set-up for Pound-Drever frequency stabilization is schematically shown in Fig. 3. The Er-Yb laser output beam was phase

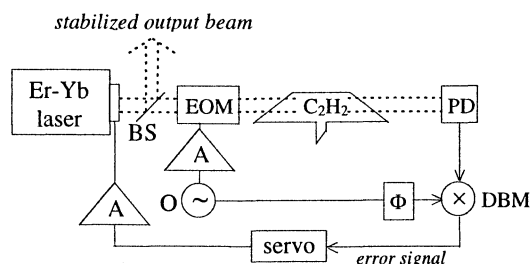


Figure 3. Pound-Drever stabilization set-up against  $C_2H_2$ . BS: beam splitter; O: oscillator; A: amplifier;  $\Phi$ : phase shifter; DBM: mixer

modulated by passing through a bulk  $LiTaO_3$  (New Focus, mod. 4004) electro-optic modulator (EOM) driven at 100 MHz with a phase modulation index of 0.16 rad. The phase-modulated beam is passed through the  $C_2H_2$  gas cell and impinges on a fast

photodetector (New Focus, mod. 1811-FS). The Pound-Drever error signal is demodulated in a double balanced mixer (Mini-Circuits, mod. ZAD-1H) by beating with a fraction of the 100 MHz modulating signal. The obtained DC error signal is then integrated and servoed to the PZT amplifier, thus closing the frequency control loop.

Before closing the frequency stabilization loop, we recorded the open-loop error signal profile when scanning the laser frequency through the molecular absorption line. The Pound-Drever discriminating curves were measured with a detection scheme, similar to the one described in Fig. 1, where the phase modulated beam senses the absorption line and the voltage error signals after the mixer are recorded as functions of the laser to resonance frequency detuning. These frequency discriminating curves are shown in Fig. 4 for the three different  $C_2H_2$  pressures. The best discriminator slope of 0.52 mV/MHz was obtained when using the 2-kPa

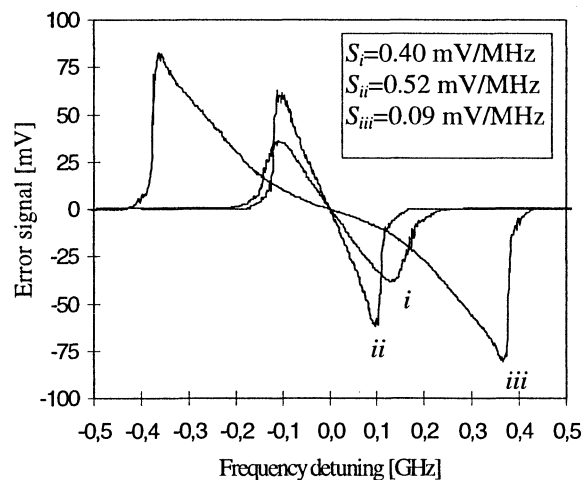


Figure 4. Optical frequency to voltage error signal curves at different gas pressures,  $p$ , for the P(15) line. (i)  $p=1$  kPa, (ii)  $p=2$  kPa and (iii)  $p=5$  kPa.

$C_2H_2$  cell. In general, when increasing the gas pressure over an optimum value, linewidth collision broadening results in a less steep zero crossing of the error signal, while, reducing the pressure below the optimum value, the signal weakening is no more compensated by a significant linewidth reduction, thus resulting in a discriminator slope decrease.

### STABILITY RESULTS ON $C_2H_2$

To evaluate the attained frequency stability by the Pound-Drever method, two identical Er-Yb:glass lasers have been frequency stabilized to the absorption peaks of three  $C_2H_2$  lines, namely P(13), P(15) and P(17), by this external frequency modulation and synchronous detection technique. In all cases the adopted modulation frequency was 100 MHz with a modulation index limited to

0.16 rad by the available EOM voltage amplifiers. Similar stability results were obtained for the three absorption lines and only the stabilization experiment and measurements on P(15) line at 1534.099 nm will be described hereafter.

The first qualitative measurements of laser frequency stability were performed recording the closed-loop error signal and converting, dividing by the measured discriminator slope, the voltage fluctuations into the corresponding frequency fluctuations. A 24-h measurement of the stabilized laser residual frequency fluctuations is shown in Fig. 5. In this case, the Er-Yb laser was locked to

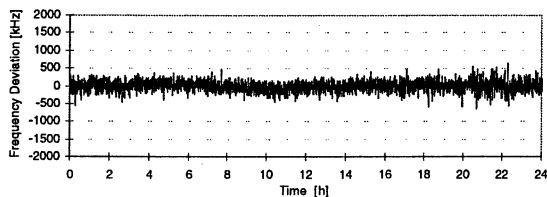


Figure 5. 24-h frequency fluctuations calculated from the recorded voltage error signal.

the P(15) line with a previously measured discriminator slope of  $\sim 0.5$  mV/MHz. From the recorded error signal of Fig. 5, a peak-to-peak frequency stability below 1 MHz is observed with a rms stability of 160 kHz over the 24-h period (8).

Beat note measurements between two identical Er-Yb lasers, independently frequency stabilized have been performed using two 1 kPa  $C_2H_2$  cells and locking to the P(15) line. One of the two stabilized laser beams was frequency shifted by an acousto-optic modulator driven at 40 MHz to observe an AC beat note signal. Figure 6 shows the Allan standard deviation of the beat note frequency,

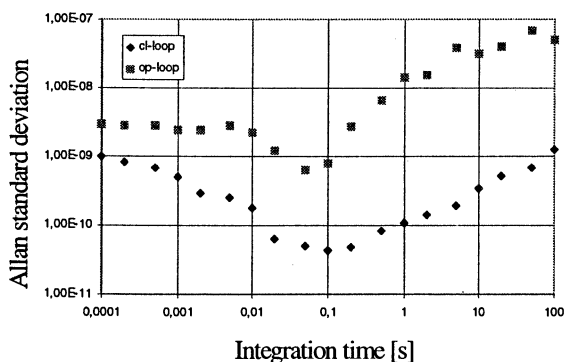


Figure 6. Beat note frequency Allan standard deviation between two Er-Yb microlasers.

as a function of the integration time,  $\tau$ . An optimum value of  $4 \times 10^{-11}$  was obtained for an integration time of 100 ms and standard deviation values below  $10^{-9}$  were obtained for  $\tau$  varying between 100  $\mu$ s and 100 s.

The short-term laser linewidth, as confirmed by beat note spectral analysis, is below 50 kHz for an observation time of 1 ms. This is a typical value even for a free-running diode-pumped Er-Yb:glass microlaser (6). However, linewidth reduction is under study and development by means of a fast electro-optic control loop to be used in conjunction with a steep frequency reference.

Possible significant improvements of these stability results, obtained with the Pound-Drever technique, could be achieved by increasing the phase modulation index. Furthermore an active temperature control of the laser cavity shall allow for a less environment sensitive frequency stability: in fact, in all the previously described experiments, a room temperature stability of  $\pm 2$  °C was needed to avoid exhausting the PZT dynamic. At the end, the ultimate stability limits (below the kHz level) could be reached by locking to Doppler-free absorption lines as obtainable with  $C_2H_2$  by an intracavity saturated spectroscopy and frequency locking (9).

## FRINGE-SIDE LOCKING EXPERIMENTS ON NINE LINES OF $^{13}C_2H_2$

A recently demonstrated and extremely important property of Er-Yb:glass lasers is their wide wavelength tunability at around 1.5  $\mu$ m. In fact, just one of these lasers can be continuously tuned for more than 36 nm (10) still keeping an output power of several milliwatt. A frequency stabilization experiment against different  $^{13}C_2H_2$  absorption lines has been performed employing these widely tunable sources and a simple fringe-side locking technique (11). In Fig. 7 we report the measured frequency fluctuations, observed over a 50 s time interval and with 50 kHz recording system bandwidth, as obtained from the closed-loop error signal, at the different stabilization wavelengths corresponding to P(13) up to P(29) absorption lines of  $^{13}C_2H_2$ . In general, a rms frequency stability below 1 MHz is observed with a slight decrease in the stability performance with increasing wavelengths due to the weaker absorption lines. Anyway, it is worthwhile reminding that for  $^{13}C_2H_2$

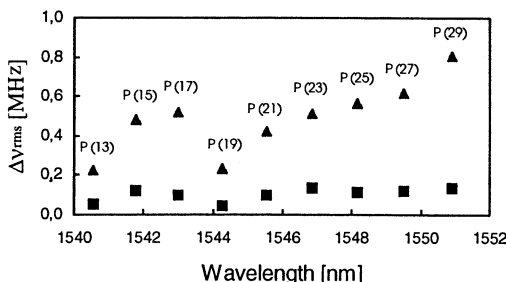


Figure 7. Frequency fluctuations of a stabilized Er-Yb laser against  $^{13}C_2H_2$ . Frequency data are sampled at 20 Hz frequency. Triangles correspond to an averaging time of 50 ms; squares do refer to a longer averaging time of 1 s.

the odd absorption lines are weaker than the even ones so that, if necessary, the number of reference lines could be easily doubled.

Beat frequency experiments between two Er-Yb lasers locked to the strongest absorption line, i.e. line P(13) at 1540.567 nm wavelength, have been conducted by calculating the Allan standard deviation of the beat frequency. The measured deviations are plotted in Fig. 8 as a function of the used integration time. Another method used to

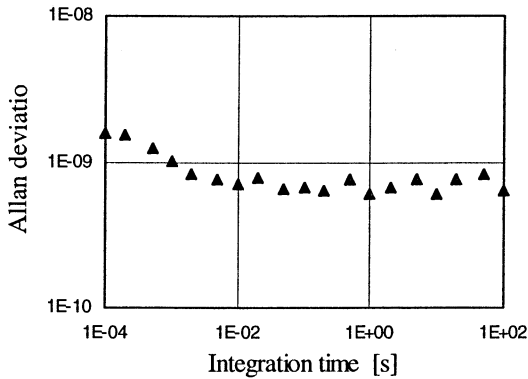


Figure 8. Beat note frequency Allan standard deviation between two Er-Yb microlasers when fringe-side locked to  $^{13}\text{C}_2\text{H}_2$  P(13) absorption line.

evaluate the long-term frequency stability of the beat note frequency was based on the digital acquisition of frequency samples by means of a frequency to voltage converter. Deviations from the central beat frequency have been recorded over a 5-h period, as shown in Fig. 9, resulting in a rms stability of 440 kHz.

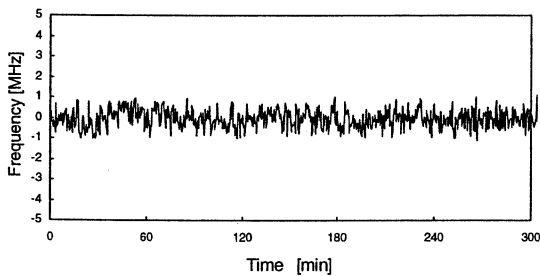


Figure 9. Beat frequency fluctuations between two identical Er-Yb lasers stabilized against the  $^{13}\text{C}_2\text{H}_2$  P(13) absorption line at 1540.567 nm wavelength.

## CONCLUSIONS

Diode-pumped Er-Yb:glass microlasers have been frequency stabilized against different  $\text{C}_2\text{H}_2$  and  $^{13}\text{C}_2\text{H}_2$  absorption lines in the 1530-1550 nm wavelength region. Pound-Drever stabilization schemes, even with Doppler broadened absorption profiles, provided for a frequency stability down to a  $4 \times 10^{-11}$  Allan standard deviation. Exploiting the extremely wide wavelength tunability of the Er-Yb laser sources, frequency locking at nine different wavelengths of the  $^{13}\text{C}_2\text{H}_2$  absorption spectrum has

been obtained with a stability level around  $10^{-9}$ . Significant improvements in both short- and long-term frequency stability can still be achieved and further experiments in this sense are under development. All of the obtained stability results are perfectly compatible with the present needs of optical fiber WDM communication systems and they also seem quite promising when looking for novel laboratory frequency references in the 1.5  $\mu\text{m}$  spectral region.

## REFERENCES

1. Y. C. Chun and C. B. Roxlo, 1988, "Frequency-locking of 1.5  $\mu\text{m}$  DFB laser to an atomic krypton line using optogalvanic effect", *IEE Electron. Lett.*, **24**, 1048-1049.
2. M. Ohtsu and E. Ikegami, 1989, "Frequency stabilisation of 1.5  $\mu\text{m}$  DFB laser using internal second harmonic generation and atomic  $^{87}\text{Rb}$  line", *IEE Electron. Lett.*, **25**, 22-23.
3. S. Sudo, Y. Sakai, H. Yasaka, and T. Ikegami, 1989, "Frequency-stabilized DFB laser module using 1.53159  $\mu\text{m}$  absorption line of  $\text{C}_2\text{H}_2$ ", *IEEE Photon. Technol. Lett.*, **1**, 281-283.
4. F. Bertinetto, P. Gambini, R. Lano, and M. Puleo, "Stabilization of the emission frequency of 1.54  $\mu\text{m}$  laser diodes to hydrogen iodide", 1993, *IEEE Photon. Technol. Lett.*, **4**, 472-474.
5. M. de Labachellerie, K. Nakagawa, Y. Awaji, and M. Ohtsu, 1995, "High-frequency-stability laser at 1.5  $\mu\text{m}$  using Doppler-free molecular lines", *Opt. Lett.*, **20**, 572-574.
6. S. Taccheo, P. Laporta, S. Longhi, G. Svelto, and C. Svelto, 1996, "Diode-pumped bulk erbium-ytterbium lasers", *Appl. Phys. B*, **63**, 425-436.
7. 'Optical Interfaces for Multichannel Systems with Optical Amplifiers', *ITU-T Draft Recommendation G.692*, May 1997.
8. C. Svelto, E. Bava, S. Taccheo, and P. Laporta, 1998, "Frequency-stabilised Yb-Er:glass laser at 1.534097  $\mu\text{m}$  on  $\text{C}_2\text{H}_2$  molecule by the Pound-Drever technique", *Electron. Lett.*, *in press*.
9. M. de Labachellerie, K. Nakagawa, and M. Ohtsu, 1994, "Ultrastable  $^{13}\text{C}_2\text{H}_2$  saturated-absorption lines at 1.5  $\mu\text{m}$ ", *Opt. Lett.*, **19**, 840-842.
10. S. Taccheo, P. Laporta, and O. Svelto, 1996, "Linearly polarised, single-frequency, widely-tunable Er:Yb bulk laser at around 1550 nm wavelength", *Appl. Phys. Lett.*, **69**, 3128-3130.
11. S. Taccheo, S. Longhi, L. Pallaro, P. Laporta, and C. Svelto, 1995, "Frequency stabilization to a molecular line of a diode-pumped Er-Yb laser at 1533-nm wavelength", *Opt. Lett.*, **20**, 2420-2422.
12. S. Taccheo, G. Sorbello, P. Laporta, and C. Svelto, 1998, "Analysis of long-term absolute-frequency stabilisation of a bulk 1.5  $\mu\text{m}$  erbium microlaser to a grid of nine different wavelengths", *IEE Electron. Lett.*, **34**, 81-82.

# A POTASSIUM VAPOR MAGNETOMETER OPTICALLY PUMPED BY A DIODE LASER

N. Beverini<sup>a, b</sup>, E. Alzetta<sup>a</sup>, C. Carmisciano<sup>b</sup>, O. Faggioni<sup>b</sup>, F. Francesconi<sup>a</sup>, E. Maccioni<sup>a</sup>

<sup>a</sup>Dipartimento di Fisica dell'Università di Pisa, and INFN (Italy)

<sup>b</sup>Consorzio Universitario della Spezia (Italy)

## INTRODUCTION

The magnetometer, that is described here, has been developed to be used in geomagnetic surveys. Since optical pumping was proposed by Kastler (1), as a powerful method to produce large changes in the relative population of Zeeman sublevels or hyperfine levels of the ground states of atoms through optical irradiation, the precise measurement of weak magnetic fields has been one of the many practical applications. A number of optically pumped magnetometers are currently in use for the measure of the geomagnetic fields near the earth surface, in the earth magnetosphere, or of planetary and interplanetary fields in the outer space. The ground state of alkali atoms is particularly suitable for this kind of application; in particular, devices working with cesium have been commercially developed and are currently in use from many years.

## ALKALI VAPOR OPTICALLY PUMPED MAGNETOMETERS

Essentially, an optically pumped atomic magnetometer measures the Zeeman splitting of an atomic state, which is approximately proportional to the magnetic field value. In 1957 Bell and Bloom (2) analyzed the possible operating schemes for measuring the Zeeman resonance frequency. In the first one (*locked magnetometer* or  $M_z$  *magnetometer*) the atomic sample is optically pumped in the direction of the static magnetic field (z-direction), and a VCO is phase-locked to the transition. In the second scheme (*self-oscillating magnetometer* or  $M_x$  *magnetometer*) the atomic sample is pumped in a direction transverse to the static magnetic field (at an angle close to 45°). If a resonant rf field drives in phase the precession motion of the oriented atoms, a macroscopic rotating magnetic moment is generated, that modulates the atomic sample transmission. By sending the amplified photodiode signal in positive feedback on the rf coils, a self-oscillating system at the Larmor frequency is thus generated. A third scheme is also possible, in which no rf. field is applied to the cell while the light source is modulated in amplitude at the resonance frequency (3). This scheme suffers however of a theoretical signal-to-noise ratio a factor 2 lower than in the other two cases.

In the presence of an external magnetic field  $\mathbf{B}$ , the frequencies of the Zeeman transitions in an alkali atom with a nuclear spin  $I$  are given by the well known Breit-Rabi formula:

$$\nu_{F, m_F \rightarrow F, m_F - 1} = g_I \frac{\mu_B}{h} B \pm \frac{W}{2} \left[ \sqrt{1 + \frac{4m_F}{2I+1} x + x^2} - \sqrt{1 + \frac{4(m_F - 1)}{2I+1} x + x^2} \right] \quad (1)$$

where  $F=I \pm 1/2$  is the total angular momentum of the two hyperfine levels of the ground state,  $W$  is the hyperfine frequency separation,  $g_J$  and  $g_I$  are the electronic and the nuclear Landé factors,  $\mu_B$  is Bohr's magneton, and  $x = (g_J - g_I) \mu_B \cdot B / hW$ .

Eq. (1) can be expanded in series of powers as:

$$\nu_{F, m_F \rightarrow F, m_F - 1} = \gamma_F B + \alpha_m^{(2)} \cdot \gamma^{(2)} B^2 + \alpha_m^{(3)} \cdot \gamma^{(3)} B^3 + \dots \quad (2)$$

where  $\gamma_F = \frac{\mu_B}{h} [(g_J - g_I) / (2I+1) + g_I]$ ,

$$\gamma^{(2)} = \frac{1}{W} \left( \frac{\mu_B}{h} \frac{g_J - g_I}{2I+1} \right)^2,$$

$$\gamma^{(3)} = \frac{1}{W^2} \left( \frac{\mu_B}{h} \frac{g_J - g_I}{2I+1} \right)^3,$$

$$\alpha_m^{(2)} = (1 - 2m_F),$$

$$\alpha_m^{(3)} = 2 \left( 1 - 3m_F + 3m_F^2 \right) - \frac{1}{2} (2I+1)^2.$$

The most important parameters for the naturally available isotopes of Cs, Rb and K are reported in Table I.

The presence of non-linear terms produces a slight difference between the frequencies of the Zeeman transitions. Cesium has the largest hyperfine structure, and thus the smallest  $\gamma^{(2)}$  factor, while the opposite appears for the two potassium isotopes. At a typical earth field level ( $B \approx 50000$  nT) the separation between two nearby transitions is 6.67 Hz and 958.3 Hz in the case of Cs and <sup>41</sup>K, respectively.

Because the typical linewidth of the Zeeman transitions in a magnetometer is in the range 10 - 100 Hz, in the case of Cs the different transitions overlap, producing a non-symmetrical profile with the peak shifted in frequency. The relative weight of the different transitions is a complex function of all the physical conditions of the magnetometer (temperature of the vessel, intensity of the pumping source, relative alignment of the magnetometer and the local magnetic field, ...), this effect is the source of relative large errors, of the order of 10 nT or more. A skilled design of the magnetometer allows to compensate this asymmetry by combining the signals of two apparatus acting with opposite polarization (4). This design, in the self-oscillating scheme is applied to the commercial Cs magnetometers. The exact balance between the two signals is

however critical and limits the accuracy to some hundreds pT, while the sensitivity can be up to three order of magnitude better.  $^{87}\text{Rb}$  magnetometer is very similar, but a bit more sensitive because of the doubled gyromagnetic ratio. On the contrary, in the case of K, it is quite easy to obtain well resolved lines, and a very good laboratory self-oscillating magnetometer was realized by Alexandrov and al. (5).

The choice of Cs or Rb for commercial application is due to the difficult operation of K low pressure spectral lamp, because its vapor attacks and darkens usual glasses, reducing the lifetime of the lamp. Moreover, the two fine components of an alkali atom resonance line  $D_1$  and  $D_2$  pump the vapor in opposite directions, imposing a filtering. This can be easily done for Cs and Rb, but it is rather difficult for K, whose fine structure is only 3 nm.

The use of a diode laser as optical source overcomes all these difficulties connected with potassium spectral lamps.

## EXPERIMENTAL APPARATUS

The experimental apparatus is schematized in fig. 1. Our magnetometer uses a single mode diode laser, working in free-running mode. The radiation is tuned at the exact wavelength of the potassium  $D_1$  line (769.9 nm), by carefully controlling the temperature and the current in the diode. Low power lasers, developed for compact disk drivers, are suitable for our apparatus. The diode laser is connected to the probe by a 15 m long multimode optical cable. The radiation exiting the cable is circularly polarized and sent in the vapor cell, parallel to its axis, as a cylindrical beam of about 15 mm of diameter. The transmitted radiation is focused on a silicon photocell.

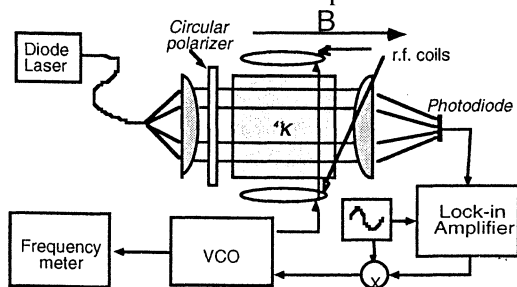


Figure 1: Experimental apparatus

The magnetometer works presently in the locked configuration. The resonant rf, produced by a frequency synthesizer, is applied to the vapor cell by a couple of Helmholtz coils, placed orthogonally to the cell axis. A frequency modulation at 10 - 20 Hz is superimposed to the rf, and the in-phase signal is detected through a lock-in amplifier. The lock-in output is sent to control the synthesizer frequency through a servo loop with an attack time variable between 400 ms and 2 s.

The probe is a sealed off Pyrex cell, 25 mm in length and 22 mm in diameter, filled of atomic potassium by vacuum distillation. In order to avoid the

fast relaxation of the atomic spin in the collision against the walls, we added a diamagnetic buffer gas. We chose to use nitrogen, that is also very effective in quenching the fluorescence from the excited K atoms, thus avoiding the presence of resonance radiation, that could perturb the pumping process. A  $\text{N}_2$  pressure of the order of some kPa produces also a broadening of some hundreds MHz (6), that is of the same order of the hyperfine structure and of the Doppler thermal linewidth. Thus, each atom can interact with the radiation, independently from its velocity and its hyperfine level, increasing the optical pumping efficiency. The cell is warmed by an antiinductive wired resistor, powered in a.c. at a frequency ( $\approx 1.5$  kHz), high enough to avoid interference with the optical pumping, and the temperature is controlled with a precision better than  $0.1^\circ\text{C}$ .

Preliminary we measured the relaxation time of the potassium spin orientation at different  $\text{N}_2$  pressures (Fig. 2) in identical cells, in order to find the optimum pressure values. Some cells were previously coated by a silicon diamagnetic film. This coating appears effective in reducing the relaxation rate, avoiding the use of a too high buffer gas pressure and a consequent too large line broadening. The coated cells, however, present a lower K vapor pressure at a given temperature and have a working temperature higher of almost  $10-20^\circ\text{C}$ .

Finally, we have made as magnetometer probe a coated cell, filled with isotopically enriched potassium (99.17%  $^{41}\text{K}$  and 0.83%  $^{39}\text{K}$ ) in presence of 6.1 kPa (at  $0^\circ\text{C}$ ) of  $\text{N}_2$ .

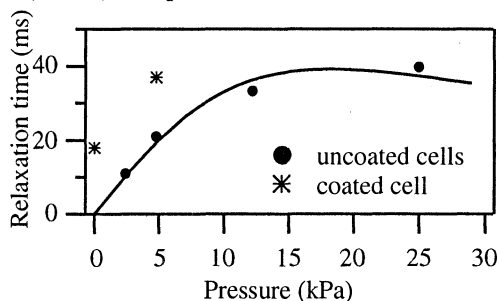


Figure 2: Relaxation time as a function of the pressure.

## EXPERIMENTAL RESULTS

The whole Zeeman spectrum, recorded by sweeping the rf around the resonance and detecting directly the photodiode signal in a cell filled with natural K (91%  $^{39}\text{K}$  and 9%  $^{41}\text{K}$ ), is shown in Fig. 3. The pumping power is about  $10\ \mu\text{W}$ , while rf power is about  $-55\ \text{dBm}$ . The absorption signal shows the well resolved different Zeeman components of  $^{39}\text{K}$  and  $^{41}\text{K}$ . We observe a resonance linewidth  $\Delta\nu \leq 80$  Hz, limited by the field inhomogeneity.

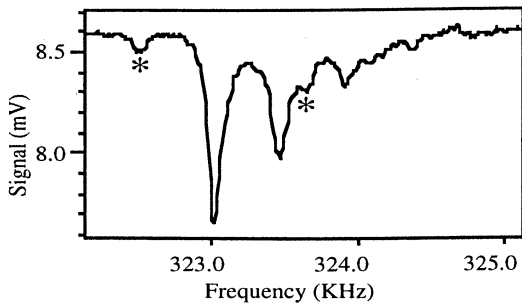


Figure 3: Absorption spectrum in a cell with natural potassium.  $^{41}\text{K}$  transition are indicated by \*.

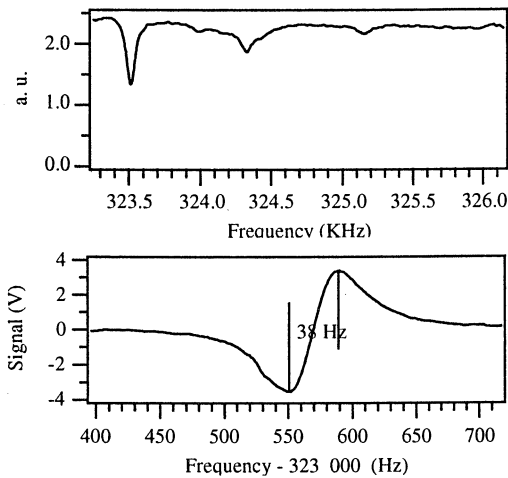


Figure 4: upper side, the Zeeman spectrum of the  $^{41}\text{K}$  ; lower side, the magnetometer transition.

By using isopically enriched potassium in a magnetically cleaner location, the spectrum of Fig. 4 was obtained. The derivative signal obtained from the lock-in amplifier (at right) demonstrate a linewidth of the order of 38 Hz. The actual values of the linewidth and of the S/N ratio gives an instrumental sensitivity  $(\delta B)_{\min} \approx 1.5 \text{ pT} \cdot \text{Hz}^{-1/2}$ .

The magnetometer has been tested in a location satisfying the condition for a magnetic observatory for a period of 60 minutes. The integration time of the loop was chosen of the order of 1 s, and the geomagnetic field value was read every 2 s. The recorded magnetogram is shown in Fig. 5, together with the magnetogram recorded by a commercial proton resonance magnetometer, whose sample time was setted at 1 minute. The probes of the two instru-

ments were kept quite far ( $\approx 10 \text{ m}$ ) one from the other, in order to avoid reciprocal perturbation, and this explicates the small difference in the readings.

## CONCLUSION

Work is in progress in order to build a magnetometer in self-oscillating configuration. The apparatus appears particularly suitable for application of the kind of field gradient measurement. In this case a single diode laser may pump two identical cells, placed at a fixed distance. The different sources of unaccuracy of the field reading (light shift, pressure shift, frequency pulling by the nearby transition,...) are then identical. With a distance between the two probes compatible with a portable instrument, gradient sensitivities better than 1 pT/m can be easily achieved.

## REFERENCES

- (1) A. Kastler: Production et détection optique d'une inégalité de population, *J. Phys. Rad.* **11**, 255-265 (1950)
- (2) W.E. Bell, and A.L. Bloom: *Phys. Rev.* **107**, 1559 (1957)
- (3) W.E. Bell, and A.L. Bloom: *Phys. Rev. Lett.* **6**, 623 (1961)
- (4) T. Yabuzaki, and T. Ogawa: Frequency shifts of self-oscillating magnetometer with cesium vapor, *J. Appl. Phys.* **45**, 1342-1355 (1974)
- (5) E.B. Alexandrov, M.V. Balabas, V.A. Bonch-Bruevich, S.V. Provotorov, and N.N. Jacobson: Fast optically pumped potassium magnetometer of high precision, in *Geomagnetics Measurements and devices*, pp. 5-23. Moscow, IZMIRAN (1986); E.B. Alexandrov, V.A. Bonch-Bruevich: Optically pumped atomic magnetometers after three decades, *Opt. Engin.* **31**, 711-717 (1992)
- (6) N. Allard and J. Kielkopf: The effect of neutral nonresonant collisions on atomic spectral lines, *Rev. Mod. Phys.* **54**, 1103-1182 (1982)

## JULIAN DAY 1998.26

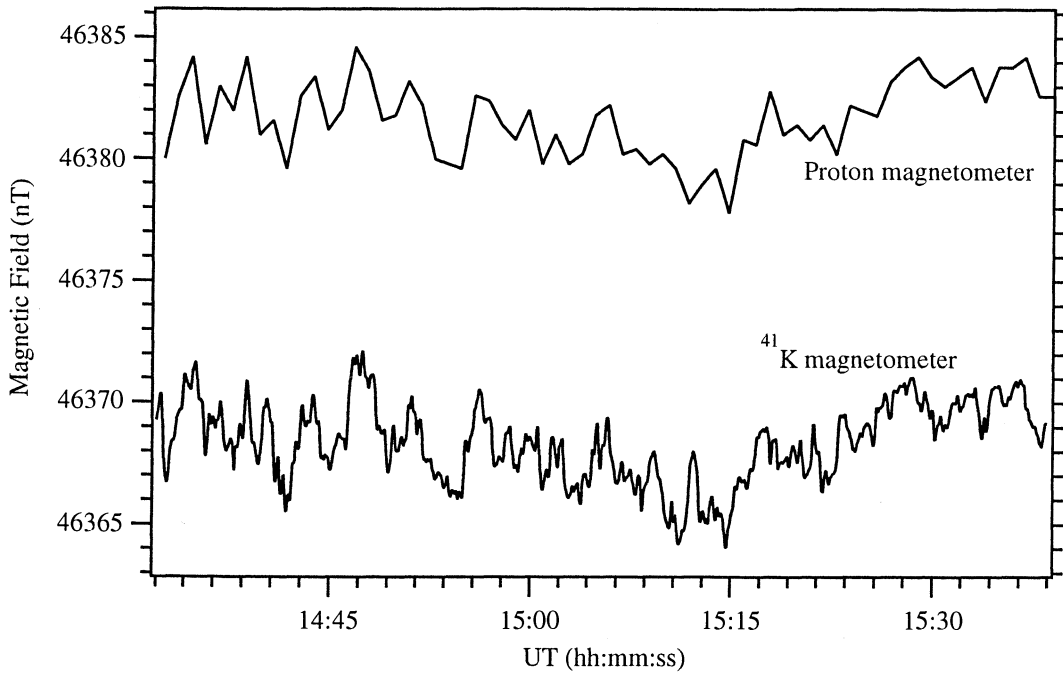


Figure 6: Magnetogram recorded by potassium magnetometer in locality Corvara (La Spezia, Italy)

TABLE I - Ground state alkali atoms parameters important for magnetometric application.

	<b>Cs</b>	<b><sup>85</sup>Rb</b>	<b><sup>87</sup>Rb</b>	<b><sup>39</sup>K</b>	<b><sup>41</sup>K</b>
<b><i>I</i></b>	7/2	5/2	3/2	3/2	3/2
<b><i>W</i> (MHz)</b>	9192.631770	3035.732439	6834.682613	461.7197202	254.013871
<b><i>g<sub>J</sub></i></b>	2.00254032	2.00233113	2.00233113	2.00229421	2.00229421
<b><i>g<sub>I</sub></i></b>	$-3.9885395 \cdot 10^{-4}$	$-2.936400 \cdot 10^{-4}$	$-9.951414 \cdot 10^{-4}$	$-1.4193489 \cdot 10^{-4}$	$-0.779060 \cdot 10^{-4}$
<b><math>\gamma_F</math> (Hz/T)</b>	$3.49862 \cdot 10^9$	$4.66743 \cdot 10^9$	$6.99583 \cdot 10^9$	$7.00466 \cdot 10^9$	$7.00533 \cdot 10^9$
<b><math>\gamma^{(2)}</math> (Hz/T<sup>2</sup>)</b>	$1.33579 \cdot 10^9$	$7.18879 \cdot 10^9$	$7.18932 \cdot 10^9$	$1.06327 \cdot 10^{11}$	$1.93257 \cdot 10^{11}$
<b><math>\gamma^{(3)}</math> (Hz/T<sup>3</sup>)</b>	$5.0920 \cdot 10^8$	$1.1062 \cdot 10^{10}$	$7.3735 \cdot 10^9$	$1.6135 \cdot 10^{12}$	$5.3306 \cdot 10^{12}$
<b><i>v</i> @ 50000 nT</b>	≈174.90 kHz	≈233.28 kHz	≈349.77 kHz	≈349.43 kHz	≈348.82 kHz
<b><math>\delta v</math> @ 50000 nT</b>	6.67 Hz	35.9 Hz	35.9 Hz	529.2 Hz	958.3 Hz



*12th E F T F* - 10÷12 March 1998 - **Warsaw - POLAND**

**SAW II**

Chairman:

*George D. Mansfeld*



**TEMPERATURE SENSITIVITY OF SURFACE TRANSVERSE WAVE  
RESONATORS BUILT USING DIFFERENT COMBINATIONS OF  
GROOVES AND STRIPS**

S. Ballandras, W. Daniau, E. Bigler, G. Martin, G. Marianneau

*Laboratoire de Physique et Métrologie des Oscillateurs du C.N.R.S.  
associé à l'Université de Franche-Comté - Besançon  
32 avenue de l'Observatoire - 25044 Besançon Cedex - France*

**ABSTRACT**

This paper is devoted to investigate the influence of the gratings of surface transverse wave (STW) devices on their temperature stability. A review of previous work in that field is proposed first, showing significant efforts performed by different research groups since 1977. It is also shown that various structures of STW-like devices have been tested, but very little work has been done on the thermal stability of real groove grating architecture. In a second part of the paper, perturbation models applied to STW are recalled and even extended to more inhomogeneous gratings combining strips and grooves. Finally, experimental frequency-temperature measurements are presented and compared to theoretical predictions. The purpose of the work is to find out a STW structure improving the reproducibility of such devices.

**1. INTRODUCTION**

The most attractive properties of Surface Transverse Waves (STW) resonators consist in a high propagation velocity (up to  $5100 \text{ m.s}^{-1}$  on AT cut of quartz) allowing the design of high frequency devices exhibiting a low sensitivity to thermal variations (AT cut quartz exhibits a parabolic frequency-temperature behavior and BT cut a cubic one at room conditions). A lot of work has been devoted to optimize the design and fabrication of STW devices, but most of the authors publishing in that field have pointed out the large dependence of STW characteristics to technological parameters. This yields a rather poor wafer to wafer reproducibility, and even on a same wafer it appears difficult to avoid a large dispersion of the devices central frequency  $F_c$  (currently up to 1% variations of  $F_c$ ), which is incompatible with the production of high quality resonators or filters.

One of the most important factors controlling the quality of STW devices is the profile and homogeneity of metal strips generally used to build their mirror gratings and their interdigital transducers. Previous work shows that slight variations of technological parameters in the fabrication process are enough to strongly modify the frequency response of the resonator. These results have been experimentally established by many authors for STW on AT cut quartz. As in the case of Rayleigh wave on (ST,X) quartz, STW on AT cut quartz was experimentally found sensitive to metallization but this sensitivity seems to be conditioned by the grating structure. The first part of the paper is then devoted to review major contributions in that field. Also, some results concerning reproducibility are reported. State of the art shows that there is still a lack in modeling the influence of the gratings on STW thermal properties, and that groove grating structures have rarely been used for frequency-temperature measurements. Using a perturbation approach based on Tiersten and Sinha work, it is possible to correctly predict the first order temperature coefficient of frequency (TCF) including a corrective term due to the corrugation (groove or strip). The theoretical approach used in that way is presented in the second part of the paper.

Finally, experiments have been performed on different kind of devices combining strips and grooves. The frequency versus temperature stability of these devices

has been measured and compared to theoretical perturbation model results. The dependence of the first order TCF versus groove depth has been tested for one of the proposed device. The purpose of this work is to find a possible optimal STW structure exhibiting a robust behavior with respect to technological parameter variations.

**2. STATE OF THE ART**

Surface waves exhibiting a pure shear horizontal polarization have been widely studied by most of the research groups involved in the development of advanced SAW devices. The possibility to excite bulk waves purely polarized using an interdigital transducer was first introduced by Mortley in 1962 [1], three years before the well-known paper of White and Voltmer announcing the excitation of surface wave by the means of such a transducer [2]. In 1970, much more work was already performed to improve the characterization of IDT's properties as a bulk-surface wave transducer (see ref. [3, 4] as examples among numerous of others). However, during the following years, a major drawback was identified in the use of IDT for the fabrication of surface acoustic wave (SAW) devices, consisting in spurious signals superposed on the fundamental response the Rayleigh wave and clearly associated to unwanted bulk wave excitation and detection. In 1974, enough work was done on this subject to allow Mitchell to present a review paper [5] with more than 12 references published since 1970 directly related to spurious bulk waves in SAW devices.

Although a large majority of the research in this field was devoted to suppress this unwanted phenomenon, the basic idea of Shallow Bulk Acoustic Waves (SBAW) was growing. In 1976, Auld & al [6] proposed a new concept for SAW design, consisting in trapping bulk-like polarized shear waves at the surface of isotropic material by the use of groove gratings. The same idea was developed separately by Gulyaev and Plesskii and proposed less than one year later [7]. Whatever, the first propositions of SBAW devices on quartz were published in 1977 by Browning and Lewis [8] and Yen & al [9] during the same event. A particular attention has to be devoted to the paper of Browning and Lewis [8], which can be considered as the first evidence of STW propagation because of the length of the IDT they used for their experiments ( $2500$  wavelengths  $\lambda$ ) and which presents frequency-temperature measurements for various orientations of singly rotated quartz cuts close to AT and BT orientations, propagation direction lying along the rotated Z axis of the plate. It is also relevant to note that in ref [8, 9], SSBW or SBAW devices operating at frequencies close or even higher than 2 GHz. A few more experimental data were proposed some months later by Lewis [10]. In this paper, a question reported in appendices concerned the influence of the metallization on the thermal stability of the proposed devices. Lewis had no definitive response at this time, but only a general conviction that the strip height of the IDTs strongly influences the working principle of the SSBW delay lines.

First quantitative answers were given three years later by Lau & al [11] and Nishikawa & al [12]. In ref [11], a comparison between a theoretical analysis of temperature

stability of SBAW and experiments performed on a 2 GHz delay line is reported. The model used, based on the thermal variations of the SSBW parameters [13], accurately predicted the frequency-temperature behavior of the AT cut (parabolic) and BT cut (cubic) devices but did not take into account the presence of IDTs. As a consequence, the rather large difference between theoretical and measured turnover temperatures  $T_{turn}$  was related to the influence of the metallization on the thermal sensitivity of SBAW. However, the second order temperature coefficient of frequency (TCF) was given, accurately at  $-52$  ppb/K<sup>2</sup>. It must be precised that these results were obtained using recessed metal gratings.

As for ref [8], it is very interesting to closely inspect the results of ref [12] for different reasons. First, the paper presents a simple method to take into account the metallization on what is generally called by its authors shear horizontal (SH) type waves. Second, the experimental devices have been build including a metal strip grating between the IDTs, since its presence was found theoretically to increase the electromechanical coupling factor. Hence, increasing the metal thickness of the gratings was found experimentally to reduce the Insertion losses. Finally, using the proposed model together with a thermal variation procedure in accordance to what proposed Minowa [14] allows a precise prediction of the turnover temperature ( within  $5^\circ\text{C}$ , p.288 of [12] ) and of the second order TCF ( $-56$  ppb/K<sup>2</sup> theoretical,  $-60$  ppb/K<sup>2</sup> experimental). These values were obtained for a  $h/\lambda$  equal to 0,7 %. The studied devices can be considered as one of the very first STW delay line ever tested, together with a pertinent attempt to take into account the influence of the metallization on the SH wave properties. Moreover, those who are used to STW resonator's electrical response can recognize in fig.12 of [12] the familiar signature of surface transverse waves resonators. In 1981, Renard & al also presented STW delay lines working close to 160 Mhz but no frequency-temperature measurements were performed [15].

More exhaustive measurements have been done then a few years later by Duquesnoy and Gautier [16] to better characterize experimentally the influence of the metallization on the properties of SH mode SAW delay line. The proposed structure of the device was a mixed version of IDT architectures presented in [11] and [12], combining recessed metal strips and a trapping grating between the IDTs. In this paper the kind of wave propagating under the gratings are identified as a trade-off between Love [17] and Bleustein-Gulyaev waves [18, 19], which appears as a good definition of STW. The most interesting results presented in [16] in the systematic measurement of the influence of the relative metal strip height  $h/\lambda$  and of the cut angle in the vicinity of AT cut quartz ( $\theta = 36^\circ$ ) on the velocity and thermal properties of the SH waves. As in ref [11], a rather high sensitivity to the metal thickness was measured in terms of center frequency, up to 1 MHz for a 2nm variation, for metallization ratio of 0,72 (strip width/period). As in the case of Rayleigh waves on (ST,X) cut of quartz, the Turnover Temperature decreases when the strip height increases, with a rate of  $-20^\circ\text{C}$  per percent of  $h/\lambda$  (metal ratio still equal to 0,7). This result can be compared to the  $-12^\circ\text{C}$  per percent of Rayleigh waves on (ST,X) quartz.

The authors proposed a parabolic eyeball fit of the curve  $T_{turn}$  versus  $h/\lambda$ , but it can be remarked that a linear law also fits the experiments.

Whatever might have been the interest in this topic, the activity in the field of SSBW or SBAW or more generally SH surface modes has decreased during the following years. Auld and Thompson proposed in 1984 [20] a model assumed to correctly predict the influence of groove depth or metal height on the frequency-temperature low of STW devices. However, the same authors announced two years later in a short part of ref [21] bad news about the agreement between their model and experiments. They gave in [20] a dependence of  $T_{turn}$  to  $(h/\lambda)^4$ , providing a temperature shift of  $86^\circ\text{C}$  when increasing  $h/\lambda$  from 1,75% to 3,75%, which is two times higher than the experimental results of Duquesnoy and Gautier [16]. But unfortunately,

experimental results of Auld and Thompson, summarized in two parts of measurements, gave a rate of  $11^\circ\text{C}$  per percent of  $h/\lambda$  in the variation of  $T_{turn}$  (8 times smaller than the proposed theory).

Although more experiments should have been performed to definitively conclude about these results, the authors proposed an explanation of the discrepancy between theory and experiments. Following their own denomination, it was due to "static strain effect" related to the difference of thermal expansion between metal and substrate, causing significant changes of thermoelastic properties of the latter. Considering results shown by Nishikawa, another reason of such a discrepancy may be searched in Auld and Thompson model. Furthermore, even if static strain effect does change the effective material properties, no evidence was given by the authors because no values were calculated to compare with the simple thermal expansions of metal and substrate and to check the effective importance of the phenomenon. Ref [22] gives a good synthesis of the work of Auld and Thompson on STW. During the same event, the first STW resonators were presented by Bagwell and Bray [23] and a fine analysis of their electrical response was proposed by Flory and Baer [24]. In ref [23], the temperature compensation was experimentally studied and found highly sensitive to cut angle (but not more that what was found by Lewis [10], Lau & al [13] or Duquesnoy & al [16]). A more interesting point is the shape of the frequency-temperature curve obtained for a cut angle  $\theta = 36^\circ$ . The authors pointed out that it was a combination of parabolic and cubic orders, which was never found for delay lines [10-13, 16, 20]. For STW resonators on ( $Y + 38,4^\circ, Z$ ) cut, the curve was found parabolic with  $T_{turn}$  close to  $120^\circ\text{C}$  which is in good agreement with previous work (see the above mentioned references). Whatever, very nice results were presented in [23] considering high Q factors and relatively low insertion losses, improving the state of the art of surface wave resonators. Very little work was then devoted to understand the thermoelastic properties of STW on quartz until the paper of Avramov in 1991 [25], which presents many frequency-temperature measurements performed on a selection of STW resonators built on AT cut-like substrates with different metal thickness. The dependence of thermal compensation at room conditions versus cut angle  $\theta$  found experimentally by Avramov agrees well with previous work [10-13, 16, 20, 23]. The temperature-frequency behavior versus relative metal thickness  $h/\lambda$

appears more surprising. First, the turnover temperature is experimentally shifted down with a rate of  $-75^\circ\text{C}$  to  $-85^\circ\text{C}$  per percent of  $h/\lambda$ . This agrees fairly well with theoretical data of Auld and Thompson [21, 22] but with none of the above mentioned experimental work. Furthermore, a cubic shape of the frequency-temperature is found at very low temperature (below  $-50^\circ\text{C}$ ) which is a result quite unusual. The conclusion of the author is that this phenomenon occurs because "it would be well known that STW on AT cut properties are similar to those of bulk waves resonators" (with an abusive mention to [23] as an evidence of the proposition). Many authors have clearly demonstrated the SH surface waves on rotated  $Y + \theta$  cuts of quartz exhibit acoustic properties similar to those of bulk waves on the same substrate but taking into account an extra rotation  $Y + \theta \pm 90^\circ$ . Experimental evidences have been presented in many papers (see above mentioned references) that SH surface wave on AT cut exhibit properties similar to bulk waves on BT cut and vice-versa. Even if the conclusions of Avramov are questionable, the scientific material presented in this paper is of particular interest because measurements of frequency-temperature dependence at temperature below  $-50^\circ\text{C}$  have been rarely presented, and because the cubic law he measured presents a third order temperature coefficient with a negative sign, opposite to the one of classical bulk waves on AT cut quartz (consequently of SH surface wave on BT cut) and even of doubly rotated Rayleigh wave quartz cuts proposed in [26]. This means that an unusual mechanism may be responsible of such a result, but it is clear that it must be verified by a separate research group to be reliably confirmed and then considered.

Another study has to be mentioned concerning frequency-temperature experiments on STW resonators performed by

Almar & al [27]. In their paper, the authors show the dependence of the turnover temperature of a STW resonator built on an AT cut ( $\theta = 36^\circ$ ) of quartz versus metal thickness which is found equal to  $-13,25^\circ \text{C}$  per percent of  $h/\lambda$ . This additional data agrees rather well with previously published ones [16, 21]. However, an interesting point of these measurements is the rather small value of the second order TCF ( $-45 \text{ ppb}/^\circ \text{C}^2$  instead of  $-55$  or  $-60 \text{ ppb}/^\circ \text{C}^2$  [12, 16, 23, 25]). Unfortunately, there is not enough material in ref [27] to propose any explanation of such results. Whatever, another point emphasized by the authors is the variation of insertion losses versus temperature which appears less than 1dB per  $100^\circ \text{C}$ , which is a rather satisfying feature. It can be added that non cubic behavior of the frequency-temperature dependence of the devices was pointed out in ref [27].

This presentation gives an overview of the work performed on temperature stability of surface transverse waves on Y cuts of quartz corresponding to the best of the authors knowledge. The work performed by the authors since ref [27] will be developed in the next part of the present paper. To conclude this section, some remarks should be added concerning reproducibility of SH surface wave devices on quartz.

Very soon, some authors [11, 16] have pointed out experimentally the large sensitivity of STW or SH-SAW to metallization, in opposition to Browning and Lewis opinion that SSBW filters should be only a little more

complicated to design than the classical SAW devices [8]. Also, the dual nature of SH-SAW or STW (i.e., partly surface and partly bulk waves) was identified in ref [15] as a possible drawback in the design of STW resonators. Furthermore, the authors of [15] pointed out space harmonic interferences perturbing the response of their devices, and related to dimensional tolerances in the design of the gratings. This problem was emphasized one more time in [21] and associated to reflections at the end of the grating. Large efforts have been done to model this phenomenon, [28, 29], but no efficient solution has been proposed to solve the problem.

In ref [23], the difficulty to control repeatably optical lithography with linewidths smaller than 1 micron was underlined, but the authors also reported an excellent consistency of their results using E-beam exposure. However, they did not give any extra information in the following years about their work. Avramov also underlined the fact that STW results were difficult to design [25].

The experiments performed by our group using different resonators operating close 500 MHz, 1 GHz or even 3 GHz have also yield identical conclusions concerning reproducibility of the electrical responses of STW devices [30,31]. Most of published work on STW resonators has been performed using classical aluminum strip gratings deposited at the propagation surface. Considering the possibility to implement groove gratings [15-21] or combined strip and groove structures [11-16], preliminary work has been done to emphasize the properties of STW resonators built using mixed strip and groove grating mirrors [32], exhibiting the influence of grooves in grating mirrors on the STW electrical response. This work has been continued to check the influence of the grooves on the temperature stability of STW from both theoretical and experimental point of view.

### 3. THEORETICAL ANALYSIS OF STW AND COMBINED STRIP AND GROOVE GRATING

#### 3.1 Propagation

In this section, the basic principles of the calculation procedure for modeling STW propagation are briefly recalled, more detailed calculations are given in [32]. In opposition to Bagwell and Bray opinion concerning grooved gratings ruled out due to their less efficient trapping of the shear wave, it has been shown theoretically that groove and strip grating of identical dimensions exhibit a similar trapping efficiency [33]. This result

indicates that strip gratings may be replaced by groove gratings in order to reduce the proportion of metal in STW devices and to check any improvement in the reproducibility of the results.

The model used to calculate the STW propagation characteristics in a periodic grating of period  $p$  is based on a Floquet development of the fields associated with the wave, yielding the following form of mechanical displacement  $u_1$  and electrical potential  $\Phi$ :

$$u_1 = \sum_{n=-\infty}^{+\infty} \left( \sum_{r=1}^2 A_{nr} e^{-\alpha_{nr} a_2} \right) e^{-j\beta_n a_3} e^{j\omega t} \quad (1)$$

$$\Phi = \sum_{n=-\infty}^{+\infty} \left( \sum_{r=1}^2 D_{nr} A_{nr} e^{-\alpha_{nr} a_2} \right) e^{-j\beta_n a_3} e^{j\omega t}$$

Where  $\beta_n = \beta_0 + 2n\pi/p$  is the wavenumber of the  $n$ th spatial harmonic of the wave, which exhibits two partial waves  $r$  as in Bleustein-Gulyaev models [33,34].  $\alpha_{nr}$  are penetration coefficients of the wave into the substrate,  $A_{nr}$  are the mechanical amplitudes and  $D_{nr} A_{nr}$  the electrical amplitudes of the wave, both related via the Poisson's condition. Propagation direction is along  $a_3$  according to fig.1, which shows the general shape of the problem considered in the present work. The boundary conditions can be considered as a superposition of shallow groove and thin metal strip gratings.

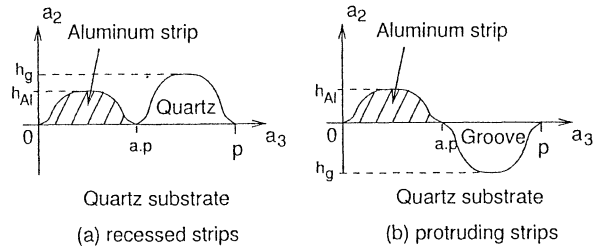


fig. 1 general shape of the gratings considered in the present work.  
a) recessed metal strip structure  
b) protruding metal strip structure

According to ref [32], the mechanical boundary conditions are written as follows:

$$T_{12}(0, a_3) = h_{A\ell} \left[ \frac{\partial f_{A\ell}(a_3)}{\partial a_3} T_{13}(0, a_3) + f_{A\ell}(a_3) \left( \rho_0 \omega^2 u_1(0, a_3) + \frac{\partial T_{13}}{\partial a_3}(0, a_3) \right) \right]$$

and  $u_1(0, a_3) = u_1(0, a_3)$  along  $0 < a_3 < r.p$

$$T_{12}(0, a_3) = h_g \left[ \frac{\partial f_g(a_3)}{\partial a_3} T_{13}(0, a_3) - f_g(a_3) \frac{\partial T_{13}}{\partial a_3}(0, a_3) \right]$$

along  $r.p < a_3 < p$

In eq. (2),  $h_{A\ell}$  and  $h_g$  represent respectively the strip height and the groove depth (or height, see fig. 1), and  $f_{A\ell}(a_3)$  and  $f_g(a_3)$  describe the profiles of the aluminium metal strip (underscript  $A\ell$ ) and of the groove (underscript  $g$ ). The primed terms in eq. (2) are relative to the contribution of the metal strip.

The electrical boundary conditions correspond to a started metal strip and to the continuity of electrical displacement normal to the surface of the groove:

Where  $\sigma(a_3)$  is the unknown electrical charge distribution at the interface between the substrate and the strip. More developments can be found in [32]. The way the resulting algebraic system is solved is carefully described in ref [30, 33].

$$\left. \begin{aligned} D_2^{substrate}(0, a_3) - D_2^{vacuum}(0, a_3) &= \sigma(a_3) \\ \Phi^{substrate}(0, a_3) &= \Phi^{vacuum}(0, a_3) = 0 \end{aligned} \right\} \text{along } 0 \leq a_3 < p$$

$$\left. \begin{aligned} \left( D_j^{substrate}(0, a_3) - D_j^{vacuum}(0, a_3) \right) \cdot V_j &= 0 \\ \Phi^{substrate}(0, a_3) &= \Phi^{vacuum}(0, a_3) \end{aligned} \right\} \text{along } rp \leq a_3 < p$$

### 3.2 Perturbation equation and temperature effects

Previous study [35] has demonstrated the possibility to use perturbation equations proposed by Tiersten and Sinha for classical BAW and SAW [36, 37] for the prediction of STW sensitivity to first order temperature effects. An extension of the proposed approach is shown here to take into account the influence of the groove or strip dimensions on the first order TCF. According to usual assumptions [35-38], the basic form of the perturbation equation to be considered is as follows:

$$\frac{\Delta\omega}{\omega_0} = \frac{\int_0^p \int_{-\infty}^{\infty} \left[ \frac{h_g f_g(\alpha_3)}{\rho_0} \frac{\partial u_1}{\partial \alpha k} \frac{\partial u_1}{\partial \alpha k} - \frac{\partial u_1}{\partial \alpha k} \frac{\partial u_1}{\partial \alpha k} \right] da_2 + \int_{-\infty}^{\infty} \left[ \frac{h_{Al} f_{Al}(\alpha_3)}{\rho_0} \frac{\partial u_1}{\partial \alpha k} \frac{\partial u_1}{\partial \alpha k} - \frac{\partial u_1}{\partial \alpha k} \frac{\partial u_1}{\partial \alpha k} \right] da_3}{2\omega_0^2 \left[ \rho_0 \int_0^p \int_{-\infty}^{\infty} u_1 u_1 da_2 da_3 + \rho_0 \int_0^p \int_{-\infty}^{\infty} u_1 u_1 da_2 da_3 \right]} \quad (4)$$

Where  $H_{ijkl}$  is a perturbation tensor representation of the linear and non-linear thermoelastic properties of the substrate, and proportional to the temperature variation [35].

$$H_{1k1\ell} = \theta_{1k1\ell} (T - T_0) \quad (5)$$

All the primed terms of eq. (4) are relative to the metal strips. To is the reference temperature set to 25° C according to the definition of the fundamental constants used to calculate  $H_{ijkl}$ .

Computation of eq. (4) requires the explicit expression of  $u_1$  and  $u_1'$ . According to [39],  $u_1$  can be developed under a form very close to the one used for  $u_1$  (eq. (1)), as follows:

$$u_1 = \sum_{n=-\infty}^{+\infty} \sum_{r=1}^2 B_{nr} e^{-\gamma_{nr} a_2} e^{-j\beta_n a_3} \text{ with } \gamma_{nr} = (-1)^r \sqrt{\frac{\omega}{V_T} - \beta_n^2} \quad (6)$$

Inserting eq. (1) and (5) into eq. (4) allows the development of the perturbation equation under the following form:

$$\frac{\Delta\omega}{\omega_0} = \frac{\sum_{n,m=-\infty}^{+\infty} \sum_{r,s=1}^2 \left( \theta_{nmrs} I_{nmrs}' + \theta_{nmrs}' I_{nmrs} \right) (T - T_0)}{2\omega_0^2 \sum_{n,m=-\infty}^{+\infty} \sum_{r,s=1}^2 \left( \rho_0 A_{nr}^* A_{ms} I_{nmrs}' + \rho_0 B_{nr}^* B_{ms} I_{nmrs}' \right)}$$

with

$$\theta_{nmrs}' = \left( \theta_{1212} \alpha_{nr}^* \alpha_{ms} + j \theta_{1213} \left( \alpha_{nr}^* \beta_m - \alpha_{ms} \beta_n^* \right) + \theta_{1313} \beta_n^* \beta_m \right) A_{nr}^* A_{ms}$$

$$\theta_{nmrs}' = \left( \theta_{1212} \gamma_{nr}^* \gamma_{ms} + j \theta_{1213} \left( \gamma_{nr}^* \beta_m - \gamma_{ms} \beta_n^* \right) + \theta_{1313} \beta_n^* \beta_m \right) B_{nr}^* B_{ms}$$

$$I_{nmrs}' = \int_0^p \int_{-\infty}^{\infty} \frac{h_g f_g(\alpha_3)}{\rho_0} e^{-(\alpha_{nr}^* + \alpha_{ms}) a_2} e^{j(\beta_n^* - \beta_m) a_3} da_2 da_3$$

$$I_{nmrs}' = \int_0^p \int_{-\infty}^{\infty} \frac{h_{Al} f_{Al}(\alpha_3)}{\rho_0} e^{-(\gamma_{nr}^* + \gamma_{ms}) a_2} e^{j(\beta_n^* - \beta_m) a_3} da_2 da_3$$

Since  $h_g$  and  $h_m$  are generally small compared to the acoustic wavelength, both integrals  $I_{nmrs}$  and  $I_{nmrs}'$  can be simplified by using the series development of the exponential along  $a_2$  as follows:

$$I_{nmrs} = - \int_0^p \left( \frac{1 - (\alpha_{nr}^* + \alpha_{ms}) h_g f_g(\alpha_3)}{\alpha_{nr}^* + \alpha_{ms}} \right) e^{j(\beta_n^* - \beta_m) a_3} da_3 \quad (8)$$

$$I_{nmrs}' = h_{Al} \int_0^p f_{Al}(\alpha_3) e^{j(\beta_n^* - \beta_m) a_3} da_3$$

Considering the boundary conditions of eq. (2) and the definition of  $f_g(\alpha_3)$  and  $f_{Al}(\alpha_3)$  conformally to fig. 1, the final form of integrals (8) is obtained:

$$I_{nmrs} = j \left[ \frac{e^{j(\beta_n^* - \beta_m)p} - 1}{(\beta_n^* - \beta_m)(\alpha_{nr}^* + \alpha_{ms})} + h_g \frac{e^{j(\beta_n^* - \beta_m)p} - e^{-j(\beta_n^* - \beta_m)p}}{\beta_n^* - \beta_m} \right] = \Delta_{nmrs} + h_g \Gamma_{nm}^g$$

$$I_{nmrs}' = j h_{Al} \left[ \frac{1 - e^{j(\beta_n^* - \beta_m)p}}{\beta_n^* - \beta_m} \right] h_{Al} \Gamma_{nm}^{Al}$$

Another simplification is proposed for the calculation eq. (7). Since the denominator is only a normalization factor it still because  $h_g$  and  $h_{Al}$  are very small compared to the wave length, it is assumed independent on the grating dimension. Finally, the frequency variation due to first order temperature effects can be simply written under the following expression:

$$\frac{\Delta\omega}{\omega_0} = \left( \theta_{\alpha} + h_g \theta_{\alpha g} + h_{Al} \theta_{\alpha Al} \right) (T - T_0)$$

with

$$\theta_{\alpha} = \frac{\sum_{n,m=-\infty}^{+\infty} \sum_{r,s=1}^2 \theta_{nmrs} \Delta_{nmrs}}{2 \rho_0 \omega_0^2 N} \quad (10)$$

$$\theta_{\alpha g} = \frac{\sum_{n,m=-\infty}^{+\infty} \sum_{r,s=1}^2 \theta_{nmrs} \Gamma_{nm}^g}{2 \rho_0 \omega_0^2 N}$$

$$\theta_{\alpha Al} = \frac{\sum_{n,m=-\infty}^{+\infty} \sum_{r,s=1}^2 \theta_{nmrs}' \Gamma_{nm}^{Al}}{2 \rho_0 \omega_0^2 N}$$

$$\text{and } N = \sum_{n,m=-\infty}^{+\infty} \sum_{r,s=1}^2 A_{nr}^* A_{ms} \Delta_{nmrs}$$

Both terms  $\theta_{\alpha g}$  and  $\theta_{\alpha Al}$  can be considered as correction coefficients of the first order TCF  $\theta_{\alpha}$  proportional to the height (or depth) and the width of the strips and the grooves. It can be emphasized that the expression of  $\theta_{\alpha}$  is exactly the same than the one obtained when completely neglecting the gratings (see ref [35]).

### 3.3 Numerical computation

Results concerning the propagation of STW under mixed strip and groove gratings have been already published and

commented in [32]. The most attractive result emphasized in this paper was the possibility to strongly reduce the bulk wave radiation at the end of the stop band using strip and groove gratings and also to obtain rather large values of reflexion coefficients improving the rejection after the resonance.

In this section, theoretical calculation results are exposed to check the efficiency of the developments of section II.2. Unperturbed propagation characteristics of STW ( $u_1^0$  and  $u_1^0$ ) are calculated using Slobodnik's set of constants for quartz [40] and using  $\rho'_0 = 2695 \text{ kg/m}^3$  and  $C'_{55} = 25 \text{ GPa}$  for Aluminum (metal of the strips). Nonlinear coefficient of quartz are those of Thurston [41], and can be found in [42] for Aluminum. The first derivatives of the elastic constants of quartz are given by Sinha and Tiersten [43] and those of Aluminum are calculated conformally to [38] (see also ref [44]).

Fig. 2 shows a comparison between theory and our experiments for the dependance of the resonance frequency versus groove depth up to values of  $0.55 \mu\text{m}$  which corresponds to a frequency shift at least two orders of magnitude bigger than would be necessary for a precision frequency trimming.

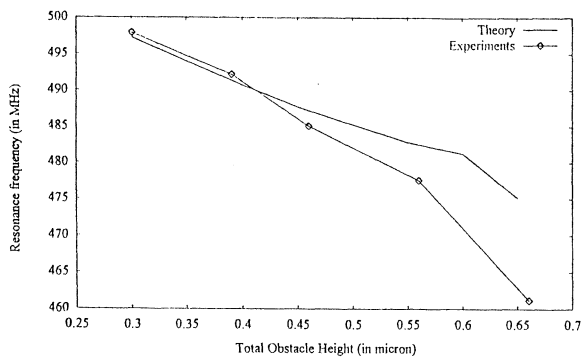


Fig. 2. Comparison between theory and experiments for the dependance of the resonant frequency vs groove depth at room temperature for a mixed strip-groove structure (protruding strips, see fig. 1a)

A point must be precised before discussing theoretical results on temperature effects. For each height  $h_g$  or  $h_{A\ell}$ , propagation characteristics of the unperturbed wave are first calculated and then inserted in eq. (10). As a consequence, the three coefficient  $\theta_\alpha$ ,  $\theta_{\alpha_g}$  and  $\theta_{\alpha_{A\ell}}$  exhibit a dependance on  $h_g$  and  $h_{A\ell}$  which is emphasized when plotting them separately. In fig. 3.a, the first order TCF of a groove grating STW device on AT quartz ( $Y+36^\circ$ ) is reported, showing that the correction factor  $\theta_{\alpha_g}$  acts a very little on the frequency shift value due to temperature. One can conclude that in this case, the main effect is correctly represented by  $\theta_\alpha$ .

On the other hand, fig. 3a. shows that for metal strip grating on AT-cut devices, the most significant term is  $\theta_{\alpha_{A\ell}}$  for a correct modeling of the metal thickness on the first order TCF. Moreover, it can be shown that the calculation is weakly sensitive to the value of the Aluminium shear elastic constant  $C'_{66}$ , but more dependant on the values of the non linear constants.

Nevertheless, fig.3a and b emphasize that the first order temperature coefficient of aluminum strip grating devices is more sensitive to the surface corrugation geometry than groove grating ones on AT-cut-quartz. As a consequence, variations of turnover temperature versus obstacle height should be larger for STW under aluminum gratings than

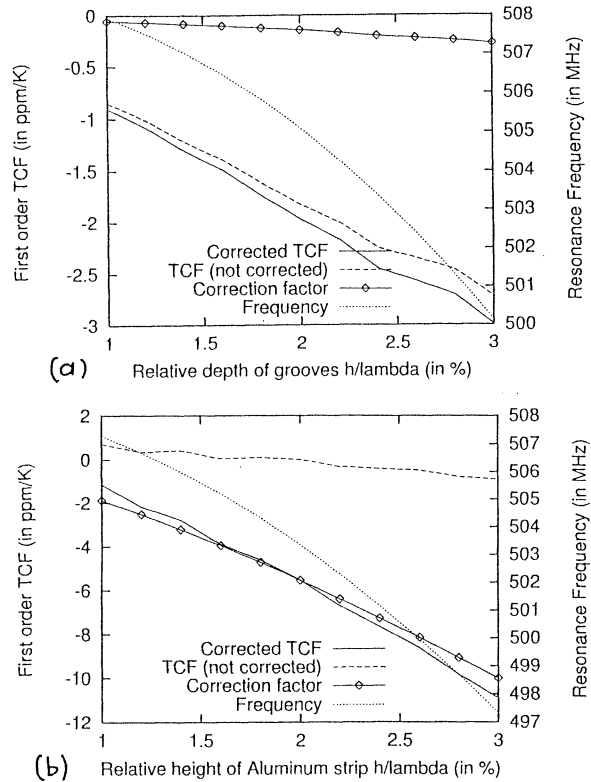


Fig. 3. Theoretical predictions for the first order temperature coefficient of frequency vs metal thickness or groove depth  
a) For metal strip STW resonators without grooves  
b) For groove STW resonators without metal strips

for STW under groove gratings. Considering results fig. 3a and b, it is found according to [44] and using a second order TCF of  $-66 \text{ ppb per } ^\circ\text{C}^2$  that an increase of 1 % of  $h/\lambda$  induces a  $-8^\circ\text{C}$  turnover temperature shift in the case of STW under grooves instead of  $-32^\circ\text{C}$  for STW under aluminum strips. The latter value appears too large when compared with experiments [11, 16, 21, 27]. However, physical properties of thin films are known to be very dependent on the process used to deposit them, which may partly explain this discrepancy. Whatever might be the differences between theory and experiments, it must be noted that Almar & al [27] have measured a rather small sensitivity of the turnover temperature to metal thickness together with a small second order TCF. On the contrary, Duquesnoy & al [16] have found large experimental second order TCF together large turnover temperature shifts versus metal thickness. Even, if the structures they used was different, both groups have proposed contradictory data considering the theoretical calculation of the turnover temperature presented in [44].

Then, more reliable experimental work is required to conclude on the efficiency of the proposed analysis. If confirmed, the theoretical work proposed in this paper clearly shows that using grooves instead of aluminum strips allows a smaller sensitivity of the turnover temperature of STW devices on AT quartz to the grating geometry.

## 4. EXPERIMENTAL RESULTS

STW resonators have been built on AT-cut quartz plates. The acoustic wavelength was close to  $10 \mu\text{m}$  with an operating frequency close to 500 MHz. A conventional design with a purely synchronous structure was used. Metal thickness was 300 nm and metallization ratio was about 55% before etching.

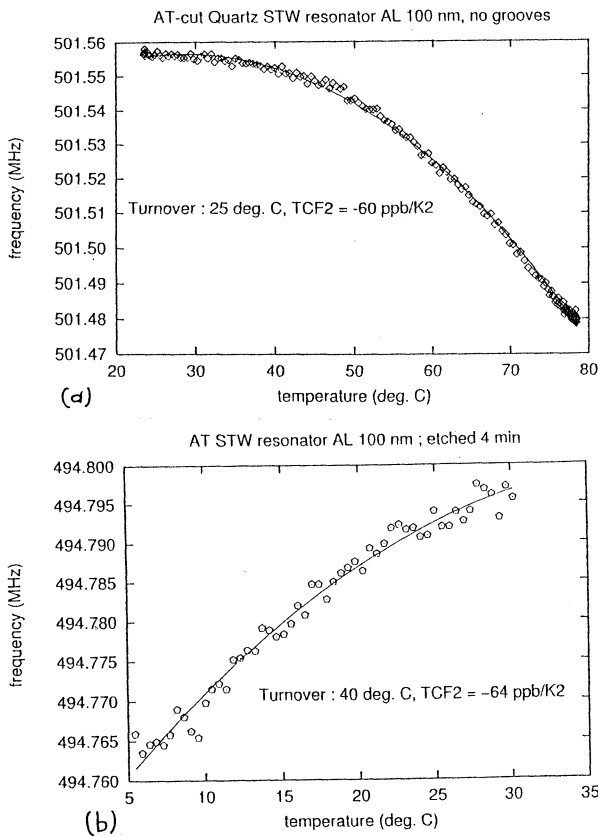


Fig.4. Experimental results

- a) Frequency vs temperature curve of an AT cut STW resonator on quartz,  $f_0 = 500$  MHz,  $h = 300$  nm,  $h/\lambda = 3\%$   
 b) Temperature sensitivity of the same resonator after 4 minutes of reactive ion etching

A positive shift of the turnover temperature is observed i.e. the opposite sign of what would be expected from metal strips only or grooves only

Fig. 4a shows the frequency vs temperature curve of the device before etching. A classical parabolic curve with a second order TCF =  $-60$  ppb/ $^{\circ}$ C $^2$  is observed in accordance to already published data. The same device was etched for 4 minutes in a reactive ion etching process used for silicon micromachining. A frequency shift of about 6 MHz at room temperature is observed, corresponding to a groove depth of about 100 nm (see fig. 2) i.e 1% of  $h/\lambda$ . As mentioned in the previous section, a change of 1<sup>st</sup> order TCF can be directly related to a shift in turnover temperature if the 2<sup>nd</sup> order TCF is supposed to stay constant which is experimentally verified since the 2<sup>nd</sup> order TCF can be estimated to about  $-64$  ppb/ $^{\circ}$ C $^2$  after etching (fig. 4b). However, a negative shift of the turnover temperature between  $-8^{\circ}$  C and  $-32^{\circ}$ C was expected from the model; but this was not observed experimentally. On the contrary a positive shift of about  $+15^{\circ}$ C was

measured. the origin of this discrepancy is still not well understood; however some hypothesis can be made:

- the period-to-mark ratio may have been altered by the etching process,
- the mechanical properties of aluminum may also have been altered, even if metal thickness does not significantly change in the etching process,
- if static strain actually play a role in temperature compensation effects, the reactive ion etching process may have altered the state of surface strains by removing part of the quartz substrate altered by polishing,

- finally, other sources of experimental arte facts should be investigated e.g. thermoelastic mounting stresses: a whole wafer was used where as tests with single diced resonators should be performed also.

## CONCLUSION

STW resonators built with a combination of grooves and strips have been fabricated and tested. A good agreement between the proposed model and measured values is found for the dependency of the resonant frequency versus groove depth. This allows frequency trimming of the devices provided that a lower etch rate is used.

A perturbation method has been proposed to model the temperature dependance of the resonant frequency versus groove depth or metal strip height. For the moment, prediction of temperature effects can be made for groove-only or strip-only resonators. Experiments confirm that the second order temperature coefficient of frequency is weakly sensitive to the etching process.

The change of turnover temperature versus groove depth is predicted to be in the range of  $-8^{\circ}$  C to  $-32^{\circ}$  C per  $\% h/\lambda$  on AT-cut quartz; an experimental value of the right order of magnitude but with an opposite sign has been found for 500 MHz STW resonators with 300 nm metal thickness and 100 nm groove depth. Further investigation are required to solve this problem. However it can be already stated that frequency trimming by reactive on etching of STW resonators will induce a negligible shift in turnover temperature, which is an important result for volume production of these devices.

## ACKNOWLEDGEMENTS

The authors thank the Thomson Microsonics Research department for giving them a full access to its scientific library. Thanks are also due to S. Calisti and J. Hector for the preparation of the quartz wafers.

## REFERENCES

- [1] W. S. Mortley, UK patent 988102 (1962).
- [2] R.M. White, F.W. Voltmer, Direct piezoelectric coupling to surface elastic waves, Appl. Phys. Letters, Vol 7, pp 314-316 (1965).
- [3] L.J. Van der Pauw The planar transducer a new type of transducer- cf transducer for longitudinal waves, J. Appl. Phys. 9, 3 p 129 (1966).
- [4] H. Thomann, New type of Rayleigh wave on piezoelectric ceramics Electronics Letters 6,22, p 716 (1970).
- [5] R. F. Mitchell, Spurious bulk wave signals in acoustic surface wave devices, Proc of the IEEE US Symposium, IEEE cat. 74CH0896-1SU, pp 313-320 (1974).
- [6] B. A. Auld, J.J. Gagnepain, M.S. Tan, Horizontal shear waves on corrugated surfaces, Electronics Letters, vol.12, n 24, pp 650-651 (1976).
- [7] Yu.V. Gulyaev, V. P. Plesskii, Sov. Tech. Phys. Letters, vol. 3, n $^{\circ}$ 3, pp.87-88.
- [8] T. I. Browing, M. F. Lewis, A new class of quartz crystal oscillator controlled by surface skimming bulk waves, Proc. of the 31th AFCS, pp 258-265, (1977).
- [9] K. M. Yen, K. L. Wang, R. S. Kagiwada, K. F. Lau, Interdigitaltransducers a means of efficient bulk wave excitation, Proc of the 31th AFCS, pp 266-270 (1977).
- [10] M. F. Lewis, Surface Skimming Bulk Waves, SSBW, Proc. of the IEEE US, IEEE cat 77CH12644-1SU, pp. 744-752 (1977)

- [11] K.F. Lau, K. H. Yen, R. S. Kagiwada, A. M. Kong, A temperature stable 2ghz SBAW delay line oscillator, Proc. of the 34th AFCS, pp 237-242 (1980).
- [12] T. Nishikawa, A. Tani, K. Shirai, C. Takeuchi, SH - type surface acoustic waves on rotated Y-cut quartz, Proc. of the 34th AFCS, pp 286-291 (1980).
- [13] K.F. Lau, K.H. Yen, J. Wilcox, R.S. Kagiwada, Analysis of shallow bulk waves excitation by interdigital transducers, Proc. of the 33th AFCS, pp. 388-395 (1979).
- [14] J. Minowa, A method for accurately adjusting center frequency of surface acoustic wave filters , Review of the Electrical Communications Lab., 26 (5- 6), pp 797-807 (1978).
- [15] A. Renard, J. Henaff, B.A. Auld, SH surface wave propagation on corrugated surfaces of rotated Y-cut Quartz and Berlinite crystals, Proc. of the IEEE US, pp. 123-128 (1981).
- [16] J. Y. Duquesnoy, H. Gautier, 2,2 Ghz SH-mode delay line , proc. of the IEEE U.S. ,pp 57-62 (1982).
- [17] A. E. H. Love, Some problems of Geodynamics, Cambridge University Press (1911).
- [18] J.L. Bleustein, A new surface wave in piezoelectric materials , Appl. Phys. Letters, vol 13, n°12, pp 412-413 (1968).
- [19] Y. V. Gulyaev, Electroacoustic surface waves in solids, JEPT Letters, vol 9, pp 37-38 (1968).
- [20] B.A. Auld, D.F. Thompson, Temperature compensation of surface transverse waves for stable oscillator applications using shallow gratings , Proc. of the IEEE US, pp 213-217 (1984).
- [21] D.F. Thompson, B.A. Auld, Surface transverse wave propagation under metal strip grating , Proc. of the IEEE US, pp 261-266 (1986).
- [22] B.A. Auld, D.F. Thompson, Temperature compensation of surface transverse waves for stable oscillator applications, Proc. of IEEE U.S, pp 305-312 (1987).
- [23] T. L. Bagwell, R.C. Bray, Novel surface transverse wave resonators with low loss and high Q , Proc. of the IEEE U.S, pp 319-324 (1987).
- [24] C.A. Flory, R. L. Baer, Surface transverse wave mode analysis and coupling to interdigital transducers, Proc. of the IEEE U.S, pp 313-318 (1987).
- [25] I.D. Avramov, Microwave oscillators stabilized with surface transverse wave resonant devices , Proc. of the 45th AFCS, pp 29-31 (1991).
- [26] D. F. Williams, F.Y. Cho, A. Ballato, T. Lukaszek, The propagation characteristics of surface acoustic waves on singly and doubly rotated cuts of quartz , Proc. of the 35th AFCS, pp376-382 (1981).
- [27] R. Almar, B. Horine, J.Andersen, High frequency STW resonator filters Proc of the IEEE U.S., pp. 51-56 (1992).
- [28] V. Plesskii, Two parameters Coupling of Modes model for shear horizontal type SAW propagation in periodic gratings, Proc. of the IEEE U.S., pp 195-200 (1993).
- [29] B.P. Abbott, K. Hashimoto, Acoupling-of-modes formation for surface transverse wave devices Proc of the IEEE U.S., pp 239-245 (1995).
- [30] E. Gavignet, S.Ballandras, E. Bigler, Analysis and experimental study of surface transverse wave resonators on quartz, J. Appl. Phys. vol 79, n°12, pp. 8944-8950 (1996).
- [31] E. Bigler, E. Gavignet, S. Ballandras, S. Denissenko, E. Cambriel, "Design and test of 3 GHz, fundamental mode STW resonators on quartz", IEEE Trans. on UFFC, vol. 44, n° 2, pp. 399-405 (march 1997).
- [32] W. Daniau, S. Ballandras, J.B. Briot, "Groove gratings surface transverse wave resonators", 1997 IEEE Int. Freq. Cont. Symp. (51st), Orlando, 28-31 may 1997.
- [33] E. Gavignet, S. Ballandras, E. Bigler, "Theoretical analysis of surface transverse waves propagating on a piezoelectric substrate under shallow-groove or thin metal strip grating", J. Appl. Phys., vol. 77, n° 12, pp. 6228-33 (1995).
- [34] V.M. Bright, W.D. Hunt, Analysis of Bleusteingulyaev wave propagation under thin periodic metal electrode , J. Appl. Phys., vol 70, n°2, pp 594-602 (1991).
- [35] E. Gavignet, S. Ballandras, E. Bigler, "A perturbation method for modelling the thermal sensitivity of Surface Transverse Waves" IEEE Trans. UFFC, vol. 44, no1, pp201-207, (janv. 1997).
- [36] H.F. Tiersten and B.K. Sinha, "A perturbation analysis of the attenuation and dispersion of surface waves", J. Appl. Phys., vol. 49, n° 1, pp. 87-95 (jan. 1978).
- [37] B.K. Sinha and H.F. Tiersten, "On the temperature dependence of the velocity of surface waves in quartz", J. Appl. Phys., vol. 51, n° 1, pp. 4659-4665 (jan. 1980).
- [38] S. Ballandras, E. Gavignet, E. Bigler, E. Henry, "Temperature derivatives of the fundamental elastic constants of isotropic materials" Appl. Phys. Letters, vol. 71, no 12, pp 1625-1627 (1997).
- [39] S. Ballandras, E. Gavignet, E. Bigler, "A perturbation method for modelling the thermal sensitivity of Surface Transverse Wave (STW) propagation on a piezoelectric substrate", Proc. 1994 I.F.C.S., Boston (USA), june 1-3, IEEE cat. 94CH3446-2, pp. 184-191.
- [40] A.J. Slobodnik, E.D. Conway, R.T. Delmonico, "Microwave Acoustics Handbook, vol. 1A : Surface Wave Velocities", Air Force Cambridge Research Labs, 1973.
- [41] R.N. Thurston, H.J. McSkimin, P. Andreacht, "Third order elastic coefficients of quartz", J. Appl. Phys., vol. 37, pp. 267-275 (1966).
- [42] Landolt-Börnstein, Numerical Data and Functional Relationships in Science and Technology, group III : Crystal and Solid State Physics, vol. 11, Springer-Verlag Berlin - Heidelberg - New York, 1979.
- [43] B. K. Sinha, H. F. Tiersten, "First temperature derivatives of the fundamental elastic constants of quartz", J. Appl. Phys., Vol. 50, n° 4, pp. 2732-2739 (1979).
- [44] S. Ballandras, E. Henry and E. Bigler, "Influence of metal thickness on the temperature sensitivity of surface acoustic waves using a perturbation method", Proc. 9th E.F.T.F., march 1997, (Neuchâtel, Switzerland), pp 249-254.

# Theoretical Analysis of a Reciprocal BAW to SAW coupler

Bernard Dulmet and Hervé Watchueng

Laboratoire de Chronométrie Electronique et Piézoélectricité  
Ecole Nationale Supérieure de Mécanique et des Microtechniques, F 25000 Besançon

## Abstract

This paper presents a theoretical analysis of BAW to SAW reciprocal transformations occurring in periodic gratings with a the period very close to the wavelength of surface waves propagating on the substrate outside the couplers's region. An essential feature of here-presented method is the use of integral boundary conditions instead of Brekhovskikh's expansion which we used in previous work. The basics of this method are first presented in the case the study of a SAW reflector in anisotropic substrate. Then, following the method proposed in [1], we use a combination of eigensolutions obtained for semi-infinite gratings to model the behavior of a coupler of finite length, with excitation by either SAW or BAW incident wave in isotropic substrates, and we obtain an analytical dispersion equation in case of STW in  $Y + \Theta$  cuts of class-32 crystals.

## Introduction

We mainly study the strong coupling which arises between surface and bulk acoustic waves when the surface of substrate exhibits periodic corrugations with a period  $\Lambda$  very close to the the wavelength  $\lambda$  of SAW. A standard approach in case of corrugated substrates consists of expanding the solutions in terms of Bloch harmonic functions to derive the dispersion curve  $f(\delta, \omega)$  where  $\delta$  denotes the wavenumber component governing the behavior of Bloch sum. Ref [1] outlines a theoretical analysis and gives closed-form results for a reciprocal coupler when surface waves are of the Rayleigh type and propagate onto an isotropic substrate. Boundary conditions are then "projected" onto the average plane of profile by means of Brekhovskikh expansion and combined with Fourier expansion of the surface profile, thereby allowing to take into account the effect of various profiles. Obtained inter-mode couplings between Bloch harmonics when  $\Lambda \approx \lambda$  are of the second order in terms of a small dimensionless parameter  $\varepsilon$  characterizing the surface profile, whereas they are of the first order for Bragg's reflection. In the present paper, we do not make use of Brekhovskikh expansion. Instead, we multiply the boundary conditions by  $\exp(-jq_n x)$  where  $q_n = \delta +$

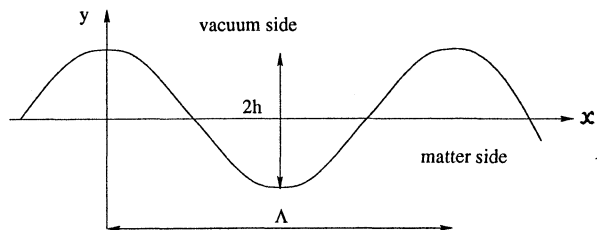


Figure 1: Surface profile

$nQ$ ,  $Q = 2\pi/\Lambda$  and  $n$  is an arbitrary integer, and we integrate the boundary condition over one period of the surface profile. Inter-harmonic couplings are then governed by integrals which can be expanded in terms of powers of  $\varepsilon$  or a related small parameter. Of course, expansion to the second order is required to get results when  $\Lambda \approx \lambda$ . Effect of Piezoelectricity is not taken into account in the present paper.

## I. Surface waves on periodic gratings

As a matter of fact, integrals appearing in the proposed approach remain quite identical for the study of a coupler between BAW and STW or Rayleigh waves, the latter case on either isotropic or anisotropic substrates. Let us consider a surface with profile defined at Fig.1. The height of profile  $2h$  is supposed to be very small with respect to period of corrugation  $\Lambda$ . Then, assuming  $\bar{y}$  is the direction of the average normal to substrate (outwardly orientated), and  $x$  is the direction of propagation (in suitable rotated axes, of course), we can write :

$$y = \xi(x) = h\bar{\xi}(x) = \varepsilon/Q\bar{\xi}(x) \quad (1)$$

(where  $-1 \leq \bar{\xi} \leq 1$ ,  $Q$  being the "corrugation wavenumber"  $Q = 2\pi/\Lambda$ ), in such a way that the dimensionless parameter is small in any case :

$$\varepsilon \ll 1 \quad (2)$$

We may start with a general problem (SAW on anisotropic substrate). Due to the periodic nature of corrugations, Floquet's theorem allows to seek mechanical displacements as sums of Bloch functions :

$$u_\alpha = \sum_{k \in \mathbb{Z}} U_\alpha^{k,n} e^{j[(\delta+kQ)x + \beta_k^n y - \omega t]} \quad (3)$$

where  $k$  is the harmonic rank,  $\alpha$  indicates the component and  $n$  determines which solution is taken in the determinantal equation obtained when substituting above-mentioned form into the 3 by 3 partial derivative equations of dynamics for the  $k$ -th harmonic.  $U_\alpha^{k,n}$  represents the normalized amplitudes for this  $k$ -th harmonic and the  $n$ -th solution  $\beta_k^n$  of the determinant of PDEs. The small wavenumber component  $\delta$  governs the whole behavior of Bloch series with respect to  $\omega$ .

An exact writing of mechanical boundary conditions on the free surface would be :

$$(T_{\alpha\beta}n_\alpha)_{[x,y=\xi(x)]} = 0 \quad \alpha = 1, 2 \quad \beta = 1 \dots 3 \quad (4)$$

on the free surface, where  $T_{\alpha\beta}$  is the stress tensor and  $n_\alpha$  is the outward unit normal on some point of the surface profile  $y = \xi(x)$ . Exactly solving the whole problem on uneven surfaces is a difficult problem. So, we may arbitrarily multiply the boundary conditions by  $\exp(-jq_l x)$  with  $q_l = \delta + lQ$ ,  $l$  being some arbitrary integer, and we integrate over one period of profile (See [4] for justifications) :

$$\int_\Lambda T_{\alpha\gamma} e^{-jq_l x} n_\gamma(x) dx = 0 \quad \alpha = 1 \dots 3 \quad (5)$$

Thus, we obtain the following algebraic system :

$$\sum_{\alpha=1,2} \sum_{n=1}^3 \sum_{k \in \mathbb{Z}} C_{k,n} \mathcal{T}(\alpha, \gamma, n) I_\alpha(k-l, \beta_k^n) = 0 \quad (6)$$

where  $\mathcal{T}(\alpha, \gamma, n)$  stress terms are defined by :

$$\mathcal{T}(\alpha, \gamma, n) = j [c_{\alpha\gamma 1} \epsilon q_k + c_{\alpha\gamma 2} \epsilon] U_\epsilon^{k,n} \quad (7)$$

and :

$$I_\alpha(k-l, \beta_k^n) = \int_\Lambda n_\alpha(x) e^{j[(k-l)Qx + \beta_k^n \xi(x)]} dx \quad (8)$$

In the linear system (6), the column indexes are obtained by combination of harmonic  $k$  and number of EDP solution  $n$ , while row indexes come from the combination of stress component  $\alpha$  and index  $l$  governing the exponential factor in Eq (5)

Components of the unit normal can be expressed in terms of the profile function  $\xi(x)$  :

$$n_2(x) = \frac{1}{\sqrt{1 + \xi'(x)^2}} \quad n_1(x) = -\xi'(x) n_2(x) \quad (9)$$

Now, considering that the parameter of profile  $\epsilon$  is small, we can expand one part of the integrand of  $I_\alpha(k-l, \beta_k^n)$  :

$$e^{j\beta\xi} \approx 1 + j\beta h \bar{\xi} - \frac{(\beta h)^2 \xi^2}{2} + \dots \quad (10)$$

which, considering that  $-1 \leq \bar{\xi} \leq 1$ , is justified provided that  $\beta h$  be sufficiently small. Also, whenever the slope of profile is sufficiently small :

$$n_2(x) \approx 1 - \frac{1}{2} \xi^2 + \dots \quad (11)$$

Then, after some easy calculations, we obtain :

$$I_2(m, \beta) \approx \Lambda \delta_{m0} + j\beta h I_2^1 - \frac{h^2}{2} [\beta^2 I_2^1 + Q^2 I_2^3] \quad (12)$$

with :

$$\left. \begin{aligned} I_2^1 &= \int_0^\Lambda \bar{\xi}(x) e^{jmQx} dx \\ I_2^2 &= \int_0^\Lambda \bar{\xi}^2 e^{jmQx} dx \\ I_2^3 &= \int_0^\Lambda \frac{\bar{\xi}^2}{Q^2} e^{jmQx} dx \end{aligned} \right\} \quad (13)$$

Above-mentioned expansions hold if the complex quantity  $\beta$ , homogeneous to a wavenumber, remains of the order of magnitude as the profile wavenumber  $Q$ . The other integral  $I_\alpha(k-l, \beta_k^n)$  corresponding to  $\alpha = 1$ , can be obtained in a similar manner, after performing integration by parts on factors  $\exp(j\beta)$  from one hand, and  $n_2(x) \exp(jmQx)$  from another hand. Taking advantage of the periodicity of profile, we obtain :

$$I_1(m, \beta) = \frac{mQ}{\beta} I_2(m, \beta) + \int_0^\Lambda \frac{n_2'}{j\beta} e^{j(\beta\xi(x) + mQx)} dx$$

Remarking that  $n_2' \equiv -h^2 \bar{\xi}' \xi'' n_2^3$ , we can reiterate integration by parts and we easily obtain the second order expansion of  $I_1(m, \beta)$  :

$$I_1(m, \beta) \approx mQh \left[ jI_2^1 - \frac{\beta h}{2} I_2^2 + \dots \right] \quad (14)$$

In this way, substituting the proper values of  $k-l$  and  $\beta_k^n$  into the dummy parameters  $m$  and  $\beta$  in above formula, we can compute all terms of the linear system (6), while taking into account any number of harmonics. The determinant of  $C_{k,n}$  can thereafter be solved by means of Newton's method. Following this approach, we obtained results of Fig. 2, which presents a plot of the real and imaginary parts of small wavenumber  $\delta$  in the case of purely cosine profile and trapezoid profiles, in the Bragg's band, *ie* in the vicinity of  $\omega_B = \frac{1}{2} Q V_R$ , where  $V_R$  is Rayleigh waves celerity. Since, in such case,  $\delta \approx Q/2$ , the plots actually represent  $\delta/k - 0.5$  in terms of  $\Omega = (\omega - \omega_B)/\omega_B$ . For symmetric trapeze profile, two values of the slope  $h/a$  of the oblique edge of trapeze are considered. The value  $a = 0.25$  corresponds in fact to the particular case of a sawtooth profile. Results were obtained with  $\epsilon = 0.16$  and  $\omega_B = 100$  MHz for a 42.75 ST cut.

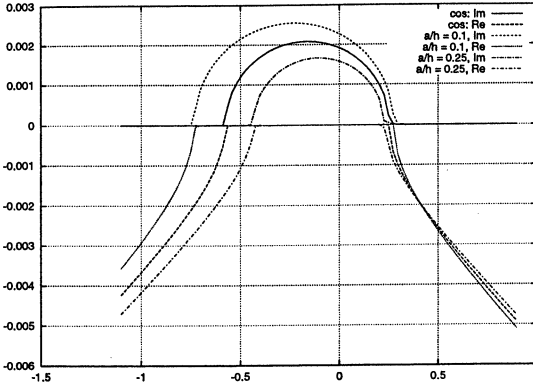


Figure 2:  $\delta_Q = f(\Omega)$  for SAW and  $\lambda \approx \Lambda/2$

## II. Rayleigh waves on isotropic substrate

Now looking at the simpler case of Rayleigh waves propagating in isotropic substrates, we know that we can derive the mechanical displacement from longitudinal  $\phi$  and transverse  $\psi$  potentials :

$$\vec{u} = \nabla\phi + \nabla \times \vec{\psi} \quad (15)$$

Then, Bloch series of interest become :

$$\begin{aligned} \phi &= e^{j(\delta x - \omega t)} \sum_{k \in \mathcal{Z}} \varphi_k e^{(p_k y + jkQx)} \\ \psi &= e^{j(\delta x - \omega t)} \sum_{k \in \mathcal{Z}} \psi_k e^{(s_k y + jkQx)} \end{aligned} \quad (16)$$

and the equations of dynamics for each harmonic take then very simple forms :

$$\begin{aligned} q_k^2 - p_k^2 &= k_t^2 = \rho\omega^2 / (\lambda + 2\mu) \\ q_k^2 - s_k^2 &= k_t^2 = \rho\omega^2 / \mu \end{aligned} \quad (17)$$

where  $\lambda$  and  $\mu$  are Lamé coefficients for isotropic body. In this case, it is possible to analytically carry out the analysis of a BAW to Rayleigh waves reciprocal coupler. Assuming that  $\delta \rightarrow 0$ , it is clear that

$$\left. \begin{aligned} k \neq 0 & \quad p_k \rightarrow (k^2 Q^2 - k_t^2)^{1/2} \\ k = 0 & \quad p_0 \rightarrow \pm j k_t \\ k \neq 0 & \quad s_k \rightarrow (k^2 Q^2 - k_t^2)^{1/2} \quad k \neq 0 \\ k = 0 & \quad s_0 \rightarrow \pm j k_t \end{aligned} \right\} \quad (18)$$

## Dispersion Equation

When one considers an eigenvalues problem, *ie* without any incident wave, only the  $-$  sign must be retained, since it corresponds to bulk waves carrying away energy from the free surface. Boundary conditions can be treated exactly in the same manner as in the previous section, provided that  $p/j$  or  $s/j$  exactly correspond to  $\beta$  parameter of integrals  $I_\alpha(m, \beta)$ . The

only stresses relevant in this case are  $T_{12}, T_{11}, T_{22}$  if we stick calling the sagittal plane  $(X, Y)$ . Then, the integral boundary conditions can be written as :

$$\begin{aligned} 2jq_l p_l I_1(0, -jp_l) \varphi_l - (q_l^2 + s_l^2) I_2(0, -js_l) \psi_l \\ + \sum_{k \neq l} A_k^l \varphi_k - B_k^l \psi_k = 0 \\ (q_l^2 + s_l^2) I_1(0, -p_l) \psi_l + 2jq_l s_l I_2(0, -js_l) \varphi_l \\ + \sum_{k \neq l} C_k^l \varphi_k - E_k^l \psi_k = 0 \end{aligned} \quad (19)$$

and the complex coefficients  $A_k^l \dots E_k^l$  take analytical expressions in terms of  $I_\alpha(m, \beta)$  integrals, which can themselves be carried analytically for cosine and trapeze profiles :

$$\begin{aligned} A_k^l &= \frac{j}{p_k} [2q_k p_k J_1(m, p_k) - mQ(k_t^2 + 2p_k^2) J_2(m, p_k)] \\ B_k^l &= (q_k^2 + s_k^2) J_1(m, s_k) - 2mQq_k J_2(m, s_k) \\ C_k^l &= (q_k^2 + s_k^2) J_1(m, p_k) - 2mQq_k J_2(m, p_k) \\ E_k^l &= \frac{j}{s_k} [mQ(q_k^2 + s_k^2) J_2(m, s_k) - 2q_k s_k^2 J_1(m, s_k)] \end{aligned}$$

where we introduced the notation  $J_\alpha(m, p) = I_\alpha(k - l, -jp)$  to shorten the writing of formulas. To facilitate understanding, we wrote those formulas with the same naming convention for indexes as we did in the first section. Thus  $l$  is still the integer appearing in Eq (5).

Now, go back for a moment considering an even, flat surface. Then, the exact local boundary conditions are satisfied when the very well-known Rayleigh equation is satisfied, *ie* :

$$D(q, \omega) = (q^2 + s^2)^2 - 4q^2 p s = 0 \quad (20)$$

Rayleigh determinant  $D$  has useful properties : first, it is even with respect to  $q$ , which is obvious examining (17) with  $p = p_k, q = q_k, s = s_k$ . Due to that, it can be written as a function of  $V = \partial\omega / \partial q$ . Thus we can establish the following properties :

$$\begin{aligned} D(q, \omega) &= D(-q, \omega) \quad \forall q \\ \frac{\partial D}{\partial \omega} \Big|_{V_R} &= \frac{-1}{V_R} \frac{\partial D}{\partial q} \Big|_{V_R} ; \frac{\partial D}{\partial q} \Big|_{V_R} = -A k_t^3 \end{aligned} \quad (21)$$

where  $A$  is a dimensionless constant depending on Poisson's ratio.

Multiplying the first kind of equation of system (19) by  $2jq_l p_l$  and the second kind by  $-(q_l^2 + s_l^2)$  and combining two by two the resulting equations, the sequence of integral boundary condition becomes :

$$\begin{aligned} D_l I_1(0, s_l) \varphi_l + \\ \sum_{k \neq l} [(2jq_l p_l C_k^l - (q_l^2 + s_l^2) A_k^l) \varphi_k \\ - (2jq_l p_l E_k^l - (q_l^2 + s_l^2) B_k^l) \psi_k] = 0 \end{aligned} \quad (22)$$

where  $D_l$  is Rayleigh determinant for  $l$ -th harmonic :

$$D_l(q, \omega) = (q_l^2 + s_l^2)^2 - 4q_l^2 p_l s_l \quad (23)$$

Of course, if  $\delta = 0$ , and  $\omega = \omega_c = QV_R$ , then  $D_{\pm 1}$  vanish since they correspond to Rayleigh equations for waves propagating along  $x+$  and  $x-$  on a flat surface. Thereby, at the limit, the ratios  $\psi_{\pm 1}/\varphi_{\pm 1}$  take the same finite values as in simple propagation on flat surface. Properly using (21) of  $D$ , it is then possible to expand  $D_{\pm 1}$  in the vicinity of  $\delta = 0, \omega = \omega_c$  :

$$D_n = k_t^3 (\varepsilon^2 k_t \Omega - nA\delta) + \mathcal{O}(\varepsilon^4) \quad n = \pm 1 \quad (24)$$

where  $A$  is the dimensionless constant appearing in (21) and  $\Omega$  is a normalized frequency deviation :

$$\Omega = \frac{A\Delta\omega}{\varepsilon^2 k_t V_R},$$

Since  $D_0 \approx k_t^4$  in the same region, it is possible to express  $\varphi_0$  and  $\psi_0$  in terms of other  $\varphi_k$  and  $\psi_k$  with help of (22) when ( $l = 0$ ), and another equivalent equation privileging  $\psi_l$  instead of  $\phi_l$  by another combination of both kinds of equations (19). The study of the sequence of boundary conditions (19) for  $|l| \geq 1$  shows that amplitudes  $\varphi_k$  and  $\psi_k$  decrease rapidly with  $|k|$ . In this way, it can be shown ([1], Chap 8) that asymptotic behavior of the whole system is given by the following equation of dispersion :

$$[\varepsilon k_t^2 (\Omega + \mathbb{E}) - nA\delta] \varphi_n - \varepsilon^2 k_t \mathcal{B}_n \varphi_{-n} = 0 \quad n = \pm 1 \quad (25)$$

where  $\mathbb{E}$  and  $\mathcal{B}_n$  are complex coefficients that can be expressed in terms of  $J_\alpha$  integrals, and of the limit values of  $p$  and  $s$  wavenumbers of Rayleigh waves on a flat surface, when  $\omega = \omega_c$ . Using (24), and because  $\mathcal{B}_{-1} = \mathcal{B}_{+1} = \mathcal{B}$ , one obtains simple solutions of (25), with a closed form of the dispersion equation :

$$\mathcal{E} = \Omega + \mathbb{E}; \quad \delta = \pm \frac{\varepsilon^2 k_t}{A} (\mathcal{E}^2 - \mathcal{B}^2)^{1/2} \quad (26)$$

The solution  $\delta_+$ , with a positive imaginary part, governs the eigenmode system physically meaningful in semi-infinite gratings extending in  $x+$  direction, since it corresponds to surface waves  $k = \pm 1$  damped toward  $x > 0$ , whereas the solution  $\delta_-$  with negative imaginary part holds for corrugation semi-ininitely extending toward  $x-$ . Correspondingly, we obtain the reflection coefficient of semi-infinite structures :

$$\left. \begin{aligned} R_+ = \frac{\varphi_{-1}}{\varphi_1} |_{\delta_+} = R_- = \frac{\varphi_1}{\varphi_{-1}} |_{\delta_-} = R_\infty \\ R_\infty = \frac{\mathcal{B}}{(\mathcal{E}) + (\mathcal{E}^2 - \mathcal{B}^2)^{1/2}} \end{aligned} \right\} \quad (27)$$

The two independent eigenmodes are given by :

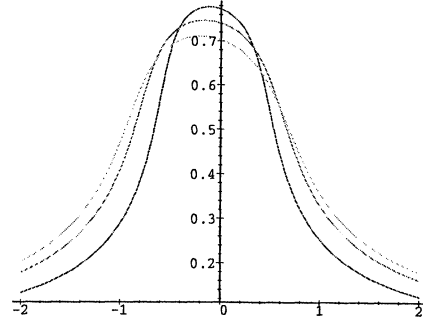


Figure 3:  $|R_\infty| = f(\Omega)$

$$\varphi^1 = [\varphi_0^1 e^{-ik_l y} + \Phi^1 e^{py} (R_\infty e^{-iQx} + e^{iQx})] \times e^{i(\delta x - \omega t)}$$

$$\varphi^2 = [\varphi_0^2 e^{-ik_l y} + \Phi^2 e^{py} (e^{-iQx} + R_\infty e^{iQx})] \times e^{-i(\delta x + \omega t)} \quad (28)$$

where  $\Im(\delta) > 0$ ,  $\Phi^1$  and  $\Phi^2$  are arbitrary complex constants, and corresponding values of  $\varphi_0^1$  and  $\varphi_0^2$  can be obtained with help of (22) with  $l = 0$ . Fig.3 gives  $|R_\infty|$  for cosine (middle curve) and trapeze profiles ( $a/h = 0.1$  and  $0.25$ ) in silica, and with the same values as in Fig.2 ( $\Lambda = 31.6 \mu m$  and  $\varepsilon = 0.16$ ).

## Finite length coupler

A practical device shall convert some significant part of the energy of an incident SAW into BAW propagating into the substrate, or convert into SAW the energy of a BAW coming toward the surface from the depth of substrate. The coupler length  $L$  in the  $x$  direction has a significant influence on the behavior of the system. The cases of incident SAW and BAW require slightly different treatments.

First, we consider a bulk acoustic wave coming from the depth of substrate and reaching the surface under purely normal incidence. Then, as described in Ref[1], the study of a finite length coupler must be split in two steps : first, getting the solutions in an infinite system under excitation by incident BAW thereby defining *forced* solutions, and second, combining forced solutions and previously obtained eigenmodes to satisfy end-conditions at both ends of the finite coupler.

So, we must start setting up the forced solutions in an infinitely long system. Then, the whole mechanical displacement in the structure consists of this wave plus the sum of Bloch functions previously considered, where  $\delta$  is set to zero :

$$\begin{aligned}\bar{\varphi} &= \tilde{\Phi}_0 e^{j(k_t y - \omega t)} + \sum_{k \in Z} \varphi_k e^{(p_k y + jkQx)} \\ \bar{\psi} &= \tilde{\Psi}_0 e^{j(k_t y - \omega t)} + \sum_{k \in Z} \psi_k e^{(s_k y + jkQx)}\end{aligned}\quad (29)$$

Additional terms driven by  $\tilde{\Phi}_0$  and  $\tilde{\Psi}_0$  are independent since the incident BAW can be either longitudinal or transverse. Of course, they create additional stress terms  $\tilde{T}_{11}$ ,  $\tilde{T}_{12}$ ,  $\tilde{T}_{22}$  in integral boundary conditions. Those terms are relatively simple and can be transferred to second member of those boundary conditions, while the first members remain the same as in the study of dispersion equation, except that now  $\delta = 0$ , imposed by the incident wave. In this manner, all previously carried calculations can be very easily reused, provided that the proper second members are added to existing formulae, and we get the following non homogeneous 2 by 2 system instead of the previous homogeneous system (25) :

$$\varepsilon k_t^2 (\Omega + E) \varphi_n - \varepsilon^2 k_t \mathcal{B}_n \varphi_{-n} = \frac{C_n}{\Lambda k_t} \quad (30)$$

where  $n = \pm 1$ , indeed, and  $C_n$  is another complex constant, which is a linear combination of  $\tilde{\Phi}_0$  and  $\tilde{\Psi}_0$ . The coefficients of this combination only depend on  $Q$ , on vertical components of Rayleigh wavevectors for the flat surface problem,  $p$  and  $s$ , and on above-mentioned  $J_\alpha$  integrals. All remaining unknown potential can be obtained upon solving the linear system (30). It can be observed that harmonic 0 in Bloch series then corresponds to a reflected BAW driven by the incident potentials  $\tilde{\Phi}_0$  and  $\tilde{\Psi}_0$ .

Once the forced solutions  $(\bar{\varphi}, \bar{\psi})$  of (29) are obtained, one must add to them a linear combination of the two independent eigenmodes of (28). At  $y = 0$ , one obtains :

$$\begin{aligned}\varphi|_{y=0} &= \bar{\varphi}_1 e^{iQx} + \bar{\varphi}_{-1} e^{-iQx} \\ &+ \Phi^1 (R_\infty e^{-iQx} + e^{iQx}) e^{i\delta x} \\ &+ \Phi^2 (e^{-iQx} + R_\infty e^{iQx}) e^{-i\delta x}\end{aligned}\quad (31)$$

where  $\bar{\varphi}_1$  and  $\bar{\varphi}_{-1}$  depend on  $(\tilde{\Phi}_0, \tilde{\Psi}_0)$  through  $C_{\pm 1}$ . Then, in the coupler, the "local" amplitudes of parts of the whole system travelling to the "right"  $x > 0$  and to the "left"  $x < 0$  are given by :

$$\begin{aligned}\varphi_+ &= \bar{\varphi}_1 + \Phi^1 e^{i\delta x} + \Phi^2 R_\infty e^{-i\delta x} \\ \varphi_- &= \bar{\varphi}_2 + \Phi^1 R_\infty e^{i\delta x} + \Phi^2 e^{-i\delta x}\end{aligned}\quad (32)$$

Since all energy put into the system comes from the incident BAW, it is mandatory to satisfy the following end-conditions :

$$\varphi_+(-L/2) \equiv 0 \quad \varphi_-(L/2) \equiv 0 \quad (33)$$

from which every quantities are completely determined. The case of incident Rayleigh wave on the structure is different because, then the incident SAW is seen as

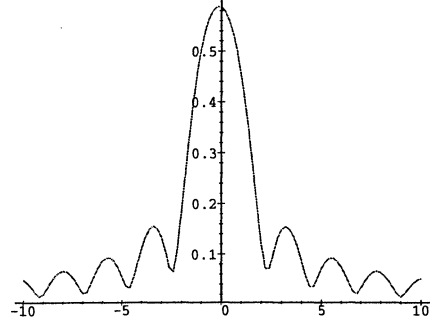


Figure 4:  $|R_{x=0}| = f(\Omega)$

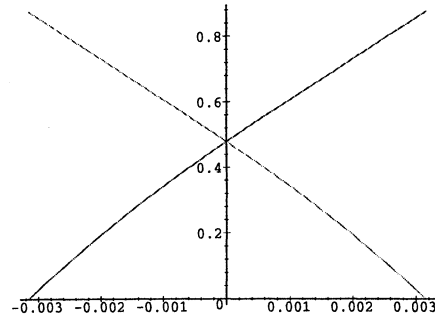


Figure 5:  $|\frac{\varphi_{\pm}}{\tilde{\Psi}_0}| = f(x)$

a part of Bloch series itself, thereby allowing to shortcut the forced solution introduced in the treatment of incident BAW. We have just to add the eigenmodes and fix up the combination so that :

$$\varphi_+(0) \equiv \varphi^1 \quad \varphi_-(L) \equiv 0 \quad (34)$$

The results directly depend on the coupler's length, indeed, and more precisely on its order of magnitude with respect to  $L^* = A/\varepsilon^2 * k_t$ . We present on Fig.4 the reflexion coefficient (case of incident SAW from the left), at the left end of a structure with  $L = 200\Lambda$  ( $L \approx 1.3L^*$ ) as a function of  $\Omega$ . Fig. 5 shows the amplitude of excited surface waves for  $-L/2 \leq x \leq L/2$  for an incident transverse wave of unit amplitude. Conversely, Fig.6 gives the amplitude of surface waves in the coupler, for an incident Rayleigh wave at the left end. All these results are for cosine profile.

### III. STW in Class-32 Crystals

The study of coupler between SH-BAW and STW propagating along  $Z'$  axis in  $Y + \Theta$  cuts of class-32 crystals exhibit similarities and differences with above-mentioned analysis. Then, only one component  $u$

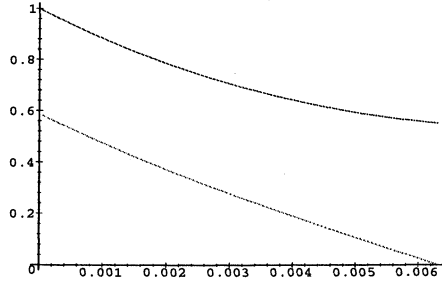


Figure 6:  $|\varphi_{\pm}| = f(x)$

should be considered, since the other are uncoupled with  $u_1$  :

$$u = e^{-j\omega t} \sum_{k \in \mathbb{Z}} u_k e^{j(p_k y + q_k z)} \quad (35)$$

Thus, dynamics equation for  $k$ -th harmonic is simply :

$$C_1 p_k^2 + 2C_2 p_k q_k + q_k^2 - k_t^2 \quad (36)$$

with  $C_1 = c_{66}/c_{55}$  and  $C_2 = c_{56}/c_{55}$ ,  $k_t = \rho\omega^2/c_{55}$ . Following the same approach as before, we find the following equation :

$$\begin{aligned} \{ \varepsilon^2 k_t [a^2 \sqrt{C} (K + nC_2) - \Omega] + nA\delta \} u_n \\ + \varepsilon^2 k_t \sqrt{C} \{ a^2 K + nC_2 (a^2 + 2b) \} u_{-n} = \\ -2\varepsilon k_t a \sqrt{C} \tilde{u}_0 \end{aligned} \quad (37)$$

where  $n = \pm 1$  and :

$$\begin{aligned} A = \frac{C_1}{C_2} K \quad a = \frac{I_n^p}{\Lambda h p} \quad b = \frac{I_{2n}^p}{\Lambda h p} \\ C = 1 - \frac{C_2^2}{C_1} \quad K = \sqrt{c_{\mathcal{G}}} \quad \Omega = \frac{A \Delta \omega}{\varepsilon^2 k_t V_S} \end{aligned}$$

In (37)  $\tilde{u}_0$  is the amplitude of incident transverse BAW on the coupler. This equation becomes the dispersion equation upon removal of the second hand member, of course, which leads to the following solutions :

$$\delta = \frac{\varepsilon^2 k_t}{A} \left[ a^2 c_2 \sqrt{C} \pm \sqrt{\Delta} \right] \quad (38)$$

$$\Delta = \Omega^2 - 2a^2 K \sqrt{C} \Omega + C C_2^2 (a^2 + 2b)^2$$

This results exhibits a significant difference from the case of Rayleigh waves on isotropic substrate : the pair of solutions  $\delta$  are not exactly opposite in the bandwidth of coupler, thereby providing with different values of  $R_{\infty}$  in  $+z$  and  $-z$  direction of propagation. Fig. 7 shows both real and imaginary parts of  $\delta$  for sawtooth profile on 42.75 ST cut (same values of  $\Lambda$  as previously). Nevertheless, the treatment of a coupler of finite length can be achieved if we assume that

there exist different kinds of corrugations outside the coupler's region, so that the  $y$  variation of  $\pm 1$  harmonics in the coupler are quite similar to the  $y$  variation of STW outside the coupler. This is required since, if the surface is flat outside the coupler, only SSBW will propagate there.

## References

- [1] S.V. Biryukov, Y. Gulyaev, V. Krylov, V. Plesky, *Surface Acoustic Waves in Homogeneous Media*, Springer, 1995.
- [2] B. Dulmet and H. Watchueng, Proc of IEEE Symp on Ultrasonics, pp 587–591, Seattle, Nov 1995.
- [3] H. Watchueng and B. Dulmet, EFTF 1996, pp 165–169, Brighton, March 1996.
- [4] Tuan and Parekh, IEEE SU-24, N 6, pp 384-391 Nov 1977.
- [5] H. Watchueng, Ph.D thesis, to be submitted at University of Franche Comté, May 1998.

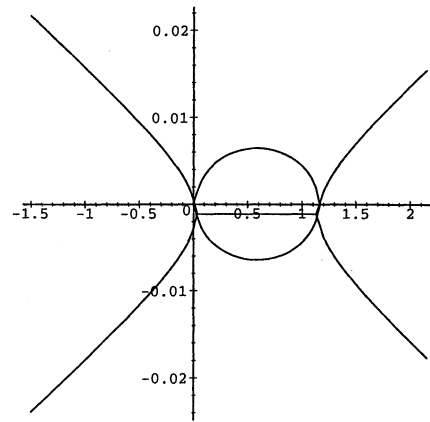


Figure 7:  $\Im(\delta), \Re(\delta) = f(\Omega)$ , STW, sawtooth

## GHZ RANGE STW RESONATORS ON QUARTZ AND LANGASITE

Alexander V. Grouzdev, Stanislaw I. Kort, Igor S. Mitrofanov, Alexander V. Perevalov

Avangard-Elionica Co., St. Petersburg, 195271, Russia

Sylwester Gawor, Andrzej Milewski

Tele and Radio Research Institute, Warsaw, 03450, Poland

## ABSTRACT

In recent years there is an increasing practice interest to the acoustoelectronics devices on surface transverse waves (STW) as analogous one on widely used surface acoustic waves (SAW). It is known that using STW versus SAW in resonator application gives the better quality factor and the higher resonant frequency with the same resonator structure step and high temperature stability. This allows to receive low loss high quality resonators up to GHz range, but industry implementation demands more detail experimental data on dependencies between the main resonator parameters and manufacturing factors. A few of these information cause significant difficulties for high yield processing.

This paper presents data on design and experimental research of two-port STW resonators (STWR) on quartz and langasite substrates. The main aim of present work is attempt to search and analyze important relationships of the resonator electrical characteristics and design parameters. In results, there are experimental temperature characteristics and functions of the resonant frequency, quality factor, and insertion loss from to structure and thickness of the film metallization. It is shown the ability of frequency trimming with close tolerance about  $\pm 40$  ppm.

*Keywords: STW resonator frequency trimming.*

## 1. INTRODUCTION

Now the intensive investigations are carried out in the field of STW device design and technology. This is caused by the superior parameters in some cases of SAW device comparison. For example, the STW signal processing devices use bulk acoustic waves that spread close to the surface of the piezoelectric substrate. And hence the surface imperfection and pollution effects are greatly reduced for a device performance. As a result for the high stable oscillators on STWR the signal power may be significantly increased or the aging will be slower. In addition, the STW velocity is higher then SAW velocity. This yields to rise up frequency limit on about 1.6 times with the same lithography process.

We are interesting in GHz range high quality one-pole resonators with high temperature stability in wide range. In this connection we have designed and produced the GHz STWR on quartz ( $\text{SiO}_2$ ) and langasite ( $\text{LGS}$ ,  $\text{La}_3\text{Ga}_5\text{SiO}_{14}$ ).

## 2. RESONATOR DESIGN

Two-port synchronous resonant structure on STW with metal strip reflectors was selected as the base construction that is suitable for technology equipment. Two-port resonators are need not in matching and allow receive higher stop-band level in comparison one-port resonators. The piezoelectric substrates for the resonators are the monocrystal plates of quartz  $\text{YXl}+36^\circ$ -cut and langasite Y cut (convention on cut angles according to Ref. 1) and spread of STW is normal to X crystallographic axis. Electrode material is aluminum with using thin sublayer of vanadium (several percents of summary layer thickness). Design parameters were adapted according to lift-off lithography and reactive ion-beam etching with aim to obtain the control on frequency respond.

The schematic layout of the resonant structure is shown at the Fig. 1. Geometry characteristics of effective resonant structures on quartz and langasite are summarized in the Table 1.

The resonant structure has two interdigital transducers (IDT), two reflective arrays (RA), and central "holder" array (HA) for the effective STW control in cavity. Arrays are the sets of shorted finger electrodes. IDT is continued the RA structure and have periodicity same to RA periodicity.

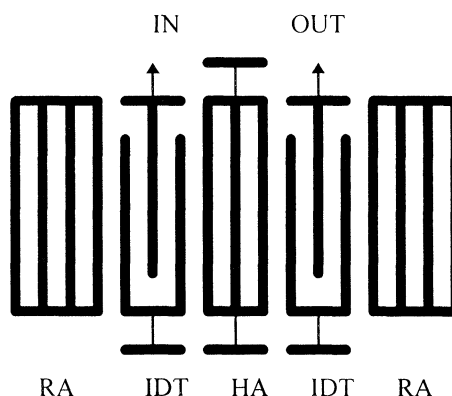


Figure 1: Resonant structure scheme.

TABLE 1 – Resonator geometry.

Finger feature	Parameter value
Aperture, $\mu\tilde{N}$	300 ( $\approx 90 \lambda$ )
Thickness, nm	35...45 ( $\approx 1.2\% \lambda$ , on quartz) 30...40 ( $\approx 1.0\% \lambda$ , on LGS)
Width, $\mu\tilde{N}$	0.8...0.9 ( $\approx 0.25 \lambda$ , on quartz) 0.7...0.8 ( $\approx 0.22 \lambda$ , on LGS)
Step, $\mu\tilde{N}$	1.69 ( $\approx 0.5 \lambda$ , in RA)
	1.69 ( $\approx 0.5 \lambda$ , in IDT)
	1.68 or 1.67 ( $< 0.5 \lambda$ , in HA)
Quantity	1000 (in RA)
	150 (in IDT)
	25 (in HA)

A model of two-port STW resonator was designed for exploring of correlation between design and electrical characteristics. There was realized Common-Of-Modes (COM) model base on data from Krasnikova, et al, Ref. 2 and Write in Ref. 3, that is tunable using a treatment of device tests for the precise determination of COM-model fundamental parameters. This technique was applied for study dependence of response from layout variations. Fig. 2 presents response changes with metal thickness (80, 60, 50, 40, 30, 20 nm from left to right) that are closed to experiment.

The main tendency is that insertion loss and quality factor both have minimum about 50 nm thickness. When raising quality factor we must increase or reduce the layer thickness and insertion losses are raised too.

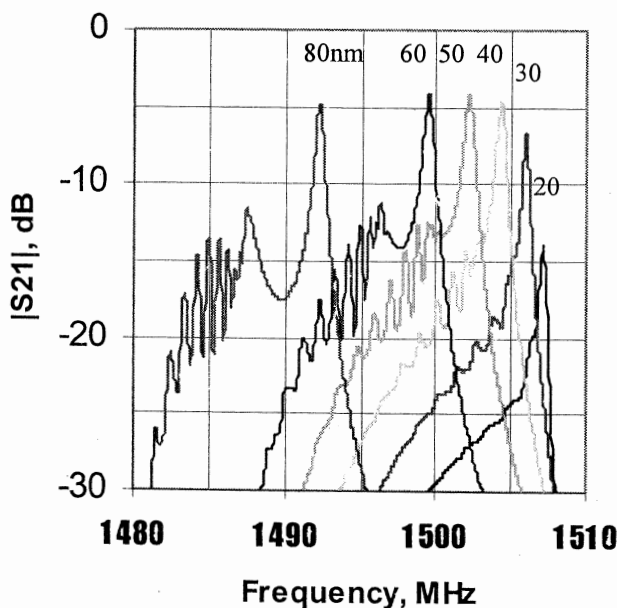


Figure 2: STWR response changes with metal thickness.

### 3. EXPERIMENTS

Several sets of STW resonators were designed and tested. Fig. 3 and Fig. 4 show frequency response for quartz and langasite devices according with Table 1. Their main electrical parameters are shown in Table 2.

TABLE 2 – Quartz and langasite resonator characteristics.

Parameter	Quartz STWR	Langasite STWR
Resonant frequency, MHz	1501.260	688.750
Insertion loss, dB	8.5	18.3
Loaded Q-factor	2380	1180

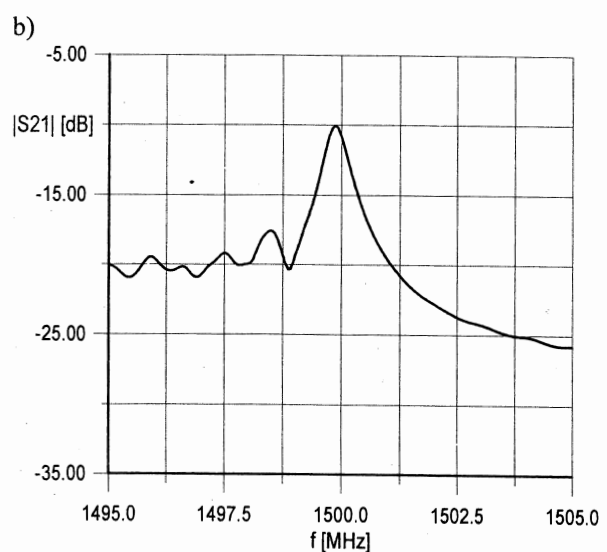
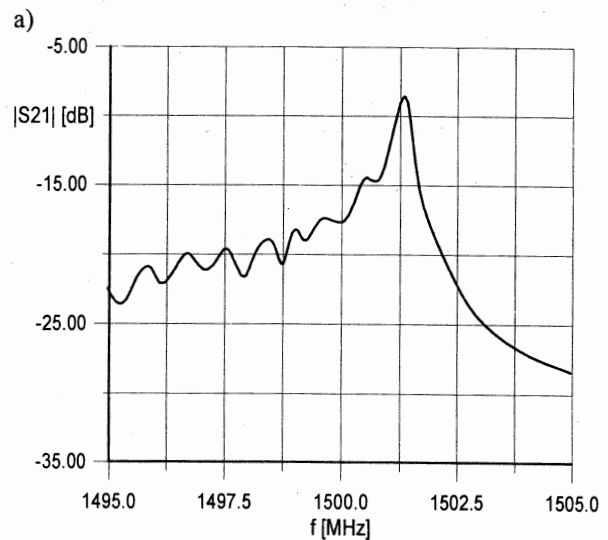


Figure 3: Frequency response for STWR on quartz. a) without trimming, b) after trimming.

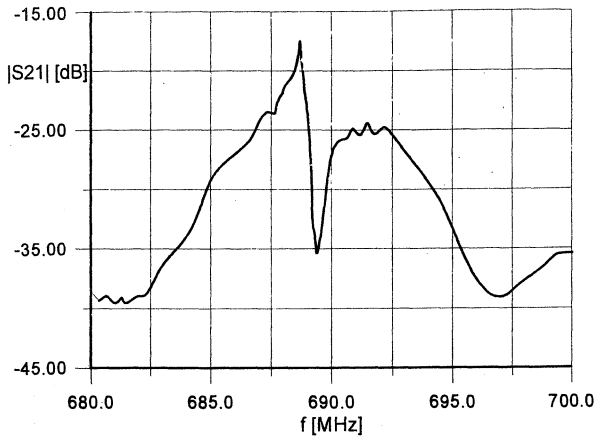


Figure 4: Frequency response for STWR on langasite.

Condition of STW existing in resonant cavity demands surface periodicity structure. It is the HA, that “holding” the acoustic wave near the surface and prevents energy loss. Due to HA be residing inside cavity, it has very strong influence on resonator characteristics. As were shown Bigler, et al, in Ref. 4, best values of Q-factor and insertion loss being obtained with the resonant frequency at lower edge of the stopband. Adjustable geometric characteristics of HA are, the main, quantity, periodicity, width and thickness of their fingers. The optimum finger quantity for HA is about 25. Any deflection from this value is not desirable. When reducing number of HA fingers the magnitude of sidelobes also increasing and appears the multimode response. The other hand, when increasing number of HA fingers the Q-factor is strong worst and insertion loss increases. The step of finger periodicity for HA is connected with the step one for RA and both must be close for the residing resonant frequency at lower edge of the stopband. Account for providing one-mode work and sufficiently low sidelobe level the HA step must be a little less than RA step. The optimum relationship of RA and HA steps was define for the quartz resonator as shown in Table 3. The value of step changing is discrete due to photomask performance limits and the minimum change value is about  $0.01 \mu\text{m}$ . They were fabricate and tested set of resonators with HA step both  $1.68 \mu\text{m}$  and  $1.67 \mu\text{m}$ . Really all samples in these groups have significant difference and fabrication with this minimum step difference  $0.01 \mu\text{m}$  give a better characteristics (about 50% for the insertion loss and loaded Q).

Frequency trimming of resonators was followed by definition of frequency trimming range limits and corresponding behavior both insertion loss and quality factor when using reactive ion-beam etching. It is known that although resonator frequency parameters have depend on layout geometry the good precise value can not be achieve by only with metric measuring due to high accuracy demands ( $10^{-5} \dots 10^{-6}$  from resonant frequency).

TABLE 3: The comparison of response parameter data in dependence from RA and HA relationship.

Parameter	HA step, $\mu\text{m}$ (1.69 $\mu\text{m}$ RA step)	
	1.68	1.67
Resonant frequency, MHz	1504.127	1506.080
Insertion loss, dB	8.7	12.9
Loaded Q	3400	2160

Electrical measuring of device frequency response controlled trimming process by means of reactive ion-beam etching with  $\text{CF}_4$ -plasma medium. For good yield was used reduced etching speed with ion current density about  $3 \text{ A/m}^2$ . The effective velocity of trimming varies in the range from 100 to 125 ppm/min. It was enough to receive repeatable tuning accuracy up to  $\pm 40$  ppm and higher.

Experiments show ability of frequency trimming in the range up to about 3000 ppm else begin the response destruction process. When starting the trimming up to 500 ppm insertion loss are reduced and Q-factor increase up to 7% and return to origin value at about 1000 ppm. In the range between 1000 and 3000 insertion loss increase and Q-factor decrease with the rate of 20% on each 1000 ppm from resonant frequency.

Temperature stability of resonators both quartz and langasite was investigate in range from  $-60^\circ\text{C}$  to  $+85^\circ\text{C}$  and temperature characteristics of resonant frequency are shown on Fig. 5 and Fig. 6.

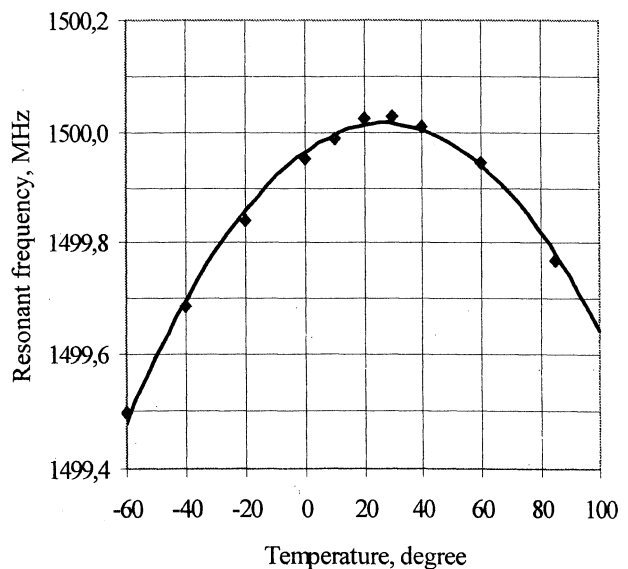


Figure 5: Temperature characteristic for quartz STWR.

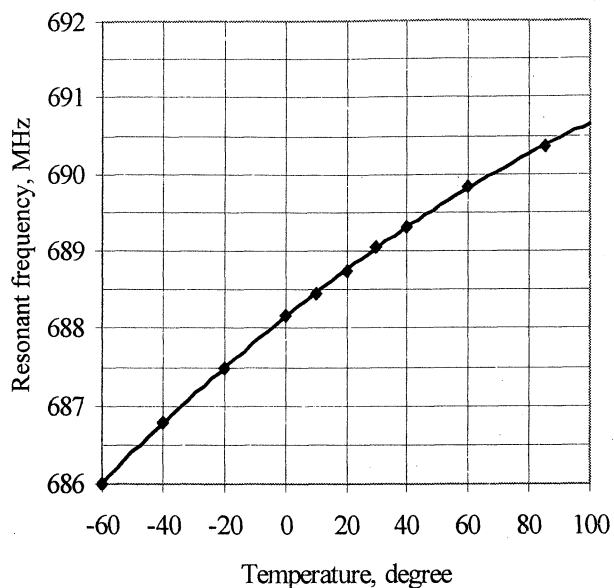


Figure 6: Temperature characteristic for langasite STWR.

#### 4. CONCLUSION

This paper presents data on modeling and experimental work with some of STWR sets on quartz and langasite. There were reported about design and fabrication methods, experimental research of two-port STWR and were analyzed important relationships of the resonator electrical characteristics and design parameters. In results, there are experimental temperature characteristics and functions of the resonant frequency, quality factor, and insertion loss from to structure and thickness of the film metallization. It is shown the ability of frequency trimming with close tolerance about  $\pm 40$  ppm.

#### REFERENCES

1. IEEE Standard on Piezoelectricity 176-1949, Proc. IRE, 37, pp. 1378-1395.
2. Krasnikova S., et al, "COM Parameter Extraction for STW Resonator Design", 11th EFTF, 1997, pp. 440-444.
3. Wright P.V., "Coupling-Of-Modes Modelling of SAW Devices", Proc. Int. Symp. Devices for Mobile Comm., 77-84, 1992, pp. 77-84.
4. Bigler E., et al, "Surface Transverse Wave (STW) Quartz Resonators in the GHz Range", 6th EFTF, 1992.



*12th E F T F* - 10-12 March 1998 - Warsaw - POLAND

**Piezoelectricity & measurement techniques**

*(posters)*



## IMPROVEMENTS OF X-RAY ORIENTATION DETERMINATION METHODS APPLICABLE IN QUARTZ RESONATOR INDUSTRY

Hans Berger

EFG International Berlin, Germany

**Abstract.** Using the  $\Omega$ -scan method two X-ray reflection pairs are measured, from which the angles describing the orientation of *AT*-cut and *SC*-cut quartz blanks can be determined with standard deviations of few arcsec. In order to correct systematic errors and to estimate the reproducibility limits due to the pulse statistics, the reflection profiles are simulated including the statistic fluctuations. This allows to optimize the evaluation conditions and also to estimate the influence of some instrumental errors. The possibility of determining the absolute orientation of *AT* cuts is discussed.

### 1. INTRODUCTION

The industrial application of quartz resonators needs an exact determination of the orientation, i.e. of the angular coordinates of the plate (blank) surface related to the crystal lattice. These angular coordinates must be known with a standard deviation down to few seconds of arc. This can be reached only by means of sophisticated X-ray diffraction methods.

Several years ago the so-called  $\Omega$ -scan method has been developed, which allows the quick automatic orientation measurement and sorting of quartz blanks [Nestler et al (1), Morys et al (2)]. The method can be applied to blanks of arbitrary (not only rectangular) shape. It was originally developed for *AT*-cut resonators. Recently, the method has been modified to become applicable to doubly rotated quartz blanks, especially for *SC*- and *FC*-cut resonators [Berger et al (3)].

While the  $\Omega$ -scan method as developed for *AT* cuts is a relative method giving the orientation related to a standard, the modified method for *SC* and *FC* cuts allows the absolute determination of the orientation. Therefore, it is desirable to enable such measurements also with *AT*-cut blanks. Besides that, the  $\Omega$ -scan apparatus should be usable for all relevant cutting angles of quartz resonators applying only small modifications.

To utilize the potentialities of the absolute orientation determination, any systematic errors have to be avoided or corrected carefully. Systematic errors caused by the problem of defining the exact peak position have been shown to be especially critical [Berger et al (4)]. They can be evaluated by simulation of the line profiles.

There are steadily increasing demands for higher precision, for shorter measuring times as well as for

smaller blank sizes. Hence, the principal potentialities of the  $\Omega$ -scan method have to be analyzed. This analysis must include the finding of the theoretic limits as well as the contribution of instrumental errors in order to diminish them.

In this contribution, the state of the  $\Omega$ -scan method applied to the orientation determination and sorting of quartz blanks will be briefly described. The limits and possible modifications of the method as sketched before will be discussed from the theoretic point of view.

### 2. THE $\Omega$ -SCAN METHOD - PRINCIPLE AND APPLICATION

In the usually employed geometry an X-ray reflection for monochromatic radiation on a certain lattice plane of a single crystal is obtained turning the crystal around an axis perpendicular to the plane which contains the incident beam, the lattice plane normal and usually the surface normal ( $\Theta$  scan). In the  $\Omega$ -scan method, the crystal is rotated around the surface normal (Fig. 1). Then two reflections at this lattice plane will arise when the incidence angle deviates somewhat from that for maximum intensity in the  $\Theta$  scan. From the angular difference of both reflection positions on the measuring ( $\Omega$ ) circle the angle between surface and

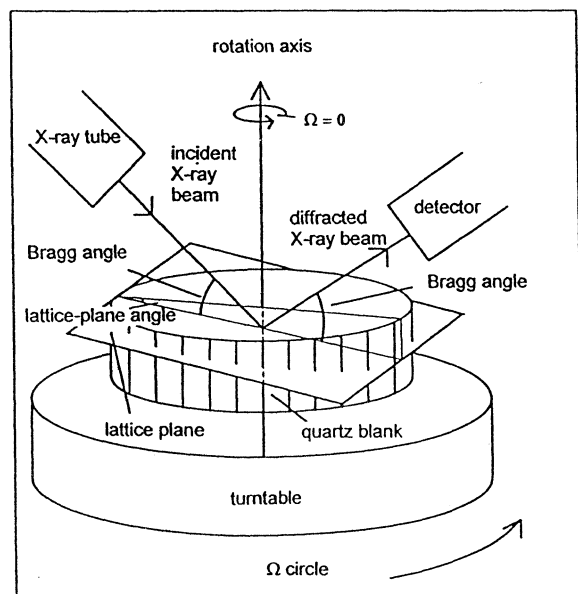


Figure 1. Scheme of the measuring arrangement

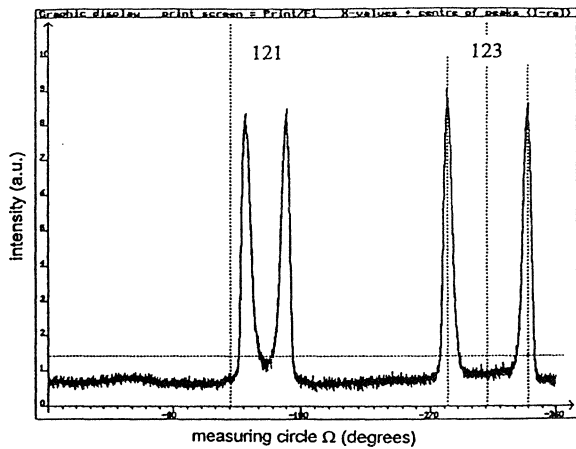


Figure 2. Measuring curve ( $\Omega$  circle) of an SC cut.  $\text{CuK}\alpha$ ; reflections 211 and 213; average over eight turns

lattice plane can be calculated. The reflection distance is especially sensitive for this angle when both the angle and this distance are small. So the lattice-plane angle can be determined with high precision.

If the geometric conditions are chosen in such a way that two lattice planes reflect at the same incidence angle, two reflection distances and additionally the distance between the centers of both reflection pairs can be taken from the measuring curve (Fig. 2). From these values, two angular coordinates,  $\Theta$  and  $\Phi$ , describing the orientation in the general case (doubly rotated blanks), can be calculated. Besides the conditions mentioned above, certain geometric relations between both lattice planes must exist to make the errors of  $\Theta$  and  $\Phi$  sufficiently small. As three measuring values are available, the incidence angle can be calculated additionally so that in principle absolute measurements can be performed.

The cutting angle and the  $XX'$  miscutting (corresponding to  $\Theta$  and  $\Phi$ ) of AT-cut quartz blanks are presently measured by means of the reflection combination 202/203 using one rotation of the  $\Omega$  circle (needing 2 sec cycle time). Standard deviations of the cutting angle of about 3 arcsec have been obtained. However, the evaluation does not allow to determine the incidence angle with sufficient precision so that the measurement is to be related to a standard blank.

TABLE 1 - Measuring example: SC cut;  $\text{CuK}\alpha$ ; average over eight turns (15 sec)

reflection	2 1 1	2 1 3
Bragg angle	29.98°	39.95°
incidence angle	47.06°	
<i>measured values</i>		
reflection distance	37.576°	66.703°
distance between reflection pairs	146.883°	
<i>results</i>		
$\Theta$	34.0283°	
$\Phi$	23.064°	
<i>experimental standard deviations</i> (include lifting of the blank after each measurement)		
reflection distance	0.016°	0.023°
distance between reflection pairs	0.024°	
$\Theta$	1.8"	
$\Phi$	8.5"	

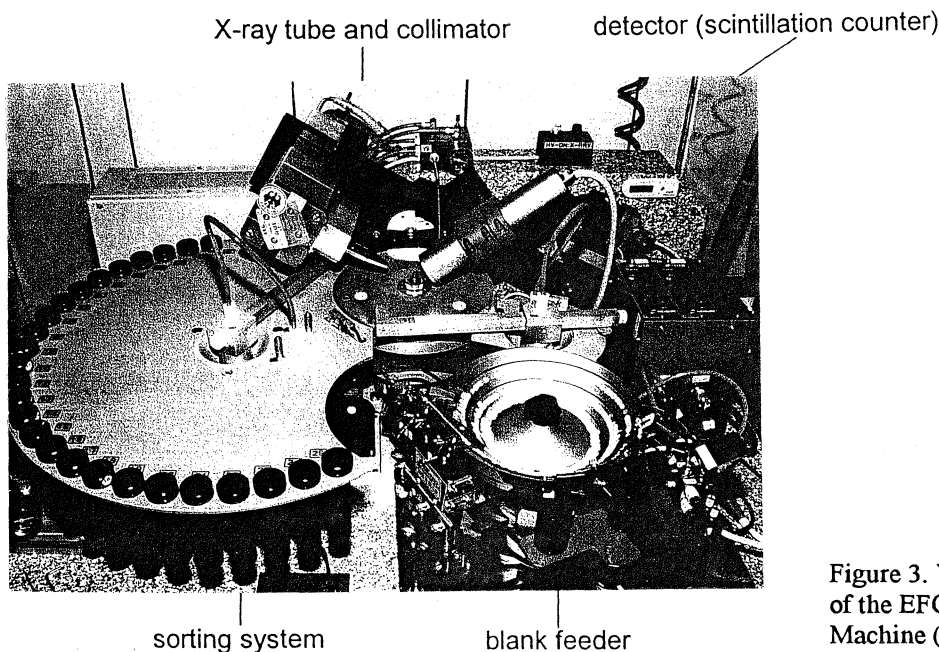


Figure 3. View of the main parts of the EFG Automatic Sorting Machine (for AT cuts)

TABLE 2 - Calculated systematic errors. CuK $\alpha$ ; diameter of the collimator holes: 0.5 and 0.8 mm, resp., distance 133 mm; peak position determination: centroid (AT), fit by 2nd order polynomial (SC), resp.

orientation	$\Theta$		reflection	peak distance		corrections	
	$\Theta$	$\Phi$		peak distance	$\Theta$	$\Phi$	
AT	35.25°	0	2 0 2	70°	-1.07°	66"	0"
SC	34.25°	21.5°	2 1 1	33.7°	-0.31°	17"	-2.5"
			2 1 3	43.1°	-0.70°		

For SC cuts, a number of reflection combinations was checked, from which a few deliver good results. The reflections 211 and 213 have been chosen (Table 1) that give sufficiently small errors in the angular coordinates  $\Theta$  and  $\Phi$  as well as in the incidence angle for the relevant range of possible orientations (a few degrees for both angular coordinates). Using the same reflections, also the absolute orientation of FC cuts and, with some limitations, of IT cuts can be determined.

Based on the X-ray orientation determination as described above, the EFG Automated (optionally Manual) Quartz Sorting Machines available for AT-cut as well as for SC-cut round and rectangular blanks have been developed (Fig. 3).

As the X-ray measurement is related to the axis of the  $\Omega$  measuring circle, the orientation of the blank surface assumed to be perpendicular to this axis must be known exactly. Therefore, the surface orientation is measured additionally by simultaneous registration of a reflected laser beam [Bradaczek et al (5)].

### 3. ERROR ANALYSIS BY SIMULATION OF THE REFLECTION PROFILES

#### 3.1. Calculation of the Reflection Profiles

As the basis for the following considerations on systematic and statistic errors the reflection profiles have to be simulated as exactly as possible. Neglecting the influence of the intrinsic reflection curve and assuming the crystal to be perfect, the intensity distribution on the  $\Omega$  circle,  $I(\Omega)$ , results as

$$I(\Omega) = \int_{-\infty}^{\infty} S(\Theta_B) \cdot D(\Omega, \Theta_B) d\Theta_B \quad (1)$$

( $S$ : spectral distribution;  $D$ : collimator function;  $\Theta_B$ : Bragg angle). The collimator function has to be described for the skew diffraction geometry of the  $\Omega$  scan. It can be relatively simply derived for a collimator bounded of two round holes with different radii assuming an extended homogeneous X-ray source. The detailed derivation of the collimator function is given in (4).

As the widths of the spectral lines K $\alpha_1$  and K $\alpha_2$  are small compared to that of the collimator curve, the reflection profile may be approximated by the superposition of collimator curves at the corresponding angular positions of the spectral lines. Because the CuK $\alpha_1$  and K $\alpha_2$  lines are distinctly asymmetric, each of them can be described as to be composed by two single lines of different height [Berger (6)]. Therefore, the intensity distribution follows as

$$I(\Omega) = \sum_{i=1}^4 Q_i(\Theta_{Bi}) \cdot D(\Omega, \Theta_{Bi}) \quad (2)$$

( $Q_i$ : relative peak height of the single line  $i$ ). An example of a calculated intensity distribution is shown in Fig. 4.

#### 3.2. Systematic Errors Caused by the Peak Determination

The peak positions of measured X-ray reflection profiles are usually determined by calculating the centroid of the curve or applying an appropriate fit procedure (cf. 3.3.). This peak position is an arbitrary value and may deviate essentially from the reference value to which the evaluation is related. The peak shift can be calculated by applying the

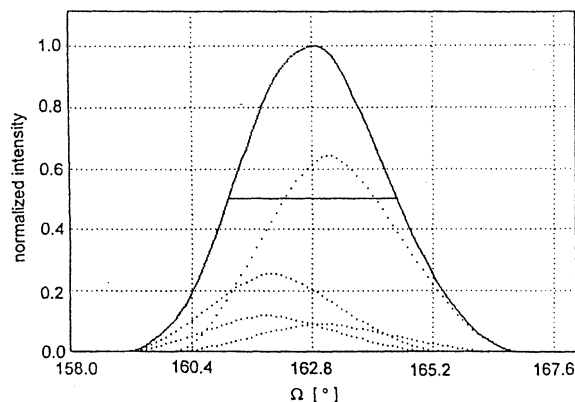


Figure 4. Calculated reflection profile (full line) as superposition of the four spectral contributions (dashed lines) of the CuK $\alpha$  spectrum. SC cut; reflection 211; collimator conditions see Table 2

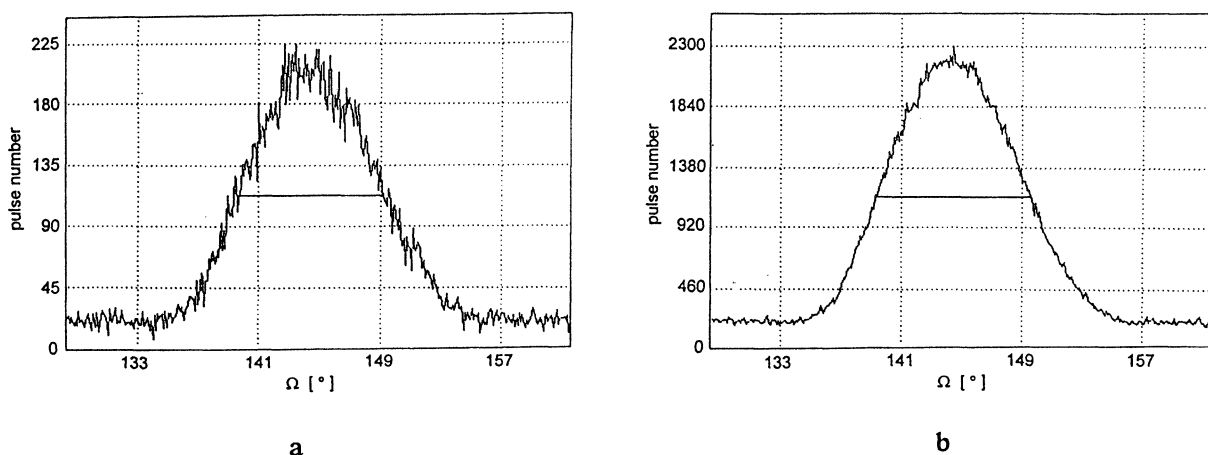


Figure 5. Calculated reflection profiles including constant noise, with Gaussian distributions of the pulse numbers. CuK $\alpha$ ; AT cut; reflection 202; collimator conditions see Table 2; a) without smoothing; b) smoothing range 1.1°

same peak determination procedure to the simulated as to the measured curves. In this way, the systematic errors in the measured values can be determined and the values can be corrected.

Table 2 shows examples of peak shifts for typical cases of AT- and SC-cut blanks calculated for conditions as used in the EFG Sorting Machines and applying the usual peak determination and evaluation methods. Peak shifts in the order of one degree may occur, leading to errors in the angular coordinates up to 0.5 arcmin.

The simulation of the reflection profiles allows also to estimate the profile widths and the conditions for reflection resolution in order to realize the minimum distances of resolved profiles.

As the calculation of an intensity profile on the PC demands a few seconds computing time, for the blanks of one charge the following procedure has been proved to be suitable: The corrections are calculated for the extreme values of both angular coordinates. After measuring a blank the individual correction can then be estimated by two-dimensional interpolation. Such procedure can not be applied for blanks with stronger deviating orientations (different charges).

### 3.3. Pulse Statistics and Limits of Reproducibility

The limit of reproducibility of the measurement of a reflection profile is determined by the pulse statistics. For given measuring conditions defining the total number of available pulses, the optimum evaluation method has to be found, which gives the highest precision in the peak position.

The standard deviation of the peak position,  $\sigma_P$ , can be generally written as

$$\sigma_P^2 = \sum_{j=1}^n N_j \cdot [\partial \Omega_P(N_1, \dots, N_n) / \partial N_j]^2 \quad (3)$$

( $\Omega_P$ : peak position;  $N$ : pulse number;  $n$ : number of evaluated measuring values). Because this expression can be evaluated only numerically and, besides that,  $\sigma_P$  does not include the error at fixing the boundaries of the range of utilized measuring values, another procedure has been used:

Gaussian or Poisson distributions, respectively, were applied to the simulated intensity profiles (cf. 3.1.). As there are no significant differences for the relevant pulse numbers, the easier calculable Gaussian statistics has been used further on. Examples of such curves are shown in Fig. 5. The standard deviation is calculated from a large number (a few hundred) of successive applications of the Gaussian statistics.

Peak determination procedures have been compared varying the following parameters: angular distance of the measuring points at constant total measuring time; number of measuring points, over which a simple smoothing (summation) of the original pulse numbers is carried out (Fig. 5b); ranges of measuring values and kind of their definition; powers of the original pulse numbers; calculation of the centroid or polynomial fit of second (or higher) order, respectively.

The minimum standard deviations are obtained using the following conditions: centroid, squared pulse numbers (corresponds to the weighting of every value with its squared statistic error), wide angular range of evaluated values (a few times the halfwidth), smoothing over a range in the order of magnitude of the halfwidth. The angular distance of the measuring points is not critical. The minimum standard deviations of the peak positions and of the cutting angle of AT cuts compared to those valid for the present evaluation procedure are given in Table 3. By modification of this procedure, the improvement of the reproducibility by a factor two should be possible. However, as follows from the comparison with the measured reproducibility (3 arcsec), there

TABLE 3 - Calculated pulse-statistic errors for *AT* cuts.  $\text{CuK}\alpha$ ; maximum puls number per channel: 200; size of angular steps:  $0.1^\circ$

reflection	2 0 2	2 0 3
<i>present state</i>		
smoothing range	$1.1^\circ$	$1.1^\circ$
<i>standard deviations</i>		
peak position	$0.012^\circ$	$0.005^\circ$
cutting angle		$1.0''$
<i>XX'</i> miscutting		$1.5''$
<i>minimum values</i>		
smoothing range	$10^\circ$	$1.1^\circ$
<i>standard deviations</i>		
peak position	$0.005^\circ$	$0.005^\circ$
cutting angle		$0.5''$
<i>XX'</i> miscutting		$0.8''$

TABLE 4 - Calculated minimum pulse-statistic errors for *AT* cut. Reflections 203/302;  $\text{CuK}\alpha$ ; maximum puls number per channel: 200; size of angular steps:  $0.1^\circ$

reflection	2 0 3	3 0 2
smoothing range	$2.1^\circ$	$5.1^\circ$
<i>standard deviations</i>		
<i>with unknown incidence angle</i>		
cutting angle		$1.3''$
<i>XX'</i> miscutting		$1.9''$
incidence angle		$1.2''$
<i>with known incidence angle</i>		
cutting angle		$0.6''$
<i>XX'</i> miscutting		$1.3''$

exist still other sources of statistic errors. For *SC* cuts result similar relations (reproducibility limits in the angular coordinates  $\Theta$  and  $\Phi$  of about 0.2 and 0.5 arcsec, respectively).

### 3.4. Additional Statistic Errors

In order to see the influence of some instrumental errors deteriorating the reproducibility, a similar procedure as used for the calculation of the pulse-statistic error has been used.

The presence of a constant statistic oscillation of the pulse numbers (i.e., independent of their values), which could be due to noise of the electronic devices, can be simulated analogously to the pulse-statistic error. As expected, for comparable standard deviations of the pulse numbers this effect would

produce errors in the peak positions being in the same order of magnitude.

The angular steps on the  $\Omega$  circle correspond to channels defined by electronic signals which are produced synchronously to the rotation of the turntable. As results from corresponding simulations, any statistic fluctuation of the channel width leads only to small, probably neglectable error contributions. Finally, the influence of a non-uniform rotation of the turntable has been regarded, described as sinusoidal modulation of the channel widths. Assuming statistic fluctuations of the phase of this modulation, statistic errors in the peak distances and the positions of the centers of the reflection pairs are expected. For *AT* cuts (conditions as given in Table 3) and an amplitude of  $0.05^\circ$ , this would lead to standard deviations in the cutting angle as observed (3 arcsec). The presuppositions for this estimation would be fulfilled at least when the blank is lifted after each measuring. However, also an irregular phase fluctuation during the rotation would have a similar effect.

## 4. ABSOLUTE MEASUREMENT OF *AT*-CUT BLANKS

The absolute orientation determination is possible when the angular coordinates can be calculated from the measuring values with sufficiently high precision without exact knowledge of the incidence angle, as it is possible for the measuring variant for *SC* cuts (cf. 2.). The set incidence angle is chosen before so that the peak distances are optimum for evaluation.

For *AT* cuts no reflection combination could be found which enables an analogous evaluation. There are reflections for which this evaluation gives a small error in the incidence angle, but the error in the cutting angle and/or the *XX'* miscutting can not be accepted. However, with known incidence angle the cutting angle and the *XX'* miscutting can be determined with sufficient reproducibility. In this case the measuring procedure has to be modified: Starting the measurements of a new charge the incidence angle must be determined first with adequate precision (measuring time). Then all blanks of the charge are to be measured and evaluated using this incidence angle, the error of which arises now as a constant systematic error.

As mentioned above, the reflections presently used for measuring *AT* cuts yield too large errors in the incidence angle. Besides the precision and the general demands for searching alternative reflections it is to consider that the incidence angle ranges should be compatible to that of the established *SC*-cut method. On these premises, the reflection combinations 303/302 and 203/302 seem to be similarly acceptable. The reflections 203 and 302 deliver somewhat larger errors in the incidence angle. An

advantage is the higher intensity of the 203 reflection. The minimum statistic errors estimated according to the regardings in 3.3. are given in Table 4.

Using the discussed reflections for *AT* cuts, the measurement of all relevant orientations of quartz resonator blanks (*AT*, *SC*, *IT* and *FC*) on one  $\Omega$ -scan machine would be possible if the incidence angle can be set in a range of about 4° and the detector can be adjusted accordingly. The requirements for a "universal" sorting machine would be fulfilled.

## 6. CONCLUSIONS

The  $\Omega$ -scan method and the EFG Sorting Machines based on it have been proved its usefulness for industrial application since a few years. It was to be shown that the potentialities of this method are not yet exhausted also from the theoretic point of view. It is principally possible to construct an universal arrangement being able to measure all relevant absolute orientations of quartz blanks. It can be expected that this will be true also for further orientation requirements.

The theoretic limits of statistic errors are valid for the present instrumental conditions. They can be still improved using more sophisticated evaluation methods and eventually higher X-ray intensities. On the other hand, there is a large contribution of instrumental errors at present, which should be diminished in the future in order to fulfill the forthcoming demands. From the simulation of possible error influences the kind and order of magnitude of such errors can be estimated.

Smaller blanks (width about 1.5 mm) can be measured using smaller beam sections. This leads to lower intensities and, hence, to the diminution of the precision. The application of higher X-ray power to compensate the lost of intensity can be avoided if more sophisticated systems of beam collimation like glass capillaries [Arkadiev et al (7)] will be used.

As shown earlier (4), the angular coordinates obtained by means of the  $\Omega$ -scan method depend still on the lattice parameters of the quartz material. It will be the aim of further efforts to find a solution of this problem.

**Acknowledgement.** The author wishes to thank Mr. Tran Tham Anh for programming essential parts of the simulation procedure. He is indebted to Prof. H.A. Bradaczek, Prof. G. Hildebrandt and Dr. H.-A. Bradaczek for kind cooperation.

## REFERENCES

1. Nestler B, Kuhr H-J, Hildebrandt G, Bradaczek H, 1991, "Novel Use of a Commercial Goniometer for Sorting Round Quartz Blanks", Meas. Sci. Technol. 2, 528-531
2. Morys B, Bradaczek H, Hildebrandt H, 1994, "Improved  $\Omega$ -Scan for Separate Measurement of True AT-Cutting Angles and X-Miscutting Angles for Round Quartz Blanks", Proc. Intern. Freq. Contr. Symp., 237-240
3. Berger H, Bradaczek H, Bradaczek H-A, Hildebrandt G, 1996, "Application of the  $\Omega$ -Scan to the Sorting of Doubly Rotated Quartz Blanks", Proc. Intern. Freq. Contr. Symp., 412-415
4. Berger H, Bradaczek H, Hildebrandt G, 1997, "Improvements of the  $\Omega$ -Scan Method by Eliminating Systematic Errors", Proc. 19th Piezoelectr. Dev. Conf., 15/1-15/15
5. Bradaczek H-A, Lim T, Pianowski H, 1997, "Optical Surface Scan by Laser Device, an Improvement in the Cutting Angle Determination of Round Quartz Blanks", Proc. 19th Piezoelectr. Dev. Conf., 12/1-12/8
6. Berger H, 1986, "Study of the  $K\alpha$  Emission Spectrum of Copper", X-Ray Spectrom. 15, 241-243
7. Arkadiev V A, Bzhaumikhov A A, Gorny H-E, Langhoff N, Schmalz J, 1996, "Capillary-Based X-Ray Filters", SPIE 2859, 220-226

## ULTRA STABLE OSCILLATORS

Vincent Candelier\*, Jacques Chauvin\*, Claude Gellé\*, Gérard Marotel\*, Michel Brunet\*\*, Roger Petit \*\*\*

\* CEPE, Groupe C-MAC, 44, Avenue de la Glacière 95100 ARGENTEUIL - FRANCE

\*\* CNES, "Centre National d'Etudes Spatiales" 18, Avenue Edouard Belin - 31055 TOULOUSE -FRANCE

\*\*\* CELAR, "Centre d'Electronique de l'Armement" Route de Redon - 35998 BRUZ - FRANCE

### Abstract

Telecommunication and measurement systems used in space applications (for example in flight equipment and ground station of navigation and accurate orbitography systems) require more and more demanding performances. This will apply to near future civil and military programmes.

Works conducted at CEPE allowed us to identify the various design key factors which are contributing to reach and limit present performances of Ultra Stable Oscillators.

A new generation of Ultra Stable Oscillation has been designed and developed in the aim of improving highest frequency stability, mainly :

- within temperature range :  $\Delta f/f < 2E - 11$  (-20°C, +60°C),
- short term with temperature variation :  $\sigma_y (10s) < 2E-13$  with a variation of 10°C per hour.

Works performed in this frame took into account :

- oscillator structures for mechanical and thermal aspects,
- electrical designs (schemes, lay out and locations),
- component and materials selection.

Several breadboards were manufactured and tested/characterised on thermal, electrical and mechanical topics.

Qualification of materials, components, processes and measurement sets has been carried out in order to permit EQM device launch (for flight purposes) and industrialisation of devices (dedicated to ground stations).

This paper summarises main results achieved with this new generation of ULTRA STABLE OSCILLATORS.

### 1. INTRODUCTION

Telecommunication and measurement systems require more and more demanding performances from ultra stable oscillators (USO) in each type of application (Space, Avionics and Professional).

Some tens of first generation USO flight modes are actually on board [2].

In the aim of improving this type of device, a specific study and development has been contracted by CEPE with French MOD (DGA - Délégation Générale de

L'armement) and French Space Agency (CNES - Centre National d'Etudes Spatiales).

### 2. OSCILLATORS REQUIREMENTS

The major characteristics to be improved on Ultra Stable Oscillators for space applications (time keeping, Doris system) are :

- The short term stability in Allan or Picinbono variance,
- The medium term stability (over the duration of 15 min in the DORIS configuration [1]).

Following table 1 gives on board (OB) and ground base station (GB) specifications/requirements for the new generation of USO (DORIS system).

	OB and GB 1st generation	OB and GB new generation
Allan variance $\tau = 10 s$	$\leq 5.10^{-13}$	$\leq 1,5.10^{-13}$
Slopes (MQ)	$\leq 4.10^{-13}/min$	$\leq 4.10^{-13}/min$
Residuals (1 sigma)	$\leq 1.10^{-12}$	$\leq 1.10^{-12}$
Temperature sensitivity	$\leq \pm 2.10^{-10}$	$\leq \pm 1.10^{-11}$
Environmental Conditions	OB : thermal vacuum GB : temperature in air	OB : thermal vacuum and magnetic filed GB : temperature in air

Table 1 : DORIS USO SPECIFICATIONS

### 3. TECHNICAL APPROACH

Taking into account typical performances of existing Ultra Stable Oscillators, designed and developed by CEPE [2], the technical approach was first based on identifying key limiting factors which are contributing to wards frequency stability (short term, mid term, thermal variation).

#### 3.1. - Short term stability

- First step of this analysis was dedicated to identify all the various noise sources in the oscillator electronic circuit.
- Second step was focused on the impact assessment of those "noise generators" to short term stability.

For this, we used a non linear simulation software after defining theoretical model of noise generation for each critical components [9].

Afterwards, we characterized by measurement the noise generated by these critical components for :

- validating theoretical models,
- sorting them.

The short term limitation that we achieved for electronics (circuit and selected components) is estimated around some  $10^{-14}$  on 10 seconds.

Quartz crystal resonator itself presents an important contribution [3], [4], [5] and [6]. Parker has indeed established a direct relation between frequency noise ( expressed in  $f^{-1}$  ) and quartz crystal Q factor [4].

At low frequency, spectrum density of resonator frequency relative variations is given for the best ones by :

$$S_y(f) = \frac{10^{14}}{f \times F_0^2 \times Q^4} \quad (1)$$

Where  $F_0$  is the nominal frequency of quartz crystal resonator and  $f$  is the Fourier frequency.

When cut type, overtone and quantity of material are defined and fixed, the value  $QF_0$  is constant for quartz crystal resonators.

$$QF_0 = K_p \quad (2)$$

Allan variance  $\sigma_{y_q}^2(\tau)$  due to the quartz crystal contribution is deduced from (1) and (2). [7]

$$\sigma_{y_q}^2(\tau) = 2 \ell_n(2) \times \frac{10^4 \times F_0^2}{K_p^4} \quad (3)$$

Conclusion of (3) is lower the frequency  $F_0$  is, better the short term stability shall be.

In case of use of SC cut and 3 rd overtone crystal in an HC40 U package, available low frequency quartz resonators are :

$$\begin{aligned} F_0 &= 5 \text{ MHz (QHS resonator),} \\ F_0 &= 10 \text{ MHz (QAS or BVA resonators)} \\ \text{and } QF_0 &\cong 1.3 \times 10^{13} \end{aligned} \quad (4)$$

Best theoretical values of short term stability are given by (3) and (4) :

$$\text{at 5 MHz } \sigma_{y_q}(\tau) = 3.5 \times 10^{-14}$$

$$\text{at 10 MHz } \sigma_{y_q}(\tau) = 7 \times 10^{-14}$$

However, those intrinsic stabilities, for a given quartz crystal design, are only achievable with a very good control of resonator manufacturing processes, at each stage, and mainly :

- cutting,
- contouring,
- polishing,
- cleaning,
- assembly,
- encapsulation conditions.

### 3.2. - Thermal stability

Environmental constraints, as temperature variation, present also an important effect on short term characteristics. In order to improve thermal stability of

the oscillator, two designs have been selected, which present different mechanical and thermal structures :

- ① single hermetic and compact oven,
- ② double oven with Dewar vessel.

For both cases, we got a temperature stability in the oven lower than  $10^{-2}^\circ\text{C}$  (some  $10^{-3}^\circ\text{C}$ ) for an external temperature range of  $80^\circ\text{C}$  ( -  $15^\circ\text{C}$ , +  $65^\circ\text{C}$ ).

## 4. - PRODUCT DEFINITION AND CONFIGURATION

USO for ground base stations at 5 MHz is built on structure 1 (single oven), with a more simple design than the one proposed in reference [10]. On board USO is built on structure 2, which is larger - Photograph 1 and 2 give illustrations of those two types of USO.

Material of resonator blanks is swept quartz for 10 MHz corresponding to on board oscillators, high quality, quartz (IR absorption lower than  $0.02 \text{ cm}^{-1}$ ) for 5 MHz relative to ground base ones.

Resonators used are packaged in HC 40 U holder and are SC cut/3 rd overtone.

Mechanical structure for 10 MHz resonator is self suspended (QAS - BVA 4 type) which insures now compatibility to ARIANE 5 mission profile (vibration, shocks).

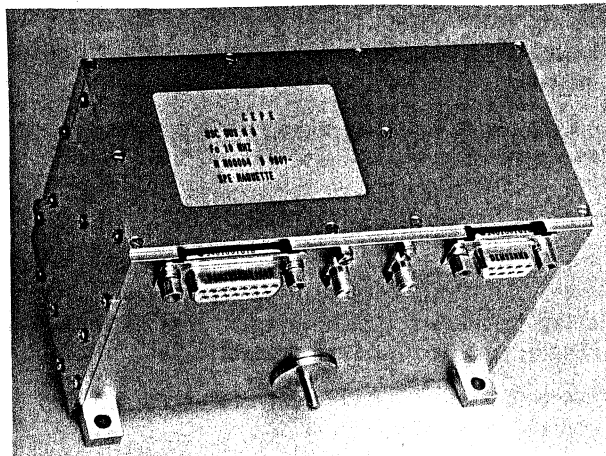
Manufacturing process of QAS - 10 MHz is in accordance to ESA rules described in CEPE PID for space applications.

Concerning USO components, most of them are procured with an ESA-SCC C quality level for flight models. However, due to the performances required for critical components, we procured some commercial components which were qualified in order to be used on space application.

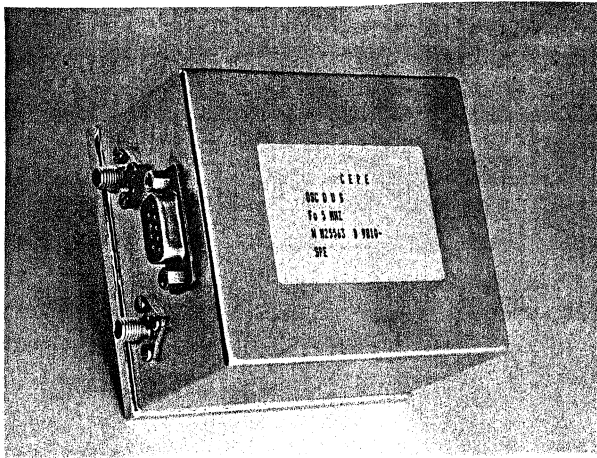
The Bread Boards were manufactured and the qualification model is on going.

Ground base station USO is under transfer to manufacturing line after industrialization..

Measurement on the two types of USO are described in the next chapter.



Photograph 1 : 10 MHz OB USO



Photograph 2 : 5 MHz OG USO

### 5. - MEASUREMENT AND TEST METHOD

For second generation USO done in chapter 2, we have developed new methods of measurement in short term and in temperature. The characterization of these oscillators in short term, with an uncertainty better than  $1.10^{-13}$ , has been possible by using the test bench presented in figure 1.

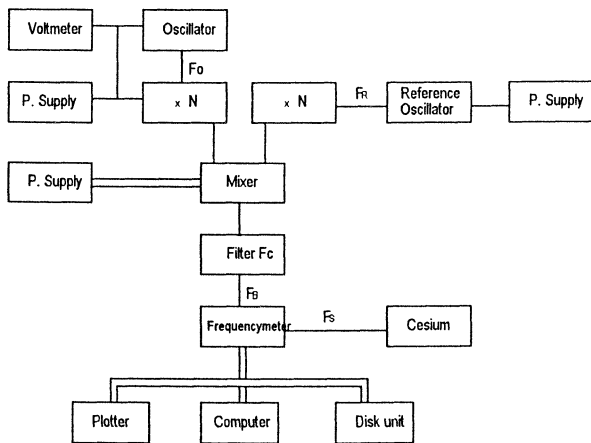


Figure 1 : Short term test bench

That is a frequency measurement by mixing. After filtering, we count the frequency of beating  $F_b$ . The relative fluctuations of frequency  $F_o$  are deduced with the following relation :

$$\frac{\Delta F_o}{F_o} = \left( \frac{F_b}{NF_o} \right) \times \left[ \frac{\Delta F_b}{F_b} + \frac{\Delta F_m}{F_m} \right] + \frac{\Delta F_r}{F_r} \left( \frac{F_r}{F_o} \right) \quad (5)$$

Where  $\frac{\Delta F_m}{F_m}$  is the frequency counter uncertainty,

$F_r$  the reference frequency,  
 $N$  the multiplication rank.

The two samples variance of the oscillator on the integration time  $\tau$  results from equation (5) :

$$\sigma_o^2(\tau) = \left( \frac{F_b}{NF_o} \right)^2 \left[ \sigma_b^2(\tau) + \sigma_m^2(\tau) \right] + \left( \frac{F_r}{F_o} \right)^2 \sigma_r^2(\tau) \quad (6)$$

The indices o, b, m, r represent respectively, the oscillator under test, the beating, the frequency counter, the reference frequency. The measurement uncertainty

is principally done by the counter uncertainty  $\sigma_{yr}(\tau)$  and the reference oscillator uncertainty. The counter uncertainty is limited by its frequency reference standard and the resolution for the chosen integration time  $\tau$ . With the used counter, we have :

$$\sigma_{ym}(\tau) = \sigma_{ys}^2(\tau) + \frac{4.10^{-18}}{\tau^2} \quad (7)$$

A frequency measurement of  $F_o$ , more stable than  $1.10^{-13}$ , require, with respect of (5), (6), (7) :

$$\left( \frac{F_b}{NF_o} \right)^2 \left[ \sigma_{ys}^2(\tau) + \frac{4.10^{-18}}{\tau^2} \right] + \left( \frac{F_r}{F_o} \right)^2 \sigma_{yr}^2(\tau) \ll 1.10^{-26} \quad (8)$$

Also, we may share the uncertainty budget as follows :

$$\left. \begin{aligned} \sigma_{yr}(\tau) &< 1.10^{-14} \\ \sigma_{ys}(\tau) &< \left( \frac{NF_o}{F_b} \right) \cdot 10^{-14} \\ F_o &< \tau \times N \times F_o \times 5.10^{-6} \end{aligned} \right\} \quad (9)$$

The short term stability in stable environment have been measured at the L.H.A. (Laboratoire de l'Horloge Atomique, Orsay) and at the LPTF (Laboratoire Primaire du Temps Français, Paris), which have a MASER. With these conditions, we have :

- $F_b \cong 10$  Hz
- $N = 1$  or  $N = 10$
- Frequency standard for counter : Cesium or Maser
- Reference frequency : MASER such as in table 2.

$\tau$ in (s)	$\sigma_{yr}(\tau)$
0,1	$3 \times 10^{-13}$
1	$1 \times 10^{-13}$
5	$4 \times 10^{-14}$
10	$1 \times 10^{-14}$
100	$< 1 \times 10^{-14}$
1000	$< 1 \times 10^{-14}$

Table 2 : MASER ALLAN STANDARD DEVIATION

On the one hand, only, the MASER limite the measure uncertainty between 0.1 s and 5 s. Above 5 secondes the test bench uncertainty is in accordance with conditions (8).

On the other hand, the filtering of the equipments power supplies and the filtering, after the mixer in the test bench seen in figure 1, must be the most efficient possible.

For a first order filter after mixer the frequency cut off,  $F_c$ , may be like that :

$$F_c = 3 F_b$$

and  $F_c > \frac{1}{2\pi\tau}$ , (10)

to let go through the spectral density  $S_{y_o}(f)$ , necessary for the variance calculation [7].

The variances, used for the caracterisation of the short-term and the medium term stability are :

- The ALLAN variance (two samples variance) [11],

$$\sigma_y^2(\tau) = \frac{1}{2NF_0^2} \sum_{K=1}^N (F_{K+1} - F_K)^2 \quad (11)$$

N = 30 samples

- The Picinbono variance(three samples variance) [11],

$$\sigma_{y_p}^2(\tau) = \frac{4}{9NF_0^2} \sum_{K=1}^N \left( \frac{F_{K+2} + F_K}{2} - F_{K+1} \right)^2 \quad (12)$$

N = 30 samples

- The CNES variance (regression, least squares line variance) [8],

$$\sigma_{y_c}^2(\tau) = \frac{1}{NF_0^2} \sum_{K=1}^N (F_k - p \cdot X_k - F_{00})^2 \quad (13)$$

N = 90 samples

Progression, least-squares line coefficients :

P = Mean slope

F<sub>00</sub> = Origin ordinate.

The relation between the CNES variance and the frequency noise density was studied by F. VERNOTTE [12]. It offers a possible comparison with the other variances.

The figures 2 and 3 display the obtained result with a great number of samples. The Allan and Picinbono variances are calculated with N samples sweeping by step of one unity on index K. The variances mean is done in legend.

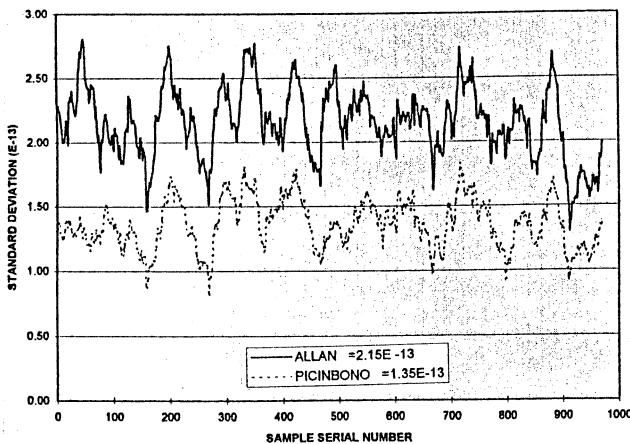


Figure 2 : 10 MHz USO N° 4 - Short term frequency stability (integration time : 10 s)

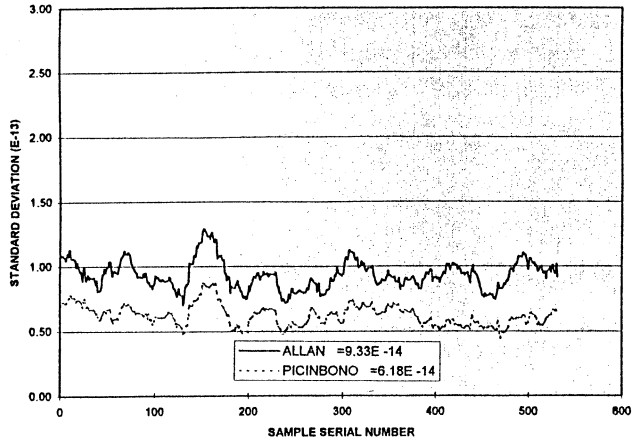


Figure 3 : 5 MHz USO N° 69404 - Short term frequency stability (integration time 10 s)

The figure 4 shows, for five GB USO 5 MHz, the Picinbono standard deviation mean according to  $\tau$  varying from 5 seconds to 1000 seconds . They ever stay lower than  $2 \times 10^{-13}$  from 5 s to 1000 s. It's principally due to the good temperature stability of the oscillators, even with a great thermal gradient.

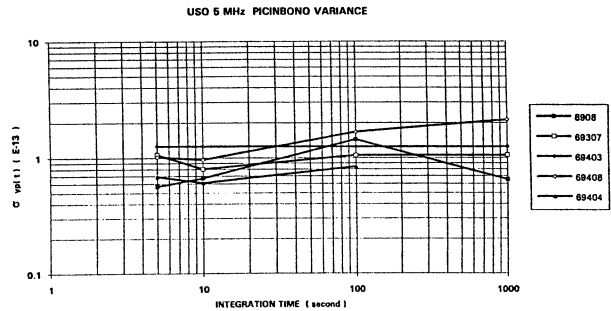


Figure 4 : 5 MHz USO Picinbono standard deviation

For the times below 5 seconds, the MASER standard is replaced by an oscillator of same type than the oscillator in test and the phase noise measurement is preferred. By applying a  $\sqrt{2}$  ratio for the same weight oscillators, we get for the OB USO and the GB USO the phase noise curves seen in figures (5) and (6)

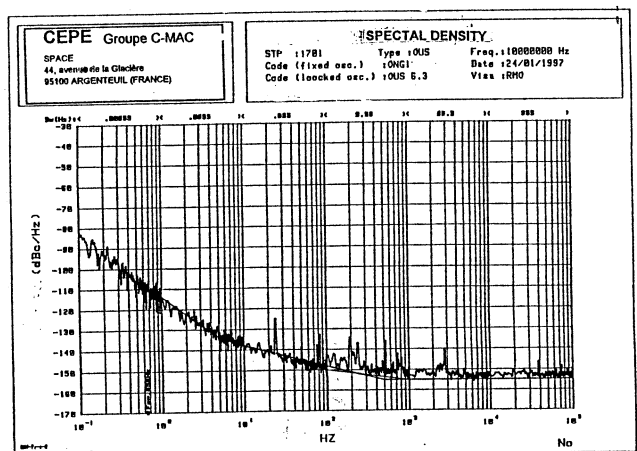


Figure 5 : 10 MHz OB USO BBM1 - Phase noise density L(f)

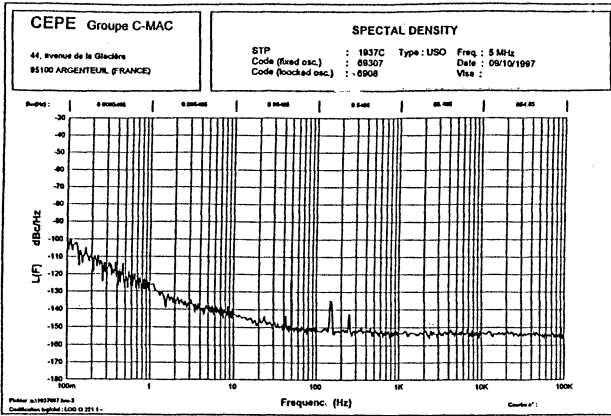


Figure 6 : 5 MHz GB USO N° 69307 - Phase noise density  $L(f)$

By using a temporal conversion as precised in [7], we may calculate the corresponding Allan variance  $\sigma_y(\tau)$

$$\sigma_y^2(\tau) = 4 \int_{f_{min}}^{f_{max}} \left(\frac{f}{F_c}\right)^2 \frac{L(f)}{1 + f^2/f_c^2} \frac{\sin(\pi f \tau)^4}{(\pi f \tau)^2} df \quad (14)$$

The cut off frequency of filter is fixed to  $3/\tau$  and for  $\tau$  upper than  $1/10 \times F_{min}$ , the calculation of  $\sigma_y^2(\tau)$  is correct. Then for the calculation at  $\tau$  equal to 1 s, we need the points of the measured phase noise curve above  $f = F_{min} = 0.1$  Hz. When we draw, on the same graph, the calculated points short term below  $\tau$  equal to 1 s and the measured points in the test bench with MASTER standard, we obtain the figure 7.

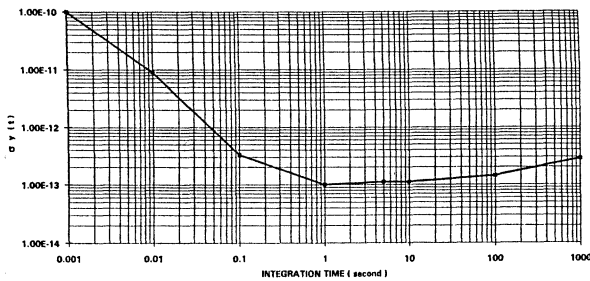


Figure 7 : 5 MHz USO N° 69307 Allan standard deviation

The figures 8, 9 and 10 show the thermal frequency drift of OB USO and GB USO. (at atmospheric pressure and under vacuum for OB USO and only at atmospheric pressure for the GB USO).

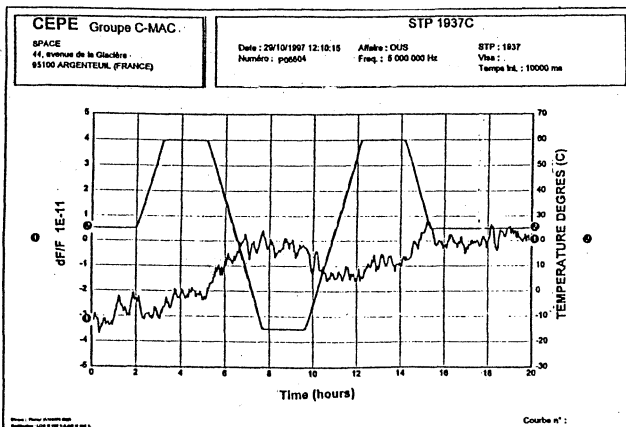


Figure 8 : 5 MHz GB USO N° 6604 - Thermal frequency drift under atmospheric pressure

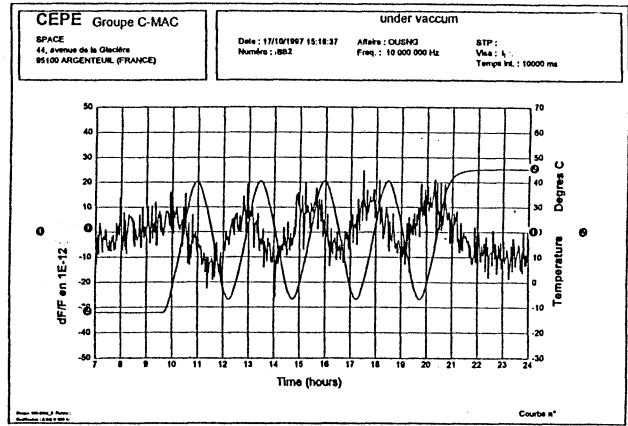


Figure 9 : 10 MHz OB USO BBM2 - Thermal frequency drift under atmospheric pressure

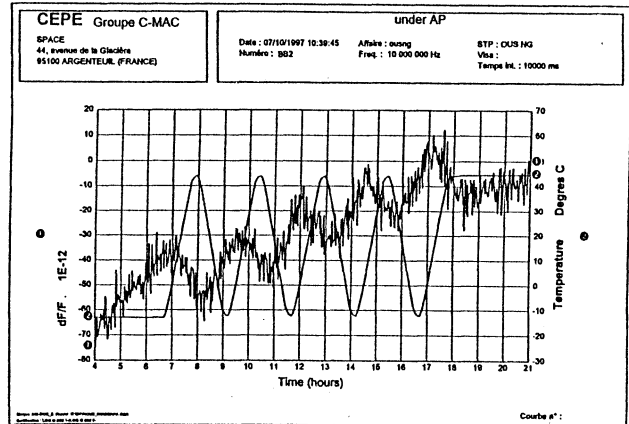


Figure 10 : 10 MHz OB USO BBM2 - Thermal frequency drift under vacuum

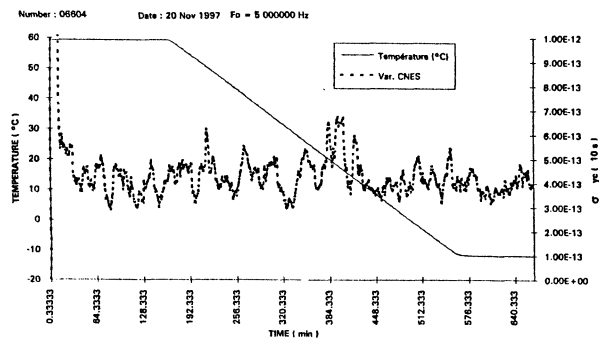


Figure 11 : 5 MHz GB USO N° 6604, CNES variance frequency standard deviation during temperature drift

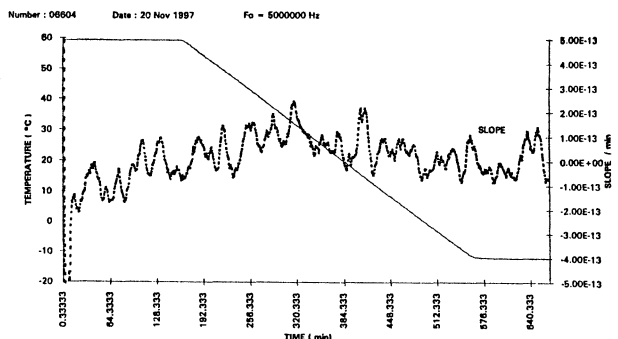


Figure 12 : 5 MHz GB USO N° 6604, CNES variance, mean slope during temperature drift

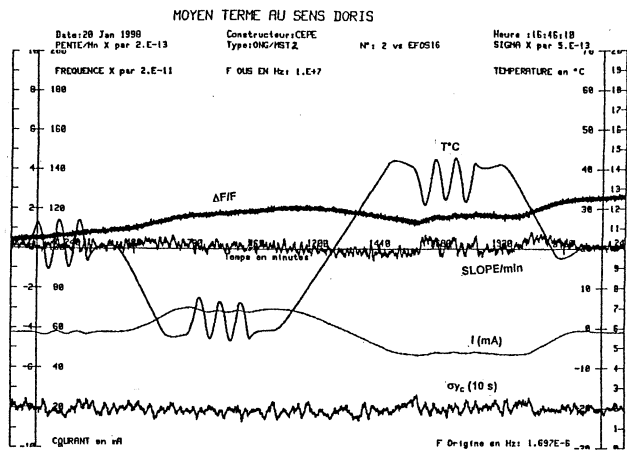


Figure 13 : 10 MHz OB USO BBM 2 medium term stability

The figures 11, 12 and 13 show the medium term stability, characterized by the CNES standard deviation  $\sigma_{v\tau}(\tau)$  and the mean slope P. This slope is not very dependant to the fast drift of the temperature.

With these performances, the needs for the second generation oscillator are satisfied.

The table 3 summarize the typical values obtained by these on board and ground base oscillators.

Parameters	OB. USO	GB USO
Frequency	10 MHz	5 MHz
DC. Supply variation (1%)	$\pm 2 \times 10^{-13}$	$\pm 5 \cdot 10^{-13}$
Load variation (10%)	$\pm 1,5 \times 10^{12}$	$\pm 1,5 \times 10^{-12}$
Pressure variation	$\pm 2 \times 10^{-9}/\text{bar}$	$< \pm 1 \times 10^{-12}/\text{mb}$
Acceleration variation	$\pm 2 \times 10^{-10}/\text{g}$	$\pm 2 \cdot 10^{-9}/\text{g}$
Vibrations (sine, random)	$\pm 1 \times 10^{-9}$	-
Magnetic variation	$\pm 5 \times 10^{-12}/\text{gauss}$	-
Temperature variation	$\pm 1 \times 10^{-11}$ (air, vacuum - 20 to 40°C)	$\pm 1 \times 10^{-11}$ (- 20 to 60°C)
Short term stability $\tau = 10$ s (Picinbono variance)	$1,4 \times 10^{-13}$	$8 \cdot 10^{-14}$
Doris mid term stability with $\theta = 0.1^\circ\text{C}/\text{min}$	0 to 40°C $\pm 1 \times 10^{-13}/\text{min}$	- 20 to 60°C $\pm 1 \times 10^{-13}/\text{min}$
R.M.S. SLOPE	$5 \times 10^{-13}$	$4 \times 10^{-13}$
Residual (1 $\sigma$ )		
Long term aging after 1 month		
1 day	$\pm 2 \times 10^{-11}$	$\pm 3 \cdot 10^{-11}$
1 month	$\pm 6 \times 10^{-10}$	$\pm 1 \cdot 10^{-9}$
Phase noise dBc/Hz		
10 Hz	- 140	- 140
1 KHz	- 155	- 155
DC. Power		
Air, 0°C	3 W	3 W
Vacuum, 0°C	2 W	-
Power supply	24 VDC	12 VDC
Random vibration	30 grms	-
Sine vibration	20 g-10 to 100 Hz	2 mm 5 - 25 Hz
Radiations	TOPEX	-

Table 4 : USO main characteristics typical values

## 6. - CONCLUSION

The results described in this paper regarding the 5 MHz ground base USO and 10 MHz space on board USO, demonstrate that the expected performances in short term and thermal stabilities have been successful and are ensured in a reproducible way :

$$\sigma_y(10 \text{ s}) < 1.5 \times 10^{-13}$$

$$\ln(-20^\circ\text{C}, 60^\circ\text{C}) \frac{\Delta F}{F} < 2 \times 10^{-11}$$

The works conducted in this study have been directly re-used for the design of our space and professional devices (mainly telecommunication) ; the technical standards have been optimized and rationalized to achieve demanding performances in thermal and short term stabilities and phase noise.

The USO for ground base station is now in production phase, (in a volume close to 0,15 l) based on structure 1.

The space qualification of OB USO will be completed in Q3/1998. Some flight models USO are now planned for 1999.

With the products and results presented here, it is now realistic for CEPE to reach higher performances as :

$$\sigma_y(10 \text{ s}) \leq 1 \times 10^{-13}$$

$$\sigma_y(10000 \text{ s}) \leq 5 \times 10^{-13}$$

and for the environmental frequency sensitivity

thermal	$10^{-13}/^\circ\text{C}$
magnetic	$10^{-12}/\text{gauss}$
irradiation	$10^{-2}/\text{rad}$ .

These performances should be necessary for next generation of space USO, requiring smaller dimensions and better time keeping stability.

We would like to thank Mr. SANTARELLI of L.P.T.F. and Mr. BARILLET of L.H.A. for their help in the frequency short term measurement of CEPE USO.

## REFERENCES

- [1] M. Brunet, A. Auriol, J.P. Berthias, M. Costes, J.K. Issler, P. Sengenès, "DORIS precise orbit determination and localization - Performances in orbit and preliminary studies of DORIS-NG", 11<sup>th</sup> European Frequency and Time Forum Neuchâtel - Mars 1997.
- [2] E. Gerard and R. Molle, "Design and Qualification of an Ultra Stable Oscillator for Space Applications, Proceedings of the 5<sup>th</sup> EFTF., Besancon 1991, pp 347.
- [3] J. Gros Lambert, "Ultimate Performances of Oscillators in Time Domain" AFCS 1996.
- [4] T.E. Parker, "1/f Frequency Fluctuations in Acoustic and Other Stable Oscillators", Proceedings 39<sup>th</sup> Annual Frequency Control Symposium, pp. 97-106, May 1985.

- [5] J.J. Gagnepain, R.J. Besson : "Non Linear Effects in Piezoelectric Quartz Crystals", Physical Acoustics (Vol. XI), pp. 245-288, Academic Press Inc. NY 1975.
- [6] E.S. Ferre-Pikal, F.L. Walls, J.F. Garcia nava : "Relationship of Amplitude and Resonant Frequency in Quartz Crystal Resonators", 10<sup>th</sup> Europ. Freq. Time Forum 1996.
- [7] C. Audoin, Reprint from "Metrology and Fundamental Constants", 1980 LXVIII Corso Soc. Italia di Fisica, Bologna (Italia).
- [8] R.J. Besson, J.J. Boy, M. Mourey, E.S. Ferre-Pikal, F.L. Walls, "Phase Noise Limitation due to Amplitude Frequency Effects in State-Of-The-Art Quartz Oscillators" AFCS 1996.
- [9] Ph. Cathelin, B. Nasreddine, P. Canzian, V. Candelier, "Short Lead Time for the Design of High Performance Airborne Oscillators", Proceedings of 8<sup>th</sup> EFTF, 1994.
- [10] R.K. Karlquist, L.S. Cutler, E.M. Ingman, J.L. Johnson and Parisek " A Low-Profile High-Performance Crystal Oscillator for Timekeeping Applications", Proceedings IFCS, 1997.
- [11] J. Rutman, "Characterization of Phase and Frequency instabilities in precision frequency Sources : fifteen years of progress", Proceedings IEEE 66, 1048-1075, 1978.
- [12] F Vernotte, M. Vincent, "Estimation of the measurement uncertainty of versus the noise levels", Proceedings of the 12<sup>th</sup> EFTF, WARSAW, POLAND.

## NONLINEARLY GENERATED 1/f FREQUENCY NOISE IN MODELOCKINGS

Serge DOS SANTOS, Franck LARDET-VIEUDRIN and Michel PLANAT

*Laboratoire de Physique et Métrologie des Oscillateurs du CNRS associé à l'Université de Franche Comté  
32, Av. de l'Observatoire, 25044 BESANÇON CEDEX, FRANCE*

The phase locked loop (PLL) which is used in a phase noise measurement set up shows a synchronization zone related to the open loop gain. The voltage fluctuations measured in the zone should be proportional to the fluctuations of the oscillator under test. But an increase is in fact observed when we go from the center of the zone to its ends. The phase locking zone of the fundamental mode may be explained from the dynamics of a nonlinear integrable equation. Introducing intermodulation products, the first odd products lead to a perturbation of the integrable equation. We performed numerical simulations in agreement with the fluctuation dependence observed experimentally. Besides we developed an Hamiltonian approach; by defining an action-angle space, we found a relation between the increase of fluctuations and the hyperbolic curvature of this space. We found that frequency noise transforms from white to 1/f noise when we go from the center of the phase locking zone to its ends, or from outside the locking region to its vicinity.

## I. INTRODUCTION

Despite a lot of efforts the ubiquitous 1/f noise phenomenon is still not well understood [1]. In the field of frequency standards such a noise limits the long term stability and as such it is very desirable to improve our knowledge of its generation. In this paper we questioned a physical set-up which allows to extract the frequency noise of a clock to be qualified, that is the phase locked loop (PLL) [2].

In this paper we propose to study the transformation of white frequency noise in a classical first-order PLL under high nonlinear configuration. It seems that 1/f noise is generated (or amplified) by the presence of nonlinearity.

An Hamiltonian description was chosen in order to apply the powerful approach called Riemannian description of Hamiltonian systems. It allows us to extract a curvature property related to synchronization and fluctuations in the PLL which agrees with similar results obtained in areas such as thermodynamics [3] or mechanics [4].

## II. NONLINEAR STUDY OF THE ELECTRONIC LOOP

The electronic loop under study is a basic part of a PLL. The loop realizes frequency locking between an reference oscillator (RF) and a local oscillator (LO) (Fig.1). The signal  $u(t)$  at the output of the mixer results from the frequency conversion of input signals with angular frequency  $\omega_0$  and  $\omega_1$  given by  $u(t) = \mu(\sin(\omega_0 - \omega_1)t + \sin(\omega_0 + \omega_1)t)$ , where  $\mu$  represents the sensitivity of the mixer. At the output of the filter only the down converted product remains. The Voltage Controlled Oscillator (VCO) produces a signal whose angular frequency  $\omega_1$  depends linearly on the incoming voltage  $v(t)$ ,  $\omega_1 = \omega_{vco} + k.v(t)$ , where  $\omega_{vco}$  is the central angular frequency of the VCO and  $k$  its sensitivity. Putting  $\Phi = (\omega_0 - \omega_1)t$ , the following differential equation governs the phase error signal:

$$\dot{\Phi}(t) + K \sin \Phi(t) = \Delta\omega, \quad (1)$$

where  $\Delta\omega = \omega_0 - \omega_{vco}$  is the angular frequency deviation and  $K = \mu k$  the coupling coefficient (also called open loop gain).

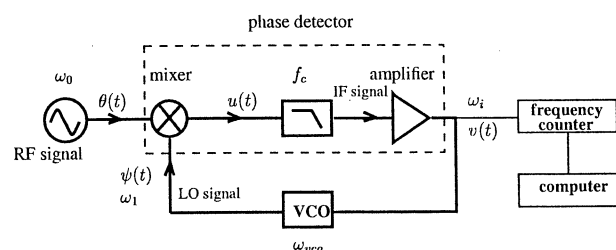


FIG. 1. Schematic of the voltage controlled electronic loop used in the experiment. A high accuracy quartz oscillator with relative stability of  $10^{-11}$  constitutes the RF stable reference. A low phase noise frequency synthesizer is used as the VCO.

Equation (1) is the model equation of a first-order PLL, and its solution is given by (Fig.2),

$$\Phi(t) = 2 \arctan \left( u^{-1} \left( 1 + 2Z/K \tan(Z(t - t_0)) \right) \right), \quad (2)$$

where  $u = \frac{\Delta\omega}{K}$  and  $Z = \frac{K}{2} \sqrt{u^2 - 1}$ .

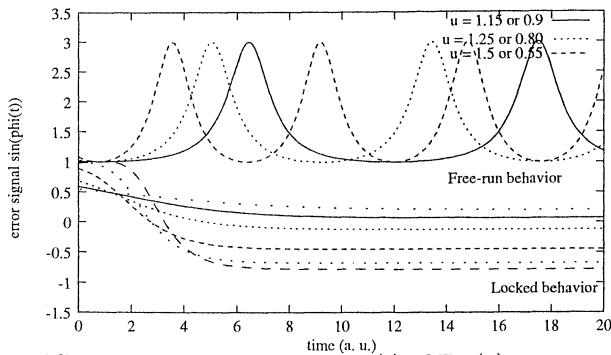


FIG. 2. Plots of time solution  $\Phi(t)$  of Eq.(1) versus  $u$ . The two different behaviors of the system (synchronized when  $u < 1$  and beat shape when  $u > 1$ ) are visible. When  $u \rightarrow 1^+$ , the angular beat frequency  $\omega_B \rightarrow 0$ ; when  $u \rightarrow 1^-$  the transient tends towards  $\infty$ .

The first order PLL is also integrable in the sense of Liouville [5], and can be associated to an Hamiltonian  $\mathcal{H}(\Phi, \dot{\Phi})$  expressed in action-angle coordinates  $\Phi$  and  $\dot{\Phi}$ ,

$$\mathcal{H} = T + V(\Phi) = \frac{1}{2}\dot{\Phi}^2 - \int \ddot{\Phi} d\Phi, \quad (3a)$$

$$= \frac{1}{2}(\dot{\Phi}^2 + K^2 \cos^2 \Phi) + K\Delta\omega \sin \Phi, \quad (3b)$$

$$= \frac{1}{2}(\Delta\omega^2 + K^2) = E_{tot}, \quad (3c)$$

which verify the Hamilton equations:  $\frac{d\Phi}{dt} = \frac{\partial \mathcal{H}(\Phi, \dot{\Phi})}{\partial \dot{\Phi}}$  and  $\frac{d\dot{\Phi}}{dt} = -\frac{\partial \mathcal{H}(\Phi, \dot{\Phi})}{\partial \Phi}$ . As seen in Eq.(3c), the Hamiltonian  $\mathcal{H}(\Phi, \dot{\Phi})$  is in involution and is called an integral of motion, commonly called mechanical total energy  $E_{tot}$ . The explicit expression of the solution of this Hamiltonian system is dependent on the parameter  $u$ . In the phase tracking range of width  $2K$  the input signals are also frequency locked. Outside the modelocking zone there is a sech shape beat signal of angular frequency

$$\omega_B = \langle \dot{\Phi}(t) \rangle = K\sqrt{u^2 - 1}, \quad (4)$$

converging to the open loop frequency beat  $\Delta\omega$  when  $u \gg 1$ . The theoretical limit  $u = 1$  constitutes a frontier between two physical different behaviors, one associated to a synchronization state (locked state) and the other to an oscillating behavior (free-run state) as seen in Fig.2.

### A. Separatrix property of the limit $u = 1$

The PLL which is described by  $\mathcal{H}(\Phi, \dot{\Phi})$  can be compared to a mechanical overdamped system with an associate periodic potential  $V(\Phi)$  given by

Eq.(3b). The unidimensional system will have an oscillating behavior if its total energy  $E_{tot}$  is higher than its potential energy, i.e.  $E_{tot} = 1/2(\Delta\omega^2 + K^2) > V(\Phi), \forall \Phi$ . The maxima of  $V(\Phi)$  are given for  $\Phi = \pi/2$  which give  $E_{tot} - V(\Phi) > 0$  since  $(\Delta\omega - K)^2 > 0$ . The case  $\Delta\omega = K$  is then the only one singular case. The potential  $V(\Phi) = K^2$  equals the total energy  $E_{tot}$  and the phase  $\Phi$  of the error signal  $v(t)$  would take an infinite time to reach each maxima of the potential. This property explains the curves given for  $u = 0.99$  and  $u = 1.01$  in Fig.2. This particular case  $\Delta\omega = K$  is then called a separatrix which is extremely dependent on external perturbations as we will see in section III.

We are then interested in the characterization of the locked and the beat regions near the separatrix. Recently, some authors [3,4,6] have associated instability and intrinsic curvature of the action-angle configuration space in domains like mechanics and thermodynamics. The Riemannian description of Hamiltonian systems developed by Pettini [4] is useful for the calculation of the curvature related to the configuration space of the first-order PLL. An integrable property of a system yields to a zero curvature of the configuration space. Let us show it in the first-order PLL case. It is well known that trajectories of an Hamiltonian system can be viewed as geodesics of a Riemannian manifold with a suitable metric. Actually, it is always possible to define a proper Riemannian metric  $g$  in the configuration space of the PLL because it is an integrable case. The associated metric tensor  $g_{ij}$  follows the simple expression (cf Eq.(6) of [4])

$$g_{ij} = g_{\Phi\Phi} = \dot{\Phi}^2 = (\Delta\omega - K \sin \Phi)^2. \quad (5)$$

The associate scalar curvature can be calculated from the classical formula involving Christoffel and Ricci tensors, and yields to zero curvature in this one dimensional particular case. We then verify that integrable system can be associated to an underlying space which shows a zero curvature property.

### B. Characterization in the phase space

Hamiltonian description of the PLL is interesting because it allows to obtain general properties in the phase space  $(\Phi, \dot{\Phi})$ . Physically, the relevant signal is the error voltage correction  $v(t) \sim \sin \Phi(t)$ . A characterization in the phase space  $(\Psi, \dot{\Psi})$  where

$\Psi = \sin \Phi$  and  $\dot{\Psi} = \dot{\Phi} \cos \Phi$  will be better from the electrical point of view. The Hamiltonian  $\mathcal{H}(\Phi, \dot{\Phi})$  can be expressed in the  $(\Psi, \dot{\Psi})$  coordinates as

$$\mathcal{H}(\Psi, \dot{\Psi}) = \frac{\dot{\Psi}^2 + K^2(1 - \Psi^2)^2}{2(1 - \Psi^2)} + \Delta\omega K\Psi, \quad (6)$$

which gives the phase portraits (Fig.3a,b,c) obtained from numerical and experimental study. We verify that the configuration  $u = 1$  is a separatrix.

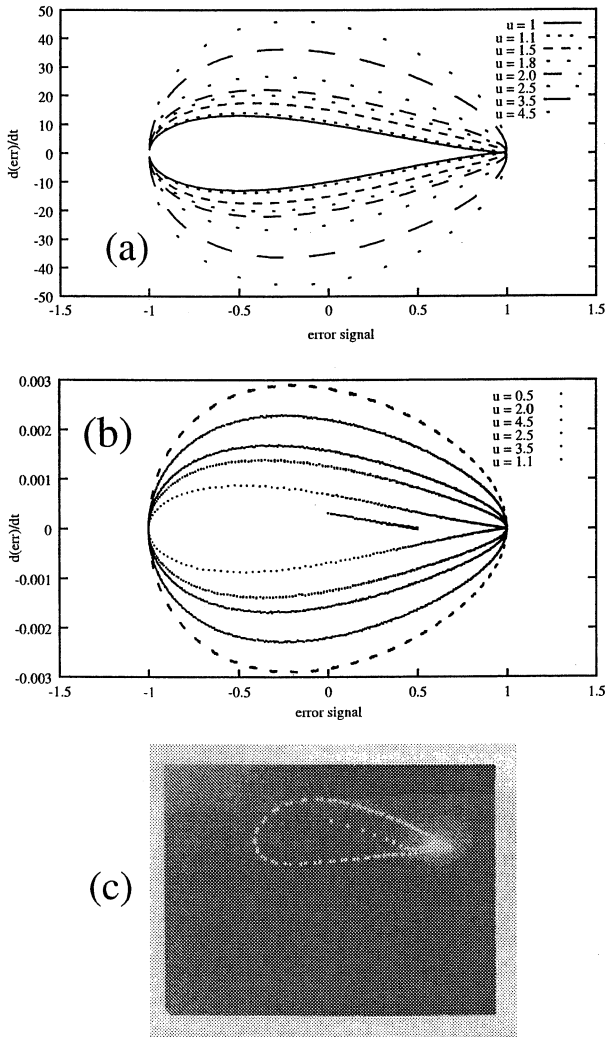


FIG. 3. (a): Plots of the Hamiltonian  $\mathcal{H}(\Psi, \dot{\Psi})$  in the phase space  $(\Psi, \dot{\Psi})$  given by Eq.(6) for different values of  $u$ . The separatrix is the curve given for  $u = 1$ . (b): Plots of the phase portrait given with a numerical simulation of the first order PLL. We plot a transient for  $u = 0.5$  in order to see the asymptotic evolution in the phase space. (c): An experimental phase portrait seen in an oscilloscope running in XY mode.

### III. PERTURBATION OF THE PLL HAMILTONIAN : 1/F NOISE NEAR THE SEPARATRIX

The Hamiltonian  $\mathcal{H}(\Phi, \dot{\Phi})$  given by Eq.(3) is only a first nonlinear approximation of the PLL running

under these conditions. It does not take into account some possible perturbations created by the environment of the system. These perturbations are principally given by the other intermodulation products elaborated by the mixer (as studied in Ref. [7]), and by the internal noise of oscillator under test. These perturbations have already been studied and can generate chaos and instability under particular conditions [8–10].

We chose to study experimentally noise and harmonic perturbations. The noise perturbation was elaborated by an external perturbation of a stable oscillator by a pseudo-random signal generator. Harmonic perturbation has been studied by putting the PLL into particular conditions where two harmonics ( $\omega_0 - \omega_{vco}$ ) and  $(3\omega_0 - \omega_{vco})$  amplitude are closeby. We have supposed that the other kind of perturbations described above are negligible.

#### A. Noise perturbation

The noise perturbation of the PLL has been studied experimentally and numerically. We modulated our stable oscillator of frequency 5.020626 MHz with white frequency noise given by a pseudo random signal generator with 15 kHz bandwidth. The modulation level has been chosen in order to be higher than the oscillator intrinsic noise. The differential equation governing the system is then given by

$$\ddot{\Phi}(t) + K \sin \Phi(t) = \Delta\omega + \Gamma(t), \quad (7)$$

where  $\Gamma(t)$  denotes the Gaussian white noise contribution.

##### 1. Observation in the time domain

We have made four records of the beat frequency  $\dot{\Phi}(t)$  versus  $u$ . Each calculation of the Allan deviation  $\sigma_{\dot{\Phi}}^{(N)}(\tau)$  was done with 2000 points with an integration time  $\tau_0 = 0.02$  s. An increasing fluctuation has been observed and is detailed in [11].

Nevertheless we can directly observe that the nature of the fluctuation is modified when we go near the limit  $u = 1$ . The slope of the Allan deviation is transformed from  $\sigma_{\omega_B}(\tau) \sim \tau^{-1/2}$  to  $\sigma_{\omega_B}(\tau) \sim \tau^0$ . The initial white frequency noise is transformed into flicker frequency noise (1/f noise) in long time domain.

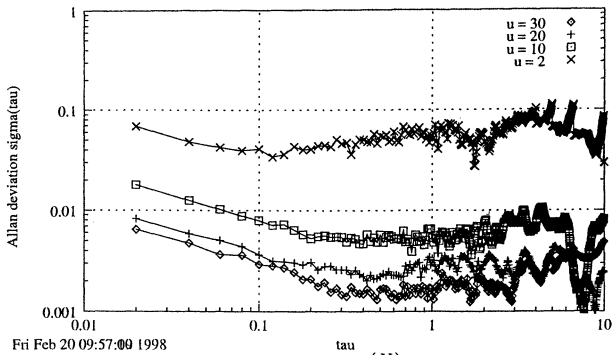


FIG. 4. The Allan deviation  $\sigma_{\Phi}^{(N)}(\tau)$  ( $N = 2000$ ) of frequency beat  $\Phi$  for different values of  $u$ . The RF oscillator is the quartz oscillator of frequency  $f_0 = 5.020626$  MHz modulated by a white frequency noise. A high open loop gain  $K = 1.5$  kHz was chosen in order to amplify the nonlinear effects. The transformation of the noise is detected in the range  $\tau \in [0.1; 0.5]$ . The white frequency noise ( $\tau^{-0.5}$ ) is changed into  $1/f$  noise ( $\tau^0$ )

Under these particular experimental conditions, a nearest value of  $u$  yields to a possible desynchronization of the system. The most important result of this experiment was the observation of  $1/f$  fluctuation when we are under nonlinear conditions. Yamaguchi [12] has shown the same effect considering chaotic motion in a whisker mapping. Wischert *et al* have observed the same phenomenon in a first-order delayed PLL [9]. Then, the presence of the separatrix in the system is certainly responsible of this kind of fluctuations. It is well known that chaos appears near the separatrix [13], so the origin of  $1/f$  fluctuations seems to be related to the presence of chaos.

## 2. Observation in the frequency domain

$1/f$  noise has been observed for  $u > 1$  when the PLL is in the beat state. The motivation to verify the fluctuation transformations in the frequency domain led us to consider the same experiment when the PLL is locked. The experimental set-up is the same as above, except that the frequency shift  $\Delta\omega$  is lower than the open loop gain  $K$ . A smaller cut-off frequency was chosen ( $K = f_c^{(ass)} = 450$  Hz) in order to realize a compromise between nonlinear effects and a good characterization in the random generator bandwidth.

We verify that the cut-off frequency of the spectrum divides it in two areas according to the classical results. Fig.5 shows different spectra of the error signal versus  $u$ . The spectrum for  $u = 0$  is the classical noise measurement of the external modulated fluctu-

ations. We confirm in the Fourier domain that  $1/f$  noise is generated when we go from the center of the zone ( $u = 0$ ) to its end ( $u = 1$ ). This  $1/f$  fluctuation appears in the Fourier frequency spectrum between 50 and 300 Hz.

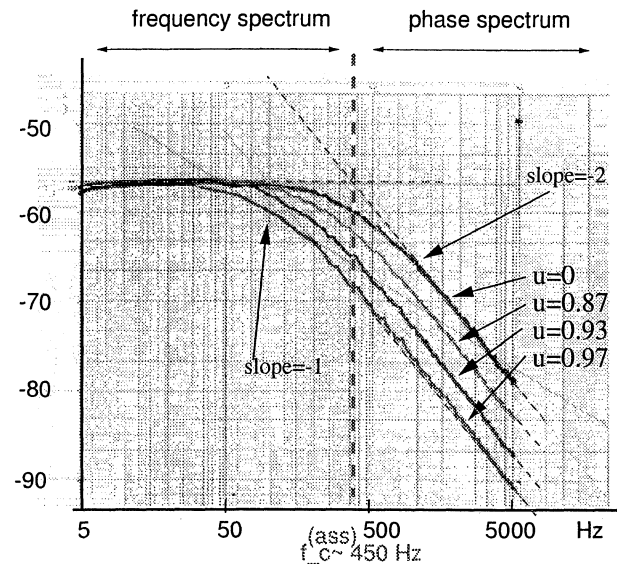


FIG. 5. RMS spectrum of the error signal  $v(t)$  for  $u = \{0; 0.87; 0.93; 0.97\}$ . This spectrum is proportional to the frequency spectrum for  $f \in [0; 450]$  and proportional to the phase spectrum ( $f^{-2}$ ) of the white frequency fluctuation modulating the oscillator  $\omega_0$ . For  $u = 0.97$ , we see that a slope of  $f^{-1}$  appears in the frequency spectrum area when, for  $u = 0$ , the slope is related to white noise.

This result is analog to thus obtained in the time domain via the Allan variance; it confirms that we have observed the same phenomenon but with a lower precision.

The experimental result was difficult to obtain because of a possible desynchronization. It helps us to confirm that  $1/f$  noise and synchronization phenomenon are certainly very closeby related. The fact that the system is near a synchronization area generates naturally a kind of fluctuation with  $1/f$  power law.

From the theoretical point of view, the resolution of the nonlinear differential equation (7) with the stochastic term  $\Gamma(t)$  is difficult to realize. The linear approximation  $\sin \Phi \sim \Phi$  can be done and the system can be solved classically in Laplace's variable or with a powerful algebraic method used to solve the Fokker-Planck (FP) equation [14]. Both methods produce the same result for the spectral density of the error signal. Moreover, the algebraic formalism used for the resolution of the FP equation can be used in few nonlinear cases where the Laplace's

method fails.

## B. Harmonic perturbation

It is known that the PLL can be locked for all harmonics of the input signals such that  $\frac{\omega_0}{\omega_1} = p/q$  with  $p$  and  $q$  integers [7]. We have shown that the PLL is a complex system where many intermodulation products interact to each other.

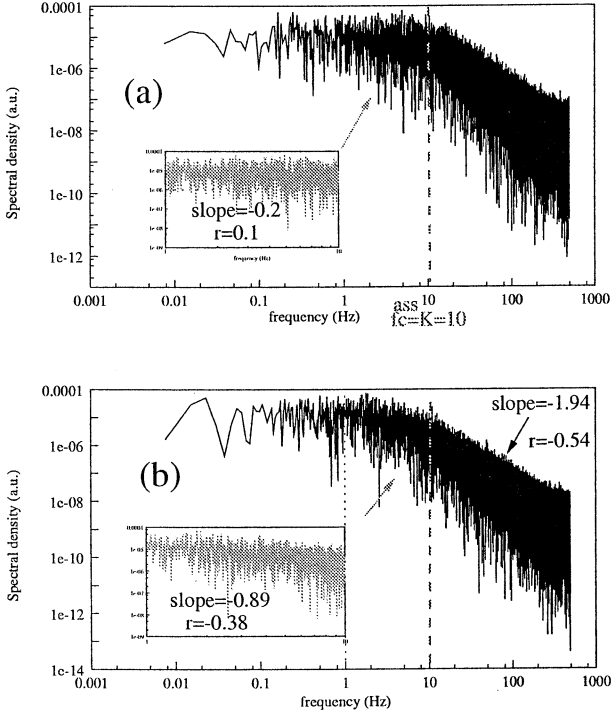


FIG. 6. Numerical spectra of  $v(t)$  showing the same results as the experimental ones (Fig.5). The harmonic of the perturbation is the intermodulation product  $\frac{\omega_0}{\omega_{vco}} = 1/3$ . In the frequency range  $f \in [1, 10]$ , the slope follows a  $f^{-0.89}$  law for  $u = 0.9$  (b). Spectra have been obtained performing a numerical FFT with  $N = 2^{17}$  points.

Audoin [15] has shown that intermodulation effects are responsible of additional perturbations in noise measurements. We can select an experimental configuration where only two harmonics are important with respect to the others. In this case, we can study the perturbation of the equation (1) by an harmonic. In fact, the ratio  $\frac{\omega_0}{\omega_{vco}} = 1/3$  generated by the mixer produces the higher perturbation. So, we have studied the following system from the both numerical and theoretical point of view:

$$\dot{\Phi}(t) + K \sin \Phi(t) + K_3 \sin(\Phi + 2\omega_0 t) = \Delta\omega. \quad (8)$$

For numerical simulation, we have observed the noise transformation near the locking region  $\Delta\omega =$

$K$  in the band  $f \in [1, 10]$  Hz. Fig.6 shows that white noise is transformed from white noise into  $f^{-0.89}$  noise when we go from the center ( $u = 0$ ) to the end ( $u = 0.9$ ) of the locking region. We obtain the same results as the experimental curve shown in Fig.5. We confirm the transformation of white noise into  $1/f$  noise with these simulations.

### 1. Theoretical study

We can write Eq.(8) into the 2-dimensional autonomous system:

$$\begin{cases} \dot{\Phi} + K \sin \Phi + K_3 \sin \chi = \Delta\omega \\ \dot{\chi} + K \sin \Phi + K_3 \sin \chi = \Delta\omega_1 \end{cases}, \quad (9)$$

where  $\chi = \Phi + 2\omega_0 t$  and  $\Delta\omega_1 = 3\omega_0 - \omega_{vco}$ . Let us evaluate the curvature  $R$  associated to this 2-dimensional system as done in section II A for the Hamiltonian case. Ruppeiner [3] showed that the curvature  $R$  associated to an 2-dimensional system is given by (Eq.(6-11) of [3])

$$R = \frac{1}{\sqrt{g}} \left[ \frac{\partial}{\partial \Phi} \left[ \frac{1}{\sqrt{g}} \frac{\partial g_{11}}{\partial \Phi} \right] + \frac{\partial}{\partial \chi} \left[ \frac{1}{\sqrt{g}} \frac{\partial g_{22}}{\partial \chi} \right] \right] \quad (10)$$

where  $g = \det[g_{ij}]$ . Considering the relation between  $\Phi$  and  $\chi$  (i.e.  $\frac{\partial}{\partial \Phi} = \frac{\partial}{\partial \chi}$ ) and the symmetry property, the curvature  $R$  can be approximated as

$$R \sim \frac{2}{\sqrt{g}} \left[ \frac{\partial}{\partial \Phi} \left[ \frac{1}{\sqrt{g}} \frac{\partial g_{11}}{\partial \Phi} \right] \right]. \quad (11)$$

The metric element  $g_{11} = g_{\Phi\Phi}$  tends towards Eq.(5) when  $K_3 \rightarrow 0$ , the asymptotic value of  $R$  is also obtained by putting Eq.(5) into (11);

$$R \sim \frac{\sin \Phi}{u - \sin \Phi}. \quad (12)$$

The curvature can be also evaluated in the locked and the free-run region of the PLL.

If  $0 < u < 1$ , the PLL is locked and the phase  $\Phi(t)$  of the system is globally constant. Then, as seen in Fig.2,  $\lim_{t \rightarrow \infty} \dot{\Phi} = 0^-$  yields to  $\lim_{t \rightarrow \infty} \sin \Phi = u^+$ ; then  $\forall u, 0 < u < 1$ ; and when  $t \rightarrow \infty$ ,  $R \sim \frac{u}{u - \sin \Phi} - 1 < 0$ . The curvature of the underlying space is negative and yields to an hyperbolic space with the limits  $\lim_{u \rightarrow 0} R = -1$ , and  $\lim_{u \rightarrow 1} R = -\infty$ . This result about the curvature shows the difficulty to describe the signal evolution in the PLL synchronized state.

If we suppose that the difference  $\Delta\omega$  could be variable, that yields an instantaneous variation of the curvature as shown in relation (12). But the most important result is that the global evolution is done in a space of which the curvature is negative.

It is interesting to determine the space property when the PLL is unlocked ( $u > 1$ ) in order to extract informations that are probably not present in the classical approach. For  $u > 1$ , the instantaneous frequency  $\dot{\Phi}$  is not constant and the curvature  $R$  defined by (12) verifies  $R \geq 0, \forall u > 1$ . The space is also an elliptic space (positive curvature) characterized by an oscillating behavior (the beat angular frequency  $\omega_B$  physically represents this oscillation). When  $u$  is near 1, the curvature can increase and becomes infinite in the limit.

The second limit is when  $u$  tends towards infinity by positive value. The curvature  $R$  tends towards zero, synonymous of an integrable system. The  $u \rightarrow \infty$  is obtained in the system (9) when  $\Delta\omega \rightarrow \infty$ . The two constants  $K_1$  and  $K_3$  then become smaller than  $\Delta\omega$  and the system (9) can be approximated by

$$\begin{cases} \dot{\Phi} + K\Phi + K_3\chi = \Delta\omega \\ \dot{\chi} + K\Phi + K_3\chi = \Delta\omega_1 \end{cases}, \quad (13)$$

where solutions are easy calculable by classical linear algebra.

We see that the curvature tends towards infinity when  $u \rightarrow 1$ . This result confirms the high complexity of this region. Let us write the relative frequency variation  $\sigma_{\dot{\Phi}} = \frac{\delta\dot{\Phi}}{\dot{\Phi}}$  versus  $\sigma_{\Delta\omega} = \frac{\delta(\Delta\omega)}{\Delta\omega}$ . From Eq.(1), we get  $\frac{\delta\dot{\Phi}}{\dot{\Phi}} = \frac{\delta(\Delta\omega)}{\dot{\Phi}}$  or

$$\frac{\delta\dot{\Phi}}{\dot{\Phi}} = \frac{\delta(\Delta\omega)}{\Delta\omega - K \sin \Phi} \quad (14)$$

from Eq.(12), we can express (14) versus  $R$ , and when  $u \rightarrow 1$ , the curvature  $|R|$  tends towards infinity, and finally we get the asymptotic behavior

$$\sigma_{\dot{\Phi}} = |R|\sigma_{\Delta\omega}. \quad (15)$$

We obtain an interesting result which associates the fluctuation of  $\dot{\Phi}$  and the curvature. The fluctuations are then proportional to the curvature. Analog results have been obtained by Ruppeiner and Pettini in Refs. [3,4]. We can say now that an increasing of the fluctuations are due to the presence of the separatrix which can be now associated to a configuration space with high curvature.

#### IV. CONCLUSION

We have developed an Hamiltonian description of the first order PLL in order to extract a new property, never given in the frequency standards domain. The curvature of the Hamiltonian configuration space seems to be responsible of an increase of fluctuations near high nonlinear conditions of the system. Moreover the nature of the fluctuations is transformed from white frequency noise to  $1/f$  noise. Is  $1/f$  noise an intrinsic property of nonlinearity?

- 
- [1] P. H. HANDEL. *The Nature of Fundamental 1/f Noise*. In *Noise in Physical Systems and 1/f fluctuations*, page 162, Saint-Louis, 1993. Peter H. Handel and Alma L. Chung.
  - [2] J. KLAPPER and J. T. FRANKLE. *Phase-Locked and Frequency-Feedback systems*. Academic Press, New York, 1972.
  - [3] G. RUPPEINER. *Riemannian geometry in thermodynamic fluctuation theory*. Reviews of Modern Physics, **67**, 605, (1995).
  - [4] M. PETTINI and R. VALDETTARO. *On the Riemannian description of chaotic instability in Hamiltonian dynamics*. Chaos, **5**, 646, (1995).
  - [5] V. ARNOLD. *Méthodes Mathématiques de la Mécanique Classique*. MIR, Moscou, 1976.
  - [6] G. RUPPEINER. *New thermodynamic fluctuation theory using path integrals*. Phys. Rev. A, **27**, 1116, (1983).
  - [7] S. DOS SANTOS, J.F. MOUGIN, F. LARDET-VIEUDRIN, J. GROSLAMBERT, and M. PLANAT. *Non linear approach of the spectrum and stability of frequency lockings*. Proc. 11<sup>th</sup> Ann. European Time and Frequency Forum EFTF, Neuchatel, Suisse, , (1997).
  - [8] W. WISCHERT, A. WUNDERLIN, A. PELSTER, M. OLIVIER, and J. GROSLAMBERT. *Delay induced instabilities in nonlinear feedback systems*. Phys. Rev. E, **49**, 203, (1994).
  - [9] W. WISCHERT, M. OLIVIER, and J. GROSLAMBERT. In *Noise in Physical Systems and 1/f fluctuations*, page 333, New York, 1993. Peter H. Handel and Alma L. Chung.
  - [10] M. DE SOUSA VIEIRA, A. J. LICHTENBERG, and M. A. LIEBERMAN. *Nonlinear dynamics of digital phase-locked loops with delay*. Int. J. Bifurcation and Chaos, **4**, 715, (1994).
  - [11] M. PLANAT and S. DOS SANTOS. *The Arithmetic of Frequency Mixing in an Electronic Loop*. in these proceedings, , (1998).
  - [12] Y. YAMAGUCHI and K. SAKAI. *1/f noise spectrum of the chaotic motion in a whisker mapping*. Physics Letters A, **117**, 387, (1986).
  - [13] B. V. CHIRIKOV. Phys. Rep., **52**, 265, (1979).
  - [14] H. RISKEN. *The Fokker-Planck Equation*. Springer Verlag, Berlin, 1989.
  - [15] C. AUDOIN, V. CANDELIER, and NOËL DIMARCO. *A Limit to the Frequency Stability of Passive Frequency Standards Due to an Intermodulation Effect*. IEEE Trans. Instrum. Meas., **2**, 121, (1991).

## A NEW 5 MHz MINI-BVA OCXO

Gilles ROBICHON  
bva INDUSTRIE SA  
1 boulevard Fleming - BP 61923 - 25020 BESANÇON Cedex 07

Tel. : 33 3 81 41 13 09 - Fax : 33 3 81 41 01 11

### Abstract

Up to now, Mini-BVA quartz crystal resonators (in T 21 11 cans) have been manufactured at and around 10 MHz. We are now able to produce these crystals (SC-cut, 3rd overtone) at 5 MHz in the identical package. These units exhibit higher Q-factors and lower agings than the crystals around 10 MHz.

We use the 5 MHz crystals in the same, OCXO than this used for the 10 MHz resonators (about 100 cm<sup>3</sup>). A comparison of the two OCXOs will be presented and their relative advantages shown with respect to parameters as phase noise, short term stability, aging and gravitational sensitivity.

### I - INTRODUCTION

The electrodeless BVA technology resonators have proved their capabilities [1, 2, 5] at 5, 10 and 50 MHz. bva INDUSTRIE has developed an OCXO ref. bvap022 at 10 MHz, an other one ref. bvap016 at 8.192 MHz. Both were 0.1 liter volume and exhibit frequency shifts versus temperature better than  $5 \cdot 10^{-10}$  in the full range. The 5 MHz request not covered by the same way due to the resonator size difficulty. Recent progress in the resonator design permit to obtain SC-cut 3rd overtone at 5 MHz in the same package (T2111 or HC-40/U). So, some minor changes in the OCXO electronic were achieved in order to manufacture this new bva OCXO at 5 MHz.

### II - THE 5 MHz RESONATOR

#### 2.1 - The size target

Our target is to keep the size of T2111 package (or HC-40/U) with electrodeless technology at 5

MHz. Recent progress concerning the mounting structure enable us to reject mechanical frequency resonances above 3 kHz. At the same time, more free place was available. So, the greatest possible diameter is taken for the "sandwich" of quartz (see fig. 1) (condensator - resonator - condensator). We have realized some prototypes with geometrical definition assistance from Dr J.J. BOY of the ENSMM/LCEP.

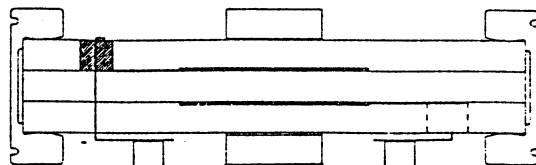


Figure 1 - Quartz crystal "sandwich"

#### 2.2 - Motional parameters at 5 MHz

The T2111 package implied that we use an SC-cut 3rd overtone resonator. We were ready to assume a not "optimized" resonator and our objectives were not too much ambitious.

Frequency :  $4\,999\,991 \pm 4$  Hz  
Turn over point :  $78^\circ\text{C} \pm 4$   
Quality factor :  $> 1.6 \cdot 10^6$   
Serial resistance :  $< 100 \Omega$   
Motional inductance :  $> 4$  H  
Aging :  $< 3 \cdot 10^{-11}$ /day  
First anharmonic mode :  $> 30$  kHz  
Encapsulated in HC-40 can (or T2111).

### 2.3 - Results

Two batches have been manufactured. The first one is to confirm the good geometrical design, as the second is to optimize the final frequency adjustment. That one has to be better than  $\pm 4$  Hz when  $\pm 8$  Hz is required at 10 MHz. That point is not really a problem because our manufacturing line is able to adjust the final frequency at  $\pm 2$  Hz by chemical etching. A dispersion and a frequency deviation after enclosure has to be taken into account when customer's specification is written. Raw data are presented on Table 1.

N°	Freq (Hz)	Ttop (°C)	Q x10 <sup>6</sup>	Rr (Ohm)	L1 (H)
55.03	4 999 989.2	75.4	2.1	73	5.2
55.08	4 999 989.3	74.4	2.3	77	5.6
55.10	4 999 997.2	76.6	2.5	72	5.7
55.11	4 999 997.3	77.4	2.4	72	5.7
55.13	4 999 995.5	77	2.4	72	5.5
60.01	4 999 995.5	74	2.4	68	5.2
60.02	4 999 989.2	74	2.4	68	5.2
60.03	4 999 991.5	75	2.3	75	5.4
60.04	4 999 991.3	74.4	2.3	70	5.2
60.05	4 999 988.3	74	2.1	79	5.2
60.06	4 999 986.6	75	2.4	69	5.3
60.07	4 999 990.5	76.2	2.0	81	5.1

Table 1

Frequency and resistance deviations versus temperature are presented fig.2. This test is made according to CEI 444 method. The turn over point temperature is calculated by the best 3rd order fit of the measured data. The cubic coefficients are :

$$\begin{aligned}
 a &= 0.86 \cdot 10^{-6}/^{\circ}\text{C} \\
 b &= -12.68 \cdot 10^{-9}/^{\circ}\text{C}^2 \\
 c &= 54 \cdot 10^{-12}/^{\circ}\text{C}^3
 \end{aligned}$$

Generally, the experimental points are close to the fitted curve and the difference is lower than  $1 \cdot 10^{-8}$  in frequency fractionnal part :

$$\Delta F/F = a(T-T_0) + b(T-T_0)^2 + c(T-T_0)^3$$

with  $T_0 = 25^{\circ}\text{C}$ .

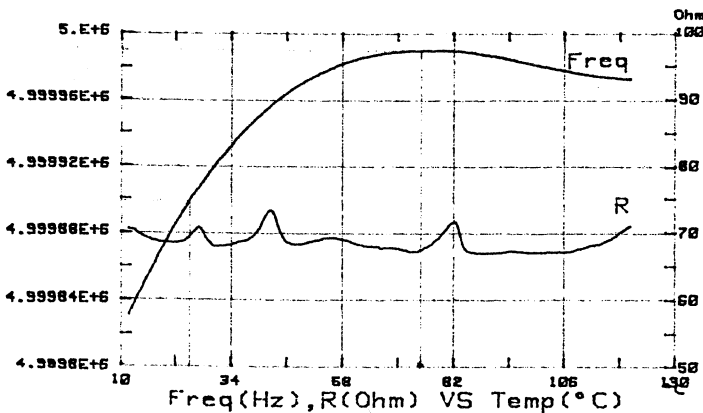


Figure 2

The impedance of the crystal is recorded fig. 3. The first significant unwanted mode is at about 5.070 MHz with a 1 k $\Omega$  motional resistance.

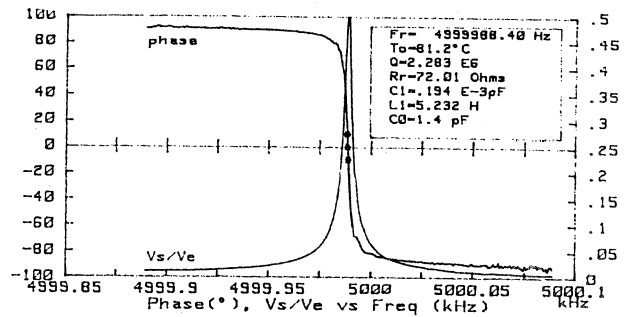


Figure 3

### III - THE 5 MHz OCXO

#### 3.1 - Context

A few years ago, we have designed a small size 10 MHz OCXO (0.1 liter), with very good phase noise and short term stability. Our electronic is perfectly known, tested and produced. Some minor changes have permitted to produce a lot of 8.192 MHz OCXO with acceptable yield concerning the frequency deviation versus temperature range :  $\Delta F/F \leq 5 \cdot 10^{-10}$  with  $0 < T < 70^{\circ}\text{C}$ , and  $\Delta F/F \leq 2 \cdot 10^{-10}$  for  $20 < T < 57^{\circ}\text{C}$ .

#### 3.2 - Development

The 5 MHz 3rd overtone SC-cut presents a typical resistance of 75  $\Omega$ . This value is an advantage for the power dissipated inside the crystal. Anyway, we are sure to keep our same PC board. The phase noise and the computed short term, stability are presented on fig. 4 and 5.

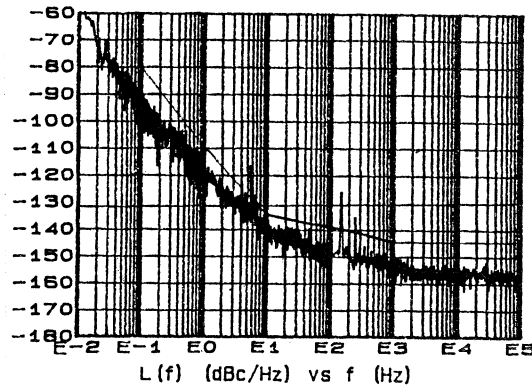


Figure 4

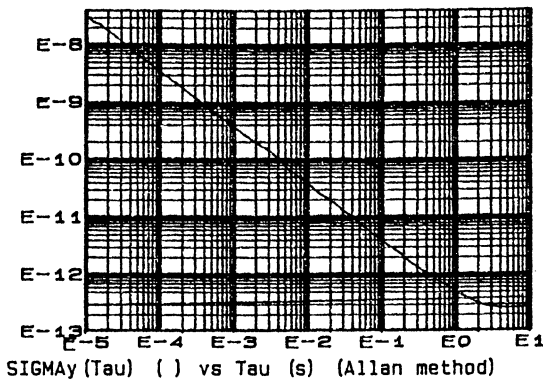


Figure 5

We note the value of  $\sigma = 3.10 \cdot 10^{-13}$  at 3 Hz.

The aging of the best piece (two were tested) is presented in fig. 6 with extrapolation over 10 years, figure 7.

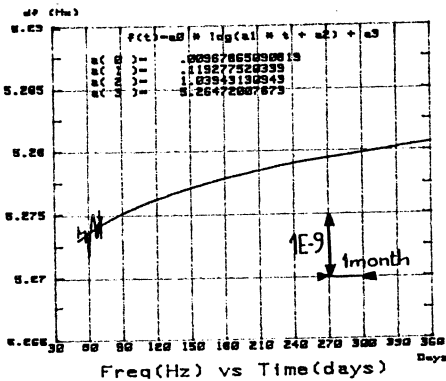


Figure 6

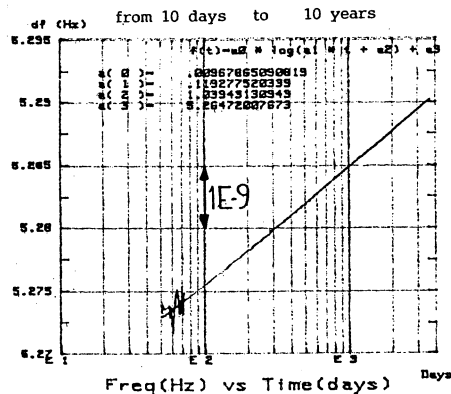


Figure 7

### 3.3 - g-sensitivity and vibration

The accelerometric sensitivity was measured on 1 piece by 2g-tip over method. Results are presented in table 2

N°	OX	OY	OZ	Γ
55.26	$2.10 \cdot 10^{-10}$	$8.10 \cdot 10^{-10}$	$2.10 \cdot 10^{-9}$	$2.2.10 \cdot 10^{-9}$

Table 2

A validation test of our mounting structure inside the resonator has been performed using a rugged OP22 type. For the three axes, frequency is recorded and the main frequency shift is obtained when shaker amplifier is switched ON. Probably, its magnetic field is the origin of the phenomena. We note several time domains:

1. Stabilisation.
2. Switch ON.
3. Vibration.
4. Vibration STOP.
5. Switch OFF.
6. Stabilisation.

We note that frequency drift between 1 and 6 is about  $2.10 \cdot 10^{-9}$ , so, no subsequent remaining effect has been noticed. This test is presented figure 8.

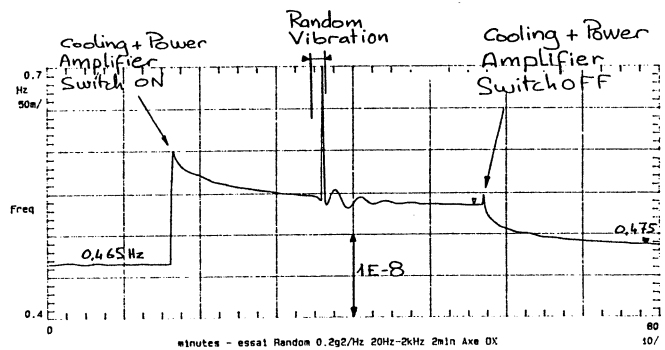


Figure 8

### IV - 10 MHz or 5 MHz ? : COMPARISON

The user who multiply the frequency up to hyper frequency domain will appreciate the table here below :

Item	5 MHz (first piece)	10 MHz (the best L(R))
L(f)		
0.1 Hz	-92 dBc/Hz	-90dBc/Hz
1 Hz	-120 dBc/Hz	-120 dBc/Hz
10 Hz	-140 dBc/Hz	-142 dBc/Hz
100 Hz	-150 dBc/Hz	-153 dBc/Hz
1 kHz	-155 dBc/Hz	-154 dBc/Hz
$\sigma_y(\tau)$		
10 $\mu$ sec	$3E-8$	$1.8E-7$
100 $\mu$ sec	$3E-9$	$1.8.E-9$
1 msec	$3E-10$	$1.8E-10$
10 msec	$3E-11$	$1.8E-11$
100 msec	$4E-12$	$1.8E-12$
1 sec	$5E-13$	$2.2E-13$
10 sec	$3E-13$	$1.8E-13$
Aging		
/day	$3E-11$	$5E-11$
/month	$1E-9$	$1.5E-9$
(typic. /year results) /15 years	$7E-9$	$1E-8$
	$6E-8$	$1.E-7$
g-sensitivity on the worst axis	$2E-9/g$	$1.5.E-10/g$

Table 3

Here below some comments about table 3:

4.1 -  $L(f)$  is not directly comparable. If  $N$  is the multiplication factor, we have :

$$L_m(f) = L(f) + 20 \log N$$

where  $L_m(f)$  is the phase obtained after multiplication. It means that 6 dB have to be added to the 5 MHz  $L(f)$  before comparison to the 10 MHz  $L(f)$ .

bva INDUSTRIE has more experience at 10 MHz so, the values of  $L(f)$  presented are those obtained for phase noise reference at 10 MHz. At 5 MHz,  $L(f)$  is for our first piece.

4.2 - *Short term stability* is not degraded by multiplication. This point can influence the choice of 5 MHz.

4.3 - *Aging is normally better at 5 MHz* due to the more important material working compared to the exchange surface. The yield of aging is better at 5 MHz for  $5 \cdot 10^{-11}$ /day for example but some performance like  $3 \cdot 10^{-10}$  per year was obtained at 10 MHz. Our first piece at 5 MHz seems to exhibit a  $2 \cdot 10^{-9}$  for the first year (see fig. 6) and  $4 \cdot 10^{-9}$  for the next 15 years (see fig. 7).

## V - CONCLUSION

bva INDUSTRIE is able to supply OCXO at 5 MHz in the same volume than 10 MHz using a BVA crystal at 5 MHz, with BVA electrodeless technology of course, the crystal shall be available with high reliability option like 10 MHz which is used now as Fly Model for space application.

## VI - ACKNOWLEDGMENTS

The author wishes to thank Prof. R.J. BESSON and Dr J.J. BOY of LCEP for their help for geometric choice guidance.

## VII - BIBLIOGRAPHY

- 1 J. NORTON, R.J. BESSON, 1993, "Tactical BVA quartz resonator performance"  
Proc., IEEE Frequency Control Symp. pp 609-613.
- 2 J. NORTON, May 1991, "BVA type oscillators for spacecraft"  
Proc. of the 45th Annual Symposium on Frequency Control, pp 426-430.
- 3 R.J. BESSON, June 1977, "A new electrodeless resonator design"  
Proc. of the 31st Annual Symposium on Frequency Control.
- 4 R. DELAITE, March 1989, "Special miniaturized SC-cut quartz resonator for severe environment applications"  
Proc. of the 3rd EFTE, pp 296-300.
- 5 Ch. LONGET, G. ROBICHON, March 1995, "An electrodeless BT cut, 5th overtone quartz crystal resonator at 50 MHz"  
Proc. of the 9th EFTE, pp 141-145.

## NEW THERMAL TRANSIENT MODEL OF CRYSTAL RESONATOR OF THICKNESS-SHEAR VIBRATIONS

Yuriy S Shmaliy

"Sichron" Center, 4 Skripnika Str., Kharkiv, 310057, UKRAINE, yush@sichr.kharkov.ua

### ABSTRACT

This paper presents a new effective model of frequency thermal transient of vacuum quartz crystal resonator of thickness-shear vibrations. There are introduced the response times  $\tau_i$ ,  $i = \overline{1,4}$  and thermal dynamic coefficient  $S_D$  which are coupled with A. Ballato's coefficient  $\tilde{\alpha}$  by the relationship  $S_D = -\tilde{\alpha}\varphi(\tau_i)$ , where  $\varphi(\tau_i)$  is the coefficient defined by the resonator design. The method has been worked out of  $\tau_i$  calculation. The model has been used, in particular, for data approximation of the frequency thermal transient of AT-cut resonator  $h_{513}$  mode, 5.16 MHz excited by the modulation method within an oven controlled Colpitts oscillator. A good prediction agreement with experimental data in the different temperature ranges is shown.

### INTRODUCTION

Thermal frequency instability, as well as an aging, is one of the most significant limitations of BAW crystal resonators. Its control is possible by filtering methods if the model is known of thermal transient frequency characteristic of resonator. Attempts to create such models had been under-taken more than once [1-5]. Nevertheless, only Ivlev's thermal dynamic frequency coefficient for a frequency range [1,2] and Ballato's  $\tilde{\alpha}$  coefficient [3] for a time range of temperature changes has gained currency. In [4-6] and then in [7-10] there had been carried out theoretical investigations of resonator frequency processes coupled with dynamic influence of ambient temperature. Special significance has the paper [11] in which the results are given of experimental studies of thermal flows and their contributions (in percents) into the processes of heat transport as for the vacuum resonator. Results of these and some other papers had further been used in [12-14] for the evaluation of the frequency change in self-contained crystal plate.

In this paper, creation of a thermal transient frequency model is carried out with general positions of a dynamic characteristic theory on a ground of physical analysis of proceeding thermal processes in resonator and oscillator within an oven system. The method and algorithm are worked out to calculate the model response times. This had been done as for the different insights on an integral temperature influence of a piezo plate to the static and dynamic behavior of its frequency. The model has been used for the experimental data approximation of the frequency thermal transient of AT-cut resonator  $h_{513}$

mode, 5.16 MHz that was excited by the modulation method [15] within an oven controlled Colpitts oscillator [18]. A good agreement between data and prediction is shown. Also, there are given the experimental and calculated plots of frequency thermal transients.

### THERMAL TRANSIENTS IN CRYSTAL RESONATOR

Below we will consider a quartz crystal unit that operates under the temperature influence within an OCXO. We will select as main resonator parts a crystal plate, crystal holders, and an enclosure.

#### Justification of the thermodynamic model

Taking results obtained by Valentin et al [9], let us separate general thermal flows in vacuum resonator as follows.  $T_k^{in}$  is the internal flow that forms closed way through the parallel parts of oscillator electronic plate and resonator enclosure, crystal holders, and piezo plate.  $T_k^{1ex}$  is the first external flow closed through the resonator enclosure.  $T_k^{2ex}$  is the second external flow formed by an oscillator body. It may be also more than one external flow within an OCXO as for the resonator. As the heat transfer and exchange by radiation make less significant effect particularly in a vacuum crystal unit [13], the model of the main resonator thermal circuits may be presented as shown in figure 1. Here A is a part of a crystal holder; B and C are edges and center of a crystal plate. In the general case there is hard to simulate the inter space between oscillator and resonator. Let us mark it as D and consider as delay line with  $\tau_z$  response time. Here  $\tau_z = 0$ , if a resonator has only the one external circuit.

#### Partial functions of thermal transient

Considering crystal holders as thin shafts with axes are started at points of their contacts with a piezo plate, let us write the thermal conductivity equation in a form of  $\frac{\partial u}{\partial t} = \frac{k_c}{c_c \rho_c} \frac{\partial^2 u}{\partial x^2}$ , where  $u$  is an ambient temperature,  $0 \leq x \leq l$  is a current coordinate,  $l$  is a crystal holder length,  $k_c$ ,  $c_c$  and  $\rho_c$  are the heat conductivity coefficient, specific heat and density of holder material,  $t$  is a current time. According to [11] one may consider a crystal holder sides and its part at the point of  $x = 0$  as heat isolated, and at the point of  $x = l$  as supported with the

surrounding temperature  $\tilde{u}_1$ . It leads to the boundary conditions in the form of  $\left. \frac{\partial u}{\partial x} \right|_{x=0} = 0$  and  $u|_{x=l} = \tilde{u}_1$ . With this, for uniform start conditions  $u|_{t=0} = u_0$  the solution of equation at the point of  $x = 0$  is given as

$$u(t) = \tilde{u}_1 + \frac{4\Delta u}{\pi} \sum_{n=0}^{\infty} \frac{(-1)^n}{2n+1} e^{-\frac{(2n+1)^2 t}{\tau_c}}, \quad (1)$$

where  $\Delta u = u_0 - \tilde{u}_1$  and  $\tau_c = 4l^2 c_c \rho_c / \pi^2 k_c$ . Calculation shows that while neglecting in (1) all rows terms excluding the first one we may get the averaged in time error no more than few percents. Thus, for creation of the thermal transient model we may use the approximate solution in a form of

$$\Delta u_1 \cong \Delta \tilde{u} \left( 1 - e^{-\frac{t}{\tau_c}} \right), \quad (2)$$

where  $\Delta u_1(t) = u_1(t) - \tilde{u}_1$ ,  $u_1(t)$  is function (1) for  $n = 0$ ,  $\Delta \tilde{u}$  is a temperature increment.

For evaluation of the thermal transient parameters of crystal plate let us study a main heat conductive equation  $c\rho \frac{du}{dt} - \text{div}(\kappa \text{grad}u) = F(x, y, z, t)$ , where  $c$ ,  $\rho$  and  $\kappa$  are the specific heat, density and heat conductivity of quartz,  $F(x, y, z, t)$  is a function of internal sources of heat. On cylindrical  $r$ ,  $\varphi$ ,  $z$  coordinates of a disk piezo plate this equation has the form [6]

$$c\rho \frac{\partial u}{\partial t} - \bar{\kappa}_1 \left\{ (1 - \bar{\alpha} \cos 2\varphi) \left( \frac{\partial^2 u}{\partial r^2} + \frac{\partial u}{r \partial r} \right) + [(1 + \bar{\alpha} \cos 2\varphi) \frac{\partial^2 u}{\partial \varphi^2} - 2\bar{\alpha} \frac{\partial u}{\partial \varphi} \sin 2\varphi] \right\} - \bar{\kappa}_3 \frac{\partial^2 u}{\partial z^2} = F(r, \varphi, z, t), \quad (3)$$

where  $\bar{\alpha} < 0.53$ ,  $\bar{\kappa}_1$  and  $\bar{\kappa}_3$  are the components of conductivity tensor in directions of turned crystal axis  $x$  and  $z$  of quartz respectively. Accounting special features of a resonator operation (the initial heat distribution in a volume of a piezo plate) and a resonator structural features, the nonstationary solution of (3) for an arbitrary initial and boundary conditions in a general case has a form

$$u = u_0 + \Delta u + \sum_{k=0}^{\infty} \sum_{m=0}^{\infty} \sum_{l=0}^{\infty} \left( a_{kml} - b_{kml} e^{-\frac{t}{\tau_{kml}}} \right) \chi_{kml}(r, \varphi, z), \quad (4)$$

where  $u_0$  and  $\Delta u$  are the initial environmental temperature and its increment,  $k$ ,  $m$  and  $l$  are integer numbers corresponding to  $\chi_{kml}(r, \varphi, z)$  basic functions of equation (3) in directions of  $z$ ,  $\varphi$  and  $r$  respectively. Here also  $a_{kml}$  and  $b_{kml}$  are the coefficients, and  $\tau_{kml}$  is the response time of system of functions [4-6].

The equation (4) describes the temperature behavior both at the center ( $r = 0$ ) and on the edges ( $r = R$ ) of a crystal plate. Meanwhile, supposing the solution error in

few percents for the real coefficient  $h = 1 \dots 1000$  [4] of a crystal plate thermal exchange with environment, one may restrict this solution (4), as in the case of (2), with the approximation form of

$$\Delta u_{QK, Q0} \cong \Delta u \left( 1 - e^{-\frac{t}{\tau_{QK, Q0}}} \right), \quad (5)$$

where  $\Delta u_{QK, Q0} = u_{QK, Q0} - u_0$ ,  $\tau_{QK, Q0}$  are response times correspondingly for edges and a center of crystal plate.

## THE MODEL OF FREQUENCY THERMAL TRANSIENT

For the thermal difference between center and edges of a piezo plate  $\Delta u_Q = u_{Q0} - u_{QK}$  that causes a frequency offset  $\Delta f(\Delta u_Q)$  due to a force-frequency effect in crystal [16], we will use the linear transform operator [13]

$$L\{\Delta u_Q\} = \delta f(\Delta u_Q) = 2\beta_f H D a_f \overline{K_f}(\varphi) \Delta u_Q, \quad (6)$$

where  $\beta_f = 3.85 \times 10^6 \text{ NK}^{-1} \text{ m}^{-2}$  [13],  $a_f = f_0 \eta / Dn$ ,  $H$  and  $R$  are thickness and radius of a crystal plate,  $f_0$  is a vibration frequency of resonator,  $\eta \approx 1$  is the correction coefficient,  $n$  is a number of resonator mechanical vibration harmonic,  $\overline{K_f}(\varphi)$  is an averaged over  $\varphi$  value of Rataiski coefficient [16].

## Operator model

Basing upon the thermal flows model (fig.1), let us define the operator circuit of resonator as a converter of the ambient temperature variations  $\Delta T$  into its frequency changes  $\delta f$  (fig.2). The delay operator we will write as

$$K_z(p) = k_z e^{p\tau_z}, \quad (7)$$

where  $p$  is Laplace operator,  $k_z$  is an attenuation coefficient of ambient temperature influence that determine the effectiveness of the heat isolation ( $k_z < 1$ ) and oven ( $k_z \ll 1$ ) systems. Circuit gains corresponding to parts of crystal holders  $K_C(p)$  (A), crystal plate edges  $K_{QK}(p)$  (B), and center of crystal plate  $K_{Q0}(p)$  (C) we will write according to (2) and (5) in the form of

$$K_{C, QK, Q0}(p) = \frac{k_{C, QK, Q0}}{1 + p\tau_{C, QK, Q0}}, \quad (8)$$

where for a vacuum unit one may take  $k_{C, QK, Q0} \cong 1$ . A gain  $K_Q(p)$  correspond to the integral plate temperature  $T_i$  that causes an offset of frequency with respect to non-linear static frequency-temperature characteristic of resonator within in oven

$$\delta f_1(t) = \eta_1 [T_i(t)] = c'_1 T_{ov}(t) + c'_2 T_{ov}^2(t) + c'_3 T_{ov}^3(t), \quad (9)$$

where  $T_{ov} = T_l - T_0$ ;  $c_1'$ ,  $c_2'$  and  $c_3'$  are the approximation polynomial factors;  $T_0$  is an oven temperature at NTP ( $T_0 = 20^\circ\text{C}$ ). A characteristic slope of a differential temperature  $\Delta T_D = \Delta T_{Q0} - \Delta T_{QK}$  transformation into dynamic frequency change  $\delta f_D$  we will define as

$$S_D = \frac{L\{\Delta T_D\}}{\Delta T_D} = \frac{\delta f_D}{\Delta T_D} \quad (10)$$

### Functions of a differential thermal transient

Let us consider the formation processes of portion temperature and frequency changes in resonator. After a temperature step action with the value of  $\Delta T$ , the crystal holders and crystal plate edges start to warm-up with a delay time  $\tau_Z$  (7) and with  $\tau_C$  and  $\tau_{QK}$  (8) response times by the low of

$$\Delta T_{QK}(t) = \Delta T k_z k_c k_{QK} \left( 1 - b_1 e^{-\frac{t'}{\tau_C}} + b_2 e^{-\frac{t'}{\tau_{QK}}} \right), \quad (11)$$

where  $t' = t - \tau_Z$ ,  $b_1 = \tau_C / (\tau_C - \tau_{QK})$ ,  $b_2 = \tau_{QK} / (\tau_C - \tau_{QK})$ . The low of a temperature change at a center of crystal plate is defined as

$$\Delta T_{Q0}(t) = -\Delta T k_Q \left( 1 - a_1' e^{-\frac{t'}{\tau_C}} - a_2' e^{-\frac{t'}{\tau_{QK}}} - a_3' e^{-\frac{t'}{\tau_{Q0}}} \right), \quad (12)$$

where  $a_1' = \tau_C^2 (\tau_{QK} - \tau_{Q0}) / Y$ ,  $a_2' = \tau_{QK}^2 (\tau_{Q0} - \tau_C) / Y$ ,  $a_3' = \tau_{Q0}^2 (\tau_C - \tau_{QK}) / Y$ ,  $k_Q = k_z k_c k_{QK} k_{Q0}$ ,  $Y = \tau_C^2 (\tau_{QK} - \tau_{Q0}) + \tau_{QK}^2 (\tau_{Q0} - \tau_C)$ . Function of a difference low of a temperature change with account of (11) and (12), and with  $k_{Q0} \cong 1$ , that holds true for a vacuum resonator, is

$$\Delta T_D(t) = -\Delta T k_z k_c k_{QK} \left( a_1' e^{-\frac{t'}{\tau_C}} + a_2' e^{-\frac{t'}{\tau_{QK}}} + a_3' e^{-\frac{t'}{\tau_{Q0}}} \right), \quad (13)$$

where  $a_1' = -\frac{\tau_C}{\tau_C - \tau_{QK}} + \frac{\tau_C^2 (\tau_{QK} - \tau_{Q0})}{Y}$ ,  $a_2' = \frac{\tau_{Q0}^2 (\tau_C - \tau_{QK})}{Y}$ ,

$a_3' = \frac{\tau_{QK}}{\tau_C - \tau_{QK}} + \frac{\tau_{QK}^2 (\tau_{Q0} - \tau_C)}{Y}$ . Finally, a frequency drift corresponding to (13) has a form of

$$\delta f_D(t) = S_D \Delta T_D(t), \quad (14)$$

### Functions of an integral thermal transient

Let us take that the distribution of resonator vibration amplitudes is a subject to the Hermite-Gauss' low [17]

$$v_{npq} = e^{-x^2 \frac{\alpha_n}{2}} H_p(x \sqrt{\alpha_n}) e^{-z^2 \frac{\beta_n}{2}} H_q(z \sqrt{\beta_n}), \quad (15)$$

where  $n$  is a number of mechanical harmonic,  $x$  and  $z$  are the coordinates in a plane of plate,  $p, q$  is an index of anharmonic vibrations,  $\alpha_n$  and  $\beta_n$  are determined

in [17],  $H_p$  and  $H_q$  are Hermite's polynomials. Distribution (15) causes the correspondent temperature field. Thus, an integral temperature change  $\Delta T_l$  is determined with (4) by an integral temperature averaged over the crystal plate volume. Here, a transient function is

$$h_l(t) = \frac{\bar{u}(r, \varphi, z, t) - \bar{u}(r, \varphi, z, 0)}{\bar{u}(r, \varphi, z, \infty) - \bar{u}(r, \varphi, z, 0)}, \quad (16)$$

where  $\bar{u}(r, \varphi, z, t) = \frac{1}{2\pi R H} \int_0^R \int_0^{2\pi H} u(r, \varphi, z, t) dr d\varphi dz$ ,  $t \in \tau_Z, \infty$ .

An argument increment in (9) for (16) we will write as  $\Delta T_q(t) = \Delta T k_l h_l(t)$  where  $k_l$  is a static coefficient.

### Resulting function of a frequency thermal transient

Let us determine a resulting function of thermal transient of frequency with account of (9) and (14) as

$$\delta f(t) = \delta f_D(t) + \delta f_l(t), \quad (17)$$

where for calculation of  $\delta f_l(t)$  according to (9) we will transform  $T_l$  into the change of the ambient temperature  $\Delta T(t) = T_b - T_0 + \Delta T h_l(t)$ , where  $T_b$  is its initial value. Proceeding from  $\delta f_l(t) = \eta_l[\Delta T_l(t)] = \eta_Q[\Delta T(t)]$  let us write

$$\eta_Q(t) = c_1 \Delta T(t) + c_2 \Delta T^2(t) + c_3 \Delta T^3(t), \quad (18)$$

where  $c_1 = c_1' k_l$ ,  $c_2 = c_2' k_l^2$  and  $c_3 = c_3' k_l^3$ . Now we will find the transient function (17) supposing that (16) is defined by integral low from differential function (14). Here  $S_R \int_{\tau_Z}^t \Delta T_D(t) dt = -S_R \Delta T \varphi_3 h_l(t)$  is validated,

where  $\varphi_3 = a_1' \tau_C + a_2' \tau_{QK} + a_3' \tau_{Q0}$ ,

$$h_l(t) = 1 - \frac{1}{\varphi_3} \left( a_1' \tau_C e^{-\frac{t'}{\tau_C}} + a_2' \tau_{QK} e^{-\frac{t'}{\tau_{QK}}} + a_3' \tau_{Q0} e^{-\frac{t'}{\tau_{Q0}}} \right), \quad (19)$$

For the frequency change corresponding to (19) we may finally write

$$\begin{aligned} \delta f^l(t) = & c_1 \Delta T h_l(t) - S_D \Delta T \left( a_1' e^{-\frac{t'}{\tau_C}} + a_2' e^{-\frac{t'}{\tau_{QK}}} + a_3' e^{-\frac{t'}{\tau_{Q0}}} \right) + \\ & + c_2 \Delta T^2 h_l^2(t) + c_3 \Delta T^3 h_l^3(t), \end{aligned} \quad (20)$$

Comparing (20) with Ballato's form

$$\delta f^B(t) = c_1 \Delta T(t) + \bar{\alpha} \frac{dT(t)}{dt} + c_2 \Delta T^2(t) + c_3 \Delta T^3(t), \quad (21)$$

we come to conclusion that these models are equal. It is easy to show from (20) and (21) comparison that

$$\tilde{a} = -S_D \varphi_3 = -S_D \frac{\tau_{Q0}(\tau_{QK} - \tau_C)(\tau_{Q0} - \tau_C)(\tau_{Q0} - \tau_{QK})}{\tau_C^2(\tau_{Q0} - \tau_{QK}) + \tau_{Q0}^2(\tau_{QK} - \tau_C) - \tau_{QK}^2(\tau_{Q0} - \tau_C)}. \quad (22)$$

So, we have worked out the model of vacuum resonator frequency thermal transient (20) defined as reaction to the sudden rise of an ambient temperature. Further, we will use this model (20) practically. In addition, we will take the differential and integral functions (14) and (18) accounting that  $h_f(t)$  is given by the low (20).

### CALCULATION OF THE MODEL PARAMETERS

The task of parameters  $\tau_Z$ ,  $\tau_C$ ,  $\tau_{QK}$ ,  $\tau_{Q0}$  and  $S_D$  calculation is reduced to approximation of the experimental thermal transient data. Here the following algorithm is turned out to be more convenient. Let us find out with the help of iteration procedure the initial values  $\tau_Z^0$ ,  $\tau_C^0$ ,  $\tau_{QK}^0$ ,  $\tau_{Q0}^0$  and  $S_D^0$ . Then let us seek the precision solution of the equation system forming from (20) with criteria of minimum of root-mean-square error and with the use of the start values. In particular case, for the linear form of frequency versus temperature characteristic  $\delta f_f(t) = c_1 \Delta T$  after determination of the above mentioned initial values, we may bring (20) into the form

$$y(t) = \delta f(\infty) - g_1 e^{-\alpha_1 t} - g_2 e^{-\alpha_2 t} - g_3 e^{-\alpha_3 t}, \quad (23)$$

where  $g_{1,2,3} \equiv S_D \Delta T a_{1,2,3} e^{-\alpha_{2,3,4} t}$ ,  $\alpha_{2,3,4} = 1/2 \tau_{C,QK,Q0}$ ,  $z \in [-1, 1]$ . Also, let us use an expansion  $e^{\alpha z} = I_0(z) + 2 \sum_{k=1}^{\infty} I_k(\alpha) T_k(z)$ , where  $T_k(z)$  is Chebyshev series,  $I_k(\alpha)$  is modified Bessel function of imaginary argument. After that we will transform (23) into the form of  $y(z) = \sum_{j=0}^{\infty} d_j T_j(t)$ , where

$$d_0 = \delta f(\infty) - \sum_{k=0}^{\infty} \frac{1}{2^{2k} (k!)^2} (g_1 \alpha_2^{2k} + g_2 \alpha_3^{2k} + g_3 \alpha_4^{2k}), \quad (24)$$

$$d_n = \sum_{k=0}^{\infty} \frac{(-1)^{n+1} (t')^{n+2k}}{2^{2n+4k-1} k! (n+k)!} \left( \frac{g_1}{\tau_C^{n+2k}} + \frac{g_2}{\tau_{QK}^{n+2k}} + \frac{g_3}{\tau_{Q0}^{n+2k}} \right), \quad (25)$$

Here, corresponding alternative coefficients  $e_k^0$  and  $e_k^n$  of (24) and (25) series are found respectively by  $e_k^0 = e_{k-1}^0 \frac{\alpha^2}{4k^2}$  and  $e_k^n = e_{k-1}^n \frac{\alpha^2}{4k(n+k)}$  recurrent relationships. Coefficients of (24) and (25) rows determine the

equation system that has to be resolved about  $\tau_Z$ ,  $\tau_C$ ,  $\tau_{QK}$ ,  $\tau_{Q0}$  and  $S_D$  parameters. It may mark that in our case we had  $k < 15$ . However, precision calculation of the model parameters may be unnecessary if an iteration procedure brings quickly to the anticipated results by criteria of minimum of root-mean-square error.

### EXPERIMENTAL RESULTS

Let us consider the results of the model (20) usage for the experimental data processing of vacuum resonator thermal transients. Experimentally the vacuum quartz crystal resonator of PK-187 type, AT-cut had been placed into the oven with the temperature  $T_{ov} = 65^\circ C$  of frequency-temperature characteristic minimum of the main mode  $h_{511}$  (5 MHz). By the modulation method [19] it had been measured the thermal transients of the mode  $h_{513}$  (~5.16 MHz) that has slope of frequency-temperature characteristic at the point of oven approximately of  $\approx 1 Hz / K$ . The approximation coefficients of the mode  $h_{513}$  frequency-temperature characteristic (18) under the oven condition with  $T_0 = 20^\circ C$  had been  $c_1 = 7.226 \times 10^{-12} / K$ ,  $c_2 = -1.886 \times 10^{-11} / K^2$  and  $c_3 = 7.74 \times 10^{-14} / K^3$ .

A step changes of ambient temperature caused the oven response to heating-cooling and brought to resonator frequency transfer from one point of frequency-temperature characteristic to another by the transient low. The averaged approximation results obtained for the model (20) in the different ranges of temperature are  $\bar{\tau}_Z = 4.676$  min,  $\bar{\tau}_C = 4.647$  min,  $\bar{\tau}_{QK} = 4.310$  min,  $\bar{\tau}_{Q0} = 16.996$  min, and  $S_D = (-0.28 + 0.21T) \times 10^{-10} / K$ . The discordance of  $\bar{\tau}_Z$ ,  $\bar{\tau}_C$ ,  $\bar{\tau}_{QK}$ ,  $\bar{\tau}_{Q0}$  valuations with regard to the particular cases had not been more that ten percents.

Figures 3 through 5 show the results of measurements and prediction of frequency thermal transient in the high, middle and low temperature ranges. There are given also the functions of the errors calculated as «prediction minus data». One may see from these figures that the individually found approximation functions pass near the data with the lowest distance. The accurate prediction curves fit to the data good and the coarse ones (with  $\pm 1^\circ K$  error of  $T_b$  and  $\Delta T$  measurement) are less precision. These coarse valuations bring significant errors of the model in high and low temperature ranges (figures 3 and 5). In the middle range (fig.4) the errors appeared as less visible. In the fig.8, there are shown the calculated functions of the dynamic frequency drifts (14) for the all considered cases. As it may be seen, all these prediction curves have similar behaviors in time. Here, the bold type line corresponds to the averaged magnitudes of parameters  $\bar{\tau}_Z$ ,  $\bar{\tau}_C$ ,  $\bar{\tau}_{QK}$  and  $\bar{\tau}_{Q0}$ .

Figure 7 shows the changes on temperature the Ballato's and thermal dynamic coefficients  $\tilde{a}$  and  $S_D$ . It may mark here that behavior of  $S_D(T^\circ)$  has more systematic character in opposite to  $\tilde{a}(T^\circ)$ . It is explained by the fact that Ballato's coefficient  $\tilde{a}$  is a function on temperature and response times (22). On the contrary, the thermal dynamic coefficient  $S_D$  depends only on temperature. It had been considered during studies the surface plots of the thermodynamic frequency drifts measured after a temperature step decrease and increase within the different temperature ranges. It is follows from these plots analysis that the best prediction results in our case took place for the temperature step decrease. With the temperature increase, there had not been a success in getting the accurate temperature step. Only by this reason, we have gotten the great resulting errors in this case.

## CONCLUSION

Analyzing results of these studies, we came to the following conclusions. The model (20) is effective for thermal frequency behavior prediction of a vacuum crystal resonator in an arbitrary range of ambient temperature. The magnitudes  $\tau_z$ ,  $\tau_C$ ,  $\tau_{OK}$  and  $\tau_{Q0}$  are constant for each resonator unit. A thermal dynamic coefficient  $S_D$  is a function of temperature, and its behavior obeys to the low closed to the linear one. The dependence on temperature of Ballato's coefficient  $\tilde{a}$  is also closed to the linear low but has greater dispersion (fig.7). Each thermal frequency drift (fig.6) is a subject to the low (13), and its maximum is proportional to  $S_D$  and  $\Delta T$  according to (14).

The approximation errors caused by thermal hysteresis effect in resonator, AT-cut, PK-187 in a steady state regime constituted of  $(-24...+39) \times 10^{-10}$  and had tendency to 2-3 times increase as the error of an ambient temperature measurement is  $(1-2)^\circ K$ . This error has the greatest appearance in the transient range where its speed of change the largest and, in our cases, constituted of  $(32.9...7.36)\%$  for all data. At the same time the averaged and root-mean-square errors of approximation constituted of  $(-1.5...4.6) \times 10^{-10}$  and  $(1.3...2.5) \times 10^{-10}$  respectively. The predicted effectiveness of the thermal transient model with its use for the digital temperature filtering may be determined as a ratio of non-linearity maxima of the measured curves and calculated curves of errors in time. Calculations shown that the effectiveness of the model (20) is 3.0...13.6 with the averaged value of 7.0 for the all data.

Finally, we may mark that the model (20) is being used for the algorithm creation of digital temperature filtering in an OCXO and crystal standard have been realized with the use of the modulation method [15]. The results of these studies will be published later.

## REFERENCES

1. Ivlev L, 1965, "On thermodynamic coefficient of resonator frequency", *Voprosy radioelektroniki, Seria 3, Detali i komponenty apparatury, Vol.2*, (in Russian)
2. Ivlev L, 1967, "Thermal coefficient of frequency and temperature dynamic characteristics of precision quartz crystal resonators", *Elektronnaia tehnika, Seria 9, Radiokomponenty, Vol.4*, 20-28. (in Russian)
3. Ballato A, 1979, "Static and dynamic behavior of quartz resonators", *IEEE Trans. Sonics and Ultrason.*, SU-26(4), 299-306.
4. Holland R, 1974, "Non uniformly heated anisotropic plates: I Mechanical distortion and relaxation", *IEEE Trans.*, SU-21, N3, 171-179.
5. Holland R, 1974, "Non uniformly heated anisotropic plates: II Frequency transients in AT and BT quartz plates", in Proc. of IEEE Ultrasonics Symp., 582-588.
6. Barjin V, Krutophalov E, Tartakovsky I, 1975, "Studies of non stationary temperature field of piezo plate", *Elektronnaia tehnika, Seria 5, Radiodetali i radiokomponenty, Vol.5*, 56-58. (in Russian)
7. Stevens D, Tiersten H, 1980, "Transient thermally induced frequency excursions in AT- and SC-cut quartz trapped energy resonators", in Proc. of 34<sup>th</sup> IEEE AFCS, 208-217.
8. Janiaud D, Besson R, Gagnepain J, Valdois M, 1981, "Quartz resonator thermal transient due to crystal support", in Proc. of 35<sup>th</sup> IEEE AFCS, 340-344.
9. Valentin J, Theobald G, Gagnepain J, 1984, "Frequency shifts arising from in-plane temperature gradient distribution in quartz resonators", in Proc. of 38<sup>th</sup> IEEE AFCS, 157-163.
10. Valentin J, 1984, "Thermal gradient distributions in trapped energy quartz resonator", in *J.Appl. Physic*, 128-132.
11. Valentin J, Decailliot M, Besson R, 1984, "New approach of fast warm-up for crystal resonators and oscillators", in Proc. of 38<sup>th</sup> IEEE AFCS, 366-373.
12. Yevdokimenko Yu, Shmaliy Yu, 1991, "Thermal dynamic frequency instability of crystal oscillators", *Izvestia VUZov, Radioelektronika, N.5*, 49-55.
13. Yevdokimenko Yu, Shmaliy Yu, 1992, "Thermal dynamic frequency instability of bulk acoustic vibrations of quartz crystal piezo plate", *Akustichesky Jurnal, Vol.2(38)*, 283-289. (in Russian)
14. Yevdokimenko Yu, Shmaliy Yu, 1993, "A thermodynamic resonance in piezoelectric crystal plates of thickness-shear vibrations", in Proc. of 47<sup>th</sup> IEEE AFCS, 193-201.
15. Shmaliy Yu, 1995, "The modulation method of the precision quartz crystal oscillators and standards frequency stabilization", in Proc. of IEEE AFCS, 579-589.
16. Rataiski J, 1968, "Force-frequency coefficient of singly rotated vibrating quartz crystals", in *IBM J.Res.Dev.*, No.1(12), 92-99.
17. Stevens D, Tiersten H, 1985, "An analysis of doubly-rotated contoured quartz crystal resonators", in Proc. of 39<sup>th</sup> IEEE AFCS, 436-447.

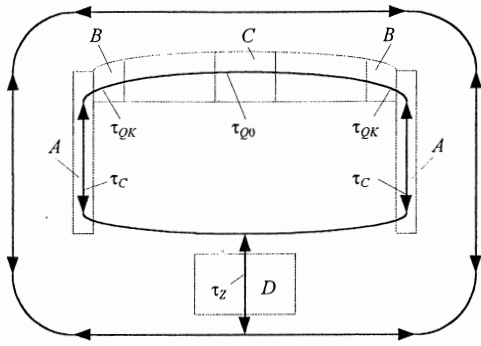


Figure 1. Model of the main internal and external thermal flows in quartz crystal resonator.

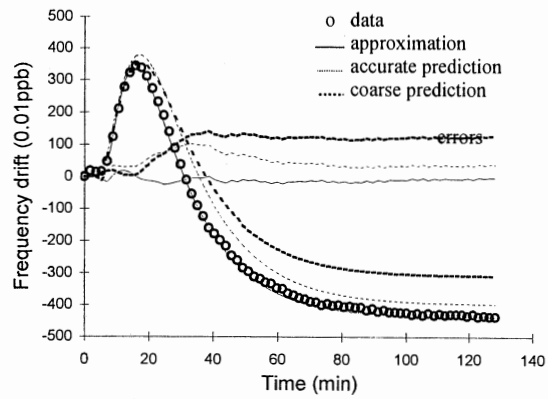


Figure 5. Frequency thermal transients and errors in the low temperature range (25.5→5.3)°C

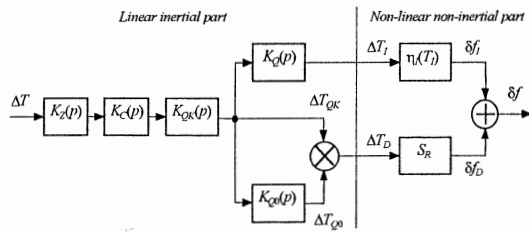


Figure 2. Thermal operator model of a crystal resonator

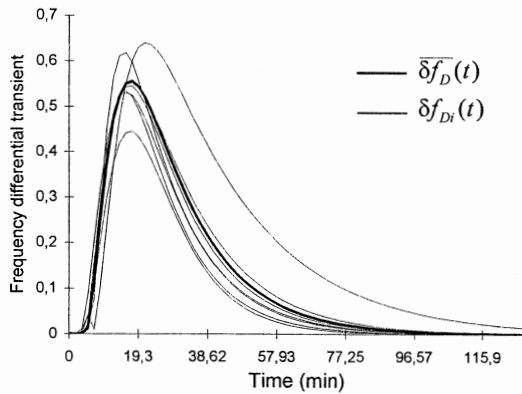


Figure 6. Thermal frequency drifts in the different temperature ranges:  $\delta f_{D_i}(t)$  are special cases,  $\bar{\delta f}_D(t)$  is averaged curve.

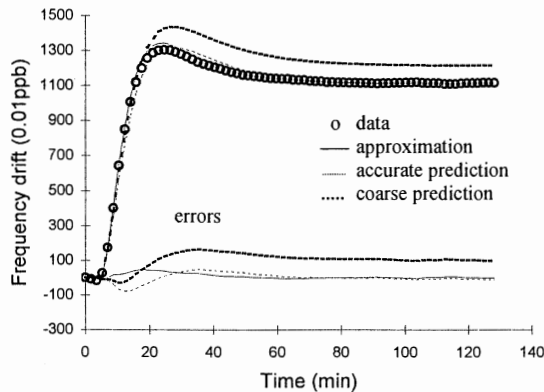


Figure 3. Frequency thermal transients and errors in the high temperature range (44.9→26.1)°C

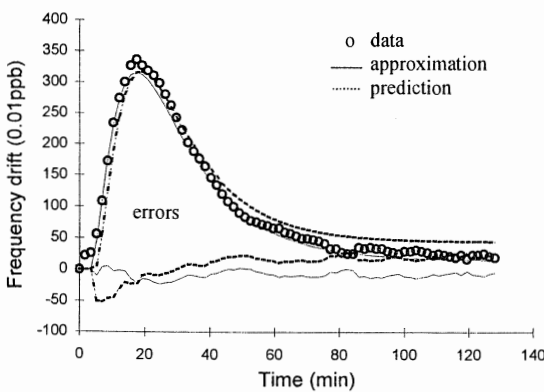


Figure 4. Frequency thermal transients and errors in the middle temperature range (26.1→15.0)°C

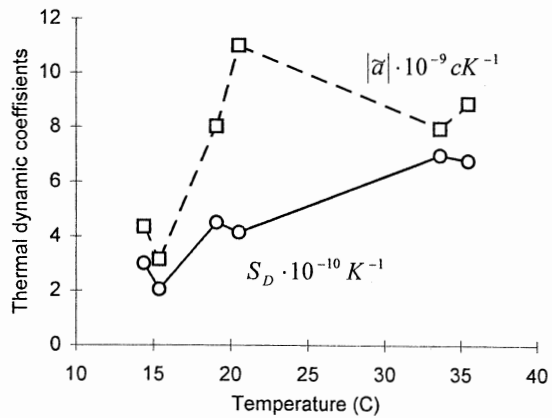


Figure 7. Dependencies on temperature of Ballato's coefficient  $\tilde{\alpha}$  and thermal dynamic coefficient  $S_D$

## CALCULATION AND MEASUREMENT OF ANHARMONIC VIBRATION MODES IN SC-CUT QUARTZ RESONATORS

*Krzysztof Weiss\**, Irina Mateescu, Gabriela Pop, Christina Ghita

\*Tele & Radio Research Institute, Ratuszowa 11, 03-450 Warsaw, Poland

National Institute of Materials Physics, PO Box MG 7, 76900 Bucharest - Magurele, Romania

### 1. INTRODUCTION

In quartz resonators the fundamental vibrations are accompanied by anharmonic mode of vibrations. They are given by nonuniform electric field distribution due to the limited quartz plate contour and electrode dimensions. Anharmonic mode vibrations in quartz resonators have been investigated since many years. For AT-cut quartz resonators, theoretical equations of calculation of anharmonic modes frequencies in plan-convex plates were presented in 1974 by Wilson (1). In (1) Wilson refers to previous works of Stoddard (1963) and Beaver (1973). This problem for SC resonators was also discussed by Tiersten and Smythe (2) and Tiersten and Stevens (3) but only in 1986 Stevens and Tiersten presented a completely analysis (4). The practical utilization of SC-cut resonators operating in  $n 1 0$  or in  $n 0 1$  anharmonic mode was presented by Bourquin, Dulmet and Boy in 1996 (5) and in 1997 (6). The advantage of such resonators is the reduction of intensity of B mode vibrations below that of C mode. In these papers were presented calculated and measured dispersion constants  $M'_n$  and  $P'_n$  for fundamental, third and fifth overtones. These parameters make possible calculation of anharmonic vibrations modes frequencies.

The purpose of this work is to check the conditions when the same dispersion constants are valid for antisymmetric anharmonic mode resonators with lateral field excitation as for classic SC-cut anharmonic mode resonators.

### 2. ANTISYMMETRIC ANHARMONIC MODE RESONATORS WITH LATERAL FIELD EXCITATION

Four semicircle electrodes with gap between them, alternately connected to electrical connectors, were used for resonator in (5) and (6). In this configuration the electrodes excites the thickness shear vibrations with the movements, in two adjacent regions of quartz plate, in opposite directions. These vibrations are mechanically coupled and they give  $n 0 1$  or  $n 1 0$  antisymmetric anharmonic vibrations modes depending on the gap between electrodes and on its orientation. In the optimum position of electrodes is possible to obtain the motional resistance of C mode about  $160\Omega$ , Q factor  $\approx 10^6$  and B mode resistance  $\approx 200\Omega$ .

In classic resonators with two electrodes deposited on opposite sides of quartz plate symmetric anharmonic modes  $n 0 2$ ,  $n 2 0$  and higher can be excited. The same modes can be excited too in classic lateral field resonators (7). The antisymmetric anharmonic modes

there are in quartz plates with two (or more) regions where lateral field is applied in opposite directions. Three parallel finger electrodes where the external electrodes are shortened excite this kind of modes (figure 1).



Figure 1: Electrode configuration

The operation way can be explained by analogy with surface acoustic waves excitation model presented in figure 2.

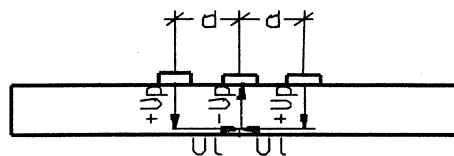


Figure 2: Electric field distribution

The  $U_p$  values are symmetric to plate axis and can excite the symmetric anharmonic vibration modes. The  $U_1$  excite the antisymmetric vibration modes. The value of  $U_p / U_1$  ratio can be changed by the electrode spacing  $d$  but always  $U_1 > U_p$  and the intensity of antisymmetric vibration modes is higher than that of symmetric vibration modes. If  $d$  value is larger than quartz plate thickness the antisymmetric modes prevail.

### 3. DETERMINATION OF THE DISPERSION CONSTANTS

The dispersion constants have been determined by the measurements of anharmonic mode frequencies on standard SC-cut quartz plates with crystallographic orientation  $\phi = 22^\circ 10'$  and  $\theta = 34^\circ 05'$ , 14 mm diameter and 500 mm curvature radius. The third overtone frequency ( $3 0 0$  mode) is about 8.2 MHz. The quartz plates were lapped with final abrasive corundum 1200/3 and after that were etched using ammonium bifluoride with polishing additives. Frequency measurements were performed with electrodes configuration presented in figure 3. For frequency measurements the Wandel & Goltermann vobuloscope set with  $50\Omega$   $\pi$  network was used. This set consists of level generator PSS-1, level meter SPM-16 and storage display unit SG-

4. Initial measurements were performed with the same electrodes configuration and  $\pi$  network using HP 8753 D network analyzer. For these measurements quartz plates were positioned by rotation to obtain for 3rd overtone the same signal level of 3 0 1 and 3 1 0 mode or for 5th overtone 5 0 1 and 5 1 0 mode. Using the relation:

$$f_{nmp} = \frac{n}{2h_0} \times \sqrt{\frac{\bar{c}_{66}}{\rho}} \times \frac{0.969}{(2n-1)^2 \pi^2} \times \sqrt{1 + \sqrt{\frac{h}{n^2 \pi^2 R c} [(2m+1)\sqrt{M_n} + (2p+1)\sqrt{P_n}]}} \quad (1)$$

where:  $n$  – order of overtone;  $m, p$  – orders of anharmonic vibration mode;  $h_0$  – maximum quartz plate thickness;  $h$  – quartz plate thickness;  $\bar{c}_{66}$  – effective elastic constant;  $\rho$  – quartz density;  $R$  – radius of curvature;  $M_n, P_n$  – dispersion constants,

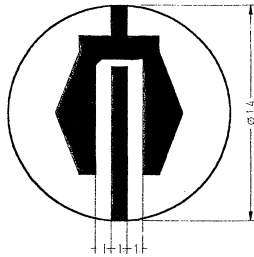


Figure 3: Practical electrodes configuration.

the anharmonic modes frequencies were calculated. The dispersion constants were chosen so to give the best agreement between the measured and the calculated anharmonic modes frequencies. In table 1 the theoretical and practical dispersion constants obtained by Bourquin, Dulmet and Boy (6) and the calculated values obtained in this paper are presented.

TABLE 1 - Dispersion constants of C-mode SC-cut resonators

$M_n (10^9 \text{ N/m}^2)$			
Overtone order	Bourquin et al		
	theoretical	practical	practical
3	53.1	57	55.4
5	71.0	69	66.8
$P_n (10^9 \text{ N/m}^2)$			
Overtone order	Bourquin et al		
	theoretical	practical	practical
3	63.3	67	65.1
5	78.2	80	76.1

Measured and calculated antisymmetric anharmonic modes frequencies of SC-cut resonators with 14 mm quartz plate diameter and 500 mm radius of curvature are presented in table 2.

TABLE 2 - Measured and calculated antisymmetric anharmonic modes frequencies

3 <sup>rd</sup> overtone / without electrodes				
No	Mode n m p	$f_1$ = measured frequency (Hz)	$f_2$ = calculated frequency (Hz)	$f_1 - f_2$ (Hz)
1	3 0 0	8216362		
	3 1 0	8255783	8255950	-167
	3 0 1	8259343	8259274	69
	3 1 1	8298811	8298657	154
	3 3 0	8335520	8334562	958
	3 0 3	8346234	8344435	1799
2	3 0 0	8216406		
	3 1 0	8255665	8255997	-332
	3 0 1	8259070	8259320	-250
	3 1 1	8298485	8298703	-218
	3 3 0	8335173	8334608	565
	3 0 3	8345426	8344481	945
	3 1 0	8255571	8255685	-114
	3 0 1	8258916	8259008	-92
	3 1 1	8298573	8298391	182
	3 3 0	8335458	8334294	1164
	3 0 3	8345548	8344167	1381
5 <sup>th</sup> overtone / without electrodes				
1	5 0 0	13671534		
	5 1 0	13715547	13715110	437
	5 0 1	13718112	13718050	62
	5 1 1	13761778	13761480	298
	5 3 0	13801852	13801850	2
	5 0 3	13810557	13810610	-53
2	5 0 0	16671684		
	5 1 0	13715449	13715260	189
	5 0 1	13718076	13718200	-124
	5 1 1	13761539	13761630	-91
	5 3 0	13801456	13802000	-544
	5 0 3	13810332	13810760	-428
3	5 0 0	13671562		
	5 1 0	13715421	13715140	281
	5 0 1	13718192	13718080	112
	5 1 1	13761753	13761510	243
	5 3 0	13801588	13801800	-212
	5 0 3	13811166	13810640	526

From this table we observe a little difference between Bourquin et al (6) results and ours.

#### 4. ANHARMONIC MODE OF SC-CUT CLASSIC RESONATORS

A comparison between the calculated and experimental measured anharmonic modes frequencies of SC-cut resonators with 14 mm plate diameter and 500 and 750 mm radius of curvature was performed. The 7mm

diameter silver electrodes were deposited with 75, 100, 125, 150, and 175 nm thickness. For all of the plates the harmonic and the nearest anharmonic modes frequencies of 3<sup>rd</sup> and 5<sup>th</sup> overtones were measured. The anharmonic modes frequencies were calculated using the above relation modified in function of the electrode thickness. We observed that the energy trapping effect due to the electrode thickness is similar with the curvature radius change. So the electrode effect was considered by curvature radius modification according to relation:

$$R' = R \left( 1 + k_a \frac{2 h_e \rho_e}{h_k \rho_k} \right) \quad (2)$$

where  $\rho_e$  - electrode density;  $h_e$  - electrode thickness;  $\rho_k$  - quartz density;  $h_k$  - quartz plate thickness;  $k_a = -R^2 6 \times 10^{-11}$ ;  $k_a$  - empirical coefficient

The measured and calculated anharmonic modes frequencies for 3<sup>rd</sup> and 5<sup>th</sup> overtone are presented in the tables 3 ; 4 ; 5 and 6.

## 5. CONCLUSIONS

The dispersion constants determined in the present work and those obtained in (6) have closed values. This is probably due to the little differences between values of quartz plates parameters ( curvature radius and nominal frequency ). Small errors of curvature radius can cause important variations of these constants, e.g. a 10% error of R value giving a deviation with  $\approx 0.05\%$  of calculated anharmonic modes frequencies. In the case of 8MHz resonator the difference is about 4kHz and can result in error over 10% of dispersion constants determination. There was not a significant influence of quartz plate excitation method on obtained values of dispersion constants. The same formula can be used for the calculation of symmetric and antisymmetric anharmonic modes frequency. For the plates with 500 mm curvature radius the agreement of calculated and measured values of anharmonic modes is very good ( $\approx 2\text{kHz}$  is the maximum difference). For radius of 750mm the differences are larger probably because of spread in R values. The differences could be a result of small energy trapping effect in these resonators.

The anharmonic and harmonic frequencies decrease due to the increase of the electrode thickness for all the curvature radii used (500 mm, 750 mm). The frequency spectrum is influenced more by the mass-loading than by the curvature radius.

These results show that is a possibility to find the properly technological parameters of resonators using the anharmonic modes frequencies spectrum.

## 6. ACKNOWLEDGMENTS

We wish to thank Dr B Dulmet from LCEP for his help in the explanation of anharmonic modes vibrations theory and formulas presented in references.

## 7. REFERENCES

1. Wilson C.J., 1974, "Vibration modes of AT - cut convex quartz resonators", J. Phys.. D7, 2449-
2. Tiersten H.F., Smythe R.C., 1979, "An analysis of contoured crystal resonators operating in overtones of coupled thickness shear and thickness twist", J. Acoust. Soc. Am. 65 (6), 1455-1460
3. Stevens D.S., Tiersten H.S. 1986, "An analysis of doubly rotated quartz resonators utilizing essentially thickness modes with transverse variation", J. Acoust. Soc. Am. 79(6), 1811-1826
4. Stevens D.S., Tiersten H.S. 1985, "An analysis of doubly rotated contoured quartz crystals resonators", Proc. of 39<sup>th</sup> IEEE AFCS,
5. Bourquin R., Dulmet B. and Boy J.J, 1996, "SC - cut resonator operating in anharmonic modes with B mode reduction", Proc 10<sup>th</sup> EFTF, 463-468
6. Bourquin R., Dulmet B. and Boy J.J, 1997, "Characterization of SC-cut resonators operating in anharmonic mode", Proc of 11<sup>th</sup> EFTF, 168-172
7. Masiukiewicz A., Gniewinska B., Szulc W. and Weiss K., 1985, "Study of SC cut lateral field excited resonators features", Proc. of 39<sup>th</sup> IEEE AFCS

TABLE 3 - Comparative data between measured and calculated frequencies for three plates with radius of curvature  $R = 500$  mm, 3<sup>rd</sup> overtone;  $f_m$  - measured frequency;  $f_c$  - calculated frequency;  $df = f_m - f_c$

Electrode thickness (nm)	Mode n m p	plate no.1			plate no.2			plate no.3		
		$f_m$ (Hz)	$f_c$ (Hz)	$df$ (Hz)	$f_m$ (Hz)	$f_c$ (Hz)	$df$ (Hz)	$f_m$ (Hz)	$f_c$ (Hz)	$df$ (Hz)
75	3 0 0	8195602			8196118			8196418		
	3 2 0	8275458	8275026	432	8276144	8275545	599	8276426	8275846	580
	3 0 2	8281958	8281677	281	8282182	8282196	-14	8282716	8282497	219
100	3 0 0	8193354			8192988			8192492		
	3 2 0	8273398	8272949	449	8273072	8272582	490	8272406	8272083	323
	3 0 2	8279728	8279614	114	8279122	8279247	-125	8278882	8278748	134
125	3 0 0	8190402			8190082			8189622		
	3 2 0	8270472	8270166	306	8270216	8269844	372	8269574	8269381	193
	3 0 2	8276856	8276845	11	8276276	8276523	-247	8276056	8276061	-5
150	3 0 0	8186984			8186598			8186206		
	3 2 0	8267120	8266915	205	8266682	8266526	156	8266236	8266131	105
	3 0 2	8273564	8273608	-44	8272968	8273219	-251	8272874	8272826	48
175	3 0 0	8182202			8181946			8181748		
	3 2 0	8262558	8262294	264	8261912	8262036	-124	8261948	8261837	111
	3 0 2	8268992	8269000	-8	8268402	8268743	-341	8268644	8268544	100

TABLE 4 - Comparative data between measured and calculated frequencies for three plates with radius of curvature  $R = 750$  mm, 3<sup>rd</sup> overtone;  $f_m$  - measured frequency;  $f_c$  -calculated frequency;  $df = f_m - f_c$

Electrode thickness (nm)	Mode n m p	plate no.1			plate no.2			plate no.3		
		$f_m$ (Hz)	$f_c$ (Hz)	$df$ (Hz)	$f_m$ (Hz)	$f_c$ (Hz)	$df$ (Hz)	$f_m$ (Hz)	$f_c$ (Hz)	$df$ (Hz)
75	3 0 0	10005410			10255916			10004792		
	3 2 0	10079114	10078180	934	10331418	10329640	1778	10080112	10078590	1522
	3 0 2	10087584	10084280	3304	10337792	10335820	1972	10086672	10084780	1892
100	3 0 0	10001060			10000358			10246638		
	3 2 0	10074752	10074290	462	10075676	10073590	2086	10324204	10320820	3384
	3 0 2	10077902	10080430	-2528	10082264	10079730	2534	10329160	10327040	2120
125	3 0 0	9996442			10246484			9995922		
	3 2 0	10070116	10070140	-24	10322030	10321170	860	10071178	10069520	1658
	3 0 2	10078728	10076320	2408	10328392	10327430	962	10077738	10075700	2038
150	3 0 0	9991092			10240686			9990748		
	3 2 0	10064752	10065260	-508	10316258	10315860	398	10065792	10064930	862
	3 0 2	10073392	10071480	1912	10322662	10322160	502	10072354	10071130	1224
175	3 0 0	9984590			10233194			9982958		
	3 2 0	10058442	10059240	-798	10309098	10308860	238	10058598	10057600	998
	3 0 2	10067116	10065490	1626	10315644	10315210	434	10065070	10063850	1220

TABLE 5 - Comparative data between measured and calculated frequencies for three plates with radius of curvature  $R = 500$  mm, 5<sup>th</sup> overtone;  $f_m$  - measured frequency;  $f_c$  - calculated frequency;  $df = f_m - f_c$

Electrode thickness (nm)	Mode n m p	plate no.1			plate no.2			plate no.3		
		$f_m$ (Hz)	$f_c$ (Hz)	$df$ (Hz)	$f_m$ (Hz)	$f_c$ (Hz)	$df$ (Hz)	$f_m$ (Hz)	$f_c$ (Hz)	$df$ (Hz)
75	5 0 0	13637892			13638772			13639302		
	5 2 0	13725544	13725390	154	13726764	13726280	484	13726968	13726810	158
	5 0 2	13730790	13731290	-500	13731258	13732170	-912	13732106	13732700	-594
	5 4 0	13811842	13812340	-498	13813012	13813230	-218	13813518	13813760	-242
	5 2 2	13817126	13818200	-1074	13817912	13819080	-1168	13818558	13819620	-1062
	5 0 4	13823760	13824050	-290	13823978	13824940	-962	13825018	13825470	-452
100	5 0 0	13634182			13633588			13632748		
	5 2 0	13721842	13721870	-28	13721548	13721280	268	13720394	13720440	-46
	5 0 2	13727002	13727780	-778	13726042	13727180	-1138	13725604	13726340	-736
	5 4 0	13808506	13809010	-504	13807880	13808410	-530	13806764	13807570	-806
	5 2 2	13813512	13814880	-1368	13812758	13814280	-1522	13811980	13813430	-1450
	5 0 4	13820092	13820750	-658	13818924	13820150	-1226	13818652	13819300	-648
125	5 0 0	13629282			13628768			13627968		
	5 2 0	13716898	13717160	-262	13716692	13716650	42	13715598	13715840	-242
	5 0 2	13722146	13723080	-934	13721212	13722560	-1348	13720808	13721760	-952
	5 4 0	13803676	13804480	-804	13803184	13803960	-776	13802074	13803160	-1086
	5 2 2	13809902	13810360	-458	13807998	13809840	-1842	13807222	13809040	-1818
	5 0 4	13815356	13816240	-884	13814238	13815720	-1482	13813962	13814920	-958
150	5 0 0	13623586			13623144			13622102		
	5 2 0	13711226	13711650	-424	13711134	13711210	-76	13709932	13710160	-228
	5 0 2	13716392	13717580	-1188	13715574	13717140	-1566	13715044	13716090	-1046
	5 4 0	13798080	13799150	-1070	13797628	13798710	-1082	13796504	13797660	-1156
	5 2 2	13803028	13805050	-2022	13802414	13804600	-2186	13801684	13803550	-1866
	5 0 4	13809876	13810940	-1064	13808750	13810490	-1740	13808592	13809440	-848
175	5 0 0	13615588			13615126			13614604		
	5 2 0	13703394	13703830	-436	13703244	13703370	-126	13702532	13702840	-308
	5 0 2	13708396	13709770	-1374	13707736	13709310	-1574	13707792	13708790	-998
	5 4 0	13790552	13791510	-958	13789904	13791040	-1136	13789430	13790520	-1090
	5 2 2	13795386	13797410	-2024	13794822	13796950	-2128	13794438	13796420	-1982
	5 0 4	13802248	13803320	-1072	13801238	13802850	-1612	13801596	13802330	-734

TABLE 6 - Comparative data between measured and calculated frequencies for three plates with radius of curvature R = 750 mm. 5<sup>th</sup> overtone;  $f_m$  - measured frequency;  $f_c$  - calculated frequency;  $df = f_m - f_c$

Electrode thickness (nm)	Mode n m p	plate no.1			plate no.2			plate no.3		
		$f_m$ (Hz)	$f_c$ (Hz)	$df$ (Hz)	$f_m$ (Hz)	$f_c$ (Hz)	$df$ (Hz)	$f_m$ (Hz)	$f_c$ (Hz)	$df$ (Hz)
75	5 0 0	16655776			17073216			16654568		
	5 2 0	16737714	16735880	1834	17159994	17154360	5634	16738288	16734670	3618
	5 0 2	16744942	16741280	3662	17161886	17159830	2056	16743428	16740070	3358
	5 4 0	16818216	16815600	2616	17239404	17235130	4274	16820374	16814390	5984
	5 2 2							16825718	16819760	5958
	5 0 4	16825742	16826350	-608	17251016	17246020	4996	16831862	16825130	6732
100	5 0 0	16648526			17065534			16647166		
	5 2 0	16730422	16729130	1292	17149326	17147210	2116	16730854	16727770	3084
	5 0 2	16737712	16734570	3142	17154184	17152710	1474	16736036	16733210	2826
	5 4 0	16810958	16809360	1598	17231790	17228490	3300	16812988	16807990	4998
	5 2 2	16818526	16814760	3766	17236852	17233970	2882	16818286	16813400	4886
	5 0 4	16826478	16820170	6308	17243388	17239450	3938	16824504	16818800	5704
125	5 0 0	16640852			17057496			16639664		
	5 2 0	16722702	16721980	722	17141256	17139710	1546	16723308	16720790	2518
	5 0 2	16730012	16727450	2562	17146114	17145250	864	16728490	16726250	2240
	5 4 0	16803232	16802710	522	17223774	17221520	2254	16805568	16801520	4048
	5 2 2	16810812	16808150	2662	17235356	17227040	8316	16810764	16806960	3804
	5 0 4	16818842	16813590	5252				16817022	16812400	4622
150	5 0 0	16631906			17047824			16630652		
	5 2 0	16721032	16719060	1972	17131532	17130580	952	16714274	16712300	1974
	5 0 2	16713744	16713550	194	17136114	17136150	-36	16719434	16717800	1634
	5 4 0	16794314	16794800	-486	17214116	17212930	1186	16796566	16793540	3026
	5 2 2	16801852	16800280	1572	17219126	17218480	646	16801758	16799020	2738
	5 0 4	16810000	16805760	4240				16807992	16804490	3502
175	5 0 0	16621116			17035402			16618172		
	5 2 0	16703054	16703290	-236	17119452	17118700	752	16702026	16700340	1686
	5 0 2	16710396	16708830	1566	17124418	17124320	98	16707024	16705880	1144
	5 4 0	16783790	16785060	-1270	17202348	17201590	758	16784642	16782100	2542
	5 2 2	16791362	16790570	792	17207264	17207118	146	16789722	16787160	2562
	5 0 4	16799656	16796080	3576	17286712	17289650	-2938	16795874	16793120	2754

**SIMULATION OF PIERCE OSCILLATORS WITH DIGITAL INVERTERS USING THE NEGATIVE RESISTANCE MODEL**

Detlef Göhrig, Jörg Haffelder

TELE QUARZ GmbH, D-74924 Neckarbischofsheim, Germany

**1 INTRODUCTION**

In standard applications like microcontrollers, DECT systems and other low-cost crystal oscillators, the pierce oscillator with a digital inverter used as oscillator amplifier is the most common one. Due to the lack of precision high frequency analog models for digital inverters it is nearly impossible to simulate these oscillators with SPICE.

This article shows a method to simulate the oscillation startup condition and the oscillator frequency in steady state operation using the negative resistance model.

The first step is to generate a model for the digital inverter over the desired frequency range for small and large signal condition at different supply voltages. This model is a s-parameter model which can be easily implemented into the simulation circuit used for the SPICE simulation.

The second step is to redraw the pierce oscillator schematic in a special way, so that the AC-Simulation using the negative resistance model method [1] can be used. With this method it is possible to simulate very fast and accurate the frequency and the oscillation startup condition of pierce oscillators.

As a final step a comparison between the SPICE simulation and a real oscillator is shown.

**2 THE DIGITAL INVERTER USED AS OSCILLATOR AMPLIFIER AND MEASUREMENT TECHNIQUES**

**2.1 Basic Circuit Of Pierce Oscillators**

The following schematic shows the typical simple pierce oscillator using a digital inverter as oscillator amplifier.

This basic circuit contains the feedback resistor  $R_{fb}$  to generate the operating point, a resistor ( $R_v$ ) connected to the inverter output to reduce the crystal drive level and to provide an

additional phase shift especially at lower frequencies, the crystal itself and the two capacitors connected between the crystal's leads and ground and the crystal itself.

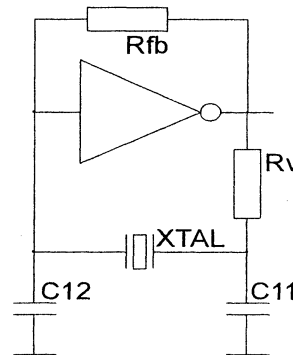


fig.1 basic circuit

As other oscillator types like VCXO's and overtone oscillators are only modifications of this basic circuit we'll reduce our reflection to this basic circuit.

**2.2 The Digital Inverter**

**2.2.1 Linearisation Using A Feedback Resistor**

When using a CMOS or compatible digital inverter as amplifier in the pierce oscillator, it is necessary to set the inverter operating point near to it's switching voltage. Thus it is possible to achieve large output voltage swings with a small input signal level.

By connecting the inverter output pin with a high-ohmic resistor ( $100k\Omega$  up to  $5M\Omega$ ) to the inverter input pin, the digital inverter is forced into a selfadjusting operating point near the half value of the supply voltage [4].

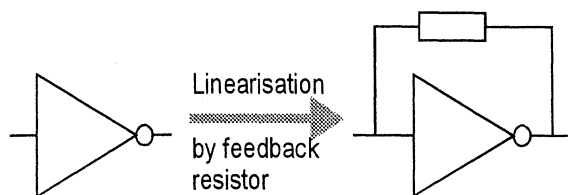


fig.2 inverter linearisation

The digital inverter has been "linearized" to a high gain amplifier.

## 2.2.2 Characteristics Of The Linearized Inverter

### 2.2.2.1 Input Impedance

It is very useful to describe the input impedance as a parallel connection of R and C. Typical values for these components are about 10k and from 2pF up to 5pF for the capacitor. The measurement of these parameters can be realized by a capacitive decoupled impedance analyzer. Another method to describe the port characteristics is to measure the s11 parameter of the device.

It is very easy to develop an oscillator circuit with optimized crystal drive level and high startup reserve, if the oscillator input impedance is high-ohmic.

### 2.2.2.2 Output Impedance

The output impedance (source impedance) can also be described as a paralleled RC-network. The output impedance is mainly dependent from the DC operating point of the inverter [4]. It is very low when the inverter output is low or high and increases to very high values around the selfadjusting operating point like shown in the following graph.

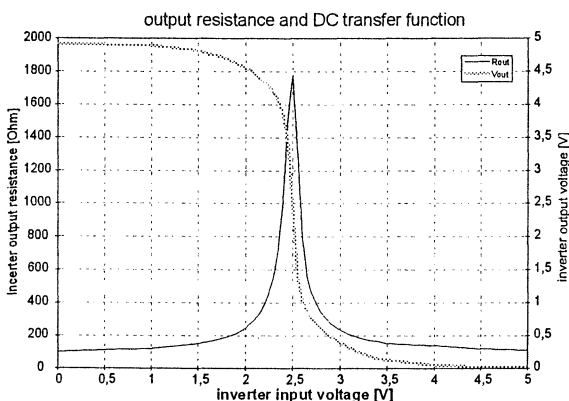


fig.3 output impedance and DC transfer function

During a steady state operation the output signal of the inverter is a squarewave signal. The inverter changes very fast from low to high and back.

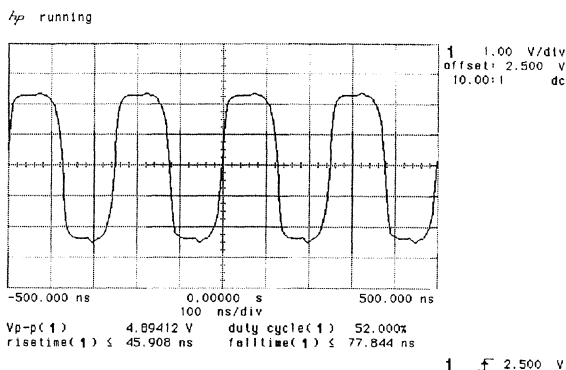


fig.4 typical inverter output signal

This is the reason why it is necessary to distinguish between small signal condition (oscillation startup in the selfadjusting operation point) and large signal condition (steady state operation mainly high and low) when determining the output impedance.

To build a model of the output impedance we can use the same method like we used it for the model of the input impedance (measurement of S22)

### 2.2.2.3 Transfer Function

It is very important to know the exact values of the amplifier transmission gain and phase over the whole frequency range depending on the signal power. It is impossible to assess the oscillation startup or to guarantee a reliable operation of the oscillator without knowledge of these parameters [4]. The amplifier transfer function is dependent on the frequency, the supply voltage and especially on the signal power. The following two diagrams show the magnitude of the S21 parameter in small signal and large signal condition traced over frequency and supply voltage.

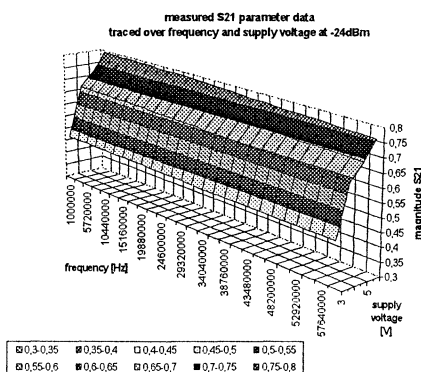


fig.5 small signal S21-parameter data

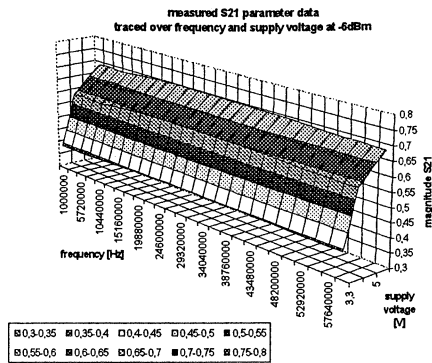


fig.6 large signal S21-parameter data

### 2.2.3 Model

A very simple and common method to determine all necessary parameters of the linearised inverter is to build a whole s-parameter model including S11, S12, S21 and S22. S-Parameter models can be used in nearly every simulation software

The model used for the simulation of the pierce oscillator is splitted into small signal condition (oscillation startup) and large signal condition (steady state operation). We decided to build the s-parameter model at small signal condition (-24dBm) at 4 different DC supply voltages of the inverter (3.3V, 4.5V, 5V and 5.5V) and at large signal condition (6dBm) at the same DC supply voltages.

For the frequency range we decided to measure 26 points from 1MHz up to 60MHz. The result is a model containing 208 (2\*4\*26) measurement points.

The following diagram shows the measurement points in the three dimensions "supply voltage", "signal power" and "frequency".

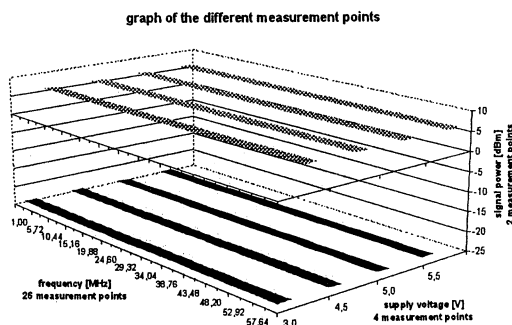


fig.7 measurement points

The following model represents the measured s-parameter data at different values of signal power, supply voltages and frequencies.

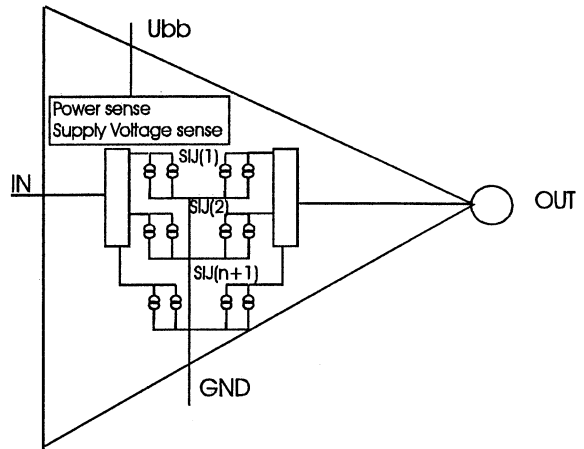


fig.8 structure of the S-parameter model

For the simulation the model represent an S-parameter model [5] depending on supply voltage, signal power and frequency . To detect the bias point of the model, a separate input for the supply voltage is implemented. The signal power was defined by an parameter statement.

### 3 PIERCE OSCILLATOR SIMULATION

When simulating the Pierce oscillator it is not possible to cut between the passive and active part, because the quartz crystal is in the feedback loop of the oscillator. For a simulation with the „negative resistance model“ it is necessary to separate into passive and active part.

For the redrawing of the circuit in passive and active part it is necessary to delete the real ground and add a virtual ground [1] [2]. A standard Pierce oscillator with BJT can redrawn as shown in figure 9.

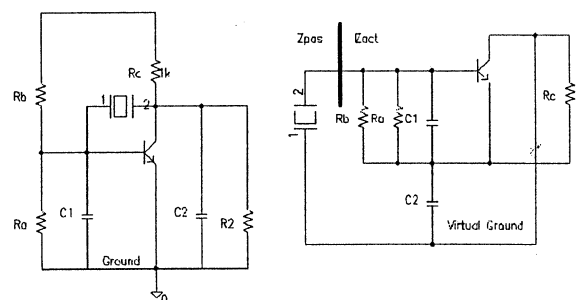


fig.9 virtual ground at Pierce oscillator with BJT

As an digital inverter (180 ° amplifier) can be compared with a transistor in emitter mode, the pierce oscillator with digital inverter can

redrawn very easy as shown in the following example.

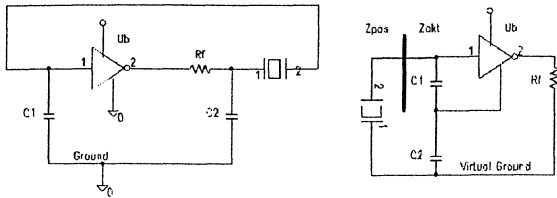


fig.10 pierce oscillator

By inserting the virtual ground in the circuit it is possible to simulate the oscillator with the „negative resistance model“ [3]. When using this method it is not possible to work with normal spice transistor model or an analog inverter model, because a biasing of the transistor can not be realised in the redrawn circuit. For the simulation the use of an analog model for the digital inverter with internal biasing is necessary. To get better results a S-parameter model which is depending on signal power is required. The structure of these model is shown by figure 8.

After redrawing the circuit the passive and active part can be defined by an section of the crystal unit and the digital inverter. At this point two AC-current sources with a current value of 1A are introduced (see figure 11).

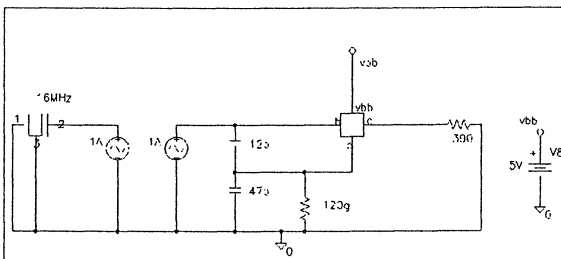


fig. 11 example circuit

The voltage of these current sources are the impedance of  $Z_{pas}$  and  $Z_{akt}$ . The oscillator operates in a steady state condition with the following conditions:

$$|R_{act}| = |R_{pas}| \text{ und } X_{pas} = -X_{akt} \quad (1)$$

If the imaginary part of  $Z_{total} = Z_{akt} + Z_{pas}$  is depicted as a function of frequency, the oscillator frequency is represented as the point of intersection with the x-axis.

To get some information concerning the oscillator start up reliability it is very useful to simulate the negative impedance of the circuit. The result of the negative resistance simulation in the example is  $-668\Omega$  at 16MHz.

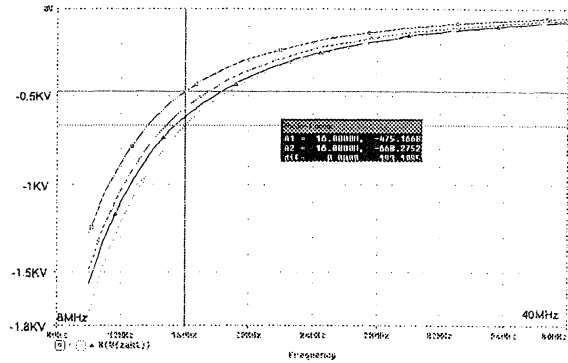


fig.12 negative input resistance

A reliable oscillator startup is given if the negative input resistance is five times bigger than the maximum crystal resonance resistance.

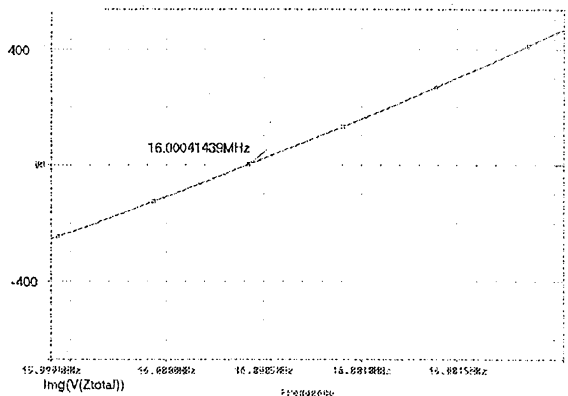


fig.13 frequency of the oscillator

To define the oscillation frequency it is necessary to find the first point of intersection of the imaginary part of  $V(z_{total})$  and 0. In the example the oscillation frequency is 16,00041439 MHz. Between the measured and calculated frequency is a difference of  $-31,2\text{ppm}$ .

The following figure shown the frequency versus supply voltage.

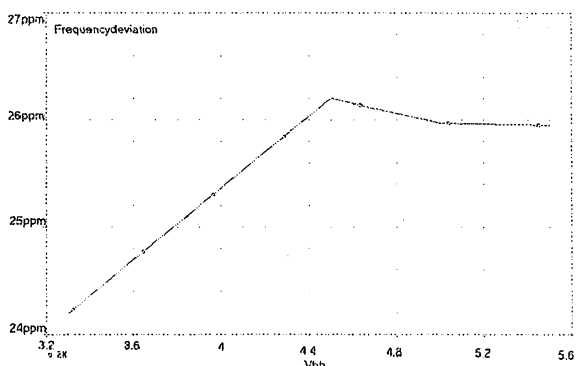


fig.14 frequency vs. supply voltage

The following graph shows a comparison between simulated and measured frequencies relative to the frequency at 5V supply voltage from the example above (oscillator working at 16MHz).

[4] Haffelder J., 1997, "Pierce Oscillator Fundamentals", Application Note TELE QUARZ GmbH, page 2ff

[5] Timmermann, C.C., 1995, "Exact S-Parameter Models Boost SPICE", IEEE: Circuit & Devices, September 95, page 17ff

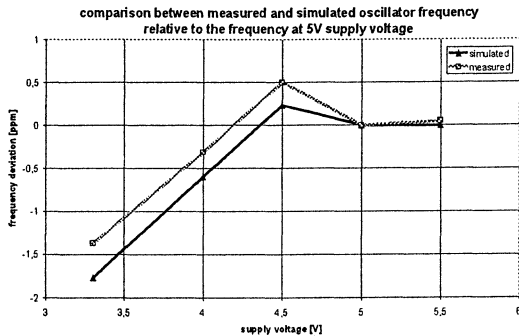


fig.15 comparison between measurement and simulation

#### 4 CONCLUSION

The method of redrawing a pierce oscillator with digital inverter from a two port model into a one port model allows to use the method of the "negative input resistance" when simulating oscillation startup reserve and the oscillation frequency.

To get simulation results which correlate with the reality it is necessary to have a very accurate RF-model of the oscillator amplifier (the digital inverter). Especially when simulating the steady state operation it is necessary to have an S-Parameter model containing measurement data at the same level of signal power like in the real oscillator (up to 5Vpp).

#### 5 REFERENCES

[1] Omlin L., 1977, "Analyse und Dimensionierung von Quarzoszillatoren", Elektroniker Hefte 6,9,12

[2] Alechno S., 1997, "Analysis Method Characterizes Microwave Oscillators", Microwave & RF, Nov.97, page 82ff

[3] Göhrig D., 1997, "AC-Spice Simulation Of Quartz Crystal Oscillator With The Negative Resistance Model", 11<sup>th</sup> European Frequency and Time Forum

# OCXO OSCILLATOR WITH DIRECT TEMPERATURE MEASUREMENT OF QUARTZ VIBRATOR

A. Smolarski, W. Szulc, B. Gniewińska, K. Weiss, A. Masiukiewicz, B. Kalinowska  
 Tele & Radio Research Institute, Ratuszowa 11, 03-450 Warsaw Poland

## 1. Introduction

To improve static and dynamic behavior of the newly designed miniature OCXO oscillator, the direct temperature measurement and direct heating of quartz vibrator was applied. The multilayer thin metal structure was applied directly on quartz surface around the electrode beside the active part of the plate. This structure fulfills simultaneously both functions: the temperature sensor and the heater. Such solution offers very good thermal coupling of sensor-heater and ovenized element (vibrator). This leads to very short warm up time, assures the aperiodic character of frequency stabilization process and significantly reduced energy consumption.

## 2. Resonator construction

The SC cut 5 and 10MHz (of 10.2mm diameter) crystal plates were used for experiments. These plates were placed in HC 37/U (T0-8) cold welded enclosures with four leads (two for the resonator and two for the sensor-heater). The examples of plate constructions are shown in fig. 2.1.



a/ b/  
 Fig. 2.1. Two different constructions of the sensor-heater

The sensor-heater is placed around the active part of the plate. Several different

constructions were tested. Among them different material of heater, different shapes and technology. Results of experiments are presented in Table 2.1.

Table 2.1.

No	LAYERS PARAMETERS	RH [ $\Omega$ ]	RHvT coefficient	FEATURES
1.	1 layer, Au, 1000 $\text{Å}$	45	0.3%/K	not sufficiently adhesive to quartz plate
2.	2 layers, Cr $\rightarrow$ 100 $\text{Å}$ , Au $\rightarrow$ 1000 $\text{Å}$	65	0.16%/K	not stable in time
3.	2 layers, Ti $\rightarrow$ 100 $\text{Å}$ , Au $\rightarrow$ 1000 $\text{Å}$	70	0.2%/K	fulfills all requirements

where:

$RH$  the sensor-heater resistance,  
 $RHvT$  the sensor-heater resistance versus temperature coefficient,

The examples of resistance versus temperature characteristics are presented in fig. 2.2.

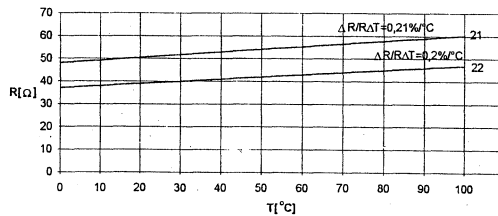


Fig.2.2. Resistance versus temperature characteristics of the sensor-heater (2 layers construction, Ti  $\rightarrow$  170  $\text{Å}$ , Au  $\rightarrow$  1000  $\text{Å}$ ).

The final 5MHz vibrators were made using one mask and all elements were deposited in one processes. The thickness of the sensor-heater is the same as the electrode.

The shape of the sensor-heater structure could be changed (fig. 2.1. a, b) to obtain proper value of the resistance and the uniform thermal energy distribution.

The basic parameters of the resonators and the sensor-heater are presented in Table 2.2.

Table 2.2

No	RH [ $\Omega$ ]	RHvTC [%/K]	Te [ $^{\circ}$ C]	RI [ $\Omega$ ]
28	61.6	0.22	85	10
29	63.8	0.22	>90	10
30	61.4	0.22	85	10
31	61.8	0.22	85	10.5
32	61.6	0.22	87	10.5
33	61.9	0.22	90	10.5
34	67.9	0.22	>90	10

where:

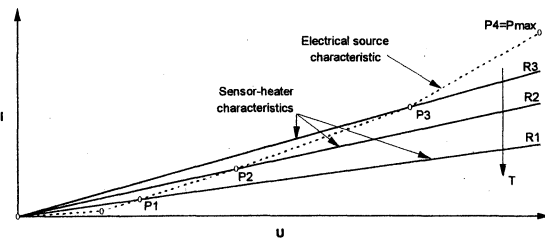
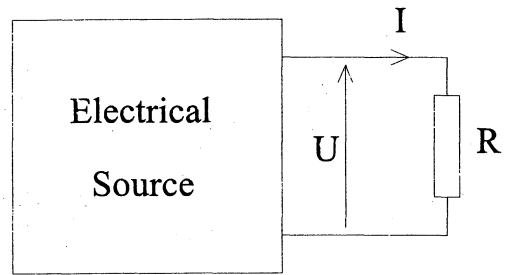
- RH *the sensor-heater resistance,*
- RHvTC *the sensor-heater resistance versus temperature coefficient,*
- Te *resonator turn over temperature,*
- RI *resonator dynamic resistance.*

These resonators has Q factor  $\geq$  than 1E6, and others parameters comparable with typical SC cut resonators. Long term resistance stability measurements of the sensor-heater were carried out. The temperature change which correspond to resistance versus time change was below 0.2K/year.

### 3. Temperature control circuit

The supply source for the sensor-heater of the nonlinear output characteristic was used as temperature control circuit. The cross points between this source characteristic and the family of the sensor-heater characteristics for different temperatures corresponds to the heating power necessary in each temperature to obtain steady state. The basic principles of circuit operation are shown in fig.3.1.

The experimentally obtained heating power characteristic versus temperature deviation close to the oven operating temperature is shown in fig.3.2.



T-temperature of R

$$P1 < P2 < P3 < P4$$

$$P = f(T) = U \times I$$

Fig. 3.1 The basic principle of temperature control circuit operation

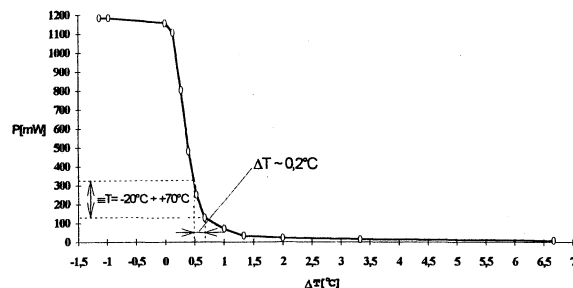


Fig. 3.2. Heating power versus temperature characteristic

### 4. Oscillator construction

The oscillator block diagram is shown in fig. 4.1.

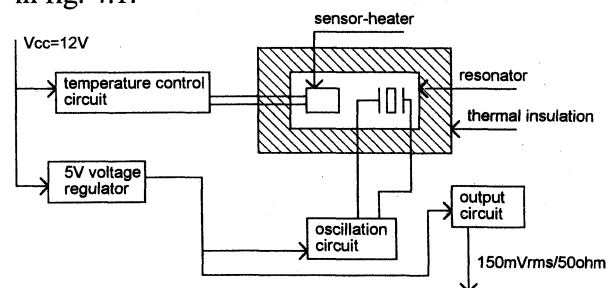


Fig. 4.1 The oscillator block diagram

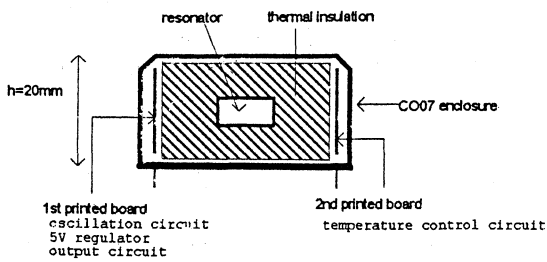


Fig. 4.2. Oscillator construction

## 5. Measurement results

Experiments confirmed that very short and aperiodic frequency stabilization characteristic could be achieved. An example of this characteristic is shown in fig. 5.1.

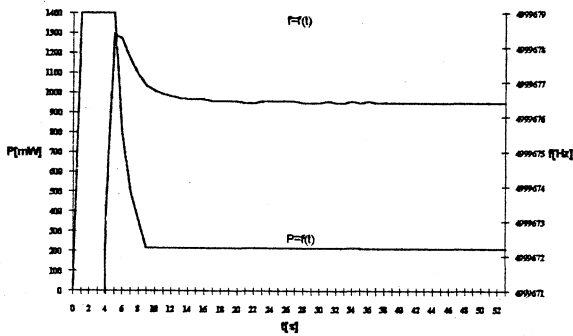


Fig 5.1. Oscillator frequency (f) and power (P) stabilisation characteristics.

The aging characteristics of three oscillators were measured. After the 1st month of operating all oscillators achieved the stability better than  $5E-9$ /day.

The aging parameters of the oscillator nr. 30 are presented in fig. 5.2 and 5.3.

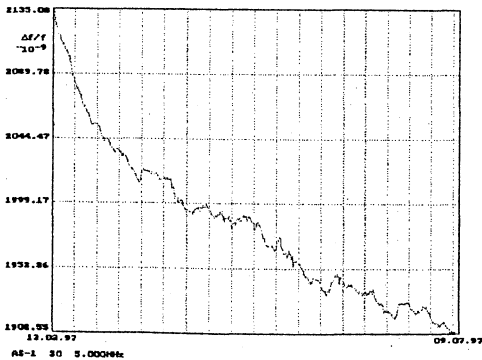


Fig.5.2 Aging characteristic after two weeks of continuous operation

Data concerning aging of all models are shown in table 5.1, while other average parameters are collected in table 5.2.

Table 5.1

Osc nr.	$\Delta f/f$ /month	$\Delta f/f$ /day after 1 month of operating	$\Delta f/f$ /day after 5 months of operating
28	-1.6E-7	-1.3E-9	-1.1E-9
30	-1.1E-7	-0.6E-9	-0.3E-9
31	-4.1E-7	-3.4E-9	-1.1E-9

Table 5.2

Parameter	Measurement results
frequency versus temperature stability $T = -20 \div 70^\circ\text{C}$	$\leq 5E-8$
frequency stabilization time at $20^\circ\text{C}$ with accuracy $1E-7$ with accuracy $1E-8$	$\leq 10\text{s}$ $\leq 40\text{s}$
energy consumption during warm up at $20^\circ\text{C}$	$\leq 10\text{Ws}$

## 6. Conclusions

Due to application of the specially developed sensor-heater, very short (9 sec at  $20^\circ\text{C}$ ) and aperiodic frequency stabilization character was achieved. This led to low energy consumption during warm up (about 10 Ws at  $20^\circ\text{C}$ ).

Despite the presence of the additional structure on the vibrator plate quite good long term stability was obtained (better than  $5E-9$ /day after one month of continuous operation).

Further improvement of thermal parameters is possible however requires changes in the resonator construction or thicker layer of thermal isolation. At present the main energy loss is through the four leads and to reduce heat leaks the elements of the plate mounting construction have to be changed.

Type = "AS-1"

Fnom = "5.0"

Number = 30

Measurement\_period = "29.01.97-08.07.97"

Calculation\_period = "15.06.97-08.07.97"

### Calculation results

A. Not corrected    B. Corrected

Average twenty-four hours frequency change /E-11/ -->

$\delta f = -88.01$

$\delta f_{sk} = -24.91$

Calculation accuracy /E-11/ -->

$\epsilon = 9.13$

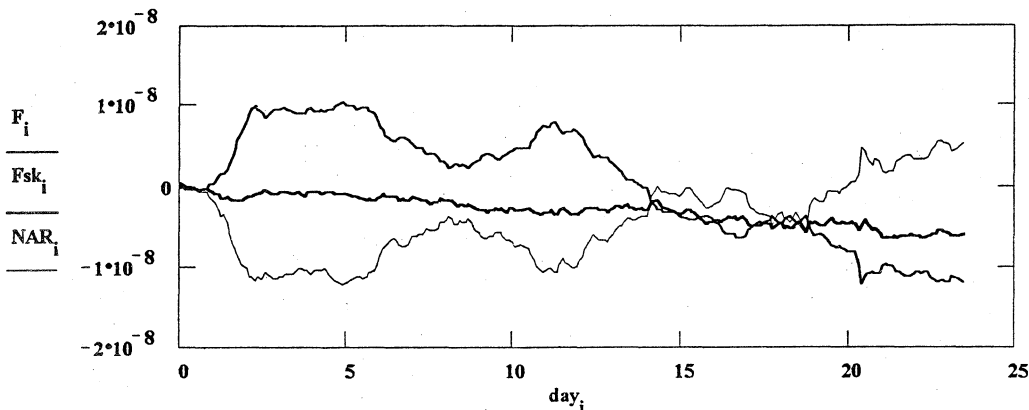
$\epsilon_{sk} = 2.35$

Standard deviation /E-10/ -->

$\sigma = 35.49$

$\sigma_{sk} = 5.46$

AMBIENT\_FACTOR="H"

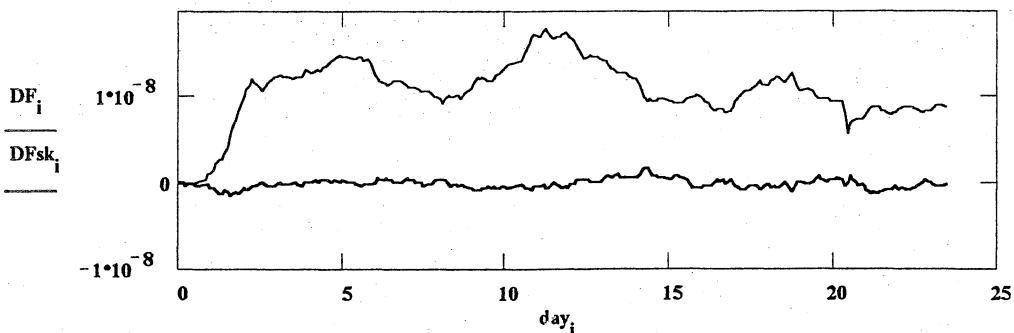


$F_i$  – measured frequency changes

$F_{sk_i}$  – corrected frequency changes

$NAR_i$  – one of three values T, P or H

$\Delta NAR = \text{"humidity change=24.3 \%"}$



$DF_i$  – deviation from the straight line, approximating non corrected response

$DF_{sk_i}$  – deviation from the straight line, approximating corrected response

Sensitivity coefficients due to: temperature -  $ST[1/K]$ , pressure -  $SP[1/hP]$ , humidity -  $SH[1/\%]$  and accuracy of their determination :  $\delta ST[1/K]$ ,  $\delta SP[1/hP]$ ,  $\delta SH[1/\%]$

$ST = -1.65 \cdot 10^{-9}$       with accuracy       $\delta ST = 2.1 \cdot 10^{-10}$

$SP = -1.01 \cdot 10^{-10}$       with accuracy       $\delta SP = 3.02 \cdot 10^{-11}$

$SH = -7.15 \cdot 10^{-10}$       with accuracy       $\delta SH = 2.37 \cdot 10^{-11}$

Fig.5.3 Long term frequency stability after 5 months of continuous operation with environmental stress correction.

## 7. References

1. A.Smolarski, W.Szulc, Quartz resonator with direct temperature measurement for oscillators, Proc.of PIEZO'96 Conference, Waplewo 1996
2. B.Long, G.Weaver, Quartz crystal oscillators with direct resonator heating, Proc.of 1991 ASFC
3. I.Abramson, R.Boroditsky, High stability resonator-thermostat packaged in TO-8 vacuum holder, Proc. of 11th EFTF, Neuchatel 1997
4. The quartz resonator with the heater on the quartz plate, Patent application, RP:/P319794, 1997 (in Polish)
5. The method of temperature control of the quartz resonator with the heater on the quartz plate, Patent application, RP:/P324098, 1997 (in Polish)

## STUDIES OF CRYSTAL OSCILLATOR WITH OUTPUT SIGNAL CONTROLLED PHASE

Anatoliy S Vasilenko, Yuriy S Shmaliy

“Sichron” Center, 4 Skripnika Str., Kharkiv, 310057, Ukraine, tel/fax: 380 572 45 09 55;  
e-mail: [yush@sichr.kharkov.ua](mailto:yush@sichr.kharkov.ua)

## ABSTRACT

The quartz crystal oscillator circuit that is performed on a base of crystal resonator with additional electrodes, the use of which allows to combine functions of generation, frequency stabilization and control over the output signal phase within one device, is discussed in this paper. Dependencies of both a slope and stability of device characteristics from resonator parameters, that are essential for control of an output signal phase, has been found. It is shown that the quartz crystal oscillator with such type of resonator has high slope of control characteristics as well as high stability level of output amplitude in regime of phase control. In particular, the slope of static modulation characteristic  $S_{fm}$  had reached the level of 20000 degree/V within the  $\Delta\varphi = \pm 85^\circ$  phase range.

*Keywords: quartz crystal resonator, quartz crystal oscillator, frequency control, phase control*

## INTRODUCTION

Control of an output signal phase of high stability quartz crystal oscillator is one of the important practical tasks. As examples one may take ensembles of phase-coupled oscillators, coherent crystal oscillators of on-board indicators of impulse-phase systems, phase shifts control blocks of receiving tracts of phase measuring systems and the steering oscillators of the reference frequency and time positional GPS NAVSTAR and GLONASS systems as well [1].

As a rule, an external (in reference to oscillator) phaser controls a phase of high stability oscillations. However, their usage leads to undesirable consequences: the constructions of oscillatory systems are complicated, and the operating, mass and overall dimension parameters are getting worse. Moreover, influence of non-stabilizing factors does not allow us to obtain simultaneously the high slope and control function characteristics stability of the output signal.

As regards to stable oscillations, the frequency  $\omega_0$  of these ones is located within the limits of a crystal resonator gap. Due to interactions between a perpendicular exciting field (between the main electrodes) and parallel one (between the main and additional electrodes) in such type of resonator, the phase ratio of oscillations on the

load resistor appears to be sensitive to the complete resistance changes of the external  $T$ -shape  $RC$  circuit. This property is used for mechanical or electronic control of the output signal phase by change of loaded resistance. The controlling function can be performed with any active element, for example, with a use of a field transistor.

## DESIGN OF A MULTIELECTRODE RESONATOR

To extension a tuning range and increase a frequency stability Barjin *et al* in [2] had offered the design of quartz crystal resonator of AT-cut of thickness-shear vibrations, which is differed from traditional ones by special additional electrodes (fig.1).

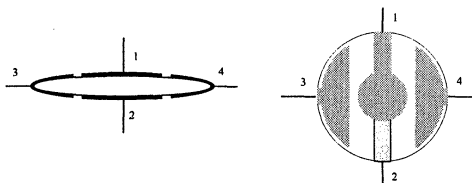


Figure 1. Design of the quartz crystal resonator with main (1,2) and additional (3,4) electrodes

Such resonator consists of the lens form piezo plate with 1<sup>st</sup> and 2<sup>nd</sup> main electrodes. Also, there are 3<sup>rd</sup> and 4<sup>th</sup> additional electrodes of the segment form, which located on both sides of the plate. The chords of additional electrodes are perpendicular to  $z'$  axis of a piezo plate, and the square of these ones is approximately equal to square of the main electrodes. The plate and holders are located into the vacuum glass of cylinder type.

The resonator has particular properties that differ from well-known ones and are subject to further investigations in direction of phase modulator creation. It had been found out under a resonator excitation in a perpendicular electric field by means of 1<sup>st</sup> and 2<sup>nd</sup> main electrodes that between 3<sup>rd</sup> and 4<sup>th</sup> additional ones there is a voltage, which form has the phase shift of  $\pm 180^\circ$  with respect to each main electrodes. Moreover, resonator parameters are differed one from another under the resonator excitation in perpendicular and parallel fields that is obtained by combination of electrodes.

## A CRYSTAL OSCILLATOR CIRCUIT

Figure 2 shows the circuit of quartz crystal oscillator with four-electrode resonator that allows us to simulta-

neously combine the functions of oscillation and stabilization, and output signal phase control as well. The oscillator is a subject to Colpitts circuit with the resonator, which 1<sup>st</sup> and 2<sup>nd</sup> electrodes is connected to oscillatory circuit as the frequency determining and stabilizing unit. Between main 1<sup>st</sup> and additional 4<sup>th</sup> electrodes of resonator there is incorporated the  $RC$   $T$ -type circuit, which consists of  $C_1$  and  $C_2$  capacities, and  $R_1$  resistor. The capacity  $C_3$  allows to carry out the oscillator frequency steering and afford the regime of effective control of the output signal phase. On the resistors  $R_2$  and  $R_3$  there are extracted correspondingly the phase-modulated and reference oscillations.

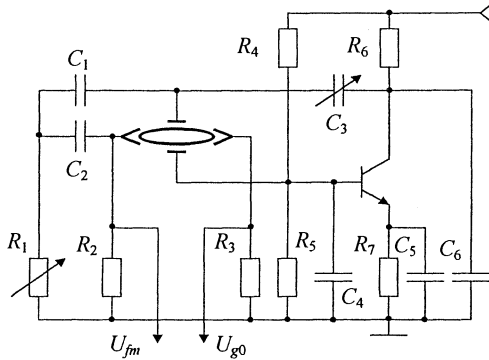


Figure 2. The crystal oscillator circuit with four-electrode resonator.

The frequency  $\omega_0$  in a steady-state mode of oscillations is determined within an inter resonance gap of resonator. Due to interaction between perpendicular (between main 1<sup>st</sup> and 2<sup>nd</sup>, and additional 3<sup>rd</sup> and 4<sup>th</sup> electrodes) and parallel (between 1<sup>st</sup> and 3<sup>rd</sup>, 1<sup>st</sup> and 4<sup>th</sup>, 2<sup>nd</sup> and 3<sup>rd</sup>, 2<sup>nd</sup> and 4<sup>th</sup> electrodes) excitation fields in a quartz resonator, the phase ratios of oscillations on the loading  $R_2$  resistor are very sensitive to the change of complex resistance of the outside  $T$ -type circuit [3]. This change is necessary for the phase control and obtained by  $R_1$  resistor. The function of this resistor one may be fulfilled with an active unit, a field transistor in regime of resistor control, in instance.

### AN ANALYSIS OF THE OSCILLATORY CIRCUIT

During the circuit (fig.2) analysis, it has been necessary to account both parameters of the outside controlling circuit units and inside processes in multielectrode resonator. At present, we have worked out the multiresonance bridge equivalent circuit of a resonator. However, taking into consideration its complexity, let us carry out an analysis of the simplified equivalent circuit (fig.3), in which the real parameters of resonator and oscillator changed to their equivalent values (fig.3b).

Let us introduce the following designations:  $\dot{U}_1 = U_1 e^{j\varphi_1}$  is a voltage on the 1<sup>st</sup> main electrode of resonator,

$\dot{U}_2 = U_2 e^{j\varphi_2}$  is a voltage on the 4<sup>th</sup> additional electrode of resonator,  $\varphi_2 - \varphi_1 = \pi$  is the phase shift between  $\dot{U}_1$  and  $\dot{U}_2$ ,  $\dot{z}_{in} = R_{in} + jx_{in}$  is a resonator input resistance between 1<sup>st</sup> main electrode and common line,  $\dot{z}_{eq} = R_{eq} + 1/(j\omega C_{eq})$  is an equivalent resistance between 4<sup>th</sup> and 2<sup>nd</sup> electrodes of resonator.

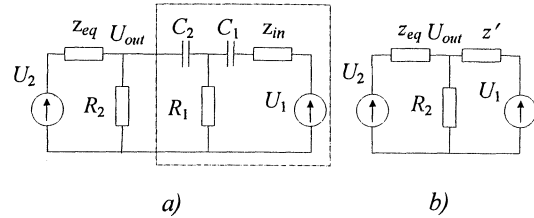


Figure 3. Equivalent circuits of the quartz crystal oscillator: a) complete; b) transformed

As usually,  $x_{in}$  have an inductive character, and  $z_{eq} \cong 1/(j\omega C_{eq})$  since  $\omega_{q12} < \omega_0 < \omega_{q24}$ , where  $\omega_{q12}$  and  $\omega_{q24}$  are the frequencies of series resonances of a resonator between 1<sup>st</sup> - 2<sup>nd</sup> and 2<sup>nd</sup> - 4<sup>th</sup> electrodes correspondingly.

Using the theorem of equivalent generator, let us exchange the part of the circuit (this one picked out in the fig.3a by dotted line) to that of equivalent electromotive force (e.m.f.) one and go to the circuit (fig.3b), where an e.m.f.-input resistance is described by the function

$$z' = \frac{R_1[z_{in} + 1/(j\omega C_1)]}{R_1 + z_{in} + 1/(j\omega C_1)} + \frac{1}{j\omega C_2}, \quad (1)$$

and its e.m.f. is described as

$$\dot{U}'_1 = \dot{U}_1 \frac{R_1}{R_1 + z_{in} + 1/(j\omega C_1)}. \quad (2)$$

The expression for  $\dot{U}_{out}(R_1) = \dot{U}_{PM}$ , which defined by applying method in accordance with fig.3b, appears as

$$\dot{U}_{out} = \frac{(\dot{U}'_1 z_{eq} + \dot{U}_2 z') R_2}{z_{eq} z' + z_{eq} R_2 + z R_2}. \quad (3)$$

Substituting (1) and (2) into (3) and carrying out the correspondent one transformation, we write the expression in closed form

$$\dot{U}_{out}(R_1) = \frac{(\dot{U}_1 \dot{A}_1 + \dot{U}_2 \dot{A}_2) R_2}{\dot{A}_2 (z_{eq} + R_2) + z_{eq} R_2}, \quad (4)$$

where

$$\dot{A}_1 = \frac{j\omega R_1 C_1 z_{eq}}{j\omega C_1 (R_1 + z_{in}) + 1},$$

$$\dot{A}_2 = \frac{\omega^2 C_1 C_2 R_1 z_{in} - 1 - j\omega (C_1 R_1 + C_1 z_{in} + C_2 R_1)}{\omega^2 C_1 C_2 (R_1 + z_{in}) - j\omega C_2}.$$

Since  $\dot{U}_{out}(R_1) = U_{out}(R_1)e^{j\varphi_{out}(R_1)}$ , the (4) describe the output amplitude  $U_{out}(R_1)$  and phase  $\varphi_{out}(R_1)$  characteristics.

Figures 4 and 5 show the phase  $\varphi_T(R_1)$  and the amplitude  $U_T(R_1)$  characteristics theoretically calculated in accordance with (4).

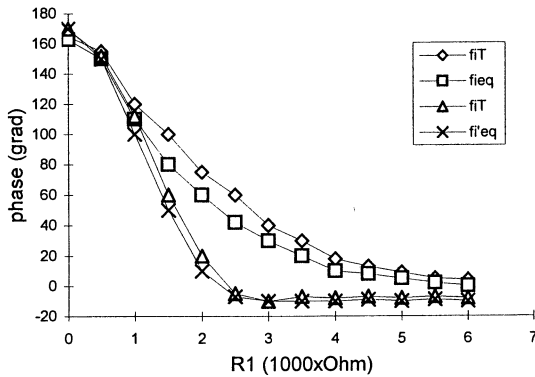


Figure 4. Phase performances of the oscillator output signal:  $fiT$  and  $fi'T$  are theoretical valuations for the basic and optimized circuits correspondingly,  $fieq$  and  $fi'eq$  are experimental values for the basic and optimized circuits correspondingly.

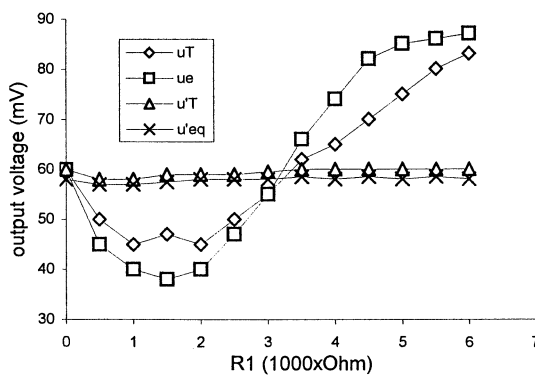


Figure 5. Output signal amplitude performances of the oscillator with controlled phase:  $uT$  and  $u'T$  are theoretical valuations for the basic and optimized circuits correspondingly,  $ue$  and  $u'eq$  are experimental values for the basic and optimized circuits correspondingly.

Results have been obtained for the following parameters of the oscillator equivalent circuit:  $C_1 = 91pF$ ,  $C_2 = 33pF$ ,  $R_{in} = 3000Ohm$ ,  $R_2 = 4700Ohm$ ,  $R_3 = 5100Ohm$ ,  $U_1 = 3U_2$ ,  $C_{eq} = 50pF$ ,  $x_{in} = 3000Ohm$ , and resonator:  $C_{q12} = 0.0198pF$ ,  $R_{12} = 7000Ohm$ ,  $L_{q12} = 1.43H$ ,  $C_1 = 91pF$ ,  $f_0 = 1MHz$ , and  $Q = 5.6 \cdot 10^{-5}$  is Q-factor. As it follows from (1) – (4), with a change of  $R_1$  from 0Ohm to 6000Ohm there is the output phase  $\Delta\varphi$  shift about  $170^\circ$ . Also, the slope of the controlling characteristic  $S_{fm}$  has

reached the level of  $0.04^\circ/Ohm$  with the small nonlinearity factor of 8% of the phase response and with rather small variations of  $\sim 10\%$  of the amplitude one. In addition, it has given here the experimental phase  $\varphi_{eq}(R_1)$  and amplitude  $U_{out}(R_1)$  responses of the quartz crystal oscillator circuit (fig.2) with the same parameters of units and voltages. Some comparative disadvantage of theoretical curves and data is explained by a resonator approximate model have been used in analysis.

Let us carry out an evaluation of the oscillator frequency change depending on the total loading resistance of the output signal phase controlling circuit for both extreme values of  $R_1$ . With  $R_1 = 0$  the capacity  $C_1$  is connected in parallel to  $C_6$  (fig.2). With  $R_1 = R_{max}$  there is connection of  $C_1$  through the  $R_1$  to the oscillator circuit. It may be marked here that the change of  $R_1$  leads to the change of capacity between transistor collector and emitter. Hence, it causes the frequency offset described by the form of [4]

$$\left(\frac{\Delta f}{f}\right)_g = \frac{C_{q12}}{2} \left[ \left(1 + \frac{R_{q12}}{R_{eq}}\right) \frac{1}{C_6} + \frac{1}{C_4} \right], \quad (5)$$

where  $R_{eq}$  is an equivalent resistance of the oscillator feedback circuit. In practice, one may get  $R_{q12}/R_{eq} \ll 10^{-3}$ . Moreover, we also obtained  $C_4 = C_6 = 6.8 \cdot 10^{-9}$ , in our case. As follows from (5), a frequency shift for these parameters has the level  $\Delta f/f = 1.1 \cdot 10^{-6}$  that corresponds to the long-term aging range of quartz crystal oscillator.

## THE QUARTZ CRYSTAL OSCILLATOR CIRCUIT OPTIMIZATION

The form of output phase and amplitude performances depends on circuit unit parameters, oscillatory regime, and performances of resonator. An analysis of (4) has been carried out with a help of PC/AT and had the aim of a range determination of the circuit units parameters possible changes for the given output characteristics. The values, that had been gotten, were used for the output oscillator parameters statistical optimization with Monte-Carlo method. During the optimization process the output parameters are given in a form of  $\Delta\varphi$ ,  $K_{hd}$ ,  $du_{out}/dR_1$ , and  $S_j^{n-1}$  random vectors. An exhaustion of set of admissible states of optimizing object on the forming of  $N$ -set of distributed numbers of  $P^N$  is effected in a range of admissible values of  $x_{i_{max}}^k - x_{i_{min}}^k$  input parameters or in a range of admissible changes of the oscillator circuit units parameters values. When we will get near an aim, a search zone will be contracted and a possibility of optimal magnitude determination will be increased.

Optimization of the oscillator circuit has been carried out on criteria of controlling  $S_{jm}$  slope characteristics maximization. The other output parameters (maximum of  $\Delta\varphi_{\max}$  range with simultaneous minimum of  $k_{hd}$  and  $du_{out}/dR_1$  coefficient of harmonic distortion) had given the limitations for random vectors distribution space. The optimization algorithm block diagram is shown in the fig.6.

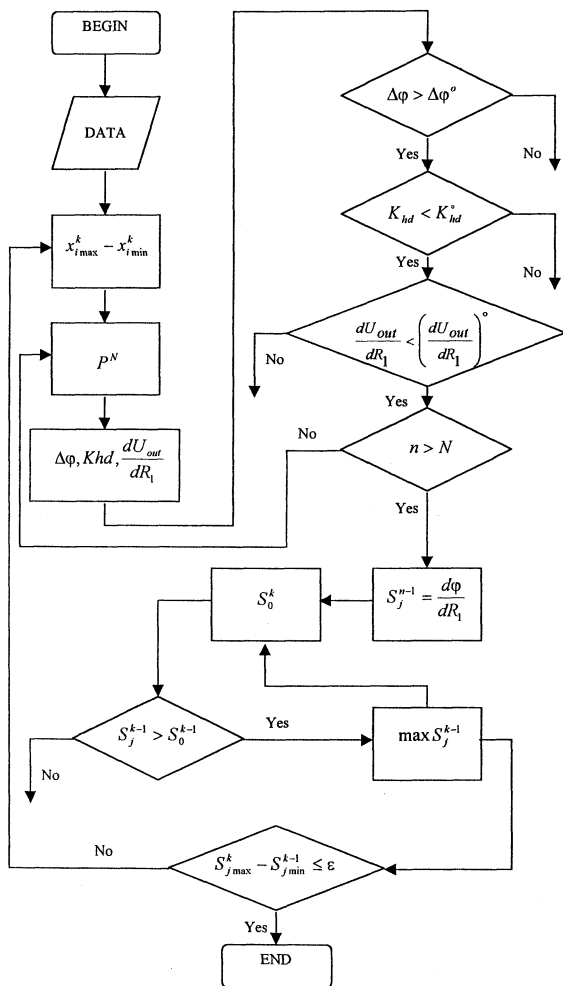


Figure 6. Block diagram of the optimization algorithm

As a result of optimization there is obtained a quartz crystal oscillator circuit with parameters of its units:  $C_1 = 51 pF$ ,  $C_2 = 27 pF$ ,  $C_{eq} = 10 pF$ ,  $R_{in} = 5000 \text{ Ohm}$ ,  $x_{in} = 10000 \text{ Ohm}$ ,  $R_2 = R_3 = 5600 \text{ Ohm}$ ,  $U_1 = 2U_2$ ,  $R_1 = 0..6000 \text{ Ohm}$ , and special parameters of resonator:  $f_0 = 1 \cdot 10^6 \text{ Hz}$ ,  $L_{q12} = 1.43 \text{ H}$ ,  $C_{q12} = 0.0198 \text{ pF}$ ,  $R_{q12} = 7000 \text{ Ohm}$ ,  $C_0 = 6.3 \text{ pF}$ ,  $Q = 5.6 \cdot 10^5$ . Theoretical  $\varphi_T(R_1)$  and  $U_{out}(R_1)$ , and experimental

$\varphi_{ex}(R_1)$  and  $U_{out.ex}(R_1)$  performances of optimized oscillator circuit with output parameters of  $S_{PM} > 0.1^\circ / \text{Ohm}$ ,  $dU_{out}/dR_1 < 1\%$ ,  $\Delta\varphi \cong 180^\circ$ , and  $k_{hd} < 2\%$  are shown in the figures 4 and 5 as well. Under the electrical phase control of output oscillations, a  $S_{jm}$  slope had reached the value of  $(2 \cdot 10^4)^\circ / V$ .

## CONCLUSION

We had shown in the report that the multielectrode quartz crystal resonator gives a possibility to create high stability oscillator devices with an output signal controlled phase. The method had been used here for such devices analysis and discussed above allows us to calculate their general characteristics with engineering accuracy. During such analysis with the use of the method of statistical optimization, there is a possibility to define the oscillator circuit units parameters closed to optimal.

In whole, the analysis had shown that the quartz crystal oscillator with controlled phase of its output signal has gotten rather great slope of the control characteristics and high stability of the output oscillation amplitude in the controlling process.

## REFERENCES

1. Douglas R, Boulanger J, 1992, "Local Oscillator Requirements for Timekeeping in the  $10^{-14} \tau^{-1/2}$  Era", in Proc. of 46<sup>th</sup> IEEE IFCS, 6-26.
2. Barjin V, Zelenkov A, Karaulnik A, 1972, "Quartz crystal resonator", Patent #349078 (USSR).
3. Barjin V, Vasilenko A, Zelenskiy A, 1978, "Experimental Studies of Frequency-Phase Response characteristics of the Complex Quartz Crystal Resonator", Radioelektronika letatelnykh apparatov, **10**, 11-17 (in Russian).
4. Vasilenko A, Kolesnik E, Sorokoput V, 1985, "Phase Control of Output Oscillations in Quartz Crystal Oscillators", Elektronnaya tehnika. Radiodetali i radiokomponenty, **1(58)**, 71-74 (in Russian).

RANDOM WALK AND FIRST CROSSING TIME: APPLICATIONS IN METROLOGY

Laura Di Piro, Elena Perone  
 Università di Torino, Dip. Matematica  
 Via Carlo Alberto 10, 10124 Torino, Italy  
 Tel. +39-11-3919238, Fax +39-11-3487046

Patrizia Tavella  
 Istituto Elettrotecnico Nazionale G. Ferraris  
 Strada delle Cacce 91, 10135 Torino, Italy  
 Tel. +39-11-3919235, Fax +39-11-3487046, [tavella@tf.ien.it](mailto:tavella@tf.ien.it)

ABSTRACT

Random walks have a large interest in metrology, in fact they may describe the evolution in time of the values of reference measurement standards. In particular, random walk limited by barriers may be useful to study the probability that the error of a metrological standard doesn't exceed some tolerance thresholds at a certain time after calibration. A brief mathematical description is reported and, as an example, the behaviour of an atomic clock is investigated by a suitable random walk model.

1. INTRODUCTION

The evolution in time of many physical systems may be described by a series of random steps, whose integrated effect is often referred as a random walk. Well known are the phase and frequency random walk noises, which affect the signal of frequency standards.

Random walks have the interesting peculiarity that many of their properties can be exactly studied by means either of combinatorial analysis, or of recursive expressions. In particular, the probability that, at a certain instant  $t$ , the random walk crosses for the first time a tolerance level is of particular importance and suggests different applications in metrology also.

For example, let's suppose that a random walk may describe the error of a clock. At a certain instant the clock is synchronised, i.e. its error is set to about zero. It may be interesting to know which is the probability that such error exceeds a threshold level after a certain time. In the case of national reference time scales, the threshold level should be 100 nanoseconds as recommended by the CCTF. If a lower quality clock is used, the threshold may be any limit of permissible error.

The study of the threshold crossing probability helps in individuating how long a clock can stand alone with a reasonable probability not to exceed the permissible error or how often the clock has to be re-synchronised.

More in general, the analysis of random walks seems useful to determine the optimal calibration intervals of any measuring instrument or standard, from the industrial laboratory level, up to primary standards.

The mathematical description of the random walk is briefly reported and, as an example, an application to atomic clock is examined by a suitable random walk model and by studying the expected probability of level crossing.

2. MATHEMATICAL BACKGROUND

Let's consider a simple symmetrical random walk in which each jump is either +1 or -1 [1, 2]. Let  $S_n$  be a random variable denoting the position at time  $n$  of a moving particle. Initially the particle is at the origin,  $S_0=0$ . At  $n=1$  there is a jump, upwards to position 1 with probability 1/2, and downwards to position -1 with probability 1/2. At  $n=2$  there is a further jump, again of one step. The jumps at all times are independent.

We shall denote the individual steps generically by  $X_1, X_2, \dots$  and the positions of the particle by  $S_1, S_2, \dots$ . Steps  $X_i$  are independent and identically distributed random variables, thus the random walk results

$$S_n = X_1 + \dots + X_n, S_0 = 0. \tag{1}$$

The event "at epoch  $n$  the particle is at the point  $r$ " will be denoted by  $\{S_n = r\}$ . We will denote its probability by  $p_{n,r}$  and it can be written as [1]:

$$P\{S_n = r\} = p_{n,r} = \binom{n}{\frac{n+r}{2}} 2^{-n} \tag{2}$$

Let's now consider the motion of the particle to be restricted by the presence of barriers. By using the reflection principle [1, 2] and combinatorial methods [3], the following theorem can be proved.

**Theorem 1:**

Let  $a$  and  $b$  be positive, and  $-b < c < a$ . The probability that the particle arrives to the point  $(n, c)$  without having touched the barrier  $-b$  and  $a$  is given by:

$$P\{S_n = c, -b < S_i < a, \forall i = 0, \dots, n-1 \mid S_0 = 0\} = \sum_{k=-\infty}^{+\infty} (p_{n, 2k(a+b)+c} - p_{n, 2k(a+b)+2a-c}) \tag{3}$$

Where the series has only finitely many non-zero terms. Therefore, the probability that the particle is still inside the barriers at the epoch  $n$  is given by:

$$P\{-b < S_i < a, \forall i=0, \dots, n | S_0 = 0\} = \left[ \sum_{c=-b+1}^{a-1} \left[ \sum_{k=-\infty}^{+\infty} (p_{n,2k(a+b)+c} - p_{n,2k(a+b)+2a-c}) \right] \right] \quad (4)$$

An analogous result can be obtained in the case of more general random walks [3], where the steps can assume the values  $-1, 0, 1$  with  $P\{X_i=1\}=p$ ,  $P\{X_i=0\}=1-p-q$ ,  $P\{X_i=-1\}=q$ , where the probability has not necessary to be symmetric ( $p \neq q$ ), or when the process is continuous [2].

In the following example of application to atomic clocks, the continuous process of random walk will be used. In such case, the analogous of probability (2) that the particle starting from  $s_0$  at the time  $t=0$  arrives in  $s$  at the time  $t$  is given by:

$$p(s_0, s; t) = \frac{1}{\sigma\sqrt{2\pi t}} \exp\left\{-\frac{(s - s_0 - \mu t)^2}{2\sigma^2 t}\right\} \quad (5)$$

A Gaussian density function can be recognised with average value equal to  $\mu t$  and variance equal to

$\sigma^2 t$ . Such expression, usually referred as Wiener process with drift, is a solution of the diffusion equation used in different application fields [2].

The probability that the process evolves inside two barriers, without touching them can be written by a generalisation of (3). Such a generalisation requires particular care because now the process is no more symmetric and the demonstration of the analogous of Theorem 1 requires the introduction of suitable corrective factors [2, 3]. For processes starting from the origin ( $s_0=0$ ), the final expression results:

$$\bar{p}(c, t) = \sum_{k=-\infty}^{+\infty} \left[ \exp\left\{-\frac{2k(a+b)\mu}{\sigma^2}\right\} p(2k(a+b)+c; t) - \exp\left\{-\frac{2(k(a+b)+a-c)\mu}{\sigma^2}\right\} p(2k(a+b)+2a-c; t) \right]$$

where the symbol  $\bar{p}(c, t)$  stands for "probability that the process arrives in  $c$  at time  $t$  without having touched the barriers  $-b$  and  $a$ ". Thus the final survival probability is:

$$\bar{p}(t) = \int_{-b}^a \bar{p}(c; t) dc \quad (7)$$

### 3. APPLICATION TO ATOMIC CLOCK

Random walks have a large interest in metrology, in fact they may describe the evolution in time of the values of reference measurement standards. In particular, random walk limited by barriers may be useful to study the probability that the error of a metrological standard doesn't exceed some tolerance thresholds at a certain time after calibration.

As an example the behaviour of atomic frequency standards was examined. In Fig. 1 the values of the difference UTC-UTC(k) are reported for some different country and it appears that a random walk model could be usefully applied.

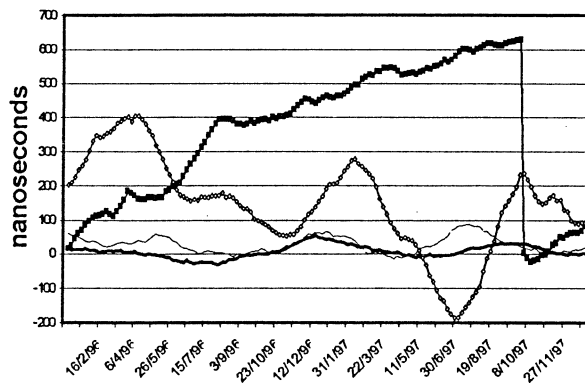
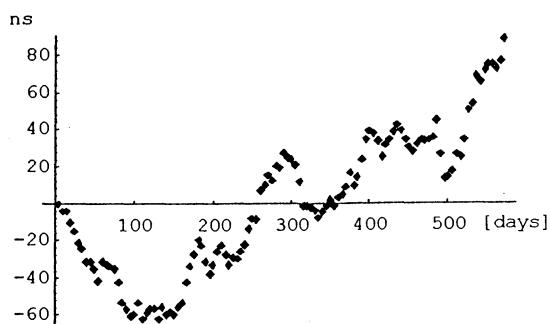


Fig. 1 Examples of UTC-UTC(k) from BIPM Circular T data. The black line with squares represents UTC-UTC(IEN).

In particular, we studied a random walk model for representing the behaviour of a primary atomic clock maintained at the Istituto Elettrotecnico Nazionale G.Ferraris of Turin, Italy, which generates the reference time scale UTC(IEN). The final aim is of estimating the survival probability function inside two barriers, by applying the method described in the previous section.

The study was performed on the behaviour of the clock after having removed all the time and frequency steps intentionally applied to maintain the agreement with UTC. For the same two year period considered in Fig. 1, the behaviour of the IEN master clock is that reported in Fig. 2, where a constant drift of about +13 ns/day was removed to concentrate the attention only on the random part of the process.



**Fig.2 Measures of UTC-IEN master clock (drift of  $\approx 13$  ns/day removed)**

From the knowledge of the noise affecting the atomic clock under consideration and from the experimental measures at disposal, it appears that the time deviation (UTC - Master clock) is mostly due to a phase random walk as obtained from the integration of a white frequency noise. In fact, the measurements at disposal are time deviations of the clock estimated any 5 days and, for integration time in the region of  $\tau=5$  days, it can be assumed that the predominant noise is white FM. As long as the predominant noise is due to white FM, the following model can be applied. From the analysis of experimental data and from consideration about the physical nature of the clock system, it seems that the continuous process model is the best suited for representing the behaviour of the clock.

The probability that such process is in position  $s$  at the time  $t$  having started from  $(t=0, s=0)$  is given by (5), where, from the analysis of experimental data, the estimates  $\mu \approx 0.7$  ns/day and  $\sigma^2 \approx 37.8$  ns<sup>2</sup>/day were inferred.

At this point, we have all the information necessary to evaluate equation (7) and to estimate the probability of remaining within two barriers for a certain period after synchronisation.

For example, the threshold levels equal to  $\pm 100$  ns are the tolerance levels recommended by the CCTF. By substituting  $a = b = 100$  ns in the (7), with the estimated values of  $\mu$  and  $\sigma$ , the survival probability inside the barriers is estimated as a function of time. Such probability is depicted in Fig. 3, with other different values for the threshold levels.

From Fig. 3 we can see that, with probability 90% (horizontal line to 0.90), the process would be inside the tolerance range of  $\pm 100$  ns for about one year. When the barriers are fixed at  $\pm 200$  ns, the probability that the process remains inside the tolerance range would be high enough and it would not decrease below 0.75 for a period of about 1000 days. Decreasing the tolerance thresholds, there

would be a need of re-synchronising the clock more often. If the barriers were equal to  $\pm 50$  ns or  $\pm 20$  ns, the time interval between two successive synchronisation would decrease to a few days, at a confidence level of 90%.

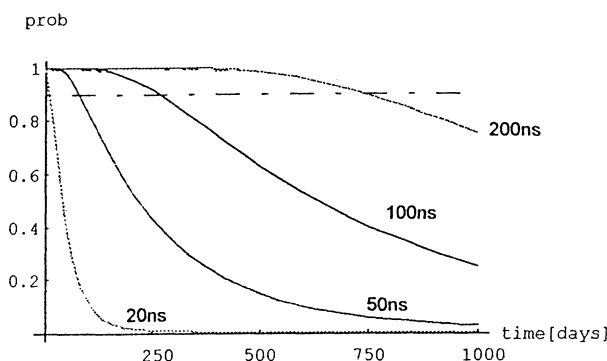


**Fig. 3: Probability that the process remains within two fixed levels.**

Such results are to be considered as approximate and related to a provisional analysis with a small amount of experimental data, being the aim of this study only the demonstration of the utility of the method, rather than a complete characterisation of the clock at hand. The good stability of the considered clock and the fact of having a good estimate of its drift, *a posteriori*, lead to the estimate that the clock, due to its natural behaviour, could remain inside the tolerance thresholds for a long period of time. Actually, it is known that the aim of remaining inside the tolerance range of  $\pm 100$  ns is a rather challenging aim. In particular, for integration time  $\tau$  longer than one month the clock could show a predominant noise not only due to a white FM, but also to some other slower modulations. In this case, the model would not be applicable as such, but it would require the addition of another slower process. Nevertheless, for integration time from one day to approximately one month, the assumption of phase random walk remains valid and the method described could be a valuable help in estimating the performance of the clock.

#### 4. OTHER APPLICATION IN METROLOGY

The same evaluations could be of interest for other metrological standards. For example, the application to Weston cell voltage standards is currently under study [3].

More in general, the problem of how often a "calibration" or "adjustment" should be repeated has a large interest in metrology either at the primary standard level or at the industrial level. In the former case, the international metrological bodies are discussing an "Agreement on equivalence of national standards and recognition of calibration certificates issued by national metrology institutes

[4]. One consensus already reached is that the technical basis for equivalence will be a series of carefully selected measurement comparisons, to be known as the key comparisons, which will be repeated at appropriate intervals of time. "The periodicity of the comparisons is set to ensure continuity of the equivalence ..." [4], but no quantitative criteria are established at the moment.

As far as metrology in industry is concerned, the importance of establishing appropriate calibration intervals for each instrument is well recognised in the international and European standards. Among the standards concerning quality programs for industries, for example, the EN ISO 9001 [5], prescribes that measurement and testing instruments shall be periodically confirmed through a calibration and verification. The same concept is extensively reformulated in the ISO 10012 [5]. EN ISO 9001, in paragraph 4.11, says: "Measuring equipment ... shall be confirmed at appropriate intervals (usually periodic) established on the basis of their stability, purpose and usage. The intervals shall be such that confirmation is again carried out prior to any probable change in accuracy that is of significance in the use of the equipment". However, in the mentioned standards there is a surprising lack of established methodologies or recipes for estimating the calibration intervals and the periodicity of calibration is often established only qualitatively. The definition of quantitative techniques for evaluating the calibration intervals may constitute a valuable support for integrating the actual standards with updated methodologies and to help European industries to achieve a good compliance to standards. Some preliminary results obtained by the mathematical modelling of calibration intervals were reported in [6], and the study reported in this paper constitutes its further development.

## 5. CONCLUSIONS

The evolution in time of the behaviour of a metrological standards can often be modelled by a suitable random walk obtained as the integration of different independent perturbations. Random walks of different nature have a powerful mathematical description that permits the evaluation of many interesting features. In particular, the study of the probability that the random walk doesn't exceed some tolerance barriers for a certain period of time suggests interesting applications to metrology, where the tolerance barriers can be some limits of permissible errors. An application to atomic clock was presented, with the general aim of explaining by an example the possible information that may be inferred by a random walk modelling.

## ACKNOWLEDGEMENTS

The authors are largely indebted to Daniela Meo of the University of Turin for her kind support during the preparation of this work.

## REFERENCES

- [1] W. Feller, An introduction to probability theory, Wiley, New York, 1968, Cap. 3,14.
- [2] D.R.Cox, H.D.Miller, The theory of stochastic processes, Science Paperbacks, Chapman and Hall, London, 1965, Cap. 2,5.
- [3] L. Di Piro, "Passeggiate casuali e probabilità di primo attraversamento: applicazione alla metrologia", and E. Perone, "Cammini aleatori limitati da barriere: modello per i campioni metrologici primari", Degree thesis in Mathematics, University of Turin, Italy, 1998 [in Italian].
- [4] CIPM/97 (a) "Agreement on equivalence of national measurement standards and recognition of calibration certificates issued by national metrological institutes", Draft, Aug. 1997. (b) "Guidelines for the Consultative Committee key comparisons", Comite International des Poids et Mesures, Draft Aug. 1997.
- [5] EN ISO 9001: "Quality system: Model for quality assurance in design, development, production, installation and servicing", Sec. 4.11, 1994, ISO 10012 (EN 30012): "Quality assurance requirements for measuring equipment - Part I (1992, now under revision), Part II (1997)", International Standardisation Organisation, Geneva.
- [6] A. Bobbio, P. Tavella, A. Montefusco, S. Costamagna, "Monitoring the calibration condition of a measuring instrument by a stochastic shock model", IEEE Trans. Instr. Meas. Vol. 46, n. 4, pp. 747-751, 1997.

# About the radiofrequency spectrum of a phase noise-modulated carrier

A. Godone and F. Levi

Istituto Elettrotecnico Nazionale "G. Ferraris"

Str delle Cacce 91, 10135 Torino, Italy. E-Mail: Levi@tf.ien.it

## ABSTRACT

The RF spectrum of a carrier modulated by a phase noise with spectral density of the form  $|\omega|^{-\alpha}$  ( $0 \leq \alpha < 3$ ) is analyzed and closed form expressions are reported in terms of hypergeometric functions for the white phase noise ( $\alpha=0$ ) and white frequency ( $\alpha=2$ ) noise, and in terms of modified Bessel functions for the flicker phase noise ( $\alpha=1$ ). Moreover the behavior of the RF spectrum near the carrier frequency is examined for every  $\alpha$  in the range  $0 \leq \alpha < 3$ .

## I INTRODUCTION

The radiofrequency (RF) spectrum of a phase-noise modulated carrier has been widely examined in the past, in particular by the communication and time and frequency communities (see for example [1,2,3] and references therein). Recently the problem has been faced also for carriers in the visible range, [4,5], when modulated by white or frequency noises.

In this work we reconsider the problem *ab initio*, reaching a closed form expression for the RF spectrum in the case of white phase and frequency noises in terms of generalized and confluent hypergeometric functions respectively; these special functions can now be easily handled analytically and numerically, due to the recent development of powerful software programs, such as [6]. This formulation allows also a full description of the RF multiplied spectrum without approximations.

Moreover the general case of a phase flicker noise ( $|\omega|^{-\alpha}$  with  $0 < \alpha < 2$ ) is examined with particular care for the RF spectrum near the carrier frequency: completely different behaviors are found for the three cases  $0 < \alpha < 1$ ,  $\alpha=1$  and  $1 < \alpha < 2$ ; a closed form expression for the full RF spectrum is also reported when  $\alpha=1$ .

The effect of the low-pass filter and of its slope, defining the bandwidth of the modulating noise, is then discussed for all the random processes considered in this work ( $0 \leq \alpha < 3$ ).

## II GENERAL THEORETICAL CONSIDERATIONS

We state the problem in the following way: given a sinusoidal signal

$$v(t) = V_0 \sin[\omega_0 t + \varphi(t)] \quad (1)$$

where  $\varphi(t)$  is a stationary random process with Gaussian distribution and zero mean value,  $\omega_0$  is the carrier angular frequency and  $V_0$  the amplitude (we assume  $V_0 = \text{constant}$  that means no amplitude modulation), we want to determine the power spectral density  $S_v(\omega)$  of  $v(t)$  (RF spectrum) assuming the knowledge of the phase spectral density  $S_\varphi(\omega)$  of  $\varphi(t)$ . Taking into account the Wiener-Khinchine theorem [1,7], the RF spectrum is the Fourier transform of the signal autocorrelation function  $R_{vv}(\tau)$ :

$$S_v(\omega) = \int_{-\infty}^{+\infty} R_{vv}(\tau) e^{-i\omega\tau} d\tau \quad (2)$$

In the hypothesis above reported (stationary and Gaussian random process),  $R_{vv}(\tau)$  is given by [1]:

$$R_{vv}(\tau) = \frac{1}{2} V_0^2 \cos \omega_0 \tau e^{-\Omega_\varphi(\tau)} \quad (3)$$

with:

$$\Omega_\varphi(\tau) = R_{\varphi\varphi}(0) - R_{\varphi\varphi}(\tau) \quad (4)$$

In equation (4)  $R_{\varphi\varphi}(\tau)$  is the autocorrelation function of  $\varphi(t)$ ; taking again into account the Wiener-Khinchine theorem, we have:

$$R_{\varphi\varphi}(\tau) = \frac{1}{2\pi} \int_{-\infty}^{+\infty} S_\varphi(\omega) e^{i\omega\tau} d\omega \quad (5)$$

The function  $\Omega_\varphi(\tau)$  satisfies the following conditions [1,7]:

$$\Omega_\varphi(0) = 0, \quad \Omega_\varphi(\tau) \geq 0 \quad \forall \tau$$

The equations from (2) to (5) lead to the evaluation of RF spectrum once the phase noise spectral density is specified. In the case of high frequency stability oscillators,  $S_\varphi(\omega)$  may be expressed as a sum of statistically independent terms of the form  $K_\alpha |\omega|^{-\alpha}$  [2] where  $K_\alpha$  is a constant related to the integrated noise power and  $0 \leq \alpha \leq 4$ . We assume moreover that the modulating noise is a band-limited process as always happens in the practical

situations: we consider than noise processes of the type:

$$S_\varphi(\omega) = K_\alpha |\omega|^{-\alpha} |H(i\omega)|^2 \quad (6)$$

where  $H(i\omega)$  is a low-pass transfer function. In this work we consider the different noise processes separately. The expressions (4), (5) and (6) yield:

$$\Omega_\varphi(\tau) = \frac{K_\alpha}{\pi} \int_0^\infty \frac{1 - \cos \omega \tau}{\omega^\alpha} |H(i\omega)|^2 d\omega \quad (7)$$

Finally the RF spectrum is obtained from (2),(3) and (7):

$$S_v(\omega) = V_0^2 \int_0^\infty \cos(\omega - \omega_0)\tau e^{-\Omega_\varphi(\tau)} d\tau \quad (8)$$

In the formulas (7) and (8) we have taken into account that, for a real physical process,  $\Omega_\varphi(\tau)$  and  $S_v(\omega)$  are even functions [1].

It is clear from (8) that many fundamental properties of  $S_v(\omega)$  may be deduced from  $\Omega_\varphi(\tau)$  directly. In particular the integral (7) is not defined for  $\alpha \geq 3$  (infrared divergence) and then the RF spectrum doesn't exist for the flicker ( $\alpha=3$ ) and random walk ( $\alpha=4$ ) frequency noises; in order to evaluate the stability characteristics of an oscillator in presence of these non-stationary noises, the analysis may be performed in the time domain through filtered variances as the Allan variance [2]. In the following we limit our analysis to  $0 \leq \alpha < 3$ .

When  $|H(i\omega)|^2 = 1$  (all-pass filter), equation (7) leads to [8]:

$$\Omega_\varphi(\tau) = -\frac{K_\alpha}{\pi} \Gamma(1-\alpha) \cos \frac{\pi}{2}(1-\alpha) |\tau|^{\alpha-1} \quad 1 < \alpha < 3 \quad (9)$$

which implies that the high-pass filter is not mathematically necessary in the range  $1 < \alpha < 3$  for ensuring the existence of the RF spectrum.

As far as the phase variance  $\sigma_\varphi^2$  is concerned, it is given by [7]:

$$\sigma_\varphi^2 = R_{\varphi\varphi}(0) = \frac{K_\alpha}{\pi} \int_0^\infty \frac{|H(i\omega)|^2}{\omega^\alpha} d\omega \quad (10)$$

and is defined for  $0 \leq \alpha < 1$  ( for  $1 < \alpha < 3$  a frequency variance  $\sigma_\varphi^2$  will be introduced further on).

In Tab I all the above considerations are summarized.

Range	Low-pass filter	phase variance
$0 \leq \alpha < 1$	necessary	exists
$\alpha = 1$	necessary	Not defined
$1 < \alpha < 3$	not necessary	Not defined

Tab I General Considerations

It follows moreover from (8) that  $\lim_{\tau \rightarrow \infty} \Omega_\varphi(\tau)$

defines the behavior of  $S_v(\omega)$  at  $\omega = \omega_0$ ; careful considerations lead to the possible cases summarized in TAB III. They will be very helpful in carrying the computations reported in the next paragraphs; since now it may be observed that the RF spectrum at  $\omega = \omega_0$  may preserve the carrier (Dirac  $\delta$ ), may be divergent or finite.

$\lim_{\tau \rightarrow \infty} \Omega_\varphi(\tau)$	$\lim_{\tau \rightarrow \infty} R_{vv}(\tau)$	RF spectrum @ $\omega = \omega_0$
Positive constant	positive constant	$\delta(\omega - \omega_0)$
Logarithmic divergence	$\approx \lim_{\tau \rightarrow \infty} \tau^{-\beta}$	$\left\{ \begin{array}{ll} \text{divergence} & 0 < \beta < 1 \\ \text{log div} & \beta = 1 \\ \text{finite} & \beta > 1 \end{array} \right.$
divergence	0	finite

TAB II Behavior of the RF spectrum at  $\omega = \omega_0$ , related to the behavior of  $\Omega_\varphi(\tau)$  at  $\tau = \infty$ ;  $\beta$  is a real positive number.

### III WHITE PHASE NOISE $\alpha=0$

We assume a single pole filter (RC or Lorentzian filter) for the spectrum of  $\varphi(t)$ :

$$S_\varphi(\omega) = \frac{K_0}{1 + (\omega / \omega_n)^2} \quad (11)$$

where  $\omega_n$  is the -3dB filter bandwidth. Introducing (11) in (7) we obtain:

$$\Omega_\varphi(\tau) = \sigma_\varphi^2 \left( 1 - e^{-\omega_n |\tau|} \right) \quad (12)$$

being  $\sigma_\varphi^2 = k_0 \omega_n / 2$  (from eq. 10). From TAB II and (12) we see that a white phase noise modulation preserves the carrier. From the definition of the generalized functions  ${}_2F_2$  [8], the RF spectrum may be expressed in the closed form:

$$S_v(\omega) = \frac{V_0^2}{\omega_n} \left\{ \pi e^{-\sigma_\varphi^2} \delta(\Delta) + \sigma_\varphi^2 e^{-\sigma_\varphi^2} \Re e \left[ \frac{{}_2F_2(1, 1-i\Delta; 2, 2-i\Delta; \sigma_\varphi^2)}{1-i\Delta} \right] \right\} \quad (13)$$

where  $\Delta = (\omega - \omega_0) / \omega_n$  is the normalized detuning. This expression, also reported in [4], describes the well-known spectrum shown in Fig 1.

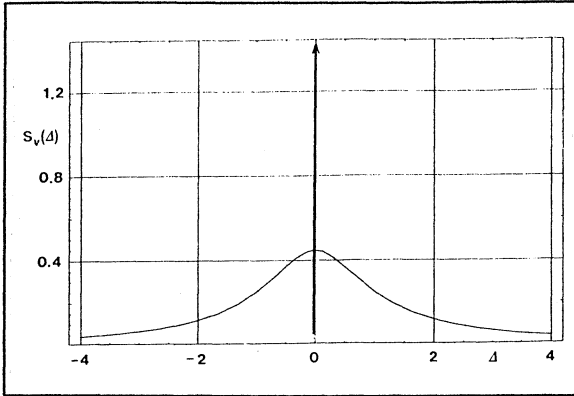


Fig. 1 - RF spectrum of a carrier modulated by a white phase noise.

The pedestal height  $h_p$  and width  $\Delta_{1/2}$  are reported in Fig 2 versus the phase variance, as obtained from (13); they allow also a generalization of the theory reported in [9], regarding the spectrum of a multiplied signal. The shape of the spectrum is Lorentzian both for  $\sigma_\phi^2 \rightarrow 0$  and for  $\sigma_\phi^2 \rightarrow \infty$ .

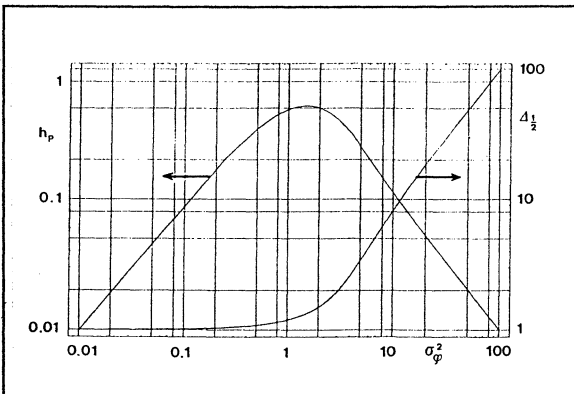


Fig. 2 - Height and width of the RF spectrum. The height is reported in units of  $V_0^2 / \omega_n$ .

#### IV WHITE FREQUENCY NOISE $\alpha=2$

Assuming also in this case a Lorentzian filter, we have from (7):

$$\Omega_\phi(\tau) = \mu_f^2 \left[ \omega_n |\tau| - 1 + e^{-\omega_n |\tau|} \right] \quad (14)$$

Where  $\mu_f$  is the modulation index, defined through the frequency variance  $\sigma_f^2$  by:

$$\mu_f^2 = \frac{\sigma_f^2}{\omega_n^2} = \frac{1}{\pi \omega_n^2} \int_0^\infty \omega^2 S_\phi(\omega) d\omega = \frac{K_2}{2\omega_n} \quad (15)$$

From (14) we see that  $\lim_{\tau \rightarrow \infty} \Omega_\phi(\tau) = \infty^1$  and then the RF spectrum is limited at  $\omega = \omega_0$ ; it may be expressed via the confluent hypergeometric function  ${}_1F_1$  as:

$$S_v(\omega) = \frac{V_0^2}{\omega_n} \Re e \left[ \frac{{}_1F_1 \left( 1; 1 + \mu_f^2 - i\Delta; \mu_f^2 \right)}{\mu_f^2 - i\Delta} \right] \quad \mu_f^2 > 0 \quad (16)$$

The typical spectrum is shown in Fig-3; it is Lorentzian when  $\mu_f^2 \rightarrow 0$  and Gaussian when  $\mu_f^2 \rightarrow \infty$ , a well known property [1] which is included in the behavior of  ${}_1F_1$ .

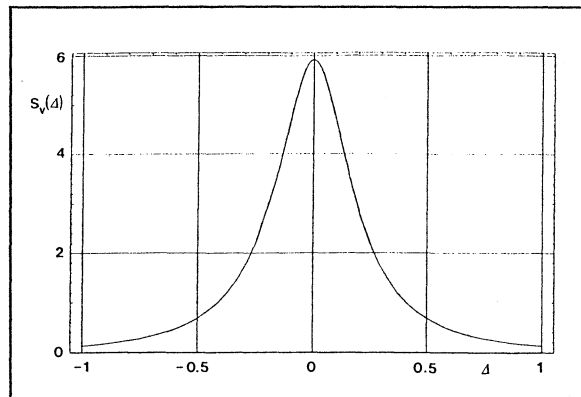


Fig. 3 - RF spectrum of a carrier modulated by white frequency noise.

The value of the spectrum at  $\omega = \omega_0$  and of its width  $\Delta_{1/2}$  are reported in Fig 4 versus  $\mu_f^2$ ; it is interesting to observe the behavior of  $\Delta_{1/2}$ : it increases as  $\mu_f^2$  for  $\mu_f^2 < 1$  (limiting spectrum shape Lorentzian) and as  $\mu_f$  for  $\mu_f^2 > 1$  (limiting spectrum shape Gaussian).

It is interesting to note that with an all-pass filter (pure white frequency noise) we obtain from (8) a pure Lorentzian spectrum:

$$S_v(\omega) = V_0^2 \frac{K_2 / 2}{(K_2 / 2)^2 + (\omega - \omega_0)^2} \quad (17)$$

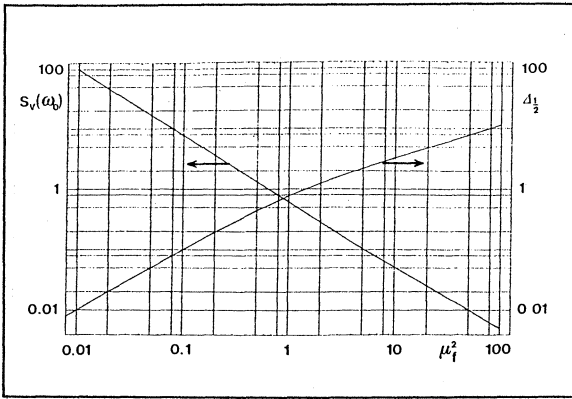


Fig. 4 - Value of  $S_v(\omega_0)$  in units of  $V_0^2/\omega_n$  and of  $\Delta_{1/2}$  versus  $\mu_f^2$ .

## V FLICKER PHASE NOISE $0 < \alpha < 2$

We consider the flicker phase noise in the wide sense of a phase spectral density of the type  $|\omega|^{-\alpha}$  with  $0 < \alpha < 2$ ; this situation is of practical interest because in many measurements the value of  $\alpha$  is found in this range [10]. It is convenient from the mathematical point of view to examine separately the cases  $\alpha=1$  and  $0 < \alpha < 2$  with  $\alpha \neq 1$

### The case $\alpha=1$

We consider two different filters which allow a simple analytical solution for  $\Omega_\varphi(\tau)$ , namely the rectangular and exponential filters:

$$\text{rect.} \quad |H(i\omega)|^2 = \begin{cases} 1 & \forall |\omega| \leq \omega_n \\ 0 & \forall |\omega| > \omega_n \end{cases} \quad (18a)$$

$$\text{exp} \quad |H(i\omega)|^2 = e^{-|\omega|/\omega_n} \quad (18b)$$

From (7) we obtain the two interesting expressions:

$$\text{rect} \quad \Omega_\varphi(\zeta) = \mu^2 [\gamma + \ln \zeta - Ci(\zeta)] \quad (19a)$$

$$\text{exp.} \quad \Omega_\varphi(\zeta) = \frac{1}{2} \mu^2 \ln(1 + \zeta^2) \quad (19b)$$

Where  $\gamma$  is the Euler constant,  $Ci(\zeta)$  is the cosine integral,  $\zeta = \omega_n \tau$  and  $\mu^2 = K_f/\pi$ . In both cases  $\lim_{\zeta \rightarrow \infty} \Omega_\varphi(\zeta) = \mu^2 \ln \zeta$  which corresponds to the second situation considered in Tab II with  $\beta = \mu^2$ .

When the exponential filter is used, an analytical expression for the RF spectrum is found [11] in terms of the modified Bessel functions  $K_\nu(z)$  with  $\nu = (\mu^2 - 1)/2$ :

$$S_v(\Delta) = \frac{V_0^2}{\omega_n} \frac{\sqrt{2\pi}}{2^{\mu^2/2} \Gamma(\mu^2/2)} \Delta^\nu K_\nu(\Delta) \quad (20)$$

The RF spectrum is shown in Fig 5; it is important to note that for  $\alpha=1$  and  $\mu^2 \leq 1$  an ordinary divergence is present at  $\omega = \omega_0$  and not a generalized function (Dirac  $\delta$ ), which means that the carrier is no more existing.

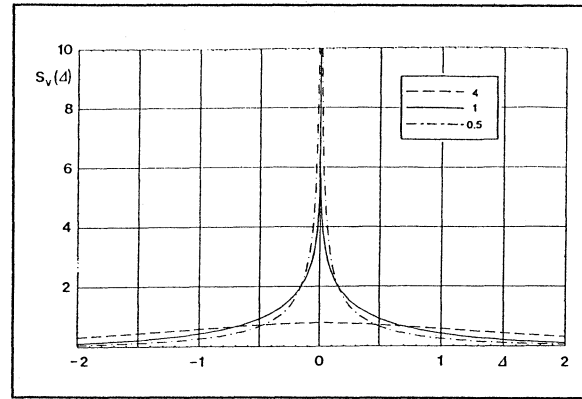


Fig. 5 - RF spectrum of a carrier modulated with flicker phase noise ( $\alpha=1$ ) when a gaussian filter is used in the calculations:  $\mu_f^2 = .5, 1, 4$  respectively.

### The case $0 < \alpha < 2, \alpha \neq 1$

The exponential filter (18b) leads in this case to a significant analytical expression for  $\Omega_\varphi(\tau)$  [6]:

$$\Omega_\varphi(\zeta) = \frac{K_\alpha}{\pi} \Gamma(1-\alpha) \omega_n^{1-\alpha} \left\{ 1 - \frac{\cos[(1-\alpha) \arctg \zeta]}{(1 + \zeta^2)^{(1-\alpha)/2}} \right\} \quad (21)$$

which clearly provides the behavior of the RF spectrum at  $\omega = \omega_0$ . In fact we have, taking into account (10), that:

$$\lim_{\zeta \rightarrow \infty} \Omega_\varphi(\zeta) = \frac{1}{\pi} K_\alpha \Gamma(1-\alpha) \omega_n^{1-\alpha} \equiv \sigma_\varphi^2 \quad 0 < \alpha < 1$$

$$\lim_{\zeta \rightarrow \infty} \Omega_\varphi(\zeta) = \infty^{\alpha-1} \quad 1 < \alpha < 2$$

The carrier  $\delta(\omega - \omega_0)$  is preserved when  $0 < \alpha < 1$  as in the white phase noise case, while the RF spectrum is finite at  $\omega = \omega_0$  when  $1 < \alpha < 2$  as for the white frequency noise.

Due to the limited space and for sake of simplicity, in this paragraph we have not reported all the results referring to the examined filters (Lorentzian, Gaussian, rectangular, exponential and all-pass) for every type of noise also because the properties reported so far turned out to be independent from the filter shape. This remark is fundamental

anyway, because only the Lorentzian filter satisfies the Paley-Wiener condition (causality principle) [12].

The solution (21) is valid also for  $2 < \alpha < 3$  and then applies up to the flicker frequency limit.

## VI CONCLUSIONS

The results obtained in this work concerning the behavior of the RF spectrum near the carrier frequency are summarized in TAB III. Even if some of them are well known, it turns out from the analysis that the random phase modulating spectra here considered ( $|\omega|^{-\alpha}$ ) shows a behavior of the type white phase noise when  $0 < \alpha < 1$  and of the type white frequency noise when  $1 < \alpha < 3$ ; The case  $\alpha = 1$  is very peculiar, because the spectrum shape near the carrier frequency depends critically on the power level.

$( \omega ^{-\alpha})$	$\lim_{\tau \rightarrow \infty} \Omega_{\varphi}(\tau)$	$S_v(\omega_0)$
$0 \leq \alpha < 1$	$\sigma_{\varphi}^2$	$\delta(\omega - \omega_0)$
$\alpha = 1$	$\lim_{\tau \rightarrow \infty} \mu^2 \ln \omega_n \tau$	$\begin{cases} \infty^{1-\mu^2} & 0 < \mu^2 < 1 \\ \log \text{ div} & \mu^2 = 1 \\ \text{finite} & \mu^2 > 1 \end{cases}$
$1 < \alpha < 3$	$\infty^{\alpha-1}$	finite
$\alpha \geq 3$	RF spectrum not existing	

TAB III Behavior of the RF spectrum near the carrier frequency

Moreover we have reported closed form expressions of  $S_v(\omega)$  without any approximations in the cases  $\alpha = 0$ ,  $\alpha = 1$  and  $\alpha = 2$  which may be very useful to evaluate the spectra at the output of frequency multipliers or the spectra of free running laser sources where the noise level may be very high. The effect of the shape of the low-pass filter, always present in the practical situations, has been carefully examined and it turns out quite unimportant to describe the RF spectrum near the carrier frequency.

## ACKNOWLEDGMENTS

This work has been partially supported by ASI (Italian Space Agency).

We would like to thanks P. Tavella and A. De Marchi for their cooperation.

## REFERENCES

- [1] D. Middleton Statistical Communication Theory Mc Graw-Hill New York 1960
- [2] J. Rutman Proc IEEE, Vol 66, p 1048 (1978)
- [3] J. Vanier C. Audoin The Quantum Physics of Atomic Frequency Standards, 1989, (Adam Higler, Bristol)
- [4] M. Zhu and J.L. Hall J. Opt. Soc. Am B Vol 10 p 802 (1993)
- [5] M. Prevedelli, T. Ferregarde and T.W. Hänsch Appl Phys B 60 s241 (1995).
- [6] Mathematica 3 by Wolfram Research
- [7] A. Papoulis Probability, Random Variables and Stochastic Processes, MC Graw-Hill New York (1965)
- [8] I.S. Grdsteyn and I.M. Ryzhik Table of Integral Series and Products Academic Press, New York (1965)
- [9] E. Bava, A. De Marchi and A. Godone IEEE Trans. IM-26 p 128 (1977)
- [10] F. L. Walls, E.S. Ferre-Pikal and S. R. Jefferts, IEEE Trans on Ultrasonic Ferroelectrics and Frequency Control, Vol 44 n 2 p 326.
- [11] M. Abramowitz and I. Stegun Handbook of Mathematical Functions
- [12] A. Papoulis The Fourier Integral and its applications Mc Graw-Hill, New York (1962)

## New approach to long term frequency stability measurement data analysis

B.Kalinowska, B.Gniewińska

Tele & Radio Research Institute, Ratuszowa 11, 03-450 Warsaw, Poland

### 1. INTRODUCTION

System for long term frequency stability measurement which was developed at ITR, enables simultaneous measurement of 100 oscillators. Measurements are made every two hours. The system accuracy is about  $1E-11$  while the measurement resolution is better than  $5E-12$  /1 sec.

Oscillators and system are placed in the nonairconditioned room. Monitoring of such environmental parameters as temperature, humidity and pressure is carried out together with frequency measurements.

Several data concerning frequency versus time characteristics could be available due to applied measurement method, among them:

- \* frequency versus time characteristic in the presence of environmental parameters changes,
- \* oscillators frequency sensitivity to temperature, humidity and pressure changes,
- \* frequency versus time characteristics after removing the environmental stresses influence,
- \* frequency stability per day in chosen time period,
- \* evaluation and prediction of future frequency changes in long time periods.

Basing on these data the day and month long term stability in accordance with IEC recommendation could be evaluated.

Another advantages of this approach ( nonairconditioned environment, large number of measurement points - 12 per day) are:

- \* estimation of oscillator parameter in real environmental circumstances,
- \* possibility of investigations of power supply breaks influence on aging characteristics,
- \* observation of aging characteristic nonregularity such as jumps and slow variable fluctuations.

### 2. METHODS OF CALCULATIONS

The least square method was the basic instrument for the oscillators sensitivity to environment stresses calculations and for removing influence of these stresses from measurement data.

Following assumptions were made:

- \* linear frequency dependence on all considered stresses and time,
- \* correlation between stresses in time domain are possible

To solve this problem from mathematical point of view it is necessary to evaluate linear functions of parameters:

$$a = g_1 a_1 + \dots + g_n a_n$$

for indirect observations basing on overdetermined set of equations:

$$y_i = l_i + \Delta i = \sum_{j=1}^n a_j x_{ij}$$

where:

- $a_j$  parameters,
  - $x_{ij}$  variables,
  - $\Delta_i$  errors,
  - $l_i$  measured values,
  - $i = 1 \dots N$  number of measurements,
  - $n$  number of parameters.
- Unbiased function estimation  $\tilde{a} = g_1 \tilde{a}_1 + \dots + g_n \tilde{a}_n$  and unbiased  $\tilde{s}$  estimation of  $D^2(\tilde{a})$  deviation were determined.

The function:

$$\frac{\tilde{a} - a}{s^2} = t_{N-n}$$

has Student t distribution with  $N-n$  degrees of freedom under following conditions:

- \*  $y$ -is the unbiased random variable ( $E(\Delta i) = 0$ ,  $D^2(\Delta i) = \sigma^2$ ); but the normal distribution is not necessary,
- \*  $a_j$  - independent parameter,
- \*  $x_{ij}$  - known values.

Calculations were made using the least square method with additional assumption that accuracy of  $l_i$  is uniform.

Parameters of both functions corrected and not corrected were determined.

Noncorrected function of one variable is described as:

$$\Delta F = S1t \cdot \Delta t$$

While the corrected function of four variables as:

$$\Delta F_{SK} = St \cdot \Delta t - ST \cdot \Delta T - SP \cdot \Delta P - SH \cdot \Delta H$$

where:

$\Delta F, \Delta F_{SK}$  fractional frequency changes of corrected and noncorrected characteristics,  
 $\Delta t, \Delta T, \Delta P, \Delta H$  changes of time, temperature, pressure and humidity,  
 $S1t, St$  frequency versus time slope coefficients for noncorrected and corrected functions,  
 $ST, SP, SH$  frequency versus temperature, pressure and humidity slope coefficients.

Following additional parameters were calculated:

- confidence intervals of calculated values for confidence level 99% ( $\varepsilon, \varepsilon_{SK}, \delta_{ST}, \delta_{SP}, \delta_{SH}$ ),
- average square deviation of measurement points from evaluated straight lines ( $\sigma, \sigma_{SK}$ )

Set of developed and produced at ITR oscillators was continuously measured for very long period of time (longer than 1 year) to deliver data for developing principles of long term frequency change prediction. Basing on obtained results the best fitted (to the resonators produced at ITR) function (1) was chosen:

$$f(t) = A + B\sqrt{t} + c \ln(1 + Dt) \quad (1)$$

This function enables prediction of a few years aging of oscillators with sufficient accuracy. The aging results of the first month are the base for calculations, however these calculations are valid only for the oscillators whose aging have growing monotone character (this is about 80% of investigated population).

### 3. MEASUREMENT RESULTS

Examples of data analysis concerning the oscillators of long term frequency stability better than 2E-10/day are presented in fig.1. Results confirmed the high efficiency of applied method of removing the influence of environmental stresses. Quite evident frequency versus humidity dependence was observed. Aging characteristic for the same type oscillator after hermetization is shown in fig.2. The correlation between frequency changes and humidity changes are now negligible.

The effects of applied frequency changes prediction procedure are presented in fig.3 and 4.

Accordance between real and theoretical characteristic for calculation based on the first month measurement results is better than 10%, while the calculation carried out according to MIL recommendation gives the error of 50% in the best case (fig. 4).

Some nonregular aging characteristics and the effects of power supply breaks are shown in fig.5 to 7. Slow variable fluctuations of frequency which are not correlated with environmental parameters changes are observed practically in all measured oscillators. These fluctuations are probably connected with fluctuations processes which occurred in the oscillators.

### 4. REFERENCES

1. B.Kalinowska, S.Gawor, Automated system for investigation of long term instability of precise quartz oscillators, Proc. of PIEZO'94, Zakopane, 1994
2. B.Kalinowska, B.Gniewińska, Analysis of medium term frequency instability of high stability quartz oscillators, Proc. of 10th EFTF, Brighton, 1996
3. B.Kalinowska, B.Gniewińska, Slow variable frequency fluctuations in high stability oscillators, Proc. of Winter School of Acustoelectronics, Ustroń, 1997

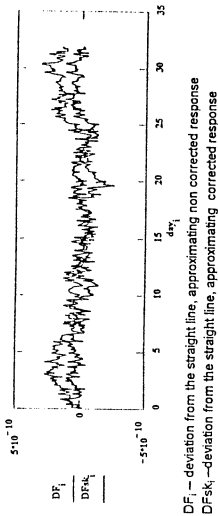
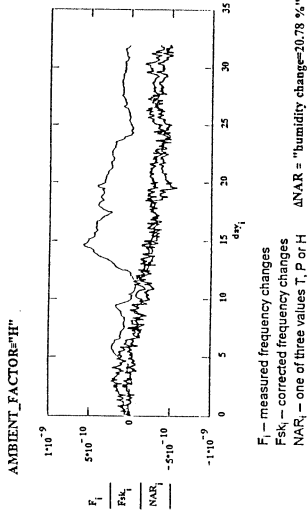
DESIGNATIONS in fig.3 and 4

g oscillator frequency changes  
W1, W2, WC fitting from 1st month, 2nd month and all measurement data (according to equation 1)  
gw1, gw2, gwc prediction errors for different analysis periods  
M1, M2, MC fitting frequency from 1st month, 2nd month and all measurement data (according to MIL recommendation)

Type = "OCO-80" From = "5.0" Number = 2 Measurement\_period = "20.10.95-19.01.98"  
 Calculation\_period = "25.10.97-25.11.97"

**Calculation results**

Average twenty-four hours frequency change /E-11/ →  $\delta f = -1.61$  **A. Not corrected** **B. Corrected**  
 $\delta f_k = -1.48$   
 Calculation accuracy /E-11/ →  $\epsilon = 0.18$   
 Standard deviation /E-10/ →  $\sigma = 1.1$   
 $\epsilon_k = 0.09$   
 $\sigma_k = 0.54$



Sensitivity coefficients due to: temperature - ST, pressure - SP, humidity - SH and accuracy of their determination:  $\delta ST, \delta SP, \delta SH$

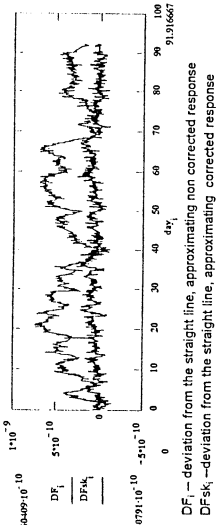
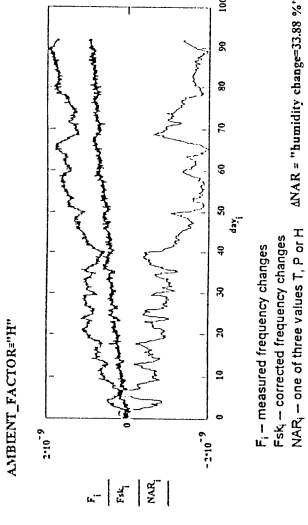
ST =  $-9.01 \cdot 10^{-11}$  with accuracy  $\delta ST = 1.4 \cdot 10^{-11}$   
 SP =  $3.51 \cdot 10^{-12}$  with accuracy  $\delta SP = 1.21 \cdot 10^{-12}$   
 SH =  $-7.16 \cdot 10^{-12}$  with accuracy  $\delta SH = 2.13 \cdot 10^{-12}$

Fig. 2  
 Hermetized OCO-80 oscillator long term frequency measurement results

Type = "OCO-80" From = "5.0" Number = 2 Measurement\_period = "28.11.96-23.01.98"  
 Calculation\_period = "01.09.97-01.12.97"

**Calculation results**

Average twenty-four hours frequency change /E-11/ →  $\delta f = 1.7$  **A. Not corrected** **B. Corrected**  
 $\delta f_k = 0.98$   
 Calculation accuracy /E-11/ →  $\epsilon = 0.06$   
 Standard deviation /E-10/ →  $\sigma = 1.89$   
 $\epsilon_k = 0.04$   
 $\sigma_k = 0.65$



Sensitivity coefficients due to: temperature - ST, pressure - SP, humidity - SH and accuracy of their determination:  $\delta ST, \delta SP, \delta SH$

ST =  $-8.25 \cdot 10^{-11}$  with accuracy  $\delta ST = 5.36 \cdot 10^{-12}$   
 SP =  $-1.17 \cdot 10^{-12}$  with accuracy  $\delta SP = 8.21 \cdot 10^{-13}$   
 SH =  $-2.77 \cdot 10^{-11}$  with accuracy  $\delta SH = 1.24 \cdot 10^{-12}$

Fig. 1  
 Typical OCO-80 oscillator long term frequency measurement results

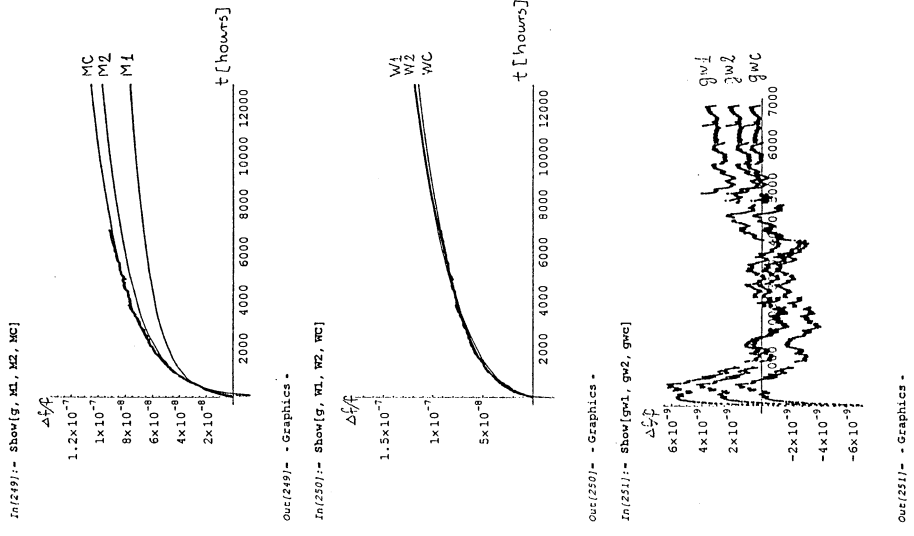


Fig. 4 Aging results fitting according to the equation (1) (OCXO-80 oscillator, 8,192 MHz, SC cut resonator, 3rd overtone), K=5

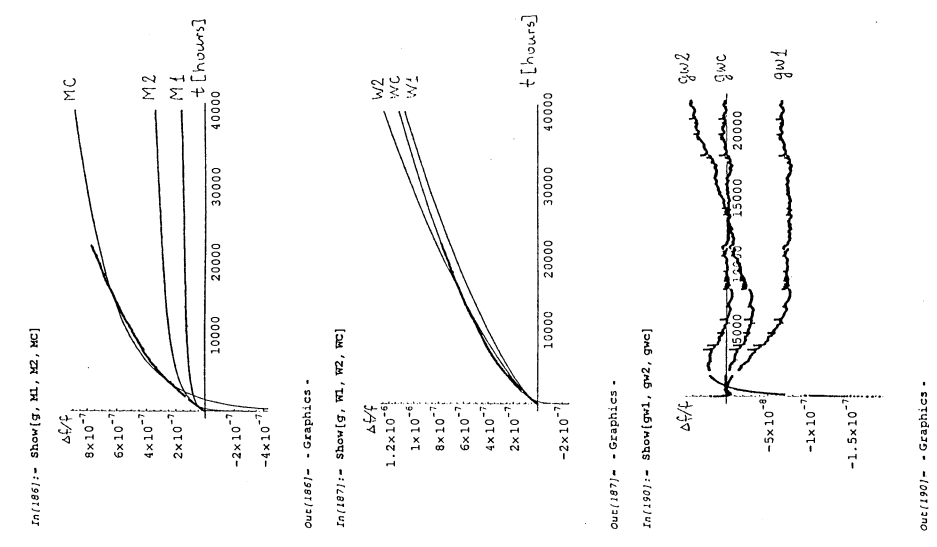


Fig. 3 Aging results fitting according to the equation (1) (OCXO-100 oscillator, 5MHz, SC cut resonator, fundamental mode), K=1.5

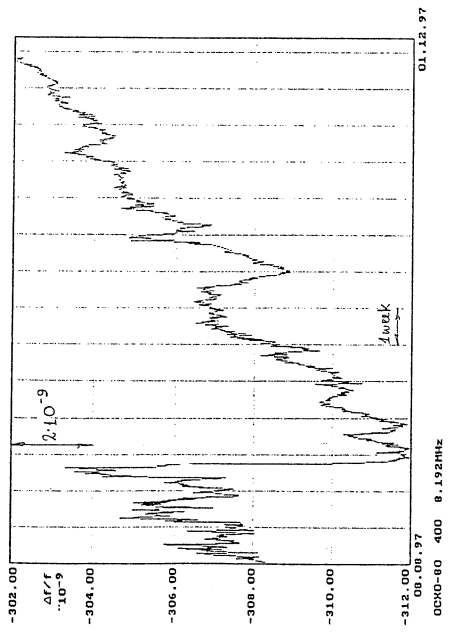


Fig. 5  
An example of nonregular aging characteristic

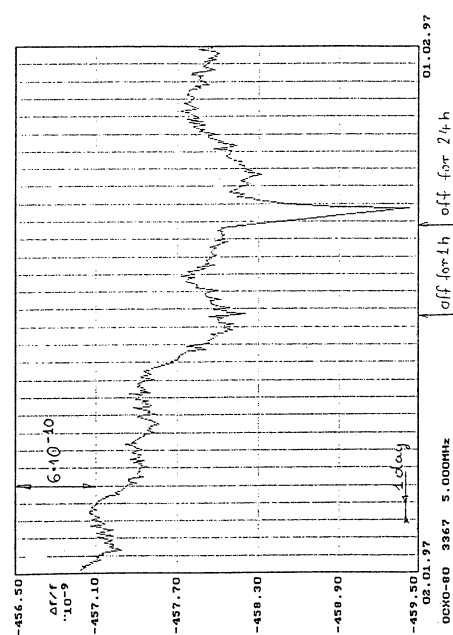
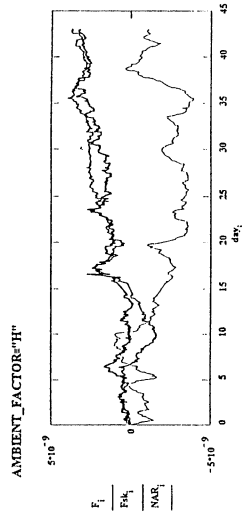
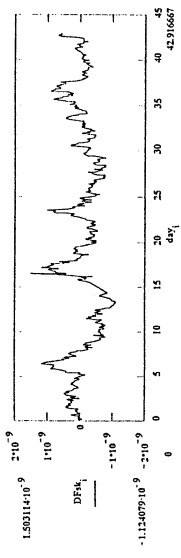


Fig. 6  
Effects of supply breaks on aging characteristic

Type = "OCXO-80" Fnom = "8.192" Number = 400 Measurement\_period = "08.08.97-02.12.97"  
 Calculation\_period = "01.10.97-12.11.97"  
 Calculation results **A. Not corrected** **B. Corrected**  
 Average twenty-four hours frequency change /E-11/ →→ δfk = 10.63 δfk = 7.24  
 Calculation accuracy /E-11/ →→ ε = 0.76 ε = 0.6  
 Standard deviation /E-10/ →→ σ = 7.22 σ = 4.57



$F_i$  — measured frequency changes  
 $F_{sk}$  — corrected frequency changes  
 $NAR_i$  — one of three values T, P or H ANAR = "humidity change=24.08 %"



$DP_i$  — deviation from the straight line, approximating non corrected response  
 $DF_{sk}$  — deviation from the straight line, approximating corrected response

Sensitivity coefficients due to: temperature - ST, pressure - SP, humidity - SH  
 and accuracy of their determination: δST, δSP, δSH

ST =  $-6.5 \cdot 10^{-10}$  with accuracy δST =  $9.42 \cdot 10^{-11}$   
 SP =  $1.35 \cdot 10^{-11}$  with accuracy δSP =  $7.6 \cdot 10^{-12}$   
 SH =  $-2.17 \cdot 10^{-11}$  with accuracy δSH =  $1.24 \cdot 10^{-11}$

Fig. 7  
The oscillator of nonregular characteristic, long term frequency stability measurement results

## THE ARITHMETIC OF FREQUENCY MIXINGS IN AN ELECTRONIC LOOP

Michel PLANAT and Serge DOS SANTOS

*Laboratoire de Physique et Métrologie des Oscillateurs du CNRS associé à l'Université de Franche Comté  
32, Av. de l'Observatoire, 25044 BESANÇON CEDEX, FRANCE*

Frequency mixing is widely used in communication receivers or in a frequency measurement set up. It is often associated to a frequency feedback loop or a phase locked loop of which the basic function is to track the frequency or phase of the output signal which may thus be demodulated.

Models of the mixing of frequencies and loop signals hardly account for the whole spectrum of intermodulation products and this has consequences in our ability to separate contributions due to the signal to be demodulated and those generated in the mixer and propagated in the loop.

In this paper we develop an alternative way of thinking the spectrum of frequency mixings in a voltage control electronic loop. It is based on elementary number theory and specifically on continuous fractions expansions of frequency ratios of signals at the inputs of the mixer.

The model is applied to a loop with different stages of filtering (from 300 KHz to 1 kHz). It provides a good account of the observed spectrum outside the modelocking zones. At or closed to the modelocking zones it is completed satisfactorily by deriving a cross section map of the nonlinear differential equation governing the phase dynamics in the loop.

In a second part of the study it is found for the first time that  $1/f$  frequency noise occurs in the vicinity of modelockings with a magnitude scaled by the non-linearity.

## I. INTRODUCTION

A complex system needs a variety of independent constraints to ensure the coherence and stability of the whole. In some cases the nature of its most elementary pieces is defined (physical particles, biological cells, or economical agents...) or the subsystem is defined from aggregates (molecules, organs, human groups), or from differential (equ-)actions and the associated observables. Many models do not account on the pieces but on the dynamics, morphology, structure... Concepts such as indiscernability, singularity, fractal dimension... are introduced to describe the system with a surprising high level of efficiency.

In this paper the complex object under study is a

voltage controlled electronic loop. It is too complex to be defined from the elementary physics of its constituents and as such is typical of an electronic circuit; observables are oscillator frequencies, complexity arises in the sequence of countings versus time or versus the frequency of one local oscillator and as such the problem is typical of signal processing; it will be shown that the biggest constraint has a number theoretical origin.

## II. THE EXPERIMENTAL SET-UP

The voltage controlled electronic loop under study (Fig.1) is a basic piece of a FM radio receiver (or transmitter).

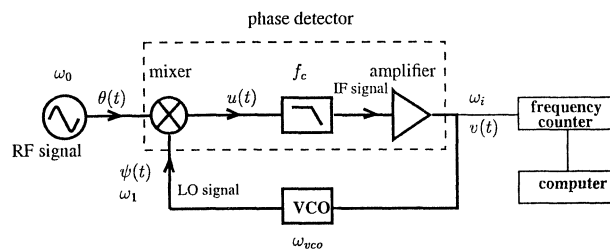


FIG. 1. Schematic of the voltage controlled electronic loop used in the experiment

It may also be used to register minute frequency fluctuations of an external oscillator under test (RF) versus the frequency of a local oscillator (LO). The loop includes a wide band mixer, a filter of low frequency cut-off  $f_c$ , a low noise amplifier and the local oscillator is voltage controlled (VCO). Mixing operation results from the frequency conversion in the time varying conductance of a diode, or the transductance from gate to drain in a field effect transistor (or FET). Here we used Schottky barrier diodes in a doubly balanced structure that produce isolation between the inputs and some rejection of spurious signals.

In the open loop configuration the ideal mixer multiplies the RF signal to be received of frequency  $\omega_0$  by the reference sinusoid of the LO of frequency  $\omega_1$  shifting it to both the sum frequency and the dif-

ference frequency  $\omega_0 \pm \omega_1$ . The down conversion is usually desired and is often associated to the low frequency feedback loop shown in Fig.1. Its basic operation is to track the phase of the LO (or VCO) to that of the RF, hence it is called a phase locked loop (PLL) [1]. The practical operation of the mixer (and of the PLL) always involves many down converted products at intermodulation frequencies (IF) given by

$$\omega_i^{(p,q)} = |p\omega_0 - q\omega_1| \quad (p \text{ and } q \text{ integers}), \quad (1)$$

in the bandwidth of the loop.

In the standard model [2] the diode (or FET) mixer and its embedding circuit are described separately. The time domain differential equations describing the nonlinear circuit are analyzed under L0 excitation only, assuming the RF excitation is negligible. The external circuit is represented in the frequency domain as a set of impedances at the  $q$  harmonics of the L0, each in series with an ideal filter. This leads to a set of  $q$  loop equations which have to be solved by trial and error using optimization routines. Several drawbacks are inherent to the standard approach: calculations are always cumbersome and need the resort to some type of general purpose nonlinear-circuit simulator; convergence is not always ensured due to the lack of knowledge of the embedding circuit and numerical errors in solving the differential equations; more severe is the fact that this harmonic-balance simulation fails to account for the intermodulation products originating from harmonics of the RF signal.

### III. ARITHMETICAL EFFECTS

We found an alternative global way of thinking the spectrum of frequency mixings based on elementary number theory and specifically on continuous fraction expansion (CFE) of frequency ratios of signals at the input of the mixer. Let  $\nu = \omega_1/\omega_0$  the LO to RF frequency ratio and  $\mu = \omega_i/\omega_0$  the IF to RF frequency ratio, the three frequencies operation may be rewritten as:

$$\mu = q | \nu - p/q |. \quad (2)$$

From this form one can guess the device tries to approximate the frequency ratio  $\nu$  from its best interaction product  $p/q$  allowed by the physical constraints in the loop, that is the amplitude, bandwidth and

finite resolution. Best rational approximations of a real number  $\nu$  are given from CFE, that is

$$\nu = a_0 + 1/\{a_1 + 1/\{a_2 + \dots + 1/\{a_i + \dots\}\}\}; \quad (3)$$

and the  $a_i$ 's are positive integers which are readily obtained from the formulas:  $a_0 = [\nu]$ ,  $\alpha_0 = \{\nu\}$  and if  $i \geq 1$ ,  $a_i = [1/\alpha_{i-1}]$ ,  $\alpha_i = \{1/\alpha_{i-1}\}$ , where  $[\nu]$  denotes the integral part of  $\nu$  and  $\{\nu\} = \nu - [\nu]$  is its fractional part. Successive best approximants of  $\nu$ , that is convergents  $p_i/q_i$  are obtained by truncating Eq. (3) at some stage  $i$ . Our task is to determine how physical parameters govern the truncation at stage  $i = imax$ .

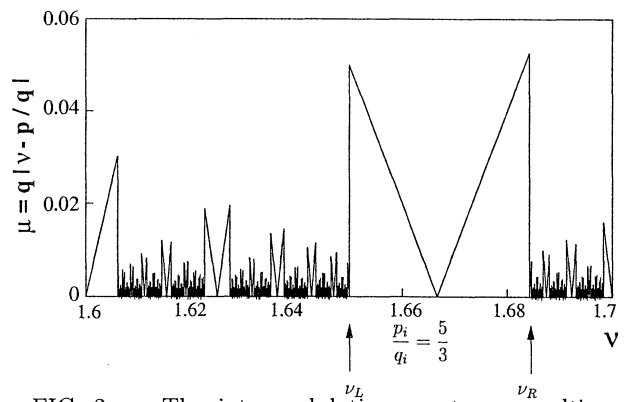


FIG. 2. The intermodulation spectrum resulting from the truncation at  $amax = 5$  in the continuous fraction expansion. The window  $1.6 < \nu < 1.7$  has been selected. The larger basin is at the rational  $\frac{p_i}{q_i} = \frac{5}{3} = [1; 1, 2]$  with  $\nu_R = [1; 1, 2, 5] = \frac{27}{16}$  and  $\nu_L = [1; 1, 1, 1, 5] = \frac{28}{17}$ . The asymmetry is given by  $\delta\nu = |5/3 - 27/16| - |5/3 - 28/17| = \frac{1}{3.16 \cdot 17}$ .

Any rational number  $p_i/q_i$  has two CFE given by  $p_i/q_i = [a_0; a_1, a_2, \dots, a_i]$  and  $p_i/q_i = [a_0; a_1, a_2, \dots, a_i - 1, 1]$ . Let us consider truncation at a given value  $amax$  and numbers  $\nu$  which are very close to  $p_i/q_i$  on the right (resp. on the left); they should be approximated as  $p_{i+1}/q_{i+1} = [a_0; a_1, a_2, \dots, \hat{a}_i, a_{i+1}]$  (resp.  $p_{i+1}/q_{i+1} = [a_0; a_1, a_2, \dots, a_i - 1, 1, a_{i+1}]$ ) with  $a_{i+1} > amax$ . But as a result of the truncation at  $amax$  those numbers will be approximated as  $\nu = p_i/q_i$  instead; the result will be a set of two straight lines  $\mu = q_i | \nu - p_i/q_i |$  as expected from Eq. (2). The last numbers in the basin of  $p_i/q_i$  will be at  $\nu_R = [a_0; a_1, a_2, \dots, a_i, amax]$  (resp.  $\nu_L = [a_0; a_1, a_2, \dots, a_i - 1, 1, amax]$ ) given by

$$| \nu_R - \frac{p_i}{q_i} | = \frac{1}{q_i q_{i+1}}, \quad (4a)$$

and

$$|\nu_L - \frac{p_i}{q_i}| = \frac{1}{q_i(amax + q_i - q_{i-1})}, \quad (4b)$$

We see that a significant asymmetry results in most cases. Fig.2 illustrates the results obtained by taking  $amax = 5$  and the window  $1.6 < \nu < 1.7$ .

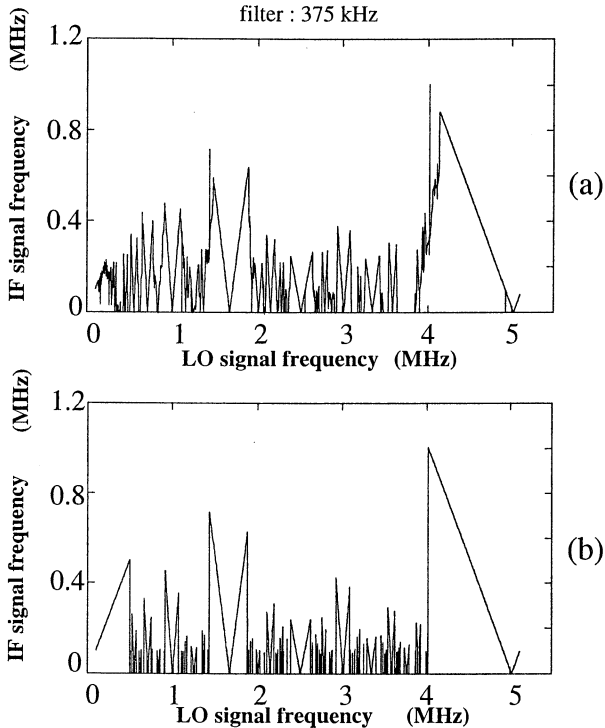


FIG. 3. (a) The intermodulation spectrum for the loop shown in Fig.1 and cut-off frequency  $f_c = 375$  KHz. The RF signal has ultrastable constant frequency  $\frac{\omega_0}{2\pi} = 5.02062628$  MHz. (b) The theoretical spectrum as predicted from Eqs. (2-4). For the fit we chose  $amax = 3$  for the fundamental mode  $1/1$ ,  $amax = 2$  for products  $p/q$  with  $p$  and  $q$  odd and  $amax = 20$  for products with  $p$  or  $q$  even.

In order to check the validity of the above arithmetical approach we registered the intermodulation spectrum for the device in Fig.1, using a constant frequency RF signal, a variable frequency LO signal and a low frequency cut-off  $f_c = 375$  kHz. Acquisition of data was performed using a digital counter with an integration time  $\tau_0 = 0.1$  s. Results are shown in Fig.3a. A good fit of the data was obtained accounting of the physical device: products with  $p$  and  $q$  even were strongly rejected due to the doubly balanced phase bridge structure of the mixer. The theoretical curve is shown in Fig.3b.

The filtering rate was found to govern the truncation level of CFE in the loop. Using selective filters at 58 kHz (resp 3 kHz) we found truncations at val-

ues  $amax = 9$  (resp 65) allowing a good fit of the experimental curves [3]. We just saw the intermodulation spectrum may be roughly described from CFE and a resolution increasing with the degree of filtering. It is convenient to represent the error  $\mu$  versus  $\nu$  on a tree with the number of leaves given from a Farey criterion

$$q_i < N. \quad (5)$$

The Farey series  $F_N$  of order  $N$  is defined as the set of irreducible fractions  $p_i/q_i$  between  $0/1$  and  $1/1$  whose denominators do not exceed  $N$ . Thus  $F_5$  is  $\{0/1, 1/5, 1/4, 1/3, 2/5, 1/2, 3/5, 2/3, 3/4, 4/5, 1/1\}$ . Between two leaves ending on the real axis at  $p/q$  and  $p'/q'$  there is one at  $(p+p')/(q+q')$  provided  $q, q'$  and  $q+q'$  do not exceed  $N$ . It arises at the node  $((p+p')/(q+q'), 1/(q+q'))$  as shown in Fig.4.

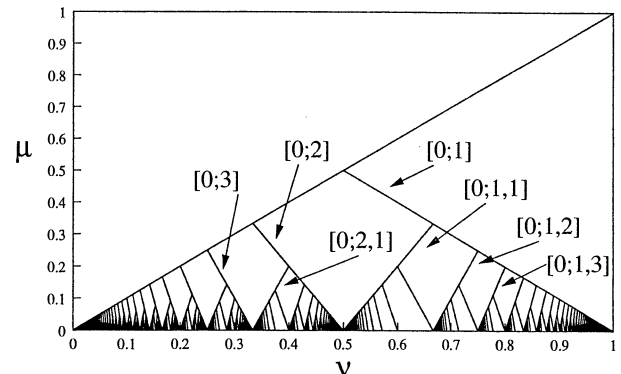


FIG. 4. The increased resolution spectrum as calculated from CFE of  $\nu$  from  $i = 1$  to  $i = 3$ .

In contrast to criterion (5) a finite resolution experiment is governed by the truncation trick

$$i < imax. \quad (6)$$

The first steps are easily obtained. If  $imax = 1$ ,  $\nu = [0; a_1] = 1/a_1$  so that  $\mu = -a_1\nu + 1$ . They are infinitely many leaves with  $a_1 = 1, 2, \dots$  accumulating at the origin. At the second stage  $imax = 2$ ,  $\nu = [0; a_1, a_2] = a_2/(1+a_1a_2)$  so that  $\mu = (1+a_1a_2)\nu - a_2$ ; they are infinitely many leaves accumulating at the bottom  $\nu = 1/a_1$  of the leaves of the preceding stage. So on up to the limit of resolution of the experiment. Fig.4 illustrates the result if  $imax = 4$ .

The finite resolution effect is unavoidable in our experiment. If we agree the device tries to produce the best rational approximation as shown before, there will be fluctuations in the basin  $\delta\nu \sim 2/N^2$  defined from (4) and (5) due to the finite resolution. They will depend on the location of the  $k^{th}$  beat sig-

nal  $\mu^{(k)}$  on the  $\nu$  axis with respect to the vicinity of a low level rational.

The arithmetical error is defined as

$$|\delta\mu^{(k)}| = \left| \mu^{(k)} - \frac{p_i^{(k)}}{q_i^{(k)}} \right|. \quad (7)$$

Some filtering of this error may be accounted for if we introduce the fluctuations as

$$\epsilon^{(k)} = |\delta\mu^{(k+1)} - \delta\mu^{(k)}|. \quad (8)$$

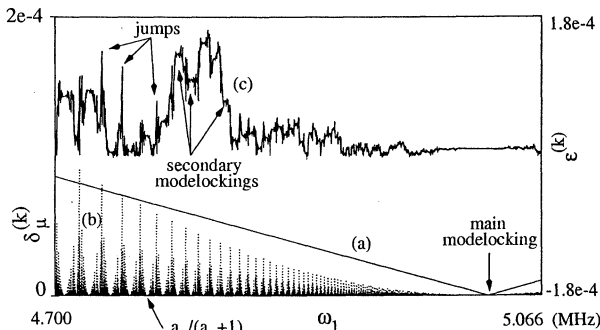


FIG. 5. The arithmetical and fractal structure of the fundamental beat mode 1/1. (a) Beat signal frequency at mode 1/1 (see Fig.2). (b) Arithmetical error  $\delta\mu^{(k)}$  as defined from Eq.(7). (c) Beat signal fluctuations as defined from Eq.(8).

The magnitude of the arithmetical error is very dependent on the number to be approximated. For the fundamental mode 1/1 in Fig.5 minima of the arithmetical error are found at  $a_2/(a_2 + 1)$ ,  $a_2 \geq 5$  as expected from Fig.4. In between there is a fractal structure similar to Fig.4 due to the badly approximated numbers. As for the fluctuations (8) some filtering of the arithmetical error may be obtained if adjacent samples  $k$  leads to the same rational approximations  $p_i/q_i$ . At the opposite a badly approximated number is responsible for a jump in  $\epsilon^{(k)}$ .

#### IV. NONLINEAR EFFECTS

Until now we did not introduce nonlinearity in the description of the set-up. This is because at the scale of Fig.3 the open and closed loop configuration are similar. Nonlinearity is present only if  $\nu \sim p_i/q_i$  in the modelocking zone of width  $2K \ll 2/N^2$  as shown now. In such a case the open loop behaves as a PLL, the output signal becomes continuous and proportional to sine of the instantaneous phase difference at the inputs [1];

$$v(t) = a \sin[\theta(t) - \Psi(t)], \quad (9)$$

where  $\theta(t)$  and  $\Psi(t)$  are the instantaneous phases of the RF and LO oscillators. The dynamics of the loop is well described by introducing the phase difference  $\Phi(t) = \theta(t) - \Psi(t)$ . Using  $\dot{\theta} = \omega_0$  and  $\dot{\Psi} = \omega_1 + b v(t)$  with  $b$  the sensitivity of the VCO one obtains the nonlinear differential equation:

$$\dot{\Phi}(t) + K \sin \Phi(t) = \omega_i, \quad (10)$$

with  $\omega_i = \omega_0 - \omega_1$  as the frequency shift and the frequency  $K = ab$  as the coupling coefficient (also called open loop gain). Eq.(10) is integrable and its solution is complex. It is illustrated in Fig.6. If the frequency shift  $\omega_i$  does not exceed the frequency gain  $K$ , the averaging frequency  $\langle \dot{\Phi} \rangle$  vanishes after a finite time to reach the stable steady state  $\Phi(\infty) = 2l\pi + \arcsin(\frac{\omega_i}{K})$ ,  $l$  integer.

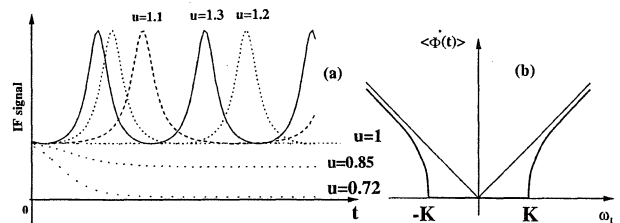


FIG. 6. (a) Shape of the beat signal  $v(t) = a \sin \Phi(t)$  with  $\Phi(t)$  and several values of the shift  $u = \omega_i/K$  in the mode-locked regime  $u < 1$  or the free regime. (b) Mean frequency  $\langle \dot{\Phi}(t) \rangle$  of the beat signal as calculated from Eq. (11). The mode-locked zone has width  $2K$

In this phase tracking range of width  $2K$  the RF and LO oscillators are also frequency locked. Outside the modelocking zone there is a sech shape beat signal of frequency

$$\omega_B = \langle \dot{\Phi}(t) \rangle = K \sqrt{u^2 - 1}, \quad (11a)$$

$$= \sqrt{\omega_i^2 - K^2}, \quad (11b)$$

with  $u = \omega_i/K$  converging to the open loop frequency  $\omega_i$  as  $u \ll 1$ .

In the extended range of operation of the electronic loop, there are harmonics products in addition to the fundamental one and phase differences  $\Phi^{(p,q)} = p\theta(t) - q\Psi(t)$  may be shown to obey the non-integrable equation

$$\begin{aligned} \dot{\Phi}^{(p,q)} = & \omega_i^{(p,q)} \\ & - q \sum_{r,s} K^{(r,s)} \sin \left( \frac{r}{q} \Phi^{(p,q)} \right. \\ & \left. - \frac{\omega_0 t}{q} (rp - sq) + \Phi_0^{(r,s)} \right), \end{aligned} \quad (12)$$

where  $\Phi_0^{(r,s)}$  is the initial phase at the harmonic  $(r, s)$ . In the simplest case the interaction of one product with another is neglected so that  $\frac{r}{s} = \frac{q}{p}$ . In such a case an equation similar to Eq. (10) is recovered so that we expect a phase tracking zone similar to the fundamental one at each product  $(p, q)$ . In the general case it is observed from Eq.(12) that the RF signal acts as a periodic perturbation for the standard phase locked loop. Modelocking zones can be described asymptotically: we assume that the condition  $\dot{\Phi} = Cte$  holds over each cycle provided the counting time is large in comparison to the period. The result is a recurrence formula mapping the phase  $\Phi_{n+1}$  at time  $t + \frac{2\pi}{\omega_0}$  to that  $\Phi_n$  at time  $t$ , that is an Arnold type map [4,5].

We found experimentally a remarkable similitude between the shape and magnitude of the beat signal  $\dot{\Phi}(t)$  and its time fluctuations. First of all the Allan variance defined as the mean squared value of the frequency deviation between adjacent samples of length  $\tau$  was found remarkably flat, that is  $\sigma_{\dot{\Phi}}^2(\tau) \sim Cte$  all over the zone near a modelocking. It is associated to the well known power spectrum [6]  $S_{\dot{\Phi}}(f) = \frac{Cte}{2 \ln^2 f}$ .

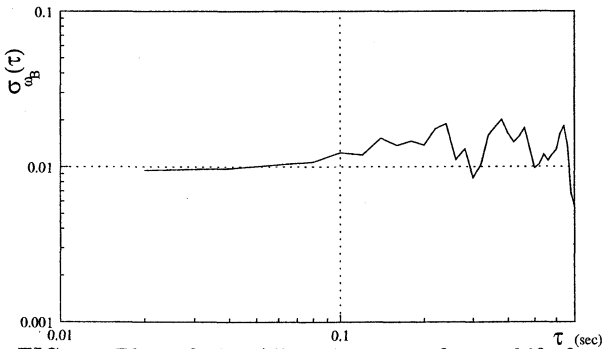


FIG. 7. Plot of the Allan deviation for a shift frequency  $\omega_i \sim 450$  Hz closed to the 1/1 modelocking

Since the most visible effect of nonlinearity near a modelocking is the frequency beat dependence versus the gain  $K$  and the bare frequency deviation  $\omega_i$  through the relation (11), it was interesting to study the dependence of  $1/f$  noise on those parameters. In our experiment the external oscillator of frequency  $\omega_0$  was chosen far more stable than the VCO oscillator of frequency  $\omega_1$  so that we could approximate the frequency beat fluctuation as  $\delta\omega_i = \delta\omega_0 - \delta\omega_1 \sim \delta\omega_1$ . Performing differentiation on (11) as  $\delta\omega_B/\omega_B = (\delta\omega_i/\omega_i)(\omega_i^2/\omega_B^2)$  and using the notation  $\sigma_{\omega_1}(\tau) \sim \delta\omega_1/\omega_1$  and  $\sigma_{\omega_B}(\tau) \sim \delta\omega_B/\omega_B$  we

obtained the relation

$$\sigma_{\omega_B}(\tau) \sim A \left( 1 + \frac{K^2}{\omega_B^2} \right), \quad (13a)$$

$$\sim A' \frac{\omega_i}{\omega_i^2 - K^2}, \quad (13b)$$

with the multiplication constants  $A = (\omega_1/\omega_i)\sigma_{\omega_1}(\tau)$  and  $A' = \omega_1\sigma_{\omega_1}(\tau)$ .

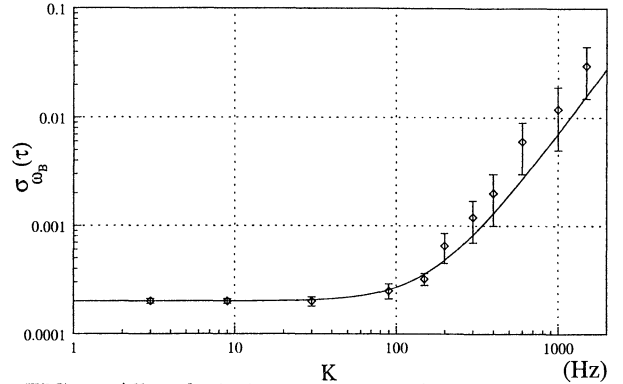


FIG. 8. Allan deviation versus open loop gain  $K$  for a constant beat signal  $\omega_B \sim 170$  Hz. The continuous line is the theoretical result in Eq.(13)

Fig.7 to 9 illustrate noise measurements performed from the device in Fig.1 closed to the main modelocking 1/1. Fig.7 is a typical plot of Allan deviation. Fig.8 illustrates the parabolic dependence of noise on gain at constant beat frequency  $\omega_B \sim 170$  Hz as predicted from the first part of Eq.13. Extrapolating at  $K \sim 0$ , this leads to an estimate of constant  $A \sim 2.10^{-4}$ , that is an estimated Allan deviation associated to the VCO oscillator  $\sigma_{\omega_1}(\tau) \sim 7.10^{-9}$ . Fig.9 illustrates the hyperbolic dependence of noise on  $\omega_i$  at constant gain  $K = 1500$  Hz. It leads to the same estimation of  $\sigma_{\omega_1}(\tau)$  than that derived above. Finally Eq.13 attributes the generation of  $1/f$  type noise to the synchronization process involved in the voltage controlled oscillator. The explanation of noise dynamics needs the understanding of the non integrable Eq.12, which accounts for harmonic interactions at all orders. This is a difficult task which is left to future work.

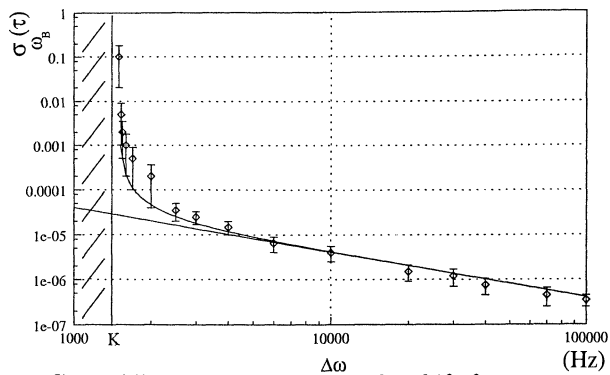


FIG. 9. Allan deviation versus the shift frequency  $\omega_i$  with a constant open loop gain  $K = 1.5$  kHz. The continuous line is the theoretical result in Eq.(13).

## V. CONCLUSION

We studied in detail the structure of phase and frequency shift between two oscillators in a voltage controlled electronic loop. We found experimentally  $1/f$  frequency noise of the beat note in the vicinity of modelockings; its magnitude is related to nonlinearity; its arithmetical structure is related to the rational approximations of frequency ratio between the two oscillators.

This paper follows two recent attempts to explain  $1/f$  frequency noise of oscillators from synchronization processes [7,8]. It opens a bridge between studies in dynamical systems, fractals and number theory.

- 
- [1] J. KLAPPER and J. T. FRANKLE. *Phase-Locked and Frequency-Feedback systems*. Academic Press, New York, 1972.
  - [2] S. A. MAAS. *Microwave mixers*. Artech House, Inc, Norwood, 1986.
  - [3] S. DOS SANTOS and M. PLANAT. *Arithmetic of Frequency Mixing in an Electronic Loop*. (submitted), 1998.
  - [4] P. CVITANOVIC. *Circle maps : Irrationally winding in From Number Theory to Physics*, page 631. Springer Verlag, New York, 1992.
  - [5] M. PLANAT and P. KOCH. *Plurifractal Signature in the Study of Resonances of Dynamical Systems*. *Fractals*, 1, 727, (1993).
  - [6] D. W. ALLAN. *Time and frequency (Time Domain) characterization, estimation and prediction of precision clocks and oscillators*. *IEEE Trans. on Ultras. Ferroelect. and Freq. Control*, 34, 647, (1987).
  - [7] M. PLANAT, V. GIORDANO, G. MARIANNEAU, F. VERNOTTE, M. MOURET, C. ECKERT, and J. MIEHE. *Is the Frequency Noise of an Oscillator*

*of Deterministic Origin ?* *IEEE Trans. on Ultras. Ferroelect. and Freq. Control*, 43, 326, (1996).

- [8] M. PLANAT, F. LARDET-VIEUDRIN, G. MARTIN, S. DOS SANTOS, and G. MARIANNEAU. *Frequency stability enhancement from carrier-envelope resonance in a surface acoustic wave delay line oscillator*. *J. Appl. Phys.*, 80, 2509, (1996).

## MICROWAVE SYNTHESIZER

Wojciech Wojtasiak, Tadeusz Morawski, Daniel Gryglewski, Ryszard Michnowski.

Institute of Radioelectronics, Warsaw University of Technology,  
ul. Nowowiejska 15/19, 00-665 Warszawa, Poland

### 1. INTRODUCTION

For the last few years fast development of microwave synthesizers for high stability carrier has been spotted. They are widely applied in telecommunication and radiocommunication systems, wherever modulated signal (for example FM and AM modulated) on microwave frequencies is transmitted. In this case efficiency of signal source is not so important. The most important thing is to obtain high frequency stability and low power level of phase noise. At the Institute of Radioelectronics of Warsaw University of Technology research over this synthesizer have been carried out. The paper describes a flexible architecture of synthesizer. The architecture permits to construct synthesizers for arbitrary microwave frequency bands.

### 2. ARCHITECTURE OF SYNTHESIZER.

The block diagram of synthesizers is shown on fig.1. The microwave synthesizers are based on QUALCOMM DDS and PLL MIC [1] circuits. This architecture allows to flexible design synthesizers characterized by:

- wide tuning band,
- every kind of phase(frequency) modulation easy realization,
- low phase noise power level,
- low spurious level,
- short time hopping.

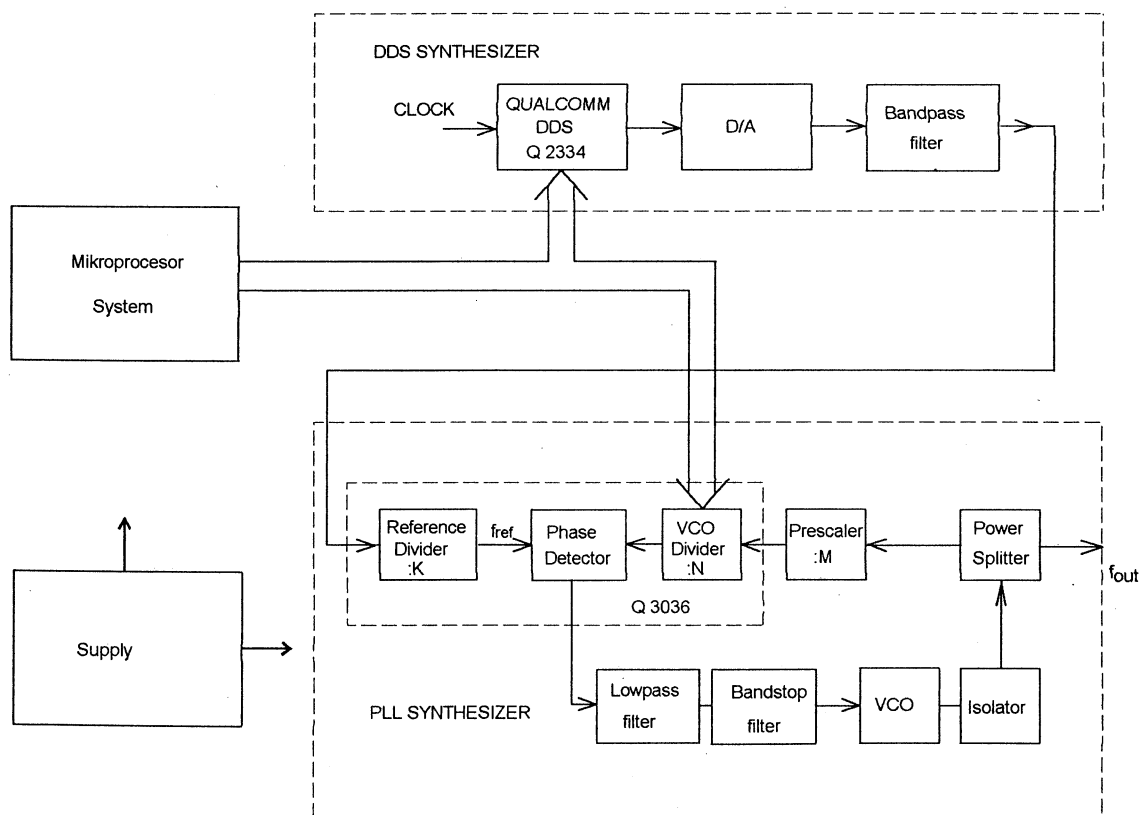


Fig.1. The block diagram of synthesizers.

## 2. THE DDS SYNTHESIZER.

The first part of synthesizer is DDS. It generates a reference signal for PLL. The synthesizer parameters are the same for each band solutions. The DDS consist on Qalcomm Q2334 DDS MIC circuit, D/A (CX20202A-1 Sony) converter and bandpass filter. In our system the clock frequency was 30MHz (the maximum clock frequency for Q2334 is 80MHz). The Q2334 has 32-bit phase accumulator, so the DDS output frequency step is (1, 2):

$$\Delta f_{\text{DDS}} = \frac{f_{\text{clock}}}{2^N} \quad (1)$$

$$\Delta f_{\text{DDS}} = \frac{30 \text{ MHz}}{2^{32}} \approx 0.007 \text{ Hz} \quad (2)$$

There is easy to perform each kind of phase modulation using software for DDS control. Output frequency of DDS (reference for PLL) was assumed about 10MHz. This frequency value arise from compromise between bandpass filter performance, low power phase noise level and time hoping. The output signal power spectrum of D/A converter is presented in fig.2. (the DDS output frequency is fixed on 10MHz.) The output bandpass filter selects the desired part of the signal power spectrum.

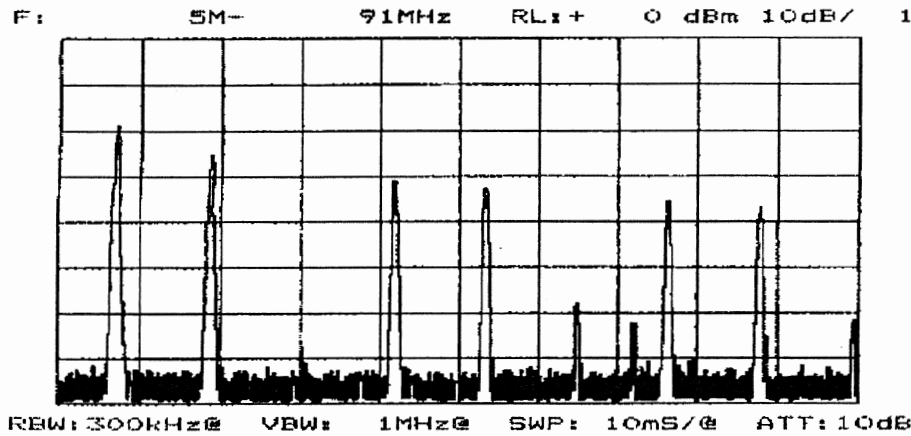


fig. 2. The output signal power spectrum of D/A converter

## 2. THE PLL SYNTHESIZER.

The second part of synthesizer consist of the PLL (fig.1). The PLL multiplies the DDS frequency into desired microwave frequency band. The main architecture of the PLL synthesizer remains unchanged. Only VCO generator and accurately chosen prescaler are needed to construct the PLL synthesizer for the desired frequency band. The loop low-pass filter parameters should be fitted accurately too. The Q3036 is the basic part of PLL synthesizer. It consist of the phase detector, VCO divider and reference divider. The Q3036 maximum reference frequency is 100MHz and VCO frequency is 1.5GHz. The division ratio of reference divider could be changed from 1 up to 16 and VCO divider properly from 90 up to 1295. The reference divider is fixed on position 1

in the proposed solutions. If the output frequency is higher than 1.5GHz the external prescaler is needed. The step frequency of DDS-PLL synthesizer could be obtained from equation:

$$\Delta f_{\text{DDS-PLL}} = \Delta f_{\text{DDS}} \cdot M \cdot L \quad (2)$$

where

$M$  - the external prescaler  
division ratio

$L$  - the internal prescaler  
division ratio

## 2. THE MEASUREMENT RESULTS OF DESIGNED SYNTHESIZERS.

The L-band, S-band and X-band synthesizers using described structure of DDS-PLL have been worked out at the Institute of Radioelectronics .

**L- band synthesizer.**

The L-band synthesizer for 0.6-1.3GHz frequency range has been designed. Because this band, the external prescaler has not been required. The VCO Q3500C-0613T made by

Qalcomm has been applied. The maximum frequency step is:  $\Delta f_{DDS-PLL} \approx 0.91\text{Hz}$ . The output signal power spectrum is shown in fig.3÷6.

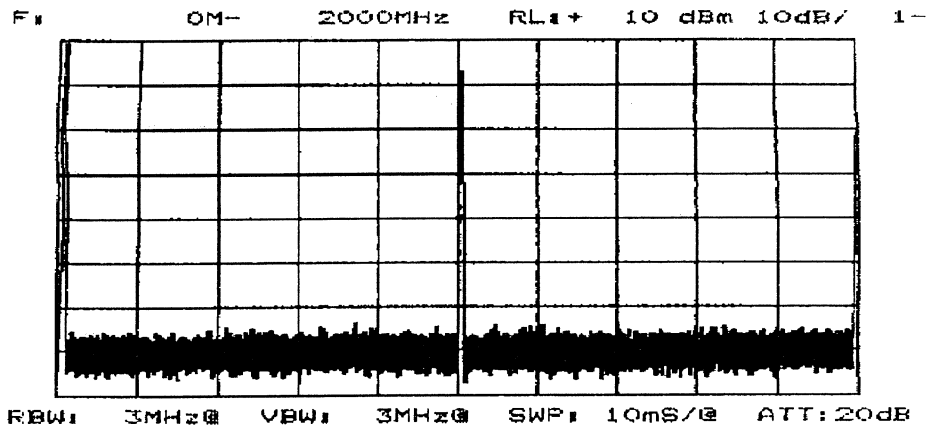


Fig.3. The main harmonic of the output signal of L-band synthesizer.

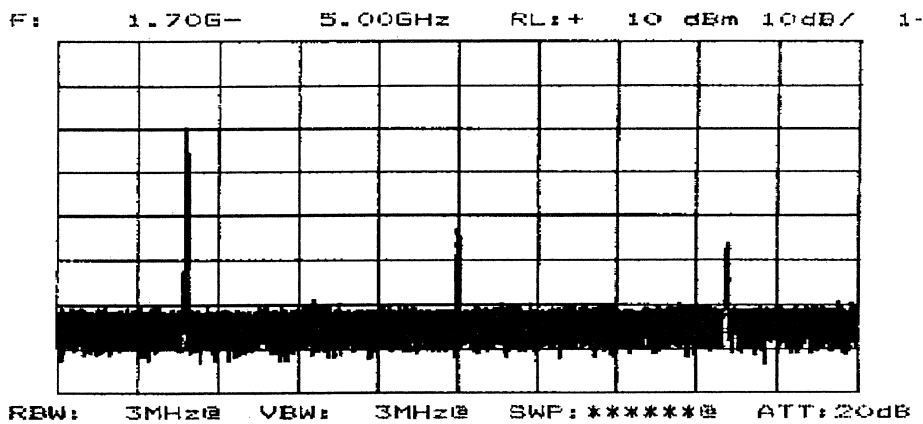


Fig.4. The reminded harmonics of the output signal of L-band synthesizer.

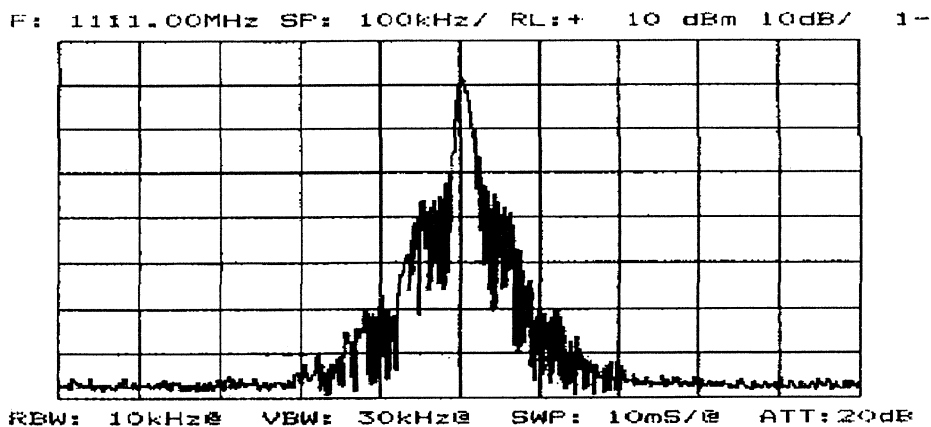


Fig.5. The main harmonic of the output signal of L-band synthesizer in the band 100kHz/div.

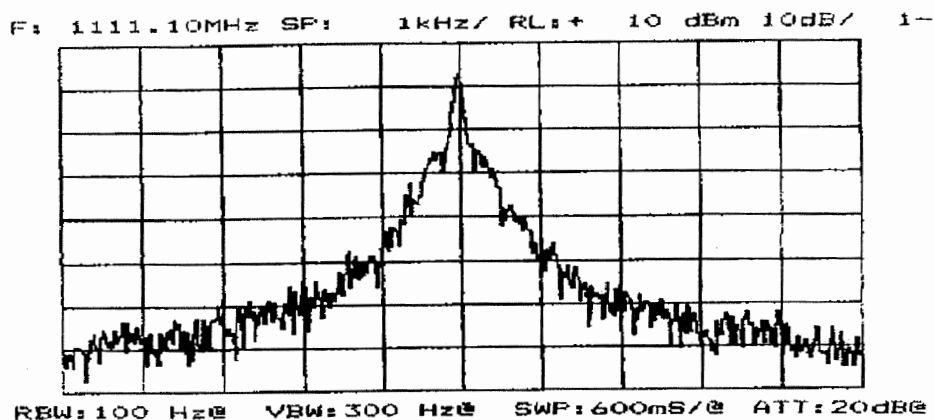


Fig.6. The main harmonic of the output signal of L-band synthesizer in the narrow band 1kHz/div.

### S- band synthesizer.

The designed S-band synthesizer works in 3.1-3.6GHz frequency range. There was used the external prescaler :4  $\mu$ PG501 made by NEC.

The VCO V-3350 made by Z-COMM has been applied. The maximum frequency step is:  $\Delta f_{DDS-PLL} \approx 2.6$  Hz. The output signal power spectrum is shown in fig.7÷9.

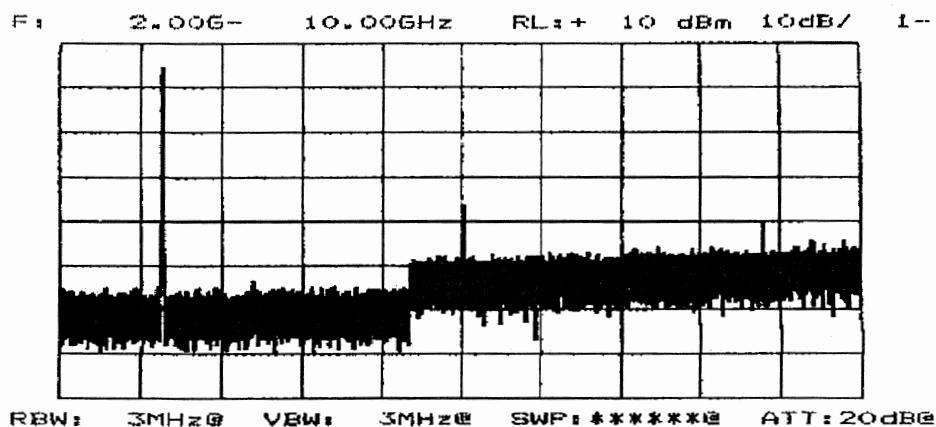


Fig.7. The 1st, 2nd, 3rd harmonic of the output signal of the S-band synthesizer.

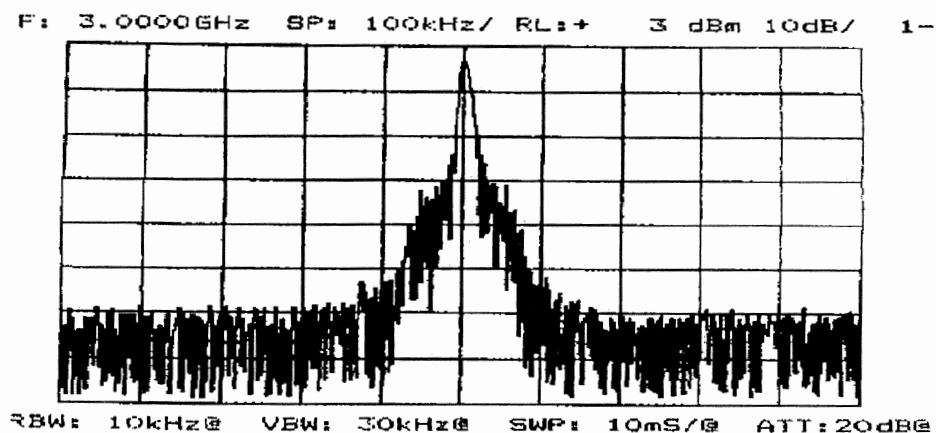


Fig.8. The main harmonic of the output signal of S-band synthesizer in the band 100kHz/div.

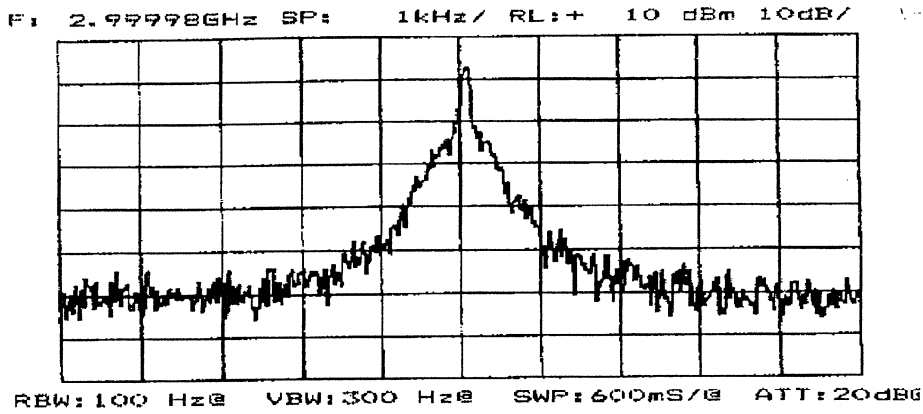


Fig.9. The main harmonic of the output signal of S-band synthesizer in the narrow band 1kHz/div.

**X- band synthesizer.**

The X-band synthesizer for 9.1-10.3GHz frequency range has been designed. There was used the external prescaler :8  $\mu$ PG506 made by NEC [2]. The self-invented VCO has been

applied. The VCO has been designed using CFX16 transistor (RFC) and varactor diode MA 46471 made by MA/COM [3]. The maximum frequency step is:  $\Delta f_{DDS-PLL} \approx 7\text{Hz}$ . The output signal power spectrum is shown in fig.10÷12.

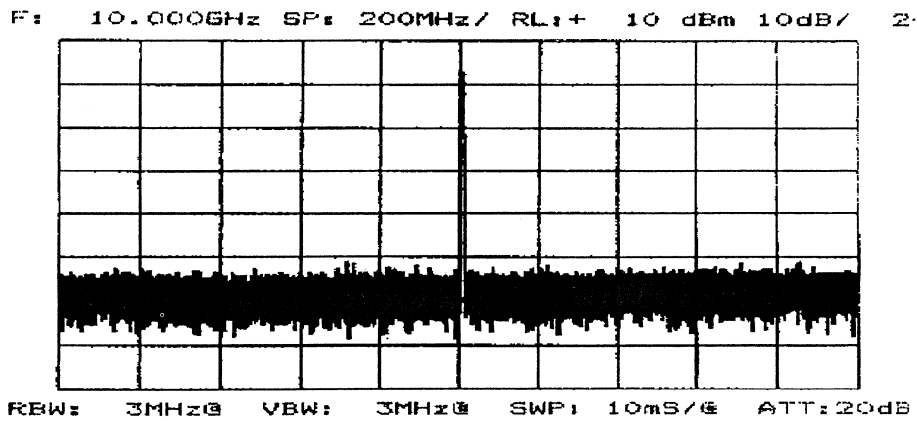


Fig 10. The main harmonic of the output signal of X-band synthesizer.

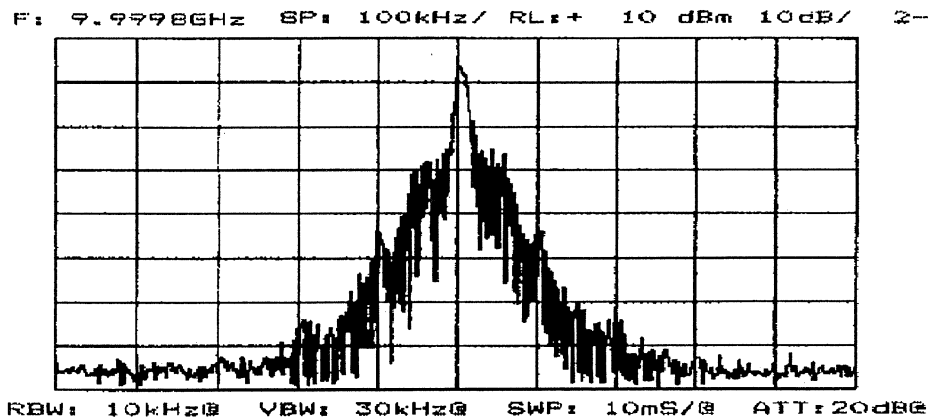


Fig.11. The main harmonic of the output signal of X-band synthesizer in the band 100kHz/div.

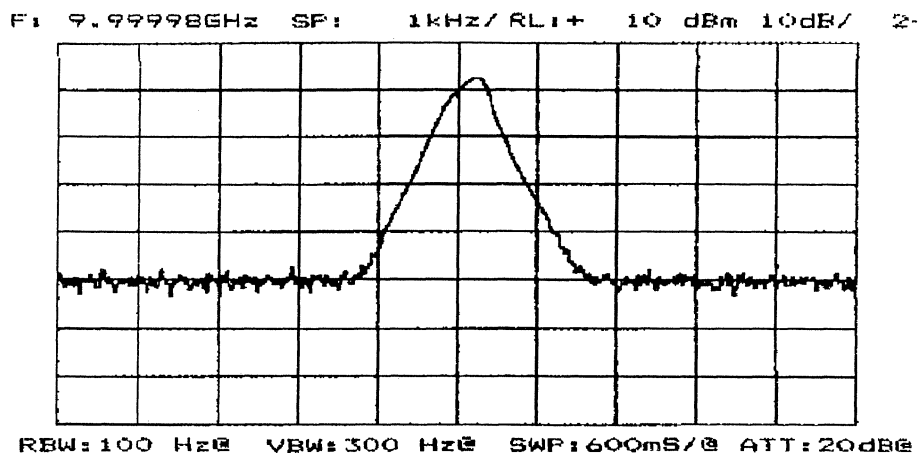


Fig.12. The main harmonic of the output signal of X-band synthesizer in the narrow band 1kHz/div.

### 3. CONCLUSIONS.

Tab. 1. Technical parameters.

Parameters	DDS synthesizer	L - band synthesizer	S - band synthesizer	X - band synthesizer
frequency range	0÷15MHz	0.6÷1.3GHz	3.1÷3.6GHz	9.1÷10.3MHz
resolution	≈0.007Hz	≈0.91Hz	≈2.6Hz	≈7Hz
phase noise level	<-120dBc/Hz	<-70dBc/Hz	<-60dBc/Hz	<-50dBc/Hz
output power	≥ 2dBm	≥ 2dBm	≥ 3dBm	≥ 2dBm

The measurement results obtained for the synthesizers have proved accuracy of circuit solution. The most important parameters of the synthesizers are presented in the tab. 1.

The stability of frequency with the DDS internal reference is better than  $10^{-7}$ . The obtained results satisfy the most of the requirements of RF laboratories. The presented architecture of the synthesizers permits to get much more better parameters (i.e. phase noise level, stability) using

proper reference source for DDS. One of the advantages of the designed synthesizers are the output power levels ( $\geq 2\text{dBm}$ ). It allows to use these synthesizers directly into a laboratory as well as utilize them into the radiolocation and radiocommunication systems.

### 4. REFERENCES.

1. Qualcomm 1991 "User's Guide For Q410 Phase Locked Oscillator"
2. NEC 1989-1990 "Microwave and RF Semiconductors "
3. M/A-COM 1988 "Semiconductor Products Master Catalog # SP101"

## TWO DETECTION AXIS VIBRATING GYROSCOPE STRUCTURE INTENDED FOR NAVIGATION

Y. Ansel, P. Lerch, P. Renaud

Institute of Microsystem (IMS), EPFL, 1015 Lausanne, Switzerland

### ABSTRACT

A vibrating gyroscope [1,2] with a new planar mechanical structure is presented allowing two perpendicular gyroscopic detection axis. The presented vibrating gyroscope uses a piezoelectric excitation/detection reference motion transducer and a differential inductive proximity sensor [3] to detect gyroscopic motion. This structure works simultaneously as an accelerometer with detection axis perpendicular to the two gyroscopic detection axis.

*N.B: Bold notations are mathematics vectors in the text.*

### INTRODUCTION

By definition, inertial systems have to compute the position and the orientation of a vehicle relying on the measurements of inertial sensors. Inertial systems are usually coupled with absolute reference systems, which leads to the concept of navigation systems. Navigation system is an end-user product providing trajectory information.

In automotive applications [4], inertial sensors can be used as a complement to GPS (Global Positioning System), to calculate the vehicle trajectory (especially in urban areas where loss of GPS signals often happens). Due to the precision increase of accelerometers and angular rate sensors for a constant cost, inertial sensors become key devices in navigation systems.

Vibrating gyroscopes measure the Coriolis acceleration. A vibrating structure with a mass  $m$  and a velocity  $v$  perpendicular to an external angular speed rotation  $\Omega$  generates the Coriolis force  $F=2m\Omega v$ . Consequently, a gyroscopic motion appears perpendicular to the reference motion  $v$  and to the rotation speed vector  $\Omega$ . This gyroscopic motion is transduced and converted into a voltage.

In figure 1, the schema of a two-mass vibrating gyroscope is represented. A reference rotation vibrating motion around the torsion bar is induced with driving elements. The two masses have

velocities collinear but opposite in sign and generate, during rotation  $\Omega$ , opposite Coriolis force components. This produces opposing deflections between the two masses. An advantage can be gained from this phenomenon using differential measurement. In this way, the external acceleration sensitivity of the vibrating gyroscope can be cancelled.

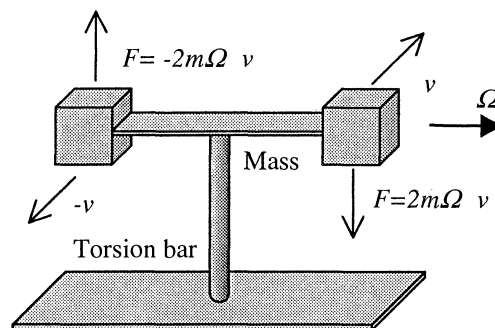


Figure 1: Two masses vibrating gyroscope schema with differential measurement capabilities.

Various microstructure geometries exist [1,2]. Two of the most popular structure geometries are beams (triangular or quadratic sections) and tuning fork (simple or H shaped) made in silicon, metals or quartz. In addition to the vibrating microstructure, vibrating gyroscopes have at least two transducers: the reference motion excitation transducer and the Coriolis force detection transducer. Figure 2 is a flow diagram of vibrating gyroscopes system.

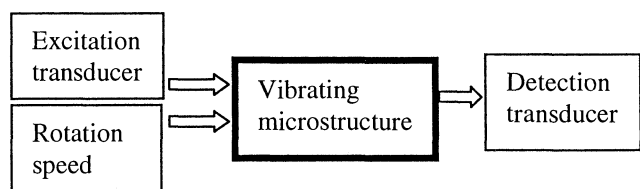


Figure 2: Flow diagram of a vibrating gyroscope structure with the input/output transducers.

The output transducer voltage is synchronously demodulated with respect to a  $90^\circ$  shift of the reference signal motion to extract the angular velocity signal. A reference loop electronics is also necessary to control the reference motion amplitude.

## SENSOR DESIGN

In order to fulfil possible demand for combined accelerometer and gyroscope device [5], a new vibrating mechanical structure was designed and developed. An inertial sensor based on this one block mechanical structure was partially tested. This inertial sensor includes the feature of two vibrating gyroscopes and one accelerometer.

The inertial sensor is adapted for land navigation (figure 3) where one acceleration  $a$  (vehicle direction) and two rotations directions  $\Omega$  and  $\Omega'$  (yaw and pitch rotations of the vehicle) are detected. The three vectors,  $a$ ,  $\Omega$  and  $\Omega'$  are perpendicular to each other.

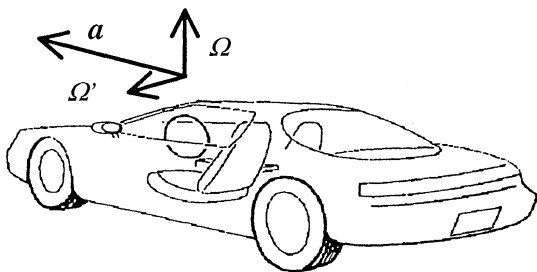


Figure 3: Land navigation directions: vehicle acceleration  $a$ , yaw  $\Omega$  and pitch  $\Omega'$ .

Practically, the inertial sensor is a vibrating mechanical structure (figure 5) mounted between two printed circuit boards, each equipped with eight piezoceramic transducers and five coils with their detection circuits (figure 4).

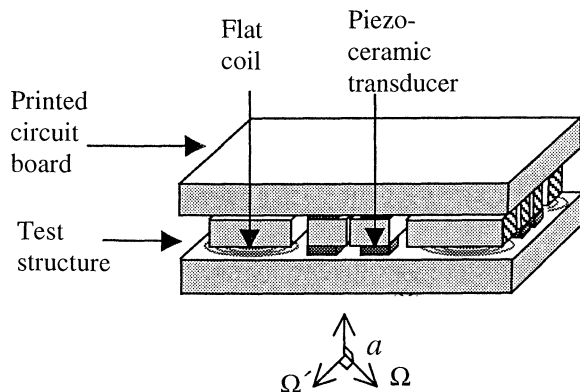


Figure 4: Mounting schema of the vibrating structure between two printed circuit boards.

Figure 5 shows the vibrating structure in chrome steel made by electro-discharge machining. Sixteen shear piezoceramic transducers are clamped to the vibrating structure on the piezoelectric supports. Structure's springs transmit the driving motion of the actuators to the structure centre. Lever arm effect of this structure centre amplify mechanically the piezoelectric driving motion. An amplification rate of 10 was designed and measured. The function of

the angular rate sensitive masses is similar to the masses in figure 1.

The first resonance mode of the structure (excitation mode) is the gyroscopic vibration reference motion: the four surrounding masses have rotation vibration around the vibrating structure gravity centre. This reference motion is generated by fourteen piezoactuators and the two last are employed to detect the excitation mechanical resonance.

When two perpendicular angular speed rotations  $\Omega$  or  $\Omega'$  occur with axis included into the 2D structure plane, Coriolis forces are generated and a gyroscopic motion appears perpendicular to the reference motion and to the rotation speed: an out of the plane movement of the surrounding masses is produced (detection mode).

Design of the structure using finite element model [7] allows frequency matching between the excitation and the detection modes in order to optimise gyroscopic coupling between modes. Nevertheless, this matching can not be perfect. It is the reason why that the fundamental resonance of the driving mode can be shifted by applying tuning DC voltages on the piezoactuators.

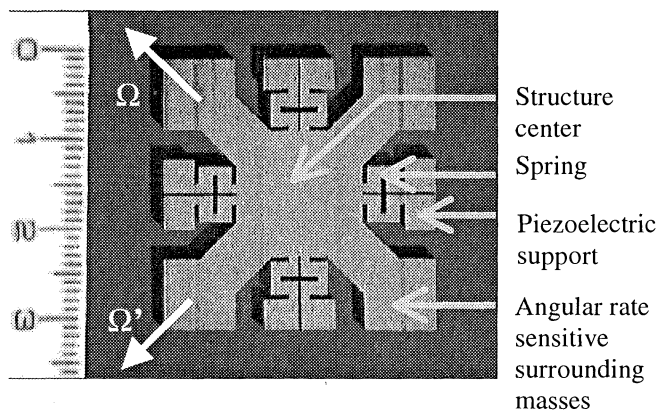


Figure 5: Photo of a vibrating structure made by electro-discharge machining.

During external rotation  $\Omega$ , two rate sensitive masses are vibrating out of plane with a phase shift of  $180^\circ$  allowing differential displacement measurement [6] to avoid acceleration sensibility. Differential displacement measurement is performed using coil inductive proximity sensors placed in front of the angular rate sensitive masses [3]. In order to detect the acceleration  $a$  perpendicular to the structure plane, a coil inductive proximity sensor is placed in front of the structure centre. Inductive sensors are connected to a RC relaxation oscillators where the output signal frequency change as a function of the distance of the coil to the targets.

## SENSOR MODEL

The mechanical equation behaviour of the vibrating structure is derived from the motion equation of solid bodies. The structure centre and the surroundings masses are assumed to be rigid which is the solid body into interest. This approximation is valid for low excitation frequency (below the seventh resonance frequency of the vibrating structure). The five first harmonic modes and the fundamental mode of the vibrating structure are in fact the six degrees of freedom of the solid body: three translations (translation vector  $\mathbf{x}$ ) and three rotations (rotation vector  $\theta$ ).

For symmetry reason, the non-newtonian coordinate system  $(G, \Omega, \Omega', \mathbf{a})$  or  $(G, i, j, k)$  is chosen to derive the mechanical equations where  $G$  is the gravity centre of the solid body. In this frame, the inertia matrix  $[I]$  of this solid body is a diagonal matrix because the frame axis  $(i, j, k)$  are symmetry axis for the solid body. The mass of the solid body is  $m$ . The motion equations of the solid body yields:

$$\int \vec{F}(P) dv = m \frac{d^2 \bar{\mathbf{x}}}{dt^2} \quad (1)$$

$$\int \overline{GP} \wedge \vec{F}(P) dv = [I] \frac{d^2 \bar{\theta}}{dt^2} \quad (2)$$

where  $F(P)$  are the external forces applied in a point  $P$  of the solid body. Four types of forces are applied on the mechanical structure: the piezoelectric excitation forces, the inertial forces, the springs recall forces and the damping forces.

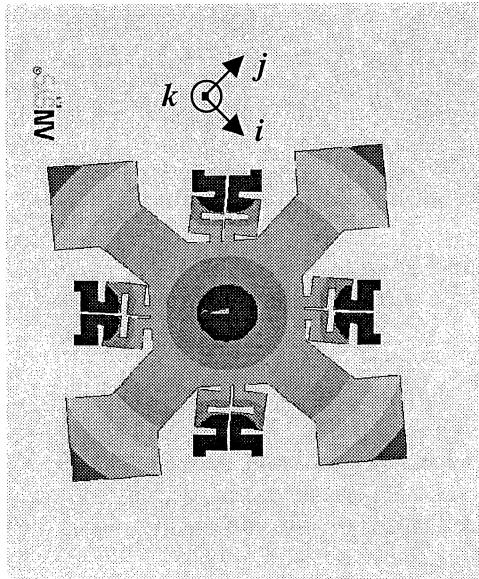


Figure 6: FEM structure excitation mode (sum translation vector are represented by grey level).

First, the piezoelectric excitation loads  $F_p(P)$  are localised on the piezoelectric support. They are transmitted to the solid body through the springs. Due

to the topology of the piezoelectric transducers, the sum of the piezoelectric excitation forces is zero but the global moment  $M_p$  with respect to  $G$  is not. This moment generates the reference motion of the structure: the vibration rotation around  $k$  axis (figure 6).

Secondly, the solid body is subject to inertial forces like miscellaneous accelerations (centrifugal forces, accelerations) and to the Coriolis forces. The global moment of the accelerations with respect to  $G$  is zero but the sum  $F_a$  of accelerations is not, because the acceleration forces are spatially constant around the symmetrical structure. On the contrary, taken into account only the reference motion speed of the solid body, the sum of the Coriolis forces is zero but their moments are not. The rotation speed  $\Omega$  (respectively  $\Omega'$ ) generates the global moment  $M_n$  collinear with  $j$  and proportional to the rotation speed (respectively the global moment  $M_n \cdot$  collinear with  $i$ ). Figure 7 displays the mode shapes of the vibrating structure excited by the rotation speed  $\Omega$ .

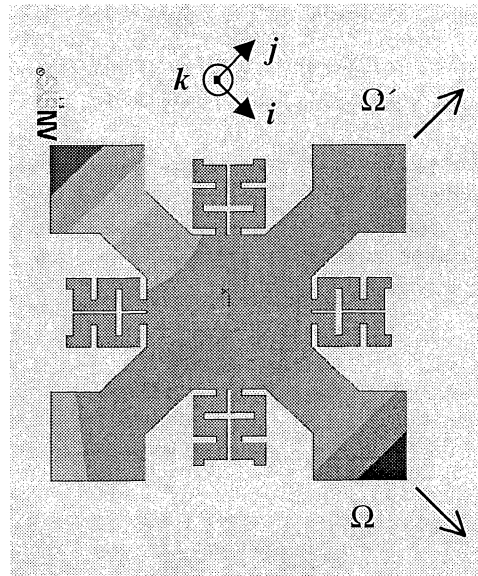


Figure 7: FEM structure detection mode (sum translation vector are represented by grey level).

Finally, the springs forces and the damping forces acting upon the solid body are represented through the translation elastic matrix  $[K_x]$  (respectively the rotational elastic matrix  $[K_\theta]$ ) and the damping matrix  $[C_x]$  and  $[C_\theta]$ . Taking advantage of the fact that the first six degrees of freedom of the solid body are the six principal mode shapes of the structure, the elastic matrices are diagonal.

The motion equations become:

$$m \frac{d^2 \bar{\mathbf{x}}}{dt^2} + [C_x] \frac{d \bar{\mathbf{x}}}{dt} + [K_x] \bar{\mathbf{x}} = \vec{F}_a \quad (3)$$

$$[I] \frac{d^2 \bar{\theta}}{dt^2} + [C_\theta] \frac{d \bar{\theta}}{dt} + [K_\theta] \bar{\theta} = \bar{M}_p + \bar{M}_\Omega + \bar{M}_{\Omega'}$$

(4)

Equation 3 represents the accelerometer behaviour of the structure. The  $k$  translation mode is induced with the acceleration  $a$ , which demonstrate the seismic mass function of the structure. Accelerations in  $i$  and  $j$  directions can also be detected with specific transducers not implemented in the actual device.

Equation 4, the linear differential equations in  $\theta_1$ ,  $\theta_2$  and  $\theta_3$  of the rotation angles around  $i$ ,  $j$ ,  $k$ , describes the gyroscopic behaviour of the vibrating structure. The rotation speed  $\Omega$  generates the rotation mode around  $\Omega'$  and vice versa. In order to calculate the resonance frequencies of the vibrating structure, the mass, the inertial matrix and the elastic matrix can be estimate.

Nevertheless, due to the complex geometry of the structure, a finite element model [7] of the structure is used. ANSYS finite element modal analysis [8] permits the matching of the resonance frequencies of the excitation mode with the detection modes. In the case of a constant rotation speed, the maximum gyroscopic sensitivity can be derived from (4) and is given by equations 5:

$$\frac{\theta_2}{\Omega} = \frac{Q \theta_3}{\pi f_0}; \quad \frac{\theta_1}{\Omega'} = \frac{Q \theta_3}{\pi f_0} \quad [s] \quad (5)$$

with  $f_0$  and  $Q$  the rotation resonance frequencies and the quality factor of the gyroscopic sensing modes. Decreasing  $f_0$  increases the sensitivity and, on the contrary to translation type vibrating gyroscope, the acceleration sensitivity can be kept unchanged. This is due to the uncoupling of the acceleration and the gyroscopic effects in this inertial sensor.

## DETECTION METHOD

A new inductive differential detection interface is used to detect the solid body rotation around  $\Omega$  and  $\Omega'$  axis. In this electronic interface, a metallic target (the angular rate sensitive surrounding masses) is inserted between the two coils (figure 8) with inductance  $L_1$  and  $L_2$ . Using two identical coils, the target deflection  $\Delta d$  normalised with respect to  $d_0$  (the distance between the two coils) is expressed in terms of the inductances with a good approximation by:

$$\frac{\Delta d}{d_0} = \frac{L_1 - L_2}{L_1 + L_2} \quad (6)$$

The equation 6 shows that the target deflection is proportional to the inductance difference (the inductance sum is in fact constant with a second order approximation).

In order to estimate this difference, a differential relaxation oscillator circuit is used (figure 8). In this circuit, in the oscillation mode, the electronic comparator compares increasing (or decreasing) voltages  $V_+$  and  $V_-$  from positive and negative relaxation branches.

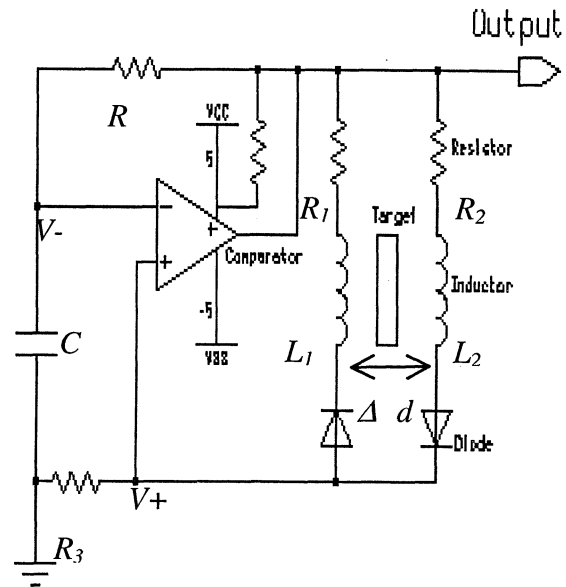


Figure 8: Detection electronic schema of the differential oscillator circuit.

The negative branch ( $RC$ ) is a capacitive type circuit and the positive branch is an inductive type circuit ( $R_1 L_1 R_3$  or  $R_2 L_2 R_3$ ). The time constant of the negative branch is constant, while the time constant of the positive branch is alternatively function of the inductance  $L_1$  and  $L_2$  depending of the sign of the comparator output saturated voltage. Two opposite mounted diodes adjust the current flow in the displacement sensitive inductive branches.

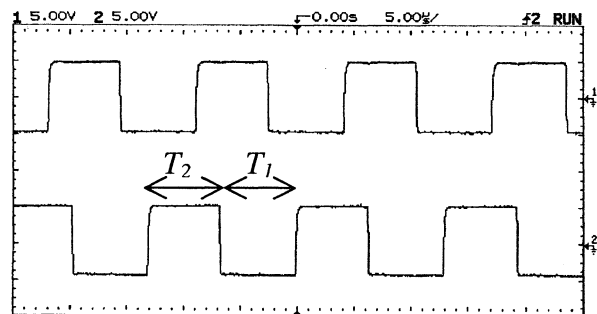


Figure 9: The differential relaxation oscillator circuit output signals.

The consequence is that the differential relaxation oscillator circuit generates a rectangle signal with one

half period  $T_1$  function of  $L_1$  and the other period  $T_2$  function of  $L_2$ . Appropriate signal processing allows finally to estimate the inductance difference. Figure 9 shows the two output signals from the differential relaxation oscillator circuits formalised with a second comparator.

It can be shown that [3] the oscillation condition is the crossing condition of the two voltage signals  $V_+$  and  $V_-$ . The two signals are competing during the charging of the two branches. Considering perfect components (ideal comparator, ideal diodes), the oscillation occurs when the following condition is fulfilled:

$$RC \frac{R_3}{L_i} > 1 \quad (7)$$

where the index  $i$  is alternatively 1 and 2. The maximum sensitivity of the oscillating signal periods caused by an inductance change is obtained when the oscillation condition 7 is hardly verified.

A second relation useful to calculate the passive component optimum value is given experimentally. Figure 10 shows, for several frequencies, the measured coil inductance for different gap distances between the coil and the solid body target. The direct inductance over displacement sensitivity increases with the period signal.

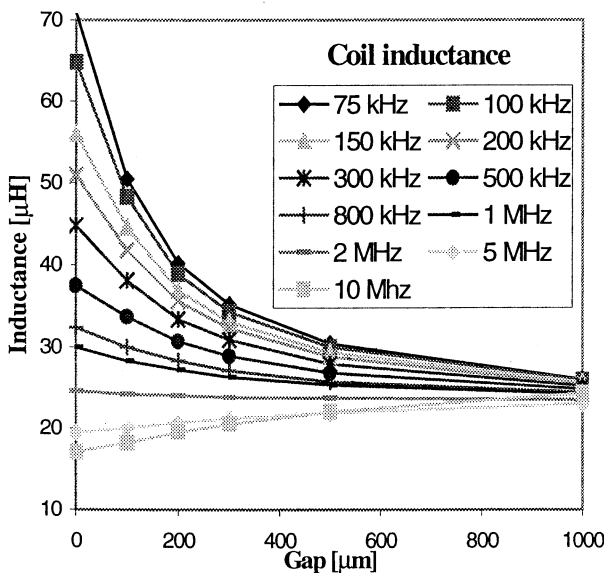


Figure 10: Coil inductive response for different gap distances between the coil and the solid body target and for several frequencies.

But the differential relaxation oscillator circuit global sensitivity is given by the direct inductance over displacement sensitivity multiplied by the sampling rate (the relaxation oscillator signal

frequency). Considering experimental result of figure 10 for a commercial coil, the absolute maximum sensitivity is obtained for frequencies around 300kHz.

This differential relaxation oscillator allows no common ground with the excitation circuit and very low impedance compared with piezoactuators. The electrical independence is then fully obtained between the detection circuit and the excitation circuit where hundreds of volts are employed for piezoactuation.

A presetable binary up/down counter can then be used as the first stage of the digital processing to evaluate the half periods difference. Due to the time coded output of the sensor, a reference clock signal is used. In order to get  $n$  binary digit output, the clock frequency should be  $2^n$  times greater than the differential relaxation oscillator one.

## TEST RESULTS

Two vibrating gyroscopes prototype were realised in chrome steel (Young modulus: 210 MPa, Poisson ratio: 0.3, density: 7.7 g/cm<sup>3</sup>). They were packaged between two 3.2 mm thick printed circuit boards made in Epoxy (Young modulus: 17 MPa). The shear piezoceramic transducers (Philips PXE71 components) were inserted in sandwich.

	#1	#2
Computed resonance frequency [Hz]	5310	1170
Measured resonance frequency [Hz]	5380	1070
Difference [Hz]	70 (+1.3%)	-100 (-9.3%)
Measured quality factor	30	130

Table 1: Computed and measured excitation resonance and quality factors.

The excitation vibration amplitude, piezoelectrically generated, was measured at ambient temperature and pressure using an interferometer. Table 1 displays the measured quality factor and resonance frequencies. Computed resonance frequencies compared with measured values are in good agreement for the 5 kHz structure.

Figure 11 displays the magnitude response of the 5 kHz vibrating structure from 1 kHz to 12 kHz. A

second resonance pick around 10 kHz is detected. Any parasitic effect of this higher frequency mode does not affect the excitation mode working several thousands Hertz below.

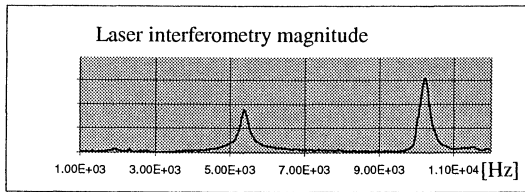


Figure 11: Magnitude response in arbitrary unit of the 5kHz test structure from 1kHz to 12kHz.

Without rotation, the excitation vibration amplitude was compared to the detection one in order to estimate the piezoelectric excitation transducer mode selectivity. An amplitude ratio of 5% were measured between the amplitudes. This low selectivity is due to mechanical coupling between the two modes. The mechanical coupling is, in our case, a consequence of the vibrating gyroscope mounting procedure leading to excitation force transducers misalignment with the vibrating structure.

Low quality factors were measured. Better quality factor should be obtained if crystalline material like silicon or quartz [9] is employed instead of iron. From the packaging point of view, vacuum encapsulation of the prototype will lower the air damping of the structure. Another reason of the poor quality factor obtained is due to the energy losses in the mount. The moment reaction of the rotation inertia of the structure around the  $k$  axis generates vibration in the surrounding packaging. A possible cure of the problem for lowering the energy loss is to stack two vibrating structure cores and drive them in antiphase excitation vibrations. For that, mechanical coupling between the two structure can be employed. In this configuration, the rotation inertia around the  $k$  axis of the whole device is constantly zero.

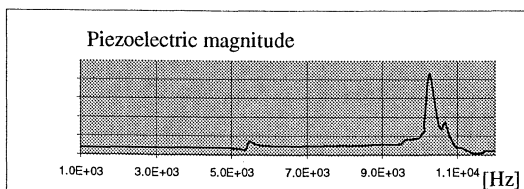


Figure 12: Piezoelectric response in arbitrary unit of the 5kHz test structure from 1kHz to 12kHz.

The measured piezoelectric response (figure 11) of the vibrating structure gives similar compared to interferometry result (figure 12). Gyroscopic response of the vibrating structure is under investigation.

## CONCLUSION

In this abstract, a new planar mechanical structure is presented allowing two perpendicular gyroscopic detection axis and one acceleration detection axis with high sensitivity displacement measurement due to the oscillator based read out electronics. The driving of the excitation mode and the differential measurement technique was experimentally demonstrated. This structure, suitable for land navigation system where two rotations and one direction are useful, allows low cross sensitivities due to the symmetry of the structure and due to differential measurement capabilities.

## ACKNOWLEDGMENTS

This work has been funded by the Swiss National Science Foundation (FNSRS) and the Swiss Foundation for Research in Microtechnology (FSRM) within the framework of an international exchange between French and Swiss institutions of microtechnology (PICS = Projet International de Coopération Scientifique).

## REFERENCES

- [1] Söderkvist J., 'Micromachined gyroscopes', 7th Inter. Conf. on Solid-States Sensors and Actuators, pp. 638-641.
- [2] Söderkvist J., 'Micromachined gyroscopes', Sensor and Actuators A, 43 (1994), pp. 65-71.
- [3] P. Passeraub, P-A. Besse, C. de Raad and R. Popovic, 'A differential relaxation oscillator as a versatile electronic interface', Sensors and Actuators A 58 (1997) 141-148.
- [4] Zhao Y. 'Vehicle location and navigation systems', Artech house, Norwood MA (1997).
- [5] Ansel Y., P. Lerch, P. Renaud, F. Paoletti, M.A. Grétilat, N.F. de Rooij, G. Schöpfer, S. Ballandras, M. De Labachellerie, C. Marselli, H.P. Amann, F. Pellandini, 'Simulation and design of a three axis navigation microsystem based on micromachined sensors', Microsim II, Computational Mechanics Publications, pp. 107-116, Lausanne, Switzerland, September 1997.
- [6] Paoletti F., Grétilat G.-A., De Rooij N.F., 'A silicon micromachined vibrating gyroscope with piezoresistive sensors detection and electromagnetic excitation', MEMS, San-Diego, (1996), pp. 162-167.
- [7] Ansel Y., Lerch P., Renaud P., 'Mode coupling aspects in a vibrating gyroscope', Sensors and Actuators, Vol. A62, 1997, pp. 576-581.
- [8] Swanson Analysis Systems, ANSYS User's Manual, version 5.3.
- [9] Söderkvist J., 'Design of a solid-state gyroscopic sensor made of quartz', Sensor and Actuators A21-A23, (1990), pp. 293-296

**TWO CLASSES OF TRANSITIONAL FILTER TRANSFER FUNCTIONS APPLIED IN CRYSTAL FILTER DESIGNING**

Snezana Dedic - Nestic

Institute "Mihajlo Pupin" Quartz Crystal Division, Belgrade, Yugoslavia

**Abstract**

*Transitional filters with characteristics between equal ripple linear phase filter and constant amplitude filters (Chebyshev, Butterworth) are presented.*

*Two types of transitional filters are obtained :*

1. *Transitional Linear Phase - Chebyshev*
2. *Transitional Linear Phase - Butterworth*

*Resulting transfer functions are used in crystal filter designs and comparisons between different approximations are made. Frequency and time domain characteristics are presented. It was shown that many filter specifications can be covered with these transfer functions. Some practical results of crystal filter realisation are presented.*

**Introduction**

There are many applications for transitional filters as compromise filters which have frequency and time domain characteristics between those of the constant amplitude filters and those of the constant group delay filters. When some amount of degradation of passband delay is allowed transitional filters can be used to improve selectivity.

Crystal narrow band filter designing is based on low pass prototype network. One of the starting point in crystal filter designing is to find the low pass transfer function that satisfies filter specification. The main problem is to find the transfer function that achieves requirements regarding shape factor and phase linearity of the filter.

In this article transitional filters obtained by combining equiripple phase approximation with constant amplitude approximations, Chebyshev and Butterworth, are introduced. Transfer function poles incorporate a variable parameter that gives responses whose characteristics lie between these approximations. An equiripple approximation of linear phase is chosen because, comparing with ideal linear phase approximation, it gives better results, approximating a linearity over a wider interval and providing higher attenuation in the stop band.

Calculating results of crystal filter designs based on the transitional low pass prototypes are presented for different values of variable parameter. Amplitude and group delay characteristics and pulse responses of the filters are presented.

Results of crystal filter realisation are presented. Filter network is realised as a cascade junction of semilattice sections.

**Transfer function**

Transfer function is of the all-pole type and is found by combining two different transfer functions, one of them realising linear phase, the other constant amplitude characteristic.

For the n-th order filter, transfer function is represented in the form :

$$T(s) = \frac{1}{\prod_{i=1}^n (s - s_i)} \dots\dots\dots(1)$$

Transfer function poles,  $s_i$ , are found according to the relation :

$$s_i = s_{pi}^m \cdot s_{ai}^{(1-m)} \dots\dots\dots(2)$$

$s_{pi}$  is the i-th pole of the linear phase filter and  $s_{ai}$  is the i-th pole of the constant amplitude filter (Chebyshev, Butterworth).  $m$  is a variable parameter,  $0 \leq m \leq 1$ .

Computer program is made for determining the value of variable parameter and for making transfer function that satisfies filter specification regarding group delay distortion and filter selectivity.

**Crystal filter characteristics**

For different values of  $m$  a set of low pass prototype transfer functions is obtained.

To illustrate behaviour of these transfer functions in crystal filter realisation the results of the analysis of 6-th order crystal band pass filters are presented for center frequency 20 Mhz and 3-dB bandwidth 18 Khz.

Following design parameters are used :

- crystal motional capacitance,  $C_1=0.0085$  pF
- capacitance ratio,  $r = 260$
- crystal quality factor,  $Q_x = 60000$
- coil quality factor,  $Q_t = 80$

Figures 1. and 2. represent computed attenuation, group delay and pulse responses to a unit - step input of crystal filters for  $m = 0, 0.4, 0.8, 1$ , obtained from transitional Linear Phase - Chebyshev and Linear Phase - Butterworth prototypes. Linear phase is approximated in equiripple sense, phase error  $0.5^\circ$ .. Chebyshev approximation with 0.1 dB ripple is used.

Comparing characteristics of these two classes of transitional filters some advantages of transitional Linear Phase - Chebyshev filters are found with respect to transitional Linear Phase - Butterworth filters. At the same fixed stopband attenuation transitional Linear Phase - Chebyshev filter provides less delay distortion and better transient response.

### Crystal filter realisation

An example of crystal filter realisation is presented. Filter has to achieve the following requirements :

- Center frequency ,  $f_0 = 10.7$  MHz
- 3 dB bandwidth ,  $\Delta f_{3dB} = 30$  KHz
- 30 dB bandwidth ,  $\Delta f_{30dB} = 100$ KHz
- 60 dB bandwidth ,  $\Delta f_{60dB} = 200$  KHz
- Group delay distortion ,  $\Delta t_g = 3 \mu s$   
in the band  $f_0 \pm 15$  KHz.

Above specification is met with a 4-th order transfer function , transitional Linear Phase - Chebyshev approximation,  $m=0.8$ . Filter is realised as a semilattice network with a 4 crystal units and 3 coils. Crystal parameters have the following values :

- Crystal motional capacitance ,  $C_1 = 0.0098$  pF
- Capacitance ratio,  $r = 220$
- Minimum crystal quality factor,  $Q_x = 80000$
- Coil quality factor  $Q_t = 60$

Attenuation and group delay characteristics of the realised filter are presented by fig 3.

### Conclusion

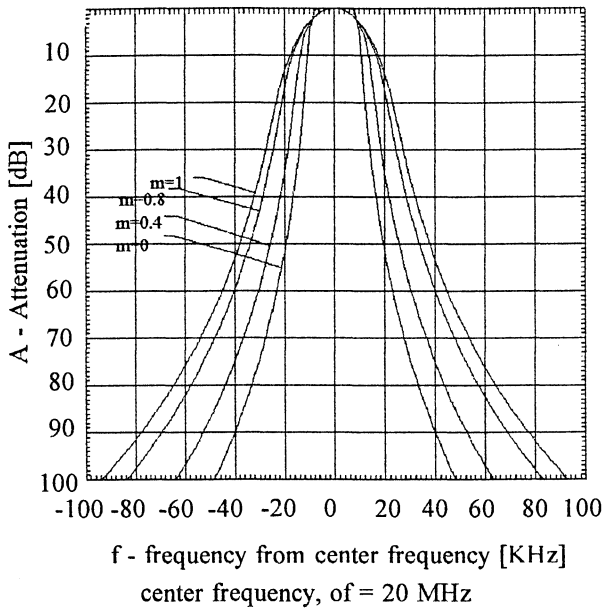
Some results obtained by analysing crystal bandpass filters realising two types of transitional responses are presented. Characteristics between equiripple phase and Chebyshev and equiripple phase and Butterworth filters are obtained. These characteristics are seen to be a very good solution and are well used in many crystal filter applications giving a compromise between the shape factor and phase linearity of the filter.

### Acknowledgement

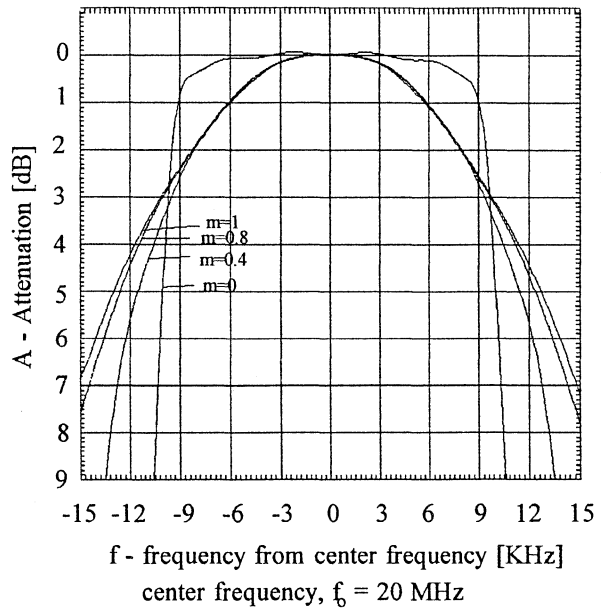
I have to express my appreciation to Mr. Camil Zabeljaj for his crystal filter realisation.

### References :

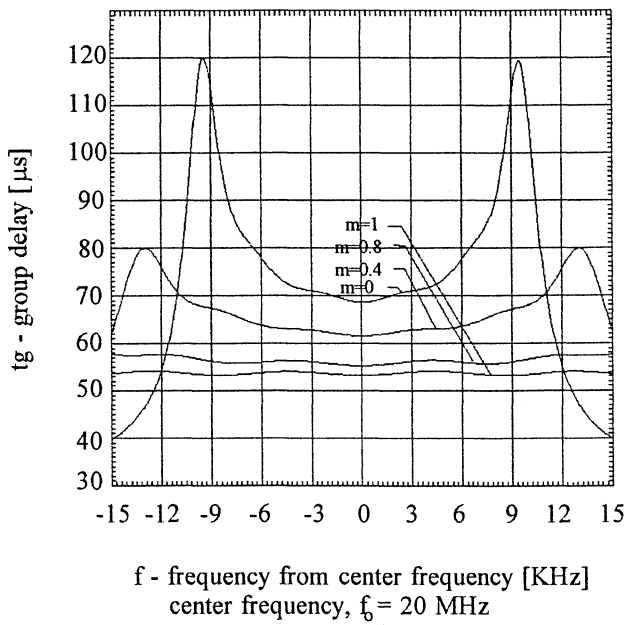
1. A.I. Zverev : Handbook of Filter Synthesis  
John Wiley and Sons, Inc. 1967.
2. D.S.Humpherys : The Analysis, Design and Synthesis of Electrical Filters  
Prentice Hall, Englewood Clifs N.J. 1970.
3. L.Weinberg : Network Analysis and Synthesis  
Mc. Graw - Hill Company , Inc. 1962



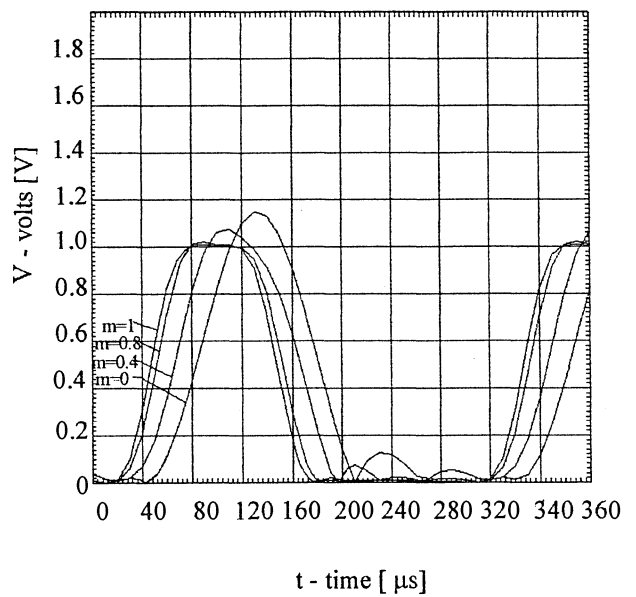
(a) Stopband attenuation



(b) Passband attenuation

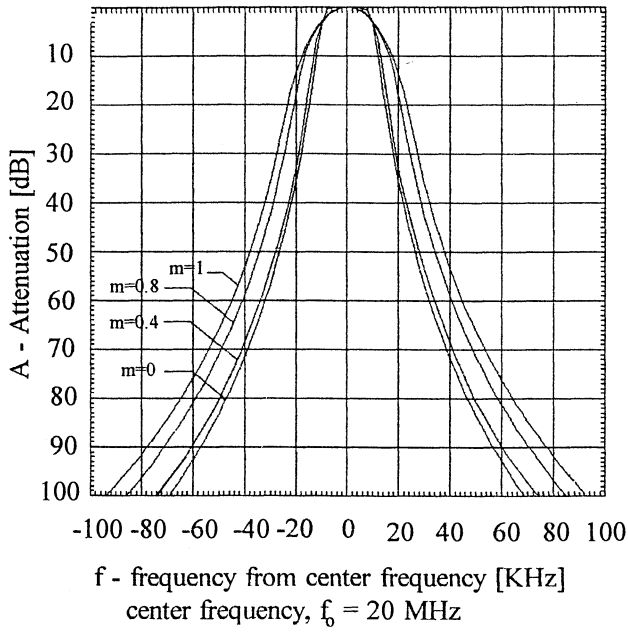


(c) Group delay characteristics

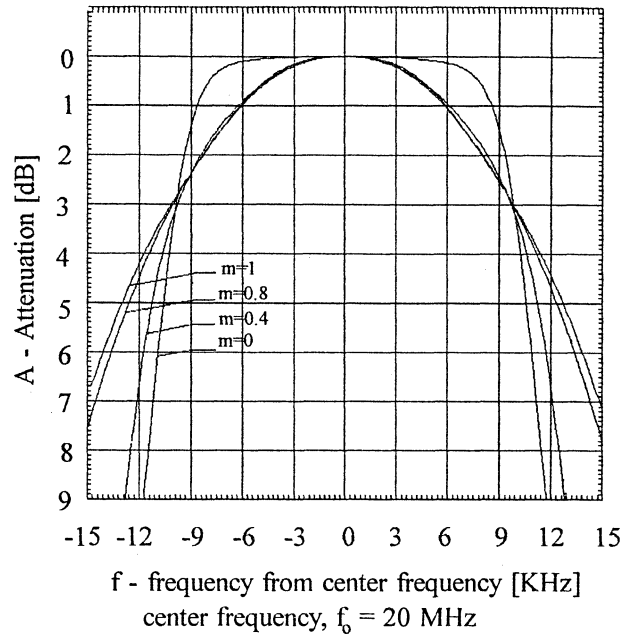


(d) Pulse response

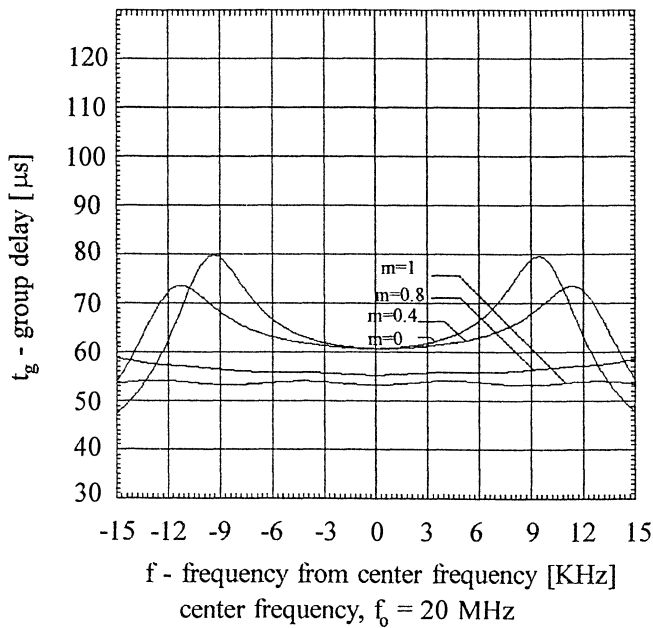
Fig 1. Characteristics of the 6-th order crystal filters based on transitional Linear Phase - Chebyshev prototype for different values of variable parameter



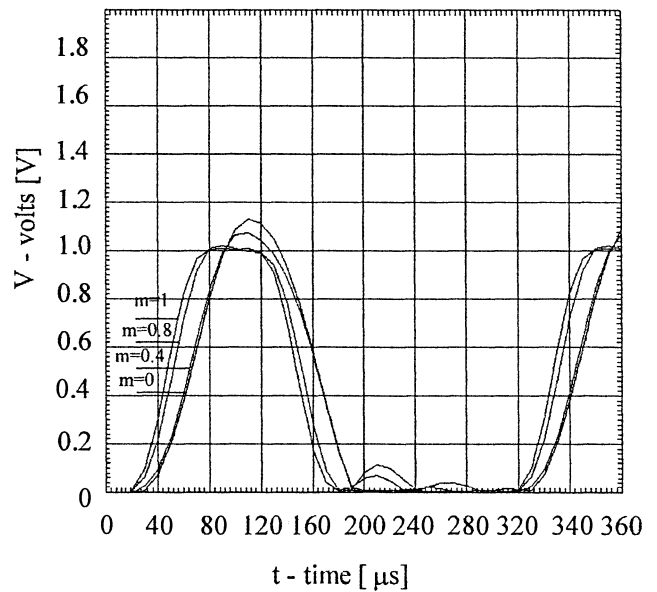
a) Stop band attenuation



b) Pass band attenuation



c) Group delay characteristics



d) Pulse response

Fig 2. Characteristics of the 6-th order crystal filters based on transitional Linear Phase - Butterworth prototype for different values of variable parameter

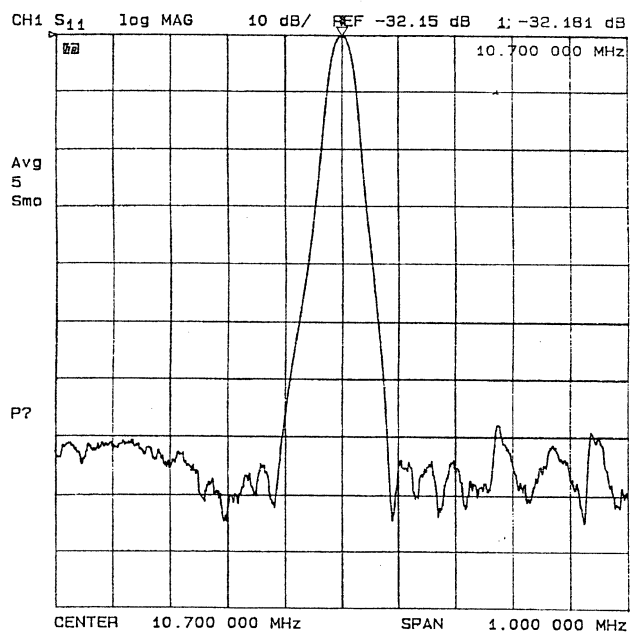
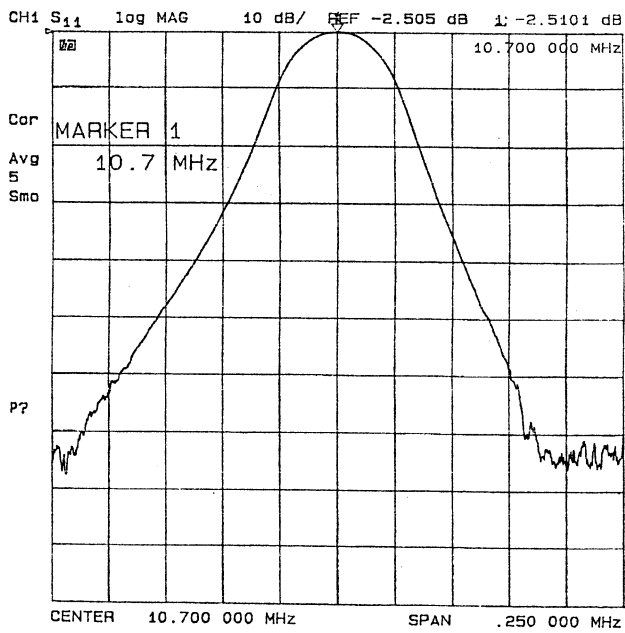
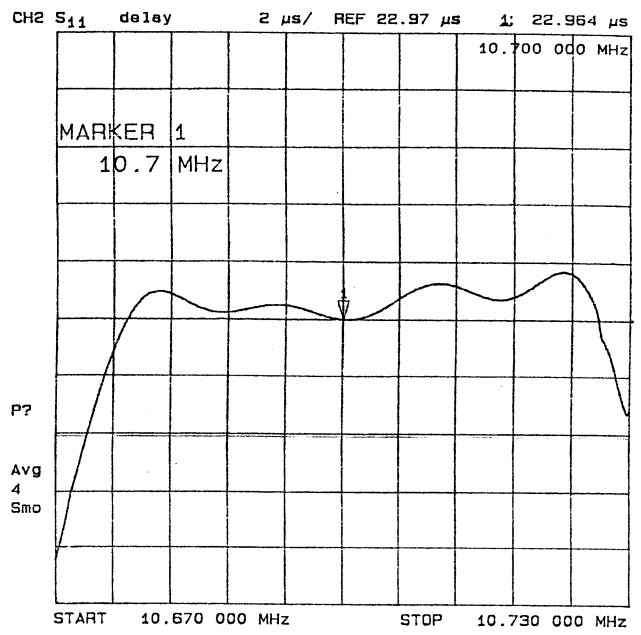
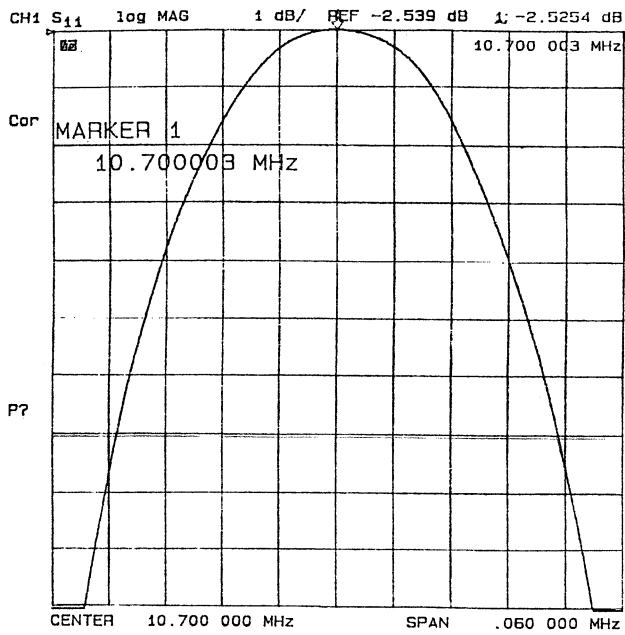


Figure 3. Characteristics of the realised 4-th order crystal filter, center frequency 10.7 MHz

## COMPARISON OF $TE_{01N}$ AND WHISPERING GALLERY MODES FOR DIELECTRIC RESONATOR FREQUENCY STANDARDS.

Ling Hao, John Gallop, Norbert Klein

National Physical Laboratory, Teddington, TW11 OLW, UK

\*Forschungszentrum, Jülich, D-52425, Germany

### ABSTRACT

Cryogenic high Q dielectric loaded microwave resonators provide a means to realise low phase noise oscillators and, when fabricated in composite dielectric form to give temperature compensation [1,2] can also provide good long term stability for use as secondary frequency standards. High Q values can be provided by two distinct resonator configurations: fundamental  $TE_{01n}$  modes or higher order 'whispering gallery' modes which have a high azimuthal node number. The first type of mode requires a very low loss conducting housing to reduce radiation losses which may be provided by a superconducting enclosure. The second, whispering gallery, configuration has very high levels of field confinement within the dielectric so that the conducting enclosure may be made of normal metal without seriously compromising the Q values obtained.

### INTRODUCTION

We present here calculations and experiments comparing the performance of the two types of resonator with particular emphasis on long term stability, and overall resonator size for a given frequency. Loaded Q values above  $10^6$  have been achieved with both configurations in a temperature compensated structure using a combination of single crystal sapphire and rutile ( $TiO_2$ ) elements. The relative advantages of each type are summarised and application areas where each may have advantages are discussed. We also consider the potential performance of other resonator and transmission line structures employing temperature compensated mixed dielectrics.

### ANALYSIS

Consider the simple cylindrical dielectric puck configuration shown in figure 1. For many

applications to frequency standards and low phase noise oscillator design one wishes to maximise the loaded Q value of the dielectric resonator. This will usually require cooling the single crystal dielectric (often sapphire is used) if Q values  $>10^6$  are to be achieved. In addition separation of the puck from contact with the surface of its enclosing conducting (or superconducting) housing is often necessary and this is achieved by low loss low permittivity spacers (not shown in Fig.1).

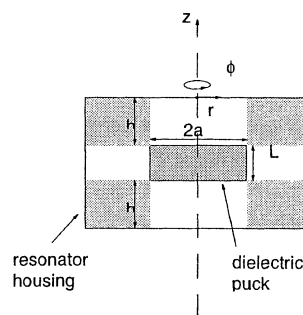


Fig.1 Schematic of dielectric puck supported in centre of radiation shield enclosure by low permittivity low loss dielectric spacers (not shown). Volume represented by lightly shaded areas is excluded from calculations below.

The loaded  $Q_l$  of the resonator may be expressed as the sum of at least five components:

$$\frac{1}{Q_l} = \frac{1}{Q_d} + \frac{1}{Q_s} + \frac{1}{Q_{cf}} + \frac{1}{Q_{cc}} + \frac{1}{Q_e} \quad (1)$$

The first term on the right hand side represents the dielectric loss within the puck. The second represents the loss in the dielectric spacers and will be assumed to be negligible throughout this paper. The third represents the losses due to the finite conductivity of the material of the flat end-plates from which the radiation screen is made. The fourth term represents the loss in the curved side wall of the screen (the material from which the screen is made may be a superconductor or a normal metal or even a

combination of the two). The final term  $1/Q_e$  represents the contribution to the loss from the externally coupled environment.

There are two distinct design routes which may be followed. A mode with low  $l$  value ( $\sim 1$ ) may be chosen, for which the dielectric puck size will be minimised. Another strategy involves choosing a 'whispering gallery' mode ( $1\sim 10$ ) for which the stored energy is concentrated in a region around the perimeter of the puck. For the same frequency the puck will be considerably larger than for a low  $l$  mode but, as compensation, the electromagnetic fields are more fully confined within the puck volume. The main issue of this paper considers which choice of mode will minimise the volume, surface area (and also mass) of the resonator.

It is important to consider the attenuation of the evanescent electromagnetic fields in the regions outside the puck but within the resonator housing, both for the variation in radial and axial directions.

### Axial Attenuation of Fields

For both low-order and whispering gallery mode families the attenuation of the electric and magnetic fields in the regions of the spacers is given by the simple relationship:

$$E(z), H(z) \propto \exp(-\alpha z) \quad (2)$$

where  $z$  is the axial distance measured from either face of the single crystal dielectric puck, towards the spacer region and  $\alpha$  is the real propagation constant (corresponding to an evanescent mode) in the spacer regions, being given by

$$\alpha^2 = \left( \frac{\chi_{lm}}{a} \right)^2 - k_0^2 \epsilon_{rs} \quad (3)$$

Here  $\chi_{lm}$  is the value of the argument which produces the  $m$ th zero of the  $l$ th order Bessel function of the first kind  $J_l$ ,  $a$  is the puck radius,  $k_0$  is the free space wave number corresponding to the resonant frequency  $\omega_m$  of the mode and is given by

$$k_0 = \omega / c \quad (4)$$

while  $\epsilon_{rs}$  is the effective relative permittivity of the spacer regions, assumed below to equal unity. To reduce the volume of the resonator as much as possible, as is required for many applications but especially for space borne resonators, one requires that, for a given frequency,  $\alpha$  should be as large as possible.

To select the minimum length of the housing one must make some arbitrary selection of how much of the total resonator loss occurring within the housing can be tolerated. This clearly depends in turn on the loss in the dielectric puck. As a general basis for comparison of resonator designs we select here the condition that the loss in either curved or flat walls of the housing should be no more than 10% of the loss in the dielectric. Assuming that for the best available sapphire at 10GHz and 77K the loss tangent  $\tan \delta \sim 10^{-7}$  allows us to calculate the minimum dimensions of the electromagnetic radiation confining housing which will not significantly compromise the overall resonator  $Q$  value.

The ratio of the  $Q$  value of the dielectric puck to that arising from the losses from the flat faces of the housing is defined by :

$$\frac{Q_d}{Q_{cf}} \sim \frac{(\epsilon_0 / \mu_0) R_s \int_{flats} E_\phi^2(\pm h).dS}{\epsilon_0 \tan \delta \int_{puck} E_\phi^2(r).dv} < 0.1 \quad (5)$$

Here the top integral is over the flat end plates whereas the integral in the numerator is a volume integral over the puck. Replacing the integrals over surface and volume by crude averages does not introduce significant error in estimating the values for  $R$  &  $h$  since the values of  $Q_{cc}$  &  $Q_{cf}$  depend exponentially on  $R$  &  $h$  respectively. Replacing the integrals by averages in the above expression allows the  $Q$  contribution ratio to be reduced to the simple form:

$$\frac{Q_d}{Q_{cf}} \sim \frac{R_s}{L\mu_0 \tan \delta} \left[ \frac{E_\phi(\pm h)}{E_\phi(0)} \right]^2 = \frac{10R_s}{L\mu_0 \tan \delta} (\exp(-\alpha h))^2 \quad (6)$$

### Radial Attenuation of Fields

In the radial direction the field of the same mode (approximately  $TE_{lmn}$ ) will vary in the region outside the dielectric puck as

$$K_1(k_2 r) \quad (7)$$

where  $K_1$  is the modified Bessel function of order 1 and the radial propagation constant  $k_2$  in the vacuum gap outside the puck is given by

$$k_2^2 = \left( \frac{n\pi}{L} \right)^2 - \left( \frac{\omega}{c} \right)^2 \quad (8)$$

The radial dependence of the electric field will be dominated by the variation of  $K_l$  and it is well known [3] that these functions approximate to

$$K_l(k_2 r) \propto \exp(-k_2 r + (2l + 1) \frac{\pi}{4}) \quad (9)$$

in the limit of large  $k_2 r$ . By a similar argument presented above for axial fields we may show that the minimum radius  $R$  of the housing which will not compromise the overall  $Q$  of the resonator is set by the condition:

$$\frac{Q_d}{Q_{cc}} \sim \frac{(\epsilon_0 / \mu_0) R_s \int_{\text{curved\_wall}} E_\phi^2(\pm R).dS}{\epsilon_0 \tan \delta \int_{\text{puck}} E_\phi^2(r).dv} < 0.1 \quad (10)$$

Assuming that the integral may be required only over a length  $L$  of the housing since for regions more distant from the centre plane the e.m. fields at the curved housing surfaces are even more attenuated this above equation reduces to:

$$\frac{4RR_s \exp(-2k_2(R-a))}{\omega\mu_0 a^2 \tan \delta} < 0.1 \quad (11)$$

This expression may be simply solved for  $R$  using a mathematical software package or even using graphical techniques

### Volume of the Resonator Housing

First consider a housing made from copper for which  $R_s$  at 10GHz and 77K is assumed equal to 0.03Ω whereas  $\tan\delta$  for high quality single crystal sapphire at the same frequency and temperature is assumed to be  $10^{-7}$ . Then the values required for  $R$  and  $h$  to satisfy the conditions embodied in equations (6) and (11) above for the case of 'typical' low-order resonator mode TE011 and whispering gallery mode

WG911 are as shown in Table 1. (Note that for a fixed value of  $\omega$  and  $n$  the value of  $k_2$  is essentially independent of mode and thus the rate of decay of electromagnetic field in the evanescent field region is also. This perhaps surprising result suggests at first sight that the gap between inner radius of the housing and outer radius of the puck is approximately a fixed quantity once  $n$  and  $\omega$  have been chosen, and is independent of the mode order  $l$  &  $m$ .

Now consider the situation with a housing made entirely from a high temperature superconductor, such as thin film epitaxial YBCO for which the surface resistance at 10GHz and  $T=77K$  is of order  $150\mu\Omega$ . Using the same criteria as above the dimensions of the housing are now significantly altered for both of the modes selected and the recalculated values are summarised in Table 2.

### Surface Area of the Resonator Housing

Another important issue from the viewpoint of provision of a stable cryogenic environment for the puck resonator, with the requirement of minimal cooling power (such as would be required for a space environment) concerns the external surface area of the resonator housing. This would clearly be treated to ensure minimum emissivity to reduce as much as possible the absorption of room temperature black body radiation from the interior of the cryocooler vacuum enclosure (by gold plating, for example) but minimising the surface area is also a requirement. Tables 1 and 2 include figures for the two different modes using copper or HTS shielding respectively. Note again that there are only relatively small differences between the surface area values required for each of the two mode types.

Table 1

Mode	Freq	a	L	R	h	Sur.Area m <sup>2</sup>	Vol (l)
TE011	10GHz	6.5	10	0.031	0.022	0.016	0.16
WG911	10GHz	19	10	0.040	0.008	0.017	0.13

Table 2

Mode	Freq	a	L	R	h	Sur.Area m <sup>2</sup>	Vol (l)
TE011	10GHz	6.5	10	0.019	$7 \times 10^{-3}$	$5.3 \times 10^{-3}$	0.029
WG911	10GHz	19	10	0.028	$2.6 \times 10^{-3}$	$7.7 \times 10^{-3}$	0.038

The results summarised in Tables 1 and 2 are at best qualitative. To obtain better values for the parameters  $R$  &  $h$  it is necessary to solve the field distributions numerically [4] (using for example the MAFIA finite difference package). Nevertheless the naïve calculation performed above gives an indication of the way in which the housing design parameters are influenced by choice of resonant mode and of the conductivity and surface resistance of the radiation enclosure. For a fixed frequency (10GHz) the overall volume of the resonator housing to achieve a  $Q$  value approaching  $10^7$  is seen to be rather insensitive to the choice of mode though note that for the TE011 mode the housing is considerably longer but of smaller radius than for the WG911 mode. For either mode choice the use of a superconductor shield reduces the resonator housing volume by a factor of between 4 and 5.

### EXPERIMENTAL RESULTS

The above analysis indicates that the use of HTS superconducting shields can in principle reduce dramatically the overall size of a dielectric resonator whether using whispering gallery or low order TE01n resonant modes. We have already performed initial experiments on copper shielded sapphire puck whispering gallery modes and HTS shielded sapphire puck TE011 modes which we present below and compare qualitatively with the above preliminary calculations.

At present we have experimental results on one example of each resonator type. No attempt has yet been made to minimise the housing volume but the results we present here are examples which can be compared with the above calculations. In both cases the simple puck geometry has been slightly complicated by the inclusion of a subsidiary dielectric element made of single crystal rutile ( $TiO_2$ ) [5].

Such a compound puck is used to try to produce a compensation of the temperature coefficients of the resonant frequency at a particular temperature, usually in the range 40K to 70K, so that the centre frequency of the chosen mode is stable when operated at this compensation point [1],[2]. The configurations and dimensions of the two pucks are shown in Fig. 2.

Fig. 3 shows the temperature dependence of the  $Q$  of the TE011 mode for the resonator of Fig. 2a, at 7.88 GHz, showing that the peak loaded  $Q$  value of  $2 \times 10^6$  is attained at a temperature of 10 K. Note that there is no separation between the sapphire puck and the lower HTS thick film.

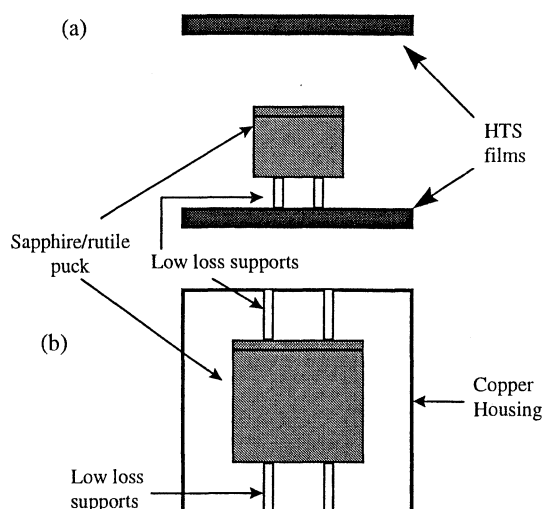


Fig. 2 Schematics of composite puck geometries reported in this paper. a) TE011 rutile/sapphire puck. b) whispering gallery mode composite rutile/sapphire puck.

We have attempted to model the lower superconductor film loss and subtract it from the loaded  $Q(T)$  curve to show the dashed line which represents the temperature dependence of the remaining  $Q$  contributions.

Fig. 4 shows the  $Q_i(T)$  variation for a whispering gallery mode (believed to be the WG711 mode) in the resonator outlined in fig. 2b. Here the simple model for a Cu housing with the dimensions shown predicts a loaded  $Q$  of  $5 \times 10^6$  at  $T=40K$ , in reasonable agreement with that observed. Further housing designs will be tested shortly to optimise the operating frequency, turning point and housing volume.

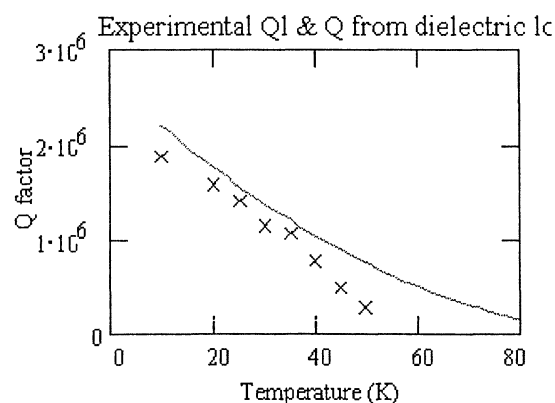


Fig. 3 Temperature dependent  $Q$  for the TE011 mode of the resonator shown in fig. 2a. Dashed line shows expected dielectric puck loss contribution.

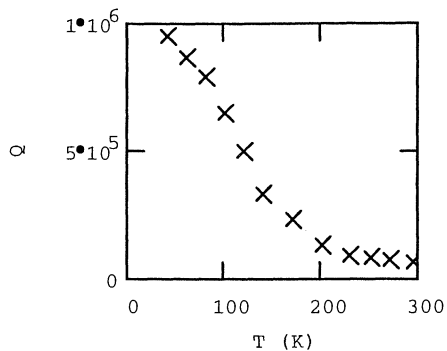


Fig.4 Temperature dependent Q for the WG711 mode of the resonator shown in fig. 2b.

## DISCUSSION

Use of a high temperature superconducting enclosure has some additional implications. The superconductor has a finite, temperature dependent penetration depth which contributes to the reactance of the resonator as a whole. The temperature dependence will give rise to a negative temperature coefficient of frequency which will be added to the sapphire temperature dependent permittivity. The size of the superconductor contribution only become significant above about 65K for typical designs. More importantly the superconductor response is to some extent non-linear in the microwave field strength and this may limit the stability of an oscillator based on such a resonator or may introduce unacceptable intermodulation distortion etc. for some applications of these devices. Normal conductors and single crystal dielectrics are in most cases far more linear in their electromagnetic response than are superconductors.

For the case of a housing with cylindrical geometry one requires a superconducting coating on the curved wall of the housing. This precludes the use of HTS thin films epitaxially grown on single crystal substrates. However this is not a serious problem since melt textured thick films on, for example, yttria stabilised zirconia show microwave losses which are only about a factor of 3-5 worse than the best epitaxial thin films.

## CONCLUSIONS

The calculations performed in this paper give a strong indication that, if small volume, surface area and mass are important requirements for a cryogenic high Q dielectric resonator then the use of a high temperature superconducting shield represents a significant advantage over the use of a high conductivity normal metal housing. A volume reduction by of order a factor of four and a surface area reduction factor between 2 and 3 can be expected.

Perhaps unexpectedly, the results indicate that there is no great advantage in size from using a whispering gallery resonance as opposed to a low order mode resonance, for a given operating frequency. This conclusion has been deduced from the assumption that the housing size for each mode type is chosen so as not to compromise the loaded Q value attainable with a single crystal sapphire puck ( $\sim 10^7$  at 10 GHz and for  $T < 70$  K). For widely different temperature ranges, dielectric materials or frequencies the conclusions may not hold.

Low noise, ultra-stable oscillators based on cryogenic dielectric resonators have many potential uses outside of the laboratory. The actual future demand for such systems will demand to a large extent on ease of use, reliability and compactness of the oscillators. The latter issue has been addressed in this paper and we have proposed that the use of high temperature superconducting shielded resonator housing is an important consideration in many situations.

## REFERENCES

- [1] J C Gallop, C D Langham & F Abbas, Proc. 10<sup>th</sup> European Frequency & Time Forum, IEE Conference Publication 418, pp270-3, (1996)
- [2] J C Gallop, C D Langham, L Hao & F Abbas, IEEE Trans. Instrum. Meas. 46 pp122-5 (1997)
- [3] Waldron, 'Theory of Guided Electromagnetic Waves' van Nostrand Reinhold (London) (1969)
- [4] Ghosh I S, Tellmann N, Schemion D, Scholen A & Klein N, IEEE Trans. Appl. Supercond. 7 pp 3071-4 (1997)
- [5] Klein N, Zuccaro C, Daehne U, Schulz H, Tellmann N, Kutzner R, Zaitsev A G & Woerdenweber R, J. Appl. Phys. 78 pp 6683-7 (1995)

## QUARTZ-CRYSTAL TUNING-FORK TACTILE SENSOR

Hideaki Itoh, Masataka Nomura and Mitsuo Nakazawa

Shinshu University, 500 Wakasato, Nagano-shi 380, Japan

**Abstract** - Sensing behaviour of a quartz-crystal tuning-fork tactile sensor was tested using the several sorts of materials (metals and slide glass) and the several sheets of sandpaper of different roughnesses fixed on copper or aluminum plates with acrylic resin paste. Sensing mechanisms on the longitudinal plane wave transmission model are discussed. For materials with roughnesses in the range of sandpaper roughnesses, this sensor functions as a simple roughness sensor in a stationary state.

### 1. Introduction

Usually, tactile senses include pressure sense, hardness sense, slipping sense, etc. as well as touch sense[1]. Up to date, several tactile sensors for detecting the hardness of materials have been proposed which make use of piezoelectric ceramics[2][3] or quartz resonator[4]. These sensors utilize longitudinal[2][4] or flexural mode vibration[3] in respect of vibration mode, making use of their change in frequency induced when their vibrating sections are brought into contact with an object. For example, Kosawada[3] reported that a tactile sensor, with a piezoelectric ceramics attached to a stainless steel bar, was capable of sensing the softness of an object, brought into contact with the tip of the bar in flexural mode vibration, on the basis of the induced shift in frequency. This method is applicable only to such soft materials as not to stop the sensor's vibration. On the other hand, Omata[2] pointed out a possible sensor, capable of sensing hardness and softness, based on the principle that, when the tip of a piezoelectric ceramics in longitudinal mode vibration is brought into contact with an object, the resonant frequency of the tactile sensor is caused to decrease by a soft object, whereas it is caused to increase by a hard object. Tactile sensors based on this principle have been effectively applied to on a range of materials from human skin to iron, but they are inapplicable for sensing roughness, smoothness, or texture of an object.

When a common tuning fork for tuning musical instruments is made to vibrate and then has its base brought into contact with various sorts of materials, the time required for the vibration to cease depends on the sort of materials; in other words, the degree of the leakage of vibration from the base depends on the sort of objects. It is empirically known that the magnitude of the leakage of vibrational energy depends on the rigidity of materials. Upon observing the vibration phenomena of a tuning fork

as mentioned above, the authors hit upon an idea of the quartz-crystal tuning-fork tactile sensor.

In this research, the authors developed a tactile sensor capable of sensing an object, which makes use of the increase in quartz-crystal tuning-fork impedance at resonant vibration due to the leakage of longitudinal vibrational energy from the sensor's base to an object in contact when the base gets brought into contact with the object. The advantage of this sensor lies in that the vibrational part in a flexural mode vibration is separated spacially from the base in contact with the object. The flexural vibrational energy of the quartz-crystal tuning fork is preserved in the arm part, and a leakage of the longitudinal vibrational energy occurs at the base in contact with the object. The flexural and the longitudinal vibration are combined with each other in energy and cause the energy leakage to increase the quartz-crystal tuning-fork impedance. It follows that this sensor may continue to operate without its flexural vibration stopped even when any materials ranging from soft silicone rubber to hard metal are brought into contact with the base. The following section describes the structure of the tactile sensor, the fixing stand for the sensor, the measurement system, and contacting measurements on metals and sandpapers, with emphasis upon the sensor's applicability as a simple roughness sensor.

### 2. Experiment and Discussion

The quartz-crystal tuning fork used was the same as that for wrist watch application, which operated at 32.768 kHz and had the dimensions of 5.9 mm in length, 1.35 mm in width, and 0.75 mm in thickness. Since it was too small for our hand to hold it to bring it into contact with an object, the quartz crystal blank was held in an acrylic resin case. The reason for the use of the acrylic resin case for holding, is that, since acrylic resin is a good insulator and can be easily processed, the use of the acrylic resin case is convenient to carry out preliminary experiments to grasp sensor characteristics. Figure 1 shows the structure of the tactile sensor fabricated. The section, in the base of the quartz-crystal tuning fork, corresponding to the nodal point of the flexural vibration, was clamped by an acrylic resin case 30.0 cm in length, 15.2 mm in width, and 1.0 mm in thickness, in such a way that the base was projected a few hundreds  $\mu$ m out of the case. The lead wires were soldered on both the Au electrodes of the quartz crystal; the soldered sections were so weak in

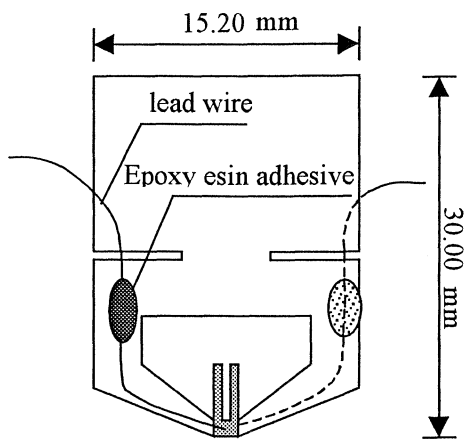


Fig. 1 Structure of the tactile sensor

mechanical strength as to be easy to separate, so that the lead wires were bonded halfway on the acrylic resin case with epoxy resin adhesive to protect the soldered sections.

The quartz-crystal tuning fork clamped by the acrylic resin case was further held on a fixing stand as shown in Fig. 2. The quartz-crystal tuning-fork tactile sensor, fastened with a clip, is vertically brought into contact with an object according as a bar connected to the clip is made to move up and down along the guide hole. This arrangement is effective for keeping the condition of contact unchanged with repetition of contact examinations. The set of the sensor, clip, and bar shown in Fig. 2 weighs 50 g, and thus a weight of 50 g is applied on an object under contact examination.

Figure 3 shows the measurement system used in this experiment. The impedance of the sensor was obtained with an impedance analyzer (HP-4194A), to which the lead wires of the quartz-crystal tuning-fork tactile sensor was connected, and which used a built-in program to calculate equivalent circuit constants from measured impedance characteristics for executed frequency variations. The impedance difference ( $\Delta R$ ) was calculated between the sensor in contact with an object ( $R_c$ ) and the free sensor ( $R_0$ ) at room temperature. A Drift of  $R_0$  as much as about 200 k $\Omega$  to about 900 k $\Omega$  results from the vibration of the quartz-crystal tuning fork in air and from the changeable condition for clamping the quartz crystal by the acrylic resin case. The frequency of the sensor, as measured with the impedance analyzer, is caused to increase several tens mHz for the 32.768 kHz quartz resonator by a contact operation. The smaller  $R_0$  is, the stabler the tactile sensor is. In contrast to the frequency change, the impedance increases from about several tens k $\Omega$  for silicone rubber to about 100 k $\Omega$  for metals. This large change in impedance was utilized for the present tactile sensor. In contact experiments using the tactile sensor, three  $R_0$  measurements were made for

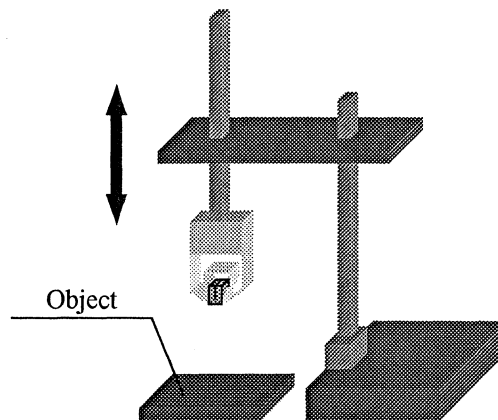


Fig. 2 Fixing stand

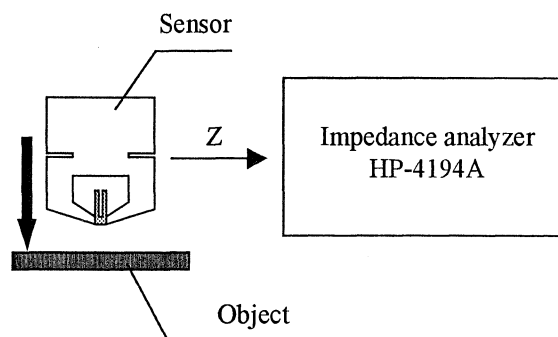


Fig. 3 Measurement system

each object, and the average of the three  $R_0$  values is indicated in both Figs. 4 and 5.

For  $R_0$  measurements, the quartz-crystal tuning-fork tactile sensor was applied on the following samples: slide glass (76.0  $\times$  26.0  $\times$  1.2 mm), aluminum (30.0  $\times$  20.0  $\times$  12.0 mm), lead (33.0  $\times$  30.0  $\times$  1.0 mm), brass (41.0  $\times$  39.0  $\times$  5.3 mm), stainless steel (58.0  $\times$  58.0  $\times$  5.0 mm), and copper (16.0  $\phi$   $\times$  14.0 mm). The measured values are shown in Fig. 4, where the acoustic impedance of the longitudinal plane wave for the object is plotted on the X-axis and  $\Delta R$  on the Y-axis. As seen from Fig. 4,  $\Delta R$  changes with the acoustic impedance of the longitudinal plane wave. At the interface between the quartz resonator and the object under measurement, the difference in acoustic impedance of materials causes the energy of the longitudinal plane wave to be transmitted and reflected. Let the acoustic impedance of the longitudinal plane wave for a quartz crystal be  $Z_1$  and that for an object be  $Z_2$ , and the energy transmittance  $T$  is given, as well known, by

$$T = \frac{4Z_1Z_2}{(Z_1+Z_2)^2} \quad (1)$$

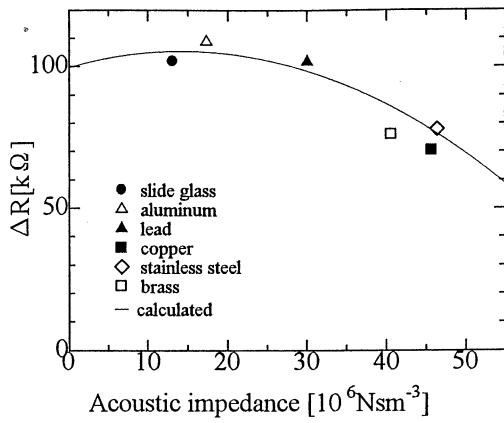


Fig. 4 Crystal impedance change  $\Delta R$  vs. acoustic impedance

The energy transmittance given by eq. (1) is 1 when quartz is subject to the measurement. The acoustic impedance of the longitudinal plane wave in the direction of the length of the quartz-crystal tuning fork is  $14.65 \times 10^6 \text{ Nsm}^{-3}$ . Since this value is intermediate between the acoustic impedances for slide glass and aluminum, the proportional coefficient of eq. (1) was derived on the basis of an approximation that the crystal impedance change  $\Delta R$  is equal to the average value of  $\Delta R$ 's for slide glass and aluminum. The solid line in Fig. 4 indicates the other values calculated. Figure 4 shows that the experimental results are in good agreement with the calculated. Therefore, the crystal impedance change  $\Delta R$  for quartz is proportional to the transmitting energy of the longitudinal plane wave from the base to an object. As far as hard materials such as metals are concerned, these facts may be taken as evidence that this sensor has identified the quality of material. The cause for the drift in the experimental results may be that even the guide hole provided on the fixing stand, shown in Fig. 2, cannot completely prevent the vertical bar from shaking, resulting in the failure to put the sensor in the identical contact state for every operation.

Another series of  $\Delta R$  measurements was made on five sheets of sandpaper of different roughnesses (#1000, #500, #240, #120, and #40) fixed on copper plates ( $20.0 \times 30.0 \times 5.0$  mm) and aluminum plates ( $20.0 \times 30.0 \times 12.0$  mm) with acrylic resin paste. The measured values are shown in Fig. 5, with the roughness of sandpaper on the X-axis and  $\Delta R$  on the Y-axis. As seen from Fig. 5, the crystal impedance change  $\Delta R$  decreases as the surface roughness of sandpaper increases. This would be because the increase in roughness of sandpaper causes the contact area between the base of the quartz resonator and the sandpaper to decrease, which in turn leads to decrease in the transmitting energy. It is seen that the plot for copper may be made to coincide with the plot for aluminum when transferred

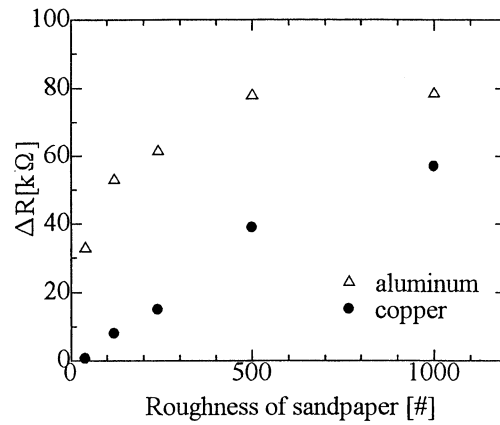


Fig. 5 Crystal impedance change  $\Delta R$  vs. roughness of sandpaper

in parallel. From this coincidence it follows that the observed difference between the plots for copper and aluminum has resulted from the difference between the acoustic impedances of the longitudinal plane waves for copper and aluminum, in accord with the result of Fig. 4. This system may be dealt with in terms of the longitudinal plane wave propagation through the set of the three media, quartz, sandpaper, and metal (copper or aluminum), and the roughness of sandpaper is considered to control the contact area between the quartz and the sandpaper. From the results of Figs. 4 and 5, it may be concluded that this tactile sensor uses, for its sensing operation, the combination of the difference in acoustic impedance of objects brought into contact and the difference in contact area due to the roughness of sandpaper. This conclusion leads to a possibility that a positive utilization of the properties with respect to the difference in contact area, will allow this sensor to serve as a simple roughness sensor applicable to the range of sandpaper roughnesses. We, human beings, sense the roughness of materials from the vibrational sense obtained in an active touch with a finger tip tracing a rough surface. In contrast to our dynamic sensing, this sensor is a novel one which, in a stationary state, is capable of sensing the roughness of materials.

### 3. Conclusion

The authors have developed a tactile sensor capable of sensing an object, which makes use of the increase in quartz-crystal tuning fork impedance at resonant vibration while the base of its quartz-crystal tuning-fork for wrist watch application is in contact with an object. Experimental findings are as follows: (1) the contact experiment with slide glass, aluminum, lead, brass, stainless steel, and copper, has revealed that the impedance change is proportional to the transmitting energy resulting from the difference in acoustic impedance of the longitudinal plane wave of the object brought into contact with the quartz-

crystal tuning fork; (2) the contact experiment with sheets of sandpaper fixed on copper or aluminum plates with acrylic resin paste, has revealed that the impedance change decreases with increasing roughness of sandpaper brought into contact with the base of the quartz-crystal tuning fork.

It follows from the above findings that this sensor may be used as a simple roughness sensor capable of sensing such degrees of roughness as sandpaper roughnesses, which have been beyond the power of the conventional sensors.

#### **4. Acknowledgements**

The authors wish to thank Professor Emeritus Isao Matsuzaki of Shinshu University for reading and criticizing the manuscript. This work was partly supported by a Grant-in-Aid for Scientific Research (C) from the Ministry of Education, Science, Sports and Culture of Japan.

#### **References**

- [1] K. Tanie, "Tactile Image Sensor," OYO BUTURI, vol. 54, pp. 373-379, 1985.
- [2] S. Omata, "Development of Tactile Sensor for Sensing Hardness," SENSOR TECHNOLOGY, vol. 10, pp.27-31, 1990.
- [3] T. Kosawada, "Softness Sensor for Soft Material Using Piezoelectric Resonator," ULTRASONIC TECHNOLOGY, vol. 9, pp. 25-30, 1997.
- [4] H. Itoh, N. Horiuchi, and M. Nakazawa, "An Analysis of the Longitudinal Mode Quartz Tactile Sensor Based on the Mason Equivalent Circuit," Proc. 1996 Frequency Control Symposium, pp. 572-576. 1996.

THE SAW ACCELERATION SENSOR

Jerzy Filipiak, Cezary Kopycki, Jerzy Ostrowski, Lech Solarz

Military University of Technology, Institute of Applied Physics, 2 Kaliskiego St., 01-489 Warsaw, Poland

INTRODUCTION

Measuring acceleration variable in time is difficult because:

- a) acceleration is not an electrical quantity,
- b) acceleration is a vector quantity.

The accelerometer must allow to measure all perpendicular components of the acceleration vector. The main structural components of the three-axes-accelerometer are three perpendicular

sensors. Each of them measures a selected component of the acceleration vector. The design condition of the accelerometer is a possibility of constructing a sensor allowing to measure one component of the acceleration vector. It can be done by using sensors based on surface acoustic waves [1]-[3].

THE PRINCIPLE OF OPERATION OF THE SAW ACCELERATION SENSOR

The main structural component of the acceleration sensor based on surface acoustic waves (SAW) is piezoelectric delay line (Fig. 1). The interdigital transducer generates a surface wave which

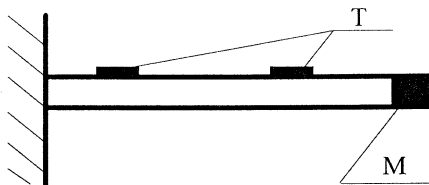


Fig. 1. Mechanical model of the accelerometer based on SAW  
 T - interdigital transducers,  
 M - aggregated mass

propagates in the surface region of the piezoelectric substratum [4, 5]. The dimensions of the transducer are properly chosen to the frequency of the electric signal which is transmitted by the wave. The wave reaches the receiving transducer after the delay time which is proportional to the distance between the transducers and inversely proportional to the velocity of the wave. The inertial force of the accelerated motion changes both the distance between the transducers and the stresses in the region where the surface wave propagates. Both, the changing distance and the changing state of stress influence the delay time of the wave. The device works properly in a frequency range for which the change of the delay-time is proportional to the measured acceleration. The principle of operation of the sensor is based on measurements of changes of the delay time of SAW of the line

mentioned. These measurements are taken by measuring the frequency of the generator with delay line in its phase-locked feedback loop, because precise measurement of the delay time is rather difficult. The change of the delay-time leads to changing the generator frequency [6]-[8]. The idea is schematically shown in Fig. 2.

The frequency of the SAW generator may be between a few tenth up and several hundreds MHz. The range depends on required parameters and the construction of the device. The changes of frequency caused by the measured acceleration are about 2 Hz to 90 kHz, so they are small in comparison to the frequency of the generator. The second generator with the constant frequency nearly the same as the frequency of the main one must be used, and only measuring of the beat frequency allows us precise measurement of the acceleration.

Each of the generators must hold high stability and cleanliness of its spectrum. These parameters allow to obtain measurements of high accuracy. In the sensor's design a system separating the work of both generators (their frequency is nearly equal) from accompanying systems is required. This allows to connect the sensor or the second generator with constant frequency to the measuring system by one concentric cable of freely chosen length and it will not be a reason of generators' retuning. Special system can change the beat frequency as an output signal to square-wave. This waveform make easy measurements of a beat frequency or its period.

High stability of both SAW generators allows to use signal of the generator constant frequency to

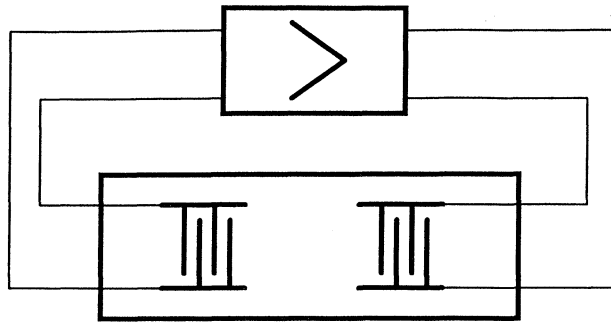


Fig. 2. Parts of the generator based on SAW

measure frequency or period of the output signal. Then change of sinusoidal signal to square-wave is required. Obtaining both signals like this makes easy the measurement of beat frequency or duration, using easy counting system. The signals in this form may be easily processed or sent.

The accuracy of frequency measurement depends on the environment temperature. This influence depends on the way of measurement. If the sensor and the generator of constant frequency work at the same temperature, beat frequency quantity will not be dependant on the temperature. The change of frequency of both generators as a function of

temperature should be identical. In other cases the accuracy of measurement will depend on temperature sensitivity of SAW generators. The temperature sensitivity of quartz YX used in the model of presented acceleration sensor is 20 ppm. Temperature stability of the sensor may be corrected using quartz ST. Its temperature sensitivity is equal zero [9].

The considerations presented above concern only the problems of beat frequency measurements of generator-sensor and generator's constant frequency.

#### DESCRIPTION OF DEVICE AND ACOMPANYING ELEMENTS

The device is made for measurement of acceleration, constant or variable, as a function of time during objects' motion (traffic, space navigation, navigation situated on the ground, geodesy and geology). The sensor mentioned above may be used for determining an object's position by acceleration measurement and its double integral. This method can be a supplement for using GPS (the position of tanks, cars, underwater divers). The

SAW acceleration sensor consists of two SAW generators, measurement and recording system. The output signal may be either analog or numerical. The working frequencies of the generators are nearly equal 75 MHz. The beat frequency of the generators is 200 kHz. In the presented sensor beat frequency is equal 2 kHz for change of acceleration equal 2g.

TABLE 1 - Selected technical data of SAW acceleration sensor

Measurement range	$\pm 10$ g
Sensitivity	$>10^{-3}$ g
Accuracy of measurement	2%
Structural resonance	100 Hz
Power supply	$\pm 12$ V
Current consumption	300 mA
Cleannes of the spectrum	-55 dB
Output signal	the change of frequency as a function of acceleration may be either analog (in the presented model) or numerical signal
Measurement duration	measurement in the real time, limited duration of numerical processing

The presented way of measurement using the SAW acceleration sensor allows to automatise it, measure in the short time. The processing and sending information is easy. By selecting dimensions of

piezoelectric beam and frequency of the generator, we may obtain different measurements ranges of device in the varying resolution range.

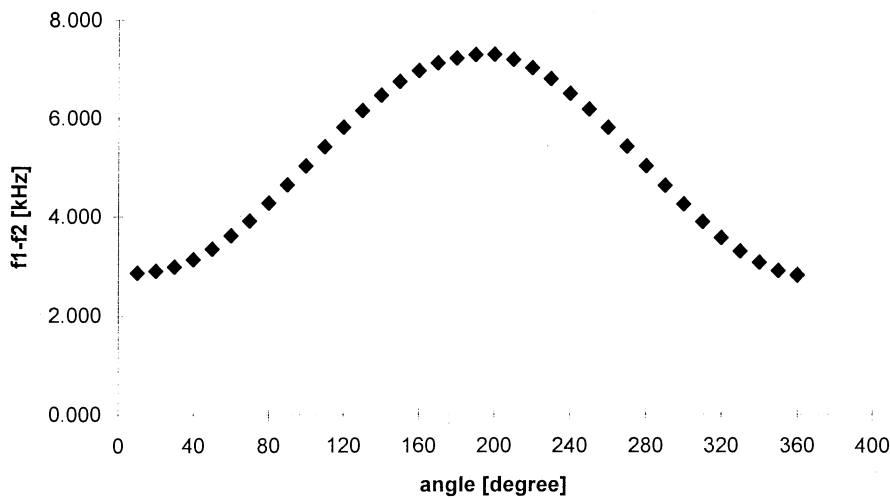


Fig. 3. The generators beat frequency as a function of an angle of rotation in the gravitational field

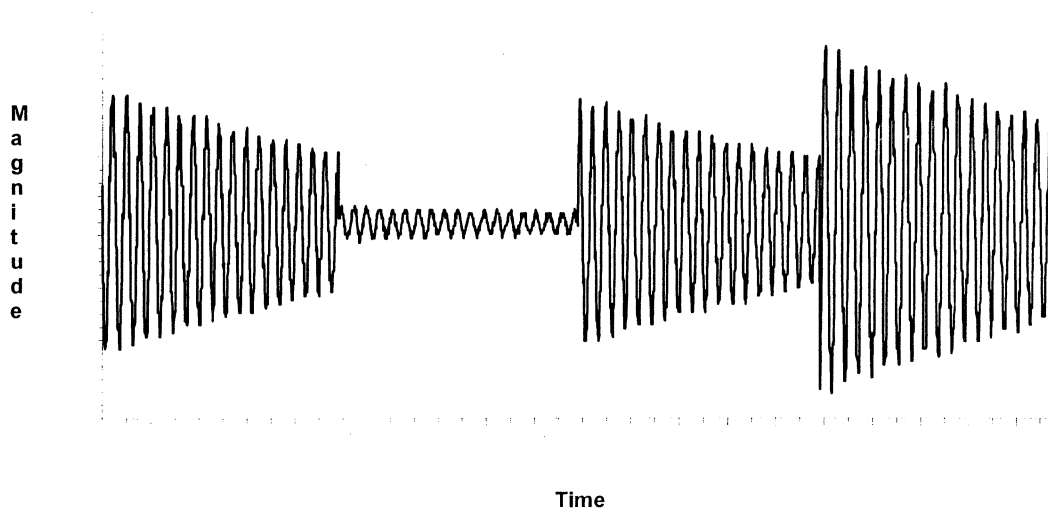


Fig. 4. The response of the measuring system working as a seismic sensor based on SAW

The possibility of constructing the acceleration sensor other wanted parameters are known. The presented device may be designed as a remote or reactive sensor of acceleration [10]-[12]. The possibility of constructing a high sensitivity

acceleration sensor allows to use it as a seismic sensor (recording small vibrations) of continuous monitoring. Using free vibration of a piezoelectric beam [13] during recording vibrations' allows to identify a working sensor.

#### REFERENCES

1. D.HAUDEN, *Elastic waves for miniaturized piezoelectric sensors: applications to physical quantity measurements and chemical detection*, Archives of acoustics, vol. 16, nr 1, Warszawa 1991.
2. J.FILIPIAK, L. SOLARZ, J. OSTROWSKI, C. KOPYCKI, *Lithium niobate as the substratum for the SAW acceleration sensor*, Solid State Crystals in Optoelectronics and Semiconductors Technology, Proc. SPIE 1997

- The International Society for Optical Engineering, **3179**, p. 156.
3. D.HAUDEN, S. ROUSSEAU, J.J. GAGNEPAIN, *Sensitivities of SAW oscillators to temperature, forces and pressure: application to sensors*, 34th Ann. Freq. Cont. Symp. (Electronic Industries Association), Washington D.C., 1980.
  4. K. A. INGEBRITSEN, *Surface waves in piezoelectrics*, J. Appl. 40, (1969), 2681-2686.
  5. J.FILIPIAK, *Zagadnienia syntezy podzespołów z akustyczną falą powierzchniową do obróbki sygnałów złożonych typu „chirp”*, WAT, Warszawa 1993.
  6. J.FILIPIAK, A. KAWALEC, M. RYGLEWICZ, *Czujnik siły i przemieszczenia wykorzystujący akustyczne fale powierzchniowe*, Elektronika, **10**, (1993), 17-21.
  7. A.BRYANT, D.L. LEE AND J.F. VETELINO, *A surface acoustic wave gas detector*, Proc. 1981 Ultrason. Symp, 171-174.
  8. A.W.BARANDSZ, J.C. VIS, M.S. NIEUWENHUIZEN AND E. NIEWKOOP, *A SAW-chemosensor for NO<sub>2</sub> gas concentration measurement*, Proc. 1985 Ultrason. Symp, cat. nr 5 CH2209-5, (1985), 589-590.
  9. W. SOLUCH, *Wstęp do piezoelektroniki*, WKŁ, Warszawa 1980.
  10. W.BUFF, F. PLATH, O. SCHMECKEBIER, M. RUSKO, T. VANDAHL, *Remote sensor system using passive SAW sensors*, 1994 Ultrasonics Symposium, Proc. IEEE, p. 585.
  11. G.C.FRYE, S.J. MARTIN, R.W. CERNOSEK, K.B. PFEIFER AND J.S. ANDERSON, *Portable acoustic wave sensor system*, 1991 Ultrasonics Symposium, Proc. IEEE, p. 311.
  12. F.SCHMIDT, O. SZCESNY, L. REINDL, V. MAGORI, *Remote sensing of physical parameters by means of passive surface acoustic wave devices*, 1994 Ultrasonics Symposium, Proc. IEEE, p. 589.
  13. C.KOPYCKI, *Zastosowanie akustycznych fal powierzchniowych do analizy drgań belki*. Praca magisterska, WAT, Warszawa 1995.

#### ACKNOWLEDGEMENTS

Research was supported by Polish State Committee for Scientific Research (contract nr 8T10C03708)

**INVESTIGATIONS ON BEHAVIOUR OF COUPLING COEFFICIENT OF MONOLITHIC STRUCTURE**

Irina Mateescu, Gabriela Pop, Adrian Manea, Mihai Lazarescu, Christina Ghita

National Institute of Materials Physics, PO Box MG 7, 76900 Bucharest - Magurele, Romania

1. INTRODUCTION

New piezoelectric crystals are produced now with the aim to improve the quality of electronic devices. So that for the obtaining of monolithic filters with average values of the bandwidth is necessary to use such new materials other than quartz and lithium tantalate (1). Also these crystals must present a high stability and small insertion attenuation. The langasite (LGS) is a leading candidate able to satisfy these requirements .

The langasite crystal ( $La_3Ga_5SiO_{14}$ ) belongs to the trigonal system, class 32 and, due to its acoustic characteristics, is a promising material for bulk and surface acoustic wave devices. Some important properties of the langasite which make it better than quartz are: (i) electromechanical coupling factor (three or four times higher), (ii) thermal stability, (iii) equivalent inductance and series resistance (smaller values) (2).

The monolithic filters on Y - cut langasite crystal are able to operate in fundamental shear mode over the frequency range from 5 MHz to 18.5 MHz with relative pass bandwidth of 0.3 % to 0.8 % of the central frequency of the filter (3), while the monolithic band-pass filters using quartz crystal are realised in the frequency range of 4-20 MHz for the fundamental mode with the bandwidth between 0.01 % and 0.35 % of the central frequency.

In some of our previous contributions (4), (5), (6) we have elaborated an accurate method to design narrow-band quartz monolithic filters and wide-band langasite monolithic filters. We have shown that in order to get a much better agreement between input data and experimental results than that obtained with the relation currently used (3) it is necessary to calculate rigorously the dependence of coupling coefficient on geometrical dimensions and mass-loading. Also, we have described some experimental details as concern the LGS synthesis. Afterwards we have developed a suitable chemical technique for the better purification of the raw oxides ( $La_2O_3$ ).

This paper presents a theoretical approach based on Tiersten's analysis (7). The influence of various material parameters and of mass-loading on coupling coefficient behaviour have been evaluated. The investigations have revealed that the mass-loading effect on coupling coefficient of langasite structure is lower than in the case of quartz structure, which could be a new advantage of langasite over quartz crystal.

2. THEORETICAL MODEL

The calculation of geometry of the two - pole structure using the relations between parameters of electric equivalent circuit (deduced from synthesis) and geometrical dimensions represents an important step of monolithic filters design. A relation (I) between coupling coefficient and dimensions ( plate thickness, electrode lengths, electrode spacing) is proposed in (3) and another one (II) is deduced by us using an original program based on Tiersten's analysis. This one allows a better correlation of the input data of filters with experimental results.

In the method described by Tiersten the three-dimensional equations of elasticity are converted into a series of two-dimensional equations by expanding the mechanical displacement and electrical displacement in a series of powers of the thickness coordinate of the plate. It was considered an infinite Y-cut rotated plate of thickness  $t$  with two pairs of strip electrodes deposited on it. The width of each electrodes is  $lx$  and the space between electrodes is  $d$ . For a narrow frequency range near the cut-off fundamental thickness-shear frequency only the contributions of the fundamental thickness-shear and fundamental flexure mode are retained. The method was applied on electroded and unelectroded regions of the plate and at the boundaries between them was imposed that the displacements  $u_1, u_1^{(e)}$  and also the derivation of the displacements  $u_{1,1}, u_{1,1}^{(e)}$  to be continuous. These conditions yield the following relation:

$$\begin{vmatrix} H_{11} & H_{12} & 0 & 0 & 0 & H_{16} & 0 & 0 \\ 0 & H_{22} & H_{23} & 0 & 0 & H_{26} & H_{27} & 0 \\ 0 & 0 & H_{33} & H_{34} & 0 & 0 & H_{37} & H_{38} \\ 0 & 0 & 0 & H_{44} & H_{45} & 0 & 0 & H_{48} \\ H_{51} & H_{52} & 0 & 0 & 0 & H_{56} & 0 & 0 \\ 0 & H_{62} & H_{63} & 0 & 0 & H_{66} & H_{67} & 0 \\ 0 & 0 & H_{73} & H_{74} & 0 & 0 & H_{77} & H_{78} \\ 0 & 0 & 0 & H_{84} & H_{85} & 0 & 0 & H_{88} \end{vmatrix} = 0 \quad (1)$$

in frequency range:

$$1 - R - 4 \frac{k_{26}^2}{\pi^2} < \Omega < 1$$

where

$$H_{11} = 1 \qquad H_{12} = -\cos\left(\xi \frac{l_x}{t}\right)$$

$$\begin{aligned}
H_{16} &= \sin\left(\frac{\bar{\xi} l_x}{t}\right) & H_{22} &= \cos\left(\frac{\bar{\xi} l_x}{t}\right) \\
H_{23} &= -\cosh\left(\xi \frac{d}{t}\right) & H_{26} &= \sin\left(\frac{\bar{\xi} l_x}{t}\right) \\
H_{27} &= \sinh\left(\xi \frac{d}{t}\right) & H_{33} &= \cosh\left(\xi \frac{d}{t}\right) \\
H_{34} &= -\cos\left(\frac{\bar{\xi} l_x}{t}\right) & H_{37} &= -\sinh\left(\xi \frac{d}{t}\right) \\
H_{38} &= \sin\left(\frac{\bar{\xi} l_x}{t}\right) & H_{44} &= \cos\left(\frac{\bar{\xi} l_x}{t}\right) \\
H_{45} &= -1 & H_{48} &= \sin\left(\frac{\bar{\xi} l_x}{t}\right) \\
H_{51} &= -\xi & H_{52} &= -\bar{\xi} \sin\left(\frac{\bar{\xi} l_x}{t}\right) \\
H_{56} &= -\bar{\xi} \cos\left(\frac{\bar{\xi} l_x}{t}\right) & H_{62} &= -\bar{\xi} \sin\left(\frac{\bar{\xi} l_x}{t}\right) \\
H_{63} &= \xi \sinh\left(\xi \frac{d}{t}\right) & H_{66} &= \bar{\xi} \cos\left(\frac{\bar{\xi} l_x}{t}\right) \\
H_{67} &= \xi \cosh\left(\xi \frac{d}{t}\right) & H_{73} &= \xi \sinh\left(\xi \frac{d}{t}\right) \\
H_{74} &= -\bar{\xi} \sin\left(\frac{\bar{\xi} l_x}{t}\right) & H_{77} &= -\xi \cosh\left(\xi \frac{d}{t}\right) \\
H_{78} &= -\bar{\xi} \cos\left(\frac{\bar{\xi} l_x}{t}\right) & H_{84} &= -\bar{\xi} \sin\left(\frac{\bar{\xi} l_x}{t}\right) \\
H_{85} &= -\xi & H_{88} &= \bar{\xi} \cos\left(\frac{\bar{\xi} l_x}{t}\right)
\end{aligned}$$

$\bar{\xi}$  is the wave number in electroded part of the plate

$$\bar{\xi}^2 = \frac{\pi^2 c_{66}}{2(\bar{\gamma}_{11} + \bar{\kappa}_6^2(1 + 2R)c_{66})} \cdot \left(1 + 2R - \frac{4\bar{k}_{26}^2}{\pi^2}\right) \cdot \left(\Omega - 1 + R + \frac{4\bar{k}_{26}^2}{\pi^2}\right)$$

$\xi$  is the wave number in unelectroded part of the plate

$$\xi^2 = \frac{\pi^2 c_{66}}{2(\gamma_{11} + \kappa_6^2 c_{66})} (1 - \Omega) \quad \text{and}$$

$$\kappa_6^2 = \frac{\pi^2}{12}; \quad \bar{\kappa}_6^2 = \frac{\pi^2}{12} \left(1 + R - \frac{8\bar{k}_{26}^2}{\pi^2}\right); \quad \bar{k}_{26}^2 = \frac{e_{26}^2}{c_{66}\epsilon_{22} + e_{26}^2}$$

$$\bar{\gamma}_{11} \approx \gamma_{11}; \quad \Omega = \frac{\omega}{\omega_0}; \quad \omega_0 = \frac{\pi}{t} \sqrt{\frac{c_{66}}{\rho}}$$

$$\gamma_{rs} = c_{rs} - c_{rv} c_{vw} (c_{vw})^{-1}; \quad r, s = 1, 3, 5; v, w = 2, 4, 6$$

The inter-resonator coupling coefficient was computed from the relation:

$$k_i = 2 \cdot \frac{\Omega_2 - \Omega_1}{\Omega_1 + \Omega_2}, \quad \text{where } \Omega_1 \text{ and } \Omega_2 \text{ are the first two roots of the equation (1).}$$

### 3. RESULTS AND DISCUSSION

#### *The Effects of the Mass-Loading and the Electrode Spacing on the Coupling Coefficient Behaviour*

The dependence of coupling coefficient on ratio between electrode spacing and plate thickness for three values of mass-loading has been calculated by the two methods previously mentioned.

The results for two-pole quartz and langasite filters are presented in figure 1, respectively figure 2.

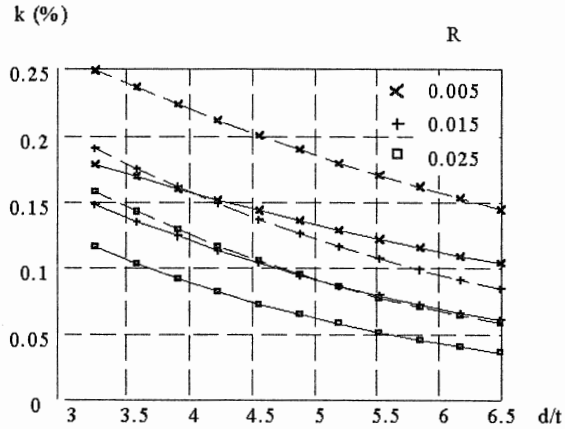


Figure 1: The dependence of  $k=f(d/t)$  for various mass-loading  $R$  of quartz filter; method I -dashed line; method II -solid line

Figure 1 shows that for small mass-loading (0.005), the difference between  $k$  values obtained by methods I and II is higher than those obtained for larger mass-loading.

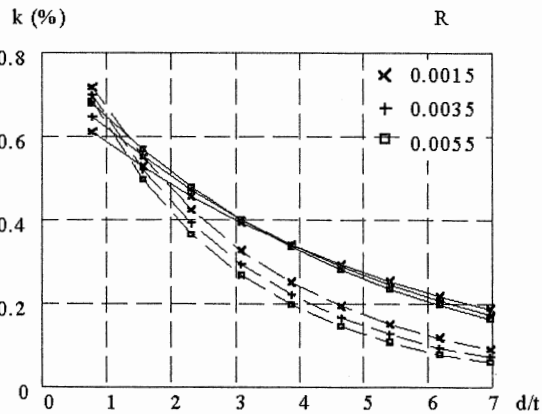


Figure 2: The dependence of  $k=f(d/t)$  for various mass-loading  $R$  of langasite filter; method I- dashed line; method II-solid line

Figure 2 reveals that the  $k$  values obtained with these two relations are more closed than in the case of quartz, especially in the  $d/t=0.5\pm 2.5$  range. The variation of coupling coefficient with mass-loading is greater for quartz than for langasite filters (figure 3, 4).

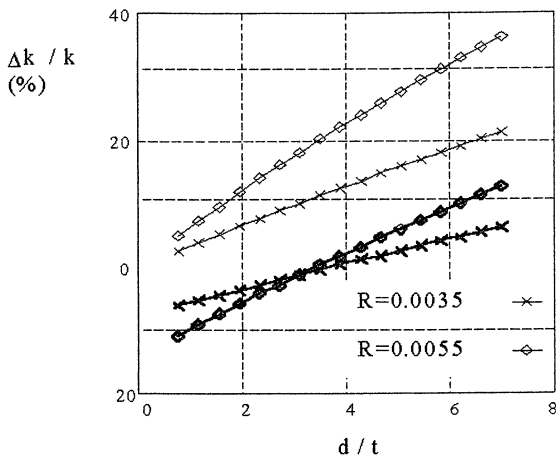


Figure 3: The relative variation of  $k$  for langasite;  $\Delta k/k=(k(R=0.0015)-k(R))/k(R=0.0015)$ ; method I -solid line; method II – bold solid line.

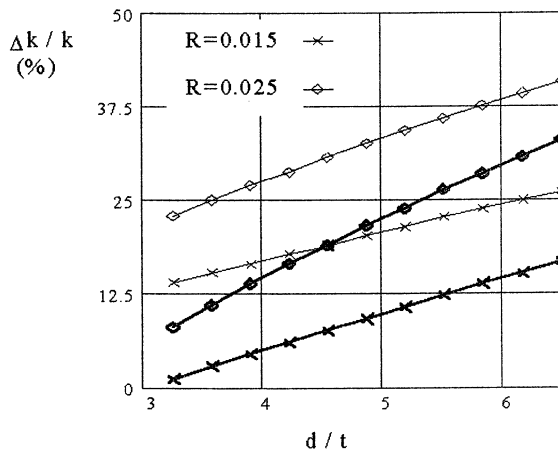


Figure 4: The relative variation of  $k$  for quartz;  $\Delta k/k=(k(R=0.005)-k(R))/k(R=0.005)$ ; method I -solid line; method II – bold solid line.

The method II gives smaller relative variation of  $k$  with  $R$  than method I for both piezoelectric crystals used.

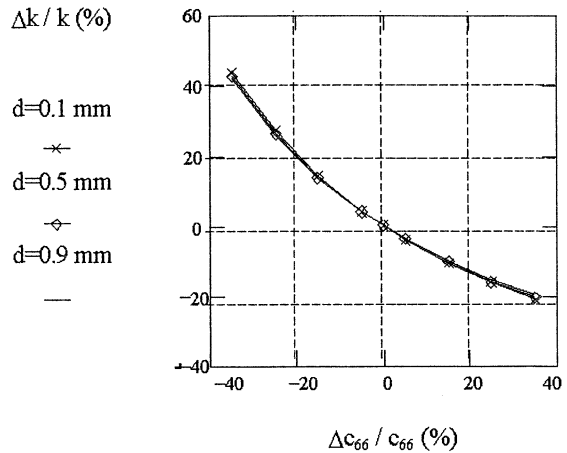
### The Influence of Materials Constants on the Coupling Coefficient

The physical properties of the crystal strongly influence the relation between the coupling coefficient and the geometrical dimensions of the bipolar structure. So, the behaviour of coupling coefficient are influenced by the material constants, but the effects of these constants are very different. For applications is interesting to know

which is weight of each constant on the control of the coupling coefficient value. That is why we tried to make a systematic study of the influence of material constants on the piezoelectric coupling coefficient behaviour.

The calculations were performed using the relation deduced from Tiersten's analysis in which was retained only thickness shear and flexure modes of vibration. As a consequence only the influence of elastic constant  $c_{66}$ , piezoelectric constant  $e_{26}$  and Voight's elastic constant  $\gamma_{11}$  was studied.

Figure 5: The relative variation of  $k$  versus relative variation of elastic constant  $c_{66}$ .



To evaluate the effects of these material constants we defined three sensitivity coefficients:  $(\Delta k/k)/(\Delta c_{66}/c_{66})$ ,  $(\Delta k/k)/(\Delta \gamma_{11}/\gamma_{11})$  and  $(\Delta k/k)/(\Delta e_{26}/e_{26})$ . These coefficients are calculated for various electrode spacing of langasite two-pole structure with parameters  $R=0.0015$ ,  $lx=9t$ .

The relative variation of  $k$  versus relative variation of material constants is not changed by the electrode spacing values for  $c_{66}$ , but it is changed for  $e_{26}$  and  $\gamma_{11}$ . The sensitivity coefficient of  $k$  with  $c_{66}$  is  $-1.246$  in the left side of  $(0, 0)$  point and  $-0.6$  in the right side (figure 5).

In figure 6 is presented the dependence of relative variation of  $k$  on relative variation of  $e_{26}$  for three values of electrode spacing. On observe that the  $k$  behaviour is strongly modified by  $e_{26}$  value when the electrode spacing has small values. For relative variation of  $e_{26}$  below zero we obtained the next values for the sensitivity coefficient 1.18 ( $d=0.1$  mm), 0.12 ( $d=0.9$  mm) and above zero the values of this coefficient are 0.67 ( $d=0.1$  mm),  $-0.57$  ( $d=0.9$  mm).

Another kind of influence has the electrode spacing on the relative variation of  $k$  with the relative variation of  $\gamma_{11}$  (figure 7): for small values of  $d$ , the values of  $\gamma_{11}$  give small changes of coupling coefficient. The sensitivity coefficient for the negative values of  $\Delta \gamma_{11}/\gamma_{11}$  is 0.39 for  $d=0.1$  mm, 0.99 for  $d=0.9$  mm; for positive values of  $\Delta \gamma_{11}/\gamma_{11}$  this coefficient is 0.22 for  $d=0.1$  mm and 0.88 for  $d=0.9$  mm.

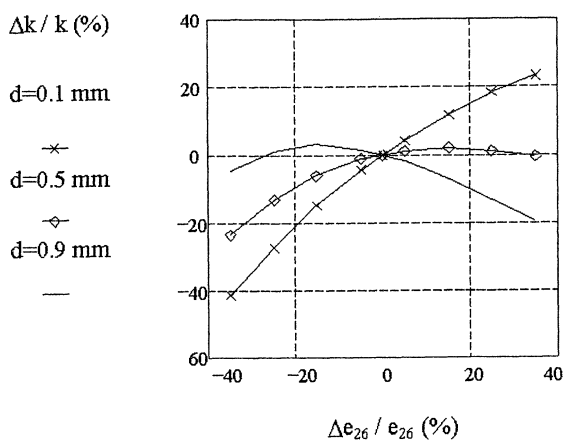


Figure 6: The relative variation of  $k$  versus relative variation of piezoelectric constant  $e_{26}$ .

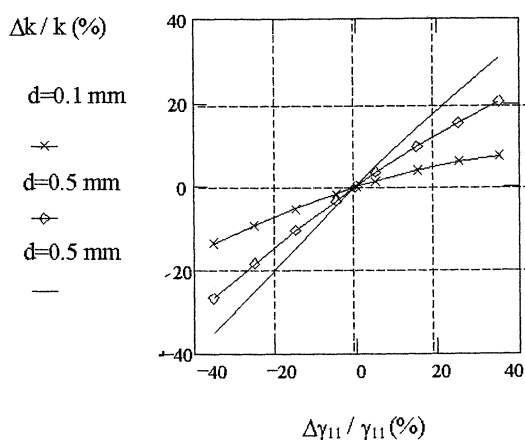


Figure 7: The relative variation of  $k$  versus relative variation of piezoelectric constant  $\gamma_{11}$ .

Two-pole langasite filters with 10.7 MHz central frequency and 40 kHz bandwidth were realised in our laboratory on langasite plates obtained from Dr. A. Gotalskaya. We used the method based on Tiersten's analysis (II) for the geometrical design of these filters. In figure 8 is presented the attenuation characteristic of one of these filters.

### 3. CONCLUSIONS

In order to improve the geometrical design method of monolithic filters we developed an original program based on Tiersten's analysis to establish an accurate relationship between coupling coefficient and bipolar structure parameters.

The influence of mass-loading on coupling coefficient behaviour for langasite and quartz two-pole monolithic filters has been evaluated. An interesting conclusion is that the variation of coupling coefficient with mass-loading is greater for quartz than for langasite filter,

which could be a new advantage of langasite over quartz crystal.

The effect of some material constants on coupling coefficient behaviour was estimated for langasite structure by the calculation of sensitivity coefficients of elastic constant  $c_{66}$ , piezoelectric constant  $e_{26}$  and Voight's elastic constant  $\gamma_{11}$ .

The relative variation of  $k$  with relative variation of material constants is not changed by the electrode spacing values for  $c_{66}$ , but it is changed for  $e_{26}$  and  $\gamma_{11}$ . The coupling coefficient behaviour is strongly modified by  $e_{26}$  for small electrode spacing values and by  $\gamma_{11}$  for large electrode spacing values.

This study of the change of the coupling coefficient behaviour through the mass-loading and the material constants could be useful for a better characterisation of piezoelectric crystals.

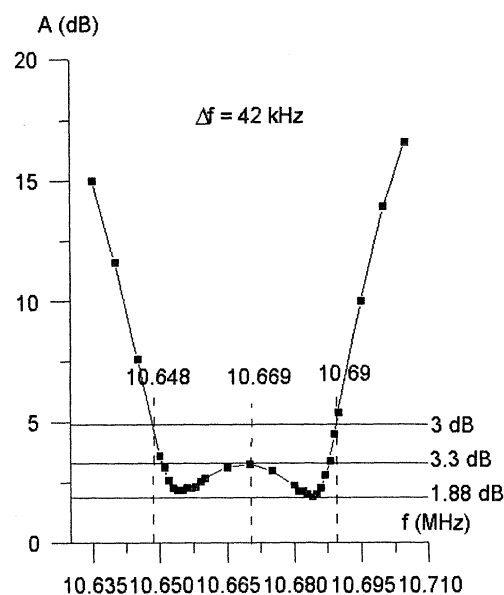


Figure 8: Attenuation characteristic of two-pole langasite filter

### 5. ACKNOWLEDGEMENTS

The authors thank Dr. Mihai Popescu for his precious advises and Dr. Alla Gotalskaya for the langasite samples.

### 6. REFERENCES

1. Shimamura K., Takeda H., Kohno T. and Fukuda T., 1996, "Growth and characterisation of lanthanum gallium silicate  $\text{La}_3\text{Ga}_5\text{SiO}_{14}$  single crystals for piezoelectric applications", *Journal of Crystal Growth*, **163**, 388-392
2. Gotalskaya A., Drezin D.I., Bezdolkin V.V and Stassevich V.N, 1993, "Peculiarities of technology,

physical properties and applications of new piezoelectric material langasite ( $\text{La}_3\text{Ga}_5\text{SiO}_{14}$ )", Proc. of IEEE Frequency Control Symposium, 339-344

3. Sakharov S.A., Larionov I.M. and Medvedev A.V., 1992, "Application of langasite crystals in monolithic filters operating in shear modes", Proc. of IEEE Frequency Control Symposium, 713-718

4. Mateescu I., Serbanescu A., Pop G. and Ghita C., 1997, "The influence of the piezoelectric crystal properties on the monolithic filters design", Ann. Chim. Sci. Mat., 22, 713-716

5. Mateescu I., Zelenka J. and Serbanescu A., 1996, "Contribution to the design of the wave filters composed from the elastically coupled two resonators structure", Proc. of the 10th European Frequency and Time Forum, 132-137

6. Manea A. Lazarescu M., Mateescu I., Pop G. and Ghita C., 1997, "Influence of the melt growth configuration on the structural properties of langasite crystals", Ann. Chim. Sci. Mat., 22, 735-738

7. Tiersten H.F., 1969, "Linear piezoelectric plate vibrations", Plenum Press, N.Y., 183 - 201

## EXPERIMENTAL VERIFICATION OF NON - LINEAR DRIVE LEVEL DEPENDENCE OF THE RESONANT FREQUENCY IN BAW QUARTZ RESONATORS

Jaroslav Nosek

Technical University of Liberec, Hálkova 6, CZ - 461 17 LIBEREC, Czech Republic

E-mail: jaroslav.nosek@vslib.cz

### ABSTRACT

Theory of non-linear behaviour of the drive level dependence of the AT-cut quartz resonant frequency was given by Tiersten (1). Nosek in (2) respects the non-linear properties by the non-linear impedance of the piezoelectric resonator using the change of the parameters of the electric equivalent circuit. Now, some results of the experimental verifications of this theory for the AT- cut quartz resonators, using HP 4195A Network/Spectrum Analyser and Saunders test temperature chamber 2250, are presented.

### 1. INTRODUCTION

Piezoelectric resonators have been studied at the Department of Electrical Engineering at Technical University of Liberec for tens of years. Beside the others, our work is focused namely on the following fields:

1. precise determination of temperature and power fields dependence of resonant frequency of quartz resonators by the use of non-linear theory,
2. calculation of frequency spectra and electrical equivalent circuit parameters of quartz cuts and application of results in the resonator design.

All the research results were applied in practise and resulted in the improvement of resonator production in former Tesla Works, now Crystals Co., Hradec Králové in the Czech Republic. A small group of about 10 persons was established in order to solve other specific partial theoretical and experimental problems, for example surface acoustic wave filters, piezoelectric resonator sensors, applications of piezoelectric composites. The main output of this activity was the establishment of the *Resonant Method Laboratory* in 1997.

Our first experiments provided the verification of some theoretical results, namely on the field 1 mentioned above.

It is known that the linear theory of piezoelectricity is a suitable tool for describing the propagation of acoustic waves with small amplitudes, without any elastic or strong electric field pre-stressing. In general, the non-linear theory takes into consideration the electro-elastic equations containing terms up to cubic in the small mechanical displacement field, but no higher than linear in the electric variables Ref. (1). In the simplified pure elastic case, the description of

propagation of a finite amplitude wave in a non-linear medium leads to the wave propagation equation with effective non-linear elastic constants of the 3<sup>rd</sup> and 4<sup>th</sup> orders. In the presented problem these non-linearities are at the origin of harmonic generation with its consequences: amplitude - frequency effect, and intermodulation.

### 2. AMLITUDE – FREQUENCY EFFECT

To some extent, the resonant frequency of piezoelectric resonators depends on the magnitude of excitation current passing through the resonator. Considering the results of Ref.(2), the following approximate relationship for the relative change in the resonant frequency of AT-cut and trapped energy plan-convex resonator is used:

$$\frac{\Delta f}{f} = \frac{9}{16} \cdot \frac{\gamma}{c_{66}^D} \cdot \frac{h^2 \pi^2}{8 \cdot e_{26}^2}$$

$$\left[ \frac{\varepsilon_{22}}{(2a)^2} \left( 1 + \hat{k}_{26}^2 \right) V_K^2 + \frac{I_K^2}{\omega_0 (S_{red})^2} \right] \quad (1)$$

where

$$\gamma = \frac{1}{2} \tilde{c}_{22}^E + \tilde{c}_{266}^E + \frac{1}{6} \tilde{c}_{6666}^E \quad (2)$$

is the effective elastic stiffness,  $\hat{k}_{26}$  is given in (1),  $2a$  is the central resonator thickness,  $\tilde{c}_{22}^E$ ,  $\tilde{c}_{266}^E$ ,  $\tilde{c}_{6666}^E$  are effective elastic stiffness of the second, third and fourth orders, respectively, measured under a constant electric field,  $h$  is order of the harmonics,  $e_{26}$  is the piezo-electric stress coefficient,  $k_{26}$  is the electro-mechanical coupling coefficient,  $\varepsilon_{22}$  is the permittivity along the thickness axis of the plate,  $S_{red}$  is the reduced surface of the electrode of trapped energy AT-cut resonator Ref. (2),  $\omega_0$  is the angular resonant frequency,  $V_K$  is the voltage applied to the resonator and  $I_K$  is the excitation current. The influence of the excitation current on the frequency and its mathematical description makes necessary to introduce a non-linear impedance characteristic of the piezoelectric resonator. This influence was modelled by the non-linear

equivalent circuit, with non-linear capacitance, resistance and inductance in general - Ref. (2).

### 3. NON – LINEAR ELECTRICAL EQUIVALENT CIRCUIT

We research the dominant non-linear elements of dynamical branch of electrical equivalent circuit. We express the angular frequency

$$\omega^2 = \omega_0^2(1 + 2BI_k^2 + B^2I_k^4), \quad (3)$$

where  $\omega_0$  is angular frequency in the linear case (infinitely small amplitude of excitation), the term  $B^2I_k^4$  can be neglected.

If  $\omega = \omega_s = \omega(I_k^2)$ , the non-linear elements  $C$  and  $L$  depend on the current  $I_k$ , too.

The Eqn. (9) is an analytical description of non-linear dependence of frequency vs. voltage and current on the resonator. In this case, a small electromechanical coupling and dominant elastic stiffness including stiffness of 3<sup>rd</sup> and 4<sup>th</sup> order are supposed.

It follows, that only  $C(I_k)$ , which depend on the elastic stiffness, and  $R(I_k)$  with a complicated origin of dependence, are considered to be a dominant non-linearity of the dynamical branch of the electrical equivalent circuit:

$$C(I_k) = \frac{1}{1 + \omega_0^2(1 + 2BI_k^2)} = \frac{1}{1 + 2BI_k^2} \quad (4)$$

For preferred inverse capacitance

$$\Gamma_C = \frac{1}{C} \quad \text{and} \quad \Gamma_{Ch} = \frac{1}{C_h},$$

the dependence on current is

$$\Gamma_C(I_k) = (1 + 2BI_k^2)\Gamma_{Ch} = a_0 + a_2I_k^2, \quad (5)$$

where

$I_k$  is amplitude of the excitation current (in the serial resonance),

$C_h$  is the dynamical linear capacitance (for infinitely small amplitude of excitation).

The second considered, non-linear element is the non-linear resistance  $R(I_k)$ .

It is difficult to determine the  $R(I_k)$  characteristic analytically. In accordance with experimental results, we can approximate the measured dependence  $R(I_k)$  in the area of  $10^{-5}$  to  $2 \cdot 10^{-4}$  A by the function

$$y = b_0 + b_1 \cdot x + b_2 \cdot x^2 + \dots = \sum_{n=0}^N b_n x^n \quad (6)$$

with constant coefficients  $b_0, b_1, b_2, \dots, b_N$ .

If we suppose an absence of dumping coefficient of 3<sup>rd</sup> order and a limited influence of the coefficient  $r_{6666}$  of 4<sup>th</sup> order, it follows that

$$R(I_k) = R_h(1 + \beta I_k^2) = b_0 + b_2 I_k^2 \quad (7)$$

for  $b_1 = 0$ .

It is obvious from comparison of  $C(I_k)$  with  $R(I_k)$ , that the dominant influence of  $C(I_k)$  is valid for the resonator with high quality coefficient  $Q$ .

The dependence of parallel capacitance  $C_o$  on the current  $I_k$ , in consequence of non-linear permittivity coefficient  $\epsilon_{2222}$  and his slight influence on the elements of dynamical branch, is negligible.

The non-linear equivalent electrical circuit valid for a piezoelectric BAW resonator is shown in Fig. 1.

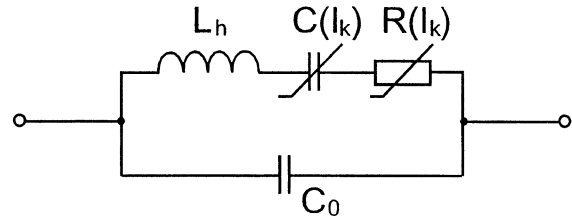


Figure 1: Non-linear electrical equivalent circuit for piezoelectric BAW resonator vibrating on the harmonics overtone h

### 4. DETERMINATION OF COEFFICIENTS OF APPROXIMATES DEPENDENCES

The first term in the square brackets in the Eqn. (1) is usually negligible compared to the second term, and Eqn. (1) acquires the form

$$\frac{\Delta f}{f} = BI_k^2, \quad (8)$$

where

$$B = \frac{9}{16} \frac{\gamma}{c_{66}^D} \frac{h^2 \pi^2}{8e_{26}^2} \frac{1}{\omega_0 (S_{red})^2} \quad (9)$$

From Eqn. (5) is obvious that coefficients  $a_0$  and  $a_2$  of the approximate dependence on current are

$$a_0 = \frac{1}{C_h} = \Gamma_{ch}, \quad a_2 = 2B.\Gamma_{ch}. \quad (10)$$

We read from Eqn. (7)

$$b_0 = R_h, \quad b_2 = \beta.R_h. \quad (11)$$

The plane-convex AT resonator operating at 5 MHz, vibrating on the 5<sup>th</sup> harmonic of the thickness-shear vibrations, was measured.

The diameter of the resonator is 17 mm, the diameter of the electrodes 5 mm, the curvature radius of the convex plane 100 mm.

The constants  $2B = 2 \times 0.574 \text{ A}^{-2}$  and  $\beta = 5 \times 10^4 \text{ A}^{-2}$ ,  $L_h = 4 \text{ H}$ ,  $R_h = 165 \text{ } \Omega$ ,  $Q = 0.8 \times 10^6$ ,

$$\omega = 2\pi \times 5 \times 10^6 \text{ s}^{-1}, \quad C_h = \frac{10^{-14}}{4\pi^2} \text{ F}.$$

Using the above mentioned values, the desired coefficients are

$$a_0 = 4\pi \times 10^{14} \text{ F}^{-1}, \quad a_2 = 45.32 \times 10^{14} \text{ F}^{-1} \text{ A}^{-2}$$

$$b_0 = 165 \text{ } \Omega, \quad b_2 = 825 \times 10^4 \text{ } \Omega \text{ A}^{-2}.$$

## 5. RESONANT METHOD LABORATORY AND EXPERIMENT

The base of the Laboratory is made by two wide-known instruments:

- Network/spectrum analyser HP 4195A for the measurement of all circuit parameters with high accuracy in frequency range from 10 Hz to 500 MHz,
- Temperature Test System from Saunders and Assoc., Inc. that allows practically all types of temperature measurements in technically interesting range.

A connection with other additional standard devices, as for example digital oscilloscopes, and very special instruments prepared by the group, allows all the measurements including the very special ones.

At present time, the Laboratory is focused to the measurement of:

- a) temperature behaviour of plate and bar piezoelectric resonators in wide frequency range,
- b) electrical equivalent circuit parameters and non-linear properties of resonators,
- c) elastic, dielectric and piezoelectric parameters of piezoelectric crystals.

The *Resonance Methods Laboratory* (and *Laser Interferometry Laboratory*) are built up thanks to the government grants, especially The Grant for Study of Properties of Special Piezoelectric Materials (Grant Agency of Czech Republic) and The Grant for Support of Research at Czech Universities (Ministry of Education). The Laboratory co-operates with industrial companies in the Czech Republic and with foreign universities and institutions in the USA, France, Poland and Austria. We suppose that great amount of work will be done in the form of PhD study, therefore the Laboratory is open for both Czech and foreign postgraduate students.

The HP 4195A Network/Spectrum Analyser can be used, among many other things, for the impedance measurements. As for this applications, it operates at frequencies from about 300 kHz to 500 MHz with an accuracy near 1%, therefore resonators in the highest frequency range can be measured by this instrument. Since its minimum resolution bandwidth is 3 Hz, these measurements could be very accurate. An additional impedance test adapter and test fixture must be connected to the analyser to perform precise impedance measurements. The main disadvantage is the necessity to perform complicated calibration procedure of these devices at the start of impedance measurement. The measurement accuracy depends strongly on both the impedance test adapter calibration and test fixture compensation. In order to verify the possibility of precise impedance measurement of high frequency resonators we have made some measurements on resonators in 10 MHz range. We have had strong problems with the apparatus calibration and compensation. Nevertheless, the measurement of 10 MHz commercial resonator confirmed our expectations. We have found a lot of resonant frequencies near 10 MHz with the typical resistance and reactance curves for a relative wide measuring range. If we neglect problems with instrument calibration and compensation, the impedance measurement is very convenient. We can find a lot of resonator parameters, including its equivalent circuit parameters and approximating curves. Its characteristic can be displayed by many forms. Since we plan the routine measurements with this new apparatus, we have prepared fully automated resonator measurements by the HP-IB interface.

## 6. CONCLUSION

The measurements results shown, that the parameters of the non-linear electrical equivalent circuit depend on the drive level applied on the resonator. The static capacitance  $C_0$  and motional inductance has not measurable dependence. Statistically, dependence of  $C_h$  and  $R_h$  is in agreement with theory, but the results are on the limits of accuracy of the Test temperature chamber. Neglecting the problems with calibration and compensation of new HP4195A analyser, many valuable measurements are achieved.

## ACKNOWLEDGEMENT

This work was supported in part by the Grant of Ministry of Education of the Czech Republic under Contract No. VS 96006 and No. G388.

## REFERENCES

1. Tiersten,H.F., Stevens,D.S.,1986, An Analysis of non-linear resonance in countered quartz crystal resonators. J.Acoust.Soc.Am., Vol. 80, 1122-1132.
2. Nosek,J., 1997, Drive Level Dependence of the Resonant Frequency in BAW Quartz Resonators and his Modelling. Proc. 1977 IEEE International Frequency Control Symposium, Orlando, USA, pp. 687 - 695. IEEE Transactions on Ultrasonics, Ferroelectrics, and Frequency Control (to be published).
3. Nosek,J., Zelenka,J.,1997, Recent Activities in the Research of Piezoelectric Crystal Properties at the Technical University of Liberec. Annales de Chimie. Science des Matériaux. Masson Paris, Milan, Barcelone,Vol.22, 8, 661-668.
4. Nosek,J.,1997, New Experimental Possibilities of Investigation of Basic Properties of Crystals and Smart Materials at the Technical University of Liberec. 2<sup>nd</sup> European Workshop on Piezoelectric Materials, Montpellier, France, Annales de Chimie. Science des Matériaux. Masson Paris, Milan, Barcelone, Vol.22, 8, 691-693.
5. Nosek,J.,1997, Some Second-order Effects in the Electromechanical Systems with Bulk- and Surface Acoustic Waves. Proc.11<sup>th</sup> European Frequency and Time Forum 1997, EFTF 97, Neuchatel, Switzerland, pp. 243-248.

## TEMPERATURE DEPENDENCE AND COMPENSATION OF GaPO<sub>4</sub> THICKNESS RESONATORS

C. REITER<sup>1</sup>, H. THANNER<sup>2</sup>, W. WALLNÖFER, P.W. KREML

AVL List GmbH, Hans-List-Platz 1, A-8020 Graz, Austria

<sup>1</sup>also Institute for Solid State Physics, Technical University Graz, A-8010 Graz, Austria

<sup>2</sup>also Institute for Experimental Physics, University of Graz, A-8010 Graz, Austria

### ABSTRACT

The properties of singly-rotated y cut thickness shear resonators and singly-rotated x cut thickness extensional resonators of the quartz-homeotypic piezoelectric crystal material gallium (ortho-) phosphate, GaPO<sub>4</sub>, have been experimentally studied. The temperature dependence of the relevant elastic constants in the range -50°C...700°C were determined. The main temperature-compensated rotated y cut at 25°C has a parabolic f(T) curve. A rotated y cut was found with cubic temperature compensation near 500°C.

### INTRODUCTION

Gallium (ortho-)phosphate, GaPO<sub>4</sub>, is a quartz-homeotypic piezoelectric crystal of considerable interest for technical applications (1). A promising segment is the use of thickness shear bulk acoustic wave devices, since there have been shown temperature compensated cuts with stronger coupling than in quartz (2,3). We present the results of experimental studies done with high-quality material.

### EXPERIMENTAL

An automatized measuring apparatus was built for the measurements (Fig. 1). An evacuated cell with resistive heaters and insulation allows measurements up to 900°C. The cell can also be cooled with liquid from a nearby cryostat to -50°C. The temperature is stabilized by a PID controller. A desktop computer steps through the measurement range by giving out the step temperature, checking if it is stably attained and then starting the resonance measurement by a HP 4195A network analyzer which transmits the admittance curve around fundamental, 3rd and 5th harmonic.

The resonators (Fig. 2) were cut from GaPO<sub>4</sub> material grown at AVL with IR values  $\alpha_{3400}$  between 0.8 and 1.6 cm<sup>-1</sup>, corresponding to estimated OH contents of 50...100 ppm/wt. The rotation around the x axis, which is given relative to a y cut, was measured by Laue backscattering with an accuracy of about 0.1°. The outer diameter was 7.4mm, the diameter of the central electrode region 3.6mm. The ranges outside this region was convexly bevelled with a curvature radius of 90mm. Gold electrodes with 100nm thickness were used. The resonators were mounted with conductive glue in standard crystal holders.

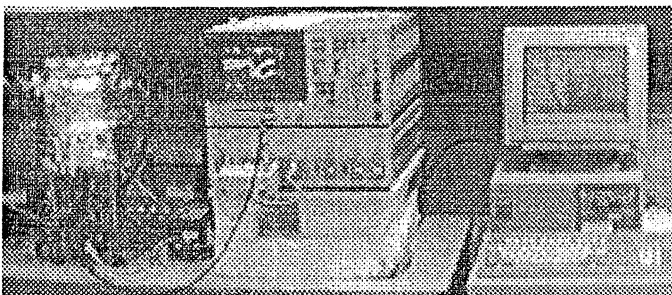


Figure 1: Measuring apparatus; l. to r.: evacuable cell with temperature controller, network analyzer, controlling computer.

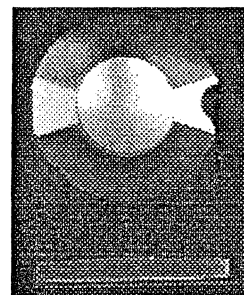


Figure 2: Thickness shear resonator mounted in crystal holder.

## RESONATOR PROPERTIES

Typical resonance curve for a thickness shear resonator is shown in (Fig. 3), for a thickness extensional resonator in (Fig. 4). The Q factors of the thickness extensional resonators are not as high as the Q factors of the thickness shear resonators. In fundamental mode of the thickness shear resonators, series and parallel resonance frequencies could usually be measured. The determination of the series and parallel resonance frequencies of the thickness extensional resonators is not so accurate, but still possible.

After the first heating to 700°C, the frequency is slightly decreasing. This is due to the reduction of stresses, which appears by mounting the resonator in the holder and sputtering the electrodes. The frequency stays stable upon further heat-ups. Also, the Q factors only reaches its stable higher value after the first heating. We achieved Q factors between 100 000 and 200 000 for the fundamental mode, between 200 000 and 300 000 for the harmonics.

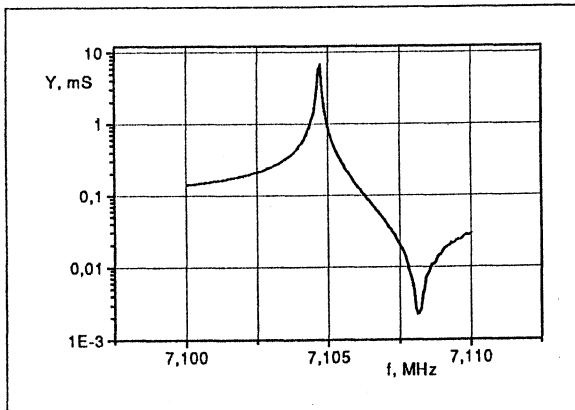


Figure 3: Resonance curve of thickness shear resonator (fundamental mode)

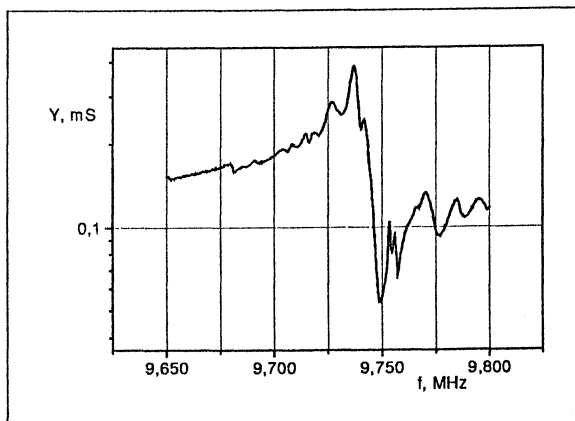


Figure 4: Resonance curve of thickness extensional resonator (fundamental mode)

The measurements were made in the temperature range -50°C...700°C. In (Fig. 5) and in (Fig. 6) the typical relative temperature dependence of frequency for thickness shear resonators (6 different rotation angles) and thickness extensional resonators (4 different rotation angles) are shown. The fit on this dependences leads to the elastic constants and the temperature coefficients.

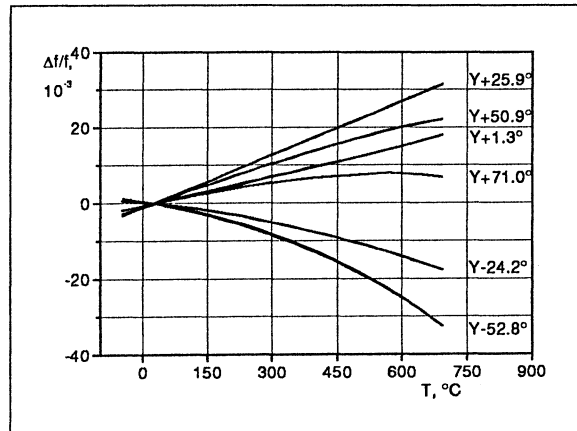


Figure 5: Relative frequency vs. temperature dependence of thickness shear resonators

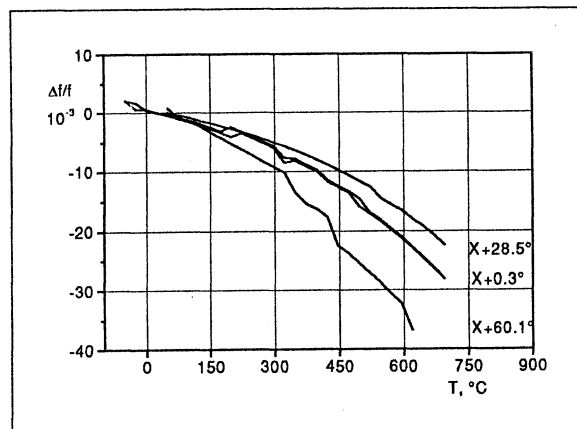


Figure 6: Relative frequency vs. temperature dependence of thickness extensional resonators

TABLE 1 - Elastic constants and their temperature coefficients

	$c^E$ GPa	$T^{(1)}c^E$ $10^{-6}K^{-1}$	$T^{(2)}c^E$ $10^{-9}K^{-2}$	$T^{(3)}c^E$ $10^{-12}K^{-3}$
$c_{11}$	69.09	-17	-158	85
$c_{12}$	21.97	-143	-497	283
$c_{13}$	19.10	-44	5	-121
$c_{14}$	4.66	414	197	25
$c_{33}$	106.96	-65	-243	89
$c_{44}$	39.33	2	-64	-13
$c_{66}$	23.56	41	0	-7

The coupling is somewhat lower than previously expected, but about twice the value of quartz. Coupling for thickness shear resonators for the different rotation angles is very stable up to 600°C, above it starts to decrease slightly.

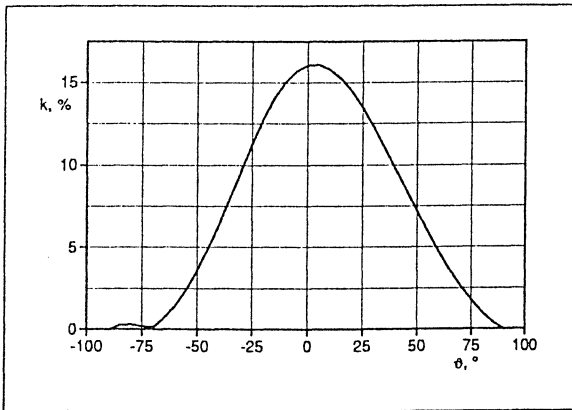


Figure 7: Coupling factor of thickness shear wave at 25°C as function of rotation angle (fitted to experimental data)

### TEMPERATURE COMPENSATED CUTS

There are two singly rotated y-cuts with temperature compensation at room temperature. One is located near y-85° and has very low coupling, so that it seems without technical interest. The other one is in the region of high coupling, near the minimum of the velocity curve ( $v = 2540$  m/s). This orientation was also found by J. Détaint on material grown in  $H_2SO_4$  in Montpellier (2). As shown in (Fig. 8), the agreement between his and our measurements is very good. This shows that even with different growth media, producing and measuring laboratories, the quality of  $GaPO_4$  crystals is now high enough to allow matching results. The measured coupling factor is 12..13%. We attribute the earlier reports on AT-like behaviour by Détaint and us to samples with high OH defect density.

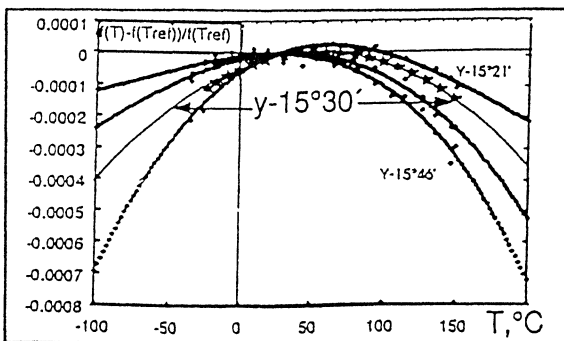


Figure 8: Relative frequency-temperature curves of temperature compensated cuts; cuts near y-15°30'; thick lines: Détaint (4), thin line: this work

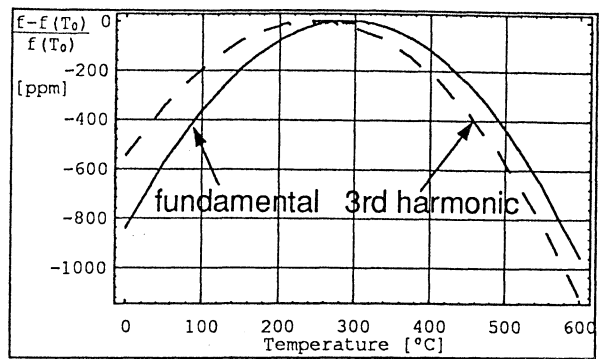


Figure 9: Relative frequency-temperature curves of temperature compensated cuts; y-11,8° cut

The second temperature coefficient of frequency (2.TCF) is near  $20 \cdot 10^{-9}/K^2$ . When the cut angle is shifted from -15.5° nearer to the y cut, the inversion temperature ( $T_0$ ) increases, and the 2.TCF decreases (Fig. 10, 11);  $T_0$  is usually somewhat lower in the overtones, as shown in (Fig. 9). In (Fig. 12), the 2.TCF achievable for a given inversion temperature is compared for  $GaPO_4$  and for the quartz AT and BT branches (minimum at higher temperature for AT branch). It shows that above 100°C, with  $GaPO_4$  better stability is achievable than with quartz.

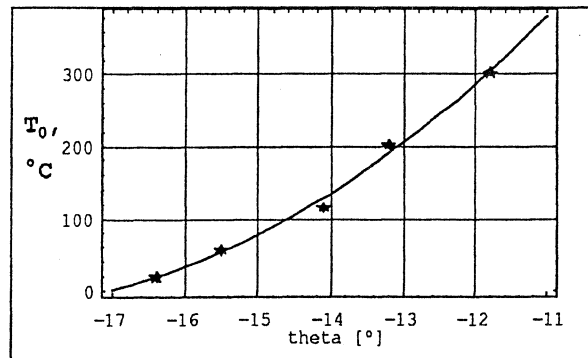


Figure 10: Angular dependence of inversion temperature

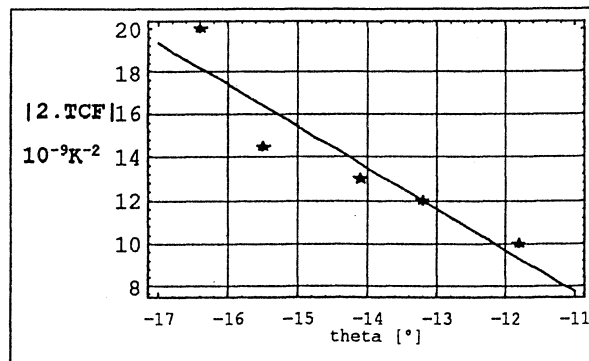


Figure 11: 2nd temperature coefficient at inversion temperature

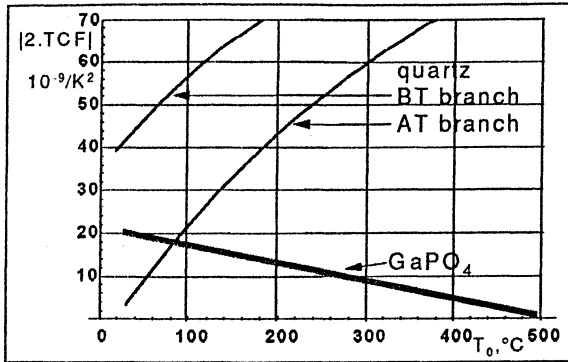


Figure 12: Dependence of 2nd temperature coefficient on inversion temperature for GaPO<sub>4</sub> (main TC cut at -11°...-17°) and quartz (AT and BT branch).

At 500°C, a second-order temperature compensation is possible. This was experimentally verified with the resonators shown in (Fig. 13). This cut and nearby cuts allow a very low temperature dependence over large temperature ranges; the frequency stays in a range of ±20ppm for 350...650°C. This makes GaPO<sub>4</sub> a very suitable material for demanding high-temperature applications of bulk wave resonators.

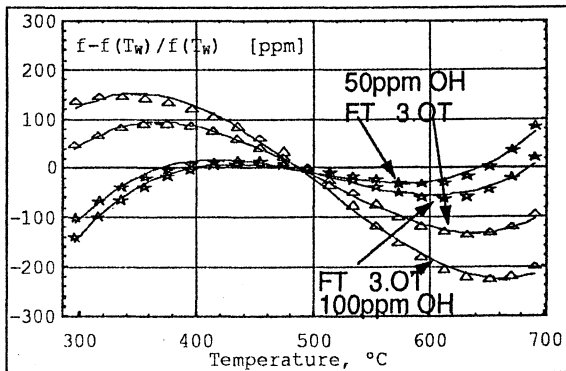


Figure 13: Relative frequency-temperature curves of cuts with cubic behaviour; fundamental and 3rd harmonic of two resonators with different OH content.

This work was supported in part by the European Communities by the Brite-EuRam projects BE96-3246 and BE96-3105.

## REFERENCES

1. KREMPL P.W, KRISPEL F, WALLNÖFER W, Industrial development and prospects of GaPO<sub>4</sub>; *Ann. Chim. Sci. Mat.* 1997, 22, pp. 623-626
2. DETAINT J, CAPELLE B, ZARKA A, PALMIER D, PHILIPPOT E, Frequency Control and filtering

applications of the new piezoelectric materials of class 32; *Ann. Chim. Sci. Mat.* 1997, 22, pp. 651-660

3. WALLNÖFER W, STADLER J, KREMPL P.W, *Proc. 7<sup>th</sup> European Frequency and Time Forum*, Neuchâtel 1993, p. 653-657

4. DETAINT J, private communication

## A new miniature quartz Y+5 temperature sensor

K. Weiss, W. Szulc, E. Żuchowski, M. Tupaj, Tele & Radio Research Institute, Warsaw, POLAND  
B. Dulmet, ENSMM/LCEP, Besançon, FRANCE

### 1. Introduction

The temperature sensors with quartz resonator are well known since many years. The most popular quartz temperature sensor is so called Y+5 one rotation resonator with  $\Theta = 5^\circ$ . This resonator exhibits the biggest temperature - frequency characteristic slope, and is easy to manufacture. It's disadvantage is nonlinear temperature - frequency characteristic. The linear temperature - frequency characteristic exhibits LC cut resonator. The LC cut is doubly rotated cut with  $\phi = 11^\circ 10'$  and  $\Theta = 9^\circ 35'$ . This resonator is more difficult to manufacture and has lower temperature sensitivity. In both kinds of temperature sensors there are round quartz plate vibrators with diameter over 5 mm. The sensor diameter is about 10 mm. The LC temperature sensors have been manufacture in Tele and Radio Research Institute since 1974 year.

### 2. Y+5 strip resonator design

The AT strip resonator have been known since over 10 years. This resonator is working in temperature range  $-25 \div 70^\circ\text{C}$ . In the Y+5 strip resonator design the main problem was the wide range of working temperature,  $-60 \div 150^\circ\text{C}$ .

In Tele and Radio Research Institute, using computer program based on complex wave numbers method, the strip Y+5 resonator was designed. Calculated relative dimensions of this resonator were:

$$L = 8,1; \mu = 0,016; W = 10,5; \Theta = 5^\circ; B = 33$$

where: L - relative width of resonator  $L = l_1/l_2$

$\mu$  - relative electrode thickness

$$\mu = \frac{\rho_m \cdot 2h}{\rho_k l_2}$$

W - relative length of electrodes

$$W = l_e/l_2$$

B - relative resonator length

$$B = l_3/l_2$$

$\Theta$  - angle of cut

$\rho_m$  - electrode metal density

$\rho_k$  - quartz density

Resonator dimensions are presented in fig. 1.

Calculated temperature - frequency and temperature - resistance characteristics of designed resonator are presented in fig 2 and fig 3.

### 3. Experimental results

At the basis of this calculation was designed strip Y+5 resonator with resonant frequency 10 MHz.

The quartz vibrator dimensions were: length - 6 mm; width - 1,52 mm; thickness - 0,188 mm and electrodes length 2 mm. Measured resonator frequency was 10 120 kHz. In resonator spurious vibration was observed in temperature about  $50^\circ\text{C}$ . This fact shows that theory is not corresponding to practice with satisfactory accuracy. Next there were carried out experiments with different quartz plate width and with different electrode length. As a result we did obtain resonator without spurious modes in temperature range  $-196 \div 170^\circ\text{C}$ . The quartz vibrator dimensions were:  $L_{9,6 \div 9,7}$ ;  $\mu = 0,007$ ;  $W = 16$ ;  $B = 33$  and  $\Theta = 5^\circ$ . For this resonator calculated characteristics  $\Delta f/f = f(T)$  and  $\Delta R/R = f(T)$  exhibit in temperature about  $80^\circ\text{C}$  a little disorder showing in this region existence of spurious vibration (see fig.4 and 5).

Resonator of this design worked correctly and had dimensions : length 6 mm; width 1,8 mm; thickness 0,186 mm. This resonator with resonant frequency in room temperature 10020 kHz exhibited spurious vibration in temperature about  $190^\circ\text{C}$ . The measured temperature - frequency characteristic of this resonator is presented in fig .6.

This resonator was analyzed in LCEP in France using Finite elements method . Results of this analysis are presented in fig. 7 ÷ 12.

From this analysis we can see that the spurious resonance appears in temperature about  $200^\circ\text{C}$  and belongs to flexion vibration modes. Correlation between experimental results and theoretical calculations realized by finite elements method is very good.

### 4. Conclusions

Presented above experimental results did show possibility of miniature temperature sensor design. Theoretical calculations with complex wave numbers method utilization exhibit too big differences with practical results, and it's impossible to use it for Y+5 temperature sensor design. The finite elements method is significantly better and gives possibility not only of this vibrator design but also the kind of spurious mode definition. In presented investigations results we did obtain miniature temperature sensor with enclosure diameter 3 mm and length 8mm. This sensor can be used for temperature measurement in range  $-200 \div +170^\circ\text{C}$  with resolution of 0,001 K.

Table 1. Initial data for Y+5 temperature sensor design

Case	cylindrical DV type
Frequency (25°C)	10 000 kHz ± 150 kHz
Overtone	fundamental
Motional resistance	lower than 120 Ω
Main slope of frequency temperature characteristic	~ 1000 Hz/K
Working temperature range	60°C to +150°C
Maximal dimensions of quartz element	width 1,8 mm height 6,0 mm
Fixing in enclosure	one side
electrode material	gold on chromium

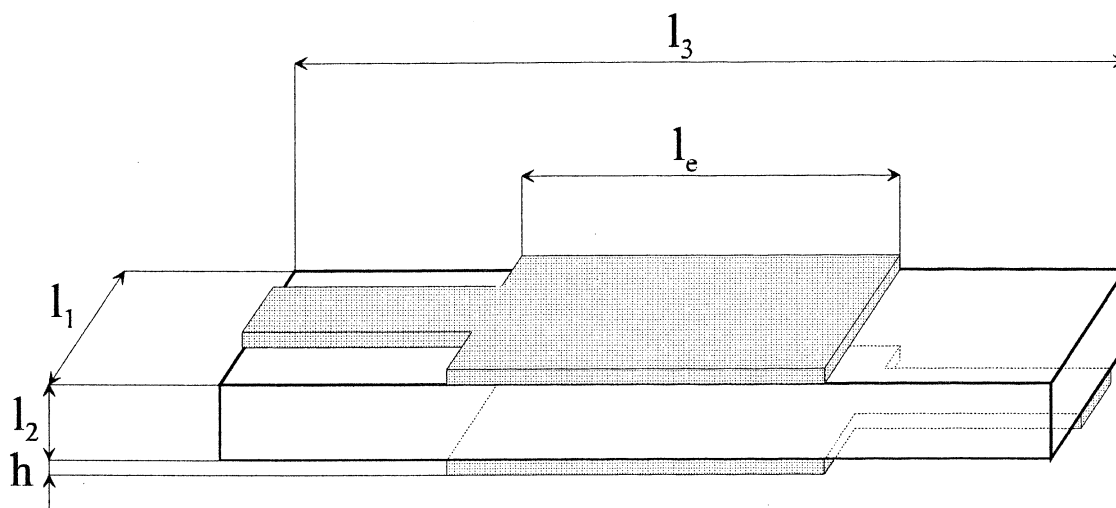


Fig 1. Y+5 strip resonator dimensions

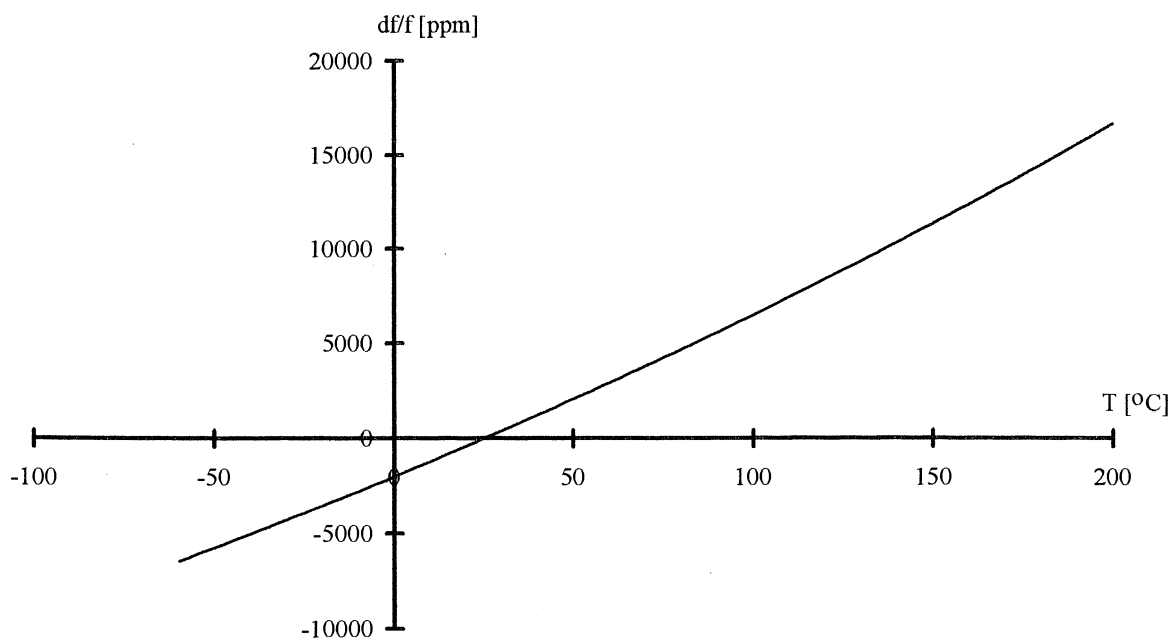


Fig. 2. Calculated  $\Delta f/f = f(T)$  characteristic of 10 MHz Y+5 strip resonator with width 1,52 mm

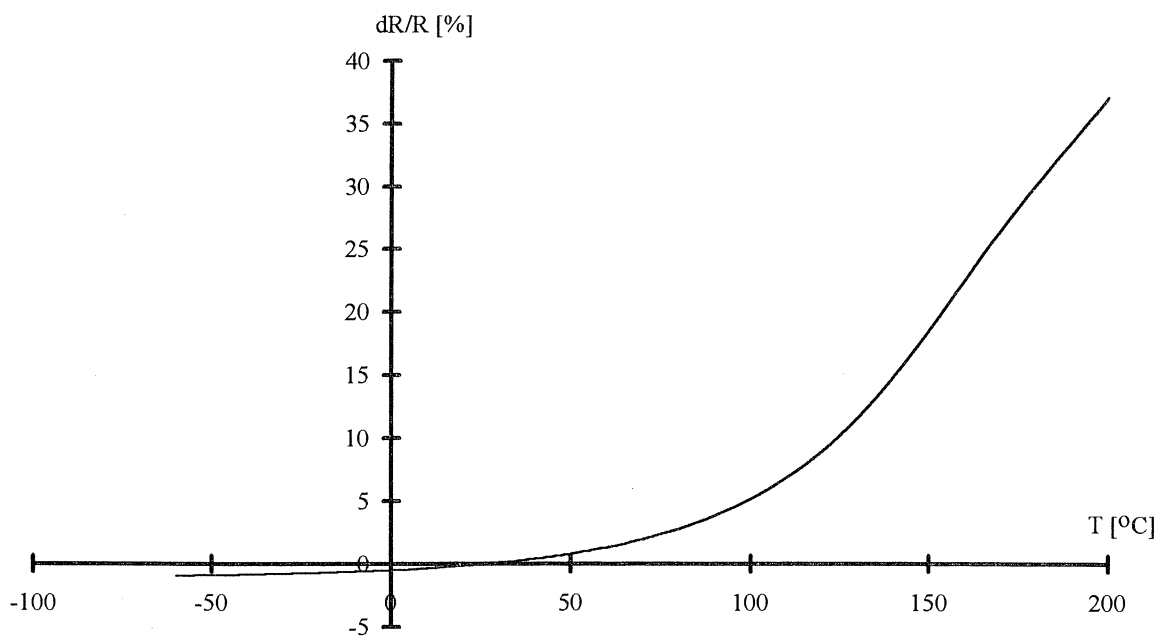


Fig. 3. Calculated  $\Delta R/R = f(T)$  characteristic of the same resonator.

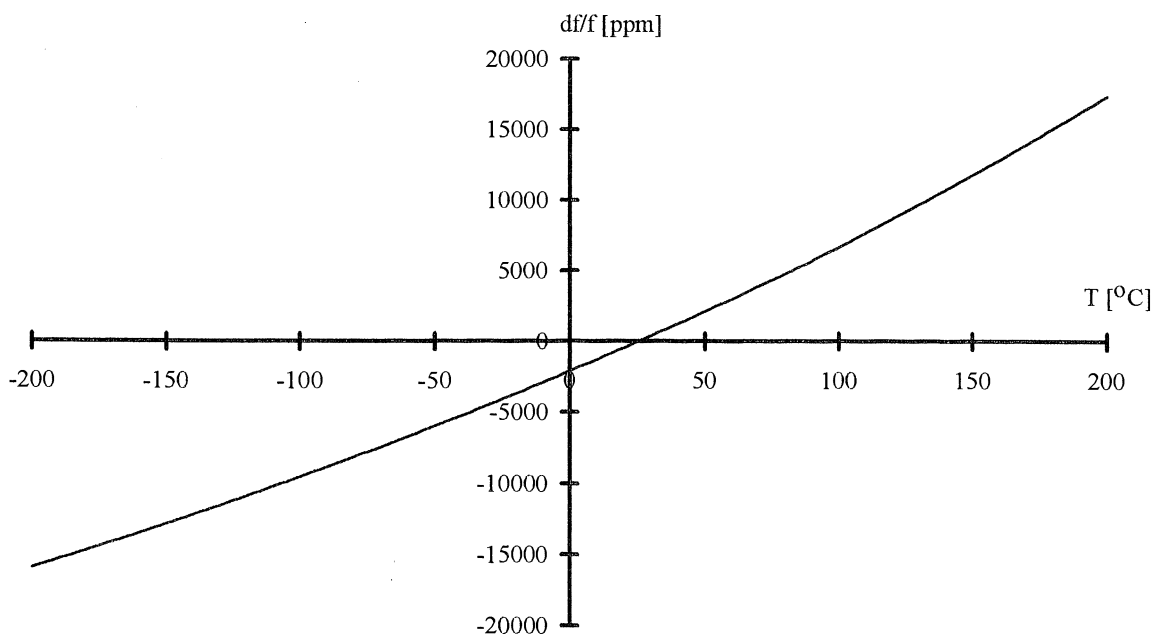


Fig. 4. Calculated  $\Delta f/f = f(T)$  characteristic of 10 MHz Y+5 strip resonator with width 1,8 mm

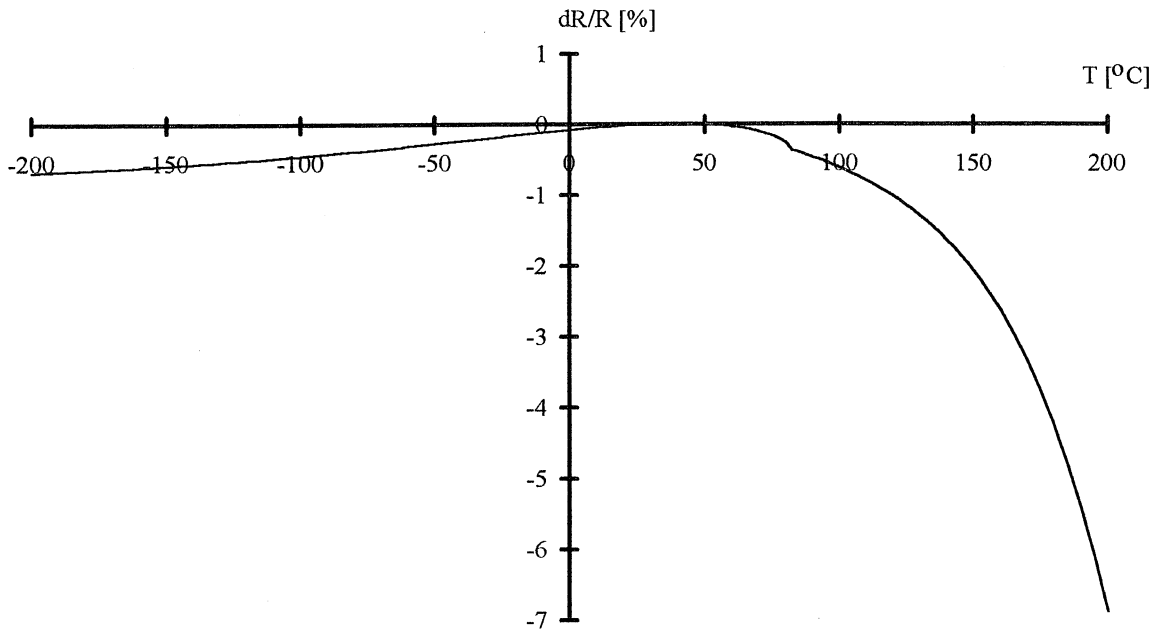


Fig. 5. Calculated  $\Delta R/R = f(T)$  characteristic of the same resonator.

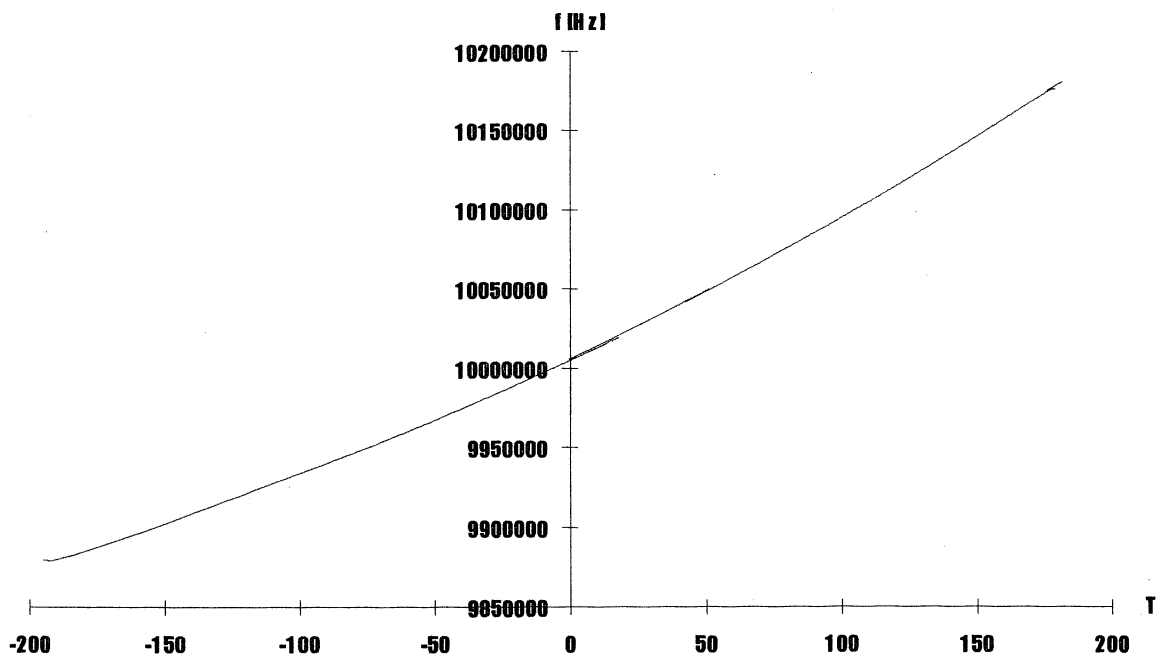
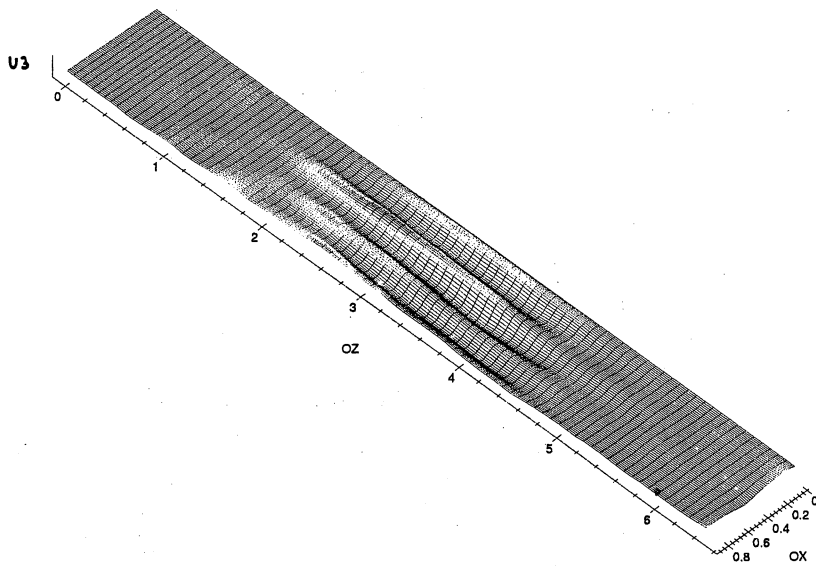
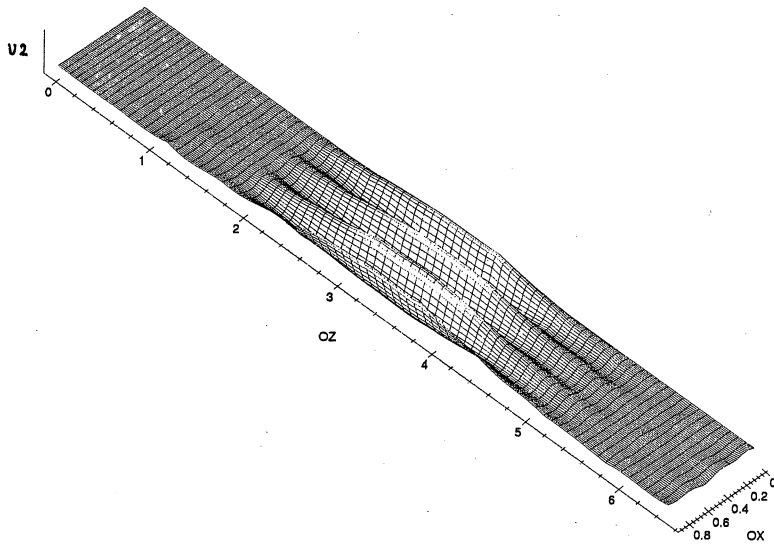
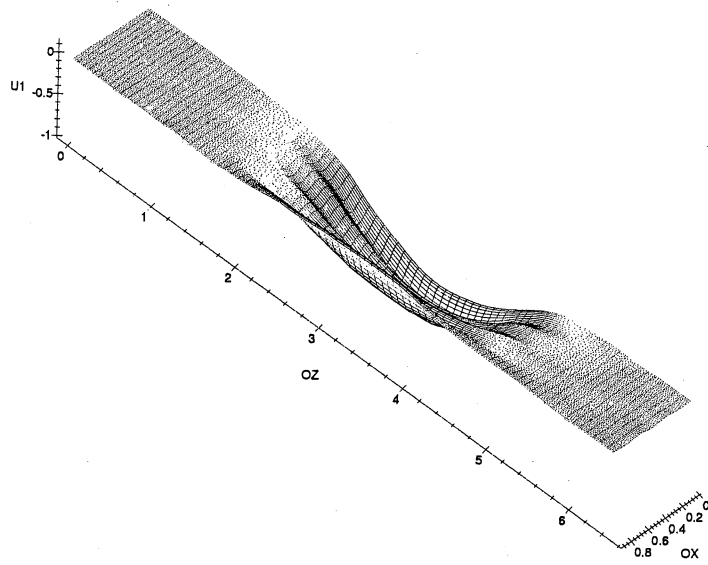
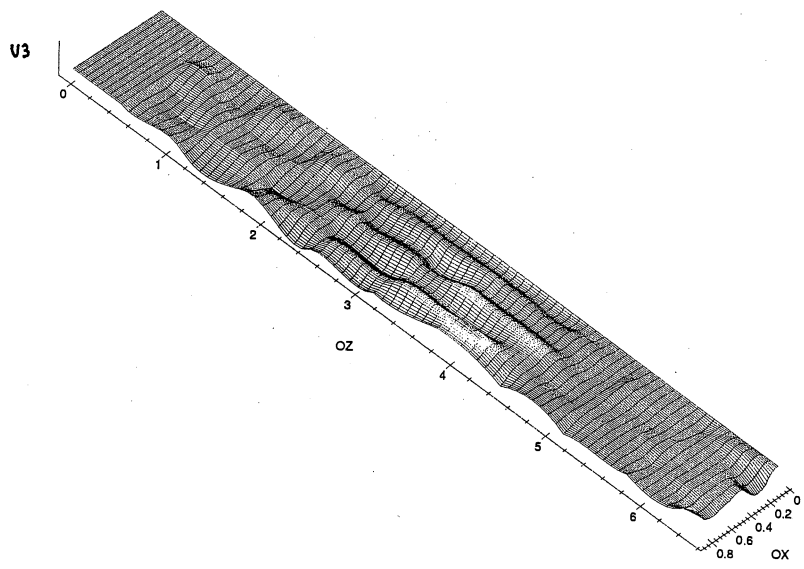
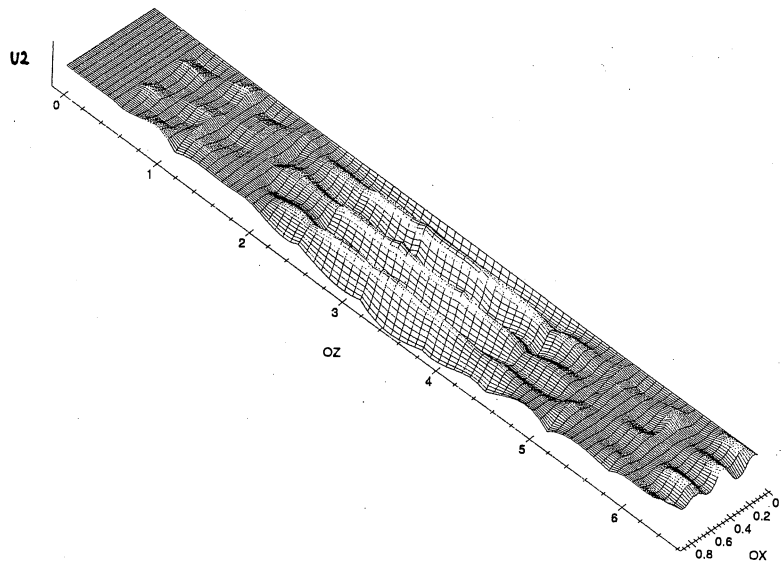
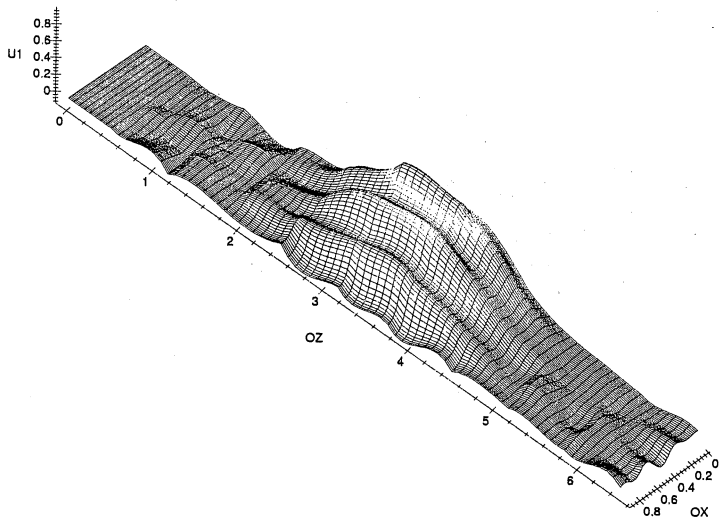


Fig.6. Measured  $\Delta f/f = f(T)$  characteristic of resonator with width 1,8 mm





## ONE-PORT SAW RESONATOR USING SERIES CONNECTED IDTS AND ITS APPLICATION

Toshihiro Kojima and Noriyuki Kawai  
Faculty of Engineering, Tamagawa University  
Tokyo 194-8610, JAPAN

### 1. INTRODUCTION

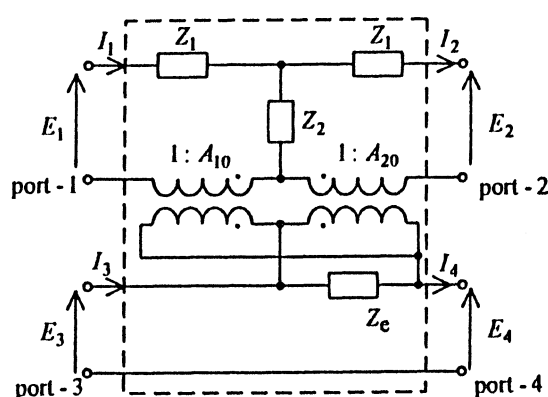
The higher impedance level of the SAW devices can be obtained by series connecting split IDTs, Yamamizu et al [1], Vandewege [2], Kojima and Shibayama [3].

In the present paper, we have derived a simple four-port equivalent circuit of an  $N$ -pair of IDT for series connection of IDTs by adding one more electric port to the three-port equivalent circuit using force factors, Kojima and Suzuki [4], Kojima and Yabuno [5]. From this circuit, we have derived the four-port transfer matrix which is very useful for series connection of IDTs. The individual elements of the matrix are expressed in closed and simple forms. Next, we analyzed a one-port SAW resonator composing of series connected IDTs and reflectors by using newly developed equivalent circuits and their transfer matrices. As one of applications of this type of resonators, the use for the element of broadband voltage controlled oscillator (VCO) is proposed. Finally, numerical calculation examples of the driving-point impedance for this type of resonators on  $\text{LiNbO}_3$  (128 Y,X) and the resonance characteristics including varactor diode for VCO are shown. The symbols used this paper are the same those used in the reference of Kojima and Yabuno [6], and they are listed again in Table I.

### 2. Equivalent four-port networks for series connection of IDTs

The four-port network theory by using the transfer matrices is known to be useful for analysis of series connection of bulk-acoustic-wave (BAW) transducers, Sittig [7].

In this section, the equivalent four-port circuit of an IDT having  $N$ -pair of finger pairs for series connection of electric terminals has been derived from the three-port equivalent circuit of an IDT using force factors [4], [5]. The circuit obtained here are shown in Fig.1. In this paper, the acoustic variables and impedances are converted into electrical variables and impedances [6]. In this figure, the connection of elements in electric ports is different from the case of the equivalent four-port circuits for parallel connection in ref.[6]. Fig.1 is the circuit for  $N$  being an integer, where  $A_{10}$  and  $A_{20}$  ( $A_{10} = -A_{20}$ ) are force factors. In this figure, the expressions for force factors  $A_{10}$  and  $A_{20}$  and impedance  $Z_e$  are given in eq.(3) described below. The  $F_s$  and  $\gamma_s$  are the image parameters of the unit cell of an IDT [5], and they are given again in Table II, since they are key parameters in the present paper.



$N$ : integer

$$Z_1 = \frac{R_0}{F_s} \tanh N\gamma_s, \quad Z_2 = \frac{R_0}{F_s} \operatorname{cosech} 2N\gamma_s$$

port-1, port-2 : acoustic port

(a) port-3, port-4 : electric port

Fig.1 Equivalent four-port circuit of an  $N$ -pair of IDT for series connection.

Table I Symbols and parameters

$k^2$ : electromechanical coupling factor  
 $v_0$ : surface wave velocity in the free region  
 $v_m$ : surface wave velocity in the metallized region  
 $r_v = \frac{v_0}{v_m}$ : velocity ratio  
 $G_0$ : acoustic characteristic admittance in the free region  
 $G_m$ : acoustic characteristic admittance in the metallized region  
 $R_0 = 1/G_0$ : acoustic characteristic impedance in the free region ( $G_0, G_m, R_0$ : in electrical system of unit)  
 $\tau = \frac{G_m}{G_0}$ : discontinuity factor  
 $l_m$ : width of a finger (or metal strip)  
 $l_g$ : width of gap between adjacent fingers (or metal strips)  
 $l_p = l_m + l_g$ : length of unit cell of IDT (or metal strip)  
 $l = 2l_p$ : periodic length of a finger pair  
 $\eta = \frac{l_m}{l_p}$ : metallization ratio  
 $G_s$ : conductance of losses due to the bulk-wave conversion at metal edges.  
 $B_s$ : susceptance of phase-shift due to the energy storage effect at metal gap boundary and piezoelectric shorting.  
 $H$ : thickness of a finger (or metal strip)  
 $\alpha_0$ : attenuation constant per unit length in the free region  
 $\bar{\alpha}_0 = \alpha_0 l$ : attenuation value per length  $l = 2l_p$   
 $\alpha_m$ : attenuation constant per unit length in the metallized region  
 $\bar{\alpha}_m = \alpha_m l$ : attenuation value per length  $l = 2l_p$   
 $C_s$ : capacitance for one pair of IDT  
 $C_{s0}$ :  $C_s$  for the case of  $\eta = 0.5$   
 $C_T = NC_s$  (capacitance for  $N$ -pairs of IDT)  
 $C_s = C_{s0} M_1(\eta)$        $M_1(\eta) = K(q_m) / K(q'_m)$   
 $f_{00} = \frac{v_0}{l}$ : (reference frequency)  
 $f_0 = \frac{1}{2} \left( \frac{l_g}{v_0} + \frac{l_m}{v_m} \right)^{-1} = \frac{1}{1 + \eta(r_v - 1)} f_{00}$ : (center frequency)  
 $f_c = \left( 1 - \frac{b_s}{\pi} \right) f_0 = \frac{1}{1 + \eta(r_v - 1)} \left( 1 - \frac{b_s}{\pi} \right) f_{00}$ : (actual center frequency)  
 $\Omega_w = \frac{f}{f_{00}}$ : reference normalized frequency  
 $\Omega = \frac{f}{f_0}$ : normalized frequency  
 $\omega_0 = 2\pi f_0$ ,       $\bar{\omega}_0$ : center angular frequency for  $\eta = 0.5$   
 $M_3(\eta) = K(1/\sqrt{2})/K(q_m)$ ,       $q_m = \sin \eta \frac{\pi}{2}$ ,       $q'_m = \cos \eta \frac{\pi}{2}$   
 $K(q_m)$ ,  $K(q'_m)$ : the complete elliptic integral of the first kind with  $q_m$  and  $q'_m$  respectively  
 $K(1/\sqrt{2})$ : the complete elliptic integral of the first kind with  $q_m = q'_m = 1/\sqrt{2}$  ( $\eta = 0.5$ )  
 $\hat{G}_s = \frac{4}{\pi} k^2 \bar{\omega}_0 C_{s0} N^2$  (reference conductance),  $\hat{G}_s = 8N^2 G_0 / \{M_3(\eta)\}^2$

3. Four-port transfer matrix for series connection of IDT

From the circuits in Fig.1, the relation between the input variables ( $E_1, I_1, E_3, I_3$ ) and the output variables ( $E_2, I_2, E_4, I_4$ ) can be obtained by the straightforward circuit analysis. The results are given by eq.(1), where  $[b_{ij}]$  is the transfer matrix.

Table II Image parameters ( $Y_s, \gamma_s$ ) \*

$Y_{is} = G_0 F_s$ ,  $F_s = \sqrt{pq}$  Image admittance  
 $\gamma_s = \alpha + j\beta = 2 \tanh^{-1} \sqrt{\frac{p}{q}}$  Image transfer constant  
 where  

$$p = \frac{\tanh \phi + \tau \tanh \frac{\psi}{2} + y_s}{1 + \tanh \phi \cdot \left( \tau \tanh \frac{\psi}{2} + y_s \right)}$$

$$q = \frac{\tanh \phi + \tau \coth \frac{\psi}{2} + y_s}{1 + \tanh \phi \cdot \left( \tau \coth \frac{\psi}{2} + y_s \right)}$$
 Complex transit angle  

$$\phi = \left( \alpha_0 + j \frac{\omega}{v_0} \right) \frac{l_g}{2} = \frac{1}{4} (1 - \eta) \bar{\alpha}_0 + j \frac{\pi}{2} (1 - \eta) \Omega_w$$

$$\psi = \left( \alpha_m + j \frac{\omega}{v_m} \right) l_m = \frac{1}{2} \eta \bar{\alpha}_m + j \pi \eta \tau_v \Omega_w$$

$$Y_s = G_s + jB_s, \quad y_s = \frac{Y_s}{G_0} = g_s + jb_s$$

\* This Table is used both for an IDT and a reflector.

$$\begin{bmatrix} E_1 \\ I_1 \\ E_3 \\ I_3 \end{bmatrix} = \begin{bmatrix} b_{11} & b_{12} & 0 & b_{14} \\ b_{21} & b_{22} & 0 & b_{24} \\ b_{31} & b_{32} & 1 & b_{34} \\ 0 & 0 & 0 & 1 \end{bmatrix} \begin{bmatrix} E_2 \\ I_2 \\ E_4 \\ I_4 \end{bmatrix} \quad (1)$$

where

$$\left. \begin{aligned} b_{11} &= b_{22} = \frac{Z_1 + Z_2(1 + s_a)}{Z_2(1 - s_a)} \\ b_{12} &= \frac{1}{Z_2(1 - s_a)} (Z_1 + 2Z_2)(Z_1 + 2s_a Z_2) \\ b_{14} &= b_{32} = \frac{s_a(Z_1 + 2Z_2)}{A_{10}(1 - s_a)}, \quad b_{21} = \frac{1}{Z_2(1 - s_a)} \\ b_{24} &= b_{31} = \frac{s_a}{A_{10}(1 - s_a)}, \quad b_{34} = \frac{Z_e}{1 - s_a} \end{aligned} \right\} (2)$$

$$\left. \begin{aligned} s_a &= \frac{A_{10}^2 Z_e}{Z_2}, \quad A_{10} = -A_{20} = \tanh \frac{\gamma_s}{2} \cdot \tanh N\gamma_s \\ Z_e &= (j\omega C_T + Y_{3m})^{-1} \\ Y_{3m} &= 2G_0 F_s \tanh \frac{\gamma_s}{2} \cdot \left[ 2N - \tanh \frac{\gamma_s}{2} \cdot \tanh N\gamma_s \right] \end{aligned} \right\} (3)$$

In eq.(2),  $Z_1$  and  $Z_2$  are the impedances in acoustic ports of Fig.1, and they are given by

$$Z_1 = \frac{R_0}{F_s} \tanh N\gamma_s, \quad Z_2 = \frac{R_0}{F_s} \operatorname{cosech} 2N\gamma_s \quad (4)$$

The calculation of the determinant of the transfer matrix  $b_{ij}$  results in;

$$|b_{ij}| = 1 \quad (5)$$

#### 4. Analysis of one-port SAW resonator

we have analyzed the one-port SAW resonators composing of series connected IDTs and shorted metal strip arrays (SMSA), as shown in Fig. 2. As the figure connecting electrically IDTs in series, Fig.2(a) shows practically preferable electrode pattern. Fig.2 (b) shows the reference planes of an IDT and a reflector. Here, the structure and the characteristics of the reflector on both sides of IDT are assumed to be symmetrical. The number of electrode pairs of IDT is  $N_1$  and  $N_2$  (here,  $N_1 = N_2$ ,  $N = 2N_1$ ). The number of strips of the reflector is  $N_s$ , the distances between two IDTs is  $d_c$ , and the distance between IDT and the reflector is  $d_R$ .

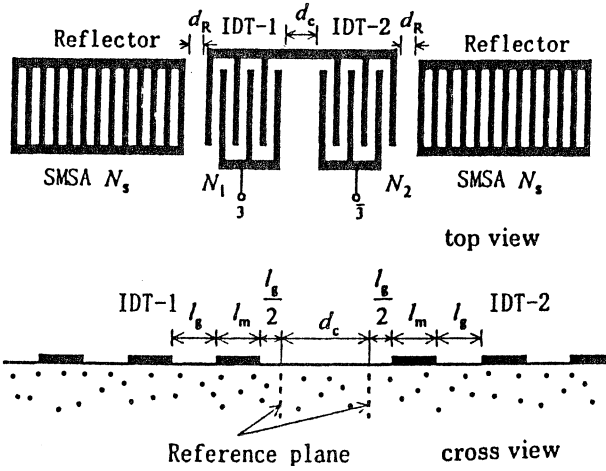
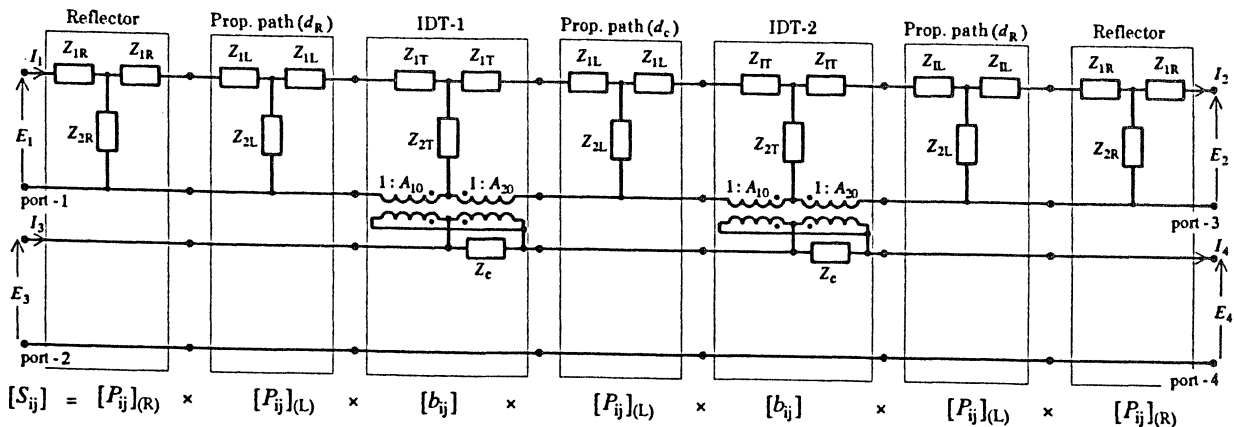


Fig.2 Configuration of one-port SAW resonator using series connected IDTs.



$$Z_{1T} = \frac{R_0}{F_s} \tanh N\gamma_s, \quad Z_{2T} = \frac{R_0}{F_s} \operatorname{cosech} 2N\gamma_s, \quad (N_1 = N_2 = N)$$

$$\left. \begin{aligned} Z_{1R}, Z_{2R}, Z_{1L}, Z_{2L} & \text{ see ref. [6]} \\ A_{20} = -A_{10} \text{ (Force factor)} \\ Z_c & \end{aligned} \right\} \text{ see eq. (3)}$$

Fig.3 Equivalent circuit of one-port SAW resonator using series connected IDTs.

By combing each equivalent circuit of the IDTs, propagation paths and reflectors, the entire equivalent circuit of the SAW resonator can be obtained, as shown in Fig.3, where the equivalent circuit of IDT is given in Fig.1 and the equivalent circuits of path and reflector are given in Fig.2 in ref.[6].

If we put  $S_{ij}$  as the entire transfer matrix of the resonator,  $S_{ij}$  can be obtained by cascading connection of the matrix for each element :

$$[S_{ij}] = [P_{ij}]_{(R)} [P_{ij}]_{(L)} [b_{ij}] [P_{ij}]_{(L)} [b_{ij}] [P_{ij}]_{(L)} [P_{ij}]_{(R)} \quad (6)$$

where  $[b_{ij}]$ ,  $[P_{ij}]_{(R)}$  and  $[P_{ij}]_{(L)}$  are the transfer matrixes for the IDT, the reflector and the free surface distance, respectively. The elements of  $[b_{ij}]$  are given by eq.(2) and  $[P_{ij}]_{(R)}$  and  $[P_{ij}]_{(L)}$  are given in Table III of ref.[6]. The relation between the input variables ( $E_1, I_1, E_3, I_3$ ) and the output variables ( $E_2, I_2, E_4, I_4$ ) of the entire equivalent four-port circuit of the resonator of Fig.3 is given by,

$$\begin{bmatrix} E_1 \\ I_1 \\ E_3 \\ I_3 \end{bmatrix} = \begin{bmatrix} S_{11} & S_{12} & 0 & S_{14} \\ S_{21} & S_{22} & 0 & S_{24} \\ S_{31} & S_{32} & 1 & S_{34} \\ 0 & 0 & 0 & 1 \end{bmatrix} \begin{bmatrix} E_2 \\ I_2 \\ E_4 \\ I_4 \end{bmatrix} \quad (7)$$

where  $S_{22} = S_{11}$ ,  $S_{14} = S_{32}$  and  $S_{24} = S_{31}$  (8)

Here, we assumed that boundary conditions at the acoustic ports (port-1 and port-2) are given by,

$$E_1 = -R_0 I_1, \quad E_2 = R_0 I_2, \quad E_4 = 0, \quad I_4 = I_3 \quad (9)$$

where  $R_0$  is characteristic impedance ( $R_0 = 1/G_0$ ).

By applying eqs.(8) and (9) in eq.(7), and analyzing the driving-point impedance of the resonator of Fig.2,  $Z^{(E)} = E_3 / I_3$ , the following equation can be obtained.

$$Z^{(E)} = S_{34} - \frac{(S_{14} + S_{24}R_0)^2}{S_{21}R_0^2 + 2S_{11}R_0 + S_{12}} \quad (10)$$

## 5. Numerical calculations of $Z^{(E)}$

In this section, we present numerical calculations of  $Z^{(E)}$  of SAW resonators on  $\text{LiNbO}_3(128^\circ \text{Y,X})$  by use of newly developed expression eq.(10).

The one-port SAW resonators investigated in this section consist of series connected IDTs ( $N_1 = N_2 = 15$  pairs, the number of total pair is 30 pairs) and SMSA reflectors ( $N_s = 120$  sections). Regarding the structure parameters, the values are as follows. The metallization ratio  $\eta$  ( $\eta_I$ : for IDT,  $\eta_R$ : for SMSA) is  $\eta_I = \eta_R = 0.5$  (standard value), Aluminum thickness  $H$  is  $H/l_p = 0.01$ , and the distance  $d_R$  between IDT and reflector is  $d_R/l = 0.375$ . And regarding the equivalent circuit parameters ( $\tau_v, \tau, b_s$ ) required for the calculations, Koshiba's values calculated by FEM method [8] were used. Propagation loss  $\tilde{\alpha}_0$ ,  $\tilde{\alpha}_m$  and scattering loss  $g_s$  are assumed to be  $\tilde{\alpha}_0 = \tilde{\alpha}_m = 10^{-3}$  dB (this value corresponds to the attenuation per wavelength) and  $g_s = 0$ , respectively.

First of all, Fig.4 shows the frequency response of  $Z^{(E)}$  ( $= |Z^{(E)}| \angle \theta$ ) of SAW resonators for two cases of the short distance  $d_c$  between IDTs. The magnitude  $|Z^{(E)}|$  is normalized by  $\hat{R}_a (= 1/\hat{G}_a)$  and the frequency  $f$  is normalized by  $f_{00}$ . Solid line shows  $d_c = 0$ , while dotted line shows  $d_c/l = 0.125$ . After this, we refer to "case 1" as the former and "case 2" as the latter. Next, Fig.5 shows the frequency responses of the resonator for two cases of the long distance  $d_c$ . The solid line (case1) shows  $d_c/l = 10.00$ , while dotted line shows  $d_c/l = 10.30$ . These

examples are the case of resonators having more pair of fingers than usual case.

In general, such resonators with many finger pairs have the advantage of high  $Q$  and low capacitance ratio, but have the disadvantage of large spurious response (longitudinal mode) near the main resonance. However, if we set a suitable distance  $d_c$  between split IDTs as shown Fig.2, we can control the resonance characteristics and suppress the spurious response to some content. In the case 1 of Figs.4 and 5, the large spurious response ( $\theta > 0$ ) occurs in the higher frequency region than the main resonance. However, in the case 2 of Figs.4 and 5, this large spurious response can be suppressed lower than case 1.

The phase characteristic in spurious region is desired to be negative (the negative phase ( $\theta < 0$ ) means capacitive) for the use of oscillator application. The impedance level  $Z^{(E)}$  of case 1 (the case dividing an IDT into two equal IDTs) is just 4 times (12dB) as large as that of the resonator before dividing. The Tables III and IV shows the comparison of the characteristics of two cases, respectively. The comparison items are the resonance and antiresonance frequencies ( $f_s, f_p$ ), the resonance and antiresonance quality factors ( $Q_s, Q_p$ ), capacitance ratio  $r_c$  and the figure of merit  $M$  (the symbol  $\Omega_s$  and  $\Omega_p$  denote  $\Omega_s = f_s/f_{00}$ ,  $\Omega_p = f_p/f_{00}$ , and  $M = Q_s/r_c$ ).

Finally, we have investigated the possibility of application to voltage controlled oscillator (VCO) Here, the practical case of series connection of the SAW resonator and the varactor diode is investigated. Fig.6 shows the relation between the resonance frequency including varactor diode and the capacitance of varactor diode. In this figure,  $\delta_v$  is normalized capacitance. that is  $\delta_v = C_v / C_T$ , where  $C_v$  is the capacitance of varactor diode and  $C_T$  is the capacitance of usual SAW resonator ( $N=30$ , not dividing). In Fig 6. case 1 shows the characteristic of the use of the resonator of case 1 in Fig.4, while case 2 shows the characteristic of the use of usual SAW resonator ( $N=30$ , not dividing). From this figure, it is apparent that the value of capacitance of varactor diode for case 1 is 1/4 times as low as that for case 2, when they are compared at the

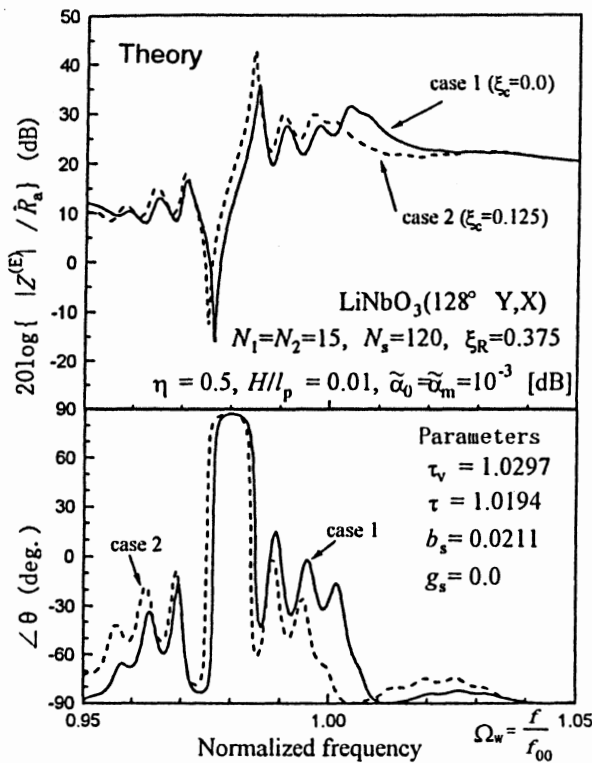


Fig.4 Frequency responses of  $Z^{(E)}$   
(case-1 :  $d_c = 0$ , case-2 :  $d_c = 0.125 l$ )

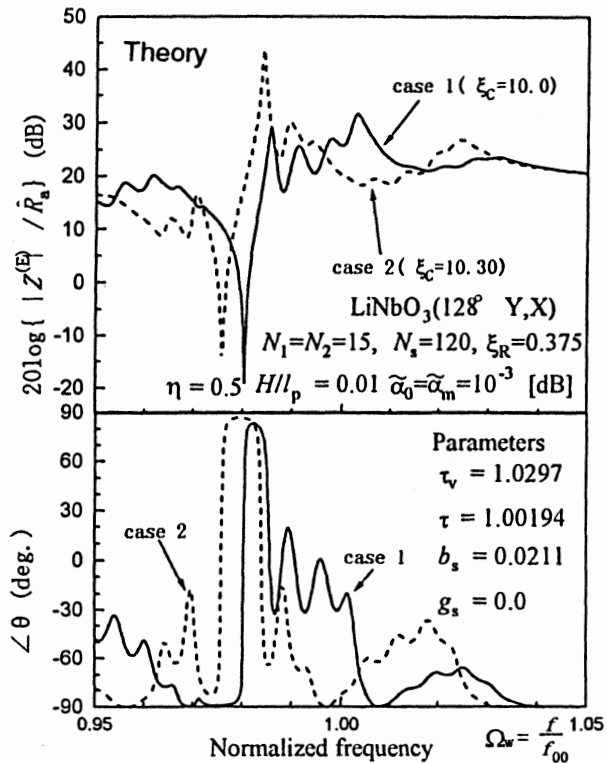


Fig.5 Frequency responses of  $Z^{(E)}$   
(case-1:  $d_c = 10.0 l$ , case-2 :  $d_c = 10.3 l$ )

Table III Evaluation for the resonator of Fig.4.

	case 1	case 2
$\Omega_s$	0.9765	0.9752
$Q_s$	3150	2480
$\Omega_p$	0.9850	0.9842
$Q_p$	955	1390
$r_c$	57.2	54.4
$M$	55.1	45.5

Table IV Evaluation for the resonator of Fig.5.

	case 1	case 2
$\Omega_s$	0.9804	0.9775
$Q_s$	4806	3148
$\Omega_p$	0.9856	0.9840
$Q_p$	768	1598
$r_c$	93.4	59.9
$M$	51.4	52.6

$$\xi_c = d_c / l$$

$$\xi_R = d_R / l$$

$$N_1 = N_2 = 15$$

$$N_1 + N_2 = 30$$

same resonance frequency  $f_s$ , since the static capacitance of case 1 is 1/4 times as low as that of case2.

In Fig. 6, the frequency band between the anti-resonance frequency  $f_p$  and the resonance frequency  $f_s$  is the important inductive region for the VCO.

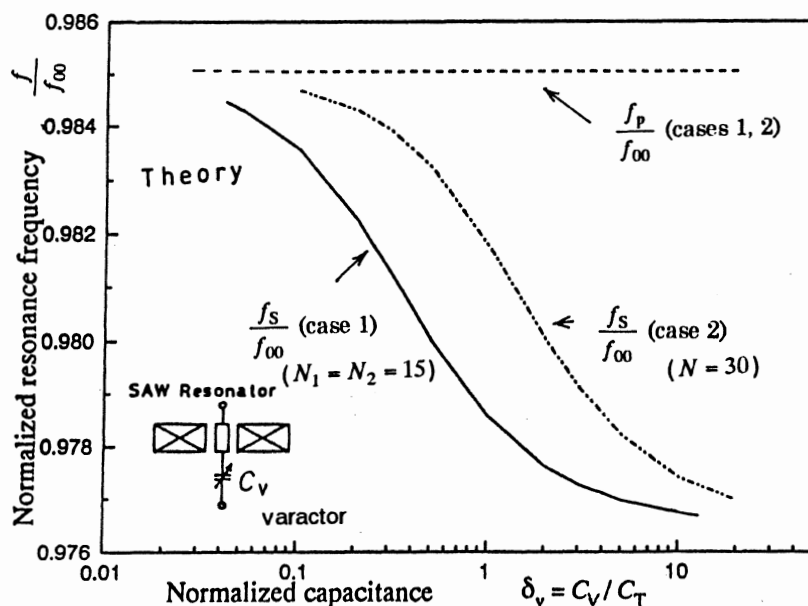


Fig. 6 Relation between the resonance frequencies  $f_s$ ,  $f_p$  and the capacitance  $C_v$  of varactor diode.

## CONCLUSION

The results of the analysis of the SAW resonators using series connected IDTs, as newly developed by the authors, are simple and useful for the design of the resonator, although they contain a large number of parameters. This type of resonator described in the present paper should find many applications. Particularly, It is practically useful for a broad band VCO, since it has a high figure of merit (a high Q and a low capacitance ratio) and a lower static capacitance than the conventional SAW resonator. If we set the long distance  $d_c$  between IDTs as the sensitive region, we can apply this type of resonator to the sensor.

## ACKNOWLEDGMENT

The authors are deeply grateful to Prof. Hiroaki Sato, Prof. Masao Takeuchi of Tamagawa University and Prof. Kazuhiko Yamanouchi of Tohoku University for useful discussions. And the author would like to thank to Dr. Tatsuo Suzuki who has always remained the good advisor for the authors.

## REFERENCES

- [1] S.Yamamizu, N.Chubachi and Y. Kikuchi, 1974, "Acoustic Surface Wave Transducers with Divided Interdigital Electrodes Connected in Series", Jpn. Jn. Acoust. Society. 541-548 [in Japanese].
- [2] J.Vandewege, P.E. Lagasse and T.Naten, 1978, "Distributed Feedback Acoustic Surface Wave Resonators", Proc.IEEE Ultrasonics Symps., 438-441.
- [3] T.Kojima and K.Shibayama 1985, "Investigation of SAW Resonators", Proc. Jpn.Acoust.Society,629-630 [in Japanese].
- [4] T.Kojima and T.Suzuki, 1994," Fundamental Equations of Electro-Acoustic Conversion for an IDT Using Force Factors",1994, Proc.IEICE Fall Conf.1-224 [in Japanese].
- [5] T.Kojima and R.Yabuno,1994, "Equivalent Four-port Networks Using Force Factors for SAW Interdigital Transducers", Proc.IEEE Ultrasonics Symps., 227-232.
- [6] T.Kojima and R.Yabuno, 1995, "A Simple Analysis of SAW Resonators by Using Force Factors" Proc.IEEE Ultrasonics Symps. 329-334.
- [7] E.K.Sittig, 1967, "Transmission parameters of Thickness Driver Piezoelectric Transducers Arranged in Multilayer Configurations", IEEE Trans. on Sonics & Ultrason. SU-14,167-174.
- [8] M.Koshiba and S.Mitobe, 1988, "Equivalent networks for SAW grating" IEEE Trans. Ultrason. Ferro. Freq. Contr. 35, 531-535.

## SAW CONVERSION IN CHIRP PULSE EXPANDERS AND COMPRESSORS

Valery F. Dmitriev, Igor S. Mitrofanov

Avangard-Elionica Co. Ltd, 195271 ,St.Petersburg, Russia

The experimental investigation of the possibility of forming a chirp-signal of great duration with the low phase distortion by the cascade of a DDL on the SAW has been performed. On the base of the summation model of the partial reflected waves the expressions for the calculation of the frequency responses a DDL with the slanted topology are presenting. The experimental results on forming and compression of the chirp-signals with the central frequency of 150 MHz, by 40 MHz bandwidth, by duration of 150 mks and 300 mks at the time-bandwidth product of the chirp-signals 6000 and 12000 accordingly are presenting. For the chirp-signals by the duration of 150 mks and 300 mks the sidelobe level of the compressed signals -25...-30 dB and - 22...-30 dB accordingly has been received.

### 1. INTRODUCTION

Aside from well known using of the SAW dispersive delay lines (DDL) in radars, important using of the DDL there is in dispersive receivers and spectrum analyzers. Fourier-processor is a main module which define parameters of the dispersive receive the spectrum analyzer, but their parameters, in turn, is defines by DDL.

A radar range of action and a radar resolution, or a frequency resolution and the number of points of resolution in a dispersive receiver or a spectrum analyzer are straight proportional to the duration and the bandwidth of the chirp-signal. For this reason at present the prevailing trend in the development of SAW devices is being the increasing of the duration and bandwidth of the chirp-signal.

Now there are two of the main ways of increasing of the chirp-signal duration, formed by the DDL. The first is increasing of a length of the piezoelectric substrate and using of a substrate. The second is using of a substrate with the low velocity. However, the length of substrates are limited by technical possibilities on growing the monocrystal and processing piezoelectric substrates. For instance, the DDL with the 100 mks dispersive delay time is possible to realize on the substrate of the LiNbO<sub>3</sub> YZ-cut [1]. The using of the material with the relatively small SAW velocity, (such as bismuth germanat) is acceptable only for the relatively low-frequency devices [2], since the smaller velocity in the substrate material expects the smaller size elements of the topology. Taking into account the restrictions which has been considered, it is of interest to research cascade connection of several DDLs as a way of the forming a chirp-signal of great duration.

### 2. METHOD OF FORMING A CHIRP-SIGNAL

The YZ-cut LiNbO<sub>3</sub> is the most suitable piezoelectric material for broadband DDL. At

present an industrial fabrication of LiNbO<sub>3</sub> substrates by the length up to 260 mm, that corresponds to 120 mks of a chirp-signal duration are available. The DDL fabrication forming the chirp-signal by 100 mks duration on the LiNbO<sub>3</sub> substrate by the length of 250 mm has been reported in [1]. However, the DDL presented in [1] had the essential distortion of the amplitude and phase responses. The unflatness of the frequency response has been more than 4 dB and the deviation of the phase response from square-law (RMS) has been require to perform the phase compensation for acceptable compression of the chirp-signal.

The crystalline quartz substrates are suitable only for narrow-band devices forming a chirp-signal of great duration. Main parameters of broadband DDLs (the amplitude unflatness and RMS deviation of the phase) in the event of using the quartz substrate are degraded. For instance, the DDL being developed on the quartz substrate and forming a chirp-signal of 38 mks duration, of 50 MHz bandwidth and 125 MHz of central frequency have been presented in [3]. The DDL had unevenness of amplitude response ~ 15 dB and RMS ~ 10°. Should be noted that the frequency response ripples < 1dB and RMS < 3° are necessary for compression of a chirp-signal with the sidelobe level 28-30 dB.

The promising material for the DDL forming the chirp-signal of a great duration is bismuth germanium (BGO). About the development of the DDL forming the chirp-signal of 140 mks duration, of 20 MHz bandwidth and centered at the 51 MHz has been reported in [2]. However, parameters of the compressed signal do not present in [2]. BGO is the extremely not technological material, that is expressed in comparatively low of the chemical and thermal stability. Moreover, as far as the SAW velocity of the BGO is approximately one half of the SAW velocity in the LiNbO<sub>3</sub>, for the DDL with the 150 mks chirp-signal duration centered at the 150 MHz, the topology of a DDL includes more than 12000 elements by the size about 2.5 mkm, which should be performed with the accuracy better, than 0.1 mkm on the length of the substrate 150 mm. The technological problems do not allow to get good parameters of the DDL of such difficulty level. In connection with restrictions of the DDL fabrication on one substrate which had been considered above, the perspective technique of the forming the broadband chirp-signal by the duration of more than 80 mks can be proposed a chirp-module with cascade connection several of the DDL. In this case the chirp-signal is formed by several DDLs connected in series. The amplifier is placed between the DDLs for matching and of the compensation of

the insertion losses. The duration of the chirp-signal formed by such a module will be equal to the total durations of the chirp-signal formed by each DDL and composed the chirp-module. The central frequency and bandwidth of each DDL must be equal to each other and correspond to required values. The choice of the chirp-signal duration which is formed by the single DDL, is based on the results of calculations but taking into account the technological equipment possibilities which are using. So, at the requirement to the sidelobe level of the compressed signal less than 30 dB or of the accuracy of the Fourier transformation better than 3 %, the ripples of the frequency response must be less than 0.5 dB, and  $RMS < 3^\circ$ . Besides, the output signal of each DDL must exceed a noise level.

When forming a chirp-signal the total losses in the DDL is equal to a sum of  $K(\omega)$  (DDL transduction losses in frequency domain and are being calculated in following section) and of losses of the expansion, in accordance with the expansion of input pulse in the DDL. The losses for the first DDL of the module on the expanding of the input pulse are equal  $10 \lg(BT)$ , where B is a bandwidth and T is a dispersive delay time in the DDL. The losses on the expanding of the input pulse for the following DDLs will not exceed 6 dB. The value of T should be chosen taking into account the inequality  $T < T_{max}$ , where  $T_{max} [U_{inp} K(\omega_0) / (S K_N E_N)]^2 / B$ , where  $U_{inp}$  is the amplitude of the input pulse, S is the signal to noise ratio on the input of the amplifier, which is required,  $K_N$  is the noise factor of the amplifier,  $E_N$  is the input noise of the amplifier.

The gain factor of the amplifier should be chosen so, that the amplitude of the signal on the output of the next DDL of the module was more, than on the output of the previous DDL. Theoretical and experimental data analysis has show that for the chirp-module with parameters which are required, dispersive delay time in single DDL of 70... 80 mks, should be considered as optimum.

### 3. DESIGN THE SLANTED DDL

The essential influence upon the parameters of a broadband DDL with great duration of a chirp-signal renders a process of the SAW conversion, bringing about the degradations of a DDL frequency response. Here and hereinafter under the SAW conversion shall understand a transformation of the part of power, which falls on RA grooves, into the bulk waves. The result of the manifestation of the SAW conversion by grooves RA are increasing of the insertion losses in the DDL and changing of the frequency response envelope. A slanted topology of a DDL is allows somewhat weakening an undesirable the SAW conversion at the passing of a SAW through the RA. In the slanted topology the channels of spread and reflection a SAW of different frequencies are space divided, due to that the SAW of the certain frequency interacts mainly with the area RA, where occurs a reflection of main part of energy a SAW of given frequency.

The calculation of the  $K(\omega)$  of a DDL with the slanted topology is based on well developed of the

theory a DDL with in-line topology and includes calculations of active parts -  $G_1(\omega)$ ,  $G_2(\omega)$  and of reactive parts -  $Y_1(\omega)$ ,  $Y_2(\omega)$  of the input and output transducers impedances as well as transfer function of reflective array. The calculations of  $G_1(\omega)$ ,  $G_2(\omega)$ ,  $Y_1(\omega)$ ,  $Y_2(\omega)$  DDL with the slanted topology is based on the model in which the IDT and RA are divided on the channels with the help of some principle, suitable for the calculations (for instance, on the  $N_K$  equal parts). Then, by summarizing of the partial conductances of radiating in all  $N_K$  channels, may be received

$$G_1(\omega) = \sum_{i=1}^{N_K} G_{1i}(\omega), \quad Y_1(\omega) = \sum_{i=1}^{N_K} Y_{1i}(\omega), \quad (1)$$

$$G_2(\omega) = \sum_{i=1}^{N_K} G_{2i}(\omega), \quad Y_2(\omega) = \sum_{i=1}^{N_K} Y_{2i}(\omega), \quad (2)$$

where  $G_1(\omega)$ ,  $G_2(\omega)$ ,  $Y_1(\omega)$ ,  $Y_2(\omega)$  is the partial active and reactive parts of the radiating conductances in i-th channel, accordingly, for the input IDT (subscript 1) and for the output IDT (subscript 2) and are calculated as for usual IDT with the aperture equal to the aperture of channel. The DDL transduction losses in the frequency domain may be received from the conditions of matching on the input and output IDT:

$$K_1(\omega) = 2 G_G G_1(\omega) / \{ [G_G + G_1(\omega)]^2 + Y_1(\omega) \}, \quad (3)$$

$$K_2(\omega) = 2 G_G G_2(\omega) / \{ [G_N + G_2(\omega)]^2 + Y_2(\omega) \}, \quad (4)$$

where  $G_G, G_N$  is the conductances of the generator and load, accordingly. The partial radiating conductances are defines as the part of the power which are led to the DDL and then are being sended in the i-th channel. Then, from the conditions of the matching IDT on the input and output, the transfer function of the channel may be written as

$$K(\omega) = 2 G_G G_1(\omega) K_{RA} K_2(\omega) / \{ [G_G + G_1(\omega)]^2 + Y_1(\omega) \}, \quad (5)$$

Then, for the DDL transfer function may be received

$$K(\omega) = \sum_{i=1}^{N_K} K_i(\omega) + TL(\omega), \quad (6)$$

where  $TL(\omega)$  is the DDL propagation losses. The calculation of the  $K_{RA}(\omega)$  by means of the analytical expression [4] allows only evaluate the frequency response of the slanted DDL.

The calculation of the  $K_{RA}(\omega)$  on the base of the model of summing of the partial reflected waves, allows to reveal a some of the essential particularities of the frequency responses of DDL, which will be considered below. The summing of the partial reflected waves, brings about the expression for the transfer function of the  $i$ -th channel:

$$K_{RA}(\omega) = \sum_{n=N_i}^i \sum_{m=N_i}^{M_i} \gamma_{nm} \rho_m \rho_n \xi_n \xi_m \exp[-i\beta(z_n + z_m + k_v x_n - k_v x_m)], \quad (7)$$

where in each channel from first groove of the channel -  $N_i$  up to the last groove of channel -  $M_i$ , the SAW passing through the RA are being summed,  $\gamma_{nm}$  is the coefficient of the overlapping of the  $m$ -th and  $n$ -th grooves in the  $i$ -th channel;  $\rho_n$ ,  $\rho_m$  is the reflecting factors defined by usual method;  $\xi_m$  and  $\xi_n$  is the coefficients of passing up to the  $m$ -th and  $n$ -th grooves accordingly;  $z_n$ ,  $x_n$ ,  $z_m$ ,  $x_m$  is the coordinates of the centre of the  $n$ -th and  $m$ -th grooves accordingly;  $\beta = \omega/v_z$ ,  $k_v = v_x/v_z$ ,  $v_x$ ,  $v_z$  is the SAW velocities in  $x$  and  $z$  directions, accordingly. During the passing of the SAW through the RA takes place a process of the reflecting and conversion. Then, with provision for conversions of the part of the SAW energy into the bulk waves, the coefficients of the passing are equals:

$$\xi_m = \prod_{k=N_i}^m (1 - \zeta_k) [1 - (\rho_k)^2]^{1/2}, \quad (8a)$$

$$\xi_n = \prod_{k=N_i}^n (1 - \zeta_k) [1 - (\rho_k)^2]^{1/2}, \quad (8b)$$

$$\zeta_k = 1 - \exp[-\eta_k(\omega) (h_k/\lambda)^2], \quad (9)$$

where  $\eta_k(\omega)$  is coefficient, which defines the part of the power transformed into the bulk wave, when the SAW is passing through the  $h$ -th groove,  $h_k$  is the depth of the  $k$ -th groove,  $\lambda$  is the wavelength of a SAW on the frequency  $\omega$ . The calculation method of the frequency-dependent factor  $\eta(\omega)$  was given in [5].

The essential moment at the deduction of the equations (5)-(7) is the following. The more rigorous model is expects that to the expression (6) is necessary to add a summation by over all overlaid channels. However, this is doing an expression for  $K(\omega)$  unfitted for the practical using because of the greater expenses of the machine time (calculation of one point of the frequency response on PC AT 486DX4-100 will occupy more than 8 hours for the DDL with parameters which are considered). Together with that fact at the determination of the

$\gamma_{nm}$ , the good results are gives an account of the channels interactions by means of using full grooves aperture (not limited by edges of channel).

The phase response of the DDL will be define as sum of the phase responses of the reflective array and IDT:

$$\Phi(\omega) = \arctg \left[ \frac{\text{Im} \left\{ \sum_{i=1}^{N_K} K_{RA}(\omega) \right\}}{\text{Re} \left\{ \sum_{i=1}^{N_K} K_{RA}(\omega) \right\}} \right] + \Phi_O(\omega), \quad (10)$$

where  $\Phi_O(\omega)$  is the IDT phase response.

After choice of the preliminary parameters slanted DDL, analysis by means of equations (1)-(9), should be done. In the process of the calculations of the frequency response of the DDL a required depth profile and(or) aperture of the grooves along the RA which has gives a required envelope of the frequency response should be defined. The calculation of the phase response by means of the equation (10) is required for the checking a DDL dispersive curve.

#### 4. THE RESULTS OF INVESTIGATIONS OF THE MODULE

For forming a chirp-signal by the duration of 150 mks the composite variant of a chirp-module was chosen. The chirp-module had included the two DDL-F by the 75 mks of the dispersive delay time each. Between the DDL-Fs and after the second DDL-F the amplifiers were using for the compensation of the insertion losses. Each of the amplifier has the 60 dB gain, 50...210 MHz range of the frequencies, the unevenness of the gain in the bandwidth of DDL-F not more than 0.3 dB and the noise factor 2.5 dB. The amplifiers had provided by adjustment of the amplification within 10 dB and by the possibility of the correction of the gain in the frequency domain for the equalizing the envelope of the chirp-signal.

The most complex chirp device, which mainly define the finished parameters of the compressed signal is DDL-F.

The particularities of designing and fabricating the DDL-F are considered hereinafter. The DDL-F is forming chirp-signal by duration of 75 mks centered at 150 MHz and with the bandwidth of 40 MHz. The slanted topology of the DDL-F and the LiNbO3 YZ-cut as the substrate were chosen as most suitable for such a device. When the design of the slanted IDT has performs exactly, frequency response of the slanted IDT has a square-wave form. The frequency response of the slanted RA with the constant depth of the grooves and with the aperture corresponding to the slanted IDT is increasing with the increasing of the frequency. For the DDL-F which is considered the unevenness of the RA frequency response is reaches 12 dB. The unevenness of the frequency response of the RA are defines, mainly, three factors: increasing the reflection of the grooves with increasing of the

frequency; the conversion losses of the RA (transformation of the part of the SAW energy into the bulk waves) and the propagation losses of a SAW. For the equalizing of the noted unevenness of the frequency response a DDL-F with the negative slopping of the dispersive response is possible two ways. Changing of the grooves depth along the RA is the first way. The using an additional apodization of the aperture RA is the second way. The preliminary calculations by means of equations (1) - (10) have show that of the linear changing of an aperture of 3 times insufficiently for the equalizing a frequency response of the DDL-F with the constant depth of grooves. The remaining unevenness of the frequency response of the monotonous nature ( the linear slopping ) is about 3-4 dB. Changing of the RA aperture more than in 3 times is not reasonable, since it is brings about the increasing of the insertion losses more than 50 dB. The best results ( smaller unevenness of a frequency response and RMS) should be expected in the event of using of changing along RA depths of the grooves. This way is allows to receive minimum insertion losses in the DDL-F, but this one technologically more difficult. The calculation analysis according to equations (1) - (10) have been showed that the main influence upon the form of a frequency response has the two factors, connected between itself. The correspondence of the received in the process of the ion etching of the RA grooves depth profile to the required linear law is the first factor. The second factor is a conversion of a SAW into a bulk waves. The more the depth of grooves, the more is the influence of the conversion, but the less is the distortion of a frequency response, connected with the deviation of the groove depth from the required linear law. The effects of conversion may be reduced up to the acceptable level by the choice of the grooves depth from 0.08 mkm - near IDT to 0.16 mkm - in the end RA. The results of the calculation by means of equations (1)-(10) are submitted in Fig. 1,a. The results of measurement of the amplitude and phase responses such DDL-F are submitted in Fig.1,b. The ripples of the amplitude response is  $\pm 0.5$  dB, and the RMS of the phase response is  $2.5^\circ$ . The linear law of the grooves depth profile is accepted at the calculations. In this case the resultant a frequency response an up-chirp is the most close to the desired square-wave form. Moreover in this case the monotonous slope of a frequency response and the peak on the high-frequency end of a frequency response are absent (both take place in the case of the equalizing the frequency response by means of the changing an aperture of the RA). However, since the absolute values of the grooves depths are small, the small deviations of the depth of the grooves from the linear law result in the significant unevenness of a frequency response. Should be noted, that is essential not only the value of the deviation of the grooves depth, as well as the form of the deviation. So, deviation of the type "step" brings about the sharp peak on the frequency response with total unevenness about 6 dB.

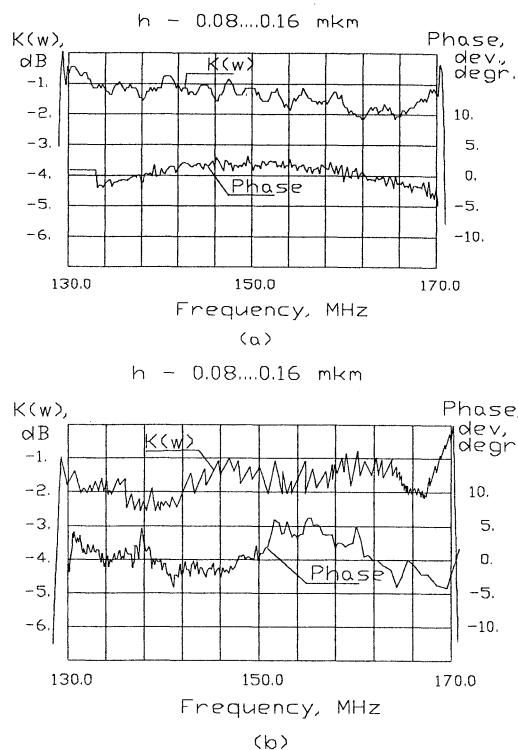


Figure1: Frequency responses of the DDL-F:  
a-calculated, b-measured

Resulting the amplitude and phase responses of a modula are equal to the sum of the corresponding responses of the up-chirps and amplifiers. The results of measurements of the amplitude and phase responses of the module are presented in Fig.2. The ripples of the amplitude response have not exceed  $\pm 0.7$  dB, and the RMS is  $4.4^\circ$ . The module forms a chirp-signal by the 1V amplitude, by the 150 mks duration, by the 40 MHz bandwidth and centered at the frequency of the 150 MHz under the exciting of the module by the short videopulse by the amplitude of  $\sim 4$  V and by the duration of 3 ns. The envelope of a chirp-signal repeats all the particularities of a frequency response and unevenness of the chirp-pulse amplitude corresponds to the unevenness of the amplitude response of the module (Fig.2).

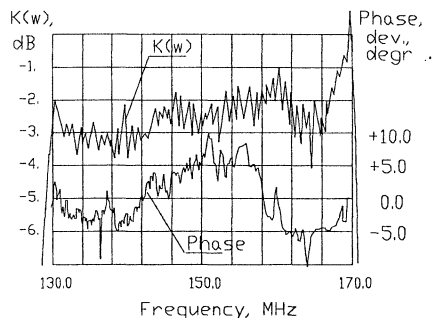


Figure2: Frequency responses of the chirp-module,  
forming the chirp-signal by duration of 150 mks.

The chirp-signal duration may be increased up to 300 mks. In order to receive such a chirp-signal quite sufficiently to connect two a chirp-module which have been presented in series. In this case the four DDL-F connected in series forms a chirp-signal. The compensating amplifiers are connected between the DDL-F. The experimentally observed chirp-signal formed by two modules connected in series is presenting in Fig.3. Increasing of the chirp-signal duration by the connections of the additional DDL-Fs (more than two) is possible. However, unevenness of a frequency response in the DDL-F for such modules should be reduced.

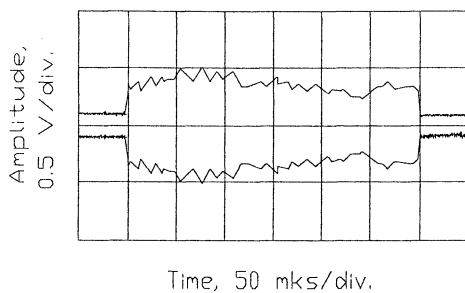


Figure3: Measured chirp-signal by duration of 300 mks, formed by the two cascade chirp-modules

### 5. RESULTS OF THE EXPERIMENT ON COMPRESSION OF A CHIRP-SIGNAL

The experiment on the compression of a chirp-signal was performed according to the block diagram submitted in Fig.4. As a compressor was

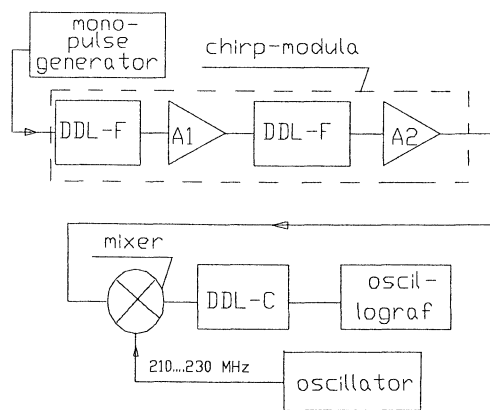


Figure4: Block diagram of the measurement pulses compression.

used the DDL-C centred on the frequency of 75 MHz, the bandwidth of 20 MHz and the dispersive delay time of 75 mks. The Taylor's apodization function was used in one of the IDT of the DDL-C. The second IDT of the DDL-C was without apodization. The slope of the DDL-C dispersive response was negative. For equalizing of the

frequency response the changing along the RA depth of the grooves from 0.17 mkm (near IDT) up to 0.35 mkm (in the end RA) have been used. As far as the absolute values of the grooves depth was sufficiently greater, small deviations of the grooves depth from the linear law, connected with the inaccuracy of the technological process of the ion etching and the irregularities of the substrate properties did not influence upon the frequency response. The frequency response of the compressing DDL-C are submitted in Fig.5.

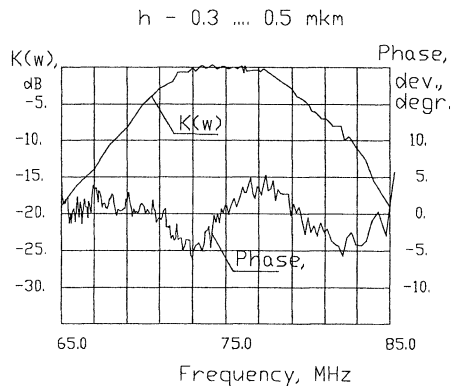


Figure5: Measured frequency responses of DDL-C

The module has been excited by the short videopulse by duration of 3 ns and by amplitude of 4 V. The chirp-signal of the 75 mks duration and of the 40 MHz bandwidth was forming on the output of the first DDL-F and then was sending on the input of the broadband amplifier A1 with the gain factor of 60 dB. The duration of the formed chirp-signal is increased up to 150 mks after the passing the second DDL-F situated after the amplifier A1. The unevenness of the amplitude of the formed chirp-pulse completely corresponded to all particularities of a frequency response presented in Fig.2. The chirp-pulse amplitude on the output of the amplifier A2 was installed of 1V by adjusting the amplification of the A2. The conversion of a chirp-signal spectrum to the band of the frequencies of the compressor and inversion of the chirp-signal spectrum (changing of the slope of the dispersive response from negative to positive) was realized by means of the balanced mixer. The mixer was simultaneously fed by formed chirp-signal by duration of 150 mks and by the signal from the monopulse generator. A inverted chirp-signal is filtering on the combinational frequencies  $f_g - f$ , where  $f_g$  - a frequency of the monopulse generator. When changing the generator frequency from 210 MHz up to 230 MHz a different area of the chirp-signal spectrum are participated in the compression. The part of the chirp-signal spectrum from 130 MHz up to 150 MHz is converted to the band of frequencies of the compressor when mixer is fed by a signal from the monopulse generator of the frequency 210 MHz. The part of the chirp-signal spectrum, which is compressing by the DDL-C, is

displaced in the area of more high frequencies under increasing a frequency of the signal from the monopulse generator. An area from 150 MHz up to 180 MHz of the chirp-signal spectrum is converted in the band of a compressor at the frequency of the generator signal 230 MHz. Temporary position of the compressed signal is changed at changing of the frequency of the generator signal. Total displacement of the compressed signal is a half of the duration of a chirp-signal (75 mks). The parameters of the compressed signal (the sidelobe level  $\alpha$  in the compressed signal and the width of compressed signal  $\tau$  by the level of 4 dB) are given in the table1 under the different values of the signal frequency from the generator.

TABLE1 - The results of the compressions of a chirp-signal by duration 150 mks.

$f_g$ , MHz	210	212	214	216	218	220
$\tau$ , ns	69	64	65	66	70	67
$\alpha$ , dB	30	26	26	27	28	25
$f_g$ , MHz	222	224	226	228	230	
$\tau$ , ns	70	70	67	65	65	
$\alpha$ , dB	26	26	26	26	26	

The experiment of the chirp-signal compression by duration 300 mks were also performed. The chirp-signal was formed by two cascaded chirp-modules (four cascaded DDL-F). The two DDL-C were cascaded on the output of the mixer for the compression of formed chirp-signal. The sidelobe level in the compressed signal has been from -22 dB up to -30 dB and the width of the compressed signal near 80 ns at the changing of the frequency of the generator signal ( $f_g$ ) from 210 MHz up to 230 MHz, accordingly. Increasing of the sidelobe level is connected with the increasing of the distortion of the

amplitude and phase of the chirp-signal of the module. The distortion of the amplitude and phase of the chirp-signal are the sum of the distortions of the amplitude and phase of four DDL-F. The expansion of the compressed signal is connected with the using for the compressing two DDL-C, each of DDL-C has a weighting and frequency response similar to presented in Fig.5 (specially for the given experiment a DDL-C without weighting was not developed). The additional selection of the samples of the DDL-F and more hard requirements to the responses of the amplitude and phase possibly improve the parameters of the formed chirp-signal by duration of 300 mks and compressed signal.

## 6. CONCLUSION

The method of forming a chirp-signal of great duration with low distortion of the phase response have been presented. The developed DDLs allows to form a chirp-signal by duration 300 mks at the time bandwidth product 12000 and acceptable level of the distortion of the amplitude and phase. The most interesting using of the elaborated chirp-module is the dispersive receivers, spectrum analyzers and radars.

1. Meyer P.C., Tancrell R.H., Matsinger J.H. // IEEE Ultrason.Symp. ,1973, pp.498-499.
2. Zuodu Xianwen, Xie Shu, Wei Yulan. // Appl. Acoust. ,1991,V.10,N 10, p.3.
3. Oates D.E., Boroson D.M. // 1980 Ultrason. Symp. Proc., 1981, V.1, pp.272-276.
4. Dmitriev V.F., Mitrofanov I.S. // Eleventh European Frequency and Time Forum, 4-6 March 1997, Neuchatel, Switzerland, pp.405 - 409.
5. Dmitriev V.F. // Sov.Phys. Tech.Phys. 65, (8), August 1995, pp.111-123.

**INFLUENCE OF DISPERSIVE DELAY LINES MATCHING NETWORKS ON COMPRESSED SIGNAL PARAMETERS**

*W. Niemyjski<sup>1)</sup>, S. Gawor<sup>2)</sup>*

1) Telecommunication Research Institute, Warsaw, Poland

2) Tele- and Radio Research Institute, Warsaw, Poland

**INTRODUCTION**

Surface acoustic wave devices are usually made on quartz or lithium niobate substrates. Lithium niobate has gained popularity over last years due to greater coupling coefficient and in consequence much lower insertion losses. But quartz is also still used in some applications. Main advantage of quartz is its very good thermal stability. It also has many times lower effective permittivity and in consequence the input and output capacitance of the device made on quartz is lower. It is very important, especially for devices with long interdigital transducers. It will be shown, that very high insertion losses of the devices made on quartz can be significantly reduced by appropriate designing of the matching networks. The influence of the matching networks on the compressed signal parameters will be analyzed.

**ANALYZED DISPERSIVE DELAY LINES**

Within the frame of this work the influence of broad band matching networks on transfer characteristics of dispersive delay lines has been investigated. Three types of SAW devices are taken into account (fig. 1):

- a) dispersive delay line (DDL) with one dispersive transducer,
- b) dispersive delay line with two dispersive slanted transducers,
- c) reflective array compressor.

TABLE 1. Dispersive delay lines parameters.

	IDT (in line)	IDT (slanted)	RAC
Dispersion [μs]	5, 10, 20	20	40
Center freq. [MHz]	70		
Bandwidth [MHz]	6		

Main parameters of the devices are presented in the Table 1. The 40μs device is reflective array compressor with two periodic transducers and the others are dispersive delay lines with one dispersive and one periodic transducer. For comparison dispersive delay line with two dispersive slanted transducers and dispersion time 20μs was also made.

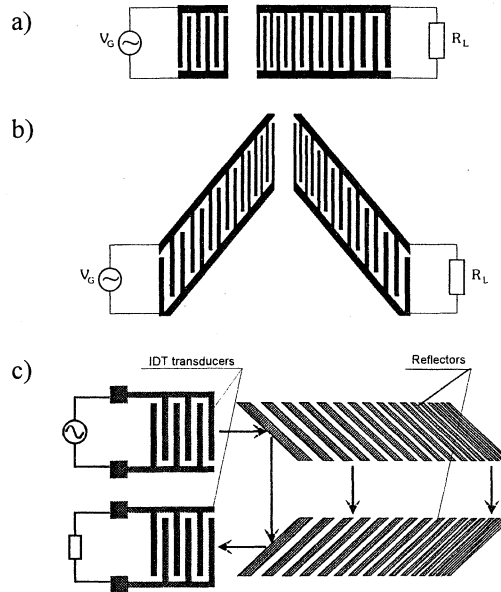


Fig. 1. Configuration of analyzed dispersive delay lines.

**MATCHING NETWORK DESIGNING**

The problem reduces to broad band matching ( $B/f_0 > 5\%$   $f_0$ - center frequency, B-bandwidth) of input and output transducers in the circuit from fig. 2. As a result [S] matrix which represents the dispersive delay line with matching networks is obtained.

In the matching structures ladder networks with LC components can be used as shown in fig 3.

The values of L, C components can be determined with the use of matching network design program on the base of measured parameters of dispersive delay lines [S] matrix. To optimize the matching network, measurement results in the  $f_0 \pm B$  bandwidth have to be known. Because of the limitations in the optimization program, the maximum number of measurements points should be less than 100.

As such small number of pints is in most cases insufficient for determination of signal after compression parameters, repeated measurement of line characteristic at greater number of points as well as determination of [S] matrix for matching networks designed previously is necessary.

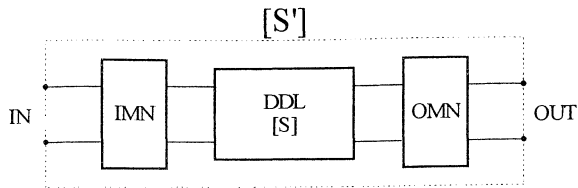


Fig. 2. Matrix representation of the dispersive delay line with matching network (IMN-Input Matching Network, OMN-Output Matching network)

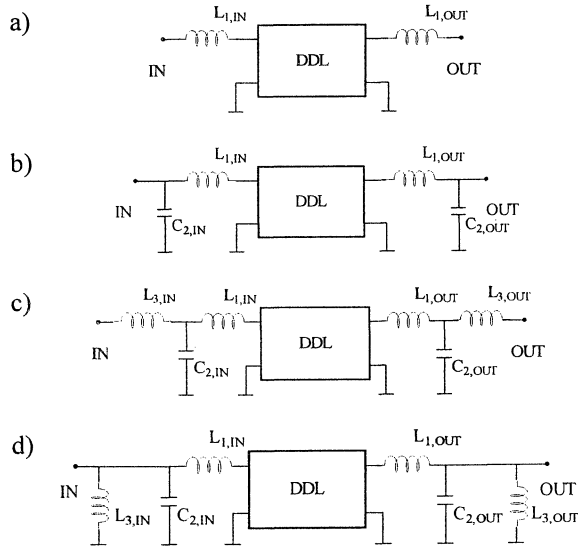


Fig. 3. Analyzed matching networks.

## RESULTS

Matching networks presented in fig. 3 have been designed and examined. For the purpose of design and optimization, the number of measurement points has been set to 41. Dispersive delay lines [S] matrices have then been determined by taking 401 points into account. The calculations were done in the range approximately equal to 2B.

Exemplary frequency characteristics of 5 $\mu$ s dispersive delay lines before and after matching are presented in fig. 4. Proper designing of matching networks enabled considerable reduction of line attenuation (fig. 5). The results presented in the diagrams refer to matching network presented in fig. 3c. The values obtained for other networks are very similar with the exception of networks from fig. 3a which are characterized by losses greater by about 3  $\div$  5dB.

On account of large impedance mismatch of non-dispersive transducers, the bigger improvement is gained for lines with these transducers.

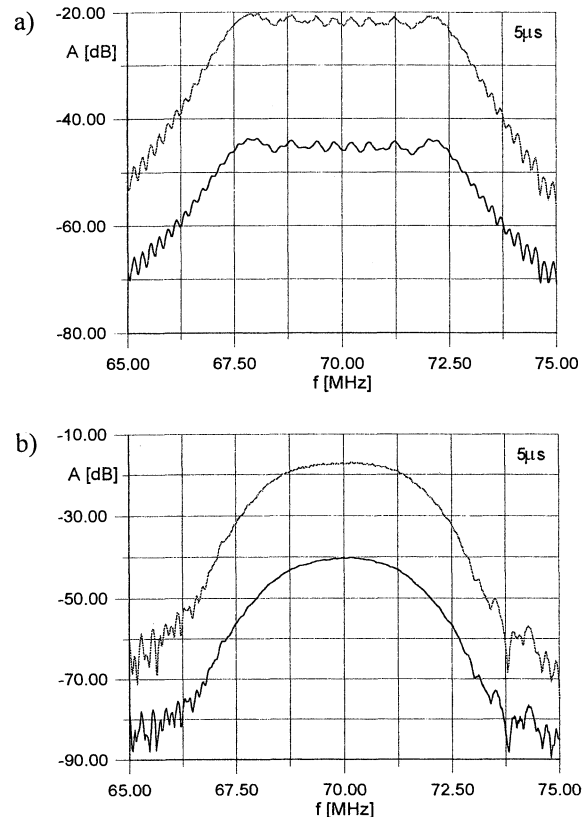


Fig. 4. Characteristics of the DDL before and after matching: a) expander, b) compressor.

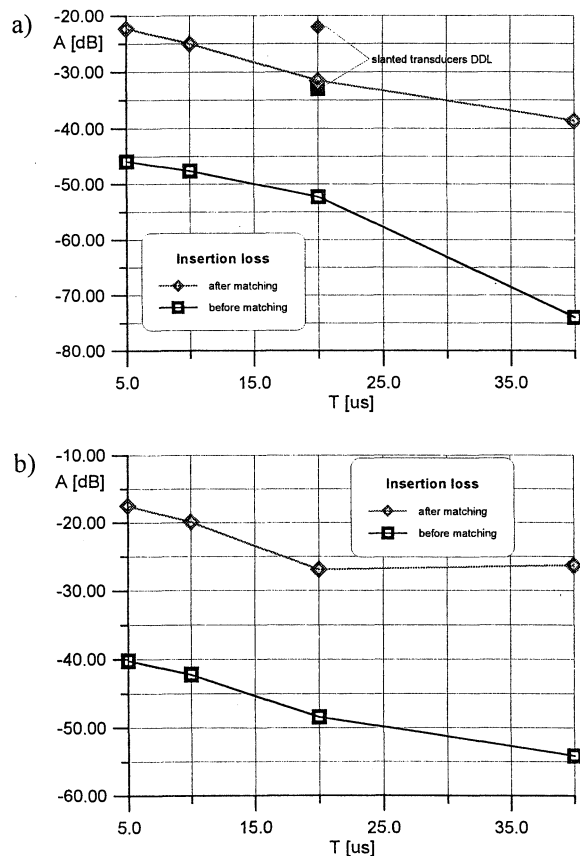


Fig. 5. Insertion losses of the DDL before and after matching: a) compressors, b) expanders.

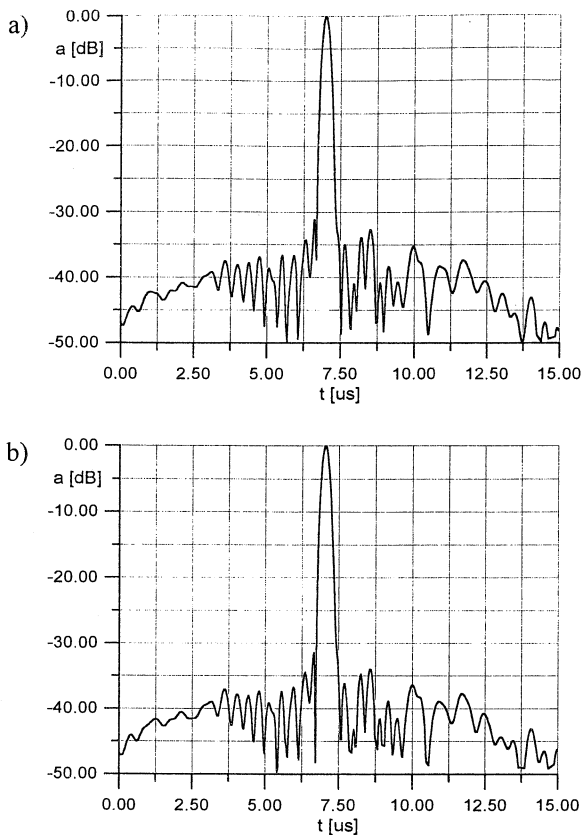


Fig. 6. Signal after compression: a) before matching, b) after matching.

Besides reducing attenuation, matching networks improve selectivity of dispersive delay lines. The improvement is bigger with greater number of L, C components applied. Larger number of matching networks elements improves the line matching, however it also increases phase distortions of frequency characteristic, which may lead to considerable worsening of sidelobes level in the compressed signal.

In the course of a number of simulations, during which matching networks with the number of

elements  $N=1..5$  were taken into account, it was established that in most cases best results were achieved for  $N=3$ . For that number of elements it is possible to obtain relatively good line matching without visible worsening of sidelobes level in compressed signal.

## CONCLUSION

As it is well known, interdigital transducers are characterized by small maximum value of input voltage which limits their use to power levels below 10 dBm. In conjunction with large transmission losses, it seriously limits dynamic range of generation and compression path.

By using the matching networks two goals are achieved: improvement of the signal to noise ratio in the pulse expander and increasing of the dynamic range of the compressed signal.

Depending on line type, considerable (20÷30 dB) increase of dynamic range of functional paths has been achieved. The biggest gain is achieved in matching short interdigital transducers.

## REFERENCES

1. Matthaei G. L., Young L., Jones, E. M. T., "Microwave filters, impedance-matching networks, and coupling structures", McGraw-Hill, Inc. New York 1964.
2. Oliner A. A., "Acoustic Surface Waves", Springer - Verlag, Berlin, Heidelberg, New York 1978.
3. Cambell C., Surface Acoustic Wave Devices and Their Signal Processing Applications, Academic Press, New York 1989.

## SURFACE MOUNT HYBRID SAW MODULES FOR MOBILE TRANSCEIVERS

S.A.Dobershtein, A.V.Martynov, V.A.Malyukhov

ONIP, Maslennikov str., 231, Omsk, 644009, Russia

## ABSTRACT

This paper presents surface mount hybrid SAW modules for 146-174 MHz mobile transceivers: the receiver module (RXM) with RF amplifier (RFA), transmitter module (TXM) and receiver module (RXM) with voltage-controlled oscillator (VCO). For the modules we used 16x7.3x2.6 mm SMD packages. The RXM with RFA contained two low-loss SAW ring filters: the first one on  $128^\circ$  YX LiNbO<sub>3</sub>, the second one on  $64^\circ$  YX LiNbO<sub>3</sub>, connected across RFA. 157 MHz RXM with RFA has shown a low amplitude ripple of 0.3 dB within a 2-dB bandwidth of 2.1 MHz, 16 dB gain, local oscillator frequency and image frequency suppressions over 90 dB. For TXM and RXM with VCO we used a SAW delay line and external electronic phase shifter in the amplifier feedback loop. The low-loss SAW ring filters having linear phase response with a phase shift of  $\pm 180^\circ$  within a 3-dB fractional bandwidth of 5% on  $49^\circ$  YX LiNbO<sub>3</sub> were used for the delay line. 157 MHz TXM and 178.4 MHz RXM with VCO provided a tuning range of 2 MHz with the control voltage varying from 0.5 to 5 V. C/N was 80 dB. New SAW modules have low power consumption, small size and are compatible with SMT.

surface mount technology (SMT). At the same time for miniaturizing the mobile transceivers hybrid SAW modules (functional devices combining low loss SAW filters, amplifiers, phase shifters) are successfully used [1,2]. It is a promising idea to combine the two mentioned technologies. In this case the parasitic coupling and phase shifts are minimized, the PCB conductor Ohmic losses are reduced, and what is more important, the size of the corresponding transceiver unit and its assembly costs are decreased. This paper presents surface mount hybrid SAW modules for 146-174 MHz mobile transceivers: the receiver module (RXM) with RF amplifier (RFA), transmitter module (TXM) and receiver module (RXM) with voltage-controlled oscillator (VCO) (Fig.1). The RXM with RFA (a bandwidth of 2 MHz) contained two SAW filters connected across RFA. This 157 MHz module was connected between an antenna and a mixer in the receiver section. The RXM and TXM with VCO (a tuning range of 2 MHz) contained a SAW delay line and external electronic phase shifter in the amplifier feedback loop. In the transceiver 178.4 MHz RXM with VCO was connected to the mixer, and 157 MHz TXM with VCO was connected to a power amplifier (Fig.1).

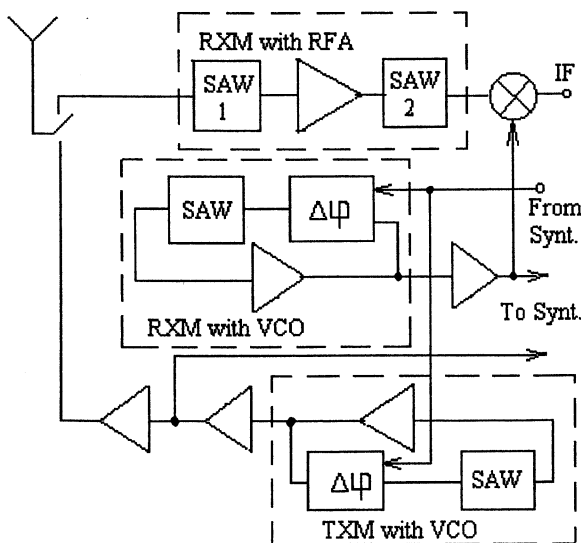


Fig.1. Block diagram of front-end and final stages of mobile transceivers

## 1. INTRODUCTION

At present for packaging SAW filters miniature SMD packages are widely used to combine SAW filters with

## 2. RFA FOR THE HYBRID MODULE

As is evident from tests of the transceivers with previously developed hybrid SAW integrated modules [2] the gain of the front-end stage must be no more than 20 dB to ensure low intermodulation distortions and to eliminate blocking. Also the high impedance mixer (an input impedance of 100-200  $\Omega$ ) is preferred for simplifying IF section. A common-emitter bipolar transistor amplifier with a cutoff frequency of 7.5 GHz is convenient for these purposes (Fig.2). It is necessary to design an amplifier circuit so that the input impedance should be close to a real value of 50  $\Omega$ , and output impedance - to a real value of 100-200  $\Omega$ . This is specified by the feedback of the transistor T (resistor R2) and its load (resistor R3). Then matching of amplifier with an antenna and mixer is easily obtained through corresponding SAW filters 1 and 2. A large body of performed calculations and experiments showed that a gain of 15-20 dB with low phase slope, noise factor of 1 dB, low consumption current of 1-2

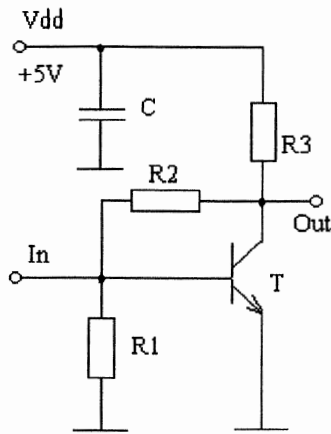


Fig.2. Circuit diagram of RFA

mA and supply voltage of 5 V were achieved in the frequency range up to 800 MHz by control of the mentioned elements. In this case the amplifier input/output impedances were close to real values of 40-70 and 100-180  $\Omega$ , respectively.

### 3. SAW FILTERS FOR RXM WITH RFA

For RXM with RFA we used previously developed self-matched low-loss SAW ring filters with a fractional bandwidth of 2% and 3.5% on  $128^\circ$  YX and  $64^\circ$  YX  $\text{LiNbO}_3$ , respectively [3]. The ring filters consisted of input/output bidirectional interdigital transducers (IDTs) placed in parallel acoustic tracks and two reflective multistrip couplers (RMSCs) which provided SAW transmission between these tracks (Fig.3).

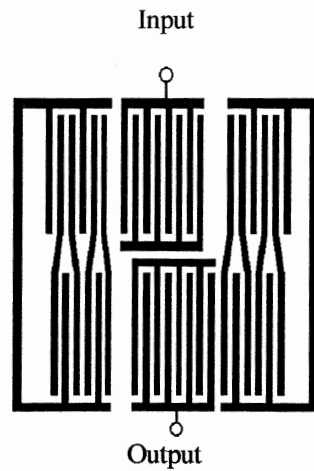


Fig.3. Schematic layout of SAW ring filter

The filters did not require matching networks because they provided the specified real input/output impedances in the passband by self-matching when a static capacitance of the IDT was compensated by radiation susceptance. Fig.4 shows the frequency response of 157 MHz SAW filter. Input/output IDT were phase weighted. In a 50  $\Omega$  system the filter had an insertion loss of 1.8 dB, passband amplitude ripple of 0.1 dB, 1-dB bandwidth about 2 MHz, stopband attenuation over 50 dB at  $\pm 10.7$  MHz offset from the center frequency. Chip size was 4x4x0.7 mm. Evidently it is appropriate to connect this filter to the input of the RXM with RFA for matching 50  $\Omega$  antenna and 50  $\Omega$  input of the RFA. The second filter of the RXM with RFA should be with high input/output impedances because the mixer has a high input impedance and RFA has a high output impedance. The ring filter on  $128^\circ$  YX with appropriately reduced aperture or filter on  $64^\circ$  YX is

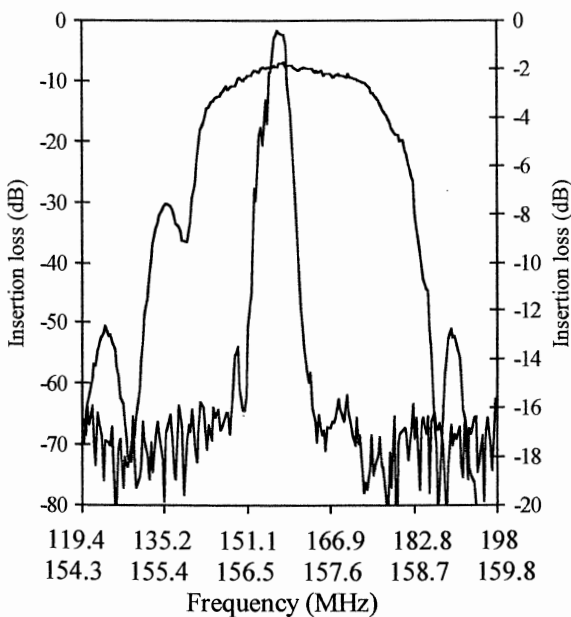


Fig.4. Frequency response of 157 MHz filter with weighting on  $128^\circ$  YX  $\text{LiNbO}_3$

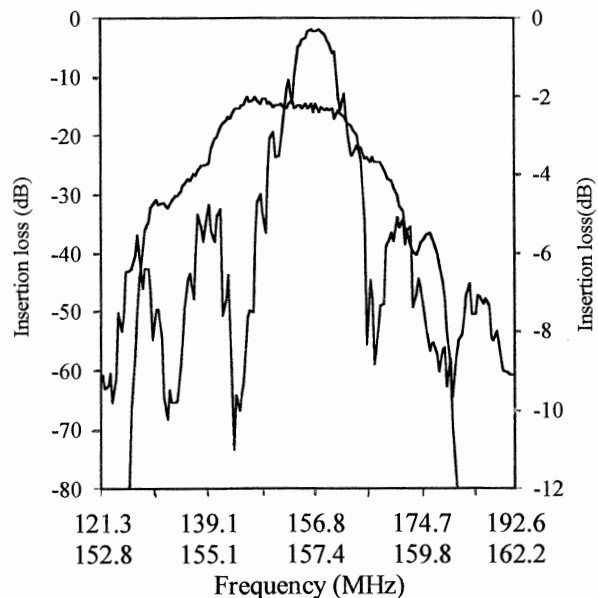


Fig.5. Frequency response of 157 MHz filter without weighting on  $64^\circ$  YX  $\text{LiNbO}_3$

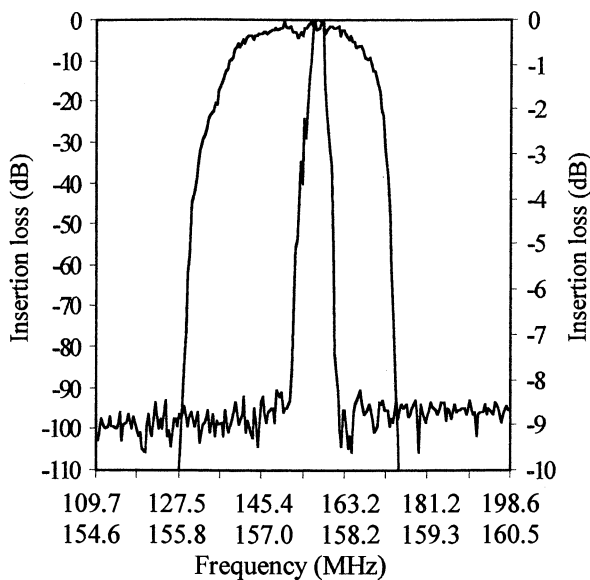


Fig.6. Normalized frequency response of 157 MHz surface mount SAW RXM with RFA

available for this purpose. As indicated in our previous investigations [3] the filter on  $64^\circ$  YX have an input impedance more than an input impedance of the filter on  $128^\circ$  YX by a factor of 2-2.5, and a number of RMSC and IDT electrodes less than number of RMSC and IDT electrodes of the filter on  $128^\circ$  YX by factor of 2 if both filter have same apertures. Thus chip size of the filter on  $64^\circ$  YX will be less than that of the filter on  $128^\circ$  YX. It is an essential advantage, since the SMD packages have a limited size. Fig.5 shows the frequency response of the ring filter on  $64^\circ$  YX. Input/output IDTs were unweighted. In a  $200 \Omega$  system the filter had an insertion loss of 2 dB, amplitude ripple in the passband of 0.2 dB, 1-dB bandwidth about 5 MHz, stopband attenuation over 50 dB at  $\pm 25$  MHz offsets from the center frequency. Chip size was  $2 \times 2 \times 0.7$  mm. Evidently this filter is well matched with an amplifier output of the RXM and mixer input in the transceiver (Fig.1).

#### 4. DEVELOPMENT OF SURFACE MOUNT HYBRID RXM WITH RFA

The RXM with RFA contained two SAW filters: the first filter with low input/output impedances on  $128^\circ$  YX, the second filter with high input/output impedances on  $64^\circ$  YX, connected across RFA (Fig.1). The first filter was with weighting, the second filter was without weighting. The high level of sidelobes of the second filter is easily suppressed by the high selectivity of the first filter. The optimization of the filter-amplifier-filter system was provided for achieving high performances of the RXM with RFA. The minimization of SAW filters and RFA mismatch was carried out by a careful selection of the RFA

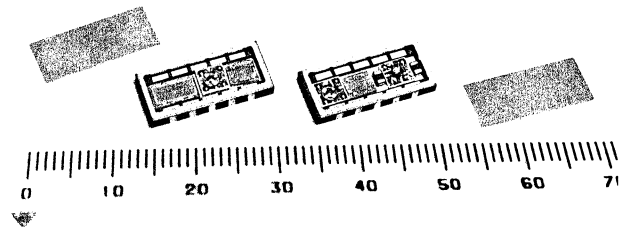


Fig.7. Photograph of the surface mount hybrid SAW modules with RFA and VCO

elements and SAW filter acoustic track apertures to achieve low passband ripple. The module topology optimization was provided to achieve high stopband attenuation over 90 dB by selection of SAW filters, RFA and ground bond wires arrangement in the SMD package. Moreover, since this module was used for the receiver front-end stage, the optimization of RFA noise factor, nonlinear distortions and current consumption was provided. Fig.6 shows normalized frequency responses of 157 MHz RXM with RFA. This module has shown a low amplitude ripple of 0.2 dB within a 2-dB bandwidth of 2 MHz, 16 dB gain, suppression over 90 dB at  $\pm 10.7$  MHz offset from the center frequency. A noise factor of 1 dB and intermodulation selectivity of 70 dB were provided with a low current consumption of 1-2 mA. The RXM was used for the local oscillator frequency and image frequency suppression. Use of SAW filters on two different  $\text{LiNbO}_3$  cuts improved matching the SAW filters with the amplifier input/output and mixer input, decreased the module size and allowed to mount it in a miniature  $16 \times 7.3 \times 2.6$  mm SMD package (Fig.7).

#### 5. SAW FILTERS FOR THE RXM AND TXM WITH VCO

For the realization of the surface mount TXM and RXM with VCO it is necessary to select a circuit with a minimum number of the elements since the SMD packages have a limited size. We used a VCO circuit with SAW delay line and external electronic phase shifter in the amplifier feedback loop [4]. For delay line we used previously developed low-loss SAW ring filter having linear phase response with a phase shift of  $\pm 180^\circ$  within a 3-dB bandwidth of 5% on  $49^\circ$  YX  $\text{LiNbO}_3$  [3]. Measured frequency and phase responses within the passband of 157 MHz filter on  $49^\circ$  YX in a  $200 \Omega$  system are presented in Fig.8 (the wideband filter frequency response and frequency response of 178.4 MHz filter are not presented in order not to overload the paper with the figures). As seen from Fig.8 the filter has insertion loss about 2 dB, linear phase response within the passband with a slope of  $42^\circ/\text{MHz}$ . Chip size was of  $2 \times 2 \times 0.7$  mm. Using such

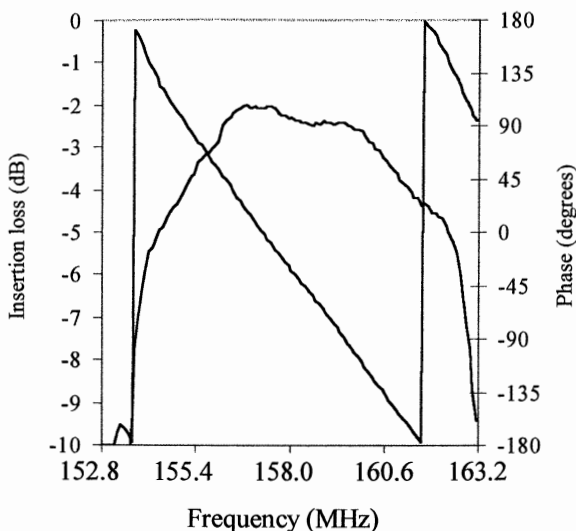


Fig.8. Frequency and phase responses of 157 MHz filter on  $49^\circ$  YX LiNbO<sub>3</sub>

frequency dependent elements with an insertion loss of 2 dB in the amplifier feedback loop it is possible to develop low power consumption VCOs. Thus considering the data for the phase response slope (Fig.8), it can be inferred that for a tuning range of 2 MHz at frequencies of 157 MHz and 178.4 MHz the phase shift of not less than  $84^\circ$  of the external electronic phase shifter is necessary.

## 6. PHASE SHIFTER FOR VCO

An electronic C-L-C phase shifter providing a phase shift of about  $100^\circ$  when the control voltage is varied on varactors V1 and V2 (Fig. 9) was selected for VCO [4]. A distinctive feature of this phase shifter is in the fact that its tuning frequency  $f_0$  (~ the center frequency of the phase tuning range) depends on the a correlation of L and  $C_j$  ( $C_j$  is the varactor's capacitance for the average value of the control voltage):  $f_0=1/2\pi\sqrt{LC_j}$ .

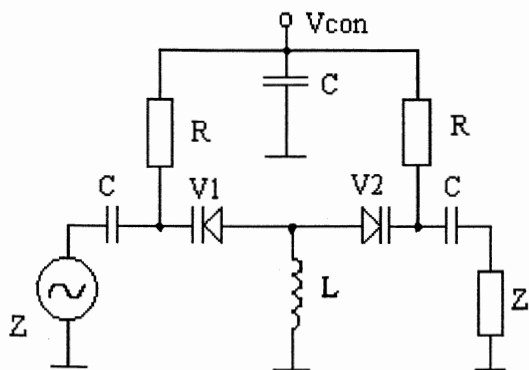


Fig.9. Schematic layout of the electronic phase shifter

Since for RF applications low noise varactors with  $C_j=5-10$  pF are usually used the calculated value of C-L-C phase shifter input impedance in 157-178 MHz frequency range is  $100-200 \Omega$ . The phase shift and insertion loss versus control voltage for this phase

shifter with  $f_0=156$  MHz using the varactors with  $C_j=10$  pF and  $Z=200 \Omega$  are shown in Fig.10. As seen from Fig.10 the C-L-C phase shifter provides the phase shift about  $100^\circ$  and low amplitude ripple about 1 dB when the control voltage is varied from 0.5 to 5 V. This shifter for hybrid module was made using miniature varactors and leadless inductor. The size of the phase shifter was  $4 \times 4$  mm.

## 7. VCO FOR HYBRID MODULE

Schematic layout of the VCO is shown in Fig.11. Since the insertion loss of the used SAW filters is about 2 dB the amplifier of VCO contained a single bipolar transistor with a cutoff frequency of 7.5 GHz. The required phase balance in the oscillator loop was provided at the expense of a phase shift in the amplifier, SAW filter and external phase shifter. The required amplitude balance in the oscillator loop in the frequency range specified by the SAW filter passband was provided by matching the input impedances of all three VCO components: an amplifier, phase shifter and SAW filter. Since self-matched SAW filters with real input/output impedances (of about  $200 \Omega$ , see previous section) are used in VCO it is desirable that the amplifier input/output impedance and phase shifter impedance should also be real values and close to SAW filter impedance on the center frequency. The first was specified by the feedback of the transistor T (resistor R4) and its load (resistor R5). The second was achieved by choosing the capacitance of the varactors V1,V2 and the inductance of the inductor L. A large body of performed experiments showed that the amplifier input/output impedance and phase shifter impedance become close to a real value of  $180 \Omega$  by adjustment of the indicated elements. In this case a phase shift of about  $100^\circ$  of the external phase was achieved with the control voltage variable from 0.5 to 5 V. It is enough for a specified VCO tuning range of 2 MHz.

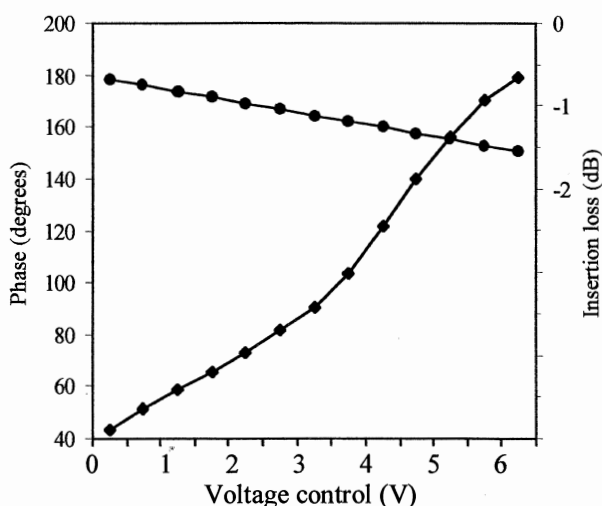


Fig.10. Phase shift and insertion loss versus control voltage of the electronic phase shifter

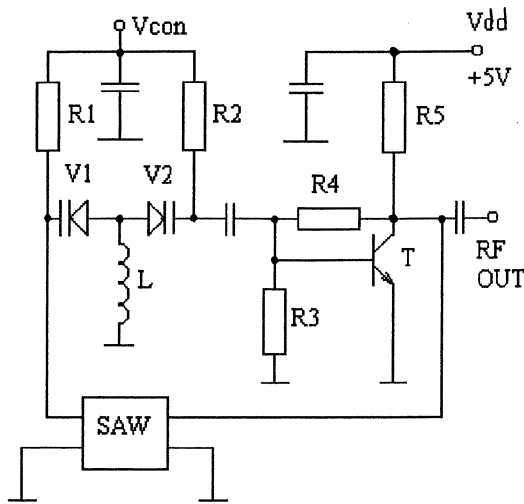


Fig.11. Schematic layout of the VCO

## 8. DEVELOPMENT OF HYBRID SAW MODULE WITH VCO

The optimization of the amplifier-phase shifter-SAW filter system was provided for achieving the optimal combination of the carrier-to-noise ratio C/N (at 25 kHz carrier offset, 3 kHz bandwidth), specified tuning range, maximal control voltage and current consumption. For this purpose the following investigations were carried out: minimization of SAW filter and amplifier mismatch; minimization of output voltage ripple in the tuning range by decreasing amplitude ripple of the phase shifter; linearization of the volt/phase characteristic of the phase shifter. Performances of 157 MHz TXM with VCO are shown in Fig.12. Similar performances were obtained for 178.4 MHz RXM with VCO. Hybrid 157 MHz TXM and 178.4 MHz RXM with VCO provided a tuning range of 2 MHz with the control voltage varying from 0.5 to 5 V. C/N was 80 dB. At a 50  $\Omega$  load connected across a buffer stage the output voltage about 0.2 V was almost constant in the tuning range. The current consumption was not more than 3 mA for a source voltage of 5 V. A combination of a single stage amplifier, low-loss wideband SAW filter and passive electronic C-L-C phase shifter allowed to obtain sufficiently high performances of hybrid SAW modules with VCO in respect of tuning range and C/N, to provide low power consumption and small size and to mount them in a miniature 16x7.3x2.6 mm SMD packages (Fig.7).

## 9. CONCLUSION

The reported results show a possibility of a combination of the two known technologies for SAW devices: SMD packages and hybrid SAW modules combining SAW filters, amplifiers, phase shifters. Surface mount hybrid SAW modules for 146-174 MHz

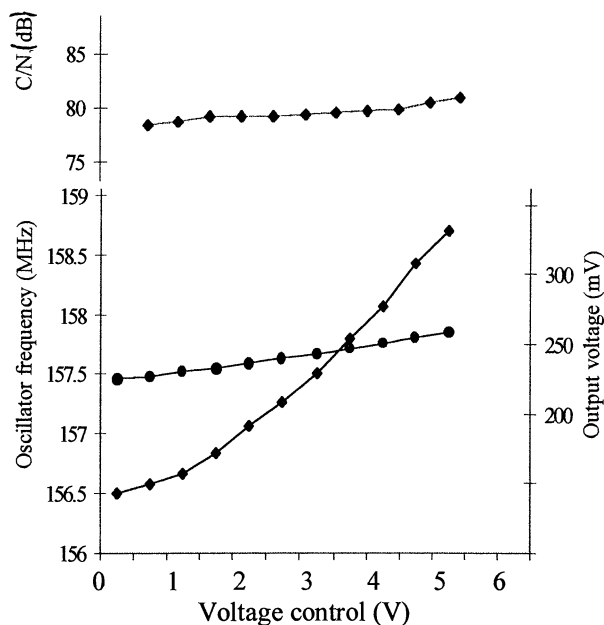


Fig.12. Performances of 157 MHz surface mount hybrid SAW TXM with VCO

mobile transceivers are presented: the receiver module (RXM) with RF amplifier (RFA), transmitter module (TXM) and receiver module (RXM) with voltage-controlled oscillator (VCO). The optimization of the filter-amplifier-filter system for the RXM with RFA and the amplifier-phase shifter-SAW filter system for the TXM and RXM with VCO was provided for achieving high performances. The RXM with RFA had 16 dB gain within a bandwidth of 2 MHz, noise factor of 1 dB, local oscillator frequency and image frequency suppressions over 90 dB. The RXM and TXM with VCO provided a tuning range of 2 MHz and C/N of 80 dB. SAW modules had low power consumption (2-3 mA current consumption, 5 V supply voltage) and small size (7.3x16x2.6 mm SMD packages were used for packaging). New hybrid SAW modules are smaller than the previous ones [2] and will be used in small mobile transceivers using SMT.

## REFERENCES

- 1.Saw J. et al., 1995, "SAW Technology in RF Multichip Modules for Cellular Systems", *Proc. IEEE Ultrason. Symp.*, 171-175.
- 2.Dobershtein S. et al., 1995, "Hybrid SAW Integrated Modules with RFA and VCO for Mobile Transceivers", *Proc. IEEE Ultrason. Symp.*, 147-150.
- 3.Dobershtein S. and Malyukhov V., 1997, "SAW Ring Filters with Insertion Loss of 1 dB", *IEEE Trans. UFFC*, 44, 590-596.
- 4.Parker T. and Montress G., 1988, "Precision Surface-Acoustic-Wave (SAW) Oscillators", *IEEE Trans. UFFC*, 35, 342-364.

**IMPROVEMENT OF SAW FILTER PARAMETERS BY THE APPLICATION OF A SINGLE-ELECTRODE INTERDIGITAL TRANSDUCER**

PIOTR NAGŁOWSKI, ELŻBIETA DĄBROWSKA

INSTITUTE OF ELECTRONIC MATERIALS TECHNOLOGY  
WÓLCZYŃSKA 133, 01-919 WARSAW, POLAND

**ABSTRACT**

This paper presents experimental results obtained for two TV-IF filters designed on 128° YX LiNbO<sub>3</sub>. One of the filter incorporates a single-electrode unapodized output IDT and second one a double-electrode. The insertion loss of the first filter is about 4dB lower than insertion loss of second filter.

**INTRODUCTION**

One of the important parasitic effects in SAW transversal filters is the triple transit signal (TTS) which degrades pulse and group delay responses of the devices. Generally TTS level grows with the decrease of the filter insertion loss. Since many modern applications require low loss filters with undisturbed pulse and group delay responses it is essential to minimize the level of TTS.

Most TV SAW filters designed and produced at the Institute of Electronic Materials Technology (ITME) consist of an apodized input transducer (IDT) and an unapodized output transducer separated by a screen. Usually both IDTs contain so-called double (or split) electrodes (Fig. 1) to prevent spurious SAW reflections from the IDT electrodes.

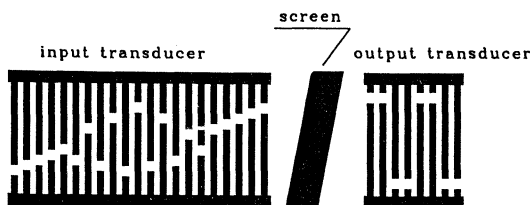


Fig.1. Typical TV-IF SAW filter structure with double electrodes in the IDTs

Recently a method of filter synthesis has been developed at ITME which makes it possible to compensate for the SAW reflections taking

place at the output uniform IDT. This enabled us to design filters containing single electrodes in the unapodized IDT (Fig. 2).

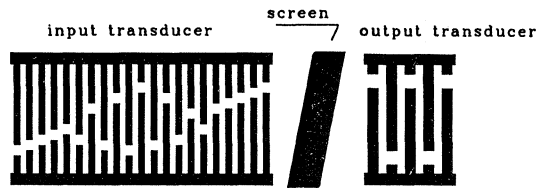


Fig.2. Typical TV-IF SAW filter structure with single electrodes in the unapodized IDT

This paper demonstrates that the use of single electrodes leads to better relations between filter insertion loss and TTS.

**CALCULATION**

Up to now the effect of SAW reflections was not included in the compensation procedure used at ITME. Consequently double electrodes were used in both IDTs.

In new mathematical model of SAW filter which was used to compute the frequency response the Remez algorithm was applied. The parabolic approximation was used to simulate diffraction. Motional admittances of the IDTs were computed as proposed in [3]. A method similar to the one shown in [4] was used to evaluate static IDT capacitances. In this model parasitic effects: SAW reflections, diffraction, and end effects in the output IDT were compensated [3,4,5].

The developed compensation method was used to design TV SAW filter (FTQW-3806) on 128°YX LiNbO<sub>3</sub> substrate. In the example presented below the source impedance of 50Ω and load impedance of 2kΩ in parallel with 3pF were assumed.

Fig. 3. illustrates considerable difference between the desired ideal response and the

response taking into account parasitic effects computed before the compensation.

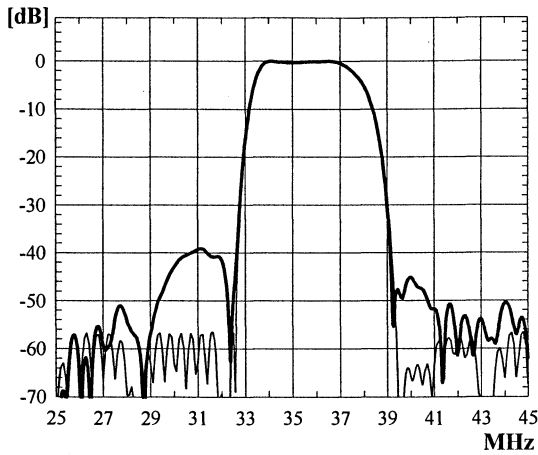


Fig.3. Theoretical amplitude responses of the FTQW-3806 filter

— including parasitic effects before compensation  
 - - - ideal

After about 1000 iterations of the compensation algorithm the theoretical amplitude response was satisfactory (Fig.4.).

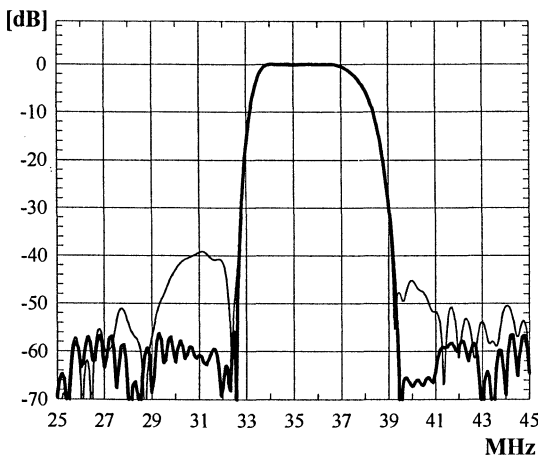


Fig.4. Theoretical amplitude responses of the FTQW-3806 filter including parasitic effects

— after compensation  
 - - - before compensation

Apodization patterns of the input transducer before and after compensation are shown in Fig.5. Instead of the electrodes themselves the gaps between the electrodes are shown only.

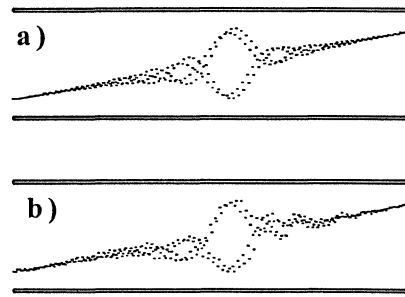


Fig.5. Apodization patterns of the input transducer  
 a) - before compensation  
 b) - after compensation

## RESULTS

FTQW-3806 filter functionally corresponds to a filter previously designed using the old method with double electrode in output transducer (FTQW-3801). Fig.6. illustrates experimental amplitude response of the FTQW-3801 and FTQW-3806 filters.

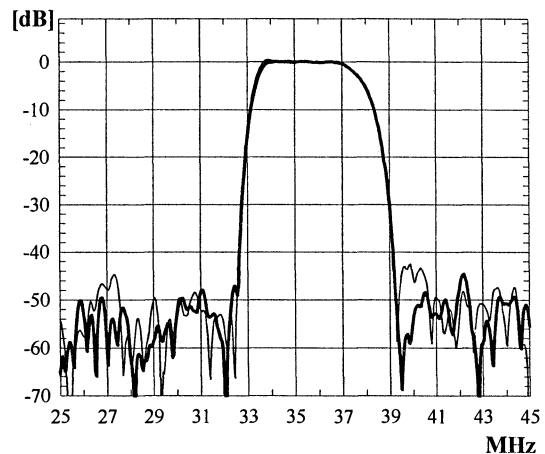


Fig.6. Amplitude responses of the filters

— FTQW-3806 (with single electrodes)  
 - - - FTQW-3801 (with double electrodes)

The responses of both filters are similar, but the insertion loss of the filter with single-electrode in the output transducer (FTQW-3806) is about 4 dB lower than the insertion loss of the filter with double-electrodes (FTQW-3801).

Impuls responses corresponding to the two filters are presented in Fig.7. The triple transit signal (TTS) for the FTQW-3806 filter is lower than TTS for the FTQW-3801 filter.

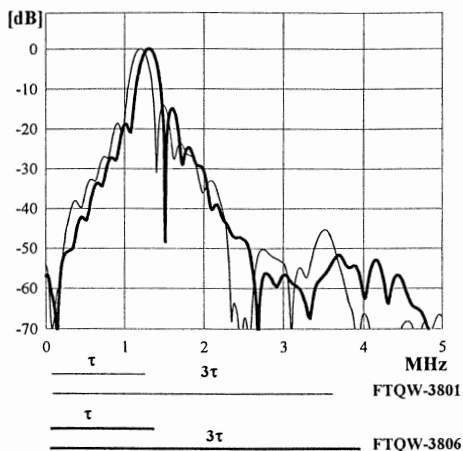


Fig.7. Pulse responses of the filters

— FTQW-3806  
 - - - FTQW-3801

Amplitude and group delay responses of the both filters are shown in Figs.8. and 9. The responses of both filters are similar.

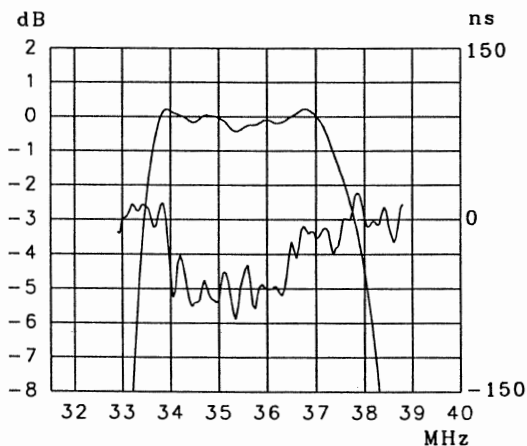


Fig.8. Amplitude and group time delay responses of the FTQW-3801 filter

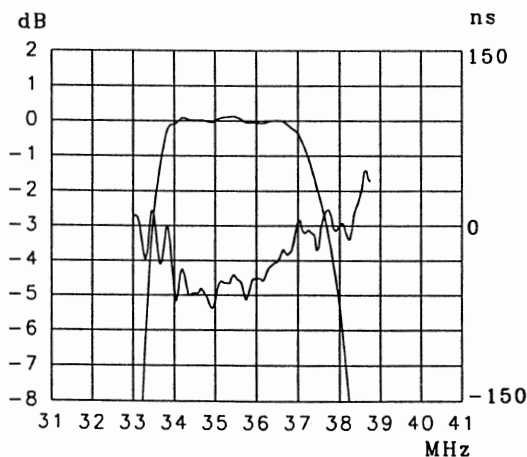


Fig.9. Amplitude and group time delay responses of the FTQW-3806 filter

## CONCLUSION

It was shown that using single electrodes in the unapodized IDT makes it possible to obtain considerably better relations between filter insertion loss and TTS.

As a result we have obtained the filter with a correct parameters. Additionally the insertion loss is lower about 4dB in comparison with insertion loss for the filter with double electrodes in unapodized IDT.

## ACKNOWLEDGEMENT

The funds for the development of the new filter synthesis method have been provided by The State-Ordered Research Program PBZ 12-05.

## REFERENCES

- [1] G.Albrecht, W.Faber, G. Tobolka, "Time Domain Texting of Surface Acoustic Wave Filters", Siemens Forsch.- u. Entwickl.-Ber. Bd. 13 (1984) Nr.4, Springer-verlag 1984, pp. 171-175
- [2] F.Z.Bi, K.Hansen, "The investigation of Diffraction Compensation at the Trap Position for TV SAW Filters", 1996 IEEE Ultrasonics Symposium, San Antonio, USA
- [3] P.Nagłowski, "Fast Computation of Finger-Length-Weighted SAW Transducer Dynamic Admittance", 1985, Electronics Letters
- [4] D.Morgan, "Surface-Wave Devices Signal Processing", 1995, Elsevier, Amsterdam
- [5] F.Z.Bi, K.Hansen, "Wideband Diffraction Methods and the Angular Spectrum of Waves (ASoW) Model for TV SAW Filters", IEEE Trans. on UFFC, vol. 44, no.4, July 1997, pp.925-934"



*12th EFTF* - 10÷12 March 1998 - Warsaw - POLAND

**T/F techniques & atomic standards**

*(posters)*



## VERY LOW AGING RATE <sup>87</sup>Rb FREQUENCY STANDARD

*Dong Taiqian*

*Liu Shuqin*

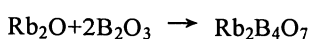
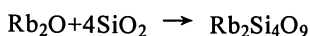
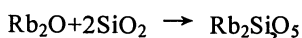
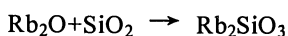
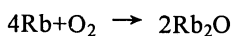
Peking University, Dept. of Electronics, P.R.China

Compared to the other atomic frequency standards, Rb frequency standard has the following advantages: Small volume. easy to make. low price. So it has been widely used. But the main disadvantage is aging. Usually the aging rate is  $1-5 \times 10^{-11}$ /mon. If the electronics is perfect, this aging rate is completely determined by the physics package. For the 0-0 transition of ground state of Rb atom, there are three kinds of frequency shift: light shift, Collision shift, microwave power shift. The microwave power shift usually manifests itself the frequency fluctuation with environment temperature. When the environment temperature is different, the input microwave power to the physics package is different. Via microwave power shift, it causes the frequency fluctuation. But it does not cause the aging. So the reasons for aging in Rb frequency standard are light shift and collision shift.

In Rb gas cell frequency standard, it is impossible to completely eliminate the light shift and collision shift. For reducing the aging rate, the light shift and collision shift must be well controlled. About how to control the light shift, there are many papers to discuss it<sup>(1)</sup>. It will not be discussed in this paper. In the following, only controlling the collision shift is discussed.

In Rb cell, there are very weak Physical reaction and chemical reaction. Physical reaction means the wall of cell will release or absorb gas. But if the temperature of cell is constant, finally the dynamic equilibrium must be established. So Physical reaction just exists for a couple of days, it can not last for long time. Therefore physical reaction is not the reason for aging.

As to chemical reaction in the Rb cell, it means the reaction between Rb atom and the glass wall of the cell. The possible chemical reactions are as follows:



All of these possible chemicals are solid state materials attached on the wall of Rb cell. No new gas produced.

In Rb cell, although Rb atoms are localized by buffer gas, but the collision between Rb atoms and wall still exists which means the wall shift still exists. Suppose the dimension of cell is  $\sim 1\text{cm}$ , the pressure of buffer gas is  $\sim 10$  torr, So the average free path of Rb atom is  $\sim 5 \times 10^{-4}\text{cm}$ . In other words, the probability of free path equal to  $1\text{cm}$  is  $\sim 5 \times 10^{-4}$ . The wall shift of Rb atom (for example, parafin coating) is  $\sim 200\text{Hz}^{(2)}$ . So the remainder wall shift is  $\sim 2 \times 10^2 \times 5 \times 10^{-4} = 0.1\text{Hz}$ , namely the fractional frequency shift is  $\sim 1.5 \times 10^{-11}$ . From preceding example, the conclusion is that in Rb cell filled with buffer gas, the remainder wall shift is still big to the order of  $10^{-11}$ . The continuously produced new solid state material attached on the wall will change the remainder wall shift. This is the reason for aging of Rb frequency standard.

There are three possible ways to reduce the aging rate caused by the remainder wall shift:

1. bigger cell and lower temperature
2. higher buffer gas pressure
3. special glass

In our Lab. the third way is used. The main specifications of our Rb frequency standard are as follows:

Aging Rate  $\leq 1 \times 10^{-12}$ /mon.

Allan Variance  $\leq 3 \times 10^{-11}$ /1s.

$\leq 1 \times 10^{-11}$ /10s.

$\leq 3 \times 10^{-12}$ /100s.

Volume of Physics Package  $\leq 0.4\text{L}$

### References

- (1) Dong Taiqian, 1981, "Reduction of Light Shift In <sup>87</sup>Rb Frequency standard Using Pulse Sampling Optical Detection Method" *Acte Physica Sinica* 30 1-11
- (2) Risely A, Jarvis S. Jr, Vanier J, 1980, "The Dependence of Frequency upon Microwave Power of Wall-Coated and Buffer-gas-filled Gas Cell <sup>87</sup>Rb Frequency Standards" *J.Appl.Phys.* 51 4571-4576

## THE MODIFICATION OF A HP 105B FREQUENCY STANDARD AND ITS USE AS A PORTABLE FREQUENCY REFERENCE

K.Kalliomäki <sup>(1)</sup>, T.Mansten <sup>(2)</sup>

1) University of Oulu, Department of Electrical Engineering, FIN-90570 Oulu, Finland

2) VTT AUTOMATION, Measurement Technology, P.O. Box 1304, FIN-2044 VTT, Finland

### ABSTRACT

In Finland there are six calibration laboratories with frequency accreditation. All of the laboratories trace their frequency either to TV line frequency derived from a rubidium oscillator and monitored by the National Standards Laboratory (VTT), or to a GPS receiver. Their best measurement capabilities are accordingly fairly good and the audit device for annually repeated proficiency tests must meet with stringent demands. Up to year 1997 VTT used a portable HP 105B crystal frequency standard for the purpose. In summer 1997 the crystal oscillator was replaced by an Efratom rubidium oscillator and a new divider for continuous monitoring via tick pulses was added. After the replacement HP105B has been used two times successfully in proficiency tests. According to the Allan variances the improvement is more than tenfold. The results show that an uncertainty level of  $1 \cdot 10^{-11}$  is achievable in those frequency proficiency tests that can be realized during a work day (7h).

### INTRODUCTION

The accreditation of calibration laboratories is a standardized procedure under which laboratories are officially verified in an internationally acceptable manner as being continuously competent to perform certain calibration tasks. As a part of the verification the accredited calibration laboratories (AKL) regularly participate in proficiency tests, in which they can show their competence by calibrating a suitable device, the properties of which are well known to the National Standards Laboratory (VTT) of the quantity under verification. In frequency there are six AKLs in Finland and the National Standards Laboratory is VTT Automation.

In Finland TV line frequency (15 625 Hz) of the national broadcasting company is locked to a rubidium oscillator and the phase and frequency of TV line signal are continuously monitored at the National Standards Laboratory (VTT). The short term stability of the line frequency phase monitored from the video signal of a commercial TV receiver

is a few ns (occasional phase jumps are not included) and daily average frequency deviation is within the limits of  $\pm 1 \cdot 10^{-11}$ .

Up to the year 1997 all calibration laboratories with frequency accreditation in Finland traced their reference frequency to the TV line frequency. The most accurate calibrations were done by comparing the phase of the device under calibration to the phase of the TV line frequency. For less stringent calibrations a counter, calibrated by comparison to TV line frequency, was used. Nowadays the laboratories are increasingly resorting to GPS receiver as a reference standard because TV signals will in a few years be distributed via digital links and the phase information will be deteriorated in the process.

The device used for the proficiency tests for frequency in Finland has for more than ten years been a portable HP 105B oven crystal oscillator, see Fig. 1 and Kalliomäki and Mansten (1). The achievable uncertainty levels of the AKLs have ameliorated during those years to meet and surpass the specifications of the HP 105B.

### MODIFICATIONS TO HP 105B

An Efratom rubidium oscillator of VTT has about the same size and power consumption but more stringent specifications than the oven crystal assem-

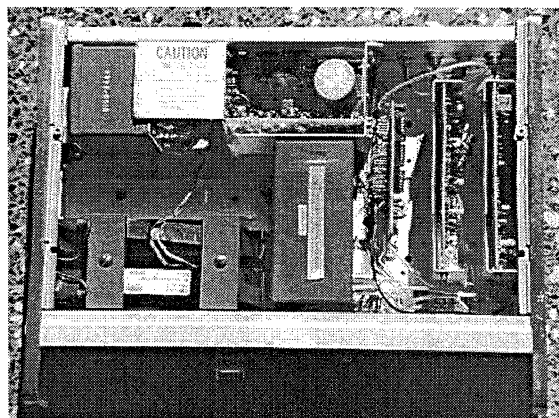


Fig. 1: HP 105B with the original OCXO

bly in the HP 105B. To meet with the demands of the proficiency tests we decided to substitute the crystal oscillator with the rubidium oscillator. For the substitution we had to do some changes to the power supply, frequency division and monitoring circuits of HP 105B. A commercial temperature meter was added to monitor and compensate for the temperature effects on the frequency of the portable device. The replacement and tests took about three weeks of work. In Fig. 2 is the rubidium oscillator and the division circuit ready for assembly.

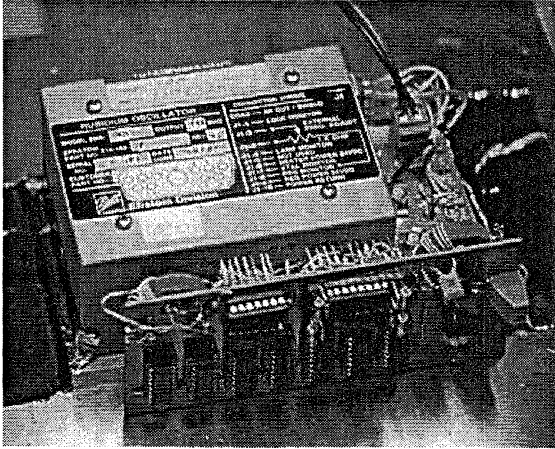


Fig. 2: Efratom rubidium oscillator and divider

### INTERFACE CIRCUITS

The 10 MHz output frequency of the rubidium oscillator is connected via a resonance circuit to a dc-biased Schmitt port and after amplification connected to an output connector via a second resonance circuit producing about 0.6 V signal level (see Fig. 3). The Schmitt port output also goes to a partially synchronous frequency divider which produces 5 MHz, 0.5 MHz, 1 kHz and 1 Hz outputs. The 5 MHz frequency goes to the original HP 105B divider, which produces three amplified frequency outputs (5 MHz, 1 MHz and 100 kHz). The 1 kHz and 1 Hz outputs go to two variable delay circuits

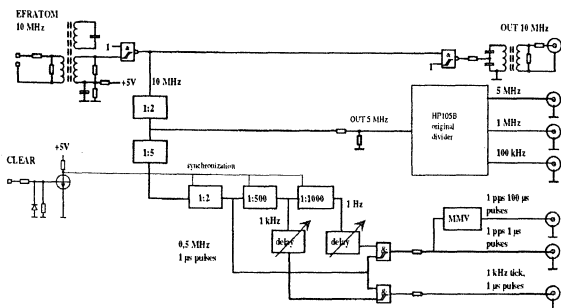


Fig. 3: Block diagram of the new divider

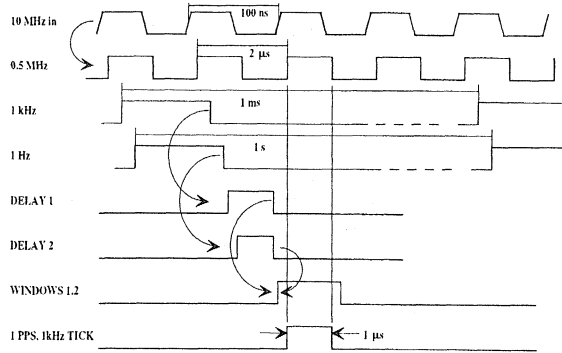


Fig. 4: Timing diagram of the divider

which produce two 1.5 μs windows. The two output ports are controlled by these windows to pass only one 1 μs pulse from the 0.5 MHz pulse train at 1 ms and 1 s intervals as depicted in Fig 4. The windows are tuned by adjustable delays to enclose symmetrically the 1 μs pulses. This rather complicated way of producing 1 kHz and 1 Hz pulse trains is chosen to reduce the jitter of the division circuitry.

In Fig. 5 the original crystal oscillator and the old, slow division circuit has been replaced by the Efratom rubidium oscillator and the new division circuit inside HP 105B.

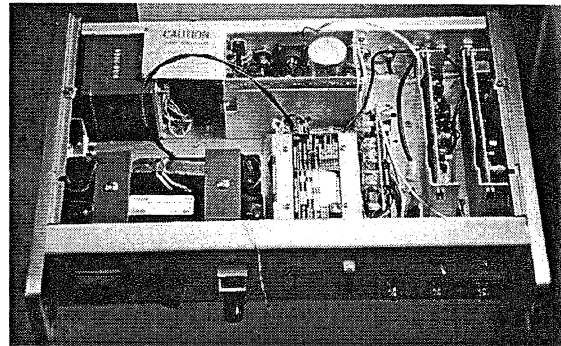


Fig. 5: HP 105B with the new rubidium oscillator

### RESULTS

Instead of frequency measurements it is customary to monitor different clocks by comparing the phases of their 1 Hz "tick" pulses to the phase of a "main" clock. The frequency differences are obtained from phase differences via differentiation. Therefore it is of utmost importance to produce stable, jitter-free pulses for phase comparison. In Fig. 6 is shown the Allan variances of the original HP 105B oscillator and the modified oscillator. According to the Allan variances the improvement has been more than ten-fold. The use of windows has dramatically reduced the short time jitter of the 1 Hz ticks. The relative increase of variance around 10 hour integration

time is caused by daily variations in laboratory temperature.

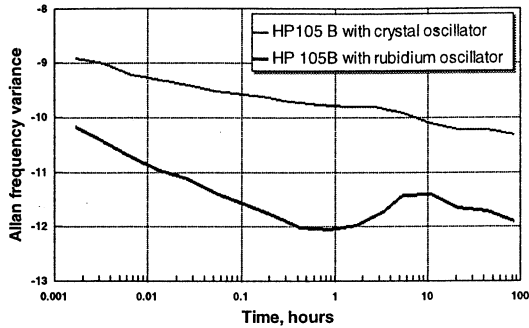


Fig. 6: Frequency Allan variances before and after modification

The AKL proficiency tests are carried out by transporting the modified HP 105B in a car. In order to keep the temperature stable during the trip the device is supplied with 220 V power via the car battery and an inverter. During the short transportation between the car and laboratory the power is supplied from the internal batteries of the device. The temperature of the Efratom base plate is monitored before, during and after the proficiency test and the measured frequencies are corrected according to the known temperature coefficient ( $+5 \cdot 10^{-12}/^{\circ}\text{C}$ ). After the modification the HP 105B has been used two times successfully in AKL proficiency tests. The results are in Figs. 7 and 8.

In Fig. 9 is the history of proficiency tests done by using HP 105B in 1993-1997. The upper bars represent uncertainties (left due to AKLs and right AKL and VTT combined). The lower bars are the corresponding relative deviations ( $|E_n|$ -values).

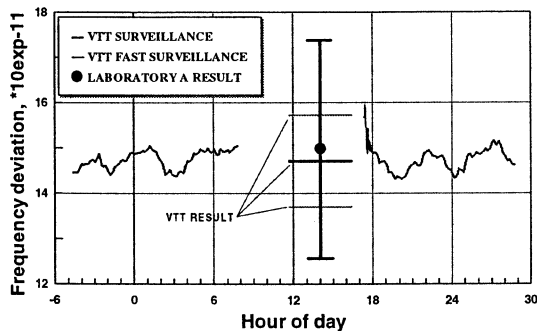


Fig. 7: Laboratory A proficiency test result

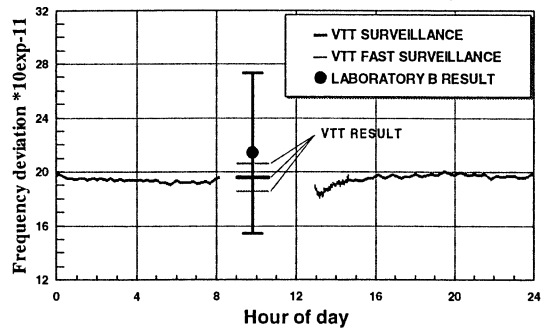


Fig. 8: Laboratory B proficiency test result

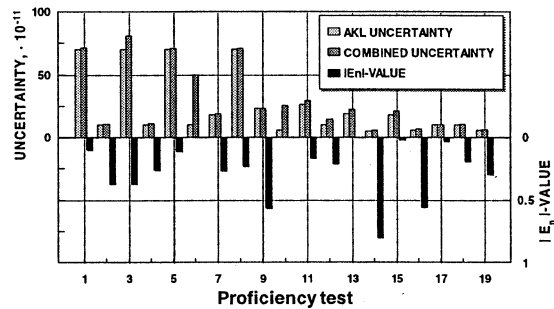


Fig. 9: History of proficiency tests done by using HP 105B in years 1993-1997

## CONCLUSIONS

The results show that the achievable uncertainty level is about  $1 \cdot 10^{-11}$  is in those frequency proficiency tests which can be realized by using a car during a work day (7h). The temperature dependence of the rubidium frequency seems to be linear and reversible, i.e. no hysteresis has been observed. The achieved uncertainty level is at the moment quite adequate for all calibration laboratories with frequency accreditation in Finland. Problems may come up if new laboratories with stringent frequency accreditations arise in the northern parts of the country and transportation by train or via air is mandatory.

1. Kalliomäki K, Mansten T, 1993, "TV-Frequency Standard as a Traceability Source in Accredited Calibration Laboratories", *Proc. 7th EFTF*, 383-385

## Polarization gradient cooling effect in the outer potential field

Masatoshi Kajita, Kyoya Fukuda, and Takao Morikawa

Communications Research Laboratory

4-2-1, Nukui-Kitamachi, Koganei, Tokyo184-8795, JAPAN

TEL: +81-423-27-6974 FAX: +81-423-27-6694 E-mail: kajita@crl.go.jp

### I. Introduction

Polarization gradient cooling (PGC) has been employed to obtain temperatures lower than the Doppler limit, so it is one of the most important techniques to develop the frequency standard based on the cold atoms. The energy distribution has been discussed assuming that it is in thermal equilibrium (for example J. Dalibard et al (1)). Actually the energy distribution after PGC is not always thermal equilibrium. J. S. Boulange et al. has experimentally shown that the energy distribution is described with two temperatures (2). Therefore, we need to examine the actual energy distribution after PGC is performed for a certain amount of time.

In this paper, we discuss the actual energy distribution after 1-dimensional PGC is given with (1) field free  $^{133}\text{Cs}$  atoms, (2)  $^{133}\text{Cs}$  atoms with gravity, and (3)  $^{24}\text{Mg}^+$  ions trapped by a harmonic oscillation potential.

### II. Theoretical basement with PGC

In this paper, we consider that PGC is performed with a linear-linear configuration in the  $z$ -direction, which makes  $\sigma^+$  at  $z = 0$ . When PGC is applied to an atom whose ground state is doubly degenerated ( $J = \pm 1/2$ ), the temporal change of atomic energy ( $E$ ) is given by

$$\begin{aligned} \frac{dE(z)}{dt} &= \frac{1}{2} \Delta \Gamma' \left\{ (\Pi_{1/2} - \Pi_{-1/2}) \cos(2kz) - 1 + \frac{1}{2} \sin^2(2kz) \right\} + \frac{D_P'}{M} \left[ 1 + \cos(2kz) (\Pi_{1/2} - \Pi_{-1/2}) \right] + \frac{D_P''}{M} \cos^4(2kz) \\ \frac{d(\Pi_{1/2} - \Pi_{-1/2})}{dt} &= -\Gamma' (\Pi_{1/2} - \Pi_{-1/2}) \cos(2kz) \\ \Delta &= \frac{2}{3} \frac{\hbar \delta \Omega^2}{\delta^2 + \Gamma^2/4} \\ \Gamma' &= \frac{2}{9} \frac{\Gamma \Omega^2}{\delta^2 + \Gamma^2/4} \\ D_P' &= \frac{11}{90} \frac{\hbar^2 k^2 \Gamma \Omega^2}{\delta^2 + \Gamma^2/4} \\ D_P'' &= \frac{4 \hbar^2 k^2 \delta^2 \Omega^2}{\Gamma (\delta^2 + \Gamma^2/4)}, \end{aligned} \quad (1)$$

where  $k$  denotes the wave number of the cooling laser,  $\delta$  is the laser frequency detuning,  $\Omega$  is the Rabi frequency,  $\Gamma$  is the rate of spontaneous emission, and  $M$  is atomic mass.  $\Delta$  denotes (optical energy shift of  $J=1/2$  atom)-(optical energy shift of  $J=-1/2$  atom) and  $\Gamma'$  is the transition rate

between  $J = \pm 1/2$  states.  $\Pi_{\pm 1/2}$  is the population at the  $J = \pm 1/2$  state.  $D_p'$  and  $D_p''$  denote heating effects caused by the photon recoil and the dipole force fluctuation, respectively. Actually,  $(\Pi_{1/2} - \Pi_{-1/2})$  can be approximately obtained to be  $\cos(2kz)$ .

First we consider the case that the atomic mobile range is much larger than  $\lambda$ . To fill this assumption, the atomic kinetic energy ( $K$ ) must be larger than the the depth of the optical potential ( $U$ ). Here we assume that the temporal change of  $\sin(2kz)$  and  $\cos(2kz)$  is much faster than that of the atomic velocity. Taking the average, Equation (1) can be rewritten as

$$\frac{dE}{dt} = -M\beta$$

$$\beta = \frac{1}{8M} \Delta\Gamma' - \frac{3D_p'}{2M^2} - \frac{3D_p''}{8M^2} \quad (2)$$

Note that  $\beta$  does not depend on the atomic velocity, so we can consider  $\beta$  as a constant value.

When the atoms are trapped within the Lamb-Dicke region (mobile range is less than  $\lambda$ ), the treatment is quite different. If the atoms are trapped at around  $z = 0$ , Eq. (1) should be solved taking

$$\cos(2kz) = 1 - 2(kz)^2. \quad (3)$$

The cooling procedure can be expressed by

$$\frac{dE}{dt} = -\gamma(E - E_{eq}), \quad (4)$$

where  $\gamma$  is the damping constant and  $E_{eq}$  is the equilibrium energy.

When the atoms (or ions) are in a certain outer potential field ( $P(z)$ ; for example, gravity, harmonic oscillation field), the motion equation is described by

$$\frac{dK}{dt} = \frac{d}{dt} \left( \frac{Mv^2}{2} \right) = \frac{dE}{dt} - \frac{dP(z)}{dt} - \frac{dP_{op}(z)}{dt}$$

$$\frac{dv}{dt} = \frac{1}{Mv} \frac{dE}{dt} - \frac{dP(z)}{Mdz} - \frac{dP_{op}(z)}{Mdz}$$

$$P_{op}(z) = -U \cos(2kz) (\Pi_{1/2} - \Pi_{-1/2}) \approx -U \cos^2(2kz), \quad (5)$$

where  $P_{op}(z)$  denotes the optical potential and  $v$  is the atomic velocity in the  $z$ -direction. When the atomic mobile range is much larger than  $\lambda$ ,  $dP_{op}(z)/dz$  is on average zero. Then Eq. (5) is given by

$$\frac{dv}{dt} = -\frac{\beta}{v} - \frac{dP(z)}{Mdz}. \quad (6)$$

When the atomic mobile range is much smaller than  $\lambda$ , Eq. (5) is given by

$$\frac{dv}{dt} = -\frac{\gamma}{Mv} (E - E_{eq}) - \frac{dP(z)}{Mdz} - \frac{dP_{op}(z)}{Mdz}. \quad (7)$$

With

$$\left| P(z) - P\left(z + \frac{\lambda}{2}\right) \right| \ll U, \quad (8)$$

Eq. (7) is approximated as

$$\frac{dv}{dt} = -\frac{\gamma}{Mv} (E - E_{eq}) - \frac{dP_{op}(z)}{Mdz} \approx -\frac{2Uk}{M} \sin(4kz) \quad (9)$$

Equation (9) shows that the atoms are trapped by the optical potential (optical lattice). Further,

we assume that Eq. (8) is valid. Then Eq. (6) should be employed with  $K > U$  and Eq. (9) with  $K < U$ . Here we consider the energy distribution, assuming that the initial energy distribution is in equilibrium (initial temperature is given by  $T_{initial}$ ). The ratio of the energy distributions ( $\rho(E)$ ) before and after PGC is given by

$$\rho(E^{final}) = \frac{dE^{initial}}{dE^{final}} \rho(E^{initial}), \quad (10)$$

where  $E^{initial}$  and  $E^{final}$  denote the energy before and after PGC, respectively. We can express the temporal change of atomic energy for the case  $K > U$  by

$$E^{final} = E^{initial} - M\beta t. \quad (11)$$

Equation (10) can then be expressed as

$$\frac{\rho(E_1^{final})}{\rho(E_2^{final})} = \frac{\rho(E_1^{initial})}{\rho(E_2^{initial})} = \text{Exp} \left[ -\frac{E_1^{initial} - E_2^{initial}}{T_{initial}} \right]. \quad (12)$$

In this case, the temperature, defined by the energy difference and population ratio, is given by  $T_{initial}$ .

For  $K < U$ , the energy loss by PGC becomes much smaller and the energy distribution is described by a temperature  $T_{final} (\approx E_{eq}^*/k_B)$ . The PGC procedure transforms atoms in the broad distribution component to the sharp distribution component. Under the actual experimental conditions, however the PGC time (on the order of 10 ms with neutral atoms) is not always long enough that the energy distribution is described by a single temperature.

### III. Energy distribution of potential free $^{133}\text{Cs}$ atoms after PGC

First, we consider the case where PGC is given to a potential free  $^{133}\text{Cs}$  atomic cloud. The kinetic energy change is obtained through numerical calculation. The wavelength ( $\lambda$ ) of the cooling laser is 852 nm. Figure 1 shows the energy distribution after PGC is performed for 13 ms. We assume that the initial energy distribution is in thermal equilibrium (400  $\mu\text{K}$ ). The Rabi frequency of  $6S_{1/2} (F=4, m_F=4) \rightarrow 6P_{3/2} (F=5, m_F=5)$  transition is  $1.4 \Gamma$  ( $\Gamma/2\pi = 5 \text{ MHz}$ ), and  $\delta$  is taken to be  $10 \Gamma$ . As suggested in Sec. II, the energy distribution is described by two sub-components, a sharp component (with a temperature 2  $\mu\text{K}$ ) and a broad component (with a temperature 400  $\mu\text{K}$ ). In this case, atoms which belong to the sharp component amount to almost 10 %, and this increases as the PGC time becomes longer.

### IV. PGC effect on atoms with gravity

Here we consider the case where PGC is given with a  $^{133}\text{Cs}$  atomic cloud in the vertical direction. In this case, the effect of gravity should be taken into account.

When the initial atomic velocity is downward, atoms are accelerated by gravity unless the initial kinetic energy is smaller than  $U$ . The absolute value of velocity increases from the initial

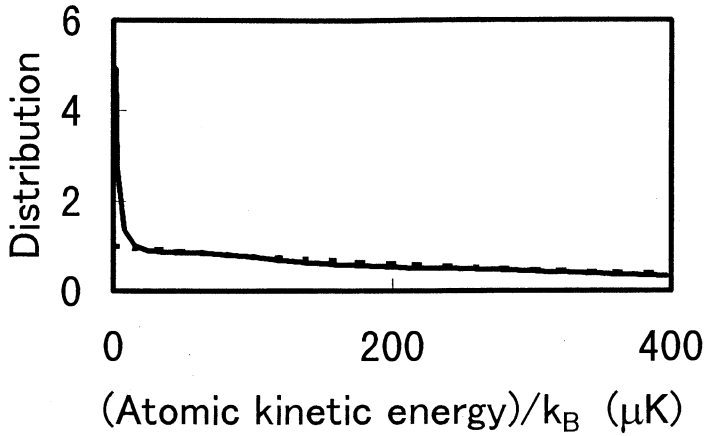


Fig. 1: The distribution of kinetic energy of potential free  $^{133}\text{Cs}$  atoms after (solid line) and before (dotted line) PGC, with the condition shown in the text (Sec. III).

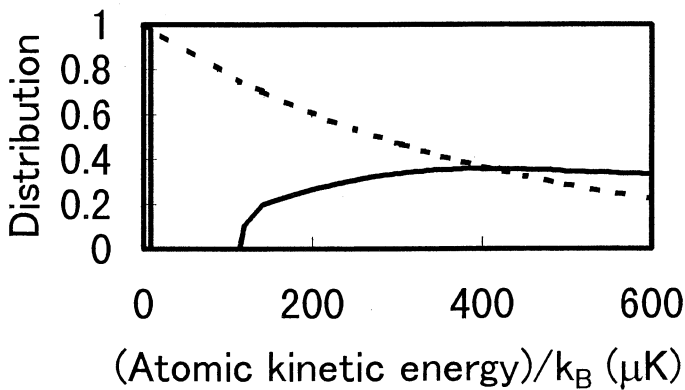


Fig. 2: The distribution of kinetic energy of  $^{133}\text{Cs}$  atoms in the gravity field after (solid line) and before (dotted line) PGC, with the condition shown in the text (Sec. III). Initial velocity is downward.

value and the deceleration force becomes very small. Figure 2 shows the kinetic energy distribution after PGC (same initial condition with Sec. III). It shows that the average kinetic energy is increased by the gravity, and that the distribution of kinetic energy is broadened more than the initial condition.

When the initial atomic velocity is upward, gravity works to decrease the absolute value of velocity. The deceleration force by PGC, which is inversely proportional to atomic velocity, becomes much larger than the case of potential free atoms. As soon as the atomic kinetic energy becomes less than  $U$ , atoms are trapped by the optical potential at that position and cannot be accelerated by gravity after that. Figure 3 shows the kinetic energy distribution after PGC

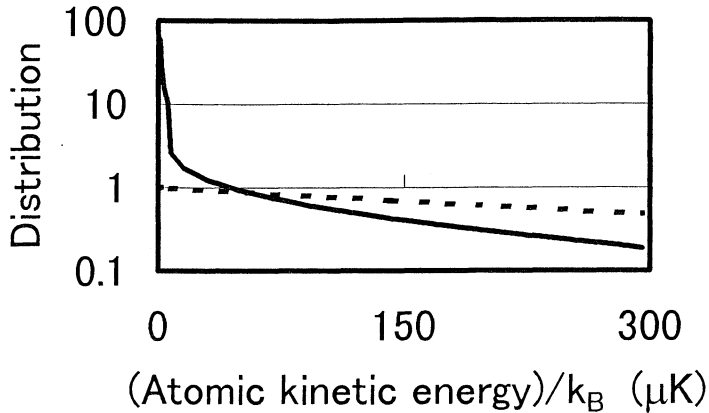


Fig. 3: The distribution of kinetic energy of  $^{133}\text{Cs}$  atoms in the gravity field after (solid line) and before (dotted line) PGC, with the condition shown in the text (Sec.III). Initial velocity is upward.

(same initial condition with Sec. III). It shows that the kinetic energy distribution is described by a sharp component and a broad component. In this case almost 50% of the atoms belong to the sharp component.

#### V. Distribution of the harmonic potential energy after PGC

Sections III-IV discuss the temporal kinetic energy distribution. In this section, we discuss the distribution of  $P(z)$  (see Sec. II) after PGC. Here we consider the case where  $P(z)$  is given by

$$P(z) = \frac{1}{2} M \omega^2 (z - z_c)^2, \quad (13)$$

where  $\omega$  is the angular oscillation frequency and  $z_c$  is the trap center of  $P(z)$ . The atomic energy is given by

$$\begin{aligned} E &= P(z) + E_{lattice} \\ E_{lattice} &= K + P_{op}(z). \end{aligned} \quad (14)$$

Once  $K$  becomes smaller than  $U$ , atoms are trapped by the optical potential (see Eq. (9)), which happens within one half period. There is no energy transfer between  $E_{lattice}$  and  $P(z)$  after that.  $P(z)$  remains constant, while there is no random walk between lattice sites. The random walk effect is negligible if  $U$  is large enough (larger than 100 times the photon recoil energy).

Actually, the harmonic oscillation potential is much easier to give for ions (with rf-trap, Penning trap, or linear trap) than for neutral atoms. We have calculated the distribution of  $P(z)$  for  $^{24}\text{Mg}^+$  ions after PGC is performed ( $\lambda = 280$  nm) for 100 ns (taking a longer PGC time, there is very little difference in the result). We assume that the initial energy distribution is thermal equilibrium (1 mK). The Rabi frequency is  $0.79 \Gamma$  ( $\Gamma/2\pi = 43$  MHz),  $\delta$  is taken to be  $2.5 \Gamma$ , and  $\omega$  is  $2\pi \times 3$  kHz. Figure 4 shows the distribution of  $P(z)$  after PGC. The distribution of  $P(z)$  is not in thermal equilibrium. It is composed by two components: a sharp distribution component and a

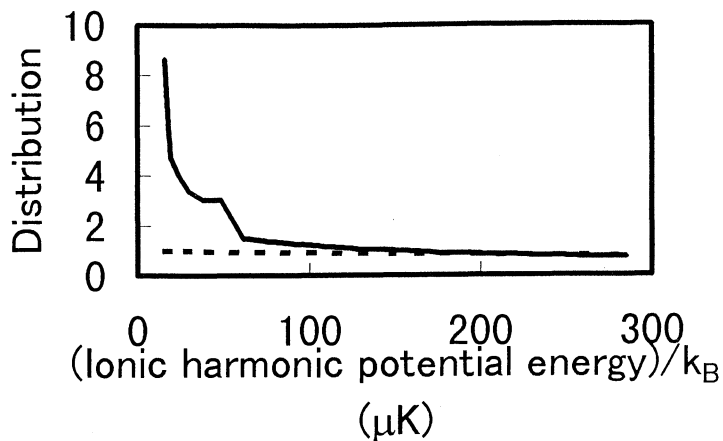


Fig. 4: The distribution of harmonic potential energy of trapped  $^{24}\text{Mg}^+$  ions. The solid line and dotted line show the distribution of  $P(z)$  after and before PGC, respectively. The condition is given in the text (Sec.V).

broad distribution component.

## VI. Conclusion

This is the first trial to analyze the energy distribution when PGC is performed with atoms or ions in some outer potential fields ( the gravity or harmonic potential etc.). When the atomic kinetic energy is larger than  $U$ , the PGC gives a deceleration force inversely proportional to the atomic velocity. Once the kinetic energy becomes smaller than the depth of the optical potential, the atoms are trapped at that position by the optical potential. Then the outer potential energy does not change after that, and its distribution is not in thermal equilibrium.

## References

- [1] J. Dalibard and C. Cohen-Tannoudji, J. Opt. Soc. Am. B, 6, 2023 (1989).
- [2] J. S. Boulanger, M. C. Gagne, and R. J. Douglas, Proceedings of "11<sup>th</sup> European Frequency and Time Forum (Neuchatel)", 567 (1997)

## RFH 100 A RUGGEDIZED TIME & FREQUENCY SYSTEM FOR NAVY

Jean-François SCHUH, Bruno CAILLIEZ, Hervé BELIVIER

MORS - Défense - BP 22 - 13610 Le Puy Sainte Réparate - France  
phone : (33) 4 - 42 33 86 00 - fax : (33) 4 - 42 61 85 31 - e mail : MORS@dialup.francenet.fr

### 1. ABSTRACT

MORS has developed for the French Navy a new Time and Frequency Equipment that provides precise time and precise frequency signals in a harsh environment.

Named **RFH 100**, it is based on dual redundant cesium beam frequency standards fixed in a ruggedized case.

It generates and distributes frequency and time information in a wide temperature, shock, vibration, electromagnetic range.

The time is periodically compared to GPS timing information. It can be automatically corrected every day, even when the GPS timing information is not available : a long term analysis, processed by the equipment itself, maintains a **1  $\mu$ sec maximum time drift over 10 days** without the GPS timing information, and within the worst environmental conditions.

The equipment drives up to 12 time and frequency outputs, and up to 60 outputs with 4 distribution units.

### 2. INTRODUCTION

Since the 80's, MORS has a defence activity based on the development and production of dedicated ruggedized equipments.

MORS is a preferred supplier for the French Navy in Time & Frequency and Navigation systems. Primary Frequency Standards, Primary Clocks, Loran C receivers are the different products installed on ships and used in operational conditions.

The need for better performances at lower price has led MORS to associate different technologies to improve system accuracy. The association of the best available technologies, as GPS, LORAN C, and Atomic clock, has conducted MORS to develop a new Primary Reference Clock based on the use of the best features in each technology to improve overall performances.

The RFH 100 is a Primary Reference Clock designed with automatic time scale monitoring. It provides efficient clock correction, and simplified directions for use. Thus, the RFH 100 Primary Reference Clock can be operated by a non-specialist crew.

The RFH 100 Primary Reference Clock have the following interfaces :

- a complete GPS receiver input, complying with ICD-GPS-060 revision A,
- a 1 PPS time reference input complying with PT&FI interface,
- a LORAN C receiver interface,
- 8 x 5 MHz outputs (1Vrms / 50  $\Omega$ ),
- 11 x 1 PPS outputs (TTL / 50  $\Omega$ ),
- 1 x 0.1 PPS output (TTL / 50  $\Omega$ ),
- 12 x time message outputs (serial time code),

The outputs can be expanded through RFH 100 Secondary Clocks whose outputs are :

- 12 x 5 MHz outputs (1Vrms / 50  $\Omega$ ),
- 12 x 1 PPS outputs (RS422),
- 12 x time message outputs (serial time code).

The RFH 100 equipments are shown figure 1.

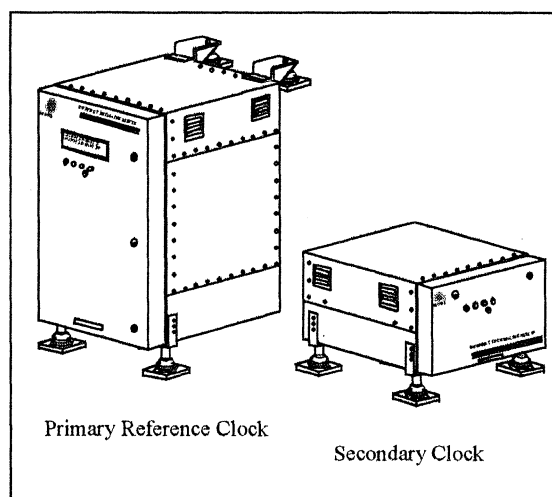


Fig 1 : RFH 100 Equipments

### 3. RFH 100 PRINCIPLES

The RFH 100 Primary Reference Clock generates and distributes precise frequency signals and precise time information to a wide diversity of users.

The heart of the system is composed of dual redundant cesium beam frequency standards whose behaviors are monitored through a complementary reference. After a learning period, the RFH 100 Primary Reference Clock is able to correct the generated time scale without human intervention.

The complementary reference can be acquired through a GPS receiver when the ship is at sea, or through a ground reference station when the ship is ashore.

The behavior analysis of cesium beam frequency standards is based on time error measurements between the "1 PPS" signal derived from the two cesium beam frequency standards and the complementary reference "1 PPS" signal. Measurements are made every second and memorised for an hour, for a day, and ten days.

A global analysis is performed per day and per ten days to determine two time correction values. The effective correction values depends on the complementary reference status to minimize errors.

The RFH 100 Primary Reference Clock block diagram is shown figure 2.

### 3.1. Cesium beam frequency standard model

The frequency inaccuracy of a cesium beam frequency standard can be expressed by the following formula :

$$\frac{\Delta F}{F}(\tau) = D \cdot \tau + \frac{\Delta F}{F}(0) + \rho_{\theta} \cdot [\Delta\theta 1(\tau) + \Delta\theta 2 \cdot \cos(2\pi \frac{\tau}{T_j}) + \Delta\theta 3 \cdot \cos(2\pi \frac{\tau}{T_a})] + \sigma_{\tau} \quad (1)$$

with the following definitions :

- D = aging,
- $\frac{\Delta F}{F}(0)$  = initial frequency offset,
- $\Delta\theta 1(\tau)$  = temperature difference at  $\tau$  time between mean ambient and adjustment temperature,
- $\Delta\theta 2$  = peak daily temperature,
- $\Delta\theta 3$  = peak annual temperature,
- $T_a$  = year duration (365,25 days)
- $T_j$  = day duration (24 hours)
- $\rho_{\theta}$  = thermal sensitivity,
- $\sigma_{\tau}$  = square root of Allan variance for a  $\tau$  time observation.

For OSA 3006-02 cesium beam frequency standard, the parameters are :

- D  $\approx$   $1 \cdot 10^{-22}$ ,
- $\frac{\Delta F}{F}(0)$  =  $\pm 2 \cdot 10^{-12}$  over a temperature range from 0°C to +50°C,

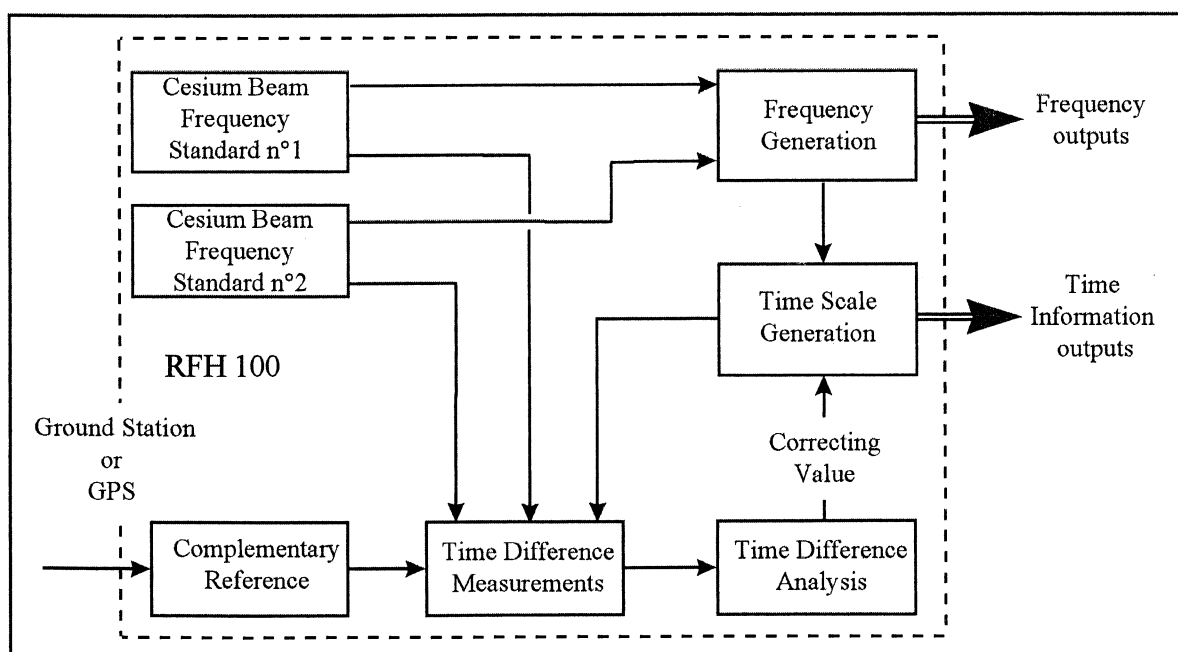


Fig 2 : RFH 100 Primary Reference Clock Block diagram

$\rho_{\theta}$	<	$5.10^{-12}$ over a temperature range from 0°C to +50°C,
$\sigma_{\tau}$	<	$2.10^{-12}$ for $\tau = 1000$ seconds, $5.10^{-13}$ for $\tau = 10.000$ seconds, $3.10^{-13}$ for $\tau = 100.000$ seconds. $1.10^{-13}$ for $\tau > 100.000$ seconds.

The RFH 100 time difference is obtained through a time integration of the frequency inaccuracy.

The time difference can be expressed by the formula :

$$\Delta T(\tau) = \int_0^{\tau} \frac{\Delta F}{F}(t) dt \quad (2)$$

The expression of time difference is :

$$\Delta T(\tau) = X_0 + \frac{D}{2} \tau^2 + \frac{\Delta F}{F}(0) \cdot \tau + \rho_{\theta} [\Delta\theta 1(\tau) \cdot \tau + \Delta\theta 2 \cdot \frac{T_j}{2\pi} \sin(2\pi \frac{\tau}{T_j}) + \Delta\theta 3 \cdot \frac{T_a}{2\pi} \sin(2\pi \frac{\tau}{T_a}) ] + \sigma_{\tau} \cdot \tau \quad (3)$$

where

$X_0$  is the initial time offset,

$$\Delta T_d(\tau) = \frac{D}{2} \tau^2 + \frac{\Delta F}{F}(0) \cdot \tau + \rho_{\theta} [\Delta\theta 1(\tau) \cdot \tau + \Delta\theta 2 \cdot \frac{T_j}{2\pi} \sin(2\pi \frac{\tau}{T_j}) + \Delta\theta 3 \cdot \frac{T_a}{2\pi} \sin(2\pi \frac{\tau}{T_a}) ] \quad (4)$$

is a deterministic time difference,

$\Delta T_r(\tau) = \sigma_{\tau} \cdot \tau$  is a random time difference.

The  $\Delta T_d(\tau)$  value is computed from the integration of the deterministic frequency inaccuracy; the value is depending from temperature profile.

The  $\Delta T_r(\tau)$  value is  $\sigma_{\tau} \cdot \tau$  and is depending from time observation.

As aging is very small, the corresponding time error value is neglected.

The daily and annual temperatures are considered as secondary terms ; the corresponding time errors are not considered.

$\Delta\theta 1(\tau)$  is supposed to be about constant over time observation.

The remaining terms are the following :

$$\Delta T(\tau) = X_0 + [ \frac{\Delta F}{F}(0) + \rho_{\theta} \cdot \Delta\theta 1(\tau) + \sigma_{\tau} ] \cdot \tau \quad (5)$$

This linear equation is the model used for time drift measurement.

### 3.2. Learning process

The learning process consists on the calculation of the two cesium beam frequency standards parameters. As precised above, a linear modelisation is considered to define the time drift related to the standards.

Every second, four time differences are measured : the first between the complementary reference and the cesium standard n°1, the second between the complementary reference and the cesium standard n°2, the third between the two cesium standards, and the fourth between the complementary reference and the RFH 100 Primary Reference Clock output.

Every hour, time differences are computed through a linear algorithm process in order to deliver, for each channel, the initial time offset, the associated time slope and standard deviation.

Every day, at 10:00:00 UTC, a similar calculation gives for the complete day, for the last ten days, and for each channel, the initial time offset, the time slope, and the standard deviation.

Each computation returns a status defining the validity of the result, depending on the complementary reference status and measurement sequence.

When the complementary reference is available, the learning process is always operational, and is realised on ten successive sliding days.

When the complementary reference is not available, the learning process is stopped, waiting for the next availability.

### 3.3. Correction process

The correction process is allowed each day at 10:00:01 UTC. It applies the corrections computed over the previous day :

- the initial time offset on the RFH 100 Primary Reference Clock output,
- the time drift on the selected cesium beam frequency standard.

The considered correction values are the values computed over the last day if the complementary reference was available.

If the complementary reference is not yet available, the considered correction values are the values computed over the last ten days with the available complementary reference.

The latter correction values have higher precision and allow the RFH 100 Primary Reference Clock to apply efficient corrections even if the complementary reference is not available for a long time.

A coherence test is performed with the successive correction values to remove unrealistic values corrupted by the complementary reference invalidity (GPS failure for instance).

In the same way, the benefit of the three sources is used to detect a faulty source (Cesium or GPS reference), and to select the best cesium beam frequency standard to be used for Time & Frequency generation.

#### 4. RFH 100 PERFORMANCES

The RFH 100 Primary Reference Clock was designed to operate in extreme environmental conditions :

- temperature range from  $-5^{\circ}\text{C}$  to  $+55^{\circ}\text{C}$ ,
- shocks up to 40g,
- vibrations from 1 Hz (1 mm) to 55 Hz ( $10\text{ m/s}^2$ ),
- electromagnetic fields,
- heavy rains (500 mm/h).

Nevertheless, the RFH 100 Primary Reference Clock operating in a temperature range from  $+15^{\circ}\text{C}$  to  $+36^{\circ}\text{C}$ , is specified to maintain a time within a maximum of 1  $\mu\text{sec}$  from UTC.

##### 4.1 Theoretical Performance

A simulation of the RFH 100 Primary Reference Clock maximum time error is shown figure 3. The assumptions related to the simulation are the following :

- at the beginning of the 1<sup>st</sup> day, an initial synchronisation is performed with GPS signals,
- the learning period lasts over 10 successive days with GPS available,
- the GPS is not available between the 11<sup>th</sup> day and the 20<sup>th</sup> day,
- the GPS standard deviation is  $\sigma_{\text{GPS}} = 100\text{ ns}$ , with TFOM parameter less or equal to 3,
- the ambient temperature profile is displayed at the bottom of figure 2 (min =  $+9^{\circ}\text{C}$ , max =  $+44^{\circ}\text{C}$ ) ; the average is stable over the first ten days, and linearly rising over the next ten days,
- the time error is given at 99.7 % ( $3\sigma$ ),
- the cesium beam frequency standards are OSCILLOQUARTZ OSA 3006-02, selected for their low temperature sensitivity.

Under these conditions, the maximum time error (at 99.7 %) is less or equal to 915 ns over the complete period of 20 days.

One can see that a daily correction is applied, based on the computed values over the previous day when GPS is available, and based on the computed values over the previous ten days when GPS is not available.

These simulation results are worst case analysis. Experimental results should be much better.

##### 4.2 Experimental Performance

Measurements were made on an operational RFH 100 Primary Reference Clock for characterization.

After environmental tests passed with success, the RFH 100 Primary Reference Clock was running and evaluated over a long period.

The experiment described here after lasted over 11 days : 5 days with a GPS receiver connected to the corresponding input, 5 days with a GPS receiver disconnected, and 1 day with a GPS receiver reconnected.

So the learning and correcting period with GPS is over 5 successive days, the correcting period without GPS is over 5 successive days, and a new learning and correcting period with GPS is over 1 day.

The experiment was done under ambient environmental conditions, without any particular precautions.

The GPS receiver used was an ONCORE Motorola model, coupled to an adapter delivering a classical ICD-GPS-060 format.

The figure 4 shows measurements performed on the RFH 100, from the 5<sup>th</sup> day to the 11<sup>th</sup> day.

The first curve is the time error between a "1 PPS" derived from one of the cesium beam frequency standards selected for Time & Frequency generation and the "1 PPS" signal from the GPS receiver.

The second curve is the time error between the RFH 100 "1 PPS" output signal and the "1 PPS" signal from the same GPS receiver.

The superposed noise is related to GPS noise.

The first curve is a typical cesium beam frequency standard time error due to frequency inaccuracy. The cesium beam frequency standard slope is evaluated at 70 ns per day (relative accuracy of  $8 \cdot 10^{-13}$ ).

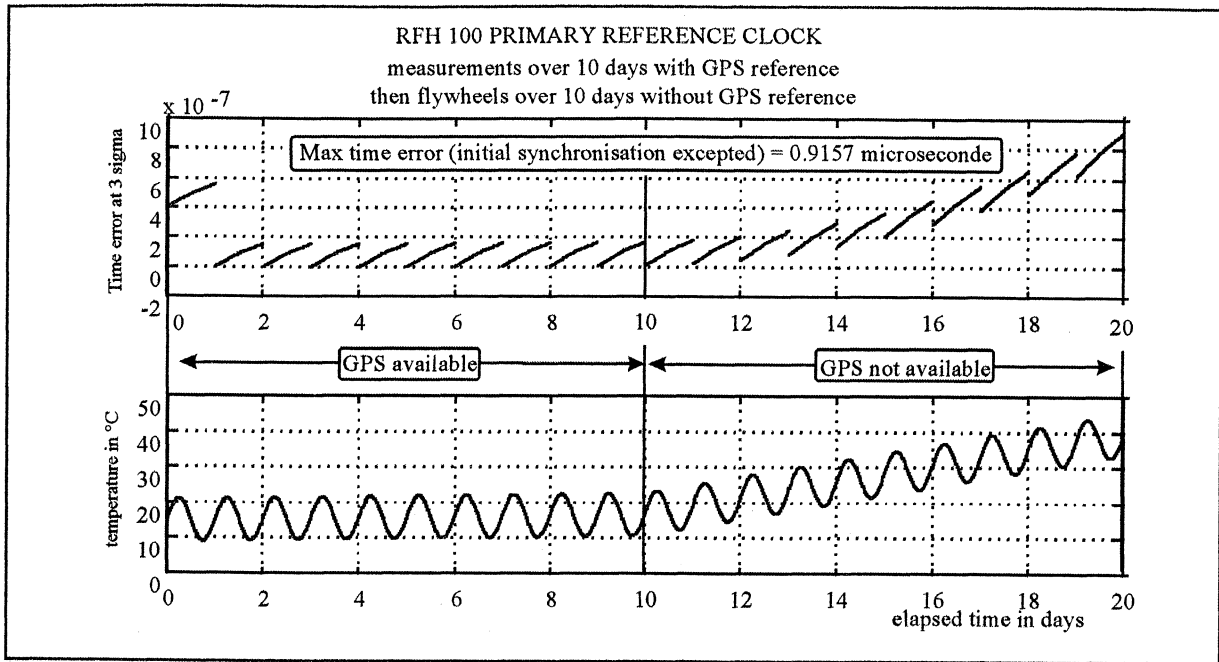


Fig 3 : RFH 100 Primary Reference Clock Theoretical Performance

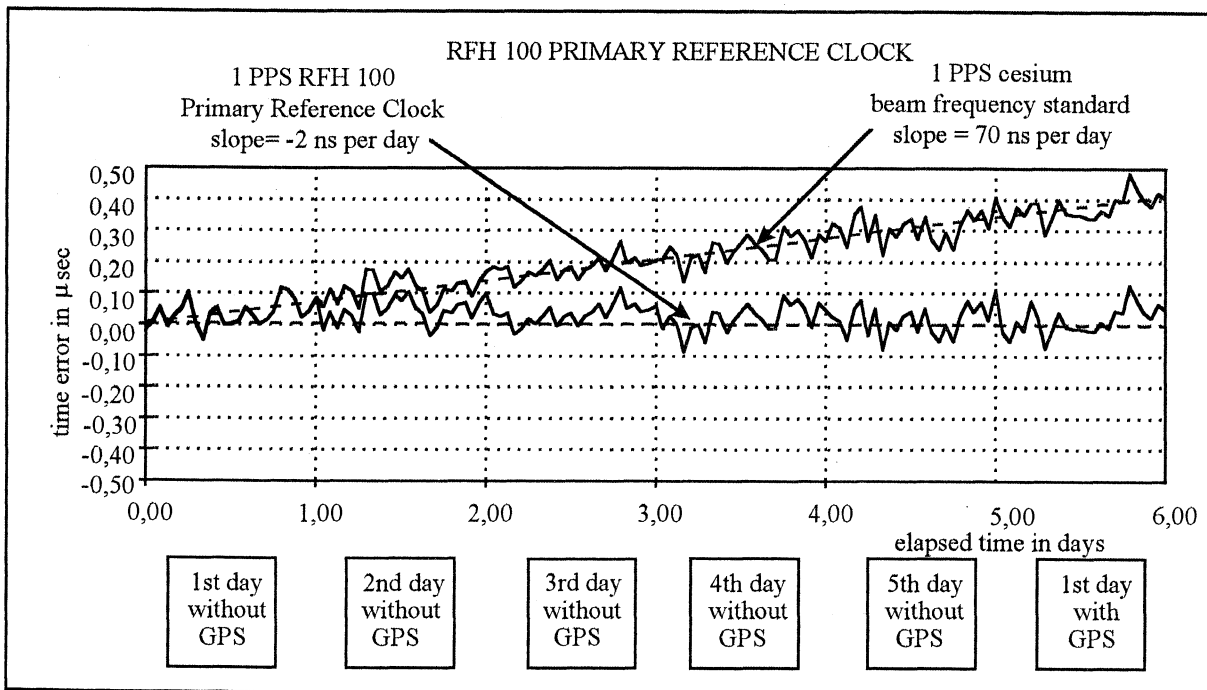


Fig 4 : RFH 100 Primary Reference Clock Experimental Performance

The second curve is the same as the first curve over the first day because the selected cesium beam frequency standard is used for Time & Frequency generation. At the beginning of the second day, the RFH 100 time output is corrected to compensate the cesium beam frequency standard drift over the previous day. And so on till the end of the 5<sup>th</sup> day where GPS is available again.

The global RFH 100 Primary Reference Clock slope is evaluated at -2 ns per day (relative accuracy of  $2.3 \cdot 10^{-14}$ ).

The experiment shows the high ability of the RFH 100 Primary Reference Clock to compensate the drift of its internal cesium beam frequency standards, even when the complementary reference is not available for several days.

No differences were detected between the duration with learning and correcting period, and the duration with correcting period only.

## 5. LORAN C RECEIVER CONTRIBUTION

The RFH 100 Primary Reference performance is related to the confidence level of the complementary reference.

If this one is acquired through a ground reference station, the confidence level is supposed to be well-known.

If this one is acquired through a GPS receiver, the intrinsic confidence level of the GPS system is not sufficient enough for military missions ; So a control of the GPS integrity is performed for proper operations. The GPS integrity is monitored through the RFH 100 Primary Reference Clock and our LORAN C receiver.

The RFH 100 Primary Reference Clock performs a crossed coherence between the two cesium beam frequency standards and the GPS information, while the LORAN C receiver computes a time difference between the RFH 100 time and LORAN C time (disciplined on UTC time scale, and independent of GPS time).

A dedicated proprietary software, implemented on the MORS LORAN C receivers, monitors time difference information.

These computations are performed in the following high performances MORS LORAN C receivers :

62 NR 15 : full military,  
RLC 100 : enhanced off the shelves.

## 6. RFH 100 FACILITIES

The RFH 100 Primary Reference Clock can be operated in two different modes :

- a fully automatic mode, without human intervention, where the best cesium beam frequency standard is selected, and where timing information is corrected every day,
- a manual mode, under human supervision, where all operations are driven by a skilled staff in Time & Frequency subject.

Besides ordinary time functions, the RFH 100 Primary Reference Clock has the convenient helpful features in Time & Frequency networks :

- GPS time offset compensation (from -1  $\mu$ sec to +1  $\mu$ sec),
- cable propagation delay compensation (from 0 meter to 150 meters),
- time scale offset (from -10  $\mu$ sec to +10  $\mu$ sec of UTC).

## 7. FUTURE DEVELOPMENTS

The new up-market RFH 100 Primary Reference Clock was developed in accordance with specific military needs.

Nevertheless, the product was designed with a high modularity level, easily adapted for other needs required by civilian or industrial applications.

Lower environmental conditions should improve the performances in a significant way, and lower performances should drastically reduce the cost through the choice of other internal oscillators.

MORS has planned the development, on the one hand, of a simplified off the shelves version (based on a single cesium beam frequency standard), on the other hand, a much more precise version (based on multiple cesium beam frequency standards), of the present RFH 100 Primary Reference Clock.

## 8. CONCLUSION

MORS thanks the French Procurement Agency and particularly the DCN INGENIERIE, for the expression of their confidence shown in this development.

The new principles implemented by MORS, give a new insight into an attractive generation of Time & Frequency equipments that combines high performances and simplicity of operation. For the first time, an original method for GPS integrity is proposed, based on the new enhancement of the LORAN C system.

With the new RFH 100 Primary Reference Clock, MORS maintains its leadership among the best companies supplying dedicated ruggedized Time & Frequency systems.

R R R R R R R R R R R R

## USE OF A DUAL-FREQUENCY MULTI-CHANNEL GEODETIC GPS RECEIVER FOR THE ESTIMATION OF IONOSPHERIC DELAYS APPLIED TO ACCURATE TIME TRANSFER

Kenneth Jaldehag<sup>1</sup>, Claudine Thomas<sup>2</sup>, and Jacques Azoubib<sup>2</sup>

<sup>1</sup>SP Swedish National Testing And Research Institute, Borås, SWEDEN

<sup>2</sup>Bureau International des Poids et Mesures, Sèvres, FRANCE

### ABSTRACT

A dual-frequency multi-channel geodetic GPS receiver (Ashtech Z12) has been used to estimate ionospheric delays which can be applied to GPS single-frequency observations. The receiver, which is located at the SP Swedish National Testing and Research Institute, Borås, Sweden, tracks the P-code on both carrier frequencies by a cross-correlation technique which makes it possible to estimate the ionospheric delay on L1 for each track of the international GPS tracking schedule issued by the BIPM (Bureau International des Poids et Mesures, Sèvres, France). Time links are computed using measured ionospheric delays and precise satellite ephemerides between the Observatoire de Paris (OP), France, the National Institute of Standards and Technology (NIST), Boulder, Colorado, USA, and the SP. A study of these time links and of the closure SP-OP-NIST-SP shows that the use of measured ionospheric corrections significantly improves the accuracy of the time links to the SP.

Keywords: GPS time transfer, common view, ionospheric delay, geodetic GPS receiver.

### 1. INTRODUCTION

Since 1985, the GPS common-view method [1] has been used with great success for the comparison of clocks on remote locations on the Earth and is, at present, the main technique on which relies the computation of international time references such as International Atomic Time (TAI). Strict common views, synchronised to within 1 s, make it possible to remove the clock-dither noise brought about by Selective Availability. The remaining error sources affecting GPS common-view results are linked to imperfections in the broadcast satellite ephemerides, to the use of a model for estimation of the ionospheric delays, and to errors in antenna coordinates on site [2]. At present, most time laboratories know their antenna coordinates with an uncertainty of 10 cm or better and errors associated with the position of GPS satellites are dealt with by using precise satellite ephemerides available via Internet from, for example, the international GPS

Service for Geodynamics [3]. The problem of estimating the ionospheric delays experienced by GPS signals along the line of sight of the satellites is still far from being solved for many time links, and independent estimates of the ionospheric delay are expected to have increased importance during the next maximum of solar activity around year 2000.

Currently, most national time laboratories are equipped with single-frequency GPS receivers, which apply ionospheric model parameters broadcast from the GPS satellites to compensate for the ionospheric delays. However, since the modelled values have a precision of about 50% [4], instruments based on code-less dual-frequency GPS observations have been developed during the last 5-10 years [5, 6, 7]. These instruments are designed to measure ionospheric delays and are in regular use at a few time laboratories. The application of ionospheric delay corrections computed on the basis of data from such instruments, located at each end of an inter-continental baseline, in conjunction with the use of precise ephemerides, has led to an improvement in time transfer accuracy which is, at present, characterized by a standard uncertainty of 4 ns for one 13 minute common-view observation [8, 9].

This paper presents results demonstrating the use of a dual-frequency multi-channel geodetic GPS receiver (Ashtech Z12) for the estimation of ionospheric delays. The receiver is located at the SP Swedish National Testing and Research Institute, Borås, Sweden, and is normally used for accurate differential positioning. It tracks the P-code on both frequencies by a cross-correlation technique and is capable of observing up to 12 satellites simultaneously which means that, in general, no scheduling or pointing system is necessary. If absolute measurements of the ionospheric delays are required there is a need to compensate for the internal differential delays between the two frequencies in both the geodetic receiver and the GPS satellites.

The routines for estimation of the ionospheric delay corrections from measurements based on the geodetic receiver at the SP and the comparison of the measured delays with those calculated from the broadcast model parameters, are described and

discussed in Section 2. The estimates are then applied to L1 C/A-code observations carried out at the SP following the international GPS tracking schedule issued by the BIPM (Bureau International des Poids et Mesures, Sèvres, France). Time links and closure conditions are computed using measured ionospheric delays and precise satellite ephemerides between the Observatoire de Paris (OP), France, the National Institute of Standards and Technology (NIST), Boulder, Colorado, USA, and the SP. These results are presented and discussed in Section 3.

## 2. ESTIMATION OF IONOSPHERIC DELAY CORRECTIONS

Since the delay of the GPS signals through the dispersive ionosphere is roughly in inverse proportion to the square of the carrier frequencies at L1 (1575.42 MHz) and L2 (1227.60 MHz), it is easily shown that the ionospheric group delay of the P1 observable,  $P1_{ion}$ , is

$$P1_{ion} = k \cdot (P2 - P1) / c \quad (1)$$

where  $P1$  and  $P2$  are measured code ranges at L1 and L2, respectively,  $k = 120^2 / (154^2 - 120^2)$ , and  $c$  is the speed of light in vacuum. If we assume that the receiver can measure the P1 and P2 observables within 1% of the signal chip-length, the precision of  $P1_{ion}$  can be estimated to be about 1 ns. The accuracy of  $P1_{ion}$  is set by the knowledge of the differential delays between the L1 and L2 channels in both the receiver and in the GPS satellites.

### 2.1 Calibration of the internal differential delay of the Ashtech Z12 geodetic GPS receiver at the SP

In order to calibrate the internal differential delay of the Ashtech Z12 geodetic receiver, the estimated ionospheric delays, as calculated using Equation (1), are regularly compared with those from another geodetic GPS receiver (Allen Osborne Associates TurboRogue) located at the Onsala Space Observatory, Onsala, Sweden, about 60 km from the SP. The TurboRogue receiver at Onsala (as well as many similar receivers in Europe) is calibrated on a daily basis by the Deutsche Forschungsanstalt für Luft- und Raumfahrt (DLR), Neustrelitz, Germany. This is done by analysis of GPS carrier phase data for the study of total electron content in the atmosphere above Europe [10, 11]. Another outcome of the DLR analysis is an estimation of each receiver's internal differential delay, between L1 and L2, for each satellite, that is, the receiver + satellite delay (referred to as bias in the following), on a daily basis. In order to calibrate the Ashtech Z12 receiver at the SP (which is not included in the

DLR analysis), that is, to find the bias of the Ashtech Z12 receiver, we use the following routine:

1. Collect the observational daily RINEX files, for the Onsala TurboRogue and the SP Ashtech Z12 receivers, consisting of code (and phase) data.
2. Use Equation (1) to estimate  $P1_{ion}$  for each code observation in the RINEX files.
3. Correct each estimate for the TurboRogue receiver on a satellite-by-satellite basis using the bias data available from the DLR analysis.
4. Find observations that are common (in time) to Onsala and the SP and calculate the difference between them (and only them).
5. Average the differential data on a satellite-by-satellite basis.

What is left after point 5 is an estimate of the bias of the SP Ashtech Z12 receiver on a daily satellite-by-satellite basis. The procedure assumes (1) that the ionosphere behaves similar over Onsala and the SP, and (2) that the biases in the receivers and satellites vary little over the course of a day. It is not possible with this procedure to separate the biases originating in the receivers from those originating in the satellites. However, this is not needed or relevant for this study as the measured delays from the systems used at the OP and the NIST both include the satellite bias; the satellite bias thus cancels in the common-view method.

In Figure 1 we plot the estimated receiver + satellite biases for the Ashtech Z12 geodetic receiver averaged over the 410 days that were used between 1 August 1996 to 17 October 1997 (MJD 50296-50738). In Figure 2 we plot, for all 410 days, the estimated daily average of the receiver + satellite bias, obtained from the satellites observed during the day. The estimated biases in Figure 2 are the values to be used in the common-view solutions to correct for the Ashtech Z12 receiver bias. These values do not include the satellite-dependent

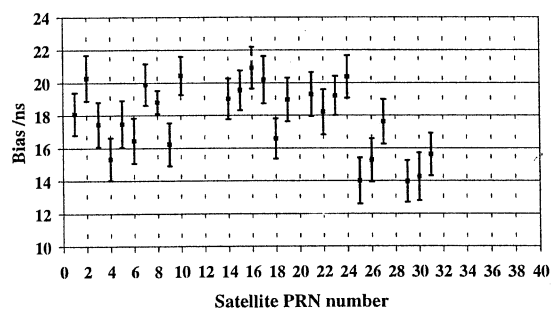


Figure 1: Estimated receiver + satellite bias for the Ashtech Z12 receiver at the SP on a satellite-by-satellite basis. Each estimate is for an average of 410 days between 1 August 1996 to 17 October 1997 (MJD 50296-50738). The uncertainty bars characterize the dispersion of the daily biases.

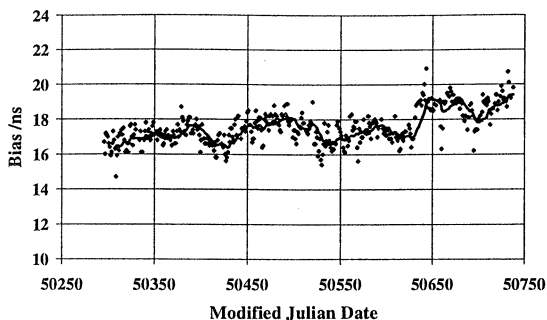


Figure 2: Estimates of the receiver + satellite bias of the Ashtech Z12 geodetic receiver at the SP. Each point is a daily average obtained from all satellites observed during the day. Included is also a 10 day average plotted as a line.

variations shown in Figure 1 but, as noted above, they should not. The uncertainties of the estimates shown in Figure 2 are probably a few nanoseconds so, instead of using one estimate for each day, we have in this study used a fixed value of 17 ns which is close to the average of all the estimates in Figure 2. The standard deviation of these estimates is about 1 ns. The estimated average bias of 17 ns is based on all GPS satellites observed by the Ashtech Z12 geodetic receiver. If for some reason specific satellites were disregarded in the international GPS tracking schedule issued by the BIPM, the value of 17 ns may differ slightly from the average value set. We judge, however, that it is a good description of the overall accuracy of the estimated bias.

## 2.2 Estimates of ionospheric delay corrections using the Ashtech Z12 geodetic GPS receiver at the SP

In Figure 3 we plot measured ionospheric delays for each common-view track of the international GPS tracking schedule issued by the BIPM as observed at the SP during the period 23 July 1996 to 6 October 1997 (MJD 50287-50727). The delays were obtained using Equation (1) with data from the Ashtech Z12 geodetic receiver. The sampling rate of the Ashtech receiver is 15 seconds which means that for a 13 minute common-view track 53 independent estimates are calculated. These 53 estimates were then combined through a linear regression to obtain one average estimate for each common-view track, a method similar to that used by the one-channel single-frequency GPS time receiver software [12]. Finally, the measured delays were corrected for the average receiver + satellite bias as described above, that is, -17 ns in this study. If data for any of the 53 estimates, necessary for the regression, was not available from the geodetic receiver, no measured ionospheric delay was calculated for that particular common-view track. An annual trend in the measured delays of Figure 3 is clearly seen where the delays are smaller during

	Ionospheric delay /ns		Difference /ns
	SP	OP	
Measured	7	14	-7
Modelled	9	10	-1
Meas. zenith	4	9	-5
Mod. zenith	6	6	0

Table 1: Average values over a 6 month period for the measured and modelled ionospheric delays at the SP and the OP.

winter time. The negative values represent an unphysical condition, but we should remember that these measured delays are not corrected for the satellite-dependent variations shown in Figure 1. We have, however, made this correction for the data from a selected period so as to compare, strictly, the measured delays with those obtained from model parameters. In Figure 4 we plot measured delays,

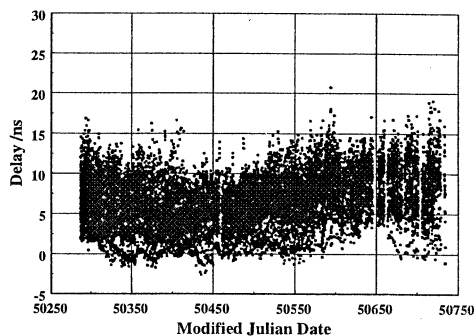


Figure 3: Measured ionospheric delays for each common-view track of the international GPS tracking schedule issued by the BIPM as observed by the SP during the period 23 July 1996 to 6 October 1997 (MJD 50287-50727).

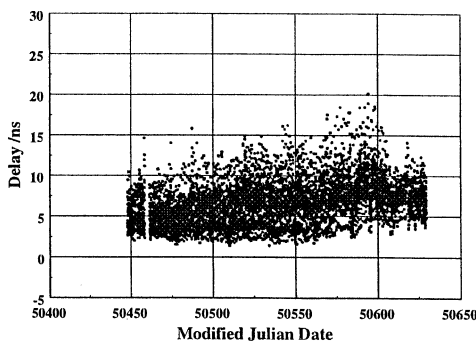


Figure 4: Measured ionospheric delays for each common-view track as observed by the SP for the period 31 December 1996 to 30 June 1997 (MJD 50448-50629), corrected for the satellite-dependent biases shown in Figure 1.

for the period 31 December 1996 to 30 June 1997 (MJD 50448-50629), corrected for the satellite-dependent biases shown in Figure 1. These ionospheric delays vary from about 2 ns to 20 ns with an average of about 7 ns, see also Table 1. The data in Figure 3 which cover the same period as in Figure 4, also has an average of about 7 ns. This suggests that over the period studied the average bias of 17 ns is a good approximation for the average delay of the satellites being selected in the international GPS tracking schedule issued by the BIPM (see discussion above). It does not, however, constitute a verification of the value 17 ns, this being obtained independently by the procedure described in Section 2.1.

The modelled ionospheric delays for the same period and for the same common-view tracks are plotted in Figure 5. These vary from about 5 ns to 25 ns with an average of 9 ns, about 2 ns higher than the measured average. This difference may be explained by the fact that the modelled delays never go below 5 ns, corresponding to a total electron content for the ionosphere of about  $10^{17}$  electrons/m<sup>2</sup>. The other entries in Table 1 correspond to the data obtained for the OP over the same period.

In order to check the quality of the model parameters and the measured delays, it is helpful to map the ionospheric delays to zenith and plot them as a function of time of day. This has been done for the data shown in Figures 4 and 5 using a  $\sin(\text{elevation})$  mapping function with the results shown in Figures 6 and 7, respectively. It may be seen that the model, Figure 7, uses about the same parameters, independent on the season, for the period between 19 h (0.8) and 7 h (0.3), that is, during night-time or when the sun is supposed to be below the horizon. The duration of "night-time" at the SP (latitude 57,7° N) varies between about 4 h in mid-summer and 20 h in mid-winter. These variations can be seen in Figure 6.

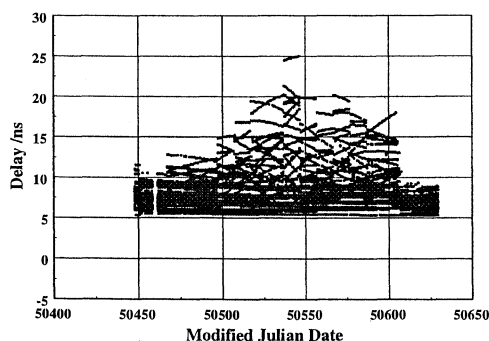


Figure 5: Modelled ionospheric delays at the SP for the same period and for the same common-view tracks as plotted in Figure 4.

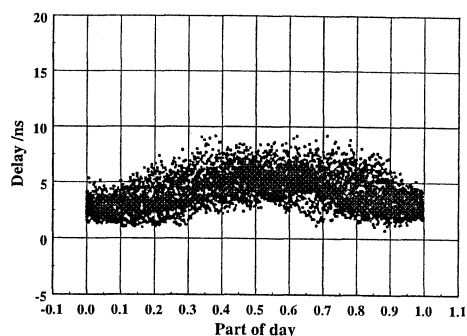


Figure 6: Measured ionospheric zenith delays at the SP for the same period and for the same common-view tracks as plotted in Figure 4, corrected for the satellite-dependent biases shown in Figure 1.

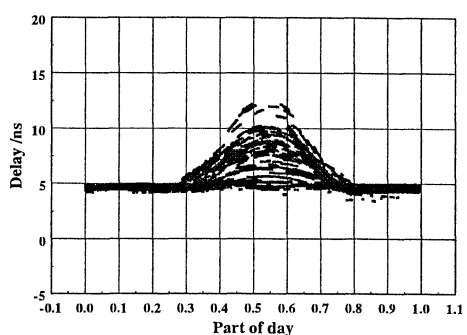


Figure 7: Modelled ionospheric zenith delays at the SP for the same period and for the same common-view tracks as plotted in Figure 4.

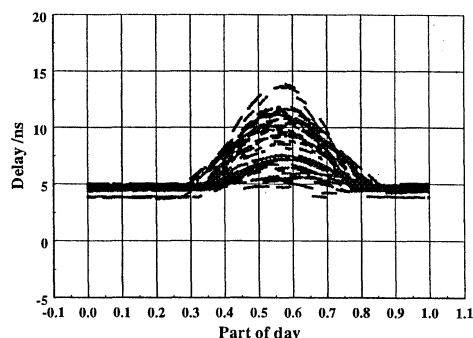


Figure 8: Modelled ionospheric zenith delays for the common-view tracks as observed at the OP during the same period as plotted for the SP in Figure 7.

The modelled ionospheric zenith delay for the OP as a function of time of day is shown in Figure 8. A comparison of Figures 7 and 8 shows that the modelled zenith delays for the OP and the SP are quite similar (which also can be seen from the average values in Table 1) despite the difference of latitude (about 9°) between the two sites. This suggests that the ionospheric model used by GPS is

not sufficient for accurate time transfer between the OP and the SP, and that separate ionospheric measurement systems, or dual-frequency GPS time receivers, must be used.

### 3. TIME TRANSFER RESULTS

In the usual TAI computation at the BIPM, the long-distance time link between the OP and the NIST is computed taking into account corrections for precise satellite ephemerides and measured ionospheric delays at the two sites. This is not the case for the link between the SP and the OP. It is treated like other continental time links, which are supposed to correspond to rather short baselines for which the use of these two corrections is not critical. In Europe, however, this link plays a special role since the corresponding baseline is about 1200 km, and it lies close to the North-South direction for which the ionospheric delays on the two branches could be significantly different.

In this study, the measured ionospheric delays deduced at the SP from the Ashtech Z12 receiver and the IGS precise ephemerides were applied to the time scale comparisons  $[UTC(SP) - UTC(OP)]$  and  $[UTC(NIST) - UTC(SP)]$  for a period of 5 months (August to December 1996). The possibilities of a gain in accuracy was tested by computing the closure  $[UTC(SP) - UTC(OP)] + [UTC(OP) - UTC(NIST)] + [UTC(NIST) - UTC(SP)]$  and by studying its deviation from zero. Possible offsets in the internal delays of the time receivers in operation in the three laboratories cancel in the closure computation, which makes it possible to investigate the role of the ionospheric corrections at the SP and ephemerides corrections on the two links.

Figure 9 shows the deviation of the closure from zero for two cases: with or without applying the corrections for the links to the SP. For the link between the OP and the NIST, measured ionospheric delays and precise ephemerides have been applied in both cases (as is normally done in the TAI computation). Without corrections for the links to the SP, the average deviation of the closure from zero is -11.8 ns over the period under study but it is reduced to -1.1 ns when measured ionospheric delays and precise ephemerides are applied to all links. An average offset of -10.7 ns is thus removed. A study of the values  $[UTC(SP) - UTC(OP)]$  and  $[UTC(NIST) - UTC(SP)]$ , corrected or not, shows that applying the corrections to the time scale comparison  $[UTC(SP) - UTC(OP)]$  removes an average value of about -7.1 ns. This value is very close to the value -6 ns which would be expected from Table 1. The average offset removed by applying corrections to the time comparison values  $[UTC(NIST) - UTC(SP)]$  is -3.6 ns. The improvement in accuracy of the closure thus

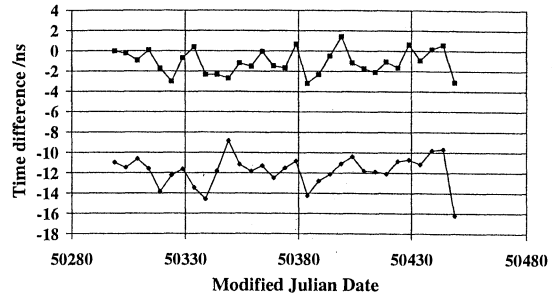


Figure 9: Deviation of the closure  $[UTC(SP) - UTC(OP)] + [UTC(OP) - UTC(NIST)] + [UTC(NIST) - UTC(SP)]$  from zero. Upper curve: measured ionospheric delays and precise satellite ephemerides for the links to the SP. Lower curve: modelled ionospheric delays and broadcast ephemerides for the links to the SP.

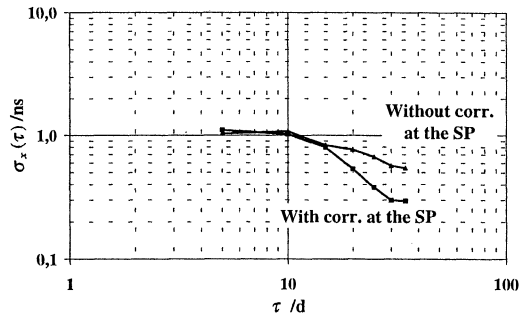


Figure 10: Time deviation  $\sigma_x(\tau)$  of the closure values shown in Figure 9.

comes from both links and it arises mainly from cancellation of the offsets between modelled and measured ionospheric delays for all links. In the usual TAI computation, in which no measured corrections are applied for the SP, these offsets are not cancelled and the closure deviates from zero.

The effects of the corrections on the precision of the links can be investigated by computation of the time deviation  $\sigma_x$  on the closure values, with or without corrections applied. The corresponding variation of  $\sigma_x(\tau)$ , for  $\tau$  ranging from 5 d to 35 d, is shown in Figure 10. For short averaging times,  $5d \leq \tau \leq 15d$ , the level of noise does not change when the corrections are applied and is characterized by  $\sigma_x(\tau)$  values ranging from 1.1 ns to 800 ps. However,  $\sigma_x(\tau)$  drops from 580 ps to 300 ps, for  $\tau = 35$  d, when the corrections are applied. There is thus a gain in precision in the long term when corrections for measured ionospheric delays and precise satellite ephemerides are applied to the two links to the SP. This may correspond to the removal of systematic effects so it is of interest for TAI computation, for which the frequency stability of the clocks is judged over a one-month averaging time. Detailed study of the level of noise affecting the time scale comparisons  $[UTC(SP) - UTC(OP)]$

shows that the  $\sigma_x(\tau)$  value corresponding to an individual 13 minute common-view track is nearly the same or slightly better when the corrections are applied. The improvement is more visible for the long-distance link between the NIST and the SP. The lack of improvement in the precision for short averaging times may be due to the fact that the code observable rather than the more precise carrier phase observable have been used in this study [13].

#### 4. CONCLUSION

Data provided by multi-channel dual-frequency geodetic GPS receivers makes it possible to measure the ionospheric delays experienced by GPS signals along the line of sight of the satellites. Nevertheless, access to some external calibration of the difference of the delays experienced by the receiver between the L1 and L2 channels is necessary to improve the accuracy of these measurements. A study carried out at the SP and the BIPM shows the feasibility of using code measurements provided by the Ashtech Z12 geodetic GPS receiver for the estimation of ionospheric delays to an uncertainty of a few nanoseconds, the calibration of the unit being obtained by comparison with another geodetic receiver, located about 60 km from the SP, itself calibrated on a daily basis by a multi-receiver geodetic treatment.

The application of measured ionospheric delays to the usual one-channel L1 data corresponding to the international GPS tracking schedule issued by the BIPM, and the use of precise satellite ephemerides provided by the IGS, make it possible to remove an offset of about 7 ns, in absolute value, from the values of the time scale comparison [ $UTC(SP) - UTC(OP)$ ] and thus to improve the accuracy of this time link. Applying corrections to the SP data also, indirectly, improves the accuracy of the link [ $UTC(NIST) - UTC(SP)$ ] deduced from BIPM publications, since the BIPM always calculates the time scale comparison [ $UTC(OP) - UTC(NIST)$ ] using ionospheric corrections and precise satellite ephemerides. The same argument applies to all links involving measured corrections.

Until now, in the TAI computation, measured ionospheric delays and precise satellite ephemerides have been applied only to two long-distance West-East links. This study shows that TAI computation could, with advantage, apply the same corrections to the middle-distance North-South link between the SP and the OP.

The results presented are based on the GPS P-code observable provided by the geodetic receiver. A future aspect of this study would be to consider the more precise carrier phase observable, also provided by the receiver.

#### Acknowledgements

The authors are grateful to the staff at Deutsche Forschungsanstalt für Luft- und Raumfahrt, Neustrelitz, Germany (among other, Esther Sardón and Stefan Schlueter) for providing bias data for the Onsala TurboRogue receiver, and to the world-wide collaboration organised by the IGS for providing precise satellite ephemerides data.

#### References

- [1] D. W. Allan and M. A. Weiss, "Accurate time and frequency transfer during common-view of a GPS satellite", *Proc. 34th Ann. Symp. on Frequency Control*, pp. 334 - 346, May 1980.
- [2] W. Lewandowski and C. Thomas, "GPS time transfer", *Proc. of the IEEE*, vol. 79, no. 7, pp. 991 - 1000, July 1991.
- [3] International GPS Service for Geodynamics, *1996 Annual Report*, editors J. F. Zumberge, D. E. Fulton, and R. E. Neilan, IGS Central Bureau, Jet Propulsion Laboratory, California Institute of Technology, Pasadena, California, USA, November 1997.
- [4] J. A. Klobuchar, "Ionospheric correction for the single frequency users of the Global Positioning System", *IEEE Trans. NTS*, 1982.
- [5] M. Imae, C. Miki, and C. Thomas, "Improvement of time comparison results by using GPS dual frequency codeless receivers measuring ionospheric delay", *Proc. 21st Ann. PTI Appl. and Planning Meeting*, pp. 199 - 204, November 1989.
- [6] M. Weiss, T. Weissert, C. Thomas, M. Imae, and K. Davies, "The use of ionospheric data in GPS time transfer", *Proc. 4th EFTF*, pp. 327 - 333, March 1990.
- [7] D. Davis, M. A. Weiss, K. Davies, and G. Petit, "Improving GPS time transfer accuracy with the NIST ionospheric measurement system", *Proc. of the Institute of Navigation Satellite Division, 4th International Technical Meeting (ION GPS-91)*, 1991.
- [8] W. Lewandowski, G. Petit, C. Thomas, and M. A. Weiss, "The use of precise ephemerides, ionospheric data and corrected antenna coordinates in a long-distance GPS time transfer", *Proc. 22nd Ann. PTI Appl. and Planning Meeting*, pp. 547 - 558, December 1990.
- [9] W. Lewandowski, G. Petit, and C. Thomas, "Precision and accuracy of GPS time Transfer", *IEEE Trans. Instrumentation and Measurement*, vol. 42, no. 2, pp. 474 - 479, April 1993.
- [10] D. S. Coco, C. Coker, S. R. Dahlke, and J. R. Clynch, "Variability of GPS satellite Differential group delay biases", *IEEE Trans. Aerospace and Electronic Systems*, vol. 27, no. 6, pp. 931 - 938, November 1991.
- [11] E. Sardón, A. Rius, and N. Zarraoa, "Estimation of the transmitter and receiver differential biases and the ionospheric total electron content from Global Positioning System observations", *Radio Science*, vol. 29, no. 3, pp. 577 - 586, May-June 1994.
- [12] D. W. Allan and C. Thomas, "Technical directives for standardization of GPS time receiver software", *Metrologia*, vol. 31, pp. 69 - 79, 1994.
- [13] G. Mirena, V. Pettiti, F. Cordara, and L. Ciralo, "A new approach to ionospheric delay corrections in single frequency GPS receivers", *Proc. 29th Ann. PTI Appl. and Planning Meeting*, 1997, in press.

## THE LOCAL RESTITUTION OF GPS TIME AT SHANGHAI OBSERVATORY

Hu Jinlun Huang Peicheng

(Shanghai Observatory, Chinese Academia of Sciences, Shanghai 200030, China)

**Abstract:** Local Restitution of GPS Time (LRGPST) at Shanghai Observatory (SO) is the synthesized results for GPS time with multi-satellites at UTC 0h. It is obtained by the method of cubic spline function to interpolate-smooth and weight averaging for the GPS time comparison data received from single satellite in the different moment.

With calculated results from the LRG PST data during 1995~1996, it shows that the effects of Selective Availability (SA) have basically been removed from the statistical characteristics which level is similar to or a little better than the results of single satellite without SA effects (such as PRN15). It can improve the long term reliability of International GPS time synchronization results. With comparison, the system deviation corrected value  $\Delta t$  for International GPS time synchronization in [BIPM-SO] and [USNO-SO] are about +3.7ns and +21.0ns respectively. Their uncertainty are 7.2ns and 8.8ns respectively.

**Key words:** GPS, Time Comparison, Time Synchronization, Data Processing, Restitution

### 1. Introduction

LRGPST is the synthesized results of GPS time with multi-satellites at UTC 0h. It is obtained by using the suitable data processing method to normalize for the GPS time comparison data received from single satellite in the different moment at time laboratory. In fact, LRG PST is one of synthesized GPS time. In statistical sense, the LRG PST data can improve the long term reliability of International GPS time synchronization results, and it can much more reduce the SA effects. In addition, it can conventionally give the precise results of time synchronization at UTC 0h between any two sites in the world, it is very significance for much scientific research

works and practical applications. Therefore, this is also a effective method to improve the level for International GPS time synchronization.

Data processing method to gain synthesized GPS time is not only. BIPM Time Section gives the synthesized GPS time is designated as a Common Time Scale of GPS Time (CTSGPST)<sup>[1]</sup>. It is obtained by the GPS data at the Paris Observatory to smooth and linear interpolate. LRG PST at USNO is obtained by the filter-smooth method with 2 day datum<sup>[2]</sup>. LRG PST at SO is obtained by the method of cubic spline function to interpolate-smooth and weight averaging for the GPS time comparison data from single satellite received in the different moment. Time Bulletin of SO gives the daily values  $C_0$  of [UTC(SO)-GPS time] at UTC 0h, and the standard deviation  $\sigma$  expressed the dispersion in individual measurements, and the global uncertainty  $\sigma / \sqrt{N}$  ( $N$  is the measurement number for the satellites to give daily values  $C_0$  within the appointed day). These parameters are similar to the one of Time Bulletin of the BIPM Time section<sup>[3]</sup>.

The practical method gained LRG PST at SO, and its comparison and analysis with International GPS time synchronization results in some Time Centres of the world are also described in this paper.

### 2. Method

LRGPST at SO is obtained by using the method of cubic spline function. The spline function is a important tool for the function approach. Because it has assembling feature, its expression is a polynomial in parts and has the continuous first and second derivations at the sampling points. Therefor, it looks much more flexible in the practical application, and its effect is very good.

The interpolated function for cubic spline has a optimum approaching properties, its expression  $S(X)$

within the given region [A,B] is as follows:

$$S(X) = A + A_0X + \frac{A_2X^2}{2!} + \frac{A_3X^3}{3!} + \sum_{j=1}^{N-1} B_j \frac{(X - X_j)^2}{3!} \quad (1)$$

$$A = X_0 < X_1 < \dots < X_n = B$$

where,  $X_0 \sim X_n$  are the jointed points of spline,  $A_0 \sim A_3$  are the coefficients to be solved. The last item of Equation (1) is the estimation for remnant error.

First, according to the requirements of interpolated conditions and the GPS time comparison data from single satellite received in the different moment, we use the least square method to evaluate the coefficients of cubic spline function, and give the concert expression to be interpolated. Then we use this expression to interpolated, the daily values of single satellite of [UTC(SO)-GPS (PRN J)] at UTC 0h (PRN J is pseudo-random numbers for different GPS satellite) are derived.

Secondly, using the polishing function in cubic spline to approach with the interpolated data, the daily smoothing values of single satellite at UTC 0h are given. The expression of polishing function in cubic spline is:

$$F_3(S_i) = S_i + (S_{i+1} - 2S_i + S_{i-1}) / 6 \quad (2)$$

(i = 0, 1, 2, ..., N)

Thirdly, using the linear regression method, the standard deviations  $\sigma_{xj}$  of [UTC(SO)-GPS(PRN J)] for every month are evaluated, and the weight  $P_j = A / (\sigma_{xj})^2$  are derived. Here, A is arbitrarily constant. If the upper limit of weight is 300 which is according to the standard deviation without SA effects  $\sigma_{xj} < 18\text{ns}$ , then  $A=100000$ .

Lastly, Doing weight-averaging to data from multi-satellites at UTC 0h every day, the daily value  $C_0$  of [UTC(SO) - GPS time] at UTC 0h and the standard deviation  $\sigma$  of the dispersion in individual measurement and the global uncertainty  $\sigma\sqrt{N}$  are derived.

To check the effectivity and practicality with this method, correlation analysis between the results obtained by the SO method and USNO method from USNO data is carried out. The analytical results show that the two methods have good conformity, the relative slope is about 1.02, and the correlation coefficient is about 0.90 (it is about 0.98 without SA effects)<sup>[4]</sup>.

### 3. Comparison of results

From statistical results for the LRGPST data at SO during 1995~1996, it shows that the SA effects are basically removed. When the measurement numbers of satellite are about 20 for every day, the standard deviation  $\sigma$  for the dispersion of individual measurements and global uncertainty  $\sigma/\sqrt{N}$  of daily  $C_0$  are 40-55ns and 10-12ns respectively. It can improve the long term reliability in GPS time synchronization data. Similar results in some Tims Centers have been compared. Besides comparing with the synthesized GPS time data, and we also compare with the single satellite result without SA effects such as PRN15. Some results for comparison and analysis during 1995~1996 are summered following<sup>[5]</sup>.

#### 3.1 Time synchronization precision and frequency stability( $\tau=1\text{day}$ )

Table 1 shows the annual mean results on time synchronization precision and frequency stability during 1995~1996, for comparison between SO and BIPM and USNO. For averaging time  $\tau$  of one day and calculating once for every month, the annual mean results are derived from data of 12 months per year. From Table 1, it indicates that the time synchronization precision and the frequency stability for comparison of SO and BIPM and USNO are about 12ns and  $1.3 \times 10^{-13}$  respectively, a little better than the results of single satellite without SA effects.

Table 1 Comparison of time synchronization precision and Frequency Stability

Classify	Time synchronization precision		Frequency Stability	
	$\sigma_x$ ns		$\sigma_y(\tau)$ $1 \times 10^{-14}$	
	1995	1996	1995	1996
UTC-GPS Time CTSGPST	5.4	7.9	3.4	3.9
UTC(USNO)-GPS Time LRGPST	6.2	6.6	4.6	4.2
UTC(USNO)-GPS(PRN15)	8.0	9.4	10.3	13.2
UTC(SO)-GPS Time LRGPST	9.6	8.4	13.9	11.4
UTC(SO)-GPS(PRN15)	11.4	13.0	14.9	14.9
UTC-UTC(USNO) by CTSGPST & LRGPST	4.8	5.8	4.8	5.8
UTC-UTC(SO) by CTSGPST & LRGPST	10.3	12.3	14.0	12.3
UTC(USNO)-UTC(SO) by LRGPST	11.1	11.6	14.9	12.2
UTC(USNO)-UTC(SO) by GPS(PRN15)	12.7	14.5	18.9	17.2

3.2 Long term frequency stability ( $\tau=1\sim 100$  days)

Table 2 shows the results of long term frequency stability during 1995-1996, for comparison of SO and BIPM and USNO. For averaging time  $\tau=1\sim 100$  day, the annual mean results are derived from calculation for step by step

with one day step length from couple years data. From Table 2, it indicates that the long term frequency stabilities in LRGPST at SO are  $1.4 \times 10^{-13} \sim 1.0 \times 10^{-14}$ , a little better than the results of single satellite without SA effects.

Table 2 Comparison of long term frequency stability

Classify	$\sigma_y(\tau)$ $1 \times 10^{-14}$											
	1d	5d	10d	20d	30d	40d	50d	60d	70d	80d	90d	100d
UTC-GPS Time	3.66	2.75	2.55	2.32	1.58	1.25	0.99	0.78	0.69	0.66	0.65	0.60
UTC(USNO)-GPS Time	4.54	2.52	2.55	2.26	1.56	1.30	1.05	0.81	0.72	0.65	0.62	0.55
UTC(USNO)-GPS(PRN15)	13.3	3.53	2.81	2.26	1.55	1.33	1.08	0.85	0.76	0.70	0.66	0.59
UTC(SO)-GPS Time	14.1	4.08	2.75	2.24	1.67	1.31	1.09	0.98	0.95	0.98	1.05	1.09
UTC(SO)-GPS(PRN15)	17.1	5.22	3.37	2.40	1.71	1.34	1.13	1.03	0.99	1.03	1.09	1.11

In the two tables mentioned, the results at SO are worse than that at BIPM and USNO. That reflects the

situation on GPS time synchronization system at SO.

### 3.3 Slope characteristics of frequency stability model

Table 3 shows the results on slope characteristics of and BIPM and USNO. According to the calculated results of  $\sigma_y(\tau)$  of step by step from the two years data for averaging time  $\tau=1\sim 100$  days, and we use the linear fit in the drawing of  $[\log \sigma_y(\tau) - \log \tau]$ , then the slope  $\mu$  and the correlation coefficients  $r$  are derived. From

frequency stability model during 1995-1996, for comparison of SO

Table 3, it indicates that the slope  $\mu$  and the correlation coefficients  $r$  of the LRG PST data are about -1.10 and -0.9~1.0 respectively, and exhibits mainly the white frequency noise, and is similar to the results of single satellite without SA effects.

Table 3 Slope characteristics of frequency stability model

Classify	Parameter	Range of averaging time and results				
		1 ~ 60day	1 ~ 70day	1 ~ 80day	1 ~ 90day	1 ~ 100day
UTC-GPS Time CTSGPST	$\mu$	-0.9191	-1.0260	-1.0926	-1.1252	-1.1458
	$r$	-0.9089	-0.9137	-0.9234	-0.9329	-0.9405
UTC(USNO)-GPS Time LRGPST	$\mu$	-0.8696	-0.9738	-1.0460	-1.0946	-1.1360
	$r$	-0.9188	-0.9196	-0.9264	-0.9340	-0.9401
UTC(USNO)-GPS(PRN15)	$\mu$	-1.1800	-1.2396	-1.2786	-1.2994	-1.3176
	$r$	-0.9808	-0.9796	-0.9807	-0.9827	-0.9827
UTC(SO)-GPS Time LRGPST	$\mu$	-1.2200	-1.2236	-1.2026	-1.1556	-1.0974
	$r$	-0.9905	-0.9920	-0.9917	-0.9862	-0.9756
UTC(SO)-GPS(PRN15)	$\mu$	-1.3506	-1.3432	-1.3102	-1.2560	-1.1958
	$r$	-0.9973	-0.9976	-0.9957	-0.9893	-0.9798

### 3.4 Estimation and verification of system deviation on GPS time synchronization

It is a validity method by using the LRG PST data to estimate and verify for the system deviation of International GPS time synchronization. Table 4 shows the correlation values  $\Delta t$  for GPS time synchronization between two sites during 1995~1996. They are derived from comparison of LRG PST data with Time Bulletin data between SO and BIPM and USNO<sup>[6]</sup>. The method obtained  $\Delta t$  are as follows:

$$\Delta t_{\text{BIPM-USNO}} = \{[\text{UTC-GPS time}] - [\text{UTC(USNO)-GPS time}]\}_{\text{by GPS}} - [\text{UTC-UTC(USNO)}]_{\text{by BUL}} \quad (3)$$

$$\Delta t_{\text{BIPM-SO}} = \{[\text{UTC-GPS time}] - [\text{UTC(SO)-GPS time}]\}_{\text{by GPS}} - [\text{UTC-UTC(SO)}]_{\text{by BUL}} \quad (4)$$

$$\Delta t_{\text{USNO-SO}} = \{[\text{UTC(USNO)-GPS time}] - [\text{UTC(SO)-GPS time}]\}_{\text{by GPS}} - \{[\text{UTC-UTC(SO)}] - [\text{UTC-UTC(USNO)}]\}_{\text{by BUL}} \quad (5)$$

The averaging time of data points are 10 days in 1995 and are 5 days in 1996. In the annual results of correlation values  $\Delta t$  the peak to peak values, the average values, and the standard deviations are given. Then they have been compared with the averaging values in couple years. From Table 4, it indicates that the correction values  $\Delta t$  on GPS time synchronization in [BIPM-SO] and [USNO-SO] are about +3.7ns and +21.0ns respectively. Their uncertainty are 7.2ns and 8.8ns respectively.

Table 4 The correction values of GPS time synchronization between two sites

Year	$\Delta t$ Results ns								
	$\Delta t_{\text{BIPM-USNO}}$			$\Delta t_{\text{BIPM-SO}}$			$\Delta t_{\text{USNO-SO}}$		
	P-P	Ave.	SD	P-P	Ave.	SD	P-P	Ave.	SD
1995	22	-16.6	6.3	28	7.0	6.4	30	23.6	8.4
1996	39	-17.8	6.7	49	0.5	7.8	40	18.3	9.2
Ave.	31	-17.2	6.5	39	3.7	7.2	35	21.0	8.8

#### 4. Conclusions

The data processing method obtained LRGPST may be different, but the conform degree of results is very satisfactory. LRGPST is also a effective method to improve the level of International GPS time synchronization.

#### 5. References

- [1] BIPM Time Section, "Annual Report of the BIPM Time Section", 1995~1996.
- [2] U. S. Naval Observatory, "Daily Time Differences, series 4", 1995~1996.
- [3] Shanghai Observatory, "Atomic Time Bulletin", 1995~1996.
- [4] Hu Jinlun, "Normalizing on GPS Time Comparison Data", Annals of Shanghai Observatory Academia Sinica, 1995, 16, 193~201.
- [5] Hu Jinlun, "Synthesized GPS Time", Chinese Journal of Radio Science, 1997, 12(3), 313~320.
- [6] Hu Jinlun, etc., "Estimation of the System Deviation on International GPS Time Synchronization", Journal Astronautic Metrolory and Measurement, 1997, 17(5), 6~11.

# GPS MULTI-CHANNEL COMMON-VIEW TIME TRANSFER USING MOTOROLA ONCORE RECEIVER WITH CCDS STANDARDS

J. Nawrocki\*, W. Lewandowski\*\*, J. Azoubib\*\*

\*Astrogeodynamical Observatory, Space Research Center, Polish Academy of Sciences, Borowiec, Poland

\*\*Bureau International des Poids et Mesures, Sevres, France

## ABSTRACT.

Most of the standard receivers used for the common view time transfer are of the single channel, single frequency, Coarse/Acquisition code type. They all are built according to the "NBS standard" prototype from the early 1980's. The uncertainty of the common view time comparisons varies between 2-3 ns RMS for the best of them. The new generation of the unexpensive, multi-channel C/A code receivers which are now available, seems to make the old standard obsolete.

One of the interesting new solutions, proposed for the time transfer, is the 8-channel Motorola VP Oncore receiver combined with a time interval counter and a microcomputer (Gifford et al., 1996), (Lewandowski et al, 1996).

Such a measurement system was tested for several months at the Time Section of the Bureau International des Poids et Mesures (BIPM) in Sevres yielding very interesting results (Lewandowski et al., 1997).

To maintain the compatibility with the old "NBS type" receivers, still in use at the majority of time laboratories, and to make use of the Motorola multi-channel capabilities, special software driving the receiver and the counter was developed at BIPM in 1997.

The results of tests in time transfer between BIPM in Sevres and AOS in Borowiec (Astrogeodynamical Observatory in Borowiec, Poland) at the baseline of about 1200 km give the uncertainty of results in the range of 1-2 ns RMS when applying recommendations of CCDS (Allan, Thomas, 1993).

## INTRODUCTION.

The common-view method of GPS time transfer is one of the most precise and accurate methods for time comparison between remote clocks. The main aim of the method, proposed at the beginning of the 80s (Allan, Weiss, 1980) was to increase the accuracy of the comparisons into the range of a few nanoseconds. The method became especially important after the implementation of SA (selective availability). The observations of the same GPS satellite are carried on simultaneously at different laboratories according to the schedule

published, usually twice a year, by the BIPM. Up to now, the common view method is applied for single frequency receivers which enable observation of up to 48 satellite passes per day.

New, unexpensive, multichannel receivers, enable observation of several satellites simultaneously. Motorola VP Oncore is especially interesting among them, because of the information available through the RS-232 communication port of the receiver. It is possible to relate generated by Motorola 1 pps pulse with nanosecond accuracy to internal time scale of the receiver. Full observed satellite information (raw satellite dispatch) and raw pseudorange measurements are also available.

It is possible to prepare the receiver independent way of time comparisons, where all the computations are carried according to rules recommended by the CCDS (Comite Consultatif pour la Definition de la Seconde, (Rapport BIPM-93/6). The essential advantage of such observations is the compatibility with old, single channel, NBS type receivers, still in use at the majority of time laboratories.

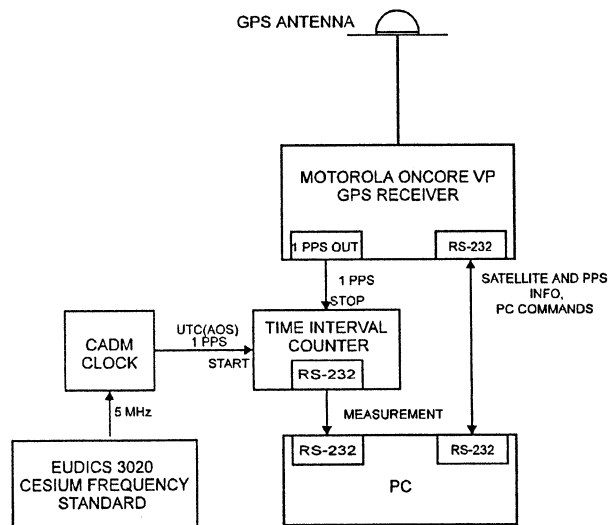


Fig. 1. Set-up of the Experiment at Borowiec Observatory.

## SET-UP OF THE EQUIPMENT.

The organization of the measurements is very similar to the setup applied at BIPM and Besancon

in the experiment carried out in 1996 (Lewandowski et al., 1997). The Stanford SR-620 time interval counter (Fig. 1) is started by the 1 pps pulse from the local UTC clock driven by the Oscilloquartz EUDICS 3020 cesium frequency standard. The counter is stopped by the 1 pps pulse from the Motorola Oncore VP receiver, working in the GPS synchronization mode. Both, the counter, and the receiver are controlled by the software installed on a PC computer. COM1 port is used for the communication with the counter: for sending commands and for gathering the readings  $1\text{PPS}(\text{local clock}) - 1\text{PPS}(\text{receiver})$ . Serial COM2 port is used for the communication with Motorola. Set-up of the experiment at BIPM in Sevres is almost identical, the only difference is that Racal-Dana counter is controlled using GPIB interface instead of a serial one. The Racal-Dana counter is driven by the 5MHz frequency signal from HP-71A cesium time and frequency standard, also generating laboratory 1pps pulse.

#### SOFTWARE DRIVING THE MEASUREMENTS.

The block diagram of the applied software is presented in Fig. 2. During the startup procedure the Motorola Oncore VP receiver is set up in the position-hold mode, with antenna coordinates known with cm accuracy in the ITRF reference frame. The 1pps signal output is formed by the internal GPS time scale of the receiver.

The reception of the measurement  $1\text{PPS}(\text{local clock}) - 1\text{PPS}(\text{receiver})$  from the counter triggers the gathering of the following data from the Motorola:

- pseudoranges for each of the observed satellites,
- corrections connecting internal software GPS time scale of the receiver to its 1pps pulse.

Every 6 seconds the orbital data of the observed satellites (raw satellite frames) are also received. Satellite clock parameters, Keplerian elements of the orbit, and their reference time are decoded. The basic condition for the proper functioning of the software was to tie the internal time scale of the receiver to the generated by the receiver 1pps pulse. The work-out of the data during the pass is done exactly according to the recommendations of the CCDS (Rapport BIPM 1993/6). The 780 measurements carried in the period of time defined by the BIPM schedule are divided into 15 s intervals. The differences between the second of the local clock and  $i$ -th satellite time second are pseudoranges. The connection between Motorola internal second and the output 1pps pulse can be written as:  $1\text{pps} + \Delta\tau$ , where  $\Delta\tau$  can be computed from the corrections transmitted one second before and one second after the 1pps pulse. The pseudorange for the  $i$ -th satellite can be thus written as:

$$\text{psd}_i = \text{UTC}(\text{loc}) - 1\text{pps}(\text{Motorola}) + 1\text{pps}(\text{Motorola}) - T(\text{sat}_i),$$

so:

$$\text{psd}_i = \text{UTC}(\text{loc}) - T(\text{sat}_i).$$

For each of the 15 s intervals, the pseudoranges are square fitted for the centre of the interval. Satellite position, geometric delay as well as ionospheric, tropospheric, Sagnac, periodic relativistic, L1-L2 corrections are computed. Then the clock corrections for access to GPS time, using the broadcasted second order polynomial are evaluated. The values obtained in this way are linear fitted. The results for each satellite are stored in the standard format on the hard disk, ready for the transfer to the other laboratory participating in the experiment.

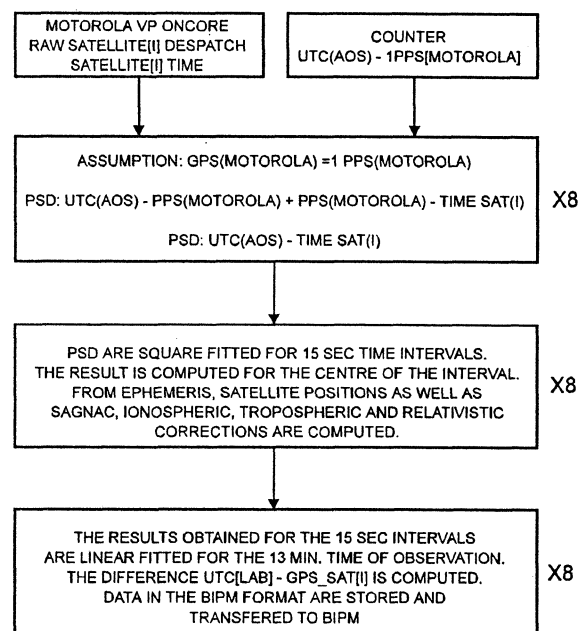


Fig. 2. General diagram of the software applied to the work-out of the Motorola VP Oncore data.

#### COMMON VIEW RESULTS OF THE EXPERIMENT.

In the experiment participated two Motorola Oncore VP receivers working simultaneously at BIPM (Sevres, France) and AOS (Borowiec, Poland). The approximate baseline is about 1200 km. The results of the observations come from the period of MJD: 50679 - 50683 (19.08 - 23.08.1997) and present the time scales comparison between the BIPM and the AOS. The comparisons were obtained using both multi-channel and single-channel observations. Fig. 3 presents raw differences BIPM - AOS obtained for multi-channel observations between the two laboratories. One-channel comparisons are presented in Fig. 4. The results of the removal of slope are shown in Fig. 5

and Fig.6 respectively. The period of observations is relatively short because of the quite significant drift of the clock at AOS. The EUDICS 3020 cesium frequency standard is at least by the order of magnitude less stable than the HP-71, equipped with high performance tube used at Sevres.

Fig. 7 presents the modified Allan deviation computed for the BIPM - AOS multi-channel observations. Similar computations obtained for the one-channel observations are shown in the Fig. 8. The results of the time stability of the multi-channel and one-channel observations are analysed in Fig. 9 and Fig. 10. The multi-channel results are more stable. The uncertainty of the comparisons (RMS) varies between 1.2 to 1.5 ns, for one channel observations it is by 1 ns worse. The certain problem for all GPS receivers are the changes of internal receiver delay caused by the changes of external temperature (Lewandowski and Tourde, 1991). Fig.11 presents the zero-baseline, one-channel comparisons between Motorola and Sercel receiver working at the BIPM time laboratory. The same 1pps pulse from local clock was used for the two receivers. The Sercel was equipped with the temperature stabilized antenna, the Motorola was equipped with typical, unstabilized antenna. For the period of MJD: 50670 - 50721 the daily average of external temperature varied between 12° to 33° C. The changes in the difference Sercel - Motorola follow the pattern of the external temperature. The temperature coefficient is equal  $\zeta = -0.27$  ns/deg.

#### CONCLUSIONS.

The best single-channel, C/A code receivers built especially for timing purposes, e.g. Allen-Osborne TTR6, NBS TTR5, or Sercel, used for common view observations for baselines 1000-2000 km give the uncertainty of 2-3 ns. They observe up to 48, 13 min. satellite passes per day. The results obtained

with the set of equipment consisting of an unexpensive, multi-channel

Motorola VP Oncore receiver, a time counter with the 1 ns resolution, and the PC computer with especially prepared software are significantly better. As it was presented above, the obtained uncertainty is well below the 2 ns level. The Motorola at Borowiec observes about 650 satellite passes per day. Moreover, the results of the multi-channel satellite observations obtained with the software used at Sevres and Borowiec are compatible with the old single-channel receivers widely used for timing purposes. The significant problem still is connected to relatively high dependence of Motorola observations on outside temperature which can be resolved by thermal protection of its antenna.

The paper was presented at the Precise Time and Time Interval Systems and Applications Meeting, Long Beach, 2-4 December 1997.

#### REFERENCES.

1. D. W. Allan, A. M. Weiss, Accurate Time and Frequency Transfer during Common-View of GPS Satellite, Proc. 34th Ann. Symp. on Frequency Control, pp. 334 - 346, 1980.
2. The Group on GPS Time Transfer Standards, Technical Directives for Standardization of GPS Time Receiver Software, Rapport BIPM 1993/6.
3. W. Lewandowski, P. Moussay, P. Guerin, F. Meyer, M. Vincent, Testing Motorola Oncore GPS Receiver for Time Metrology, EFTF '97.
4. W. Lewandowski, R. Tourde, Sensitivity to the External Temperature of some GPS Time Receivers, Proc. 22nd PTTI Meeting, pp. 307-316, 1990.

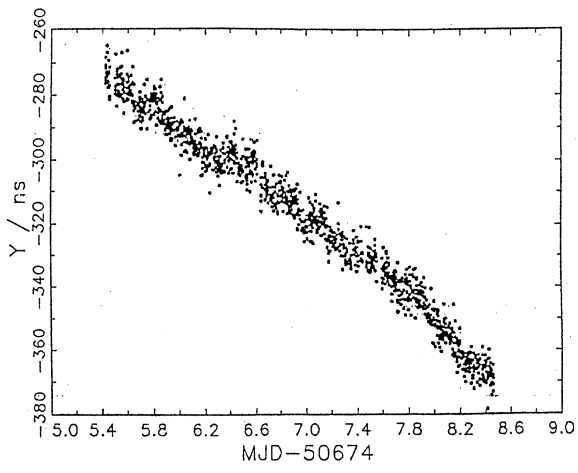


Fig. 3. Raw [BIPM clock - AOS clock] differences by Motorola multi-channel, common-view observations.

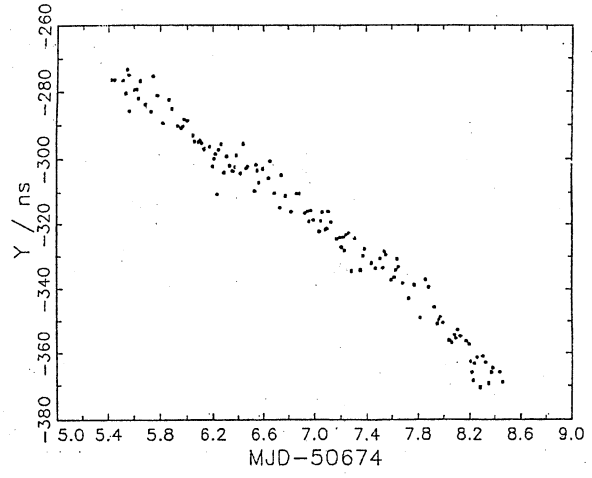


Fig. 4. Raw [BIPM clock - AOS clock] differences by Motorola one-channel observations.

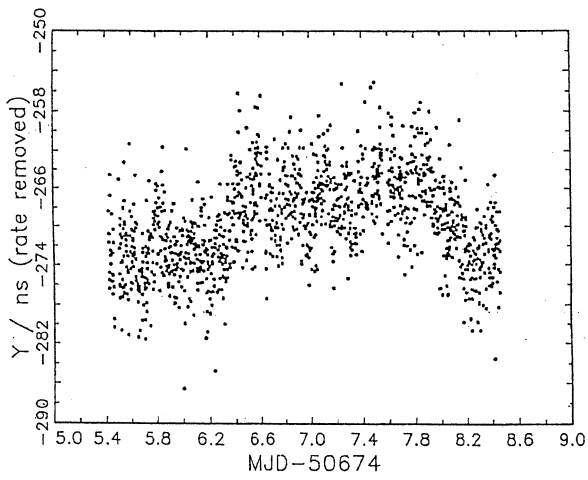


Fig. 5. Data of Fig. 3 after slope removal.

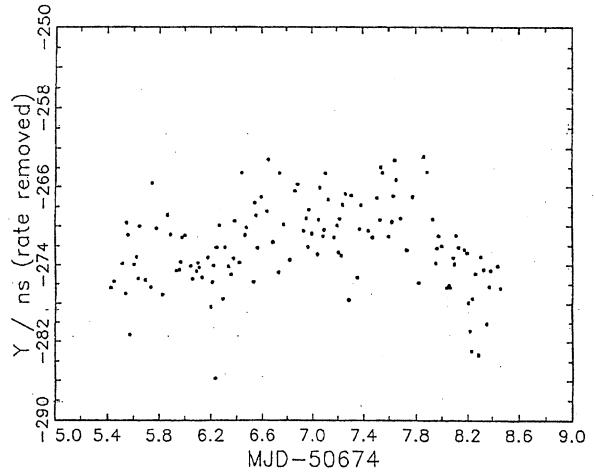


Fig. 6. Data of Fig. 4 after slope removal.

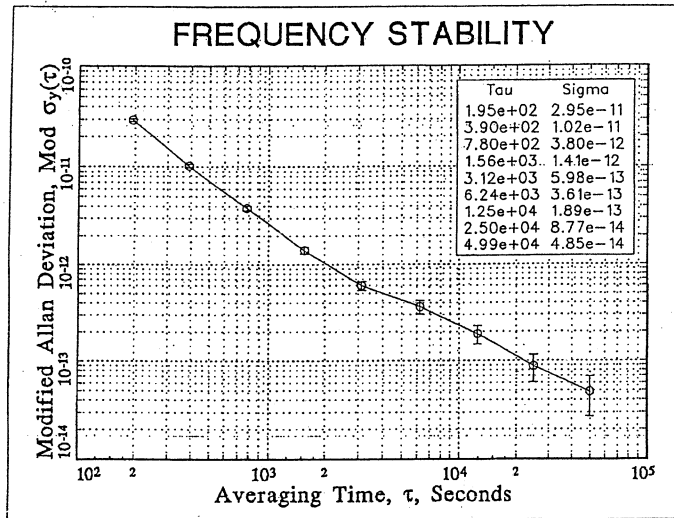


Fig. 7. Modified Allan Deviation of the [BIPM clock - AOS clock] differences from Motorola multi-channel observations.

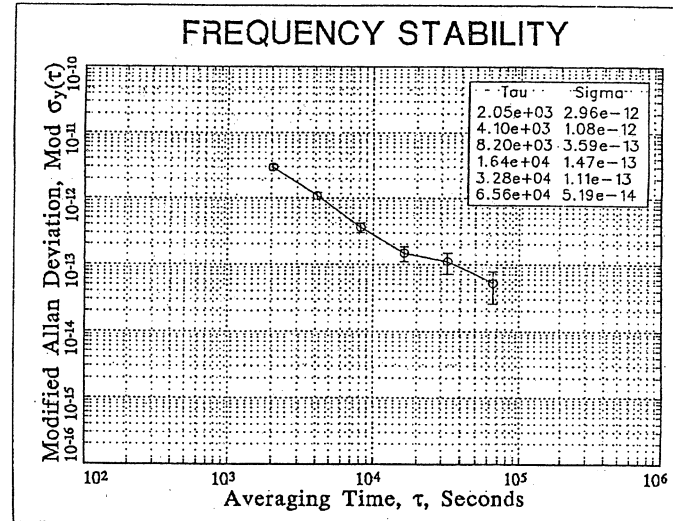


Fig. 8. Modified Allan Deviation of the [BIPM clock - AOS clock] differences from Motorola one-channel observations.

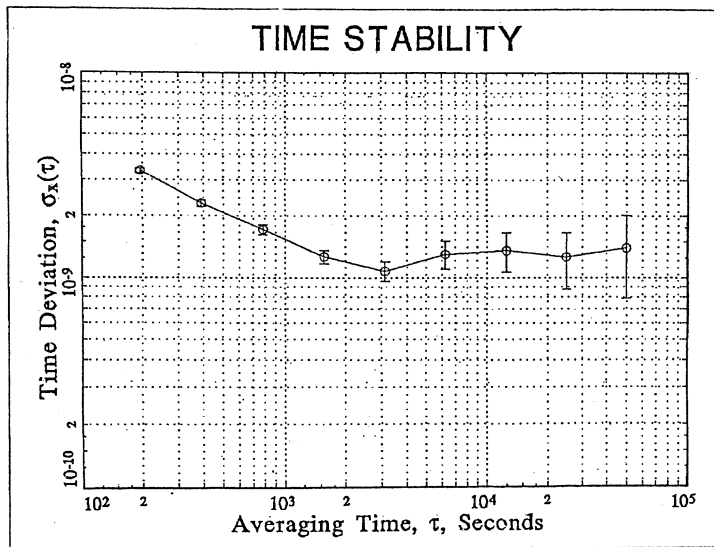


Fig. 9. Time deviation of the [BIPM clock - AOS clock] differences from Motorola multi-channel observations.

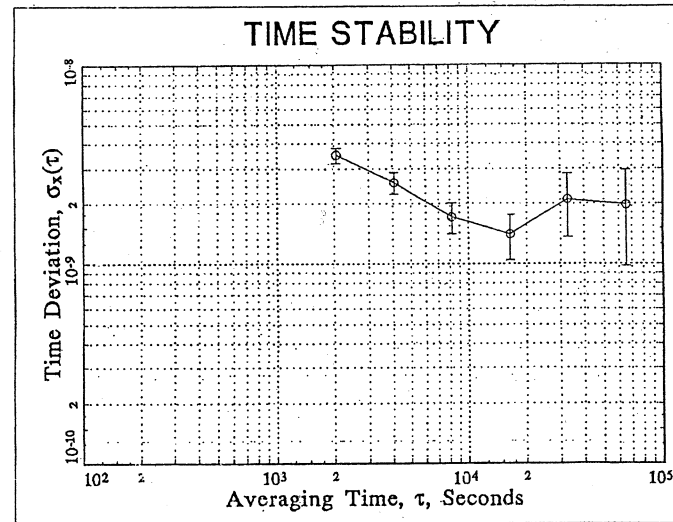


Fig. 10. Time deviation of the [BIPM clock - AOS clock] differences from Motorola one-channel observations.

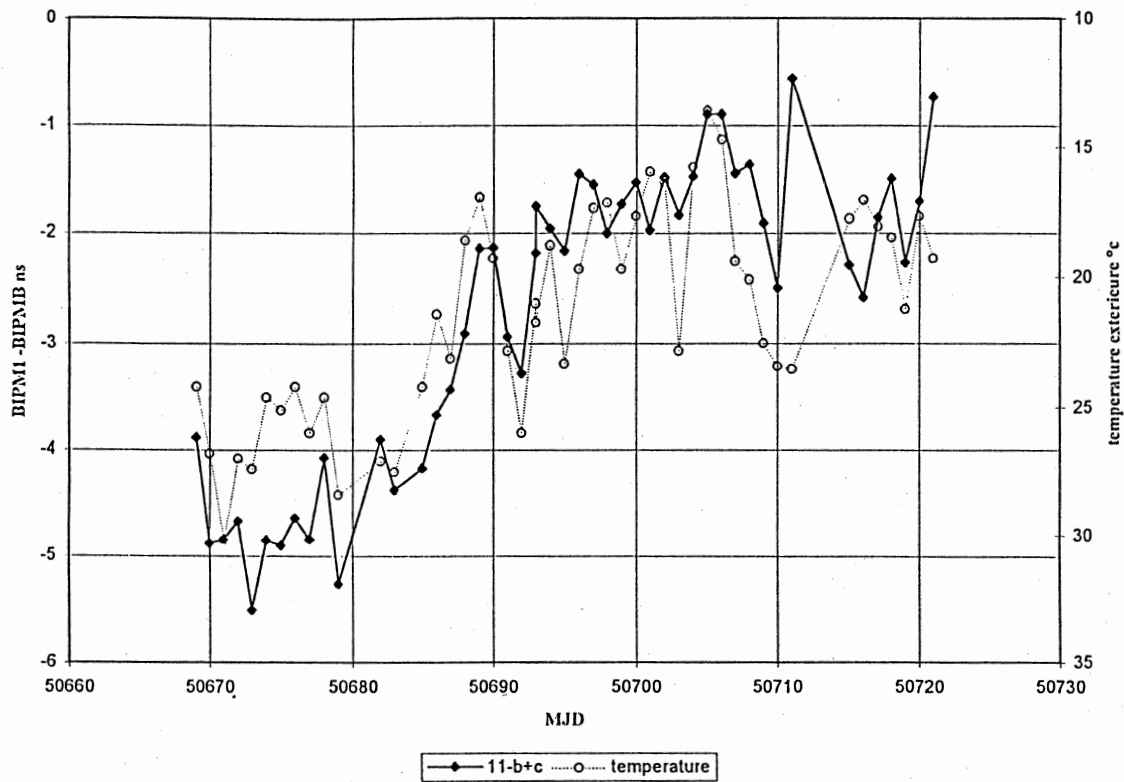


Fig. 11. Zero-baseline comparison between Sercel receiver (BIPM1) and Motorola receiver (BIPMB), and corresponding external temperature.

## REAL TIME ACCESS TO INTERNATIONAL TIME SCALE USING GPS

Anca Niculescu  
National Institute of Metrology  
Sos. Vitan – Bârzești nr. 11  
Bucharest

### 1. ABSTRACT

The Global Positioning System (GPS) is an outstanding tool for the dissemination of the time unit. Equipped with a C/A code GPS time receiver, civil users may access the GPS time scale, disseminated by the GPS satellites, and thus to the reference time scale UTC (USNO) and UTC. At any given instant, the restitution of GPS time through the satellite constellation presents a peak-to-peak discrepancy of several tens of nanoseconds without SA and several hundreds of nanoseconds with SA. This paper deals with possible solutions for the improvement real time access to the GPS time scale. One possible solution considered relies upon the statistical analysis of numerous observations of the satellites, using one channel GPS receiver.

### 2. INTRODUCTION

The Global Positioning System (GPS) program was initiated by the Department of Defence in order to provide worldwide instantaneous and continuous accurate time and position information. Practically, anyone who has a GPS receiver can have access to the data from this system of satellites.

In order to determine his position, a user must simultaneously receive signals from at least four satellites. If a user already knows his position, he needs to track only one satellite to determine the time. Thus, GPS has the capability to provide absolute time, i.e., time referenced to a specific time scale: UTC. This is extremely important, since it enables the users to synchronize or time event, to submicrosecond accuracy.

The time scale GPS time is a continuous time, not corrected for leap seconds, maintained in agreement with UTC (USNO) within 100 ns [1].

So long as the input of the time receiver is driven by 1 pps of the local clock, at date  $t$ , the user has access to the quantity:

$$x(t) = [\text{Local clock} - \text{GPS time}](t)$$

The GPS timing data can be accessed using either the common view method [2,3,4] or the single view method. The accuracy with which the time scale GPS time is accessed depends on local conditions of observations, especially on the accuracy with which the coordinates of the receiver antenna have been established.

### 3. EXPERIMENTAL RESULTS

A GPS receiver for time is based on the comparison of the calculated slant range between the receiver position and the satellite position with the measured transit time of the radio signal. The clock bias resulting from this comparison is due to the different delay time values caused by the ionosphere, the troposphere and the receiver itself. The receiver clock can be synchronized to the atomic clock on board the satellite. The difference between the GPS time and UTC (USNO) is given by the coefficients of the polynomial included in the data message transmitted together with the ranging signal. The position of the satellite has to be evaluated from ephemeris data transmitted by the satellite.

This paper presents the results of the observations data recorded with a single channel receiver for a 13-day period (4 – 17 February 1998). The data was recorded with different time steps (15 min, 30 min, 60 min) using a dedicated software package and a PC. The local reference was a commercial cesium clock installed at the National Institute of Metrology.

With ordinary conditions of observation, the real time readings of the quantity [Local clock – GPS time] for this period indicates a discrepancy that can be up to 100 ns for a measuring time interval of 15 minutes and up to 80 ns for a measuring time interval of 60 minutes. It seems that for larger time steps the predominant noise is white phase noise brought about by SA degradation. This noise can be reduced by using a data smoothing method. In our case we used a polynomial smoothing method. Fig. 1 shows the observed data, taken with a 15 minutes time step, together with the smoothed curve. Fig. 2 and Fig. 3 present the same observed data taken with 30 minutes and 60 minutes time steps, respectively, together with the smoothed curves. The precision of the GPS time restitution can be expressed in terms of the root mean square of residuals to the smoothed values. For the period 4 February – 17 February this was found to be 8.1 ns.

This value reflects the impact of error sources such as:

- residual errors in local antenna coordinates;
- errors in estimating the ionospheric delay of GPS signals;
- errors in ephemerides parameters broadcasted by the satellite;
- other minor error sources such as multipath effects and the sensitivity of the local receiver to the external

temperature.

Accuracy in GPS time restitution also calls for the calibration of the local receiver internal delay. In our case only the cable delay is known.

#### 4. CONCLUSIONS

From these results, one may conclude that a user with a single channel receiver may have access to the GPS time and eventually to reference time scales such as UTC (USNO) and UTC. For a final conclusion more observation data are needed.

#### References

- [1] Lewandowski W., Thomas C., GPS Time Transfer, IEEE Special Issue on Time, 1991, 79, 991-1000.
- [2] Allan D.W., Weiss M.A., Accurate Time and Frequency Transfer during Common -View of a GPS satellite, Proc. 34<sup>th</sup> Annual Symposium on Frequency Control, 1980, 334-346.
- [3] Thomas C., Real - Time Restitution of GPS Time, Proc 7<sup>th</sup> European Frequency and Time Forum , 1993, 141-146
- [4] Thomas C. Real -Time Restitution of GPS Time Through a Kalman Estimation, Metrologia, 1992, 29, 397- 414.

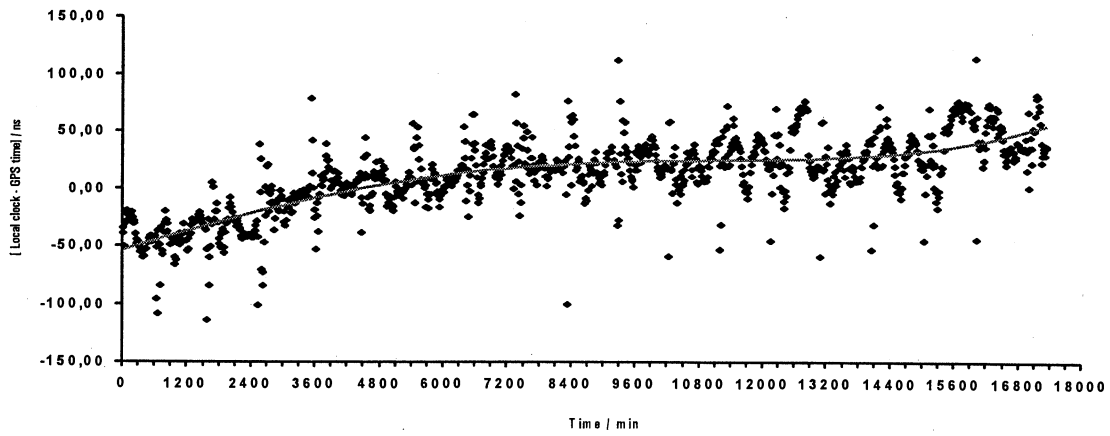


Fig.1 Raw data [Local clock – GPS time] taken at the NIMB between 4 and 17 February 1998 with 15 min time step, \_\_\_\_\_ Smoothed satellite data

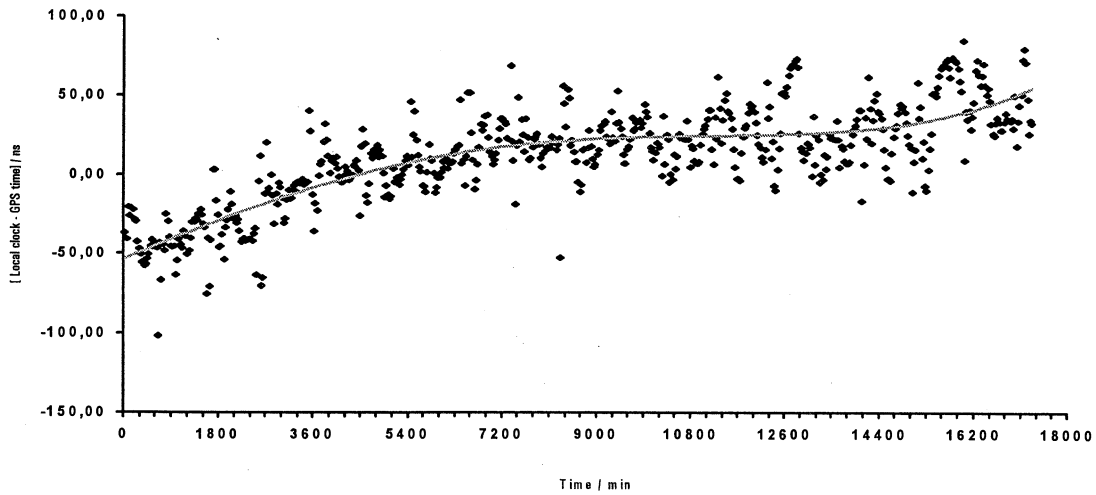


Fig.2 Raw data [Local clock – GPS time] taken at the NIMB between 4 and 17 February 1998 with 30 min time step, \_\_\_\_\_ Smoothed satellite data

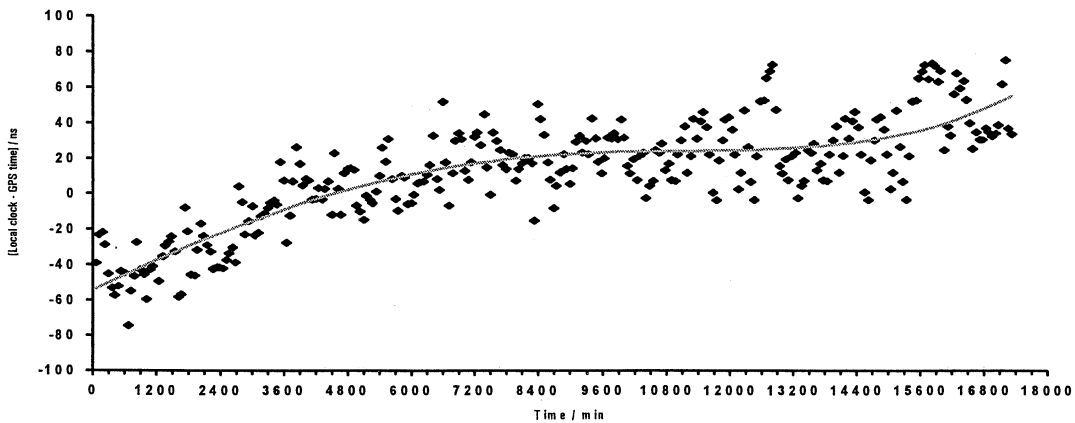


Fig.3 Raw data [Local clock – GPS time] taken at the NIMB between 4 and 17 February 1998 with 60 min time step, \_\_\_\_\_ Smoothed satellite data

## LOW-COST TIME SYNCHRONISATION AND TAGGING USING SATELLITE TV TELETEXT BROADCASTS

J J Lennon, J J O'Riordan, C T O'Sullivan, PW Twomey, and P J Murphy\*

Department of Physics, University College, Cork, Ireland.

**Abstract** -- A low-cost method of generating pulses for time synchronisation between widely spaced (~1000 km) stations is described. Using standard teletext transmissions broadcast on commercial satellite TV channels, a timing accuracy of better than  $\pm 30$  ns can be achieved. A simple extension of the technique enables the recording of date and time information.

*PACS:* 95.55.Sh 98.70.Sa

*Keywords:* time synchronisation, time transfer, time tagging

### 1. INTRODUCTION

Time synchronisation by means of signals from commercial TV stations has been developed over the past thirty years [1,2], mostly for time/frequency metrology. With the launch of the GPS constellation of satellites in 1988, a convenient alternative became available, particularly for time synchronisation over longer ( $> 1000$  km) baselines [3 - 6]. Where a large number of stations is involved, for example in the proposed Auger experiment [7,8] which envisages a cosmic ray extensive air shower array comprising up to 3000 autonomous detectors covering an area of  $5000 \text{ km}^2$ , low cost solutions become imperative. Pryke and Lloyd-Evans [9] have described a system based on GPS technology which provides 6 ns (standard deviation) accuracy with an offset error of less than 5 ns; it is expected that this solution will be adopted for the Auger project.

In this paper we describe a simple and novel alternative, based on the use of the standard teletext signals disseminated on satellite TV channels. While not capable of the accuracy of the technique employed by Pryke and Lloyd-Evans, this approach is extremely easy to implement at very low cost and, in addition, provides a convenient facility for time-of-event recording.

### 2. TELETEXT TRANSMISSIONS

Teletext information is disseminated on eight lines in each transmitted field, that is 16 lines per frame, specifically lines 11-18 and 324-331 [10]. There are two fields per frame and twenty five frames per second. Each page of teletext contains 24 rows, each row comprising up to 40 alphanumeric characters, the bit rate being 6.9375 Mbits/s. Each teletext row is broadcast on a single TV line so that, at 16 lines per frame and 25 frames per second, 400 teletext rows are broadcast per second. In a receiver equipped with a teletext card, the off-air video signal is decoded by a teletext decoder chip which presents each 8-bit ASCII character on its data bus together with a corresponding 13-bit address code. The data is recorded in RAM in the memory location specified by the address code and is continually updated as new information is received off-air. While not receiving data off-air, the RAM contents are transferred to a character generator which controls the TV screen when operating in teletext mode. The address provided for each character determines its location on screen.

The information transmitted for display on the top row (the header row) of the teletext screen contains only 32 characters (located at positions 9 to 40 on the screen, see figure 1) which include the number of the page being currently updated and the current time information (day, month, year, hour, minute, second). Each TV station has its own format for the header row but the hour-minute-second information always appears on the extreme right hand side of the header row, the latter information being retransmitted many times per frame. This provides a convenient source of time information which, as described below, can be used for both time synchronisation and time-of-event tagging within the service area of the satellite, which may include an entire continent.

Figure 1 shows the address codes corresponding to the 32 broadcast characters of the header row together with examples of the header row formats broadcast on

\* Department of Electrical Engineering & Microelectronics

position on header row	9	10	11	12	13	14	15	16	17	18	19	20	21	22	23	24	25	26	27	28	29	30	31	32	33	34	35	36	37	38	39	40	
address (hex)	008	009	00A	00B	00C	00D	00E	00F	010	011	012	013	014	015	016	017	018	019	10A	01B	01C	01D	01E	01F	3F8	3F9	3FA	3FB	3FC	3FD	3FE	3FF	
				S	K	Y										1	0	0															
	1	0	0		A	R	D	/	Z	D	F				M	O																	
	1	0	0																														
					B	A	Y	E	R	N	T	E	X	T																			

SKY NEWS: Astra 1A (11.377 GHz)  
ZDF: Astra 1C (10.964 GHz)  
Bayern 3: Astra 1C (11.141 GHz)

Figure 1. Examples of header row information and corresponding address codes for three Astra channels.

three typical commercial channels. These examples all show page 100 which is the default or menu page; the rest of the header row information is the same for all pages.

The teletext mode of the TV receiver does not have to be active for the techniques described below to be implemented, since the teletext information is always available on the teletext decoder chip. Furthermore, the teletext information remains available on channels for which the video signal has been scrambled.

### 3. TIME SYNCHRONISATION

To implement time synchronisation between widely spaced stations, it is necessary to provide at each station a pulse which originates from a source at a known distance from that station. A geostationary satellite which disseminates signals for commercial TV stations provides a convenient source from which such pulses may be generated. The circuit in figure 2 shows how a pulse per second may be generated from the information available on the address and data lines of a standard teletext card of a household TV set. A Sony model KV-M1400L TV receiver with a built in teletext card was used in our tests but the technique is applicable to any similar system. Eleven address lines (lines A10 and A11 are ignored since these merely involve recognition of sub-pages of the same page) and the lowest order bit (D0) of the data lines are extracted from the pins of the SAA 5246P-H teletext decoder chip of the teletext card.

The address lines are fed to the combination of four 7485 comparators, as shown, which are interconnected

[11] so that the A=B output from the combination goes to the logic '1' state when the information on the address lines is the same as that set by the user. When the latter is set to address 3FF (hex), for example, the output indicates that the data lines now contain the current value of the seconds (rightmost character of the header row).

The D0 data bit is gated with the WE clock on the teletext card (the WE signal is used to clock in new data being received off-air). The rest of the circuitry is designed to detect a change in D0. Thus, a pulse appears at the output (PPS out) whenever the seconds digit is incremented, the width of the output pulse being set by the value of the delay as indicated in the figure. Alternatively, a pulse per 10 seconds, a pulse per minute, etc. up to one pulse per day may be obtained by changing the address set by the user to the corresponding address given in figure 1 (3FE, 3FD, etc.).

The use of comparators to detect the appropriate address, while providing considerable versatility, is not essential. If a pulse per second alone is required, for example, the address could equally well be detected by a simple configuration of gates.

### 4. TESTING

The TV teletext signals utilised in our experiments were those received from the ASTRA satellite constellation. Two standard commercial receiving systems, each comprising dish, LNB, decoder box, TV receiver with teletext card and the additional

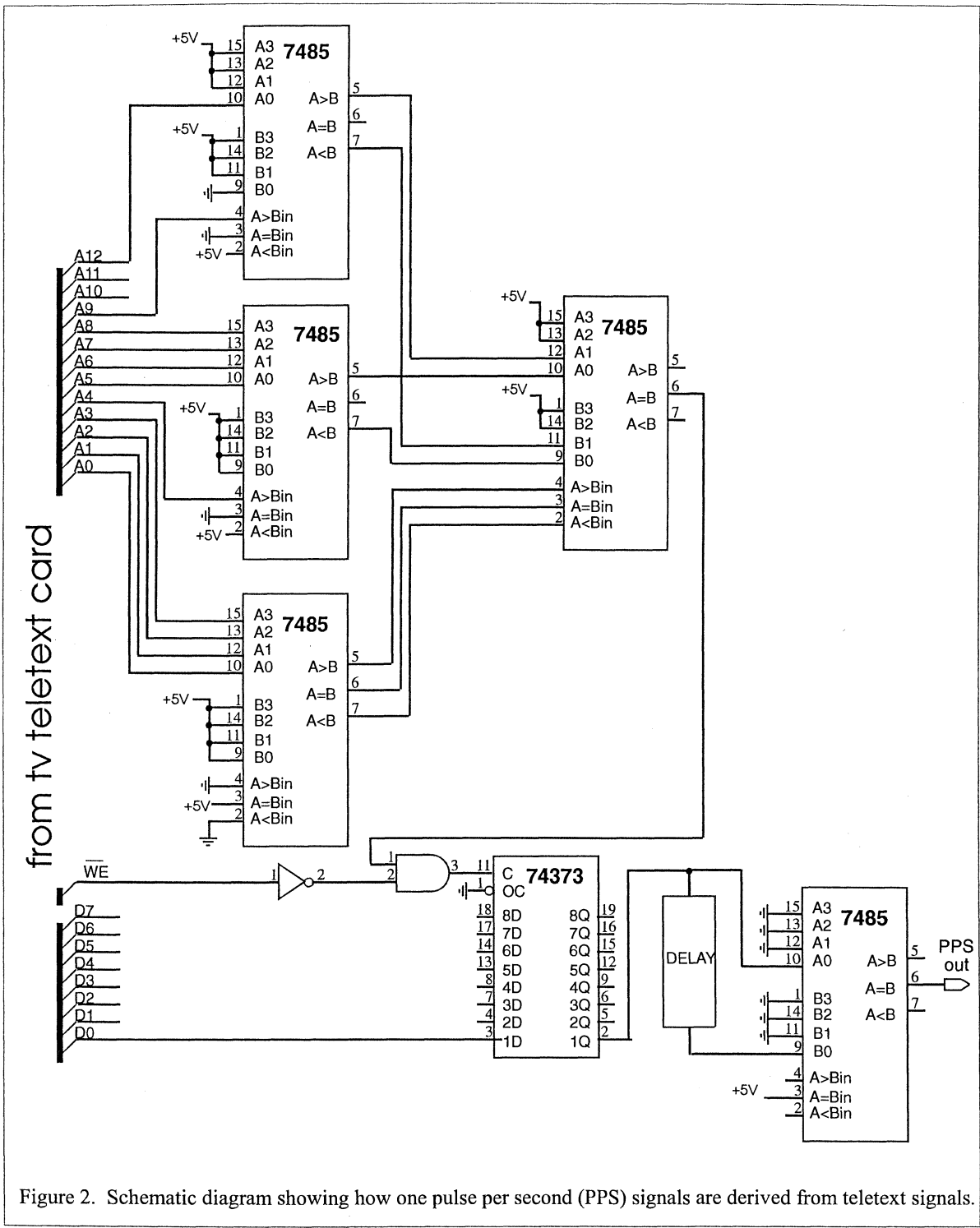


Figure 2. Schematic diagram showing how one pulse per second (PPS) signals are derived from teletext signals.

circuitry described above, were put in operation. Initially, the two dishes were placed side by side on the roof of a building and appropriate delays were introduced to compensate for any intrinsic time difference between the two arrangements, e.g. cable lengths, response times of LNBS, decoding circuits or receivers. Subsequently, one of the dishes was moved fixed distances northward along the roof relative to the other dish. The PPS output from one system was fed to the START input and the other to the STOP input of a time-to-amplitude converter whose output was fed into a multichannel analyser.

The distribution of time difference was recorded for each inter-antenna separation and displayed on the multichannel analyser screen; figure 3 shows the distribution in time difference corresponding to north-south distances between the dishes of 0.0 m, 21.1 m, 41.5 m and 75.0 m. The distributions have a FWHM of approximately 30 ns with 60% of events within  $\pm 15$  ns, 90% within  $\pm 35$  ns and 99% within  $\pm 45$  ns. The long term drift in the mean position, possibly due to degeneration of components in receivers, etc. was found to be less than 5 ns over six months of operation.

No satellite is truly geostationary and, accordingly, the accuracy of the time synchronisation technique described is limited by the precision to which the position of the transmitting satellite is known. Various methods are available for accurate determination of satellite co-ordinates [12]. Where a large number of stations is involved, a self-consistency algorithm can be applied to the arrival times of the PPS signals at any second and the most probable position, in earth co-ordinates, of the transmitting satellite determined. Alternatively, a small number of stations (say three or four adjacent stations at the centre of an array) could be interconnected by cables of known length and the transit times of the PPS pulses through these could be used to fix the corresponding satellite position. These, or similar techniques, should provide sub 25 ns accuracy (standard deviation) over ~ 1000 km baselines at low cost.

The  $\overline{OE}$  clock of the teletext card is designed for a number of functions which take place on different clock phases and consequently it has a rather complex structure. The purpose of the 74221 monostable multivibrator in figure 4 is to modify the  $\overline{OE}$  signal to provide a simple 1 MHz clock whose transitions correspond to the required 'valid data' epochs for time-of-event recording, specifically while the teletext card is writing data from its internal RAM to the character generator. This modified  $\overline{OE}$  signal is fed to the SI inputs of the FIFOs.

The four 7485 comparators in figure 4 are used to monitor the eleven bits of the address lines of the teletext card, as in figure 2. The A=B output from this combination of comparators indicates that the preset criterion is satisfied which, in this case,

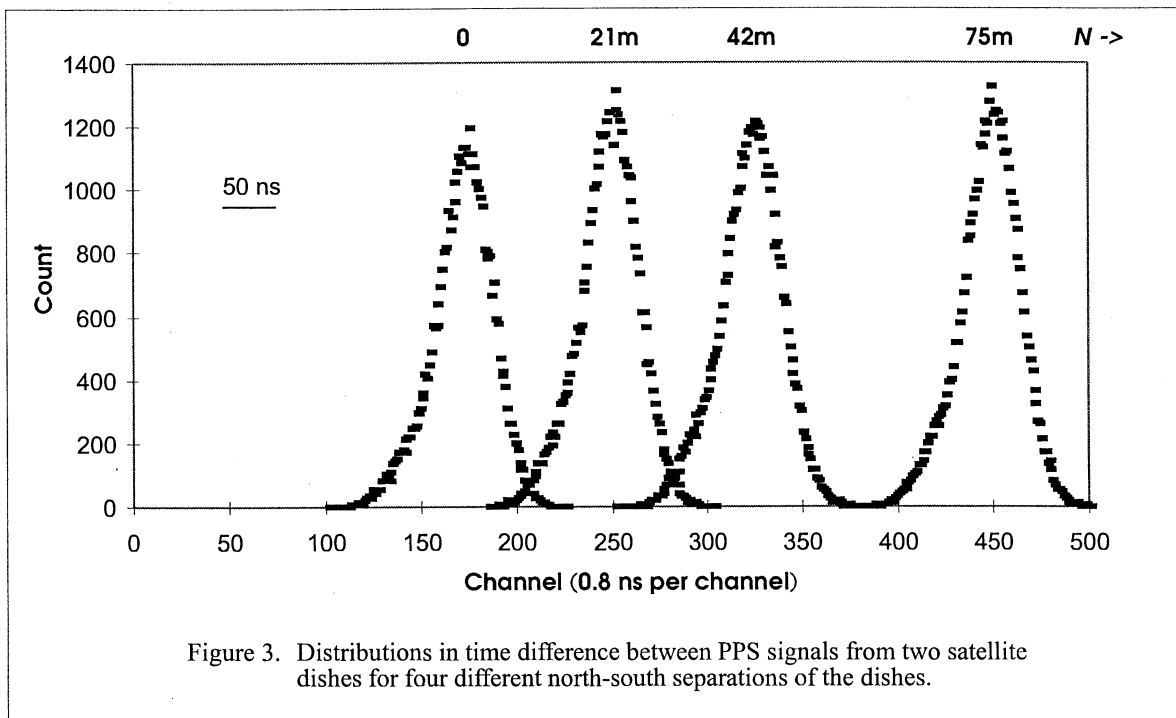


Figure 3. Distributions in time difference between PPS signals from two satellite dishes for four different north-south separations of the dishes.

## 5. TIME-OF-EVENT RECORDING

The availability of current date and time on the header row of all teletext transmissions allows a simple extension of the system described above to enable this time to be abstracted. The ability to insert a time-of-event, as required, into a data recording stream proves useful in many data acquisition applications. The schematic layout in figure 4 is designed to make available to data acquisition software the sixteen rightmost characters of a teletext header line. This data, available on the data bus (D0 - D7) of the teletext card, can be held temporarily in the two 40105 4 x 16 FIFOs.

corresponds to the address 018 (hex), the address of the first of the sixteen rightmost characters on the header line (see figure 1). This criterion is satisfied many times per second. The function of the other components of the circuit (7474 flip-flop and four simple gates) is to enable the 1 pulse per second (PPS out), generated as described in section 3, to be utilised to provide for the following action. The memory reset (MR) of the FIFOs is activated on the first occasion after each PPS that the comparator criterion is satisfied in coincidence with a pulse derived from the  $\overline{OE}$ . Subsequently, the next sixteen records on the data bus of the teletext card are read sequentially into the FIFO memory clocked by the 1 MHz modified  $\overline{OE}$

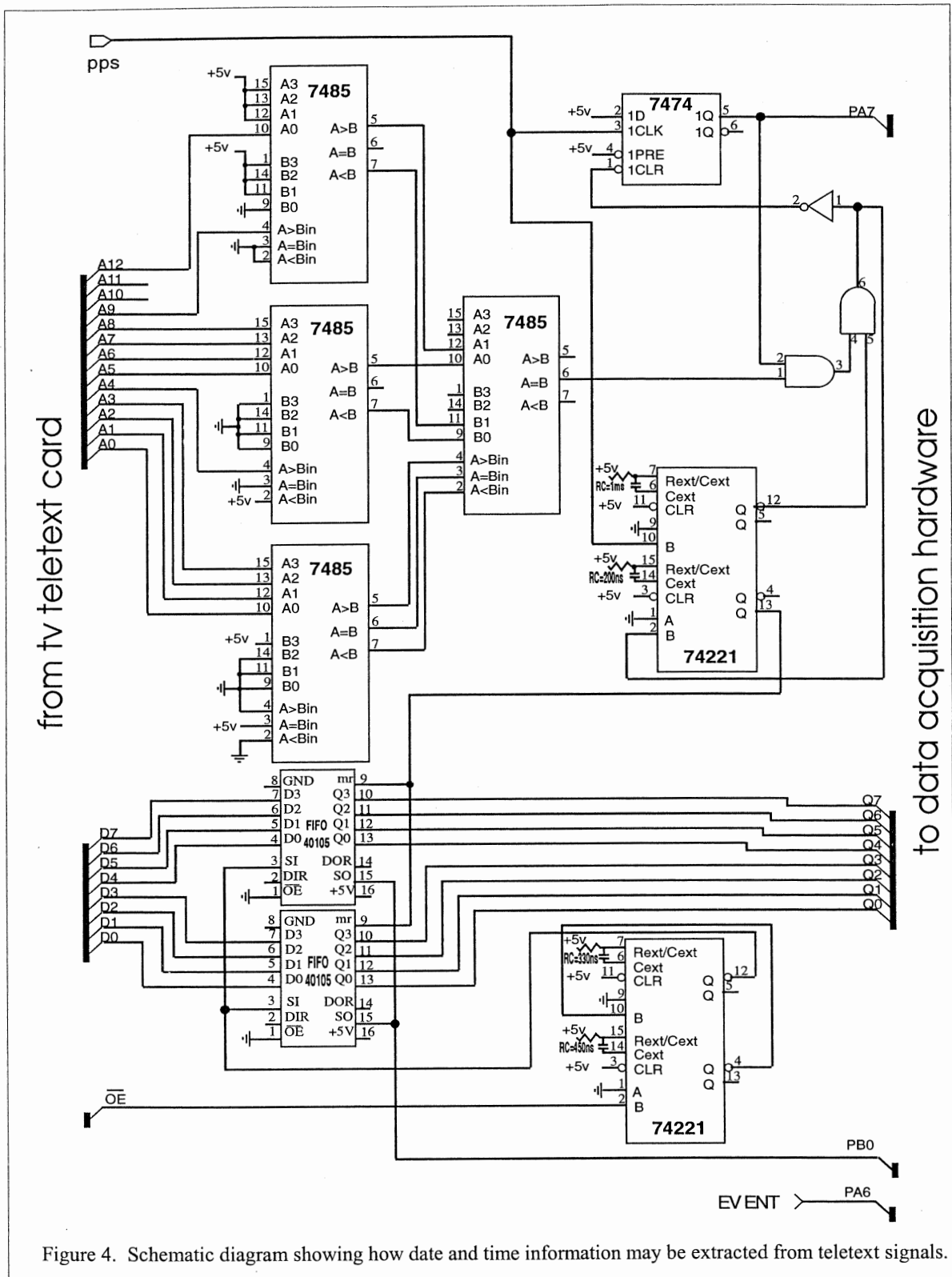


Figure 4. Schematic diagram showing how date and time information may be extracted from teletext signals.

signal. Further resets of the FIFOs are inhibited until the next second when the sequence is repeated. The output from the 7474 flip-flop is used to inform the data acquisition hardware and software that the data in the FIFOs is valid.

An 'event', for example a pulse derived from an experiment, triggers the data acquisition system to read out in sequence all sixteen characters in the FIFO

memory after the next subsequent PPS. This readout is clocked by a software generated signal which is fed to the SO inputs of the FIFOs (see figure 4). Thus, the date and time corresponding to the second immediately after any event may be recorded as required. In the case of SKY NEWS, for example, the record would have the following form  
 dd mon 1997 hhmm:ss.

It should be noted that times broadcast in this way by commercial teletext transmissions cannot be guaranteed to correspond to Universal Time and some procedure, such as the use of UTC related radio transmissions, must be used to determine any offset from Universal Time.

The hour, minute and second information on the header row is updated off-air much more frequently than the day, month and year. If time-of-day information alone is sufficient for time tagging purposes, this alternative could be implemented in a simple manner using the WE clock.

### Acknowledgements

We wish to express our thanks to Mr. Clem Pryke, Dr. Jeremy Lloyd-Evans and Prof. Alan Watson of the University of Leeds for many helpful discussions. Also, we thank Dr. P. Urich of Laboratoire Primaire du Temps et des Fréquences, Observatoire de Paris for providing important advice and information at the commencement of the project.

### References

- [1] J. Tolman et al., Trans IEEE **IM-16** (1960) 247
- [2] J. J. Lennon et al., Nuc Instrum Meth **171** (1980) 101
- [3] W. Lewandowski and C. Thomas, Trans IEEE **79** (1991) 991
- [4] J. A. Davis et al., Proc 5th EFTF, Besançon (1991) 74
- [5] F. Meyer et al., Proc 5th EFTF, Besançon (1991) 82
- [6] J. A. Davis and P. R. Pearce, Proc 6th EFTF, Noordwijk (1992) 195
- [7] K. de Souza et al., Nucl. Phys. B **22B** (1991) 116
- [8] J. W. Cronin et al., *Scientific American*, (January 1997) 32
- [9] C. L. Pryke and J. Lloyd-Evans, Nuc Instrum Meth **A 345** (1995) 560
- [10] P. L. Mothersole and N. W. White, *Broadcast Data Systems* (Butterworth: 1990) 101
- [11] *The TTL Data Book* (Texas Instruments: 1993) 3-198
- [12] F. Meyer et al., Proc 7th EFTF, Neuchâtel (1993) 129

**TIME AND FREQUENCY STANDARD OF GUM AND ACTIVITIES TOWARD ITS IMPROVEMENT**

Jerzy Siemicki

Central Office of Measures (GUM), Warsaw, Poland

**1. INTRODUCTION**

Central Office of Measures (GUM) in Poland fulfils the function of national metrology institute and maintains the standards of units of nearly all physical quantities. There also is here, in Time and Frequency Laboratory, the national standard of time and frequency units which beside the reproduction of units generates the UTC(GUM) time scale too.

**2. THE SYSTEM OF TIME SCALE GENERATION AND COMPARISONS**

Simplified block diagram of the standard is shown in Fig. 1. The basic part of the standard is a set of four cesium time and frequency standards usually called cesium clocks which are HP 5071A (two pieces), HP 5061B and HP 5061A. The time scale in this arrangement is generated directly by one of the four cesium clocks, that one of them which has the best long term frequency stability. This clock reproduces also the time and frequency units and is called the main cesium standard.

The 1 pps output signals of the main cesium standard are fed via the equal length coaxial cables to the main GPS receiver, the time interval counter

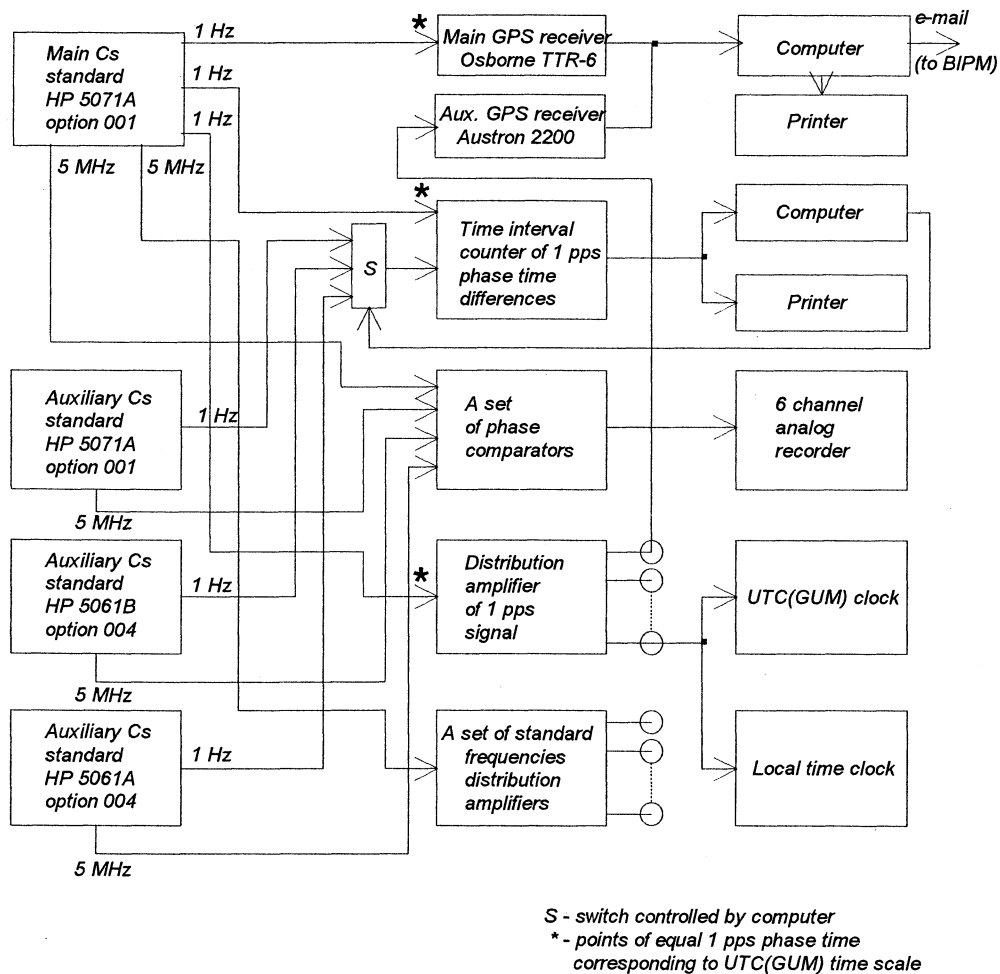


Fig. 1. Simplified block diagram of national standard of time and frequency units which also generates the UTC(GUM) time scale

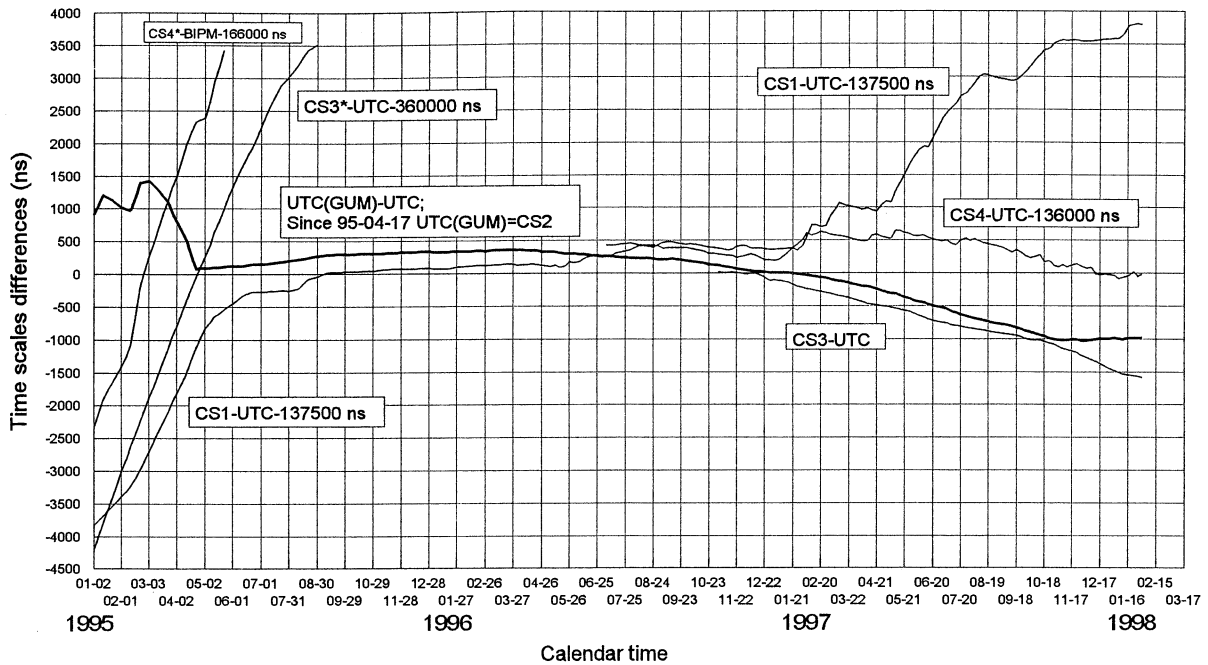


Fig.2. UTC(GUM) time scale and cesium clocks time scales differences with respect to UTC

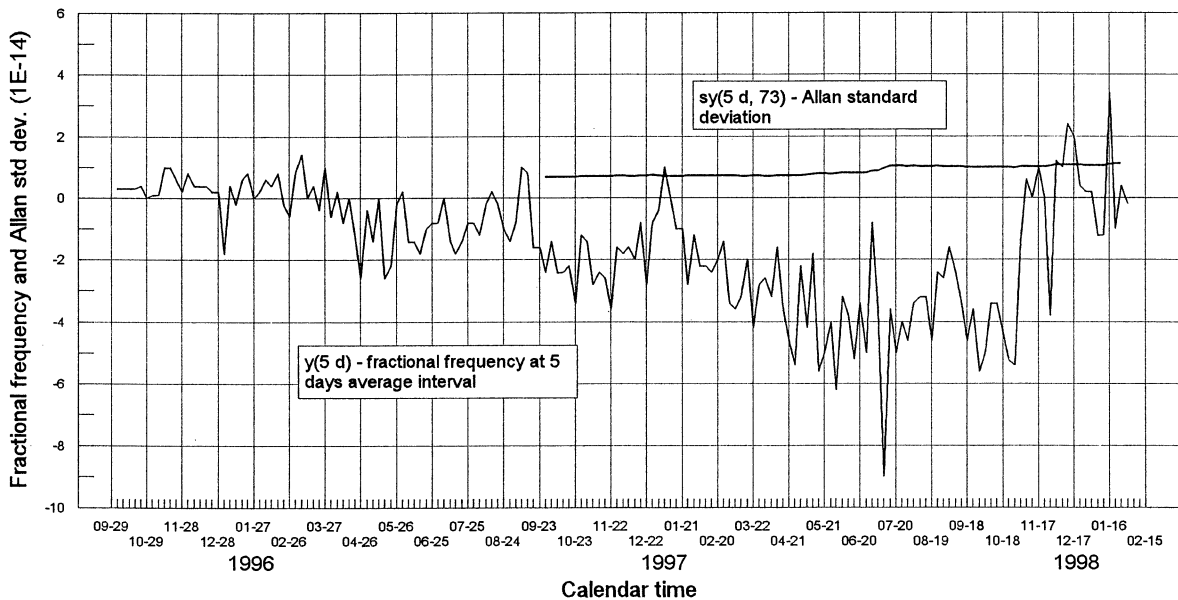


Fig.3. Fractional frequency and Allan standard deviation of GUM time and frequency standard for 5 days average interval and 1 year (strictly:  $73 \cdot 5$  days) consecutive measurement period

measuring the phase time differences between the 1 pps signals from the auxiliary cesium standards and the 1 pps signal from the main cesium standard, and the distribution amplifier of the 1 pps signal. The inputs of those three instruments are the points in which the phase time of the 1 pps signal exactly corresponds to the UTC(GUM) time scale. The advantage of that system in which there are no switched devices between the main standard and the basic measuring instruments is that the time scale generated is to considerable degree unaffected by

any accidental switching or a lack of contact in the apparatus.

The system of international comparisons of the UTC(GUM) time scale is based on the GPS common view method and is included to the general system coordinated by BIPM.

### 3. LONG TERM CHARACTERISTICS OF THE STANDARD

The graphs of the UTC(GUM) time scale and the auxiliary standards time scales for last three years

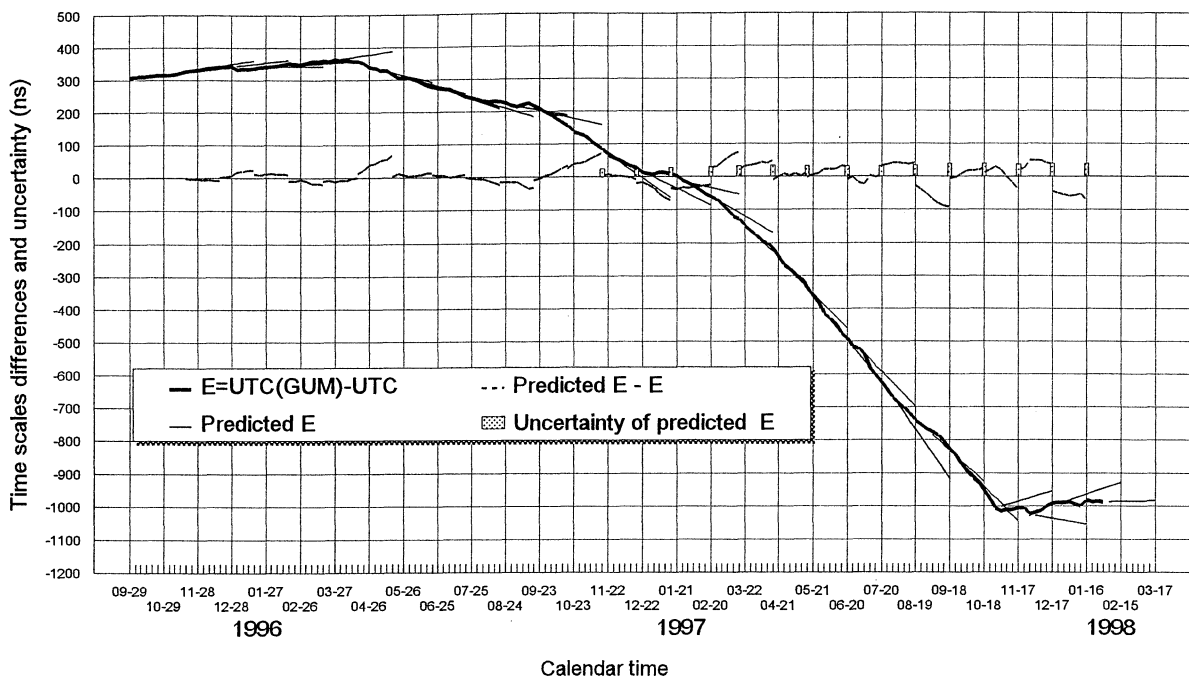


Fig. 4. Carrying out the prediction of UTC(GUM) time scale and evaluation of uncertainty of predicted values

are shown in Fig. 2. In fact, this figure presents the differences between the given time scales and the UTC being, from traditional metrological point of view, the errors of the given time scales with respect to UTC.

The graphs of fractional frequency and Allan standard deviation of the main standard output signals for 5 days average interval and one year consecutive measuring period (containing 73 average intervals) are presented in Fig. 3.

The data for graphs in Fig. 2 and Fig. 3 were taken from the BIPM Time Section circulars and the records of internal comparisons of cesium clocks.

It can be seen in Fig. 2 that the UTC(GUM) time scale (bold line graph) has had a good long term stability since April 1995. In that month the HP 5071A standard was established as the main cesium standard and begun generate the UTC(GUM) time scale in the new system shown in Fig. 1. Before that date the system based on HP 5061B standard was used in which the 5 MHz signal from HP 5061B was passing via microstepper and frequency divider to generate the 1 pps signal for UTC(GUM). That system caused much troubles in operation.

As it is seen in Fig. 2, the difference UTC(GUM) - UTC obtained the value of about -1000 ns at the end of October 1997. At that moment the first frequency correction of the main standard was carried out and since then the long term averaged fractional frequency has remained near zero which can be seen also in Fig. 3.

Fig. 2 shows also that the BIPM recommendation to maintain the time scale in  $\pm 100$  ns limits with respect to UTC was not fulfilled. The reason for that

was that up to now there was no specific need of such small differences. For instance, for measuring instruments calibration purposes the difference smaller than  $1 \mu\text{s}$  is satisfactory provided that the prediction of time scale for current day is carried out and the uncertainty of predicted values is estimated. However, in view of significance of the BIPM recommendation for international comparisons of time scales the UTC(GUM) time scale will be corrected in a short time by introducing a time step and will be maintained in  $\pm 100$  ns limits by slight frequency corrections.

#### 4. TIME SCALE PREDICTION AND UNCERTAINTY EVALUATION

The graphs shown in Fig. 4 concern the time scale prediction and the uncertainty evaluation of predicted values. The knowledge of these parameters is requested for measuring instruments calibration as it was mentioned, and in general they present important characteristics of the standard.

The outline of the evaluation of these characteristics is as follows:

1. The linear prediction of the time scale differences  $E = \text{UTC(GUM)} - \text{UTC}$  is performed using the values of  $-E$  given in the BIPM Time Section circular. The circular for previous month is received about 15th day of current month. Assuming that the prediction is done in this day, it concerns about 15 days in the past (it is the "backward" prediction) and about 30 days in the future (it is the "forward" prediction) including the period from the approximate beginning of the current month to

a date of receiving of the next circular. The forward prediction is essential one for our purposes.

2. The differences  $\Delta E_{pred} = E_{pred} - E$ , where  $E_{pred}$  is a predicted value of  $E$ , are calculated for the total period included in the circular (i.e. for calendar month approximately) assuming that at least one prediction was performed before. These differences may be treated as the prediction errors. Only the values of the forward prediction are taken to account in this calculation.

3. The uncertainty of predicted values  $E_{pred}$  for the current prediction is evaluated taking to account the prediction error values  $\Delta E_{pred}$  for last year assuming that the predictions have been performed every month since a day of about one year ago. The method of uncertainty evaluation used is based partly on experience and intuition, not strictly on the theory. An idea of this method is that it is possible, on the base of the knowledge of prediction error  $\Delta E_{pred}$  for last year, to take to account the contribution of the mid term (5 days average time), the long term (1 month average time) and the very long term (1 year average time) variations of difference  $E$  to the total uncertainty of the current prediction.

Formulas used in consecutive calculations leading to the estimation of the uncertainty are as follow (units of quantities are nanoseconds if no other unit is written):

1. Basic formula for calculation of predicted time scale differences with respect to UTC according to the linear prediction principle:

$$E_{pred} = E_e + \frac{E_e - E_s}{T}(t - t_e) \quad (1)$$

where:

$E_{pred}$  - predicted difference UTC(GUM) - UTC;  
 $E_{pred} = \{\text{UTC(GUM) - UTC}\}_{pred}$ ,

$T[\text{days}]$  - basic time interval equal to a total period included in the BIPM circular;  $T = n\tau$  where  $n = 6$  usually or  $n = 5$  or  $7$  sometimes,  $\tau = 5$  days - basic average time interval used in the BIPM circulars,  
 $E_s$  - difference UTC(GUM)-UTC in the first day of time interval  $T$ ,

$E_e$  - as above but in the last day of time interval  $T$ ,

$t[\text{MJD}]$  - date of any day in prediction interval,

$t_e[\text{MJD}]$  - date of the last day of interval  $T$ .

2. Formula for calculation of prediction errors:

$$\Delta E_{pred} = E_{pred} - E \quad (2)$$

where  $E = \text{UTC(GUM)} - \text{UTC}$  is obtained from the BIPM circular where values of  $-E$  are given.

3. Formulas for calculation and estimation of the uncertainty of the predicted time scale differences for current day:

1) experimental standard deviation of prediction errors for month interval:

$$s_{\Delta E_j} = \sqrt{\frac{1}{n-1} \sum_{i=1}^n (\Delta E_{predi} - \Delta E_{predavj})^2} \quad (3)$$

where:

$\Delta E_{predi}$  - number  $i$  prediction error in number  $j$  prediction interval;  $\Delta E_{predi} = E_{predi} - E_i$ , where  $E_i = [\text{UTC(GUM)} - \text{UTC}]_i$  is obtained from BIPM circular,

$\Delta E_{predavj}$  - arithmetic mean of prediction error in number  $j$  of prediction interval,

$j = 1, 2, \dots, m$ ; usually  $m = 12$ ,

$n$  - number of prediction error values in forward prediction; usually  $n = 6$ , sometimes  $n = 5$  or  $7$ ,

2) square mean of  $s_{\Delta E}$ :

$$s_{\Delta E}^{\#} = \sqrt{\frac{1}{m} (s_{\Delta E1}^2 + s_{\Delta E2}^2 + \dots + s_{\Delta Em}^2)} \quad (4)$$

3) arithmetic mean of prediction error values in prediction interval:

$$\Delta E_{predavj} = \frac{1}{n} \sum_{i=1}^n \Delta E_{predi} \quad (5)$$

4) experimental standard deviation of parameter  $\Delta E_{predav}$  for  $m$  observations:

$$s_{\Delta E_{av}} = \sqrt{\frac{1}{m-1} \sum_{j=1}^m (\Delta E_{predavj} - \Delta E_{predav})^2} \quad (6)$$

where  $\Delta E_{predav}$  is the total average of prediction error:

$$\Delta E_{predav} = \frac{1}{m} \sum_{j=1}^m \Delta E_{predavj} \quad (7)$$

5) type A standard uncertainty of predicted time scale differences:

$$u_A = \sqrt{(s_{\Delta E}^{\#})^2 + s_{\Delta E_{av}}^2} \quad (8)$$

6) type B standard uncertainty of predicted time scale differences which takes into account the total average of prediction error (equ.7) and enables including it to total uncertainty; it is assumed that  $\Delta E_{predav}$  has a normal probability distribution and its values are contained in  $(-2\Delta E_{predav}, +2\Delta E_{predav})$  interval with probability of 0,997 which corresponds to 3s confidence interval:

$$s_{\Delta E_{av}} = u_B = \frac{2\Delta E_{predav}}{3} = 0,67\Delta E_{predav} \quad (9)$$

7) total uncertainty of predicted time scale differences:

$$u_t = \sqrt{u_A^2 + u_B^2} \quad (10)$$

In above calculations, formulas (3) and (4), (5) and (6), and (7) and (9) give respectively a main contribution of the 5 days, the 1 month and the 1 year average time variations of difference  $E$  to the total uncertainty of the current prediction.

An example of the calculation of the time scale prediction and the evaluation of its uncertainty is presented in tables 1, 2 and 3.

TABLE 1 - Values of E obtained from the BIPM circular including the period of 27th Dec. 97 to 31st Jan. 98

Date	97-12-27	98-01-01	98-01-06	98-01-11	98-01-16	98-01-21	98-01-26	98-01-31
E (ns)	-988	-987	-993	-999	-982	-987	-985	-986

TABLE 2 - Calculation of the GUM time scale prediction for the period of 1st Feb. 98 to 17th March 98

Date	98-02-05	98-02-10	98-02-15	98-02-20	98-02-25	98-03-02	98-03-07	98-03-12	98-03-17
$E_{pred}$ (ns)	-985,67	-985,33	-985,00	-984,67	-984,33	-984,00	-983,67	-983,33	-983,00
	Backward prediction	Day of calculation of prediction	Forward prediction						

TABLE 3 - Carrying out the evaluation of the uncertainty of the time scale prediction for period of 1st Feb. 98 to 17th March 98 on the base of prediction errors data from period of Jan. 97 to Jan. 98

Months	01/02 1997	02/03 1997	03/04 1997	04/05 1997	05/06 1997	06/07 1997	07/08 1997	08/09 1997	09/10 1997	10/11 1997	11/12 1997	12.97/ 01.98
$s_{\Delta E_j}$ (ns)	4,4	20,1	9,4	7,7	11,6	10,2	3,0	25,1	11,7	25,2	12,1	8,5
$s_{\Delta E}^{\#}$ (ns)	14,3											
$\Delta E_{predavj}$ (ns)	-31,2	50,2	36,7	3,9	17,8	-6,4	39,2	-64,4	11,8	3,1	39,3	-55,1
$s_{\Delta E_{av}}$ (ns)	37,5											
$u_A$ (ns)	40,1											
$\Delta E_{predavavj}$ (ns)	3,7											
$u_b$ (ns)	2,5											
$u_t$ (ns)	40,2											

In Table 1, the values of E obtained from BIPM circular are given being the base of the prediction. The calculation of the prediction is presented in Table 2. Days in Table 2 correspond to days in the BIPM circulars. For intermediate days, predicted values  $E_{pred}$  must be obtained by interpolation. It can be seen in Table 3 that the most significant contribution to the total uncertainty is brought in by formulas (5) and (6) representing the month average time variations of difference E. On the contrary, the contribution of the year average time variations of E represented by formulas (7) and (9) is negligible.

In Table 3 is also seen that the total standard uncertainty of the time scale prediction (more strictly: of the predicted values of  $E = UTC(GUM) - UTC$ ) presented in Table 2 is  $40,2 \text{ ns} \approx 40 \text{ ns}$ . This value is represented by the last bar in the bar graph in Fig. 4.

As it was mentioned, the method is to a considerable degree based on the intuition and experience and does not strictly conform to the principles of the uncertainty theory. For instance, it does not take into account the correlation coefficients.

So the works toward improving of the method will be carried out.

### 5. NEW APPARATUS INSTALLED

Up to now, a time and frequency dissemination realized by GUM has been consisted mainly in the distribution of the acoustic time signals via public broadcasting stations and the cable transmission of the standard frequency to public telecommunication centre. In the last time, a system of coded time signals distribution via telephone lines was installed and put into provisional operation. The system consists of the time code generator and the 1 pps monitor which are manufactured by the Technical University of Graz (Austria), and also a modem, host PC computer and special software. The system enables the synchronization, according to UTC, of real time clock in remote PC computer which is equipped with a modem and special software and which will be connected to the system via a telephone line for a short time (a part of minute to 2 minutes).

The first results obtained for the synchronization error of real time clock in a PC computer working

in the DOS operation system are of  $(15 \div 20)$  ms (it is experimental standard deviation of 10 observations, several measurement series were performed, mean value was about 0). The practical accuracy of the synchronization is limited by a short term dispersion of a computer DOS clock error which approximately is of the same value and masks the synchronization error.

The time error due only to the distribution system was evaluated by the measurements of a time interval between the 1 pps signal of local time scale and the 1 pps signal taken from 1pps monitor of the distribution system. Provisional results obtained are as follow: the experimental standard deviation of 10 observations is of about 2 ms, and the mean values of several measurement series performed in the same day are in limits  $\pm 8$  ms approximately.

Above results were obtained in GUM - telephone exchange - GUM connection using the distribution system special function of measurement and compensation of the modems and telephone line delay. The modems used were Premier 33.6 model of Motorola with relatively big delay of about 230 ms (it is summary delay of sending and receiving modems).

The work toward more precise determination of time distribution error and full implementation of the system will be continued. The telephone number of this time service is: (48) (22) 654 88 72.

In recent time was also installed and put in motion a set for time scale comparisons by means of a multichannel GPS receiver. It contains the Motorola "Oncore" VP 1115 GPS receiver, HP 53132A universal counter and PC computer. The set is equipped with a software worked out by Dr J. Nawrocki from Astrogeodynamical Observatory in Borowiec (Poland). The software

enables the data processing of 89 receiving seances during a day. Each of them lasts thirteen minutes and during each of them up to eight satellites can be received simultaneously.

The set works in provisional way and up to now there are no intercomparisons results.

#### ACKNOWLEDGEMENTS

The author would like to express his gratitude to Dr D. Kirchner from Technical University of Graz and Mr H. Reßler from Space Research Institute in Graz for their help in putting in motion of the set for distribution of coded time signals by telephone lines.

The author also wish to thank Dr J. Nawrocki for his work on software for the Motorola "Oncore" GPS receiver and help in putting it in motion.

#### REFERENCES

1. Tavella P., Thomas C., 1991, "Comparative Study of Time Scale Algorithms", *Metrologia*, 28, 57 -63.
2. BIPM et al., 1993, "Guide to the Expression of Uncertainty in Measurements".
3. Kirchner D., Reßler H., 1993, "Zeitübertragung über Telefonmodems", Verlag Sprache und Technik Groß-Bieberau, 185 -199.
4. W. Lewandowski et al., "A New Approach to International Satellite Time and Frequency Comparisons: 'All in View' Multichannel GPS + GLONASS Observations", ION GPS '97, 16 - 19 September 1997, Kansas City, USA (preprint).
5. Report of the Open Forum on GPS and GLONASS Standardization, 6th CGGTTS Meeting, 1 December 1997, Long Beach, California, USA.

ON LINE UNIFORMITY OPTIMIZATION OF THE HIGH C-FIELD MAGNET IN THE POLITECNICO CESIUM BEAM STANDARD

G.A. Costanzo, V. Barychev<sup>\*</sup>, M. Siccardi, A. De Marchi

Dipartimento di Elettronica, Politecnico di Torino  
 C.so Duca degli Abruzzi, 24  
 10129 - TORINO, Italy  
 e-mail: cesio@polito.it  
<sup>\*</sup>VNIIFTRI, Mendeleevo, Russia

Abstract

A few years ago the high C-field concept was presented to the scientific community as a possible solution to reduce some sources of inaccuracy related to the C-field design in primary Cs beam frequency standards [1].

This goal appears presently within reach by "on line" optimization of the C-field spatial uniformity. The procedure calls for real time observation of the  $\nu_0$  field dependent transition linewidth and shape, while adjusting currents in a number of correction coils. Experiments and results are described.

Introduction

The Politecnico di Torino developed an experimental apparatus<sup>1</sup> in order to investigate technical and physical solutions to reduce inaccuracies in classical Cs beam frequency standards. The design was based on a high C-field approach.

The latter is set at 82mT where the Breit-Rabi formula shows a purely quadratic minimum for the  $m_F = -1, \Delta m_F = 0$  transition. This C-field setting point reduces neighboring transitions effects and shielding needs. The field along the atomic path minimizes to  $\nu_{-1} = 8900727438,257$  Hz the frequency of the clock transition.

Neighboring transitions move 600MHz away from the  $\nu_{-1}$  frequency, and the uncertainties induced by Rabi and Ramsey pulling and Majorana transitions become unimportant.

A multilambda cavity [2] is used, which allows reduction of some cavity related problems and "on line" uniformity analysis by observation of the field dependent  $\nu_0$  line.

As a trade-off, the C-field relative spatial uniformity must be about  $10^{-6}$  over the microwave interaction zone (40cm) for an accuracy target in the low  $10^{-14}$ . On-line optimization of the magnetic field uniformity seems to be a better solution than the "trial and error" procedure used in the past [3].

Description of the apparatus

The high C-field frequency standard is an operative Cs beam in the La.R.C.A. laboratory at the Politecnico di Torino (Italy).

The prototype is a vertical apparatus consisting mainly of a solenoidal magnet, which produces the 65kA/m C-field. Figure 1 depicts a simplified scheme of the whole apparatus. The oven to detector distance is about 1.4m.

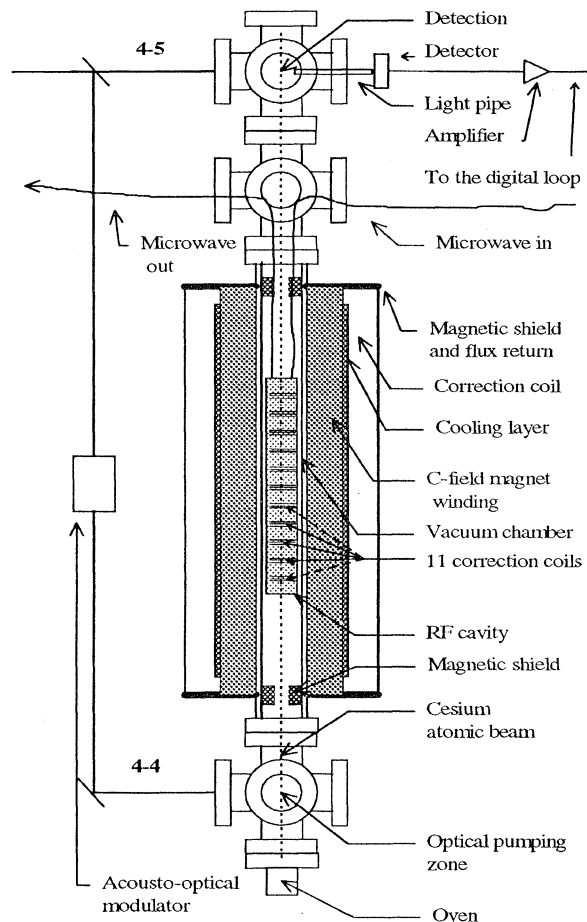


Figure 1: scheme of the high C-field device.

<sup>1</sup> This work is partially supported by INFN

Hard electrical and mechanical specifications are imposed on the C-field: if the accuracy level must be in the low  $10^{-14}$ , the exciting current must be stable to  $10^{-6}$ . This problem is solved by a control loop which adequately stabilizes the current by looking at the voltage drop across a manganin resistor [4].

The mechanical stability of the C-field solenoidal magnet is also important, and the thermal coefficient of the magnet was measured to be close to  $10^{-4}/\text{K}$ . A digital servo loop stabilizes the cooling water flux to mK level, by monitoring the winding resistance with a volt-ampereometric measurement.

For the rest, the multilambda cavity has high spatial phase uniformity, and the high quality factor of the cylindrical  $\text{TE}_{01}$  mode should reduce end to end phase shift to negligible level.

Measurements are planned to evaluate this systematic effect because of residual first order Doppler shift due to losses in end caps.

Pumping and detection are accomplished by using an extended cavity semiconductor laser diode. Absorption spectroscopy in a Cs cell is used to stabilize the laser on the 4-5 cycling transition.

Frequency modulation by an AOM is used to produce the pumping laser beam tuned to the 4-4 transition.

### C-field uniformity optimization

In the high C-field concept, rms spatial field uniformity of  $3 \cdot 10^{-6}$  is required to ensure bias in the low  $10^{-13}$ . This limit seems hard to obtain because is not easy to make repeatable measurements on the solenoidal magnet at the level of  $10^{-6}$  when it operates with or without the atomic beam active.

In fact, in the past, we measured the spatial uniformity using a NMR probe gaussmeter and a trial and error procedure was used for optimization: magnetic field measurements were performed in one hour and shim coil currents were set after computer analysis.

Trial were repeated to reach a considerably good uniformity ( $3 \cdot 10^{-5}$ ) [5]. No discrepancies were found by comparing this figure with the shape of the field dependent transition.

Shim coils wound outside the main winding were used for early trials. This caused a spatial resolution limitation for the correction.

Shim coils were ultimately wound directly on the cylindrical cavity: this solution ensures local corrections. Each Rabi interaction zone length is of the order of the cavity diameter and coils act on the local magnetic static field.

In view of field uniformity measurements, the multilambda Rabi cavity geometrical dimensions were chosen to resonate at two  $\text{TE}_{01}$  modes at the same time:  $\text{TE}_{01-7}$  at 8.900 GHz for clock transition and  $\text{TE}_{01-11}$  at 9.475 GHz. The latter is resonant at

$\nu_0$  ( $m_F=0$ ) line at 82mT which, from Breit-Rabi formula, shows a linear dependence with the magnetic field.

The eleven magnetic field lobes act as independent Rabi zones where static C-field is locally defined along 3.5cm.

Observations of the  $\nu_0$  shape allow to evaluate field uniformity through the sensitivity coefficient of 680kHz/gauss. Therefore each Rabi line contributes to the field uniformity evaluation because it is proportionally shifted from the mean average field along the atomic path.

On line optimization is performed by making the  $\nu_0$  line shape narrower, acting on the shim currents. Figure 2 shows the eleven separated Rabi zones: each peak is easily recognized by varying current of the n-th shim coil, wound around the n-th antinode of the  $\text{TE}_{01-11}$  microwave mode. In this manner all currents are manually chosen to reduce the  $\nu_0$  line shape.

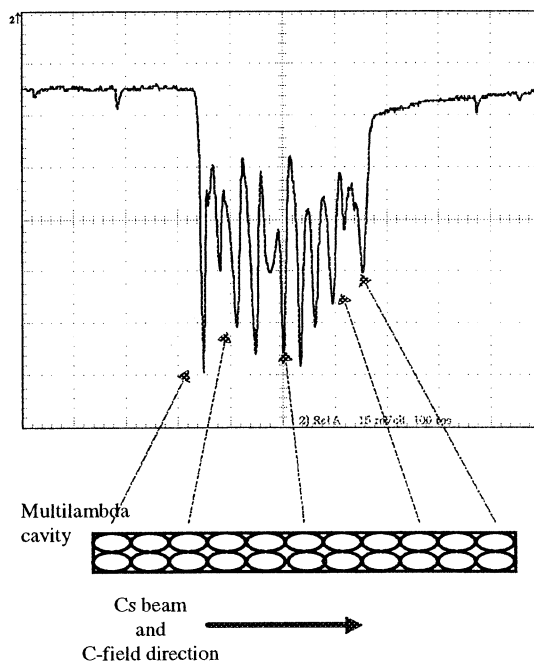


Figure 2: the 11 Rabi zones separated. The n-th peak is identified with the related n-th antinode of the  $\text{TE}_{01-11}$  mode in the multilambda cylindrical cavity (1.2MHz span, FWHM=300kHz).

Moreover, external coils wound around the main winding of the magnet are still used to reduce high disuniformities at the extremities. Few Amperes are fed in the external coils for first cut optimization, useful to reduce the natural disuniformity of the magnet (which is of the order of  $10^{-3}$ ).

Thus, when this step is accomplished, all the eleven Rabi zones are visible and coils with smaller diameter are fed with commercial current power supplies up to  $\pm 0.5\text{A}$ .

## Results and discussions

When all the 11 Rabi zones are completely resolved, an "on line" procedure is performed in order to make the  $\nu_0$  field dependent line narrower. The 11 Rabi lines then collapse in a single one. Furthermore, fine adjustments are performed maximizing the amplitude of the signal. Finally we obtained a FWHM of 15kHz as shown in figure 3. From the sensitivity coefficient, the measured linewidth ensures a uniformity of  $9 \cdot 10^{-6}$  rms. When higher uniformity will be reached, a Ramsey pattern is expected because of the interference between the 11 Rabi zones.

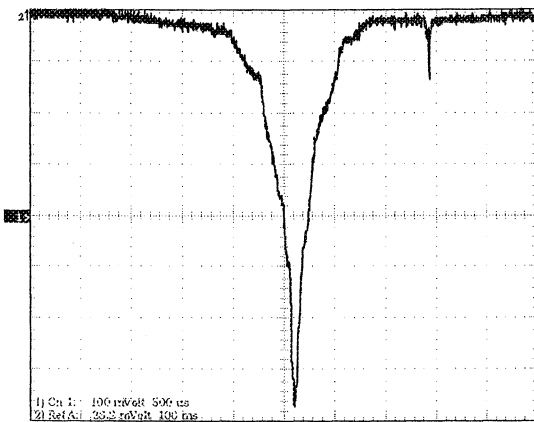


Figure 3: collapse of the 11 Rabi zone in fig.2 to a single line (span=300kHz, FWHM=15kHz).

Presently this limit is not very far. The present limit could be current stability and resolution of the eleven power supplies which excite the shim coils. A higher number of correction coils wound on the cylindrical cavity may also be necessary in order to increase spatial resolution for field optimization. Incidentally, the lineshape shown in fig.4 may be caused by Ramsey type interference. Higher contrast in the Ramsey pattern and adequate linewidth should follow from further uniformity improvement. This would hint to an uniformity in the low  $10^{-6}$ .

## Conclusions

C-field spatial uniformity is presently still the limiting factor for the frequency standard at the Politecnico di Torino. Even if high C-field value of 82mT reduces a set of inaccuracies sources, magnetic field specifications are really stringent. In fact, even if magnetic field stability (electrical and mechanical) have been overcome, problems still arise in the spatial uniformity along the interaction. By using on-line measurements of the  $\nu_0$  field dependent transition, optimization is performed.

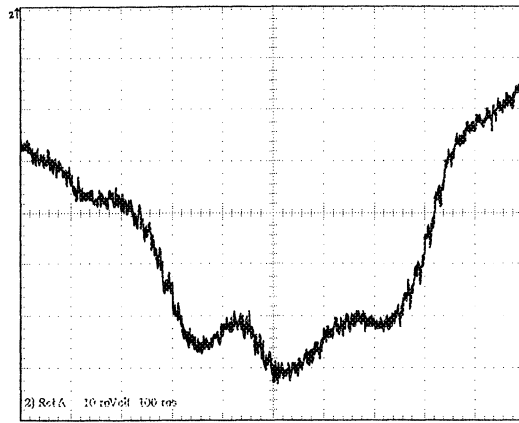


Figure 4: Ramsey type pattern between a few Rabi lines of the  $\nu_0$  field dependent transition (full span is 20kHz).

A linewidth of 15kHz was obtained, which correspond to a disuniformity of the order of  $10^{-5}$ . Finally, investigations on the central part of the resonant line allow the projection that the desired uniformity goal may be reached in the future.

## Acknowledgments

Authors wish to acknowledge useful discussions with many colleagues in the Politecnico di Torino. A particular thank goes to R.Drullinger and G.D.Rovera for invaluable help.

## References

- [1]A. De Marchi: "The high C-field concept for an accurate Cesium beam resonator"- Proc.7<sup>th</sup> European Frequency and Time Forum, pp.541-548, Neuchâtel (1993)
- [2]A. De Marchi, P. Tavella, E. Bava: "Multilambda Rabi cavities in atomic beam frequency standards", J. Appl. Phys. 82 (10), November 1997
- [3]G.A.Costanzo, M.Nervi, A. Premoli, M.Repetto, F.Levati: "Use of automated optimization techniques in the design of the magnetic system for a Cs frequency standard", Int. J. App. Electrom. and Mechanics, vol.6, pp.297-308, 1995
- [4]E. Rubiola: "High stability current control in the 10A range", IEEE Trans. on Instrumentations & Measurements, vol. 45, pp.865-871, October 1996.
- [5]G.A. Costanzo, E. Rubiola, S. Therisod, M.Siccardi, F. Periale, G.D. Rovera, V. Barichev, A. De Marchi: "The high C-field Cs beam frequency standard: present status and future improvements", Proc. 11<sup>th</sup> European Frequency and Time Forum, pp. 53-57, Neuchâtel, March 1997

## ATOMIC FOUNTAIN DEVELOPMENT AT U.S.N.O

Christopher R. Ekstrom and Eric A. Burt

U. S. Naval Observatory - Time Service Department  
 3450 Massachusetts Ave. NW  
 Washington, D.C. 20392 USA

Atomic fountain clocks are showing great promise as primary frequency standards (1). In light of this, we have started a program to develop atomic fountain clocks at the U. S. Naval Observatory. The mission of the observatory, however, dictates different design goals than that of a standards institution. In this paper we will discuss the goals of our atomic fountain project, a scheme for reducing the overall temperature sensitivity of the fountain, and the status of our efforts to launch atoms from a four beam optical lattice.

## DESIGN GOALS

We have undertaken a research program to produce atomic fountain clocks to support the timekeeping mission of the U. S. Naval Observatory. The most important feature of a fountain clock for the observatory is that it have excellent long term frequency stability. Also important is a short term frequency stability that will allow realization of the long term stability floor in a short (less than one week) time scale. Of only minor importance is the frequency accuracy of the standard, making it possible to consider atoms other than cesium for the fountain.

It is our hope to realize a fountain that has a short term stability of  $10^{-13}$  at one second and a systematic reproducibility of  $5 \times 10^{-16}$ . Initially, we will operate by reporting frequency offsets relative to a hydrogen maser that is part of our local clock ensemble.

## ATOMIC SPECIES

Recent results (2,3) have demonstrated that ultra-cold collisions between different spin states are suppressed in rubidium 87 as compared to other alkalis. This makes rubidium ( $^{87}\text{Rb}$  unless otherwise noted) a potentially attractive candidate for a stable frequency standard since the collisional frequency shifts will be greatly reduced.

We have made simple simulations of the collisional shift realized in a fountain with both rubidium and cesium at different launch temperatures. In these simulations, we assumed that the collisional shift at a given atomic density was a factor of 15 smaller for rubidium than in cesium (3,4). It appears that it should be possible to realize a reduction of the

fountain's systematic shift from these collisions by a factor of 10 for a rubidium fountain as compared to a cesium fountain with the same short term integration properties. This factor of 10 reduction was calculated in light of the different resonant frequencies, acceptable atomic cloud sizes, and realizable laser cooling temperatures.

Since we are primarily interested in stability of our fountain clock as opposed to accuracy, we will consider both rubidium and cesium atoms in this paper. It is clear that we will pursue the design and possibly the construction of rubidium fountains, but our initial apparatus uses cesium.

## TEMPERATURE COMPENSATION

To realize a stable frequency standard, we must minimize systematic frequency shifts that are driven by external parameters. One such is the temperature sensitivity of the atomic fountain "physics package". It appears that we should be able to reduce the overall temperature sensitivity of the fountain by balancing two temperature dependent effects.

The first effect is the Black Body shift. This shift is due to the AC Stark and Zeeman shifts of the atomic clock transition in the presence of Black body radiation characterized by a temperature  $T$ . The size of the Black Body shift is given by

$$\Delta y_{BB} = -A \left( \frac{T}{300} \right)^4$$

$$A_{Cs} = -1.69 \times 10^{-14} \quad (1)$$

$$A_{Rb} = -1.25 \times 10^{-14}$$

where the temperature is in Kelvin. The Black Body shift has been measured in a cesium beam standard (5) and is being measured in a cesium fountain standard (6). The DC polarizability of cesium, which is a key parameter in calculating this shift has also been measured with a cesium fountain (7).

The second temperature dependent shift, cavity line pulling, comes from the temperature tuning of the microwave cavity. If we assume that the microwave cavity is tuned so that the  $\text{TE}_{011}$  mode is resonant

with a clock transition at a frequency  $f_0$ , the shift of the cavity frequency is given by

$$\frac{d}{dT} f_{cavity} = -1.62 \times 10^{-5} f_0 \text{ Hz/}^\circ\text{C}. \quad (2)$$

This temperature tuning of the cavity creates a temperature dependent line pulling. The line pulling of the clock is (8)

$$\Delta y_{linepulling} = \frac{f_0 - f_{cavity}}{f_0} \left( \frac{Q_{cavity}}{Q_{atoms}} \right)^2. \quad (3)$$

If the atoms spend a time  $\tau$  above the microwave cavity the Q of the atomic transition is given by

$$Q_{atoms} = \frac{f_0 \tau}{2} \quad (4)$$

Using this expression for the atomic line Q and assuming that the cavity is tuned onto the atomic resonance at a temperature  $T_0$ , the line pulling reduces to

$$\Delta y_{linepulling} = 1.62 \times 10^{-5} \left( \frac{2Q_{cavity}}{f_0 \tau} \right)^2 (T - T_0). \quad (5)$$

Since the Black body and line pulling shifts have different temperature dependencies, their sum can be made insensitive to temperature (to first order) at a temperature given by

$$T = 300 \left[ \frac{Q_{cavity}^2 4.86 \times 10^{-3}}{A f_0^2 \tau^2} \right]^{1/3}. \quad (6)$$

In practice, the temperature at which the sum of these effects are insensitive to temperature would be chosen to be  $T_0$ . It remains to be seen if these temperatures allow practical construction of a device. If the temperature calculated above is too high, one can load the cavity to reduce the Q and have a comfortable operating temperature. However, this will result in a higher distributed cavity phase shift (9). The compensation temperature can also be raised by decreasing the time that the atoms spend above the microwave cavity, but this has the undesirable effect of degrading the short term stability of the fountain.

A key assumption in this analysis has been that the temperature of the cavity and the drift region are the same. In addition, it has been assumed that the AC Stark and Zeeman shifts from Black Body radiation can be characterized by this single temperature.

The theoretical maximum Q of an evacuated TE<sub>011</sub> cavity is given by

$$Q = \frac{D}{\delta} \frac{1 + \left( \frac{x'_{01}}{\pi} \right)^2 \left( \frac{D}{R} \right)^2}{1 + \left[ \frac{(x'_{01})^4 J_0^2(x'_{01})}{4\pi^2 * 1.191} \right] \left( \frac{D}{R} \right)^3} \quad (7)$$

where  $D$  is the height and  $R$  is the radius of the cavity,  $x'_{01}$  is the first root of the derivative of the zeroth Bessel function, and  $\delta$  is the skin depth of the cavity material. The Q for copper cavities resonant with both the cesium and rubidium clock frequencies are plotted in Figure 1 as a function of  $R$ .

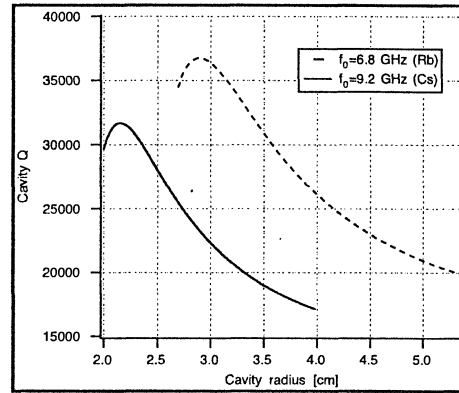


Figure 1: Maximum cavity Q for the TE<sub>011</sub> mode of a copper cavity. The cavity aspect ratio is fixed for each value of the cavity radius to keep the mode resonant with either the cesium or rubidium clock frequency.

The compensation temperature for the maximum possible Q is shown in Figure 2, where the time above the cavity is assumed to be 1/2 second. The Q used in these calculations is higher than will be realized in an actual cavity due to construction imperfections, the holes in the endcaps to allow access by the atoms, and loading from the coupling to the cavity.

If we restrict ourselves to operation of the fountain at or above 30<sup>0</sup> C, there is only a small range of cavity radii that can work for cesium. A wider range of cavity geometries will work for rubidium.

In summary, we have found a range of construction parameters that allow the cancellation of the temperature coefficients of the Black Body shift and the cavity line pulling in an atomic fountain. While the compensation is possible with both cesium and rubidium fountains, the sets of parameters that provide the cancellation appear more useful with a rubidium fountain.

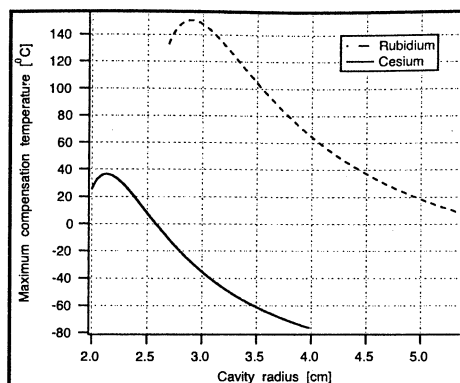


Figure 2: Upper bound on the temperature at which a fountain cancels the temperature coefficients of cavity line pulling and black body shift. The atoms are assumed to spend 1/2 second above the microwave cavity. The compensation temperature can be lowered by loading down the Q of the cavity from the value in Figure 1.

## LAUNCHING ATOMS FROM A 4-BEAM OPTICAL LATTICE

One common way of launching atoms uses two laser beams with different frequencies that are directed towards each other and aligned along the launch direction. Atoms in this optical field will accelerate and laser-cool into a moving frame where the two (Doppler shifted) laser frequencies appear to be the same to the atoms.

We have been pursuing a slightly different technique for launching our atomic sample. We are hoping to use a launching scheme built from a 4 beam optical lattice (10). The geometry of the laser beams used in the launch is shown in Figure 3. In this arrangement, there are two beams going downward with the same angle (45 degrees) from vertical and two beams going upward with the same angle from vertical. Each of the laser beams is linearly polarized such that the polarization vector lies in the equatorial plane of Figure 3. This arrangement of beams produces a three dimensional lattice of optical potential wells with either right or left circular polarization of the resulting optical field at the potential minima. One useful feature of a 4-beam lattice is that a phase shift in any beam will cause a translation of the lattice, but no distortion of the spatial potential or polarization structure seen by the atoms.

A launch can be realized by having the upward going laser beams at a higher frequency than the downward going laser beams. This creates an optical lattice that is moving upwards with a velocity that is given by  $v_{launch}[\text{meters/second}] = 0.60 \Delta\nu [\text{MHz}]$ , where  $\Delta\nu$  is the difference in the laser beam frequencies. The atoms are cooled in three dimensions into the upward moving reference frame.

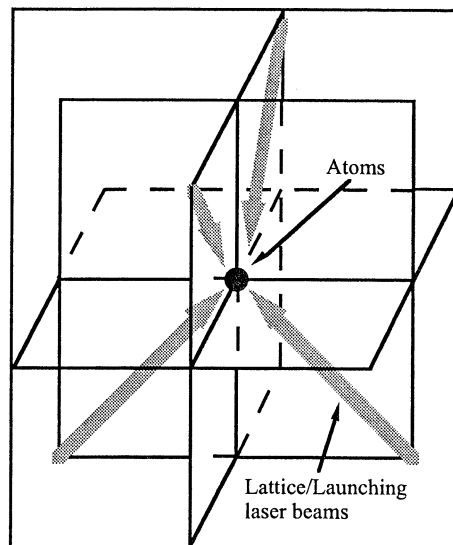


Figure 3: 4-beam optical lattice diagram. This geometry of laser beams forms an optical lattice. The atoms in the lattice can be launched as well as cooled by tuning the two upward going laser beams to a higher frequency than the downward going laser beams.

There are several potential advantages to launching atoms from a 4-beam optical lattice. The first is that there is no vertical laser beam. This is an advantage because it makes the construction of the magnetically shielded free precession region of the fountain much simpler. The ability to have the top of the magnetic shields closed and the lack of an upper optical window should allow for easier construction of a homogeneous magnetic field in this free flight zone.

A second potential advantage is that it requires only two laser frequencies, simplifying the experimental realization. In addition, because the four beam optical lattice potentials and polarizations are stable under a phase disturbance of any laser beam, it should be easier to realize adiabatic cooling (11) in the moving frame as the last phase of the atomic launch.

It should be noted that some of these advantages are also realized in a six beam launching scheme (12). The primary advantages of a 4-beam lattice launch should be in ease of realization and engineering.

We have set up a preliminary version of a launch from a four beam optical lattice. The atoms are collected in a magneto-optical trap and then cooled in a six beam  $\sigma^+ - \sigma^-$  molasses. The lattice beams are then turned on with different frequencies for the upward and downward going lattice beams.

Using this system, we have been able to accelerate the atoms from rest to launch velocities of up to 7.2 meters/second in 1.5 milliseconds. This

acceleration was achieved with the average frequency of the lattice beams at 8 MHz to the red of the atomic resonance and with an intensity of 0.6 mW/cm<sup>2</sup> in each lattice beam. By having the upward going laser beams close to resonance (roughly one half to one linewidth), the initial imbalance in the scattering rate between upward and downward going beams, and therefore the initial vertical acceleration, is maximized. It should be noted that after this initial, violent launch, the atoms are hot and will require a second stage of laser cooling in the moving frame to be useful in a fountain.

A light sheet was positioned a short distance above the launch location to monitor the initial launch conditions. We saw no change in the number of launched atoms for launch velocities from 2.4 meters/second to 7.2 meters/second. These initial velocities would correspond to launch heights of 0.29 to 2.6 meters.

We have also cooled the atoms to temperatures of less than 4  $\mu$ K in an optical lattice with no launch. These temperatures should be achievable in the moving frame as well. With the addition of a final adiabatic expansion phase (11) the temperature should be even further reduced. We are in the process of assembling more flexible frequency synthesis hardware that will allow these different launching and cooling phases.

In the near future, we plan on extending this four beam lattice launch in several ways. The first will be to have a separate initial launch phase and subsequent cooling phases in the moving frame. The last cooling phase will be an adiabatic expansion of the lattice wells by ramping down the intensity of the laser beams. In addition, all of the beams will be optical fiber coupled to the chamber, improving the spatial quality of the lattice.

## CONCLUSION

In conclusion we have outlined our goals for building an atomic fountain at the U. S. Naval Observatory. We have presented an idea for reducing the overall temperature dependence of the fountain, and given a short description of our work on a four beam optical lattice launch.

We would like to thank the Office of Naval Research and the Naval Observatory for their generous support.

## REFERENCES

1. A. Clairon, S. Ghezali, G. Santarelli, Ph. Laurent, S. N. Lea, M. Bahoura, E. Simon, S. Weyers, and K. Szymaniec, 1995, "Preliminary Accuracy Evaluation of a Cesium Fountain Frequency Standard" Proceedings of the Fifth Symposium on Frequency Standards and Metrology p. 49-59 (Woods Hole, MA) ; A. Clairon, P. Laurent, G. Santarelli, S. Ghezali, S. N. Lea, and M. Bahoura, 1995, "A Cesium Fountain Frequency Standard: Preliminary Results", IEEE Trans. Instrum. Meas. 44, pp.128-131
2. C. J. Myatt, E. A. Burt, R. W. Ghrist, E. A. Cornell, and C. E. Weiman, 1997, "Production of Two Overlapping Bose-Einstein Condensates by Sympathetic Cooling", Phys. Rev. Lett. 78, pp. 586-589
3. S. J. J. M. F. Kokkelmans, B. J. Verhaar, K. Gibble, and D. J. Heinzen, 1997, "Prediction for Laser-Cooled Rb Clocks", Phys. Rev. A 56, pp. R4389-R4392
4. Kurt Gibble and Steven Chu, 1993, "Laser-Cooled Cs Frequency Standard and a Measurement of the Frequency Shift due to Ultracold Collisions", Phys. Rev. Lett. 70, 1771-1774
5. Andreas Bauch and Roland Schroder, 1997, "Experimental Verification of the Shift of the Cesium Hyperfine Transition Frequency due to Blackbody Radiation" Phys. Rev. Lett. 78, pp.622-625
6. The group of A. Clairon at LPTF is working on a measurement of the Black Body shift in a cesium fountain. Personal communication with S. Ghezali.
7. E. Simon, P. Laurent, and A. Clairon, 1998, "Measurement of the Stark shift of the Cs hyperfine splitting in an atomic fountain", Phys. Rev. A 57, pp. 436-439
8. Jacques Vanier and Claude Audoin, 1989, "The Quantum Physics of Atomic Frequency Standards", Pub: Adam Hilger
9. G. Vecchi, and A. De Marchi, 1993, IEEE Trans. Instrum. Meas. 42, pp.434-438
10. G. Grynberg, B. Lounis, P. Verkerk, J.-Y. Courtois, and C. Salomon, "Quantized Motion of Cold Cesium Atoms in Two- and Three-Dimensional Optical Potentials", Phys. Rev. Lett. 70, pp.2249-2252
11. A. Kastberg, W. D. Phillips, S. L. Rolston, R. J. C. Spreeuw, and P. S. Jessen, 1995, "Adiabatic Cooling of Cesium to 700 nK in an Optical Lattice", Phys. Rev. Lett. 74, pp.1542-1545
12. Kurt Gibble, Seongsik Chang, Ronald Legere, 1995, "Direct Observation of s-wave Atomic Collisions", Phys. Rev. Lett 75, pp. 2666-2669

**GPS DISCIPLINED OSCILLATORS AS  
'INTERNATIONALLY' TRACEABLE TIME  
AND FREQUENCY REFERENCE**

Clive Green

Quartzlock UK LTD

**Abstract**

The calibration of time and frequency laboratory standards to nationally traceable references is expensive, cumbersome and often not possible except through intermediary accredited 'middle man' commercial laboratories.

It is rarely, if ever, possible to find a commercial standards laboratory that is both accessible, affordable and accredited to a level of uncertainty able to confirm the best GPS disciplined oscillators.

GPS disciplined oscillators that employ carrier phase tracking techniques are able to provide high stability, drift jitter and wander free frequency and time references with little measurable offset.

Throughout Europe, the USA and Pacific Rim whilst the GPS system provides a reliable if not totally robust directly traceable source that may be employed to E-13 level over appropriate measurement times the confirmation of this performance can only be achieved with Hydrogen Maser standards and high resolution frequency and phase comparators.

**Introduction**

The Result of GPS disciplined oscillator stability tests at two separate locations using near identical receivers and Hydrogen Maser references gave results as tabulated

The down converters employed at antenna locations had 80dB gain 90MHz...10.23 MHz...At this stage group delay distortion/group delay were only estimated as some 50 down converter were involved in associated tests at this time. Antenna cable lengths from 25m to 250,m were employed to demonstrate effectiveness of co-siting antenna and down converter.

The down converter design includes later SMT devices to reduce noise, consumption and increase gain without incurring instability problems. A repeatable 80dB gain and constant noise figure to within 1dB gives confidence in receiver performance in different locations.

**TIME AND FREQUENCY REFERENCE**

	CH1-76
GPS DISCIPLINED REFERENCE STEERED RUBIDIUM	A8
MEASUREMENT SET-UP	A7
FREQUENCY CONVERTER	A6
DISTRIBUTION AMPLIFIER	A5

**Peripheral equipment included**

- GT200 Time Interval counter
- Mathcad Analysis Software
- FSS 100 Phase noise detector

**Results to date**

Locations	A lat 50°25.824 long 3° 41.650
	B NPL -UK
	C KVARZ - 5U
	D BRAUNSCHWEIG.D

The British National Standards Laboratory has evaluated 15 GPSDO's (Disciplined Oscillators) and Quartzlock 8A+ and 8A-Rb clearly lead the world in this field. It must be noted that Quartzlock 8A and 8A-Rb whilst providing the best available performance, are themselves not the top Quartzlock GPSDO. The Quartzlock temperature controlled A8(O<sup>2</sup>CXO) and A8-Rb have Caesium Atomic Standard levels of performance and above. Quartzlock employ Hydrogen Masers to assess GPSDO characteristics - the best commercial Caesium, simply do not have the stability equal to Quartzlock GPSDO. A Passive Hydrogen Maser (10x more stable than the best option Caesium) meets the required level of stability - above these latest GPSDO (A8 and A8-Rb) - in order to establish credible results with required integrity margins i.e. parts in 10<sup>-14</sup> stability over 10s.

Fig 1

FREQUENCY MEASUREMENT USING PHASE DIFFERENCE METHOD  
CALCULATION OF UNCERTAINTIES

1/- REFERENCE SOURCE UNCERTAINTIES

Number of days since calibration of reference source (passive maser) days<sub>1</sub> = 27  
 Maximum drift rate of reference source drift = 1.10<sup>-13</sup>  
 Calibration temperature of reference source: T<sub>c</sub> = 68  
 Laboratory temperature at time of measurement: T<sub>m</sub> = 75  
 Reference source temperature coefficient: T<sub>coeff</sub> = 1.9.10<sup>-14</sup>  
 Uncertainty of reference source calibration: σ<sub>refcal</sub> = 1.10<sup>-14</sup>

$$\sigma_{\text{drift}} = \frac{\text{days}_1 \text{ drift}}{\sqrt{3}}$$

$$\sigma_{\text{temperature}} = \frac{(|T_m - T_c|) T_{\text{coeff}}}{\sqrt{3}}$$

$$\sigma_{\text{reference}} = \sqrt{\sigma_{\text{drift}}^2 + \sigma_{\text{temperature}}^2 + \sigma_{\text{refcal}}^2}$$

σ<sub>reference</sub> = 7.89895.10<sup>-14</sup>

2/- FREQUENCY COMPARATOR UNCERTAINTIES

Typical slope of comparator zero drift A<sup>2</sup><sub>drift</sub> = 5.10<sup>-13</sup>  
 Maximum temperature change of laboratory during measurement period: T<sub>var</sub> = 0.2 degrees C  
 Temperature coefficient of comparator: T<sub>comcoef</sub> = 5.10<sup>-12</sup> seconds/degree C  
 Measurement period: t<sub>meas</sub> = 100 seconds

$$\sigma_{\text{comparator}} = \sqrt{\left(\frac{A^2_{\text{drift}}}{\sqrt{3}}\right)^2 + \left(\frac{T_{\text{comcoef}} T_{\text{var}}}{\sqrt{3} t_{\text{meas}}}\right)^2}$$

σ<sub>comparator</sub> = 6.43497.10<sup>-13</sup>

3/- MEASUREMENT UNCERTAINTIES

Read in data file  
 #in = READPRN(datain) ; 0 las(#in) T<sub>s</sub> = 1 ; 2, T<sub>s</sub> ; N = length(#in)  
 Correct data for multiplication factor of comparator  
 $\phi_n = \frac{\phi_n - \phi_{n1}}{10000}$  ; N = 1.10<sup>7</sup>

The next section performs the least squares fit on the data

Vs = regress(z, #, 1)  
 calculated coefficients a = Vs<sub>3</sub> b = Vs<sub>4</sub> a = 7.27308.10<sup>-11</sup> b = -3.37114.10<sup>-11</sup>

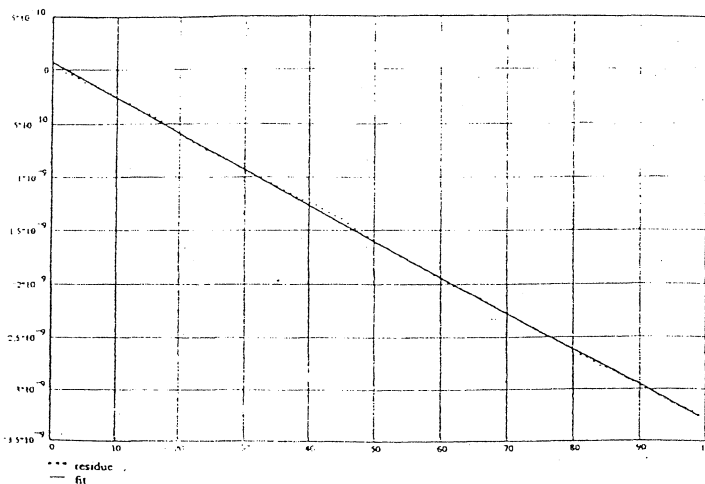
Fig 2

Sum of squared errors: SSE = [2((# - a - b z))<sup>2</sup>] ; SSE = 2.84606.10<sup>10</sup>

standard error of residuals: σ<sub>e</sub> =  $\sqrt{\frac{\text{SSE}}{N - 2}}$  ; σ<sub>e</sub> = 1.70116.10<sup>-11</sup>

Standard error of slope(frequency offset): σ<sub>slope</sub> =  $\frac{\sigma_e}{T_s \sqrt{N(N^2 - 1)}}$  ; σ<sub>slope</sub> = 5.89327.10<sup>-14</sup>

Total quoted uncertainty for measurement: σ<sub>total</sub> =  $\sqrt{\sigma_{\text{slope}}^2 + \sigma_{\text{comparator}}^2 + \sigma_{\text{reference}}^2}$  ; σ<sub>total</sub> = 9.87627.10<sup>-14</sup>



Phase Data

8A-Rb f<sub>0</sub> Offset Mean f<sub>0</sub>Free run

σ τ = 1s 8 x 10<sup>-12</sup> 1.2 x 10<sup>-11</sup> 1.2x 10<sup>-11</sup>

<sup>13</sup>1,000s 4 x 10<sup>-13</sup> 5 x 10<sup>-13</sup> 6 x 10<sup>-13</sup>

100,000s 2 x 10<sup>-13</sup> 1.6 x 10<sup>-13</sup> 6 x 10<sup>-14</sup>

Position Offsets

E + 0.9m 0.016 (sec of arc)

N - 0.7m 0.022 (sec of arc)

Alt 2.4m

Frequency Data

Time Transfer Stability 1pps data

ζ ψ 5 x 10<sup>-13</sup> 1 x 10<sup>-12</sup>

MOD 3.5x10<sup>-13</sup> 5.7x10<sup>-13</sup>

ζ x 2.1x10<sup>-10</sup> 3.6x10<sup>-10</sup>

f<sub>0</sub> 6.3x10<sup>-13</sup> 1.3x10<sup>-12</sup>

Standard Deviation 24Hrs 2.6ns

CH1-75 Passive Hydrogen Maser stability

10s 3 x 10<sup>-13</sup>

100s 9.2 x 10<sup>-14</sup>

1000s 4 x 10<sup>-14</sup>

1 Hour 2.8 x 10<sup>-14</sup>

100,000 9.5 x 10<sup>-15</sup>

1 Day 9 x 10<sup>-16</sup>

(4 weeks of ageing data at 1.9 x 10<sup>-14</sup>)

The NPL GPS Disciplined Oscillator (GSDO) report is available on request from Miss P Hack National Physical Laboratory, Queens Rd, Teddington, Middlesex.

You can fax her on Int +44 181 943 7138. The copy must be requested in person, but will be sent for no charge

**Fig 3**  
Time and Allen Variances from a set of real time difference measurements acquired using the Quartzlock model A7 frequency/phase comparator and the gt200 counter card

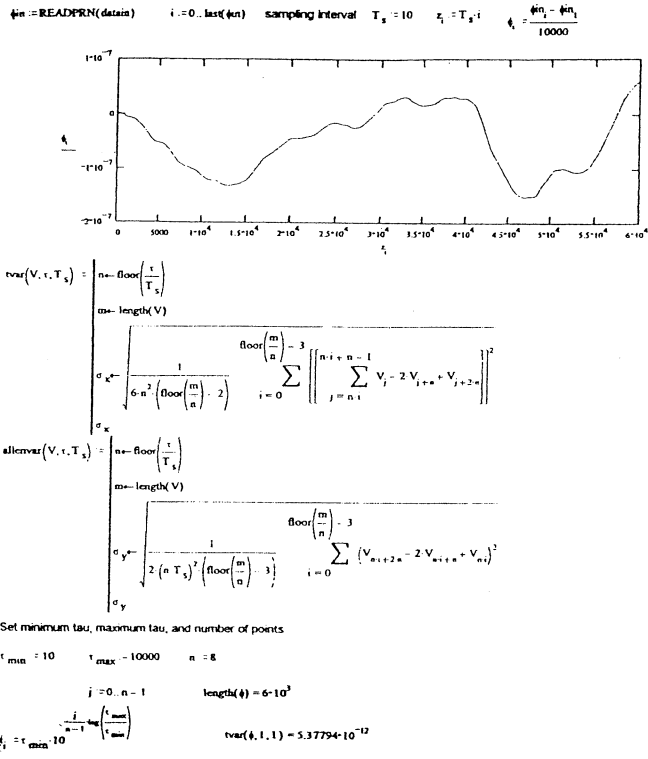
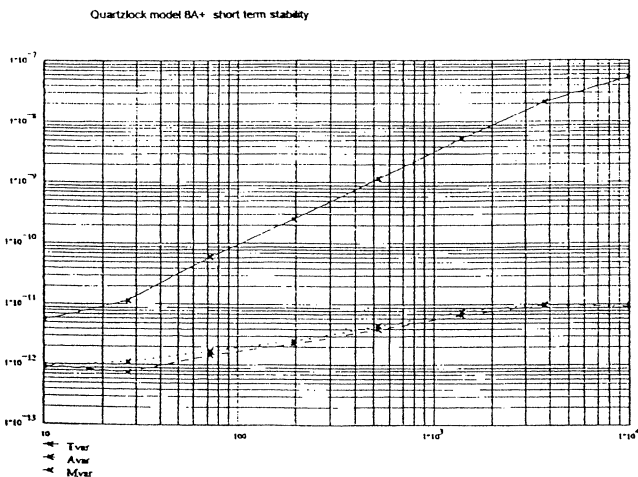


Fig 4



**Fig 5**  
first difference Variances from a set of real time difference measurements acquired using the Quartzlock model A7 frequency/phase comparator and the gt200 counter card

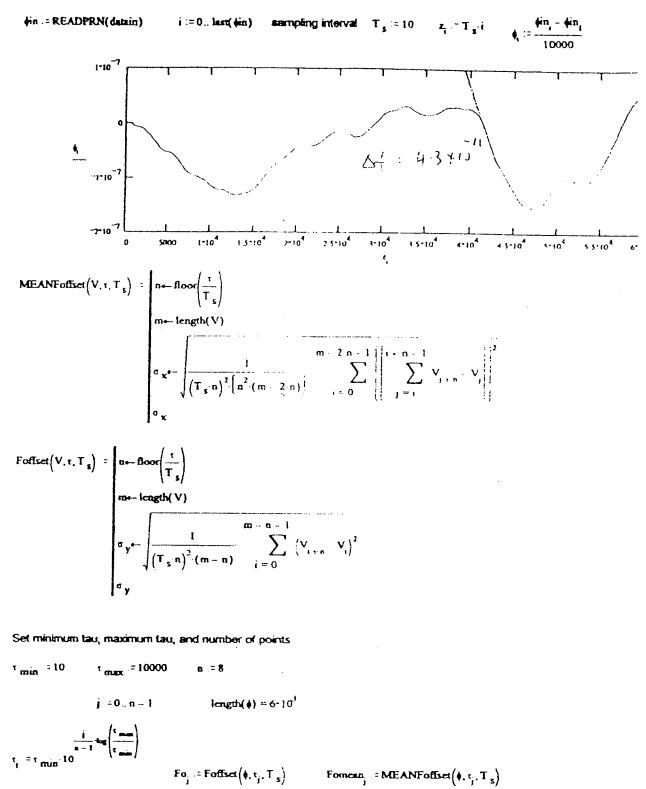
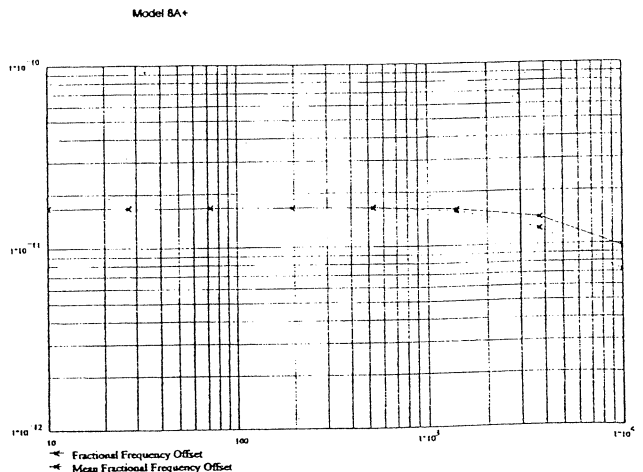


Fig 6

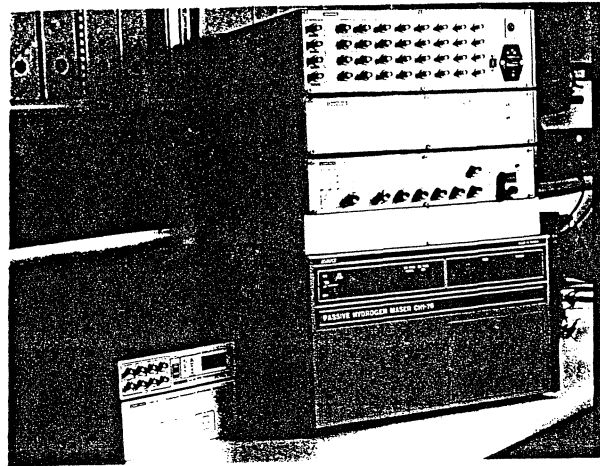


**Results of tests using 4 Active Hydrogen Masers in Nizhny Novgorod (CH1-75) Russia, with Quartzlock 8A-Rb GPS disciplined rubidium**

**Frequency Offset**

1 hour average from switch on to:

18 hours	+2.10 <sup>-13</sup>	+1 hours	-7.10 <sup>-14</sup>
19	-2.10 <sup>-13</sup>	2	-2.10 <sup>-13</sup>
20	+2.10 <sup>-14</sup>	3	-6.10 <sup>-14</sup>
21	-2.10 <sup>-13</sup>	4	-1.10 <sup>-13</sup>
22	-5.10 <sup>-14</sup>	5	-5.10 <sup>-14</sup>
23		6	+1.10 <sup>-13</sup>
24	+6.10 <sup>-15</sup>	7	+7.10 <sup>-14</sup>
		8	+2.10 <sup>-13</sup>



CH 75

**Ch1-75 Passive Hydrogen Maser stability**

$\Delta f$  10 hours average  $9 \times 10^{-14}$

=  $7 \times 10$  Allan variance  $n = 10$

Short term stability (2T)

1s	$1.4 \times 10^{-11}$
10s	$3.9 \times 10^{-12}$
100s	$1.15 \times 10^{-13}$

10s	$3 \times 10^{-13}$
100s	$9.2 \times 10^{-14}$
1000s	$4 \times 10^{-14}$
1 Hour	$2.8 \times 10^{-14}$
100,000	$9.5 \times 10^{-15}$
1 Day	$9 \times 10^{-16}$

5 day average frequency offset  
 $5 \times 10^{-14}$

(4 weeks of ageing data at  $1.9 \times 10^{-14}$ )

**Additional Technical Data**

		Min	Typ	Max	units
<b>Output level:</b> (into 50Ω load)	Square;	2.25	2.5	2.75	V (pk)
	Sine;	+12.5	+13	+13.5	dBm
	sine accuracy		±0.25	±1	dB
<b>Output purity (Square);</b>	risetime	5	10	20	ns
	overshoot	-	2	10	%
(Sine);	THD		-70	-50	dBc
	noise		-70	-60	dBc

**Output Frequency Stability**

	Model interval	8	8A	8A+	8ARb	8ARb+
$5f/f$ (estimated RMS)	100ms	$1.0 \times 10^{-10}$	$1.0 \times 10^{-11}$	$2 \times 10^{-11}$	$1 \times 10^{-11}$	$3 \times 10^{-11}$
$5f/f$ (RMS)	1s	$2.8 \times 10^{-10}$	$5 \times 10^{-11}$	$2 \times 10^{-11}$	$1 \times 10^{-11}$	$5 \times 10^{-12}$
	10s	$2.8 \times 10^{-10}$	$6 \times 10^{-11}$	$3 \times 10^{-12}$	$< 7 \times 10^{-12}$	$< 2 \times 10^{-12}$
	100s	$1.5 \times 10^{-10}$	$7 \times 10^{-11}$	$2 \times 10^{-12}$	$< 1 \times 10^{-12}$	$8 \times 10^{-13}$
	1000s	$5 \times 10^{-12}$	( $4 \times 10^{-11}$ )	$8 \times 10^{-12}$	$< 5 \times 10^{-13}$	$3.5 \times 10^{-13}$
	10000s	$5 \times 10^{-12}$	( $1 \times 10^{-11}$ )	$8 \times 10^{-13}$	$< 4 \times 10^{-13}$	$3 \times 10^{-13}$
	1 day	$< 1 \times 10^{-12}$	$1 \times 10^{-12}$	$< 8 \times 10^{-13}$	$< 2 \times 10^{-13}$	$1 \times 10^{-13}$
	1 week	$1 \times 10^{-12}$	$< 1 \times 10^{-12}$	$< 3 \times 10^{-13}$	$< 2 \times 10^{-13}$	$1 \times 10^{-13}$

(figures in parentheses are provisional)  $(5 \times 10^{-14})$   
640 Sd

## BIBLIOGRAPHY

- Allan, David. W. & Marc A. Weiss. "The Variance of Predictability of Hydrogen Masers and of Primary Cesium Standards in Support of a Real Time Prediction of UTC." National Institute of Standards and technology, Boulder, Colorado. as printed in ACTIVE HYDROGEN MASERS (CH1-75) "Seven Scientific Papers that Prove the Performance".
- Archdeacon, Timothy W. (prepared by). "The Use of US Crystal Oscillator Markets, Technologies, and Opportunities: 1991-1996 Analysis." World Information Technologies Inc, Northport, New York, 1991.
- Audoin, Claude & Jaques Vanier. The Quantum Physics of Atomic Frequency Standards. Adam Hilger Press, Bristol and Philadelphia, 1989.
- Azoubib J. & C. Thomas. "Hydrogen Masers in Tai Computation" Bureau International des Poids et Mesures Pavillon de breteuil, 92312 Sevres Cedex, France, as printed in ACTIVE HYDROGEN MASERS (CH1-75) "Seven Scientific Papers that Prove the Performance".
- Bauch, A., N.A. Demidov, E.M. Ezhov, B. Fischer, B.A. Sakharov, & B.A. Uljanov. "Investigations of the Frequency Instability of CH1-75 Hydrogen Masers." "Kvarz" Russia. as printed in ACTIVE HYDROGEN MASERS (CH1-75) "Seven Scientific Papers that Prove the Performance".
- BEMC '97. Conference Digest. Eighth International Conference on Electromagnetic Measurement 4-6 November 1997. National Physical Laboratory & Lyons Instruments, Teddington, Middlesex, 1997.
- Chernov, G.M., N.A. Demidov & V.A. Logachev. "Improvement of a Digital Automatic Cavity Tuning System in the Active Hydrogen Maser CH1-75." Institute of Electrical Measurements "Kvarz", Novgorod, Russia. as printed in ACTIVE HYDROGEN MASERS (CH1-75) "Seven Scientific Papers that Prove the Performance".
- Connect Press, Telecom 95 Press Service. Geneva, 1995.
- Danzy, Frederick, Edward C. Jones & Edward D. Powers. "Test Results of Kvarz CH1-75 Active and CH1-76 Passive Hydrogen Masers." Naval Research Laboratory, Washington DC, USA. as printed in ACTIVE HYDROGEN MASERS (CH1-75) "Seven Scientific Papers that Prove the Performance".
- Davis, J.A. & J.M. Furlong. Report on the Study to Determine the Suitability of GPS Disciplined Oscillators as Time and Frequency Standards Traceable to the UK National Time Scale UTC (NPL). Centre for Time Metrology, National Physical Laboratory, Teddington, Middlesex, October 1997.
- Davis, J.A. & M. Furlong. Report on the Suitability of GPS Disciplined Oscillators as Time and Frequency Standards Traceable to the UK National Time Scale UTC (NPL). Centre for Time Metrology, National Physical Laboratory, Teddington, Middlesex, June 1997.
- Demidov, N.A., V.A. Logachev, A.S. Marakhov, & V.A. Fedorov. "Progress in Development of Active and Passive Hydrogen Frequency Standards at IEM <<KVARZ>>". Institute of Electronic Measurements "Kvarz", 176 Prospect Gagarina, Nizhny Novgorod, Russia. as printed in ACTIVE HYDROGEN MASERS (CH1-75) "Seven Scientific Papers that Prove the Performance".
- EFTF '88. Second European Frequency and Time Forum Proceedings. Organised by the Institute of Electrical Engineers. Neuchatel, Switzerland, 1988.
- EFTF '89. Third European Frequency and Time Forum Proceedings. Organised by the Institute of Electrical Engineers. Neuchatel, Switzerland, 1989.
- EFTF '90. Fourth European Frequency and Time Forum Proceedings. Organised by the Institute of Electrical Engineers. Neuchatel, Switzerland, 1990.
- EFTF '93. Seventh. European Frequency and Time Forum Proceedings. Organised by the Institute of Electrical Engineers. Neuchatel, Switzerland, 1993.
- EFTF '95. Ninth European Frequency and Time Forum Proceedings. Organised by the Institute of Electrical Engineers. Neuchatel, Switzerland, 1995.
- EFTF '96. Third European Frequency and Time Forum Proceedings. Organised by the Institute of Electrical Engineers. Neuchatel, Switzerland, 1996.
- IEEE International Frequency Control Symposium Program 1995. Sponsored by The Institute of Electrical and Electronics

## **HORACE : a new advance for compact clocks with cold atoms**

Emmanuel GUILLOT, Pierre PETIT, Constance VALENTIN, Noël DIMARCO

Laboratoire de l'Horloge Atomique

Unité Propre de Recherche du CNRS associée à l'Université Paris-Sud

Bâtiment 220, Université Paris-Sud

F-91405 ORSAY CEDEX

Tel. 33 1 69 15 78 07

Fax. 33 1 69 15 41 10

E-mail : Emmanuel.Guillot@ief.u-psud.fr

Cold atoms have already demonstrated their great potential to improve both frequency stability and accuracy of existing atomic clocks. Such clocks essentially operate at the present time on the fountain principle. They are obviously intended to be primary frequency standards with high frequency performances.

However, the regular users of atomic clocks are broadly satisfied with the current performances of existing atomic clocks. Their main wish is to operate smaller clocks without any degradation of their performances. Our aim is to use cold atoms not to further improve the performances of frequency standards but to reduce their volume. While the size of the microwave cavity stays unchanged, cold atoms allow to increase the interrogation duration, so to reduce the linewidth of the clock signal, improving in this way the performances of the clock. In other respects, cold atoms allow to decrease the volume of the microwave cavity without altering the performances of the clock.

Unfortunately, the good running of cold atom clocks requires a good control of the optical components and a precise superposition of the laser beams for an efficient cooling. We propose a new concept of clock named **HORACE** for **HO**rloge à **R**efroidissement d'Atomes en **C**ellule. This clock uses a cylindrical microwave cavity in which cesium atoms are cooled with isotropic light. Such a cooling technique have already demonstrated a good efficiency and easiness to operate.

In our configuration, cooling, preparation and microwave interrogation of the atoms, as well as the detection of the clock signal, will be located right at the same place. This means that cooling will be performed inside the microwave cavity. The time sequence of operation could be described as successive cycles divided into four stages : cooling, preparation of atomic state, microwave interrogation and optical detection of the clock signal. Two kinds of microwave interrogation may be chosen : a Rabi-like interrogation, with one single  $\pi$  pulse, or a Ramsey-like interrogation, with two short  $\pi/2$  pulses. For a maximum atomic displacement of one millimeter, linewidths as low as 30 Hz on Earth or a few Hz in microgravity are reachable. Corresponding frequency performances should be in the  $10^{-15}$  level.

One of the main advantages of such a clock configuration is that atoms are not lost during each cycle. As a result the cooling duration could be shortened, then the cycle duration too. Moreover this new configuration will be quite flexible since each stage duration could be easily modified and adapted.

## PROGRESS OF THE PTB CAESIUM FOUNTAIN FREQUENCY STANDARD

U. Hübner, S. Weyers, J. Castellanos\*, D. Griebisch, R. Schröder, C. Tamm, A. Bauch

Physikalisch-Technische Bundesanstalt, Time-Unit Section  
 Bundesallee 100, D-38116 Braunschweig, Germany

### ABSTRACT

An atomic frequency standard based on a fountain of cold caesium atoms is under construction at PTB. Some of its components are described in this contribution. The effect of the 3-fold magnetic shielding of the C-field region was measured. A special design of the microwave interrogation cavity with low Q leads to reduced temperature stability requirements. A single sideband modulation technique is used to launch atoms and time-of-flight signals demonstrate the performance. First tests of a magnetic octupole trap have been performed.

### INTRODUCTION

The accuracy of primary frequency standards with a thermal atomic beam, as the CS2 of the PTB, is limited among others by the cavity phase shift, the second order Doppler effect, and short interrogation times. These limitations can be overcome to a large extent when using ultra-cold atoms and long interrogation times in a Ramsey geometry. Therefore, as other metrological institutions world-wide, the PTB is constructing a caesium fountain frequency standard. With such a fountain an uncertainty of  $2 \cdot 10^{-15}$  has been achieved (Clairon et al. (1), Simon et al. (2)). While building PTB's caesium fountain, manipulation of cold caesium atoms is investigated in a separate experimental setup. In the following, some details of both setups are described.

### THE EXPERIMENTAL SETUP

The experimental setup consists of a standard magneto-optical trap (MOT) with 6 cooling beams (Monroe et al. (3), Grison et al. (4)). The 2 vertical beams are used to launch the atoms. The launch height is limited to 13 cm. The detection zone is 11 cm below the center of the MOT.

Fig. 1 shows the laser diode system for launching and detecting the laser-cooled atom clouds. The setup consists of two extended cavity diode lasers locked to the  $F=4 \rightarrow F'=5$  and the  $F=3 \rightarrow F'=4$  caesium transitions, respectively. The laser locked to the  $F=4 \rightarrow F'=5$  transition is used as a master laser to injection lock a high power laser diode, which provides the six cooling laser beams. The main part of the master laser light is used for detection of the atoms. The other extended cavity diode laser serves as a repumping laser. The laser detunings required for the operation of a MOT and for optical molasses are controlled by acousto-optical modulation schemes similar to those described in (1) and (2).

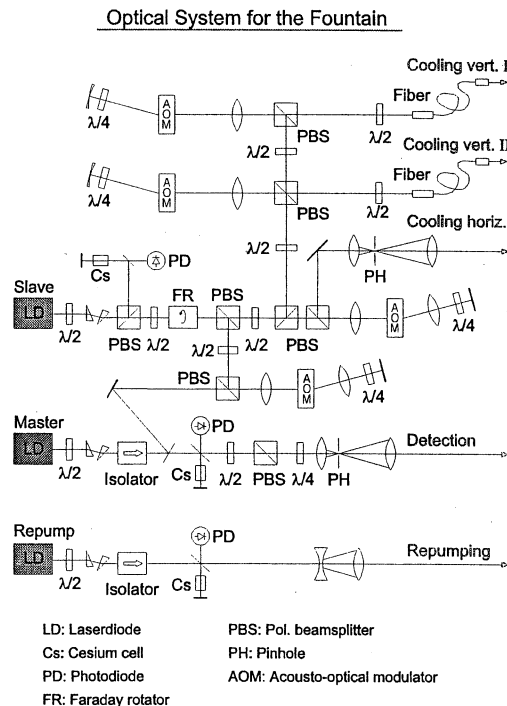


Fig. 1: Laser diode system for cooling, launching, and detecting

Laser cooling of up to  $10^7$  caesium atoms down to 2,5  $\mu$ K could be achieved in a molasses. The

temperature of the atoms was measured by a time-of-flight method. We also tested launching and pushing down of the atoms (Fig. 2) in a moving molasses. Here the frequency shifts of the vertical laser beams required for launching the atoms were obtained by means of a single-sideband modulation technique. 35% of the initially launched atoms were detected 11 cm below the MOT in case of the maximum launch height.

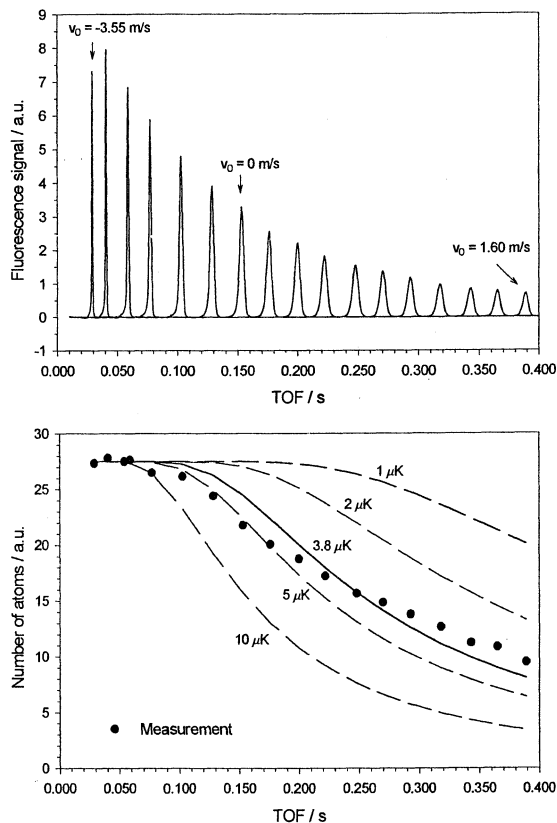


Fig. 2: Time-of-flight measurements of atoms released from the MOT. The Gaussian-like curves in the fluorescence signal plot each show one time-of-flight measurement, the parameter being the launch velocity (positive velocities stand for launching, negative for pushing down). The continuous and the dashed curves in the number-of-atoms plot are theoretical curves for a cloud diameter of 0.7 mm (visually estimated FWHM) with the temperature of the cloud as parameter. The continuous curve is the best fit to the experimental data (points).

Presently, this experimental system is being modified in order to investigate MOT operation in a higher order magnetic multipole field. By using a magnetic octupole field, one expects that the central region of low magnetic field ( $\leq 1 \mu\text{T}$ ) can be extended to several millimeters, while magnetic field gradients suitable for MOT operation exist in the surrounding volume. This approach promises to combine the trapping property of an MOT with an extended region of molasses-type polarization gradient cooling. The

magnetic vector field (one quadrant) is shown in Fig. 3 (left part), together with a cross-section of the setup (right part) containing the cell and 4 coils the setup being cylindrically symmetric around the z-axis. The four horizontal cooling laser beams are indicated. The other two laser beam are vertical to the drawing plane.

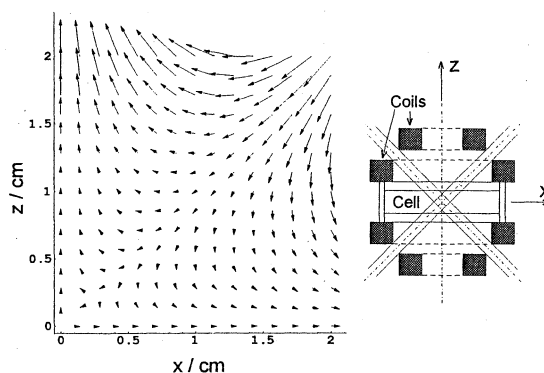


Fig. 3: Field vectors of the octupole (one quadrant). Cell, octupole, and field are cylindrically symmetric around the z-axis. The cell consists of 2 circular quartz glass plates fixed in a cylindrical stainless steel ring shown in the drawing right to the vector field. The four horizontal laser beams are indicated in the drawing.

Fig. 4 shows the very first CCD pictures of trapped caesium clouds together with vertical density plots for the quadrupole and the octupole fields.

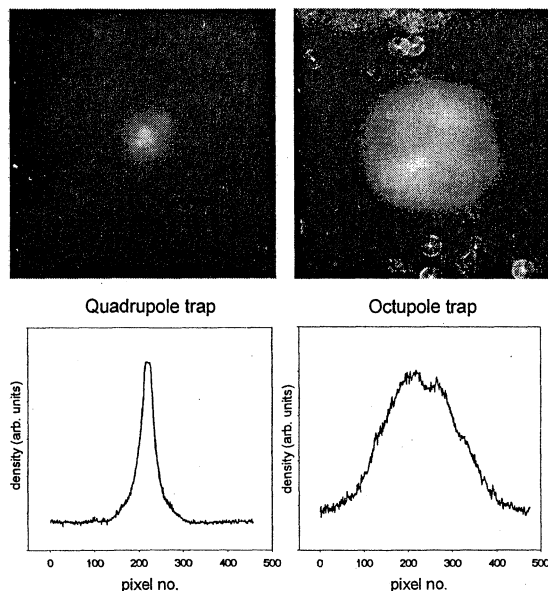


Fig. 4: CCD pictures of two trapped caesium clouds together with density plots taken vertically across the clouds. Each plot point is an average of 10 horizontal pixels. The cloud diameters calculated from the plots are 0,9 mm and 4,4 mm (FWHM).

## THE PLANNED FOUNTAIN

In the planned PTB fountain setup (Fig. 5) caesium atoms will be launched from an MOT or an optical molasses inside a titanium chamber to a height of 90 cm, 50 cm above the microwave interrogation cavity.

As others we use a cylindrical cavity with the field oscillating in the TE<sub>011</sub> mode (Fig. 6). Along the trajectory of the atoms this mode is characterized by a longitudinal magnetic field and small phase variations caused by low losses. In a previous design (1) the TE<sub>011</sub> cavity is weakly coupled, resulting in a high loaded Q. In that case, the high temperature sensitivity of the cavity resonance makes a temperature stabilization unavoidable. In our design, phase variations are minimized by using 2 opposite slits as described in (1) but strong coupling of the TE<sub>011</sub> cavity is realized by 11 mm length of the slits (2 mm width). These slits couple to a surrounding low-Q waveguide section, resulting in a loaded Q value of  $\approx 2000$  of the TE<sub>011</sub> cavity. Due to the small Q value, a temperature stabilization of the cavity appears unnecessary.

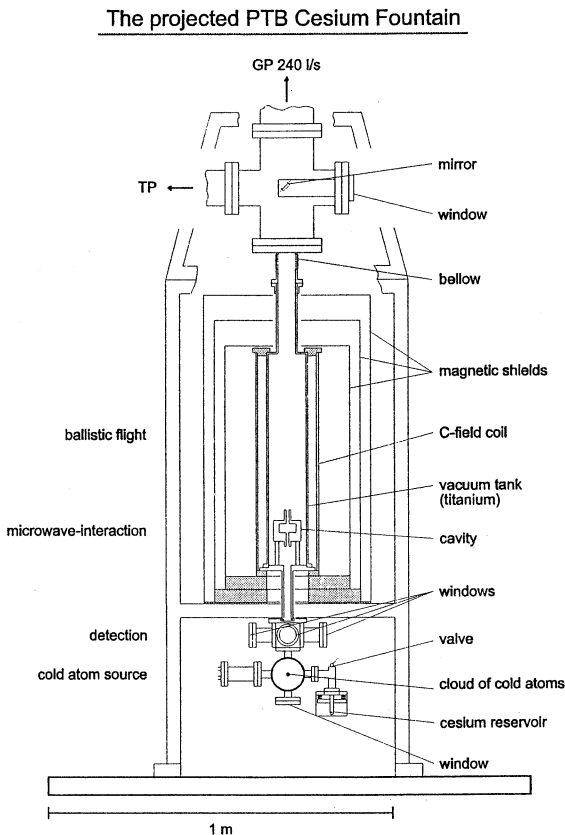


Fig. 5: Scheme of the mechanical construction of the fountain. TP: Turbo molecular pump; GP: Ion getter pump.

The threefold magnetic shielding surrounding the titanium vacuum chamber was tested (Fig. 7). After a standard demagnetization procedure the residual magnetic field along the axis was measured to be less than  $10^{-8}$  Tesla with an inhomogeneity of  $10^{-9}$  Tesla. Our design goal is the operation of the fountain with a C-field strength below  $1 \mu\text{T}$  with a relative inhomogeneity of less than 0,1 %, which seems feasible with the current shielding.

Finally, the mechanical mounting of the fountain will be isolated from the optical table which carries the laser systems for both setups. The optical connection between the fountain vacuum system and the laser systems will be realized by polarization maintaining optical fibers.

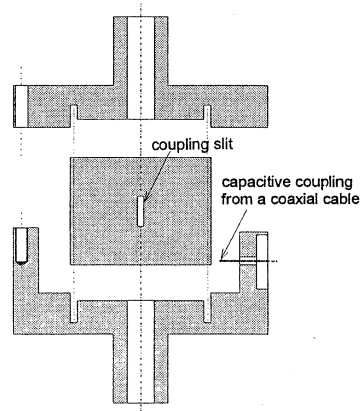


Fig. 6: The three parts of the circular microwave interrogation cavity. The central part (copper tube with two opposite slits) forms the TE<sub>011</sub> cavity. The surrounding waveguide is fed capacitively from a coaxial cable.

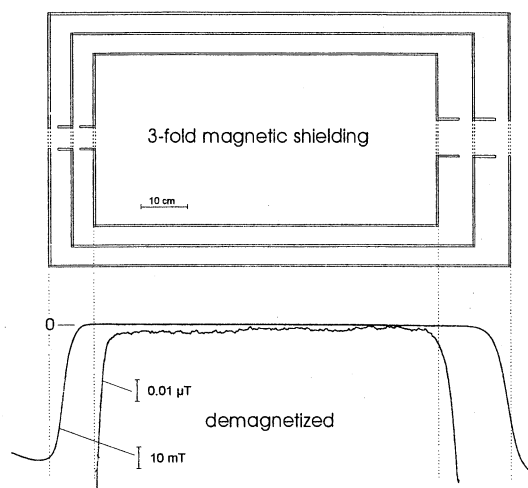


Fig. 7: Measurement of the field in the demagnetized shieldings. The residual field is below  $10^{-8}$  Tesla with an inhomogeneity of  $10^{-9}$  Tesla.

## REFERENCES

1. A. Clairon, S. Ghezali, G. Santarelli, P. Laurent, E. Simon, S. N. Lea, M. Bahoura, S. Weyers, and K. Szymaniec, in: Proceedings of the 10th European Frequency and Time Forum (EFTF), Brighton, 218 (1996)
2. E. Simon, P. Laurent, C. Mandache and A. Clairon, in: Proceedings of the 11th European Frequency and Time Forum (EFTF), Neuchâtel, 43 (1997)
3. C. Monroe, W. Swann, H. Robinson, and C. Wieman, 1990, Phys. Rev. Lett. 65, 1571
4. D. Grison, B. Lounis, C. Salomon, J. Y. Courtois, and G. Grynberg, 1991, Europhys. Lett. 15, 149

---

\* Visiting from Time and Frequency Division CENAM, Queretaro 769, Mexico

## ADVANCES IN MODULAR TIME & FREQUENCY SYSTEM DESIGN INCORPORATING POWERFUL STATUS & ALARM MANAGEMENT & GPS CORRECTED CAESIUM TECHNOLOGY.

David F. Wright, Nigel C. Helsby, Michael R. Sagin, Gary H. Smith.

Radiocode Clocks Ltd., Helston, UK. Brandywine Communications Inc., Costa Mesa, USA.

### ABSTRACT

Radiocode Clocks Ltd have developed an advanced, modular time and frequency generation and distribution strategy suitable for complex turnkey system applications. The significant developments upon existing distribution systems fall into the following four categories:

1. Active, multilayer backplane architecture facilitating "Plug and Play" interchanging of different types of distribution module in any slot without internal reconfiguration.
2. An advanced status and alarm management system providing comprehensive local monitoring together with bi-directional communication for remote control and supervision.
3. Integration of three core signals into a single composite time and frequency code for distribution over either a single copper or optical fibre transmission line for subsequent decoding into any remote time and frequency signal.
4. The development of a universal time and frequency processor designed to monitor and correct internal or external caesium references or lower grade references where applications permit.

This paper discusses these four major developments in detail and outlines how the technology can be integrated into a custom turnkey time and frequency system.

The paper also focuses upon the universal time and frequency processor module and its ability to monitor and correct errors in the outputs of caesium beam atomic clock systems, without access to internal circuits or control points, utilising information from the Global Positioning System (GPS) constellation of satellites. As part of this development, four commercially available caesium beam frequency standards from two different manufacturers were analysed and significant differences in the outputs were observed.

The paper describes the testing carried out on the caesium beam atomic frequency standards, the results of these tests and comments on how these

results justify the need for caesium monitoring and correction. It also outlines the development of the monitoring and correction technology and publishes test results for the resultant instrument.

### BACKPLANE ARCHITECTURE

A Time and Frequency Distribution System (TFDS) based on three 'core' signals distributed on a specially designed bus and backplane system has been described previously by Wright<sup>(1)</sup>. Over the past three years significant developments have been made to this strategy in response to customer specifications and requirements.

Due to the need to isolate the high stability analogue frequency core signal from the digital timecode the previous backplane design required factory configuration of chassis slots for particular types of distribution module. This caused concern with customers requiring a completely future-proof distribution solution or the ability to customise a number of similar systems in differing applications in the field.

The new backplane design incorporates active buffering of each core signal on every module slot allowing the placement of any distribution module in any slot without the need to reconfigure the wiring of the chassis. Each slot on the backplane also provides a discrete signal line to the Status & Alarm Management slot which identifies its position within the chassis. The modules themselves have also been transformed to provide module type identification to the backplane slot.

The original system strategy provided a common collector alarm output from each module to the backplane enabling the system alarm management module merely to identify the position of the faulty module. As increasing applications for turnkey distribution systems became situated in remote, unmanned sites, the requirement arose for full and detailed reporting of the mode and criticality of failure. This necessitated the conversion of the alarm LED drivers on the front panel of the module into addresses on a multiplexed

communications bus routed through the backplane of the system to a substantially upgraded alarm management module.

## STATUS & ALARM MANAGEMENT

The significant improvements made to the backplane design were carried out in tandem with the complete redesign of the original Alarm Management Module (AMM). Initial improvements requested by customers included the fitting of a processor and serial port for remote interrogation of the AMM. However, as the AMM merely reported which slot in the chassis was faulty this was of limited use to a remote user. The improvements in the design of the backplane enabled an increased level of information pertaining to the fault to be communicated to the AMM. In its current state the AMM would be unable to process this information adequately therefore a completely new module was required for this purpose.

The Status and Alarm Monitoring Module (SAM) was developed in order to provide comprehensive Local and Remote Status, Alarm Monitoring and Communication to the TFDS, the front panel allowing rapid verification of overall system status via four simple LED indicators. The design included a 4 key keypad and 2 line by 8 character display which could give access to detailed Status information on all the modules installed in a TFDS chassis. A bi-directional serial interface was included for communication of status and remote control. A further serial interface was fitted to communicate with TFDS modules for such functions as remote Time of Day setting and GPS Disable, all achievable via a single TFDS serial interface to the user. It was of the utmost importance that the module allow the user to identify fault conditions simply and rapidly.

Each slot in the redesigned chassis is equipped with a multiplexer that connects to the module status lines. Each type of single-connector module has up to 12 alarm sources; double connector modules may have a further 12 alarms. The status of the possible alarm sources for each module are configured by default values held in EPROM and transferred to battery-backed RAM when the system is first switched-on. The status of an alarm source can be user defined as: "Not used", "Priority 1", "Priority 2" or "Calibration Required" and in each case can be Latched or non-latched.

During initialisation the SAM searches for every module in the chassis requiring a power-on latched

reset clear operation and automatically clears the latched reset by writing to the latch.

Following initialisation the SAM reads the status of each installed module's 16 lines by repeatedly scanning the multiplexer at every module slot in the chassis. The 16 lines read from a slot are organised as two bytes and are connected as a parallel bus of 8 data lines through the TFDS chassis connecting all the multiplexers to the SAM. The SAM addresses each multiplexer by pulling a unique control line low for each slot; these lines are named MOD1 through MOD40 and are generated by the 40 channel Demultiplexer. Two further control lines connect in parallel to all multiplexers. They are effective only when one particular slot has its MODn line pulled low by the SAM.

Module types are identified by a 4 bit code which allows the SAM to name the alarm condition and categorise it. This code is contained in the top 4 bits of the 16 bit module data read through the multiplexer.

During normal operation the SAM reads the 16 bits at every module slot and saves the information in RAM. Unoccupied slots scanned by the SAM return all zeros. The SAM constructs in RAM three tables of "Primary 1", "Primary 2" and "Calibration Required" status from all slots and a table of "Module ID" and "ID count" for each slot. ID count is a count of the occurrence of a particular module type, counting to the right from the SAM's own position in the chassis. The SAM contains look-up tables of the status and name of each data line for every module type. If a data line for a module type indicates an alarm condition the alarm priority level is determined and that alarm is operated. If the alarm is a latched type then a memory bit is set coinciding with the alarm and its priority level. Any such bits which are set operate the appropriate alarm 'PRIORITY 1', 'PRIORITY 2' or 'CALIBRATION DUE' until they are cleared by the user by operation of the front panel key-switch or by remote command through the serial port. They also cause the named alarm to appear in the alarm list, even if the alarm condition has disappeared, until the user action has taken place.

When any change in alarm status occurs it is memorised by the SAM which time-tags the event and outputs a serial message through the user serial port naming the source of the event, its status, and the time at which it occurred. If the event is an alarm which later clears itself then another message is generated to record the change in status; however if the alarm is a latched type then the relevant alarm output remains in the

alarm condition until cleared by the user. The External Inputs and the SAM's own alarms are assigned Module ID numbers to allow the editing and reporting of these alarms in the same format as standard module alarms.

## COMPOSITE CORE SIGNAL

The original TFD8000 concept reduced the vast array of pulses, frequencies and timecode normally routed around a Timing and Frequency system to three core signals (1PPS, 10MHz and a RS422 ASCII serial string) from which any standard Time and Frequency signal could be synthesised or translated. This approach has now been taken a step further to combine the three signals into a composite core signal which can be transmitted over either copper or fibre links to provide synchronisation between remote systems.

The three signals, 1pps, 10MHz and Timecode are sent down a single coax, twisted pair or optical fibre link by using the core 10MHz to generate a reference frequency carrier which is phase-modulated by the timecode and 1pps signals. The carrier phase is reversed at the instant the 1pps commences so that the 1pps timing resolution is not limited by carrier frequency. For simplicity the timecode is in the form of asynchronous serial data which is passed through the same phase modulator.

At the transmit end the reference frequency carrier is fed into one input of an overdriven multiplier; the other input receives the combined 1pps and Timecode. The output is a carrier wave which is phase modulated by the 1pps signal for 20µs, followed by phase modulation corresponding to the timecode logical levels.

At the receiving end the demodulator works by locking a simple 20MHz VCXO to the carrier. For optimal performance, the transmit architecture is mirrored and a similar multiplier type phase-detector is used. To maintain the high phase accuracy desired the phase-detector is followed by an integrator so that any residual phase difference is driven to zero. The loop locks with precisely 90 degrees phase shift between the frequency derived from the local 20MHz VCXO and the incoming reference carrier. To demodulate the carrier, a further multiplication is carried out between the carrier, phase shifted by 90 degrees, and a frequency derived from the VCXO.

The phase-corrected demodulated output is used to control a timer. The function of the synchronised

timer is to control a receiving end demultiplexer. The demultiplexer operates in advance to select the 1pps demodulated data and then closes. When the demultiplexer 1pps channel is closed, the timecode channel is open, so that demodulated data other than the 1pps is routed to the timecode channel.

Tests of the composite core signal have shown that over 100m of standard coax 1pps can be recovered with <5ns peak-to-peak jitter over 256 samples. With an intentional variation of the 1pps phase to the carrier phase through a complete carrier cycle the resultant peak-to-peak variation in recovered 1pps timing is 10ns. Timecode can be sent as asynchronous serial data so long as the transmission period is short compared with the total 1s frame.

Frequency is recovered to better than  $\pm 1 \times 10^{-7}$  over a few milliseconds using just the demodulator's simple crystal phase-locked loop. Using an unmodified precision phase-locked loop the variation in the recovered frequency measured  $< \pm 4 \times 10^{-11}$  over 50 milliseconds.

## GPS CORRECTED CAESIUM

The characteristics of the GPS system and its application to time and frequency as a precision reference source have been extensively described by Hubner<sup>(2)</sup>. The principal error sources have been characterised under four headings as ephemeris errors, ionospheric delay, the accuracy of the clock correction polynomial, and Selective Availability (SA). Selective Availability, an intentional degradation of the system for commercial users, is the largest effect, accounting for planned accuracy of 363ns for timing. SA appears to be a pseudo random modulation of the C/A code phase essential to commercial GPS receivers. In order to attenuate SA substantially it is necessary to use phase-locked loops with a cut-off frequency as low as 50µHz and use averaging for 20,000 seconds or more. Clearly in the short term a disciplined oscillator must run virtually open loop and to date the best disciplined frequency standards have used Rubidium oscillators as their local references. The primary error source of the disciplined Rubidium in the short term is the effect of temperature upon the Rubidium frequency and the random frequency fluctuations which can occur in the order of parts in  $10^{12}$  in some of the commercial units which we have encountered. These errors can be attenuated over periods of hours by closed loop control using 1pps obtained from a board level OEM GPS receiver as long as satellites are available.

In some critical telecommunication and military projects the disciplined oscillator may be required to continue to deliver the same accuracy levels even in the absence of satellite reception for prolonged periods. The best available time and frequency accuracy is essential for synchronisation of communications, synchronisation of last resort and other projects. For these applications only a corrected Caesium has the long term open loop performance necessary.

We decided to make a general purpose corrected Caesium based on our TOC80 instrument already successfully applied to Rubidium control. This precision time and frequency source uses either a commercial GPS receiver module as its reference or the standard timecodes and 1pps delivered by ICD-GPS-060 compatible units.

The TOC80 has a standard 16 key keypad and large digit 2 line by 24 character display. The TOC80CM has had some new elements added specifically to allow the control of Caesium frequency standards, or indeed to control any other highly stable frequency source. To permit a wide range of standard Caesiums to be connected without modification the input buffering allows for two types of external frequency sources, at 5MHz or 10MHz, and provision is made for a chosen Caesium to be built into the instrument and form a compact corrected oscillator. For the latter unit, a comprehensive monitoring and control interface is provided on the TOC80 to allow the user access to such parameters as Caesium beam current, ion current and quartz oven power, all of which set an alarm if limits are exceeded.

The signal processing path from the Caesium output to the Core 10MHz output has been kept as simple as possible. In the case of the 5MHz Caesium no digital processing (other than in the controller electronics) is required from the Caesium 5MHz frequency input through to the Core 10MHz corrected output frequency. The simplicity of the signal path means that the basic, uncorrected Caesium performance remains unaffected by the controller. The core of the system is a processor controlled engine which can adjust the phase of a signal in extremely small steps. During our development work we found 1 picosecond to be the optimum step size. Because these minuscule steps can be applied at any rate (i.e. once per day) it is therefore possible to correct the smallest of frequency offsets. The step size of 1ps is smaller than the short term stability of most commercially available caesiums although this could be reduced further for reference frequency sources with higher short term stability characteristics such as Hydrogen Masers. The high

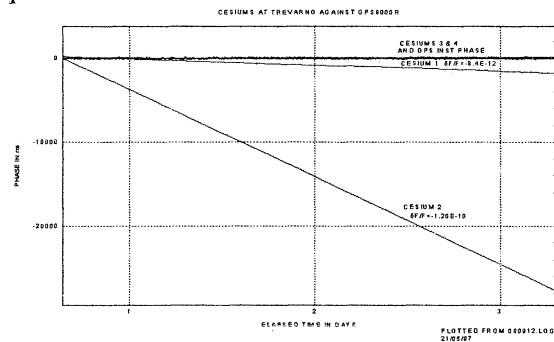
resolution phase stepper allows the controller to maintain high resolution in frequency control even when there is a large frequency offset to be removed.

Standard TOC80 electronics are employed to derive 1Hz from the corrected 5MHz and independently phase control it to track the 1pps GPS reference and maintain time from the Caesium to within 50ns of GPS time.

At the start of the development programme we measured four commercially available Caesium beam frequency standards against a GPS8000R disciplined rubidium oscillator as an independent reference. Immediately prior to these measurements this reference had been extensively tested and characterised by NPL as part of a GPS Disciplined Oscillator study, the subject of another paper being presented at this conference.

The initial analysis immediately identified significant differences in the performance of the four frequency standards. Units 3 and 4 (from the same manufacturer) exhibited almost identical short and medium term performance to the reference while unit 1 had a frequency offset of  $8.4 \times 10^{-12}$  and unit 2 had a huge offset of  $1.2 \times 10^{-10}$ .

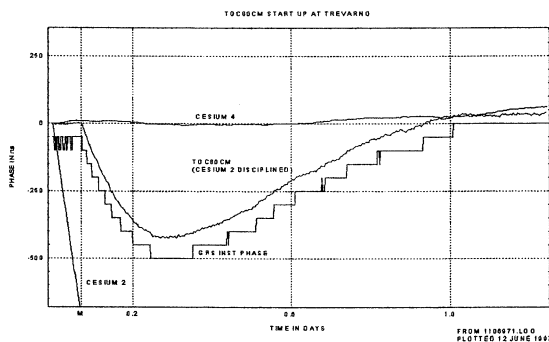
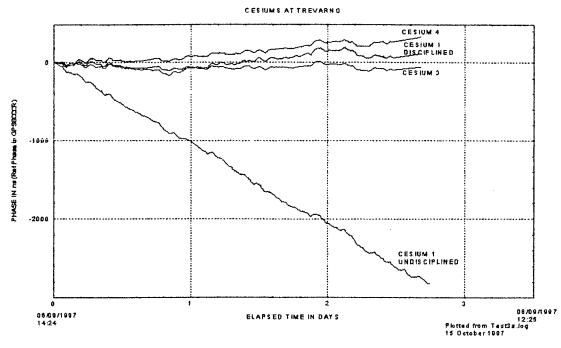
Upon closer inspection of the results units 1 and 2 also indicated significantly increased noise on the outputs compared to the reference and the other two units. Both of these latter instruments were examined in detail and it was confirmed by front panel operation, and a study of the built in test equipment, that they were operating normally to all intents and purposes. Unit 2 was examined more thoroughly and internal waveforms were examined and calibrated but no significant improvement in performance was observed.



For some years now commercially available Caesium beam atomic frequency references and clocks have been employed and trusted in critical applications. Units 1 and 2 were previously fitted singly in critical military installations where sub-microsecond timing accuracy was a paramount requirement. Following a typical 90 day operation

Caesium 2 would have had a timing error in excess of 1millisecond.

Caesium 2 is considered an extreme case but it is easily controlled by the TOC80CM. The following graph shows what happens during the start up phase when Caesium 2 is controlled by first a fast correcting algorithm, then the TOC80 automatically changes over to a medium speed algorithm (at point M on the time axis) as the performance improves. The controller works entirely by measuring phase errors between 1pps derived from the Caesium and valid 1pps pulses from the GPS receiver (in this case via a GPS060 interface). The 1pps instrument has a 50ns resolution phase measurement which is displayed on the graph together with a 1ns resolution measurement of the output frequency against the GPS8000R. This resolution is improved progressively over the averaging period and the graph illustrates both the inherent inaccuracies of the Rubidium reference and the performance limitations of GPS. From this graph we learned that the initial fast control up to point M should have been continued longer in order to build a more accurate integral for the next controller rate. However it can clearly be seen that after 1 day from 'switch-on' the controller has removed the huge offset from Caesium 1 and that it then challenges Caesium 4 with accuracy better than 1 part in  $10^{12}$ .



The TOC80 controller was then connected to Caesium 1 which has an offset of about 1 part in  $10^{11}$ , a value that is considered to be more typical of commercial Caesiums, but nevertheless at the limit of acceptable accuracy for use as a telecommunications stratum 1 frequency source. The graph below shows the start up phase of the controller has been improved and within a small fraction of a day the benefit of correcting a normal grade Caesium is clearly visible. Once again both 'before' and 'after' correcting results are shown on the same graph together with results from the two other higher grade Caesiums which are free-running, all plotted against the output of a GPS8000R.

A Caesium frequency controller has been described and demonstrated working with both inaccurate and typical commercial caesiums. A Caesium with accuracy outside of CCITT's primary reference clock accuracy (Stratum 1) is automatically corrected with no user intervention required and can then have a Maximum Time Interval Error (MTIE) which is an order better than is required. If the reference source (GPS) becomes unavailable then the correction rate established prior to the loss of reference continues to be applied. In terms of time error, an error rate of 1000ns per day (about  $1E-11$ ) has been shown to be reduced to less than 100ns per day within a day of operation. The alignment of the output with the GPS reference also eliminates the long term effects resulting from any offsets inherent to the particular Frequency Standard under control. The user receives the benefit of the results of measurements of the performance of his frequency source against GPS whilst retaining access to his uncorrected frequency output. The frequency controller requires no prior knowledge of the frequency source and the correction is applied without generating a feedback signal to the frequency source

We now intend to run a set of long term tests using a Hydrogen Maser to establish what benefits can be achieved with signals more accurate than a caesium can provide

(1) Wright D F, 1994 "Custom Turnkey Time and Frequency Systems A Structured, Expandable Approach" 26<sup>th</sup> Annual Precise Time and Time Interval (PTTI) Applications and Planning Meeting, Reston, Virginia

(2) Hubner G, 1994, "Performance of Disciplined Rubidium Oscillators under Selective Availability" 8<sup>th</sup> European Frequency and Time Forum, Munich

**A VERSATILE PC CONTROLLED SERVO SYSTEM FOR HIGH PERFORMANCE OPTICALLY PUMPED CESIUM BEAM FREQUENCY STANDARD**

F. Hamouda, R. Barillet and P. Cerez

Laboratoire de l'Horloge Atomique, Unité Propre de Recherche du CNRS associée à l'Université Paris-Sud, Bâtiment 221, UPS, 91405 - Orsay Cedex - France

**ABSTRACT**

A PC controlled servo-system has been designed and implemented in the experimental optically pumped cesium beam frequency standard using a short resonator developed at LHA [1]. This servo-system sequentially controls the frequency of the 10MHz ultra stable oscillator (USO), the level of the microwave signal which interacts with the cesium atoms and the static magnetic field applied to the atoms in the resonator.

First experimental results confirm that this new digital system does not degrade the short term frequency stability of the frequency standard, and also makes it possible to suppress the effect of slow fluctuations i) of the amplitude of the microwave probe signal and ii) of the static magnetic field. Preliminary GPS comparisons show a frequency stability about  $2.8 \times 10^{-14}$  for  $\tau = 1$  day and  $1.4 \times 10^{-14}$  for  $\tau = 4$  days.

*Keywords : atomic clocks, digital servo-systems*

**1. INTRODUCTION**

Digital servo-systems have already been used in various atomic clocks in order to control some of the operating parameters : frequency of the master U.S.O (Ultra Stable Oscillator), static magnetic field intensity [2] and also microwave signal power [3]. This kind of apparatus automatically adjusts the previous parameters and suppresses some spurious effects related to the ambient fluctuations. Recently, such a digital servo-system has been designed and implemented in our experimental optically pumped cesium beam frequency standard Cs4. This new servo-system is operated according to the results of recent investigations [4] : the microwave power servo does not require any longer a permanent level modulation - which was necessary in [3]. Consequently this new design suppresses a possible spurious effect on the USO frequency and insures that the servos are independent. Preliminary experimental results show that the short term frequency stability is not disturbed by the servo-system, and that the flicker floor previously observed at the  $2.10^{-14}$  level [5] is probably suppressed.

**2. ARCHITECTURE AND DESCRIPTION OF THE SERVO-SYSTEM**

The global architecture of the servo system, as well as its practical implementation, is shown in fig1 ; the timing inside the sequences is represented in fig2.

The aim of our design was i) to realize the sequential servo of the USO frequency, of the microwave power and of the static magnetic field, and ii) to have flexibility in the parameters configuration for the optimization of each servo and flexibility for the characterization of the physical properties of the resonator. Consequently, the three servos are independent and all the servo parameters are programmed by software.

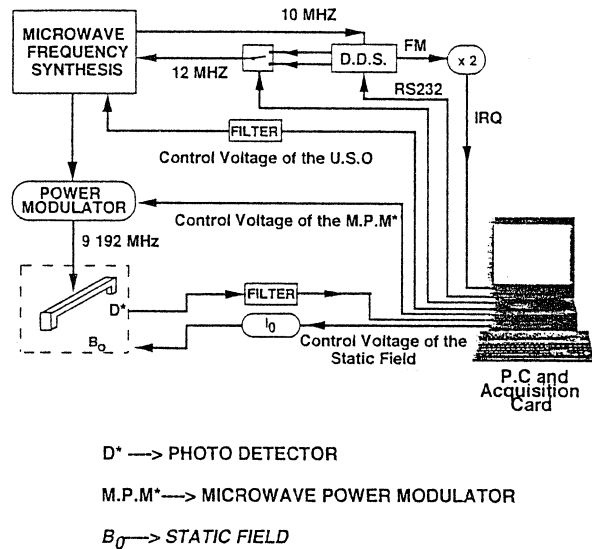


Fig.1 : the PC controlled servo system

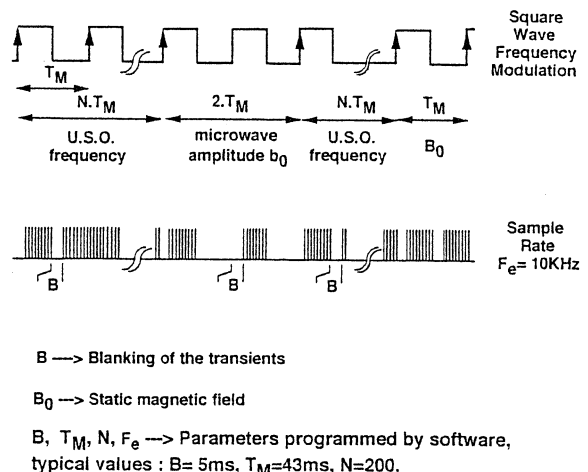


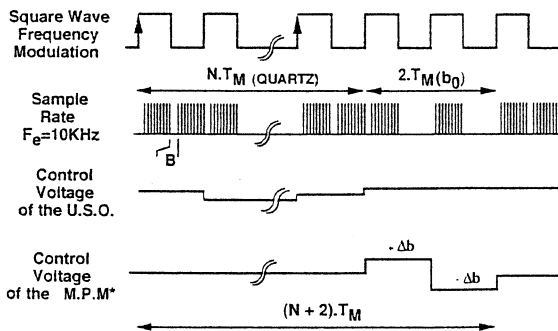
Fig 2 : timing of the 3 servo loops

The frequency of the microwave signal is permanently square wave modulated. Each servo is separately operated during an integer number of modulation periods  $T_M$ . All the parameters of the operation - modulations, demodulations, blankings, transfer functions, time constants...- may be separately adjusted by the user via the PC.

The use of a blanking at the beginning of each half-period is necessary in order to suppress the large transients of the resonator response after the frequency jumps or power jumps : these transients could induce a degraded accuracy by creating a false "error signal" or induce a degraded behavior of the input ADC by increasing the relative quantization step.

First sub-sequence

At the beginning of a typical sequence (fig.2), the USO frequency servo is activated during N periods  $T_M$  - currently  $N=200$ ,  $T_M = 43ms$ . The digital signal processing includes a square demodulation, two integrations and a phase lead in order to insure the stability of the servo loop. The two integrations are a classical means to perfectly suppress a possible frequency drift of the free-running USO. The frequency control voltage is adjusted at the end of each period  $T_M$ . The time constant of this servo is about 1s.



B -> Blanking of the transients

$b_0$  -> Microwave amplitude

M.P.M.\* -> Microwave Power Modulator

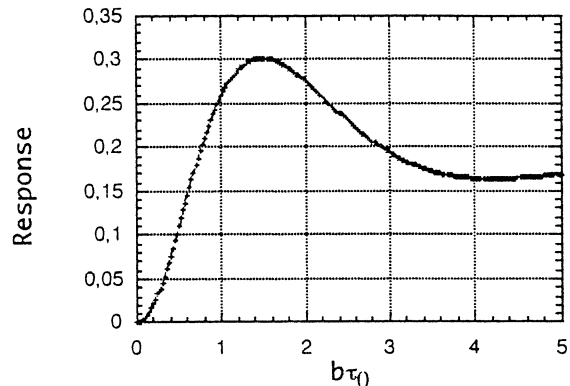
B,  $T_M$ , N,  $\Delta b$  -> Parameters programmed by software, typical values : B= 5ms,  $T_M=43ms$ ,  $N=200$ ,  $(\Delta b)/b \Leftrightarrow 1dB$ .

Fig.3 : timing of the USO and of the microwave power servos

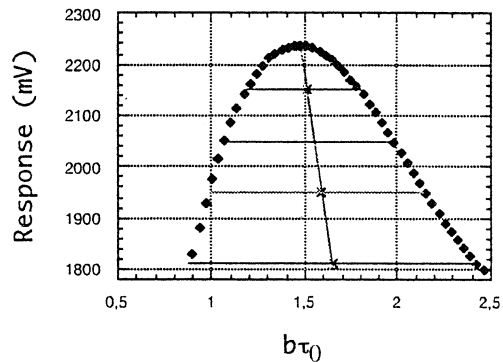
Second sub-sequence

At the end of the Nth period, the frequency control voltage of the USO is fixed at the proper value for the next 2 periods, which are used for the servo of the microwave signal level, as shown in fig.3. The microwave power servo is based on the following observation, represented in figs.4a, 4b and 4c : around its first optimum, the Ramsey Probability graph shows a very symmetrical behavior when plotted against the logarithm of the microwave amplitude. This property was experimentally verified (figs 4b and 4c) and enables

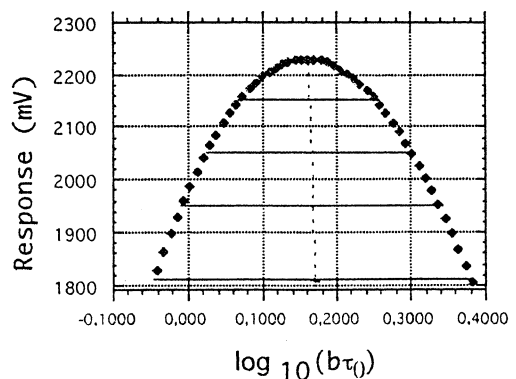
us to use a non permanent amplitude modulation with a relatively large modulation depth, typically  $\pm 1dB$  around the optimum level : the corresponding detailed information is included in a separate paper also presented at EFTF 1998 [4]. The amplitude modulation and the amplitude control are provided by a PIN attenuator : its logarithmic response naturally provides the proper scale law for the amplitude modulation. The digital signal processing includes a square demodulation and one integration. The time constant of this servo loop is currently about 30s.



4a : theoretical behavior



4b : experimental results (linear  $b\tau_0$  scale)



4c : experimental results (logarithmic  $b\tau_0$  scale)

Figs.4 : Ramsey probability against the amplitude of the microwave interrogation field  $b\tau_0$

Experimental conditions of figs 4b and 4c are  $\Phi = \pi$ ,  $\omega_0 T_0 = 1.54$ ,  $n = 3$  with the classical notations, cf [6].

### Third sub-sequence

Then the USO frequency servo is operated again during  $N$  periods as in the first sub-sequence, and finally...

### ...Fourth sub-sequence

One period is used for the magnetic field servo. During this last period, the frequency of the microwave probe signal jumps 41kHz above the atomic reference frequency in order to interrogate the  $(4,1) \leftrightarrow (3,1)$  transition and to control the magnetic field ( $58.5 \text{ mG} = 5.85 \times 10^{-6} \text{ T}$ ). This large frequency jump requires a very wide bandwidth of DRO-PLL (Dielectric Resonator Oscillator, fig 5) that generates the microwave probe signal, typically more than 100kHz. The time constant of the static magnetic field servo is less than 1 mn.

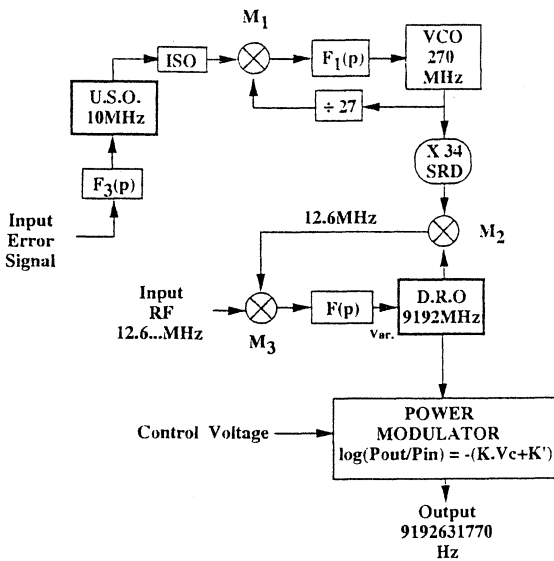


Fig.5 : microwave synthesis block diagram

## 3. EXPERIMENTAL RESULTS

Experiments concerned three domains : behavior of the servos, short term frequency stability and long term frequency stability

### 3.1. Behavior of the servos

It was observed in order to verify the coherence between the expected theoretical behavior and the real one. A preliminary FFT spectral analysis of each error signal enabled us to verify the bandwidth and to adjust the damping - when necessary - in order to prevent us from an increased noise at the limit of the servo bandwidth. After that, we verified the general behavior. For example, figures 6a and 6b show the response of the resonator when the static magnetic field servo is "off" or "on" respectively. In each figure 6, the upper curve represents the response of the resonator : the left part, with transient "down", is related to the last USO servo period, then the first transient "up" shows the beginning of the static magnetic field servo operation : during this

period  $T_M$ , the lower curves are at the "down" level. When the magnetic field is not at the proper value, we observe that the two plateaus of the upper curve (fig 6a) during this period are not at the same level. When the magnetic field servo is "on", the response of the resonator shows a steady state where the two plateaus are at the same level, as in fig.6b.

Similar observations can be made for the three servos. A detailed noise analysis of the spectrum of each "error signal" can be made in each servo in order to provide additional information about the respective contributions to the noise performance of the frequency standard. We have just verified that these contributions were negligible in the noise budget.

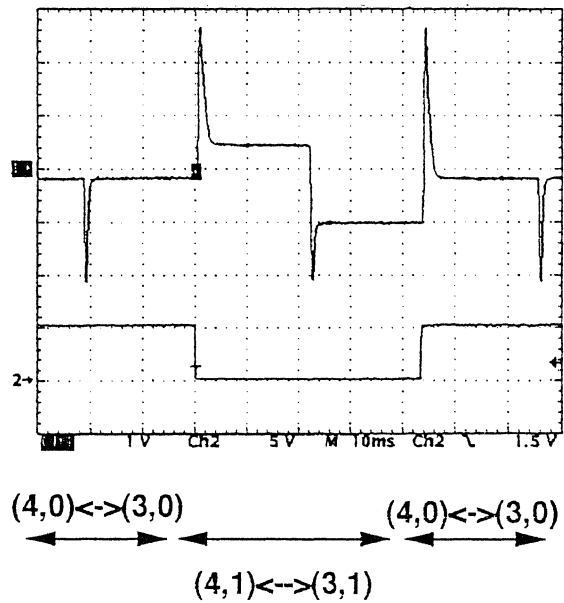


Fig.6a : Cs4 response when the static magnetic field servo is in open loop

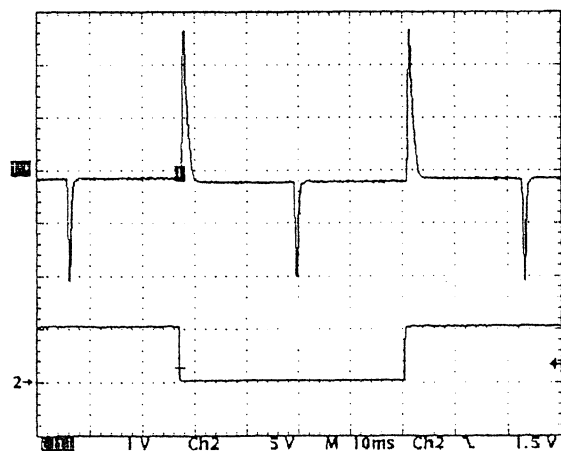


Fig.6b : Cs4 steady state response when the static magnetic field servo is in closed loop

### 3.2. Short term frequency stability

According to our expectation, the implementation of this servo system does not degrade the short term

frequency stability of the frequency standard, which is consistent with the previous observation : the noise contribution of the three servos is negligible in the noise budget of the frequency standard.

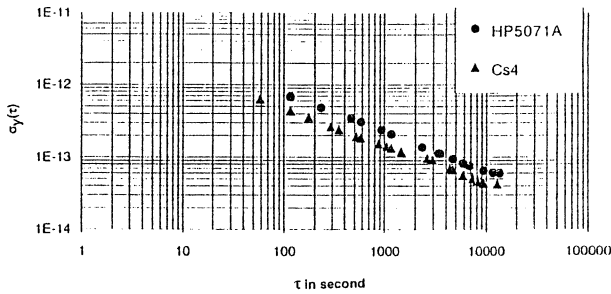


Fig.7 : frequency stability of Cs4 and of a HP5071A (opt 001)

The short term performance is shown in fig.7. The frequency stability expressed in Allan standard deviation is about  $4 \cdot 10^{-12} \tau^{-0.5}$  in the short term, measured against our H-Maser M3. This result is identical to that previously obtained, always with an oven temperature of 90°C in Cs4. The frequency stability of a HP 5071A opt. 001 frequency standard (available at LHA), compared to the H-Maser M3, is also presented in fig 7.

### 3.3 Long term frequency stability

A common view GPS link with LPTF (Laboratoire Primaire du Temps et des Fréquences) at Observatoire de Paris enabled us to compare the time scale, generated from Cs4, to UTC-OP during 28 days. The raw results are represented in fig. 8. The estimated frequency stability of Cs 4 alone is approximately 3dB lower, which corresponds to  $2.8 \cdot 10^{-14}$  ( $\tau=1d$ ) and  $1.4 \cdot 10^{-14}$  ( $\tau=4d$ ). This preliminary result shows that the previous flicker floor at  $2 \cdot 10^{-14}$  is probably suppressed by the implementation of the digital servo-system.

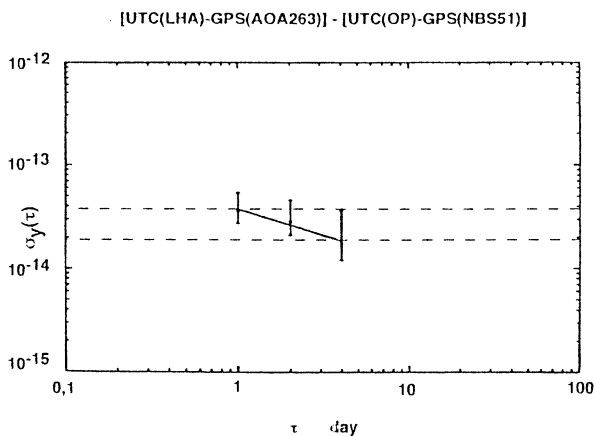


Fig.8 : first evaluation of the long term frequency stability of Cs4 against UTC(OP) by GPS link

## CONCLUSION

The new digital servo system implemented in the Cs4 frequency standard now makes it possible to suppress the spurious effect of the magnetic field fluctuations and of the microwave power fluctuations. The short term frequency stability remains identical to that previously measured, which means that there is no additional noise. Preliminary GPS measurements show that the flicker floor previously observed is probably reduced, thanks to the stabilization of the microwave amplitude and of the static magnetic field. Longer GPS measurements are now necessary to validate these promising results.

## ACKNOWLEDGEMENTS

We gratefully acknowledge Claude Audoin, whose permanent interest and suggestions have very widely contributed to our results.

## REFERENCES

1. P. Petit et al - "Miniature optically pumped cesium beam resonator", Proc. of the 6th EFTF, ESTEC, Noordwijk (the Netherlands) 17-19 march 1992, pp 83-86
2. J. Rabian, P. Rochat - "Full digital processing in a new commercial cesium standard" - 11<sup>th</sup> European Frequency and Time Forum, Neuchâtel, Switzerland, 16-18 march 1988, Proc. pp 461-465
3. L.S. Cutler and R.P. Giffard "Architecture and algorithms for new cesium beam frequency standards electronics"- 1992 IEEE Freq. Contr. Symp., 27-29 may, 1992, Hershey, USA - Proc. pp 127-133
4. C. Audoin et al - "Some properties of an optically pumped cesium beam tube depending on the microwave amplitude" presented at EFTF 1998, to be published in the Proceedings
5. B. Boussert - "Évaluation des performances en fréquence d'une horloge atomique miniature pompée optiquement", Thèse de Doctorat en Sciences, 15 nov. 1996, Université Paris-Sud, Orsay (France)
6. J. Vanier and C. Audoin, "The Quantum Physics of Atomic Frequency Standards", Adam Hilger, Bristol Philadelphia, 1989, chapter 5.

Experimental conditions of figs 4b and 4c are  $\Phi = \pi$ ,  $\omega_0 T_0 = 1.54$ ,  $n = 3$  with the classical notations, cf [6].

### Third sub-sequence

Then the USO frequency servo is operated again during  $N$  periods as in the first sub-sequence, and finally...

### ...Fourth sub-sequence

One period is used for the magnetic field servo. During this last period, the frequency of the microwave probe signal jumps 41kHz above the atomic reference frequency in order to interrogate the  $(4,1) \leftrightarrow (3,1)$  transition and to control the magnetic field ( $58.5 \text{ mG} = 5.85 \times 10^{-6} \text{ T}$ ). This large frequency jump requires a very wide bandwidth of DRO-PLL (Dielectric Resonator Oscillator, fig 5) that generates the microwave probe signal, typically more than 100kHz. The time constant of the static magnetic field servo is less than 1 mn.

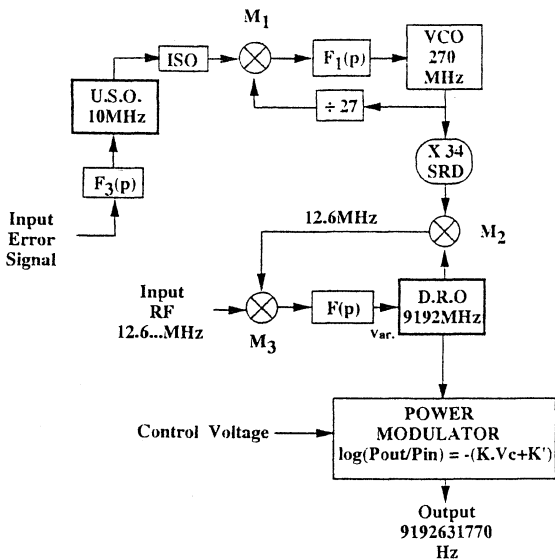


Fig.5 : microwave synthesis block diagram

## 3. EXPERIMENTAL RESULTS

Experiments concerned three domains : behavior of the servos, short term frequency stability and long term frequency stability

### 3.1. Behavior of the servos

It was observed in order to verify the coherence between the expected theoretical behavior and the real one. A preliminary FFT spectral analysis of each error signal enabled us to verify the bandwidth and to adjust the damping - when necessary - in order to prevent us from an increased noise at the limit of the servo bandwidth. After that, we verified the general behavior. For example, figures 6a and 6b show the response of the resonator when the static magnetic field servo is "off" or "on" respectively. In each figure 6, the upper curve represents the response of the resonator : the left part, with transient "down", is related to the last USO servo period, then the first transient "up" shows the beginning of the static magnetic field servo operation : during this

period  $T_M$ , the lower curves are at the "down" level. When the magnetic field is not at the proper value, we observe that the two plateaus of the upper curve (fig 6a) during this period are not at the same level. When the magnetic field servo is "on", the response of the resonator shows a steady state where the two plateaus are at the same level, as in fig.6b.

Similar observations can be made for the three servos. A detailed noise analysis of the spectrum of each "error signal" can be made in each servo in order to provide additional information about the respective contributions to the noise performance of the frequency standard. We have just verified that these contributions were negligible in the noise budget.

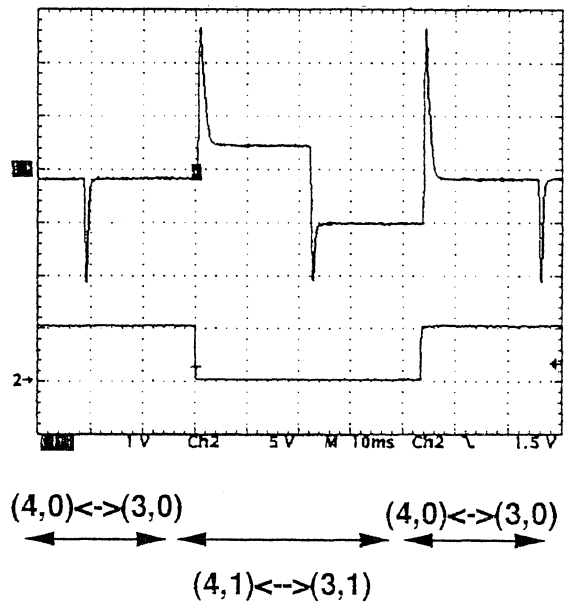


Fig.6a : Cs4 response when the static magnetic field servo is in open loop



Fig.6b : Cs 4 steady state response when the static magnetic field servo is in closed loop

### 3.2. Short term frequency stability

According to our expectation, the implementation of this servo system does not degrade the short term

frequency stability of the frequency standard, which is consistent with the previous observation : the noise contribution of the three servos is negligible in the noise budget of the frequency standard.

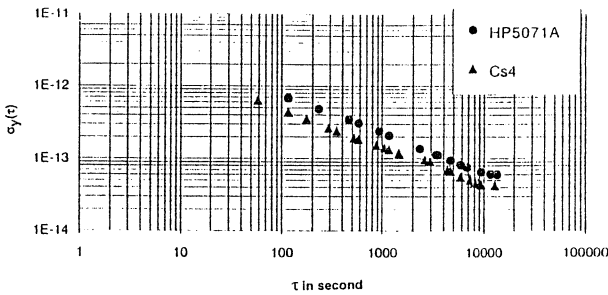


Fig.7 : frequency stability of Cs4 and of a HP5071A (opt 001)

The short term performance is shown in fig.7. The frequency stability expressed in Allan standard deviation is about  $4 \cdot 10^{-12} \tau^{-0.5}$  in the short term, measured against our H-Maser M3. This result is identical to that previously obtained, always with an oven temperature of  $90^\circ\text{C}$  in Cs4. The frequency stability of a HP 5071A opt. 001 frequency standard (available at LHA), compared to the H-Maser M3, is also presented in fig 7.

### 3.3 Long term frequency stability

A common view GPS link with LPTF (Laboratoire Primaire du Temps et des Fréquences) at Observatoire de Paris enabled us to compare the time scale, generated from Cs4, to UTC-OP during 28 days. The raw results are represented in fig. 8. The estimated frequency stability of Cs 4 alone is approximately 3dB lower, which corresponds to  $2.8 \cdot 10^{-14}$  ( $\tau=1\text{d}$ ) and  $1.4 \cdot 10^{-14}$  ( $\tau=4\text{d}$ ). This preliminary result shows that the previous flicker floor at  $2 \cdot 10^{-14}$  is probably suppressed by the implementation of the digital servo-system.

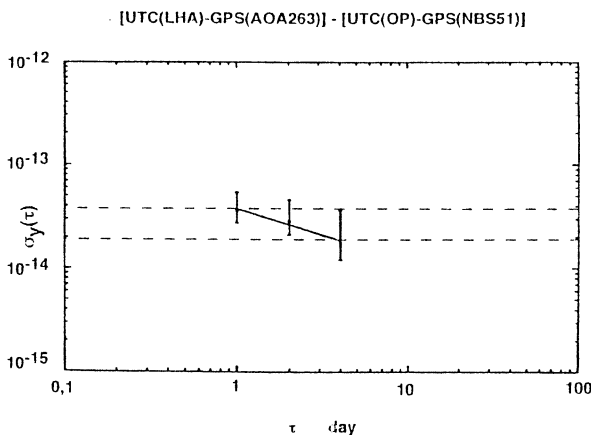


Fig.8 : first evaluation of the long term frequency stability of Cs4 against UTC(OP) by GPS link

## CONCLUSION

The new digital servo system implemented in the Cs4 frequency standard now makes it possible to suppress the spurious effect of the magnetic field fluctuations and of the microwave power fluctuations. The short term frequency stability remains identical to that previously measured, which means that there is no additional noise. Preliminary GPS measurements show that the flicker floor previously observed is probably reduced, thanks to the stabilization of the microwave amplitude and of the static magnetic field. Longer GPS measurements are now necessary to validate these promising results.

## ACKNOWLEDGEMENTS

We gratefully acknowledge Claude Audoin, whose permanent interest and suggestions have very widely contributed to our results.

## REFERENCES

1. P. Petit et al - "Miniature optically pumped cesium beam resonator", Proc. of the 6th EFTF, ESTEC, Noordwijk (the Netherlands) 17-19 march 1992, pp 83-86
2. J. Rabian, P. Rochat - "Full digital processing in a new commercial cesium standard" - II<sup>nd</sup> European Frequency and Time Forum, Neuchâtel, Switzerland, 16-18 march 1988, Proc. pp 461-465
3. L.S. Cutler and R.P. Giffard "Architecture and algorithms for new cesium beam frequency standards electronics"- 1992 IEEE Freq. Contr. Symp., 27-29 may, 1992, Hershey, USA - Proc. pp 127-133
4. C. Audoin et al - "Some properties of an optically pumped cesium beam tube depending on the microwave amplitude" presented at EFTF 1998, to be published in the Proceedings
5. B. Boussert - "Évaluation des performances en fréquence d'une horloge atomique miniature pompée optiquement", Thèse de Doctorat en Sciences, 15 nov.1996, Université Paris-Sud, Orsay (France)
6. J. Vanier and C. Audoin, "The Quantum Physics of Atomic Frequency Standards", Adam Hilger, Bristol Philadelphia, 1989, chapter 5.

**PROGRESS AT CENAM TOWARD THE CONSTRUCTION OF A SHORT CESIUM BEAM OPTICALLY PUMPED FREQUENCY STANDARD**

J.M. López-Romero<sup>1</sup>, D.A. Jennings<sup>2</sup>, J.F. García-Nava<sup>1</sup> and J.M. Figueroa-Estrada<sup>1</sup>

<sup>1</sup> Centro Nacional de Metrología  
Km. 4.5 Carretera a los Cues, Mpo. del Marqués  
C.P. 76900, Qro., México

<sup>2</sup> National Institute of Standards and Technology  
Time and Frequency Division  
Broadway 325, Boulder, CO 80303, USA

**ABSTRACT**

We report the progress at the Centro Nacional de Metrología, CENAM, toward the construction of a short Cesium beam optically pumped frequency standard. We describe the geometry of our Ramsey cavity, magnetic shield, and light collection. To pump and probe the atoms we use two 5mW DBR diode lasers with linewidth about 1MHz, the lock of this lasers to the 852nm Cesium transition line is described. The spectral purity and short time stability of the microwave synthesizer are reported.

**RAMSEY CAVITY, MAGNETIC SHIELD AND LIGHT COLLECTION**

The cesium tube we are using was previously used by NIST in early experiments to demonstrate the potential performance achievable in cesium beam frequency standards in which laser driven optical pumping is used for the atomic state selection and state detection in place of the magnetic state selection (1).

The cesium tube that we are using to built a short cesium beam frequency standard is schematically shown in figure 1, it is a modification on an commercial beam tube manufactured by Frequency Electronics Inc. The magnets "A" and "B", hot wire ionizer, electron multiplier and vac-ion pump were omitted in construction. The magnetic shields, C-field and Ramsey cavity remained unchanged from the standard commercial tube. In figure 1, the darker line shows the magnetic shield. The cesium oven is separated from the beam tube by a gate valve which could be closed when the beam tube system is opened. In "A" and "B" field regions are the optical pumping and detection optics, the fluorescence collection optics is a combination of a spherical mirror and an aspheric lens followed by lens which refocused the fluorescence onto a photodetector

mounted outside the vacuum envelope. The Ramsey cavity is 13cm long, the pumping and detection laser beams are 3,5cm apart from the ends of the cavity.

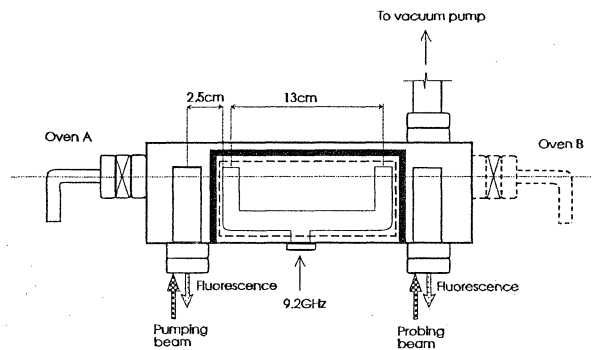


Fig. 1. Schematic of the Cesium tube.

**DIODE LASERS**

We use Distributed Bragg Reflection (DBR) type laser diodes to pump and detect the hyperfine Cesium transitions. The DBR laser used has an output power of about 5mW, a linewidth  $\approx$  1MHz and operating wavelength 852nm. The lock of the laser wavelength to the  $D_2$  line is achieved with FM sideband locking. A block diagram of the locking system is shown in figure 3. We use a 20 MHz current to be injected directly into the gain section of the laser diode giving rise to FM sidebands which are about 20 dB down from the single frequency carrier. A small part (about 5%) of the laser beam is passed through the Cesium cell and returned nearly on itself giving rise to the saturated absorption signals from the Cesium  $D_2$  transition line at 852nm. The 20MHz signal (the beat between the FM sidebands and the carrier) is amplified and quadrature phase detected in the phase-loop-filter section. The quadrature detection discriminates against the Doppler broadened background signal and the saturated signals appear as a type of dispersion. The signal obtained with the

quadrature detection is used as a discriminant to lock the emission wavelength of the diode laser to any of the  $D_2$  hyperfine transitions. Because the response time of the DBR control section is larger than  $10^{-5}$ s the gain of the control loop is rolled off at 100kHz. The DBR set-up has no gratings, PZT transducers, or laser cavities to keep aligned. In reference (2) a DBR diode laser similar to this one was found equivalent to an extended cavity diode laser when it was used as the optical source for the fluorescence detection in the USA primary frequency standard, NIST-7.

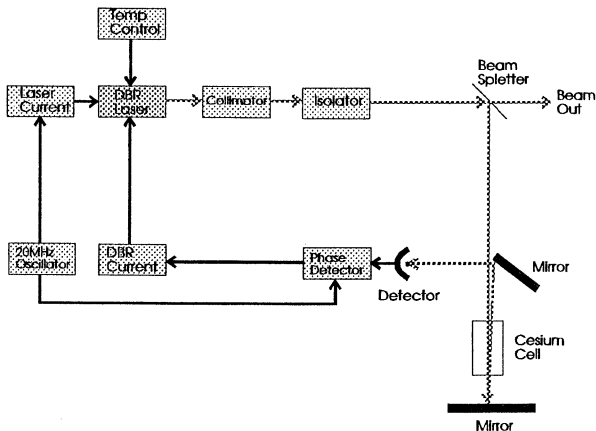


Fig. 2. Block schematic of the DBR laser stabilized to the Cs saturated absorption.

### MICROWAVE SYNTHESIZER

Our synthesizer was developed at NIST (National Institute of Standards and Technology) under a collaborative program between CENAM and NIST. The synthesizer is of the HR (high resolution) type described in reference (3), and it can be stepped  $\pm 180$ kHz at 9,192GHz to interrogate Zeeman resonance, it has a frequency resolution of  $2 \times 10^{-15}$ . The frequency stability of 100MHz to 9,192GHz is approximately  $1 \times 10^{-16}$  at 15 minutes and approaches  $1 \times 10^{-17}$  in one day in a laboratory with thermal variations of about 1K as is shown in figure 4. The temperature coefficient of this synthesizer is less than 1ps/K for synthesis from 100MHz to 9,192GHz and 10ps/K for synthesis from 5MHz to 9,192GHz. The power spectrum of the 9,192GHz output is shown in figure 5. As is shown, it has a very clean spectrum. Except for the residuals left from filtering the 10,7MHz and 510,7MHz comb product of the synthesis chain, there are no spurs higher than -73dBc (dB below de carrier). Figure 6 shows the PM noise from 1Hz to 100kHz for a pair of synthesizers and figure 7 shows the upper limit to the AM noise for Fourier offset frequencies from 1Hz to 100kHz.

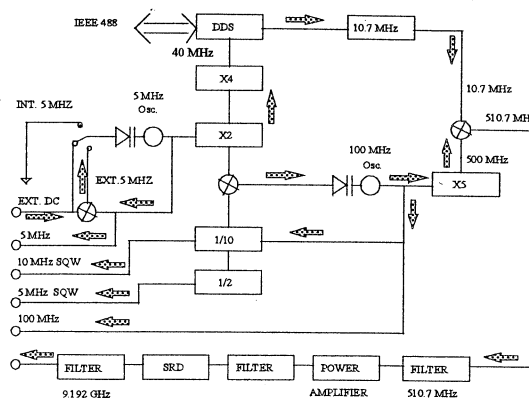


Fig. 3. Block diagram of the CENAM's HR1 type high stability synthesizers developed at NIST to interrogate passive Rb or Cs (depicted) atomic frequency standards.

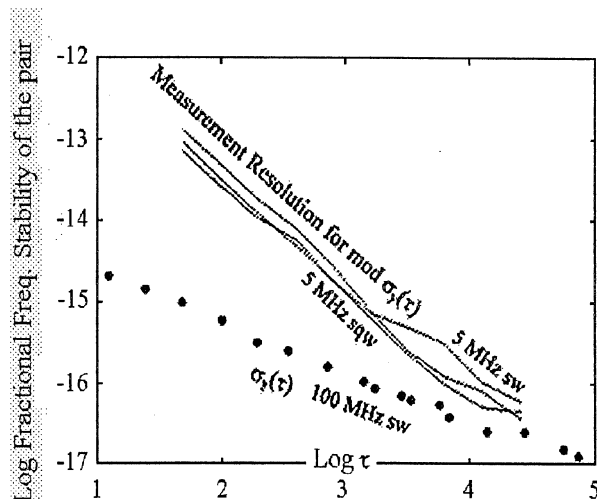


Fig. 4. Fractional Frequency stability of 100MHz output for the pair of HR1 Cs Synthesizers. The other curves show the fractional frequency stability for the 5MHz square-wave and 5MHz sine-wave outputs of the pair.

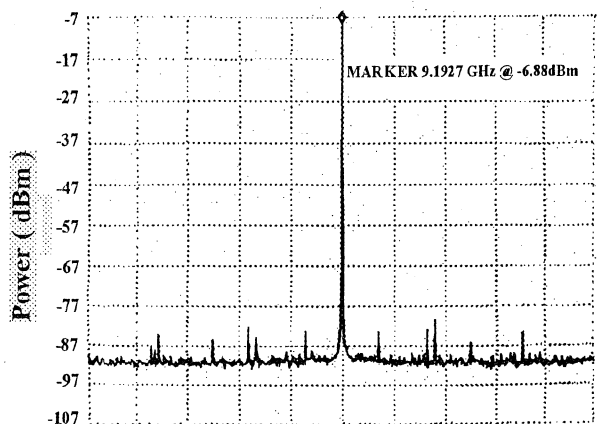
## CONCLUSIONS

We report the progress at the Centro Nacional de Metrología, CENAM, toward the construction of a short Cesium beam optically pumped frequency standard. The beam tube we are using has been derived from a commercial Cesium tube with a minimum modifications. We use DBR type diode lasers to pump and probe the Cesium atoms. The microwave synthesizer has been constructed in collaboration with the Time and Frequency Division of NIST, it has been designed to work in both Cesium thermal beam and Cesium fountain experiments.

An special acknowledge from the CENAM's authors to Dr. Donald Sullivan, Dr. Fred L. Walls, and Dr. Robert E. Drullinger from NIST for their valuable support to this work. Also we would like to thank to Dr. Hector N. Jaimes for kindly support this project.

## REFERENCES

- (1) Amy Derbyshire *et al*, 1985, "Optically Pumped Small Cesium Frequency Standard; A Status Report", Proc. of the 39th Symposium on Frequency Control, Philadelphia, 1985, pp. 18-21.
- (2) R.E. Drullinger *et al*, 1996, "DBR Laser Diodes for Optically Pumped Cs Frequency Standards", Proc. 1996 Conference on Precision Electromagnetic Measurements, pp. 260-270.
- (3) J.F. García-Nava *et al*, 1996, "Environmental Effects in Frequency Synthesizers for Passive Frequency Standards", Proc. of the 1996 IEEE International Frequency Control Symposium, pp. 973-979.



CENTER FREQUENCY 9.192 76 GHz      SPAN 20 MHz  
RESOLUTION BANDWIDTH 300 Hz      VIDEO BANDWIDTH 300 Hz

Fig. 5. Power spectrum of 9,192GHz output of the HR1 Synthesizer.

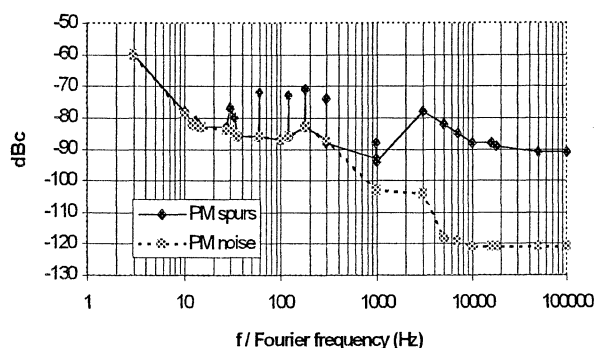


Fig. 6. Typical PM noise and upper limit to the PM spurs @ 9,192GHz for Cesium version of the HR1 synthesizers.

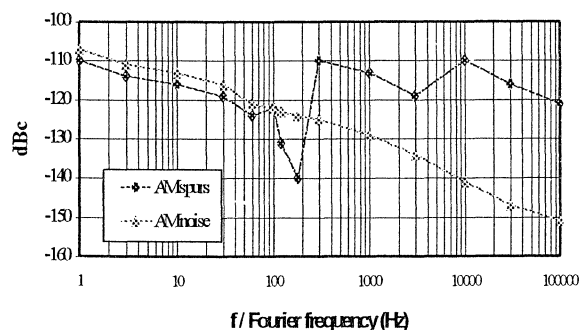


Fig. 7. Typical AM noise and upper limit to the AM spurs @ 9,192GHz for the Cesium version of the HR1 Synthesizers.

# AN EXPERIMENT IN FREQUENCY PROFICIENCY TESTING

Huang-Tien LIN & Chia-Shu LIAO

Telecommunication Laboratories,  
Chunghwa Telecom Co., Ltd.  
12, Lane 551, Min-Tsu Road Sec. 3, Yang-Mei,  
Taoyuan, Taiwan 326, ROC  
Telephone No. : +886-3-424-4066 Fax No. : +886-3-424-5474  
E-mail : htlin@ms.tl.gov.tw

## ABSTRACT

The experiment of proficiency test was launched in our BSF broadcasting station. In this experiment, the output frequency of Rubidium clock was taken as the time base, the Oven-Crystal frequency standard was used as the testing equipment, and the universal counter and PC were utilized to simulate the frequency calibration in the second-class laboratory. The experiment was supervised simultaneously by FMAS (Frequency Measurement and Analysis System), which was purchased from NIST, then proceeded an inter-comparison.

The goal of this experiment is to gain the experience of proficiency test for the future use. The method, procedure, and the equipment in this experiment can also be applied to the proficiency test between other laboratories.

## 1. INTRODUCTION

In order to satisfy the request of APLAC (Asia Pacific Laboratory Accreditation Cooperation) and CNLA (Chinese National Laboratory Accreditation) for the proficiency testing between laboratories, we try to proceed the "Frequency Proficiency Testing" and to gain the experience of proficiency testing for the future use.

The "Proficiency Testing" is an operating method and procedure, by comparing the result of the calibration or testing of different laboratories, to appraise probability of some

laboratories. One may thus say that the proficiency testing is a simple, direct, and important method to ensure the measurement quality of laboratories.

Because of the influential factors such as the environment, age, and the like other, it is hard to keep the accuracy and stability of the oscillator unchanged. The similar problem would still exist as the testing equipment was located to some other laboratory for the frequency proficiency testing. For solving this problem, the relative accuracy of the testing equipment was indirectly supervised by comparing the frequency signal of GPS and the primary signal.

The experiment of proficiency testing was launched in our BSF broadcasting station. In this experiment, the output frequency of Rubidium clock in BSF station was taken as the primary signal, the Oven-Crystal frequency standard was used as the testing equipment, and the universal counter and PC were utilized to simulate the frequency calibration in the second-class laboratory. The experiment was supervised by FMAS (Frequency Measurement and Analysis System) simultaneously, then proceeded an inter-comparison.

## 2. METHOD OF EXPERIMENT

The Frequency Measurement and Analysis System (FMAS) purchased from NIST, was used for supervising and receiving the GPS signal (see Fig.1.). FMAS together with Oven-

Crystal Oscillator, used as the testing equipment, were carried to the BSF station. The output 1MHz signal of Rubidium frequency standard HP5065A is taken as the primary input of FMAS. The calibration equipment of second-class laboratory are simulated by the universal counter and the personal computer. The Oven-Crystal Oscillator was tested by the above calibration equipment and FMAS simultaneously. This experiment can be described as following two parts (see Fig.2.) :

(a) The simulation of frequency calibration in second-class laboratory:

1. Connect the output signal of the Rubidium frequency standard to the Universal Counter(HP5345A) as the primary signal source for frequency calibration.
2. Connect the output 1MHz signal of the Oven-Crystal Oscillator to the Universal Counter(HP5345A), set the gate time, and then record the measurement frequency data by the personal computer. The accuracy of the frequency can be calculated by these data.
3. Tune the adjuster of the Oven-Crystal Oscillator for changing the frequency to get a better accuracy. The adjusted frequency data are still recorded by the personal computer, and the accuracy and the stability of the frequency are calculated by these data.

(b) The supervision of frequency calibration by FMAS:

1. The output of the Rubidium frequency standard was connected to FMAS and was taken as the primary signal of FMAS. By comparing this signal to the frequency signal of GPS, the following supervision is traceable to the national time and frequency laboratory.
2. As the recording and adjusting in procedure a) was continued, the 1MHz output signal of the adjusted testing equipment is connected to the receiving channel of FMAS simultaneously. The accuracy of the testing-object can thus be obtained from FMAS.
3. The 1MHz output signal of the adjusted testing equipment is connected to the receiving channel of FMAS, then the accuracy and the

stability of the frequency of the testing equipment can also be obtained from FMAS.

By using these two methods, two sets of accuracy and stability before and after adjustment can be obtained. Comparing these two sets of numerical result, one may obtain the frequency proficiency testing result of frequency calibration by the simulated second-class laboratory and by FMAS.

### 3. RESULTS

#### 3.1 Numerical Results

The output frequency signal of the Oven-Crystal Oscillator was connected to the universal counter and the FMAS. The data recorded for 3 days through the universal counter was calculated by PC. The calculated accuracy is  $-1.67E-09$ . The data recorded simultaneously by the FMAS is shown in Fig.3, which shows that the accuracy is  $-1.74E-09$ . Take the frequency data shown on the universal counter into account, one can adjust the Oven-Crystal Oscillator to the accurate 1 MHz. After the measurement for two days, the accuracy was calculated to be  $+1.523E-10$  by PC and  $+1.47E-10$  (see Fig.4.) by FMAS. The accuracy and stability of the Oven-Crystal Oscillator before and after adjustment is shown in TABLE 1. The stability calculated by FMAS is under the condition that "gate time =1000sec" (see Fig.5).

#### 3.2 Uncertainty Analysis

The uncertainty analysis of the frequency output of the Rubidium Frequency Standard is shown in TABLE 2.

In order to calculate the uncertainty of the measurement system, the uncertainty of the time base (output frequency of the Rubidium Frequency Standard) and the resolution of the measurement equipment should be taken into account. From TABLE 2, one can see that the combined standard uncertainty of the time base is  $5.78E-11$ . Since the resolution of the FMAS  $\leq 1E-13$ , the uncertainty of the measurement system is  $5.78E-11$  by using the FMAS. While

the universal counter HP5345A is applied (with gate time =1000 sec), the resolution of the counter is 5\*LSD=5E-12. The uncertainty of the measurement system is thus 5.78E-11, with rectangular uncertainty distribution for the resolution term.

The combined uncertainty can be calculated by the uncertainty of the measurement system and the stability obtained after measurement. As the FMAS is used, the measured stability is 2.65E-11 and thus the combined uncertainty is 6.36E-11. However, as the HP5345A is used (gate time = 1000 sec), the measured stability is 5.70E-11 and thus the combined uncertainty is 8.12E-11. With the coverage factor of k=2 (95% confidence interval), the expanded uncertainty by using FMAS and HP5345A is 1.27E-10 and 1.62E-10, respectively.

### 3.3 Statistic Method Analysis[3~5]

According to the statistical method described in the ISO/TEC Guide 43 for treatment of proficiency test data [3], let's consider the value of "En":

$$E_n = \frac{|x - X|}{\sqrt{U_m^2 + U_t^2}}$$

$$= \frac{|(1.52E - 10) - (1.47E - 10)|}{\sqrt{(6.36E - 11)^2 + (8.12E - 11)^2}}$$

$$= 0.05$$

where  $x$  is the accuracy calculated by using universal counter and PC,

$X$  is the accuracy calculated by using FMAS,

$U_m$  is the combined uncertainty calculated

by using universal counter and PC,

$U_t$  is the combined uncertainty calculated by using FMAS,

Since  $E_n < 1$ , the result conforms with the degree of acceptance.

It is worth noting that the measurement resolution is different as choosing different gate time for HP5345A, the calculated short term stability will also be influenced. The short-term

stability of the Oven-Crystal Oscillator under different gate time is shown in TABLE 3. Some results seem quite different in comparison with those obtained by FMAS. However, when gate time of HP5345A is set to be 1000 sec, high measurement resolution can be obtained and thus the short term stability by using these two equipment are of the same order.

## 4. CONCLUSION

In this experiment, the output frequency of Rubidium clock was taken as the time base, the Oven-Crystal frequency standard was used as the testing equipment, and the universal counter and PC were utilized to simulate the frequency calibration in the second-class laboratory. The experiment was supervised by FMAS simultaneously, then proceeded an inter-comparison. The measured frequency accuracy and the total measurement uncertainty are 1.52E-10 and 6.36E-11 by using the universal counter, while 1.47E-10 and 8.12E-11 by FMAS. The result of this experiment conforms with the degree of "acceptance" referenced to 「ISO/IEC Guide 43」. The method, procedure, and the equipment in this experiment can also be applied to the proficiency test between other laboratories.

## 5. REFERENCES

- [1] 1990, "ISO/IEC Guide 25", 3rd Edition 「General Proficiency Request for Calibration and Testing Laboratories」.
- [2] ISO/IEC Guide 43-1984.
- [3] 1996 「Statistical Methods for Treatment of Proficiency Test Data」, ISO/IEC Guide 43, ANNEX.
- [4] R.R. Cook & W.J. Giardini, "An Introduction to the Assessment of Uncertainty of Measurement"
- [5] 「Guide to the Expression of Uncertainty in Measurement」, ISO, 2nd Edition, 1995.

TABLE 1- The accuracy and stability of the Oven-Crystal Oscillator before and after adjustment

Methods	Before Adjustment	After Adjustment	
		accuracy	stability
Measurement by Universal Counter	-1.67E-09	+1.52E-10	+5.70E-11
measurement by FMAS	-1.74E-09	+1.47E-10	+2.65E-11
relative accuracy of (GPS-Rb) at the same time	-3.79E-12	-3.19E-12	

TABLE 2- The uncertainty analysis of the frequency output of the Rubidium Frequency Standard

Standard Uncertainty	Type B	Item	Uncertainty	k factor	Probability Distribution	Remarks
		tracing	2E-13	1	normal	2E-13
		aging	3.46E-11	$\sqrt{12}$	period	12E-11/(year) / $\sqrt{12}$
		temperature	4.62E-11	$\sqrt{12}$	period	4E-11*4 / $\sqrt{12}$
		M-field perturbation	1.45E-12	$\sqrt{12}$	period	5E-12 / $\sqrt{12}$
		voltage perturbation	2.31E-12	$\sqrt{3}$	rectangular	4E-12 / $\sqrt{3}$
	Type A	frequency stability	2.84E-13	1	normal	2.84E-13
	Combination of Standard Uncertainty		5.78E-11			

TABLE 3- The short-term stability of the Oven-Crystal Oscillator under different gate time

Gate time \ Stability	10 s	100 s	1000 s
HP5345A	1.22E-09	1.24E-10	5.70E-11
FMAS	1.2E-10	3.5E-11	2.65E-11

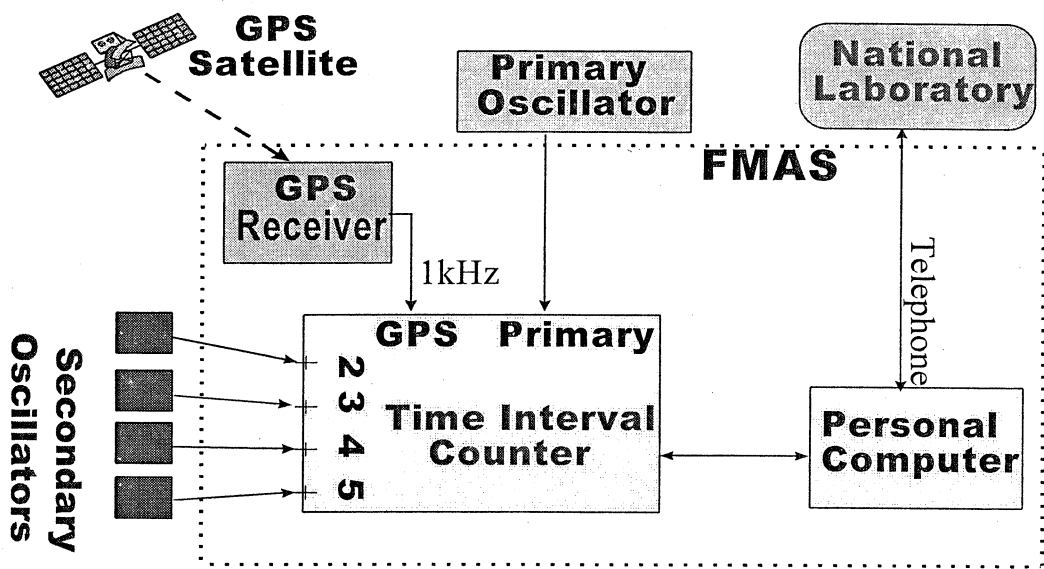


Fig.1. The block diagram of FMAS

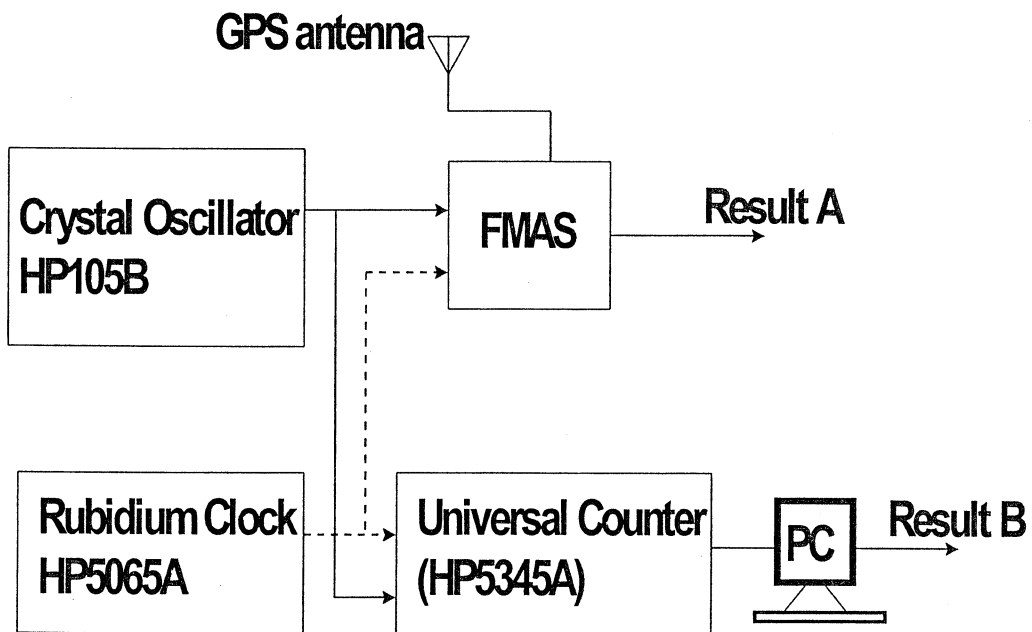


Fig.2. The block diagram of the experimental equipment

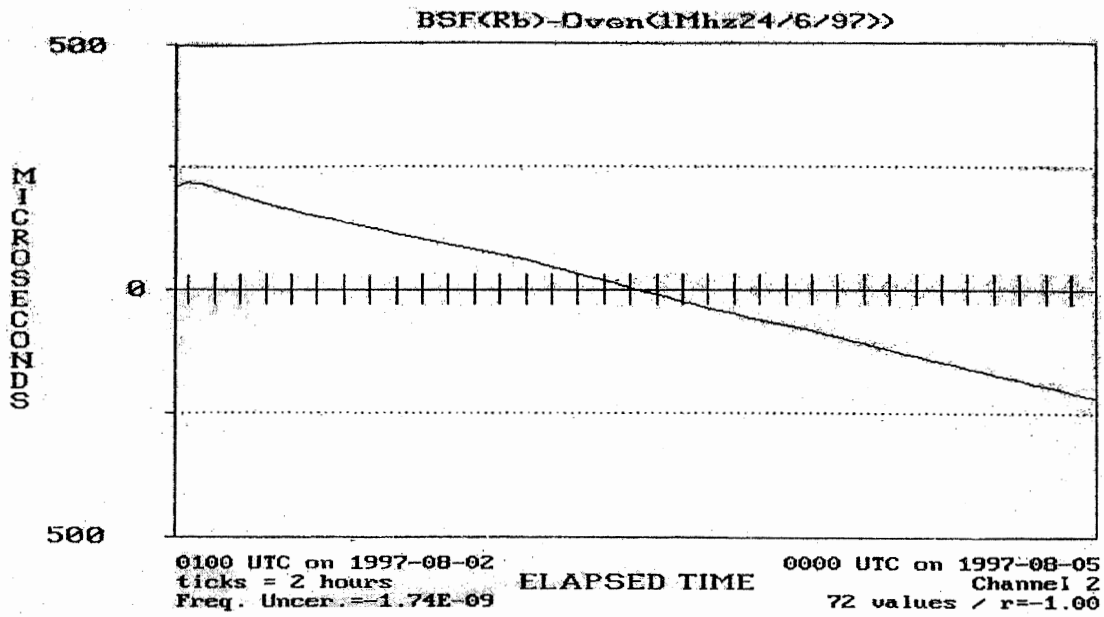


Fig.3. The accuracy of Crystal Oscillator measured by FMAS (before adjustment)

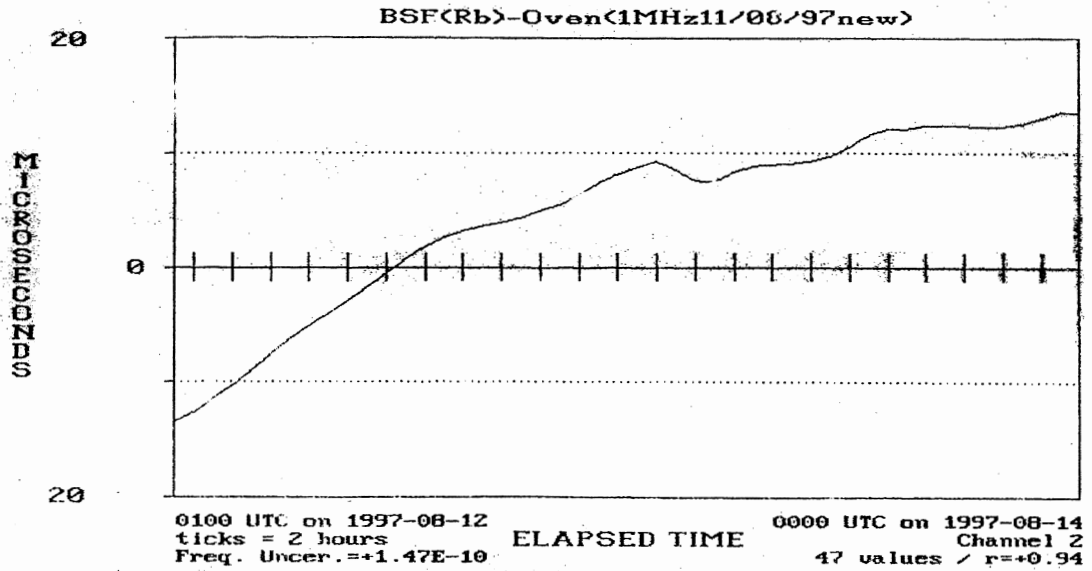


Fig.4. The accuracy of Crystal Oscillator measured by FMAS (after adjustment)

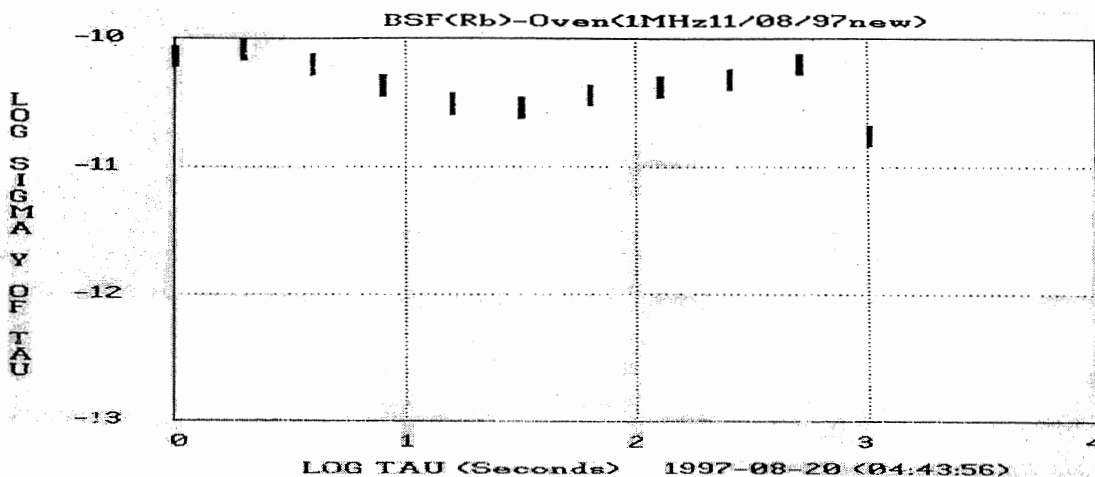


Fig.5. The stability of Crystal Oscillator measured by FMAS (after adjustment)

## GLONASS FREQUENCY AND TIME SIGNALS MONITORING NETWORK

*Y. Smirnov, M. Medvedev, N. Shienok  
Coordination Scientific Information Center (sfcsic@mx.iki.rssi.ru)  
Moscow, Russian Federation.*

### ABSTRACT

Synchronization subsystem providing frequency and time is the most important component of GLONASS and its accuracy and reliability have a great impact on overall performance of GLONASS.

Present status of GLONASS time scales and the joint effort of GLONASS authorities and State Committee For Standardization and Certification of Russia (Time Service) to improve accuracy and reliability of the GLONASS synchronization subsystem through establishment of frequency and time signals monitoring network are discussed in the paper.

The monitoring network structure based on using several frequency and time State etalons as an additional measurement facilities within State Time Service, data links and data processing, characteristics of on-board and system time scales of GLONASS as well as their behavior relative to GPS time and UTC are given.

### INTRODUCTION

Existing technology for generation and transmitting GLONASS time provides an accuracy not worse than 1 microsecond that meets specified requirements [1]. However increasing interest to GLONASS as instrument for precise timing worldwide promotes some progressive decisions towards better use of GLONASS potential in this field of application. One of approaches to it is development of monitoring network that enables to significantly improve quality of UTC transfer through GLONASS satellites.

### GLONASS TIME AND UTC

At the time being civil users community is greatly interested in combined use of GLONASS/GPS which advantages are absolutely obvious. Dedicated efforts and plans of the GLONASS administration jointly with

the Russian Federation State Committee for Standardization and Certification – Time Service (Gosstandart) were described in a greater detail in [2]. Current difference between GPS time, GLONASS time and UTC(SU), starting from GLONASS time correction on July 1, 1997, is given in Figure 1. [4].

It is well known that sub-system of synchronization is essential component of GLONASS, and its characteristics greatly affects quality of overall GLONASS performance. GLONASS time is based on time scale of the GLONASS Central Synchronizer. The Central Synchronizer consists of ensemble of CH1-80 –type hydrogen maser clocks (standards) that are steered to UTC(SU). The standards have good longtime stability and minimum systematic frequency drift (see Figure 1). However there is a problem of precise synchronization between the time scale of the Central Synchronizer and UTC(SU). Difference between UTC(SU) and GLONASS time does not affect GLONASS performance, and timing users can obtain from GLONASS navigation message (word  $\tau_c$ ) with specified accuracy [1]. Application of differential mode when synchronizing time scales allows to avoid many problems connected with system scale position and achieve accuracy about 20 nanoseconds [3].

GLONASS navigation signals have been used by State Time and Frequency Service since 1991. National etalon of time and frequency as well as all secondary etalons were equipped with stationary GLONASS receivers A724M which worked under common schedule. There are four seances of synchronization per day in differential mode. Obtained information is processed and results of the procession from every site are transmitted to all other involved sites. At the time being this synchronization network is the most accurate and rapid. Besides, it is single source of external information that is used for GLONASS time generation.

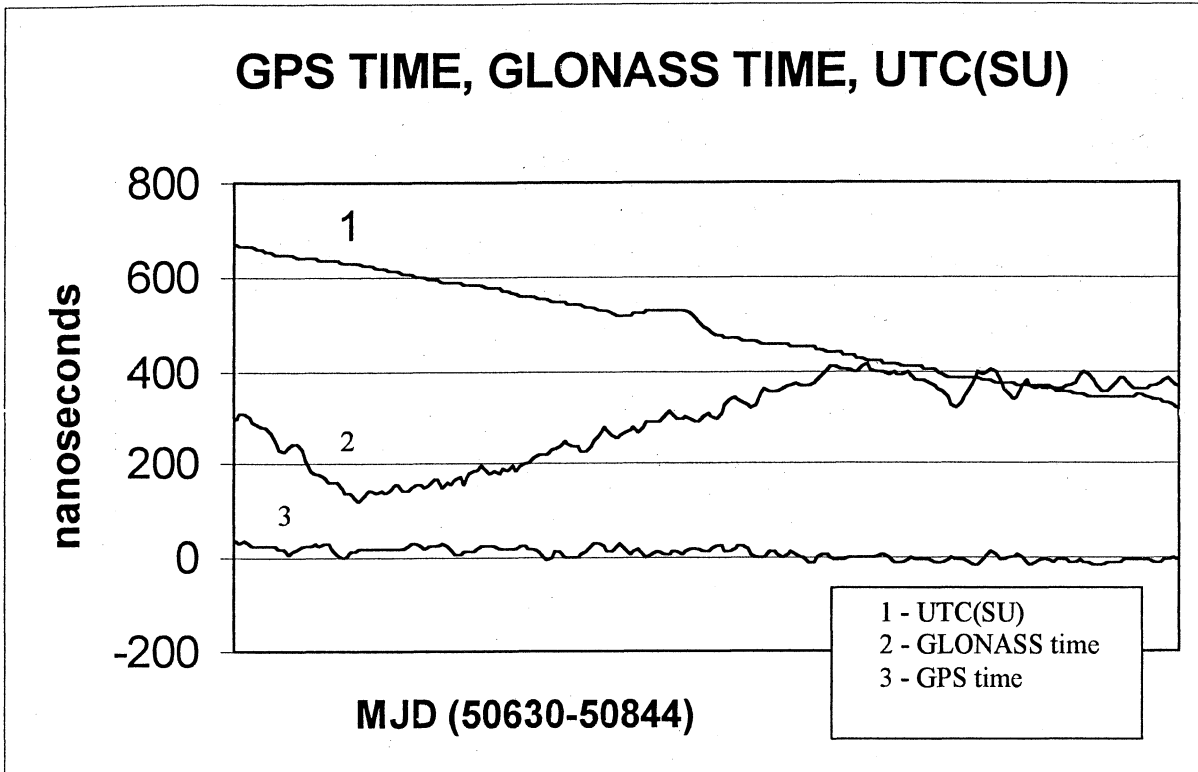


Fig.1 Difference between UTC(SU), GLONASS time, GPS time relative to UTC (1 July 1997 – 31 January 1998)

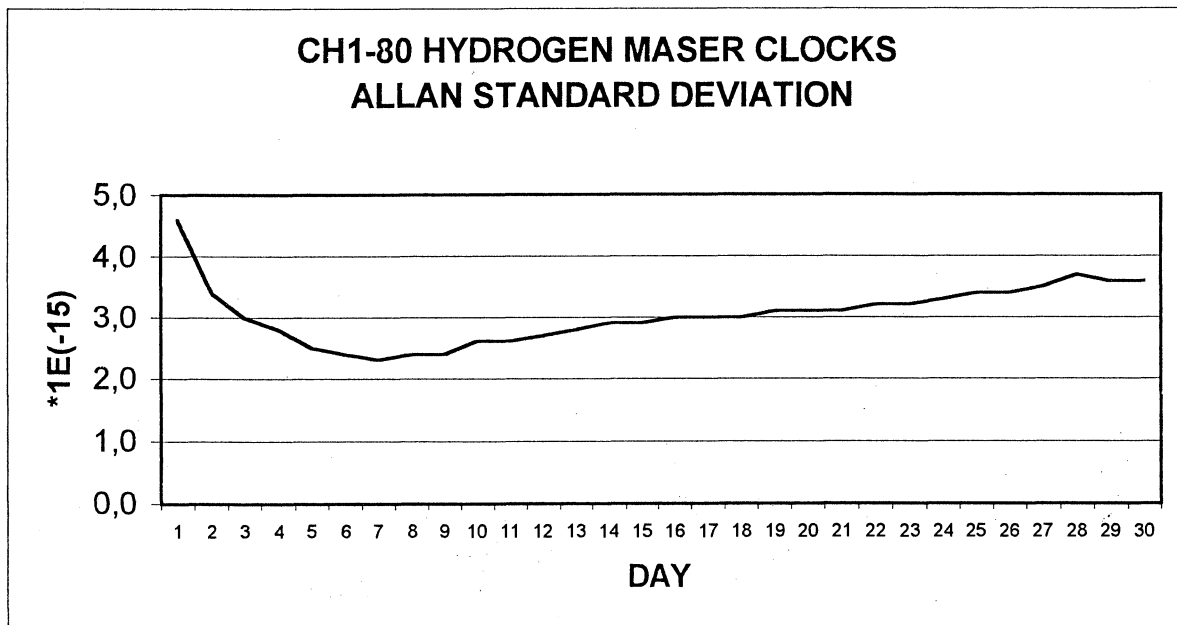


Fig.2 Allan Standard Deviation of GLONASS Master Hydrogen Maser (second half of 1997)

Some sites (secondary etalons) within the State Time and Frequency Service are equipped with other types of receivers: T4000SGL and R-100/40. However their measurements are not used for GLONASS

time generation but only as auxiliary data, because these receivers are not calibrated. It should be noted that at the time being calibrated GLONASS receivers for timing are not available for civil user community. Due to

this the values of (UTC – GLONASS time) difference obtained by various types of GLONASS receivers can vary from each other up to 1200 nanoseconds [5]. An official information about difference between GLONASS time and UTC is distributed by BIPM through Circular T [4] as well as by State Time and Frequency Service (Institute of Time and Space Metrology – IMVP) through Bulletins E [5]. Estimates of difference between UTC and GLONASS obtained on

interval from December 1997 to January 1998 (see Figure 3) show significant systematic component about 180 nanoseconds. IMVP estimates were obtained using A724 receiver. BIPM Circulars T provide data obtained by VSL laboratory (Netherlands) using 3S Navigation R-100/40 receivers. It should be noted that there is good correlation between presented estimates, and rms of both results tends to come to 20 nanoseconds.

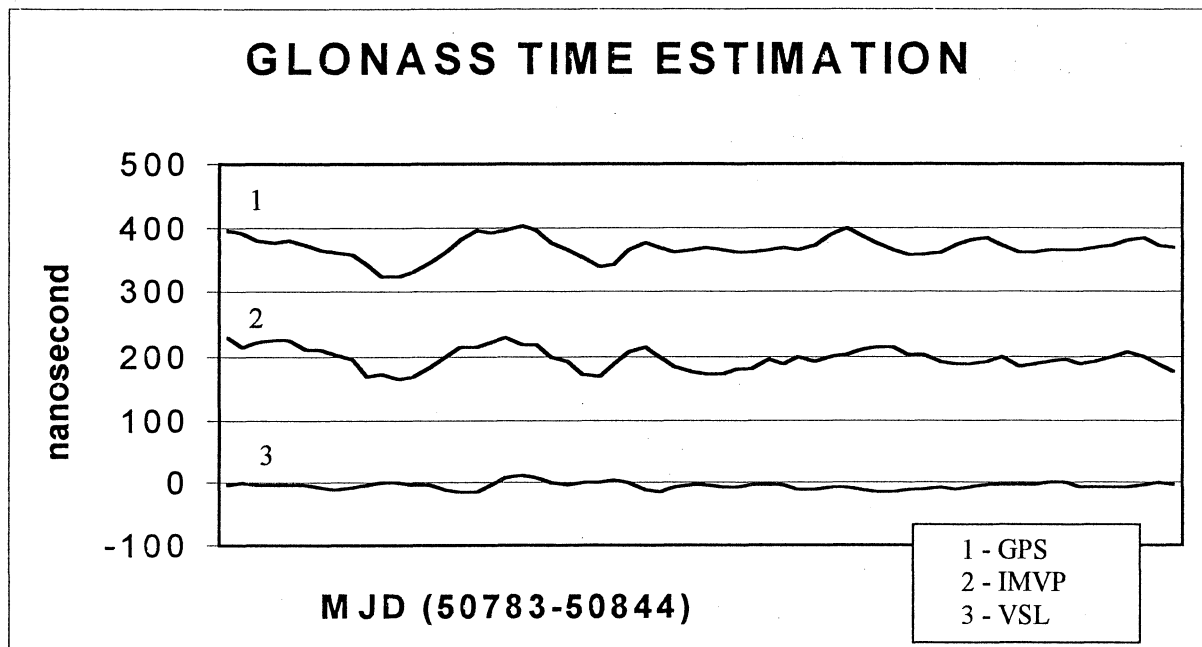


Fig.3 (GLONASS time – UTS) difference, as calculated by different laboratories (1 December 1997 – 31 January 1998)

In January of 1998 there were preliminary trials of 12-channel combined GLONASS/GPS receiver GID-12T (Russian Institute of Space Device Engineering – RNI KP, Moscow). There were obtained estimates of difference between GLONASS time and GPS time about 25 nanoseconds with rms 20 nanoseconds. So issue of calibration for GLONASS receiver used for precise timing remains open and there is urgent necessary to resolve it.

#### GLONASS FREQUENCY AND TIME SIGNALS MONITORING NETWORK

Deployment of GLONASS frequency and time signals monitoring network is in the list of planned organizational and technical

measures initiated by of GLONASS administration and Gosstandart authority to increase accuracy and reliability of timing. The Agreement on Interoperability between involved organizations has been developed. The Agreement determines aims and goals, organizational and technical structure of information interoperability as well as responsibilities of organizations-participants. Main goals of the monitoring are, as follows:

- Increasing robustness and reliability of GLONASS timing service by implementation of additional sources of measuring data on difference between GLONASS time scales;
- Adjusting technology of high accuracy timing service on a base of full account of Synchronization

sub-system equipment errors by analysis of monitoring data;

- Global UTC transfer through GLONASS with accuracy which meets the requirements of international organizations;
- Precise mutual synchronization of etalon time scales united within the State Frequency and Time Service automated network.

Obvious and the most effective way is to use etalons of the State Frequency and Time Service as components of the monitoring network. They were equipped with hydrogen maser standards CH1-75 and CH1-80 which daily stability is not worse than  $1 \cdot 10^{-14}$ , as well as with equipment of external and internal comparisons and data links.

On the first stage of experiment following sites are involved in:

- National etalon in Mendeleevo (Moscow region);
- Etalon-copy VS NIFTRI (Irkutsk);
- Etalon-copy in Golitsino (Moscow region)

It is planned to equip all these etalon sites with calibrated multi-channel combined GLONASS/GPS receivers of the same type. As a basic variant, it is scheduled to use GID-12T receivers after their tests have been completed. In the framework of the monitoring network development a GLONASS/GPS data exchange between aforementioned etalon sites has been organized under general coordination of Coordination Scientific Information Center (KNITs). Results of GLONASS/GPS measurements obtained at the sites of the monitoring network are transmitted to KNITs via e-mail. KNITs transmits collected measurements to GLONASS System Control Center where they are used as auxiliary data. Before complete deployment of the monitoring network the main problem is calibration of existing GLONASS receivers.

It appears that successful realization of planned organizational and technical measures will allow resolving issues that currently exist in GLONASS timing service

and using as much as possible GLONASS potential in terms of precise UTC transfer.

## CONCLUSION

Existing GLONASS synchronization subsystem does not enable users to obtain maximum benefit from real system potential. GLONASS administration jointly with Gosstandart authority make all possible efforts to resolve known issues. Deployment of the GLONASS frequency and time signals monitoring network over territory of Russia will allow significant decreasing difference between GPS time scale and UTC. For successful implementation of combined GLONASS/GPS use for timing worldwide there is urgent need in international cooperation and coordination.

## References

1. Global Navigation Satellite System GLONASS. Interface Control Document (October 4, 1995), Moscow, 1995;
2. GLONASS As Instrument For Precise UTC Transfer, M. Lebedev et al., KNITs, 1997
3. Estimation Of Accuracy For Channels Of Comparisons Of National Time And Frequency Etalon; A. Alshina, S. Pushkin et al (IMVP), Proc. of 5<sup>th</sup> Russian Conference "Time and Space Metrology" (Mendeleevo, 11-13 October, 1994)
4. BIPM Circular T115-T121 (Paris, monthly edition); <http://www.bipm.fr>
5. GLONASS Time Transfer and its Comparisons with GPS; W. Lewandowski et al., Proceedings of EFTF-97;
6. State Frequency and Time Service Official Bulletin (Mendeleevo, Moscow region, monthly); [http://www.rssi.ru/SFCSIC/SFCSIC\\_main.html](http://www.rssi.ru/SFCSIC/SFCSIC_main.html)

## GLONASS AS INSTRUMENT FOR PRECISE UTC TRANSFER

*M. Lebedev*

Coordination Scientific Information Center  
Moscow, Russian Federation

### ABSTRACT

Considering GLONASS as one of the principal components of future global navigation satellite system (GNSS) Russian Federation proceed with the works to integrate GLONASS with other navigation systems and facilities, to collaborate with international organizations of users, to participate in development and coordination of international standards and appropriate normative documents on GLONASS (GNSS) use, and to take into account recommendations of user's community.

GLONASS capabilities and prospects in terms of precise UTC transfer are discussed in presented material.

### INTRODUCTION

In the second half of 1996 International Civil Aviation Organization (ICAO) and International Maritime Organization (IMO) officially accepted proposal of the Russian Federation government for providing world civil user community with a standard-accuracy service through the Russian global navigation satellite system (GLONASS) as one of the principal elements of GNSS.

It is well-known that beside providing users with navigation service global navigation systems are excellent instrument for precise timing. Timing users worldwide attach great importance to GPS and GLONASS use for precise UTC transfer. Interest in capabilities and advantages of combined GLONASS/GPS use for this purpose was expressed in Recommendation S4 of 13<sup>th</sup> session of Consultative Committee for Definition of Second (CCDS) dated March 13, 1996 [1]. In the frame of GLONASS administration activity directed to extended implementation of the system into different areas of international civil application as well as to combined GLONASS/GPS use it is planned to conduct some organizational and technical measures on further improvement of accuracy of UTC transfer by GLONASS and further coordination of time and space reference frames used in GLONASS and GPS.

### GLONASS AND GPS TIME REFERENCES

Difference between GLONASS time and GPS time is one of the problems being appeared in case of combined use of both systems, specifically, for precise UTC transfer.

GPS time (GPST) takes UTC(USNO) as reference time scale, and, according to GPS SPS (2<sup>nd</sup> Edition, June 2, 1995) [2] the difference between GPS time and UTC is maintained to be within one microsecond (Modulo one second). The GPS Control Segment consistently manages GPS time coordination with UTC to better than 30 ns (1 sigma). This allows GPS user to obtain UTC practically with the same accuracy.

Time reference used in GLONASS differs from UTC. At first, GLONASS time, along with UTC(SU), is shifted relative UTC for +3 integer hours. At second, it also differed from UTC by position of time (second) mark: for example, by the end of November, 1996 the difference  $|UTC(SU) - UTC|$  was equal to approximately 8 microseconds (see Table 1).

GLONASS user, receiving navigation signals from satellites, can check his own clocks relative to GLONASS time. The GLONASS time is generated on the base of the GLONASS Central Synchronizer time scale (that is analog the GPS Master Clocks) and takes UTC(SU) as reference time scale. UTC(SU) is the time scale of the National Time and Frequency Etalon of Russia. Real technical and informational abilities of GLONASS allows user to check his clocks relative to GLONASS time with accuracy of single comparisons not worse than 30 nanoseconds (1 sigma). The GLONASS navigation message contains current value of difference between GLONASS time and UTC(SU). According to GLONASS Interface Control Document (October 4, 1995) [3] this allows user to check his clocks relative to UTC(SU) with accuracy not worse than 1 microsecond. However, really existing technical abilities of the system allows to do it with accuracy of 20 -30 nanoseconds (1 sigma). Figure 1 shows difference between UTC(SU) and GLONASS time provided that trend is excluded.

There is also another one difference between GLONASS and GPS time references connected with periodical leap second correction of UTC. The leap second correction provides difference

$$[UTC - UT] < 0.9 \text{ second, where}$$

UT (Universal Time) - is the term recommended by General Assembly of International Astronomical Union in 1928 to identify Greenwich mean solar time (aka GMT).

The GLONASS ephemeris are referenced to the UTC(SU). UTC is a discontinuous time scale, with leap seconds introduced, as needed, on 30 June or 31 December. The GLONASS time is also

corrected along with UTC and UTC(SU) during this leap second correction. GPS ephemeris are referenced to the UTC(USNO). Unlike UTC(SU) and GLONASS time UTC(USNO) and GPS time are not corrected during leap second correction of the UTC, but integer second difference between UTC(USNO) and UTC (delta time due to leap seconds) is transmitted within GPS navigation message. Therefore UTC(USNO) as reference for GPS time remains continuous time scale [4].

Experts of several international organizations and forums (e.g. ICAO, IMO, BIPM, ION, DSNS, etc.) repeatedly expressed an opinion on advantages and benefits of combined GLONASS/GPS use to improve reliability and accuracy of positioning and timing. They noted also that at the time being the GLONASS potential regarding precise UTC transfer is not fully realized yet. Besides, in order to effectively combine GLONASS and GPS it is necessary to appropriately coordinate its space and time references. Analysis shows that although the coordinate and time reference systems used in GLONASS and GPS differ from each other, these differences are not very significant and can be removed by respective translation.

#### **THE WAYS TO REALIZE GLONASS POTENTIAL REGARDING PRECISE TRANSFER OF UTC**

In June of 1996 there was joint meeting of representatives of the Russian Ministry of Defense and State Committee for Standards of the Russian Federation (Gosstandart). The meeting was dedicated to the problem of UTC transfer by GLONASS and consideration of S4 Recommendation of 13<sup>th</sup> CCDS session[1]. The meeting prepared the decision in which it is noted that considering

that international community of civil users expresses growing interest in GLONASS application;

that there is increasing interest in GLONASS as instrument of global precise timing;

that there are recommendations from international organizations on further improvement of characteristics of the UTC transfer using global navigation satellite systems;

that there are certain GLONASS potentials to be realized in the field of global precise timing for the benefit of civil users,

the meeting considers as necessary and possible to take some organizational and technical actions aimed to realization of existing GLONASS potentials regarding precise transfer of the UTC.

The decision was approved by Commander-In-Chief of the Russian Space Forces and Deputy Head of the Gosstandart. According to

the decision a special joint working group was established to prepare proposals and working plan for further improvement of frequency-time service of GLONASS users.

1. First stage of the plan was to provide GLONASS users with more accurate value of UTC. However ciphering of hour marks corresponding Moscow time (UTC + 3 hours) remains.

As a first step in this direction, National Etalon of Time and Frequency of the Russian Federation UTC(SU) was corrected on November 27, 1996 (MJD 50414) at 00 hours 00 minutes 00 seconds. The correction resulted in following difference :

$$\text{UTC(SU)}_{\text{old}} - \text{UTC(SU)}_{\text{new}} = 9 \text{ mcs}$$

This decreased difference between UTC(SU) and UTC down to 1 mcs (see Tab. 1). Data on difference between UTC(SU) and GLONASS time is transferred to the System Control Center with accuracy not worse than 100 ns. Corrections that ensure transition from GLONASS time to UTC(SU) are calculated from the data and then transferred within GLONASS navigation message to provide user with UTC with an accuracy not worse than 1 mcs.

2. Second stage of the plan is connected with modification of technology of GLONASS time generation to improve stability of the system time scale and synchronize it as close as possible to UTC(SU). The GLONASS time scale must be generated as weighted-mean group scale from observations of ground-based and onboard satellite clocks. This allows to significantly decrease existing difference between GLONASS time and UTC and maintain this difference on the level not more than 30 ns.

In this case the accuracy of UTC transfer by GLONASS will be practically the same as the one by GPS.

The meeting of the representatives of the GLONASS administration and the Gosstandart established responsibilities of agencies in implementation of above-mentioned plan as follows:

Gosstandart:

- provides maintenance of the National time scale UTC(SU);
- realizes metrological monitoring of time marks provided by GLONASS signal-in-space;
- realizes metrological monitoring of accuracy of synchronization between UTC(SU) and the Central Synchronizer time scale;

- publishes, on a regular basis, the data on the difference UTC(SU) - UTC and results of the metrological monitoring of the time marks contained in GLONASS signal-in-space.

GLONASS administration:

- provides generation of data on mutual position of GLONASS time scale and UTC(SU) that are transmitted within GLONASS signal-in-space;
- establishes monitoring of accuracy of synchronization between GLONASS time scale and UTC(SU) as well as transfer data on its mutual position through GLONASS satellites.

On 1<sup>st</sup> July of 1997 there was planned correction of GLONASS time to eliminate early existed difference about 36 mcs between this time scale and UTC(SU). Then it is planned to maintain the difference below 1 mcs.

#### **OTHER GLONASS TIME OPEN ITEMS TO BE RESOLVED**

In 1994 ICAO established GNSS Panel (GNSSP) that is responsible for development of Standards and Recommended Practices for future GNSS. GNSSP Working Group B identified some issues on GLONASS to be resolved for successful completion of SARPs [5]. These issues were addressed to the Russian Federation delegation and then were considered by GLONASS specialists.

**Provision for Leap Second.** The GNSSP Working Group B noted that periodical leap second correction of UTC(SU) and GLONASS time appears to be a problem in terms of integrity of GLONASS navigation message being transmitted to user during the correction.

In the foreseeable future it is not planned to stop consideration of UTC as reference for GLONASS. Therefore periodical leap second correction remains. However, some measures are developed to provide integrity of GLONASS navigation message during leap second correction:

a) notification within GLONASS navigation message frame about forthcoming leap second correction, its sign and magnitude. This feature should be provided on new GLONASS-M satellites. The notification should be transmitted eight weeks before the correction.

b) appropriate recommendations and procedures for users to conduct measurements during leap second correction should be included into the ICAO Standards and Recommend Practices for GNSS which are being developed.

**Parameter  $t_c$**  Currently, this parameter, broadcast as part of navigation message, relates the

GLONASS time to UTC(SU). The GNSSP WG-B noted that the LSB (7.4 ns) appears to be too coarse for the purpose of estimation of UTC(SU) in the future.

To provide more precise LSB (0.46 ns) it is planned to use 4 additional spare bits of GLONASS-M navigation message frame.

**UTC(SU) - UTC(USNO) Difference.** Currently, draft GLONASS-M ICD notes that transmission of difference UTC(SU) - UTC(USNO) within GLONASS-M navigation message should be provided using spare bits of the superframe. Calculation of the difference should be provided by GLONASS-M ground-based control complex facilities from measurements of both GLONASS and GPS.

The navigation message frame structure considering these additions it is planned to be presented in new GLONASS-M ICD in September/October of 1997.

#### **CONCLUSION**

Existing global navigation systems have excellent capabilities to provide reliable and accurate positioning and timing service for international community of civil users. But these capabilities become much better when combining measurements obtained from these systems. Therefore it appears to be reasonable to support all initiatives aimed to development of cooperation and integration in the field of space navigation technologies, search of optimal solutions to promote more complete and effective use of existing and future navigation systems for the benefit of world-wide user community.

#### **References**

- [1] Allan D. W., Harmonizing GPS and GLONASS, GPS World, # 5 (May), 1996, pp. 51-54;
- [2] GPS SPS Signal Specification, 2<sup>nd</sup> Edition, June 2, 1995;
- [3] GLONASS Interface Control Document (October 4, 1995, Coordinational Scientific Information Center of the Russian Space Forces);
- [4] Spilker J.J., Jr., GPS Navigation Data. Global Positioning System: Theory and Applications, Volume 1, p. 141, AAIA, Washington, DC, USA, 1996;
- [5] Report of GNSSP Working Group B, Annex F (Gold Coast, Australia, 17-28 February 1997).

**Difference between UTC(SU), UTC, UTC(GPS), UTC(GL) (mcs)  
as indicated in Gosstandart Bulletin E-12-96/C**

Table 1

MJD	Date	UTC(SU)- UTC(GL)	UTC(SU)- UTC(GPS)	UTC(SU)- UTC	UTC(GPS)- UTC
50407	20.11.96	-25.906	8.017	7.970	.047
50408	21.11.96	-25.934	8.017	7.971	.046
50409	22.11.96	-25.959	8.021	7.972	.049
50410	23.11.96	-25.994	8.008	7.973	.035
50411	24.11.96	-26.017	8.048	7.974	.074
50412	25.11.96	-26.060	8.028	7.976	.052
50413	26.11.96	-26.071	8.049	7.977	.072
50414	27.11.96	-35.095	-.965	-1.022	.057
50415	28.11.96	-35.121	-.954	-1.021	.067
50416	29.11.96	-35.153	-.977	-1.019	.042
50417	30.11.96	-35.180	-.941	-1.018	.077
50418	1.12.96	-35.186	-.937	-1.016	.079
50419	2.12.96	-35.205	-.958	-1.015	.057
50420	3.12.96	-35.246	-.947	-1.013	.066
50421	4.12.96	-35.277	-.938	-1.010	.072
50422	5.12.96	-35.283	-.963	-1.008	.045
50423	6.12.96	-35.300	-.933	-1.005	.072
50424	7.12.96	-35.362	-.942	-1.003	.061
50425	8.12.96	-35.394	-.939	-1.001	.062
50426	9.12.96	-35.393	-.963	-.999	.037
50427	10.12.96	-35.408	-.956	-.998	.042

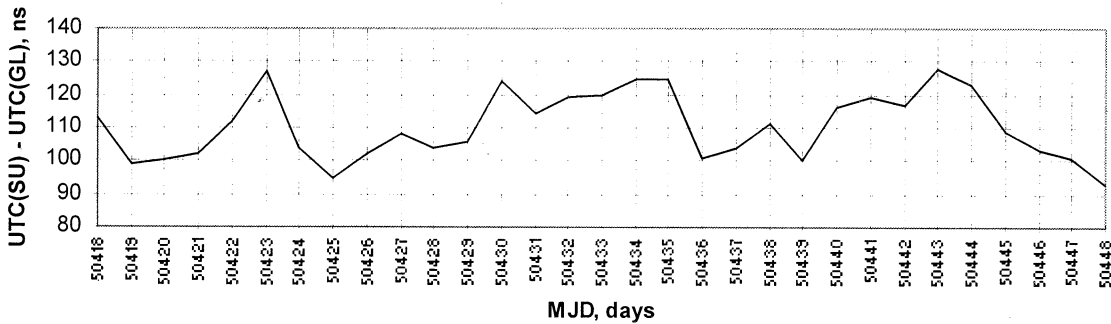


Fig.1 Difference UTC(SU) - GLONASS time

## WORK TOWARDS A CESIUM FOUNTAIN STANDARD AT PEKING UNIVESITY

Yiqiu WANG, Jidong HOU, Yimin Li, Junxian Fu, Xiaohui WANG, Xuzong CHEN, Donghai YANG

Department of Electronics, Peking University

Beijing 100871, P. R. China

A cesium atomic fountain frequency standard is being developed at Peking University, Beijing, China. A MOT with some  $10^8$  trapped atoms and an optical molasses with the cold atoms of the temperature of  $10\mu\text{K}$  have been achieved previously<sup>[1]</sup>. The atomic fountain device has been designed and is under construction.

The apparatus of our atomic fountain is composed of two parts: vacuum system and laser system. The schematic diagram of the vacuum chamber is shown in Fig.1. It has three basic parts: the collecting region (Magneto-optical trap, MOT, and optical molasses), interaction region and detection zone. Using the MOT, a few parts of  $10^7$  cesium atoms will be captured and cooled in several hundred milliseconds. Then, they are further cooled to several  $\mu\text{K}$  and launched up in the way of moving molasses. The atoms interact with microwave twice in a big C-field area when they go up and down through the two microwave cavities and will be detected by a probing laser beam in the detection zone. The function of the lower microwave cavity is to remove the unwanted atoms in the magnetic sub-levels other than the clock transition together with a laser pulse<sup>[2]</sup>. By this means we can reduce the rate of the spin-exchange collision in atomic fountain. The optics in the detection zone is carefully arranged in order to improve the fluorescence collection efficiency.

The laser system of our fountain is shown in Fig.2. The ML is a New Focus Vortex laser and is frequency-locked to the crossover of Cs  $6S_{1/2}$ ,  $F=4 \rightarrow 6P_{3/2}$ ,  $F'=4,5$ , which is 125MHz lower than the cycling transition  $F=4, F'=5$ . Before it injection-locks the first step slave laser SL1 (150mW), its frequency is blue-shifted 125MHz to the cycling transition by a double-path of

AOM1 (Modulation frequency: 62.5MHz). One of the output beams of SL1 serves as probing beams which may also injection-lock a second step slave laser SL5 (50mw) if it is necessary. After being frequency red-shifted around 200MHz, the other output of SL1 will be incident to the other two second-step slave laser (SL2, and SL3, 150mW). The fast frequency tuning in the period of forming molasses is carried out by AOM2. The output of SL2 is used as vertical beams while that of SL3 as horizontal beams. Three acoustic-optical modulators (AOM3-5) control the optical intensity of output laser and shift the laser frequency back to small red detuning to the cycling transition. AOM3 and AOM4 produce the frequency difference for moving molasses between up and down vertical beams in the phase of launching. A re-pumping laser (10mW) locked to the transition  $6S_{1/2}$ ,  $F=3 \rightarrow 6P_{3/2}$ ,  $F'=4$  is coincident with the one of output beams of SL3 and picks up the leaked atoms out of cooling transition. We use the single-mode polarization-preserving fibers to guide the laser beams into the chamber. The fibers also serve as spatial filter to maintain good beam quality.

We have changed the original retro-reflected beam arrangement for the MOT and molasses<sup>[3]</sup> and divided every of two horizontal beams into two, so the intensity symmetry of two opposite beams is much better than before. In the experiments we try to implement the idea of an asymmetric molasses. An asymmetric molasses means the atomic cloud has different equivalent temperature in different directions. Probably it can be realized by choosing suitable beams intensity, detuning and time sequence. However, the possibility and efficiency of asymmetric

molasses in lowering the spin-exchange frequency shift should be proved in our future experiment.

This work is supported by the national Natural Science Foundation of China

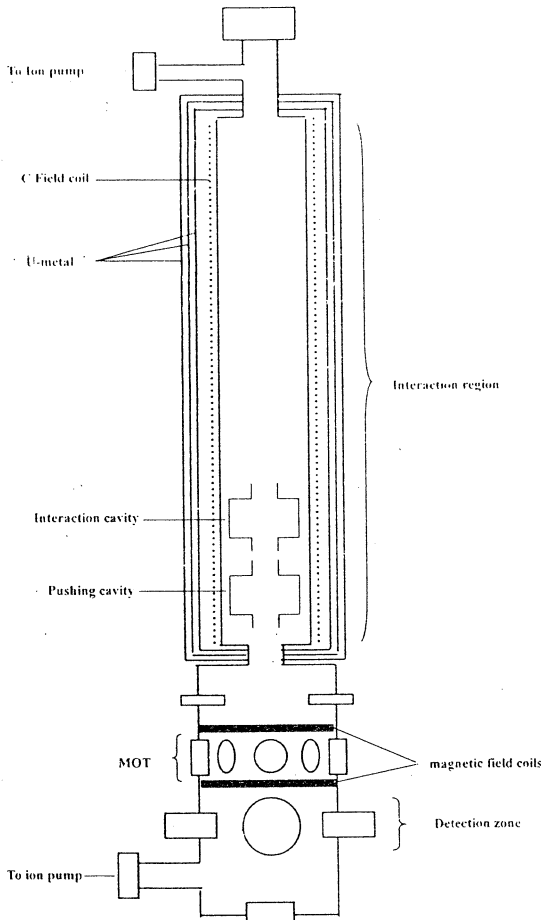


Fig 1 The apparatus of atomic fountain

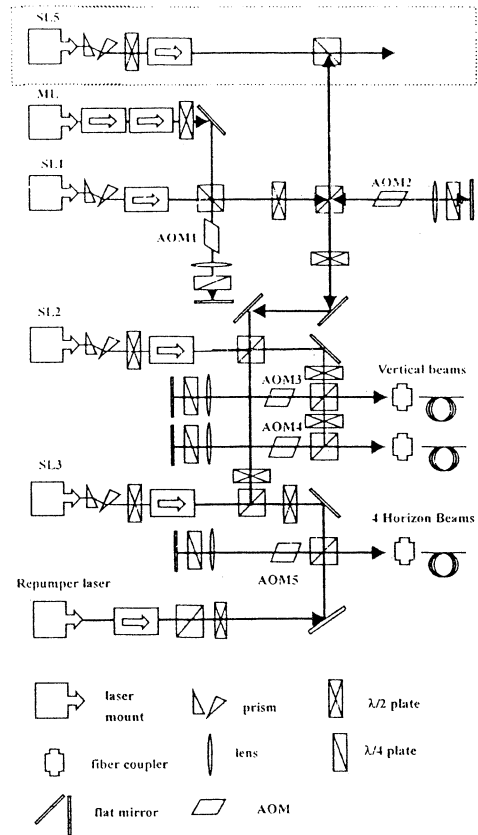


Fig 2 The laser system of atomic fountain

Reference:

[1] Hou Jidong, Li Yimin, Yang Donghai, Wang Yiqiu, 1998, "preliminary result on the first optical molasses of Cs atoms in China" Chinese Physics Letters, 6 (to be published)

[2] D. Drullinger, private communication

[3] Gan Jianhua, Li Yimin, Chen Xuzong, and Wang Yiqiu *et al*, 1996, "magneto-optical trap of cesium atoms", Chinese Physics Letter, 13, 821-824.

## Meeting report

<b>Event</b>	<b>12th European Frequency and Time Forum</b>
Date	10÷12 March 1998
Location	Warsaw - POLAND
Participants	214
Countries	25
<b>Papers</b>	<b>108</b>
- Invited	3
- Oral papers	58
- Posters	50
<b>Countries</b>	<b>25</b>
<b>Sessions</b>	<b>18</b>
<b>Exhibitors</b>	<b>11</b>

### 1. PROGRAMME

Two interesting papers were presented at the opening session. The first one was about the radio astronomy, and it reviewed the main results in the field of applied research. Areas of common interest for radio astronomers and electronics engineers, and the dependence on the frequency and time standards, were described. The second paper was a review of past and present of piezoelectricity in Poland.

The following number of oral sessions devoted to the following subjects were organized: 2 - for atomic standards, 2 - for oscillators, 2 - for time transfer and comparison, 2 - for resonators, 2 - for SAWs, 2 - for instrumentation and measurement, and 1 - for telecommunications and space applications. There were also 2 poster sessions devoted to piezoelectricity, measurement techniques, T/F techniques and atomic standards.

### 2. EXHIBITION

Between 11 exhibitors we had: 3 - from the USA, 1 - from France, 2 - from UK, 1 - from China, and 4 - from Poland.

### 3. FORUM 1999

According to the "Agreement for joint meetings between the European Frequency and Time Forum (EFTF) and the IEEE International Frequency Control Symposium (FCS)", the first of these will take place in Besançon, France in April 1999. The Chairmanship for the conference will be joint. Donald Sullivan of NIST and Raymond Besson of ENSMM will be the Co-chairmen of the meeting. The Program Committee for the joint conference will be the combination of the Scientific Committee (SC) for the EFTF and Technical Committee (TPC) for the FCS. Exhibit space will be open to US and European exhibitors. The exhibit fee will be approximately \$1600 and will include four registrations.

*Waldemar Soluch*  
1998 Scientific Committee Chairman

12th EFTF - 10÷12 March 1998 - Warsaw - POLAND

Participants by country	No of participants
AUSTRIA	3
CANADA	1
CHINA	4
CZECH REPUBLIC	4
FINLAND	6
FRANCE	42
GERMANY	13
IRELAND	1
ISRAEL	2
ITALY	14
JAPAN	8
MEXICO	1
POLAND	59
PORTUGAL	1
ROMANIA	2
RUSSIA	4
SPAIN	1
SWEDEN	1
SWITZERLAND	10
TAIWAN	1
THE NETHERLANDS	3
UKRAINE	2
UNITED KINGDOM	8
USA	22
YUGOSLAVIA	1
<b>Total: 25 countries</b>	<b>214 participants</b>

Contributed papers	No of papers
<b>Sessions</b>	
1. Opening session	2
2. Resonators I	4
3. Optically pumped & cold atom Cs standards	4
4. Materials	4
5. Time transfer & comparisons I	3
6. Resonators II (Whispering Gallery Modes)	4
7. Classical Cs standards & H masers	4
8. Oscillators I	4
9. Time transfer & comparisons II	3
10. SAW I	3
11. Instrumentation & Measurement I	4
12. Oscillators II	4
13. Telecom & space applications	4
14. Instrumentation & measurement II	4
15. Laser instrumentation & optical standards	4
16. SAW II	3
17. Piezoelectricity & measurement techniques (poster session)	28
18. T/F techniques & atomic standards (poster session)	22
<b>Total:</b>	<b>108 papers</b>
<b>16 oral sessions</b>	
<b>2 posters sessions</b>	

## List of the participants

NAME	AFFILIATION	ADDRESS	COUNTRY
<b>Abgarowicz Ewa</b>	Institute of Electronic Materials Technology	Wolczynska 133 01-919 Warszawa	POLAND
<b>Adamowicz Waldemar</b>	Centrum Badawczo-Rozwojowe TP S.A.	Obrzezna 7 02-691 Warszawa	POLAND
<b>Alwafi Ali</b>	Warsaw Univerity of Technology	Nowowiejska 15/19 00-665 Warszawa	POLAND
<b>Ansel Yannick</b>	DMT, Institute of Microsystem	EPFL -Ecublens, Room INR 118 CH-1015 Lausanne	SWITZERLAND
<b>Audoin Claude</b>	C.N.R.S. Laboratoire de l'Horloge Atomique	Bâtiment 221 - Université Paris-Sud 91405 Orsay Cedex	FRANCE
<b>Badura Heinz</b>	Datum, INC.	3 Parker 92618 Irvine, CA	USA
<b>Barillet Roland</b>	C.N.R.S. Laboratoire de l'Horloge Atomique	Bâtiment 221 91405 Orsay Cedex	FRANCE
<b>Baszun Mikolaj</b>	Warsaw Univerity of Technology	Nowowiejska 15/19 00-665 Warszawa	POLAND
<b>Baumont Françoise</b>	Observatoire de la Côte d'Azur	Av. Nicolas Copernic 06130 Grasse	FRANCE
<b>Bausk Evgeniy</b>	Russian Academy of Sciences	Acad. Lavrentyev Ave., 13 630090 Novosibirsk	RUSSIA
<b>Bava Elio</b>	Politecnico di Milano, Dip. di Elettron. e Inform.	Piazza Leonardo da Vinci, 32 20133 Milano	ITALY
<b>Bedrich Stefan</b>	GeoForschungsZentrum Potsdam	c/o DLR, P.O. Box 1116 82230 Oberpfafenhofen	GERMANY
<b>Berger Hans</b>	EFG International	Dueppelstraße 13 14163 Berlin	GERMANY
<b>Beser Jacques</b>	3S Navigation	4, Executive Circle, Suite 200 92614 Irvine, CA	USA
<b>Besson Raymond J.</b>	LCEP - ENSMM	26, Chemin de l'Epitaphe F-25030 Besançon	FRANCE
<b>Beverini Nicolo</b>	Universita di Pisa, Dip. di Fisica	Piazza Torricelli, 2 I-56126 Pisa	ITALY
<b>Bigler Emmanuel</b>	LPMO - CNRS	32 Av. de l'Observatoire 25044 Besançon	FRANCE

<b>NAME</b>	<b>AFFILIATION</b>	<b>ADDRESS</b>	<b>COUNTRY</b>
<b>Bignon Olivier</b>	TEKELEC TEMEX S.A.	29, Av. de la Baltique 91953 Les Ulis	FRANCE
<b>Bloch Martin</b>	Frequency Electronics Inc.	55 Charles Lindberg Blvd., Mitchel Field, 11553 New York	USA
<b>Boroditsky Roman</b>	Valpey - Fisher Corp.	75 South Street 01748 Hopkinton, MA	USA
<b>Bourquin Roger</b>	LCEP-ENSMM	26, Chemin de l'Epitaphe F-25030 Besançon	FRANCE
<b>Boy Jean-Jacques</b>	LCEP-ENSMM	26, Chemin de l'Epitaphe F-25030 Besançon	FRANCE
<b>Brendel Remi</b>	LPMO-CNRS	32, Avenue de l'Observatoire F-25044 Besançon Cedex	FRANCE
<b>Brunet Michel</b>	CNES	18, av. Edouard Belin F-31401 Toulouse Cedex 4	FRANCE
<b>Burt Eric</b>	U.S. Naval Observatory	3450 Massachusetts Ave, NW 20392-5420 Washington, DC	USA
<b>Busca Giovanni</b>	Observatoire Cantonal	Rue de l'Observatoire 58 2000 Neuchâtel	SWITZERLAND
<b>Cailliez Bruno</b>	MORS	BP 22 F-13610 Le Puy Sainte Réparate	FRANCE
<b>Candelier Vincent</b>	CEPE	44, Avenue de la Glaciere, BP 165 95105 Argenteuil	FRANCE
<b>Cerez Pierre</b>	C.N.R.S. Laboratoire de l'Horloge Atomique	Bâtiment 221 - Université Paris-Sud 91405 Orsay Cedex	FRANCE
<b>Chambon Maguelonne</b>	Bureau National de Métrologie	22, Rue Monge 75005 Paris	FRANCE
<b>Chan Kwok Fai Kenneth</b>	Kolinker Industrial Equipments Ltd	84-92 Chai Wan Kok Str., Shield Industrial Centre, Hong Kong	CHINA
<b>Cichocki Jacek</b>	Warsaw University of Technology	Nowowiejska 15/19 00-665 Warszawa	POLAND
<b>Clairon Andre</b>	BNM / LPTF - Observatoire de Paris	61, ave de l'Observatoire 75014 Paris	FRANCE
<b>Cordara Franco</b>	Istituto Elettrotecnico Nazionale Galileo Ferraris	Strada delle Cacce 91 10135 Torino	ITALY
<b>Costanzo Giovanni Antonio</b>	Politecnico di Torino, Dipart. di Elettronica	Corso Duca degli Abruzzi 24 10129 Torino	ITALY
<b>Couteleau Laurent</b>	LPMO-CNRS	32, Avenue de l'Observatoire 25044 Besançon Cedex	FRANCE

NAME	AFFILIATION	ADDRESS	COUNTRY
Czarnecki Andrzej	Tele & Radio Research Institute	Ratuszowa 11 03-450 Warszawa	POLAND
Davis John Anthony	National Physical Laboratory	Queens Road TW11 0LW Teddington, Middlessex	UNITED KINGDOM
Dabrowska Elzbieta	Institute of Electronic Materials Technology	Wolczynska 133 01-919 Warszawa	POLAND
de Clercq Emeric	BNM / LPTF - Observatoire de Paris	61, ave de l'Observatoire 75014 Paris	FRANCE
De Jong Gerrit	NMi Van Swinden Laboratory	P.O. Box 654 2600 AR Delft	THE NETHERLANDS
Dedic-Nesic Snezana	Institute "Mihajlo Pupin"	Volgina 15 11060 Beograd	YUGOSLAVIA
Dimarcq Noel	C.N.R.S. Laboratoire de l'Horloge Atomique	Bâtiment 220 - Université Paris-Sud F-91405 Orsay Cedex	FRANCE
Dobrogowski Andrzej	Poznan University of Technology	Piotrowo 3 A 60-965 Poznań	POLAND
Dong Taiqian	Peking University, Dept. of Electronics	100871 Beijing	P. R. China
Dorenwendt Klaus	Physikalisch-Technische Bundesanstalt	Bundesallee 100 D-38023 Braunschweig	GERMANY
Dos Santos Serge	LPMO-CNRS	32, Avenue de l'Observatoire 25044 Besançon Cedex	FRANCE
Drullinger Robert	NIST	325 Broadway 80303 Boulder, CO	USA
Dulmet Bernard	LCEP-ENSMM	26, Chemin de l'Épitaphe F-25030 Besançon	FRANCE
Dumas Joel	TEKELEC TEMEX S.A.	29, Av. de la Baltique 91953 Les Ulis	FRANCE
Ecabert Marcel	FSRM	Rue Jaquet-Droz 1 / CP20 CH-2007 Neuchâtel	SWITZERLAND
Ekstrom Christopher	U.S. Naval Observatory	3450 Massachusetts Ave, NW 20392-5420 Washington, DC	USA
Eskelinen Pekka	Lappeenranta University of Technology	PL 20 53851 Lappeenranta	FINLAND
Feltham Stephen	ESA - European Space Agency ESTEC	Keplerlaan 1 2200 AG Noordwijk	THE NETHERLANDS
Ferrand Dominique	Hewlett Packard ISSD France	1, Avenue du Canada, F 91947 Les Ulis Cedex	FRANCE

NAME	AFFILIATION	ADDRESS	COUNTRY
Finkelstein Uri	NEL Nofech Electronics Ltd.	17, Watson St. 34751 Haifa	ISRAEL
Fouilleul Bernard	Aura International SA	1, Place du Serpentaire, SILIC 122 94513 Rungis	FRANCE
Franquet Olivier	A.R. Electronique	Valparc - 14 rue de Franche Comté 25048 Besançon Cedex	FRANCE
Fukuda Kyoya	Communications Research Laboratory	4-2-1 Nukui-Kitamachi, Koganei-shi 184-8795 Tokyo	JAPAN
Gagne Marie-Claude	Institut des etalons nationaux se mesure	editice M-36, chemin de Montreal KIA OR6 Ottawa	CANADA
Gallop John	National Physical Laboratory	Queens Road TW11 0LW Teddington, Middlessex	UNITED KINGDOM
Galzerano Gianluca	Politecnico di Milano, Dip. di Elettron. e Inform.	Piazza Leonardo da Vinci, 32 20133 Milano	ITALY
Garbacz Pawel	Warsaw Univerity of Technology	Nowowiejska 15/19 00-665 Warszawa	POLAND
Garvey R. Micheal	DATUM / FTS	34 Tozer Rd. 01915 Beverly, MA	USA
Gawor Sylwester	Tele & Radio Research Institute	Ratuszowa 11 03-450 Warszawa	POLAND
Giordano Vincent	LPMO - CNRS	32 Av. de l'Observatoire 25044 Besançon	FRANCE
Girardet Emmanuel	A.R. Electronique	Valparc - 14 rue de Franche Comté 25048 Besançon Cedex	FRANCE
Gniewińska Barbara	Tele & Radio Research Institute	Ratuszowa 11 03-450 Warszawa	POLAND
Goehring Detlef	Tele Quarz GmbH	Landstrasse 74924 Neckarbischofsheim	GERMANY
Gonzales François	Centre National d'Etudes Spatiales	18, avenue Edouard Belin 31401 Toulouse	FRANCE
Green Clive Robert	Quartzlock Instruments (UK) Ltd	Gothic, Plymouth Road TQ9 5LH Totnes, Devon	UNITED KINGDOM
Gromek Józef	Tele & Radio Research Institute	Ratuszowa 11 03-450 Warszawa	POLAND
Gryglewski Daniel	Warsaw University of Technology	Nowowiejska 15/19 00-665 Warszawa	POLAND
Gufflet Nicolas	LCEP-ENSMM	26, Chemin de l'Epitaphe F-25030 Besançon	FRANCE

NAME	AFFILIATION	ADDRESS	COUNTRY
Hafner Erich	XOTEX	881 Sycamore Av. 07724 Tinton Falls NY	USA
Hahn Stefan	Warsaw University of Technology	Nowowiejska 15/19 00-665 Warszawa	POLAND
Hahn Joerg	DLR Oberpfaffenhofen, Inst. f. HF-Technik	P.O. Box 1116 D-82230 Wessling	GERMANY
Hamouda Frederic	C.N.R.S. Laboratoire de l'Horloge Atomique	Bâtiment 221 - Université Paris-Sud 91405 Orsay Cedex	FRANCE
Hao Ling	National Physical Laboratory	15 Mays Road TW11 0SQ Teddington	UNITED KINGDOM
Hauden Daniel	LPMO-CNRS	32, av. de l'Observatoire 25044 Besançon Cedex	FRANCE
Henry Briot Emmanuelle	LPMO - CNRS	32 Av. de l'Observatoire 25044 Besançon	FRANCE
Herman Gildas	TEKELEC TEMEX S.A.	29, Av. de la Baltique 91953 Les Ulis	FRANCE
Hilty Kurt	Swiss Federal Office of Metrology	Ostermundigenstr. 91-93 3000 Bern 29	SWITZERLAND
Hofman Wladyslaw	Instytut Technologii Materałów Elektronicznych	Wólczyńska 133 01-919 Warszawa	POLAND
Hübner Udo	Physikalisch-Technische Bundesanstalt, Lab. 4.32	Bundesallee 100 D-38116 Braunschweig	GERMANY
Huebner Gerhard	DATUM GmbH	Fichtenstr. 25 D-85649 Hofolding	GERMANY
Itoh Hideaki	Faculty of Engineering, Shinshu University	500 Wakasato 380 Nagano-Shi	JAPAN
Jaldehyag Kenneth	Swedish Nation. Testing & Research Institute	Box 857 501 15 Boras	SWEDEN
Jarkowski Jacek	Warsaw University of Technology	Nowowiejska 15/19 00-665 Warszawa	POLAND
Jefferts Steven	NIST, Time & Frequency Division	325 Broadway 80303 Boulder, CO	USA
Kajita Masatoshi	Communications Research Laboratory	4-2-1 Nukui-Kitamachi, Koganei-shi 184-8795 Tokyo	JAPAN
Kalinowska Barbara	Tele & Radio Research Institute	Ratuszowa 11 03-450 Warszawa	POLAND
Kalliomäki Kalevi	VIT Automation Measurement Technology	P.O. Box 1304, Otakaari 7 B FIN-02044 VTT Espoo	FINLAND

<b>NAME</b>	<b>AFFILIATION</b>	<b>ADDRESS</b>	<b>COUNTRY</b>
<b>Kasznia Michal</b>	Poznan University of Technology	Piotrowo 3 A 60-965 Poznal	POLAND
<b>Kersale Yann</b>	LPMO-CNRS	32, Avenue de l'Observatoire 25044 Besançon Cedex	FRANCE
<b>Kihara Masami</b>	NTT Optical Network Systems Laboratories	1-1 Hikari-no-oka 239-0847 Yokosuka	JAPAN
<b>Kirchner Dieter</b>	Technische Universität Graz	Inffeldgasse 12 8010 Graz	AUSTRIA
<b>Kitamura Kazunori</b>	CRIEPI	2-II-1, Iwado-kita 201-8511 Komae-shi, Tokyo	JAPAN
<b>Klepczynski William J.</b>	Innovative Solutions International	1608 Spring Hill Road, Suite 200 22182 Vienna, VA	USA
<b>Kohl Rudolf</b>	Domier Satellitensysteme GmbH	Postfach 80 11 69 D-81663 MCnchen	GERMANY
<b>Kojima Toshihiro</b>	Tamagawa University, Fac. of Engineering	6-1-1, Tamagawa-gakuen, Machida 184-8610 Tokyo	JAPAN
<b>Kolendo Wawrzyniec</b>	Centrum Radiokomunikacji i Telekomunikacji TP S.A.	Sw. Barbary 2 - Skr. poczt. P-13 00-686 Warszawa	POLAND
<b>Kolmas Maria</b>	OMIG S.A.	Stepinska 22/30 00-739 Warszawa	POLAND
<b>Koppang Paul</b>	DATUM Inc.; FTS - Sigma Tau Group	1711 Holt Road 35404 Tuscaloosa	USA
<b>Kopycki Cezary</b>	Military University of Technology	Kaliskiego 2 01-489 Warszawa	POLAND
<b>Kosinski John</b>	U.S. Army CECOM	1200 Remsen Mill Road 07753-7206 Wall TWP., NJ	USA
<b>Koziol Krystyna</b>	Centrum Radiokomunikacji i Telekomunikacji TP S.A.	Sw. Barbary 2 - Skr. poczt. P-13 00-686 Warszawa	POLAND
<b>Kretschmerova Lenka</b>	Technical University of Liberec	Háfkova 6 461 17 Liberec	CZECH REPUBLIC
<b>Kubik Lech</b>	ESO Sp. z o. o.	Stepinska 22/30 00-739 Warszawa	POLAND
<b>Kus Andrzej</b>	Centrum Astronomii UMK	Nalkowskiej 12 87-100 Toruń	POLAND
<b>Kushner Gene</b>	Frequency Electronics Inc.	55 Charles Lindberg Blvd., Mitchel Field 11553 New York	USA
<b>Lajoie Isabelle</b>	LPMO-CNRS	32, Avenue de l'Observatoire 25044 Besançon Cedex	FRANCE

NAME	AFFILIATION	ADDRESS	COUNTRY
Lea Stephen	National Physical Laboratory	Queens Road TW11 0LW Teddington, Middlessex	UNITED KINGDOM
Lee Arthur	Kolinker Industrial Equipments Ltd	84-92 Chai Wan Kok Str., Shield Industrial Centre, Hong Kong	CHINA
Leonardi Mauro	Politecnico di Torino. Dip. di Elettronica	Corso Duca Degli Abruzzi, 24 10129 Torino	ITALY
Lepek Alex	Newton Metrology Ltd.	PO Box 9769 91091 Jerusalem	ISRAEL
Levi Filippo	Istituto Elettrotecnico Nazionale Galileo Ferraris	Str. delle Cacce 91 10135 Torino	ITALY
Lewandowski Wlodzimierz	BIPM	Pavillon de Breteuil F-92310 Sevres Cedex	FRANCE
Lin Huang Tien	Chunghwa Telecom Co. Ltd.	No 12, Lane 551, Ming-Tsu Rd. Sec. 3, 326 Yang-Mei, Taoyuan	TAIWAN, R.O.C.
Lisowiec Aleksander	Tele & Radio Research Institute	Ratuszowa 11 03-450 Warszawa	POLAND
Lopez-Romero Mauricio	Centro National de Metrologia	Km. 4.5 Carretera a los Cues, Municipio el Marques. C.P. 76900 Queretaro	MEXICO
Luczynski Zygmunt	Institute of Electronic Materials Technology	Wolczynska 133 01-919 Warszawa	POLAND
Majewski Wladyslaw	Warsaw University of Technology	Nowowiejska 15/19 00-665 Warszawa	POLAND
Mannermaa Jari	Nokia Mobile Phones	P.O. Box 429 33101	FINLAND
Mansfeld George D.	Inst. of Radioengineering & Electronics,	Mokhovaya 11 103907 Moscow	RUSSIA
Mansten Tapio	VTT Automation Measurement Technology	P.O. Box 1304, Otakaari 7 B FIN-02044 VTT Espoo	FINLAND
Masiukiewicz Antoni	Tele & Radio Research Institute	Ratuszowa 11 03-450 Warszawa	POLAND
Mateescu Irina	National Institute of Materials Physic	P.O. Box MG-7 76900 Bucharest-Magurele	ROMANIA
Matsakis Demetrios	U.S. Naval Observatory	3450 Massachusetts ave., N.W. 20392-5420 Washington, D.C.	USA
Messina Filippo	Stazione Astronomica Cagliari	St. 54 loc. Poggio dei Pini 09012 Capoterra	ITALY
Michnowski Ryszard	Warsaw University of Technology	Nowowiejska 15/19 00-665 Warszawa	POLAND

<b>NAME</b>	<b>AFFILIATION</b>	<b>ADDRESS</b>	<b>COUNTRY</b>
<b>Milewski Andrzej</b>	Tele & Radio Research Institute	Ratuszowa 11 03-450 Warszawa	POLAND
<b>Mitrofanov Igor</b>	Avangard-Elionica	72, Kondratyevski av. 195271 Sankt Petersburg	RUSSIA
<b>Modelski Józef</b>	Warsaw University of Technology	Nowowiejska 15/19 00-665 Warszawa	POLAND
<b>Murphy Patrick</b>	National University of Ireland. CORK	Department of Electrical Engineering Cork	IRELAND
<b>Nafalski Lucjan</b>	Tele & Radio Research Institute	Ratuszowa 11 03-450 Warszawa	POLAND
<b>Nawrocki Jerzy</b>	Centrum Badan Kosmicznych PAN	Borowiec 62-035 Kórnik	POLAND
<b>Neubig Bernd W.</b>	Tele Quarz GmbH	Landstrasse 2 74924 Neckarbischofsheim	GERMANY
<b>Nichoga Vitalij</b>	Institute of Physics and Mechanics of N.A.S.	5, Naukova Street 290601 Lviv	UKRAINE
<b>Niculescu Anca Manuela</b>	National Institute of Metrology	Sos. Vitan-Bărzesti nr. 11 75669 Bucharest	ROMANIA
<b>Niemyjski Waclaw</b>	Przemysłowy Instytut Telekomunikacji	Poligonowa 30 04-051 Warszawa	POLAND
<b>Nosek Jaroslav</b>	Technical University of Liberec	Hávkova 6 461 17 Liberec	CZECH REPUBLIC
<b>Nowakowski Andrzej</b>	Tele & Radio Research Institute	Ratuszowa 11 03-450 Warszawa	POLAND
<b>Overney Frederic</b>	Swiss Federal Office of Metrology	Lindenweg 50 CH-3084 Wabern	SWITZERLAND
<b>Palacio Juan</b>	Real Observatorio de la Armada	11100 Cecilio Pujazon S/N	SPAIN
<b>Parker Thomas</b>	Nation Institute of Standards and Technology	325 Broadway 80303-3328 Boulder, CO	USA
<b>Perevalov Alexander</b>	Avangard-Elionica	72, Kondratyevski av. 195271 Sankt Petersburg	RUSSIA
<b>Petit Gerard</b>	BIPM	Pavillon de Breteuil F-92310 Sevres	FRANCE
<b>Pietropaoli Tomasso</b>	ISCTI - Ministero delle Comunicazioni	Viale America, 201 00144 Roma	ITALY
<b>Prost Leon</b>	Swiss Federal Office of Metrology	Lindenweg 50 3084 Wabern	SWITZERLAND

<b>NAME</b>	<b>AFFILIATION</b>	<b>ADDRESS</b>	<b>COUNTRY</b>
<b>Pyrhonen Olli</b>	Lappeenranta University of Technology	PL 20 53851 Lappeenranta	FINLAND
<b>Radecki Karol</b>	Instytut Radioelektroniki Polit. Warsz.	Nowowiejska 15-19 00-665 Warszawa	POLAND
<b>Rau Zofia</b>	Institute of Telecommunications	Szachowa 1 04-894 Warszawa	POLAND
<b>Reuning Karl</b>	DATUM / FTS	34 Tozer Rd. 01915-5510 Beverly, MA	USA
<b>Riley William J.</b>	EG & G Optoelectronics - Salem	35 Congress Street 01970 Salem, MA	USA
<b>Robichon Gilles</b>	bva Industrie	1, Bb Fleming, BP 1985 25020 Besançon	FRANCE
<b>Rochat Pascal</b>	TEKELEC TEMEX S.A.	59, Av. du Mail 2000 Neuchâtel	SWITZERLAND
<b>Roguski Wlodzimierz</b>	CERAD	Klobucka 23 00-976 Warszawa	POLAND
<b>Romisch Stefania</b>	Politecnico di Torino	Corso Duca d. Abruzzi 24 10129 Torino	ITALY
<b>Roth Hartmut</b>	DATUM GmbH	Fichtenstr. 25 D-85649 Hofolding	GERMANY
<b>Rozwadowski Mieczyslaw</b>	Tele & Radio Research Institute	Ratuszowa 11 03-450 Warszawa	POLAND
<b>Rubiola Enrico</b>	Politecnico di Torino	Corso Duca d. Abruzzi 24 10129 Torino	ITALY
<b>Sadowski Grzegorz</b>	Warsaw University of Technology	Nowowiejska 15/19 00-665 Warszawa	POLAND
<b>Saunders Steve</b>	RODITI International Corp. Ltd.	Carrington House, 130 Regent Street W1R 6BR London	UK
<b>Schäfer Wolfgang</b>	TimeTech GmbH	Nobelstr. 15 70569 Stuttgart	GERMANY
<b>Schildknecht Thomas</b>	Astronomical Institute, University of Bern	Sidlerstr. 5 CH-3012 Bern	SWITZERLAND
<b>Schlueter Bernard</b>	FSRM	Rue Jaquet-Droz 1 / CP20 CH-2007 Neuchâtel	SWITZERLAND
<b>Schuh Jean-Francois</b>	MORS	BP 22 F-13610 Le Puy Sainte Réparate	FRANCE
<b>Serizawa Yoshizumi</b>	CRIEPI	2-11-1 Iwado-kita, Komae-shi 201-8511 Tokyo	JAPAN

NAME	AFFILIATION	ADDRESS	COUNTRY
Shmaly Yuriy S.	Kharkiv Military Univ. & "Sichron" Center	4 Skripnika Street 310057 Kharkiv	UKRAINE
Siemicki Jerzy	Central Office of Measures	Elektoralna 2 00-950 Warszawa	POLAND
Sierajewski Marek	OMIG S.A.	Stepinska 22/30 00-739 Warszawa	POLAND
Silveiro Marques Fatima	Instituto Portugues da Qualidade	Rua C a Avenida dos Tres Vales 2825 Monte de Caparica	PORTUGAL
Slyusarev Sergey	National Research Laboratory of Metrology	1-1-4, Umezono, Tsukuba-shi 305 Ibaraki-ken	JAPAN
Smolarski Andrzej	Tele & Radio Research Institute	Ratuszowa 11 03-450 Warszawa	POLAND
Soluch Waldemar	Institute of Electronic Materials Technology	Wolczynska 133 01-919 Warszawa	POLAND
Šramar Jaroslav	KRYSTALY a.s.	Okruzni 1144 50003 Hradec Kralove	CZECH REPUBLIC
Stachnik Andrzej	Institute of Telecommunications	Szachowa 1 04-894 Warszawa	POLAND
Sthal Fabrice	LCEP-ENSMM	26, Chemin de l'Epitaphe F-25030 Besançon	FRANCE
Strus Janusz	Centrum Badawczo-Rozwojowe TP S.A.	Obrzezna 7 02-691 Warszawa	POLAND
Suchanek Josef	KRYSTALY a.s.	Okruzni 1144 50003 Hradec Kralove	CZECH REPUBLIC
Sullivan Donald	National Institute of Standards and Technology	325 Broadway 80304 Boulder, CO	USA
Svelto Cesare	Politecnico di Milano, Dip. di Elettron. e Inform.	Piazza Leonardo da Vinci, 32 20133 Milano	ITALY
Szulc Wieslaw	Tele & Radio Research Institute	Ratuszowa 11 03-450 Warszawa	POLAND
Szymanski Piotr	Institute of Electronic Materials Technology	Wolczynska 133 01-919 Warszawa	POLAND
Takazawa Koji	Toyocom Europe GmbH	Bollenhohe 5 40822 Mettmann	GERMANY
Tavella Patrizia	Istituto Elettrotecnico Nazionale Galileo Ferraris	Strada delle Cacce 91 10135 Torino	ITALY
Teodorczyk Marian	Institute of Electronic Materials Technology	Wolczynska 133 01-919 Warszawa	POLAND

NAME	AFFILIATION	ADDRESS	COUNTRY
<b>Thanner Herbert</b>	AVL List GmbH	Hans List Platz 1 A-8020 Graz	AUSTRIA
<b>Thomann Pierre</b>	Observatoire Cantonal	58, rue de l'Observatoire 2000 Neuchâtel	SWITZERLAND
<b>Tignanelli Gaetano</b>	ISCTI - Ministero delle Comunicazioni	Viale America, 201 00144 Roma	ITALY
<b>Trialoup Claude</b>	CEPE	44, Avenue de la Glaciere, BP 165 95105 Argenteuil	FRANCE
<b>Tupaj Mariusz</b>	Tele & Radio Research Institute	Ratuszowa 11 03-450 Warszawa	POLAND
<b>Turowski Adam</b>	Warsaw University of Technology	Nowowiejska 15/19 00-665 Warszawa	POLAND
<b>Underhill Michael J.</b>	University of Surrey	GU2 5XH Guildford, Surrey	UNITED KINGDOM
<b>Unverdross Rainer</b>	Unverdross Technik	Am Pfeifenberg 5 82237 Wörthsee	GERMANY
<b>Urbanski Robert</b>	Warsaw University of Technology	Nowowiejska 15/19 00-665 Warszawa	POLAND
<b>Vainikka Juha</b>	Lappeenranta University of Technology	PL 20 53851 Lappeenranta	FINLAND
<b>Vernotte Francois</b>	Observatoire de Besançon	41 bis avenue de l'Observatoire F-25010 Besançon	FRANCE
<b>Walnöfer Wolfgang</b>	AVL List GmbH	Kleiststrasse 48 A-8020 Graz	AUSTRIA
<b>Walter Hannes</b>	ESA - European Space Agency ESTEC	Keplerlaan 1 2200 AG Noordwijk	THE NETHERLANDS
<b>Wang Yiqiu</b>	Dept. of Electronics, Peking University	100871 Haidian	CHINA
<b>Watchueng Herve</b>	LCEP-ENSMM	3, rue de Champagne, App. 9 F-25000 Besançon	FRANCE
<b>Weaver Gregory</b>	Piezo Crystal Company	100 "K" Street, P.O. Box 619 17013 Carlisle, PA	USA
<b>Weidemann Werner</b>	Datum Efratom Division	3 Parker 92618-1696 Irvine, CA	USA
<b>Weiss Krzysztof</b>	Tele & Radio Research Institute	Ratuszowa 11 03-450 Warszawa	POLAND
<b>Wickard Timothy</b>	Piezo Crystal Company	100 "K" Street, P.O. Box 619 17013 Carlisle, PA	USA

<b>NAME</b>	<b>AFFILIATION</b>	<b>ADDRESS</b>	<b>COUNTRY</b>
<b>Wieclawski Andrzej</b>	ESO Sp. z o. o.	Stepinska 22/30 00-739 Warszawa	POLAND
<b>Wójcicki Marek</b>	Tele & Radio Research Institute	Ratuszowa 11 03-450 Warszawa	POLAND
<b>Wright David</b>	Radiocode Clocks Ltd.	Trevamo Manor TR13 0RU Helston, Cornwall	UNITED KINGDOM
<b>Wróbel Tadeusz</b>	Institute of Electronic Materials Technology	Wolczynska 133 01-919 Warszawa	POLAND
<b>Zaborowski Wacław</b>	Tele & Radio Research Institute	Ratuszowa 11 03-450 Warszawa	POLAND
<b>Zero Tadeusz</b>	Institute of Electronic Materials Technology	Wolczynska 133 01-919 Warszawa	POLAND
<b>Zuchowski Edmund</b>	Tele & Radio Research Institute	Ratuszowa 11 03-450 Warszawa	POLAND

## List of the exhibitors

COMPANY	ADDRESS	COUNTRY
<b>3S Navigation</b>	4, Executive Circle, Suite 200 92614 Irvine, CA	USA
<b>Frequency Electronics Inc.</b>	55, Charles Lindberg Blvd., Mitchel Field 11553 New York	USA
<b>Kolinker Industrial Equipments Ltd</b>	Unit H-I, 22/F., Shield Industrial Centre, 84-92 Chai Wan Kok Street, Tsuen Wan, New Territories Hong Kong	CHINA
<b>RODITI International Corp. Ltd.</b>	Carrington House, 130 Regent Street W1R 6BR London	UK
<b>TEKELEC TEMEX S.A.</b>	29, Av. de la Baltique 91953 Les Ulis	FRANCE
<b>DATUM, INC.</b>	34, Tozer Road 01915-5510 Beverly, MA	USA
<b>Institute of Electronic Materials Technology</b>	Wolczynska 133 01-919 Warszawa	POLAND
<b>Tele &amp; Radio Research Institute</b>	Ratuszowa 11 03-450 Warszawa	POLAND
<b>Omig S.A.</b>	Stepinska 22/30 00-739 Warszawa	POLAND
<b>ESO Sp. z o.o.</b>	Stepinska 22/30 00-739 Warszawa	POLAND
<b>Quartzlock Instruments (UK) Ltd</b>	Gothic, Plymouth Road TQ9 5LH Totnes, Devon	UK

## INDEX OF THE AUTHORS

<b>A</b>		<b>D</b>	
Alzetta E.	312	Daniau W.	319
Ansel Y.	414	Davis J.A.	94, 169
Audoin C.	43	Dabrowska E.	477
Azoubib J.	87, 499, 510	De Clereq E.	49
<b>B</b>		De Jong G.	79, 87, 175
Bahoura M.	54	De Marchi A.	531
Ballandras S.	193, 319	Dedic-Nesic S.	420
Barillet R.	43, 246, 553	Deyzac F.	29
Barychev V.	531	Di Monaco O.	108
Bauch A.	544	Di Piro L.	388
Bausk E.	189	Dimarcq N.	55, 543
Bava E.	301, 308	Dmitriev V.F.	463
Belivier H.	493	Dobershtein S.	472
Berger H.	339	Dobrogowski A.	253
Bernier L.G.	121	Dos Santos S.	352, 402
Bertinetto F.	301	Downie N.	292
Besson R.J.	161	Dudle G.	94
Beutler G.	94	Dulmet B.	326, 451
Beverini N.	312	Dutta-Roy R.	269
Bigler E.	193, 319	<b>E</b>	
Bird M.	269	Ekstrom C. R.	534
Bisi M.	301	Eskelinen P.	182
Bize S.	54	<b>F</b>	
Blair D.G.	115	Faggioni O.	312
Blewett M.	292	Figuroa-Estrada J.M.	557
Boy J.J.	29,66	Filipiak J.	434
Brendel R.	141	Forget S.	55
Brunet M.	345	Francesconi F.	312
Burt E. A.	534	Fu J.	574
Busca G.	121	Fukuda K.	487
<b>C</b>		Furlong J.M.	94, 169
Cailliez B.	493	<b>G</b>	
Candelier V.	345	Galliou S.	161
Carmisciano C.	312	Gallop J.C.	112, 425
Castellanos J.	544	Galzerano G.	301
Cerez P.	553	Garcia-Nava F.	557
Chassagne L.	43	Gawor S.	332, 469
Chauvin J.	345	Gelle C.	345
Chen X.	574	Ghezali S. Z.	54
Clairon F. A.	54	Ghita C.	368,438
Clarke J. D.	169	Ghosh I.S.	112
Cognet L.	54	Giordano V.	108, 286
Costanzo G. A.	531	Gniewinska B.	150, 379, 397
Couteleau L.	141	Godone A.	392

Goehring D.	374
Green C. R.	538
Griebsch D.	544
Gros Lambert J.	108, 286
Grouzdev A. V.	332
Gryglewski D.	408
Guillemot Ch.	55
Guillemot P.	141
Guillot E.	543
<b>H</b>	
Haffelder J.	374
Hamouda F.	43, 553
Hao L.	112, 425
Harnett J.G.	103, 115
Helsby N. C.	548
Henry Briot E.	193
Hetzel P.	94
Hisadome K.	258
Hofman W.	71
Hou J.	574
Hübner U.	544
<b>I</b>	
Ikegami T.	305
Itoh H.	430
Ivanov E.N.	103
<b>J</b>	
Jaldehyag K.	499
Jennings D.A.	557
Jessa M.	253
Jinlun H.	505
Jornod A.	121
<b>K</b>	
Kajita M.	487
Kalinowska B.	379, 397
Kalliomaki K.	132, 231, 484
Kaszniak M.	253
Kawai N.	457
Kersale Y.	108
Kihara M.	258
Kitamura K.	263
Klein N.	112, 425
Kohl R.	269
Kojima T.	457
Kopycki C.	434
Kort S. I.	332
Kosinski J. A.	19
Krempel P.W.	447

Kretschmer P.	72
Kretschmerova L.	72
Krupka J.	103
Kurotchka A.Ph.	234
Kus A.	3
<b>L</b>	
Lajoie I.	108
Laporta P.	308
Lardet-Vieudrin F.	352
Laurent Ph.	54
Lazarescu M.F.	438
Lebedev M.	570
Lemonde P.	54
Lennon J.J.	519
Leonardi M.	209
Lepek A.	205
Lerch P.	414
Levi F.	392
Lewandowski W.	79,87, 510
Li Y.	574
Liao C.-S.	560
Lin H.-T.	560
Lisowiec A.	280
Lopez-Romero J. M.	557
<b>M</b>	
Maccioni E.	312
Magoga D.	301
Maitre P.	29
Makdissi A.	49
Malyukhov V.A.	472
Manea A.S.	438
Mann A.G.	103
Mannermaa J.	231
Mansfeld G. D.	61
Mansten T.	132, 231, 484
Marianneau G.	141, 193, 319
Marienko A.V.	234
Marotel G.	345
Martin G.	193, 319
Martynov A.V.	472
Masiukiewicz A.	150, 379
Masui O.	263
Mateescu I.	368, 438
Matsushima T.	263
Medvedev M.	566
Michnowski R.	408
Miglietta P.	301

Milewski A.	332
Mitrofanov I.S.	332, 463
Morawski T.	408
Morikava T.	487
Mourey M.	155, 161
Murphy P.J.	519
Myoujin M.	263
<b>N</b>	
Nagłowski P.	477
Nakazawa M.	430
Nawrocki J.	510
Niculescu A.	516
Niemyski W.	469
Nomura M.	430
Nosek J.	72, 443
<b>O</b>	
O'Riordan J.J.	519
O'Sullivan C.	519
Ostrowski J.	434
Overney F.	94
<b>P</b>	
Parker T.	126
Peicheng H.	505
Pereira dos Santos F.	54
Perevalov A. V.	332
Perone E.	388
Petit P.	29, 55, 543
Petit R.	345
Planat M.	352, 402
Pop G.	368, 438
Prost L.	94
Pyrhönen O.	182
<b>R</b>	
Radcliffe W.J.	112
Radecki K.	134
Ratheesh R.	115
Ratier N.	141
Rautiainen A.	132
Reiter C.	447
Renaud P.	414
Robichon G.	358
Rubiola E.	286
<b>S</b>	
Sagin M. R.	548
Santerelli G.	54
Santos M.	54
Schildknecht Th.	94

Schröder R.	544
Schuh J.F.	493
Schweda H.	121
Sebastian M. T.	115
Serizawa Y.	263
Shienok N.	566
Shmaliy Y.S.	234, 362, 384
Shuqin L.	483
Siccardi M.	531
Siemicki J.	525
Simon E.	54
Slyusarev S.	305
Smaali M.	66
Smirnov Y.	566
Smith G. H.	548
Smolarski A.	379
Sokolynsky E.G.	234
Solal M.	193
Solarz L.	434
Solie L.	189
Soluch W.	198
Sortais Y.	54
Stavrou S.	292
Sthal F.	155
Svelto C.	308
Szulc W.	34, 379, 451
Szymaniec K.	54
<b>T</b>	
Taccheo S.	308
Taiqian D.	483
Takada R.	263
Tamm C.	544
Tavella P.	209, 388
Thanner H.	447
Thomas C.	499
Tobar M.E.	103, 115
Tupaj M.	451
Twomey P.W.	519
<b>U</b>	
Underhill M. J.	215, 292
<b>V</b>	
Vainikka J.	275
Valentin C.	55, 543
Vasilenko A.	384
Vernotte F.	222
Vincent M.	222

<b>W</b>	
Wagner K.	269
Wallnöfer W.	447
Wang X.	574
Wang Y.	574
Watchueng H.	326
Weaver G. L.	39
Weidemann W.	240
Weiss K.	34, 368, 379, 451
Weyers S.	544
Wickard T. E.	39
Wojtasiak W.	408
Wójcicki M.	9, 280
Wright D. F.	548
<b>Y</b>	
Yang D.	574
<b>Z</b>	
Zecchini P.	66
Zuchowski E.	451